©Copyright 2019

Harinder S. Oberoi

A Study of Machining Effects on the Surface Integrity, Strength Properties, Damage Evolution and Fatigue Strength of Composite Laminates

Harinder Singh Oberoi

A Dissertation submitted in partial fulfillment
of the requirements for the degree of

Doctor of Philosophy

University of Washington

2019

Reading Committee:

Ramulu Mamidala, Chair

John Kramlich

Santosh Devasia

Program Authorized to Offer Degree:
Mechanical Engineering

University of Washington

Abstract

A Study of Machining Effects on the Surface Integrity, Strength Properties, Damage Evolution and Fatigue Strength of Composite Laminates

Harinder Singh Oberoi

Chair of the Supervisory Committee:
Dr. Ramulu Mamidala
Department of Mechanical Engineering

With the increased usage of Carbon Fibre Reinforced Plastics (CFRP) Composite Laminate Materials in various industries, an understanding of changes in strength properties and fatigue performance due to manufacturing processes is becoming critical to the study of their performance characteristics. As cured laminates almost always require machining of edges and/or drilling of holes, the resultant surface integrity by such post-cure processes influences the residual strength and fatigue performance during the service life. Unfortunately post-cure manufacturing processes also result in surface and sub-surface damage which evolves during service life conditions and result in the deterioration of strength and fatigue performance. The surface conditions of any machined surface are classified as surface texture and usually represent the exterior microscale geometry of the machined surface. Surface Integrity commonly refers to the features that are sub-surface or immediately beneath the surface. In general the surface integrity consists of the structure and the stress conditions within the interior layers and subsequently dictates the surface mechanical properties. This body of work studies the influence of resultant surface integrity from trimming and drilling of composite laminates on their strength properties, damage evolution and fatigue strength.

A two phased approach was utilized in this research study. In phase 1, a 10 ply thick balanced symmetric $[0/-45/90/45/0]_s$ composite laminate of unidirectional Carbon fibre prepreg tape with an Epoxy resin was used in the study. For Phase 2, a 22 ply thick balanced symmetric $[90/-45/0/-45/90/45/0/-45/0/90/0]_s$ composite laminate of unidirectional Carbon fibre prepreg tape with an Epoxy resin was used. Machining processes used in this study included Abrasive Water Jet (AWJ) and Carbide Router Endmilling for the trimming of the laminate material. For drilling of holes in the laminate material, Polycrystalline Diamond (PCD) drills and Chemical Vapour Deposition (CVD) diamond coated carbide drills were used. Test material was machined with these processes and resultant surface integrity was recorded using a Surface Profilometer, Edge Replication using acetate tape and Scanning Electron Microscopy (SEM). Test samples were generated with varying surface integrity along differing machining processes and standard ASTM Tests conducted to study the residual strength properties. Testing was conducted on edge trimmed specimens included Monotonic Strength (Tension & Compression) as well as Cyclic Strength (Tension-Tension Fatigue). For Drilled Hole Specimens testing included Open-Hole Monotonic Strength (Tension & Compression) and Cyclic Strength (Tension-Tension Fatigue). Similar tests were conducted for Pinned-Hole strength testing for static conditions.

During Tension-Tension Fatigue Testing a percentage change in stiffness was used to determine resultant fatigue life and it correlation to surface integrity. During the fatigue testing process, damage evolution was studied using Optical Microscopy, Photography and Scanning Electron Microscopy.

The analytical modeling of Fatigue Damage composite laminates was based on damage progression. A damage model based on a change in compliance (stiffness) was used as the analytical model in this study based on the utilization of change in stiffness and resultant fatigue life to record the damage progression during the Tension-Tension Fatigue Testing.

Table of Contents

Table of Figures vii
List of Tables xxvii
Chapter 1 - Introduction 1
1.1 Overview 1
Chapter 2 – Background and Literature Review 4
2.1 Introduction 4
2.2 Machining of Composite Laminates 5
2.2.1 Edge Trimming with Cutters 6
2.2.2 Edge Trimming with Abrasive Water Jet 11
2.3 Drilling of Composite Laminates 15
2.3.1 Drill Type & Geometry, Process Parameters Effect 15
2.4 Surface Integrity of Composite Laminates 19
2.5 Defects and Damage Occurrence in Composite Laminates 23
2.5.1 Effects of Damage Due to Edge Trimming and Drilling 25
2.5.2 Surface Texture and Surface Integrity Effects on Strength Properties 30
2.6 Fatigue in Composite Laminates 39
2.6.1 Types of Damage and Fatigue Effects 40
2.6.2 Bolted Joints and Fatigue 51
2.6.3 Fatigue Damage Modeling 52
2.7 Summary 76
Chapter 3 – Motivation of Research, Goals and Objectives 78
3.1 Research Scope 78
3.2 Goals and Objectives 81
Chapter 4 – Experimental and Theoretical Methodology 83
4.1 Overview 83
4.2 Phase I Research Plan – 10 Ply Thick Laminate – Mechanical Properties Testing 83
4.3 Phase II Research Plan - 22 Ply Thick Laminate – Mechanical Properties Testing 83

4.4 Research Plan for 22 Ply Thick Laminate – Tension-Tension Fatigue Cycle Testing....84
4.5 Theoretical Strength Calculations....84
4.6 Experimental Plan....92
4.6.1 Specimen Readiness....92
4.6.2 Edge Trimming with Cutters....93
4.6.3 Edge Trimming with Abrasive Water Jet....95
4.6.4 Hole Drilling....96
4.6.5 Surface Integrity Documentation....98
4.6.5.a Surface Profilometry....98
4.6.5.b Surface Microscopy....98
4.6.5.c Mechanical Strength Testing....99
4.7 Summary....100
Chapter 5 – Experimental Testing of Static Mechanical Properties of 10 Ply Thick Laminate....101
5.1 Screening Experiments....101
5.2 Surface Integrity Observations....101
5.2.1 Machined Surfaces – Endmill Trimming Vs. AWJ....101
5.2.2 Drilled Holes – CVD Diamond Coated Vs. Polycrystalline (PCD) Drills....107
5.3 Mechanical Testing....111
5.3.1 Theoretical Strength Calculations....111
5.3.2 Specimen Readiness....112
5.3.2.1 Tensile Strength Specimens....112
5.3.2.2 Compression Strength Specimens....113
5.3.2.3 Open Hole Tensile Strength Specimens....114
5.3.3 Test Matrix....114
5.3.4 Tensile Strength Testing....115
5.3.5 Compressive Strength Testing....118
5.3.6 Open Hole Tensile Testing....119
5.4 Discussion and Summary....121

Chapter 6 – Experimental Testing of Static Mechanical Properties of 22 Ply Thick Laminate....126
6.1 Screening Experiments....126
6.2 Material Specification and Specimen Preparation....126
6.3 Surface Integrity Observations....128
6.3.1 Machined Surfaces – Endmill Trimming Vs. AWJ....128
6.3.2 Drilled Holes – CVD Diamond Coated Vs. Polycrystalling (PCD) Diamond Drills....138
6.4 Mechanical Testing....145
6.4.1 Theoretical Strength Calculations....145
6.4.2 Specimen Preparation....145
6.4.2.1 Tensile Strength Specimens....145
6.4.2.2 Compression Strength Specimens....145
6.4.2.3 Open Hole Tensile Strength Specimens....145
6.4.2.4 Open Hole Compression Strength Specimens....146
6.4.2.5 Bearing Strength Specimens....146
6.4.3 Tensile Strength Testing....146
6.4.3.1 Analysis of Tension Testing Results....170
6.4.4 Compression Strength Testing....171
6.4.4.1 Analysis of Compression Testing Results....181
6.4.5 Open Hole Tension Testing....182
6.4.5.1 Analysis of Open Hole Tension Testing Results....207
6.4.6 Open Hole Compression Testing....208
6.4.6.1 Analysis of Open Hole Compression Testing Results....234
6.4.7 Bearing Strength Testing....235
6.5 Discussion and Summary....238
Chapter 7 - Phase II – Experimental Testing – Fatigue Cycle Tension -Tension Testing – 22 Ply Thick Laminate....242
7.1 Phase II Test Materials....242
7.2 Phase II Research Plan – 22 Ply Thick Laminate....242
7.3 Fatigue Cycles Testing Readiness....243

7.3.1 Test Specimens Readiness 244
7.3.2 Test Equipment.....246
7.3.3 Machined Surfaces – Endmill Trimming vs. AWJ.....248
7.3.4 Drilled Holes – Surface Finish.....248
7.3.4 Observations from Surface Finish data and SEMs of Trimmed Edges 254
7.3.5 Drilled Holes – Surface Finish Data 254
7.3.6 Drilled Holes – SEMs 254
7.3.7 Observations from Surface Finish data and SEMs of CVD Drilled holes 256
7.3.8 Fatigue Test Loads and their derivations.....256
7.3.9 Types of Data Collected.....259
7.4 Fatigue Cycles Testing Data Review.....260
7.4.1 Unnotched Test Specimens Data Review.....260
7.4.1.1 High Load Test Specimen Data Review.....260
7.4.1.2 Medium Load Test Specimen Data Review 287
7.4.1.3 Low Load Test Specimen Data Review 317
7.4.2 Notched Test Specimens Data Review.....343
7.4.2.1 High Load Test Specimen Data Review.....343
7.4.2.2 Medium Load Test Specimen Data Review 367
7.4.2.3 Low Load Test Specimen Data Review 394
7.5 Summary 421
Chapter 8 - Phase II Testing - Damage Progression & Fatigue Life Modeling 424
8.1 Phase II Fatigue Cycling.....424
8.2 Phase II Fatigue Testing – Applied Stress Vs. (N) Cycles Data Plots 424
8.3 Phase II Fatigue Testing –Damage Progression 426
8.3.1 Damage Progression in Unnotched Specimens Testing 426
8.3.2 Damage Progression Model in Unnotched Specimens Testing.....429
8.4 Analytical Model for Damage Progression in Unnotched Fatigue Testing Specimens 434
8.4.1 Unnotched High Loading Damage Vs. Fatigue Curves from Testing Vs. Analytical Modeling Curves 434

8.4.1.1 Unnotched AWJ Trimmed Specimens – Empirical Curves Vs. Analytical Modeled Curves for High Loading 435

8.4.1.2 Unnotched CVD Endmill Trimmed Specimens – Empirical Curves Vs. Analytical Modeled Curves for High Loading.....437

8.4.2 Unnotched Medium Loading Damage Vs. Fatigue Curves from Testing Vs. Analytical Modeling Curves 438

8.4.2.1 Unnotched AWJ Trimmed Specimens – Empirical Curves Vs. Analytical Modeled Curves for Medium Loading.....439

8.4.2.2 Unnotched CVD Endmill Trimmed Specimens – Empirical Curves Vs. Analytical Modeled Curves for Medium Loading 440

8.4.3 Unnotched Low Loading Damage Vs. Fatigue Curves from Testing Vs. Analytical Modeling Curves 442

8.4.3.1 Unnotched AWJ Trimmed Specimens – Empirical Curves Vs. Analytical Modeled Curves for Low Loading.....442

8.4.3.2 Unnotched CVD Endmill Trimmed Specimens – Empirical Curves Vs. Analytical Modeled Curves for Low Loading 444

8.5 Analytical Model for Damage Progression in Notched Fatigue Testing Specimens 445

8.5.1 Notched High Loading Damage Vs. Fatigue Curves from Testing Vs. Analytical Modeling Curves 447

8.5.1.1 Notched AWJ Trimmed Specimens – Empirical Curves Vs. Analytical Modeled Curves for High Loading 447

8.5.1.2 Notched CVD Endmill Trimmed Specimens – Empirical Curves Vs. Analytical Modeled Curves for High Loading 448

8.5.2 Notched Medium Loading Damage Vs. Fatigue Curves from Testing Vs. Analytical Modeling Curves 451

8.5.2.1 Notched AWJ Trimmed Specimens – Empirical Curves Vs. Analytical Modeled Curves for Medium Loading.....451

8.5.2.2 Notched CVD Endmill Trimmed Specimens – Empirical Curves Vs. Analytical Modeled Curves for Medium Loading.....453

8.5.3 Notched Low Loading Damage Vs. Fatigue Curves from Testing Vs. Analytical Modeling Curves 455

8.5.3.1 Notched AWJ Trimmed Specimens – Empirical Curves Vs. Analytical Modeled Curves for Low Loading.....456

8.5.3.2 Notched CVD Endmill Trimmed Specimens – Empirical Curves Vs. Analytical Modeled Curves for Low Loading....458
8.6 Discussion and Summary....459
Chapter 9 Conclusions and Recommendations....466
9.1 Conclusions....466
9.2 Future Research Recommendations....473
Chapter 10 - BIBLIOGRAPHY....474
Appendix A....480
A1.1 Surface Profiles of Static Tension Testing Specimens....480
Appendix B....565
B1.1 Surface Profiles of Fatigue Testing Specimens as recorded by profilometer....565
Appendix C....589
C 1.1 Photographs of Damage Progression in Fatigue Testing of Unnotched Specimens....589
C2.2 Photographs of Damage Progression in Fatigue Testing of Notched Specimens....695

Table of Figures

Figure 1.1 Performance Map of Structural Composites (Source: Daniel et. al [1]) 2
Figure 2.1 Typical Fibre-Reinforced Laminate Construction....5
Figure 2.2 Chip Formation of 0° and 90° Fibre Orientation (Source: Koplev [6]) 8
Figure 2.3 Cutting Mechanism of CFRP (Source; Bhatnagar [8]) 9
Figure 2.4 Chip Formation in Orthogonal Trimming of Unidirectional Graphite/Epoxy Laminate, (Source: Wang, Ramulu & Arola [11]) 10
Figure 2.5 WJ/AWJ Cutting of CFRP Composite Laminate (Source: Ramulu & Arola [15]) 12
Figure 2.6 Schematic View of AWJ Cutting Head....12
Figure 2.7 Schematic View of AWJ Machined Kerf (Source: Class lectures, ME, IIT Kharagpur, [16]) 13
Figure 2.8 Photographic View of AWJ Machined Kerf (cross-section) (Source: Class lectures, ME, IIT Kharagpur, [16]) 13
Figure 2.9 Photographic View of AWJ Machined Kerf (longitudinal) (Source: Class lectures, ME, IIT Kharagpur, [16]) 14
Figure 2.10 Image of Conventional Twist Drill & Stepped Diameter Drill (Source: Shyha et. al [19]) 16
Figure 2.11 Pictorial Representation of Observed Damage as a Function of Drilling Conditions (Source: Capello & Tagliaferri [21]) 17
Figure 2.12 Twist Drill Action on the specimen and Peel Up Delamination (Source: Capello & Tagliaferri, [21]) 17
Figure 2.13 Effective Feed Rate and Push Down Delamination (Source: Capello & Tagliaferri, [21]) 18
Figure 2.14 Surface Integrity Classification of Homogeneous Materials (Source: Metcut Research Associates [23]) 19
Figure 2.15 Sample Holes, Damage & Drilling Conditions (source: Capello & Tagliaferri [21]) 26
Figure 2.16 Internal Hole Damage Forms (source: Shayla et. al. [19]) 27
Figure 2.17 Damage Mechanisms Type Occurrence Based on Cutting Direction & Fibre Orientation (source: Ramulu [31]) 27
Figure 2.18 Mechanism of Delamination (source: Shanmugam et. al [34]) 28
Figure 2.19 Schematic View of Effective Maximum Diameter (source: Rao et. al [36]) 29
Figure 2.20 Illustration of Mechanism of Outer 45/90/-45 Plies Separating from 0° Plies, (source: Wisnom & Hallett, [37]) 30
Figure 2.21 Surface Finish vs. Feed Rate, AWJ Trimming of a Graphite/Epoxy Laminate, (source: Ramulu & Colligan, [39]) 31
Figure 2.22 Ultimate Compression Strength vs. Delamination and Surface Finish, AWJ Trimming of a Graphite/Epoxy Laminate (source: Ramulu & Colligan, [39]) 32
Figure 2.23 Effect of Tool Wear on Free Edge Delamination of a Carbon/Epoxy Iosipescu Specimen (source: Ghidossi et. al [40]) 32
Figure 2.24 Microscopic Observations from a 15° Fibre Orientation showing Craters (source: Ghidossi et. al [41]) .33
Figure 2.25 Microscopic Observations from a 45° Fibre Orientation showing Subsurface Cracking (source: Ghidossi et. al [41]) 34
Figure 2.26 Ultimate Stress versus ‘‘Percentage of Damaged Surface’’ Criterion, 15° fibre Configuration (source: Ghidossi et. al [41]) 35
Figure 2.27 Ultimate Stress versus ‘‘Depth of Subsurface Cracking’’ Criterion, +45° and -45° Fibre Configurations (source: Ghidossi et. al [41]) 35
Figure 2.28 Size of Damage vs. Speed/Feed Ratio (source: Tagliaferri et.al [43]) 36
Figure 2.29 Bearing Strength vs. Size of Damage (source: Tagliaferri et.al [43]) 37
Figure 2.30 Form of the trimmed surface after machining with burr tool (a) Image topography 3D (b) SEM observation (source: Haddad et al [46]) 38
Figure 2.31 Quasi static strength responses vs. surface roughness of different samples obtained by AWJ machining, burr tool machining and Abrasive Diamond saw cutting (source: Haddad et al [46]) 39
Figure 2.32 Influence of the rectification process of specimens trimmed by ADS process on the mechanical behaviour in compression testing (source: Haddad et al [46]) 39
Figure 2.33 Details of Fibre Fracture in an Edge Replica (source: Jamison et. al [49]) 41
Figure 2.34 Typical Damage Modes for a Composite Laminate (source: Harris [47]) 42

Figure 2.35 X-ray CT micrographs showing the damage magnitude and locations at 60% ultimate loading and a stiffness loss of 15% (source: Pearson & Hallet [52]) 43
Figure 2.36 SEMs showing damage in carbon fabric/epoxy plates with (a) AWJ drilling (b) Conventional Twist Drill (source: Montesano et al [53]) 44
Figure 2.37 Damage vs. cycles for fatigue testing of Conventional Drill (CD) and AWJ drilled specimens (source: Saleem, M. et al [54]) 45
Figure 2.38 Cartography of the surface roughness of the wall of the hole obtained with (a) conventional drilling (b) AWJ drilling (source: Saleem, M. et al [54]) 45
Figure 2.39 SEM photographs of the surface roughness of the wall of the hole obtained with (a) conventional drilling (b) AWJ drilling (source: Saleem, M. et al [54]) 46
Figure 2.40 Transverse strains for different (N) cycles for tension-tension fatigue testing, (source: Venkatchalam et. al [55]) 47
Figure 2.41 Various stages of damage evolution during tension-compression testing, (source: Venkatchalam et. al. [55]) 47
Figure 2.42 S-N curves for unidirectional composite materials with different fibres (source: Ansari Alam et. al [56]) 48
Figure 2.43 Comparison of fatigue life with two different fibre volume fraction (source:Ansari Alam et. al [56]) 49
Figure 2.44 Variation of static strength with Fibre orientation angle (source: Ansari Alam et. al [56]) 49
Figure 2.45 S-N Curves for different fibre orientation angles (source: Ansari Alam et. al [56]) 50
Figure 2.46 Damage evolution stages in unidirectional composites (source: Ansari Alam et. al [56]) 50
Figure 2.47 Delamination Damage in a Bolted composite Joint under Service Life Conditions, (source: Xiao & Ishikawa, [57]) 51
Figure 2.48 Damage Evolution in a Pinned Joint in CFRP Laminate under Fatigue Loading, (source: Seike et. al [58]) 52
Figure 2.49 Factors affecting fatigue life of fibre-reinforced composites (source: Wicaksono & Chai [60]) 53
Figure 2.50 Composite failure criteria classification (source: Wicaksono & Chai [60]) 54
Figure 2.51 Three-Dimensional state of stresses (source: Wicaksono & Chai [60]) 54
Figure 2.52 Composite fatigue modeling classification (source: Wicaksono & Chai [60]) 55
Figure 2.53 Predicted versus experimental values of damage for UD GRP composites tested under various off-axis angles θ and stress amplitudes (source Shirazi & Varvani-Farahani [62]) 57
Figure 2.54 Predicted fatigue damage versus experimental data for 210 MPa stress and off-axis angle plies (a) 0 degree (b) 90 degree and for 300 MPa for (c) 0 degree (d) 90 degree (sources: Shirazi & Varvani-Farahani [62]) 58
Figure 2.55 Predicted fatigue damage versus experimental data for 424.8 MPa stress and off-axis angle plies (a) 0 degree (b) 90 degree and for 662 MPa for (c) 0 degree (d) 90 degree, (source: Shirazi & Varvani-Farahani [62)] 58
Figure 2.56 3D Damage state space showing fibre breakage, debonding and matrix cracking, (source: Senthinathan et. al. [63]) 60
Figure 2.57 Micrographs showing a) 0°fibre cracks b) 0° fibre missing c) 0°fibre/matrix debonding d) 45°fibre/matrix interfacial debonding e) 90° fibre/matrix interfacial debonding f) 90°Matrix cracking (source: Senthinathan et. al. [63]) 61
Figure 2.58 Elastic Modulus variation with respect to a) fibre damage in 0° b) interface debonding in 0° c) interface debonding in 45° (source: Senthinathan et. al. [63]) 62
Figure 2.59 Flowchart of Progress fatigue damage modeling of cross-ply laminates (source: Shokreih & Behrooz [72]) 67
Figure 2.60 Static strength test data (source: Behrooz-Taheri et. al. [73]) 69
Figure 2.61 Normalized residual strength of a unidirectional 0° ply under longitudinal tension-tension fatigue testing (source: Behrooz-Taheri et. al. [73]) 70
Figure 2.62 S-N curve of unidirectional 0° laminates in longitudinal direction (source: Behrooz-Taheri et. al. [73]) 70
Figure 2.63 Residual stiffness in transverse direction of a unidirectional 90° laminate (source: Behrooz-Taheri et. al. [73]) 71
Figure 2.64 S-N curve of unidirectional 90° laminates in longitudinal direction (source: Behrooz-Taheri et. al. [73]) 71

Figure 2.65 Stress Strain curve for [0/90$_5$/0] laminate under uniaxial tensile loading (source: Behrooz-Taheri et. al. [73]) 72
Figure 2.66 Stress Strain curve for [0/90$_5$/0] laminate under tension-tension cyclic loading, (source: Behrooz-Taheri et. al. [73]) 72
Figure 2.67 Stiffness degradation of 90° plies from first cycle to Characteristic Damage State (CDS) level (source: Behrooz-Taheri et. al. [73]) 73
Figure 2.68 Stiffness degradation of 90° plies from first cycle to delamination initiation, (source: Behrooz-Taheri et. al. [73]) 73
Figure 2.69 Fatigue life prediction of a [0/90$_5$/0] laminate (source: Behrooz-Taheri et. al. [73]) 74
Figure 3.1 Process Methodology for Surface Integrity Study of Machining Process 79
Figure 3.2 Process Methodology for Surface Integrity Study of Drilling Process 80
Figure 4.1 Construction of a Typical Carbon-Fibre Reinforced Plastic Laminate(source: Lin [59]) 85
Figure 4.2 Stacking Sequence of a Multi-Angle Laminate (source: Lin [59]) 87
Figure 4.3 Cure Cycle of a CFRP Laminate (source: Boeing [61]) 93
Figure 4.4 Machining Set-up for Edge Trimming with Endmill Cutters 94
Figure 4.5 PCD Endmill & CVD Diamond Coated Endmill 95
Figure 4.6 WaterjetPro WJP1313 Machine 96
Figure 4.7 CVD Diamond Coated and PCD Drill 97
Figure 4.8 Mahr Mahrsurf GD 25 Surface Profilometer 98
Figure 4.9 Wyko – NT2000 Surface Profiler 99
Figure 4.10 FEI Sirion Scanning Electron Microscope 99
Figure 4.11 Instron Universal Testing Machine, Model 5585H 100
Figure 5.1 Surface Roughness of Endmill Machined Edge (Longitudinal) 102
Figure 5.2 Surface Roughness of AWJ Trimmed Edge (Longitudinal) 103
Figure 5.3 Surface Comparison between Endmill vs. AWJ Trimmed – (a) schematic (b) actual specimen 104
Figure 5.4 Montage of 45 Degree Ply Fibre Pullout Area of Endmill Machined Edge 105
Figure 5.5 Micrograph showing Fibre Pullouts in 45 Degree Ply of Endmill Machined Edge 105
Figure 5.6 SEM of Fibre Pullouts in the Edge Surface of Endmill Trimmed Edge 106
Figure 5.7 SEM of Delamination in the Edge Surface of AWJ Trimmed Edge – (a- schematic (b) actual specimen ..106
Figure 5.8 Surface Roughness of PCD Drilled Hole 107
Figure 5.9 Surface Roughness of a CVD Diamond Coated Drilled Hole 108
Figure 5.10 SEM of Fibre Pullout Region in PCD Drilled Hole – (a) Fibre Pullouts (b) magnified view of fibre pullout 109
Figure 5.11 SEM of Surface Damage in CVD Diamond Drilled Hole 109
Figure 5.12 SEM of Fibre Pullout Region in CVD Diamond Drilled Hole – (a) magnified view of fibre pullout (b) magnified view of fibre pullout showing fibre fracture 110
Figure 5.13 Surface Roughness Zones on AWJ Specimen 110
Figure 5.14 Tensile Strength Test Specimen 112
Figure 5.15 Compressive Strength Test Specimen 113
Figure 5.16 Load Displacement Curve, Endmill Specimen – Tension 116
Figure 5.17 Load Displacement Curve, AWJ Specimen – Tension 116
Figure 5.18 Failure of Endmill Trimmed Specimen in Tension 117
Figure 5.19 Failure of AWJ Trimmed Specimen in Tension 117
Figure 5.20 Load Displacement Curve, Endmill - Compression 118
Figure 5.21 Load Displacement Curve, AWJ – Compression 119
Figure 5.22 Load Displacement Curve, Endmill Trimmed – PCD Vs. CVD Drill Open-Hole Tension 120
Figure 5.23 Load Displacement Curve, AWJ Trimmed - PCD Vs, CVD Drill Open-Hole Tension 120
Figure 5.24 Delamination Failure of Specimen in Open-Hole Testing 121
Figure 5.25 Matrix Cracking initiation and progress in an Endmill Trimmed Tension Specimen 123
Figure 5.26 First Ply Failure in an Endmill Trimmed Tension Specimen 124
Figure 5.27 Matrix Cracking Initiation and Progress in an AWJ Trimmed Specimen 124
Figure 6.1 Longitudinal Surface Roughness of PCD Endmill Machined Edge 130
Figure 6.2 Longitudinal Surface Roughness of AWJ (120 grit) Trimmed Edge 131

Figure 6.3 Longitudinal Surface Roughness of AWJ (80 grit) Trimmed Edge....131
Figure 6.4 SEM of AWJ trimmed Edge Surface (80 Grit)....132
Figure 6.5 SEM of AWJ trimmed Edge Surface (80 Grit)....132
Figure 6.6 SEM of AWJ (120 grit) Trimmed Edge Surface....133
Figure 6.7 SEM of AWJ (120 grit)Trimmed Edge Surface....134
Figure 6.8 SEM of PCD Endmill Trimmed Edge Surface....135
Figure 6.9 SEM of PCD Endmill Trimmed Edge Surface....135
Figure 6.10 SEM of CVD Endmill Trimmed Edge Surface....136
Figure 6.11 SEM of CVD Endmill Trimmed Edge Surface....137
Figure 6.12 Surface Roughness of PCD Drilled Hole (Feedrate 305 mm/min, longitudinal)....139
Figure 6.13 Surface Roughness of PCD Drilled Hole (Feedrate 508 mm/min, Longitudinal)....139
Figure 6.14 Surface Roughness of CVD Drilled Hole (Feedrate 305 mm/min, Longitudinal)....140
Figure 6.15 Surface Roughness of CVD Drilled Hole (Feedrate 508 mm/min, Longitudinal)....140
Figure 6.16 SEM showing damage during PCD Drilling at Feedrate = 305 mm/min....141
Figure 6.17 SEM showing damage during PCD Drilling at Feedrate = 508 mm/min....141
Figure 6.18 SEM showing damage during CVD Drilling at Feedrate = 305 mm/min....142
Figure 6.19 SEM showing damage during CVD Drilling at Feedrate = 305 mm/min....143
Figure 6.20 SEM showing damage during CVD Drilling at Feedrate = 508 mm/min....143
Figure 6.21 SEM showing damage during CVD Drilling at Feedrate = 508 mm/min....144
Figure 6.22 Tensile Stress Vs. Strain for AWJ (80 Grit) edge trimmed specimen....148
Figure 6.23 Magnified view of Tensile Stress Vs. Strain showing matrix cracking in AWJ (80 Grit) edge trimmed specimen....148
Figure 6.24 Magnified view of Tensile Stress Vs. Strain showing first ply failure and damage for AWJ (80 Grit) edge trimmed specimen....149
Figure 6.25 Failed specimen from Tensile testing of AWJ (80 Grit) edge trimmed specimen....150
Figure 6.26 SEM of failed specimen from tensile testing of AWJ (80 Grit) edge trimmed specimen....150
Figure 6.27 SEM showing brittle fracture of 90 degree fibres from tensile testing of AWJ (80 Grit) edge trimmed specimen....151
Figure 6.28 SEM showing brittle fracture of 0 degree fibres from tensile testing of AWJ (80 Grit) edge trimmed specimen....151
Figure 6.29 Tensile Stress Vs. Strain for AWJ (120 Grit) edge trimmed specimen....152
Figure 6.30 Magnified view of Tensile Stress Vs. Strain showing matrix cracking in AWJ (120 Grit) edge trimmed specimen....152
Figure 6.31 Magnified view of Tensile Stress Vs. Strain showing first ply failure and damage for AWJ (120 Grit) edge trimmed specimen....153
Figure 6.32 Failed specimen from Tensile testing of AWJ (120 Grit) edge trimmed specimen....154
Figure 6.33 SEM of failed specimen from tensile testing of AWJ (120 Grit) edge trimmed specimen....154
Figure 6.34 SEM showing brittle fracture of 0 and 90 degree fibres from tensile testing of AWJ (120 Grit) edge trimmed specimen....155
Figure 6.35 Comparative Plot of Tensile Stress Vs. Strain for Tensile Testing of AWJ (80 Grit) Vs. AWJ (120 Grit) edge trimmed specimens....156
Figure 6.36 Tensile Stress Vs. Strain for PCD endmill edge trimmed specimen....157
Figure 6.37 Magnified view of Tensile Stress Vs. Strain showing matrix cracking in PCD endmill edge trimmed specimen....157
Figure 6.38 Magnified view of Tensile Stress Vs. Strain showing first ply failure and damage for PCD endmill edge trimmed specimen....158
Figure 6.39 Failed specimen from Tensile testing of PCD endmill edge trimmed specimen....159
Figure 6.40 SEM of failed specimen from tensile testing of PCD endmill edge trimmed specimen....159
Figure 6.41 SEM showing brittle fracture of 0 and 90 degree fibres from tensile testing of PCD endmill edge trimmed specimen....160
Figure 6.42 Tensile Stress Vs. Strain for CVD endmill edge trimmed specimen....161
Figure 6.43 Magnified view of Tensile Stress Vs. Strain showing matrix cracking in CVD endmill edge trimmed specimen....161

Figure 6.44 Magnified view of Tensile Stress Vs. Strain showing first ply failure and damage for CVD endmill edge trimmed specimen....162
Figure 6.45 Failed specimen from Tensile testing of CVD endmill edge trimmed specimen 163
Figure 6.46 SEM of failed specimen from tensile testing of CVD endmill edge trimmed specimen 163
Figure 6.47 SEM showing brittle fracture of 0 and 90 degree fibres from tensile testing of CVD endmill edge trimmed specimen....164
Figure 6.48 Comparative Plot of Tensile Stress Vs. Strain for Tensile Testing of PCD endmill Vs. CVD endmill edge trimmed specimens....165
Figure 6.49 Sample Surface finish data for a AWJ (120 Grit) edge trimmed specimen for stress concentration factor calculation....165
Figure 6.50 Sample Surface profile data for a AWJ (120 Grit) edge trimmed specimen for stress concentration factor calculation....166
Figure 6.51 Sample stress concentration factor calculation for a AWJ (120 Grit) edge trimmed specimen....166
Figure 6.52 Plot of (E/E_0) Vs. Stress Concentration Factor for various edge trimmed specimens in Tensile testing 168
Figure 6.53 Plot of (E/E_0) Vs. Average Surface Roughness - R_a (μm) for various edge trimmed specimens in Tensile testing....168
Figure 6.54 Plot of (E/E_0) Vs. Surface Finish (R_z / R_t) for various edge trimmed specimens in Tensile testing....169
Figure 6.55 Damage Vs. Applied Load for edge trimmed specimens in Tensile Testing....170
Figure 6.56 Compressive Stress Vs. Strain for AWJ (80 Grit) edge trimmed compression specimen....172
Figure 6.57 Magnified view of Compressive Stress Vs. Strain showing matrix cracking in AWJ (80 Grit) edge trimmed compression specimen....173
Figure 6.58 Magnified view of Compressive Stress Vs. Strain showing ply failure due to buckling in AWJ (80 Grit) edge trimmed compression specimen....173
Figure 6.59 Failed specimen in compression testing of AWJ (80 Grit) edge trimmed specimen....174
Figure 6.60 Failed specimen in compression testing of AWJ (80 Grit) edge trimmed specimen....175
Figure 6.61 Compressive Stress Vs. Strain for CVD endmill edge trimmed compression specimen....176
Figure 6.62 Magnified view of Compressive Stress Vs. Strain showing matrix cracking in CVD endmill edge trimmed compression specimen....176
Figure 6.63 Magnified view of Compressive Stress Vs. Strain showing ply failure due to buckling in CVD endmill edge trimmed compression specimen....177
Figure 6.64 Failed specimen in compression testing of CVD endmill edge trimmed specimen....178
Figure 6.65 Plot of (E/E_0) Vs. Stress Concentration Factor for various edge trimmed specimens in compression testing....179
Figure 6.66 Plot of (E/E_0) Vs. Average Surface Roughness - R_a (μm) for various edge trimmed specimens in compression testing....179
Figure 6.67 Plot of (E/E_0) Vs. Surface Finish (R_z / R_t) for various edge trimmed specimens in compression testing.180
Figure 6.68 Damage Vs. Applied Load for edge trimmed specimens in Tensile Testing....181
Figure 6.69 Open Hole Tensile Stress Vs. Strain for PCD Drilled Hole (305 mm/min)....183
Figure 6.70 Magnified View of Open Hole Tensile Stress Vs. Strain showing Matrix Cracking in PCD Drilled hole specimen (305 mm/min)....183
Figure 6.71 Magnified view of Open Hole Tensile Stress Vs. Strain showing First Ply Failure and Damage in PCD Drilled hole specimen (305 mm/min)....184
Figure 6.72 Failed specimen from Open Hole Tensile testing of PCD hole specimen (305 mm/min)....185
Figure 6.73 SEM of failed specimen from Open Hole Tensile Testing of PCD hole specimen (305 mm/min)....185
Figure 6.74 SEM of failed specimen showing Matrix Cracks from Open Hole Tensile Testing of PCD hole specimen (305 mm/min)....186
Figure 6.75 SEM of failed specimen showing Fibre Fractures from Open Hole Tensile Testing of PCD hole specimen (305 mm/min)....186
Figure 6.76 SEM of failed specimen showing Delamination from Open Hole Tensile Testing of PCD hole specimen (305 mm/min)....187
Figure 6.77 Open Hole Tensile Stress Vs. Strain for PCD Drilled Hole (508 mm/min)....188
Figure 6.78 Magnified View of Open Hole Tensile Stress Vs. Strain showing Matrix Cracking in PCD Drilled hole specimen (508 mm/min)....188

Figure 6.79 Magnified view of Open Hole Tensile Stress Vs. Strain showing First Ply Failure and Damage in PCD Drilled hole specimen (508 mm/min) 189
Figure 6.80 Failed specimen from Open Hole Tensile testing of PCD hole specimen (508 mm/min) 190
Figure 6.81 SEM of failed specimen from Open Hole Tensile Testing of PCD hole specimen (508 mm/min) 190
Figure 6.82 SEM of failed specimen showing Matrix Cracks from Open Hole Tensile Testing of PCD hole specimen (508 mm/min) 191
Figure 6.83 SEM of failed specimen showing Fibre Fractures from Open Hole Tensile Testing of PCD hole specimen (508 mm/min) 191
Figure 6.84 SEM of failed specimen showing Delamination from Open Hole Tensile Testing of PCD hole specimen (508 mm/min) 192
Figure 6.85 Open Hole Tensile Stress Vs. Strain for CVD Drilled Hole (305 mm/min) 193
Figure 6.86 Magnified View of Open Hole Tensile Stress Vs. Strain showing Matrix Cracking in CVD Drilled hole specimen (305 mm/min) 193
Figure 6.87 Magnified view of Open Hole Tensile Stress Vs. Strain showing First Ply Failure and Damage in CVD Drilled hole specimen (305 mm/min) 194
Figure 6.88 Failed specimen from Open Hole Tensile testing of CVD hole specimen (305 mm/min) 195
Figure 6.89 SEM of failed specimen from Open Hole Tensile Testing of CVD hole specimen (305 mm/min) 195
Figure 6.90 SEM of failed specimen showing Matrix Cracks from Open Hole Tensile Testing of CVD hole specimen (305 mm/min) 196
Figure 6.91 SEM of failed specimen showing Fibre Fractures from Open Hole Tensile Testing of CVD hole specimen (305 mm/min) 196
Figure 6.92 SEM of failed specimen showing Delamination from Open Hole Tensile Testing of CVD hole specimen (305 mm/min) 197
Figure 6.93 Open Hole Tensile Stress Vs. Strain for CVD Drilled Hole (508 mm/min) 198
Figure 6.94 Magnified View of Open Hole Tensile Stress Vs. Strain showing Matrix Cracking in CVD Drilled hole specimen (508 mm/min) 198
Figure 6.95 Magnified view of Open Hole Tensile Stress Vs. Strain showing First Ply Failure and Damage in CVD Drilled hole specimen (508 mm/min) 199
Figure 6.96 Failed specimen from Open Hole Tensile testing of CVD hole specimen (508 mm/min) 200
Figure 6.97 SEM of failed specimen from Open Hole Tensile Testing of CVD hole specimen (508 mm/min) 200
Figure 6.98 SEM of failed specimen showing Matrix Cracks from Open Hole Tensile Testing of CVD hole specimen (508 mm/min) 201
Figure 6.99 SEM of failed specimen showing Fibre Fractures from Open Hole Tensile Testing of CVD hole specimen (508 mm/min) 201
Figure 6.100 SEM of failed specimen showing Delamination from Open Hole Tensile Testing of CVD hole specimen (508 mm/min) 202
Figure 6.101 Sample Surface finish data for a PCD drill hole at feedrate of 305 mm/min specimen for stress concentration factor calculation 203
Figure 6.102 Sample Surface profile data for a PCD drill hole at a feedrate of 305 mm/min for stress concentration factor calculation 203
Figure 6.103 Sample stress concentration factor calculation for a PCD drill hole at a feedrate of 305 mm/min feedrate specimen 204
Figure 6.104 Plot of (E/E_0) Vs. Stress Concentration Factor for various Open hole Tensile Testing specimens 205
Figure 6.105 Plot of (E/E_0) Vs. Average Surface Roughness - R_a (μm) for various Open Hole Tensile Testing specimens 205
Figure 6.106 Plot of (E/E_0) Vs. Surface Finish (R_z / R_t) for various Open Hole Tensile Testing specimens 206
Figure 6.107 Damage Vs. Applied Load for Open Hole Tensile Testing specimens 207
Figure 6.108 Open Hole Compressive Stress Vs. Strain for PCD Drilled Hole (305 mm/min) 209
Figure 6.109 Magnified View of Open Hole Compressive Stress Vs. Strain showing Matrix Cracking in PCD Drilled hole specimen (305 mm/min) 209
Figure 6.110 Magnified view of Open Hole Compressive Stress Vs. Strain showing First Ply Failure and Damage in PCD Drilled hole specimen (305 mm/min) 210
Figure 6.111 Failed specimen from Open Hole Compression testing of PCD hole specimen (305 mm/min) 211

Figure 6.112 SEM of failed specimen from Open Hole Compression Testing of PCD hole specimen (305 mm/min) 211
Figure 6.113 SEM of failed specimen showing buckling at 45 degrees from Open Hole Compression Testing of PCD hole specimen (305 mm/min) 212
Figure 6.114 SEM of failed specimen showing Ply Failure from Open Hole Compression Testing of PCD hole specimen (305 mm/min) 212
Figure 6.115 SEM of failed specimen showing Ultimate failure from Open Hole Compression Testing of PCD hole specimen (305 mm/min) 213
Figure 6.116 Open Hole Compressive Stress Vs. Strain for PCD Drilled Hole (508 mm/min).....214
Figure 6.117 Magnified View of Open Hole Compressive Stress Vs. Strain showing Matrix Cracking in PCD Drilled hole specimen (508 mm/min) 214
Figure 6.118 Magnified view of Open Hole Compressive Stress Vs. Strain showing First Ply Failure and Damage in PCD Drilled hole specimen (508 mm/min) 215
Figure 6.119 Failed specimen from Open Hole Compression testing of PCD hole specimen (508 mm/min) 216
Figure 6.120 Failed specimen from Open Hole Compression testing of PCD hole specimen (508 mm/min) 217
Figure 6.121 SEM of failed specimen showing buckling at 45 degrees from Open Hole Compression Testing of PCD hole specimen (508 mm/min) 217
Figure 6.122 SEM of failed specimen showing Ply Failure from Open Hole Compression Testing of PCD hole specimen (508 mm/min) 218
Figure 6.123 SEM of failed specimen showing Ultimate failure from Open Hole Compression Testing of PCD hole specimen (508 mm/min) 218
Figure 6.124 Open Hole Compressive Stress Vs. Strain for CVD Drilled Hole (305 mm/min) 219
Figure 6.125 Magnified View of Open Hole Compressive Stress Vs. Strain showing Matrix Cracking in CVD Drilled hole specimen (305 mm/min) 220
Figure 6.126 Magnified view of Open Hole Compressive Stress Vs. Strain showing First Ply Failure and Damage in CVD Drilled hole specimen (305 mm/min) 220
Figure 6.127 Failed specimen from Open Hole Compression testing of CVD hole specimen (305 mm/min) 222
Figure 6.128 Failed specimen from Open Hole Compression testing of CVD hole specimen (305 mm/min) 222
Figure 6.129 SEM of failed specimen showing Ply Failure from Open Hole Compression Testing of CVD hole specimen (305 mm/min) 223
Figure 6.130 SEM of failed specimen showing buckling at 45 degrees from Open Hole Compression Testing of CVD hole specimen (305 mm/min) 223
Figure 6.131 SEM of failed specimen showing Ultimate failure from Open Hole Compression Testing of CVD hole specimen (305 mm/min) 224
Figure 6.132 Open Hole Compressive Stress Vs. Strain for CVD Drilled Hole (508 mm/min) 225
Figure 6.133 Magnified View of Open Hole Compressive Stress Vs. Strain showing Matrix Cracking in CVD Drilled hole specimen (508 mm/min) 225
Figure 6.134 Magnified view of Open Hole Compressive Stress Vs. Strain showing First Ply Failure and Damage in CVD Drilled hole specimen (508 mm/min) 226
Figure 6.135 Failed specimen from Open Hole Compression testing of CVD hole specimen (508 mm/min) 227
Figure 6.136 Failed specimen from Open Hole Compression testing of CVD hole specimen (508 mm/min) 228
Figure 6.137 SEM of failed specimen showing Ply Failure from Open Hole Compression Testing of CVD hole specimen (508 mm/min) 228
Figure 6.138 SEM of failed specimen showing buckling at 45 degrees from Open Hole Compression Testing of CVD hole specimen (508 mm/min) 229
Figure 6.139 SEM of failed specimen showing Ultimate failure from Open Hole Compression Testing of CVD hole specimen (508 mm/min) 229
Figure 6.140 Plot of (E/E_0) Vs. Stress Concentration Factor for various Open hole Compression Testing specimens 231
Figure 6.141 Plot of (E/E_0) Vs. Average Surface Roughness - R_a (μm) for various Open Hole Compression Testing specimens 232
Figure 6.142 Plot of (E/E_0) Vs. Surface Finish (R_z / R_t) for various Open Hole Compression Testing specimens 233
Figure 6.143 Damage Vs. Applied Load for Open Hole Compression Testing specimens 234

Figure 6.144 Plot of Load Vs. Extension for Bearing Hole Test Specimens....235
Figure 6.145 Damage zone of Bearing hole test specimen – PCD drilled hole (305 mm/min)....236
Figure 6.146 Damage zone of Bearing hole test specimen – PCD drilled hole (508 mm/min)....237
Figure 6.147 Damage zone of Bearing hole test specimen – CVD drilled hole (305 mm/min) 237
Figure 6.148 Damage zone of Bearing hole test specimen – CVD drilled hole (508 mm/min) 238
Figure 6.149 Maximum Tensile Load Vs. Edge Trim & Hole Drilling Process Parameters 239
Figure 6.150 Maximum Compressive Stress Vs. Edge Trim & Hole Drilling Process Parameters 240
Figure 7.1 –Theoretical S-N Curve for Planned Fatigue Cycle Testing 245
Figure 7.2 Theoretical Modulus values for Laminate 246
Figure 7.3 –MTS Fatigue Testing Machine....246
Figure 7.4 – Test Specimen in Fatigue Test Machine....247
Figure 7.5 – Data Acquisition Set up....247
Figure 7.6 SEM of AWJ (80 Grit) Trimmed Surface 251
Figure 7.7 SEM of AWJ (80 Grit) Trimmed Surface 251
Figure 7.8 SEM of AWJ (80 Grit) Trimmed Surface 252
Figure 7.9 SEM of CVD Diamond Coated Endmill Trimmed Surface....252
Figure 7.10 SEM of CVD Diamond Coated Endmill Trimmed Surface....253
Figure 7.11 SEM of CVD Diamond Coated Endmill Trimmed Surface....253
Figure 7.12 SEM of CVD Drilled Hole 255
Figure 7.13 SEM of CVD Drilled Hole 255
Figure 7.14 SEM of CVD Drilled Hole 256
Figure 7.15 Percent Compliance Change Vs. Fatigue Cycles for A1 – H – 2....262
Figure 7.16 Damage at 20K Cycles, 7.49%, Test Specimen....262
Figure 7.17 Damage (12.8%) & Ultimate Failure at 32369 Cycles A1 – H – 2....263
Figure 7.18 Percent Compliance Change Vs. Fatigue Cycles for A1 – H – 3....263
Figure 7.19 Damage at 20K Cycles, 5.64%, Test Specimen....264
Figure 7.20 Damage (9.76%) & Ultimate Failure at 34365 Cycles A1 – H – 3....264
Figure 7.21 Percent Compliance Change Vs. Fatigue Cycles for A1 – H – 4....265
Figure 7.22 Damage at 20K Cycles, 5.76%, Test Specimen....265
Figure 7.23 Damage (25.54%) & Ultimate Failure at 31995 Cycles A1 – H – 4....266
Figure 7.24 Percent Compliance Change Vs. Fatigue Cycles for B1 – H - 1....267
Figure 7.25 Damage at 20K Cycles, 4.37%, Test Specimen....267
Figure 7.26 Damage (28.26%) & Ultimate Failure at 42045 Cycles 268
Figure 7.27 Percent Compliance Change Vs. Fatigue Cycles for B1 – H – 2....268
Figure 7.28 Damage at 20K Cycles, 3.92%, Test Specimen....269
Figure 7.29 Damage (17.1%) & Ultimate Failure at 45555 Cycles 269
Figure 7.30 Percent Compliance Change Vs. Fatigue Cycles for B1 – H – 3....270
Figure 7.31 Damage at 20K Cycles, 6.65%, Test Specimen....270
Figure 7.32 Damage (13.93%) & Ultimate Failure at 46800 Cycles 271
Figure 7.33 Summary Plot of AWJ High Load Percent Compliance Change Vs. Fatigues Cycles 272
Figure 7.34 Summary Plot of CVD End Mill Trimmed High Load Percent Compliance Change Vs. Fatigues Cycles ..272
Figure 7.35 Summary Plot of AWJ Vs, CVD End Mill Trimmed High Load Percent Compliance Change Vs. Fatigues Cycles....273
Figure 7.36 Stress Concentration Factor Calculation....273
Figure 7.37 Graphical Determination of radius (ρ) from surface profile of test specimen, A1–H-2....274
Figure 7.38 Graphical Determination of radius (ρ) from surface profile of test specimen, A1–H-3....275
Figure 7.39 Graphical Determination of radius (ρ) from surface profile of test specimen, A1–H-4....276
Figure 7.40 Graphical Determination of radius (ρ) from surface profile of test specimen, B1–H-1....277
Figure 7.41 Graphical Determination of radius (ρ) from surface profile of test specimen, B1–H–2....278
Figure 7.42 Graphical Determination of radius (ρ) from surface profile of test specimen, B1–H–3....279
Figure 7.43 Surface Finish - R_a (longitudinal) Vs. Fatigue Cycles – AWJ Trimmed High Load Test Specimens 280
Figure 7.44 Surface Finish – R_z (longitudinal) Vs. Fatigue Cycles – AWJ Trimmed High Load Test Specimens....281
Figure 7.45 Surface Finish – R_t (longitudinal) Vs. Fatigue Cycles – AWJ Trimmed High Load Test Specimens....281

Figure 7.46 Surface Finish – R_{sk} (longitudinal) Vs. Fatigue Cycles – AWJ Trimmed High Load Test Specimens.....282
Figure 7.47 Surface Finish – R_{ku} (longitudinal) Vs. Fatigue Cycles – AWJ Trimmed High Load Test Specimens.....282
Figure 7.48 Surface Finish – (R_t/R_z) (Longitudinal) Vs. Fatigue Cycles – AWJ Trimmed High Load Test Specimens ..283
Figure 7.49 Surface Integrity Stress Concentration Factor (Longitudinal) Vs. Fatigue Cycles – AWJ Trimmed High Load Test Specimens 283
Figure 7.50 Surface Finish - R_a (longitudinal) Vs. Fatigue Cycles – CVD Endmill Trimmed High Load Test Specimens 284
Figure 7.51 Surface Finish – R_z (longitudinal) Vs. Fatigue Cycles – CVD Endmill Trimmed High Load Test Specimens 284
Figure 7.52 Surface Finish – R_t (longitudinal) Vs. Fatigue Cycles – CVD Endmill Trimmed High Load Test Specimens 285
Figure 7.53 Surface Finish – R_{sk} (longitudinal) Vs. Fatigue Cycles – CVD Endmill Trimmed High Load Test Specimens 285
Figure 7.54 Surface Finish – R_{ku} (longitudinal) Vs. Fatigue Cycles – CVD Endmill Trimmed High Load Test Specimens 286
Figure 7.55 Surface Finish – (R_t/R_z) (Longitudinal) Vs. Fatigue Cycles – CVD Endmill Trimmed High Load Test Specimens.....286
Figure 7.56 Surface Integrity Stress Concentration Factor (Longitudinal) Vs. Fatigue Cycles – CVD Endmill Trimmed High Load Test Specimens 287
Figure 7.57 Percent Compliance Change Vs. Fatigue Cycles for A1 – M – 1.....289
Figure 7.58 Damage Progression in (A1 – M – 1) Test specimen to 5000 Cycles 290
Figure 7.59 Damage Progression in (A1 – M – 1) Test specimen to 40000 Cycles 291
Figure 7.60 Damage Progression in (A1 – M – 1) Test specimen to 80000 Cycles 292
Figure 7.61 Damage Progression in (A1 – M – 1) Test specimen to 150000 Cycles 293
Figure 7.62 Damage Progression in (A1 – M – 1) Test specimen to Failure at 153,399 Cycles 294
Figure 7.63 Percent Compliance Change Vs. Fatigue Cycles for (A1 – M – 2) 295
Figure 7.64 Damage at 50K Cycles, 6.9%, Test Specimen.....295
Figure 7.65 Damage (27.2%) & Ultimate Failure at 410001 Cycles 296
Figure 7.66 Percent Compliance Change Vs. Fatigue Cycles for (A1 – M – 3) 296
Figure 7.67 Damage at 50K Cycles, 10.13%, Test 297
Figure 7.68 Damage (30.07%) & Ultimate Failure at 83375 Cycles 297
Figure 7.69 Percent Compliance Change Vs. Fatigue Cycles for (B1 – M – 1) 298
Figure 7.70 Damage at 50K Cycles, 9.48%, Test Specimen.....299
Figure 7.71 Damage (18.53%) & Ultimate Failure at 68450 Cycles 300
Figure 7.72 Percent Compliance Change Vs. Fatigue Cycles for B1 – M – 2.....301
Figure 7.73 Damage at 50K Cycles, 9.09%, Test Specimen.....301
Figure 7.74 Damage (32.99%) & Ultimate Failure at 164698 Cycles 302
Figure 7.75 Percent Compliance Change Vs. Fatigue Cycles for (B1 – M – 3) 302
Figure 7.76 Damage at 50K Cycles, 9.69%, Test Specimen.....303
Figure 7.77 Damage (22.79%) & Ultimate Failure at 161693 Cycles 303
Figure 7.78 Summary Plot of AWJ Medium Load Percent Compliance Change Vs. Fatigues Cycles 304
Figure 7.79 Summary Plot of CVD Endmill Trimmed Medium Load Percent Compliance Change Vs. Fatigues Cycles 305
Figure 7.80 Summary Plot of AWJ Trimmed Vs. CVD Endmill Trimmed Specimens Medium Load Percent Compliance Change Vs. Fatigues Cycles 305
Figure 7.81 Graphical Determination of radius (ρ) from surface profile of test specimen A1–M-1.....306
Figure 7.82 Graphical Determination of radius (ρ) from surface profile of test specimen A1–M–2.....307
Figure 7.83 Graphical Determination of radius (ρ) from surface profile of test specimen A1–M–3.....308
Figure 7.84 Graphical Determination of radius (ρ) from surface profile of test specimen B1–M 1 309
Figure 7.85 Graphical Determination of radius (ρ) from surface profile of test specimen B1–M-2.....310
Figure 7.86 Graphical Determination of radius (ρ) from surface profile of test specimen B1–M- 3 311
Figure 7.87 Surface Finish - R_a (longitudinal) Vs. Fatigue Cycles – AWJ Trimmed Medium Load Specimens.....312
Figure 7.88 Surface Finish – R_z (longitudinal) Vs. Fatigue Cycles – AWJ Trimmed Medium Load Test Specimens....313

Figure 7.89 Surface Finish – R_t (longitudinal) Vs. Fatigue Cycles – AWJ trimmed Medium Load Test Specimens 313
Figure 7.90 Surface Finish – R_{sk} (longitudinal) Vs. Fatigue Cycles – AWJ Trimmed Medium Load Test Specimens ..313
Figure 7.91 Surface Finish – R_{ku} (longitudinal) Vs. Fatigue Cycles – AWJ Trimmed Medium Load Test Specimens ..314
Figure 7.92 Surface Finish – (R_t/R_z) (Longitudinal) Vs. Fatigue Cycles – AWJ Trimmed Medium Load Test Specimens 314
Figure 7.93 Surface Integrity Stress Concentration Factor (Longitudinal) Vs. Fatigue Cycles – AWJ Trimmed Medium Load Test Specimens 314
Figure 7.94 Surface Finish - R_a (longitudinal) Vs. Fatigue Cycles – CVD Endmill Trimmed Medium Load Specimens 315
Figure 7.95 Surface Finish – R_z (longitudinal) Vs. Fatigue Cycles – CVD Endmill Trimmed Medium Load Test Specimens....315
Figure 7.96 Surface Finish – R_t (longitudinal) Vs. Fatigue Cycles – CVD Endmill trimmed Medium Load Test Specimens....315
Figure 7.97 Surface Finish – R_{sk} (longitudinal) Vs. Fatigue Cycles –CVD Endmill Trimmed Medium Load Test Specimens....316
Figure 7.98 Surface Finish – R_{ku} (longitudinal) Vs. Fatigue Cycles – CVD Endmill Trimmed Medium Load Test Specimens....316
Figure 7.99 Surface Finish – (R_t/R_z) (Longitudinal) Vs. Fatigue Cycles – CVD Endmill Trimmed Medium Load Test Specimens....316
Figure 7.100 Surface Integrity Stress Concentration Factor (Longitudinal) Vs. Fatigue Cycles – CVD Endmill Trimmed Medium Load Test Specimens....317
Figure 7.101 Percent Compliance Change Vs. Fatigue Cycles for (A1 – L – 1) 319
Figure 7.102 Damage at 200K Cycles, 11.67%, Test 320
Figure 7.103 Damage (25.29%) & Ultimate Failure at 556687 Cycles 320
Figure 7.104 Percent Compliance Change Vs. Fatigue Cycles for (A1 – L – 2) 321
Figure 7.105 Damage at 200K Cycles, 11.49%, Test 321
Figure 7.106 Damage (26.43%) & Ultimate Failure at 487732 Cycles 322
Figure 7.107 Percent Compliance Change Vs. Fatigue Cycles for (A1 – L – 3) 322
Figure 7.108 Damage at 200K Cycles, 11.22%, Test Specimen (A1 – L – 2) 323
Figure 7.109 Damage (31.49%) & Ultimate Failure at 722803 Cycles 323
Figure 7.110 Percent Compliance Change Vs. Fatigue Cycles for (B1 – L – 1) 324
Figure 7.111 Damage at 200K Cycles, 11.53%, Test 325
Figure 7.112 Damage (30.46%) & Ultimate Failure at 296778 Cycles 325
Figure 7.113 Percent Compliance Change Vs. Fatigue Cycles for (B1 – L – 2) 326
Figure 7.114 Damage at 50K Cycles, 10.68%, Test 326
Figure 7.115 Damage (11.64%) & Ultimate Failure at 76783 Cycles 327
Figure 7.116 Percent Compliance Change Vs. Fatigue Cycles for (B1 – L – 3) 327
Figure 7.117 Damage at 200K Cycles, 11.07%, Test 328
Figure 7.118 Damage (31.06%) & Ultimate Failure at 562123 Cycles 328
Figure 7.119 Percent Compliance Change Vs. Fatigue Cycles for (B1 – L – 4) 329
Figure 7.120 Damage at 200K Cycles, 10.99%, Test 329
Figure 7.121 Damage (30.95%) & Ultimate Failure at 805926 Cycles 330
Figure 7.122 Summary Plot of AWJ Low Load Percent Compliance Change Vs. Fatigues Cycles 330
Figure 7.123 Summary Plot of CVD Endmill Trimmed Low Load Percent Compliance Change Vs. Fatigues Cycles ..331
Figure 7.124 Summary Plot of AWJ Vs. CVD Endmill Trimmed Low Load Percent Compliance Change Vs. Fatigues Cycles....331
Figure 7.125 Graphical Determination of radius (ρ) from surface profile of test specimen A1-L–1 332
Figure 7.126 Graphical Determination of radius (ρ) from surface profile of specimen A1–L–2....333
Figure 7.127 Graphical Determination of radius (ρ) from surface profile of specimen A1 – L – 3 334
Figure 7.128 Graphical Determination of radius (ρ) from surface profile of specimen B1 – L – 1 335
Figure 7.129 Graphical Determination of radius (ρ) from surface profile of specimen B1 – L – 3 336
Figure 7.130 Graphical Determination of radius (ρ) from surface profile of specimen B1 – L – 4 337
Figure 7.131 Surface Finish - R_a (longitudinal) Vs. Fatigue Cycles – AWJ Trimmed Low Load Specimens....338

Figure 7.132 Surface Finish – R_z (longitudinal) Vs. Fatigue Cycles – AWJ Trimmed Low Load Test Specimens.....339
Figure 7.133 Surface Finish – R_t (longitudinal) Vs. Fatigue Cycles – AWJ trimmed Low Load Test Specimens 339
Figure 7.134 Surface Finish – R_{sk} (longitudinal) Vs. Fatigue Cycles – AWJ Trimmed Low Load Test Specimens.....339
Figure 7.135 Surface Finish – R_{ku} (longitudinal) Vs. Fatigue Cycles – AWJ Trimmed Low Load Test Specimens 340
Figure 7.136 Surface Finish – (R_t/R_z) (Longitudinal) Vs. Fatigue Cycles – AWJ Trimmed Low Load Test Specimens 340
Figure 7.137 Surface Integrity Stress Concentration Factor (Longitudinal) Vs. Fatigue Cycles – AWJ Trimmed Low Load Test Specimens 340
Figure 7.138 Surface Finish - R_a (longitudinal) Vs. Fatigue Cycles – AWJ Trimmed Low Load Specimens.....341
Figure 7.139 Surface Finish – R_z (longitudinal) Vs. Fatigue Cycles – CVD Endmill Trimmed Low Load Test Specimens 341
Figure 7.140 Surface Finish – R_t (longitudinal) Vs. Fatigue Cycles – CVD Endmill trimmed Low Load Test Specimens 341
Figure 7.141 Surface Finish – R_{sk} (longitudinal) Vs. Fatigue Cycles – CVD Endmill Trimmed Low Load Test Specimens 342
Figure 7.142 Surface Finish – R_{ku} (longitudinal) Vs. Fatigue Cycles –CVD Endmill Trimmed Low Load Test Specimens 342
Figure 7.143 Surface Finish – (R_t/R_z) (Longitudinal) Vs. Fatigue Cycles –CVD Endmill Trimmed Low Load Test Specimens.....342
Figure 7.144 Surface Integrity Stress Concentration Factor (Longitudinal) Vs. Fatigue Cycles – CVD Endmill Trimmed Low Load Test Specimens.....343
Figure 7.145 Percent Compliance Change Vs. Fatigue Cycles for A2 – H – 3.....345
Figure 7.146 Damage at 80K Cycles, 7.40%, Test Specimen A2.....345
Figure 7.147 Damage (36.61%) & Ultimate Failure at 178298 Cycles, Test Specimen A2 – H - 3.....346
Figure 7.148 Percent Compliance Change Vs. Fatigue Cycles for A2 – H – 4.....346
Figure 7.149 Damage at 80K Cycles, 9.44%, Test Specimen A2.....347
Figure 7.150 Damage (32.59%) & Ultimate Failure at 153058 Cycles, Test Specimen A2 – H - 4 347
Figure 7.151 Percent Compliance Change Vs. Fatigue Cycles for B2 – H – 1.....348
Figure 7.152 Damage at 80K Cycles, 7.33%, Test Specimen B2 – H - 1 348
Figure 7.153 Damage (37.52%) & Ultimate Failure at 162095 Cycles, Test 349
Figure 7.154 Percent Compliance Change Vs. Fatigue Cycles for B2 – H – 2.....349
Figure 7.155 Damage at 80K Cycles, 10.62%, Test Specimen B2.....350
Figure 7.156 Damage (32.23%) & Ultimate Failure at 123091 Cycles, Test 350
Figure 7.157 Percent Compliance Change Vs. Fatigue Cycles for B2 – H – 3.....351
Figure 7.158 Damage at 80K Cycles, 10.63%, Test Specimen B2.....351
Figure 7.159 Damage (15.71%) & Ultimate Failure at 92663 Cycles, Test Specimen 352
Figure 7.160 Percent Compliance Change Vs. Fatigue Cycles for B2 – H – 4.....352
Figure 7.161 Damage at 80K Cycles, 7.81%, Test Specimen B2.....353
Figure 7.162 Damage (26.24%) & Ultimate Failure at 111447 Cycles, Test 353
Figure 7.163 Summary Plot of % Compliance Change Vs. (N) Cycles for AWJ Trimmed Test Specimens – High Load 354
Figure 7.164 Summary Plot of % Compliance Change Vs. (N) Cycles for CVD Endmill Trimmed Test Specimens – High Load 354
Figure 7.165 Summary of AWJ Vs. CVD Endmill Trimmed Plots of % Compliance Change Vs. (N) Cycles Test Specimens – High Load.....355
Figure 7.166 Graphical Determination of radius (ρ) from surface profile of specimen A2 – H – 3 356
Figure 7.167 Graphical Determination of radius (ρ) from surface profile of specimen A2 – H – 4 357
Figure 7.168 Graphical Determination of radius (ρ) from surface profile of specimen B2 – H – 1 358
Figure 7.169 Graphical Determination of radius (ρ) from surface profile of specimen B2 – H – 2 359
Figure 7.170 Graphical Determination of radius (ρ) from surface profile of specimen B2 – H – 3 360
Figure 7.171 Graphical Determination of radius (ρ) from surface profile of specimen B2 – H – 4 361
Figure 7.172 Surface Finish - R_a (longitudinal) Vs. Fatigue Cycles – AWJ Trimmed – Notched High Load Specimens 362

Figure 7.173 Surface Finish – R_z (longitudinal) Vs. Fatigue Cycles – AWJ Trimmed - Notched – High Load Test Specimens....363
Figure 7.174 Surface Finish – R_t (longitudinal) Vs. Fatigue Cycles – AWJ trimmed – Notched - High Load Test Specimens....363
Figure 7.175 Surface Finish – R_{sk} (longitudinal) Vs. Fatigue Cycles – AWJ Trimmed – Notched High Load Test Specimens....363
Figure 7.176 Surface Finish – R_{ku} (longitudinal) Vs. Fatigue Cycles – AWJ Trimmed – Notched High Load Test Specimens....364
Figure 7.177 Surface Finish – (R_t/R_z) (Longitudinal) Vs. Fatigue Cycles – AWJ Trimmed – Notched High Load Test Specimens....364
Figure 7.178 Surface Integrity Stress Concentration Factor (Longitudinal) Vs. Fatigue Cycles – AWJ Trimmed - Notched High Load Test Specimens....364
Figure 7.179 Surface Finish - R_a (longitudinal) Vs. Fatigue Cycles – CVD Endmill Trimmed – Notched High Load Specimens....365
Figure 7.180 Surface Finish – R_z (longitudinal) Vs. Fatigue Cycles – CVD Endmill Trimmed - Notched – High Load Test Specimens....365
Figure 7.181 Surface Finish – R_t (longitudinal) Vs. Fatigue Cycles – CVD Endmill trimmed – Notched - High Load Test Specimens....365
Figure 7.182 Surface Finish – R_{sk} (longitudinal) Vs. Fatigue Cycles – CVD Endmill Trimmed – Notched High Load Test Specimens....366
Figure 7.183 Surface Finish – R_{ku} (longitudinal) Vs. Fatigue Cycles – CVD Endmill Trimmed – Notched High Load Test Specimens....366
Figure 7.184 Surface Finish – (R_t/R_z) (Longitudinal) Vs. Fatigue Cycles – CVD Endmill Trimmed – Notched High Load Test Specimens....366
Figure 7.185 Surface Integrity Stress Concentration Factor (Longitudinal) Vs. Fatigue Cycles – CVD Endmill Trimmed - Notched High Load Test Specimens....367
Figure 7.186 Percent Compliance Change Vs. Fatigue Cycles for A2 – M – 1....369
Figure 7.187 Damage at 300K Cycles, 14.47%, Test Specimen A2 – M - 1....369
Figure 7.188 Damage (39.13%) & Ultimate Failure at 495512 Cycles, Test Specimen A2 – M - 1....370
Figure 7.189 Percent Compliance Change Vs. Fatigue Cycles for A2 – M – 2....370
Figure 7.190 Damage at 300K Cycles, 15.83%, Test Specimen A2 – M - 2....371
Figure 7.191 Damage (32.54%) & Ultimate Failure at 411828 Cycles, Test Specimen A2 – M - 2....371
Figure 7.192 Percent Compliance Change Vs. Fatigue Cycles for A2 – M – 3....372
Figure 7.193 Damage at 300K Cycles, 16.24%, Test Specimen A2 – M - 3....372
Figure 7.194 Damage (37.75%) & Ultimate Failure at 370163 Cycles, Test Specimen A2 – M - 3....373
Figure 7.195 Percent Compliance Change Vs. Fatigue Cycles for A2 – M – 4....373
Figure 7.196 Damage at 200K Cycles, 16.39%, Test Specimen A2 – M - 4....374
Figure 7.197 Damage (26.86%) & Ultimate Failure at 210389 Cycles, Test Specimen A2–M- 4....374
Figure 7.198 Percent Compliance Change Vs. Fatigue Cycles for B2 – M – 1....375
Figure 7.199 Damage at 300K Cycles, 18.49%, Test Specimen B2 – M - 1....376
Figure 7.200 Damage (40.0%) & Ultimate Failure at 377675 Cycles, Test Specimen B2 – M - 1....376
Figure 7.201 Percent Compliance Change Vs. Fatigue Cycles for B2 – M – 2....377
Figure 7.202 Damage at 300K Cycles, 19.71%, Test Specimen B2 – M - 2....377
Figure 7.203 Damage (51.05%) & Ultimate Failure at 436382 Cycles, Test Specimen B2 – M - 2....378
Figure 7.204 Percent Compliance Change Vs. Fatigue Cycles for B2 – M – 3....378
Figure 7.205 Damage at 300K Cycles, 17.07%, Test Specimen B2 – M - 3....379
Figure 7.206 Damage (43.04%) & Ultimate Failure at 540315 Cycles, Test Specimen B2 – M - 3....379
Figure 7.207 Summary Plot of % Compliance Change Vs. (N) Cycles for AWJ Trimmed Notched Specimens – Medium Load....380
Figure 7.208 Summary Plot of % Compliance Change Vs. (N) Cycles for CVD Endmill Trimmed Notched Specimens – Medium Load....380
Figure 7.209 Summary Plot of AWJ Vs. CVD Endmill Trimmed of % Compliance Change Vs. (N) Cycles – Notched Specimens – Medium Load....381

Figure 7.210 Graphical Determination of radius (ρ) from surface profile of specimen A2 – M - 1 382
Figure 7.211 Graphical Determination of radius (ρ) from surface profile of specimen A2 – M - 2 383
Figure 7.212 Graphical Determination of radius (ρ) from surface profile of specimen A2 – M – 3 384
Figure 7.213 Graphical Determination of radius (ρ) from surface profile of specimen A2 – M – 4 385
Figure 7.214 Graphical Determination of radius (ρ) from surface profile of specimen B2 – M - 1 386
Figure 7.215 Graphical Determination of radius (ρ) from surface profile of specimen B2 – M - 2 387
Figure 7.216 Graphical Determination of radius (ρ) from surface profile of specimen B2 – M - 3 388
Figure 7.217 Surface Finish - R_a (longitudinal) Vs. Fatigue Cycles – AWJ Trimmed – Notched Medium Load Specimens.....389
Figure 7.218 Surface Finish – R_z (longitudinal) Vs. Fatigue Cycles – AWJ Trimmed - Notched – Medium Load Test Specimens.....390
Figure 7.219 Surface Finish – R_t (longitudinal) Vs. Fatigue Cycles – AWJ trimmed – Notched - Medium Load Test Specimens.....390
Figure 7.220 Surface Finish – R_{sk} (longitudinal) Vs. Fatigue Cycles – AWJ Trimmed – Notched Medium Load Test Specimens.....390
Figure 7.221 Surface Finish – R_{ku} (longitudinal) Vs. Fatigue Cycles – AWJ Trimmed – Notched Medium Load Test Specimens.....391
Figure 7.222 Surface Finish – (R_t/R_z) (Longitudinal) Vs. Fatigue Cycles – AWJ Trimmed – Notched Medium Load Test Specimens.....391
Figure 7.223 Surface Integrity Stress Concentration Factor (Longitudinal) Vs. Fatigue Cycles – AWJ Trimmed - Notched Medium Load Test Specimens 391
Figure 7.224 Surface Finish - R_a (longitudinal) Vs. Fatigue Cycles – CVD Endmill Trimmed – Notched Medium Load Specimens.....392
Figure 7.225 Surface Finish – R_z (longitudinal) Vs. Fatigue Cycles –CVD Endmill Trimmed - Notched – Medium Load Test Specimens 392
Figure 7.226 Surface Finish – R_t (longitudinal) Vs. Fatigue Cycles – CVD Endmill trimmed – Notched - Medium Load Test Specimens 392
Figure 7.227 Surface Finish – R_{sk} (longitudinal) Vs. Fatigue Cycles – CVD Endmill Trimmed – Notched Medium Load Test Specimens 393
Figure 7.228 Surface Finish – R_{ku} (longitudinal) Vs. Fatigue Cycles –CVD Endmill Trimmed – Notched Medium Load Test Specimens 393
Figure 7.229 Surface Finish – (R_t/R_z) (Longitudinal) Vs. Fatigue Cycles – CVD Endmill Trimmed – Notched Medium Load Test Specimens 393
Figure 7.230 Surface Integrity Stress Concentration Factor (Longitudinal) Vs. Fatigue Cycles – CVD Endmill Trimmed - Notched Medium Load Test Specimens 394
Figure 7.231 Percent Compliance Change Vs. Fatigue Cycles for A2 – L – 1 396
Figure 7.232 Damage at 500K Cycles, 15.94%, Test Specimen.....396
Figure 7.233 Damage (20.94%) & Ultimate Failure at 546648 Cycles, Test 397
Figure 7.234 Percent Compliance Change Vs. Fatigue Cycles for A2 – L – 2 397
Figure 7.235 Damage at 500K Cycles, 12.61%, Test Specimen.....398
Figure 7.236 Damage (27.45%) & Ultimate Failure at 1000010 Cycles, Test 398
Figure 7.237 Percent Compliance Change Vs. Fatigue Cycles for A2 – L – 3 399
Figure 7.238 Damage at 500K Cycles, 8.29%, Test Specimen A2 – L - 3 399
Figure 7.239 Damage (18.84%) & Ultimate Failure at 1000010 Cycles, Test 400
Figure 7.240 Percent Compliance Change Vs. Fatigue Cycles for A2 – L – 4 400
Figure 7.241 Damage at 500K Cycles, 15.84%, Test Specimen.....401
Figure 7.242 Damage (52.18%) & Ultimate Failure at 582553 Cycles, Test 401
Figure 7.243 Percent Compliance Change Vs. Fatigue Cycles for B2 – L – 1.....402
Figure 7.244 Damage at 500K Cycles, 8.98%, Test Specimen B2-L-1.....403
Figure 7.245 Damage (18.92%) & Ultimate Failure at 1000010 Cycles, Test Specimen B2-L-1.....403
Figure 7.246 Percent Compliance Change Vs. Fatigue Cycles for B2 – L – 2.....404
Figure 7.247 Damage at 500K Cycles, 10.29%, Test Specimen B2-L-2.....404
Figure 7.248 Damage (21.16%) & Ultimate Failure at 1000010 Cycles, Test Specimen B2-L-3.....405

Figure 7.249 Percent Compliance Change Vs. Fatigue Cycles for B2 – L – 3 405
Figure 7.250 Damage at 500K Cycles, 9.27%, Test Specimen B2-L-3 406
Figure 7.251 Damage (21.23%) & Ultimate Failure at 1000010 Cycles, Test Specimen B2-L-3 406
Figure 7.252 Summary Plot of % Compliance Change Vs. (N) Cycles for AWJ Trimmed Notched Specimens – Low Load 407
Figure 7.253 Summary Plot of % Compliance Change Vs. (N) Cycles for CVD Endmill Trimmed Notched Specimens – Low Load 407
Figure 7.254 Summary Plot of % Compliance Change Vs. (N) Cycles for AWJ Vs. CVD Endmill Trimmed Notched Specimens – Low Load 408
Figure 7.255 Graphical Determination of radius (ρ) from surface profile of specimen A2 – L – 1 409
Figure 7.256 Graphical Determination of radius (ρ) from surface profile of specimen A2 – L – 2 410
Figure 7.257 Graphical Determination of radius (ρ) from surface profile of specimen A2 – L – 3 411
Figure 7.258 Graphical Determination of radius (ρ) from surface profile of specimen A2 – L – 4 412
Figure 7.259 Graphical Determination of radius (ρ) from surface profile of specimen B2 – L – 1 413
Figure 7.260 Graphical Determination of radius (ρ) from surface profile of specimen B2 – L – 2 414
Figure 7.261 Graphical Determination of radius (ρ) from surface profile of specimen B2 – L – 3 415
Figure 7.262 Surface Finish - R_a (longitudinal) Vs. Fatigue Cycles – AWJ Trimmed – Notched Low Load Specimens 416
Figure 7.263 Surface Finish – R_z (longitudinal) Vs. Fatigue Cycles – AWJ Trimmed - Notched – Low Load Test Specimens 417
Figure 7.264 Surface Finish – R_t (longitudinal) Vs. Fatigue Cycles – AWJ trimmed – Notched – Low Load Test Specimens 417
Figure 7.265 Surface Finish – R_{sk} (longitudinal) Vs. Fatigue Cycles – AWJ Trimmed – Notched Low Load Test Specimens 417
Figure 7.266 Surface Finish – R_{ku} (longitudinal) Vs. Fatigue Cycles – AWJ Trimmed – Notched Low Load Test Specimens 418
Figure 7.267 Surface Finish – (R_t/R_z) (Longitudinal) Vs. Fatigue Cycles – AWJ Trimmed – Notched Low Load Test Specimens 418
Figure 7.268 Surface Integrity Stress Concentration Factor (Longitudinal) Vs. Fatigue Cycles – AWJ Trimmed - Notched Low Load Test Specimens 418
Figure 7.269 Surface Finish - R_a (longitudinal) Vs. Fatigue Cycles – CVD Endmill Trimmed – Notched Low Load Specimens 419
Figure 7.270 Surface Finish – R_z (longitudinal) Vs. Fatigue Cycles – CVD Endmill Trimmed - Notched – Low Load Test Specimens 419
Figure 7.271 Surface Finish – R_t (longitudinal) Vs. Fatigue Cycles – CVD Endmill trimmed – Notched – Low Load Test Specimens 419
Figure 7.272 Surface Finish – R_{sk} (longitudinal) Vs. Fatigue Cycles – CVD Endmill Trimmed – Notched Low Load Test Specimens 420
Figure 7.273 Surface Finish – R_{ku} (longitudinal) Vs. Fatigue Cycles – CVD Endmill Trimmed – Notched Low Load Test Specimens 420
Figure 7.274 Surface Finish – (R_t/R_z) (Longitudinal) Vs. Fatigue Cycles – CVD Endmill Trimmed – Notched Low Load Test Specimens 420
Figure 7.275 Surface Integrity Stress Concentration Factor (Longitudinal) Vs. Fatigue Cycles – CVD Endmill Trimmed - Notched Low Load Test Specimens 421
Figure 8.1 AWJ Trimmed – Unnotched Test Specimens – Stress Vs. Log (N) cycles 424
Figure 8.2 CVD Endmill Trimmed – Unnotched Test Specimens – Stress Vs. Log (N) cycles 425
Figure 8.3 AWJ Trimmed – Notched Test Specimens – Stress Vs. Log (N) cycles 425
Figure 8.4 CVD Endmill Trimmed – Notched Test Specimens – Stress Vs. Log (N) cycles 426
Figure 8.5 Progress of Damage in an AWJ Unnotched Test Specimen 427
Figure 8.6 Damage curve for AWJ Unnotched High Load Test Specimen 431
Figure 8.7 Damage Zones for AWJ Unnotched High Load Test Specimen 431
Figure 8.8 Damage Progression for a CVD Endmill Trimmed – High Load Specimen 432
Figure 8.9 Damage zones for AWJ Trimmed Medium Load Specimen 433

Figure 8.10 Damage zones for AWJ Trimmed Low Load Specimen 434
Figure 8.11 Damage Vs. Fatigue Cycles – (Test Specimen – A1 – H – 2) Testing Vs. Analytical Modeling.....435
Figure 8.12 Damage Vs. Fatigue Cycles – (Test Specimen – A1 – H – 3) Testing Vs. Analytical Modeling.....436
Figure 8.13 Damage Vs. Fatigue Cycles – (Test Specimen – A1 – H – 4) Testing Vs. Analytical Modeling.....436
Figure 8.14 Damage Vs. Fatigue Cycles – (Test Specimen – B1 – H – 1) Testing Vs. Analytical Modeling.....437
Figure 8.15 Damage Vs. Fatigue Cycles – (Test Specimen – B1 – H – 2) Testing Vs. Analytical Modeling.....437
Figure 8.16 Damage Vs. Fatigue Cycles – (Test Specimen – B1 – H – 3) Testing Vs. Analytical Modeling.....438
Figure 8.17 Damage Vs. Fatigue Cycles – (Test Specimen – A1 – M – 1) Testing Vs. Analytical Modeling.....439
Figure 8.18 Damage Vs. Fatigue Cycles – (Test Specimen – A1 – M – 2) Testing Vs. Analytical Modeling.....439
Figure 8.19 Damage Vs. Fatigue Cycles – (Test Specimen – A1 – M – 3) Testing Vs. Analytical Modeling.....440
Figure 8.20 Damage Vs. Fatigue Cycles – (Test Specimen – B1 – M – 1) Testing Vs. Analytical Modeling.....440
Figure 8.21 Damage Vs. Fatigue Cycles – (Test Specimen – B1 – M – 2) Testing Vs. Analytical Modeling.....441
Figure 8.22 Damage Vs. Fatigue Cycles – (Test Specimen – B1 – M – 3) Testing Vs. Analytical Modeling.....441
Figure 8.23 Damage Vs. Fatigue Cycles – (Test Specimen – A1 – L– 1) Testing Vs. Analytical Modeling 442
Figure 8.24 Damage Vs. Fatigue Cycles – (Test Specimen – A1 – L– 2) Testing Vs. Analytical Modeling 443
Figure 8.25 Damage Vs. Fatigue Cycles – (Test Specimen – A1 – L– 3) Testing Vs. Analytical Modeling 443
Figure 8.26 Damage Vs. Fatigue Cycles – (Test Specimen – B1 – L– 1) Testing Vs. Analytical Modeling 444
Figure 8.27 Damage Vs. Fatigue Cycles – (Test Specimen – B1 – L– 3) Testing Vs. Analytical Modeling 444
Figure 8.28 Damage Vs. Fatigue Cycles – (Test Specimen – A1 – L– 4) Testing Vs. Analytical Modeling 445
Figure 8.29 Damage Vs. Fatigue Cycles – (Test Specimen – A2 – H – 3) Testing Vs. Analytical Modeling.....448
Figure 8.30 Damage Vs. Fatigue Cycles – (Test Specimen – A2 – H – 4) Testing Vs. Analytical Modeling.....448
Figure 8.31 Damage Vs. Fatigue Cycles – (Test Specimen – B2 – H – 1) Testing Vs. Analytical Modeling.....449
Figure 8.32 Damage Vs. Fatigue Cycles – (Test Specimen – B2 – H – 2) Testing Vs. Analytical Modeling.....449
Figure 8.33 Damage Vs. Fatigue Cycles – (Test Specimen – B2 – H – 3) Testing Vs. Analytical Modeling.....450
Figure 8.34 Damage Vs. Fatigue Cycles – (Test Specimen – B2 – H – 4) Testing Vs. Analytical Modeling.....450
Figure 8.35 Damage Vs. Fatigue Cycles – (Test Specimen – A2 – M – 1) Testing Vs. Analytical Modeling.....451
Figure 8.36 Damage Vs. Fatigue Cycles – (Test Specimen – A2 – M – 2) Testing Vs. Analytical Modeling.....452
Figure 8.37 Damage Vs. Fatigue Cycles – (Test Specimen – A2 – M – 3) Testing Vs. Analytical Modeling.....452
Figure 8.38 Damage Vs. Fatigue Cycles – (Test Specimen – A2 – M – 4) Testing Vs. Analytical Modeling.....453
Figure 8.39 Damage Vs. Fatigue Cycles – (Test Specimen – B2 – M – 1) Testing Vs. Analytical Modeling.....454
Figure 8.40 Damage Vs. Fatigue Cycles – (Test Specimen – B2 – M – 2) Testing Vs. Analytical Modeling.....454
Figure 8.41 Damage Vs. Fatigue Cycles – (Test Specimen – B2 – M – 3) Testing Vs. Analytical Modeling.....455
Figure 8.42 Damage Vs. Fatigue Cycles – (Test Specimen – A2 – L – 1) Testing Vs. Analytical Modeling 456
Figure 8.43 Damage Vs. Fatigue Cycles – (Test Specimen – A2 – L – 2) Testing Vs. Analytical Modeling 456
Figure 8.44 Damage Vs. Fatigue Cycles – (Test Specimen – A2 – L – 3) Testing Vs. Analytical Modeling 457
Figure 8.45 Damage Vs. Fatigue Cycles – (Test Specimen – A2 – L – 4) Testing Vs. Analytical Modeling 457
Figure 8.46 Damage Vs. Fatigue Cycles – (Test Specimen – B2 – L – 1) Testing Vs. Analytical Modeling.....458
Figure 8.47 Damage Vs. Fatigue Cycles – (Test Specimen – B2 – L – 2) Testing Vs. Analytical Modeling.....458
Figure 8.48 Damage Vs. Fatigue Cycles – (Test Specimen – B2 – L – 3) Testing Vs. Analytical Modeling.....459
Figure 8.49 Unnotched AWJ Trimmed Specimens, Damage Vs. Log (N) Cycles 462
Figure 8.50 Unnotched CVD Endmill Trimmed Specimens, Damage Vs. Log (N) Cycles.....463
Figure 8.51 Notched AWJ Trimmed Specimens, Damage Vs. Log (N) Cycles 464
Figure 8.52 Notched CVD Endmill Trimmed Specimens, Damage Vs. Log (N) Cycles.....465
Figure B 1.1 Surface Profile (Longitudinal) of AWJ Trimmed Fatigue Test 565
Figure B 1.2 Surface Profile (Longitudinal) of AWJ Trimmed Fatigue Test 565
Figure B 1.3 Surface Profile (Longitudinal) of AWJ Trimmed Fatigue Test 566
Figure B 1.4 Surface Profile (Longitudinal) of AWJ Trimmed Fatigue Test 566
Figure B 1.5 Surface Profile (Longitudinal) of CVD Trimmed Fatigue Test 567
Figure B 1.6 Surface Profile (Longitudinal) of CVD Trimmed Fatigue Test 567
Figure B 1.7 Surface Profile (Longitudinal) of CVD Trimmed Fatigue Test 568
Figure B 1.8 Surface Profile (Longitudinal) of CVD Trimmed Fatigue Test 568
Figure B 1.9 Surface Profile (Longitudinal) of AWJ Trimmed Fatigue Test 569
Figure B 1.10 Surface Profile (Longitudinal) of AWJ Trimmed Fatigue Test 569

Figure B 1.11 Surface Profile (Longitudinal) of AWJ Trimmed Fatigue Test 570
Figure B 1.12 Surface Profile (Longitudinal) of AWJ Trimmed Fatigue Test 570
Figure B 1.13 Surface Profile (Longitudinal) of CVD Trimmed Fatigue Test 571
Figure B 1.14 Surface Profile (Longitudinal) of CVD Trimmed Fatigue Test 571
Figure B 1.15 Surface Profile (Longitudinal) of CVD Trimmed Fatigue Test 572
Figure B 1.17 Surface Profile (Longitudinal) of AWJ Trimmed Fatigue Test 573
Figure B 1.18 Surface Profile (Longitudinal) of AWJ Trimmed Fatigue Test 573
Figure B 1.19 Surface Profile (Longitudinal) of AWJ Trimmed Fatigue Test 574
Figure B 1.20 Surface Profile (Longitudinal) of CVD Trimmed Fatigue Test 574
Figure B 1.21 Surface Profile (Longitudinal) of CVD Trimmed Fatigue Test 575
Figure B 1.22 Surface Profile (Longitudinal) of CVD Trimmed Fatigue Test 575
Figure B 1.23 Surface Profile (Longitudinal) of CVD Trimmed Fatigue Test 576
Figure B 1.24 Surface Profile (Longitudinal) of AWJ Trimmed Fatigue Test 576
Figure B 1.25 Surface Profile (Longitudinal) of AWJ Trimmed Fatigue Test 577
Figure B 1.26 Surface Profile (Longitudinal) of AWJ Trimmed Fatigue Test 577
Figure B 1.27 Surface Profile (Longitudinal) of AWJ Trimmed Fatigue Test 578
Figure B 1.28 Surface Profile (Longitudinal) of CVD Trimmed Fatigue Test 578
Figure B 1.29 Surface Profile (Longitudinal) of CVD Trimmed Fatigue Test 579
Figure B 1.30 Surface Profile (Longitudinal) of CVD Trimmed Fatigue Test 579
Figure B 1.31 Surface Profile (Longitudinal) of CVD Trimmed Fatigue Test 580
Figure B 1.32 Surface Profile (Longitudinal) of AWJ Trimmed Fatigue Test 580
Figure B 1.33 Surface Profile (Longitudinal) of AWJ Trimmed Fatigue Test 581
Figure B 1.34 Surface Profile (Longitudinal) of AWJ Trimmed Fatigue Test 581
Figure B 1.35 Surface Profile (Longitudinal) of AWJ Trimmed Fatigue Test 582
Figure B 1.36 Surface Profile (Longitudinal) of CVD Trimmed Fatigue Test 582
Figure B 1.37 Surface Profile (Longitudinal) of CVD Trimmed Fatigue Test 583
Figure B 1.38 Surface Profile (Longitudinal) of CVD Trimmed Fatigue Test 583
Figure B 1.39 Surface Profile (Longitudinal) of CVD Trimmed Fatigue Test 584
Figure B 1.40 Surface Profile (Longitudinal) of AWJ Trimmed Fatigue Test 584
Figure B 1.41 Surface Profile (Longitudinal) of AWJ Trimmed Fatigue Test 585
Figure B 1.42 Surface Profile (Longitudinal) of AWJ Trimmed Fatigue Test 585
Figure B 1.43 Surface Profile (Longitudinal) of AWJ Trimmed Fatigue Test 586
Figure B 1.44 Surface Profile (Longitudinal) of CVD Trimmed Fatigue Test 586
Figure B 1.45 Surface Profile (Longitudinal) of CVD Trimmed Fatigue Test 587
Figure B 1.46 Surface Profile (Longitudinal) of CVD Trimmed Fatigue Test 587
Figure B 1.47 Surface Profile (Longitudinal) of CVD Trimmed Fatigue Test 588
Figure C 2-1 Damage Progression in (A2-H-1) Test specimen to 2k Cycles 696
Figure C 2-2 Damage Progression in (A2-H-1) Test specimen to 6k Cycles 697
Figure C 2-3 Damage Progression in (A2-H-1) Test specimen to 10k Cycles 698
Figure C 2-4 Damage Progression in (A2-H-1Test specimen to 30k Cycles 699
Figure C 2-5 Damage Progression in (A2-H-1) Test specimen to 50k Cycles 700
Figure C 2-6 Damage Progression in (A2-H-1) Test specimen to 70k Cycles 701
Figure C 2-7 Damage Progression in (A2-H-1) Test specimen to 90k Cycles 702
Figure C 2-8 Damage Progression in (A2-H-1) Test specimen to 200k Cycles 703
Figure C 2-9 Damage Progression in (A2-H-1) Test specimen to 400k Cycles 704
Figure C 2-10 Damage Progression in (A2-H-1) Test specimen to 600k Cycles 705
Figure C 2-11 Damage Progression in (A2-H-1) Test specimen to 800k Cycles 706
Figure C 2-12 Damage Progression in (A2-H-1) Test specimen to 1000k Cycles 707
Figure C 2-13 Damage Progression in (A2-H-2) Test specimen to 2k Cycles 708
Figure C 2-14 Damage Progression in (A2-H-2) Test specimen to 6k Cycles 709
Figure C 2-15 Damage Progression in (A2-H-2) Test specimen to 10k Cycles 710
Figure C 2-16 Damage Progression in (A2-H-2) Test specimen to 30k Cycles 711
Figure C 2-17 Damage Progression in (A2-H-2) Test specimen to 50k Cycles 712

Figure C 2-18 Damage Progression in (A2-H-2) Test specimen to 70k Cycles 713
Figure C 2-19 Damage Progression in (A2-H-2) Test specimen to 90k Cycles 714
Figure C 2-20 Damage Progression in (A2-H-2) Test specimen to 200k Cycles 715
Figure C 2-21 Damage Progression in (A2-H-2) Test specimen to 400k Cycles 716
Figure C 2-22 Damage Progression in (A2-H-2) Test specimen to 600k Cycles 717
Figure C 2-23 Damage Progression in (A2-H-2) Test specimen to 800k Cycles 718
Figure C 2-24 Damage Progression in (A2-H-2) Test specimen to 1000k Cycles 719
Figure C 2-25 Damage Progression in (A2-H-2) Test specimen to Failure 720
Figure C 2-26 Damage Progression in (A2-H-3) Test specimen to 5k Cycles 721
Figure C 2-27 Damage Progression in (A2-H-3) Test specimen to 40k Cycles 722
Figure C 2-28 Damage Progression in (A2-H-3) Test specimen to 80k Cycles 723
Figure C 2-29 Damage Progression in (A2-H-3) Test specimen to Failure 724
Figure C 2-30 Damage Progression in (A2-H-4) Test specimen to 2k Cycles 725
Figure C 2-31 Damage Progression in (A2-H-4) Test specimen to 40k Cycles 726
Figure C 2-32 Damage Progression in (A2-H-4) Test specimen to 80k Cycles 727
Figure C 2-33 Damage Progression in (A2-H-4) Test specimen to 150k Cycles 728
Figure C 2-34 Damage Progression in (A2-H-4) Test specimen to Failure 729
Figure C 2-35 Damage Progression in (B2-H-1) Test specimen to 5k Cycles 730
Figure C 2-36 Damage Progression in (B2-H-1) Test specimen to 40k Cycles 731
Figure C 2-37 Damage Progression in (B2-H-1) Test specimen to 80k Cycles 732
Figure C 2-38 Damage Progression in (B2-H-1) Test specimen to 150k Cycles 733
Figure C 2-39 Damage Progression in (B2-H-1) Test specimen to Failure 734
Figure C 2-40 Damage Progression in (B2-H-2) Test specimen to 5k Cycles 735
Figure C 2-41 Damage Progression in (B2-H-2) Test specimen to 40k Cycles 736
Figure C 2-42 Damage Progression in (B2-H-2) Test specimen to 80k Cycles 737
Figure C 2-43 Damage Progression in (B2-H-2) Test specimen to Failure 738
Figure C 2-44 Damage Progression in (B2-H-3) Test specimen to 5k Cycles 739
Figure C 2-45 Damage Progression in (B2-H-3) Test specimen to 40k Cycles 740
Figure C 2-46 Damage Progression in (B2-H-3) Test specimen to 80k Cycles 741
Figure C 2-47 Damage Progression in (B2-H-3) Test specimen to Failure 742
Figure C 2-48 Damage Progression in (B2-H-4) Test specimen to 2k Cycles 743
Figure C 2-49 Damage Progression in (B2-H-4) Test specimen to 6k Cycles 744
Figure C 2-50 Damage Progression in (B2-H-4) Test specimen to 10k Cycles 745
Figure C 2-51 Damage Progression in (B2-H-4) Test specimen to Failure 746
Figure C 2-52 Damage Progression in (A2-M-1) Test specimen to 5k Cycles 747
Figure C 2-53 Damage Progression in (A2-M-1) Test specimen to 40k Cycles 748
Figure C 2-54 Damage Progression in (A2-M-1) Test specimen to 80k Cycles 749
Figure C 2-55 Damage Progression in (A2-M-1) Test specimen to 150k Cycles 750
Figure C 2-56 Damage Progression in (A2-M-1) Test specimen to 250k Cycles 751
Figure C 2-57 Damage Progression in (A2-M-1) Test specimen to 350k Cycles 752
Figure C 2-58 Damage Progression in (A2-M-1) Test specimen to 450k Cycles 753
Figure C 2-59 Damage Progression in (A2-M-1) Test specimen to Failure 754
Figure C 2-60 Damage Progression in (A2-M-2) Test specimen to 5k cycles 755
Figure C 2-61 Damage Progression in (A2-M-2) Test specimen to 40k cycles 756
Figure C 2-62 Damage Progression in (A2-M-2) Test specimen to 80k cycles 757
Figure C 2-63 Damage Progression in (A2-M-2) Test specimen to 150k cycles 758
Figure C 2-64 Damage Progression in (A2-M-2) Test specimen to 250k cycles 759
Figure C 2-65 Damage Progression in (A2-M-2) Test specimen to 350k cycles 760
Figure C 2-66 Damage Progression in (A2-M-2) Test specimen to Failure 761
Figure C 2-67 Damage Progression in (A2-M-3) Test specimen to 5k cycles 762
Figure C 2-68 Damage Progression in (A2-M-3) Test specimen to 40k cycles 763
Figure C 2-69 Damage Progression in (A2-M-3) Test specimen to 80k cycles 764
Figure C 2-70 Damage Progression in (A2-M-3) Test specimen to 150k cycles 765

Figure C 2-71 Damage Progression in (A2-M-3) Test specimen to 250k cycles 766
Figure C 2-72 Damage Progression in (A2-M-3) Test specimen to 350k cycles 767
Figure C 2-73 Damage Progression in (A2-M-3) Test specimen to Failure 768
Figure C 2-74 Damage Progression in (A2-M-4) Test specimen to 5k cycles 769
Figure C 2-75 Damage Progression in (A2-M-4) Test specimen to 40k cycles 770
Figure C 2-76 Damage Progression in (A2-M-4) Test specimen to 80k cycles 771
Figure C 2-77 Damage Progression in (A2-M-4) Test specimen to 150k cycles 772
Figure C 2-78 Damage Progression in (A2-M-4) Test specimen to Failure 774
Figure C 2-79 Damage Progression in (B2-M-1) Test specimen to 5k Cycles 775
Figure C 2-80 Damage Progression in (B2-M-1) Test specimen to 40k Cycles 776
Figure C 2-81 Damage Progression in (B2-M-1) Test specimen to 80k Cycles 777
Figure C 2-82 Damage Progression in (B2-M-1) Test specimen to 150k Cycles 778
Figure C 2-83 Damage Progression in (B2-M-1) Test specimen to 250k Cycles 779
Figure C 2-84 Damage Progression in (B2-M-1) Test specimen to 350k Cycles 780
Figure C 2-85 Damage Progression in (B2-M-1) Test specimen to Failure 781
Figure C 2-86 Damage Progression in (B2-M-2) Test specimen to 10k Cycles 782
Figure C 2-87 Damage Progression in (B2-M-2) Test specimen to 50k Cycles 784
Figure C 2-88 Damage Progression in (B2-M-2) Test specimen to 90k Cycles 785
Figure C 2-89 Damage Progression in (B2-M-2) Test specimen to 175k Cycles 786
Figure C 2-90 Damage Progression in (B2-M-2) Test specimen to 275k Cycles 787
Figure C 2-91 Damage Progression in (B2-M-2) Test specimen to 375k Cycles 788
Figure C 2-92 Damage Progression in (B2-M-2) Test specimen to Failure 789
Figure C 2-93 Damage Progression in (B2-M-3) Test specimen to 5k Cycles 790
Figure C 2-94 Damage Progression in (B2-M-3) Test specimen to 40k Cycles 791
Figure C 2-95 Damage Progression in (B2-M-3) Test specimen to 80k Cycles 792
Figure C 2-96 Damage Progression in (B2-M-3) Test specimen to 150k Cycles 793
Figure C 2-97 Damage Progression in (B2-M-3) Test specimen to 250k Cycles 794
Figure C 2-98 Damage Progression in (B2-M-3) Test specimen to 350k Cycles 795
Figure C 2-99 Damage Progression in (B2-M-3) Test specimen to 450k Cycles 796
Figure C 2-100 Damage Progression in (B2-M-3) Test specimen to Failure 797
Figure C 2-101 Damage Progression in (A2-L-1) Test specimen to 5k Cycles 798
Figure C 2-102 Damage Progression in (A2-L-1) Test specimen to 40k Cycles 799
Figure C 2-103 Damage Progression in (A2-L-1) Test specimen to 80k Cycles 800
Figure C 2-104 Damage Progression in (A2-L-1) Test specimen to 150k Cycles 801
Figure C 2-105 Damage Progression in (A2-L-1) Test specimen to 250k Cycles 802
Figure C 2-106 Damage Progression in (A2-L-1) Test specimen to 350k Cycles 803
Figure C 2-107 Damage Progression in (A2-L-1) Test specimen to 450k Cycles 804
Figure C 2-108 Damage Progression in (A2-L-1) Test specimen to Failure 805
Figure C 2-109 Damage Progression in (A2-L-2) Test specimen to 5k Cycles 806
Figure C 2-110 Damage Progression in (A2-L-2) Test specimen to 40k Cycles 807
Figure C 2-111 Damage Progression in (A2-L-2) Test specimen to 80k Cycles 808
Figure C 2-112 Damage Progression in (A2-L-2) Test specimen to 150k Cycles 809
Figure C 2-113 Damage Progression in (A2-L-2) Test specimen to 250k Cycles 810
Figure C 2-114 Damage Progression in (A2-L-2) Test specimen to 350k Cycles 811
Figure C 2-115 Damage Progression in (A2-L-2) Test specimen to 450k Cycles 812
Figure C 2-116 Damage Progression in (A2-L-2) Test specimen to 550k Cycles 813
Figure C 2-117 Damage Progression in (A2-L-2) Test specimen to 650k Cycles 814
Figure C 2-118 Damage Progression in (A2-L-2) Test specimen to 750k Cycles 815
Figure C 2-119 Damage Progression in (A2-L-2) Test specimen to 850k Cycles 816
Figure C 2-120 Damage Progression in (A2-L-2) Test specimen to 950k Cycles 817
Figure C 2-121 Damage Progression in (A2-L-2) Test specimen to Failure 818
Figure C 2-122 Damage Progression in (A2-L-3) Test specimen to 5k Cycles 819
Figure C 2-123 Damage Progression in (A2-L-3) Test specimen to 40k Cycles 820

Figure C 2-124 Damage Progression in (A2-L-3) Test specimen to 80k Cycles 821
Figure C 2-125 Damage Progression in (A2-L-3) Test specimen to 150k Cycles 822
Figure C 2-126 Damage Progression in (A2-L-3) Test specimen to 250k Cycles 823
Figure C 2-127 Damage Progression in (A2-L-3) Test specimen to 350k Cycles 824
Figure C 2-128 Damage Progression in (A2-L-3) Test specimen to 450k Cycles 825
Figure C 2-129 Damage Progression in (A2-L-3) Test specimen to 550k Cycles 826
Figure C 2-130 Damage Progression in (A2-L-3) Test specimen to 650k Cycles 827
Figure C 2-131 Damage Progression in (A2-L-3) Test specimen to 750k Cycles 828
Figure C 2-132 Damage Progression in (A2-L-3) Test specimen to 850k Cycles 829
Figure C 2-133 Damage Progression in (A2-L-3) Test specimen to 950k Cycles 830
Figure C 2-134 Damage Progression in (A2-L-3) Test specimen to Failure 831
Figure C 2-135 Damage Progression in (A2-L-4) Test specimen to 5k Cycles 832
Figure C 2-136 Damage Progression in (A2-L-4) Test specimen to 40k Cycles 833
Figure C 2-137 Damage Progression in (A2-L-4) Test specimen to 80k Cycles 834
Figure C 2-138 Damage Progression in (A2-L-4) Test specimen to 150k Cycles 835
Figure C 2-139 Damage Progression in (A2-L-4) Test specimen to 250k Cycles 836
Figure C 2-140 Damage Progression in (A2-L-4) Test specimen to 350k Cycles 837
Figure C 2-141 Damage Progression in (A2-L-4) Test specimen to 450k Cycles 838
Figure C 2-142 Damage Progression in (A2-L-4) Test specimen to 550k Cycles 839
Figure C 2-143 Damage Progression in (A2-L-4) Test specimen to Failure 840
Figure C 2-144 Damage Progression in (B2-L-1) Test specimen to 5k Cycles 841
Figure C 2-145 Damage Progression in (B2-L-1) Test specimen to 40k Cycles 842
Figure C 2-146 Damage Progression in (B2-L-1) Test specimen to 80k Cycles 843
Figure C 2-147 Damage Progression in (B2-L-1) Test specimen to 150k Cycles 844
Figure C 2-148 Damage Progression in (B2-L-1) Test specimen to 250k Cycles 845
Figure C 2-149 Damage Progression in (B2-L-1) Test specimen to 350k Cycles 846
Figure C 2-150 Damage Progression in (B2-L-1) Test specimen to 450k Cycles 847
Figure C 2-151 Damage Progression in (B2-L-1) Test specimen to 5k Cycles 848
Figure C 2-152 Damage Progression in (B2-L-1) Test specimen to 650k Cycles 849
Figure C 2-153 Damage Progression in (B2-L-1) Test specimen to 750k Cycles 850
Figure C 2-154 Damage Progression in (B2-L-1) Test specimen to 850k Cycles 851
Figure C 2-155 Damage Progression in (B2-L-1) Test specimen to 950k Cycles 852
Figure C 2-156 Damage Progression in (B2-L-1) Test specimen to Failure 853
Figure C 2-157 Damage Progression in (B2-L-2) Test specimen to 5k Cycles 854
Figure C 2-158 Damage Progression in (B2-L-2) Test specimen to 40k Cycles 855
Figure C 2-159 Damage Progression in (B2-L-2) Test specimen to 80k Cycles 856
Figure C 2-160 Damage Progression in (B2-L-2) Test specimen to 150k Cycles 857
Figure C 2-161 Damage Progression in (B2-L-2) Test specimen to 250k Cycles 858
Figure C 2-162 Damage Progression in (B2-L-2) Test specimen to 350k Cycles 859
Figure C 2-163 Damage Progression in (B2-L-2) Test specimen to 450k Cycles 860
Figure C 2-164 Damage Progression in (B2-L-2) Test specimen to 550k Cycles 861
Figure C 2-165 Damage Progression in (B2-L-2) Test specimen to 650k Cycles 862
Figure C 2-166 Damage Progression in (B2-L-2) Test specimen to 750k Cycles 863
Figure C 2-167 Damage Progression in (B2-L-2) Test specimen to 850k Cycles 864
Figure C 2-168 Damage Progression in (B2-L-2) Test specimen to 950k Cycles 865
Figure C 2-169 Damage Progression in (B2-L-2) Test specimen to Failure 866
Figure C 2-170 Damage Progression in (B2-L-3) Test specimen to 5k Cycles 867
Figure C 2-171 Damage Progression in (B2-L-3) Test specimen to 40k Cycles 868
Figure C 2-172 Damage Progression in (B2-L-3) Test specimen to 80k Cycles 869
Figure C 2-173 Damage Progression in (B2-L-3) Test specimen to 150k Cycles 870
Figure C 2-174 Damage Progression in (B2-L-3) Test specimen to 250k Cycles 871
Figure C 2-175 Damage Progression in (B2-L-3) Test specimen to 350k Cycles 872
Figure C 2-176 Damage Progression in (B2-L-3) Test specimen to 450k Cycles 873

Figure C 2-177 Damage Progression in (B2-L-3) Test specimen to 550k Cycles 874
Figure C 2-178 Damage Progression in (B2-L-3) Test specimen to 650k Cycles 875
Figure C 2-179 Damage Progression in (B2-L-3) Test specimen to 750k Cycles 876
Figure C 2-180 Damage Progression in (B2-L-3) Test specimen to 850k Cycles 877
Figure C 2-181 Damage Progression in (B2-L-3) Test specimen to 950k Cycles 878
Figure C 2-182 Damage Progression in (B2-L-3) Test specimen to Failure 879

List of Tables

Table 2.1 Definition of Surface Finish Profile Parameters 20
Table 2.2 Overview of Fatigue Damage Rate Models (source: Bak et. al [61])....75
Table 4.1 Endmill Geometries and Cutting Parameters 95
Table 4.2 Cutting Parameters for AWJ Trimming 96
Table 4.3 Drill Geometries and Drilling Parameters 97
Table 5.1 Example of Measured Surface Roughness of Edge Trimmed Surfaces....102
Table 5.2 Test Matrix for 10 Ply Thick Laminate – Static Mechanical Properties Testing 114
Table 5.3 Specimens Dimensions for 10 Ply Laminate – Static Mechanical Testing....115
Table 5.4 Static Mechanical Testing Results for 10 Ply Thick Laminate....122
Table 6.1 Ply Table for 22 Ply Laminate....127
Table 6.2 Surface Roughness (longitudinal) of Edge Trimmed Surfaces and Trimming Parameters , (a), (b) and (c) 129
Table 6.3 Surface Roughness (transverse) of Edge Trimmed Surfaces, Trimming parameters are same as Table 6.2 (a) and (b) 129
Table 6.4 Surface Roughness (longitudinal) of PCD vs CVD Drilled Holes 138
Table 6.5 Summary of surface finish recordings (longitudinal) of edge trimmed specimens for tension testing....147
Table 6.6 Summary of Tensile Strength Testing Results....167
Table 6.7 Summary of Surface finish and Compressive Strength properties 179
Table 6.8 Summary of Open Hole Tensile Testing Results....203
Table 6.9 Summary of Open Hole Compression testing Results 230
Table 6.10 Maximum Load recorded for Bearing Hole test specimens....236
Table 7.1 Ply Table for 22 Ply Laminate....243
Table 7.2 Fatigue Specimens Edge Trimming Conditions 244
Table 7.3 Fatigue Specimens Drilling Conditions....244
Table 7.4 Surface Finish Data of Test Specimens (Longitudinal) 249
Table 7.5 Surface Finish Data of Test Specimens (Transverse)....250
Table 7.6 Surface Finish Data for CVD Drilled hole....254
Table 7.7 Test Loads & Stresses for Unnotched Fatigue Testing....257
Table 7.8 Test Loads & Stresses for Notched Fatigue Testing 258
Table 7.9 Fatigue Cycles/Loads/Stress & % Compliance Change for Unnotched High Loading Testing....261
Table 7.10 Calculated Surface Integrity Stress Concentration Factors for Unnotched High Load Fatigue Test Specimens....280
Table 7.11 Fatigue Cycles/Loads/Stress & % Compliance Change for Unnotched Medium Loading Testing 288
Table 7.12 Calculated Surface Integrity Stress Concentration factors for Medium Load Test Specimens....312
Table 7.13 Fatigue Cycles/Loads/Stress & % Compliance Change for Unnotched Low Loading Testing 318
Table 7.14 Calculated Surface Integrity Stress Concentration Factor for Low Load Test Specimens....338
Table 7.15 Fatigue Cycles/Loads/Stress & % Compliance Change for Notched High Loading Testing....344
Table 7.16 Calculated Surface Integrity Stress Concentration Factor for Notched Specimens – High Load Testing.362
Table 7.17 Fatigue Cycles/Loads/Stress & % Compliance Change for Notched Medium Loading Testing....368
Table 7.18 Calculated Surface Integrity Stress Concentration Factor for Notched Specimens – Medium Load....389
Table 7.19 Fatigue Cycles/Loads/Stress & % Compliance Change for Notched Low Loading Testing....395
Table 7.20 Calculated Surface Integrity Stress Concentration factor for Notched Specimens – Low Load Testing..416
Table 8.1 Unnotched Test Specimens, Test Variables 430
Table 8.2 Notched Test Specimens, Test Variables 446

Acknowledgements:

I would like to thank my advisor Dr. Ramulu Mamidala for his teachings (technical and life lessons). Without his unwavering humility and willingness to help through all my personal difficult times, this body of work would not be complete. Special thanks to Ms. Sonja Johnson from Boeing, who's teachings, leadership and patience with me as an employee helped this work see its completion. She stood by through many difficult times offering support, guidance and caring. I am also grateful to my committee members, Dr. Kramlich and Dr. Devasia for their teachings, support and patience as I handled personal health issues through the research timeline. While the list of names who helped through the years of my research study is large, of particular mention are the following teammates from Boeing: Alan Draper, Jorge Arriaga, Michael Fink, Kevin Barrick, Richard Reese. Randy Everson, Gary Donovan, Jerry Marsh, Jason Clark and Karen Lynch

I am also grateful to my University of Washington team mates amongst which are Rishi Pahuja, Nishita Anandan, Bill Kuykendall and Wanwisa Kisalang.

I am grateful to my parents, brother and my wife Rubina and sons, Manmeet, Sahej and Lenny for all their love and support through my life.

Finally, while I have learnt many technical lessons through the years of research, the biggest lesion has been the humanity of all around me in supporting me with all the love and caring through many losses of family members and friends over the years and through some serious health issues of mine.

I have realized that the Divine resides in all beings and presents itself when you truly need the Divines presence. May the Divine bless all the beings of the Universe.

Dedication:

In Loving memory of my mother, Daljit Kaur and my friends Amod Wagh and James Zerby

"Chuppa Hua sa Mujhi Mein hai Tu Kahin ai Dost,
Meri Hansi mein Nahi toh meri Aah mein hain" part of Hindi Song

"Somewhere within me, you remain hidden my friend,
If not in my smiles, you are in my sighs" Translated into English

Poet 'Late Janab Majrooh Sultanpuri Sahab'

Chapter 1 - Introduction

1.1 Overview

A composite system is defined as a material system which includes two or more phases on a macroscopic scale whose mechanical properties and performance are designed to be superior to the properties of the individual constituents of the composite. When one of the constituents of the composite material is in the form of fibres, the material system is generally regarded as fibre-reinforced. In history the concept of fibrous reinforcement has been mentioned in biblical references such as the straw-reinforced clay bricks in ancient Egypt and the composite laminate design of the Achilles's shield [1]. For the last three decades, the use of composites has expanded in industries such as aerospace, automotive, marine, sports and others. The application of fibrous laminates has seen greater usage in aerospace due to their higher strengths and higher stiffness properties. In the recent aircraft models developed both by The Boeing Company and Airbus the use of composite material systems such as carbon/epoxy laminates and graphite/titanium has expanded to primary structures such as wings and fuselages. These material systems also provide additional benefits of corrosion and wear resistance compared to the traditionally used Aluminium alloy based material systems [1].

One of the widely used composite laminate material systems in aerospace applications is the Carbon Fibre Reinforced Plastic (CFRP) systems. Carbon Fibres with an average areal weight of 190 g/m^2 in combination with an Epoxy based thermosetting resin curing at 177 Degree C is a commonly used laminate material system. As laminates are anisotropic (mechanical properties are direction dependent), lamination is used to tailor the strength and stiffness direction properties to react to the loading conditions of the service life of the product. Specific strength and specific modulus are often used to quantify the performance characteristics of composites. In general most composites have higher specific strength and specific modulus than metals as shown in Figure 1.1. Carbon/Epoxy composites overall provide one of the best combinations of specific strength and specific modulus.

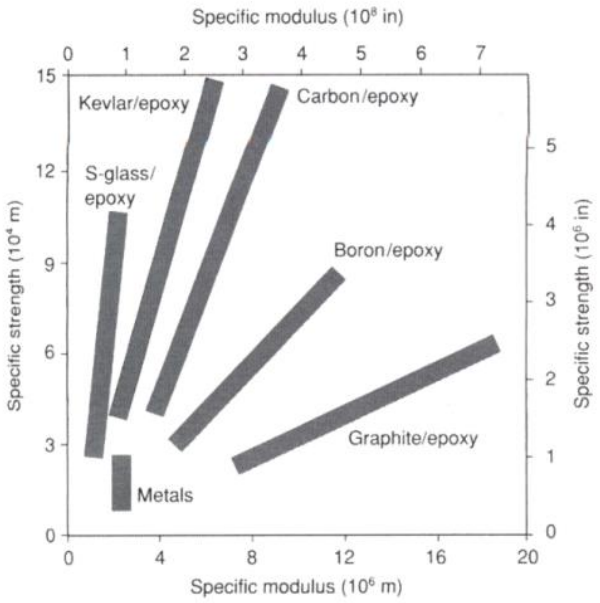

Figure 1.1 Performance Map of Structural Composites (Source: Daniel et. al [1])

Most Carbon/Epoxy composite laminates are manufactured by using the Autoclave Moulding Process. This process uses the material in the prepreg form either laid manually on the moulding tool or with an automated fibre placement machine. Curing is completed using a preset temperature-pressure-vacuum-time cycle. The cooling is controlled to minimize thermal residual stresses and prevent microcracking. While the end product is close to near net shape, post-cure machining processes are always required for edge trimming to specification or desired tolerances and drilling of holes for clearances or fasteners to be used in the end product. Traditional machining processes such as trimming utilizing carbide or polycrystalline (PCD) diamond cutters are used in machining of CFRP material systems. In addition, Abrasive Water Jet (AWJ) cutting of CFRP material systems is now a widely used process in industry. Drilling of holes for fastening for assembly is also a post-cure process that is always used in CFRP component assemblies. Carbide & PCD drills. Unfortunately these post-cure machining & drilling processes often result in defects in the CFRP laminates due to the inhomogeneity and anisotropic nature of the laminates. Defects such as Delamination and Fibre pullout often occur during trimming and drilling operations of CFRP laminates.

The resultant surface integrity of the edges and the drilled holes from the post-cure machining processes plays an important role in the engineering performance of the product.

Surface integrity is used widely to describe both, the on-surface texture (exterior) roughness characteristics and the sub-surface (interior) structure and stress conditions of materials. The sub-surface conditions play an important role in the resultant surface mechanical properties. These sub-surface conditions influence microscopic changes in the fibre/matrix constituent relationship which can result in stress concentrations altering the mechanical properties of the CFRP laminate. The machining processes also result in macroscopic defects which lead to this damage evolving with service loadings which can result in failure of the CFRP laminates in service.

This dissertation proposal focuses on the study of the effects of the resultant surface integrity from the trimming and drilling processes in CFRP Laminates on the residual mechanical strength properties and fatigue performance in service life conditions. The scope of the study also includes the understanding of the defects/damage that is created due to the machining processes and its variables and how it influences the residual monotonic static strength properties. The science of damage evolution under service fatigue conditions is also studied and documented in an effort to create an analytical progressive damage model which will quantitatively predict the progression of damage for various surface integrity conditions due to machining processes.

This dissertation is organized into nine chapters with chapter 1 as Introduction of the research subject. This is followed by Literature Review of past work conducted in the research subject area, Motivation of Research, Goals & Objectives, Research Plan Methodology – listing the plan for this study including the two phases of testing with 2 different laminate thicknesses and ply layups. This is followed by Experimental Testing – Static Mechanical Properties – 10 Ply Thick Laminate, Experimental Testing – Static Mechanical Properties – 22 Ply Thick Laminate and Experimental Testing – Fatigue Cycle Tension-Tension Testing – 22 Ply Thick Laminate. The final three chapters include Damage Progression & Fatigue Life Modeling, Conclusions & Future Work Recommendations and Bibliography.

Finally, Appendix A & B are included with Documentation of surface finish profiles and photomicrographs of damage progression in specimens during fatigue cycle testing

Chapter 2 – Background and Literature Review

2.1 Introduction

With the advent of aerospace travel and its industry in the twentieth century along with its contribution to the advancement of materials science, there has been an increase in usage of composite material systems in aerospace and other industries. The word composite in the term composite material signifies two or more materials are combined on a macroscopic scale to form a useful third material [2]. Composites have been used since ancient times with documented use during Egyptian times such as the straw-reinforced clay bricks. Today's advanced composite material systems consist of two or more phases on a macroscopic scale, whose mechanical performance and properties are designed to be superior to those of the constituent materials acting independently [1]. One of the two phases is usually a stronger and stiffer material used to reinforce a weaker compliant matrix material. The reinforcement can be in the form of:

- Particulates: roughly spherical particles with diameters typically 1-100 μm
- Whiskers: length < 10 mm
- Short (or chopped) fibres: length 10 – 200 mm
- Continuous Fibres: length is in effect infinite

All whiskers, fibres (short & continuous) have a very small diameter relative to their length (high aspect ratio) [3].

The advantages of using the advanced composite materials systems include:

- High Specific Strength (strength/density)
- High Specific Stiffness (modulus/density)
- Tailored properties in load application direction
- Tailored Coefficient of Thermal Expansion (CTE) for critical components
- Excellent Fatigue Performance

Carbon Fibre Reinforced Plastics (CFRP) material systems are used widely in aerospace applications. These systems use Carbon fibre as the reinforcement material with an epoxy based thermosetting resin as the matrix system. The matrix system governs the thermal stability and binds the fibres together. It also provides protection for the fibres from chemically and mechanically induced damage. It also helps transfer and redistribute stresses between fibres, between plies and in areas of discontinuities in load or geometry [3]. The fibres can be aligned in

using a directional approach, unidirectional (UD) for all fibres aligned in the same direction, woven for continuous fibres weaved into a fabric and braided for fibres aligned in two or three non-orthogonal directions.

A CFRP material system is generally used in aerospace applications in the form of a laminate. A single ply of fibre-reinforced plastic called lamina is used as a building block for a laminate. All fibres are anisotropic because the stiffness and strength are higher in the direction of the fibre axis than in the transverse direction. A laminate's stiffness and strength can be varied by stacking different layers of lamina in various angles to each other as shown in Fig 2.1. If the layers are same on each side of the mid plane, the laminate is considered to be symmetric and balance is all plies other than 0° and 90° occur in only plus and minus pairs and are symmetrical about the midplane.

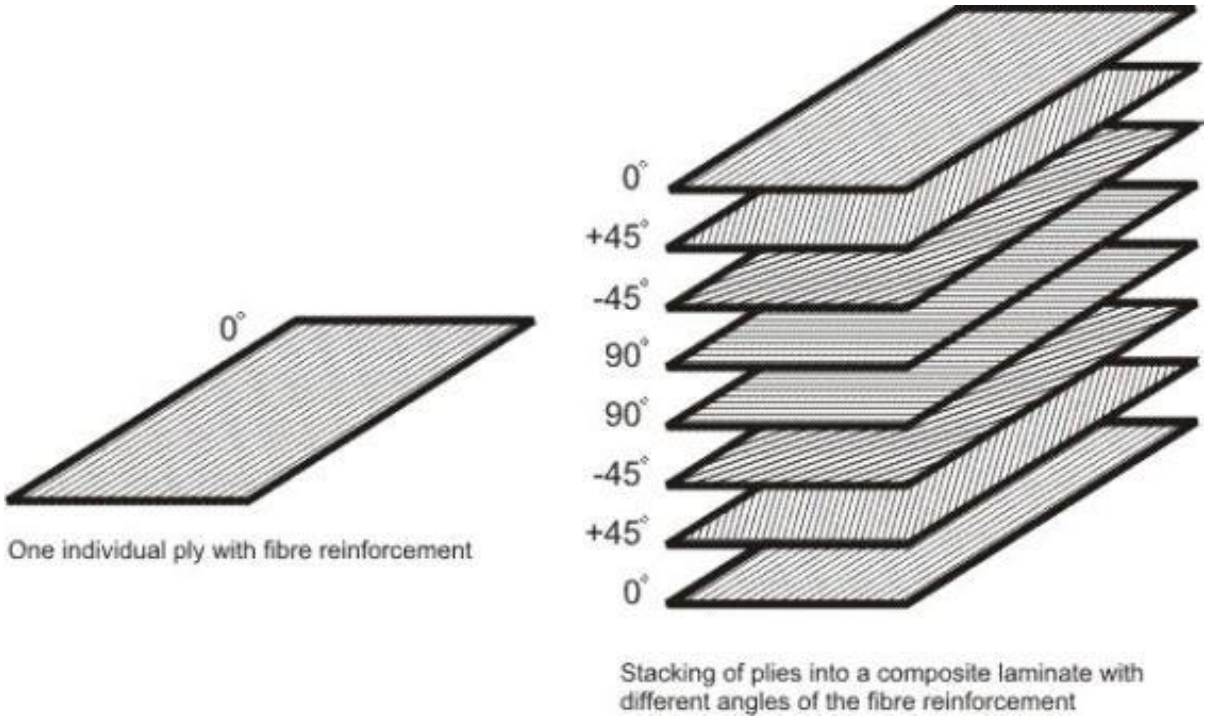

Figure 2.1 Typical Fibre-Reinforced Laminate Construction

2.2 Machining of Composite Laminates

Since CFRP's are anisotropic and inhomogeneous with low thermal conductivity matrix, heat buildup during machining of these materials is usually a problem. The behaviour of a composite material during machining depends on diverse fibre and matrix properties, the fibre orientation

and the relative volume of the matrix and the fibres [4,5]. During machining of composite laminates the tool encounters the matrix and fibre materials alternately with varying responses to machining by both of these materials. The chip formation can be due to fracture or shear or a combination of both depend on the fibre orientation and tool geometry. Since the fibres are abrasive, tooling materials resistant to abrasive wear such as Polycrystalline Diamond (PCD) are widely used in composites machining. The majority of machining operations of CFRP's are either edge machining/trimming and/or drilling of holes in laminates. The process of edge machining/trimming is usually carried out either using the principles of orthogonal cutting with cutters or using Abrasive Water Jet (AWJ) Machining. The drilling of holes in composite laminates is dependent on the drill geometry and the process variables (speed and feed rate) used. All machining processes (trimming & drilling) can cause defects and damage to the laminate both at the macroscopic and microscopic levels. Surface integrity of the machined surfaces is defined as the properties influenced by the physical and chemical effects of the machining processes. Resultant surface integrity of machined specimens depends on the process type, process variables, post-cure laminate condition as well as laminate design (ply angles etc.). The surface texture on the surface (roughness) and the residual stresses in the surface layer can cause defects and damage and stress concentrations within the laminate. This can alter the mechanical properties both monotonic (Static strength) and cyclic (Fatigue) under service life conditions.

2.2.1 Edge Trimming with Cutters

As most CFRP's are near net manufactured, trimming generally is considered a low material removal process compared to the total volume of the material. The largest influence on the machinability of any CFRP laminate is the type of fibre reinforcement used and its mechanical properties. The mechanical properties of high tensile strength, high modulus of elasticity, high yield strength and thermal properties of the fibre reinforcement have a great effect on the machinability of the laminate. To truly understand the mechanics of trimming of CFRP laminates, the cutting mechanism involved with these processes need to be studied. One of the earliest works on the study of cutting mechanisms was carried out by Koplev [6]. He conducted a series of cutting tests on CFRP composite material to study the chip formation process and the machined surface on unidirectional material. His unique methodology of capturing the small chips using the 'macrochip method' is still in use by today's experimental investigators. This method uses the

application of a rubber adhesive to the workpiece surface to collect the small chips, which are then transferred to a double-sided adhesive tape for observation and analysis. His experiments showed that the resultant surface quality of the machined surface was dependent on the fibre orientation, the smoothest surface obtained when the cutting direction was parallel to the fibre orientation. Perpendicular to fibre machining usually resulted in an increase in resultant surface roughness. His conclusions on chip formation were that chips were formed by brittle fracture of both the fibres and the matrix. The chip formation varies if the machining is perpendicular to the fibres or parallel to the fibres. During perpendicular to fibre machining, the tool exerts a compressive force with its front surface on the material causing the composite to fracture and creating a chip. Similarly, on during parallel to the fibre machining process, a compressive force is exerted causing chips to be created but it is accompanied by cracking or delamination on the front of the tool tip which helps in initiation of the next chip creation process as shown in Fig 2.2. Koplev also analyzed the relationship between cutting forces and the chip formation process and tool geometries. He concluded that the principal cutting force was proportional to the depth of cut and varied with the rake angle increasing with its increase.

Cutting Force (F_c) $\propto$ Rake angle

Cutting Force (F_c) $\propto$ Depth of Cut

His work is considered as one of the founding bodies of work in the study of mechanics of orthogonal machining of CFRP composite materials.

Another body of work on the evaluation of machinability and study of chip characteristics during machining of CFRP laminates was conducted by Hoecheng et al [7]. The researchers concluded that during machining three different types of chips are created:

- Powder like chips – produced by fracture
- Ribbon like chips – unbroken segments, produced by fracture with fibre breakage
- Large brush like chips – produced by delamination at the end of a cut

Their study also linked surface roughness to high cutting speeds and lower feed rates, an affect they attributed to heat build-up as a result of poor thermal conductivity.

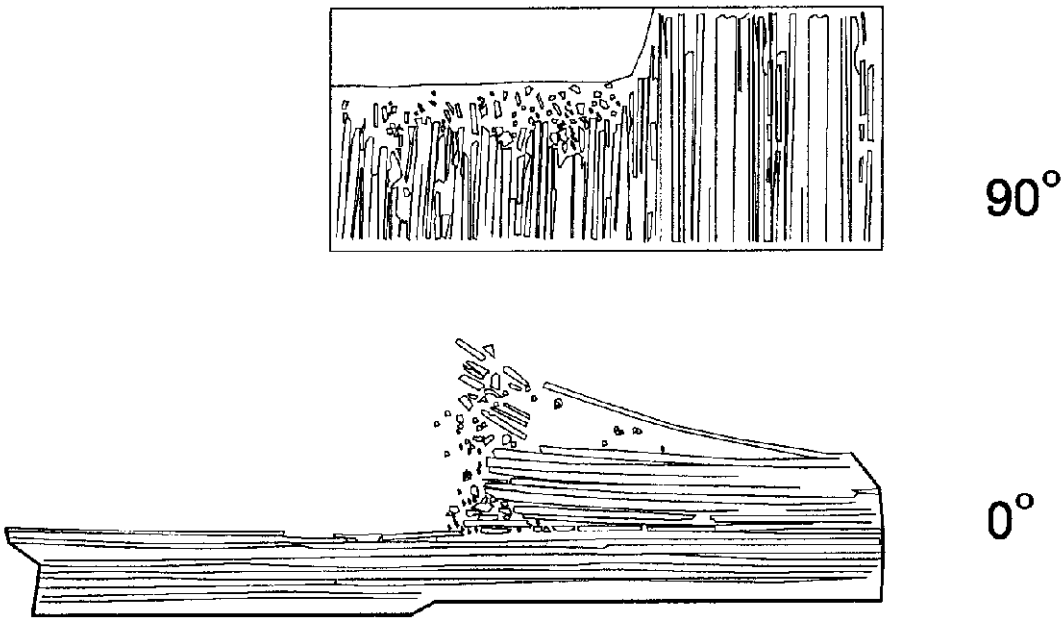

Figure 2.2 Chip Formation of 0° and 90° Fibre Orientation (Source: Koplev [6])

Bhatnagar et al. [8] in their studies observed that the in-plane shear strength of a composite material influenced its machinability. Using the Iosipescu shear test [9] they calculated the shear strength and plotted the variation of in-plane shear strength with the fibre angle. They studied the two process variables, machining direction and Fibre orientation. The machining direction being expressed as the angle between the cutting velocity vector and the fibre orientation in a plane perpendicular to the cutting edge of the tool. The fibre orientation is the angle measured counterclockwise from the datum of the machined surface. For fibre orientation less than 90°, they found that the fibres break in tension and chips are produced ahead of the cutting edge of the tool by shearing the matrix in a plane along the fibre orientation. For Fibre angles greater than 90°, they showed that the fibres experience compression and bending are broken by shearing. They used Merchant's model to create a predictive model for cutting forces by substituting the fibre angle instead of the shear plane angle as shown in Fig 2.3. They also noted that the friction condition on the rake face of the tool changes depending on the fibre orientations. This indicates that the tool wear not only depends on the direction of cutting but also on the individual fibre orientations.

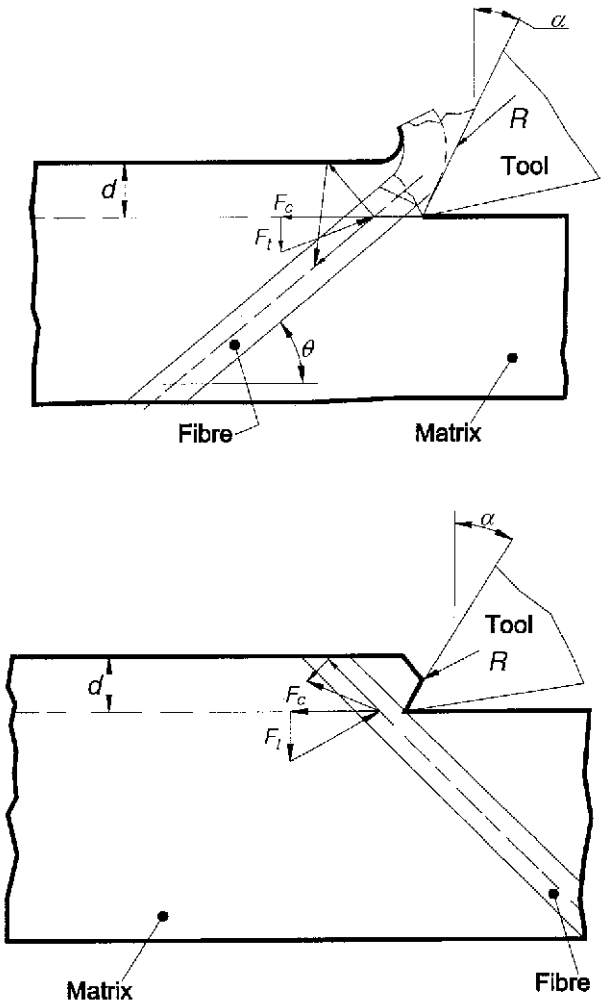

Figure 2.3 Cutting Mechanism of CFRP (Source; Bhatnagar [8])

Cutting forces were predicted by Bhatnagar et al. [8] using a modified Merchant's model.

$$F_c = \frac{\tau A \cos(\beta - \alpha)}{\sin\theta \cos(\theta + \beta - \alpha)} \qquad (2.1)$$

$$F_t = \frac{\tau A \sin(\beta - \alpha)}{\sin\theta \cos(\theta + \beta - \alpha)} \qquad (2.2)$$

F_c = principal cutting force F_t = tangential cutting force

τ = in-plane shear strength for a given fibre angle

A = area of the shear plane

θ = fibre angle

α = rake angle

β = friction angle

Chip formation in orthogonal edge trimming of graphite/epoxy composite was studied by Arola, Ramulu & Wang [10]. They found that the characteristics of chip formation were primarily dependent on Fibre orientation with only secondary effects from tool geometry and operating conditions. An increase in the rake angle of the tool was found to localize the extent of fracture from the tool nose, resulting in smaller discontinuous chips, giving better machined surface quality. They observed three different cutting mechanisms during edge trimming of the unidirectional graphite/epoxy laminate. In 0^o fibre orientations, chip formation mechanisms included failure along the fibre-matrix interface through cantilever bending and fracture perpendicular to the fibre direction. In positive fibre orientations up to 75^o chip formation involved compressive loading induced shear at the tool nose. In the 90^o and negative fibre orientations chip formation and material removal in trimming comprised out-of-plane shear with severe compressive loading induced intralaminar deformation. Chip formation during orthogonal edge trimming of unidirectional graphite/epoxy composite is shown in Figure 2.4 from Wang, Ramulu & Arola [11].

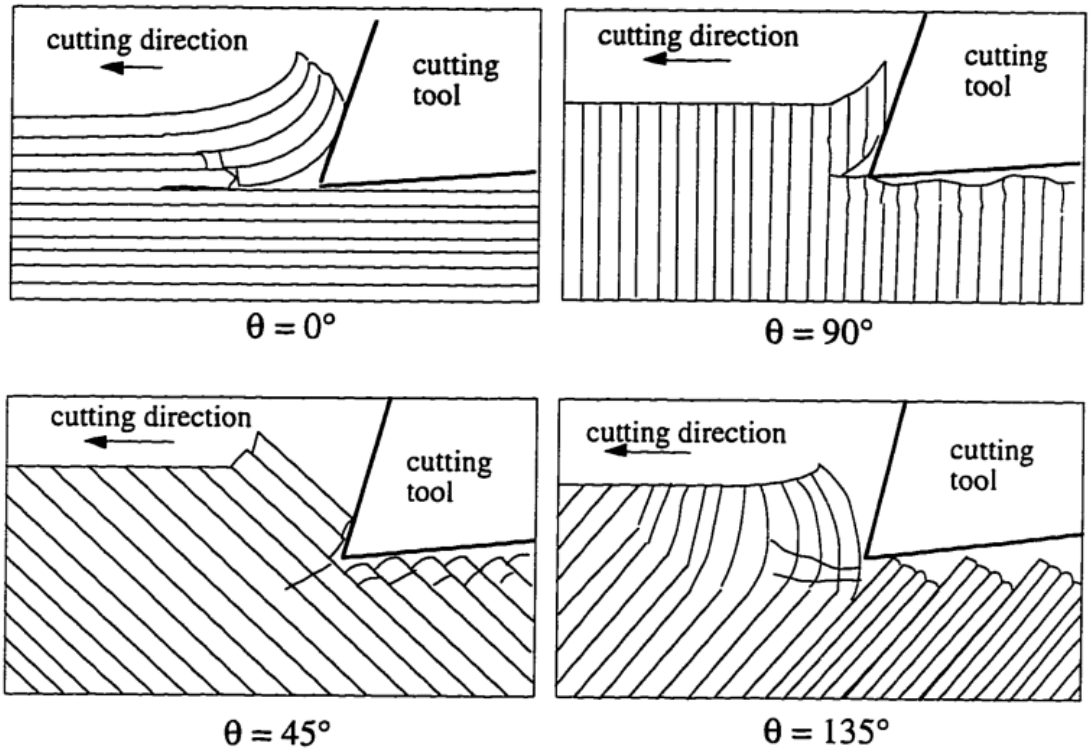

Figure 2.4 Chip Formation in Orthogonal Trimming of Unidirectional Graphite/Epoxy Laminate, (Source: Wang, Ramulu & Arola [11])

2.2.2 Edge Trimming with Abrasive Water Jet

In recent years, Water Jet (WJ) and Abrasive Water Jet cutting processes have found increased usage in machining of CFRP composite laminates. Between the two processes, AWJ dominates the non-traditional machining process used in trimming of laminates. The major advantages of using the AWJ process in trimming of composite laminates is the omnidirectional cutting capacity of the jet and its relative insensitivity to material hardness. Water is pumped at pressures up to 400 MPa and expelled through a sapphire or diamond nozzle to form a fine cutting stream. At these high pressures, the resultant jet varying in diameter from 0.07 to 1.3 mm exits the nozzle at speeds approaching 900 m/s. These high-velocity jets can be used to cut a variety of materials [12]. The basic process parameters in any water jet process are the jet pressure, the orifice diameter and the coherency of the jet. In AWJ the pressurized water jet is ejected through the small-diameter orifice which results in a vacuum being developed in the AWJ nozzle. This vacuum is instrumental in conveying the abrasives to the nozzle. Within the nozzle the abrasive particles entrained and accelerated to very high speeds with velocities in the range of 450-720 m/s. The material removal takes place due to erosion and abrasion of the target surface when abrasive particles flow past the target surface. The abrasives most widely used are the garnet abrasives. The AWJ cutting operation is controlled by the following parameters [12]:

Hydraulic Parameters

- Water Jet Pressure P
- Nozzle (orifice) diameter d_n

Abrasive Parameters

- Abrasive material (density q_a, hardness, toughness etc.)
- Abrasive particle size d_a and size distribution
- Abrasive particle shape (roundness, sphericity, etc.)
- Abrasive flow rate m_a

Mixing Parameters

- Mixing tube length l_m
- Mixing inner tube diameter d_m

Hashish [13-15] and his team have done considerable research in areas of developing the AWJ technology and have successfully commercialized the process.

A typical WJ/AWJ machining set-up is shown in Figure 2.5.

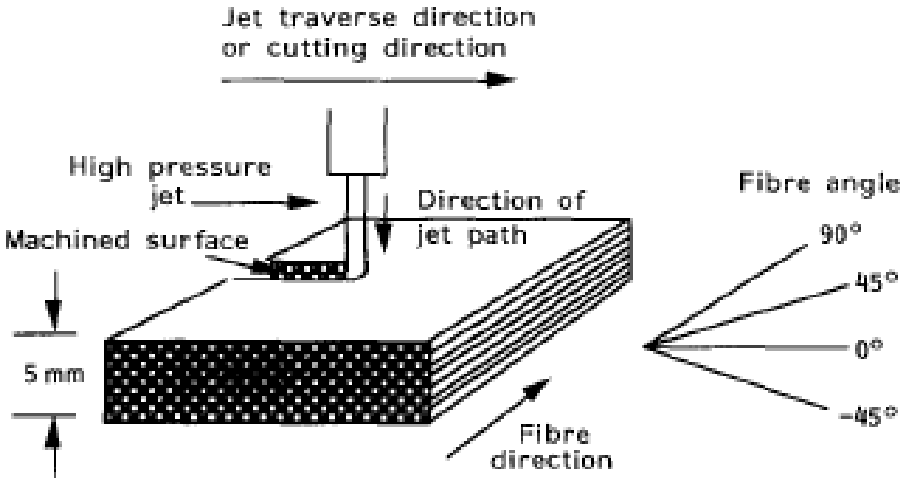

Figure 2.5 WJ/AWJ Cutting of CFRP Composite Laminate (Source: Ramulu & Arola [15])

The cutting head of an AWJ machine consists of orifice, mixing chamber and focusing tube where the water jet is formed and mixed with the abrasive particles to form the abrasive water jet as shown in Figure 2.6.

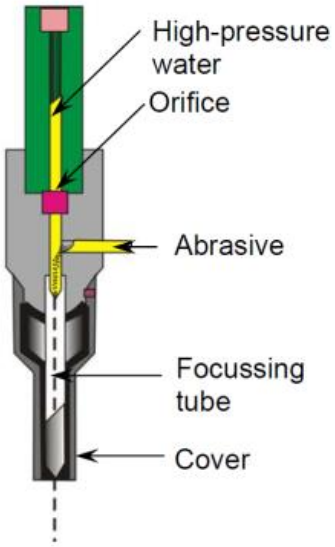

Figure 2.6 Schematic View of AWJ Cutting Head

(Schematic Courtesy - Omax Corporation, USA)

The material removal rate of an AWJ cutting process is proportional to the power of the water jet. The cut generated by an AWJ is called the kerf and its profile is shown in Figure 2.7. The top of the kerf is wider than the bottom of the kerf. Generally, the top width of the kerf is equal to the diameter of the AWJ [16]. The taper angle of the kerf can be reduced and the quality of the kerf profile improved by increasing the power of the water jet. The surface cut by an AWJ process shows striation marks along the traverse direction of the water jet. Figure 2.8 shows photographic views of the kerf profile cross-section while Figure 2.9 shows the striation marks.

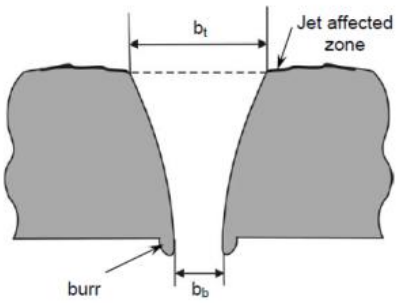

Figure 2.7 Schematic View of AWJ Machined Kerf (Source: Class lectures, ME, IIT Kharagpur, [16])

b_t = width at top of kerf

b_b = width at bottom of kerf

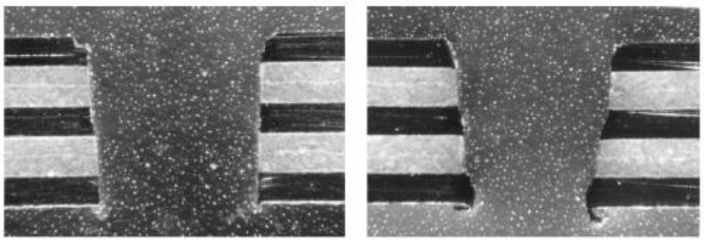

Figure 2.8 Photographic View of AWJ Machined Kerf (cross-section) (Source: Class lectures, ME, IIT Kharagpur, [16])

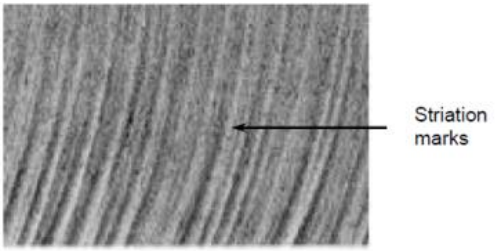

Figure 2.9 Photographic View of AWJ Machined Kerf (longitudinal) (Source: Class lectures, ME, IIT Kharagpur, [16])

The quality parameters of an AWJ machining process are striation formation, surface finish of the kerf, tapering of the kerf and burr formation on the exit side of the kerf.

The research in the field of AWJ cutting of composites have focused on studying the optimization of process parameters to improve the quality of the resultant surfaces of the machined composites. Focus has also been on studying the mechanics of the AWJ cutting of composite laminates to understand and limit the damage to laminate during the AWJ machining process. Ramulu [17] and his team of researchers have led the field of study of the micromechanics of WJ and AWJ machining of composites. Ramulu & Arola [17] were one of the earlier researchers in studying the mechanics of Water Jet and Abrasive Water Jet cutting of unidirectional graphite/epoxy composite. Their work was instrumental in establishing that the AWJ machining of unidirectional graphite/epoxy composite consists of a combination of material removal mechanisms including shearing, micromachining and erosion. They established that AWJ machining was a better process than WJ due to its material removal processes and a superior resultant quality surface that was generated.

They observed that during AWJ machining the matrix remains intact, microbending delamination which allows the matrix to be withdrawn from the kerf wall only occurs near the jet exit. Arola et. al [18] researched experimental investigations to show that from experimental data acquisition of the near field stresses during AWJ cutting, it can be concluded that material removal occurs under extremely localized mechanical and thermal loads. The cutting forces generated during AWJ are low, which makes it a better option for machining of inhomogeneous and anisotropic CFRP composite laminates.

2.3 Drilling of Composite Laminates

For CFRP composite laminates drilling operations make up the largest of the post-cure manufacturing processes. Drilling is predominant due to fastening required to assemble CFRP laminate component assemblies. The bodies of work and resultant publications available from the studies in drilling of CFRP composite laminates or other composite laminates can be characterized as follows:

a) Study of drill process parameters and their optimization. These bodies of work encompass studying the drill types in use, their point angles, speeds and feed rate parameters. These studies also include process set-up and fixturing to help the minimization of damage due to drilling.
b) Study of the types and causes of damage in CFRP composite laminates or other types of composite laminates due to drilling processes. These damage types include delamination, fibre pullouts, fibre fracture & microcracking.
c) Study of the effects of the damage on strength and performance caused due to drilling in CFRP composite laminates or other composite laminates. These include studies involving the effects of damage on tensile, compression, notched tensile/compression and fatigue properties.

2.3.1 Drill Type & Geometry, Process Parameters Effect

Various researchers have studied the importance of using different cutting tool materials such as Carbide, Polycrystalline Diamond (PCD) and Chemical Vapour Deposition (CVD) Diamond Coated Carbide drills to produce holes of good quality in composite laminates. Shyha et. al [19] studied the drill geometry and operating effects when cutting small diameter holes in CFRP composite laminates. They found that the drill type and feed rate were the main contributing factors affecting tool life and thrust force, while cutting speed and feed rate had the most significant effect on torque. Their work showed that in small diameter hole drilling (1.5 mm diameter), a 140^{o} drill point performed better with the usage of a stepped drill diameter (Figure 2.10) at higher feed rates. The use of a stepped drill and higher feed rates along with the 140^{o} point angle resulted in a lower thrust force while the increased feed rate resulted in reduced contact time between drill and the composite laminate reducing abrasive action and heat generation.

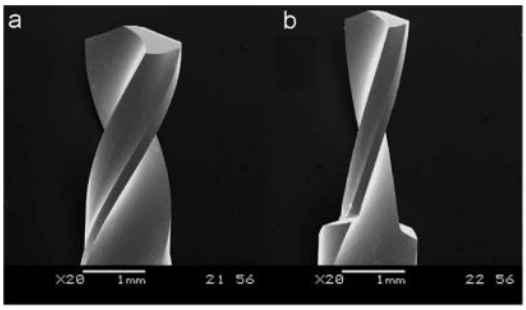

Figure 2.10 Image of Conventional Twist Drill & Stepped Diameter Drill (Source: Shyha et. al [19])

Palanikumar et. al [20] studied the influence of drill point angle in high speed drilling of Glass Fibre Reinforced Plastics (GFRP). Their theoretical and experimental study of high-speed drilling of glass fibre reinforced plastic using cemented carbide drills of different geometries showed that the 85^{o} point angle less delamination as compared to the drills with 115^{o} and 130^{o} point angles. Their study also documented that a combination of higher speed, low feed and point angle helps in the minimization of delamination in the drilling of GFRP laminates. The above two references [19] & [20] show how the difference in materials CFRP and GFRP drive different geometry of drills and process parameters. Capello & Tagliaferri [21] studied the effect of drilling damage in GFRP laminates on their residual mechanical behavior. Their study consisted of researching the influence of drilling parameters on the type and extension of damage. Their work also included the study of drilling with and without a support beneath the specimens. Results indicated that the degree of the peel-up delamination depended on the feed rate and the helix angle of the twist drill. Push-down delamination is mainly affected by the feed rate, by the presence of support beneath the specimen and by the twist drill temperature. Figure 2.11 shows the observed damage as a function of drilling conditions.

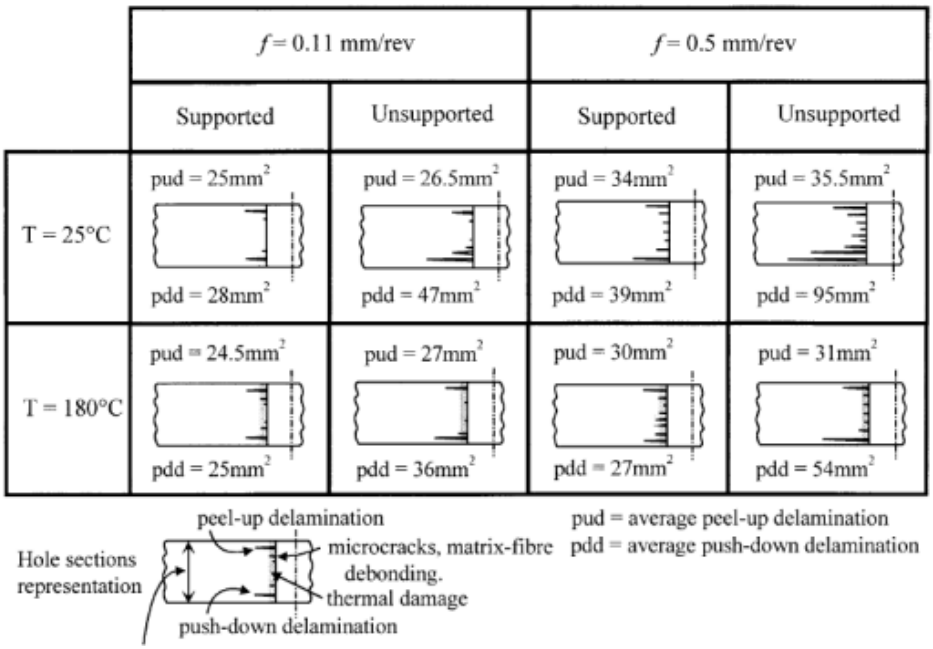

Figure 2.11 Pictorial Representation of Observed Damage as a Function of Drilling Conditions (Source: Capello & Tagliaferri [21])

Capello & Tagliaferri [21] also showed that a large helix angle influenced the peel up delamination while the presence of stiff supports reduced the peel down delamination as shown in figures 2.12 & 2.13. Feed rate influenced both peel up and peel down delamination and is a critical parameter to prevent damage during drilling of composite laminates.

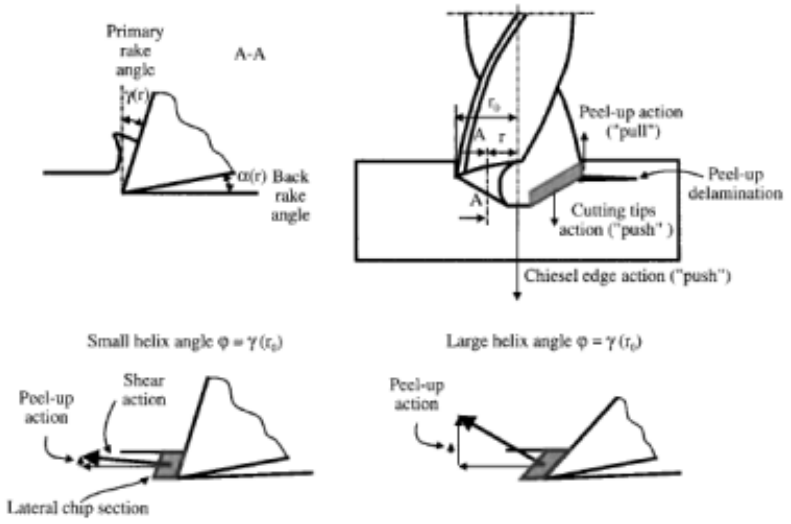

Figure 2.12 Twist Drill Action on the specimen and Peel Up Delamination (Source: Capello & Tagliaferri, [21])

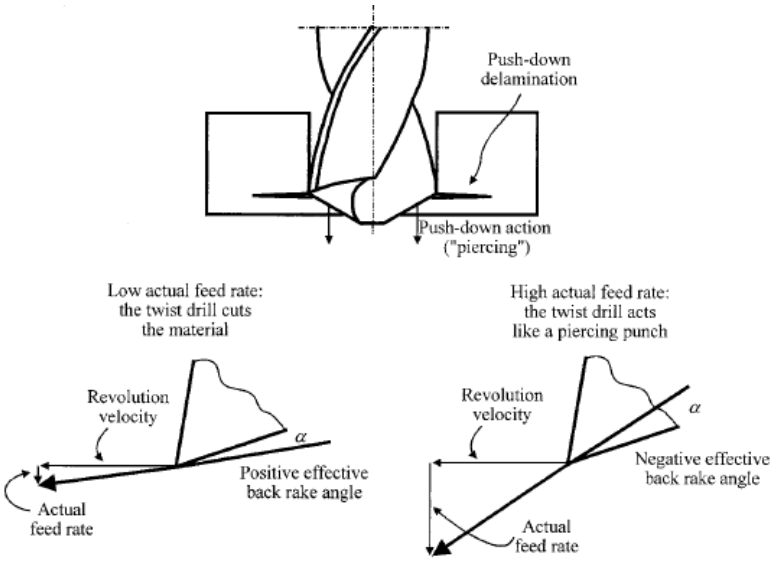

Figure 2.13 Effective Feed Rate and Push Down Delamination (Source: Capello & Tagliaferri, [21])

Different methods (techniques) of drilling holes in composite laminates to avoid the generation of damage have also been studied by various researchers. Persson et. al [22] in their study of effects of hole machining defects strength and fatigue life of carbon/epoxy laminates studied the KTH (Kungi Tekniska Hőgskolan) method of generating holes in CFRP composite laminates. Their work showed that the KTH method generated less defects compared to the drilling process using a PCD tipped drill and a cemented carbide drill both using the traditional twist drill cutting geometries. The KTH method uses the orbital drilling methodology in which the hole is machined with a cutter both axially and radially by rotating the cutter about its own axis as well as eccentrically about a principal axis while feeding the tool through the laminate. This method reduces the axial force (thrust) as there is no stationary tool centre (drill point tip). Also, as the cutter diameter is smaller than the hole diameter being drilled, clogging of the cutter flutes with graphite dust is prevented, reducing heat generation and better tool performance.

2.4 Surface Integrity of Composite Laminates

The resultant conditions of the surface and sub-surface of any composite laminates during prepreg, cure and post-cure operations influence the performance of engineering materials including composite laminates. Surface texture refers to the exterior microscale geometry of the machined surface and surface integrity includes surface texture and the features immediately beneath the surface (sub-surface) [16]. The surface integrity consists of the structure and stress conditions within the interior layers. Research has shown that surface integrity can influence mechanical properties of engineering materials. For homogeneous materials the differentiation between surface texture and surface integrity is well established. Surface texture takes into account the roughness/smoothness of the surface. For homogeneous materials, structure and stress conditions of the machined surface are often interrelated and consist of depleted alloying elements, gradients in the surface hardness and residual stresses. For homogeneous materials the surface integrity resulting from manufacturing processes is well defined and shown in the schematic diagram in Figure 2.14 by Metcut Research Associates [23].

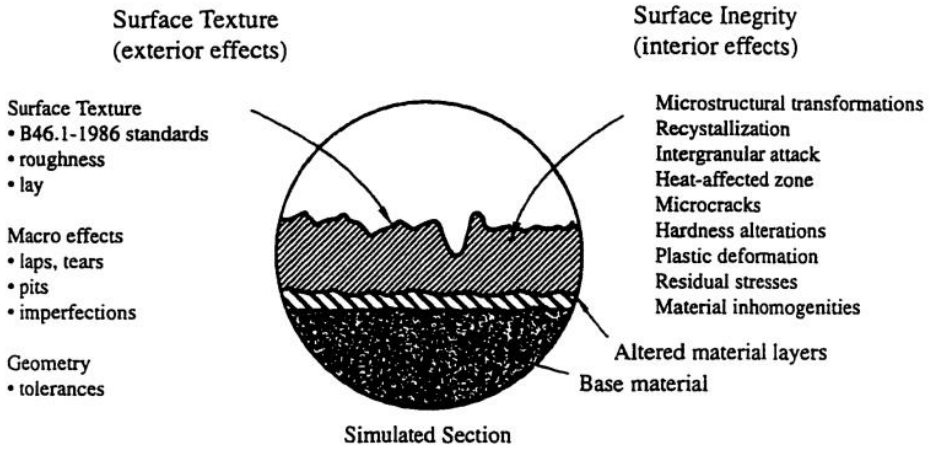

Figure 2.14 Surface Integrity Classification of Homogeneous Materials (Source: Metcut Research Associates [23])

Surface Finish Profile Parameter	Definition	Equations
R_a	Arithmetic mean deviation of the profile	$R_{\mathrm{a}} = \frac{1}{n}\sum_{i=1}^{n} \lvert y_i \rvert$
R_q	Root mean square deviation of the profile	$R_{\mathrm{q}} = \sqrt{\frac{1}{n}\sum_{i=1}^{n} y_i^2}$
R_z	Maximum height of the profile	$R_{\mathrm{t}} = R_{\mathrm{p}} + R_{\mathrm{v}}$
R_y or R_t	Total height of the profile – height between deepest valley and highest peak	$R_{\mathrm{t}} = R_{\mathrm{p}} + R_{\mathrm{v}}$
R_p	Maximum peak height of profile	$R_{\mathrm{p}} = \max_i y_i$
R_v	Maximum depth of valley of profile	$R_{\mathrm{v}} = \min_i y_i$
R_{sk}	Skewness of the profile	$R_{\mathrm{sk}} = \frac{1}{nR_{\mathrm{q}}^3}\sum_{i=1}^{n} y_i^3$
R_{ku}	Kurtosis of the profile	$R_{\mathrm{ku}} = \frac{1}{nR_{\mathrm{q}}^4}\sum_{i=1}^{n} y_i^4$

Table 2.1 Definition of Surface Finish Profile Parameters

In non-homogeneous materials the surface texture itself can be difficult to measure using the traditional surface roughness parameters such as R_a, R_t, R_y, R_z etc as defined in Table 2.1. This happens due to the inherent nature of the ply layup, surface conditions due to machining. The conditions on the external and just below the laminate surface are together described using the term “Surface Integrity”. This term will refer to both the exterior and interior structure of the machined surface. The surface integrity governs the performance of components through the stress concentrations imposed by the texture and through adverse alterations to the near-surface mechanical properties [18]. While in metals the relationship between surface integrity and its influence on mechanical properties and fatigue has been studied and documented for some time, similar works dealing with CFRP composite laminates are lacking [25].

In composite laminates surface discontinuities such as microcracks, fibre pullouts, delaminations etc. are often analyzed using a stress concentration factor such as (K_t) specially when evaluating the effects of these surface discontinuities on the strength of the composite components. The presence of the surface discontinuities results in stress localization which is usually expressed with the usage of K_t . Discontinuities have been studied as notches and their effects on the strength documented by previous researchers notably amongst them being Neuber [24].

Neuber [24] proposed a semi empirical relationship to describe the stress concentration posed by surface roughness according to

$$K_t = 1 + n\sqrt{\lambda \frac{R_z}{\rho}} \tag{2.3}$$

where R_z is the ten-point roughness and ρ is the notch radius. The stress state is represented by the empirical factor n, where $n = 1$ for shear and $n = 2$ for tension. λ refers to the ratio between spacing and height of surface irregularities.

Arola & Ramulu [25] proposed an alternative to the Neuber rule that quantifies the effects of machined surface texture on Fibre Reinforced Plastics (FRPs) in terms of an effective stress concentration factor ($\overline{K}_t$) which is given by

$$\overline{K}_t = 1 + n\left(\frac{R_a}{\overline{\rho}}\right)\left(\frac{R_y}{R_z}\right) \text{ or } \overline{K}_t = 1 + n\left(\frac{R_a}{\overline{\rho}}\right)\left(\frac{R_t}{R_z}\right) \tag{2.4}$$

where R_a ,R_y *or* R_t, R_z & $\overline{\rho}$ are the average roughness, peak-to-valley roughness, ten-point roughness and effective notch root radius respectively. The empirical constant n accounts for factors of material type and load type. For tension $n = 2$ and for shear $n = 1$ is generally recommended. This model has been used to successfully evaluate the effects of surface texture on the strength of FRPs under static and dynamic loading conditions.

Other researchers have studied the notch size effect on the normal stress distribution ahead of the discontinuity. Nuismer & Whitney [26] discussed the size effect emanating from central holes in the uniaxial failure of composite laminates. Whitney & Nuismer [27] developed two failure criteria to account for the change in normal stress conditions near the traction free boundary with different notch sizes. The first approach is referred to as the "point stress criterion" and assumes that failure occurs when the normal stress at some distance (d_0) ahead of the notch is equal to the unnotched tensile strength of the material. This was expressed as

$$\sigma_y(x,0)\big|_{x=t+d_0} = \sigma_o \tag{2.6}$$

where the unnotched tensile strength of the laminate is expressed by σ_o and t is the notch depth.
An alternative approach to the point stress criterion was also developed and accounts for the average stress ahead of the discontinuity. The "average stress criterion" assumes that failure occurs when the average stress ahead of the notch/discontinuity at a point distance a_0 reaches the unnotched tensile strength of the material and is expressed as

$$\frac{1}{a_0}\int_{a_0}^{t+a_0}\sigma_y(x,0) = \sigma_o \tag{2.7}$$

The two characteristic lengths a_0 and d_0 are associated with the "average stress criterion" and the "point stress criterion". Another body of work by Cruse [28] also researched the size effects on the strength of notched composite laminates. Cruse postulated that there exists an inherent flaw size (a) which governs the tensile strength of an unnotched composite laminate. Flaws with effective half length (λ^*) greater than the inherent flaw size will dominate failure. The degree of stress localization depends on the distance from notch root to the first fibre (r_1). The influence of the flaw size behaves according to the ratio $\left(\frac{r_1}{\bar{\lambda}}\right)$ where λ is the notch half length. For small $\left(\frac{r_1}{\bar{\lambda}}\right)$ which is large relative notch length, many fibres adjacent to the notch respond to the K_t whereas for large $\left(\frac{r_1}{\bar{\lambda}}\right)$ adjacent fibres are not influenced by K_t . For large flaws the strength of the laminate is governed by the nominal stress concentration factor. Within the transition region between inherent flaws and those which are accurately described by K_t, the strength of the laminate is governed by two superimposed criterion.
The first criterion describes a stress field for the notch using the stress intensity factor for an effective flaw as

$$\sigma_c = \frac{K_Q}{Y\sqrt{\lambda^*}} \tag{2.8}$$

where K_Q is the critical stress intensity factor of the laminate and Y is the infinite flaw size correction factor.
If the inherent flaw size (a) is modeled as a small internal crack of length ($2a$), then the strength of the unnotched specimen is

$$\sigma_\infty = \frac{K_Q}{\sqrt{\pi a}} \tag{2.9}$$

Cruse [28] showed that the application of the proposed model matched well against results from experiments for the strength of notched laminates. K_Q is estimated from the strain energy release rate (G_Q), while λ^* is obtained from numerical stress analysis for well-defined notch geometry.

Mar & Lin [29] proposed a model using a plane stress solution for the fracture stress of unidirectional composite laminates containing discontinuities. They concluded that length of the discontinuity was important in comparison to the shape which was nearly irrelevant. Considering the tip of the discontinuity as a crack, the investigators theorized that the fracture stress is governed by the equation

$$\sigma_f = H_c(2a_c)^{-m} \tag{2.10}$$

where H_c is the composite toughness and is a property of the constituents and lay-up. a_c is the length of the discontinuity. For a sharp crack, H_c is the fracture toughness and *m* is the order of the singularity at the crack tip. For isotropic materials the exponent *m* is conventionally equal to 0.5. The Mar-Lin model when applied to multi-directional laminates using surface texture, the equation uses maximum discontinuity length (R_y) and is written as

$$\sigma_f \approx H_c\left(2R_y\right)^{-m} \tag{2.11}$$

While work has been done in the areas of accounting for the notch size and shape effects on the strength of laminates, there is still development left in accounting for the effects of multiple notches and their interactions with adjacent discontinuities.

Post-cure processes such as machining processes produce surface integrity effects which are process dependent. These effects are ply dependent and hence any effective stress concentration factors should take into account the ply with the highest degree of damage. A stress concentration factor which describes the effects of surface integrity on the stress distribution must be expressed in terms of standard surface roughness parameters. Arola & Ramulu's [25] equation 2.4 represents the expression of the stress concentration factor in terms of surface texture parameters.

2.5 Defects and Damage Occurrence in Composite Laminates

Composite laminates inherently have occurrence of defects in their structure during the many stages of their manufacturing processes. Defects and Damage in composite laminates are classified primarily based on defect/damage size within each ply (intralaminar) or between plies (interlaminar). While various bodies of work and general practice use the two terms defects and

damage interchangeably, this study will classify defects as primarily occurring during the manufacturing processes up to the curing process of the laminates while damage is classified as those defects occurring during post cure processes such as edge trimming and drilling. These damage conditions further progress under service life conditions and can result in reduction of strength properties. Defects also progress and end up as damage in composite laminates. Various types of defects/damage occur at different stages of manufacturing of the composite laminates. Some of the defects that occur during processes up to complete cure of the laminates are:

Damage at Prepreg Stage – Defects at this stage usually consists of

Hollow Fibres
Excessive variability In Fibre Properties
Resin-Starved or Fibre-Starved Areas
Wrinkles, Waviness, Miscollimation
Foreign Particles, Contamination
Fuzz Balls
Non-uniform Agglomeration of Hardener
Prepreg Out of Specifications

Defects in Laminates – Defects at this stage usually consists of

Hollow Fibres Delaminations
Fibre Breaks, Ply Gaps
Excessive Porosity, Voids
Resin Rich and Resin-Stared Areas
Fibre Waviness,Wrinkles, Miscollimation
Foreign Particles, Contamination, Inclusions
Incomplete And/Or Variable Cure
Wrong Stacking Sequence
Dents,Tool Impressions, Scratches

The following post cure processes can cause damage:

Machining (edge trimming) & Drilling – Damage from these processes includes

Edge Delaminations
Edge Notches and Surface Notches
Oversize Holes/Undersize holes

Fibre Pullout
Microcracking
Heat-Damaged Machined Edges
Fibre Break-Out On Hole Exit Side
Tilted Holes
Out-Of-Round Holes
Tilted Countersinks
Improper Depth of Countersinks
Dents, Fibre Breaking from Impact
Tearout Or Pull-Through in Countersinks

Bolted Assembly Process – Damage from these processes includes

Over torqued Fasteners
Improper Fastener Seating
Missing Fasteners
Fastener Installation Damage
Oversized And Undersized Fastener

While many past studies have focused on research on the effects of laminate porosity, ply gaps and ply waviness, there have been limited bodies of work in the area of damage due to edge trimming and drilling operations. This research study will focus on the science of damage (surface integrity) due to edge trimming and drilling and its effects on strength properties.

2.5.1 Effects of Damage Due to Edge Trimming and Drilling

Past research on damage studies has concentrated on studying how edge trimming and drilling process parameters influence the generation and propagation of damage in composite laminates. Durao et. al [30] studied the effects of hole drilling process parameters in causing delaminations during of hybrid composite laminates. Their results showed that a nominal cutting speed in the range of 53 m/min and a feed rate round 0.025 mm/rev reduced the occurrence of delamination in carbon/epoxy laminates. The study also reiterated that the drill point geometry has an effect on the maximum thrust force and delamination around the hole and having a step drill with a smaller pilot hole diameter helps in the reduction of occurrence of delaminations in the drilling of carbon/epoxy laminates. As previously mentioned in section 2.4.1, Capello & Tagliaferri [21] studied the effects

of drilling parameters on the type and extent of damage generated during drilling. Their work also encompassed the influence of supports during drilling in the occurrence of damage (delaminations). Figure 2.15 shows the damage during drilling with various process parameters and the usage or lack of supports to the workpiece during drilling operations. Shyla et. al [19] as mentioned in section 2.4.1 studied the effects of drill geometry on damage during drilling of small diameter holes in CFRP composite laminates. Their work documented various forms of internal hole defects such as internal cracks, porosity (due to the absence of matrix material between layers), fibre/matrix cracking, resin loss, etc as shown in figure 2.16. They also determined that drill geometry and feed rate were the primary factors influencing damage during drilling.

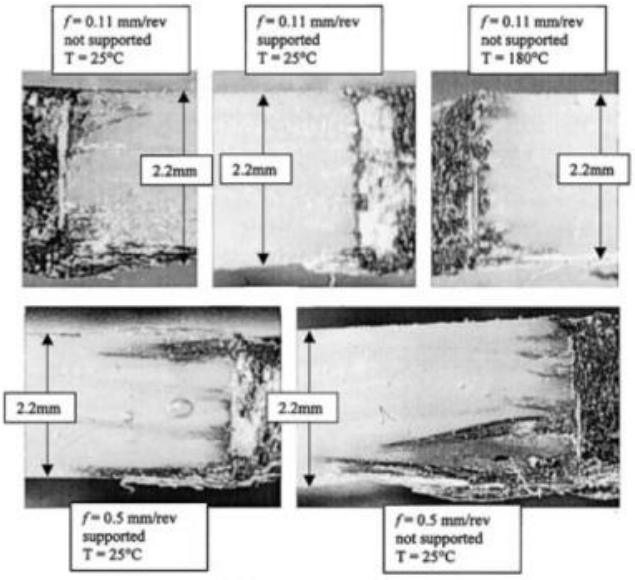

Figure 2.15 Sample Holes, Damage & Drilling Conditions (source: Capello & Tagliaferri [21])

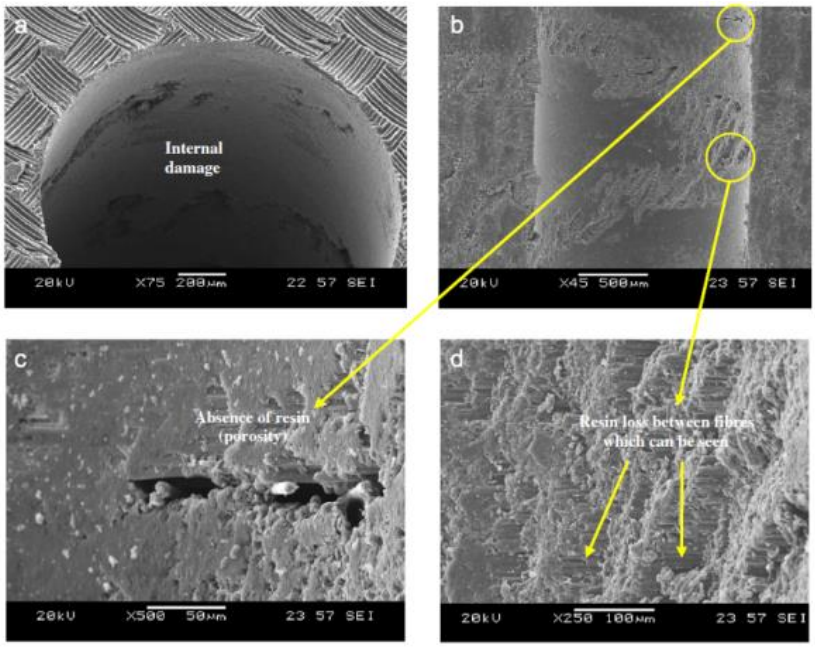

Figure 2.16 Internal Hole Damage Forms (source: Shayla et. al. [19])

Ramulu [31] has conducted extensive research in the areas of the influence of cutting direction and fibre orientation. His publications have documented the damage occurrence during drilling at various angular positions of the hole based on fibre orientations as shown in Figure 2.17.

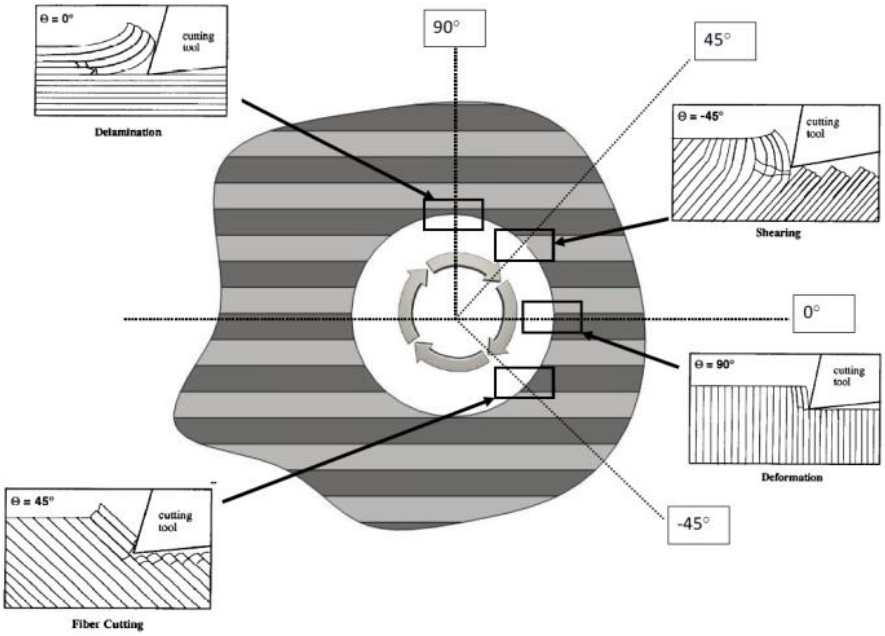

Figure 2.17 Damage Mechanisms Type Occurrence Based on Cutting Direction & Fibre Orientation (source: Ramulu [31])

Mohan et.al. [32] analyzed the delaminations in the drilling of Glass Fibre Reinforced Plastics (GFRP) composites. Their study included determining the factors and combination of factors that influence the delamination using Taguchi and response surface methodology and to achieve the optimization machining conditions that would result in minimum delamination. Similarly, Davim & Reis [33] experimented based on the techniques of Taguchi the drilling with cutting parameters of a Carbon Fibre Reinforced Plastic (CFRP) laminate. They developed a correlation between cutting velocity and feed rate with the delamination in a CFRP laminate. The correlation was obtained by multiple linear regression.

Similarly, researchers have studied damage occurrence during edge trimming processes both in the case of machining with Endmills and Abrasive Water Jet (AWJ) cutting. Shanmugam et. al [34] studied the delamination occurring in AWJ machining of graphite/epoxy laminates. They found that crack tips are generated by the shock wave impact of the waterjet at the initial cutting stage, while delamination is a result of water penetration into the crack tips that promoted water-wedging and abrasive embedment (Figure 2.18). They developed a semi-analytical model based on an energy conservation approach to predict the maximum delamination length generated by an AWJ.

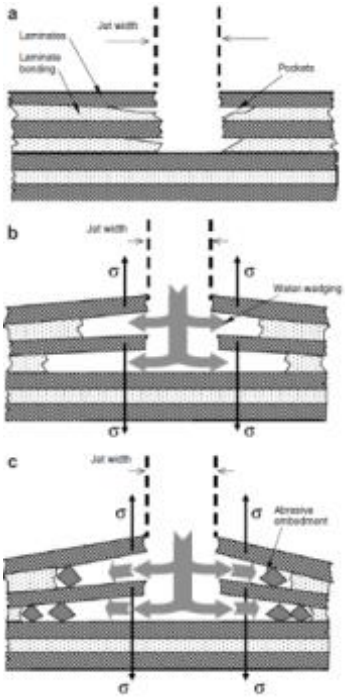

Figure 2.18 Mechanism of Delamination (source: Shanmugam et. al [34])

There have been a few studies focusing on the effects of the damage caused due to machining and drilling on the strength properties of composite laminates. Many researchers have experimented with damage documented due to edge trimming and drilling and tested the coupons/specimens under Monotonic Static Conditions as well as under cyclic Fatigue Loading Conditions. Capello & Tagliaferri [35] studied the effects of drilling damage in GFRP laminates on the static and cyclic bearing loads. They concluded that the main cause of the mechanical failure was the micro damage generated at the inner part of the hole surface while delamination played a minor role. The onset of microcracks was detrimental to the residual strength of the GFRP laminates. Their study concluded that the progression of hole deformation/damage was influenced by the feed rate used and increased with the usage of higher feed rates. Rao et. al [36] researched the effects of drilling induced damage on the notched tensile and pin bearing strengths of woven Glass Fibre Reinforced - epoxy composites. They concluded that the increase in effective diameter as a result of damage resulted in decreased notched tensile strength as well as bearing strength properties. The effective maximum diameter due to damage is shown in Figure 2.19.

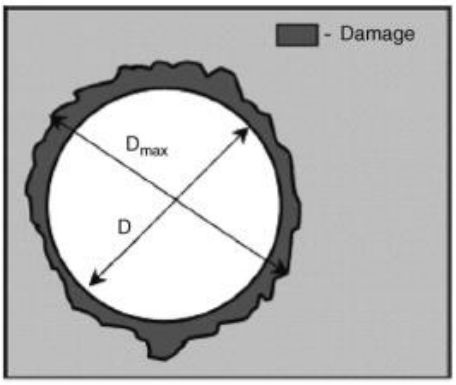

Figure 2.19 Schematic View of Effective Maximum Diameter (source: Rao et. al [36])

Persson et.al [24] researched the effects of hole machining defects on strength and fatigue life of carbon/epoxy laminates. They subjected holes with and without defects to pin loading and uniaxial compression loading at room temperatures. As mentioned in section 2.4.1 a new method based on orbital drilling, the KTH method was used to produce defect free holes. The study concluded that hole machining defects significantly reduced the static and fatigue strengths of pin-loaded

laminates. Wisnom & Hallett [37] in their work explored the role of delamination in the strength and failure mechanism in open hole testing on quasi-isotropic laminates. Their work showed that delamination plays a crucial role in the in-plane strength, failure mechanism and hole size effect in open hole tension of quasi-isotropic laminates. It can lead to premature failure, especially for small holes and thick blocks. They concluded that for thin blocks, the plies failure is dominated by fibre fracture before reaching the stress needed for delamination across the width. Their experiments studied the damage progress using testing which was interrupted to study the damage mechanism. They learnt that failure initiated from a transverse crack in the surface 45^{o} plies, followed by delamination at the 45/90 interface. This initiated first at the hole, then at the free edge, propagating towards each other. When the damage joined up across the width it then stepped down through the 90^{o} ply, delaminating at the 90/-45 interface, further stepping down through the -45^{o} ply and then delaminating at the -45/0 interface. Splitting of the 0^{o} ply also occurred at this point leaving two ligaments on either side of the hole to carry the load. This mechanism is illustrated schematically in Figure 2.20.

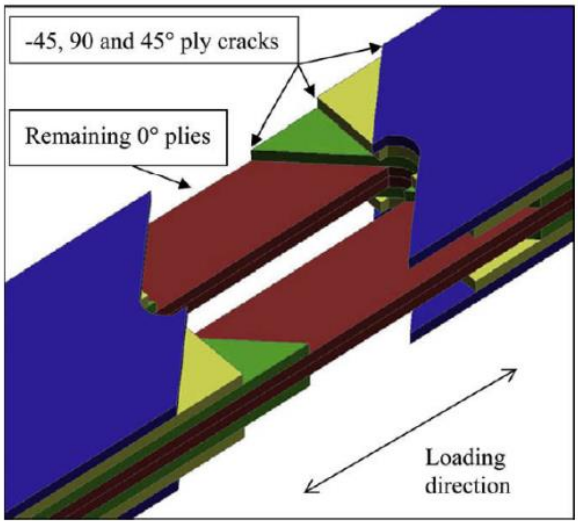

Figure 2.20 Illustration of Mechanism of Outer 45/90/-45 Plies Separating from 0^{o} Plies, (source: Wisnom & Hallett, [37])

2.5.2 Surface Texture and Surface Integrity Effects on Strength Properties

While many bodies of work have studied the effects of damage on strength of composite laminates, there have been only a handful of research efforts on relating the effects of machined surface

integrity on mechanical strength properties of composite laminates. Arola & Ramulu [38] researched the effects of surface texture on the mechanical properties of Fibre Reinforced Plastics (FRPs). Their study showed that static bending strength decreased with increasing surface roughness on net-shaped machined parts. Their experiments established that damage accumulation prior to failure was dependent on the method of machining. The location of first ply failure was influenced by the process-dependent surface structure but not by the magnitude of surface roughness. They concluded that surface integrity resulting from net shape machining with orthogonal cutting tools promoted significant reductions in the static strength of Graphite/Epoxy laminates. The static bend strength of the AWJ machined specimens also decreased with increasing surface roughness. It was also documented that laminates with the highest surface roughness around 10 μm R_a underwent a 15% reduction in the load to failure. Ramulu & Colligan [39] studied the impact of edge finishing and delamination produced by AWJ trimming of Graphite/Epoxy Laminates. They concluded that AWJ trimming of graphite/epoxy laminates is prone to producing exit ply delamination which can held apart by the abrasive particles trapped in the delaminations. Their compression strength testing of these specimens indicated that while rougher surface finish did not have a pronounce effect on the reduction of compressive strength, the delaminations produced due to the process do contribute significantly in reducing the compressive strength of the laminates. Their study showed that higher feed rates caused rougher surface finish and larger magnitude and number of delaminations occurrences. Figures 2.21 and 2.22 show the effects of feed rates on surface finish and the effect of surface finish on the ultimate compressive strength of the laminate.

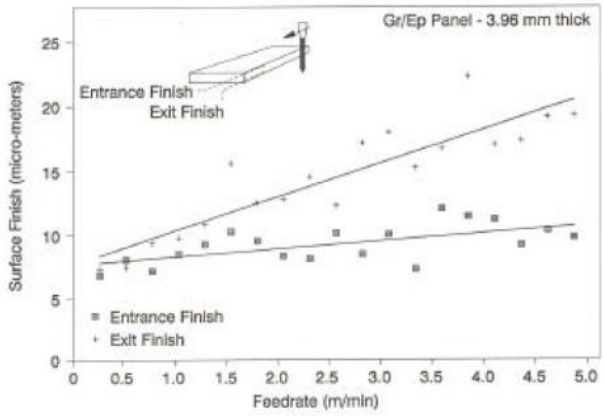

Figure 2.21 Surface Finish vs. Feed Rate, AWJ Trimming of a Graphite/Epoxy Laminate, (source: Ramulu & Colligan, [39])

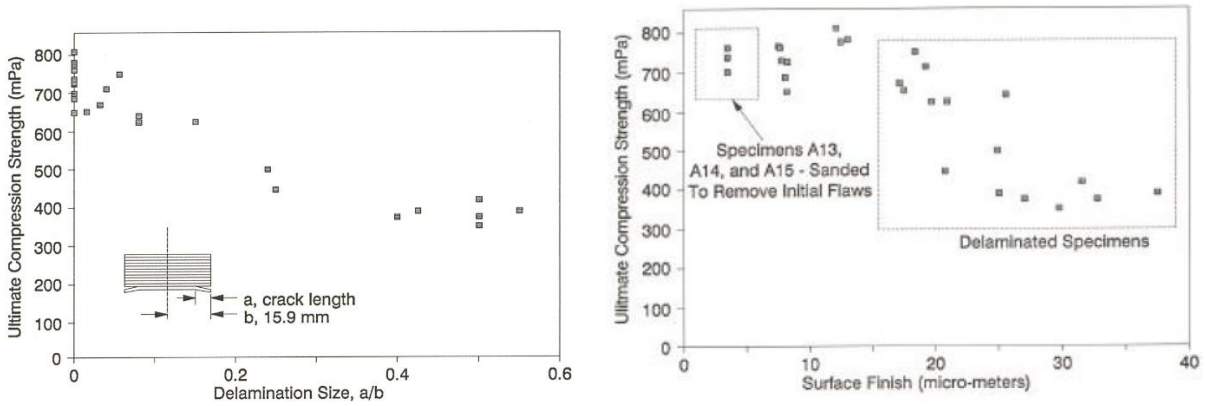

Figure 2.22 Ultimate Compression Strength vs. Delamination and Surface Finish, AWJ Trimming of a Graphite/Epoxy Laminate (source: Ramulu & Colligan, [39])

Ghidossi et. al [40] have done considerable work in research and documentation of edge machining effects on the failure of polymer matrix composite coupons. Their work documented the lack of available studies in the areas of evaluation of surface roughness effects on strength properties. They conducted various experiments using a variety of milling cutters carbide, PCD, CVD Diamond Coated Cutters to generate different surface roughness parameter magnitudes in both Carbon/Epoxy and Glass/Epoxy Laminates. Iosipescu test specimens for shear and Ring specimens for tension testing were machined. The effects of a worn tool on surface damage were also documented as shown in Figure 2.23.

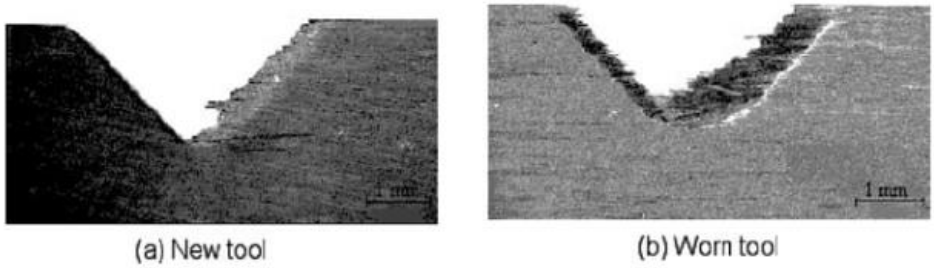

Figure 2.23 Effect of Tool Wear on Free Edge Delamination of a Carbon/Epoxy Iosipescu Specimen (source: Ghidossi et. al [40])

Their study concluded that surface roughness was not a good indicator to assess machining quality of fibre composites especially when relating it to mechanical properties. Also, sub-surface damage plays a significant role in resultant mechanical behaviours than surface texture. Ghidossi et. al [41] also studied the influence of cutting parameters on the damage level and mechanical response of off-axis glass/epoxy unidirectional coupons machined by side milling. Their work emphasized the importance of the relative orientation of the fibres with respect to the cutting direction. The study also parallels the conclusions from their previous study that the off-axis tensile failure stress of glass/epoxy composite specimens is also influenced by the machining parameters used to prepare the specimens. The type of damage is strongly influenced by the angle between the fibre direction and the cutting edge. The damage types documented were of two types: craters for the 15^{o} fibre orientations and subsurface cracks for the 45^{o} fibre orientations as shown in Figures 2.24 and 2.25. They made some recommendations on future studies which helped lay the foundation for the body of research to be conducted in this study particularly the use of Microscopic full-field strain measurements to better understand reach how the initial damage develops and propagates, particularly if linked to progressive damage computations.

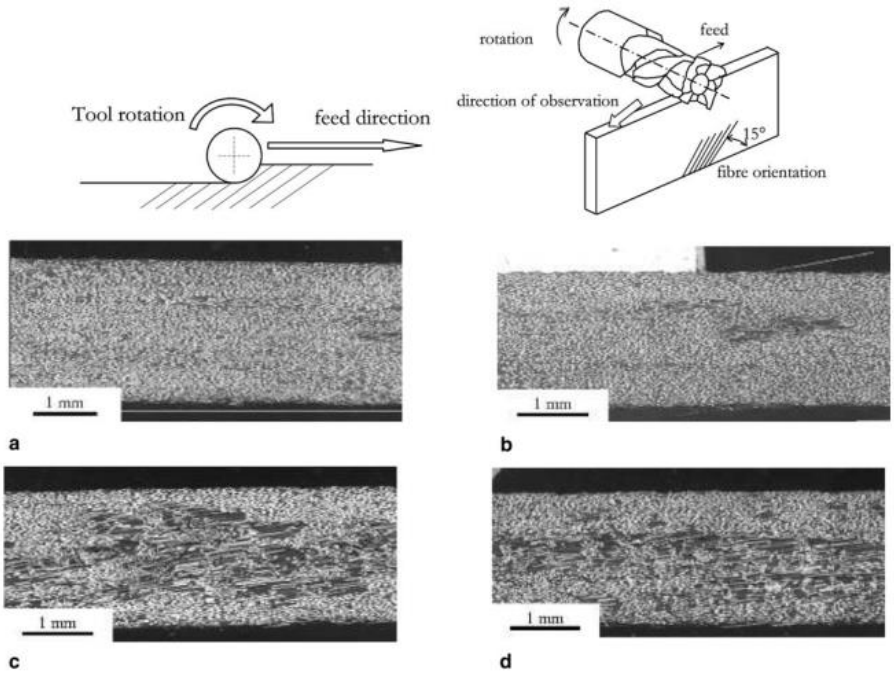

Figure 2.24 Microscopic Observations from a 15^{o} Fibre Orientation showing Craters (source: Ghidossi et. al [41])

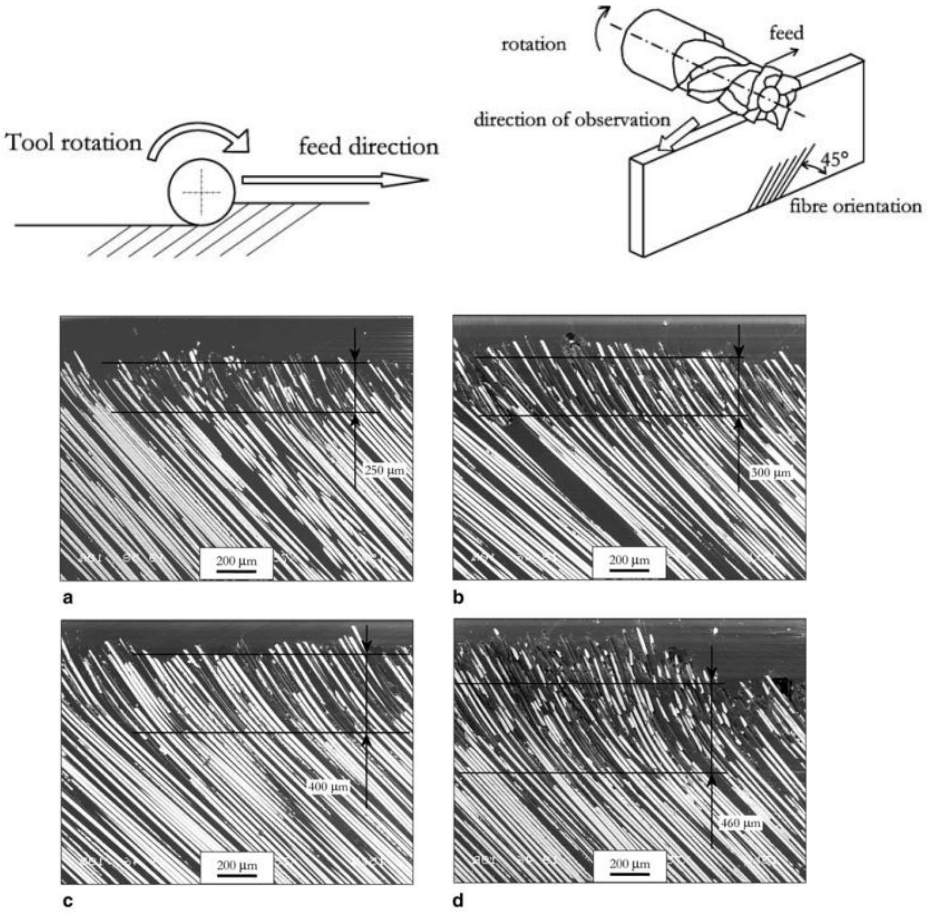

Figure 2.25 Microscopic Observations from a 45º Fibre Orientation showing Subsurface Cracking (source: Ghidossi et. al [41])

Ghidossi et. al [41] also documented the variation (reduction) in ultimate stress due to increased percentage of damage both for the 15º and 45º Fibre orientations as shown in Figures 2.26 & 2.27. Eriksen [42] studied the influence of surface roughness on the mechanical strength properties of machined short-fibre reinforced thermoplastics. The strength properties he studied were Charpy Impact, Monotonic Bending and Flexural Fatigue. He found that the mechanical strength properties were independent of the surface roughness but not necessarily for materials with a stronger bonding between matrix and the fibres or composites which have more notch sensitive matrix materials.

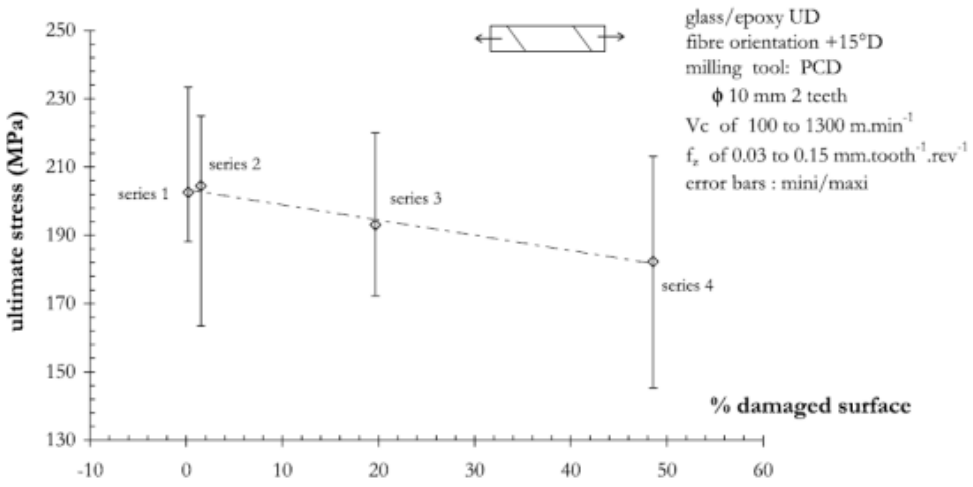

Figure 2.26 Ultimate Stress versus ‘‘Percentage of Damaged Surface’’ Criterion, 15º fibre Configuration (source: Ghidossi et. al [41])

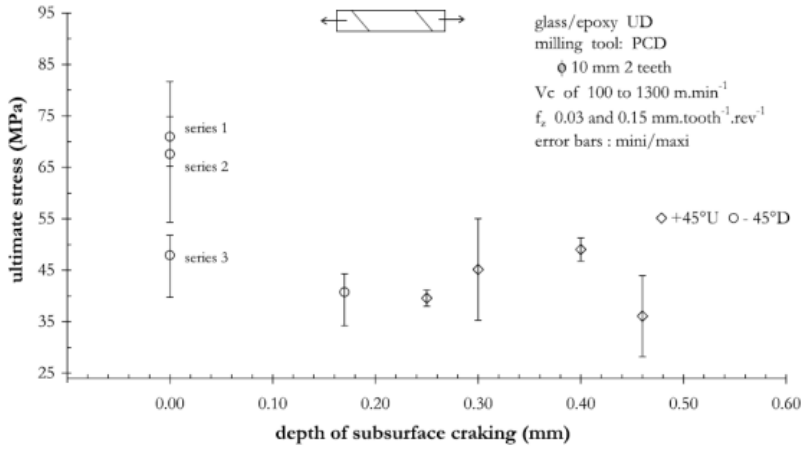

Figure 2.27 Ultimate Stress versus ‘‘Depth of Subsurface Cracking’’ Criterion, +45º and -45º Fibre Configurations (source: Ghidossi et. al [41])

One of the earlier works by Tagliaferri et. al [43] research was conducted on studying the effects of drilling parameters on the finish and mechanical properties of glass reinforced plastic composites. This work concluded that the width of the damage zone is correlated to the ratio

between drilling speed and feed rate. The higher the ratio, the better the cut and a smaller damage zone produced. While the tensile strength did not change with the size of the damage zone, the bearing strength suffered a marked decrease with the generation of a larger damage zone. Figures 2.28 and 2.29 show the relationship between size of damage zone to ratio of drilling speed to feed rate along with the relationship between bearing strength and the size of the damage zone.

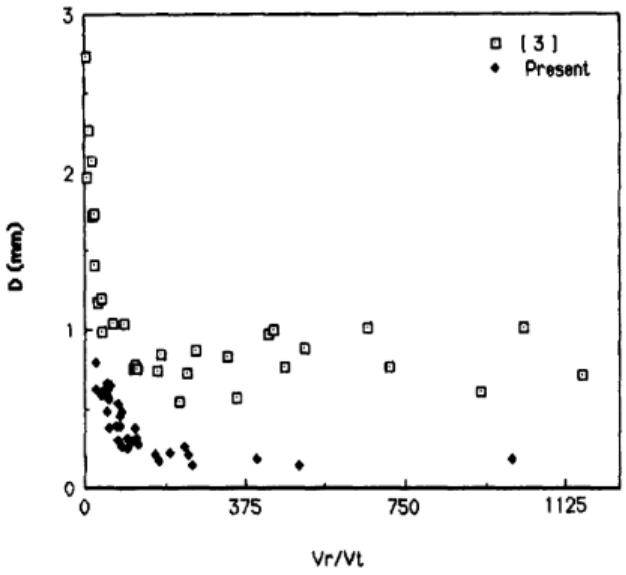

Figure 2.28 Size of Damage vs. Speed/Feed Ratio (source: Tagliaferri et.al [43])

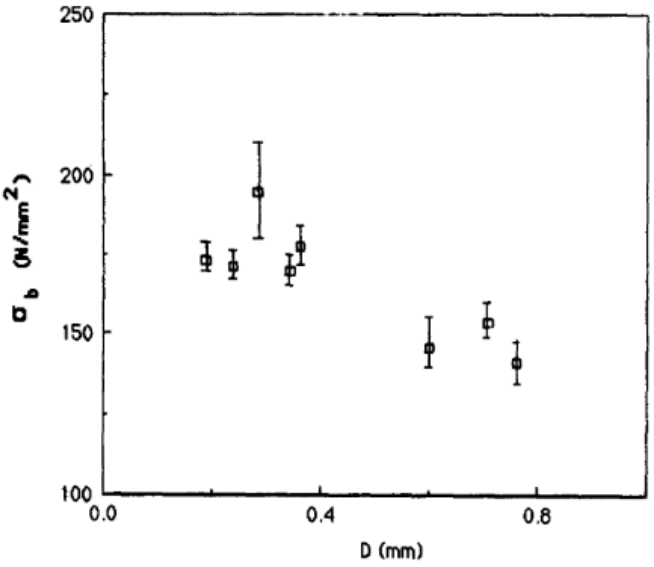

Figure 2.29 Bearing Strength vs. Size of Damage (source: Tagliaferri et.al [43])

In recent years there has been research in the area of studying the strength properties variation between holes that have been moulded into composite laminates versus holes that have been drilled. Langella & Durante [44] compared the tensile strength of composite materials with drilled and moulded holes. As drilled holes cause damage their study focused on comparing non damage moulded hole effects on strength to those with damage due to drilling. As the holes were generated by moulding directly during the impregnation phase there was no loss of continuity in fibres in these laminates. With tensile testing and analysis, they documented that maximum load supported by moulded holes was higher than the holes that were drilled. Similarly, Zitoune et. al [45] studied the behavior of composite plates with drilled and moulded holes under tensile loading. Their conclusions show that fracture strength for moulded hole specimens was higher than those obtained for drilled hole specimens, with differences being as high as 30%. The damage mechanisms also varied between drilled holes and moulded holes. The drilled holes showed sudden fracture while moulded holes underwent progressive fracture. Maximum deformations for a drilled hole were twice as high as those in the moulded holes.

The effect of machining processes using conventional (a burr tool machining and an abrasive diamond saw (ADS) cutting) and a non-conventional machining (an abrasive water jet (AWJ)) on the mechanical behaviour (compressive and inter-laminar shear strength) of composite parts made of carbon/epoxy was investigated by Haddad et al {46]. The surface defects characterized between the AWJ processes and the burr & ADS processes showed that the conventional machining processes had wrenched areas with higher peaks and valleys as shown in Figure 2.30. These damage areas resulted in stress concentrations that influenced the differences in mechanical behaviour of the composite parts that were machined with ADS and burr tools as compared to the AWJ processes.

The test specimens machined by AWJ had resultant compressive strength about 10-20% higher than those machined with conventional burr tool and ADS machining processes as shown in Figure 2.31.

The study also included the observations of the differences in the mechanical behaviour of ADS and burr tool machined composites parts after the original surface integrity was modified to remove or reduce the quantity of wrenched areas in the surface topography by additional polishing

processes. The results as shown in Figure 2.32 showed that the rectified surface specimens showed an improvement in the compressive strength behaviour. The study concluded that the machining defects are different created by different machining processes and do influence the differences in the mechanical behaviour of the composite laminates.

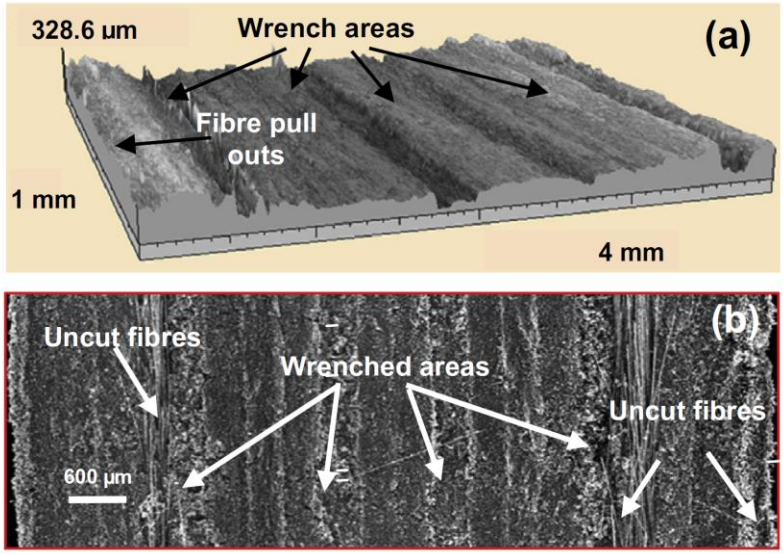

Figure 2.30 Form of the trimmed surface after machining with burr tool (a) Image topography 3D (b) SEM observation (source: Haddad et al [46])

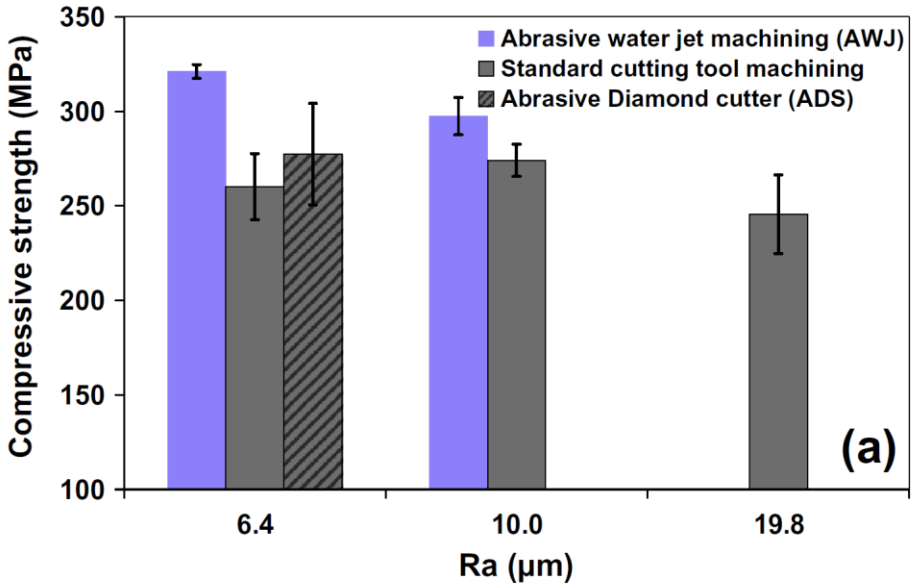

Figure 2.31 Quasi static strength responses vs. surface roughness of different samples obtained by AWJ machining, burr tool machining and Abrasive Diamond saw cutting (source: Haddad et al [46])

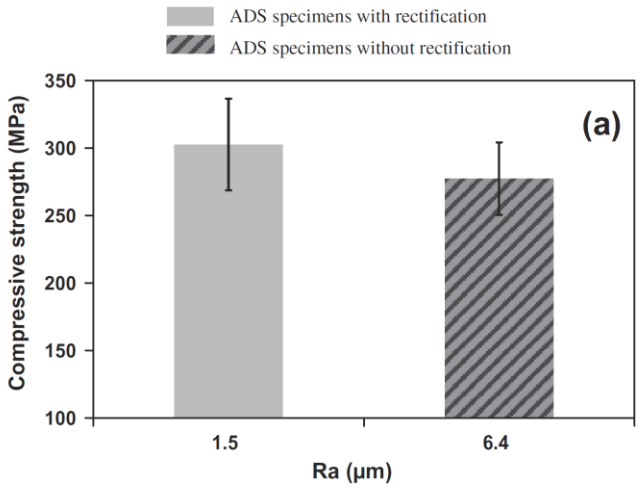

Figure 2.32 Influence of the rectification process of specimens trimmed by ADS process on the mechanical behaviour in compression testing (source: Haddad et al [46])

2.6 Fatigue in Composite Laminates

Composite materials are inhomogeneous and anisotropic accumulating damage in a general way rather than a localized manner. As in metals, failure does not always occur due to the propagation of a single macroscopic crack. The micro-structural mechanisms of damage accumulation, including fibre breakage and matrix cracking, debonding, transverse-ply cracking and delamination, occur sometimes independently and sometimes interactively and the predominance of one or the other may be strongly affected by both the materials variables and testing conditions [47].

The progression of damage in a composite laminate under fatigue loading conditions affects the mechanical properties to a magnitude which is dependent on the lay-up of the composite laminate and the loading conditions. Previous literature cited in this review confirms that the relationship between cutting direction and fibre angle orientation is critical in the type and magnitude of damage generated. Stacking sequence in composite laminates plays a vital role in the generation of damage during manufacturing processes and its propagation under service life conditions.

2.6.1 Types of Damage and Fatigue Effects

There have been a few bodies of research that have focused on the study of correlation between damage propagation to the stiffness reduction to the percent of life expended in fatigue testing of composite laminates. Reifsnider [48] and his team have been active in researching the damage mechanisms and their effects on strength in composite laminates. Jamison, Reifsnider & Stinchcomb [49] researched and documented the characterization and analysis of Damage mechanisms in Tension-Tension Fatigue of Graphite/Epoxy Laminates. They observed that the type of microdamage was related to the stacking sequence of the composite laminates. Fibre fracture occurs very early but does not progress as compared to other damage mechanisms such as delaminations that accelerate and reduce strength sharply. The damage modes were also related to each other and are interdependent. Matrix cracks can cause local fibre fracture and local interior delamination. They also concluded that the edges of laminates experience a different level of damage development due to the special stress states and the free surface deformation effects that exist at the edge locations as shown in Figure 2.33.

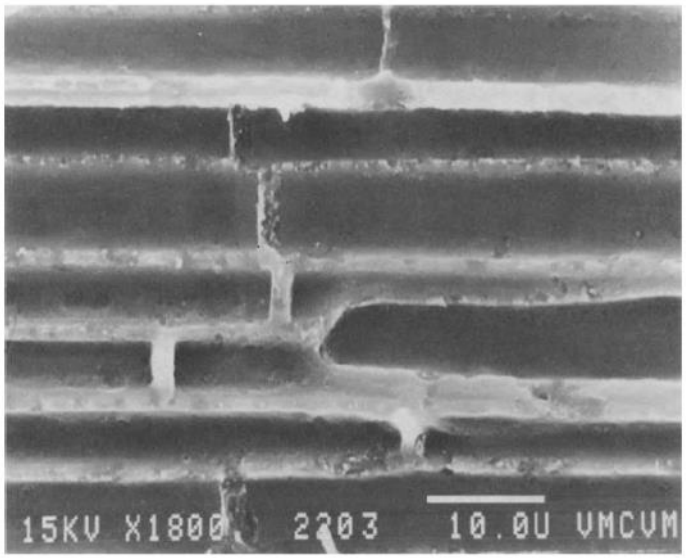

Figure 2.33 Details of Fibre Fracture in an Edge Replica (source: Jamison et. al [49])

Plumtree & Shi [50] conducted research in the fatigue damage evolution in off-axis unidirectional CFRP laminates. Their damage mechanism study showed that the variation in fatigue life for a given cyclic strain was found to be dependent upon the microstructure and the ease with which coalescence of matrix cracks occurred. When matrix cracks coalesced quickly, the fatigue life was short, while a good distribution of microcracks preventing the coalescence of microcracks resulted in better fatigue life. The fatigue life curves generated from their study were characterized by damage evolution based on modulus changes. Their work primarily focused on the study of damage mechanisms in conditions under which the matrix properties were dominant.

It has been documented through various studies that delaminations cause a larger degradation of stiffness in a composite laminate even though microcracking occurs first especially under service life conditions. Various researchers have studied the cause and effects of delaminations on the strength and fatigue life of composite laminates. Beghini et. al [51] studied the influence of crack front to the fibre orientation on fatigue delamination growth rate under mode II loading conditions (in-plane shear). Their conclusions and modeling showed that the delamination growth rate was related to the stacking sequence of the laminates but did not vary a large degree in magnitude.

Matrix Cracking and Delaminations remain the focus of damage studies in composite laminates. A schematic representation of these two types of damage mechanisms is shown in Figure 2.31.

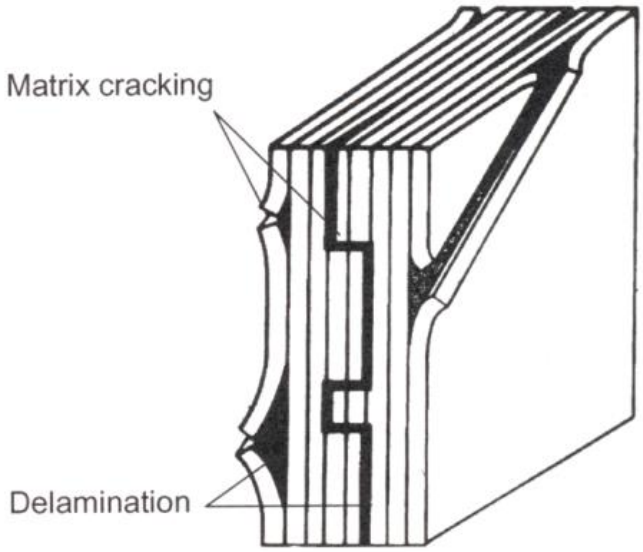

Figure 2.34 Typical Damage Modes for a Composite Laminate (source: Harris [47])

Pearson & Hallet [52] investigated the damage development and residual strengths of open hole tension specimens in fatigue. Quasi-isotropic carbon/epoxy laminates were used in their study with 45, 90- and 0-degree ply stacking directions. The study focused on the usage of X-ray CT to produce a 3D volume of the damage which was segmented to reveal the precise locations within the laminate in a non-destructive fashion as shown in Figure 2.35.

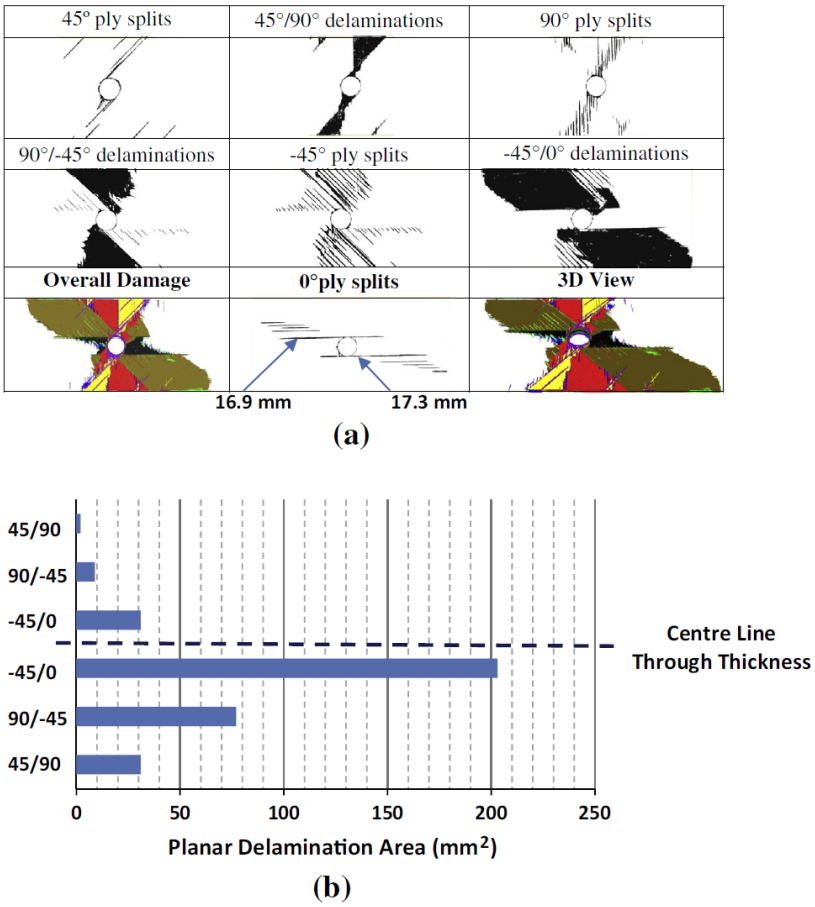

Figure 2.35 X-ray CT micrographs showing the damage magnitude and locations at 60% ultimate loading and a stiffness loss of 15% (source: Pearson & Hallet [52])

The research concluded that the dominanat mode of failure under fatigue loading was delaminations. The sub-laminate level portion of the study observed that the initial damage propagated out of the hole in terms of matrix cracks and delaminations. The failure events for the ply level and the sub-laminate level were more localized around the hole. Damage was also found to occur in the outer sub-laminates first before passing through the thickness of the laminate thus give rise to a more progressive damage sequence leading to failure [52].

Montesano et al [53] rsearched the infleucne of drilling and abrasive water jet induced damage on the performance of carbon fabric/epoxy plates with holes. The comparative study focused on the differences between drilling holes with conventional twist drills in comparisions to holes drilled with Abrasive Wate Jet (AWJ). The damage evolution with both processes is shown in figure 2.36.

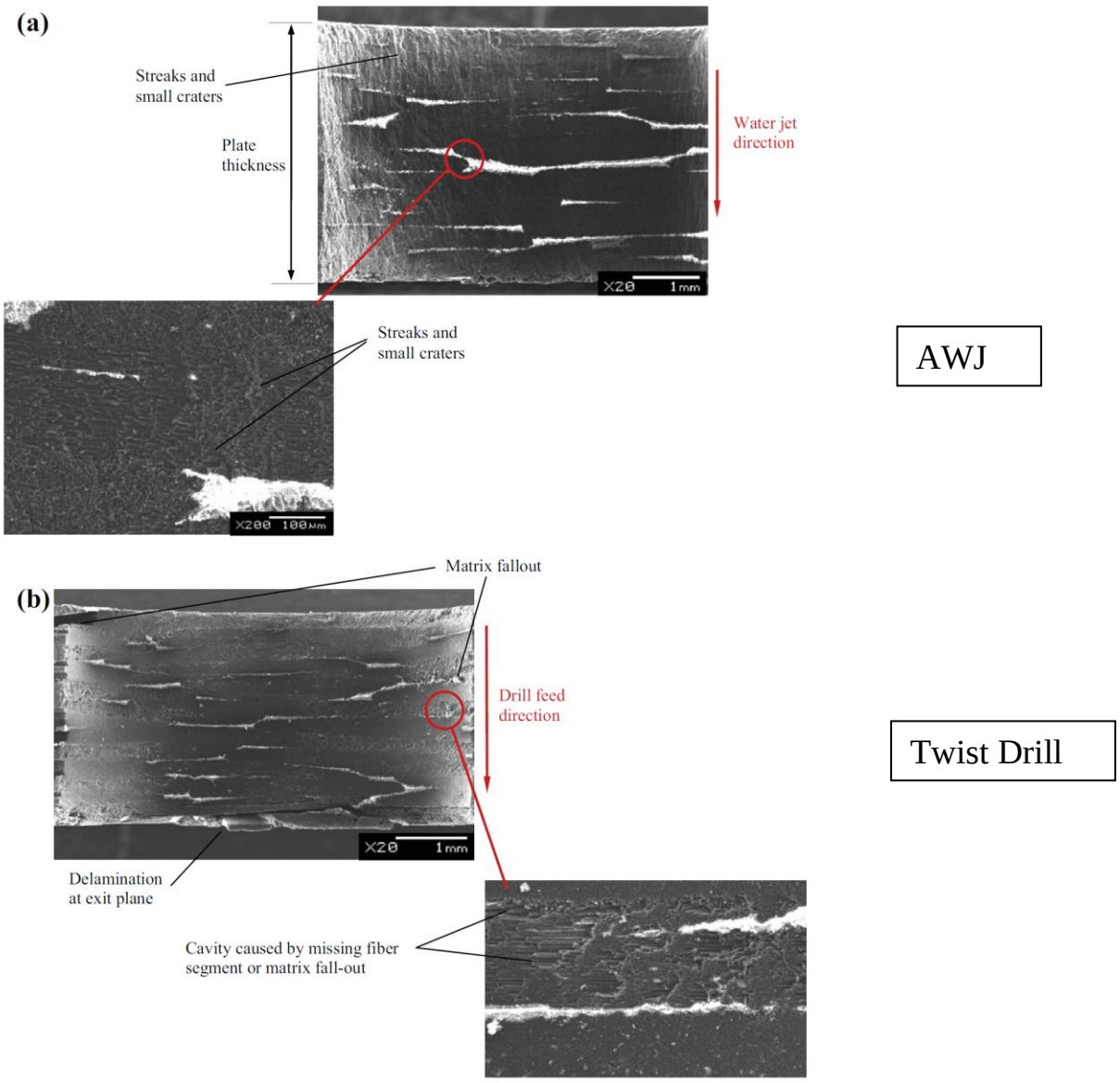

Figure 2.36 SEMs showing damage in carbon fabric/epoxy plates with (a) AWJ drilling (b) Conventional Twist Drill (source: Montesano et al [53])

The study concluded that the AWJ drilled hole specimens displayed greater than long-term fatigue performance at high stress levels in comparison to conventional twist drill hole specimens [53]. This was attributed to the severe damage modes present in the conventional drill specimens including localized delamination at hole exit plane and fibre pullouts. The AWJ specimens had streaks and craters aligned with jet direction and uniformly distributed along the hole surface.

The effect of conventional drilling processes in comparison to AWJ drilling process on the mechanical behaviour of CFRP plates with holes was also studied by Saleem, M. et al [54]. Fatigue

testing results showed that the damage accumulation in specimens drilled with conventional drilling was higher than specimens drilled with the AWJ process as shown in Figure 2.37.

$$D = 1 - (\frac{E_i}{E_o})$$

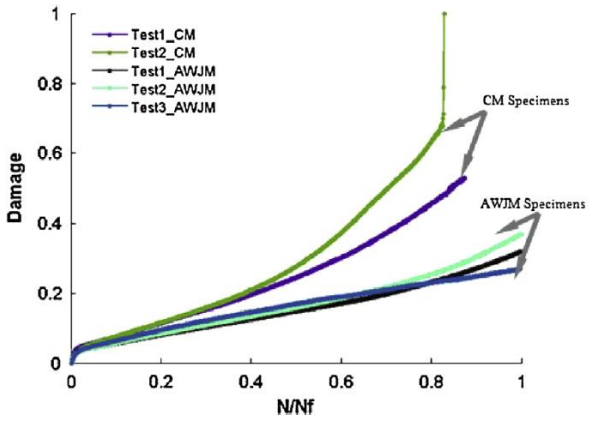

Figure 2.37 Damage vs. cycles for fatigue testing of Conventional Drill (CD) and AWJ drilled specimens (source: Saleem, M. et al [54])

The authors of the study used a Thermographic Damage Criterion (TDC) based on heat dissipation to assess the effect of two types of machining processes (conventional drilling vs. AWJ drilling on the mechanical behaviour of CFRP plates. The influence of hole surface damage on the fatigue performance was studied. The surface damage at the hole wall was studied and noted that the conventional drilled holes showed visibly district regions of fibre pullout and epoxy matrix degradation while those of AWJ drilled holes showed striation marks in the direction of water-jet [54] as shown in Figure 2.38. Also shown are SEM photographs of the damage in Figure 2.39.

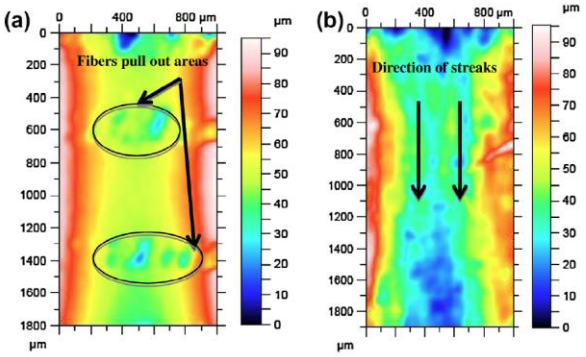

Figure 2.38 Cartography of the surface roughness of the wall of the hole obtained with (a) conventional drilling (b) AWJ drilling (source: Saleem, M. et al [54])

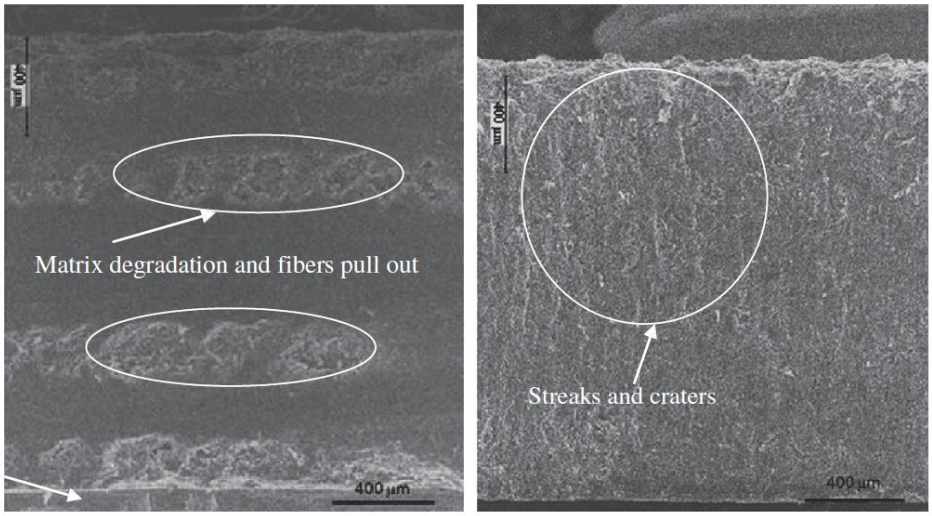

Figure 2.39 SEM photographs of the surface roughness of the wall of the hole obtained with (a) conventional drilling (b) AWJ drilling (source: Saleem, M. et al [54])

Venkatachalam et. al [55] researched the damage evolution in CFRP subjected to cyclic loading using Digital Image Correlation (DIC) to obtain full field surface strains. Their study showed that the variation of normalized local transverse strain (ratio of local transverse strain to applied stress) near the initiated delamination indicates that the damage evolution occurred over 2 to 3 stages. Each stage has a stable damage growth with a drastic increase between stages. The stages correspond to different damage mechanisms and matrix cracking, fibre-matrix debonding, delamination and fibre breakage) dominating at different periods during the fatigue life. Normalized local transverse strain plots were found to qualitatively reflect the physical extent of damage, thereby providing confidence in the methodology. The researchers found that the damage become critical after delamination became visible that occurred at nearly half the fatigue life in specimens subjected to Tension-Tension fatigue. Generally, the fibres can keep carrying the tensile loads even after debonding from the matrix until fibre fracture occurs.

The study concluded that the local transverse strain is a better indicator of damage in composites because delamination leads to a reduction in local stiffness in transverse direction due to local “bending/buckling’ of the delaminated layer.

Figure 2.40 shows the transverse strains and damage during tension-tension fatigue testing at various N cycles and with R = 0.5 value for the testing

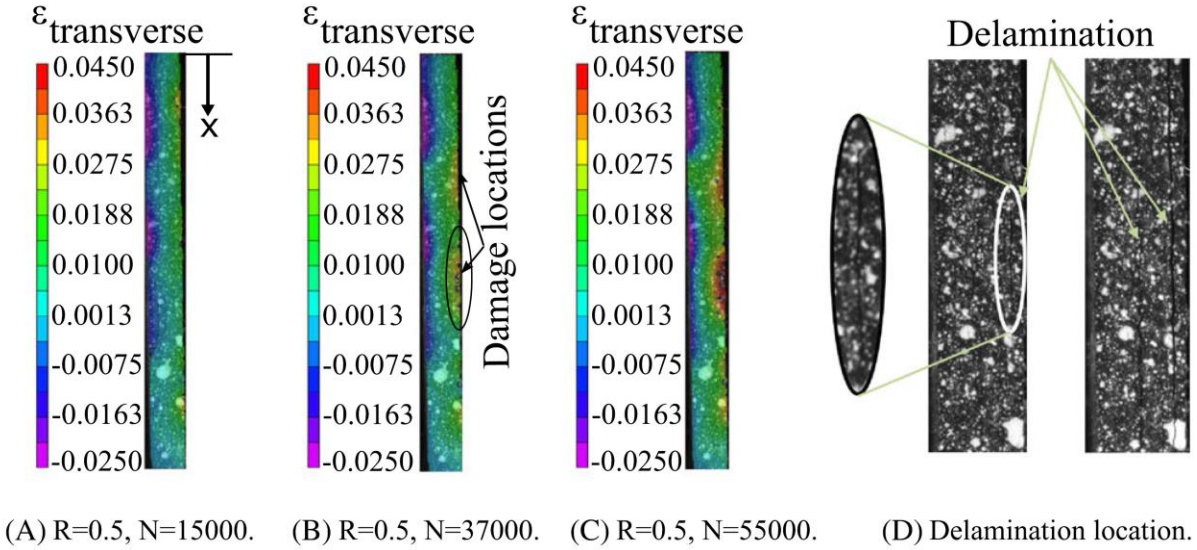

Figure 2.40 Transverse strains for different (N) cycles for tension-tension fatigue testing, (source: Venkatchalam et. al [55])

Figure 2.41 shows the various stages of damage evolution during Tension-Compression fatigue testing as documented in the study.

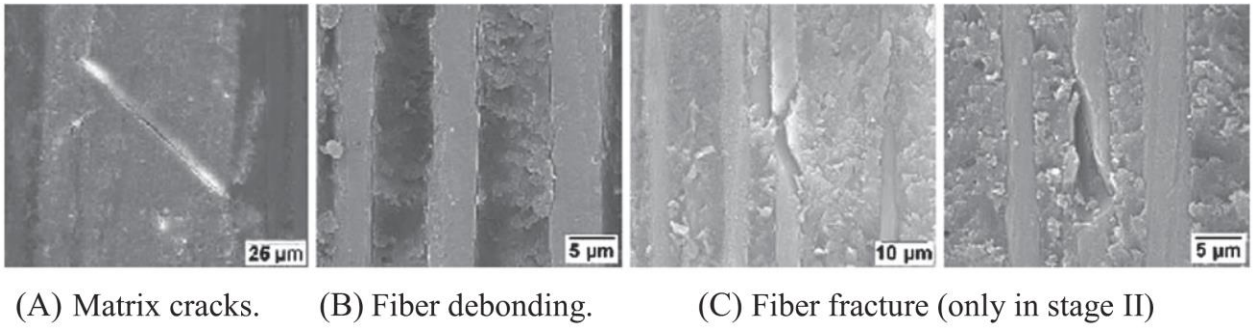

Figure 2.41 Various stages of damage evolution during tension-compression testing, (source: Venkatchalam et. al. [55])

Ansari Alam et. al. [56] explored the effects of various parameters such as fibre type, fibre orientation, fibre volume fraction etc. on the fatigue behaviour of fibre-reinforced polymer

composites. Fibres are the main load bearers in the composites so the fatigue behaviour is affected by the types of fibres used in the composites. The use of carbon fibre confines the strain in the composite thereby limiting the vast distortion in the matrix. The usage of glass fibre allows larger distortions in the matrix giving rise to the fatigue failure. It was also found that the Kevlar fibres are fatigue sensitive. Figure 2.42 shows the S-N curves for the unidirectional composite materials using different fibres.

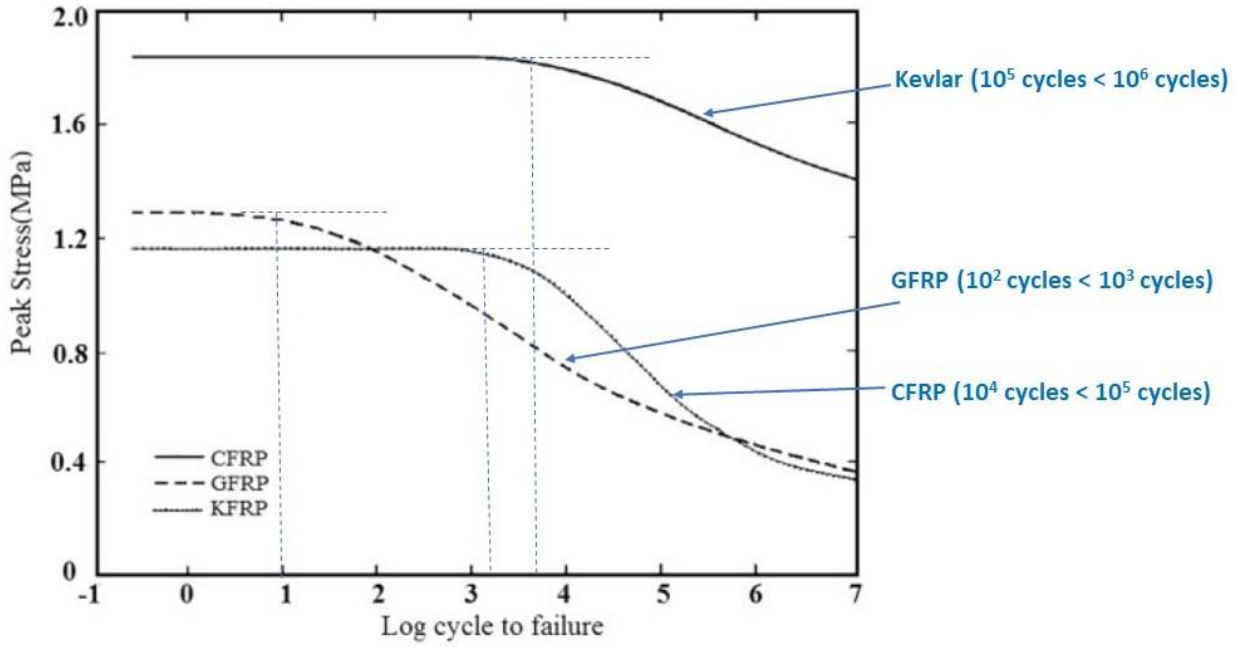

Figure 2.42 S-N curves for unidirectional composite materials with different fibres (source: Ansari Alam et. al [56])

The researchers found that the fibre volume fraction affected the static and fatigue strength properties. Stiffness, strength and load carrying capacity of a laminate are higher with a higher fibre content. When the fibre volume fraction (V_f) is high the ultimate strength decreases. With increased fibre volume fraction, the matrix content decreases which can and does affect the load carrying capacity of a laminate as the fibres and matrix carry load as a system. The researchers found that the ideal volume fraction of fibres is between 45 – 60%. If the fibre volume fraction keeps increasing, at a certain point the strength of the composite starts decreasing because of the lack of matrix to hold the fibres together.

Figure 2.43 shows the variance of fatigue life with two different fibre volume fractions.

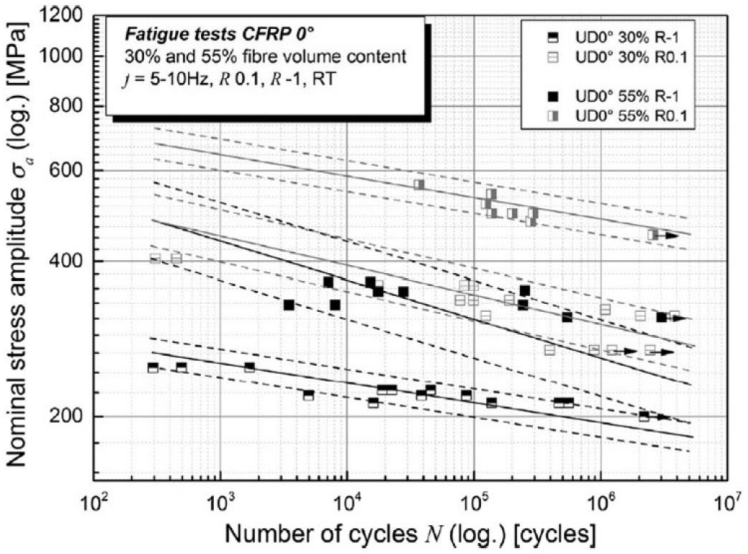

Figure 2.43 Comparison of fatigue life with two different fibre volume fraction (source: Ansari Alam et. al [56])

The study also found that the fibre orientation influenced the mechanical properties of fibre-reinforced composite laminates with decreasing strength of the laminates with increasing fibre orientation, Figure 2.44 shows the variation of static strength with fibre orientation angle, while Figure 2.45 shows the variation of fatigue strength with the fibre orientation angle.

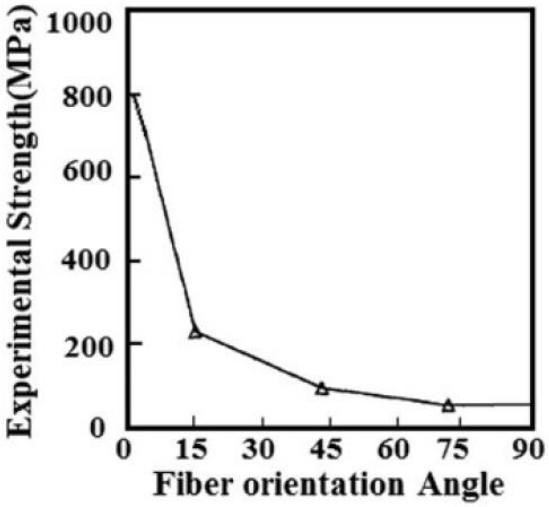

Figure 2.44 Variation of static strength with Fibre orientation angle (source: Ansari Alam et. al [56])

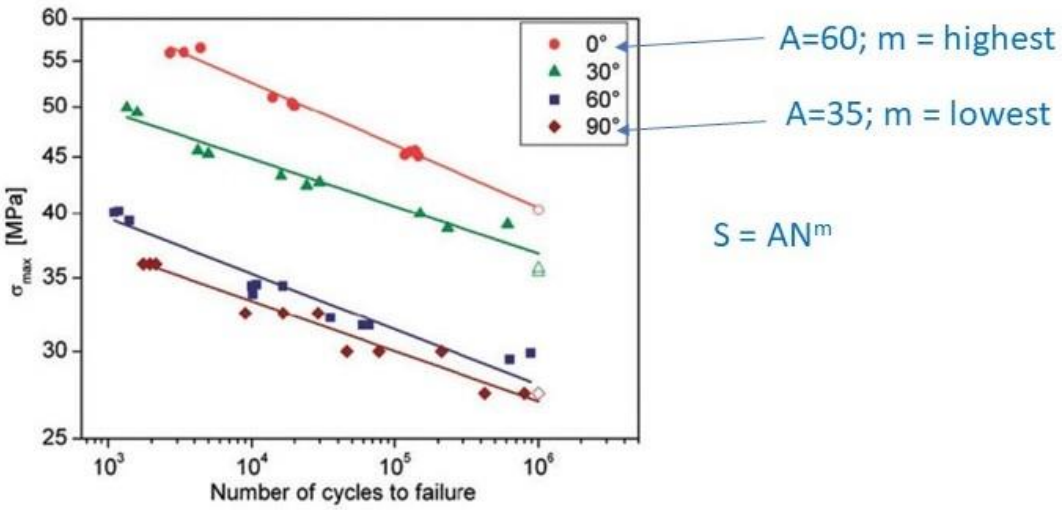

Figure 2.45 S-N Curves for different fibre orientation angles (source: Ansari Alam et. al [56])

The study by Ansari Alam et. al [56] also studied the damage mechanism indicating the 3 stages of damage evolution mainly, matrix cracking, fibre-matrix debonding and fibre fracture and delamination prior to failure. The magnitude of damage is influenced by the property of each lamina, interface property of the laminate and stacking sequence. The 3 stages of damage evolution in unidirectional composites are shown in Figure 2.46

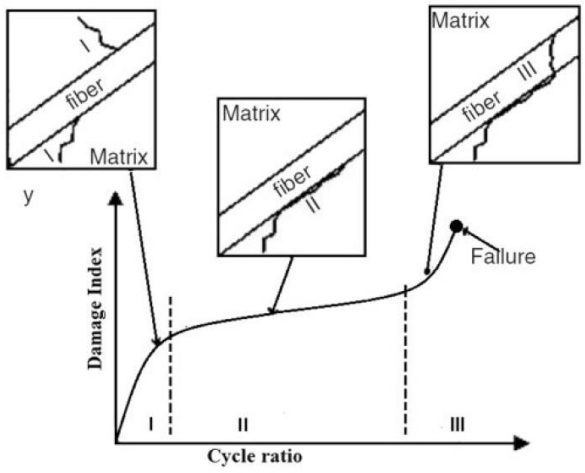

Figure 2.46 Damage evolution stages in unidirectional composites (source: Ansari Alam et. al [56])

Along with previously discussed parameters, Ansari Alam et. al [56] also studied the effects of the following on the fatigue damage of fibre-reinforced polymer composites.

a) Mean stress and stress ratio
b) Frequency and hysteresis effect
c) Environmental effects
    a. Temperature
    b. Moisture

2.6.2 Bolted Joints and Fatigue

As most composite laminates are used in assemblies, the behavior of bolted composite joints in under fatigue loading has dominated the in-service effects research studies. Xiao & Ishikawa [57] researched the bearing strength and failure behaviour of bolted composite joints. Their study concluded that bearing failure is a process of compressive damage accumulation occurring in four stages, damage onset; damage growth; local fracture; structural fracture. Delamination was one of the dominant modes of damage onset and large-scale delamination were the major cause of final fracture along with through-thickness shear cracks. Figure 2.47 shows the delamination damage in a bolted composite joint under service loading conditions.

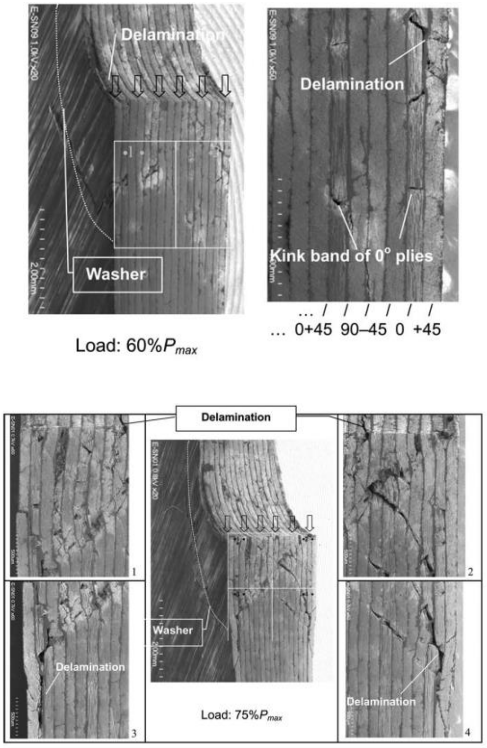

Figure 2.47 Delamination Damage in a Bolted composite Joint under Service Life Conditions, (source: Xiao & Ishikawa, [57])

Seike et. al [58] studied the Fatigue and Static Damage of a Pinned Joint in CFRP Composite Laminates. Their study concluded that there was not much difference in the macroscopic external damage between fatigue and static loading failure while the microscopic internal damage showed differences both in critical damage and damage evolution. They also found that the total delamination length was longer than the matrix crack length during fatigue failure. Figure 2.48 shows the damage growth during the fatigue loading as part of their experimental study.

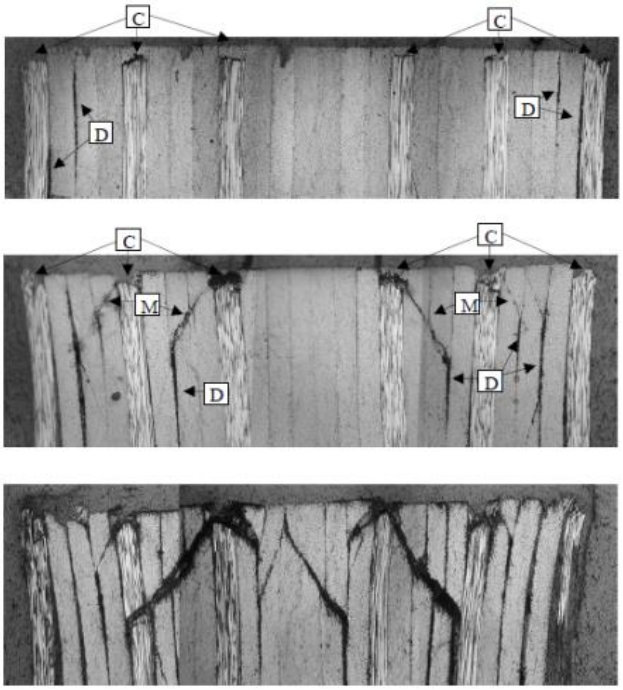

Figure 2.48 Damage Evolution in a Pinned Joint in CFRP Laminate under Fatigue Loading, (source: Seike et. al [58])

2.6.3 Fatigue Damage Modeling

Past researchers have developed fatigue models and life time prediction methodologies for fibre-reinforced polymer composites subjected to fatigue loadings. Degrieck & Paepegem [59] conducted a detailed review of fatigue damage modeling of fibre-reinforced composite materials. They classified the fatigue models into the following three categories:

a) Fatigue Life Models that do not take into account the actual degradation mechanisms but use S-N curves or Goodman-type diagrams and introduce some sort of fatigue failure criterion
b) Phenomenological models for residual stiffness/strength
c) Progressive damage models that use one or more damage variables related to measurable manifestations of damage (transverse matrix cracks, delamination size).

Progressive damage models are further subdivided into two categories:

1) Models that predict the damage growth such as number of transverse of matrix cracks per unit length, size of delamination area
2) Models that correlate the damage growth with the residual mechanical properties (stiffness/strength)

Wicaksono and Chai {[60] also conducted a review of advances in fatigue and life prediction of fibre-reinforced composites. The study categorized the review into four different groups:

1) Fatigue of fibre-reinforced composites
2) Composite damage mechanism
3) Composite failure criteria
4) Composite fatigue modeling and life prediction

The study reviewed the research conducted on various factors shown in Figure 2.49 affecting fatigue of fibre-reinforced composites

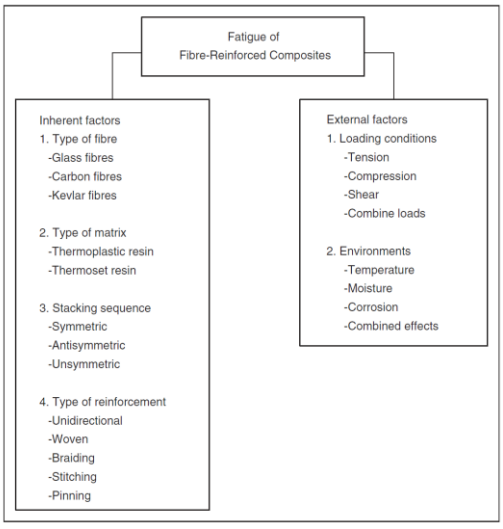

Figure 2.49 Factors affecting fatigue life of fibre-reinforced composites (source: Wicaksono & Chai [60])

For the composite damage mechanism review the study [60] focused on the research conducted on types of damage in unidirectional and multidirectional composites along with woven and three-dimensional composites. In the case of composite failure criteria, the study reviewed the mode independent and mode dependent criteria as shown in Figure 2.50 while using the fundamental three-dimensional state of stresses as shown in Figure 2.51

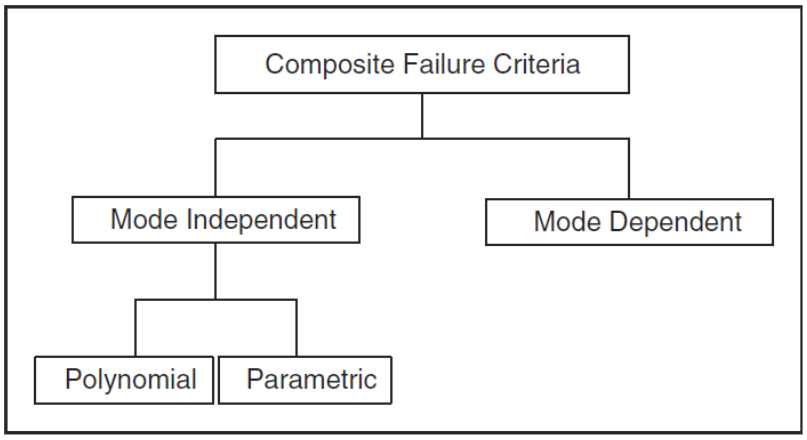

Figure 2.50 Composite failure criteria classification (source: Wicaksono & Chai [60])

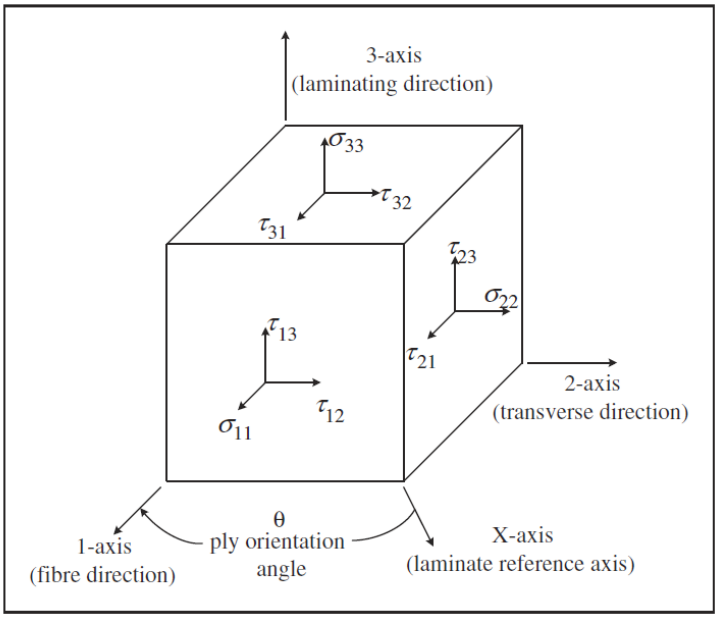

Figure 2.51 Three-Dimensional state of stresses (source: Wicaksono & Chai [60])

As part of the composite fatigue modeling and life prediction review the researchers classified the modeling into 3 categories:

1) Fatigue life
2) Phenomenological
3) Progressive Damage

Figure 2.52 shows the classification of composite fatigue modeling

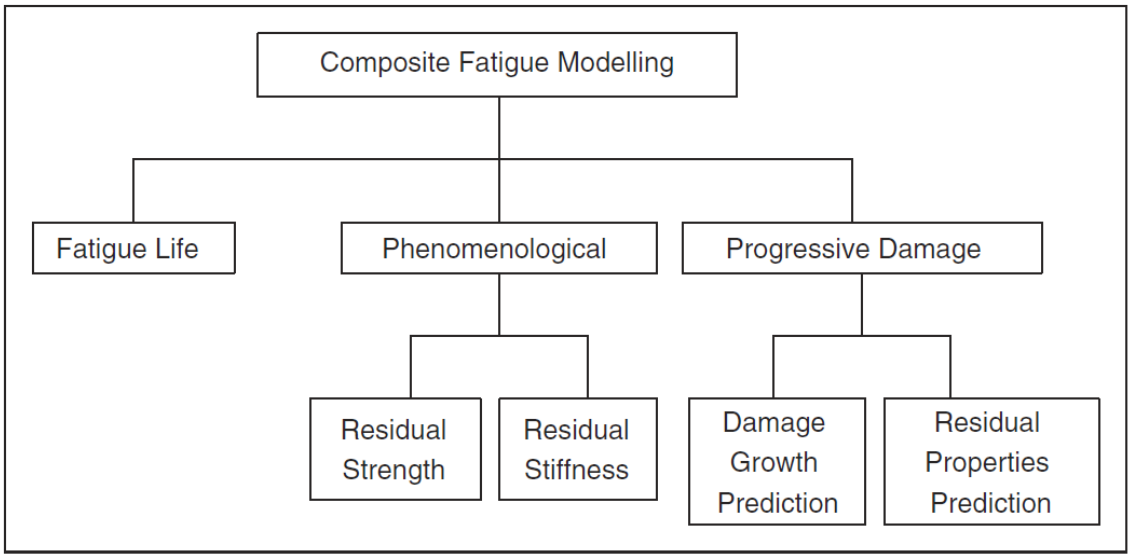

Figure 2.52 Composite fatigue modeling classification (source: Wicaksono & Chai [60])

Bak et al. [61] conducted a study of delamination under fatigue load in composite laminates and a review on the observed Phenomenology and Computational methods. Fatigue delamination was studied at three different stages initiation, onset and propagation. Phenomenological models are mainly used for delamination propagation and relate fracture mechanics quantities like energy release rates or the stress intensity factor with the crack growth rate obtained in the experiments. Simulation models that make use of computational models are based on either Linear Elastic Fracture Mechanics (LEFM) or Cohesive Zone Models (CZM).

Models based on LEFM make a direct comparison of computed values (stress intensity factor or energy release rate) with a critical value obtained with phenomenological models. They also can account for different parameters (load ratio, mixed-mode and threshold) [61].

CZMs can be used to predict delamination initiation, onset and growth in a structure. The maturity of CZMs is very low and availability for delamination onset is not there thus resulting m most availability and usage of CZMs for delamination propagation [61].

Shirazi & Varvani-Farahani [62] researched and developed a stiffness degradation based fatigue model for FRP composites of (0/θ) laminate systems. The damage model was constructed based on (i) cracking mechanism and damage progress in matrix, matrix-fibre interface and fibres and (ii) the corresponding stiffness reduction of unidirectional composite laminates as the number of cycles progresses. The overall damage was estimated by integrating the fatigue damage of the 0 degree and θ degree plies. The fatigue damage model takes into account the effects of off-axis angle θ, cyclic stress magnitude, mean stress and the fibre-matrix interfacial strength factor f and is given by

$$D = 1 - \frac{E}{E_c} = \left\{E_{m\theta}[\alpha + f(\gamma - \alpha)] + E_{f\theta}R^*\lambda\right\} \tag{2.12}$$

where

E_c= Modulus of composite laminate

$E_{m\theta}$ = Modulus of matrix accounting for off-axis angle θ

$E_{f\theta}$ = Modulus of fibre accounting for off-axis angle θ

And

$$E_{m\theta} = 1 - E_f V_f / E_c \tag{2.13}$$

$$E_{f\theta} = E_f V_f (\cos\theta)/E_c \tag{2.14}$$

where

V_f = Volume fraction of fibres

The terms α, γ and λ are functions of the number of cycles to failure N_f and progressing fatigue cycles N while n corresponds to percentage reduction in stiffness during the fatigue test and are described as:

$$\alpha = \frac{\ln(n(N+1))}{\ln(N_f)} \tag{2.14}$$

$$\gamma = \left(n\frac{N}{N_f}\right) \tag{2.15}$$

$$\lambda = \frac{\ln\left(1 - n\frac{N}{N_f}\right)}{\ln\left(\frac{n}{N_f}\right)} \tag{2,16}$$

where

n = percentage of drop in stiffness recorded for a fatigue test

f = representative of fibre/matrix interfacial shear strength and varies between 0 and 1

Equation 2.12 was used by Shirazi & Varvani-Farahani [62] to predict damage and validated with experiments as shown in Figure 2.53

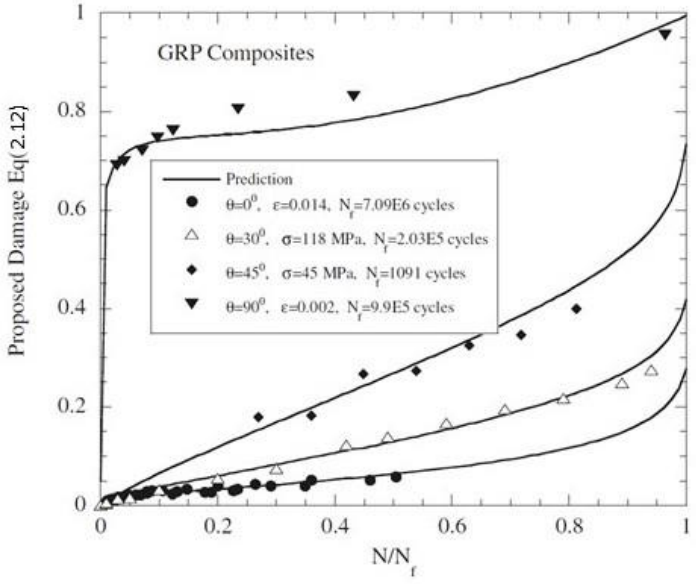

Figure 2.53 Predicted versus experimental values of damage for UD GRP composites tested under various off-axis angles θ and stress amplitudes (source Shirazi & Varvani-Farahani [62])

The authors of the study also tested experimentally and verified the model for various off-axis angle θ and stress amplitudes. Some of the results are shown in Figures 2.54 and 2.55

The results between the predictive model and those obtained with experimental testing were found to be in good agreement,

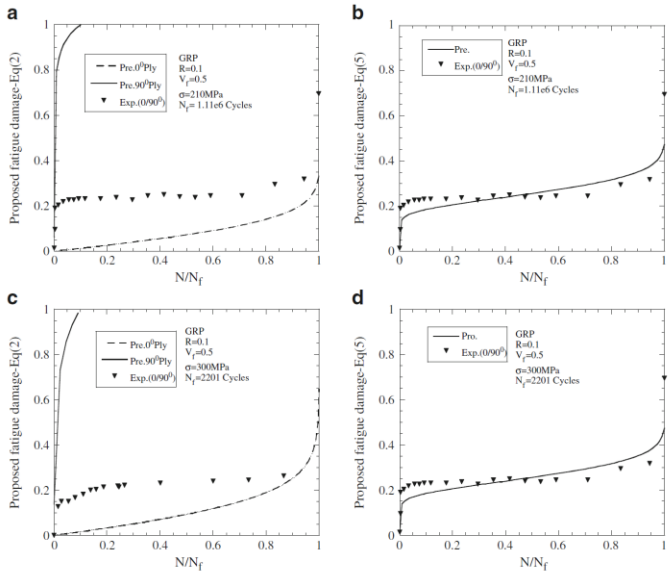

Figure 2.54 Predicted fatigue damage versus experimental data for 210 MPa stress and off-axis angle plies (a) 0 degree (b) 90 degree and for 300 MPa for (c) 0 degree (d) 90 degree (sources: Shirazi & Varvani-Farahani [62])

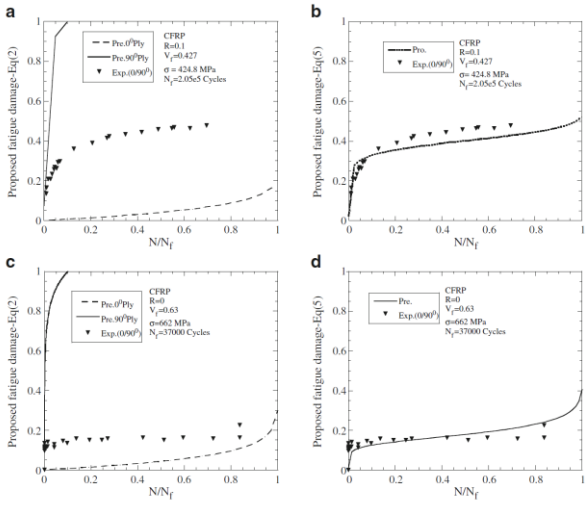

Figure 2.55 Predicted fatigue damage versus experimental data for 424.8 MPa stress and off-axis angle plies (a) 0 degree (b) 90 degree and for 662 MPa for (c) 0 degree (d) 90 degree, (source: Shirazi & Varvani-Farahani [62])]

Senthinathan et. al. [63] researched the linkage between the damage state and the stiffness degradation regardless of how the damage state was created. In the study controlled microstructural damage was created by subjecting the unidirectional CFRP specimen to tension-tension fatigue load with predetermined stress ratio, load factor and number of cycles.

For the experimental portion of the study, specimens were fabricated with 0°, 45°, 90° fibre orientations. Specimens were subjected to monotonic tensile testing to determine the modulus of elasticity. Tension-tension fatigue testing was conducted to determine the load factors for controlled damage testing in the next phase of fatigue testing. Interrupted fatigue testing was conducted to obtain varying degree of damage. The microstructure was observed using bright field imaging and digitally recorded using CCD camera.

To obtain 3D microstructural parameters, the researcher used stereology which uses the volume fraction and image analysis to convert from two-dimensional observations to 3D results. Fibre volume fraction V_v is given by

$$V_V = \frac{A_f}{A_{tot}} \tag{2.17}$$

Where

A_f = Area occupied by the fibre in μm^2

A_{tot} = Total Area of micrograph in μm^2

The quantification of damage was represented by Fibre cracks per unit volume, Fibrematrix debonding area and Crack surface area per unit volume

Fibre cracks per unit volume is calculated by:

$$(N_V)_f = \frac{(N_A)_f}{\overline{D}} \tag{2.18}$$

$$(N_A)_f = \frac{n_f}{A} \tag{2.19}$$

$$\overline{D} = 2r \tag{2.20}$$

Where

$(N_v)_f$ = Fibre cracks per unit volume (μm^{-3})

$(N_A)_f$ = Fibre cracks per unit area (μm^{-2})

n_f = number of fibre cracks

A = Area of the micrograph

r = Radius of fibre in µm

Fibre/matrix debonding area was estimated from a micrograph containing interface debonding. It was obtained by superimposing an array of grid lines, perpendicular to the fibre axis, on an image and counting the number of intersections and debonding. It was calculated by:

$$(S_V)_{db} = 2(I_L) \tag{2.21}$$

Where

$(S_v)_{db}$ = Debonding area per unit volume (μm^{-1})

I_L = Average number of intersection points per unit length of a test line (μm^{-1})

Matrix micro crack was used as a measure of crack surface density, defined as crack surface per unit volume. It was obtained by superimposing parallel grid lines on an image and counting the number of intersections of grid lines and cracks. It was calculated by:

$$(S_V)_m = 2(I_L) \tag{2.22}$$

Where

$(S_v)_m$ = Crack surface area per unit volume (μm^{-1})

I_L = Average number of intersection points per unit length of a test line (μm^{-1})

Figure 2.56 shows the 3D state of damage space showing Fibre breakage, debonding and matrix cracking.

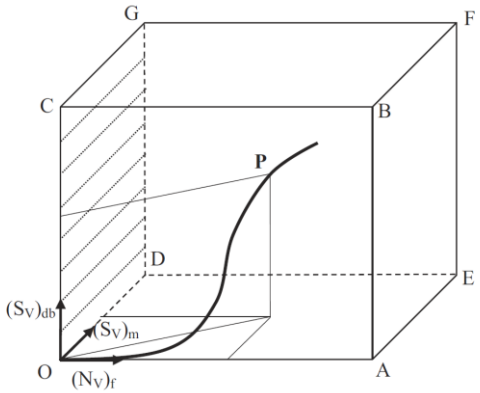

Figure 2.56 3D Damage state space showing fibre breakage, debonding and matrix cracking, (source: Senthinathan et. al. [63])

The progression of damage was observed for various orientations of fibres and micrographs are shown in Figure 2.57.

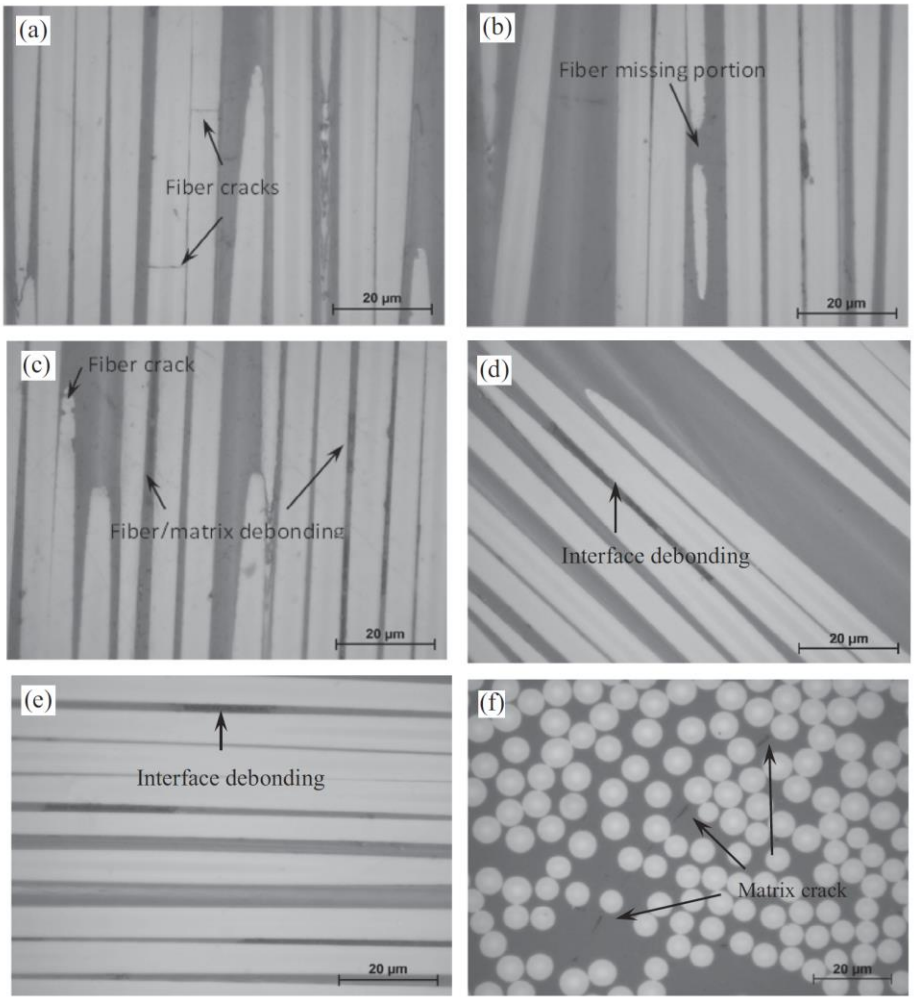

Figure 2.57 Micrographs showing a) 0°fibre cracks b) 0° fibre missing c) 0°fibre/matrix debonding d) 45°fibre/matrix interfacial debonding e) 90° fibre/matrix interfacial debonding f) 90°Matrix cracking (source: Senthinathan et. al. [63])

The research study observed that there was a steep reduction in normalized stiffness at the onset of fatigue. With further increase in number of cycles, reduction in normalized stiffness was gradual irrespective of fibre orientation and stress ratio. Microstructural damage was observed in the form of fibre cracking, interface debonding and matrix cracking. However, the damage mechanisms were different and not always occurring in all fibre orientations. Interface debonding was observed

in all fibre orientations while fibre cracking and matrix cracking were observed in the 0° and 90° fibre orientations.

The variation of the normalized elastic modulus with damage mechanisms for different fibre orientations are shown in Figure 2.58

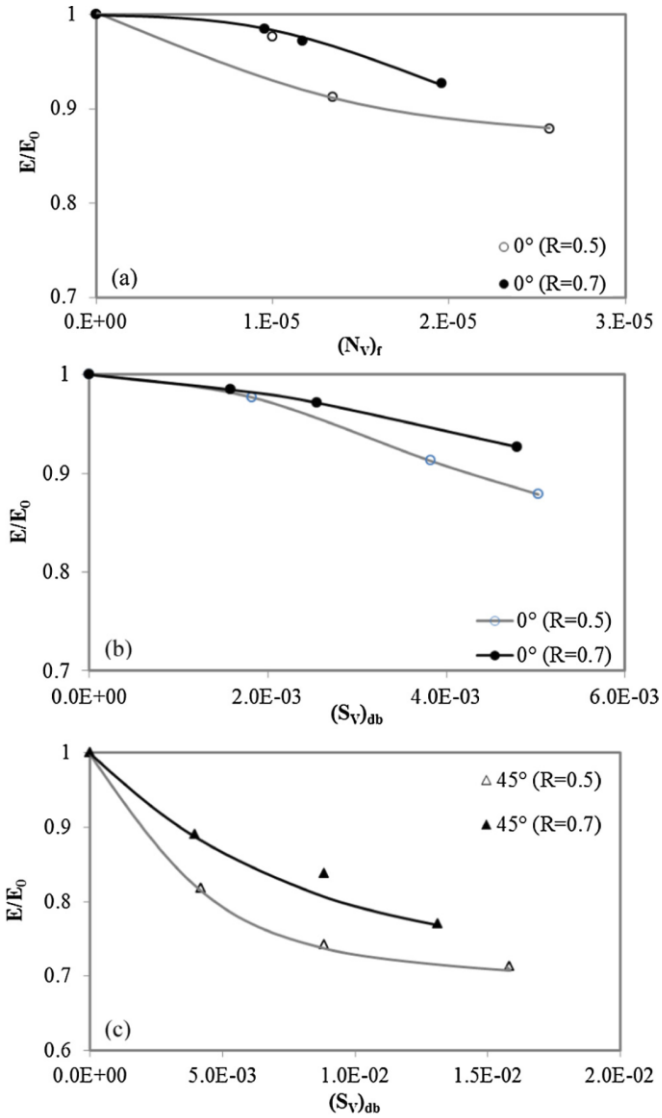

Figure 2.58 Elastic Modulus variation with respect to a) fibre damage in 0° b) interface debonding in 0° c) interface debonding in 45° (source: Senthinathan et. al. [63])

Whitworth [64] conducted a study in developing a stiffness degradation model for composite laminates under fatigue loading. The model developed was based on an assumed relationship

between the failure stiffness and the applied stress. An experimental study was conducted to evaluate the model.

The model formulation was limited to specimens subjected to constant amplitude fatigue loading with the assumption that the residual stiffness is a monotonically decreasing function of the fatigue cycles. The residual stiffness degradation is given by:

$$\frac{dE^*(n)}{dn} = \frac{-a}{(n+1)E^*(n)^{m-1}} = \frac{d\left[\frac{E(n)}{E(N)}\right]}{dn} \tag{2.23}$$

Where

$E^*(n) = E(n)/E(N)$

$E(n)$ = residual stiffness

$E(N)$ = Failure stiffness

n = number of load cycles

a, m = parameters dependent on applied stress

Integration of equation 2.24 results in equation 2.25 which represents the residual stiffness after n fatigue cycles

$$E(n) = E(N)\left[-h\ln(n+1) + \left(\frac{E(0)}{E(N)}\right)^m\right]^{1/m} \tag{2.24}$$

Where

$E(0)$ = Stiffness at 0 cycles

$h = a$ x m

Since equation 2.25 requires the determination of failure stiffness $E(N)$ which can be obtained only after failure occurs, the usage of failure strain criterion helps in development of the model. Failure strain criterion assumes that the failure of the specimen will occur when the fatigue strain reaches the tensile ultimate strain.

$$\frac{S}{S_u} = c_1\left[\frac{E(N)}{E(0)}\right]^{c_2} \tag{2.25}$$

Where

S = Applied Stress

S_u = Ultimate Strength

The stiffness life relation model was developed and is given by:

$$E(n) = E(0)\left(\frac{S}{c_1 S_u}\right)^{1/c_2}\left[-h\ln(n+1) + \left(c_1\frac{S_u}{S}\right)^{m/c_2}\right]^{1/m} \quad (2.26)$$

Where

c_1, c_2= constants obtained experimentally

The model was validated with experimental testing and comparisons between the model predictions and the experimental results were generally good [64].

Amongst the models predicting damage growth, Dahlen & Springer [65] proposed a semi-empirical model for estimating delamination growth in graphite/epoxy laminates under cyclic loading including mode I, mode II and mixed-mode conditions. They used the crack growth rate described with dimensionless grouping and a Paris similar growth law:

$$\Delta a \frac{\sigma_f^2}{E_y G_{crit}} = A\left(U\frac{G_{max}}{G_{crit}}\right)^b \quad (2.27)$$

where Δa is the delamination growth normal to the circumference of the existing delamination

σ_f is the ply strength

E_y is the transverse ply modulus

G_{crit} is the critical energy release rate with contributions from mode I and mode II

A & b are parameters which depend upon the material and the relative contributions of mode I and mode II to the delamination growth

U is a function of $\frac{G_{max}}{G_{crit}}$ and of $\frac{G_{min}}{G_{max}}$

G_{max} is the total maximum energy release rate during the cycle under consideration

Henaff-Gardin et. al [66] researched progressive matrix cracking in cross-ply laminates. They established the propagation law under fatigue loadings as:

$$\frac{dS}{dN} = A\left(\frac{G_I}{G_{max}}\right)^n \quad (2.28)$$

where S is the crack surface

G_I is the strain energy release rate for the current crack density

G_{max} is the strain energy release rate when the first matrix crack initiates

A & n are constants determined from experimental measurements of crack density

Researchers have also developed progressive damage models that relate the damage variables with the residual mechanical properties (stiffness/strength) of the laminate. The damage growth rate equations of such models are often based on damage mechanics, thermodynamics, micromechanical failure criteria or specific damage characteristics such as crack spacing, delamination area etc. [67].

Since most damages interact in composites, damage modeling with single types if damage variables is problematic. Reifsnider [68] proposed a modeling philosophy to counteract the problem of interaction of damage types. He used the approach of the representation volume concept. The representation volume is divided into critical and subcritical elements. In the subcritical elements, damage initiation and propagation is modeled on a micromechanical level and the local stress fields are calculated. Details not important for the determination of the local stress field associated with the final failure event are grouped into continuum representation of the critical elements in the representation volume. The reduction in strength is calculated by using the integral formulation:

$$\frac{S_L^r(\tau_1)}{S_{Lu}^i} = \left[\frac{(F_e/F_L)^i}{F_e(\tau)/F_{L(\tau)}}\right]_{rv} . \left[1 - \int_0^{\tau_1}(1 - F_e(\tau)k(t)^{k-1}d\tau\right] \qquad (2.29)$$

The quantity on the left side is the residual strength, normalized by the initial ultimate strength for the failure mode. The first factor on the right is the ratio of the initial stress concentration to the current stress concentration in a representative volume (rv) and *F* is a generalized failure function. The subscript *e* indicates that the value of that failure function *F* is evaluated in the critical element and the subscript *L* indicates the value of *F* in the laminate at some position from the location of the failure event. All quantities in the integral are evaluated in the critical element. The failure function is written as a function of time since the stress state in a critical element changes as damage develops in the subcritical elements around it. The Critical Element Method was used to determine the variables and uses a micro-mechanical analysis to determine local stress

redistribution caused by the failure of "subcritical elements", and phenomenological (constitutive) information to characterize the condition of the "critical elements" which control fracture. This methodology has been used by other researchers such as Diao et. al [69] and Subramanian et. al. [70].

Similarly, Bak et al. [61] conducted a study of delamination under fatigue load in composite laminates and a review on the observed Phenomenology and Computational methods. Fatigue delamination was studied at three different stages initiation, onset and propagation. Phenomenological models are mainly used for delamination propagation and relate fracture mechanics quantities like energy release rates or the stress intensity factor with the crack growth rate obtained in the experiments. Simulation models that make use of computational models are based on either Linear Elastic Fracture Mechanics (LEFM) or Cohesive Zone Models (CZM).
Models based on LEFM make a direct comparison of computed values (stress intensity factor or energy release rate) with a critical value obtained with phenomenological models. They also can account for different parameters (load ratio, mixed-mode and threshold) [69].
CZMs can be used to predict delamination initiation, onset and growth in a structure. The maturity of CZMs is very low and availability for delamination onset is not there thus resulting m most availability and usage of CZMs for delamination propagation [70].
A study of numerical modeling of damage development in open-hole composite specimens in fatigue was conducted by Pearson et al [71]. The study investigated the capability of a cohesive interface element formulation with fatigue damage capability to predict the damage development and failure of open-hole tensile specimens. The damage pattern consists of multiple delamination interfaces, matrix cracks and complex interactions between them. The study combined the modelling techniques developed for predicting the static strength of open-hole tensile specimens with the extended capability of interface elements to predict damage accumulation under fatigue loading. The numerical models used were first loaded in static conditions to determine failure loads and then used in fatigue loading using a loading envelope strategy at varying percentages of the static failure load. A detailed comparison of the predicted failure behaviour in terms of the stiffness loss and damage development was undertaken against experimental data. A very good correlation between the experiments and modelling was observed Initially damage starts to propagate out from

the hole edge in terms of matrix cracks and delamination. Once this propagates through the thickness, asymmetric -45/0 delamination occurs causing the large effective modulus drop [71].

Shokreih & Behrooz [72] developed a progressive fatigue damage model based on two assumptions. First it was assumed that off-axis plies are responsible for stress redistribution into the laminate. Second, the on-axis plies are responsible for strength reduction and control failure of the laminate.

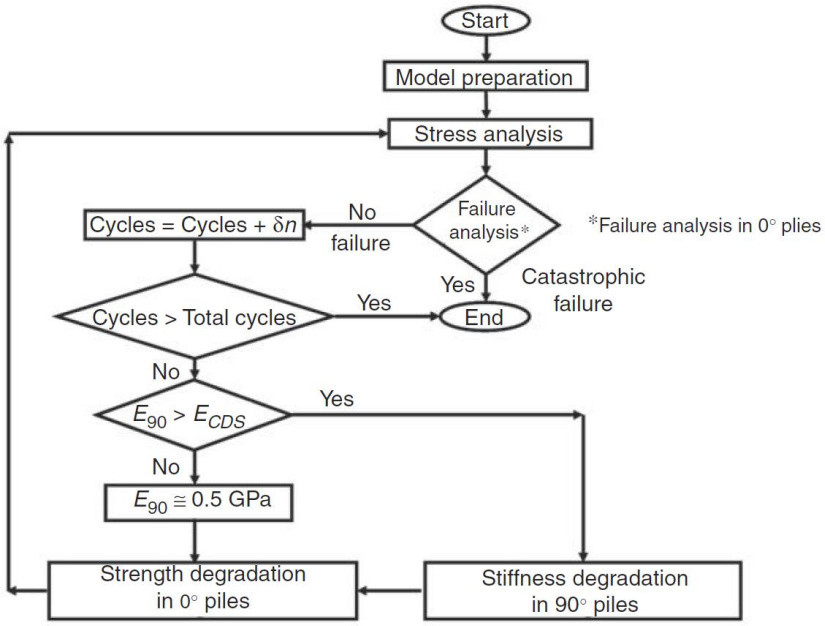

Figure 2.59 Flowchart of Progress fatigue damage modeling of cross-ply laminates (source: Shokreih & Behrooz [72])

Figure 2.59 shows the flowchart used by Shokreih & Behrooz [72] in development and experimental evaluation of a progressive fatigue damage model. Firstly, the model preparation part, material properties, maximum and minimum fatigue load, maximum number of cycles, incremental cycles etc. are defined. Then a stress analysis based on maximum and minimum fatigue load is performed. The maximum and minimum induced on-axis of all layers are calculated and the stress ratio for each layer is determined. Failure analysis is then conducted using equation 2.31.

$$\frac{\sigma_{xx}}{X_t(R,\sigma,n)} = g_f, \quad (\text{if } g_f > 1, \text{ then failure occurs}) \tag{2.30}$$

Where

σ_{xx} = Applied stress

X_t = Residual longitudinal tensile strength of a unidirectional ply under uniaxial fatigue loading

R = Stress ratio

σ = Stress state

n = Number of cycles

If there is a sudden mode of failure, the programme reports the catastrophic failure and fatigue life is reached. Otherwise additional cycles are applied. If the number of cycles exceeds the preset number of cycles, the programme is stopped, otherwise transverse stiffness of off-axis plies and longitudinal stiffness of on-axis plies along are changed according to material property degradation using strength degradation models for 0° plies (equation 2.32) and stiffness degradation models for 90° plies (equation 2.33).

$$Fr = \left[1 - \left(\frac{\log(n) - \log(0.25)}{\log(N_f) - \log(0.25)}\right)^{\beta}\right]^{\frac{1}{\alpha}} (1 - Fa) + Fa, \tag{2.31}$$

Where

$F_r = R(R, \sigma, n)/R_s$= Dimensionless residual strength

R_s= Static Strength

R = Stress ratio

σ = Stress state

n = Number of cycles

$F_a = \sigma/ R_s$= Local failure function

N_f = Cycles to failure

α = Curve fitting parameter

β = Experimental parameter

$$E(R,\sigma,n) = \left[1 - \left(\frac{\log(n) - \log(0.25)}{\log(N_f) - \log(0.25)}\right)^{\lambda}\right]^{\frac{1}{\gamma}} \left(E_s - \frac{\sigma}{\varepsilon_f}\right) + \frac{\sigma}{\varepsilon_f}, \tag{2.32}$$

Where

E = Residual Stiffness

R = Stress ratio

σ = Stress state

n = Number of cycles

N_f = Cycles to failure

Λ, γ = Curve fitting parameters

ε_f = Average strain to failure

Behrooz-Taheri et. al. [73] conducted an experimental investigation to evaluated the capability of the progressive fatigue damage model developed in study by Shokreih & Behrooz [72]. The researchers fabricated test specimens with unidirectional and cross-ply configurations.

The specimens were tested for static stiffness and strength as well as normalized residual strength in the fibre direction in tension-tension fatigue testing.

Figures 2.60 and 2.61 show the test data from the static strength and normalized residual strength fatigue testing.

Table 1. Static test results of unidirectional T700/Cycom 890 RTM carbon/epoxy laminates manufactured by VARTM technique.

Properties	Magnitudes (mean)	Standard deviation
E_{XX} (GPa)	130	4.6
$E_{YY} = E_{ZZ}$ (GPa)	7.53	0.439
$E_{XY} = E_{XZ}$ (GPa)	4.8	–
E_{YZ} (GPa)	2.72	–
$\nu_{xy} = \nu_{xz}$	0.28	–
ν_{yz}	0.382	–
X_t (MPa)	2008	261
Y_t (MPa)	58.3	4.41
$S_{xy} = S_{xz}$ (MPa)	103	6.2
ε_{uf}	0.0176	–
ε_{um}	0.0074	–
Ply thickness (mm)	0.152	–
Fiber volume fraction (%)	52	–

Figure 2.60 Static strength test data (source: Behrooz-Taheri et. al. [73])

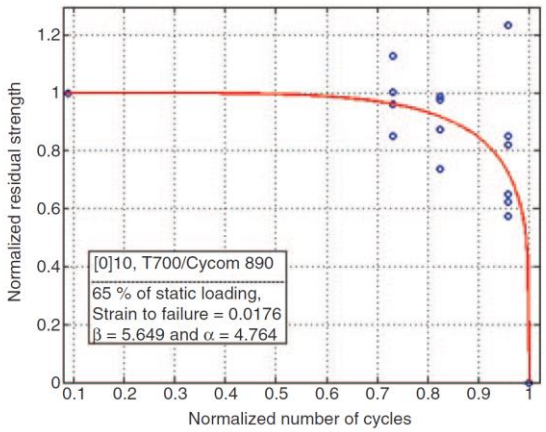

Figure 2.61 Normalized residual strength of a unidirectional 0° ply under longitudinal tension-tension fatigue testing (source: Behrooz-Taheri et. al. [73])

Figure 2.62 shows the S-N curve for the longitudinal tension-tension fatigue testing.

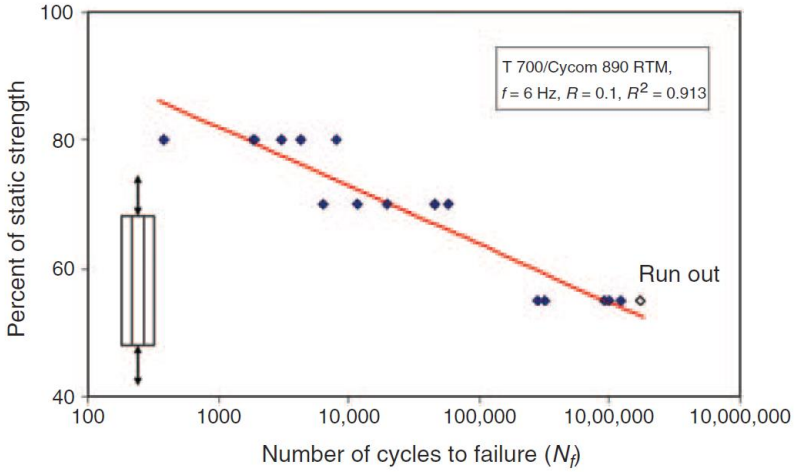

Figure 2.62 S-N curve of unidirectional 0° laminates in longitudinal direction (source: Behrooz-Taheri et. al. [73])

Transverse tensile static strength as well as tension-tension fatigue testing was conducted on the 90° laminates. Figures 2.63 and 2.64 show the residual stiffness and the S-N curve for transverse direction testing.

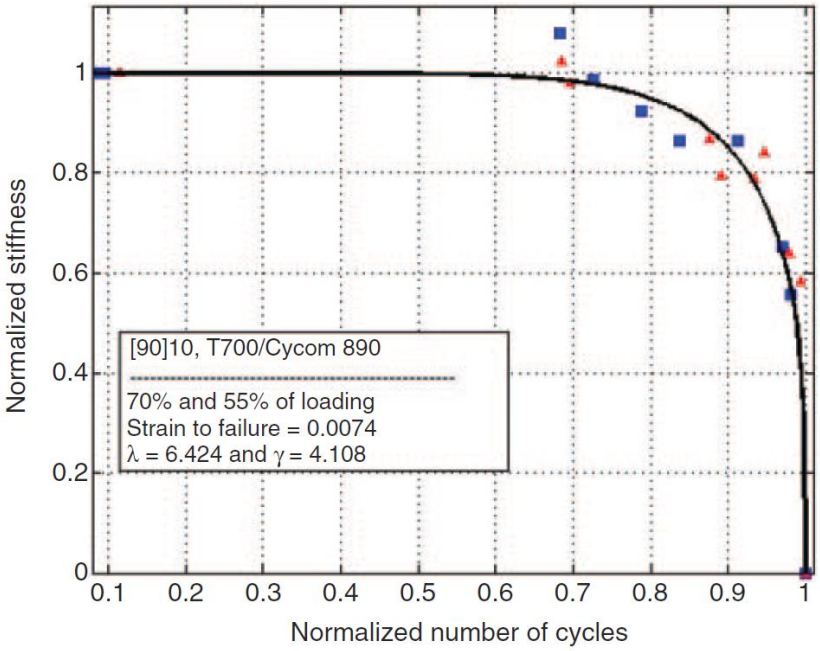

Figure 2.63 Residual stiffness in transverse direction of a unidirectional 90° laminate (source: Behrooz-Taheri et. al. [73])

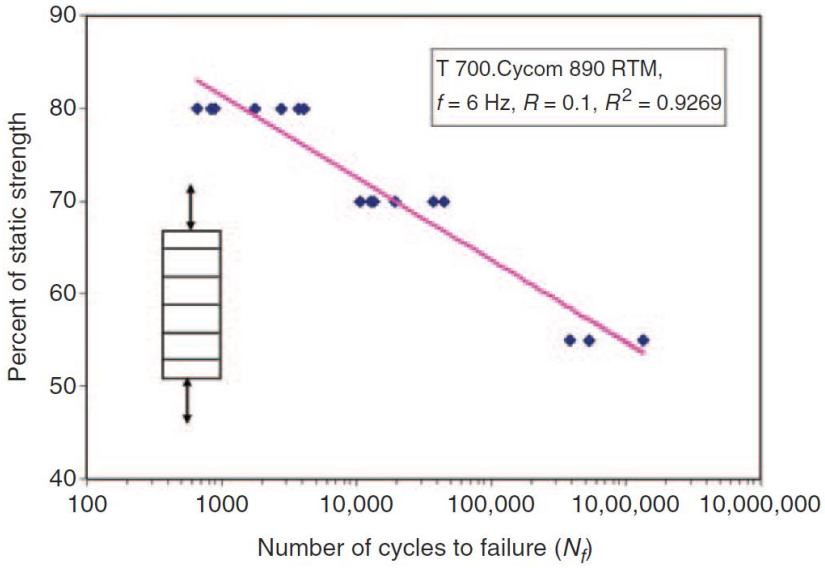

Figure 2.64 S-N curve of unidirectional 90° laminates in longitudinal direction (source: Behrooz-Taheri et. al. [73])

For cross-ply laminates testing was conducted to determine the tensile loading behaviour as well as the tension-tension cyclic testing. Figures 2.65 and 2.66 show the stress strain curves from the uniaxial tensile testing as well as the cyclic loading testing.

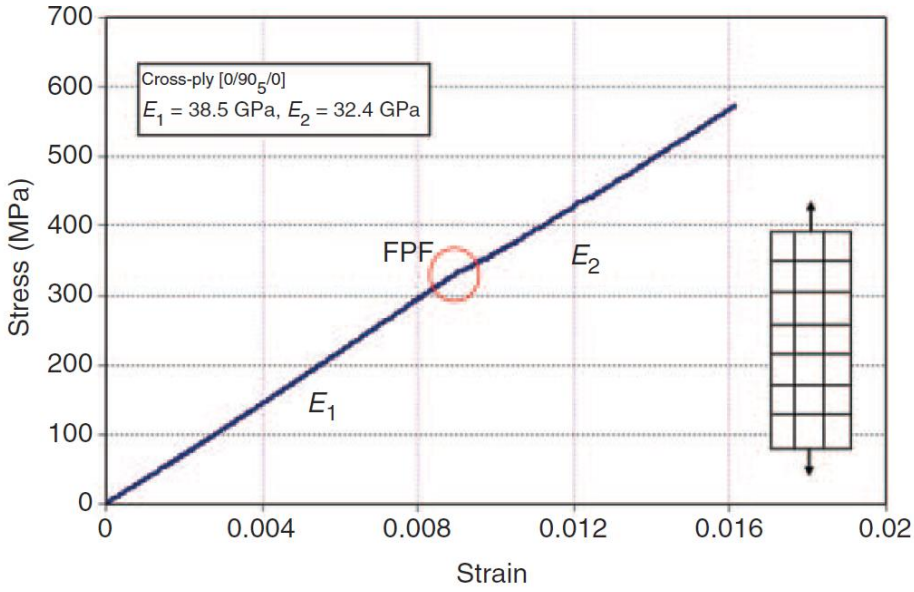

Figure 2.65 Stress Strain curve for [0/90$_5$/0] laminate under uniaxial tensile loading (source: Behrooz-Taheri et. al. [73])

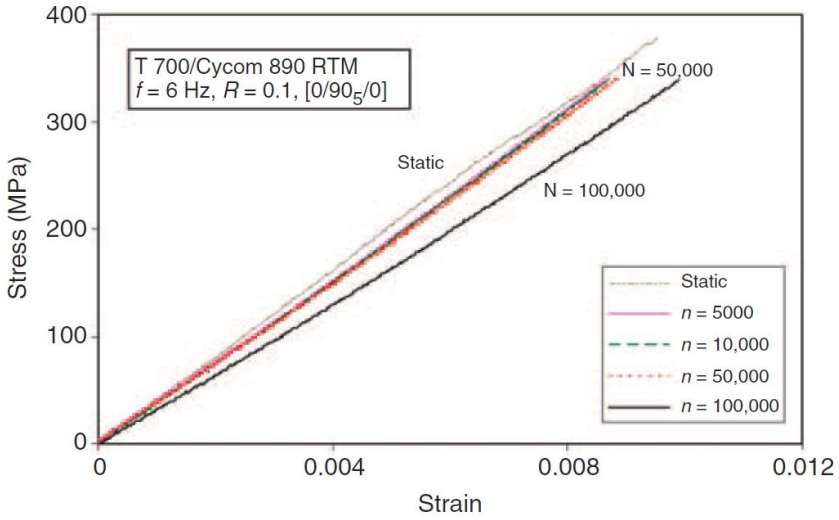

Figure 2.66 Stress Strain curve for [0/90$_5$/0] laminate under tension-tension cyclic loading, (source: Behrooz-Taheri et. al. [73])

The stiffness degradation was also studied in the cross-ply laminates and plotted first to the characteristic damage state (CDS) which is the saturation level of interlaminar crack density and is shown in Figure 2.67. The stiffness degradation was also plotted to the initiation of delamination and is shown in Figure 2.68.

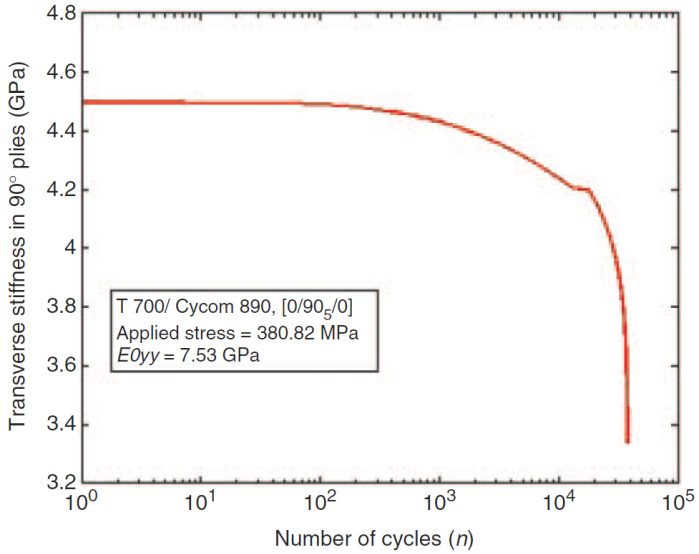

Figure 2.67 Stiffness degradation of 90° plies from first cycle to Characteristic Damage State (CDS) level (source: Behrooz-Taheri et. al. [73])

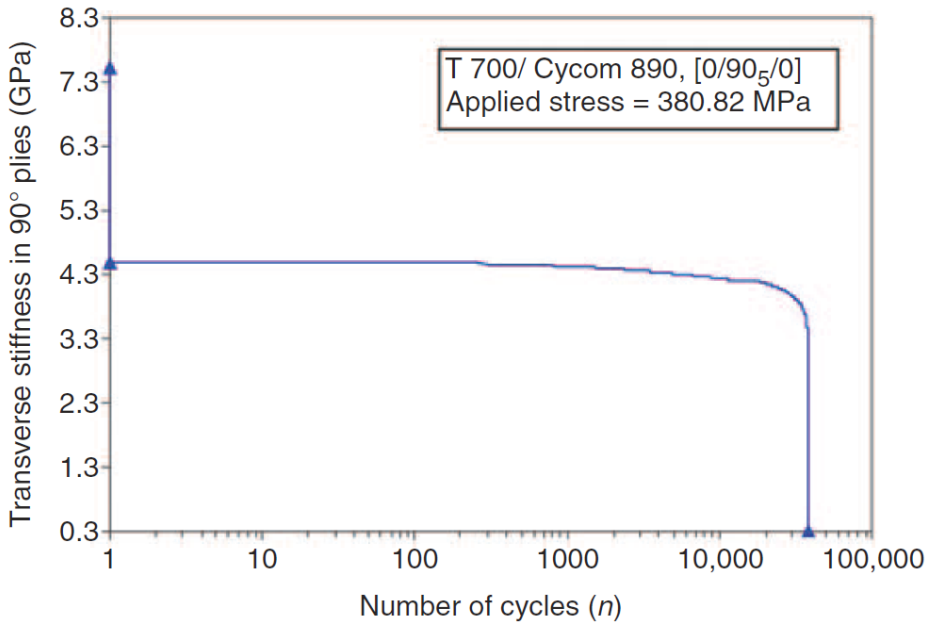

Figure 2.68 Stiffness degradation of 90° plies from first cycle to delamination initiation, (source: Behrooz-Taheri et. al. [73])

Figure 2.69 shows the fatigue life prediction of a cross-ply laminate.

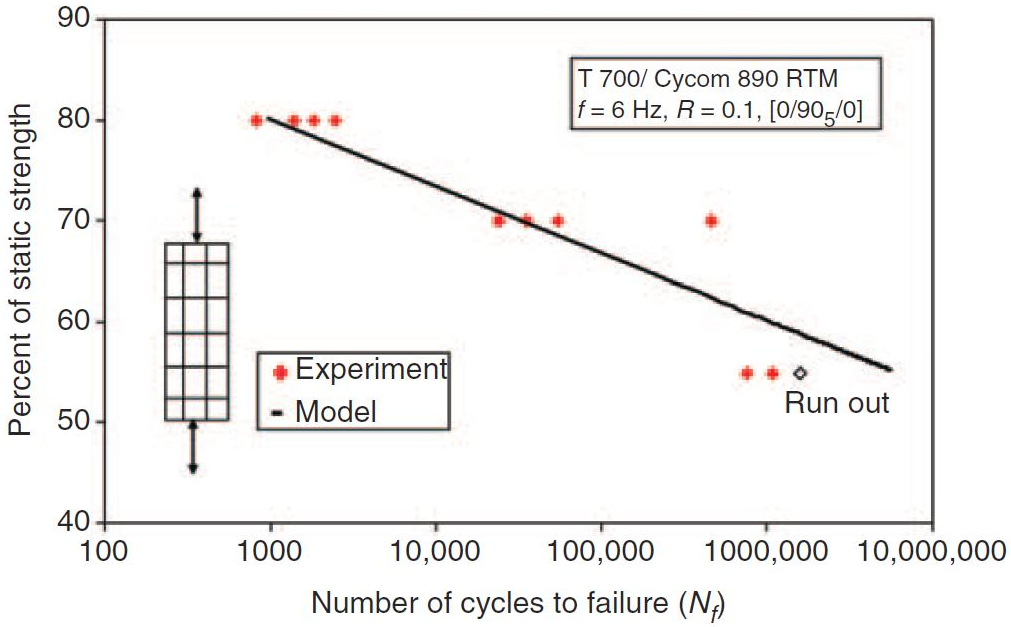

Figure 2.69 Fatigue life prediction of a $[0/90_5/0]$ laminate (source: Behrooz-Taheri et. al. [73])

Overall the authors were able to validate the progressive damage model proposed in study [72] by conducting experiments and validating it as part of the Phase II of the research study [73]

Table 2.2 shows an overview of Fatigue Damage rate models developed by various researchers. DM and FM stand for damage mechanics and fracture mechanics.

Authors	Fatigue damage rate $\frac{\partial D}{\partial N}$	Nomenclature	Capabilities and properties				Framework
			Mode mixity	Stress ratio	Fatigue threshold	Model parameters	
Robinson et al. [11]	$\frac{C}{1+\beta}e^{\lambda D}\delta^{1+\beta}$	δ: equivalent mixed-mode opening C, β, λ: fitting parameters	—	—	—	FE model calibration	DM
Tumino and Cappello [13]	$C(\phi)e^{D}\delta^{\beta(\phi)}$	δ: equivalent mixed-mode opening C, β: fitting parameters ϕ: mode mixity	✓	—	—	FE model calibration	DM
Turon et al. [14]	$\frac{1}{d_{cz}}\frac{(\delta^f(1-D)+D\delta^0)^2}{\delta^f\delta^0}P(w_{tot})$	d_{cz}: "cohesive zone length" δ^f, δ^0: equivalent mixed-mode final and onset opening, respectively. $P(w_{tot})$: Paris' law as a function of w_{tot}	✓	✓[a]	✓	Paris law parameters	DM/FM
Pirondi and Moroni [19]	$\frac{1}{a_{cz}}P(\mathcal{G})$	$P(\mathcal{G})$: Paris' law as a function of $\mathcal{G}$ a_{cz}: length of the cohesive zone	—	✓[a]	✓	Paris law parameters	DM/FM
Harper and Hallett [20]	$\frac{1-D_s-D_{f,u}}{a_{fat}}P(w_{tot})$	a_{fat}: Length of the "fatigue part" of the cohesive zone $D_{f,u}$: fatigue damage correction term for the "quasi-static" part of the cohesive zone	✓	✓[a]	✓	Paris law parameters	DM/FM
Khoramishad et al. [17]	$\frac{\alpha}{t}(\delta-\delta_{th})^{\beta},\ \delta>\delta_{th}$ $0,\ \delta\le\delta_{th}$	δ: equivalent mixed-mode opening α, β, δ_{th}: fitting parameters t: adhesive thickness	✓[b]	—	✓	FE model calibration	DM
Kawashita and Hallett [24]	$\frac{1-D_s}{\Delta N_f},\ \Delta N_f=L_e\left(\frac{\partial a}{\partial N}\right)^{-1}$	L_e: Length of element ΔN_f: Number of cycles to propagate crack through element	✓	✓[a]	✓[c]	Paris law parameters	FM

[a]The Paris law parameters are modeled as independent of the R-ratio. The R-ratio is used only in the determination of $\Delta\mathcal{G}$.
[b]Fitting parameters are assumed to be independent of the mode mixity, which indicates that the mode mixity capabilities are questionable.
[c]This is not stated in the paper, but follows from the direct use of Paris' law; which means that $\mathcal{G}_{th}$ can be taken into account in a straightforward manner.

Table 2.2 Overview of Fatigue Damage Rate Models (source: Bak et. al [61])

2.7 Summary

Literature review was made with intent to have a methodological approach to understand and explain the published research that have related surface integrity to changes in mechanical strength properties and fatigue strength. An initial study of differences in surface integrity due to machining processes with cutters and AWJ was presented along with resultant surface integrity studies due to drilling. A brief discussion of the basics of surface integrity in composites was presented leading to the review of past works conducted researching the defects & damage and their effects on the strength properties of composite laminates. Research conducted in the areas of fatigue and the effects of damage on fatigue strength, bolted joints bearing strength and damage was then reviewed along with fatigue damage modeling work done to date.

While past work has focused on studying defects and damage in test coupons there has been a shortage of research and publications in the area of relating surface integrity of post-cure processes to strength properties and behaviour under service life conditions. Real life manufacturing processes primarily in the aerospace operations utilize edge trimming and drilling processes extensively in the final component size and shape and assembly. Fibre pullouts and delaminations are the two type of defects during these manufacturing processes whose occurrence increases the cost and schedule of usage of composite laminates while affecting the overall quality and business plan of any manufacturing operations. Fibre pullouts eventually result in delaminations and delaminations once initiated will eventually grow under fatigue loadings. Fibre pullouts can be large in size as much 1 ply (200 μm) in width and ½ ply in depth (100 μm). There has been no work to date on the study of fibre pullouts and their effects on the strength properties of composite laminates. During delamination growth, the structural loads may redistribute such that a new delamination occurs in another location. Delaminations potentially are the critical mode of damage and their occurrence may cause reduction of load bearing properties leading to failure. All of the above discussion points to a need for truly understanding the effects of these defects on the stiffness/strength properties and their behaviour under service life fatigue loadings and the following questions arise:

a) How do delaminations and fibre pullouts affect the bolted joints when they are subjected to service life loadings?

b) What is the magnitude of the effects of machined and drilled surface integrity on stiffness/strength properties?
c) How do these initial defects from machining and drilling processes behave under service life conditions especially in terms of damage growth and propagation?
d) Does the damage growth and propagation change the failure loadings and fatigue life limits?
e) Can a reduced stiffness and a progressive damage model be created that uses initial defects as a starting point of failure and can then predict the damage growth and correlate it to residual strength properties and fatigue life?

The above questions when answered could not only help in understanding the fabrication effects but also help design engineers of composite laminate structures fine tune the damage allowances on the components. Most importantly, production engineers can better understand the long-term effects of delaminations and fibre pullouts to reduce the magnitude and occurrence of the critical damage variables.

Chapter 3 – Motivation of Research, Goals and Objectives

3.1 Research Scope

With increased usage of CFRP Laminates in many industries including aerospace, there has been substantial work in the research and development of machining processes for these material systems. Developments in the area of trimming include use of Polycrystalline Diamond (PCD) based cutting technologies as well as Abrasive Water Jet (AWJ) cutting. PCD Drills as well as Chemical Vapour Deposited (CVD) Diamond coated carbide drills have been developed and in use for the drilling of holes in the CFRP laminates. As most CFRP material systems are near net shape, post-cure machining processes have to be efficient for material removal. Machining process variables in combination with heat build-up and the abrasive nature of CFRP laminate systems cause damage to the cutting tools as well as the CFRP laminates. While there has been significant research conducted in improving the cutting tools and processes in an effort to reduce damage to both the material systems and tools, there have been very few significant bodies of work studying the effect of the machining processes on the mechanical performance of the CFRP material systems.

CFRP laminate composites undergo damage during machining and also during service life loading conditions. The damage mechanisms consist of delaminations, fibre rupture, fibre pullout, fibre/matrix debonding and matrix micro-cracking. These damage mechanisms affect mechanical properties such as tensile strength, compressive strength, notched tensile and compressive strength and bearing strengths. While past researchers have studied the influence of surface integrity on monotonic static properties, the influence of damage and its progression during cyclic loading on residual strength and fatigue life are still being explored.

The scope of the research was to characterize the influence of damage caused by machining (trimming) and drilling operations and its progression on monotonic static strength and Fatigue strength of CFRP laminates. The differences between resultant surface integrity for two different types of trimming operations (Edge Milling & AWJ) was studied.

Figure 3.1 Process Methodology for Surface Integrity Study of Machining Process

For Edge Milling PCD endmills and Carbide Endmills with CVD diamond coated were used. In order to document and observe damage caused by trimming, surface roughness measurements (R_a – Roughness Average, R_z – Mean Roughness Depth) were recorded and then optical microscopy was used to observe macroscopic and mesoscopic damage on the surfaces and edges of the specimen. Scanning Electron Microscopy (SEM) was also used to observe microscopic damage. Monotonic Static Strength Testing (Tensile & Compressive) was conducted to document differences in strength based on surface integrity variability based on type of trimming conducted. Tension-Tension Fatigue cycle testing was also conducted to study the effects of damage and its

progression on Fatigue Strength. Damage progression was monitored using photography and changes in stiffness. The proposed process methodology used for the surface integrity study for machining process is shown in the above Fig 3.1.

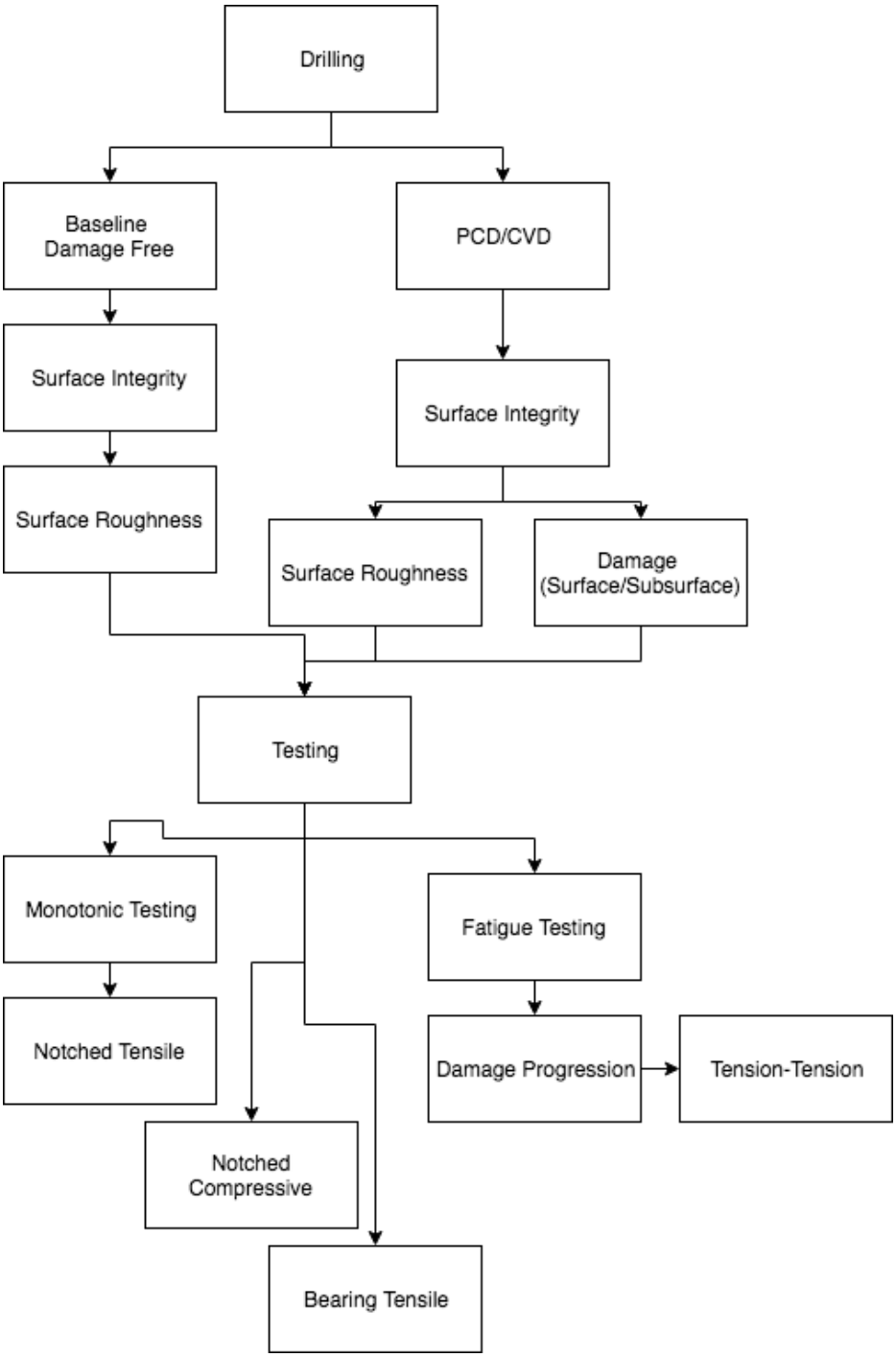

Figure 3.2 Process Methodology for Surface Integrity Study of Drilling Process

For the drilling surface integrity, PCD drills and CVD Diamond Coated Carbide drills were used. Drill point angle study is also included with a study of 2 drill point angles, 90^0 and 120^0. Surface roughness measurements (R_a – Roughness Average, R_z – Mean Roughness Depth) were recorded and then optical microscopy was used to observe macroscopic and mesoscopic damage on the surfaces and edges of the specimen. Scanning Electron Microscopy (SEM) was also used to observe microscopic damage. A baseline almost damage free hole drilling process was used as a benchmark to document and analyze the monotonic strength properties as well as fatigue strength based on tension-tension fatigue testing. Notched Tensile and Compressive Strength testing was conducted as well as pinned bearing strength (tensile) testing. Fatigue cycle testing was conducted with open hole and unnotched specimens along with the study of damage progression. Damage progression was monitored using photography and changes in stiffness of test specimens. The proposed process methodology of the surface integrity study used for drilling process is shown in Fig 3.2.

3.2 Goals and Objectives

The Goal of this research was to study the effects of resultant surface integrity from post-cure machining processes such as trimming and drilling on the mechanical performance of CFRP laminates.

1) One of the principal objectives of this study was to investigate the relationship if any of the machining process damage to a change in monotonic static strength properties and fatigue strength. As a baseline the classical lamination theory is used to calculate the longitudinal Youngs Modulus and Poisson's Ratio (v_{12}) which are then validated against empirical values obtained from mechanical testing with the machined specimens of varying damage intensities. Theoretical Tensile and Compressive Strength values obtained from calculations using the classical lamination theory were compared to those obtained from empirical data from testing.
2) Another major objective of this study was to truly understand the science of machined surface and subsurface damage in CFRP laminates. Initial damage at the fabrication of CFRP laminate components and their assembly propagates and influences the mechanical performance of the laminates. The goal of this study was to help develop a progressive damage model and its relationship to fatigue life to help fatigue life prediction of CFRP

laminates. As damage in CFRP laminates starts early during the post-cure machining operations, the size of the damage zone grows steadily along with the type changing (matrix microcracking can lead to large delaminations). This can lead to gradual deterioration of the CFRP requiring knowledge of the progression of damage for predicting fatigue life and failure.

Fatigue life models are classified into three categories [53] which are:

a) Fatigue life models that do not take into account the actual degradation mechanisms, but use *S-N* curves or Goodman diagrams and introduce some sort of fatigue failure criterion
b) Phenomenological models for residual stiffness/strength
c) Progressive damage models which use one or more damage variables which are measurable damage characterizations such as transverse matrix cracks or delamination size

Progressive damage models are also of two types:

1) Progressive damage models that predict damage growth such delamination area size and/or microcrack density
2) Progressive damage models that correlate the damage growth with the residual mechanical properties (stiffness/strength)

For this study, the development of the progressive damage model will be based on percentage change in compliance (damage) versus number of cycles is modeled from test data. This model is dependent on the applied stress, surface integrity and notch factors and based on predictive damage, the number of cycles to fatigue failure are predicted.

The damage model will focus on the 3 distinctive damage zones which constitute matrix cracking, matrix-fibre interface debonding, delamination, fibre fracture and failure. The testing conducted, static and fatigue will be depicted in the following chapters in terms of test results, photo micrographs and scanning electron microscopy for damage mechanisms and surface profilometry for surface integrity observations.

Chapter 4 – Experimental and Theoretical Methodology

4.1 Overview

This body of work comprises a two-phase approach to study the effects of surface integrity on mechanical properties and fatigue life on CFRP laminates. In phase 1, a 10 ply thick balanced symmetric $[0/-45/90/45/0]_s$ composite laminate of unidirectional Carbon fibre prepreg tape with an Epoxy resin was used in the study. For Phase 2, a 20 ply thick balanced symmetric $[0/45/90/45/0]_{2s}$ composite laminate of unidirectional Carbon fibre prepreg tape with an Epoxy resin was used. The resin used in the laminate is a 350 degree F curing epoxy based thermosetting resin. By weight the resin content of the laminate is 35.5 % of the total weight of the laminate.

4.2 Phase I Research Plan – 10 Ply Thick Laminate – Mechanical Properties Testing

The 10 ply thick balanced symmetric $[0/-45/90/45/0]_s$ laminate used in the study had a nominal thickness of 1.91 mm and with an average ply thickness of 190 μm. The prepreg tape material used was approximately 305 mm in width and all layup was done manually as a 1220 x 1220 mm wide sheet. The sheet was cut into smaller coupons using Abrasive Water Jet (AWJ). The coupons were then machined either using endmill cutters or AWJ into smaller specimens for mechanical testing. Prior to mechanical testing, surface integrity (roughness and Scanning Electron Microscopy) was documented. The following mechanical testing was conducted:

1) Tensile Strength Testing
2) Compression Strength Testing
3) Open Hole Tensile Strength Testing

4.3 Phase II Research Plan - 22 Ply Thick Laminate – Mechanical Properties Testing

The 22 ply thick balanced symmetric $[90/-45/0/-45/90/45/0/-45/0/90/0]_s$ laminate used in the study had a nominal thickness of 4.52 mm and with an average ply thickness of 190 μm. The laminate had a top layer of woven fabric material [0/90] and a bottom layer of fiberglass skin material. The coupons were machined either using endmill cutters or AWJ for edge trimming for mechanical testing. Holes were also drilled using test drills as described later in the chapter for open hole

testing. Prior to mechanical testing, surface integrity (roughness and Scanning Electron Microscopy) was documented. The following mechanical testing was conducted:

1) Tensile Strength Testing
2) Compression Strength Testing
3) Open Hole Tensile Strength Testing
4) Open Hole Compression testing
5) Pinned Bearing Testing

4.4 Research Plan for 22 Ply Thick Laminate – Tension-Tension Fatigue Cycle Testing

The 22 ply thick balanced symmetric $[90/-45/0/-45/90/45/0/-45/0/90/0]_s$ laminate used in the study had a nominal thickness of 4.52 mm and with an average ply thickness of 190 μm. The laminate had a top layer of woven fabric material [0/90] and a bottom layer of fiberglass skin material. The coupons were machined either using endmill cutters or AWJ for edge trimming for fatigue cycle testing. Holes were also drilled using test drills as described later in the chapter for notched specimen fatigue testing. Prior to fatigue cycle testing, surface integrity (roughness and Scanning Electron Microscopy) was documented. The following fatigue cycle testing was conducted:

1) Unnotched Specimen Testing
    a. High Load
    b. Medium Load
    c. Low Load
2) Notched Specimen Testing
    a. High Load
    b. Medium Load
    c. Low Load

4.5 Theoretical Strength Calculations

A lamina is a single ply whose thickness can range from 0.143 to 0.191 mm. A laminate is composed of multiple plies of different orientations. The common fibre orientation angles are 0^o, 90^o, 45^o, -45^o. A unidirectional composite (0 ply) has the largest tensile and compressive stiffness and strength in the fibre direction. A 45 ply has the highest shear stiffness and strength. The

stresses/strains, strength and the apparent (or effective, equivalent, average) stiffness of a laminate can be predicted using “Classical Lamination Theory” (CLT) [11]. CLT is a theory for predicting (force/moment) and strain/curvature) relations of a generally flat laminate based on the properties of a single ply (a lamina) and is based on the following assumptions [65];

a) The plane stress form of Hooke’s Law for a single ply in the arbitrary (x-y) coordinates
b) “Kirchhoff Hypothesis” – The normal to the midplane remains normal to the midplane after deformation i.e. transverse shear strains are zero.
c) Small deformation, perfect bonding between plies.

Fig 4.1 shows the construction of a typical carbon-fibre reinforced plastic laminate. Laminates can be of 4 types:

1) Symmetric unbalanced – example $(0 / 45 / 90)_s$
2) Symmetric balanced – example $(45 / 0 / - 45 / 90)_s$
3) Unsymmetric balanced – example (0 / 45 / 90 / 90 / - 45 / 0)
4) Unsymmetric unbalanced – example (0 / 45 / 90 / 0 / 45 / 90)

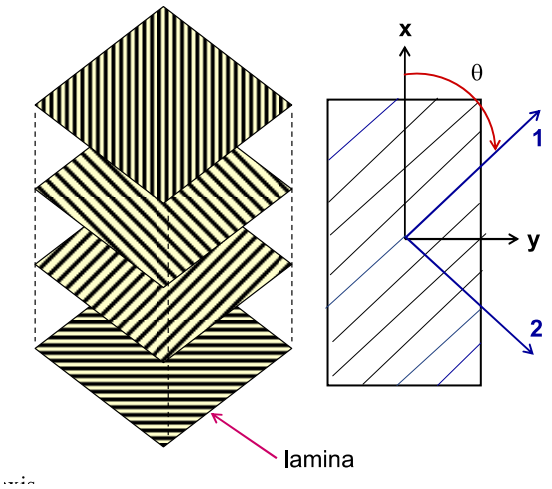

Figure 4.1 Construction of a Typical Carbon-Fibre Reinforced Plastic Laminate(source: Lin [59])

x, y : reference axes

1, 2: material axes

θ = angle between x and 1 axis

Most laminate applications use plates as the basic structural form and most require the plate geometry to be thin (longitudinal and transverse dimensions of plate are greater than 10 times the thickness of the plate). Thin laminates are usually characterized by three stiffness matrices which are denoted by [A], [B] & [D]. Since the plate is "thin", a state of plane stress can be assumed with out of plane normal stress (σ_z) equal to zero and the shear stresses (τ_{xz} & τ_{yz}) are equal to zero.
The displacements of a point in the laminate under loading and in the x, y & z direction are denoted by u, v & w. The displacements in the midplane are denoted by u^o, v^o & w^o. Using Kirchoff's hypothesis it can be shown that the strains (ϵ_x, ϵ_y & γ_{xy}) can be calculated using the following relationships:

$$\epsilon_x = \frac{\partial u^o}{\partial x} - z\frac{\partial^2 w^o}{\partial x^2} \tag{4.1}$$

$$\epsilon_y = \frac{\partial v^o}{\partial y} - z\frac{\partial^2 w^o}{\partial y^2} \tag{4.2}$$

$$\gamma_{xy} = \frac{\partial u^o}{\partial y} + \frac{\partial v^o}{\partial x} - z\frac{2\partial^2 w^o}{\partial x \partial y} \tag{4.3}$$

These equations can be written as:

$$\begin{Bmatrix} \epsilon_x \\ \epsilon_y \\ \gamma_{xy} \end{Bmatrix} = \begin{Bmatrix} \epsilon_x^o \\ \epsilon_y^o \\ \gamma_{xy}^o \end{Bmatrix} + z\begin{Bmatrix} \kappa_x \\ \kappa_y \\ \kappa_{xy} \end{Bmatrix} \tag{4.4}$$

where $\epsilon_x^o, \epsilon_y^o$ & γ_{xy}^o are the strains in the reference midplane and κ_x, κ_y & κ_{xy} are the curvatures of the reference midplane and given by:

$$\kappa_x = -z\frac{\partial^2 w^o}{\partial x^2}, \quad \kappa_y = -z\frac{\partial^2 w^o}{\partial y^2} \quad \& \quad \kappa_{xy} = -z\frac{2\partial^2 w^o}{\partial x \partial y}$$

Using Three-Dimensional (3-D) Anisotropic Constitutive Relations, Hooke's law can be written as:

$$\sigma_i = C_{ij} \cdot \epsilon_j \text{ where } (i, j = 1, 2, ...6) \tag{4.5}$$

C_{ij} = Elastic Stiffness Matrix

Equation (4.5) can also be written as:

$\epsilon_i = S_{ij} \cdot \sigma_j$ where $(i, j = 1, 2,...6)$ (4.6)

S_{ij} = Elastic Compliance Matrix

The stacking sequence of a multi-angle laminate is denoted as shown in Fig 4.2

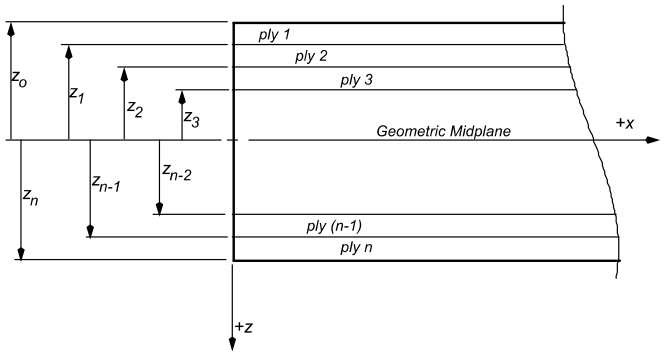

Note:

- Outer surface of ply 1 is at the most negative z - position: $z_0 < 0$

- Outer surface of ply n is at the most positive z - position: $z_n > 0$

- Plies can be composed of different materials

Figure 4.2 Stacking Sequence of a Multi-Angle Laminate (source: Lin [59])

If N_x , N_y & N_{xy} are the in-plane loadings and M_x , M_y & M_{xy} are the applied moments then their relationship to in-plane stresses is given by:

$$N_x = \int_{-h/2}^{h/2} \sigma_x \, dz$$

$$N_y = \int_{-h/2}^{h/2} \sigma_y \, dz$$

$$N_{xy} = \int_{-h/2}^{h/2} \tau_{xy} \, dz$$

and for the moments it is given by:

$$M_x = \int_{-h/2}^{h/2} \sigma_x \, z dz$$

$$M_y = \int_{-h/2}^{h/2} \sigma_y \, z dz$$

$$M_{xy} = \int_{-h/2}^{h/2} \tau_{xy} \, z dz$$

The stress-strain relationship for a given ply in a laminate is given by:

$$\begin{Bmatrix} \sigma_x \\ \sigma_y \\ \tau_{xy} \end{Bmatrix} = \begin{bmatrix} \bar{Q}_{11} & \bar{Q}_{12} & \bar{Q}_{16} \\ \bar{Q}_{12} & \bar{Q}_{22} & \bar{Q}_{26} \\ \bar{Q}_{16} & \bar{Q}_{26} & \bar{Q}_{66} \end{bmatrix} \begin{Bmatrix} \epsilon_x \\ \epsilon_y \\ \gamma_{xy} \end{Bmatrix} \tag{4.7}$$

where [$\bar{Q}$] is the stiffness matrix of the ply in the x-y coordinate system and its components are given by:

$$\begin{aligned}
\overline{Q}_{11} &= Q_{11}\cos^4\theta + 2(Q_{12} + 2Q_{66})\sin^2\theta\cos^2\theta + Q_{22}\sin^4\theta \\
\overline{Q}_{12} &= (Q_{11} + Q_{22} - 4Q_{66})\sin^2\theta\cos^2\theta + Q_{12}(\sin^4\theta + \cos^4\theta) \\
\overline{Q}_{22} &= Q_{11}\sin^4\theta + 2(Q_{12} + 2Q_{66})\sin^2\theta\cos^2\theta + Q_{22}\cos^4\theta \\
\overline{Q}_{16} &= (Q_{11} - Q_{12} - 2Q_{66})\sin\theta\cos^3\theta + (Q_{12} - Q_{22} + 2Q_{66})\sin^3\theta\cos\theta \\
\overline{Q}_{26} &= (Q_{11} - Q_{12} - 2Q_{66})\sin^3\theta\cos\theta + (Q_{12} - Q_{22} + 2Q_{66})\sin\theta\cos^3\theta \\
\overline{Q}_{66} &= (Q_{11} + Q_{22} - 2Q_{12} - 2Q_{66})\sin^2\theta\cos^2\theta + Q_{66}(\sin^4\theta + \cos^4\theta)
\end{aligned}$$

For specially orthotropic materials,

$$Q_{11} = \frac{E_1}{1 - \upsilon_{12}\upsilon_{21}}, \quad Q_{12} = \frac{\upsilon_{12}E_2}{1 - \upsilon_{12}\upsilon_{21}}, \quad Q_{16} = 0$$

$$Q_{22} = \frac{E_2}{1 - \upsilon_{12}\upsilon_{21}} \qquad Q_{26} = 0, \qquad Q_{66} = G_{12}$$

where E_1 , E_2 are the Youngs Modulus in 1 & 2 direction,

υ_{12} = Poisson's ratio in direction 2 due to applied stress in direction 1

υ_{21} = Poisson's ratio in direction 1 due to applied stress in direction 2

G_{12} = Shear Modulus in 1-2 direction

Combining equations (4.4) and (4.7) we get,

$$\begin{Bmatrix} N_x \\ N_y \\ N_{xy} \end{Bmatrix} = \int_{-h/2}^{h/2} \begin{Bmatrix} \sigma_x \\ \sigma_y \\ \tau_{xy} \end{Bmatrix} dz = \sum_{k=1}^{n} \int_{z_{k-1}}^{z_k} \begin{Bmatrix} \sigma_x \\ \sigma_y \\ \tau_{xy} \end{Bmatrix}_k dz$$

$$= \sum_{k=1}^{n} \begin{bmatrix} \overline{Q_{11}} & \overline{Q_{12}} & \overline{Q_{16}} \\ \overline{Q_{12}} & \overline{Q_{22}} & \overline{Q_{26}} \\ \overline{Q_{16}} & \overline{Q_{26}} & \overline{Q_{66}} \end{bmatrix}_k \left[\int_{z_{k-1}}^{z_k} \begin{Bmatrix} \varepsilon_x^o \\ \varepsilon_y^o \\ \gamma_{xy}^o \end{Bmatrix}_k dz + \int_{z_{k-1}}^{z_k} \begin{Bmatrix} \kappa_x \\ \kappa_y \\ \kappa_{xy} \end{Bmatrix} z\, dz \right]$$

which can be written as

$$\begin{Bmatrix} N_x \\ N_y \\ N_{xy} \end{Bmatrix} = \begin{bmatrix} A_{11} & A_{12} & A_{16} \\ A_{12} & A_{22} & A_{26} \\ A_{16} & A_{26} & A_{66} \end{bmatrix} \begin{Bmatrix} \varepsilon_x^o \\ \varepsilon_y^o \\ \gamma_{xy}^o \end{Bmatrix} + \begin{bmatrix} B_{11} & B_{12} & B_{16} \\ B_{12} & B_{22} & B_{26} \\ B_{16} & B_{26} & B_{66} \end{bmatrix} \begin{Bmatrix} \kappa_x \\ \kappa_y \\ \kappa_{xy} \end{Bmatrix}$$

$$where \quad A_{ij} = \sum_{k=1}^{n} (\overline{Q}_{ij})_k (z_k - z_{k-1}) \qquad Extensional\,(or\ Stretching)\ Stiffness$$

$$B_{ij} = \frac{1}{2} \sum_{k=1}^{n} (\overline{Q}_{ij})_k (z_k^2 - z_{k-1}^2) \qquad Bending - Stretching\ Coupling\ Stiffness$$

similarly the moment equations can be written as

$$\begin{Bmatrix} M_x \\ M_y \\ M_{xy} \end{Bmatrix} = \int_{-h/2}^{h/2} \begin{Bmatrix} \sigma_x \\ \sigma_y \\ \tau_{xy} \end{Bmatrix} z dz = \sum_{k=1}^{n} \int_{z_{k-1}}^{z_k} \begin{Bmatrix} \sigma_x \\ \sigma_y \\ \tau_{xy} \end{Bmatrix}_k z dz$$

$$= \sum_{k=1}^{n} \begin{bmatrix} \overline{Q_{11}} & \overline{Q_{12}} & \overline{Q_{16}} \\ \overline{Q_{12}} & \overline{Q_{22}} & \overline{Q_{26}} \\ \overline{Q_{16}} & \overline{Q_{26}} & \overline{Q_{66}} \end{bmatrix}_k \left[\int_{z_{k-1}}^{z_k} \begin{Bmatrix} \varepsilon_x^o \\ \varepsilon_y^o \\ \gamma_{xy}^o \end{Bmatrix}_k z\,dz + \int_{z_{k-1}}^{z_k} \begin{Bmatrix} \kappa_x \\ \kappa_y \\ \kappa_{xy} \end{Bmatrix} z^2\,dz \right]$$

which can be written as

$$\begin{Bmatrix} M_x \\ M_y \\ M_{xy} \end{Bmatrix} = \begin{bmatrix} B_{11} & B_{12} & B_{16} \\ B_{12} & B_{22} & B_{26} \\ B_{16} & B_{26} & B_{66} \end{bmatrix} \begin{Bmatrix} \varepsilon_x^o \\ \varepsilon_y^o \\ \gamma_{xy}^o \end{Bmatrix} + \begin{bmatrix} D_{11} & D_{12} & D_{16} \\ D_{12} & D_{22} & D_{26} \\ D_{16} & D_{26} & D_{66} \end{bmatrix} \begin{Bmatrix} \kappa_x \\ \kappa_y \\ \kappa_{xy} \end{Bmatrix}$$

$$where \;\; D_{ij} = \frac{1}{3} \sum_{k=1}^{n} (\overline{Q}_{ij})_k \, (z_k^3 - z_{k-1}^3) \qquad Bending\ Stiffness$$

Thus the [A], [B] & [D] matrices are given by

$$A_{ij} = \sum_{k=1}^{n} \overline{Q}_{ij}^{(k)} \, t_k \qquad (Stretching\ Stiffness\ Matrix)$$

$$B_{ij} = \frac{1}{2} \sum_{k=1}^{n} \overline{Q}_{ij}^{(k)} (z_k^2 - z_{k-1}^2) \quad (Coupling\ Stiffness\ Matrix)$$

$$D_{ij} = \frac{1}{3} \sum_{k=1}^{n} \overline{Q}_{ij}^{(k)} (z_k^3 - z_{k-1}^3) \quad (Bending\ Stiffness\ Matrix)$$

where t is ply thickness, and h is the thickness of a laminate.

In general, the inverse matrices of [A], [B] & [D] denoted by [a], [b] & [d] are used in laminate properties calculations.

For a symmetrical balanced laminate as such used in this study, the [b] matrix is zero. The strains cause by N_x are given by:

$$\begin{Bmatrix} \varepsilon_x^o \\ \varepsilon_y^o \\ \gamma_{xy}^o \\ \kappa_x \\ \kappa_y \\ \kappa_{xy} \end{Bmatrix} = \left[\begin{array}{ccc:ccc} a_{11} & a_{12} & 0 & 0 & 0 & 0 \\ a_{21} & a_{22} & 0 & 0 & 0 & 0 \\ 0 & 0 & a_{66} & 0 & 0 & 0 \\ \hdashline 0 & 0 & 0 & d_{11} & d_{12} & d_{16} \\ 0 & 0 & 0 & d_{21} & d_{22} & d_{26} \\ 0 & 0 & 0 & d_{61} & d_{62} & d_{66} \end{array}\right] \begin{Bmatrix} N_x \\ 0 \\ 0 \\ 0 \\ 0 \\ 0 \end{Bmatrix} = \begin{Bmatrix} a_{11}N_x \\ a_{21}N_x \\ 0 \\ 0 \\ 0 \\ 0 \end{Bmatrix}$$

The nominal (or "effective") uniaxial stress applied to the laminate is:

$$\overline{\sigma}_x = \frac{N_x}{h}$$

Hence, the effective Young's modulus and Poisson's ratio *for a laminate with thickness h* is:

$$E_x = \frac{\overline{\sigma}_x}{\varepsilon_x} = \frac{N_x}{h(a_{11}N_x)} = \frac{1}{ha_{11}}$$

$$\nu_{xy} = -\frac{\varepsilon_y}{\varepsilon_x} = -\frac{a_{21}N_x}{a_{11}N_x} = -\frac{a_{21}}{a_{11}}$$

Using the above theoretical formulas many companies have developed lamination theory software systems to accelerate the calculations of the laminate properties. The theoretical values of the effective Youngs Modulus and the Poissons's ratio were determined using the "Laminator" [66] software which calculated the apparent laminate material properties, ply stiffness and compliance matrices, laminate "ABD" matrices, laminate loads and mid-plane strains, ply stresses and strains in global and material axes for the laminate used in the study for Phase 1. Input to the software consisted of ply material properties, material strengths, ply-fibre orientations, stacking sequence and mechanical loading.

4.6 Experimental Plan

The goal of this experimental study was to characterize the effects of surface integrity of machined composites laminates on their strength properties. The study also attempted to characterize the influence of the variability of surface integrity on the fatigue life of the composite laminates while documenting the evolution of damage under cyclical loading conditions.

Composite Laminate material coupons were machined using different machining processes to generate a variety of surface integrity conditions on the edges of the laminates. Mechanical testing was conducted on these specimens and the change in their strength properties with changing surface integrity conditions was evaluated and compared amongst the specimens. Fatigue strength testing and the progression of damage in the laminate with cyclical loading was also evaluated with varying surface integrity specimens.

As part of the experimental study the generation of data for the following properties of the composite laminate specimens was planned.

- Tensile Strength
- Compressive Strength
- Open-Hole Tensile Strength
- Open-Hole Compressive Strength
- Pinned Bearing Strength (Tensile)
- Tension – Tension Fatigue Stress Cycles (S-N)

4.6.1 Specimen Readiness

Composite laminate material was laid up manually with prepreg tape and cured in an autoclave with the cure schedule shown in Fig 4.3. For both the 10 ply thick and 22 ply thick, a composite laminate of unidirectional Carbon fibre prepreg tape with an Epoxy resin was used in the study. All specimens were machined by either endmilling of surface edges or using an Abrasive Water Jet (AWJ) process for edge trimming. All edge machining and drilling processes were performed on a HAAS Tool Room Mill, M 1P with a 7.5 HP spindle with max speed of 6000 RPM.

Abrasive Water Jet (AWJ) machining of coupon edges was performed using a WaterJet Pro WJP1313 Water Jet Machine. The surface roughness of all specimens was then recorded on the trimmed edges as well as the surface of the hole. The surfaces were also examined under a microscope and damage areas were studied using Scanning Electron Microscopy (SEM). Aluminium tabs which were machined to the size and shape per each ASTM mechanical test standard were then adhesive bonded to the specimens to be used for gripping during the mechanical testing of the specimens on the Instron Test Machine, Model 5585H.

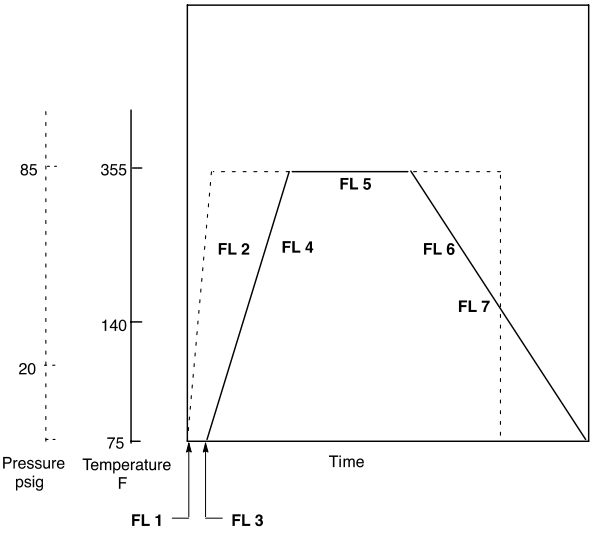

FL 1 Apply 22 inches Hg minimum vacuum to bag.

FL 2 Pressurize autoclave to 85 psig. Vent vacuum bag to atmosphere when pressure reaches 20 +10/-0 psig. Keep vented until end of cure. Pressure under vacuum bag shall be 0 +5/-0 psig throughout remainder of cure cycle.

FL 3 Apply heat after full pressurization of autoclave.

FL 4 Heat-up rate shall be 1 to 5 F/minute.

FL 5 Hold for 120 +60/-0 minutes at 355 ± 10 F and 85 +15/-0 psig. Temperature is based on lagging thermocouple. Cure begins when last thermocouple reaches the minimum cure temperature. All thermocouples shall remain in cure temperature range.

FL 6 Cool under pressure until the part temperature reaches 140 F or below. Natural pressure drop (19 psig max.) in autoclave due to cool down is allowed. Cool-down rate shall be 5 F/minute maximum.

FL 7 When part temperature reaches below 140 F, release pressure and remove part.

Figure 4.3 Cure Cycle of a CFRP Laminate (source: Boeing [61])

4.6.2 Edge Trimming with Cutters

End milling was performed using a 6.35 mm Diameter, Chemical Vapour Deposition (CVD) Diamond Coated, 4 flute endmill. The helix angle of the endmill used was 18 degrees. Also End

Milling using a 6.35 mm Diameter Polycrystalline Diamond (PCD). 2 flute, 0 degree helix cutter was performed. The following machining parameters were used for endmilling with both types of cutters:

Speed ‘N’ = 6000 RPM

Feed rate ‘F’ = 635 mm/min

The following Fig 4.4 shows the machining set-up of the edge trimming operation using the HAAS machining centre.

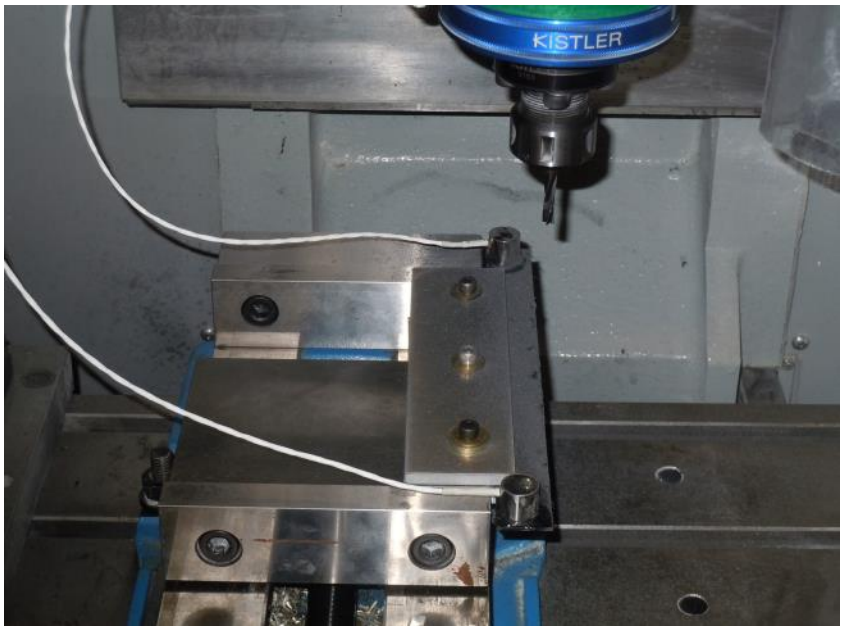

Figure 4.4 Machining Set-up for Edge Trimming with Endmill Cutters

The machining set-up used a Kistler Rotating dynamometer for capturing cutting force data. Acoustic Emission Data was also recorded during the cutting process. Cutting using a PCD endmill, 6.35 mm diameter, 0 degree helix, 4 flutes was conducted along with cutting using a 6.35 mm diameter, 18 degree, 4 flutes CVD diamond coated endmill. Both climb milling and conventional milling processes were used for edge trimming. Both the 0 degree and the 18 degree helix cutter machined samples were used for mechanical strength testing as well as surface integrity analysis. The 0 degree PCD and the 18 Degree CVD Diamond coated cutters are shown in Figure 4.5.

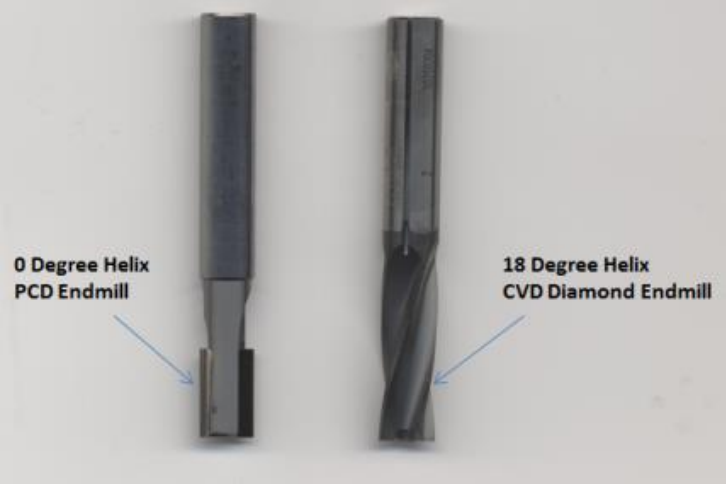

Figure 4.5 PCD Endmill & CVD Diamond Coated Endmill

Table 4.1 Shows the Endmill geometries and cutting Parameters

Cutting Parameters							
Diameter (mm)	*Type of Endmill*	*Radial Depth of cut (mm)*	*Axial Depth of Cut (mm)*	*Feed Rate (mm/min)*	*Speed (RPM)*	*Linear Cutting Speed (m/min)*	*Type of Cut*
6.35	*PCD, 2 flutes, 0 degree Helix*	*0.76*	*2.0*	*635*	*6000*	*120*	*Climb*
6.35	*CVD, 4 flutes 18 degree Helix*	*0.76*	*2.0*	*635*	*6000*	*120*	*Climb*

Table 4.1 Endmill Geometries and Cutting Parameters

4.6.3 Edge Trimming with Abrasive Water Jet

Edge trimming with an Abrasive Water Jet cutting machine was conducted using the WaterjetPro WJP1313 Machine (Figure 4.6). The abrasive used for cutting was a 120 grit Garnet and the feed rate used was 1444 mm/min.

Figure 4.6 WaterjetPro WJP1313 Machine

Table 4.2 shows the cutting parameters for AWJ trimming

Cutting Parameters			
Abrasive	*Feed Rate (mm/min)*	*Pressure (bar)*	*Flow Rate (L/min)*
120 Grit Garnet	*1444*	*3447*	*3.0*

Table 4.2 Cutting Parameters for AWJ Trimming

4.6.4 Hole Drilling

For Open Hole Testing and for Bearing response of pinned holes in CFRP composite laminates holes were drilled in the specimens. The two types of drills used were a Precorp Polycrystalline

Diamond (PCD) drill and a Sumitomo CVD Diamond Coated drill (Figure 4.7). The Precorp Inc. PCD drill is 4 facet drill with 118 degree cutting angle and a 24 degree helix. The Sumitomo Corp. CVD drill is a 4 facet, 90 degree cutting angle with a 30 degree helix. The diameter of both drills and holes drilled was 6.35mm. All drilling operations were conducted using the following parameters:

Speed 'N' = 6000 RPM

Feed rate 'F' = 305 mm/min

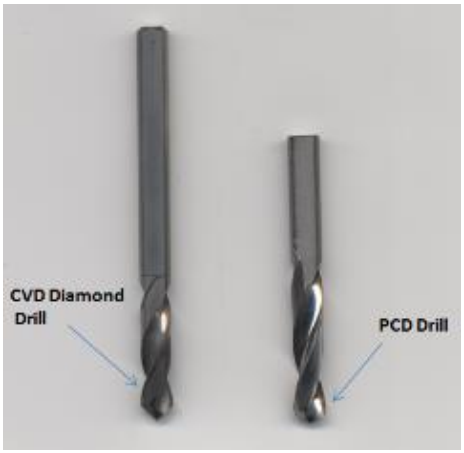

Figure 4.7 CVD Diamond Coated and PCD Drill

Table 4.3 shows the drill geometries and drilling parameters

Drilling Parameters				
Diameter (mm)	*Type of Drill*	*Feed Rate (mm/min)*	*Speed (RPM)*	*Linear Cutting Speed (m/min)*
6.35	*PCD, 4 facet, 118 degree cutting angle 24 degree Helix*	*305*	*6000*	*120*
6.35	*CVD, 4 facet, 90 degree cutting angle 30 degree Helix*	*305*	*6000*	*120*

Table 4.3 Drill Geometries and Drilling Parameters

4.6.5 Surface Integrity Documentation

The surface integrity was documented using surface roughness measurement equipment, surface microscopy and scanning electron microscopy for both surface and sub-surface damage documentation.

4.6.5.a Surface Profilometry

The surface roughness of all machined and drilled specimens was documented using the Mahr Mahrsurf GD 25 profilometer (Figure 4.8). Surface roughness readings were taken in the longitudinal and transverse directions for the edge trimmed specimens (cutters and AWJ trimmed). Detailed surface roughness parameters such as R_a, R_z, R_q, R_{max}, R_t, R_p, R_v, R_{sk}, R_{ku} were documented. Detailed surface roughness profile was also recorded for all the specimens. The profile length is 4.0 mm and the cutoff length is 0.8 mm.

Figure 4.8 Mahr Mahrsurf GD 25 Surface Profilometer

4.6.5.b Surface Microscopy

The machined surfaces were examined with a Wyko – NT 2000 Surface Profiler (Figure 4.9) which uses a halogen light source (with or without a filler), with an interferometer and a Charged Coupled Display (CCD) camera inside the microscope. For scanning electron microscopy (SEM), an FEI Sirion SEM was used (Figure 4.10).

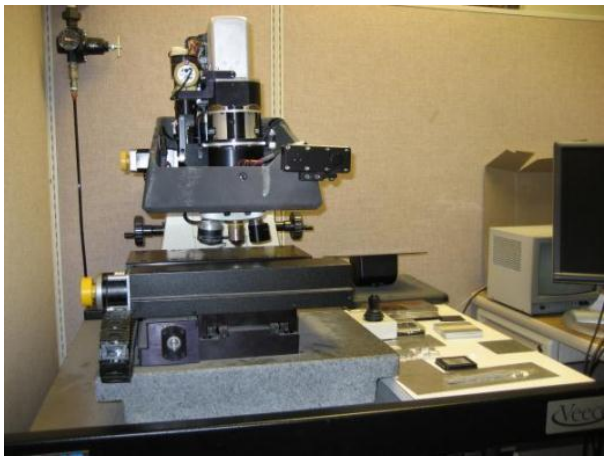

Figure 4.9 Wyko – NT2000 Surface Profiler

Figure 4.10 FEI Sirion Scanning Electron Microscope

4.6.5.c Mechanical Strength Testing

For monotonic static strength testing with the machined and drilled specimens an Instron Universal Testing machine, model 5585H (Figure 4.11) was used. Bi-axial Strain Gauges were used to record displacement of the test specimens under loading conditions.

Figure 4.11 Instron Universal Testing Machine, Model 5585H

4.7 Summary

In summary the research plan methodology is primarily based on the usage of different machining processes resulting in varying surface integrity amongst the different specimens. The specimens were the tested in static conditions subjected to different types of loadings and the resultant strengths documented both for specimens without holes and with holes.

For fatigue cycle testing, specimens with varying surface integrity due to different machining processes were tested under varying loading conditions in tension-tension cycle testing. The progress of damage in both static and fatigue testing was documented during the testing and its influence on both residual strength as well as cycles to failure for fatigue testing was documented.

A model for damage progression during fatigue testing as well as predictive cycles to failure was developed and tested against empirical data obtained from testing.

Chapter 5 – Experimental Testing of Static Mechanical Properties of 10 Ply Thick Laminate

5.1 Screening Experiments

Test specimens were edge trimmed with endmills and also using AWJ trimming. The surface roughness of the edges was measured using the MAHR surface profilometer. Similarly, for Open-Hole Testing holes were drilled using PCD and CVD Diamond Coated drills. Surface roughness was also measured using the profilometer. The machined and AWJ trimmed specimens were also examined using the Wyko surface profiler. Scanning Electron Microscopy (SEM) was used to examine the damage from each process including the surface of the drilled holes. Specimens were then bonded with aluminium tabs per the ASTM standards and mechanically tested to failure for the tensile strength, compressive strength and open-hole tensile strength. The failure mode of the test specimens for each case was examined and recorded.

5.2 Surface Integrity Observations

5.2.1 Machined Surfaces – Endmill Trimming Vs. AWJ

Surface roughness parameters were recorded for both the endmill trimmed and AWJ trimmed surface edges. The readings were taken both in the longitudinal and transverse direction. The surface roughness for the endmill machined surfaces was a lower value (R_a) in the longitudinal direction while the AWJ trimmed edge had a lower (R_a) value in the transverse direction, as shown in Table 5.1. The cutting parameters are as follows:

Endmill Trimming: Spindle Speed = 6000 RPM, Cutting Speed = 1.9 m/s, Feed Rate = 635 mm/min

AWJ Trimming: Linear Cutting Feed Rate = 1444 mm/min

The above parameters were chosen due to both limitations of the equipment used as well as cutting parameters recommend by endmill and drill manufacturers.

Type of Edge Trimming	Longitudinal R_a (μm)	Transverse R_a (μm)
Endmill	0.662	1.209
AWJ	4.491	0.816

Table 5.1 Example of Measured Surface Roughness of Edge Trimmed Surfaces

The surface profile readings in the longitudinal direction obtained from the two types of edge trimming operations are shown in Figure 5.1 & Figure 5.2.

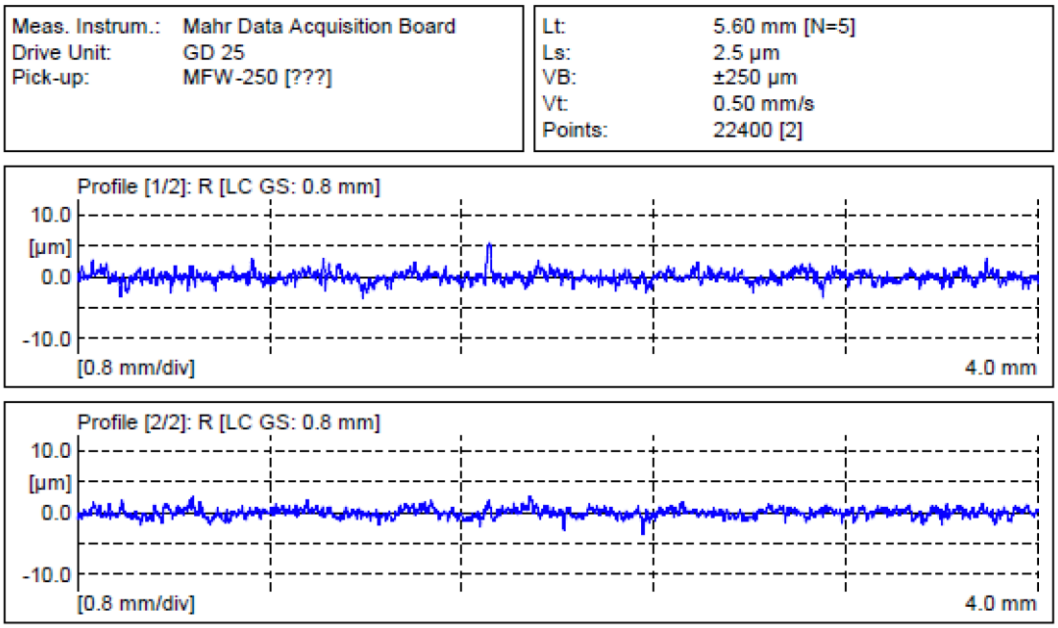

	Ra µm	Rq µm	Rz µm	Rmax µm	Rt µm	Rp µm	Rv µm	R Sm µm	R S µm	R Sk	R Ku	R Mr ... %	R Mr ... %
1:	0.662	0.892	6.232	8.01	8.97	3.38	2.85	39.95	26.34	0.57	6.58	29.11	78.56
2:	0.557	0.711	4.298	6.09	6.11	2.09	2.20	47.73	23.74	-0.11	3.73	43.02	88.80
Xb:	0.609	0.802	5.265	7.05	7.54	2.74	2.53	43.84	25.04	0.23	5.15	36.06	83.68
S:	0.074	0.128	1.368	1.36	2.02	0.91	0.46	5.50	1.84	0.48	2.02	9.83	7.24
Max:	0.662	0.892	6.232	8.01	8.97	3.38	2.85	47.73	26.34	0.57	6.58	43.02	88.80
Min:	0.557	0.711	4.298	6.09	6.11	2.09	2.20	39.95	23.74	-0.11	3.73	29.11	78.56
R:	0.104	0.181	1.934	1.92	2.85	1.29	0.65	7.78	2.60	0.68	2.85	13.91	10.24

Figure 5.1 Surface Roughness of Endmill Machined Edge (Longitudinal)

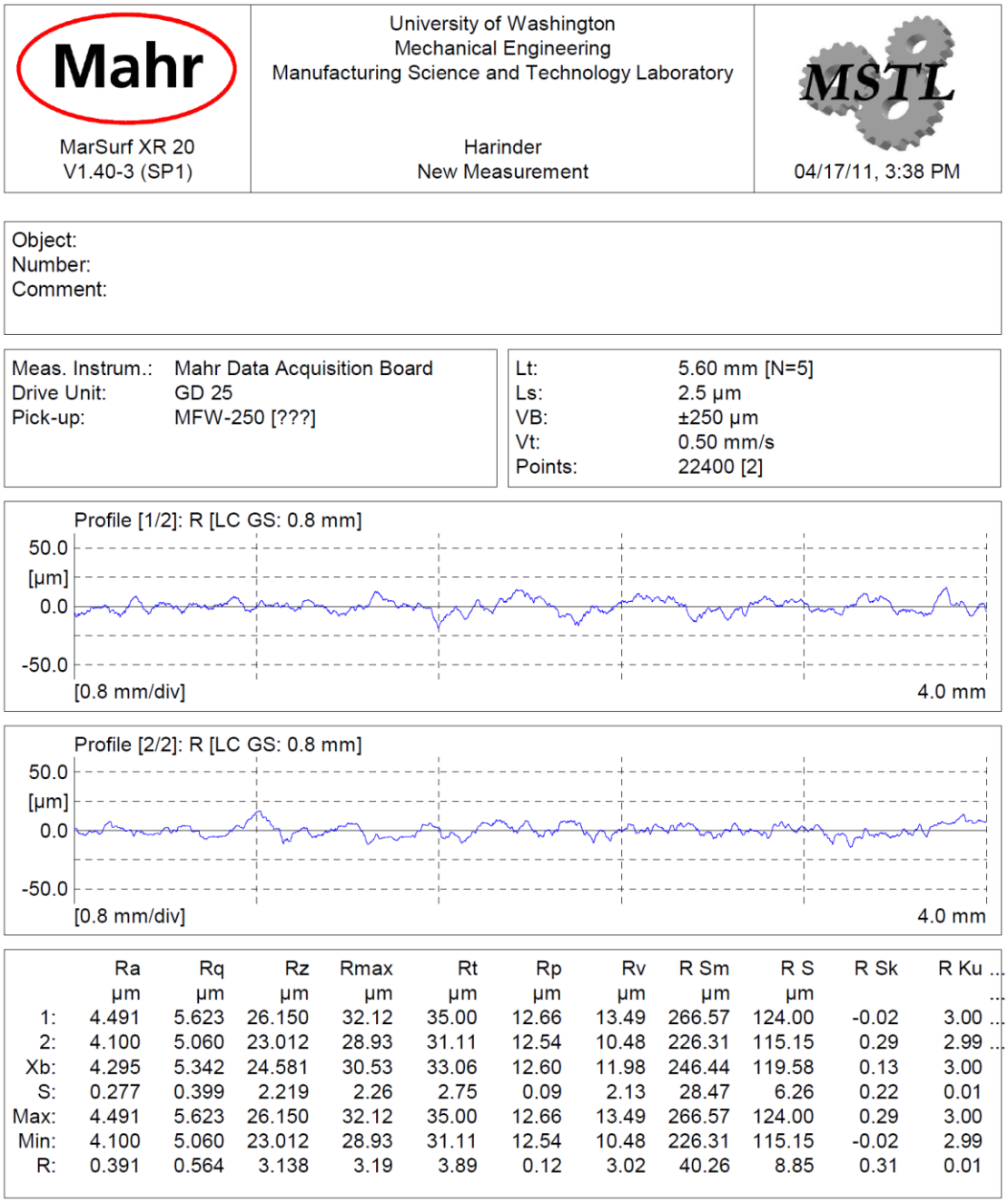

	Ra µm	Rq µm	Rz µm	Rmax µm	Rt µm	Rp µm	Rv µm	R Sm µm	R S µm	R Sk	R Ku ...
1:	4.491	5.623	26.150	32.12	35.00	12.66	13.49	266.57	124.00	-0.02	3.00 ...
2:	4.100	5.060	23.012	28.93	31.11	12.54	10.48	226.31	115.15	0.29	2.99 ...
Xb:	4.295	5.342	24.581	30.53	33.06	12.60	11.98	246.44	119.58	0.13	3.00
S:	0.277	0.399	2.219	2.26	2.75	0.09	2.13	28.47	6.26	0.22	0.01
Max:	4.491	5.623	26.150	32.12	35.00	12.66	13.49	266.57	124.00	0.29	3.00
Min:	4.100	5.060	23.012	28.93	31.11	12.54	10.48	226.31	115.15	-0.02	2.99
R:	0.391	0.564	3.138	3.19	3.89	0.12	3.02	40.26	8.85	0.31	0.01

Figure 5.2 Surface Roughness of AWJ Trimmed Edge (Longitudinal)

Next the two types of resultant surfaces were examined using an SEM and the Wyko surface profiler. Damage was observed using both pieces of equipment. A comparative view of the differences between the two types of surfaces is shown in Figure 5.3.

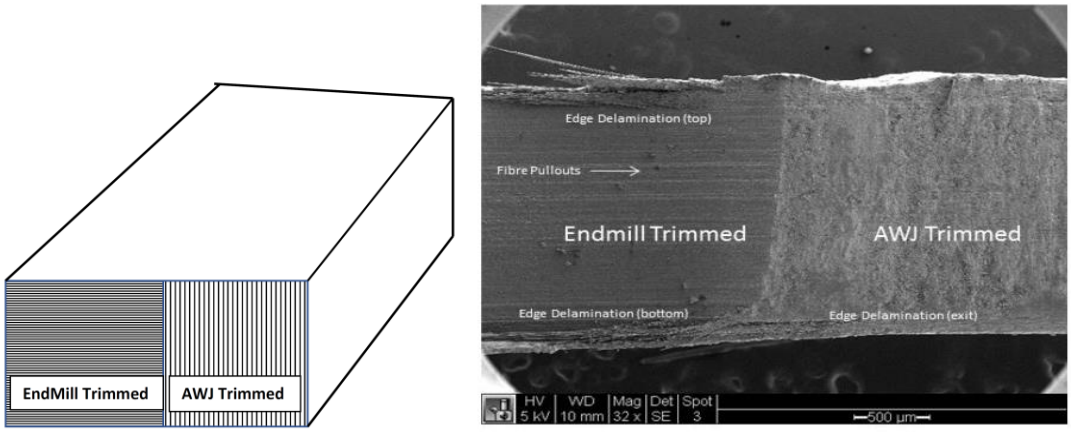

(a) (b)

Figure 5.3 Surface Comparison between Endmill vs. AWJ Trimmed – (a) schematic (b) actual specimen

It was observed that the AWJ trimmed surface showed evidence of edge delamination the exit side of the waterjet. The endmill trimmed surface though a smoother surface than the AWJ surface, had more damage on the top and bottom edge in the delamination mode of damage. The endmill machined edge also had evidence of fibre pullouts. These fibre pullouts were in the 45 degree ply and occur due to the way the cutting angle presents itself to the fibre orientation. The pattern of fibre pullouts repeats itself for the 45 degree ply as shown by the surface profile montage mapped by the Wyko surface profiler and shown in figure 5.4, while Figure 5.5 shows a micrograph with the fibre pullout areas. The two types of damage that dominate the machining processes remain fibre pullouts and delaminations. The occurrence of the fibre pullouts was more dominant during endmilling than delaminations although both occurred during trimming of each specimen with endmills. Exit delaminations during AWJ trimming were also noticed for each test specimen that was AWJ trimmed. Figures 5.6 & 5.7 show the detail damage on the endmill and AWJ trimmed edge surfaces.

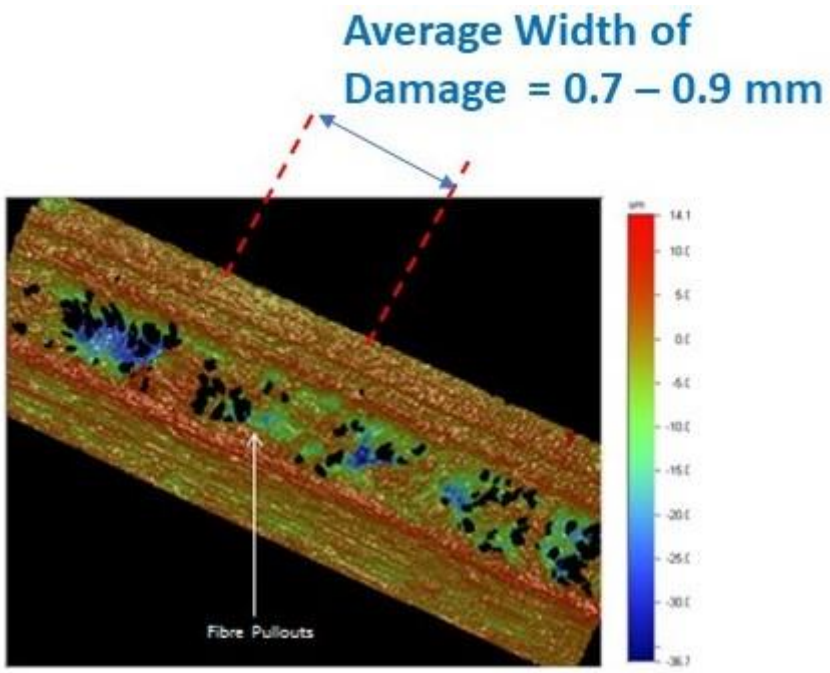

Figure 5.4 Montage of 45 Degree Ply Fibre Pullout Area of Endmill Machined Edge

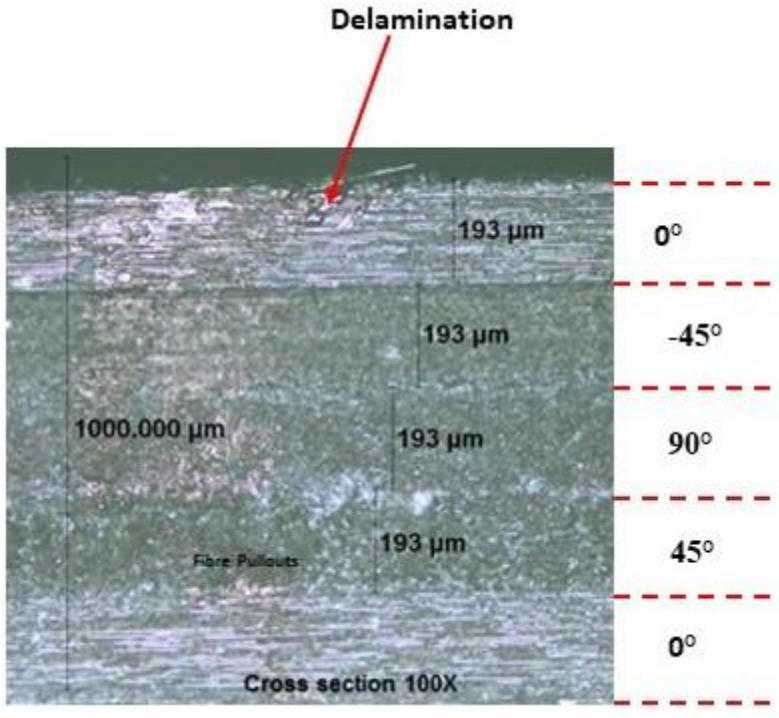

Figure 5.5 Micrograph showing Fibre Pullouts in 45 Degree Ply of Endmill Machined Edge

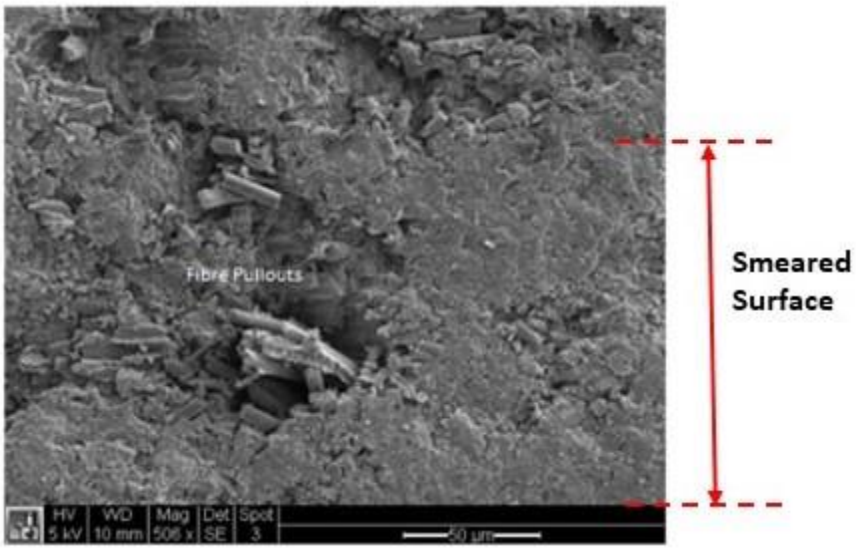

Figure 5.6 SEM of Fibre Pullouts in the Edge Surface of Endmill Trimmed Edge

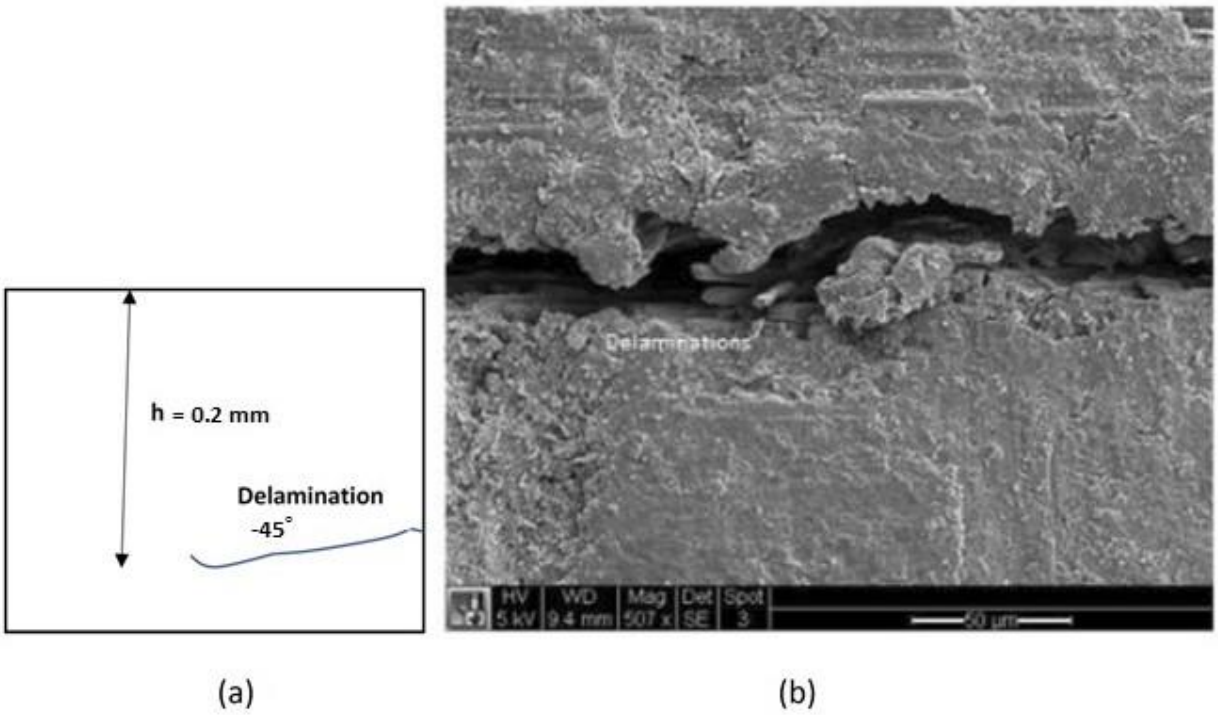

Figure 5.7 SEM of Delamination in the Edge Surface of AWJ Trimmed Edge – (a- schematic (b) actual specimen

5.2.2 Drilled Holes – CVD Diamond Coated Vs. Polycrystalline (PCD) Drills

Surface roughness parameters were recorded for holes drilled with CVD Diamond Coated and PCD drills. The surface roughness readings were lower (better surface) for the PCD drilled holes compared to the CVD Diamond drilled holes. This is due to the fact that the PCD edge is polished and smooth compared to the CVD coating which is not polished. CVD coatings are chemically deposited and are pure coatings without any binder. They are also thin coatings and cannot be polished as during polishing they can dis-bond from the substrate and strip off. The average surface roughness parameters for the two surfaces were:

PCD – Drilled Surface, R_a = 0.506 µm

CVD – Drilled Surface, R_a = 1.241 µm

The surface profile readings obtained from the hole surfaces on the PCD and the CVD Drilled holes are shown in Figures 5.8 & 5.9

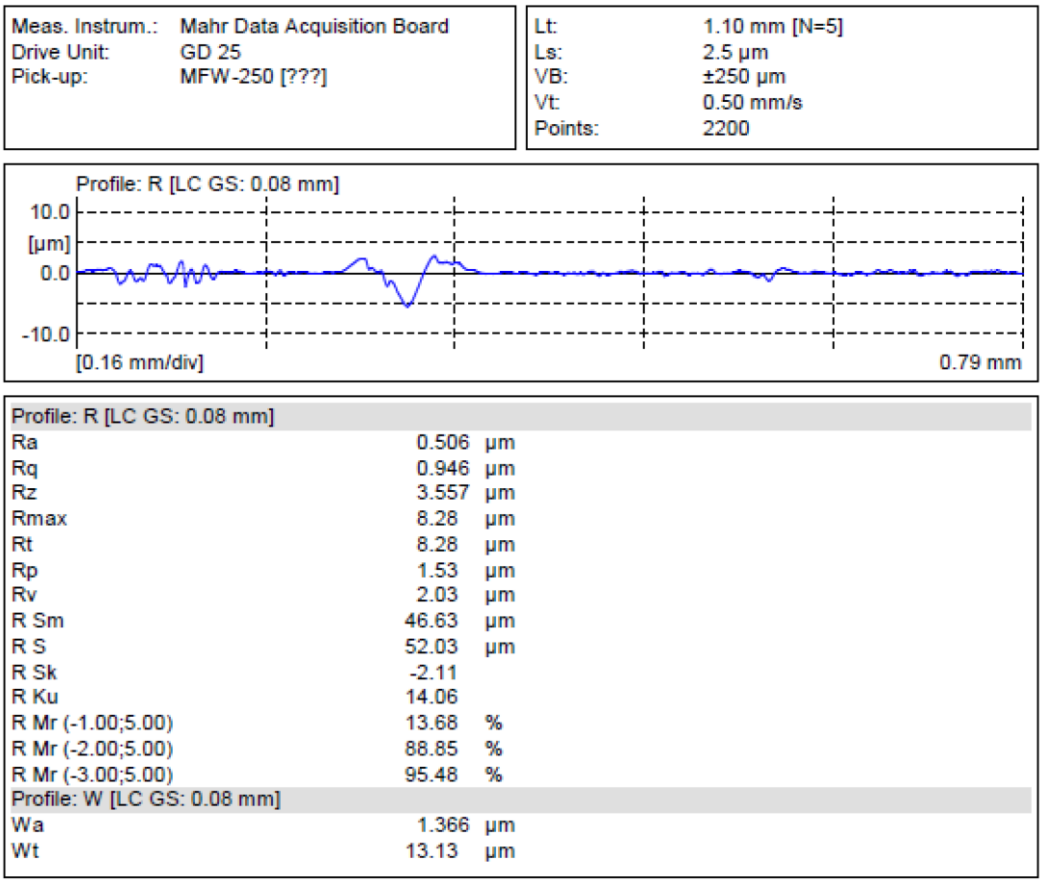

Figure 5.8 Surface Roughness of PCD Drilled Hole

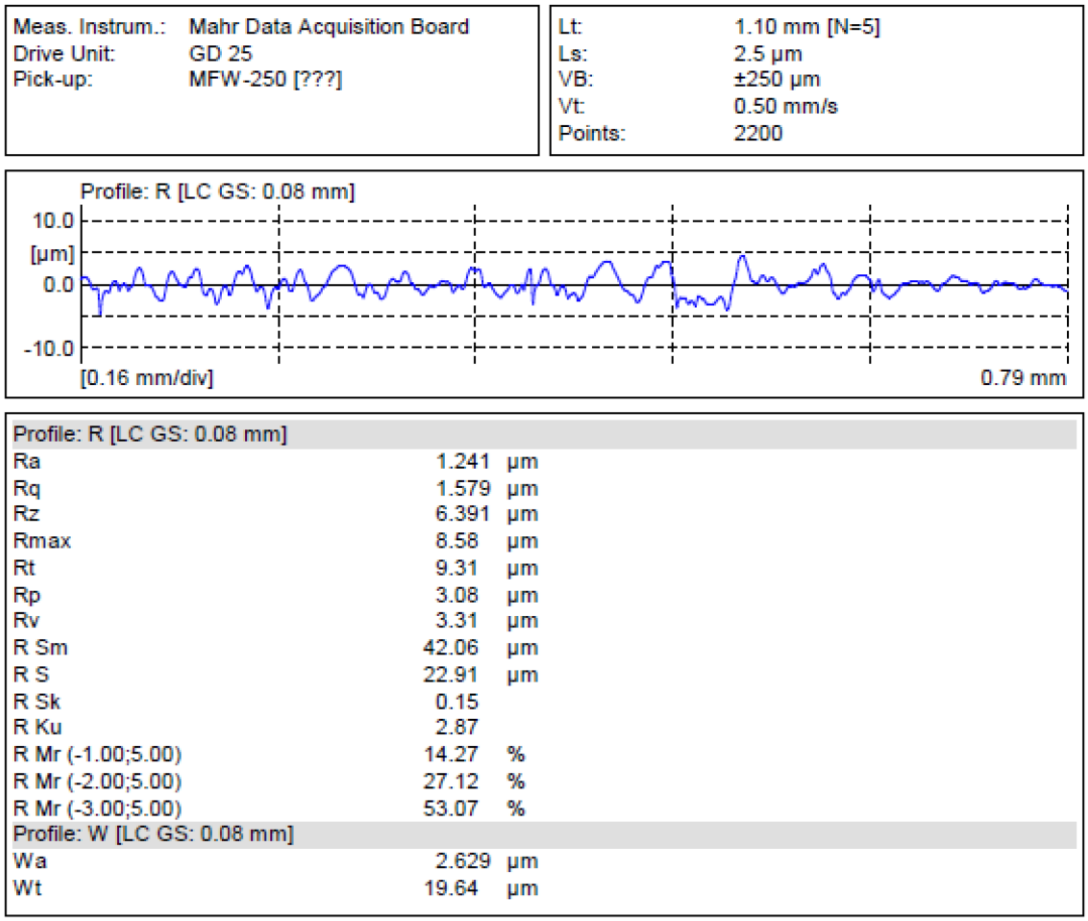

Figure 5.9 Surface Roughness of a CVD Diamond Coated Drilled Hole

Next the two types of drilled holes were examined under a Scanning Electron Microscope. Damage was noticed on the hole surfaces with both types of drills used. The SEM micrographs from holes with both types of drills are shown in Figures 5.10 through 5.14.

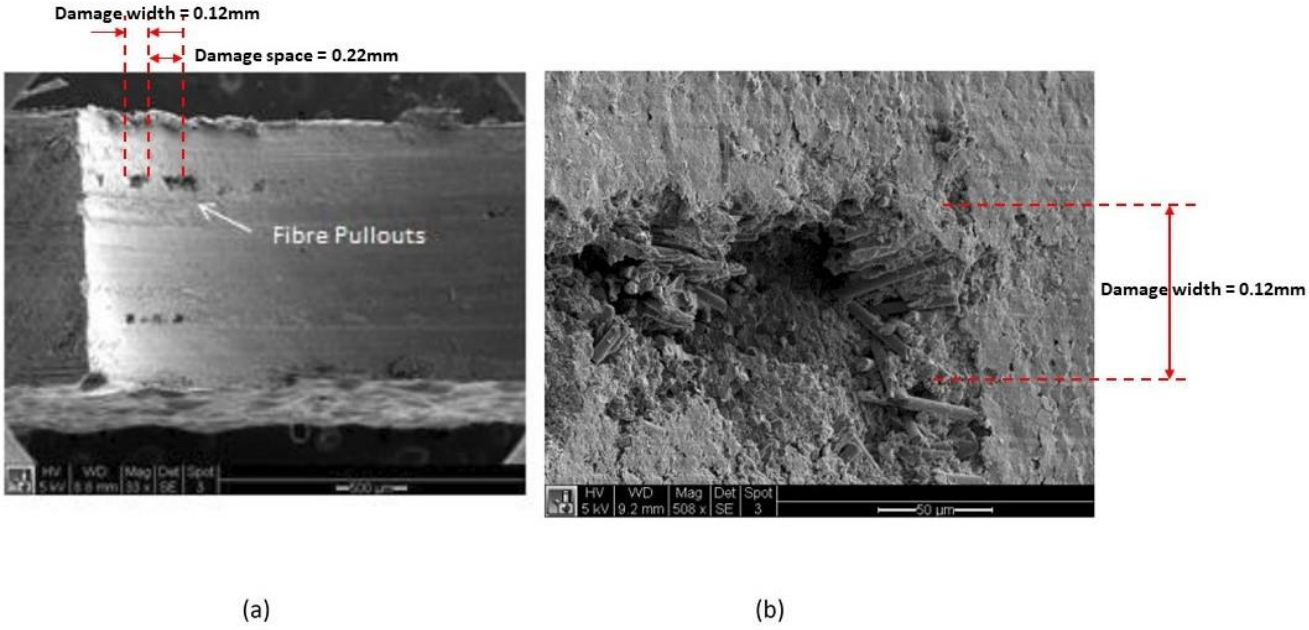

Figure 5.10 SEM of Fibre Pullout Region in PCD Drilled Hole – (a) Fibre Pullouts (b) magnified view of fibre pullout

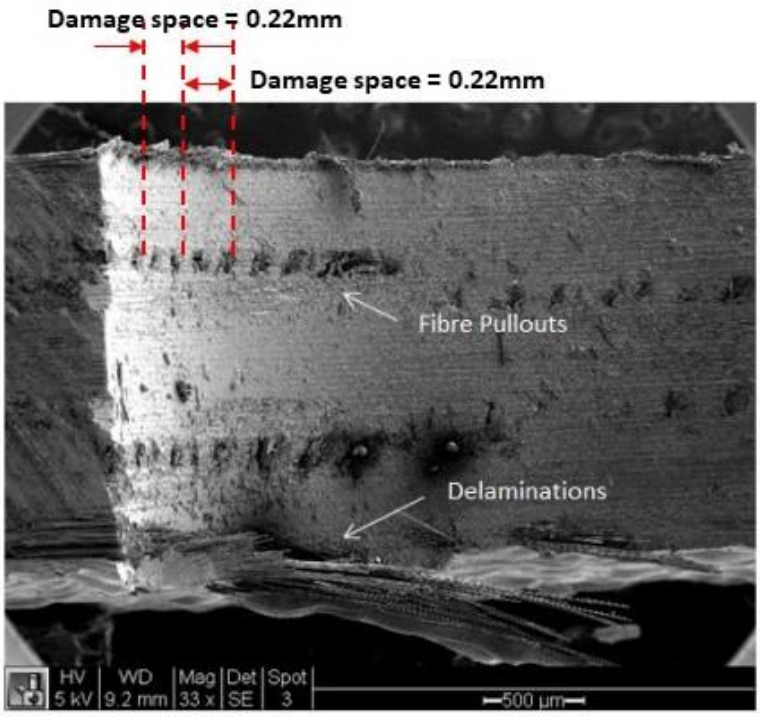

Figure 5.11 SEM of Surface Damage in CVD Diamond Drilled Hole

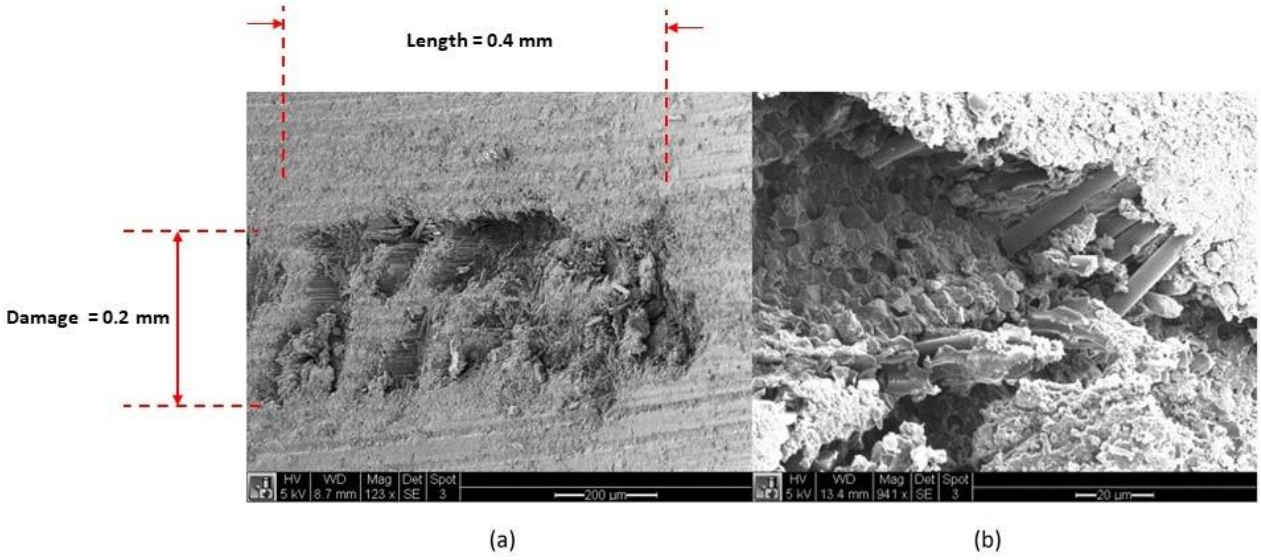

Figure 5.12 SEM of Fibre Pullout Region in CVD Diamond Drilled Hole – (a) magnified view of fibre pullout (b) magnified view of fibre pullout showing fibre fracture

The following observations were made on the surface integrity features for the 3 different machining processes used

AWJ Trimming - The AWJ timed specimens overall displayed a smooth surface with 3 distinct zones from the top of jet entry to the bottom of jet exit as shown in Figure 5.13.

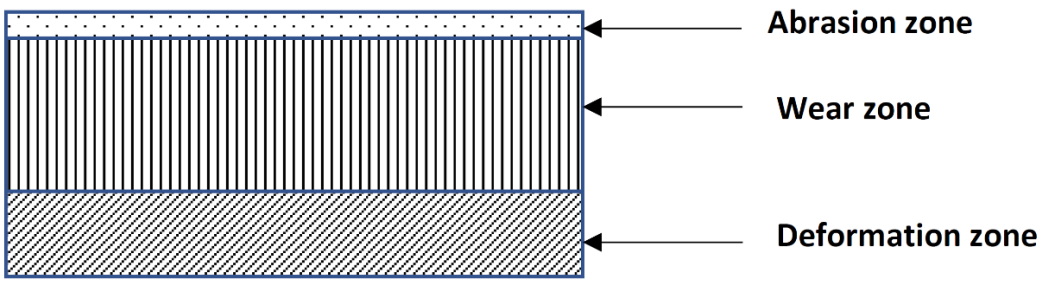

Figure 5.13 Surface Roughness Zones on AWJ Specimen

The top zone at the entry of the jet is the abrasion zone where the jet stream with particles enters the material. The wear pattern in this zone is abrasion occurring due the abrasion impact by the particles in the jet stream. The second zone is the wear zone where the cutting occurs and is smoother than the other 2 zones. The bottom zone is the deformation zone and occurs between the cutting zone and the exit edge of the specimen. This zone has a waviness pattern which is

primarily linked to the deflection of the just as the depth of the material increases. The AWJ trimmed surface also had striations along the surface and also displayed evidence of matrix cracking.

PCD Endmill Trimming - The PCD endmill used was a 0 degree helix endmill, so the orientation of the fibres to the cutting edge determined the resultant surface integrity. Fibre fractures were noticed on the plies that were parallel to the cutting edge while in plies parallel to the cutting edge, the surface was smooth. Fibre pullouts ere present predominantly in the 45 degree plies and based on the orientation of the fibres (positive or negative) and the angle of engagement to the cutting edge and cutting direction, the surface was smooth with fibre fracture being smoother under tension or rougher with fibre fracture due to shear. The cutting flutes of the PCD Endmill were polished and resulted in a smoother surface finish compared to other processes. Exit delamination (bottom edge) were present while there was a small occurrence of entrance delamination. Matrix cracking was also present through the thickness of the laminate. The damage zones were about 0.12 mm in size.

CVD Endmill Trimming - The CVD endmill used was an 18 degree helix endmill, resulting in a different angle of engagement with the orientation of the fibres resulting is surface integrity different in comparison to PCD Endmill and AWJ trimmed surfaces. The cutting edges of the endmill were not as sharp as compared to the PCD endmill to allow for effective adhesion of the diamond coating to the cutting edge. This resulted in an increased density of fibre pullouts in comparison to PCD endmill and AWJ trimmed surfaces. The higher density was also a resultant of the multi-faceted cutting edges of the diamond coating. Exit delamination were present on the trimmed surface and entrance delamination at the op edge was also present. The surface finish of the CVD Endmill trimmed surface was smooth and better than AWJ trimmed but slightly worse than PCD Endmill trimmed surfaces, the damage zones were approximately 0.2mm in size.

5.3 Mechanical Testing

5.3.1 Theoretical Strength Calculations

The laminator software was used to calculate the effective laminate strength based on the material strengths and the ply make up. The loading direction is X axis. The software returned the following theoretical Apparent Laminate Stiffness Properties:

Apparent Modulus in X direction, E_x = 91.95 GPa

Apparent Modulus in Y direction, E_y = 59.6 GPa

Apparent Shear Modulus, G_{xy} = 22.94 GPa

5.3.2 Specimen Readiness

5.3.2.1 Tensile Strength Specimens

Specimens were prepared and tested per ASTM D3039/D3039M for standard test method for tensile properties of Polymer Matrix Composite Materials. The specimens (Figure 5.14) were prepared per the standard and aluminium tabs were adhesively bonded on the ends using an epoxy adhesive. Both machined specimens using cutters and AWJ trimmed specimens were prepared and tested per the tensile properties test standard.

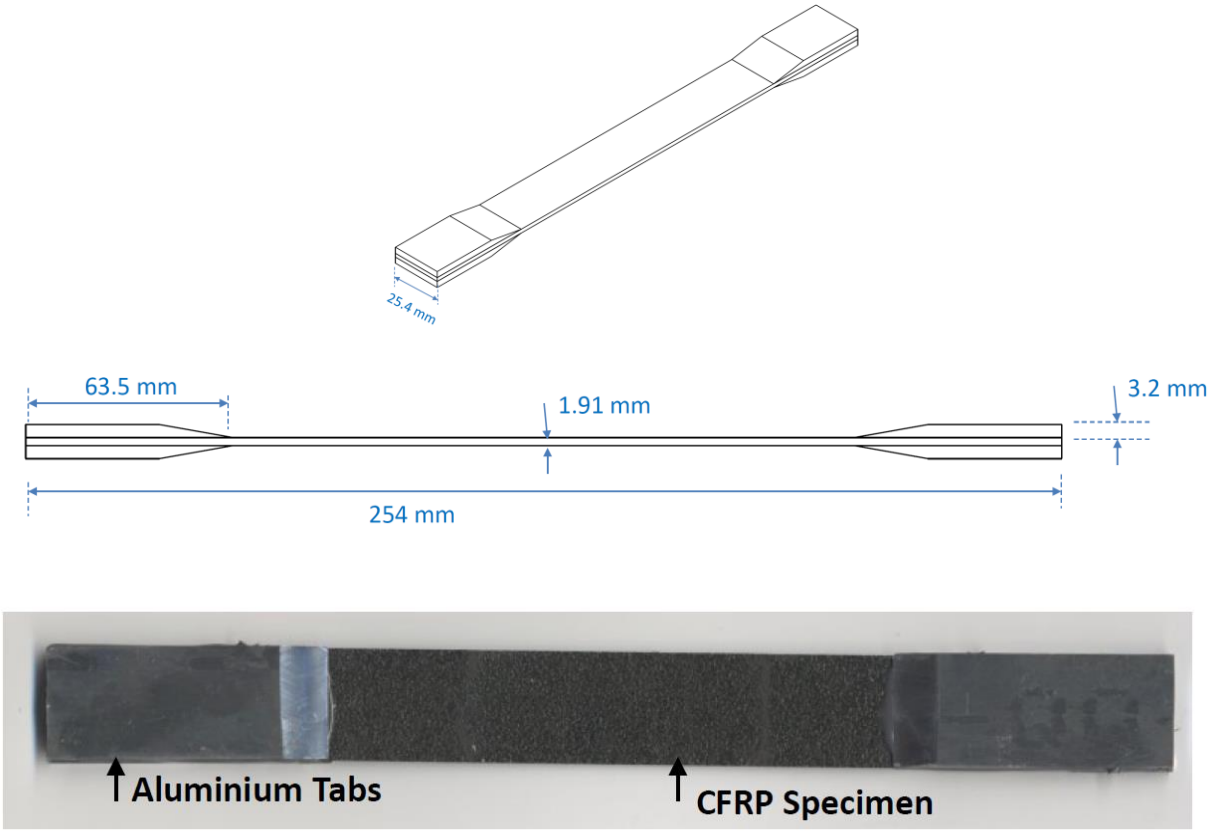

Figure 5.14 Tensile Strength Test Specimen

5.3.2.2 Compression Strength Specimens

Specimens were prepared and tested per ASTM D3410/D3410M for standard test method for compressive properties of Polymer Matrix Composite Materials. The specimens (Figure 5.15) were prepared per the standard and aluminium tabs were adhesively bonded on the ends using an epoxy adhesive. Both machined specimens using cutters and AWJ trimmed specimens were prepared and tested per the compressive properties test standard.

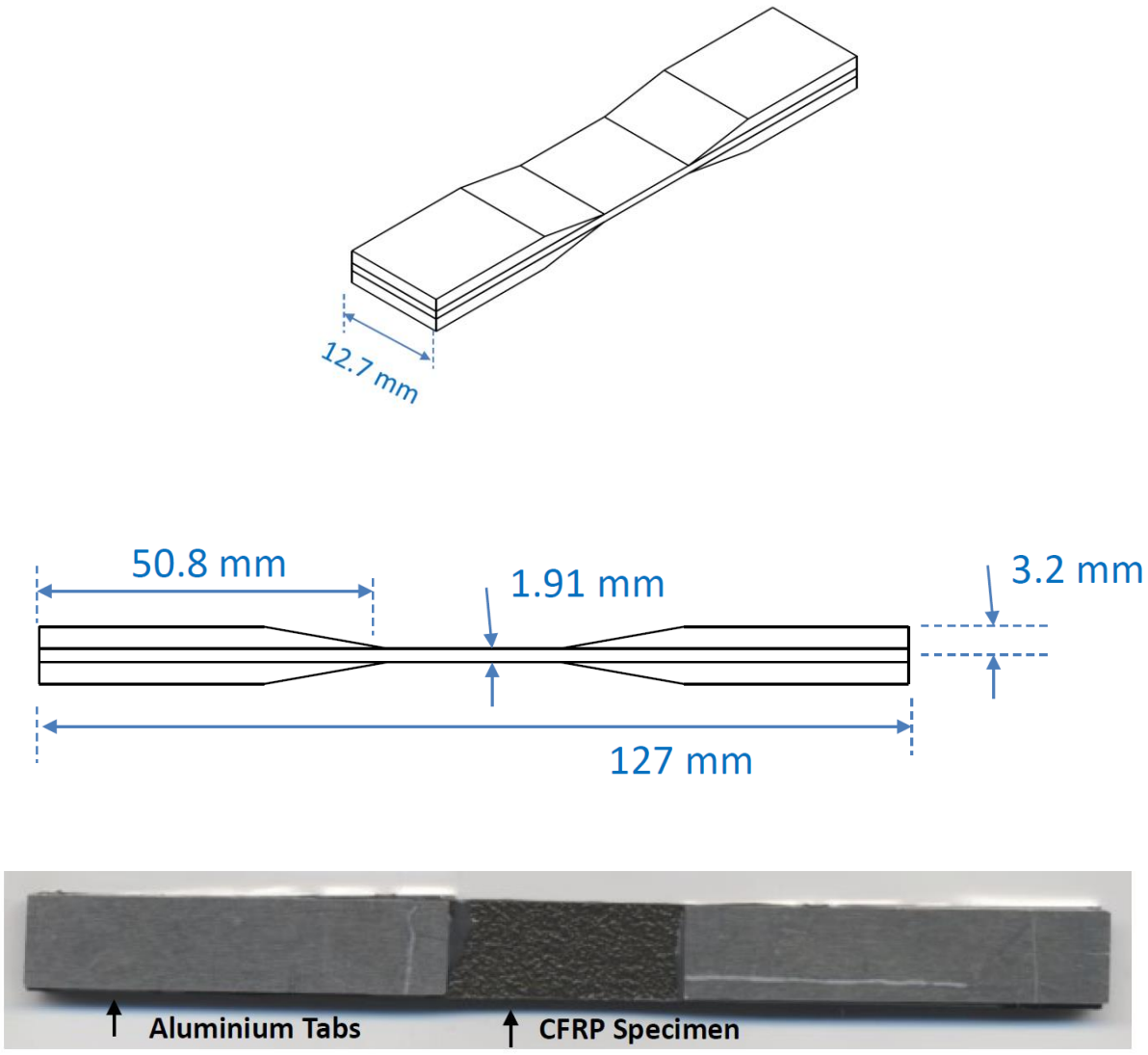

Figure 5.15 Compressive Strength Test Specimen

5.3.2.3 Open Hole Tensile Strength Specimens

Specimens were prepared and tested per ASTM D5766/D5766M for standard test method for Open-Hole Tensile Strength of Polymer Matrix Composite Laminates. The specimens were prepared per the standard and aluminium tabs were adhesively bonded on the ends using an epoxy adhesive. Both machined specimens using cutters and AWJ trimmed specimens were prepared by drilling holes using PCD and CVD drills and tested per the Open-Hole Tensile Strength Test Standard.

5.3.3 Test Matrix

A test matrix shown in Table 5.2 was developed for the test specimens used along with the processes used for trimming.

10 Ply Thick Laminate - Static Mechnical Properties Testing - Test Matrix								
Specimen Name	Trim	Hole	Test	Surface Finish - R_a	Surface Finish - R_z	Surface Finish - R_t	Surface Finish - R_{sk}	Surface Finish - R_{ku}
A1	AWJ -120		Tension	4.686	25.232	34.41	-0.19	2.55
A2	AWJ -120		Tension	5.945	32.473	42.56	-0.21	3.37
M1	CVD Endmill		Tension	0.541	4.4	5.072	NA	NA
M2	CVD Endmill		Tension	0.841	2.64	4.22	NA	NA
A3 - C	AWJ -120		Compression	4.491	26.15	35.00	-0.02	3.00
A4 - C	AWJ -120		Compression	4.099	23.012	31.109	0.289	2.99
M3 - C	CVD Endmill		Compression	0.79	1.751	2.19	NA	NA
M4 - C	CVD Endmill		Compression	0.661	2.077	2.988	NA	NA
A5 - OHT - P	AWJ -120	PCD Drill	Open Hole Tension	0.407	2.744	4.9112	NA	NA
A6 - OHT - P	AWJ -120	PCD Drill	Open Hole Tension	0.566	3.531	4.991	NA	NA
A7 - OHT - C	AWJ -120	CVD Drill	Open Hole Tension	0.985	6.00	10.547	NA	NA
A8 - OHT - C	AWJ -120	CVD Drill	Open Hole Tension	0.531	4.597	12.64	NA	NA
B5 - OHT - P	CVD Endmill	PCD Drill	Open Hole Tension	0.301	2.502	4.588	NA	NA
B6 - OHT - P	CVD Endmill	PCD Drill	Open Hole Tension	0.5062	3.557	8.277	NA	NA
B7 - OHT - C	CVD Endmill	CVD Drill	Open Hole Tension	0.998	5.601	7.867	NA	NA

Table 5.2 Test Matrix for 10 Ply Thick Laminate – Static Mechanical Properties Testing

The following test conditions were implemented after screening of machining processes for testing

a) For AWJ trimming 120 grit size was used for trimming
b) For Endmill trimming, CVD diamond coated endmills were used

c) For the Tension and compression testing, the surface finish parameters in the longitudinal direction were documented
d) For open hole tensile testing, the surface finish parameters for the holes were recorded in the transverse (thickness direction
e) Not all skew and kurtosis values were recorded due to a breakdown in the lab profilometer recording software

The following specimen dimensions were used in the mechanical testing as shown in Table 5.3

Test	Dimensions (W x L x T) in mm
Tensile Strength	25.4 x 254 x 2.0
Compressive Strength	12.7 x 127 x 2.0
Open Hole Tensile Strength	25.4 x 254 x 2.0 with a 6.35 hole in centre

Table 5.3 Specimens Dimensions for 10 Ply Laminate – Static Mechanical Testing

5.3.4 Tensile Strength Testing

Both endmill trimmed and AWJ specimens were mechanically tested in tension and the results tabulated. Strain gauges were used to capture the strain under tension loading conditions. All the specimens were taken to failure during the testing process. Figures 5.16 and 5.17 show the load displacement curves to failure of the endmill and the AWJ trimmed specimens.

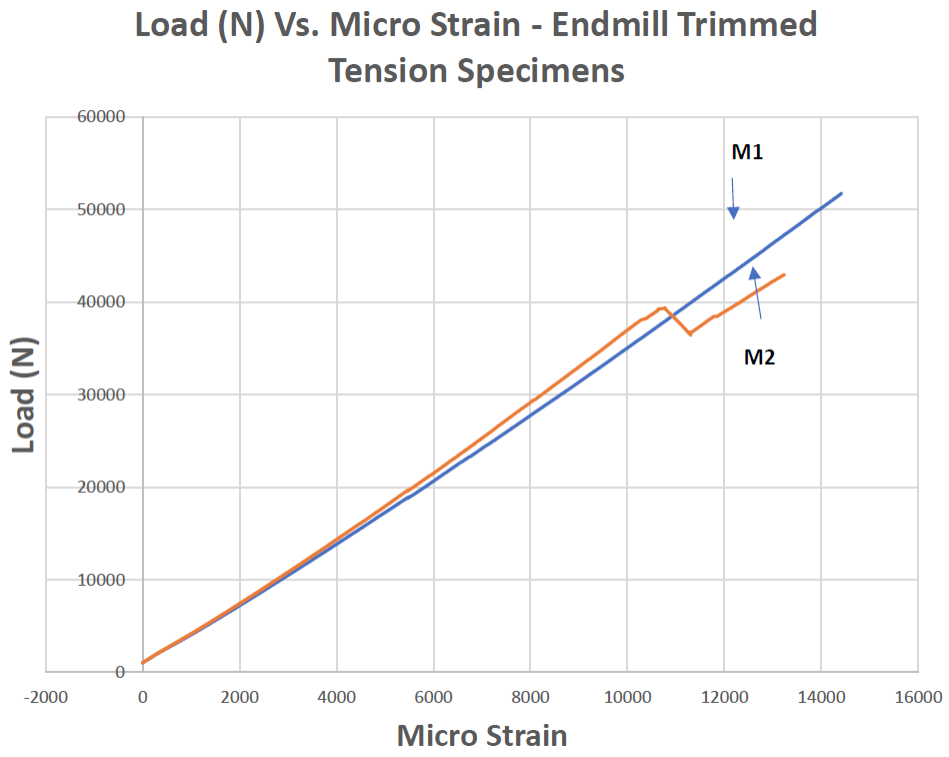

Figure 5.16 Load Displacement Curve, Endmill Specimen – Tension

Figure 5.17 Load Displacement Curve, AWJ Specimen – Tension

The results from the testing process showed the following Modulus for the tested specimens;

a) Endmill Trimmed Specimen – E_x = 70.7 GPa & 64.7 GPa
b) AWJ Trimmed Specimen – E_x = 72.5 GPa & 73.0 GPa

As seen from the above results there is a drop in the stiffness from the theoretical apparent stiffness calculations.

When analyzed for the failure mode, it was observed that the endmill trimmed specimen failed along the top ply as well as internal ply failure. The stiffness loss in this specimen was slightly larger compared to the AWJ specimen. SEM micrographs had shown evidence of fibre pullout in the endmill trimmed specimens as compared to the AWJ trimmed specimens. Figures 5.18 & 5.19 show the failure of the two types of specimens tested.

Figure 5.18 Failure of Endmill Trimmed Specimen in Tension

Figure 5.19 Failure of AWJ Trimmed Specimen in Tension

5.3.5 Compressive Strength Testing

Figures 5.20 & 5.21 show the load displacement curves of the endmill and AWJ trimmed specimens to failure in compression.

The results from the compression testing process showed the following Modulus for the tested specimens;

a) Endmill Trimmed Specimen – E_x = 54.9 GPa & 70.7 GPa
b) AWJ Trimmed Specimen – E_x = 49.2 GPa

As seen from the above results there is a drop in the stiffness from the theoretical apparent stiffness calculations.

In compression testing, the AWJ specimens showed a larger reduction in stiffness properties which is in line with research conducted by Ramulu & Colligan [39].

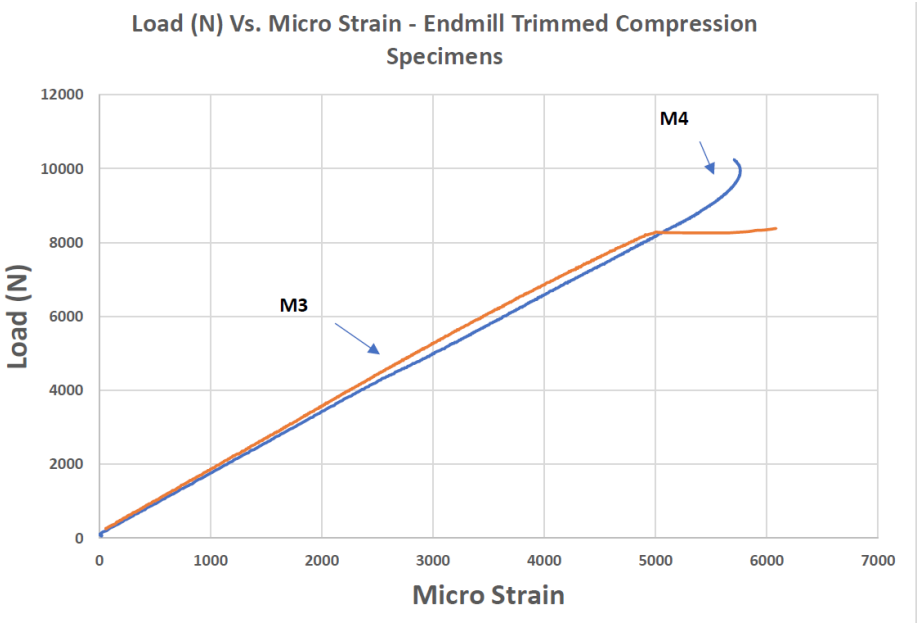

Figure 5.20 Load Displacement Curve, Endmill - Compression

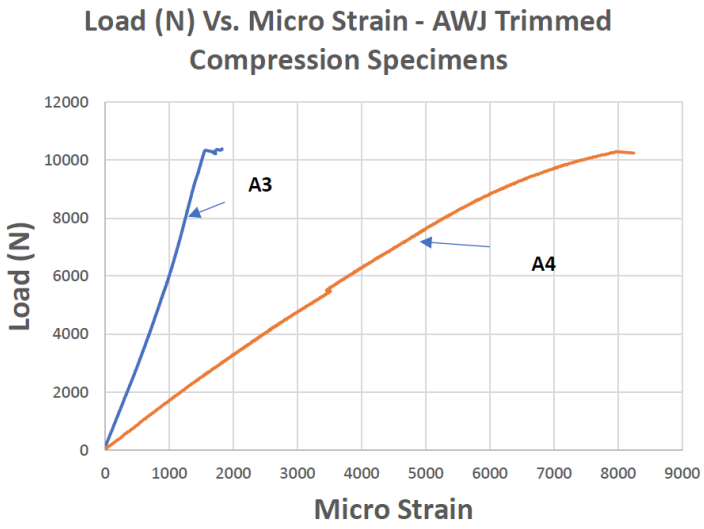

Figure 5.21 Load Displacement Curve, AWJ – Compression

In case of specimen A3 for the AWJ trimmed specimens, there was slippage between the grippers and the metallic tabs which resulted in collected strain gauge data to be inaccurate.

5.3.6 Open Hole Tensile Testing

Both PCD drilled holes and CVD drilled holes were tested in the open-hole tensile testing and their results documented. Figure 5.22 and Figure 5.23 show the Load Displacement Curves for Open-Hole Testing with PCD and CVD Drilled Holes for Endmill Trimmed and AWJ trimmed specimens.

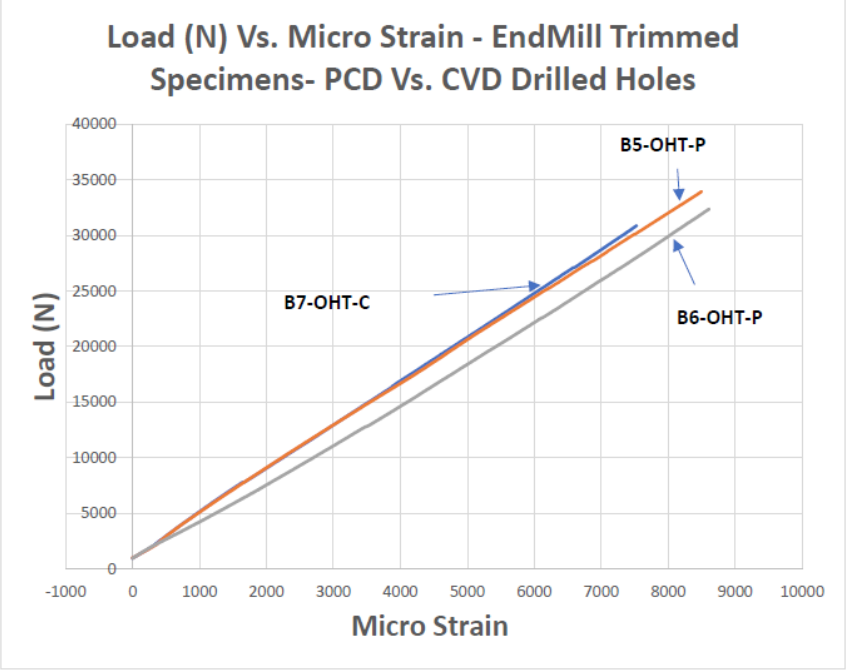

Figure 5.22 Load Displacement Curve, Endmill Trimmed – PCD Vs. CVD Drill Open-Hole Tension

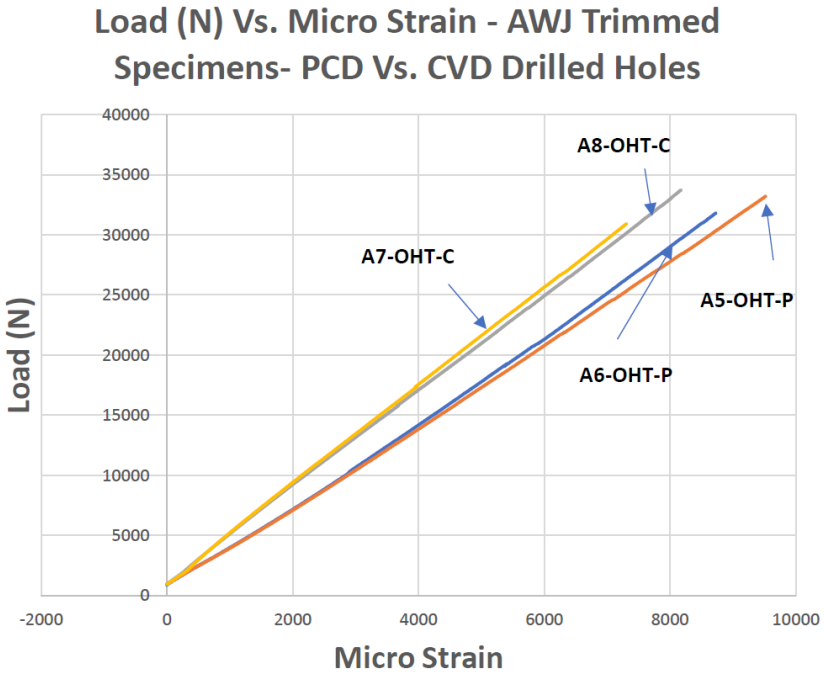

Figure 5.23 Load Displacement Curve, AWJ Trimmed - PCD Vs, CVD Drill Open-Hole Tension

From the test data, it was observed that the reduction in strength was larger for the CVD holes that had more damage on the surface area of the hole. The failure for the CVD specimens occurred on an average 2000 N lower load than the PCD drilled specimens.

The failure mode was internal delamination in both PCD and CVD drilled holes as shown in Figure 5.24

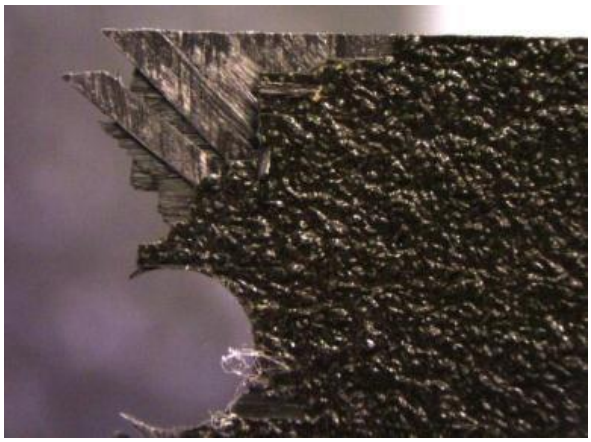

Figure 5.24 Delamination Failure of Specimen in Open-Hole Testing

From the damaged specimens it was observed that damage initiation was at the 45 degree plies in the hole. Damage progressed along the varies plies on the surface of the hole. Predominant damage was delamination along the 45 degree plies and failure was due to fibre fracture.

5.4 Discussion and Summary

This portion of the research study with a 10 ply thick laminate was conducted as a screening study to understand the processes, resultant surface integrity and the static mechanical testing that was conducted in the next phase with a 22 ply thick laminate. The following Table 5. 3 shows the results from the static mechanical testing conducted.

10 Ply Thick Laminate - Static Mechanical Properties Testing - Results Matrix												
Specimen Name	Trim	Hole	Test	Surface Finish - R_a	Surface Finish - R_z	Surface Finish - R_t	Surface Finish - R_{sk}	Surface Finish - R_{ku}	Maximum Load (N) at Failure	Maxium Stress (MPa) at Failure	Maxium Strain (mm/mm) at Failure	Modulus(GPa) at Failure
A1	AWJ -120		Tension	4.686	25.232	34.41	-0.19	2.55	52350	1030.00	0.014	73.00
A2	AWJ -120		Tension	5.945	32.473	42.56	-0.21	3.37	47902	942.9	0.013	72.5
M1	CVD Endmill		Tension	0.541	4.4	5.072	NA	NA	51740	1018.5	0.0144	70.7
M2	CVD Endmill		Tension	0.841	2.64	4.22	NA	NA	42935	845.17	0.0132	64.02
A3 - C	AWJ -120		Compression	4.491	26.15	35.00	-0.02	3.00	10394	409.20	0.0018	NA
A4 - C	AWJ -120		Compression	4.099	23.012	31.109	0.289	2.99	10249	403.5	0.0082	49.2
M3 - C	CVD Endmill		Compression	0.79	1.751	2.19	NA	NA	8380	329.9	0.006	54.9
M4 - C	CVD Endmill		Compression	0.661	2.077	2.988	NA	NA	10249	403.5	0.0057	70.78
A5 - OHT - P	AWJ -120	PCD Drill	Open Hole Tension	0.407	2.744	4.9112	NA	NA	33238	654.29	0.0095	NA
A6 - OHT - P	AWJ -120	PCD Drill	Open Hole Tension	0.566	3.531	4.991	NA	NA	31812	626.22	0.0087	NA
A7 - OHT - C	AWJ -120	CVD Drill	Open Hole Tension	0.985	6.00	10.547	NA	NA	30942	609.09	0.0073	NA
A8 - OHT - C	AWJ -120	CVD Drill	Open Hole Tension	0.531	4.597	12.64	NA	NA	33742	664.2	0.0081	NA
B5 - OHT - P	CVD Endmill	PCD Drill	Open Hole Tension	0.301	2.502	4.588	NA	NA	33925	667.8	0.0084	NA
B6 - OHT - P	CVD Endmill	PCD Drill	Open Hole Tension	0.5062	3.557	8.277	NA	NA	32361	637.02	0.0086	NA
B7 - OHT - C	CVD Endmill	CVD Drill	Open Hole Tension	0.998	5.601	7.867	NA	NA	30858	607.44	0.0075	NA

Table 5.4 Static Mechanical Testing Results for 10 Ply Thick Laminate

The results from the mechanical testing of the 10 ply thick laminate provided the following observations:

1) Overall the maximum loads for a given test or loads at failure generally were slightly lower for specimens with a rougher surface finish.
2) The maximum stress at failure was also lower for specimens with a rougher surface finish.
3) For the open holes specimens both maximum load at failure and maximum stress at failure were lower as compared to specimens with no holes. This is attributed to the stress concentration factor due to the presence of notch (hole) which is discussed in detail in chapter 6 and 7 during the testing of the 22 ply thick laminate.
4) The test specimens displayed higher strength properties in Tension in all cases as the fibres that carry the load are stronger in tension versus compression.
5) For the tension properties, the effect of surface integrity did result in slight reduction in stiffness from the theoretical calculated stiffness. Both the AWJ trimming and Endmill Trimming processes resulted in tension strength close to each other even though the surface roughness values were different between the 2 processes. This effectively pointed

to the surface integrity factor as having a dominant effect versus surface roughness. This was taken into accounted and discussed in detail in chapter 6.

The progress of damage during the testing was evaluated by reviewing the magnified views of the load versus displacement curves an example of which is shown in Figure 5.25 through Figure 5,27

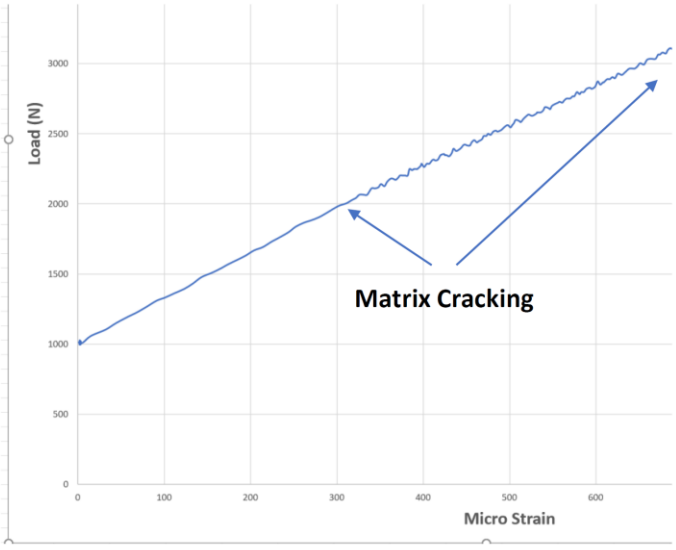

Figure 5.25 Matrix Cracking initiation and progress in an Endmill Trimmed Tension Specimen

From the Figure 5.25, it was observed that matrix cracking in an Endmill trimmed specimen under tension loading starting at around 2000N of loading and about 0.03% strain.

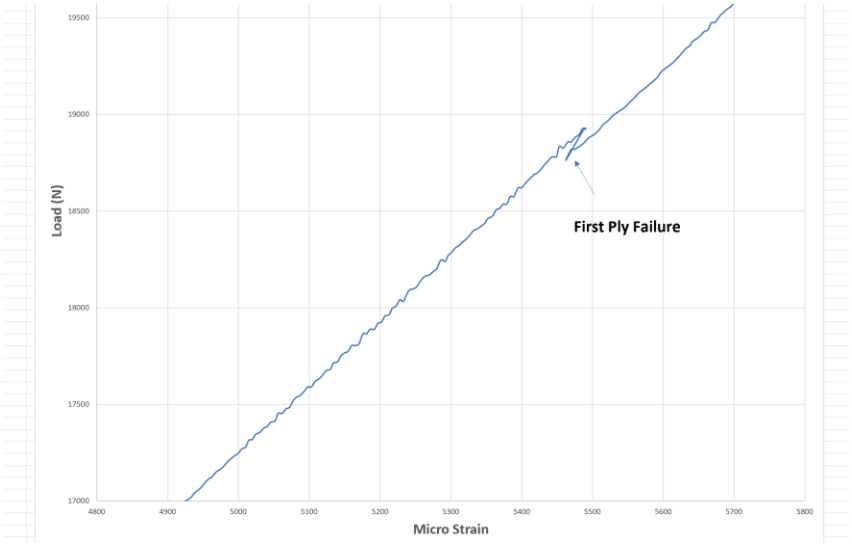

Figure 5.26 First Ply Failure in an Endmill Trimmed Tension Specimen

From Figure 5.26 it was observed that Frist Ply Failure for an endmill trimmed specimens occurred at around 0.55% strain and around a load of 18750 N.

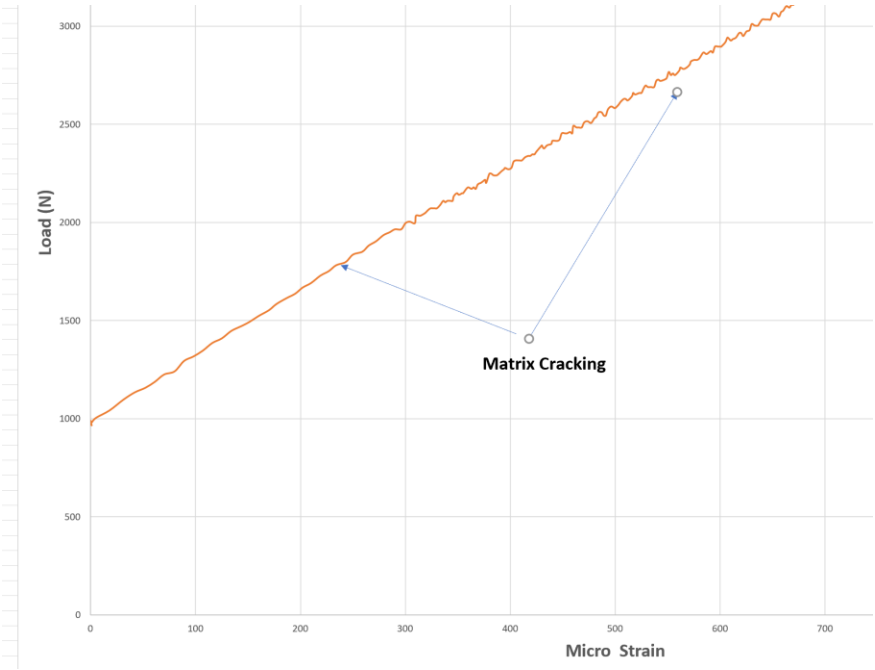

Figure 5.27 Matrix Cracking Initiation and Progress in an AWJ Trimmed Specimen

From Figure 5.27 it was observed that Matrix Cracking in an AWJ trimmed specimen under tension loading initiated at around a load of 1750N and around a strain of 0,025%.
It was observed that in AWJ trimmed specimens matrix cracking was dominant as a damage mode and first ply failure occurred also around 0.5% strain values.
This methodology of review of damage progress was used in the static mechanical properties testing of the 22 ply thick laminate as described and discussed in Chapter 6.

The damage progress mechanism constituted initial brittle nature in terms of matrix cracking. Once matrix cracking progresses, it starts with the debonding of the matrix-fibre interface. This mechanism is first inter-ply due to the shear modulus effect and soon it progress to intra-ply with initiation of delamination and first ply failure. As the fibres debond from the matrix, load transfer reduces with individual fibres carrying the load. This eventually results in fibre fracture with ply separation and eventual failure. This mechanism is studied in detail with the 22 ply thick laminate testing, both static and fatigue cycling as described in chapters 6 and 7.

The initial screening testing of all the 10 ply thick specimens led to some observations on the effects of surface integrity on the strength of CFRP laminates. Initial screening data showed a trend in reduction in stiffness and strength due to surface integrity effects. While the screening testing pointed in the direction of the magnitude of the correlation between surface integrity and stiffness/strength of the laminates, it also helped the author to understand that there is a link between the two. The effects of surface integrity were studied by including the surface integrity stress concentration factor in the static and fatigue cycle testing of the 22 ply thick laminate in chapters 6 & 7. All specimens with larger amounts of surface damage had lower loads to failure in every mode of testing. The type of failure resulting in lower loads had been predominantly the occurrence of Fibre pullouts in the specimens due to both trimming and drilling processes. This quantifies to some extent that fibre pullouts cannot be ignored in their detrimental effects on the Mechanical properties of CFRP laminates. It is an area that has not been studied by past researchers and was researched as a major part of the study by the author during the 22 ply thick laminate testing portion of the study. Initial screening tests also validated some of the results of past researchers that the surface integrity efforts from manufacturing processes do influence the mechanical properties of the CFRP laminates.

Chapter 6 – Experimental Testing of Static Mechanical Properties of 22 Ply Thick Laminate

6.1 Screening Experiments

Test specimens were edge trimmed with endmills and also using AWJ trimming. The surface roughness of the edges was measured using the MAHR surface profilometer. Similarly, for Open-Hole Testing holes were drilled using PCD and CVD Diamond Coated drills. Surface roughness was also measured using the profilometer. Scanning Electron Microscopy (SEM) was used to examine the damage from each process including the surface of the drilled holes. Specimens were then bonded with aluminium tabs per the ASTM standards and mechanically tested to failure for the tensile strength, compressive strength, open-hole tensile strength, open hole compressive strength and bearing strength. The failure mode of the test specimens for each case was examined and recorded.

6.2 Material Specification and Specimen Preparation

The 22 ply thick balanced symmetric $[90/-45/0/-45/90/45/0/-45/0/90/0]_s$ laminate used in the study had a nominal thickness of 4.52 mm and with an average ply thickness of 190 μm. The laminate had a top layer of woven fabric material [0/90] and a bottom layer of fiberglass skin material with material specification as defined in the Boeing Material Specification BMS 8-276 [67]. The Ply table is shown inn Table 6.1 The prepreg tape material used was approximately 305 mm in width and all layup was done manually as a 1220 x 1220 mm wide sheet. The sheet was cut into smaller coupons using Abrasive Water Jet (AWJ). The coupons were then machined either using endmill cutters or AWJ into smaller specimens for mechanical testing. For open holes and bearing testing, holes were drilled using PCD and CVD Diamond Coated Drills with a diameter of 6.35 mm. Prior to mechanical testing, surface integrity (roughness and Scanning Electron Microscopy) was documented.

Material	Orientation*
Fiberglass scrim	0/90
BMS 8-276 TY 40 CL 2 Form 1 6K-70-PW	0/90
BMS Spec 8-276 Type II CL 10 or 11 GR 190 Form 3	90
BMS Spec 8-276 Type II CL 10 or 11 GR 190 Form 3	45
BMS Spec 8-276 Type II CL 10 or 11 GR 190 Form 3	0
BMS Spec 8-276 Type II CL 10 or 11 GR 190 Form 3	-45
BMS Spec 8-276 Type II CL 10 or 11 GR 190 Form 3	90
BMS Spec 8-276 Type II CL 10 or 11 GR 190 Form 3	45
BMS Spec 8-276 Type II CL 10 or 11 GR 190 Form 3	0
BMS Spec 8-276 Type II CL 10 or 11 GR 190 Form 3	-45
BMS Spec 8-276 Type II CL 10 or 11 GR 190 Form 3	0
BMS Spec 8-276 Type II CL 10 or 11 GR 190 Form 3	90
BMS Spec 8-276 Type II CL 10 or 11 GR 190 Form 3	0
BMS Spec 8-276 Type II CL 10 or 11 GR 190 Form 3	90
BMS Spec 8-276 Type II CL 10 or 11 GR 190 Form 3	0
BMS Spec 8-276 Type II CL 10 or 11 GR 190 Form 3	-45
BMS Spec 8-276 Type II CL 10 or 11 GR 190 Form 3	0
BMS Spec 8-276 Type II CL 10 or 11 GR 190 Form 3	45
BMS Spec 8-276 Type II CL 10 or 11 GR 190 Form 3	90
BMS Spec 8-276 Type II CL 10 or 11 GR 190 Form 3	-45
BMS Spec 8-276 Type II CL 10 or 11 GR 190 Form 3	0
BMS Spec 8-276 Type II CL 10 or 11 GR 190 Form 3	45
BMS Spec 8-276 Type II CL 10 or 11 GR 190 Form 3	90
BMS 8-276 TY 40 CL 2 Form 1 6K-70-PW	0/90

Table 6.1 Ply Table for 22 Ply Laminate

6.3 Surface Integrity Observations

6.3.1 Machined Surfaces – Endmill Trimming Vs. AWJ

Surface roughness parameters were recorded for both the endmill trimmed and AWJ trimmed surface edges. The readings were taken both in the longitudinal and transverse direction. The surface roughness for the endmill machined surfaces was a lower value (R_a) in the longitudinal direction while the AWJ trimmed edge had a lower (R_a) value in the transverse direction. Table 6.2 shows the longitudinal surface finish values while Table 6.3 shows the transverse direction values.

Specimen Type	*Diameter (mm)*	*Type of Endmill*	*Radial Depth of cut (mm)*	*Axial Depth of Cut (mm)*
AWJ (80 Grit)	N/A	N/A	N/A	N/A
AWJ (120 Grit)	N/A	N/A	N/A	N/A
PCD Endmill	*6.35*	*PCD, 2 flutes, 0 degree Helix*	*0.76*	*2.0*
CVD Endmill	*6.35*	*CVD, 4 flutes 18 degree Helix*	*0.76*	*2.0*

(a)

Specimen Type	*Speed (RPM)*	*Linear Cutting Speed (m/min)*	*Type of Cut*	*Feed Rate (mm/min)*	*Pressure (bar)*	*Flow Rate (L/min)*
AWJ (80 Grit)	N/A	N/A	N/A	*1444*	*3447*	*3.0*
AWJ (120 Grit)	N/A	N/A	N/A	*1444*	*3447*	*3.0*
PCD Endmill	*6000*	*120*	*Climb*	*635*	N/A	N/A
CVD Endmill	*6000*	*120*	*Climb*	*635*	N/A	N/A

(b)

Specimen Type	Average Surface Finish - R_a (µm)	Surface Finish – R_z (µm)	Surface Finish – R_t (µm)	Readings at depth (mm)
AWJ (80 Grit)	4.613	25.315	31.70	2
AWJ (120 Grit)	3.467	21.416	31.31	2
PCD Endmill	0.473	3.907	5.51	2
CVD Endmill	1.358	8.312	10.5	2

(c)

Table 6.2 Surface Roughness (longitudinal) of Edge Trimmed Surfaces and Trimming Parameters , (a), (b) and (c)

Specimen Type	Average Surface Finish - R_a (µm)	Surface Finish – R_z (µm)	Surface Finish – R_t (µm)
AWJ (80 Grit)	1.424	7.801	14.295
AWJ (120 Grit)	1.404	8.277	12.285
PCD Endmill	1.614	9.142	14.06
CVD Endmill	1.994	9.904	20.575

Table 6.3 Surface Roughness (transverse) of Edge Trimmed Surfaces, Trimming parameters are same as Table 6.2 (a) and (b)

The cutting parameters used are as follows:

Endmill Trimming: Spindle Speed = 6000 RPM, Cutting Speed = 1.9 m/s, Feed Rate = 635 mm/min

AWJ Trimming: Linear Cutting Feed Rate = 1444 mm/min

The surface profile readings obtained from the two types of edge trimming operations are also shown in Figure 6.1 thru Figure 6.3.

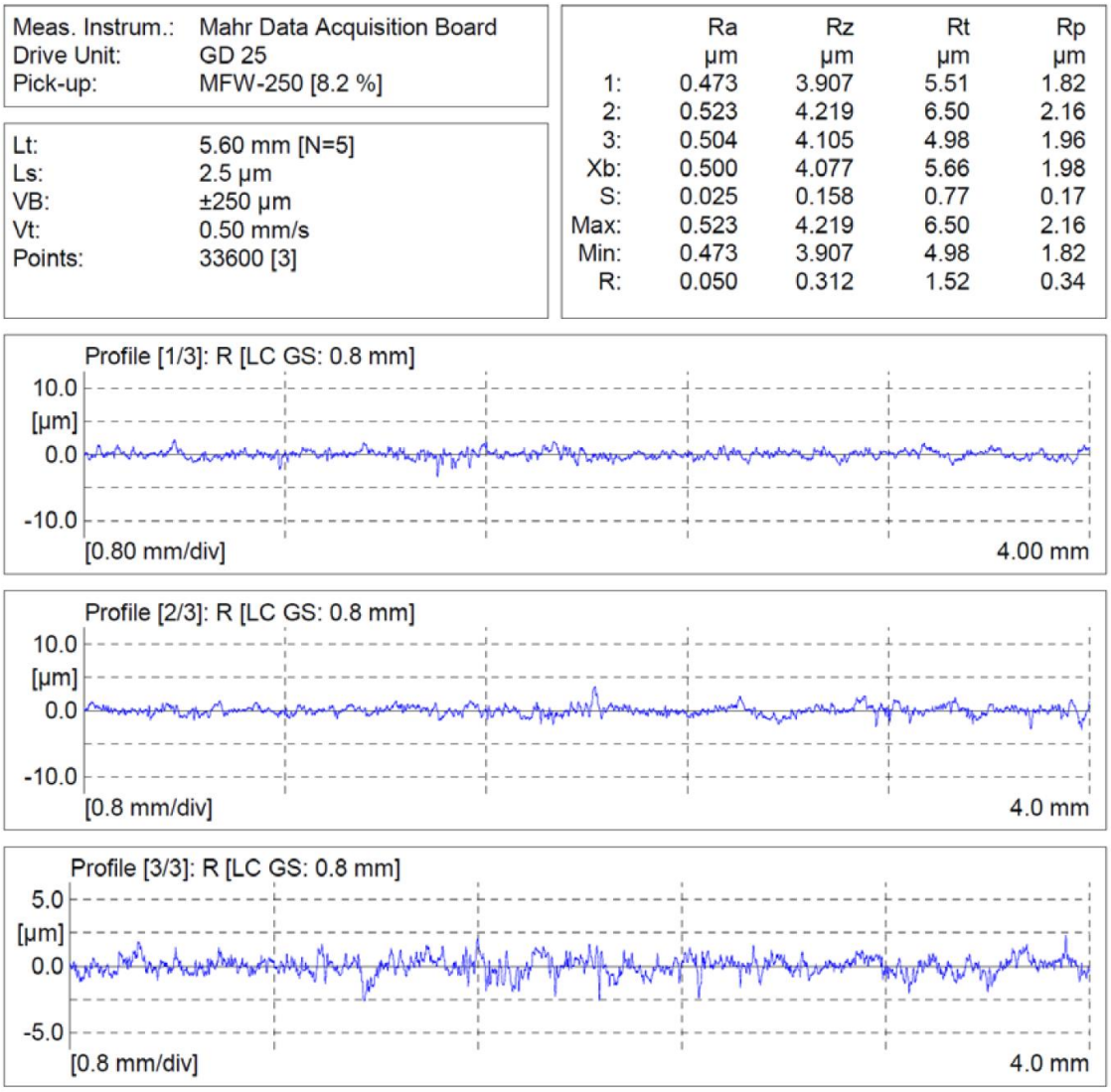

Figure 6.1 Longitudinal Surface Roughness of PCD Endmill Machined Edge

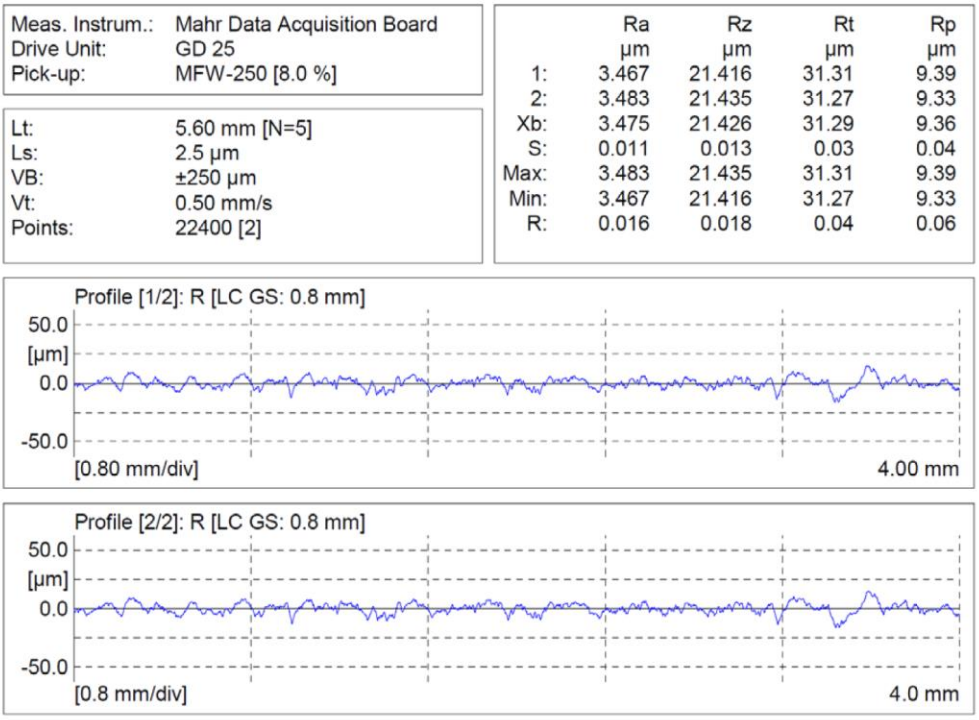

Figure 6.2 Longitudinal Surface Roughness of AWJ (120 grit) Trimmed Edge

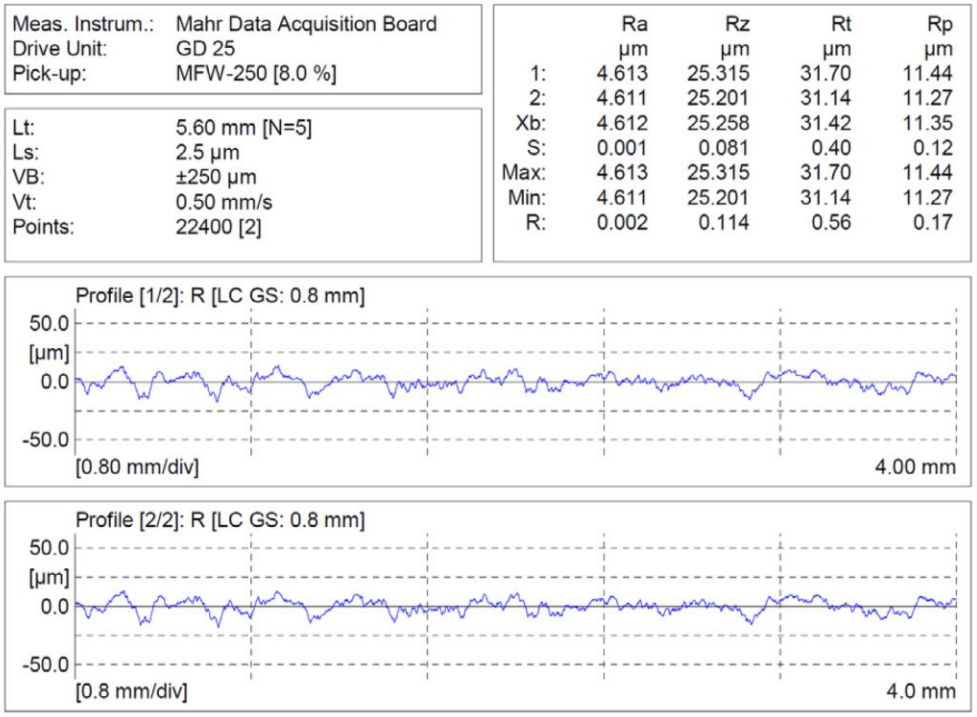

Figure 6.3 Longitudinal Surface Roughness of AWJ (80 grit) Trimmed Edge

Following Figures 6.4 and 6.5 show the SEMs of AWJ (80 grit) trimmed surface.

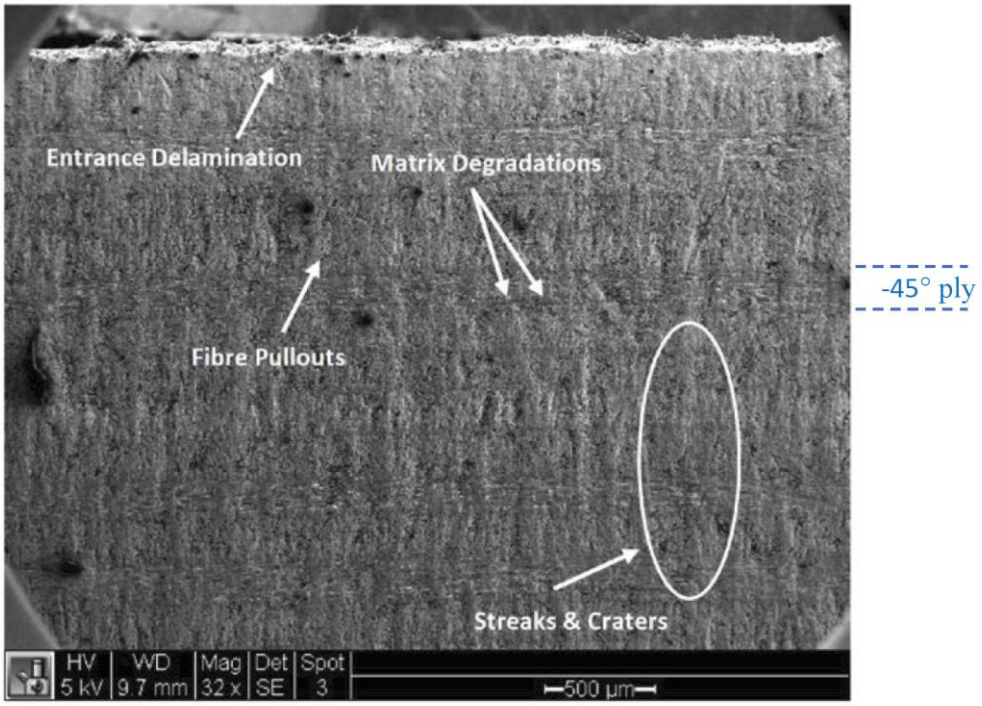

Figure 6.4 SEM of AWJ trimmed Edge Surface (80 Grit)

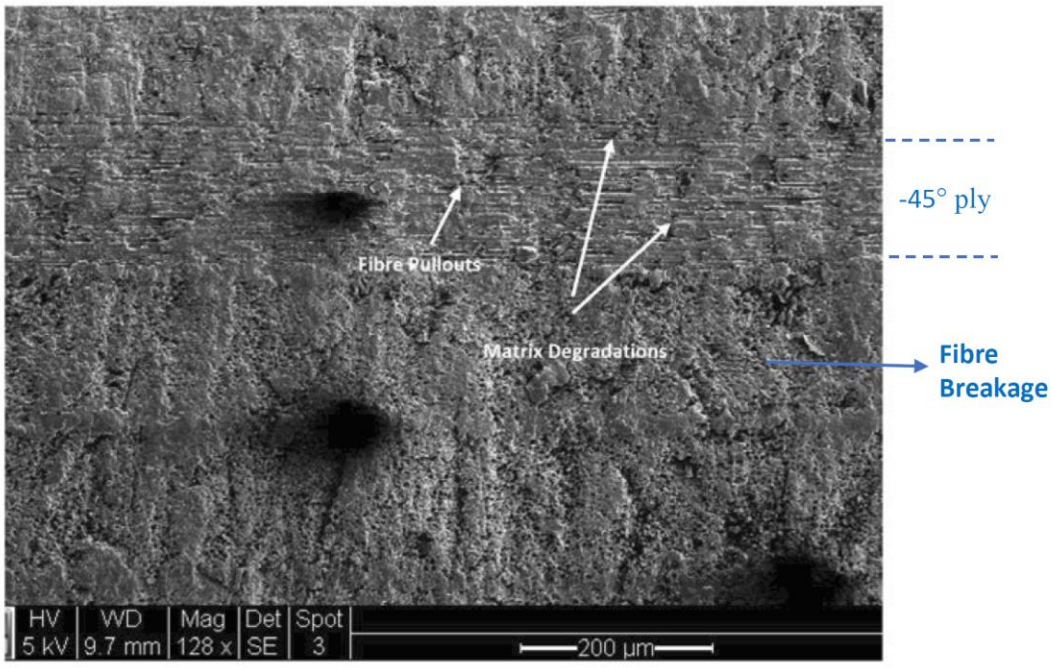

Figure 6.5 SEM of AWJ trimmed Edge Surface (80 Grit)

The following damage was observed after AWJ (80 Grit) Edge Trimming

- Streaks and Craters along the direction of the water Jet axis
- Matrix Degradation (cracks) present throughout the thickness of the specimen with approximate size of 15 µm
- Matrix Cracks are consistent in occurrence and independent of orientation of fibres with approximate size of 15 µm
- Fibre pullouts are present, lower in density and dependent on ply orientation
- Fibre pullouts are predominant along the 45 degree plies and present mostly in the bottom half of the laminate
- Exit delamination are present while there is some occurrence of entrance delamination with approximate size of 0.08 mm

Figures 6.6 and 6.7 show the SEMs of AWJ (120 grit) Trimmed edges.

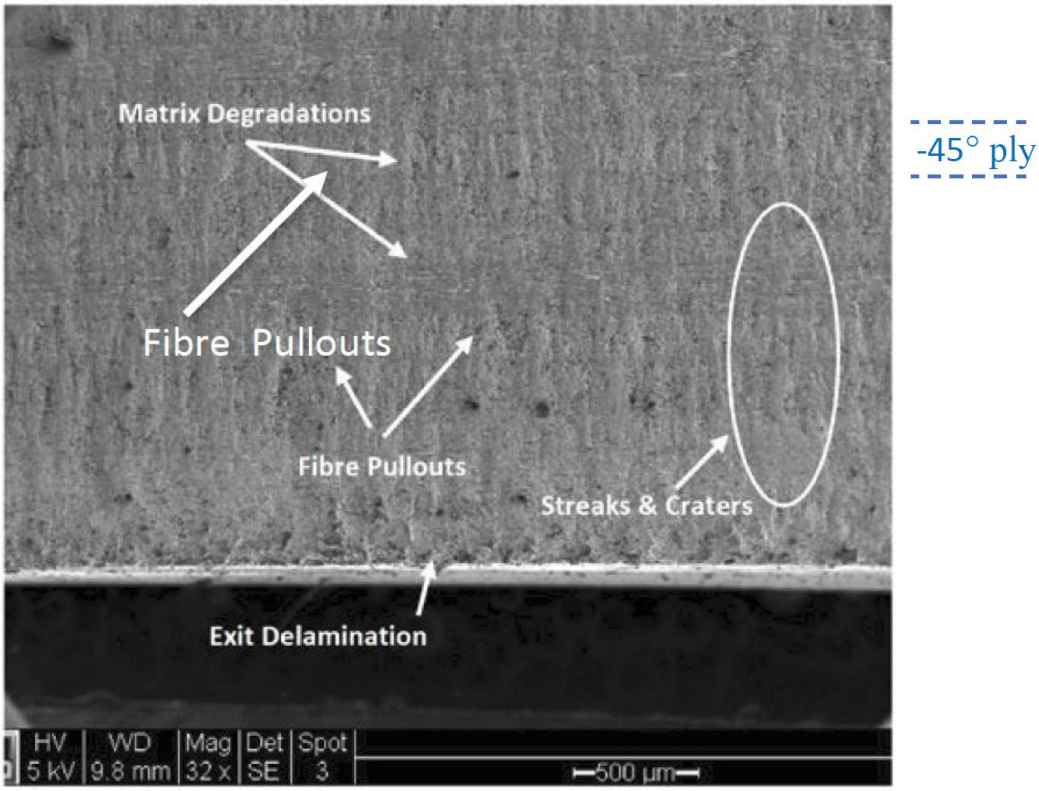

Figure 6.6 SEM of AWJ (120 grit) Trimmed Edge Surface

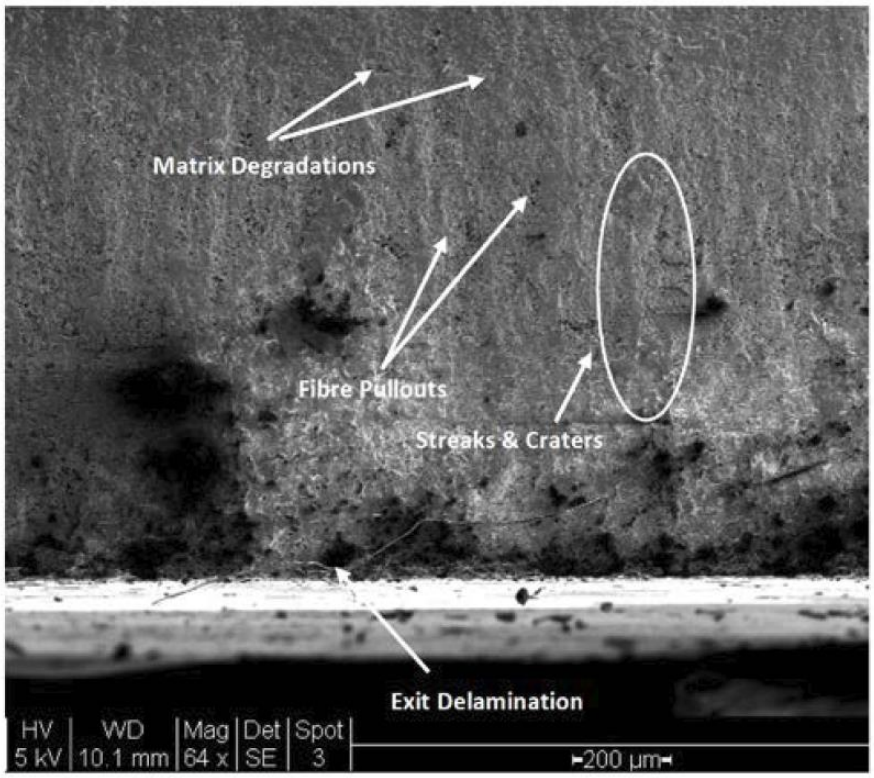

Figure 6.7 SEM of AWJ (120 grit)Trimmed Edge Surface

The following damage was observed after AWJ (120 Grit) Edge Trimming

- Streaks and Craters along the direction of the water Jet axis
- Matrix Degradation (cracks) present throughout the thickness of the specimen with approximate size of 15 µm
- Matrix Cracks are consistent in occurrence and independent of orientation of fibres with approximate size of 15 µm
- Fibre pullouts are present, lower in density and depend in ply orientation
- Fibre pullouts are predominant along the 45 degree plies and present mostly on the bottom half of the laminate
- Exit delamination are present while there is some occurrence of entrance delamination with approximate size of 0.08 mm
- Exit delamination caused by erosion effects due to water jet deflection with depth resulting in penetration between layers/plies

Figures 6.8 and 6.9 show the SEMs of PCD Endmill trimmed edges

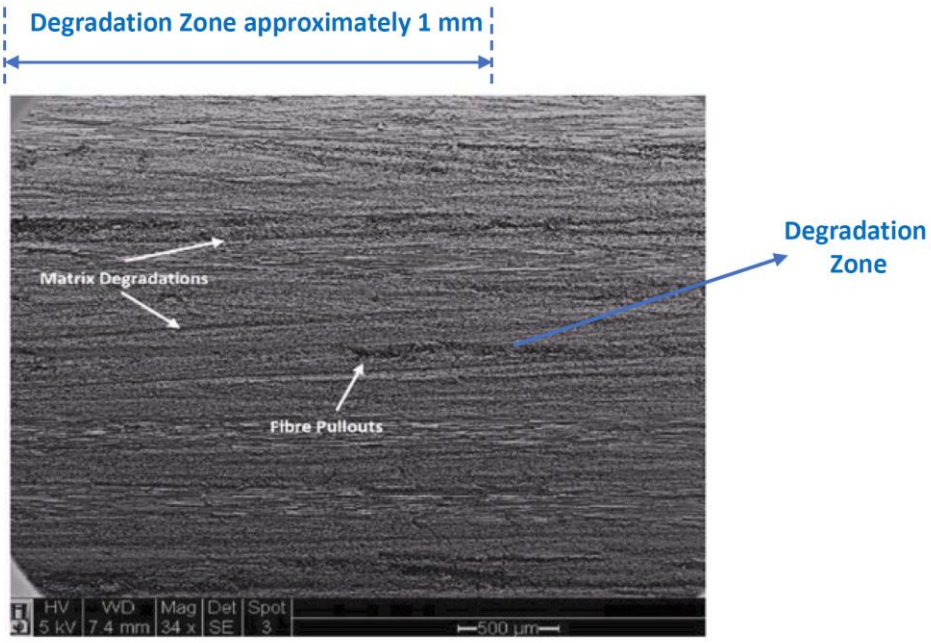

Figure 6.8 SEM of PCD Endmill Trimmed Edge Surface

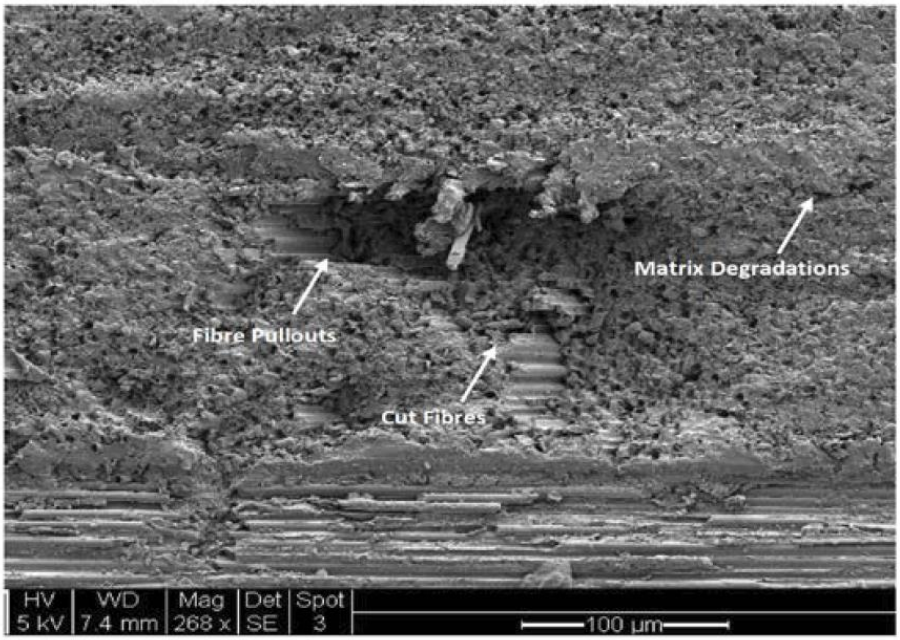

Figure 6.9 SEM of PCD Endmill Trimmed Edge Surface

The following features of surface roughness were observed after PCD Endmill Edge Trimming

- Smooth surface obtained compared to all other trimming processes
- Cutting flutes of PCD endmill polished with a sharp corner aiding in better surface finish of trimmed surface

The following damage was observed after PCD Endmill Edge Trimming

- Fibre pullouts are present, higher in density in comparison to AWJ trimmed specimens with spacing of 2 times the feedrate/rev
- Fibre pullouts are predominant along the 45 degree plies and occur through the thickness of the laminate
- Exit (bottom edge) delamination are present while there is some occurrence of entrance delamination with approximate size of 0.1 mm
- Matrix cracks also present in the PCD trimmed edge surface

Figures 6.10 and 6.11 show the SEMs of CVD Endmill trimmed edges

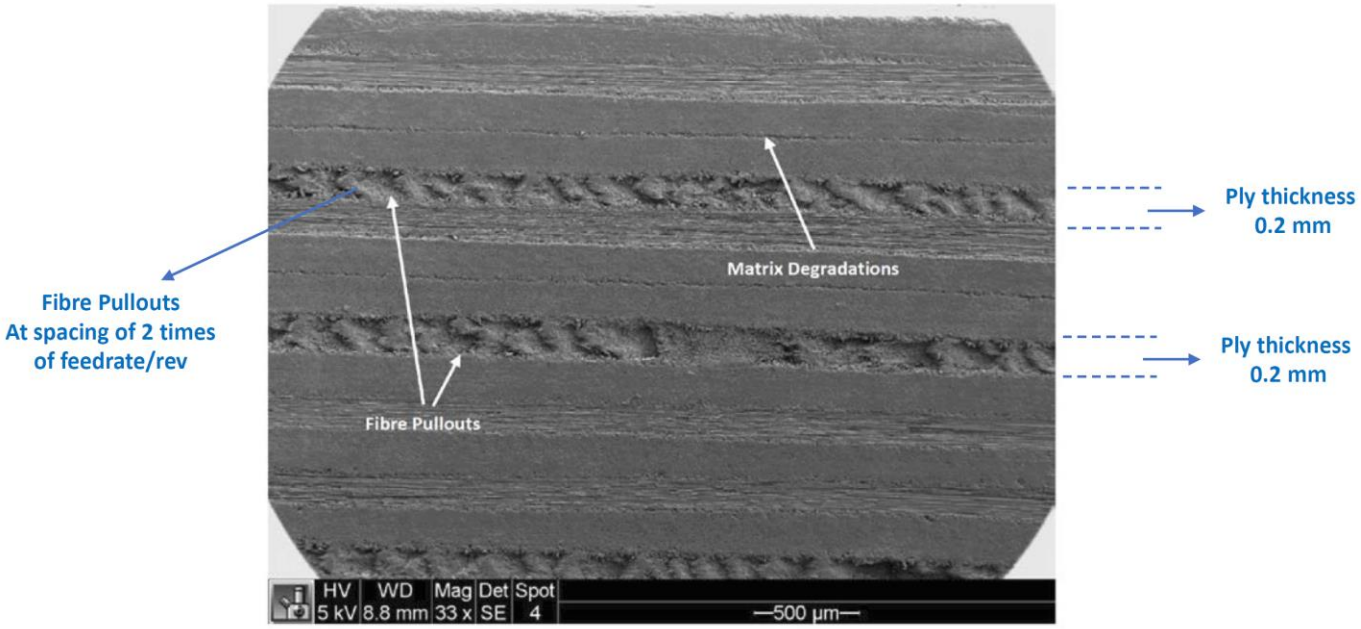

Figure 6.10 SEM of CVD Endmill Trimmed Edge Surface

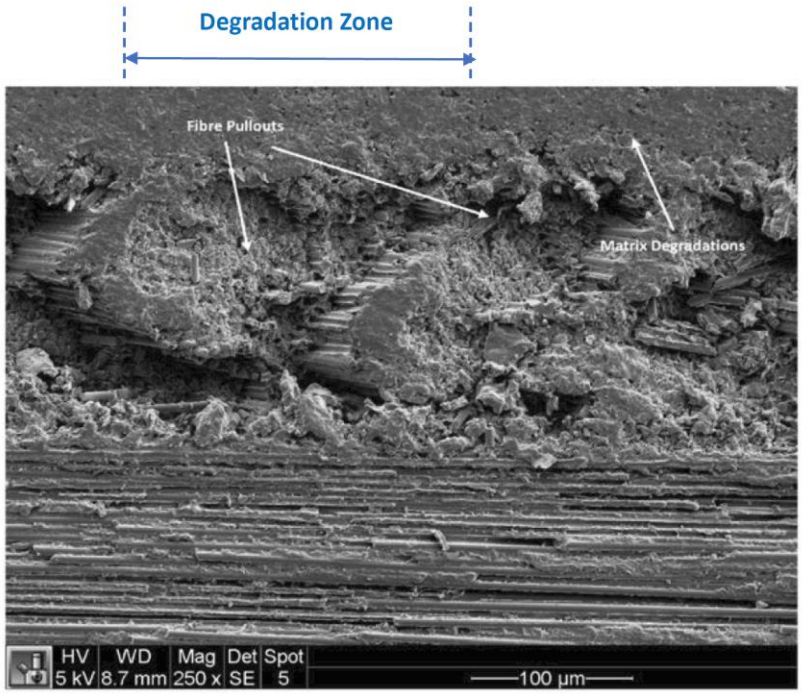

Figure 6.11 SEM of CVD Endmill Trimmed Edge Surface

The following features of surface roughness were observed After CVD Endmill Edge Trimming

- Smooth surface obtained compared to AWJ processes but rougher than PCD Endmill Trimming
- Cutting edges coated with diamond coating which is poly crystalline with large number of sharp cutting edges resulting in smoother surface

The following damage was observed after CVD Endmill Edge Trimming

- Fibre pullouts are present, higher in density in comparison to AWJ and PCD Endmill trimmed specimens
- Higher Fibre Pullouts density is attributed to the contact angle between the 18-degree helix 4 flutes and the -45 degree plies. Also contributing to this high density are the multi facet sharp edges of a CVD diamond coating. The frequency/spacing of the pullouts I greater than 2 times the feedrate/rev.
- Fibre pullouts are predominant along the 45 degree plies
- Exit (bottom edge) delamination are present while there is some occurrence of entrance delamination
- Matrix cracks also present in the CVD trimmed edge surface

6.3.2 Drilled Holes – CVD Diamond Coated Vs. Polycrystalline (PCD) Diamond Drills

Surface roughness parameters were recorded for holes drilled with CVD Diamond Coated and PCD drills. Table 6.4 shows the surface roughness comparisons between holes drilled by PCD and CVD drills.

Specimen Type	Average Surface Finish - R_a (µm)	Surface Finish – R_z (µm)	Surface Finish – R_t (µm)
PCD Drill – F1	0.445	2.91	6.15
PCD Drill – F2	0.342	2.81	5.365
CVD Drill – F1	0.965	5.632	11.597
CVD Drill – F2	0.890	5.172	11.38

Table 6.4 Surface Roughness (longitudinal) of PCD vs CVD Drilled Holes

Surface roughness parameters were recorded for both the PCD and CVD drilled hole surfaces. The readings were taken along the thickness of the hole. The surface roughness for the PCD drilled holes was a lower value (R_a) compared to the CVD drilled holes.

The drilling parameters used are as follows for both the PCD and CVD drills:

Spindle Speed = 6000 RPM

Cutting Speed = 1.9 m/s

Feed Rate = F1 = 305 mm/min and F2 =508 mm/min

Sample surface profile readings obtained from the hole surfaces on the PCD and the CVD Drilled holes are shown in Figures 6.12 to 6.15. The difference in the helix angles (24 deg for PCD and 30 deg for CVD) along with coating differences (polished for PCD while multi-faceted non polished for CVD) resulted in higher fibre pullout for CVD drilled holes.

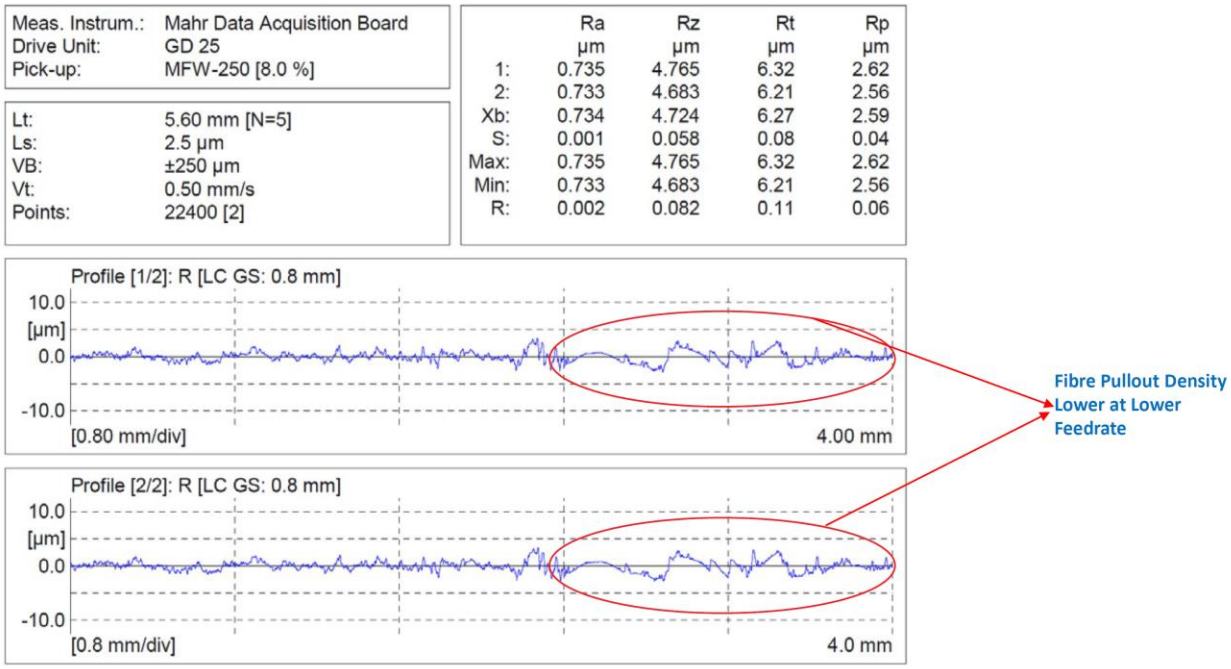

Figure 6.12 Surface Roughness of PCD Drilled Hole (Feedrate 305 mm/min, longitudinal)

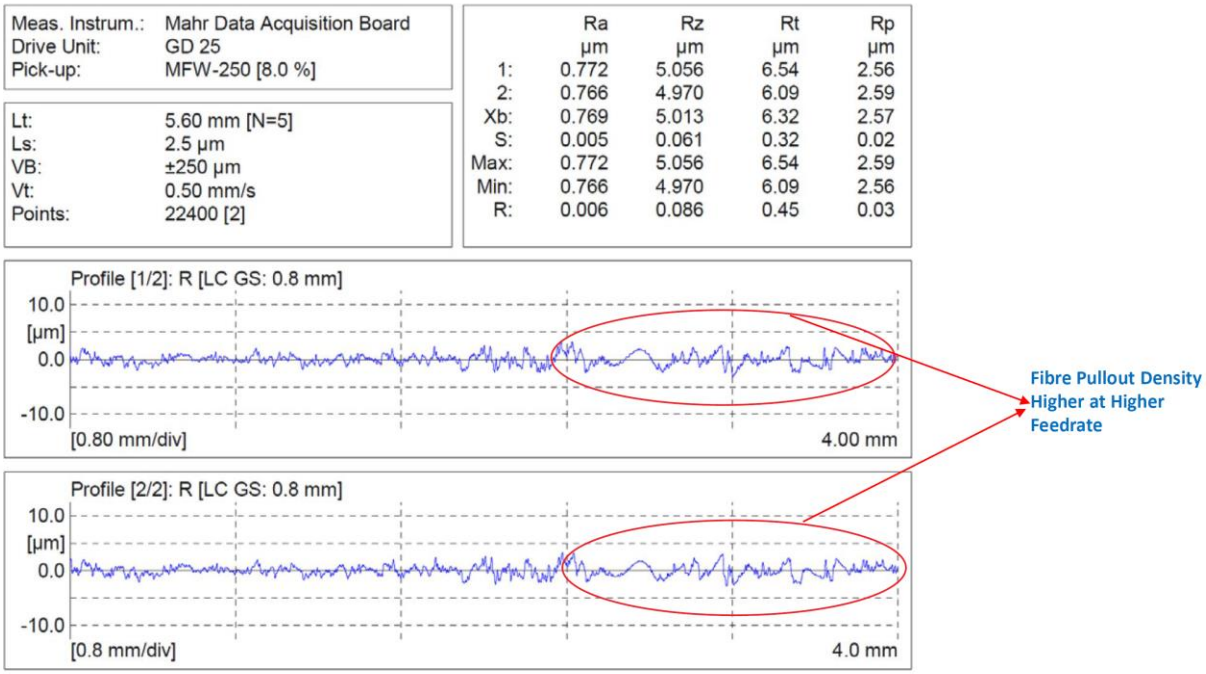

Figure 6.13 Surface Roughness of PCD Drilled Hole (Feedrate 508 mm/min, Longitudinal)

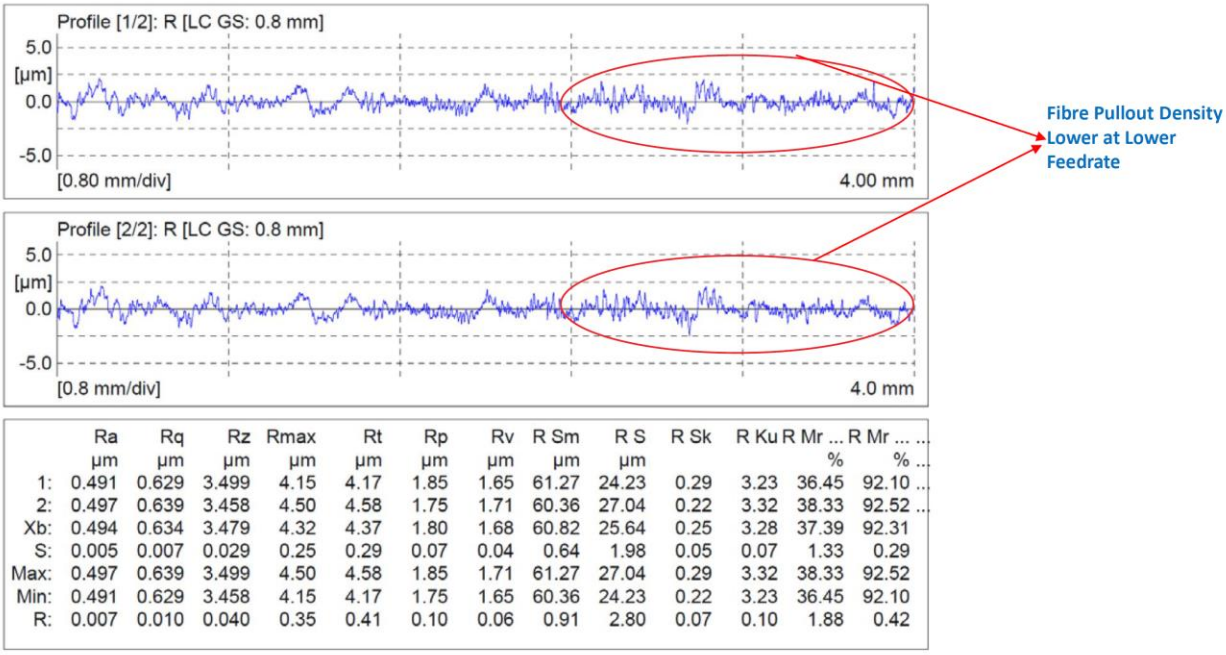

	Ra µm	Rq µm	Rz µm	Rmax µm	Rt µm	Rp µm	Rv µm	R Sm µm	R S µm	R Sk	R Ku	R Mr ... %	R Mr ... % ...
1:	0.491	0.629	3.499	4.15	4.17	1.85	1.65	61.27	24.23	0.29	3.23	36.45	92.10 ...
2:	0.497	0.639	3.458	4.50	4.58	1.75	1.71	60.36	27.04	0.22	3.32	38.33	92.52 ...
Xb:	0.494	0.634	3.479	4.32	4.37	1.80	1.68	60.82	25.64	0.25	3.28	37.39	92.31
S:	0.005	0.007	0.029	0.25	0.29	0.07	0.04	0.64	1.98	0.05	0.07	1.33	0.29
Max:	0.497	0.639	3.499	4.50	4.58	1.85	1.71	61.27	27.04	0.29	3.32	38.33	92.52
Min:	0.491	0.629	3.458	4.15	4.17	1.75	1.65	60.36	24.23	0.22	3.23	36.45	92.10
R:	0.007	0.010	0.040	0.35	0.41	0.10	0.06	0.91	2.80	0.07	0.10	1.88	0.42

Figure 6.14 Surface Roughness of CVD Drilled Hole (Feedrate 305 mm/min, Longitudinal)

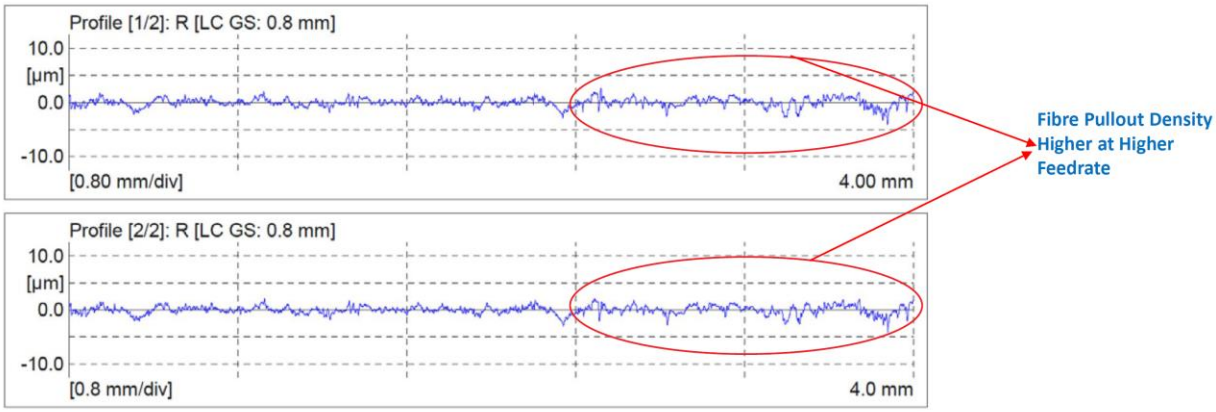

	Ra µm	Rq µm	Rz µm	Rmax µm	Rt µm	Rp µm	Rv µm	R Sm µm	R S µm	R Sk	R Ku	R Mr ... %	R Mr ... % ...
1:	0.591	0.783	4.699	5.99	6.83	1.98	2.72	74.53	35.34	-0.59	4.30	38.20	86.73 ...
2:	0.583	0.767	4.676	6.14	6.30	1.90	2.77	62.97	33.44	-0.58	4.16	40.24	87.78 ...
Xb:	0.587	0.775	4.687	6.07	6.56	1.94	2.75	68.75	34.39	-0.58	4.23	39.22	87.26
S:	0.006	0.011	0.016	0.10	0.38	0.05	0.04	8.17	1.35	0.01	0.10	1.44	0.74
Max:	0.591	0.783	4.699	6.14	6.83	1.98	2.77	74.53	35.34	-0.58	4.30	40.24	87.78
Min:	0.583	0.767	4.676	5.99	6.30	1.90	2.72	62.97	33.44	-0.59	4.16	38.20	86.73
R:	0.008	0.016	0.023	0.15	0.54	0.07	0.05	11.56	1.90	0.01	0.14	2.03	1.05

Figure 6.15 Surface Roughness of CVD Drilled Hole (Feedrate 508 mm/min, Longitudinal)

Following Figures 6.16 and 6.17 show SEMs of PCD drilled holes drilled at the 2 different feedrates.

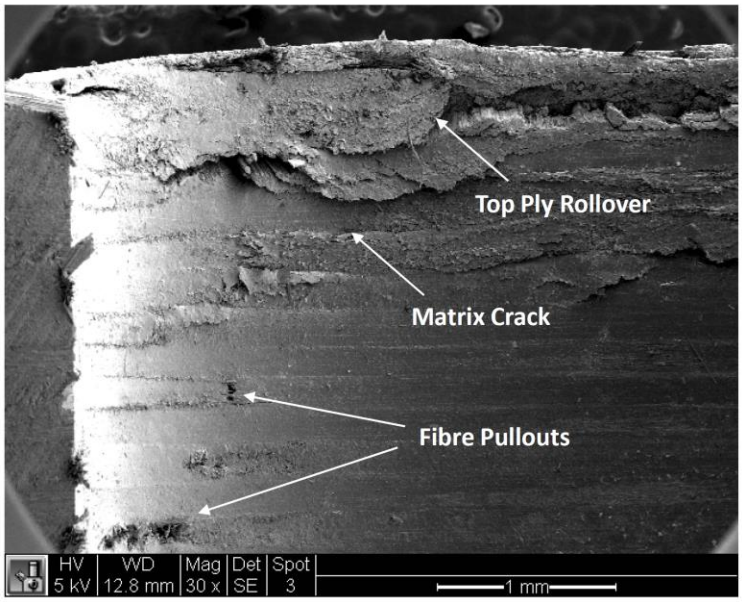

Figure 6.16 SEM showing damage during PCD Drilling at Feedrate = 305 mm/min

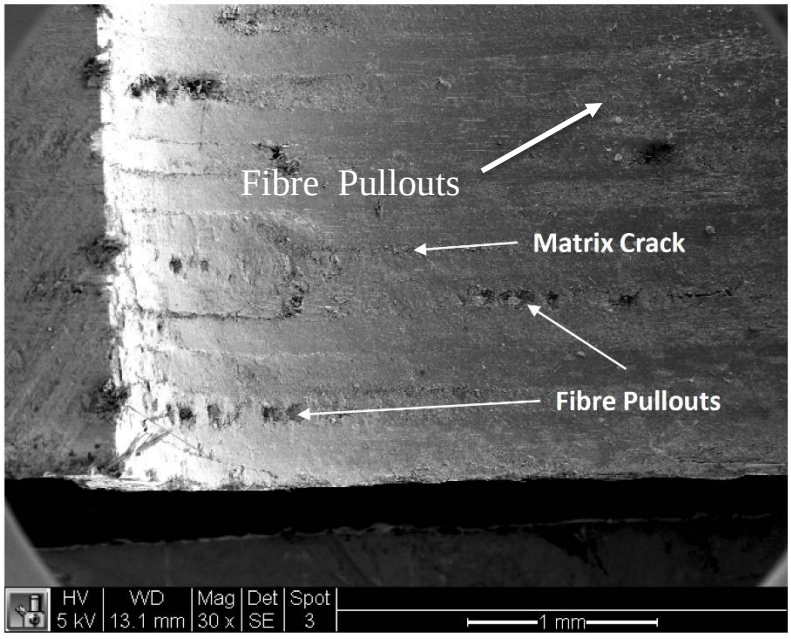

Figure 6.17 SEM showing damage during PCD Drilling at Feedrate = 508 mm/min

The following damage was observed after PCD Hole Drilling at 305 mm/min

- Top ply rolled over the hole surface along with delamination
- Delamination observed along the bottom edge of the hole surface
- Matrix Cracks are consistent in occurrence and independent of orientation of fibres

- Fibre Pullouts are present but lower in density
- Fibre Pullouts are predominant in the – 45 degree plies
- Separation of plies was also observed through the thickness of the laminate

The following damage was observed after PCD Hole Drilling at 508 mm/min

- Top ply rolled over the hole surface along with delamination
- Delamination observed along the bottom edge of the hole surface
- Matrix Cracks are consistent in occurrence and independent of orientation of fibres
- Fibre Pullouts are present and density is higher due to higher feedrate
- Fibre Pullouts are predominant in the – 45 degree plies
- Separation of plies was also observed through the thickness of the laminate

Following Figures 6.18 through 6.21 show SEMs of CVD drilled holes at 2 different feedrates

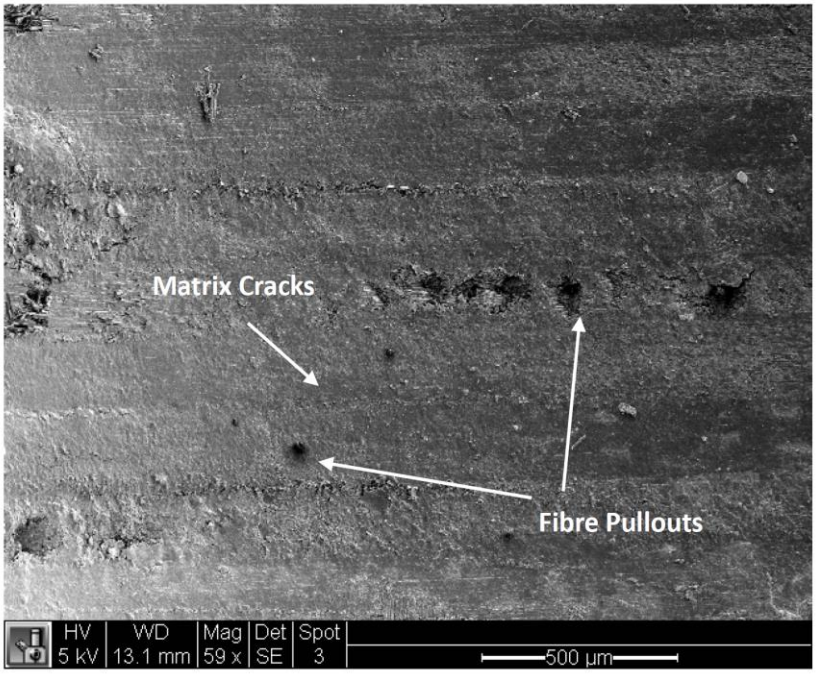

Figure 6.18 SEM showing damage during CVD Drilling at Feedrate = 305 mm/min

Figure 6.19 SEM showing damage during CVD Drilling at Feedrate = 305 mm/min

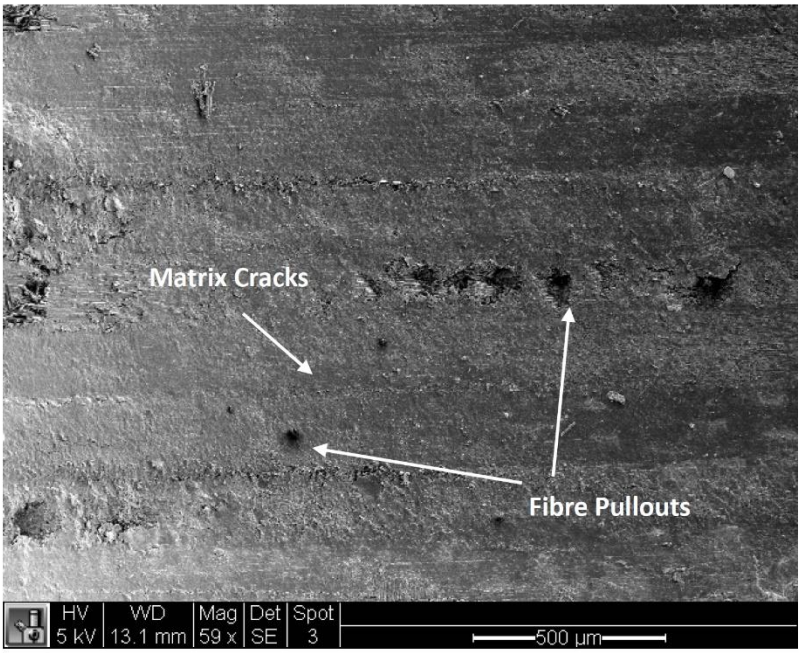

Figure 6.20 SEM showing damage during CVD Drilling at Feedrate = 508 mm/min

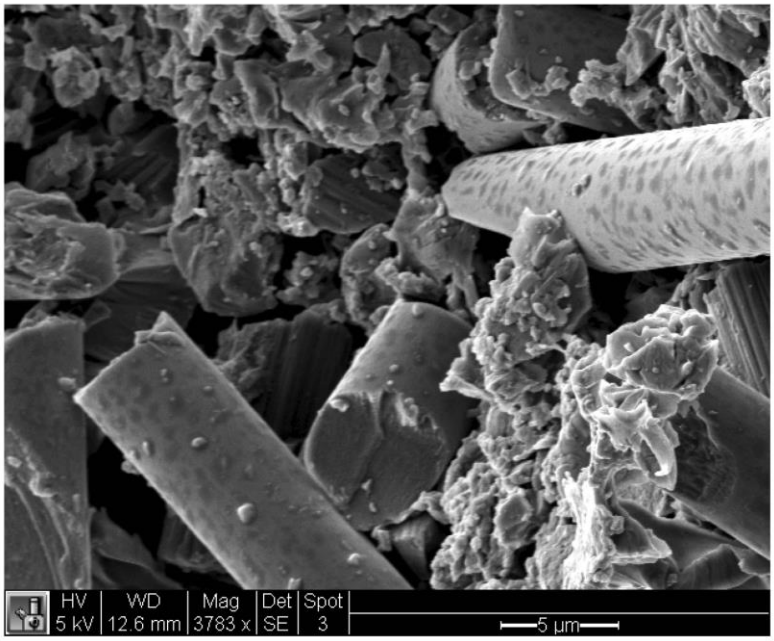

Figure 6.21 SEM showing damage during CVD Drilling at Feedrate = 508 mm/min

The following damage was observed after CVD Hole Drilling at 305 mm/min

- Delamination observed along the bottom edge of the hole surface
- Matrix Cracks are consistent in occurrence and independent of orientation of fibres
- Fibre Pullouts are present and higher in density compared to PCD drilled holes
- Fibre Pullouts are predominant in the – 45 degree plies
- Separation of plies was also observed through the thickness of the laminate

The following damage was observed After CVD Hole Drilling at 508 mm/min

- Delamination observed along the bottom edge of the hole surface
- Matrix Cracks are consistent in occurrence and independent of orientation of fibres
- Fibre Pullouts are present and density is higher due to higher feedrate
- Fibre Pullouts are predominant in the – 45 degree plies
- Separation of plies was also observed through the thickness of the laminate

6.4 Mechanical Testing

6.4.1 Theoretical Strength Calculations

The laminator software was used to calculate the effective laminate strength based on the material strengths and the ply make up. The software returned the following theoretical Apparent Laminate Stiffness Properties:

Apparent Modulus in X direction, $E_x = 78.46$ GPa

Apparent Modulus in Y direction, $E_y = 55.97$ GPa

Apparent Shear Modulus, $G_{xy} = 16.56$ GPa

6.4.2 Specimen Preparation

6.4.2.1 Tensile Strength Specimens

Specimens were prepared and tested per ASTM D3039/D3039M for standard test method for tensile properties of Polymer Matrix Composite Materials. The specimens were prepared per the standard and aluminium tabs were adhesively bonded on the ends using an epoxy adhesive. Both machined specimens using cutters and AWJ trimmed specimens were prepared and tested per the tensile properties test standard.

6.4.2.2 Compression Strength Specimens

Specimens were prepared and tested per ASTM D3410/D3410M for standard test method for compressive properties of Polymer Matrix Composite Materials. The specimens were prepared per the standard and aluminium tabs were adhesively bonded on the ends using an epoxy adhesive. Both machined specimens using cutters and AWJ trimmed specimens were prepared and tested per the compressive properties test standard.

6.4.2.3 Open Hole Tensile Strength Specimens

Specimens were prepared and tested per ASTM D5766/D5766M for standard test method for Open-Hole Tensile Strength of Polymer Matrix Composite Laminates. The specimens were prepared per the standard and aluminium tabs were adhesively bonded on the ends using an epoxy adhesive. Both machined specimens using cutters and AWJ trimmed specimens were prepared by

drilling holes using PCD and CVD drills and tested per the Open-Hole Tensile Strength Test Standard.

6.4.2.4 Open Hole Compression Strength Specimens

Specimens were prepared and tested per ASTM D6484/D6484M for standard test method for Open-Hole Compression Strength of Polymer Matrix Composite Laminates. The specimens were prepared per the standard and aluminium tabs were adhesively bonded on the ends using an epoxy adhesive. Both machined specimens using cutters and AWJ trimmed specimens were prepared by drilling holes using PCD and CVD drills and tested per the Open-Hole Compression Strength Test Standard.

6.4.2.5 Bearing Strength Specimens

Specimens were prepared and tested per ASTM D5961/D5961M for standard test method for Bearing Strength of Polymer Matrix Composite Laminates. The specimens were prepared per the standard and aluminium tabs were adhesively bonded on the ends using an epoxy adhesive. Both machined specimens using cutters and AWJ trimmed specimens were prepared by drilling holes using PCD and CVD drills and tested per the Bearing Strength Test Standard.

6.4.3 Tensile Strength Testing

Both endmill trimmed and AWJ specimens were mechanically tested in tension and the results tabulated. Strain gauges were used to capture the strain under tension loading conditions. All the specimens were taken to failure during the testing process.

The test matrix with surface roughness data for the test specimens is shown in table 6.5

The following tables and figures show the data along with the stress-strain curves and failure for both the endmill and AWJ trimmed specimens

Specimen Name	Trim	Surface Finish (L) - R_a	Surface Finish (L) - R_z	Surface Finish (L) - R_t	Surface Finish (L) - R_{sk}	Surface Finish (L) - R_{ku}
Tension Specimens						
AWJ 80 Trim						
Specimen 1	AWJ -80	3.728	24.464	27.63	-	-
Specimen 2	AWJ -80	4.612	25.258	31.42	-	-
Specimen 3	AWJ -80	3.262	17.062	24.1	-	-
AWJ 120 Trim						
Specimen 1	AWJ - 120	2.915	20.411	24.000	-	-
Specimen 2	AWJ - 120	3.557	19.299	24.52	-	-
Specimen 3	AWJ -120	3.475	21.426	31.29	-	-
Specimen 4	AWJ - 120	3.742	21.71	27.27	-	-
PCD Endmill Trim						
Specimen 1	PCD Endmill	0.664	4.722	7.23	-	-
Specimen 2	PCD Endmill	0.826	5.632	7.31	-	-
Specimen 3	PCD Endmill	0.5	4.077	5.66	-	-
Specimen 4	PCD Endmill	0.524	4.141	6.09	-	-
CVD Endmill Trim						
Specimen 1	CVD Endmill	1.189	8.05	10.79	0.54	3.97
Specimen 2	CVD Endmill	1.251	7.569	9.96	0.000	3.28
Specimen 3	CVD Endmill	1.636	9.319	10.75	-0.02	2.34
Compression Specimens						
AWJ 80 Trim						
Specimen 1	AWJ -80	3.416	22.074	27.8	-	-
Specimen 2	AWJ -80	2.891	16.155	20.58	-	-
CVD Endmill Trim						
Specimen 1	CVD Endmill	1.065	5.713	7.28	-	-
Specimen 2	CVD Endmill	0.695	4.391	5.56	-	-
Specimen 3	CVD Endmill	0.455	3.305	4.42	-	-

Table 6.5 Summary of surface finish recordings (longitudinal) of edge trimmed specimens for tension testing

Tensile Testing of AWJ (80 Grit) Edge Trimmed Specimens

Edge trimmed specimens machined with AWJ (80 Grit) were tested in tension to failure. Figures 6.22 6.23, & 6.24 show the data plots from the testing.

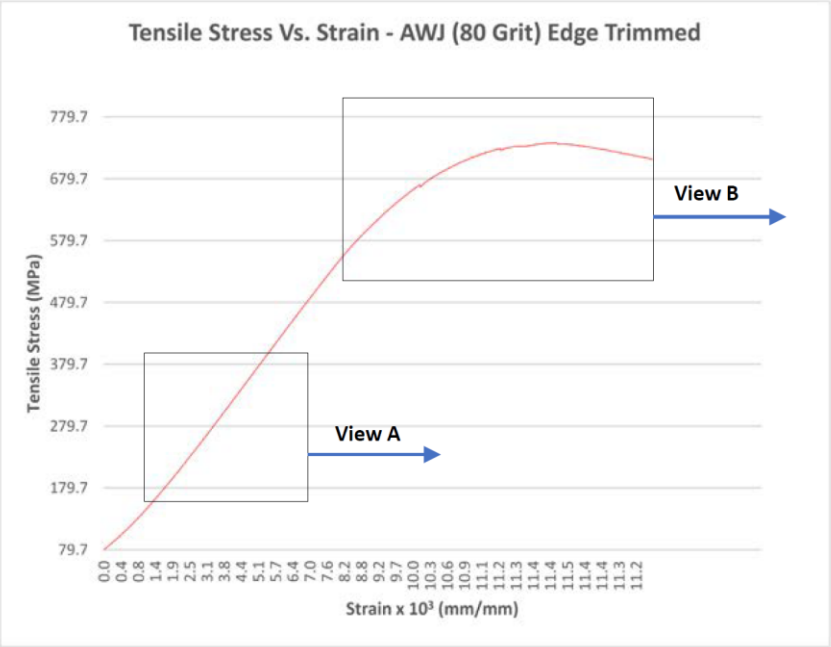

Figure 6.22 Tensile Stress Vs. Strain for AWJ (80 Grit) edge trimmed specimen

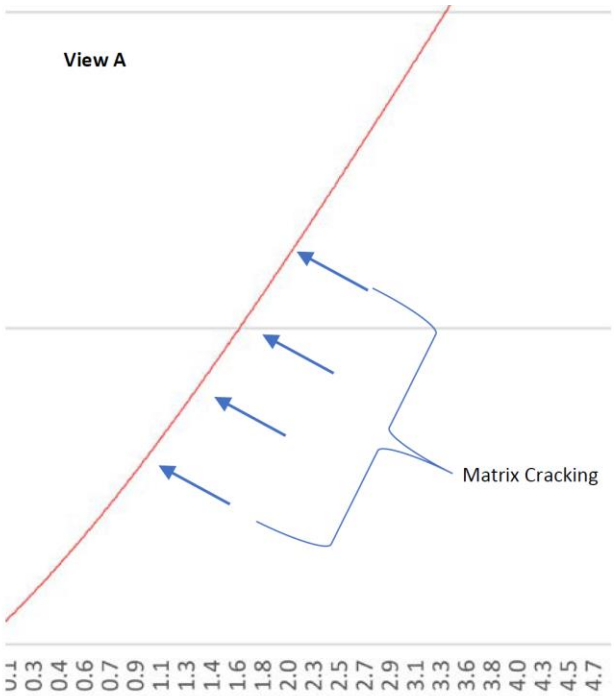

Figure 6.23 Magnified view of Tensile Stress Vs. Strain showing matrix cracking in AWJ (80 Grit) edge trimmed specimen

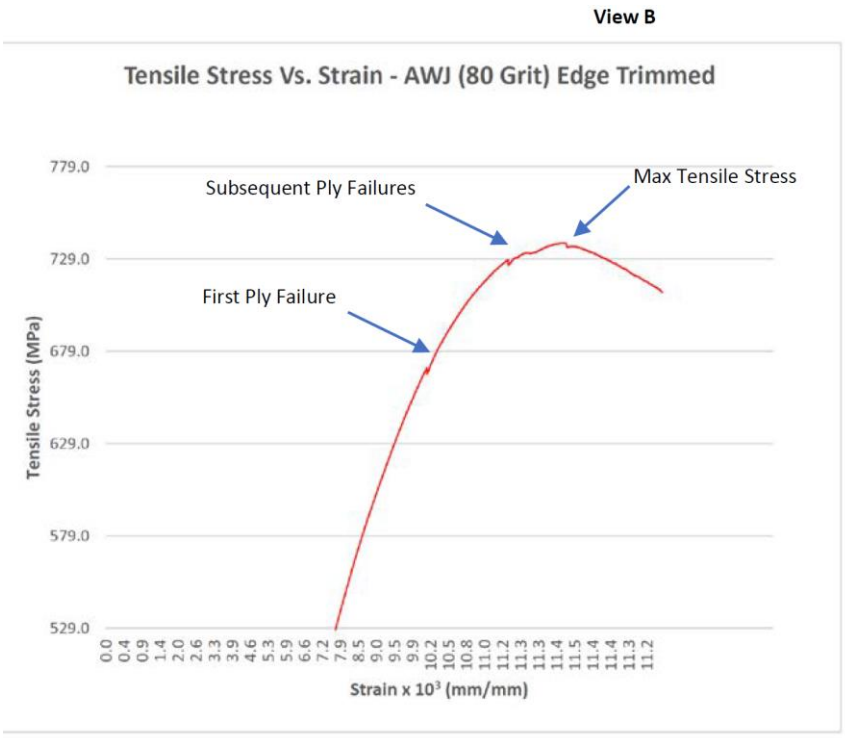

Figure 6.24 Magnified view of Tensile Stress Vs. Strain showing first ply failure and damage for AWJ (80 Grit) edge trimmed specimen

Test Data & Observations from tensile strength testing of AWJ (80 Grit) edge trimmed specimens

The following strength data was recoded from the tensile testing:
Maximum Tensile Stress = 737.5 MPa
Maximum Tensile Load = 84668 N
Strain at Maximum Tensile Stress = 0.011429 mm/mm
Youngs Modulus from Testing = 64.5 GPa

It was observed that matrix cracking started around 0.31% strain. Matrix cracking progress to 0.6% strain. First ply failure occurred around tensile stress of 668.7 MPa. Frist ply failure was around 1.01% strain. The subsequent failure zone contained ply failures (delamination) along with additional matrix cracking.

Damage observations from tensile strength testing of AWJ (80 Grit) edge trimmed specimens

Figures 6.25, 6.26, 6.37 & 6.28 show the damage recorded in the tensile strength testing of AWJ (80 Grit) edge trimmed specimens

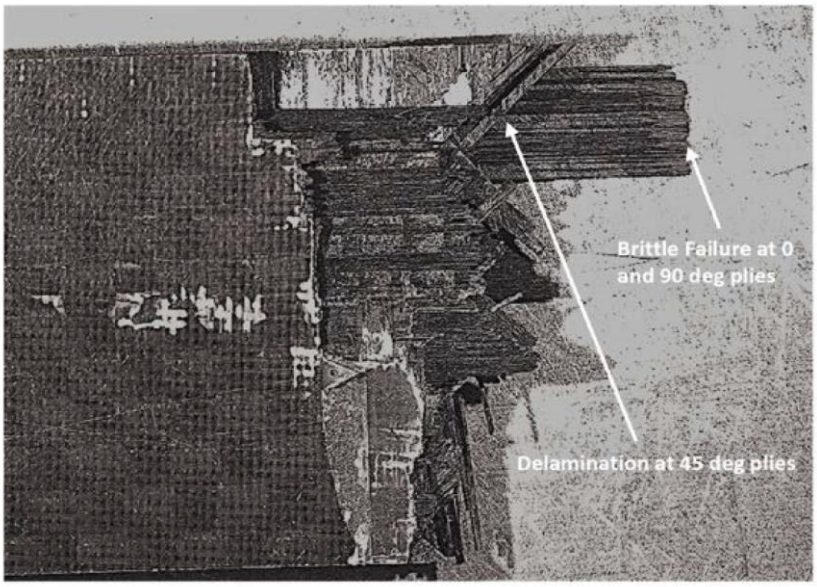

Figure 6.25 Failed specimen from Tensile testing of AWJ (80 Grit) edge trimmed specimen

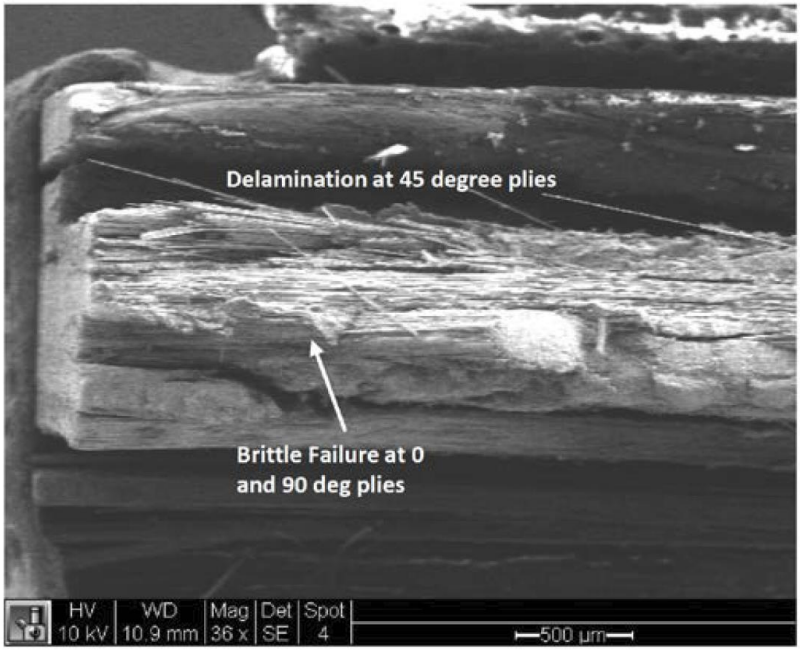

Figure 6.26 SEM of failed specimen from tensile testing of AWJ (80 Grit) edge trimmed specimen

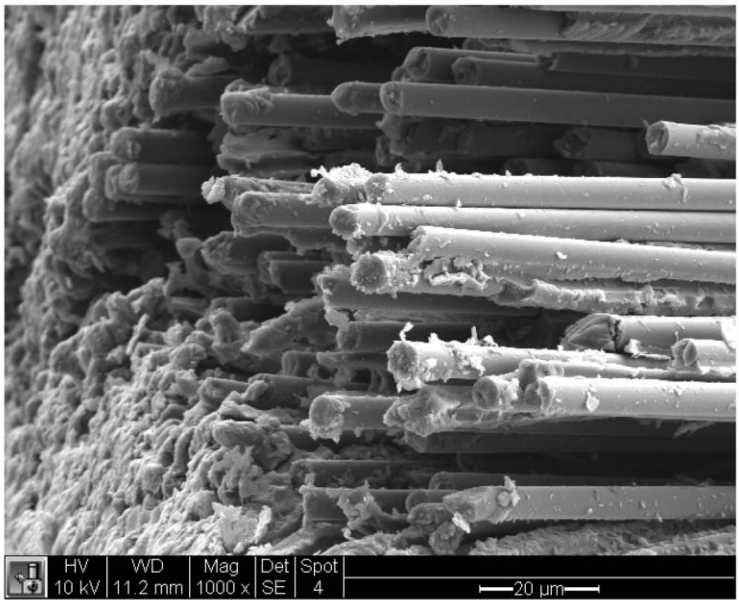

Figure 6.27 SEM showing brittle fracture of 90 degree fibres from tensile testing of AWJ (80 Grit) edge trimmed specimen

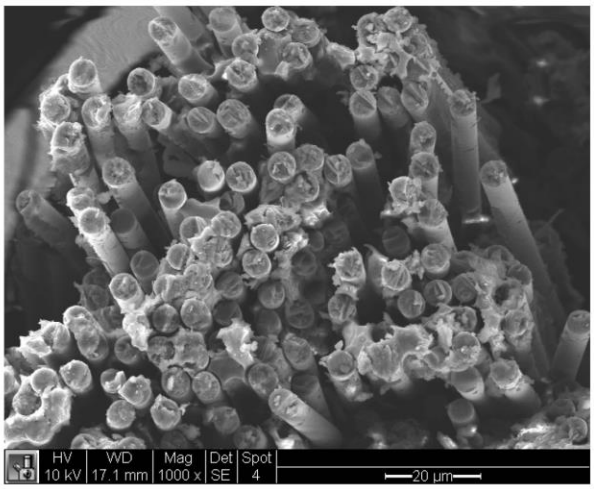

Figure 6.28 SEM showing brittle fracture of 0 degree fibres from tensile testing of AWJ (80 Grit) edge trimmed specimen

From the damage recorded it was observed that brittle fracture is the predominant failure mode in the 0 and 90 degree plies. In the 45 degree plies, delamination is the primary failure mode. It

was observed that matrix cracking precedes ply failure and delamination. Fibre-matrix debonding was seen in the SEMs showing brittle fracture of fibres.

Tensile Testing of AWJ (120 Grit) Edge Trimmed Specimens

Edge trimmed specimens machined with AWJ (120Grit) were tested in tension to failure. Figures 6.29, 6.30, & 6.31 show the data plots from the testing.

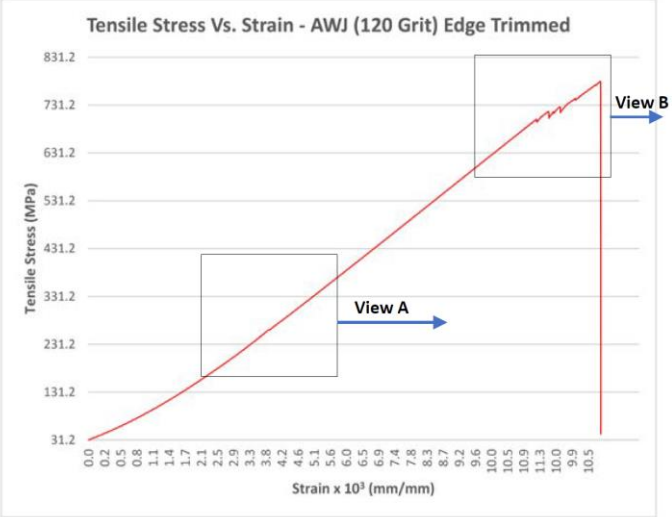

Figure 6.29 Tensile Stress Vs. Strain for AWJ (120 Grit) edge trimmed specimen

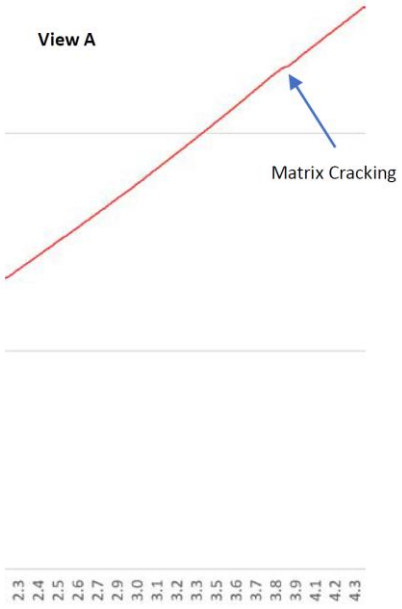

Figure 6.30 Magnified view of Tensile Stress Vs. Strain showing matrix cracking in AWJ (120 Grit) edge trimmed specimen

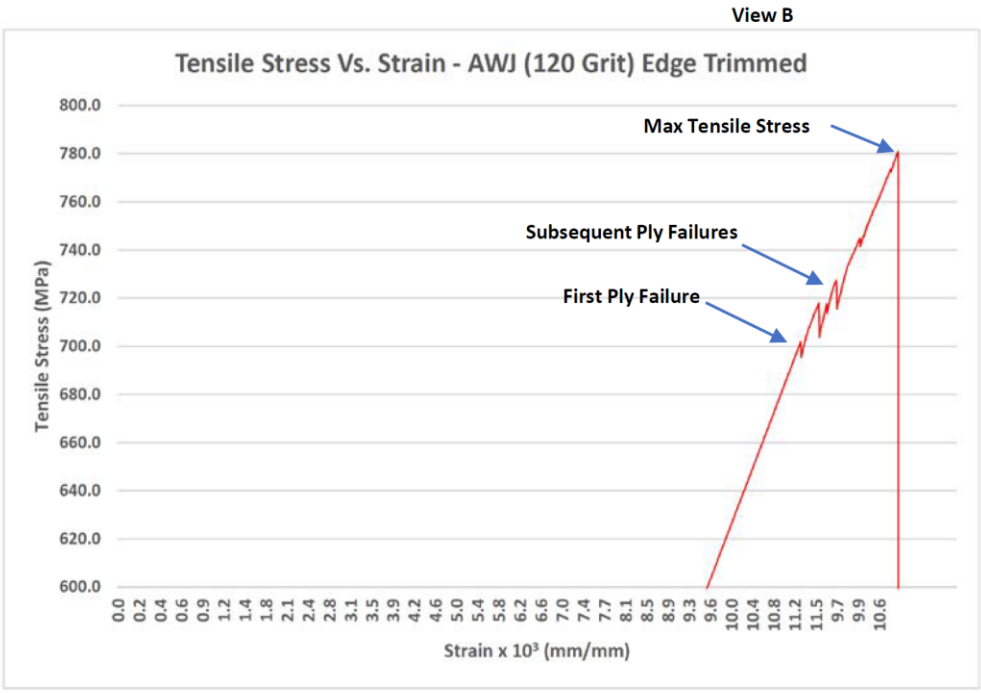

Figure 6.31 Magnified view of Tensile Stress Vs. Strain showing first ply failure and damage for AWJ (120 Grit) edge trimmed specimen

Test Data & Observations from tensile strength testing of AWJ (120 Grit) edge trimmed specimens

The following strength data was recoded from the tensile testing:
Maximum Tensile Stress = 781.0 MPa
Maximum Tensile Load = 89685 N
Strain at Maximum Tensile Stress = 0.010688 mm/mm
Youngs Modulus from Testing = 71.8 GPa

It was observed that matrix cracking started around 0.39% strain. Matrix cracking progress to 0.6% strain. First ply failure occurred around tensile stress of 701.3 MPa. Frist ply failure was around 1.13% strain. The subsequent failure zone contained ply failures (delamination) along with additional matrix cracking.

Damage observations from tensile strength testing of AWJ (120 Grit) edge trimmed specimens

Figures 6.32, 6.33 & 6.34 show the damage recorded in the tensile strength testing of AWJ (120 Grit) edge trimmed specimens

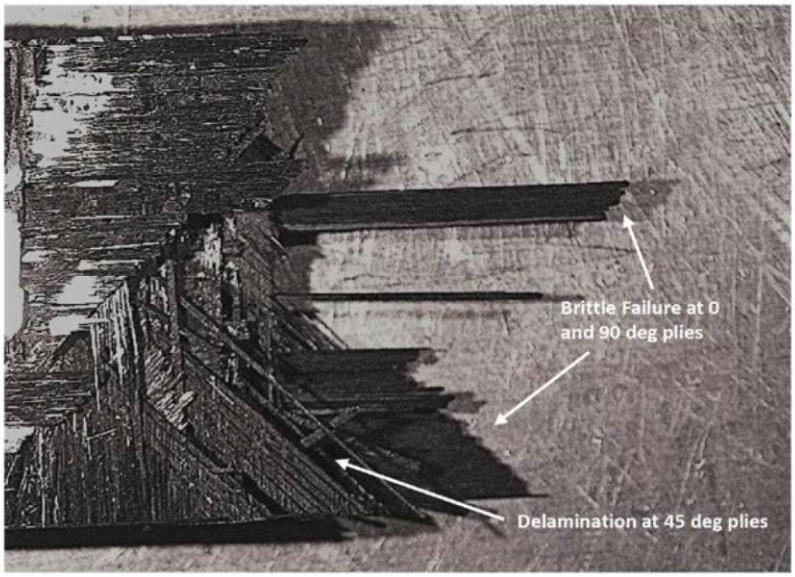

Figure 6.32 Failed specimen from Tensile testing of AWJ (120 Grit) edge trimmed specimen

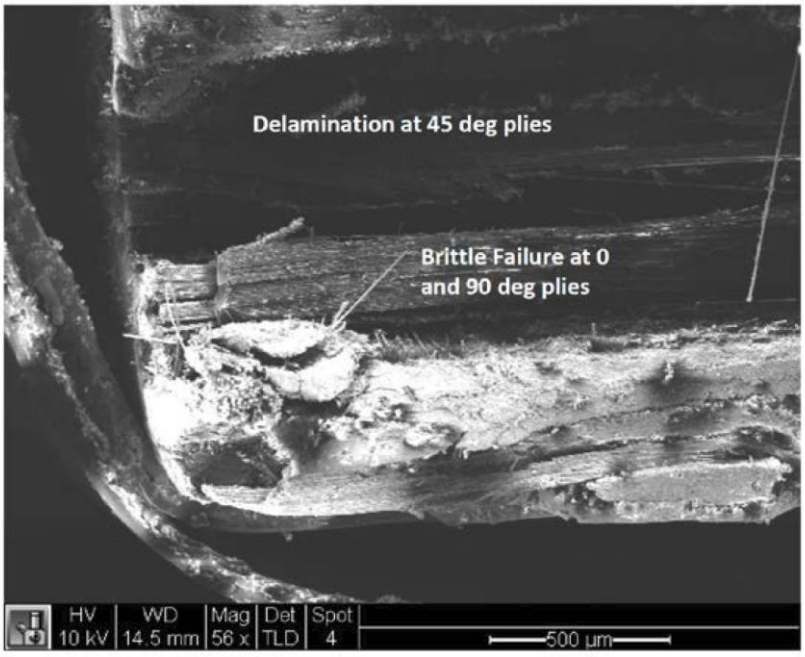

Figure 6.33 SEM of failed specimen from tensile testing of AWJ (120 Grit) edge trimmed specimen

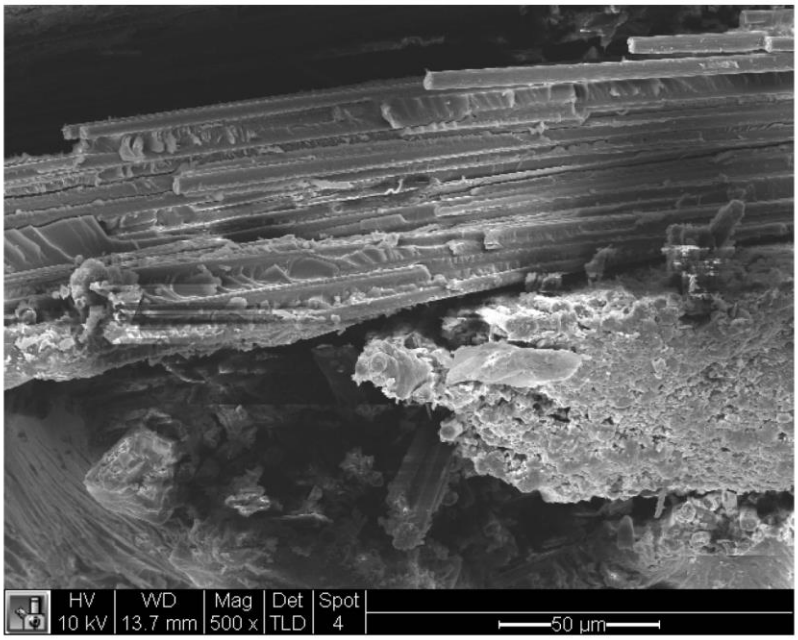

Figure 6.34 SEM showing brittle fracture of 0 and 90 degree fibres from tensile testing of AWJ (120 Grit) edge trimmed specimen

From the damage recorded it was observed that brittle fracture is the predominant failure mode in the 0 and 90 degree plies. In the 45 degree plies, delamination is the primary failure mode. It was observed that matrix cracking precedes ply failure and delamination. Fibre-matrix debonding was seen in the SEMs showing brittle fracture of fibres.

Observations on AWJ (80 Grit) Vs. AWJ (120 Grit) edge trimmed Tensile testing

It was observed that the AWJ)80 Grit) specimens had a higher load for the same magnitude of strain compared to AWJ (120 Grit) specimens. Failure in AWJ (120 Grit) specimens occurred at a higher tensile stress compared to AWJ (80 Grit) specimens. The AWJ (80 Grit) specimens displayed a higher level of damage in comparison to the AWJ (120 Grit) specimens. Fibre-matrix debonding was seen in the SEMs showing the brittle fracture in fibres. As erosion is the mechanism of cutting in AWJ edge trimming processes, the 120 grit process produces damage such as matrix cracking at lower loads but the progress of damage is slower than the 80 grit specimens resulting in lower overall damage as well as failure at higher load. Figure 6.35 shows

the comparative Tensile Stress Vs. Strain plots for the AWJ (80 Grit) and AWJ (120 Grit) edge trimmed specimens.

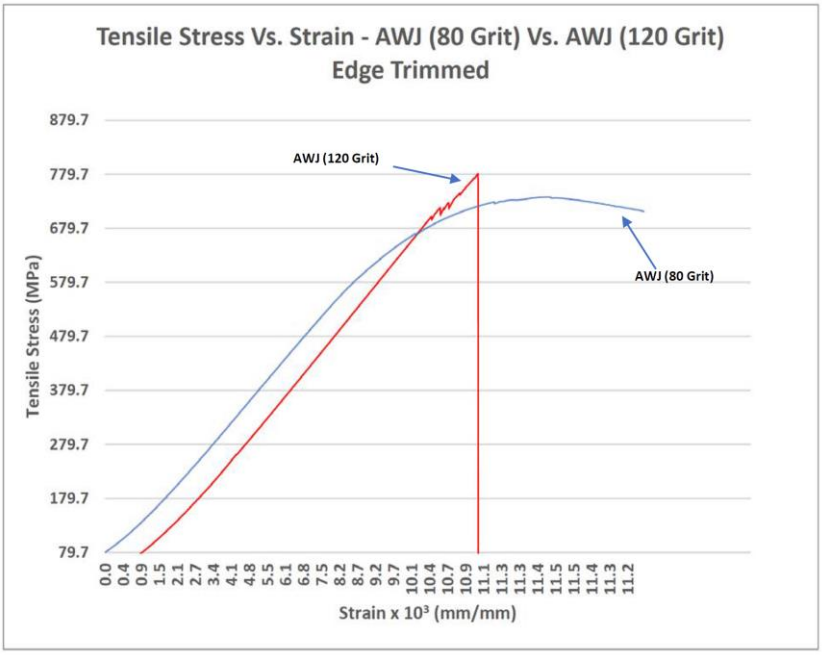

Figure 6.35 Comparative Plot of Tensile Stress Vs. Strain for Tensile Testing of AWJ (80 Grit) Vs. AWJ (120 Grit) edge trimmed specimens

Tensile Testing of PCD Endmill Edge Trimmed Specimens

Edge trimmed specimens machined with PCD Endmill were tested in tension to failure. Figures 6.36, 6.37 & 6.38 show the data plots from the testing.

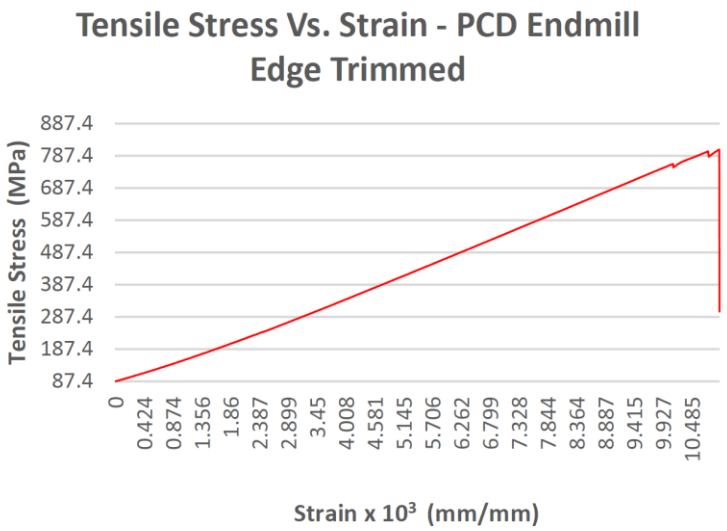

Figure 6.36 Tensile Stress Vs. Strain for PCD endmill edge trimmed specimen

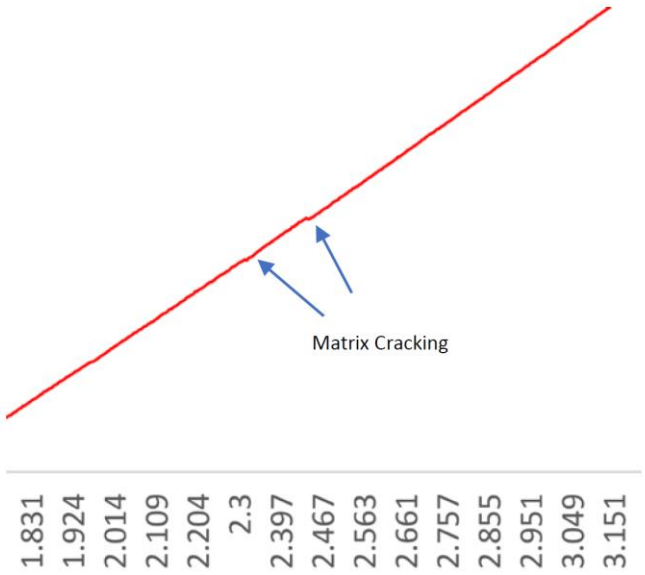

Figure 6.37 Magnified view of Tensile Stress Vs. Strain showing matrix cracking in PCD endmill edge trimmed specimen

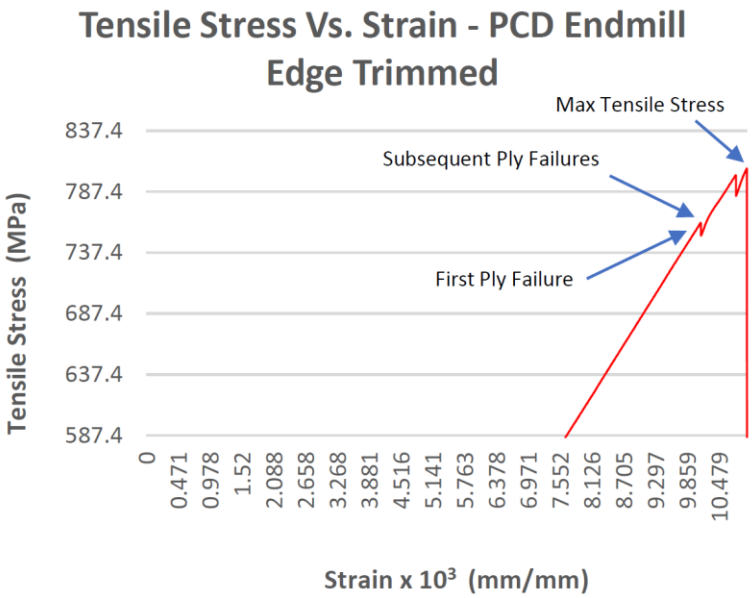

Figure 6.38 Magnified view of Tensile Stress Vs. Strain showing first ply failure and damage for PCD endmill edge trimmed specimen

Test Data & Observations from tensile strength testing PCD endmill edge trimmed specimens

The following strength data was recoded from the tensile testing:

Maximum Tensile Stress = 806.5 MPa

Maximum Tensile Load = 92594 N

Strain at Maximum Tensile Stress = 0.011157 mm/mm

Youngs Modulus from Testing = 72.3 GPa

It was observed that matrix cracking started around 0.25% strain. The magnitude of matrix cracking was found to be lower than that in AWJ trimming. First ply failure occurred around tensile stress of 759.5 MPa. Frist ply failure was around 1.01% strain. The subsequent failure zone with ply failures (delamination)was smaller before ultimate failure pointing to lower damage tolerance.

Damage observations from tensile strength testing of PCD endmill edge trimmed specimens

Figures 6.39, 6.40 & 6.41 show the damage recorded in the tensile strength testing of PCD endmill edge trimmed specimens

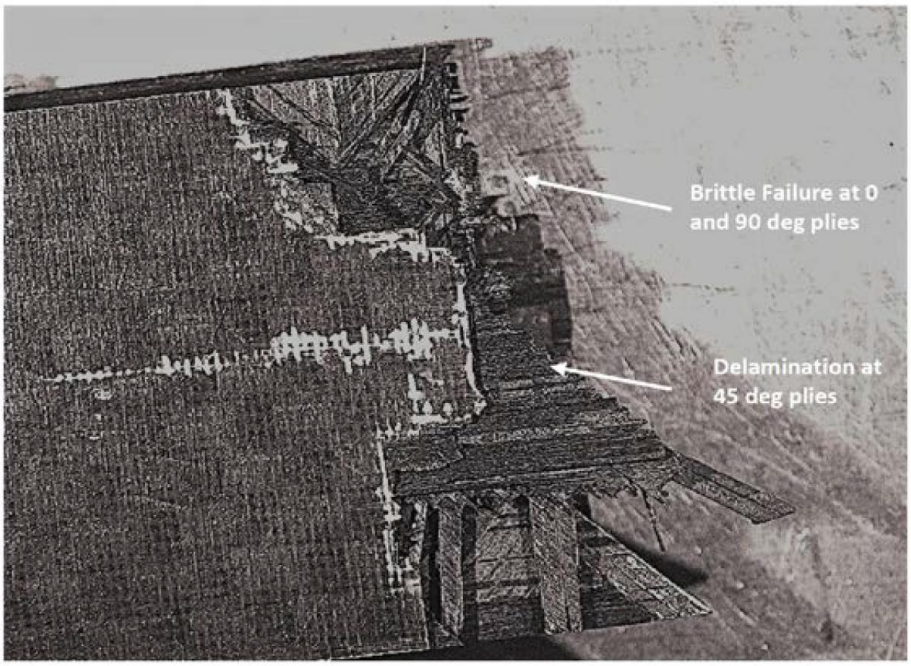

Figure 6.39 Failed specimen from Tensile testing of PCD endmill edge trimmed specimen

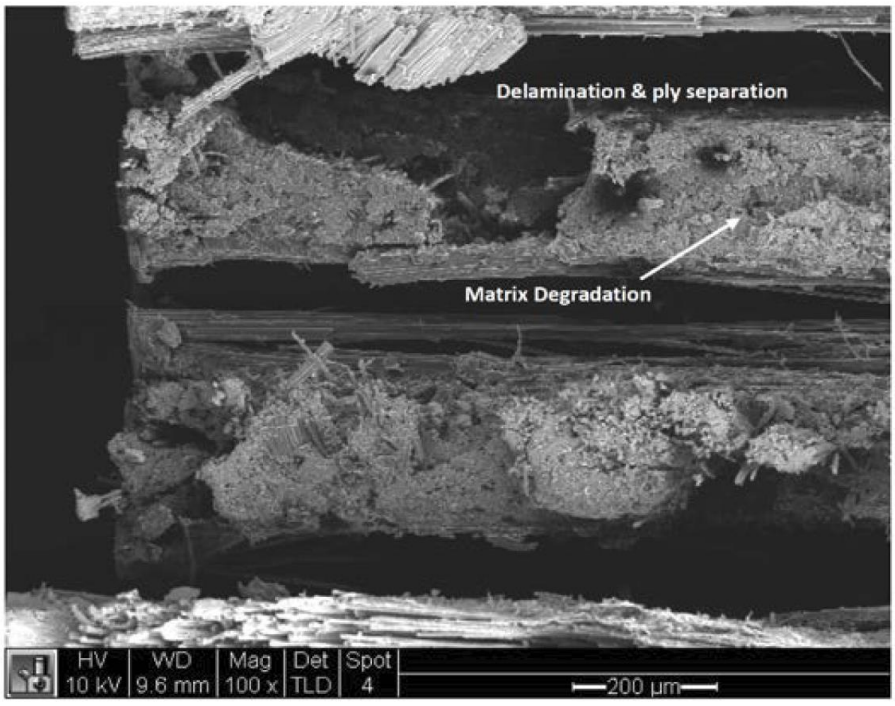

Figure 6.40 SEM of failed specimen from tensile testing of PCD endmill edge trimmed specimen

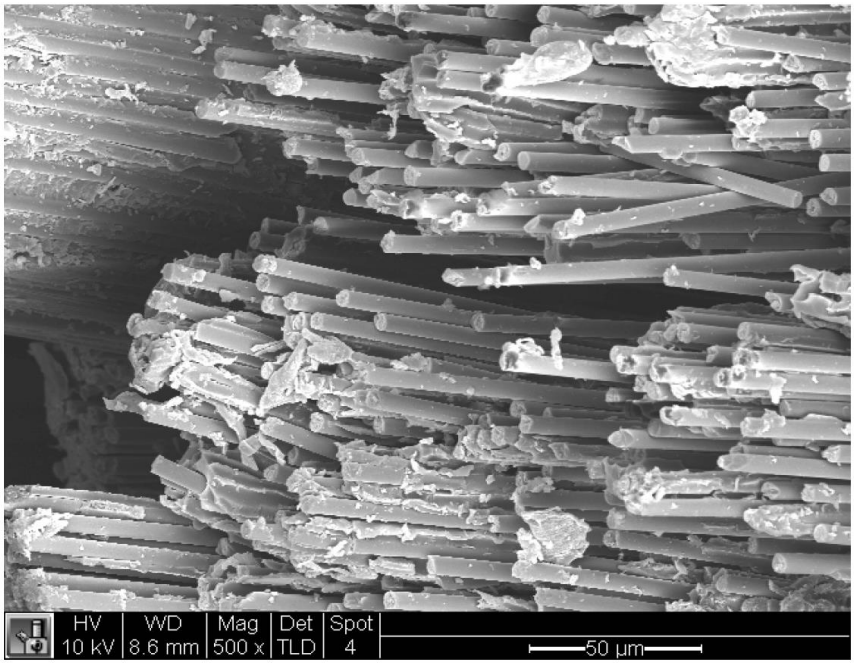

Figure 6.41 SEM showing brittle fracture of 0 and 90 degree fibres from tensile testing of PCD endmill edge trimmed specimen

From the damage it was observed that brittle fracture was predominant failure mode in 0 and 90 degree plies. In the 45 degree plies delamination was the primary failure mode. Matrix cracking preceded ply failure and delamination but was smaller in magnitude. Fibre-matrix debonding was seen in the SEMs showing brittle fracture of fibres. Exit (bottom edge) delamination was also predominant with PCD endmill trimming. Failure occurred close to after start of first ply failure. Fibre pullouts may also be contributing to reduced damage tolerance.

Tensile Testing of CVD Endmill Edge Trimmed Specimens

Edge trimmed specimens machined with CVD Endmill were tested in tension to failure. Figures 6.42 6.43 & 6.44 show the data plots from the testing.

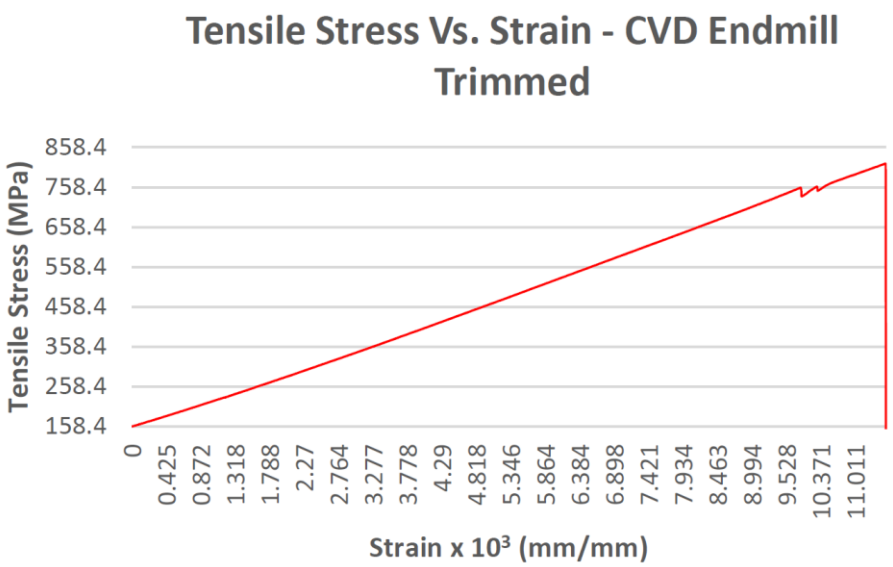

Figure 6.42 Tensile Stress Vs. Strain for CVD endmill edge trimmed specimen

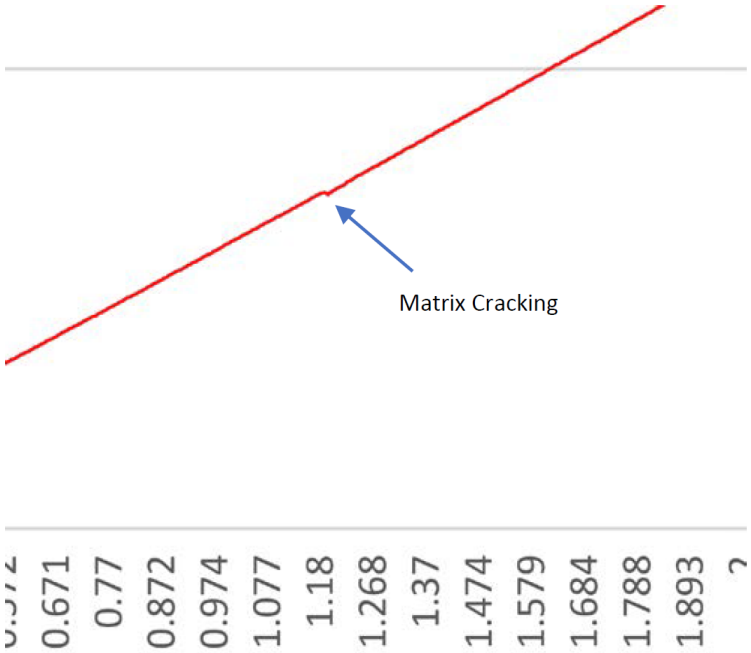

Figure 6.43 Magnified view of Tensile Stress Vs. Strain showing matrix cracking in CVD endmill edge trimmed specimen

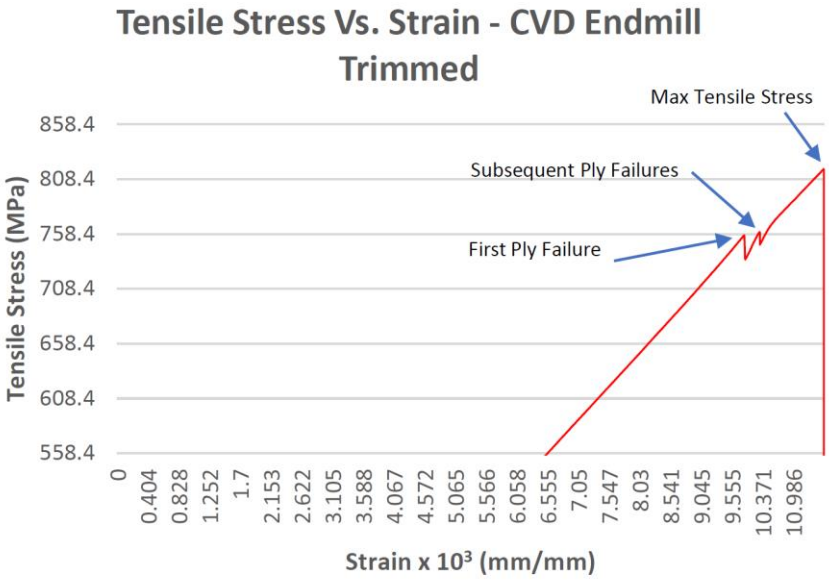

Figure 6.44 Magnified view of Tensile Stress Vs. Strain showing first ply failure and damage for CVD endmill edge trimmed specimen

<u>Test Data & Observations from tensile strength testing CVD endmill edge trimmed specimens</u>

The following strength data was recoded from the tensile testing:

Maximum Tensile Stress = 817.8 MPa

Maximum Tensile Load = 93891N

Strain at Maximum Tensile Stress = 0.011542 mm/mm

Youngs Modulus from Testing = 70.8 GPa

It was observed that matrix cracking started around 0.12% strain. The magnitude of matrix cracking was found to be lower than that in AWJ trimming. First ply failure occurred around tensile stress of 756.9 MPa. Frist ply failure was around 1.01% strain. The subsequent failure zone with ply failures (delamination)was smaller before ultimate failure pointing to lower damage tolerance. The drop in stress was also found to be larger in magnitude after first ply failure.

Damage observations from tensile strength testing of CVD endmill edge trimmed specimens

Figures 6.45, 6.46 & 6.47 show the damage recorded in the tensile strength testing of CVD endmill edge trimmed specimens

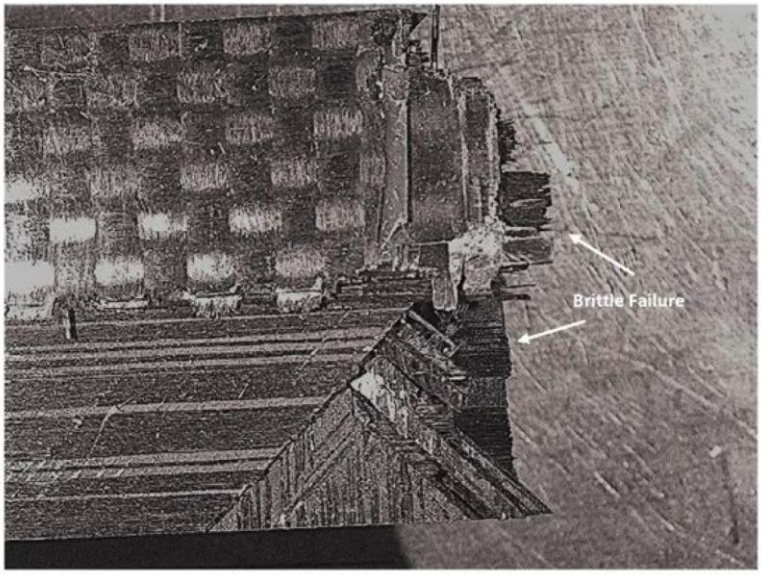

Figure 6.45 Failed specimen from Tensile testing of CVD endmill edge trimmed specimen

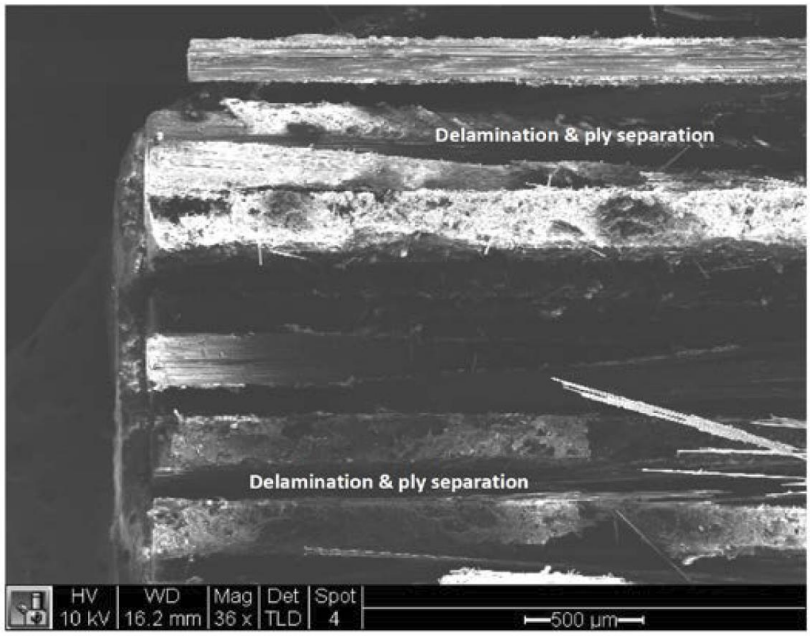

Figure 6.46 SEM of failed specimen from tensile testing of CVD endmill edge trimmed specimen

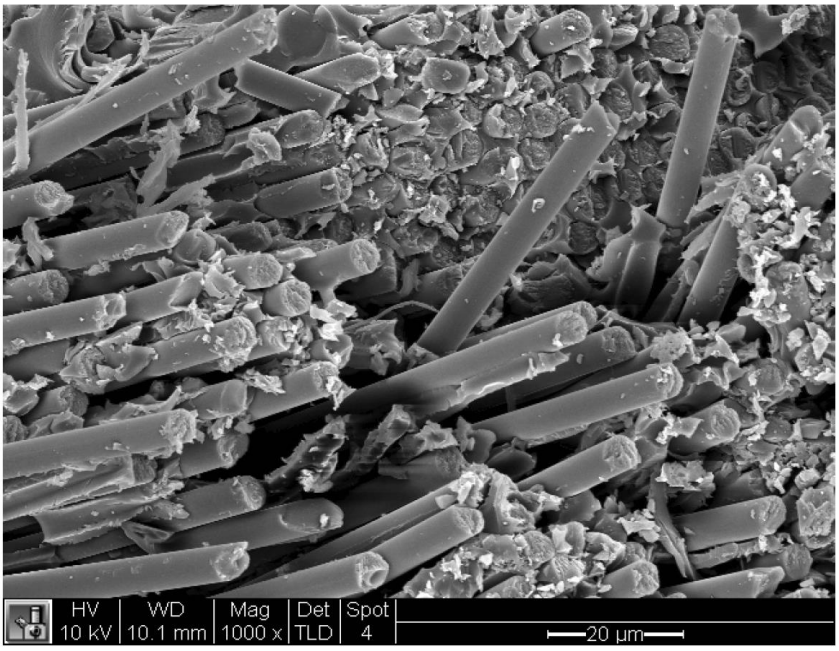

Figure 6.47 SEM showing brittle fracture of 0 and 90 degree fibres from tensile testing of CVD endmill edge trimmed specimen

From the damage it was observed that brittle fracture was predominant failure mode in 0 and 90 degree plies. In the 45 degree plies delamination was the primary failure mode. Matrix cracking preceded ply failure and delamination but was smaller in magnitude. Fibre-matrix debonding was seen in the SEMs showing brittle fracture of fibres. Exit (bottom edge) delamination was also predominant with PCD endmill trimming. Failure occurred close to after start of first ply failure. Fibre pullouts may also be contributing to reduced damage tolerance.

Observations on PCD endmill Vs. CVD endmill edge trimmed Tensile testing

In observations comparing the performance of PCD endmill Vs. CVD endmill edge trimmed specimens, it was found the CVD specimens had a higher load for same magnitude of strain compared to PCD specimens. The failure in CVD specimens was at a higher tensile stress in comparison to PCD specimens. The PCD specimens also displayed a higher level of damage in comparison to CVD specimens. Fibre-matrix debonding was also seen in the SEMs showing brittle fractures of fibres. First ply failure in PCD specimens also occurred at a higher tensile

stress compared to CVD specimens. Figure 6.48 shows the comparative Tensile Stress Vs. Strain plots for the PCD endmill Vs. CVD endmill edge trimmed specimens.

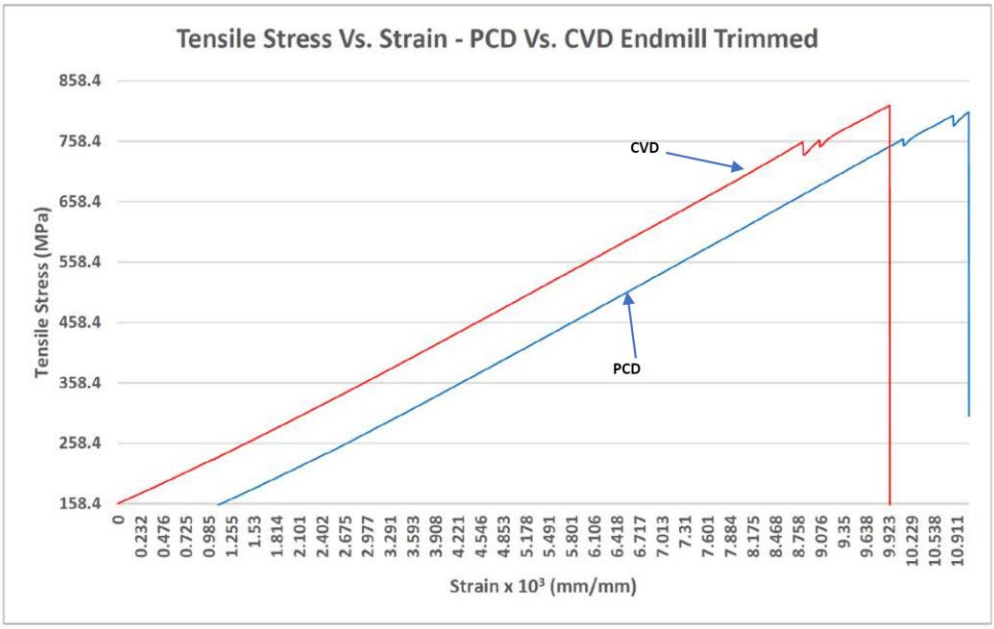

Figure 6.48 Comparative Plot of Tensile Stress Vs. Strain for Tensile Testing of PCD endmill Vs. CVD endmill edge trimmed specimens

Summary of Tensile Strength Testing Results. Observations & Conclusions

Tensile testing results were summarized and are shown in Table 6.6 along with surface roughness data. An example calculation of stress concentration factor is shown in Figure 6.49 This calculation using the notch root radius and formula shown in equation 2.4 in chapter 2 of this work. The calculation along with the graphical determination of the notch root radius is shown in Figure 6.51 along with the surface finish values. The input values of the surface finish are shown in Figure 6.49. Figure 6.50 shows the surface profile used for the graphical determination of the notch root radius.

Specimen Name	Trim	Surface Finish (L) - R_a	Surface Finish (L) - R_z	Surface Finish (L) - R_t
Specimen 4	AWJ-120	3.747	21.719	27.27

Figure 6.49 Sample Surface finish data for a AWJ (120 Grit) edge trimmed specimen for stress concentration factor calculation

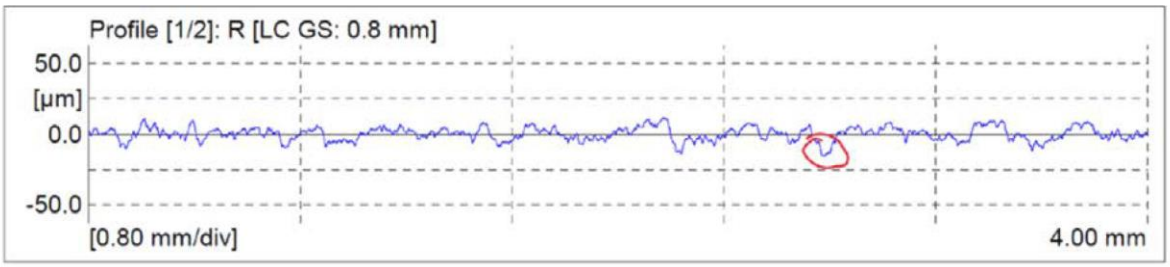

Figure 6.50 Sample Surface profile data for a AWJ (120 Grit) edge trimmed specimen for stress concentration factor calculation

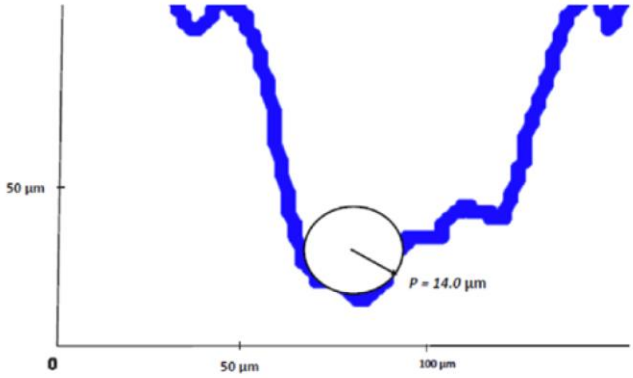

Notch Root Radius – Graphical Calculation for a AWJ (120 Grit) Edge Trimmed Specimen

$$\overline{K}_t = 1 + \eta\left(\frac{R_a}{\overline{\rho}}\right)\left(\frac{R_t}{R_z}\right) \text{ where}$$

$\eta = factor = 2(tension \,\&\, compression)$

$\overline{\rho}$ = *notch root radius*

R_a = *average surface roughness*

R_t = *peak to valley height roughness*

$R_z = 10$ *point roughness*

Figure 6.51 Sample stress concentration factor calculation for a AWJ (120 Grit) edge trimmed specimen

Specimen Type	Average Surface Finish - R_a (µm)	Surface Finish – R_z (µm)	Surface Finish – R_t (µm)	Calculated Effective Stress Concentration Factor $\overline{K}_t$	Max Tensile Stress (MPa)	Strain (mm/mm)	Youngs Modulus E_x (GPa)	Matrix Cracking Initiation – % Strain	First Ply Failure – Tensile Stress – (MPa)	First Ply Failure – % Strain
AWJ (80 Grit)	3.867	22.261	27.71	2.03	737.5	0.01142	64.5	0.31	668.7	1.01
AWJ (120 Grit)	3.315	20.71	26.77	1.67	781.0	0.01068	71.8	0.39	701.3	1.13
PCD Endmill	0.735	4.643	6.57	1.28	806.5	0.01115	72.3	0.25	759.5	1.01
CVD Endmill	1.358	8.312	10.5	1.34	817.8	0.01154	70.8	0.12	756.9	1.01

Table 6.6 Summary of Tensile Strength Testing Results

Observations from Surface Integrity plots of Tensile Testing

Surface integrity data was calculated and plots created from the surface roughness data. The plots show that the higher stress concentration factor resulted in larger reduction in stiffness compared to theoretical modulus (stiffness). Stress concentration factor is a function of surface finish parameters R_a , R_z, R_t Generally the higher the surface roughness, R_a , the large reduction in stiffness. The ratio R_z / R_t influences the reduction in stiffness. The larger the ratio the greater the reduction in stiffness. This is attributed to the larger values of the highest peaks and deepest valleys in the surface profiles. This leads to an increase in number of points of stress risers which lead to stiffness reduction and load carrying capacity. The test specimens for AWJ -120 Grit and the PCD & CVD endmill specimens had tensile properties closer to each other. The AWJ-80 grit specimens had larger variations in surface finish parameters as well as tensile properties in comparison to other trimming process specimens. Figure 6.52, 6.53 & 6.54 show the plots of various surface finish parameters Vs. the ratio of tested modules to theoretical apparent modulus (E / E_0)

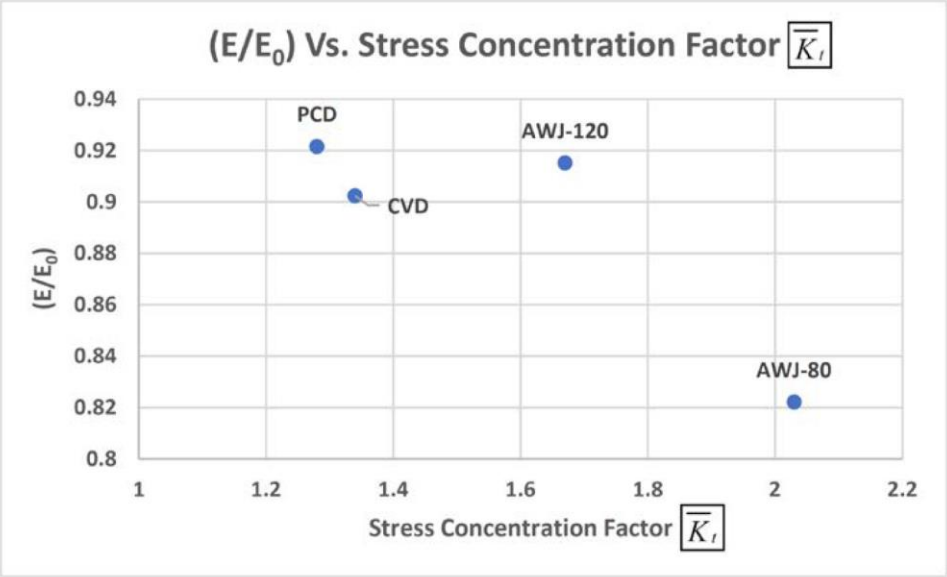

Figure 6.52 Plot of (E/E_0) Vs. Stress Concentration Factor for various edge trimmed specimens in Tensile testing

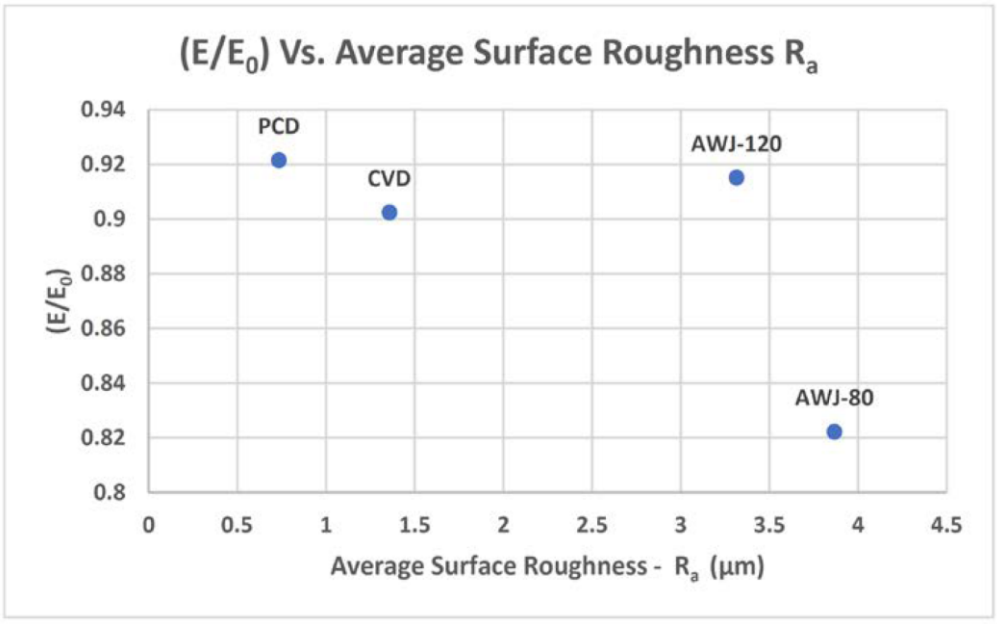

Figure 6.53 Plot of (E/E_0) Vs. Average Surface Roughness - R_a (µm) for various edge trimmed specimens in Tensile testing

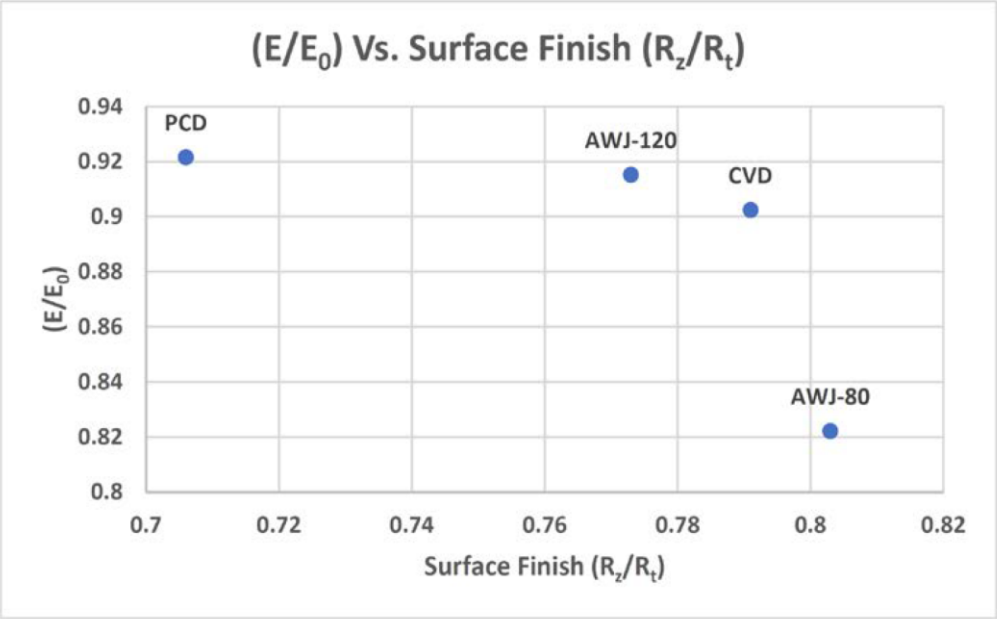

Figure 6.54 Plot of (E/E_0) Vs. Surface Finish (R_z / R_t) for various edge trimmed specimens in Tensile testing

Observations from Damage Progress Plot for Tensile Testing

Damage progress plot Vs. applied load was generated and it was observed that AWJ-80 Grit specimen showed damage starting at higher applied load and had the greatest amount of damage before failure. The plot for AWJ-80 Grit was steeper than the 120 Grit specimen. As erosion is the mechanism of cutting, the 120 grit process produces damage such as matrix cracking at lower loads but the progress of damage is slower than the 80 grit specimens resulting in lower overall damage as well as failure at higher load. The progress of damage is slower in AWJ specimens as compared to endmill trimmed specimens as matrix cracking is dominant mode of damage initially. The transition of damage from matrix cracking in delamination in AWJ is over a larger spread of applied loads. Damage tolerance of AWJ specimens was found to be better in comparison to endmill trimmed specimens. For the endmill trimmed specimens damage from matrix cracking is lower and the predominant mode is delamination. The damage initiation in endmill trimmed specimens occurred at higher loads as compared to AWJ specimens. It was also found that Delamination damage progresses faster and endmill trimmed specimens while having damage initiation at higher loads fail faster after damage initiates. For CVD specimens the

damage progress is faster compared to PCD endmills. Delamination is predominant damage and progresses faster in CVD specimens due to higher density of fibre pullouts. Damage tolerance for endmill trimmed specimens is lower in comparison to AWJ trimmed specimens. Figure 6.55 shows the damage progress plot with damage Vs. applied load for tensile testing.

$$\text{Damage} = 1 - (E/E_0)$$

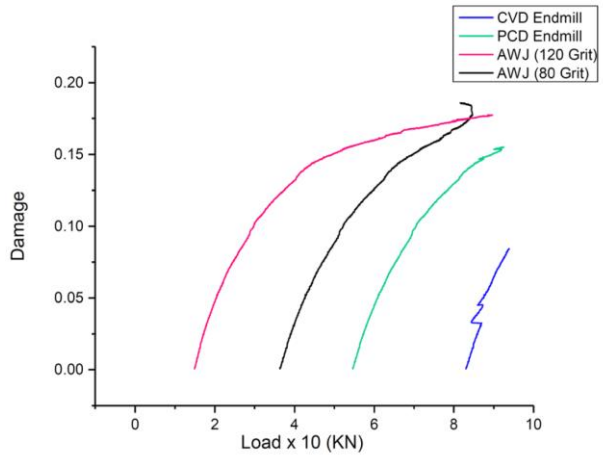

Figure 6.55 Damage Vs. Applied Load for edge trimmed specimens in Tensile Testing

6.4.3.1 Analysis of Tension Testing Results

As seen from the above results there is a drop in the stiffness from the theoretical apparent stiffness calculations. This can be attributed to resultant surface integrity from varying edge trimming operations conducted. Test specimens machined with endmills displayed better surface finish profile characteristics across variables in the longitudinal direction. Across Transverse direction, the AWJ test specimens displayed better surface profile characteristics.

AWJ trimmed specimens had a lower failure load as compared to Endmill trimmed specimens even though the fibre pullout density was lower in the AWJ specimens. The higher load carrying capacity in tension samples which were endmill trimmed was attributed to better surface finish profiles in the longitudinal direction, the direction of applied loading.

Comparing the AWJ samples, the 120 grit trimmed sample displayed slightly better load carrying capacity than the 80 grit trimmed surface. In the transverse direction, the surface finish profiles of the 80 grit trimmed surface were slightly better than the 120 grit trimmed surface.

Overall all maximum tension loads were within 10% of each other for all edge trimmed surfaces. The reduction in stiffness was the most for AWJ (80 grit) trimmed surface which displayed the roughest surface profile in the longitudinal direction, the direction of loading.

When analyzed for the failure mode, it was observed that most of the specimens in tension failed along the top ply as well as internal ply failure.

The damage mechanism is generally in 3 stages as following:

a) Stage 1 – matrix cracking
b) Stage 2 – Matrix-Fibre debonding
c) Stage 3 – Fibre Fracture

First ply failure stress is also a function of surface integrity. With the higher surface roughness value (R_a), the lower the first ply failure stress.

The reduction in stiffness is a function of the surface integrity and the resultant stress concentration factor from surface integrity

$$\frac{E}{E_0} = f(\overline{K}_t) \qquad 6.1$$

When the value of the stress concentration factor $(\overline{K}_t)$ is higher, the value of $\left(\frac{E}{E_0}\right)$ is lower

When the value of $\left(\frac{R_z}{R_t}\right)$ is higher, the value of $\left(\frac{E}{E_0}\right)$ is lower

6.4.4 Compression Strength Testing

Both endmill trimmed and AWJ specimens were mechanically tested in compression and the results tabulated. Strain gauges were used to capture the strain under tension loading conditions. All the specimens were taken to failure during the testing process.

The following tables and figures show the data along with the stress-strain curves and failure for both the endmill and AWJ trimmed specimens

Compression Testing of AWJ (80 Grit) Edge Trimmed Specimens

Edge trimmed specimens machined with AWJ (80 Grit) were tested in compression to failure. Figures 6.56, 6.57, & 6.58 show the data plots from the testing.

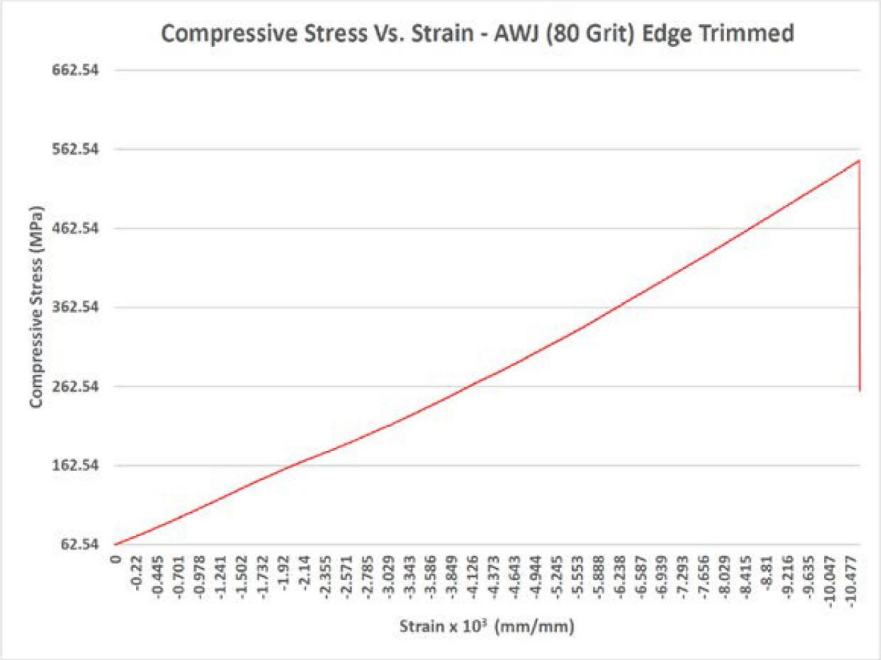

Figure 6.56 Compressive Stress Vs. Strain for AWJ (80 Grit) edge trimmed compression specimen

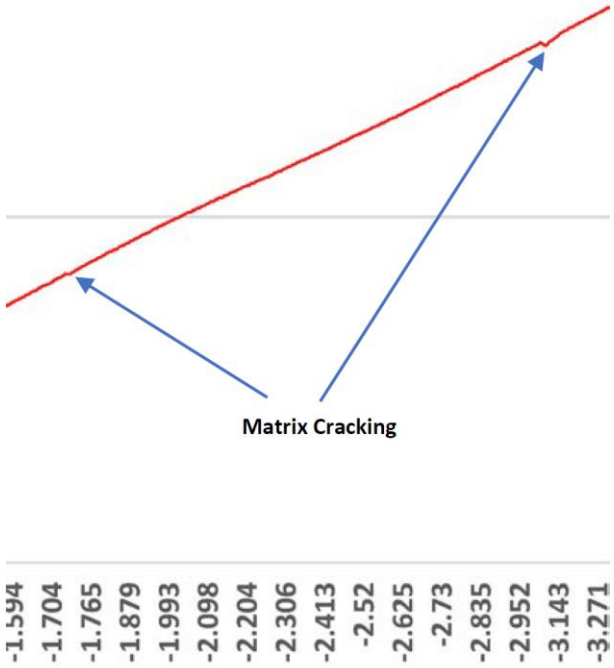

Figure 6.57 Magnified view of Compressive Stress Vs. Strain showing matrix cracking in AWJ (80 Grit) edge trimmed compression specimen

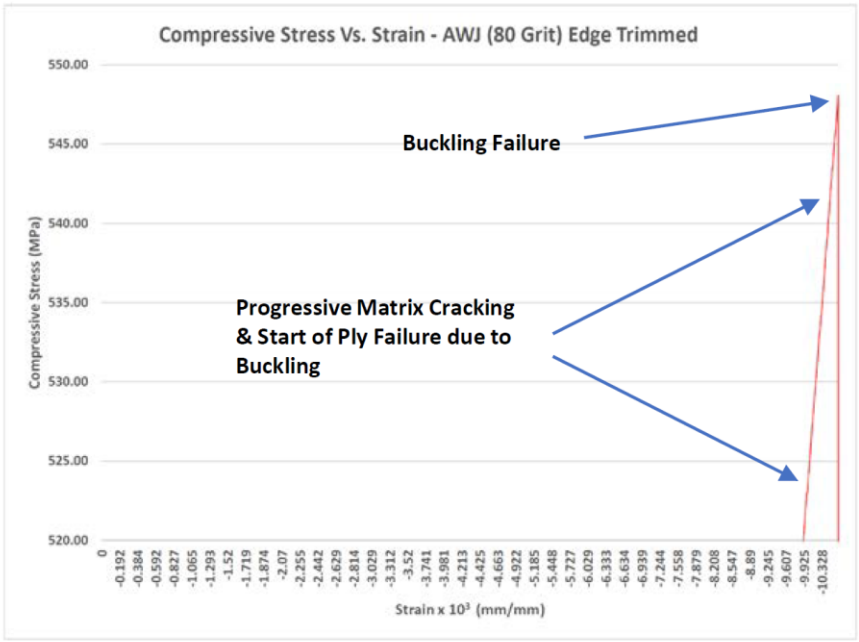

Figure 6.58 Magnified view of Compressive Stress Vs. Strain showing ply failure due to buckling in AWJ (80 Grit) edge trimmed compression specimen

Test Data & Observations from compression strength testing of AWJ (80 Grit) edge trimmed specimens

The following strength data was recoded from the tensile testing:
Maximum Compressive Stress = 548.06 MPa
Maximum Compressive Load = 31461 N
Strain at Maximum Compressive Stress = 0.010701 mm/mm
Youngs Modulus from Testing = 51.2 GPa

It was observed that matrix cracking started around 0.17% strain. Matrix cracking progresses as stress increases. First ply failure due to buckling occurred around compressive stress of 520.0 MPa. Frist ply failure was around 0.99% strain. Buckling failure occurred at a strain of 1.07%

Damage observations from compressive strength testing of AWJ (80 Grit) edge trimmed specimens

Figures 6.59 & 6.60 show the damage recorded in the compressive strength testing of AWJ (80 Grit) edge trimmed specimens

Figure 6.59 Failed specimen in compression testing of AWJ (80 Grit) edge trimmed specimen

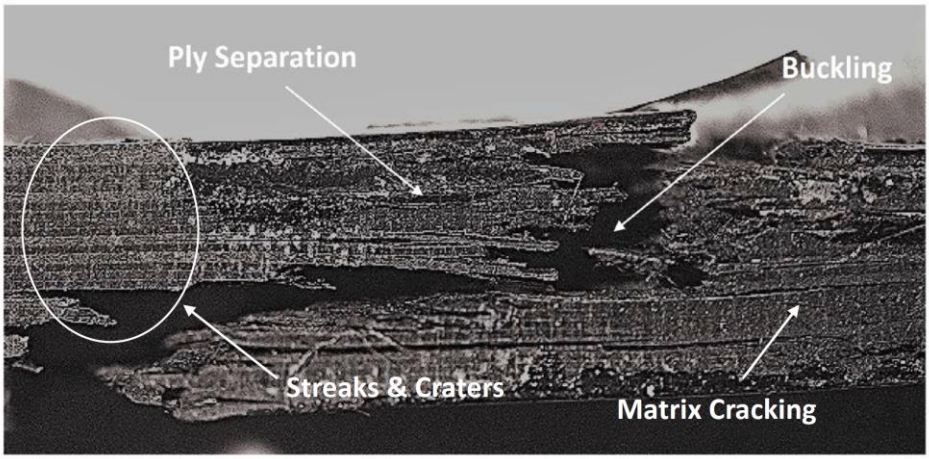

Figure 6.60 Failed specimen in compression testing of AWJ (80 Grit) edge trimmed specimen

From the damage is was observed that failed specimen showed streaks and craters from the AWJ trimming process. Matrix cracking preceded ply failure and is spread through the thickness of the laminate. Ply separation is present through the thickness of the laminate. Primary mode of failure is bucking at a 45 degree angle across the thickness of the laminate.

Compression Testing of CVD endmill Edge Trimmed Specimens

Edge trimmed specimens machined with CVD endmills were tested in compression to failure. Figures 6.61, 6.62, & 6.63 show the data plots from the testing.

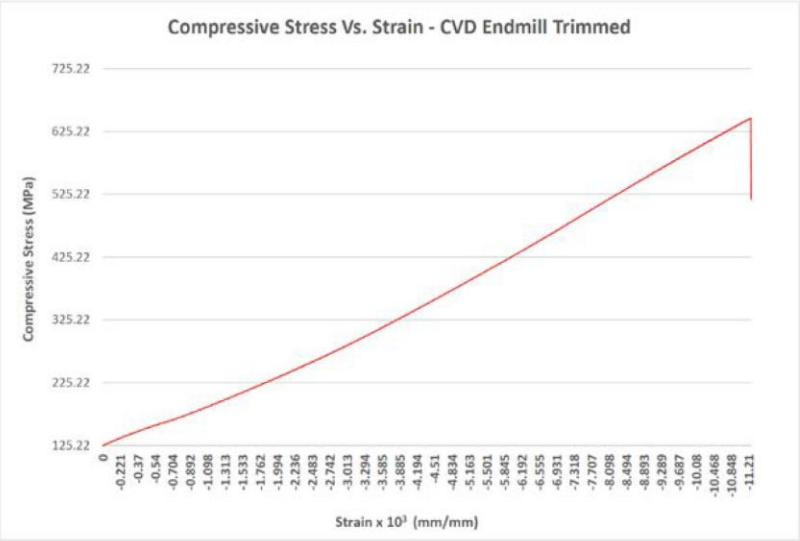

Figure 6.61 Compressive Stress Vs. Strain for CVD endmill edge trimmed compression specimen

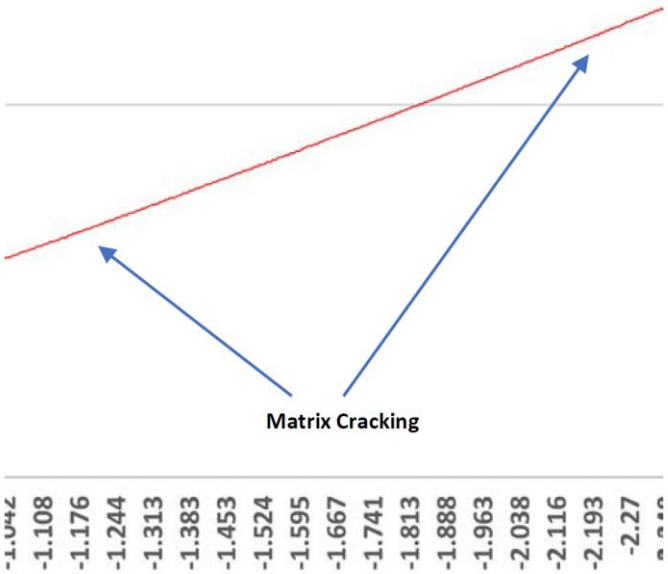

Figure 6.62 Magnified view of Compressive Stress Vs. Strain showing matrix cracking in CVD endmill edge trimmed compression specimen

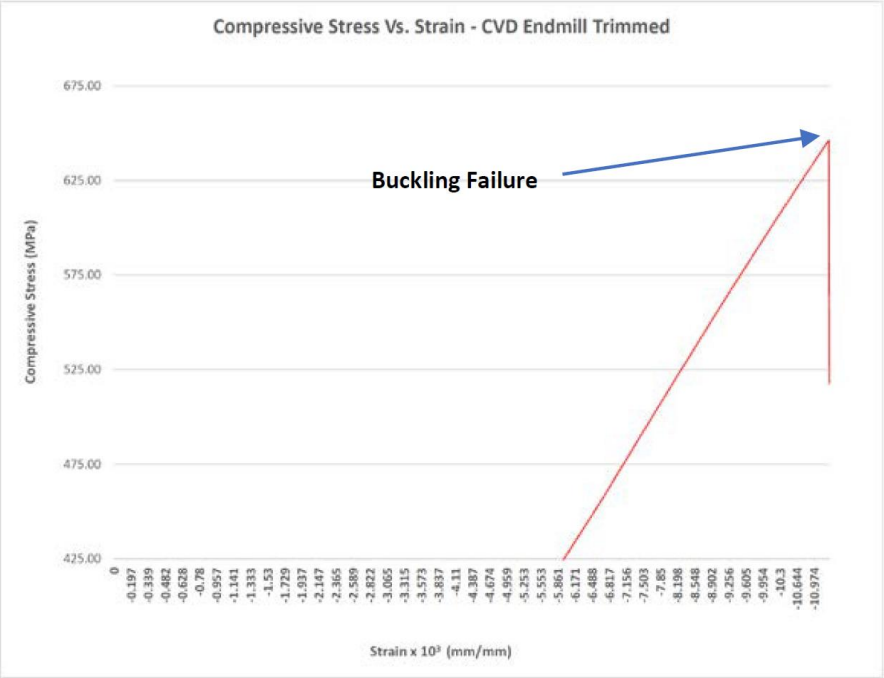

Figure 6.63 Magnified view of Compressive Stress Vs. Strain showing ply failure due to buckling in CVD endmill edge trimmed compression specimen

Test Data & Observations from compression strength testing of CVD endmill edge trimmed specimens

The following strength data was recoded from the tensile testing:
Maximum Compressive Stress = 646.4 MPa
Maximum Compressive Load = 37106 N
Strain at Maximum Compressive Stress = 0.01125 mm/mm
Youngs Modulus from Testing = 57.4 GPa

It was observed that matrix cracking started around 0.12% strain. Matrix cracking progresses as stress increases and is lower in magnitude in comparison to AWJ specimen. First ply failure due to buckling occurred around compressive stress of 575.0 MPa. Frist ply failure was around 0.99% strain. Buckling failure occurred at a strain of 1.11%

Damage observations from compressive strength testing of CVD endmill edge trimmed specimens

Figure 6.64 shows the damage recorded in the compressive strength testing of CVD endmill edge trimmed specimens

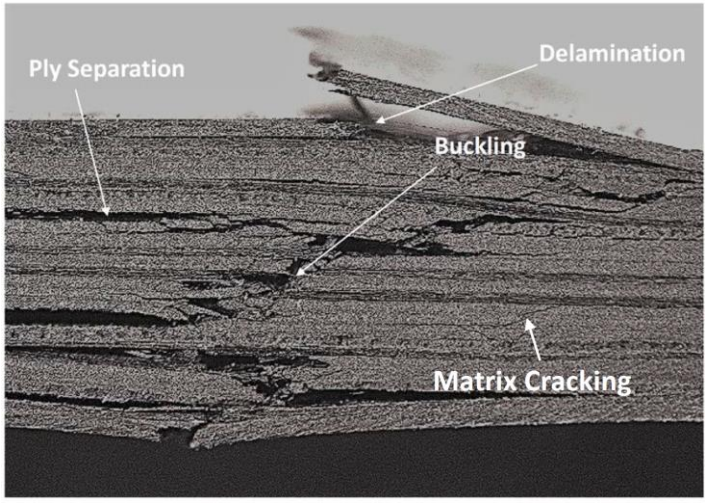

Figure 6.64 Failed specimen in compression testing of CVD endmill edge trimmed specimen

From the damage is was observed that matrix cracking was lower in magnitude compared to AWJ specimen. Matrix cracking preceded ply failure and is spread through the thickness of the laminate. Ply separation is present through the thickness of the laminate. Primary mode of failure is bucking at a 45 degree angle across the thickness of the laminate. Delamination is also present at both the top and bottom surface of the laminate.

Summary of Compressive Strength Testing Results & Surface Integrity Plots

Compressive testing results were summarized and are shown in Table 6.7 along with surface roughness data, Surface integrity data was calculated and plots created from the surface roughness data. The plots show that the higher stress concentration factor resulted in larger reduction in stiffness compared to theoretical modulus (stiffness). Stress concentration factor is a function of surface finish parameters R_a , R_z, R_t Generally the higher the surface roughness, R_a , the large reduction in stiffness. The ratio R_z / R_t influences the reduction in stiffness. The larger the ration the greater the reduction in stiffness. This is attributed to the larger values of the

highest peaks and deepest valleys in the surface profiles. This leads to an increase in number of points of stress risers which lead to stiffness reduction and load carrying capacity.

Specimen Type	Average Surface Finish - R_a (µm)	Surface Finish – R_z (µm)	Surface Finish – R_t (µm)	Calculated Effective Stress Concentration Factor $\overline{K}_t$	Max Compressive Stress (MPa)	Strain (mm/mm)	Youngs Modulus E_x (GPa)	Matrix Cracking Initiation – % Strain	First Ply Failure – Compressive Stress – (MPa)	First Ply Failure – % Strain
AWJ (80 Grit)	3.153	19.114	24.19	2.03	548.06	- 0.01071	51.2	0.71	520.0	0.99
CVD Endmill	0.738	4.469	5.753	1.34	646.4	- 0.01125	57.4	0.12	575.0	0.99

Table 6.7 Summary of Surface finish and Compressive Strength properties

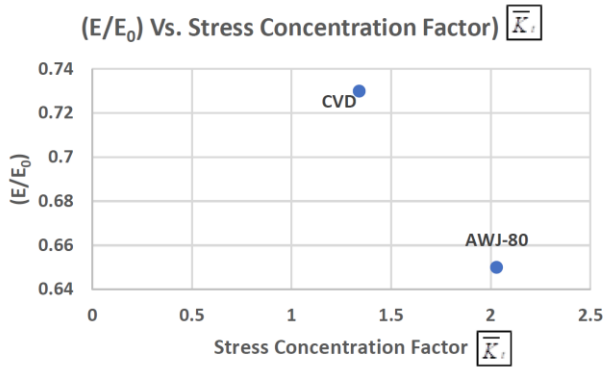

Figure 6.65 Plot of (E/E_0) Vs. Stress Concentration Factor for various edge trimmed specimens in compression testing

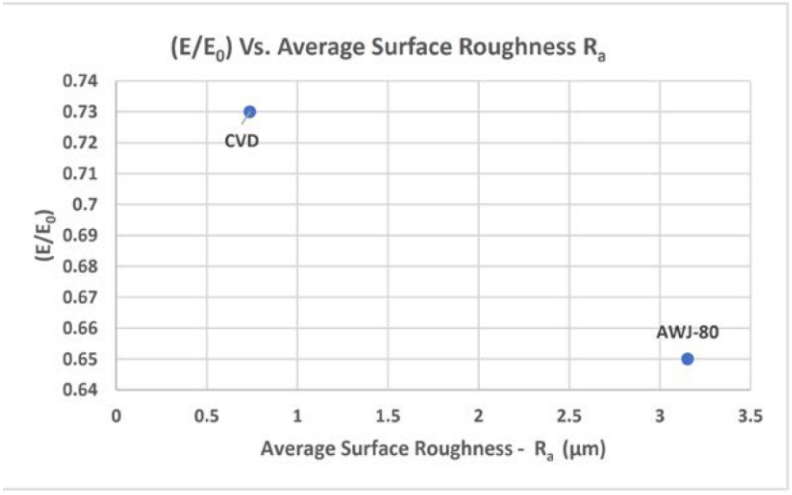

Figure 6.66 Plot of (E/E_0) Vs. Average Surface Roughness - R_a (µm) for various edge trimmed specimens in compression testing

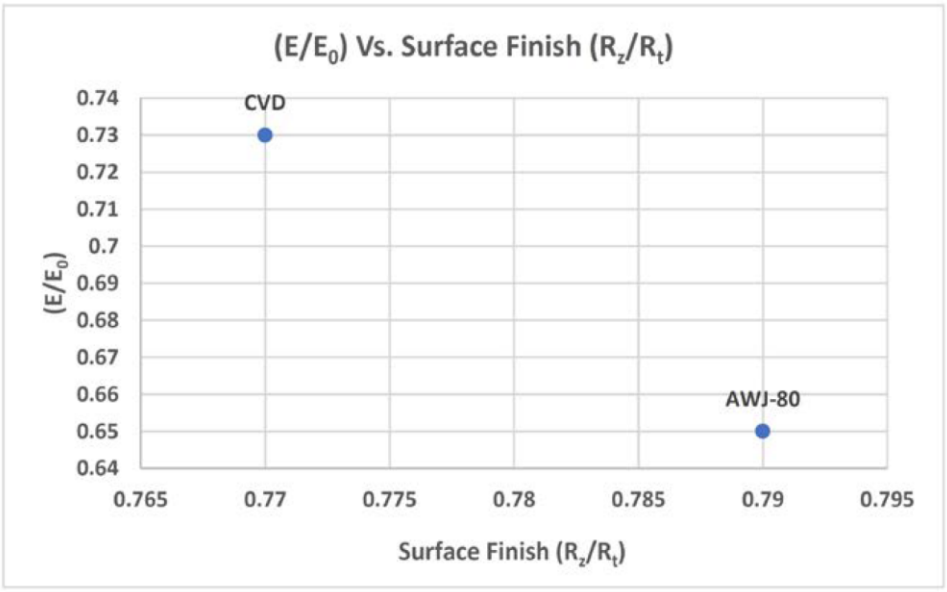

Figure 6.67 Plot of (E/E_0) Vs. Surface Finish (R_z / R_t) for various edge trimmed specimens in compression testing

Observations from Damage Progress Plot for Compression Testing

From the damage progress plot vs. applied load it was determined that the AWJ-80 Grit specimen showed damage starting at lower applied loads and had the largest amount of damage before failure. The AWJ-80 Grit specimens also is steeper than the CVD endmill trimmed specimen. The progress of damage is slower in AWJ specimen as compared to the endmill specimen as matrix cracking is the dominant mode of damage initially. The transition of damage from matrix cracking to buckling in AWJ specimen is over a larger spread of applied loads. Damage tolerance of AWJ specimen is better in comparison to endmill trimmed specimen. For endmill trimmed specimen damage from matrix cracking is lower and the predominant damage mode is ply separation and buckling. The damage initiation in endmill trimmed specimen occurs at higher loads as compared to AWJ specimen. Ply separation and buckling damage progresses faster and endmill trimmed specimens while having damage initiation at higher loads fail faster after damage initiates. Damage tolerance for endmill trimmed specimens is lower in comparison to AWJ trimmed specimens. Figure 6.68 shows the plot of damage progress Vs. applied loads.

$$\text{Damage} = 1 - (E/E_0)$$

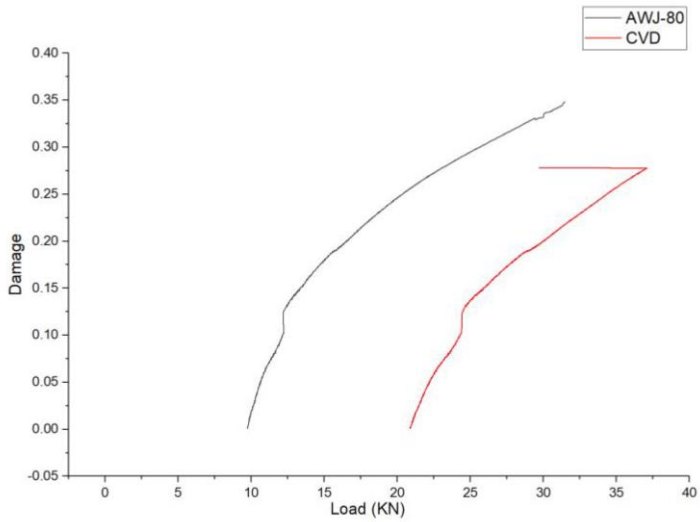

Figure 6.68 Damage Vs. Applied Load for edge trimmed specimens in Tensile Testing

6.4.4.1 Analysis of Compression Testing Results

Fibre pullouts were observed in both AWJ and Endmill trimmed specimens. The fibre pullout density was higher in endmill trimmed specimens while delaminations were observed at the exit (bottom edge) of the AWJ trimmed specimens. It was observed that the AWJ specimens failed at lower loads as compared to the Endmill trimmed specimens. The surface finish profiles for the endmill trimmed samples were better than the AWJ samples in the longitudinal direction, the direction of applied loading. In each case the maximum failure load varied within 10% across all variable test specimens. All the test results showed a drop in the stiffness from the theoretical apparent stiffness calculations.

Failure in all specimens was buckling across the 45 degree plies (Figure 6.32) before propagation through the thickness of the laminate and ultimate failure.

The damage mechanism is generally in 3 stages as following:

d) Stage 1 – matrix cracking
e) Stage 2 – Matrix-Fibre debonding

f) Stage 3 – Fibre Fracture, ply separation and buckling

First ply failure stress is also a function of surface integrity. With the higher surface roughness value (R_a), the lower the first ply failure stress.

The reduction in stiffness is a function of the surface integrity and the resultant stress concentration factor from surface integrity

$$\frac{E}{E_0} = f(\overline{K}_t) \qquad 6.1$$

When the value of the stress concentration factor $(\overline{K}_t)$ is higher, the value of $\left(\frac{E}{E_0}\right)$ is lower

When the value of $\left(\frac{R_z}{R_t}\right)$ is higher, the value of $\left(\frac{E}{E_0}\right)$ is lower

For compression loading the maximum stress values are much lower than those in tension. The values of $\left(\frac{E}{E_0}\right)$ are between 0.65 to 0.75 which are about 25% to 35% lower than those in tension.

6.4.5 Open Hole Tension Testing

Both PCD and CVD drilled specimens were tested in open hole tension and the results were tabulated. The specimens were drilled with 2 different feedrates 305 mm/min and 508 mm/min. Strain gauges were used to capture the strain under open hole tension loading conditions. All the specimens were taken to failure during the testing process. The following tables and figures show the data along with the stress-strain curves and failure for both the PCD and CVD drilled hole specimens

Open Hole Tensile Testing of PCD Drilled Hole at feedrate of 305 mm/min Specimens

PCD drilled holes at feedrate of 305 mm/min specimens were tested in open hole tension to failure. Figures 6.68, 6.69 & 6.70 show the data plots from the testing.

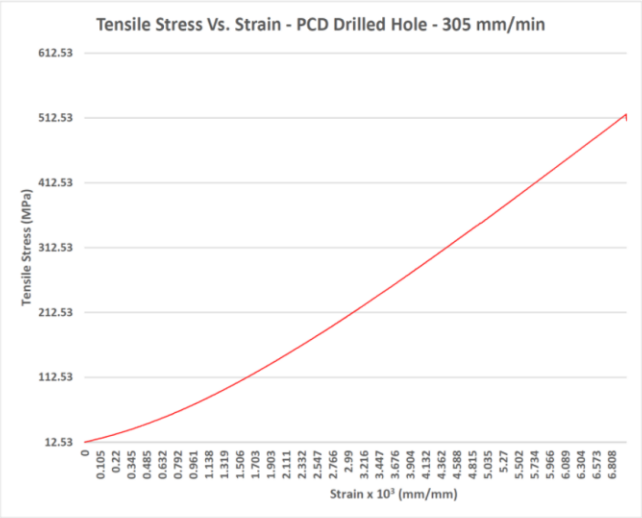

Figure 6.69 Open Hole Tensile Stress Vs. Strain for PCD Drilled Hole (305 mm/min)

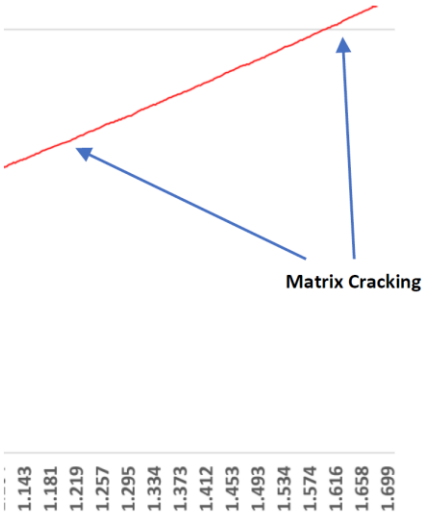

Figure 6.70 Magnified View of Open Hole Tensile Stress Vs. Strain showing Matrix Cracking in PCD Drilled hole specimen (305 mm/min)

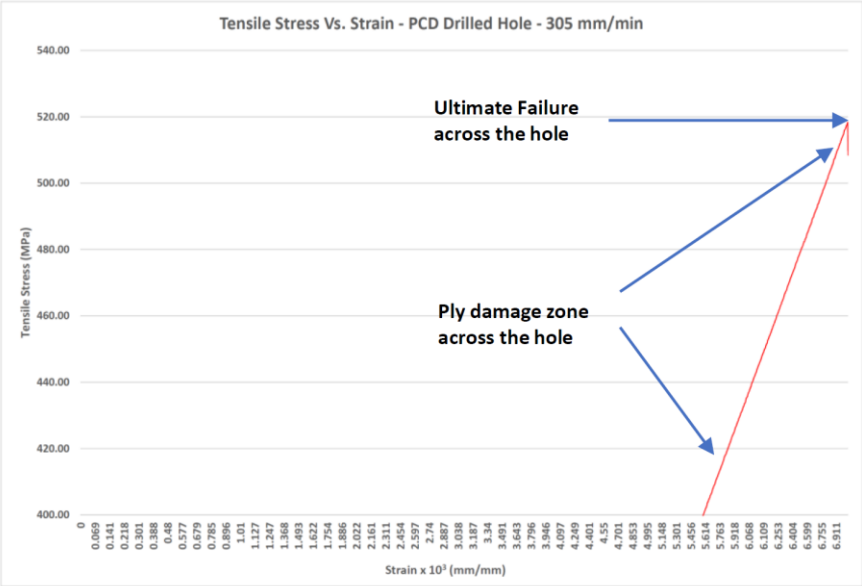

Figure 6.71 Magnified view of Open Hole Tensile Stress Vs. Strain showing First Ply Failure and Damage in PCD Drilled hole specimen (305 mm/min)

Test Data & Observations from Open Hole Tensile testing of PCD Drilled Hole at feedrate of 305 mm/min specimens

The following strength data was recoded from the open hole tensile testing of PCD Drilled hole at feedrate of 305 mm/min:

Maximum Open Hole Tensile Stress = 518.38MPa

Maximum Open Hole Tensile Load = 59514 N

Strain at Maximum Open Hole Tensile Stress = 0.007023 mm/mm

Youngs Modulus from Testing = 73.8 GPa

It was observed that matrix cracking started around 0.12% strain. Matrix cracking progressed as stress increased and first ply failure occurred around tensile stress of 420.0 MPa. First ply failure occurred around 0.57% strain. It was observed that the subsequent ply failures (delamination) was smaller before ultimate failure pointing to a smaller damage tolerance. Failure zone initiated at the 45 degree plies in the hole with ultimate failure occurring across the complete hole.

Damage observations from open hole tensile testing of PCD Drilled hole at 305 mm/min specimens

Figures 6.72 through 6.76 show the damage recorded in open hole tensile testing of PCD drilled hole at feedrate of 305 mm/min specimens.

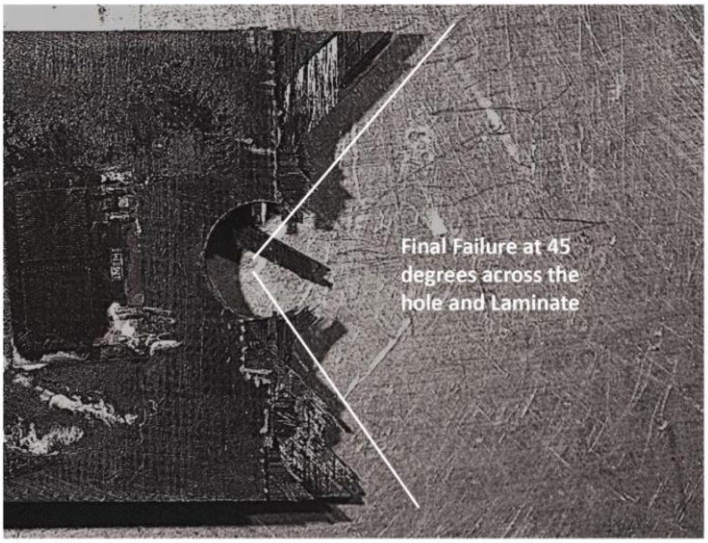

Figure 6.72 Failed specimen from Open Hole Tensile testing of PCD hole specimen (305 mm/min)

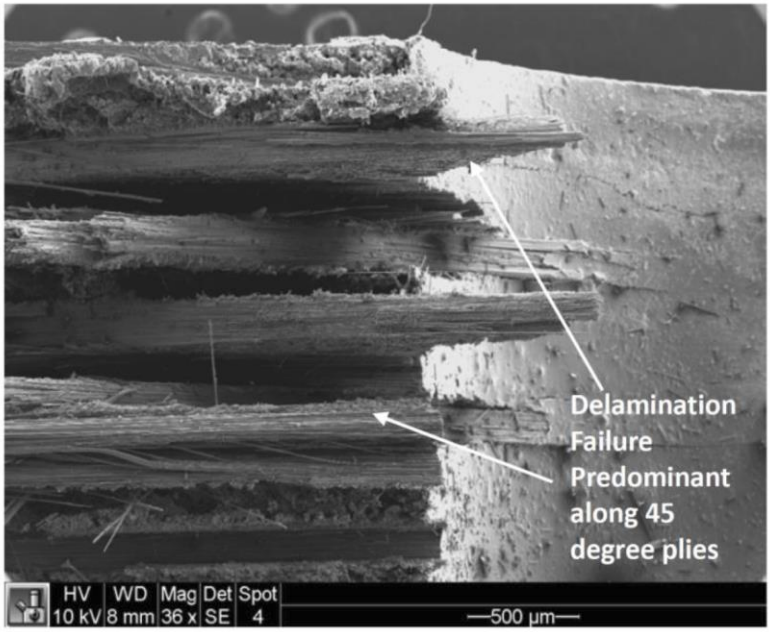

Figure 6.73 SEM of failed specimen from Open Hole Tensile Testing of PCD hole specimen (305 mm/min)

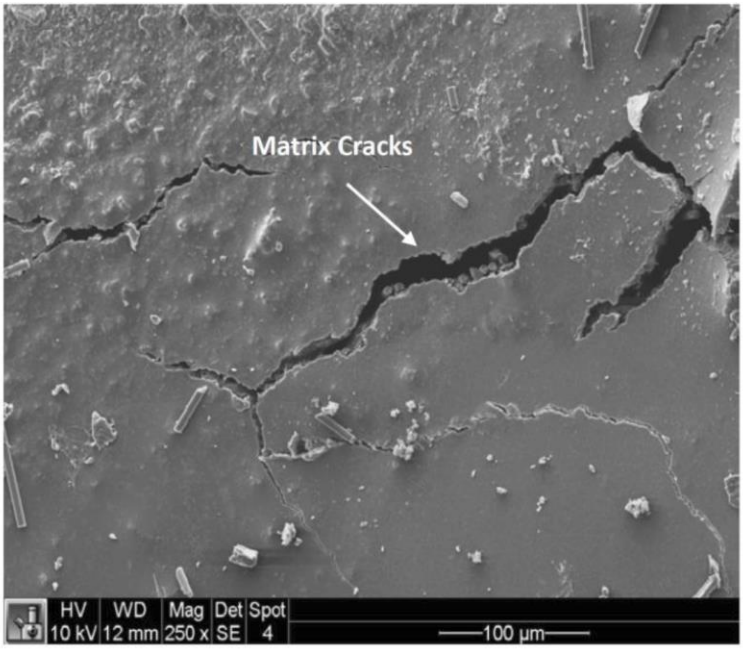

Figure 6.74 SEM of failed specimen showing Matrix Cracks from Open Hole Tensile Testing of PCD hole specimen (305 mm/min)

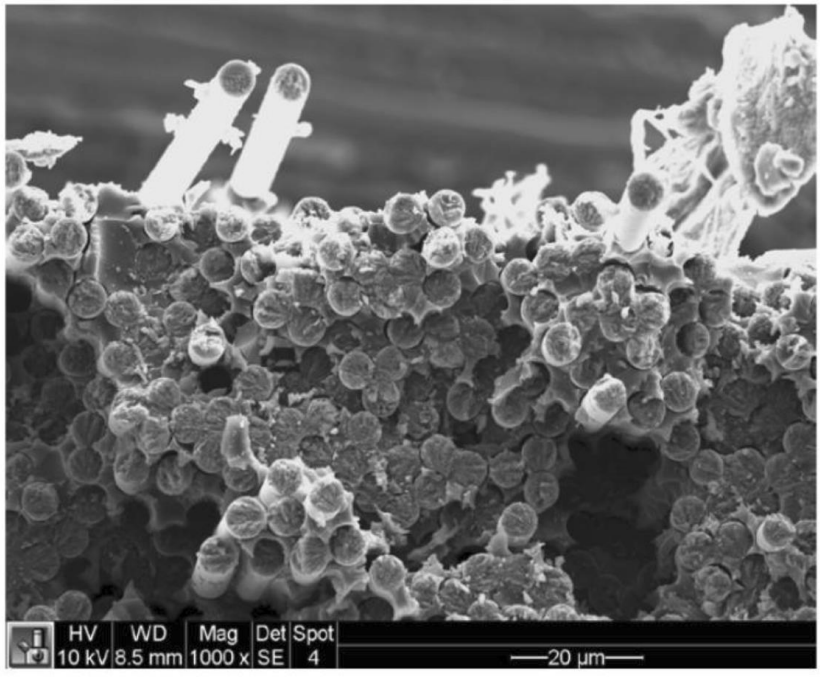

Figure 6.75 SEM of failed specimen showing Fibre Fractures from Open Hole Tensile Testing of PCD hole specimen (305 mm/min)

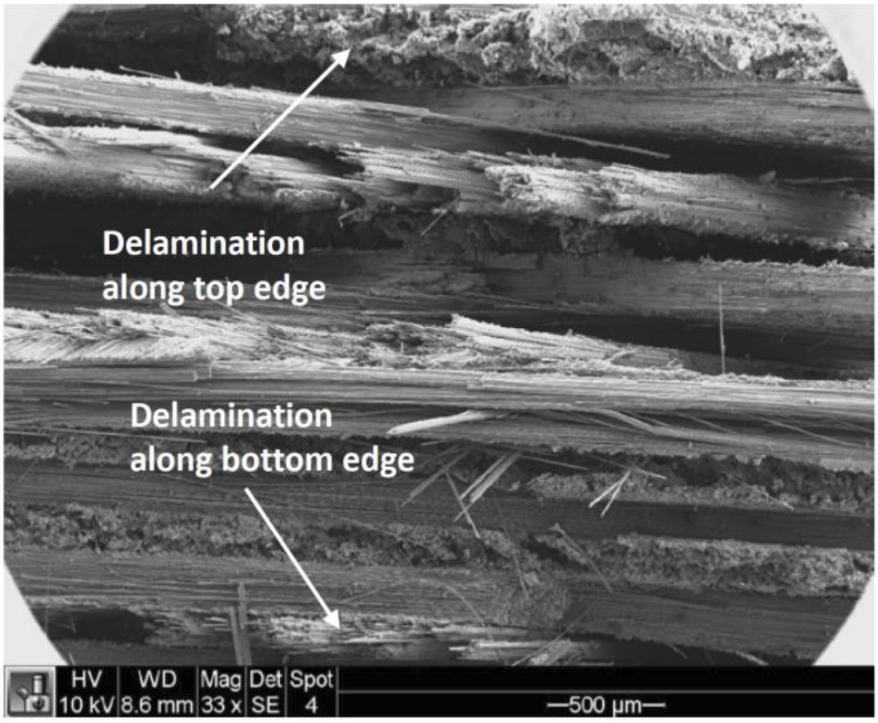

Figure 6.76 SEM of failed specimen showing Delamination from Open Hole Tensile Testing of PCD hole specimen (305 mm/min)

From the damage observations, it was noted that the damage initiation started at the 45 degree plies in the hole. The damage progressed along the various plies on the hole surface. The predominant failure was delamination along the 45 degree plies of the hole surface. Matrix cracks were present along the surface through the thickness of the laminate. Brittle fracture of fibres was observed in the failed specimens. Final failure of specimen was separation along 45 degrees across the thickness of the laminate. Fibre pullouts contributed to delamination initiation and progression starting at 45 degrees plies. Matrix cracking preceded delamination and aided in the final failure of the specimen.

Open Hole Tensile Testing of PCD Drilled Hole at feedrate of 508 mm/min Specimens

PCD drilled holes at feedrate of 508 mm/min specimens were tested in open hole tension to failure. Figures 6.77, 6.78 & 6.79 show the data plots from the testing.

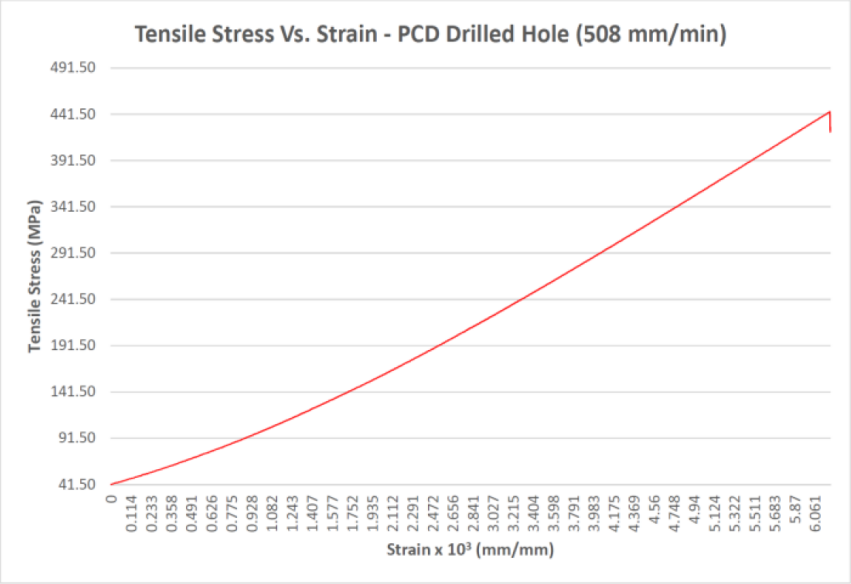

Figure 6.77 Open Hole Tensile Stress Vs. Strain for PCD Drilled Hole (508 mm/min)

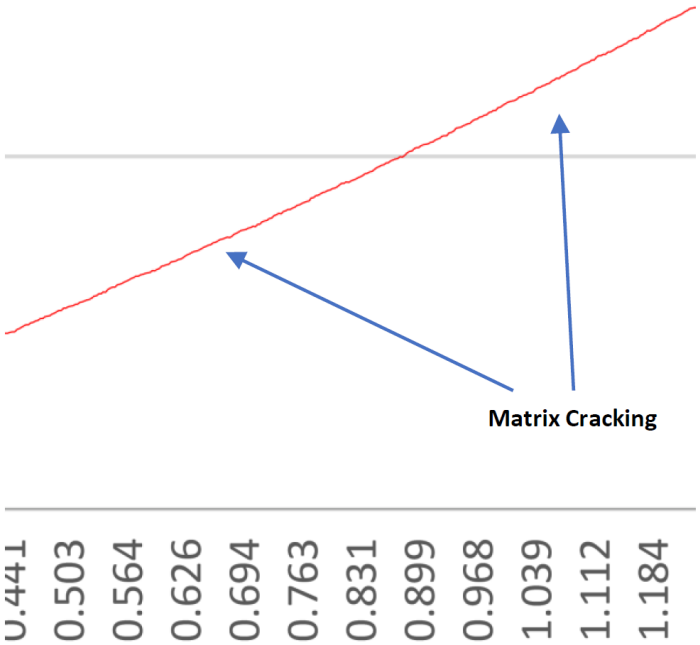

Figure 6.78 Magnified View of Open Hole Tensile Stress Vs. Strain showing Matrix Cracking in PCD Drilled hole specimen (508 mm/min)

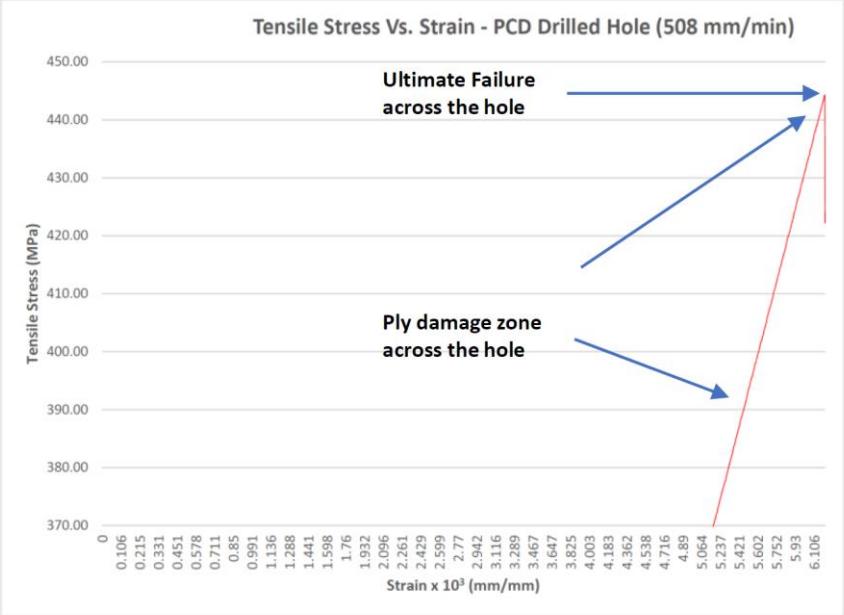

Figure 6.79 Magnified view of Open Hole Tensile Stress Vs. Strain showing First Ply Failure and Damage in PCD Drilled hole specimen (508 mm/min)

<u>Test Data & Observations from Open Hole Tensile testing of PCD Drilled Hole at feedrate of 508 mm/min specimens</u>

The following strength data was recoded from the open hole tensile testing of PCD Drilled hole at feedrate of 508 mm/min:
Maximum Open Hole Tensile Stress = 444.35 MPa
Maximum Open Hole Tensile Load = 51015 N
Strain at Maximum Open Hole Tensile Stress = 0.006197 mm/mm
Youngs Modulus from Testing = 71.7 GPa

It was observed that matrix cracking started around 0.07% strain. Matrix cracking progressed as stress increased and first ply failure occurred around tensile stress of 395.0 MPa. First ply failure occurred around 0.54% strain. It was observed that the subsequent ply failures (delamination) was smaller before ultimate failure pointing to a smaller damage tolerance. Failure zone initiated at the 45 degree plies in the hole with ultimate failure occurring across the complete hole. It was

also observed that delamination progressed faster due to higher density of fibre pullouts compared to lower drilling feedrate specimens.

Damage observations from open hole tensile testing of PCD Drilled hole at 508 mm/min specimens

Figures 6.80 through 6.84 show the damage recorded in open hole tensile testing of PCD drilled hole at feedrate of 508 mm/min specimens.

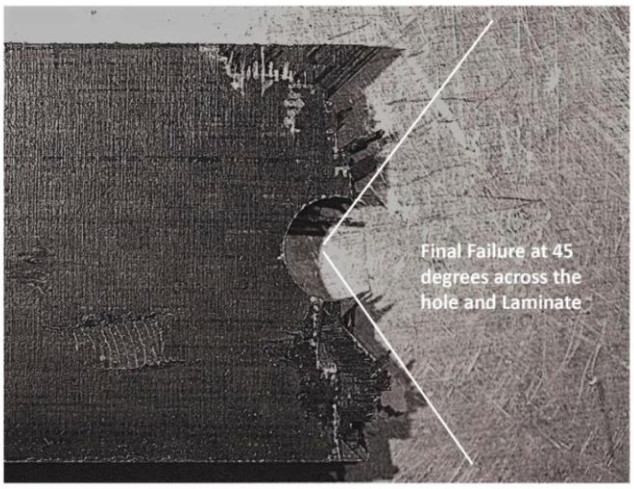

Figure 6.80 Failed specimen from Open Hole Tensile testing of PCD hole specimen (508 mm/min)

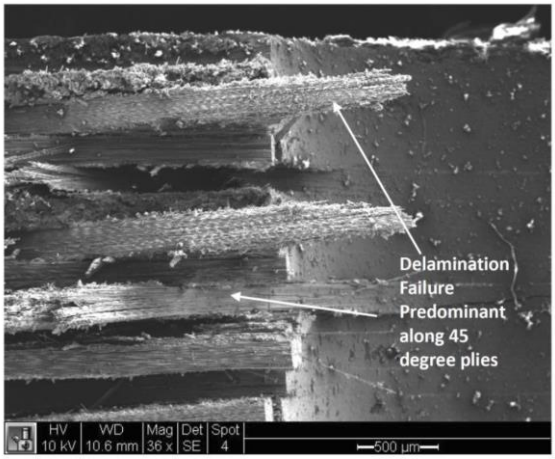

Figure 6.81 SEM of failed specimen from Open Hole Tensile Testing of PCD hole specimen (508 mm/min)

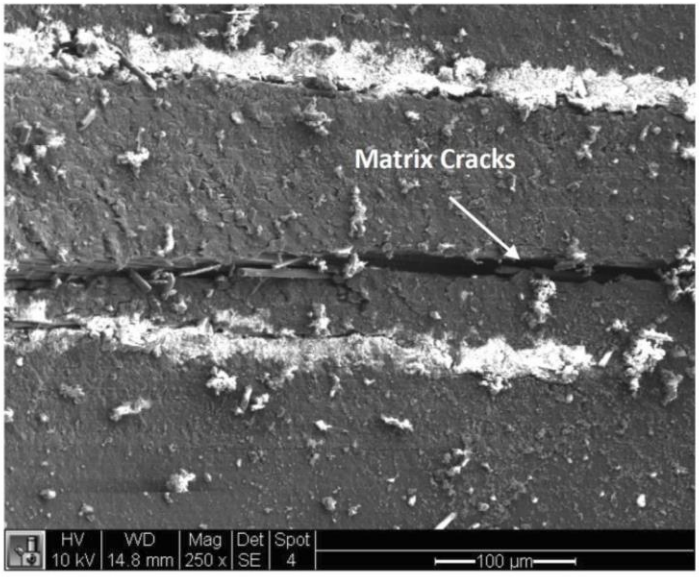

Figure 6.82 SEM of failed specimen showing Matrix Cracks from Open Hole Tensile Testing of PCD hole specimen (508 mm/min)

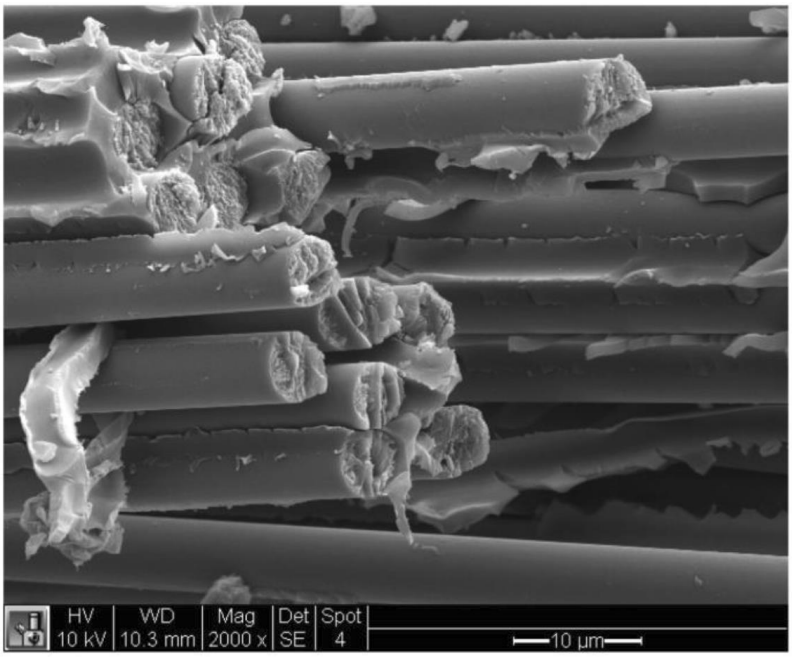

Figure 6.83 SEM of failed specimen showing Fibre Fractures from Open Hole Tensile Testing of PCD hole specimen (508 mm/min)

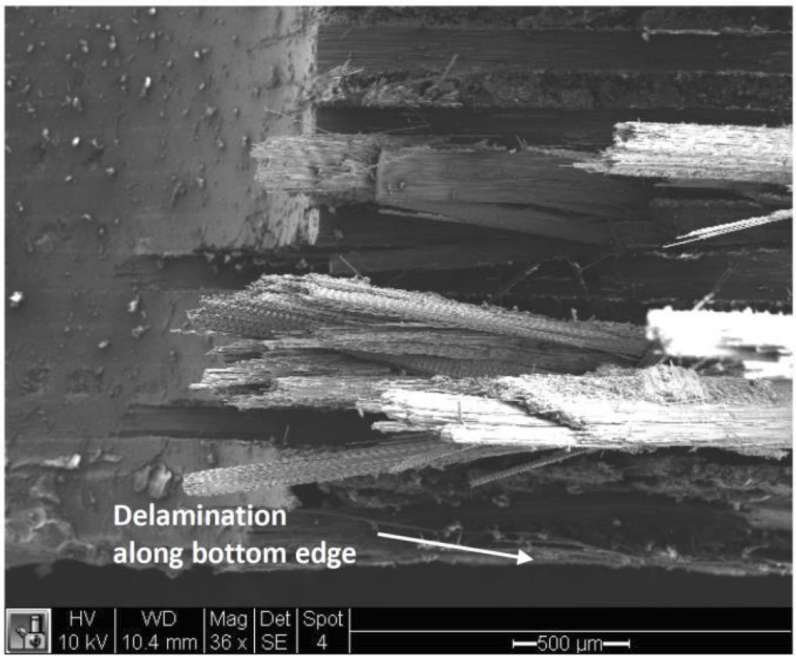

Figure 6.84 SEM of failed specimen showing Delamination from Open Hole Tensile Testing of PCD hole specimen (508 mm/min)

From the damage observations, it was noted that the damage initiation started at the 45 degree plies in the hole. The damage progressed along the various plies on the hole surface. The predominant failure was delamination along the 45 degree plies of the hole surface. Matrix cracks were present along the surface through the thickness of the laminate. Brittle fracture of fibres was observed in the failed specimens. Final failure of specimen was separation along 45 degrees across the thickness of the laminate. Fibre pullouts contributed to delamination initiation and progression starting at 45 degrees plies. Matrix cracking preceded delamination and aided in the final failure of the specimen. It was observed that the damage tolerance was lower than the PCD drilled holes at lower feedrates.

Open Hole Tensile Testing of CVD Drilled Hole at feedrate of 305 mm/min Specimens

CVD drilled holes at feedrate of 305 mm/min specimens were tested in open hole tension to failure. Figures 6.85, 6.86 & 6.87 show the data plots from the testing.

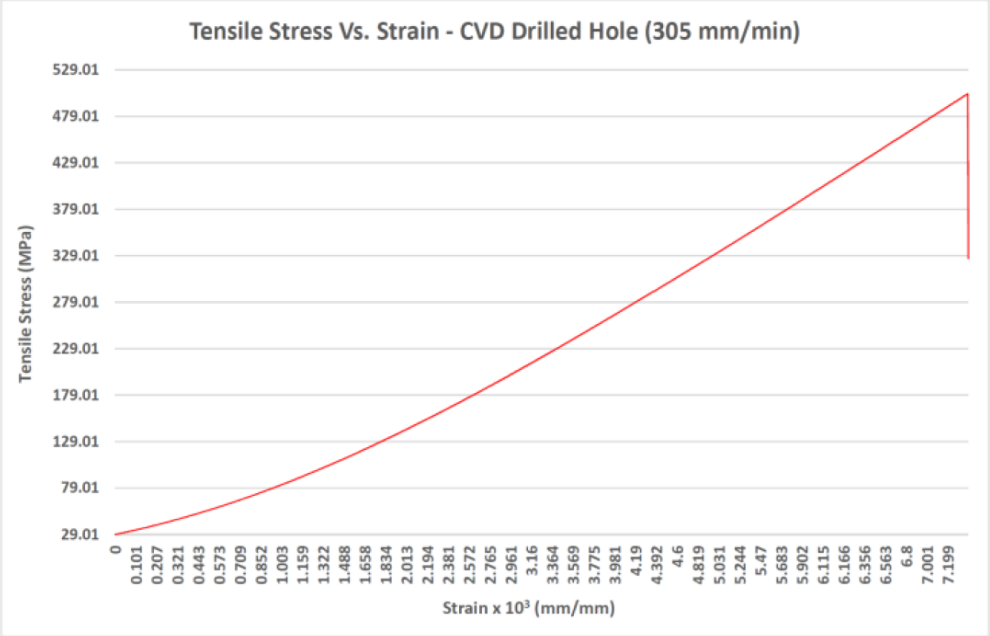

Figure 6.85 Open Hole Tensile Stress Vs. Strain for CVD Drilled Hole (305 mm/min)

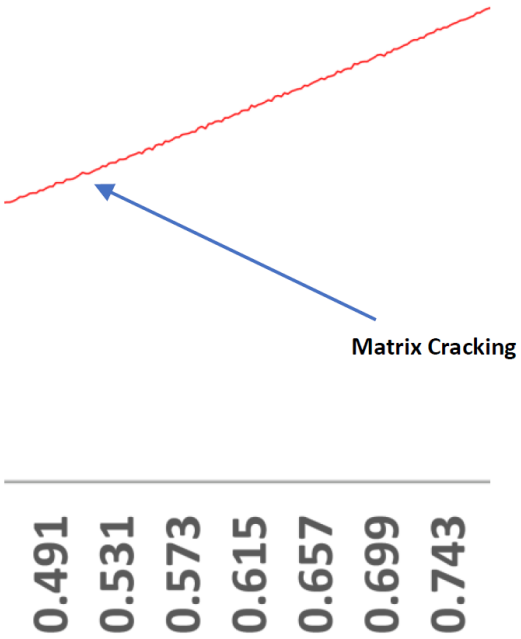

Figure 6.86 Magnified View of Open Hole Tensile Stress Vs. Strain showing Matrix Cracking in CVD Drilled hole specimen (305 mm/min)

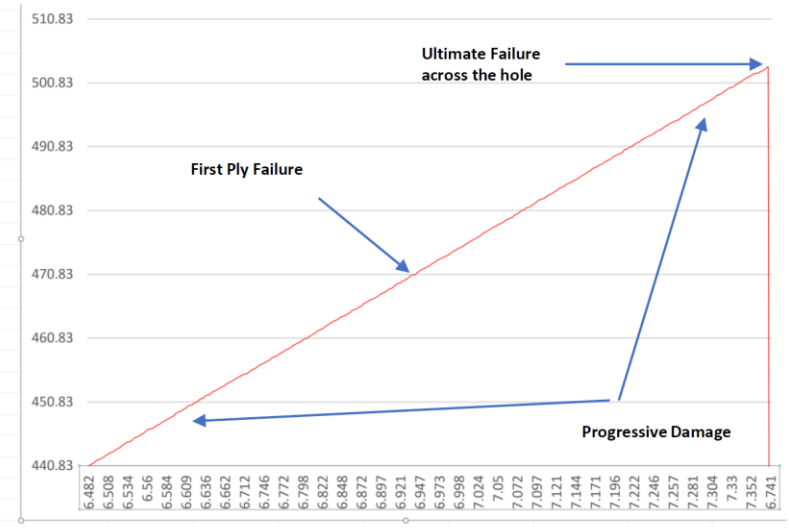

Figure 6.87 Magnified view of Open Hole Tensile Stress Vs. Strain showing First Ply Failure and Damage in CVD Drilled hole specimen (305 mm/min)

Test Data & Observations from Open Hole Tensile testing of CVD Drilled Hole at feedrate of 305 mm/min specimens

The following strength data was recoded from the open hole tensile testing of CVD Drilled hole at feedrate of 305 mm/min:

Maximum Open Hole Tensile Stress = 503.36 MPa

Maximum Open Hole Tensile Load = 57789 N

Strain at Maximum Open Hole Tensile Stress = 0.007065 mm/mm

Youngs Modulus from Testing = 71.2 GPa

It was observed that matrix cracking started around 0.05% strain. Matrix cracking progressed as stress increased and first ply failure occurred around tensile stress of 470.0 MPa. First ply failure occurred around 0.68% strain. It was observed that the subsequent ply failures (delamination) was smaller before ultimate failure pointing to a smaller damage tolerance. Failure zone initiated at the 45 degree plies in the hole with ultimate failure occurring across the complete hole. It was also observed that delamination progressed faster due to higher density of fibre pullouts

compared to lower drilling feedrate specimens. Damage tolerance was also lower than PCD drilled holes.

Damage observations from open hole tensile testing of CVD Drilled hole at 305 mm/min specimens

Figures 6.88 through 6.92 show the damage recorded in open hole tensile testing of CVD drilled hole at feedrate of 305 mm/min specimens.

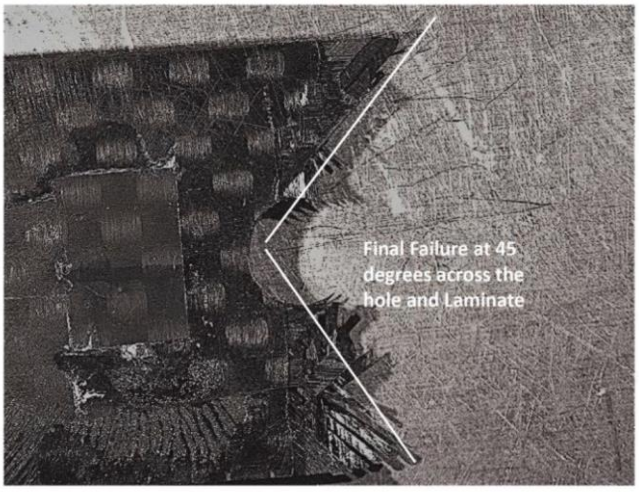

Figure 6.88 Failed specimen from Open Hole Tensile testing of CVD hole specimen (305 mm/min)

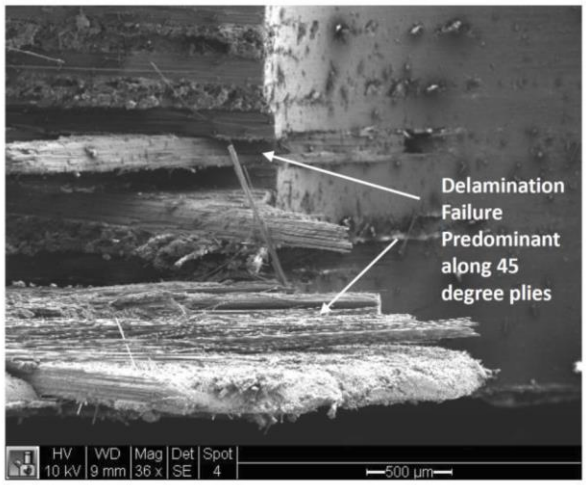

Figure 6.89 SEM of failed specimen from Open Hole Tensile Testing of CVD hole specimen (305 mm/min)

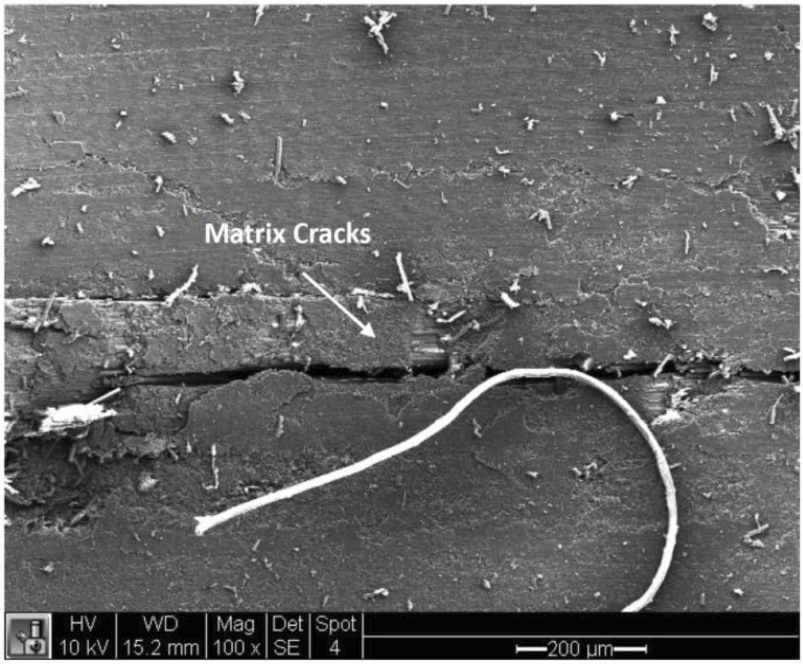

Figure 6.90 SEM of failed specimen showing Matrix Cracks from Open Hole Tensile Testing of CVD hole specimen (305 mm/min)

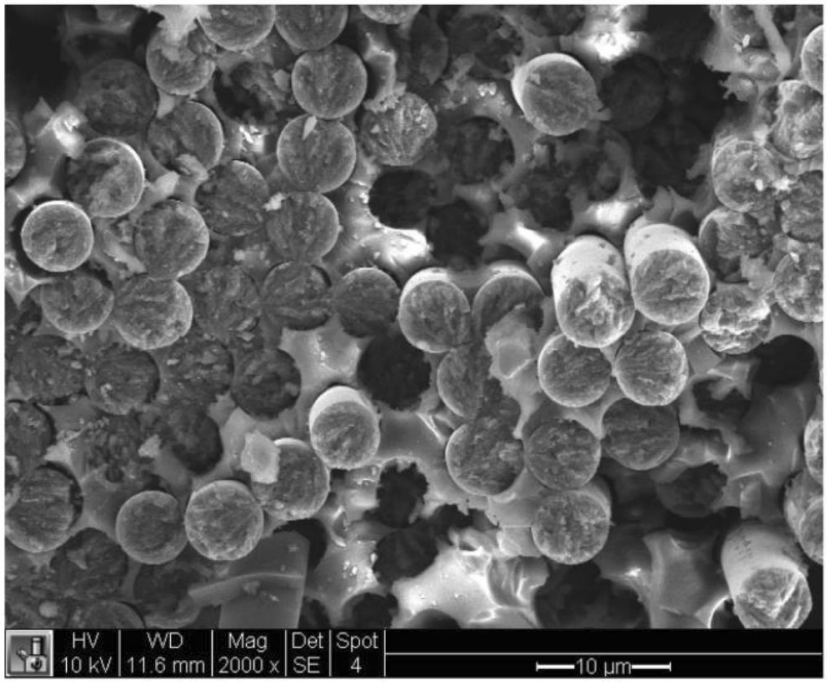

Figure 6.91 SEM of failed specimen showing Fibre Fractures from Open Hole Tensile Testing of CVD hole specimen (305 mm/min)

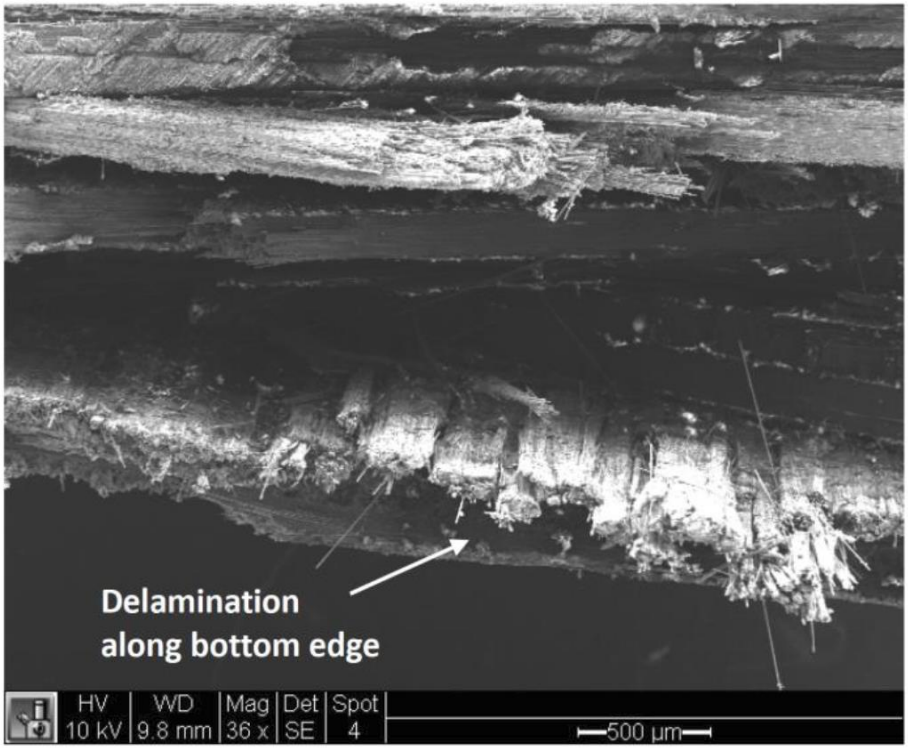

Figure 6.92 SEM of failed specimen showing Delamination from Open Hole Tensile Testing of CVD hole specimen (305 mm/min)

From the damage observations it was noted that damage initiated at the 45 degree plies in the hole. Damage progressed along the various plies on the hole surface. Predominant failure was delamination along the 45 degree plies of the hole surface. Matrix cracks were present along the hole surface through the thickness of the laminate. Brittle fracture of fibres was observed in the failed specimens. Final failure of specimen was separation along 45 degrees across the thickness of the laminate. Fibre pullouts contributed to delamination initiation and progression starting at 45 degree plies. Matrix cracking preceded delamination and aided in final failure. Damage tolerance was lower as compared to PCD drilled holes.

Open Hole Tensile Testing of CVD Drilled Hole at feedrate of 508 mm/min Specimens

CVD drilled holes at feedrate of 508 mm/min specimens were tested in open hole tension to failure. Figures 6.93, 6.94 & 6.95 show the data plots from the testing.

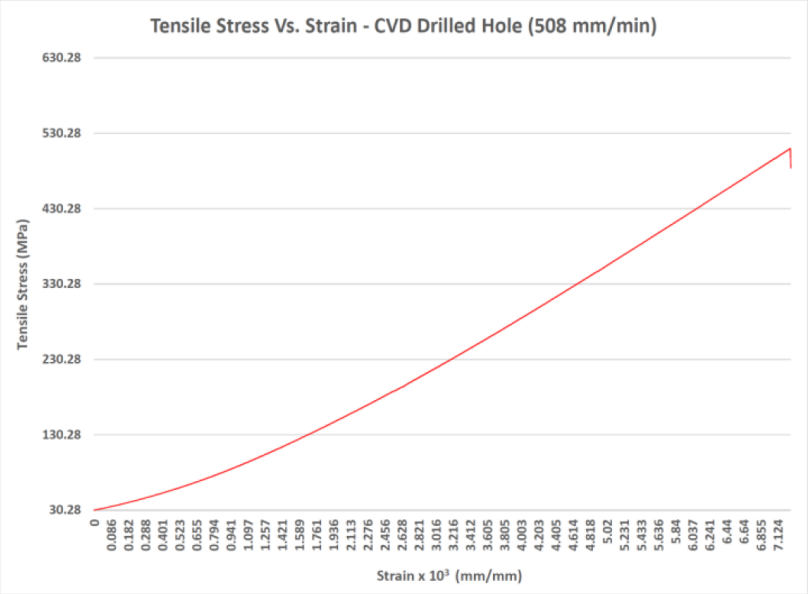

Figure 6.93 Open Hole Tensile Stress Vs. Strain for CVD Drilled Hole (508 mm/min)

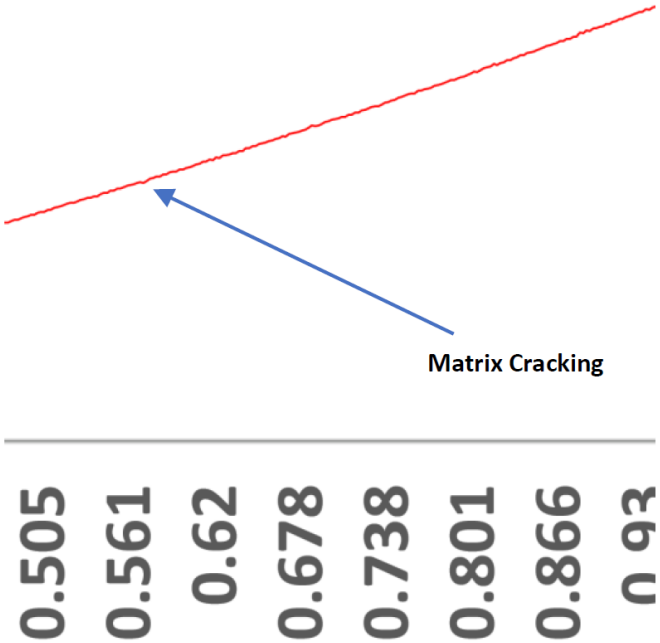

Figure 6.94 Magnified View of Open Hole Tensile Stress Vs. Strain showing Matrix Cracking in CVD Drilled hole specimen (508 mm/min)

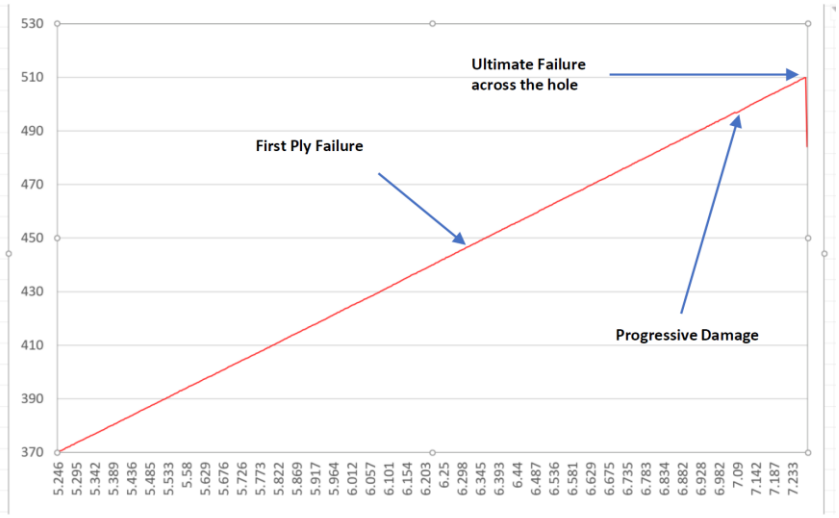

Figure 6.95 Magnified view of Open Hole Tensile Stress Vs. Strain showing First Ply Failure and Damage in CVD Drilled hole specimen (508 mm/min)

Test Data & Observations from Open Hole Tensile testing of CVD Drilled Hole at feedrate of 508 mm/min specimens

The following strength data was recoded from the open hole tensile testing of CVD Drilled hole at feedrate of 508 mm/min:

Maximum Open Hole Tensile Stress = 509.94 MPa

Maximum Open Hole Tensile Load = 58545 N

Strain at Maximum Open Hole Tensile Stress = 0.007267 mm/mm

Youngs Modulus from Testing = 70.2 GPa

It was observed that matrix cracking started around 0.056% strain. Matrix cracking progressed as stress increased and first ply failure occurred around tensile stress of 445.0 MPa. First ply failure occurred around 0.63% strain. It was observed that the subsequent ply failures (delamination) was smaller before ultimate failure pointing to a smaller damage tolerance. Failure zone initiated at the 45 degree plies in the hole with ultimate failure occurring across the complete hole. It was also observed that delamination progressed faster due to higher density of fibre pullouts

compared to lower drilling feedrate specimens. Damage tolerance was also lower than PCD drilled holes and CVD drilled with lower feedrate.

Damage observations from open hole tensile testing of CVD Drilled hole at 305 mm/min specimens

Figures 6.96 through 6.100 show the damage recorded in open hole tensile testing of CVD drilled hole at feedrate of 508 mm/min specimens.

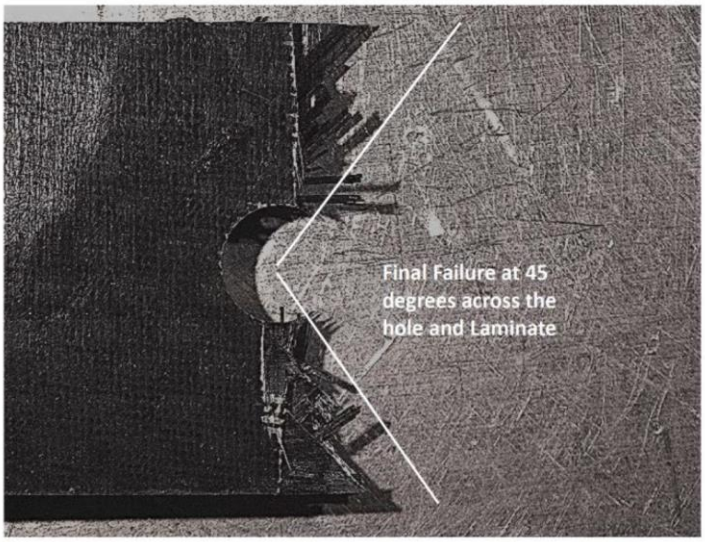

Figure 6.96 Failed specimen from Open Hole Tensile testing of CVD hole specimen (508 mm/min)

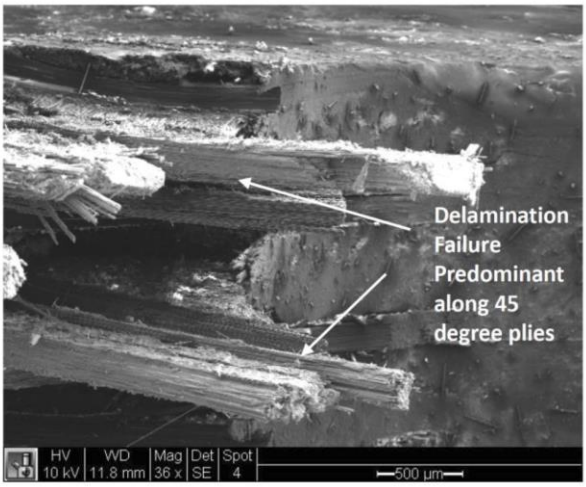

Figure 6.97 SEM of failed specimen from Open Hole Tensile Testing of CVD hole specimen (508 mm/min)

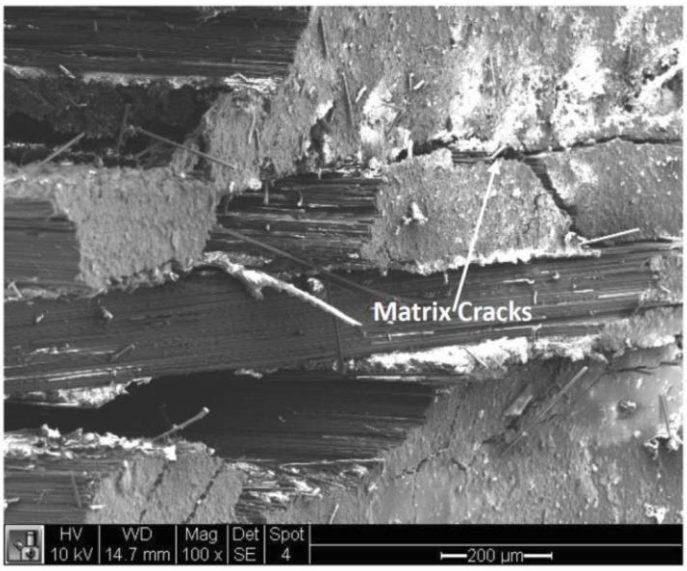

Figure 6.98 SEM of failed specimen showing Matrix Cracks from Open Hole Tensile Testing of CVD hole specimen (508 mm/min)

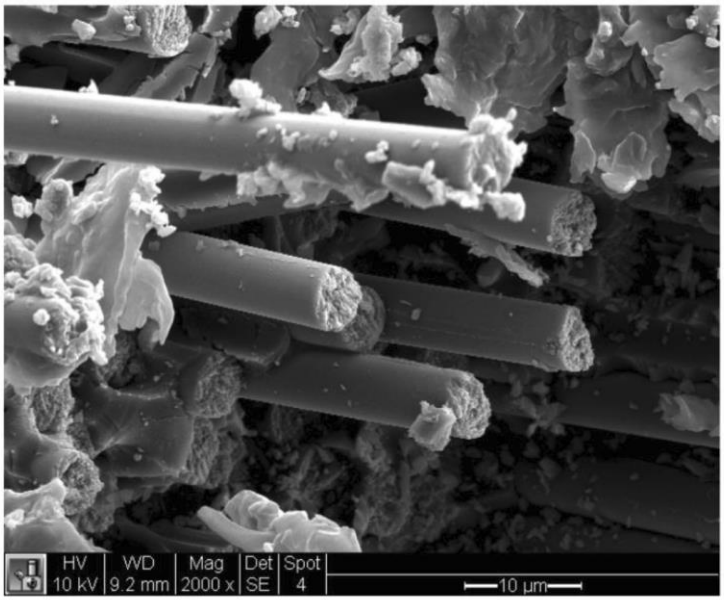

Figure 6.99 SEM of failed specimen showing Fibre Fractures from Open Hole Tensile Testing of CVD hole specimen (508 mm/min)

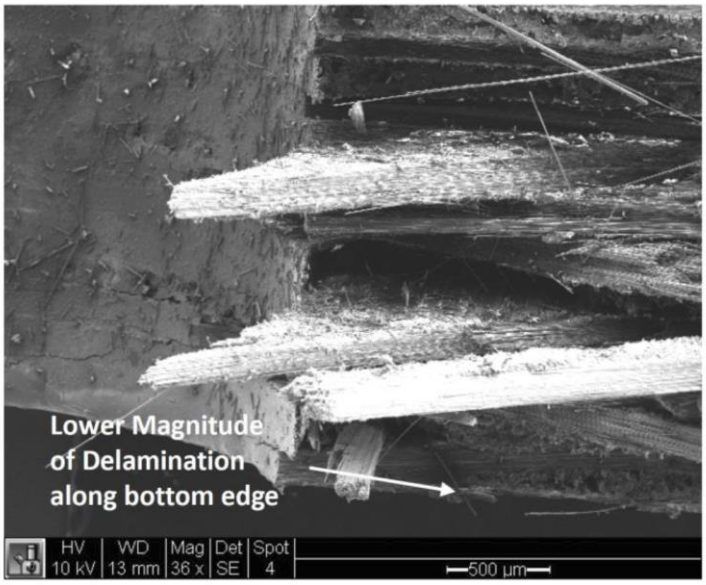

Figure 6.100 SEM of failed specimen showing Delamination from Open Hole Tensile Testing of CVD hole specimen (508 mm/min)

From the damage observations it was noted that damage initiated at the 45 degree plies in the hole. Damage progressed along the various plies on the hole surface. Predominant failure was delamination along the 45 degree plies of the hole surface. Matrix cracks were present along the hole surface through the thickness of the laminate. Brittle fracture of fibres was observed in the failed specimens. Final failure of specimen was separation along 45 degrees across the thickness of the laminate. Fibre pullouts contributed to delamination initiation and progression starting at 45 degree plies. Matrix cracking preceded delamination and aided in final failure. Damage tolerance was lower as compared to PCD drilled holes. Delamination at bottom edge was lower in magnitude compared to PCD drilled holes.

Summary of Open Hole Tensile Strength Testing Results. Observations & Conclusions

Open Hole Tensile testing results were summarized and are shown in Table 6.8 along with surface roughness data. An example calculation of stress concentration factor is shown in Figure 6.103 This calculation using the notch root radius and formula shown in equation 2.4 in chapter 2 of this work. The calculation along with the graphical determination of the notch root radius is shown in Figure 6.101 and Figure 6.103 along with the surface finish values. The input values of

the surface finish are shown in Figure 6.101. Figure 6.104 shows the surface profile used for the graphical determination of the notch root radius.

Specimen Type	Average Surface Finish - R_a (µm)	Surface Finish – R_z (µm)	Surface Finish – R_t (µm)	Calculated Effective Stress Concentration Factor $\bar{K}_t$	Max Tensile Stress (MPa)	Strain (mm/mm)	Youngs Modulus E_x (GPa)	Matrix Cracking Initiation – % Strain	First Ply Failure – Tensile Stress – (MPa)	First Ply Failure – % Strain
PCD Drill – F1	0.445	2.91	6.15	1.75	518.38	0.007023	73.8	0.12	420.0	0.57
PCD Drill – F2	0.342	2.81	5.365	1.92	444.35	0.006197	71.7	0.07	395.0	0.54
CVD Drill – F1	0.965	5.632	11.597	2.45	503.36	0.007065	71.2	0.05	470.0	0.68
CVD Drill – F2	0.890	5.172	11.38	2.88	509.94	0.007267	70.2	0.056	445.0	0.63

Table 6.8 Summary of Open Hole Tensile Testing Results

Specimen Name	Hole	Surface Finish (L) - R_a	Surface Finish (L) - R_z	Surface Finish (L) - R_t
Specimen 2	PCD Drill - F = 305 mm/min	0.770	3.875	9.51

Figure 6.101 Sample Surface finish data for a PCD drill hole at feedrate of 305 mm/min specimen for stress concentration factor calculation

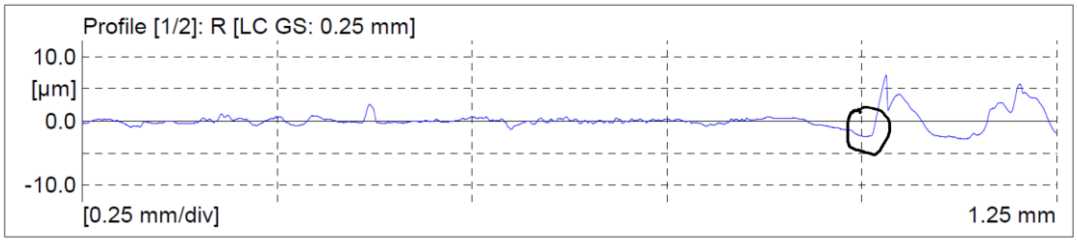

Figure 6.102 Sample Surface profile data for a PCD drill hole at a feedrate of 305 mm/min for stress concentration factor calculation

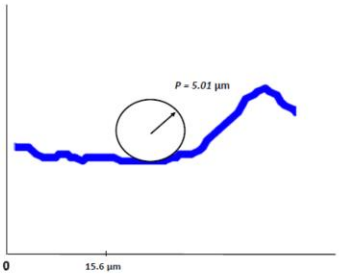

$$\overline{K_t} = 1 + \eta\left(\frac{R_a}{\overline{\rho}}\right)\left(\frac{R_t}{R_z}\right) \text{ where}$$

$\eta = factor = 2(tension \,\&\, compression)$
$\overline{\rho} = notch\ root\ radius$
$R_a = average\ surface\ roughness$
$R_t = peak\ to\ valley\ height\ roughness$
$R_z = 10\ point\ roughness$

Notch Root Radius – Graphical Calculation for a PCD Drilled (305 mm/min) Specimen

Figure 6.103 Sample stress concentration factor calculation for a PCD drill hole at a feedrate of 305 mm/min feedrate specimen

Observations from Surface Integrity plots of Open Hole Tensile Testing

Surface integrity data was calculated and plots created from the surface roughness data. The plots show that the higher stress concentration factor resulted in larger reduction in stiffness compared to theoretical modulus (stiffness). Stress concentration factor is a function of surface finish parameters R_a , R_z, R_t Generally the higher the surface roughness, R_a , the large reduction in stiffness. The ratio R_z / R_t influences the reduction in stiffness. The larger the ratio the greater the reduction in stiffness. This is attributed to the larger values of the highest peaks and deepest valleys in the surface profiles. This leads to an increase in number of points of stress risers which lead to stiffness reduction and load carrying capacity. Drilling feedrate did not influence the average surface roughness or other parameters in CVD drilling. In PCD drilling, the change in feedrates influenced a larger change in surface integrity parameters as well as strength properties. Figure 6.104, 6.105 & 6.106 show the plots of various surface finish parameters Vs. the ratio of tested modules to theoretical apparent modulus (E / E_0)

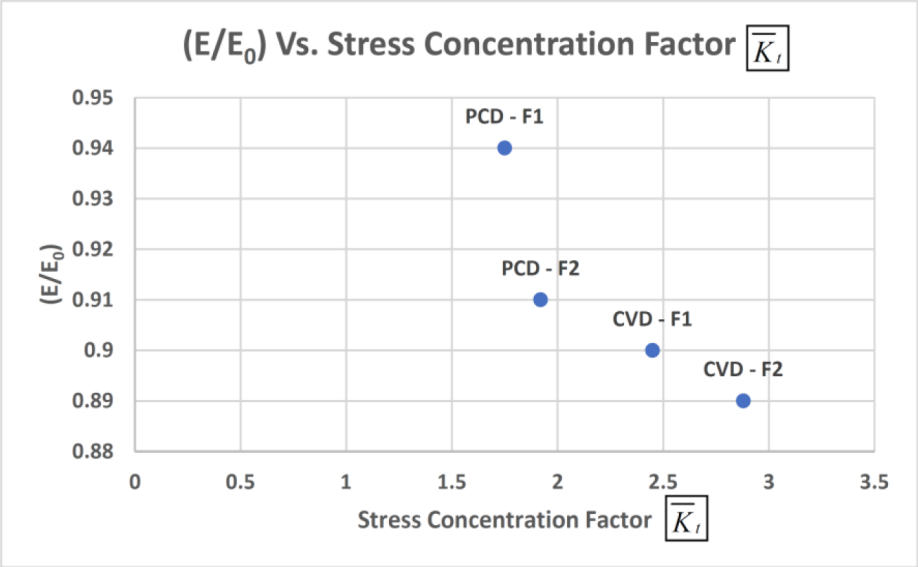

Figure 6.104 Plot of (E/E_0) Vs. Stress Concentration Factor for various Open hole Tensile Testing specimens

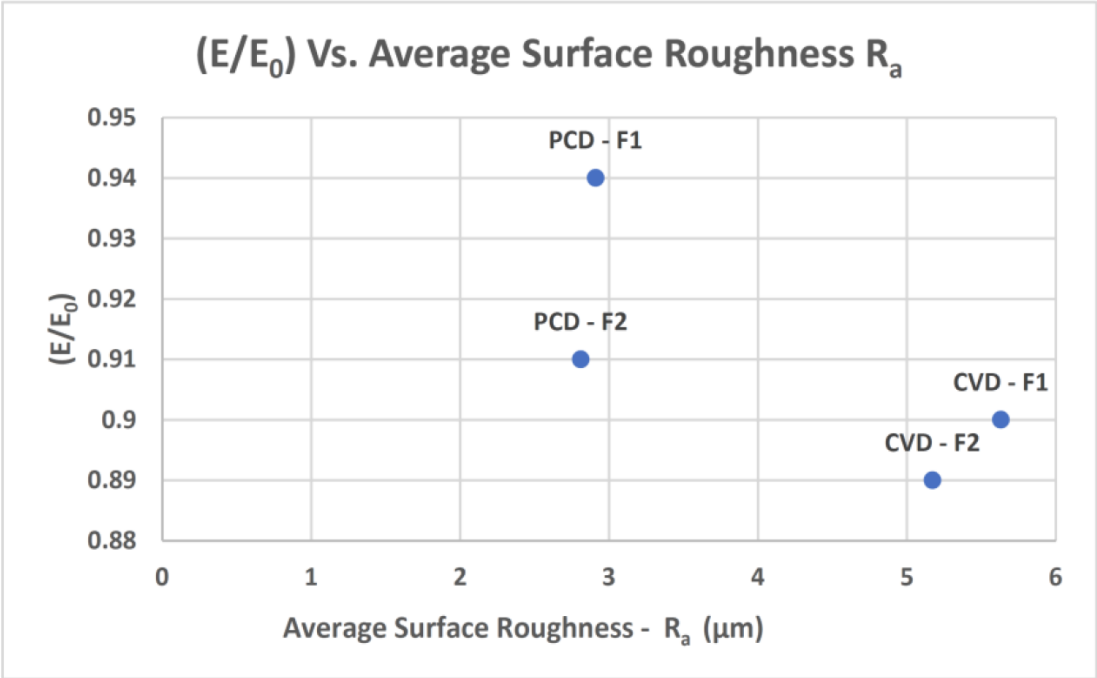

Figure 6.105 Plot of (E/E_0) Vs. Average Surface Roughness - R_a (µm) for various Open Hole Tensile Testing specimens

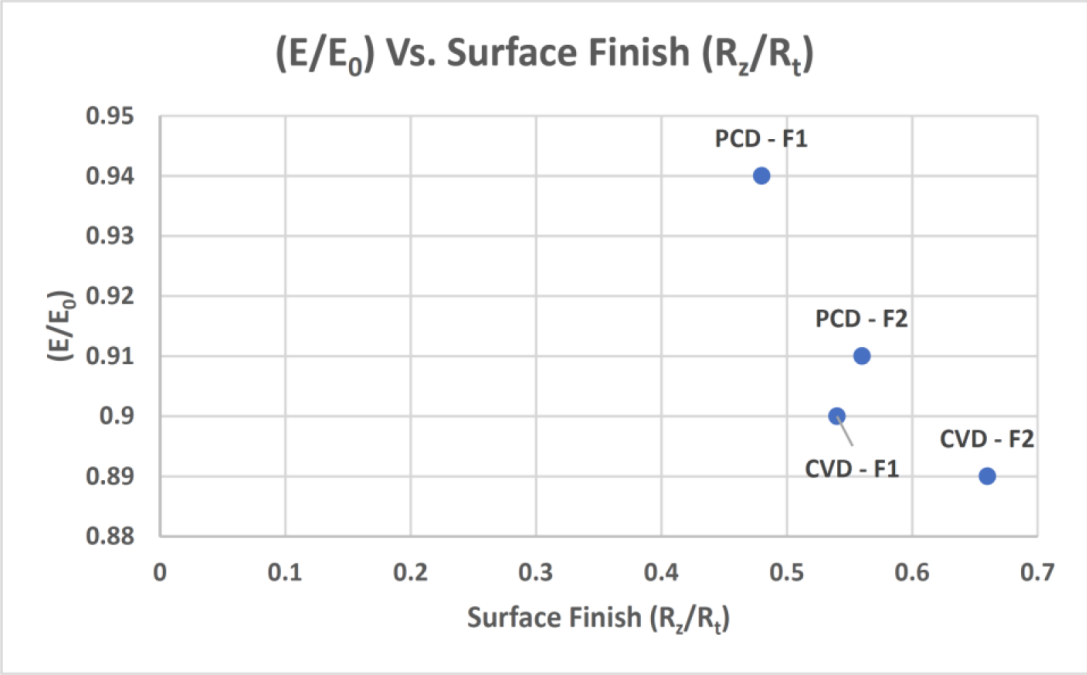

Figure 6.106 Plot of (E/E_0) Vs. Surface Finish (R_z / R_t) for various Open Hole Tensile Testing specimens

Observations from Damage Progress Plot for Open Hole Tensile Testing

Damage progress plot Vs. applied load was generated as shown in Figure 6.107 and it was observed that the drilled holes had damage start at lower loads for lower feedrate as compared to the higher feedrate. This was attributed to the longer contact time of the drill in the hole which contributed to the matrix cracking initiation. Both the PCD specimens had slightly higher damage as compared to the CVD drilled holes. This was contributed to larger magnitude of delamination at the bottom surface of the hole. The PCD drill has a 118 degree point angle as compared to 90 degree point angle of the CVD drill. This contributes to the larger delamination at the bottom surface of the hole. The progress of damage was similar in all specimens with matrix cracking being the dominant mode of damage initially. The transition of damage from matrix cracking to delamination followed a similar pattern for all PCD and CVD drilled hole specimens. Damage tolerance of CVD specimens is slightly lower in comparison to PCD drilled specimens. For both PCD and CVD drilled hole specimens, the damage tolerance is lower in specimens drilled at higher feedrates. All specimens displayed a sudden increase in damage showing the progression of damage from hole to across the width of the laminate. Ply damage

across the hole for all specimens displayed a similar path of progression. The reduction in stiffness for all drilled holes by PCD and CVD was close to each other within 5%

Damage = $1 - (E/E_0)$

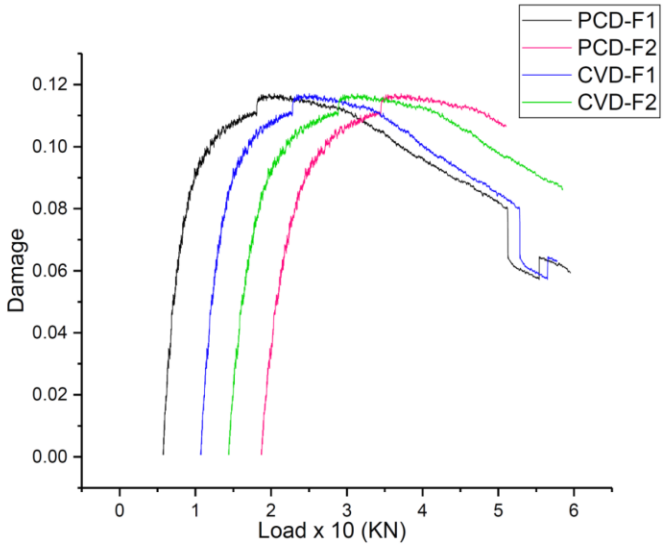

Figure 6.107 Damage Vs. Applied Load for Open Hole Tensile Testing specimens

6.4.5.1 Analysis of Open Hole Tension Testing Results

As seen from the above results there is a drop in the stiffness from the theoretical apparent stiffness calculations. This can be attributed to resultant surface integrity from varying drilling operations conducted. Test specimens drilled with PCD drills displayed better surface finish profile characteristics.

The reduction in stiffness is a function of the surface integrity and the resultant stress concentration factor from surface integrity of the drilled hole.

$$\frac{E}{E_0} = f(\overline{K}_t) \qquad 6.1$$

When the value of the stress concentration factor $(\overline{K}_t)$ is higher, the value of $\left(\frac{E}{E_0}\right)$ is lower

When the value of $\left(\frac{R_z}{R_t}\right)$ is higher, the value of $\left(\frac{E}{E_0}\right)$ is lower.

The maximum tensile stress is a function of both the hole concentration factor (K_t) as well as the surface integrity concentration factor of the hole $(\overline{K}_t)$

$$\sigma_{\max} = f(K_t, \overline{K}_t) \qquad 6.2$$

The maximum tensile stress in open hole tension testing is about 30% to 40% less than maximum tensile stress in tension testing. The presence of an hole (notch) in the specimen results in a stress concentration factor with the presence of a notch.

6.4.6 Open Hole Compression Testing

Both PCD and CVD drilled specimens were tested in open hole compression and the results were tabulated. The specimens were drilled with 2 different feedrates 305 mm/min and 508 mm/min. Strain gauges were used to capture the strain under open hole tension loading conditions. All the specimens were taken to failure during the testing process. The following tables and figures show the data along with the stress-strain curves and failure for both the PCD and CVD drilled hole specimens

Open Hole Compression Testing of PCD Drilled Hole at feedrate of 305 mm/min Specimens

PCD drilled holes at feedrate of 305 mm/min specimens were tested in open hole compression to failure. Figures 6.108, 6.109 & 6.110 show the data plots from the testing.

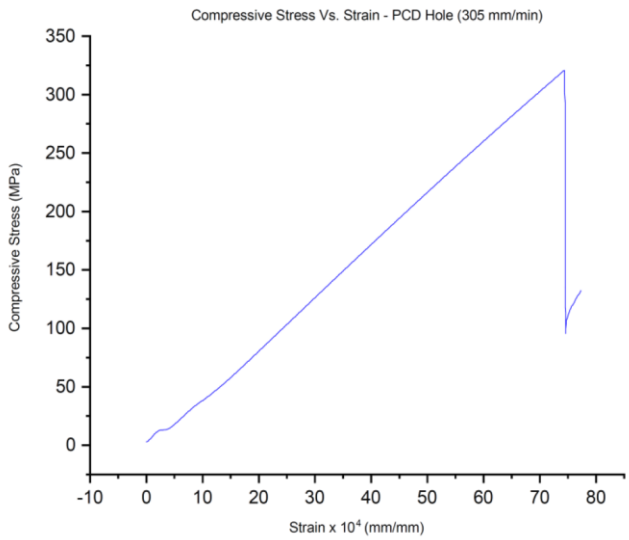

Figure 6.108 Open Hole Compressive Stress Vs. Strain for PCD Drilled Hole (305 mm/min)

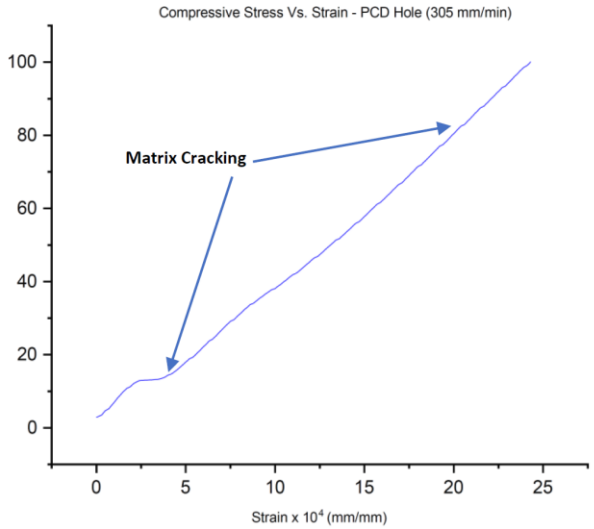

Figure 6.109 Magnified View of Open Hole Compressive Stress Vs. Strain showing Matrix Cracking in PCD Drilled hole specimen (305 mm/min)

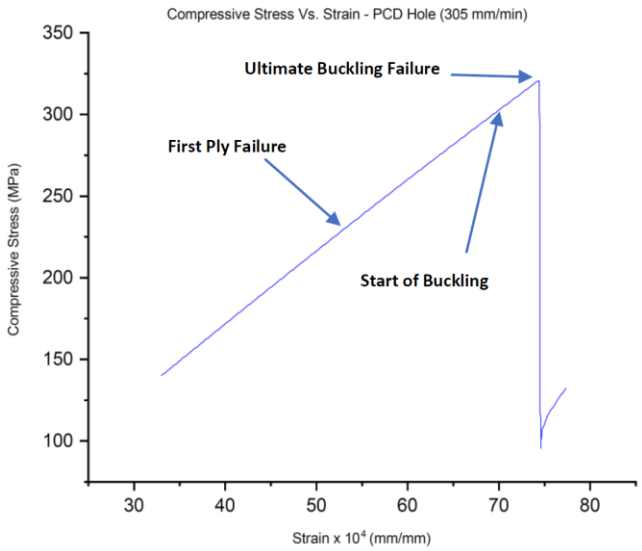

Figure 6.110 Magnified view of Open Hole Compressive Stress Vs. Strain showing First Ply Failure and Damage in PCD Drilled hole specimen (305 mm/min)

Test Data & Observations from Open Hole Compression testing of PCD Drilled Hole at feedrate of 305 mm/min specimens

The following strength data was recoded from the open hole compressive testing of PCD Drilled hole at feedrate of 305 mm/min:

Maximum Open Hole Compressive Stress = 320.8 MPa

Maximum Open Hole Compressive Load = 53892.9 N

Strain at Maximum Open Hole Tensile Stress = 0.00744 mm/mm

Youngs Modulus from Testing = 45.15 GPa

It was observed that matrix cracking started around 0.035% strain. Matrix cracking progressed as stress increased and first ply failure occurred around tensile stress of 240.0 MPa. First ply failure occurred around 0.055% strain. It was observed that failure zone initiated at 45 degree plies in the hole and ultimately resulted in failure across the complete hole. Final failure was buckling across the thickness of the laminate.

Damage observations from Open Hole Compression testing of PCD Drilled hole at 305 mm/min specimens

Figures 6.111 through 6.115 show the damage recorded in open hole compressive testing of PCD drilled hole at feedrate of 305 mm/min specimens.

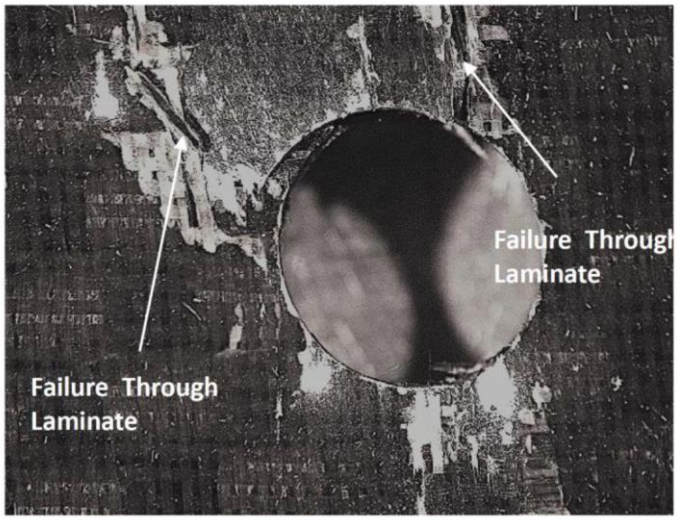

Figure 6.111 Failed specimen from Open Hole Compression testing of PCD hole specimen (305 mm/min)

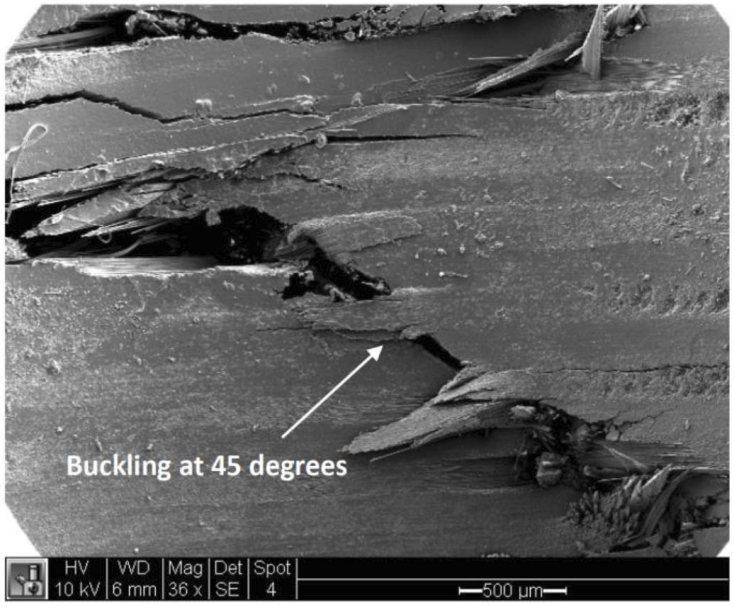

Figure 6.112 SEM of failed specimen from Open Hole Compression Testing of PCD hole specimen (305 mm/min)

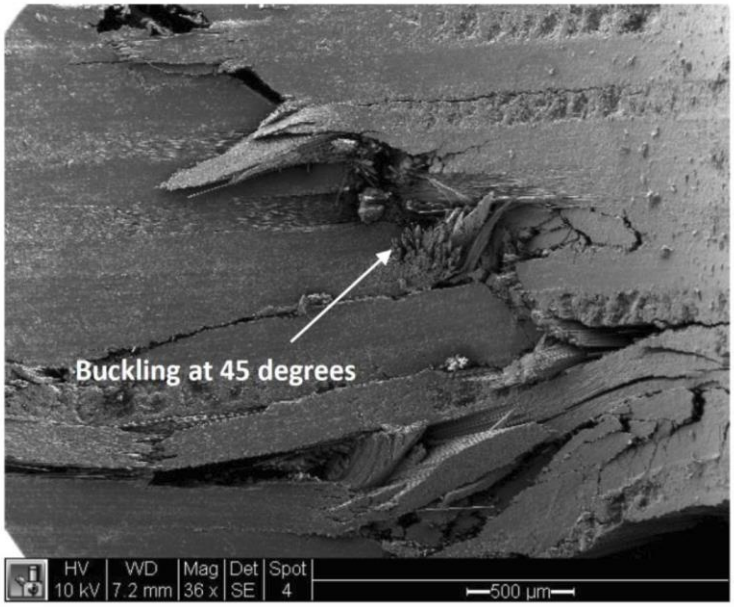

Figure 6.113 SEM of failed specimen showing buckling at 45 degrees from Open Hole Compression Testing of PCD hole specimen (305 mm/min)

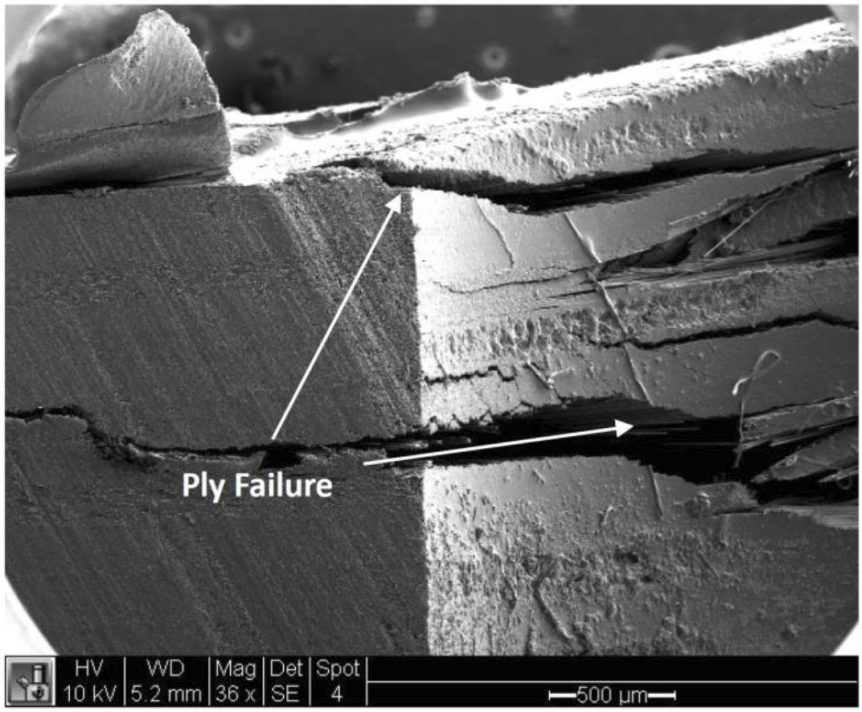

Figure 6.114 SEM of failed specimen showing Ply Failure from Open Hole Compression Testing of PCD hole specimen (305 mm/min)

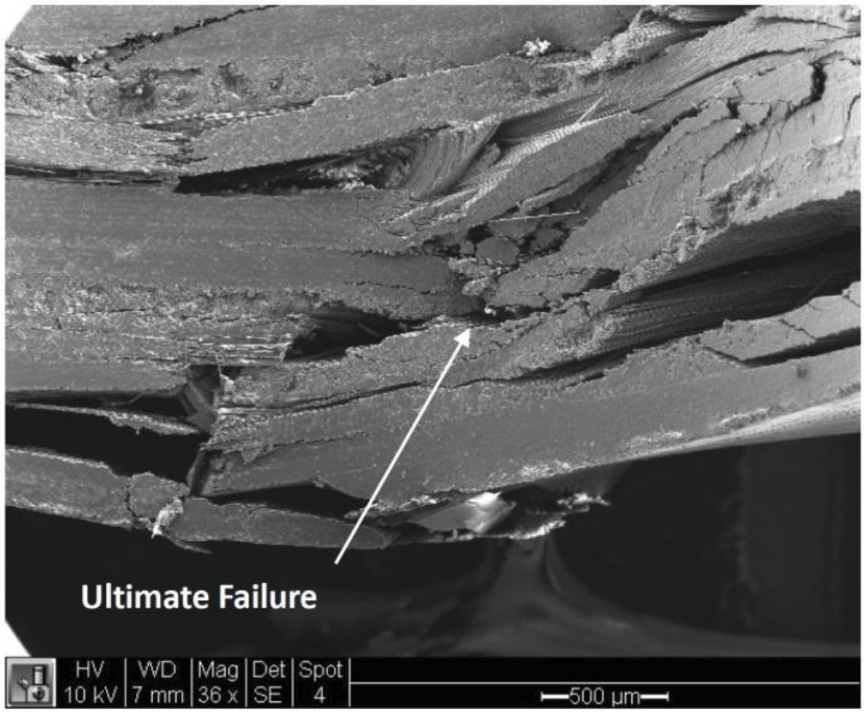

Figure 6.115 SEM of failed specimen showing Ultimate failure from Open Hole Compression Testing of PCD hole specimen (305 mm/min)

From the damage observations, it was noted that the damage initiation started at the 45 degree plies in the hole. The damage progressed along the various plies on the hole surface. The predominant failure was buckling along the 45 degree plies of the hole surface. Matrix cracks were present along the surface through the thickness of the laminate. Brittle fracture of fibres was observed in the failed specimens. Final failure of specimen was separation along 45 degrees across the thickness of the laminate. Fibre pullouts contributed to delamination initiation and progression starting at 45 degrees plies. Matrix cracking preceded delamination and aided in the final failure of the specimen.

Open Hole Compression Testing of PCD Drilled Hole at feedrate of 508 mm/min Specimens

PCD drilled holes at feedrate of 508 mm/min specimens were tested in open hole compression to failure. Figures 6.116, 6.117 & 6.118 show the data plots from the testing.

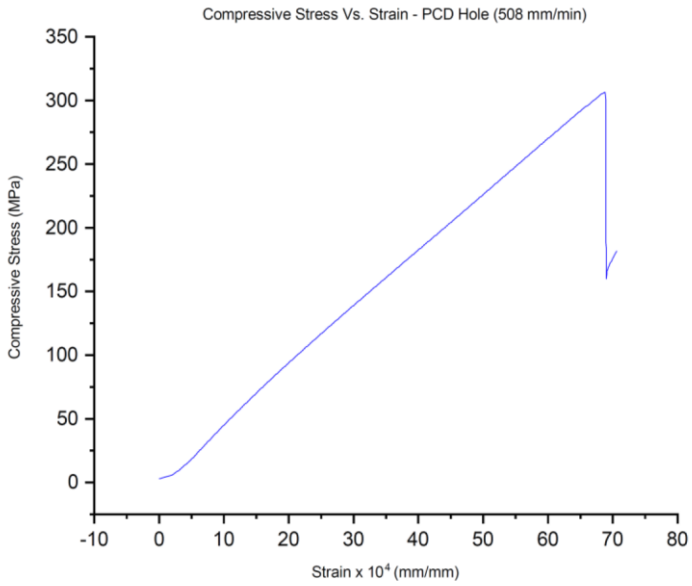

Figure 6.116 Open Hole Compressive Stress Vs. Strain for PCD Drilled Hole (508 mm/min)

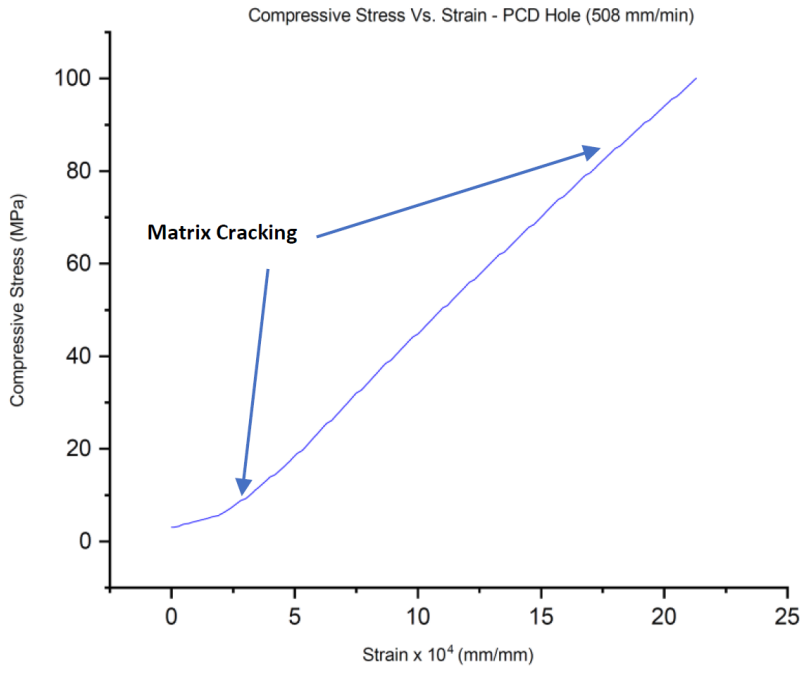

Figure 6.117 Magnified View of Open Hole Compressive Stress Vs. Strain showing Matrix Cracking in PCD Drilled hole specimen (508 mm/min)

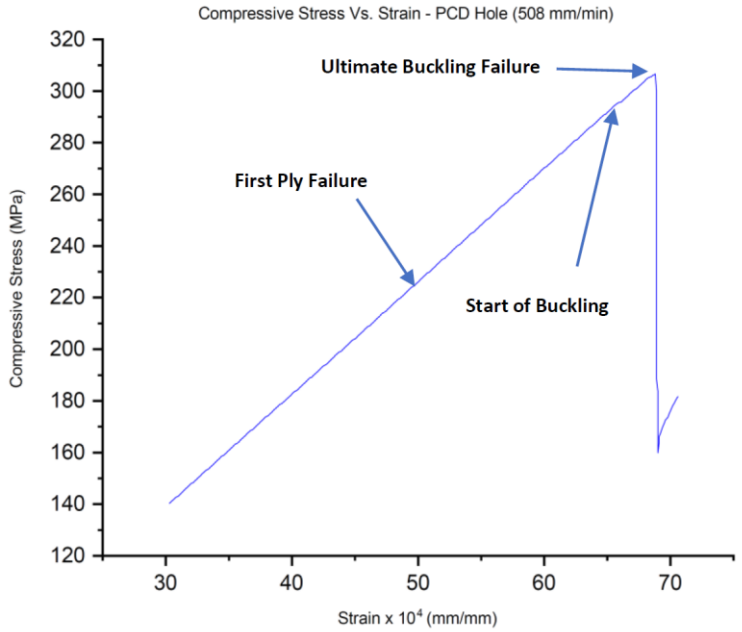

Figure 6.118 Magnified view of Open Hole Compressive Stress Vs. Strain showing First Ply Failure and Damage in PCD Drilled hole specimen (508 mm/min)

Test Data & Observations from Open Hole Compression testing of PCD Drilled Hole at feedrate of 508 mm/min specimens

The following strength data was recoded from the open hole compressive testing of PCD Drilled hole at feedrate of 508 mm/min:

Maximum Open Hole Compressive Stress = 306.6MPa

Maximum Open Hole Compressive Load = 51514.7 N

Strain at Maximum Open Hole Tensile Stress = 0.00688 mm/mm

Youngs Modulus from Testing = 46.09 GPa

It was observed that matrix cracking started around 0.025% strain. Matrix cracking progressed as stress increased and first ply failure occurred around tensile stress of 230.0 MPa. First ply failure occurred around 0.051% strain. It was observed that failure zone initiated at 45 degree plies in the hole and ultimately resulted in failure across the complete hole. Final failure was buckling across the thickness of the laminate.

Damage observations from open hole compression testing of PCD Drilled hole at 508 mm/min specimens

Figures 6.119 through 6.123 show the damage recorded in open hole compressive testing of PCD drilled hole at feedrate of 508 mm/min specimens.

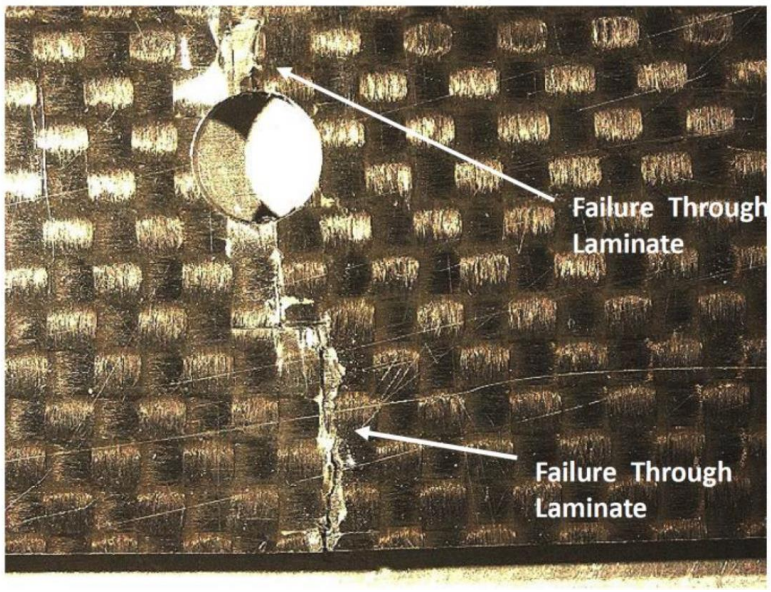

Figure 6.119 Failed specimen from Open Hole Compression testing of PCD hole specimen (508 mm/min)

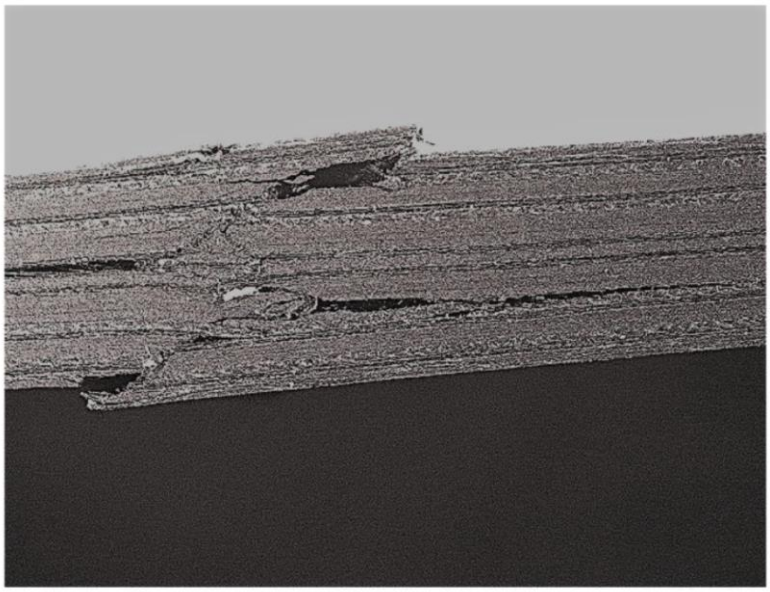

Figure 6.120 Failed specimen from Open Hole Compression testing of PCD hole specimen (508 mm/min)

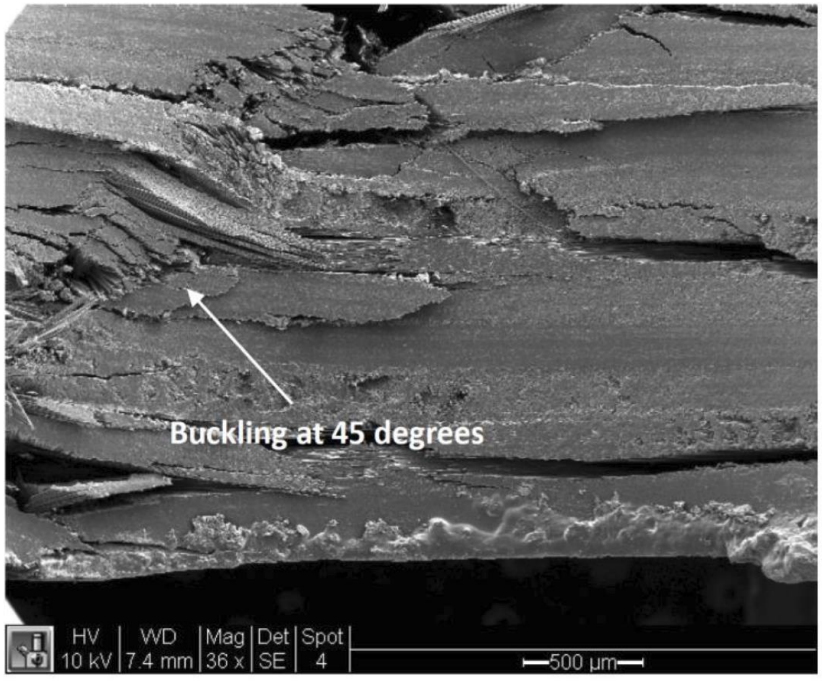

Figure 6.121 SEM of failed specimen showing buckling at 45 degrees from Open Hole Compression Testing of PCD hole specimen (508 mm/min)

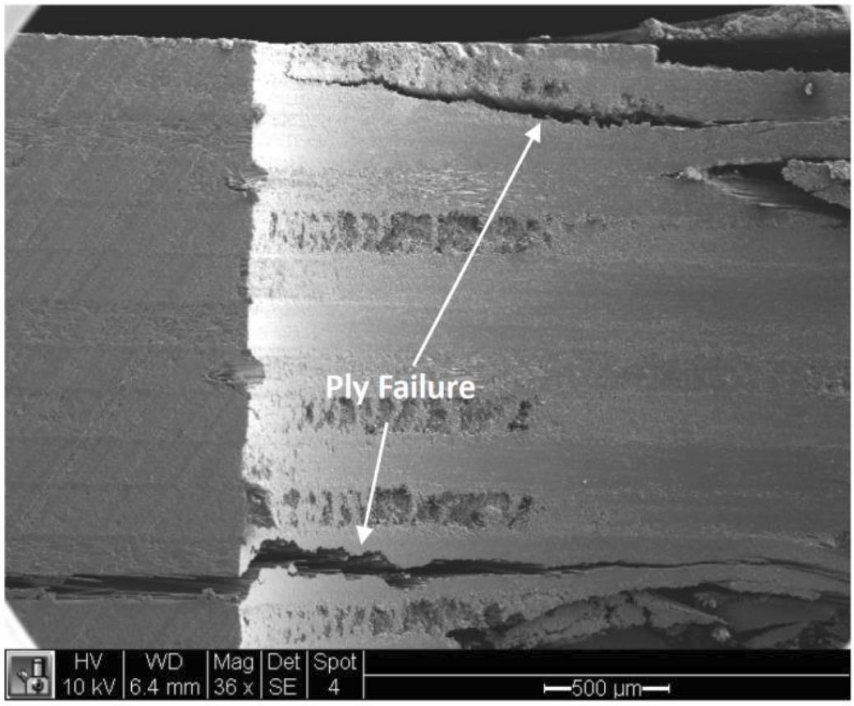

Figure 6.122 SEM of failed specimen showing Ply Failure from Open Hole Compression Testing of PCD hole specimen (508 mm/min)

Figure 6.123 SEM of failed specimen showing Ultimate failure from Open Hole Compression Testing of PCD hole specimen (508 mm/min)

From the damage observations, it was noted that the damage initiation started at the 45 degree plies in the hole. The damage progressed along the various plies on the hole surface. The predominant failure was buckling along the 45-degree plies of the hole surface. Matrix cracks were present along the surface through the thickness of the laminate. Brittle fracture of fibres was observed in the failed specimens. Final failure of specimen was separation along 45 degrees across the thickness of the laminate. Fibre pullouts contributed to delamination initiation and progression starting at 45 degrees plies. Matrix cracking preceded delamination and aided in the final failure of the specimen.

Open Hole Compression Testing of CVD Drilled Hole at feedrate of 305 mm/min Specimens

CVD drilled holes at feedrate of 305 mm/min specimens were tested in open hole compression to failure. Figures 6.124, 6.125 , & 6.126 show the data plots from the testing.

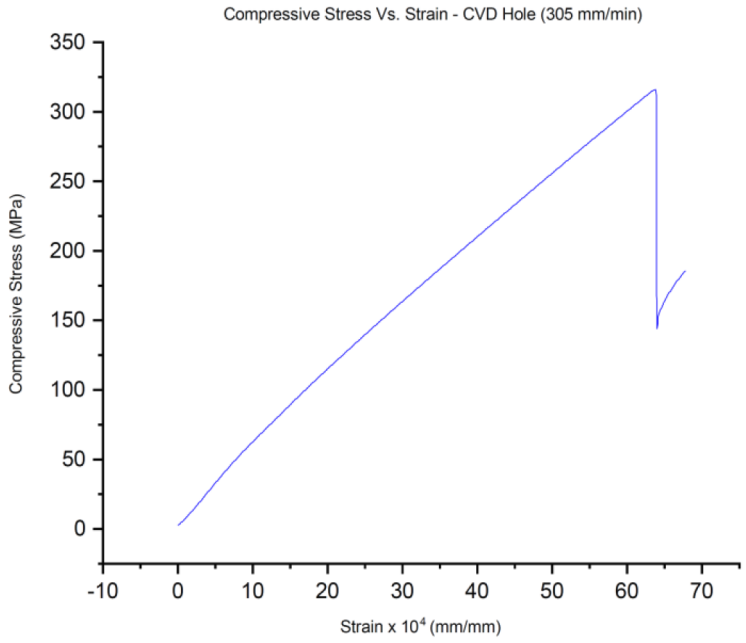

Figure 6.124 Open Hole Compressive Stress Vs. Strain for CVD Drilled Hole (305 mm/min)

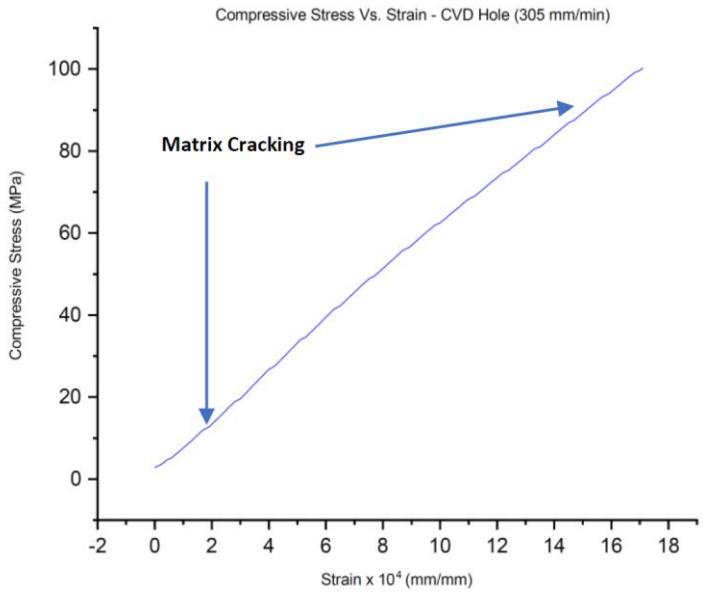

Figure 6.125 Magnified View of Open Hole Compressive Stress Vs. Strain showing Matrix Cracking in CVD Drilled hole specimen (305 mm/min)

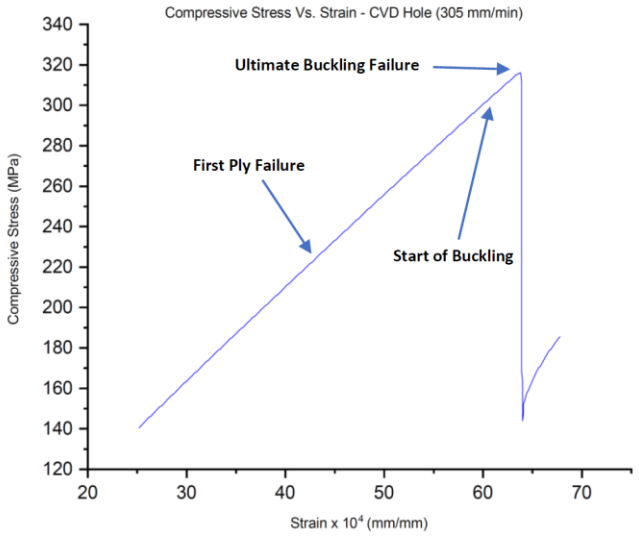

Figure 6.126 Magnified view of Open Hole Compressive Stress Vs. Strain showing First Ply Failure and Damage in CVD Drilled hole specimen (305 mm/min)

Test Data & Observations from Open Hole Compression testing of CVD Drilled Hole at feedrate of 305 mm/min specimens

The following strength data was recoded from the open hole compressive testing of CVD Drilled hole at feedrate of 305 mm/min:

Maximum Open Hole Compressive Stress = 316.0 MPa

Maximum Open Hole Compressive Load = 53103.9 N

Strain at Maximum Open Hole Tensile Stress = 0.00638 mm/mm

Youngs Modulus from Testing = 50.7 GPa

It was observed that matrix cracking started around 0.02% strain. Matrix cracking progressed as stress increased and first ply failure occurred around tensile stress of 220.0 MPa. First ply failure occurred around 0.044 % strain. It was observed that failure zone initiated at 45 degree plies in the hole and ultimately resulted in failure across the complete hole. Final failure was buckling across the thickness of the laminate.

Damage observations from open hole compressive testing of CVD Drilled hole at 305 mm/min specimens

Figures 6.127 through 6.131 show the damage recorded in open hole compressive testing of CVD drilled hole at feedrate of 305 mm/min specimens.

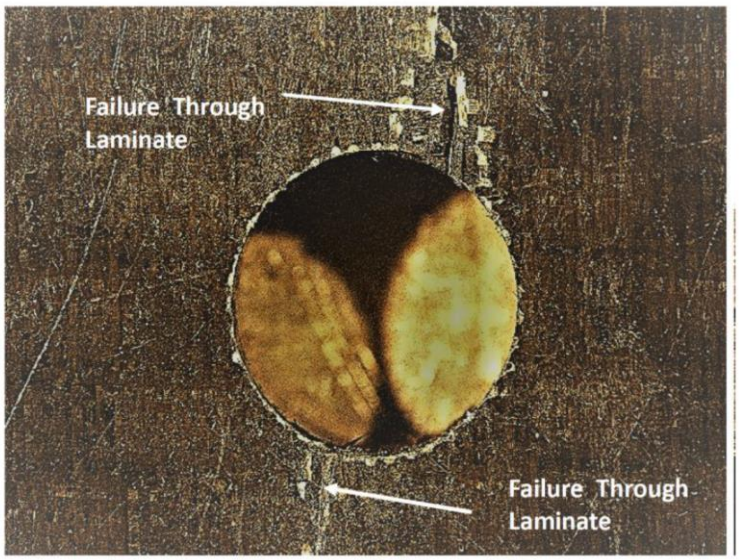

Figure 6.127 Failed specimen from Open Hole Compression testing of CVD hole specimen (305 mm/min)

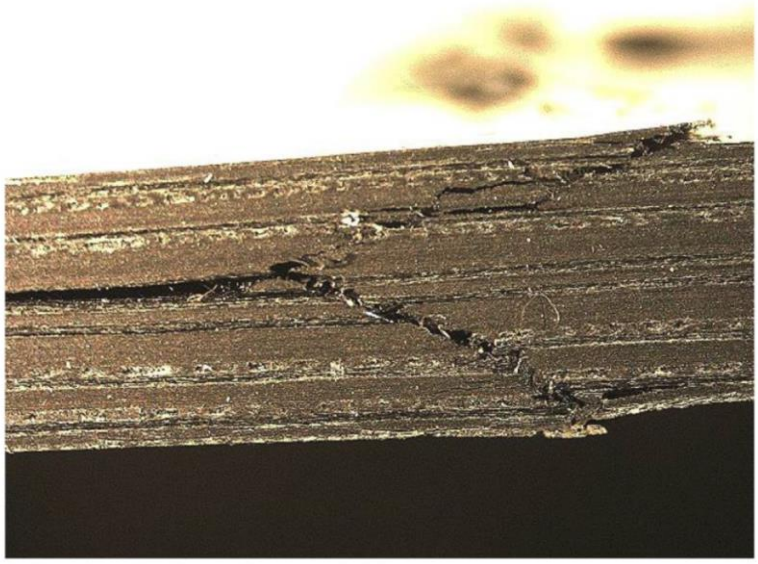

Figure 6.128 Failed specimen from Open Hole Compression testing of CVD hole specimen (305 mm/min)

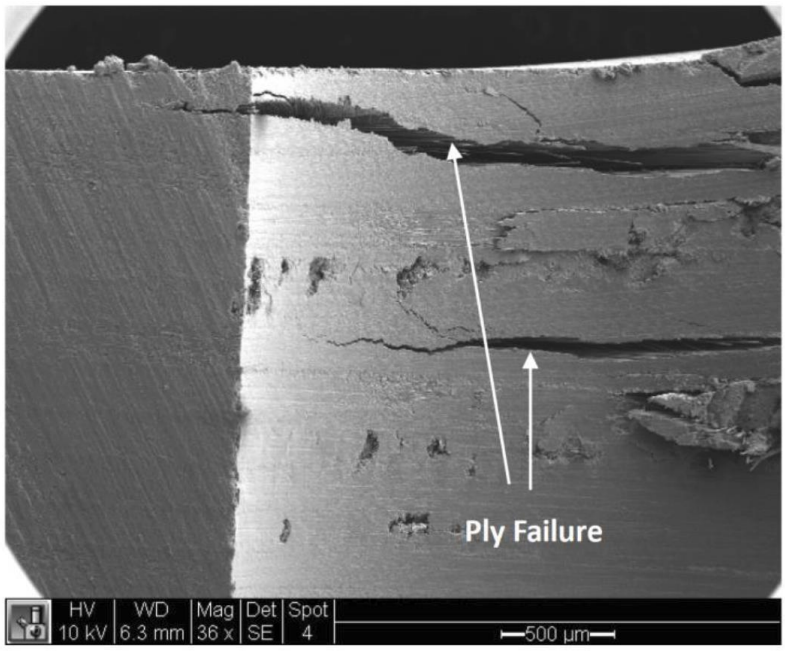

Figure 6.129 SEM of failed specimen showing Ply Failure from Open Hole Compression Testing of CVD hole specimen (305 mm/min)

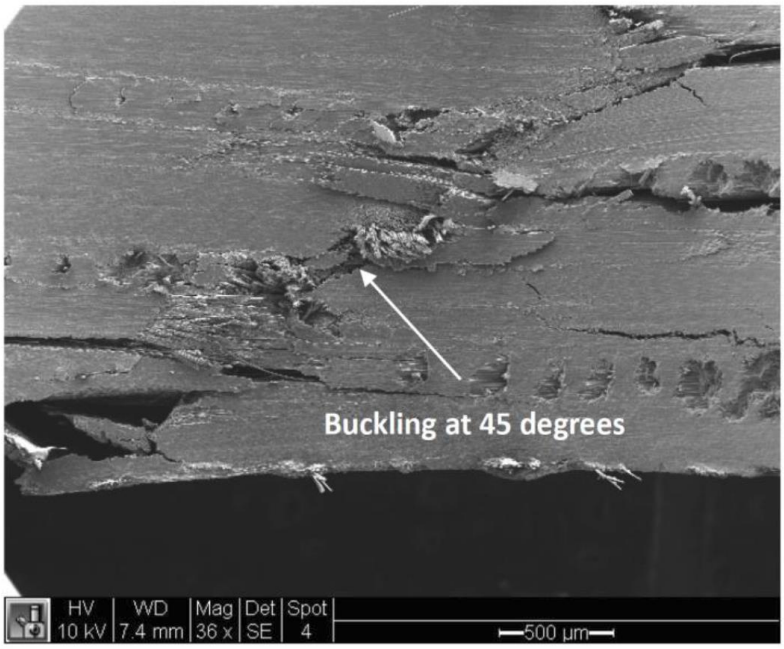

Figure 6.130 SEM of failed specimen showing buckling at 45 degrees from Open Hole Compression Testing of CVD hole specimen (305 mm/min)

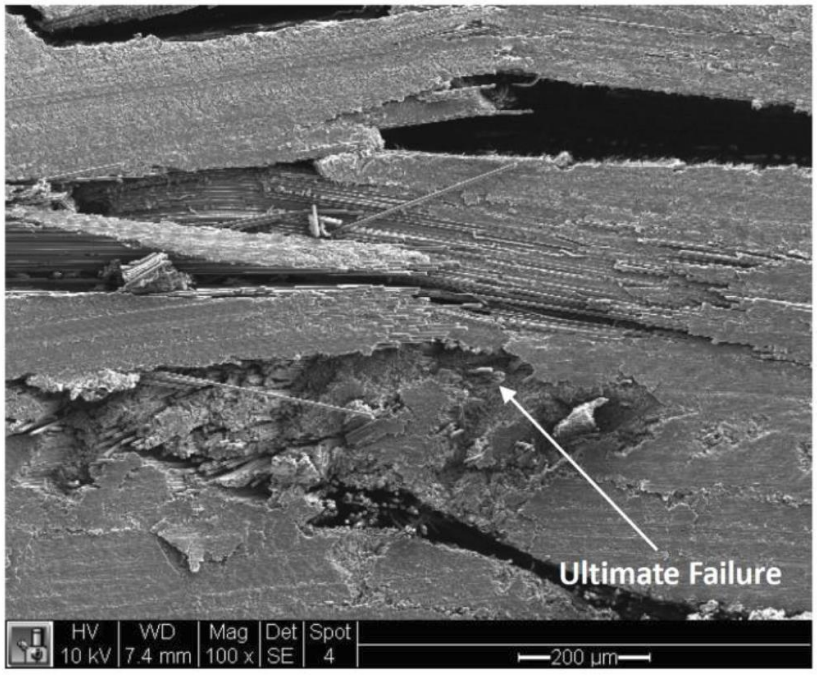

Figure 6.131 SEM of failed specimen showing Ultimate failure from Open Hole Compression Testing of CVD hole specimen (305 mm/min)

From the damage observations, it was noted that the damage initiation started at the 45 degree plies in the hole. The damage progressed along the various plies on the hole surface. The predominant failure was buckling along the 45 degree plies of the hole surface. Matrix cracks were present along the surface through the thickness of the laminate. Brittle fracture of fibres was observed in the failed specimens. Final failure of specimen was separation along 45 degress across the thickness of the laminate. Fibre pullouts contributed to delamination initiation and progression starting at 45 degrees plies. Matrix cracking preceded delamination and aided in the final failure of the specimen.

Open Hole Compression Testing of CVD Drilled Hole at feedrate of 508 mm/min Specimens

CVD drilled holes at feedrate of 508 mm/min specimens were tested in open hole compression to failure. Figures 6.132, 6.133 & 6.134 show the data plots from the testing.

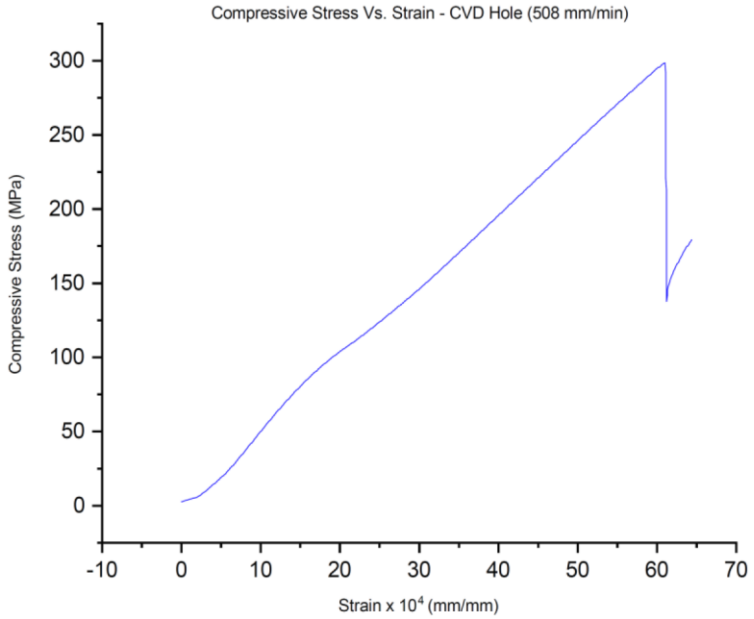

Figure 6.132 Open Hole Compressive Stress Vs. Strain for CVD Drilled Hole (508 mm/min)

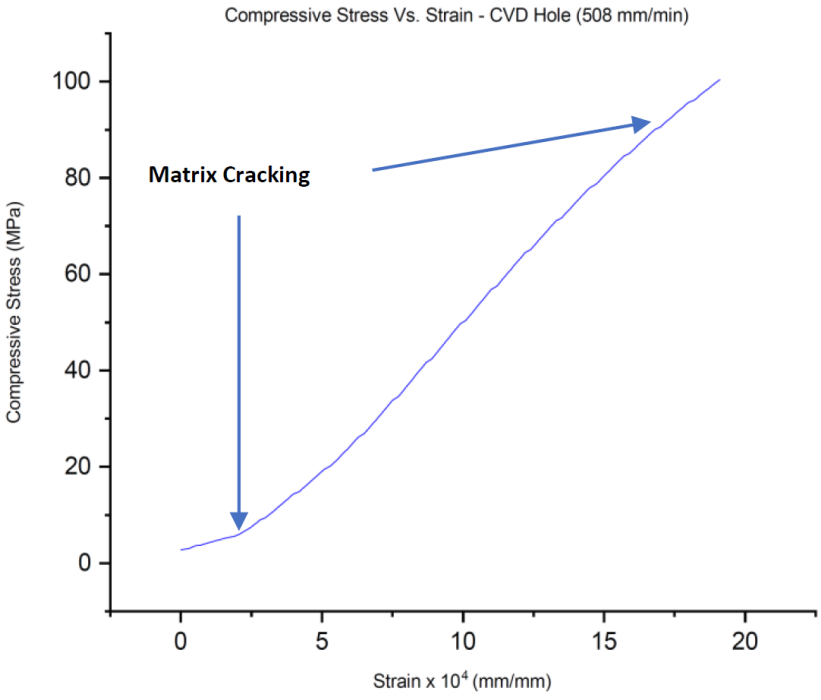

Figure 6.133 Magnified View of Open Hole Compressive Stress Vs. Strain showing Matrix Cracking in CVD Drilled hole specimen (508 mm/min)

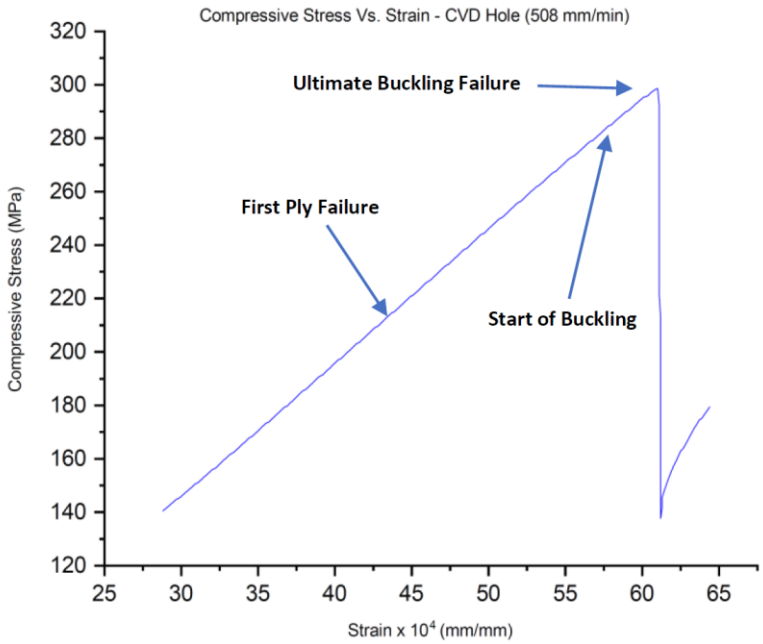

Figure 6.134 Magnified view of Open Hole Compressive Stress Vs. Strain showing First Ply Failure and Damage in CVD Drilled hole specimen (508 mm/min)

Test Data & Observations from Open Hole Compression testing of CVD Drilled Hole at feedrate of 508 mm/min specimens

The following strength data was recoded from the open hole compressive testing of CVD Drilled hole at feedrate of 508 mm/min:

Maximum Open Hole Compressive Stress = 298.6 MPa

Maximum Open Hole Compressive Load = 50175.0 N

Strain at Maximum Open Hole Tensile Stress = 0.0061 mm/mm

Youngs Modulus from Testing = 47.9 GPa

It was observed that matrix cracking started around 0.02% strain. Matrix cracking progressed as stress increased and first ply failure occurred around tensile stress of 215.0 MPa. First ply failure occurred around 0.044 % strain. It was observed that failure zone initiated at 45 degree plies in

the hole and ultimately resulted in failure across the complete hole. Final failure was buckling across the thickness of the laminate.

Damage observations from open hole compressive testing of CVD Drilled hole at 508 mm/min specimens

Figures 6.135 through 6.139 show the damage recorded in open hole compressive testing of CVD drilled hole at feedrate of 508 mm/min specimens.

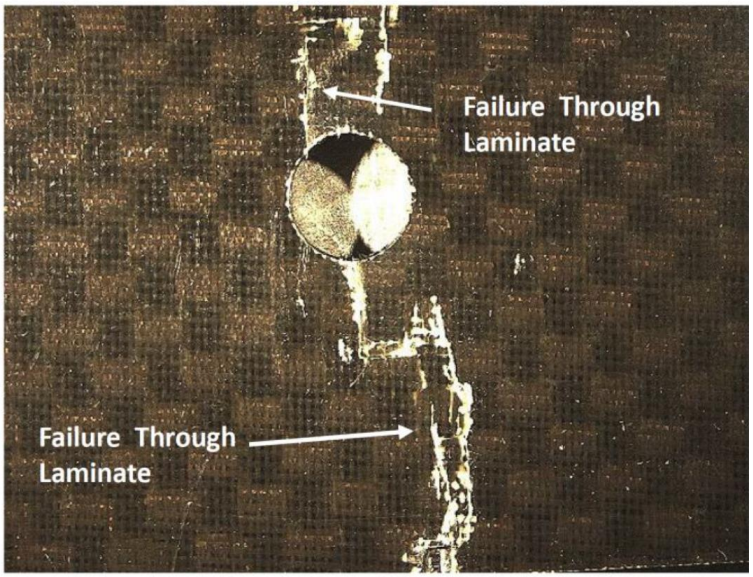

Figure 6.135 Failed specimen from Open Hole Compression testing of CVD hole specimen (508 mm/min)

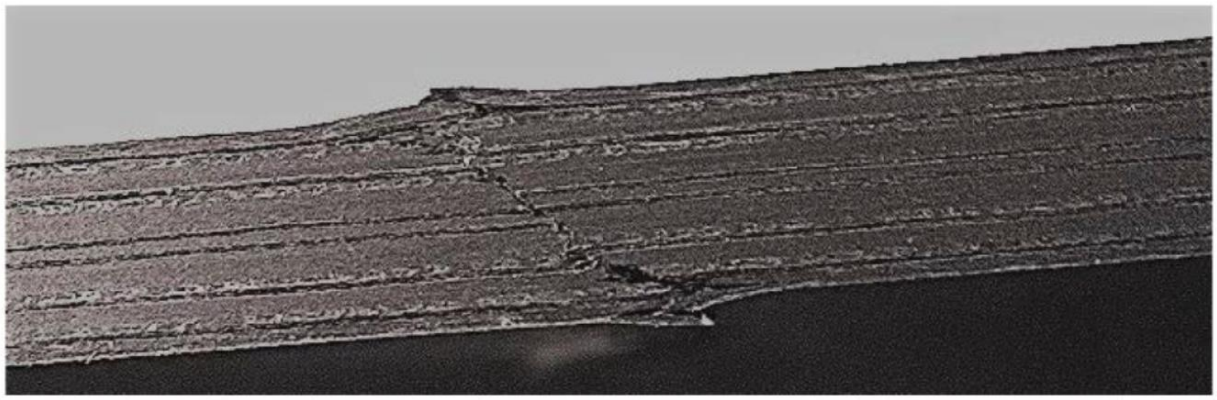

Figure 6.136 Failed specimen from Open Hole Compression testing of CVD hole specimen (508 mm/min)

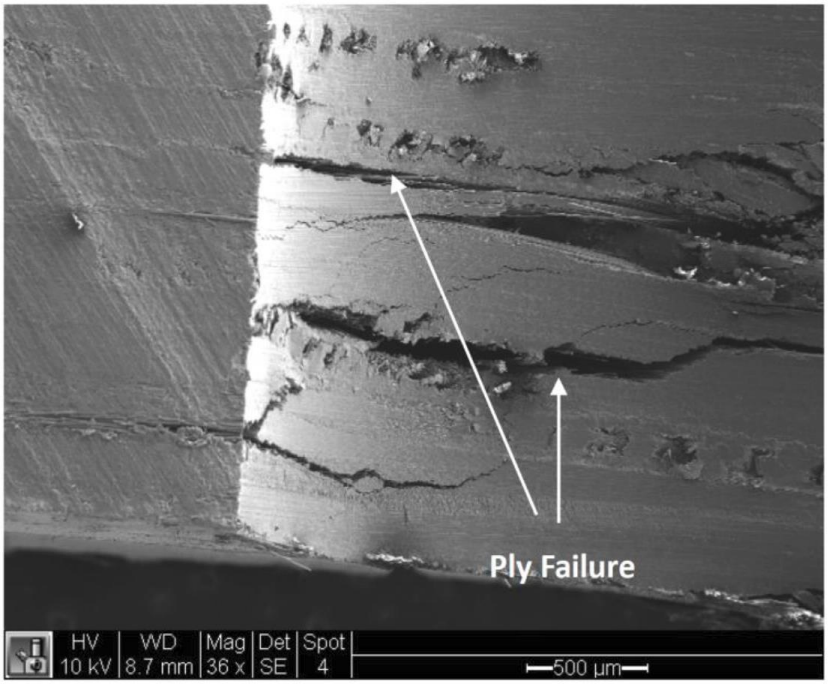

Figure 6.137 SEM of failed specimen showing Ply Failure from Open Hole Compression Testing of CVD hole specimen (508 mm/min)

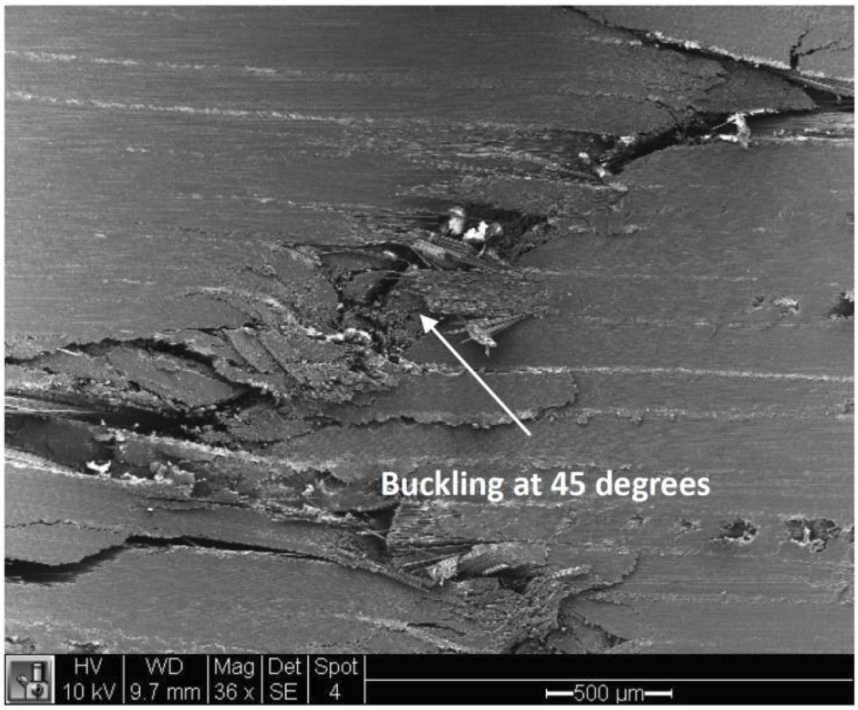

Figure 6.138 SEM of failed specimen showing buckling at 45 degrees from Open Hole Compression Testing of CVD hole specimen (508 mm/min)

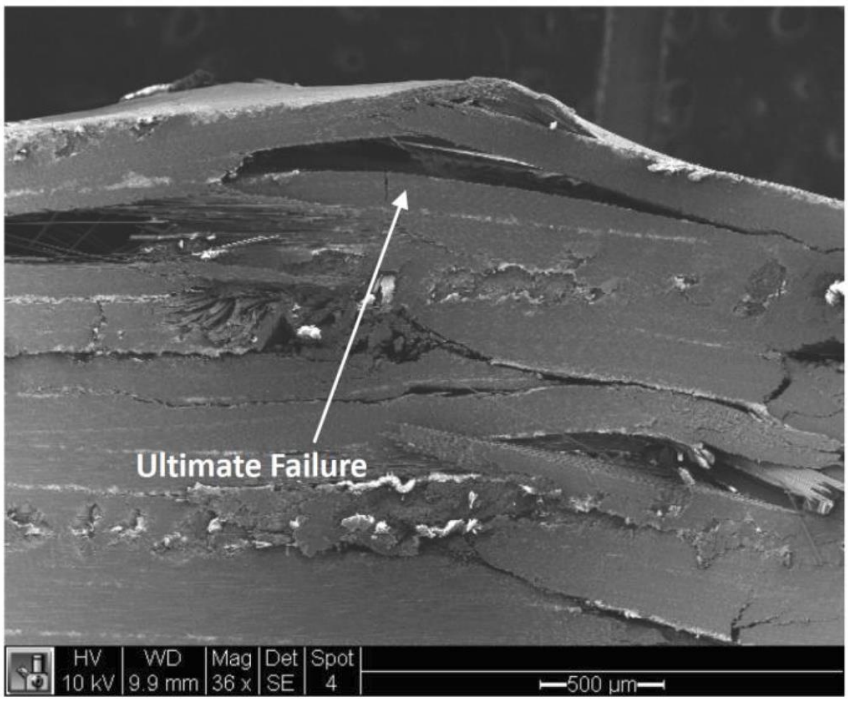

Figure 6.139 SEM of failed specimen showing Ultimate failure from Open Hole Compression Testing of CVD hole specimen (508 mm/min)

From the damage observations, it was noted that the damage initiation started at the 45 degree plies in the hole. The damage progressed along the various plies on the hole surface. The predominant failure was buckling along the 45 degree plies of the hole surface. Matrix cracks were present along the surface through the thickness of the laminate. Brittle fracture of fibres was observed in the failed specimens. Final failure of specimen was separation along 45 degress across the thickness of the laminate. Fibre pullouts contributed to delamination initiation and progression starting at 45 degrees plies. Matrix cracking preceded delamination and aided in the final failure of the specimen.

Summary of Open Hole Compression Strength Testing Results. Observations & Conclusions

Open Hole Compression testing results were summarized and are shown in Table 6.9. The table data includes surface finish data along with testing results including Youngs Modulus. First ply failure stress and strain results.

Specimen Type	Average Surface Finish - R_a (µm)	Surface Finish – R_z (µm)	Surface Finish – R_t (µm)	Calculated Effective Stress Concentration Factor $\bar{K}_t$	Max Comp Stress (MPa)	Strain (mm/mm)	Youngs Modulus E_x (GPa)	Matrix Cracking Initiation – % Strain	First Ply Failure – Comp Stress – (MPa)	First Ply Failure – % Strain
PCD Drill – F1	0.445	2.91	6.15	1.75	320.8	0.00744	45.15	0.035	240.0	0.055
PCD Drill – F2	0.342	2.81	5.365	1.92	306.6	0.00688	46.09	0.025	230.0	0.051
CVD Drill – F1	0.965	5.632	11.597	2.45	316.0	0.00638	50.7	0.02	220.0	0.044
CVD Drill – F2	0.890	5.172	11.38	2.88	298.6	0.0061	47.9	0.02	215.0	0.044

Table 6.9 Summary of Open Hole Compression testing Results

<u>Observations from Surface Integrity plots of Open Hole Compression Testing</u>

Surface integrity data was calculated and plots created from the surface roughness data. The plots show that the higher stress concentration factor resulted in larger reduction in stiffness compared to theoretical modulus (stiffness). Stress concentration factor is a function of surface finish parameters R_a , R_z, R_t Generally the higher the surface roughness, R_a , the large reduction

in stiffness. The ratio R_z / R_t influences the reduction in stiffness. The larger the ratio the greater the reduction in stiffness. This is attributed to the larger values of the highest peaks and deepest valleys in the surface profiles. This leads to an increase in number of points of stress risers which lead to stiffness reduction and load carrying capacity. Drilling feedrate did not influence the average surface roughness or other parameters in CVD drilling. In PCD drilling, the change in feedrates influenced a larger change in surface integrity parameters as well as strength properties. Figure 6.140, 6.141 & 6.142 show the plots of various surface finish parameters Vs. the ratio of tested modules to theoretical apparent modulus (E / E_0)

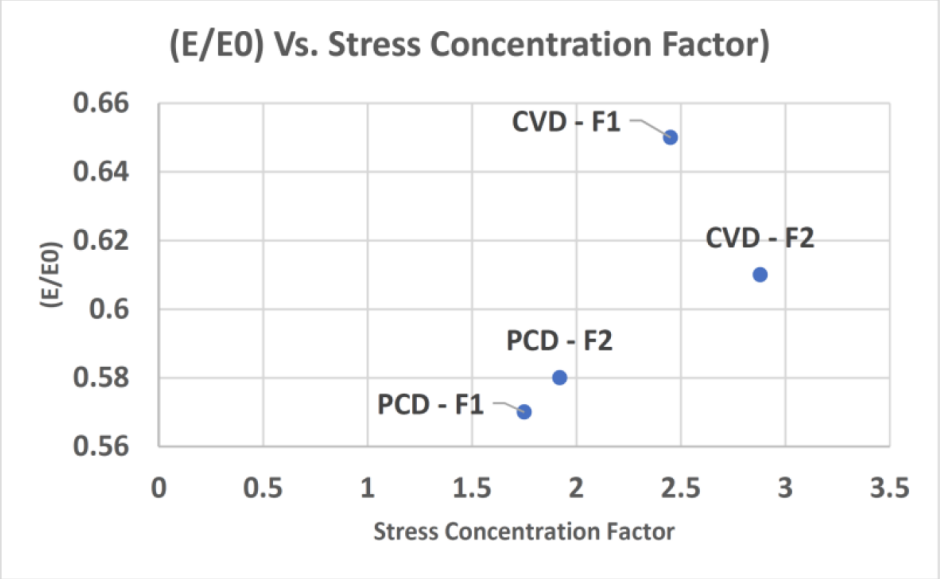

Figure 6.140 Plot of (E/E_0) Vs. Stress Concentration Factor for various Open hole Compression Testing specimens

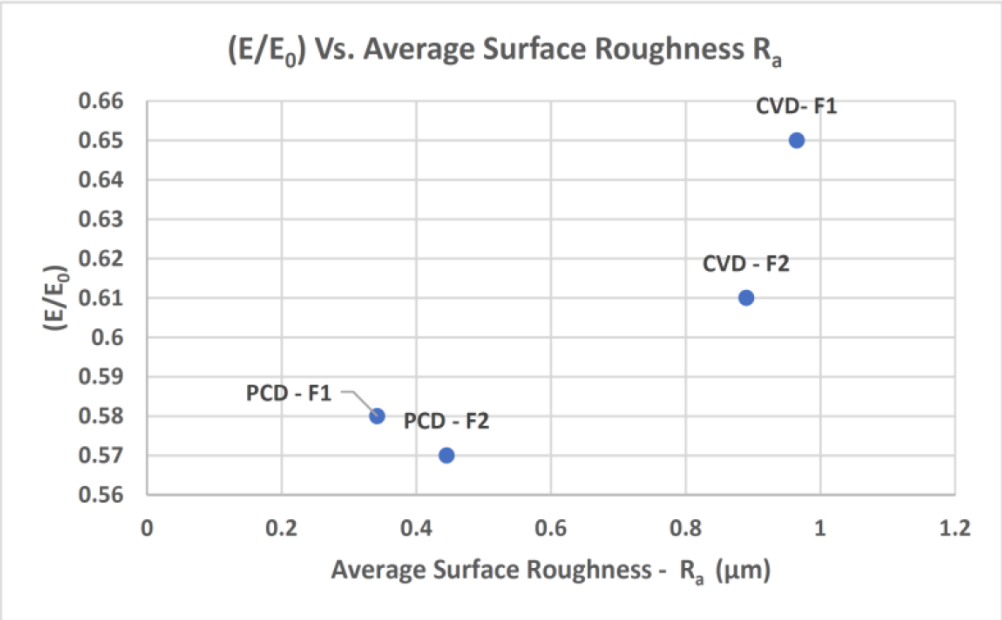

Figure 6.141 Plot of (E/E_0) Vs. Average Surface Roughness - R_a (µm) for various Open Hole Compression Testing specimens

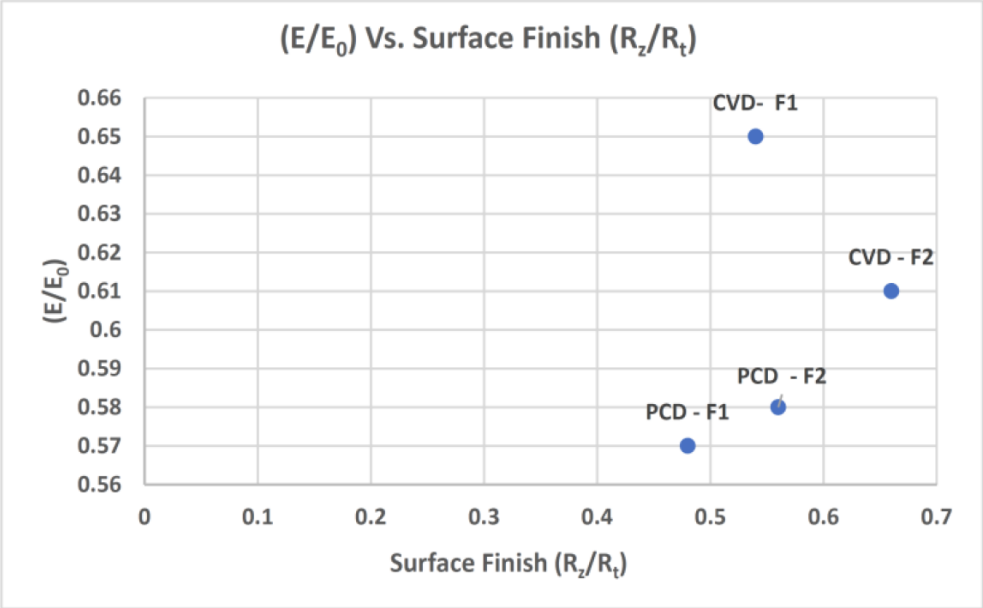

Figure 6.142 Plot of (E/E_0) Vs. Surface Finish (R_z / R_t) for various Open Hole Compression Testing specimens

Observations from Damage Progress Plot for Open Hole Compression Testing

Damage progress plot Vs. applied load was generated as shown in figure 6.143 and it was observed that the drilled holes had damage start at lower loads for lower feedrate as compared to the higher feedrate. This was attributed to the longer contact time of the drill in the hole which contributed to the matrix cracking initiation. Both the PCD specimens had slightly higher damage as compared to the CVD drilled holes. This was contributed to larger magnitude of delamination at the bottom surface of the hole. The PCD drill has a 118 degree point angle as compared to 90 degree point angle of the CVD drill. This contributes to the larger delamination at the bottom surface of the hole. The progress of damage was similar in all specimens with matrix cracking being the dominant mode of damage initially. The transition of damage from matrix cracking to delamination followed a similar pattern for all PCD and CVD drilled hole specimens. Damage tolerance of CVD specimens is slightly lower in comparison to PCD drilled specimens. For both PCD and CVD drilled hole specimens, the damage tolerance is lower in specimens drilled at higher feedrates. All specimens displayed a sudden increase in damage showing the progression of damage from hole to across the width of the laminate. Ply damage

across the hole for all specimens displayed a similar path of progression. The reduction in stiffness for all drilled holes by PCD and CVD was close to each other within 5%

Damage = $1 - (E/E_0)$

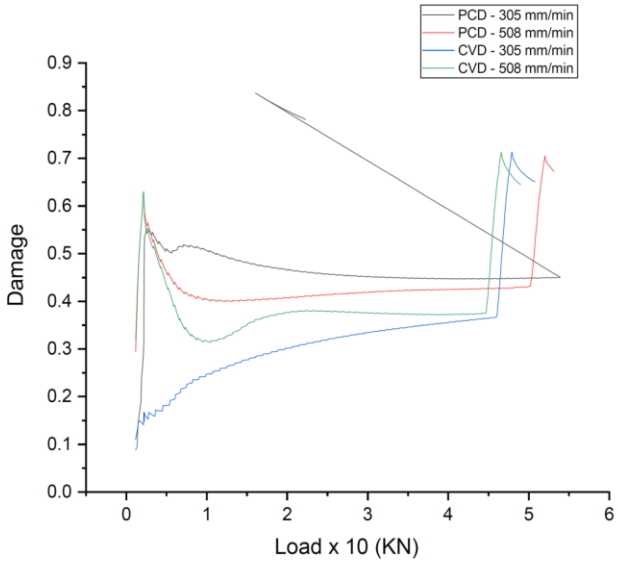

Figure 6.143 Damage Vs. Applied Load for Open Hole Compression Testing specimens

6.4.6.1 Analysis of Open Hole Compression Testing Results

As seen from the above results there is a drop in the stiffness from the theoretical apparent stiffness calculations. This can be attributed to resultant surface integrity from varying drilling operations conducted. Test specimens drilled with PCD drills displayed better surface finish profile characteristics.

The reduction in stiffness is a function of the surface integrity and the resultant stress concentration factor from surface integrity of the drilled hole.

$$\frac{E}{E_0} = f(\overline{K}_t) \qquad 6.1$$

When the value of the stress concentration factor $(\overline{K}_t)$ is higher, the value of $\left(\frac{E}{E_0}\right)$ is lower

When the value of $\left(\frac{R_z}{R_t}\right)$ is higher, the value of $\left(\frac{E}{E_0}\right)$ is lower.

The maximum compressive stress is a function of both the hole concentration factor (K_t) as well as the surface integrity concentration factor of the hole $(\overline{K}_t)$

$$\sigma_{max} = f(K_t, \overline{K}_t) \qquad 6.2$$

The maximum compressive stress in open hole compression testing is about 30% to 45% less than maximum compressive stress in compression testing. The presence of a hole (notch) in the specimen results in a stress concentration factor with the presence of notch.

6.4.7 Bearing Strength Testing

Bearing hole testing was conducted on PCD and CVD drilled hole specimens drilled at feedrates of 305 mm/min and 508 mm/min. It was found that for PCD drilled hole specimens maximum load was recorded in specimens drilled at the lower feedrate of 305 mm/min. For CVD hole specimens, the maximum load was also recorded in specimens drilled at lower feedrate of 305 mm/min.

Figure 6.144 shows the plot of the load Vs. extension for various test specimens in bearing hole testing. Table 6.10 shows the recorded values for maximum load for different test specimens.

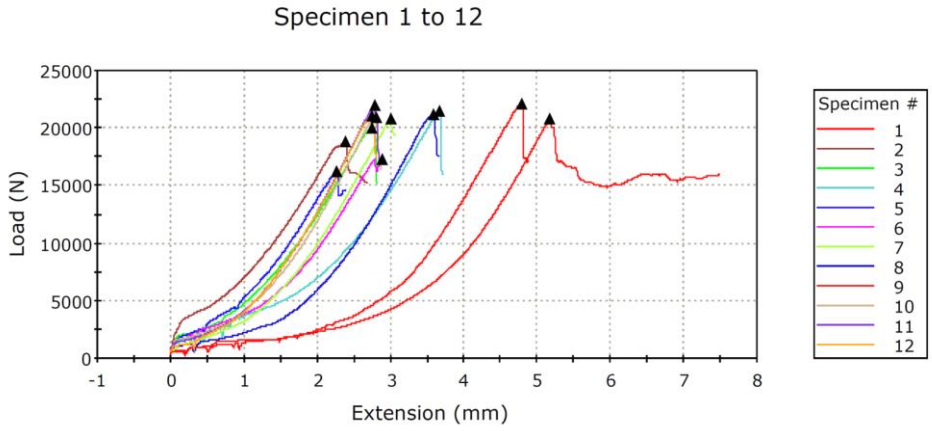

Figure 6.144 Plot of Load Vs. Extension for Bearing Hole Test Specimens

Specimen Number	Drill Hole	Load (N)
Specimen 1	PCD, 508 mm/min	20761.54
Specimen 2	PCD, 508 mm/min	18841.75
Specimen 3	PCD, 508 mm/min	20057.73
Specimen 4	PCD, 305 mm/min	21432.53
Specimen 5	PCD, 305 mm/min	16287.54
Specimen 6	PCD, 305 mm/min	17286.29
Specimen 7	CVD, 305 mm/min	20839.38
Specimen 8	CVD, 305 mm/min	21222.29
Specimen 9	CVD, 305 mm/min	22166.94
Specimen 10	CVD, 508 mm/min	21005.45
Specimen 11	CVD, 508 mm/min	21944.56
Specimen 12	CVD, 508 mm/min	21114.34
	Maximum	22166.94
	Mean	20246.7
	Minimum	16287.54
	Standard Deviation	1841.971

Table 6.10 Maximum Load recorded for Bearing Hole test specimens

Damage observations from Bearing hole testing for PCD and CVD drilled hole specimens

Figures 6.145 through 6.148 show the damage recorded in bearing hole testing of PCD drilled hole at feedrates of 305 mm/min and 508 mm/min specimens.

Figure 6.145 Damage zone of Bearing hole test specimen – PCD drilled hole (305 mm/min)

Figure 6.146 Damage zone of Bearing hole test specimen – PCD drilled hole (508 mm/min)

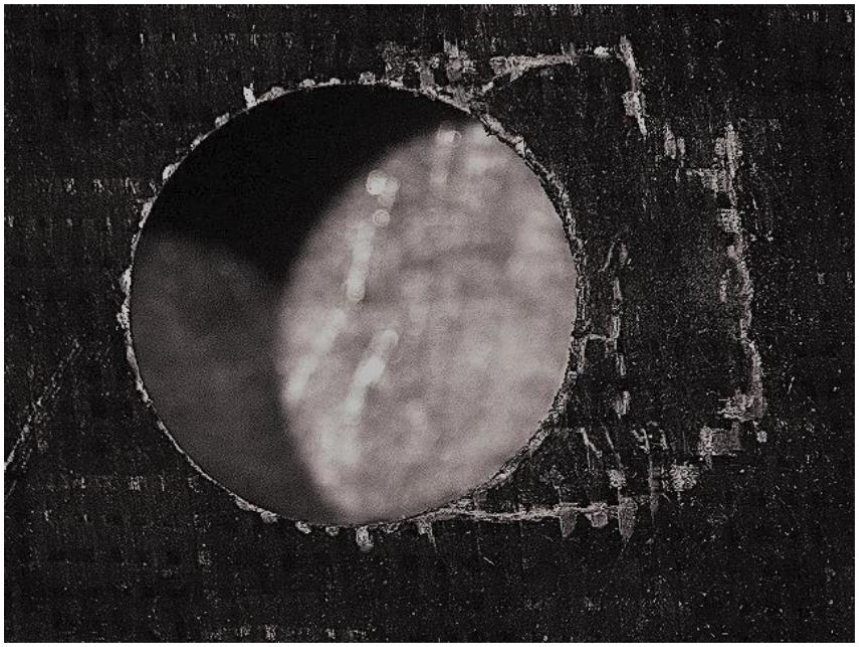

Figure 6.147 Damage zone of Bearing hole test specimen – CVD drilled hole (305 mm/min)

Figure 6.148 Damage zone of Bearing hole test specimen – CVD drilled hole (508 mm/min)

From the damage observed during the testing it was noted that in both PCD & CVD drilled hole specimens that damage zone is larger in specimens drilled at higher feedrate. In the higher feedrate specimens the damage zone was deeper in the hole.

6.5 Discussion and Summary

The maximum loads under tension vary based on the processes used for edge trimming as well as the drilling processes used. Fig 6.150 shows a comparison between maximum tensile loads for specimens trimmed with AWJ as well PCD and CVD Endmills. As expected between the AWJ trimmed and the endmill trimmed specimens, the surface integrity variance between the two results in a difference in the maximum tensile loads. It is noted that the open hole tension specimens failed at lower tensile loads than the normal tension specimens as expected.

The maximum stress under compression vary based on the processes used for edge trimming as well as the drilling processes used. Figure 6/149 shows a comparison between maximum compressive stress for specimens trimmed with AWJ as well CVD Endmills. As expected between the AWJ trimmed and the endmill trimmed specimens, the surface integrity variance between the

two results in a difference in the maximum compressive stress. It is noted that the open hole compression specimens failed at lower stress than the normal compression specimens as expected.

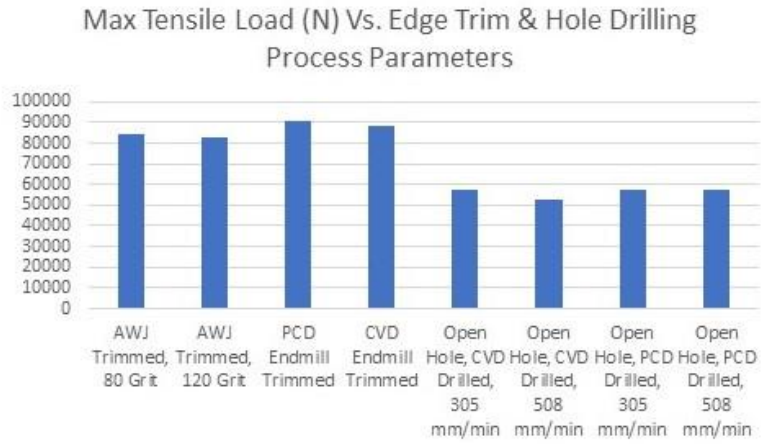

Figure 6.149 Maximum Tensile Load Vs. Edge Trim & Hole Drilling Process Parameters

The maximum stress under compression vary based on the processes used for edge trimming as well as the drilling processes used. Figure 6.150 shows a comparison between maximum compressive stress for specimens trimmed with AWJ as well CVD Endmills. As expected between the AWJ trimmed and the endmill trimmed specimens, the surface integrity variance between the two results in a difference in the maximum compressive stress. It is noted that the open hole compression specimens failed at lower stress than the normal compression specimens as expected.

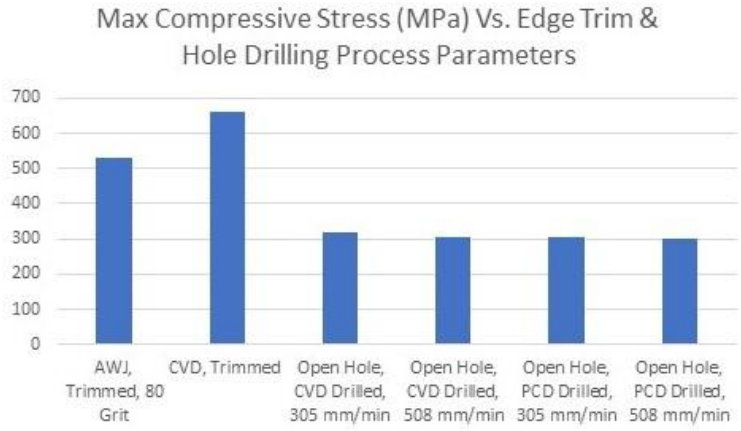

Figure 6.150 Maximum Compressive Stress Vs. Edge Trim & Hole Drilling Process Parameters

The initiation of damage and its progress followed a common path in all types of testing. Initiation starts as matrix cracking in all specimens with the initiation load being a function of the type of trimming process used (AWJ Vs. Endmilling and the resultant surface integrity of the trimmed specimen. The AWJ specimens had a lower load for matrix cracking initiation but displayed slower progress of damage in comparison to endmilled trimmed specimens. The AWJ specimens also displayed larger amount of damage at failure loads. The endmilled specimens failed at slightly higher loads and showed higher amounts of delamination and ply failure at ultimate failure. Damage tolerance was also lower in the case of endmilled specimens. In all test specimens, matrix cracking damage initiated at the free edge surfaces. The transition of damage from matrix cracking to delamination occurred over a larger spread of applied loads in AWJ specimens in tension and transition from matrix cracking to buckling in compression specimens also occurred over a larger spread of applied loads in AWJ specimens.

For testing of specimens with open holes the drilled holes had damage start at lower loads for lower feedrate as compared to the higher feedrate. This was attributed to the longer contact time of the drill in the hole which contributed to the matrix cracking initiation. The PCD specimens had slightly higher damage as compared to the CVD drilled holes. This was contributed to larger magnitude of delamination at the bottom surface of the hole attributed to the drill point. The progress of damage was similar in all specimens with matrix cracking being the dominant mode

of damage initially. The transition of damage from matrix cracking to delamination followed a similar pattern for all PCD and CVD drilled hole specimens. Damage tolerance of CVD specimens is slightly lower in comparison to PCD drilled specimens. For both PCD and CVD drilled hole specimens, the damage tolerance is lower in specimens drilled at higher feedrates. All specimens displayed a sudden increase in damage showing the progression of damage from hole to across the width of the laminate. Ply damage across the hole for all specimens displayed a similar path of progression.

In conclusion the data shows a trend in reduction in stiffness and strength due to surface integrity effects. All specimens with larger amounts of surface damage had lower loads to failure in every mode of testing. The type of failure resulting in lower loads had been predominantly the occurrence of delamination and Fibre pullouts in the specimens due to both trimming and drilling processes. This quantifies to some extent that delamination and fibre pullouts cannot be ignored in their detrimental effects on the Mechanical properties of CFRP laminates. Which type of damage is critical depends on the service loading deployed. This study has also validated some of the results of past researchers that the surface integrity efforts from manufacturing processes do influence the mechanical properties of the CFRP laminates.

Data from static testing was the foundation of selection of types of edge machining processes and type of drill as well as drilling processes to be used for Fatigue Cycle Testing in Tension that was studied and documented in Chapter 7.

Fatigue Cycle Testing Loads/Stress were also derived based on Failure Loads observed during static properties testing as described in this chapter.

Chapter 7 - Phase II – Experimental Testing – Fatigue Cycle Tension -Tension Testing – 22 Ply Thick Laminate

7.1 Phase II Test Materials

Test specimens were edge trimmed with endmills and also using AWJ trimming. The surface roughness of the edges was measured using the MAHR surface profilometer. Similarly, for Open-Hole Testing holes were drilled using CVD Diamond Coated drills. Surface roughness was also measured using the profilometer. Scanning Electron Microscopy (SEM) was used to examine the damage from each process including the surface of the drilled holes. Specimens were then tested for Tension-Tension Fatigue Cyclic Testing. The failure mode of the test specimens for each case was examined and recorded.

7.2 Phase II Research Plan – 22 Ply Thick Laminate

The 22 ply thick balanced symmetric $[90/-45/0/-45/90/45/0/-45/0/90/0]_s$ laminate used in the study had a nominal thickness of 4.52 mm and with an average ply thickness of 190 μm. The laminate had a top layer of woven fabric material [0/90] and a bottom layer of fiberglass skin material with material specification as defined in the Boeing Material Specification BMS 8-276 [61].. The Ply table is shown inn Table 7.1 The prepreg tape material used was approximately 305 mm in width and all layup was done manually as a 1220 x 1220 mm wide sheet. The sheet was cut into smaller coupons using Abrasive Water Jet (AWJ). The coupons were then machined either using endmill cutters or AWJ into smaller specimens for fatigue cyclic testing. For open holes testing, holes were drilled using a CVD Diamond Coated Drill with a diameter of 6.35 mm. Prior to fatigue cycle testing, surface integrity (roughness and Scanning Electron Microscopy) was documented.

Material	Orientation*
Fiberglass scrim	0/90
BMS 8-276 TY 40 CL 2 Form 1 6K-70-PW	0/90
BMS Spec 8-276 Type II CL 10 or 11 GR 190 Form 3	90
BMS Spec 8-276 Type II CL 10 or 11 GR 190 Form 3	45
BMS Spec 8-276 Type II CL 10 or 11 GR 190 Form 3	0
BMS Spec 8-276 Type II CL 10 or 11 GR 190 Form 3	-45
BMS Spec 8-276 Type II CL 10 or 11 GR 190 Form 3	90
BMS Spec 8-276 Type II CL 10 or 11 GR 190 Form 3	45
BMS Spec 8-276 Type II CL 10 or 11 GR 190 Form 3	0
BMS Spec 8-276 Type II CL 10 or 11 GR 190 Form 3	-45
BMS Spec 8-276 Type II CL 10 or 11 GR 190 Form 3	0
BMS Spec 8-276 Type II CL 10 or 11 GR 190 Form 3	90
BMS Spec 8-276 Type II CL 10 or 11 GR 190 Form 3	0
BMS Spec 8-276 Type II CL 10 or 11 GR 190 Form 3	90
BMS Spec 8-276 Type II CL 10 or 11 GR 190 Form 3	0
BMS Spec 8-276 Type II CL 10 or 11 GR 190 Form 3	-45
BMS Spec 8-276 Type II CL 10 or 11 GR 190 Form 3	0
BMS Spec 8-276 Type II CL 10 or 11 GR 190 Form 3	45
BMS Spec 8-276 Type II CL 10 or 11 GR 190 Form 3	90
BMS Spec 8-276 Type II CL 10 or 11 GR 190 Form 3	-45
BMS Spec 8-276 Type II CL 10 or 11 GR 190 Form 3	0
BMS Spec 8-276 Type II CL 10 or 11 GR 190 Form 3	45
BMS Spec 8-276 Type II CL 10 or 11 GR 190 Form 3	90
BMS 8-276 TY 40 CL 2 Form 1 6K-70-PW	0/90

Table 7.1 Ply Table for 22 Ply Laminate

7.3 Fatigue Cycles Testing Readiness

A total of 48 test specimens were prepared for fatigue cycles testing. ASTM Standard Test D3479/D3479M – Standard Test Method for Tension-Tension Fatigue of Polymer Matrix Composite Materials was used as the test method for fatigue testing of the specimens.

7.3.1 Test Specimens Readiness

The test batches were distributed as 24 test specimens for testing as unnotched specimens and 24 test specimens as notched specimens (open hole).

The test specimen batches were designed to evaluate the effects of surfaced integrity due to machining on the fatigue cycles and damage evolution during fatigue cycle testing.

Table 7.2 and Table 7.3 summarize the trimming and drilling conditions for the test specimens.

Trimming Operation	Speed (RPM)	Feedrate (mm/min)
AWJ (80 Grit)	-	1444
CVD Endmill	6000	635

Table 7.2 Fatigue Specimens Edge Trimming Conditions

Drilling Operation	Speed (RPM)	Feedrate (mm/min)
CVD Drill	6000	508

Table 7.3 Fatigue Specimens Drilling Conditions

Edge trimming was conducted with AWJ using a grit size of 80 for 24 of the 48 test specimens. The remaining 24 test specimens were edge trimmed using a CVD Diamond Coated Endmill.

For testing of the notched specimens, 12 AWJ Trimmed and 12 CVD Endmill Trimmed specimens were drilled with a 6.35 mm diameter hole using a CVD Diamond Coated Drill.

The number of samples used to develop the S-N curves was 12 samples for each batch with 3 to 4 specimens tested for each batch at 3 different load levels as shown in Fig 7.1

- High Load/Engineering Stress
- Medium Load/Engineering Stress

- Low Load/Engineering Stress

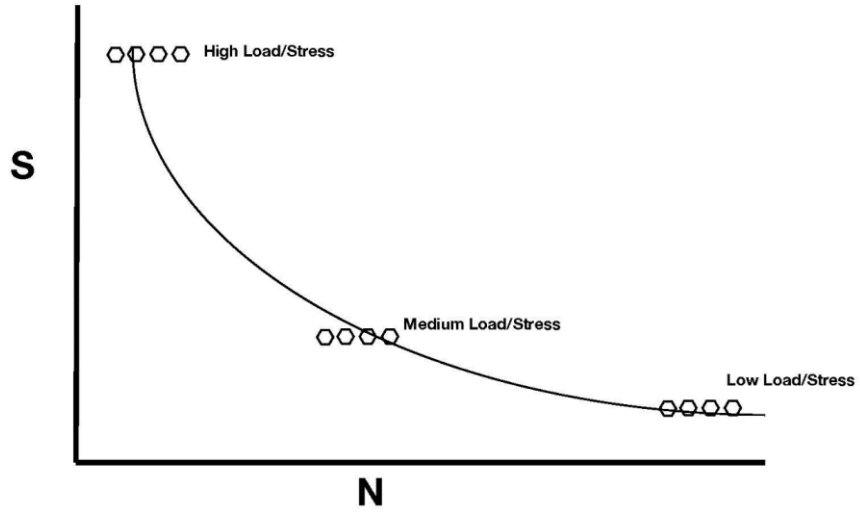

Figure 7.1 –Theoretical S-N Curve for Planned Fatigue Cycle Testing

The test specimens were designated with the following notations, an example shown below:

Specimen Name: A1 – H – 1 where the following apply:

A1 – notates AWJ trimmed with no hole

A2 – notates AWJ trimmed with hole

B1 - notates CVD Endmill trimmed with no hole

B2 - notates CVD Endmill trimmed with hole

H – notates High Load used for testing

M - notates Medium Load used for testing

L - notates Low Load used for testing

1, 2, 3, 4 – notates the test specimen number

Figure 7.2 shows the theoretical calculations for the modulus values of the laminate.

Apparent Modulus in X direction,	**E_x = 78.46 GPa**
Apparent Modulus in Y direction,	**E_y = 55.97 GPa**
Apparent Shear Modulus,	**G_{xy} = 16.56 GPa**

Figure 7.2 Theoretical Modulus values for Laminate

7.3.2 Test Equipment

The test equipment used was a Material Test Systems (MTS) Fatigue Testing Machine (shown in Figure 7.3) with a loading capacity of 88965 Newtons.

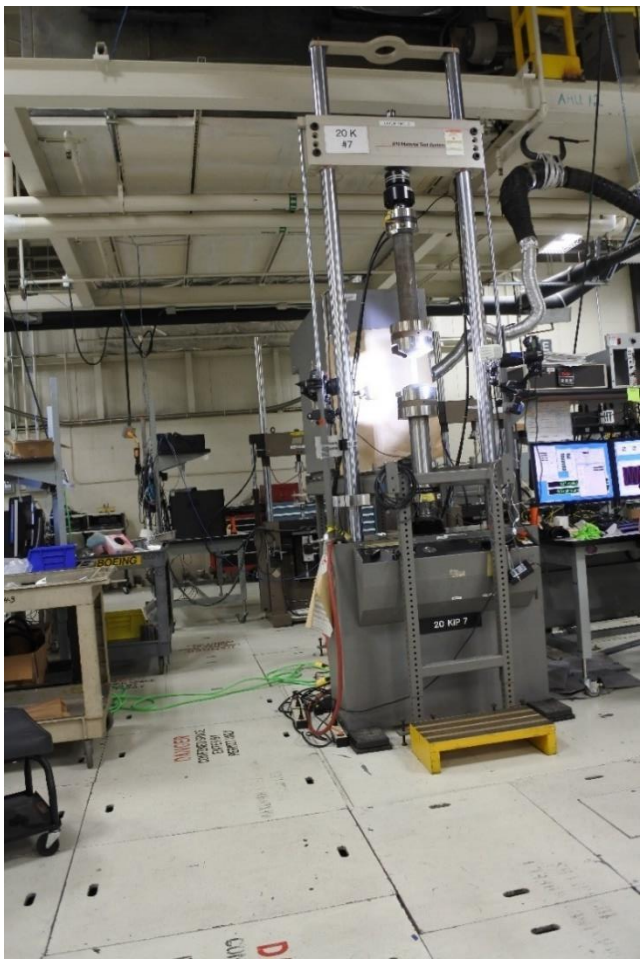

Figure 7.3 –MTS Fatigue Testing Machine

Figures 7.4 and 7.5 show the Fatigue Test Specimen Loaded in the machine for cycle testing and the data acquisition hardware and software setup for the testing.

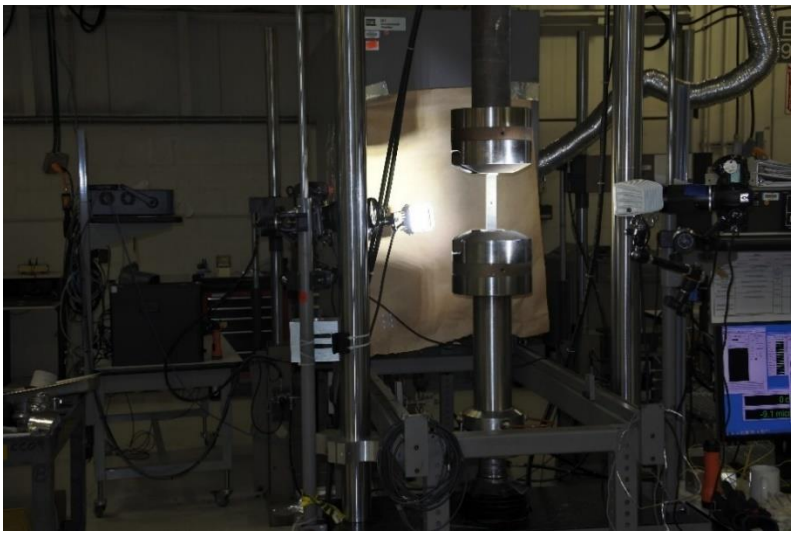

Figure 7.4 – Test Specimen in Fatigue Test Machine

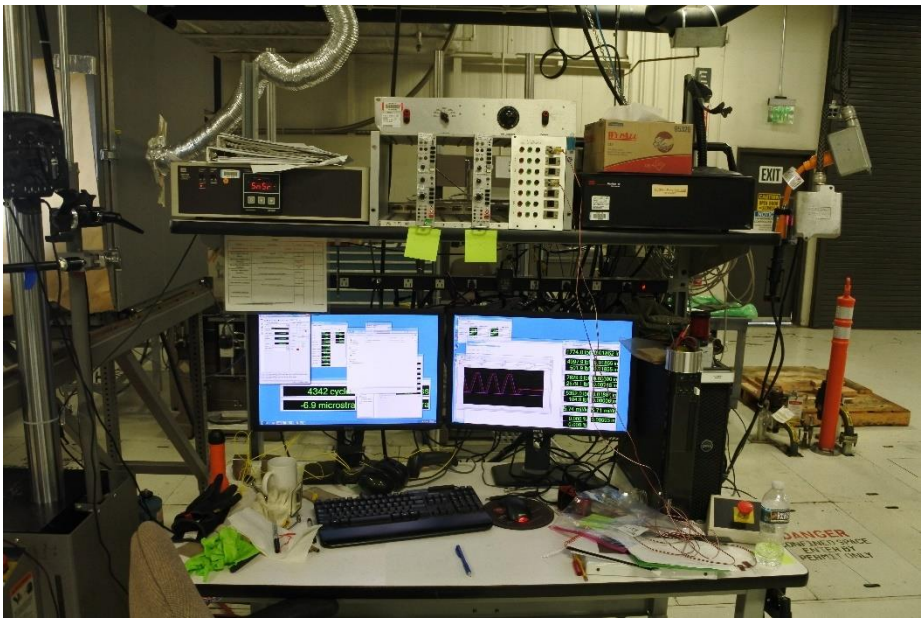

Figure 7.5 – Data Acquisition Set up

7.3.3 Machined Surfaces – Endmill Trimming vs. AWJ

Surface roughness parameters were recorded for both the endmill trimmed and AWJ trimmed surface edges. The readings were taken both in the longitudinal and transverse direction. The surface roughness for the endmill machined surfaces was in general a lower value (R_a) in the longitudinal direction while the AWJ trimmed edge had a lower (R_a) value in the transverse direction, as shown in Table 6.2.

Only CVD Diamond Coated Endmills were used for edge trimming for endmill trimming of fatigue test specimens.

The cutting parameters used are as follows:

Endmill Trimming: Spindle Speed = 6000 RPM, Cutting Speed = 1.9 m/s, Feed Rate = 635 mm/min

AWJ Trimming: Linear Cutting Feed Rate = 1444 mm/min

The surface profile readings in the obtained from the two types of edge trimming operations are documented in tables 7.4 and 7.5 for longitudinal and transverse direction. SEMs of both AWJ trimmed and CVD Diamond Coated Endmill trimming are shown in figures 7.6 through 7.11

7.3.4 Drilled Holes – Surface Finish

Since CVD drills were only used to drill holes in notched test specimens with the same drilling feedrate of 508 mm/min, only one test sample was used to record the surface finish profile. This was done due to the difficulty in recording surface finish in a non-destructive way. Surface finish data for the drilled hole is shown in Table 7.6. SEMs of the drilled hole are shown in figures 7.12 through 7.14

Phase II - Fatigue Testing Specimens - Data Summary							
Specimen Name	Trim	Hole	Surface Finish (L) - R_a	Surface Finish (L) - R_z	Surface Finish (L) - R_t	Surface Finish (L) - R_{sk}	Surface Finish (L) - R_{ku}
A1-H-2	AWJ -80		4.355	23.395	33.5835	-0.01	3.31
A1-H-3	AWJ -80		2.9725	16.2365	21.28	-0.21	3.37
A1-H-4	AWJ -80		2.807	16.164	22.75	-0.46	3.26
A1-M-1	AWJ -80		2.076	11.40635	14.383	-0.16	3.02
A1-M-2	AWJ -80		3.0335	17.00615	22.5	-0.2	3.04
A1-M-3	AWJ -80		3.118	18.838	27.465	-0.49	3.84
A1-L-1	AWJ -80		2.545	16.8135	20.033	-0.17	3.42
A1-L-2	AWJ -80		2.6275	16.946	23.33	-0.13	3.56
A1-L-3	AWJ -80		2.982	16.681	21.1	-0.19	2.73
B1-H-1	CVD Endmill		0.781	5.14815	6.633	-0.12	3.16
B1-H-2	CVD Endmill		0.3545	2.44	3.015	-0.3	3.76
B1-H-3	CVD Endmill		0.516	3.3515	4.8165	-0.59	4.99
B1-M-1	CVD Endmill		0.914	5.6225	6.133	-0.2	2.69
B1-M-2	CVD Endmill		0.986	5.5205	6.983	-0.59	3.03
B1-M-3	CVD Endmill		1.5675	11.059	18.25	0.04	4.35
B1-L-1	CVD Endmill		0.2575	2.138	2.433	0.19	3.37
B1-L-2	CVD Endmill		3.091	17.791	30.65	-0.04	4.86
B1-L-3	CVD Endmill		0.2725	2.2545	2.583	-0.23	3.37
B1-L-4	CVD Endmill		0.45715	2.851	3.2	0.42	2.76
A2-H-3	AWJ -80	CVD Drill	4.3175	21.868	24.983	-0.41	2.52
A2-H-4	AWJ -80	CVD Drill	4.268	19.9485	23.0665	-0.3	2.37
A2-M-1	AWJ -80	CVD Drill	4.149	19.636	29.75	-0.11	3.19
A2-M-2	AWJ -80	CVD Drill	3.032	13.935	17.8	0.2	2.33
A2-M-3	AWJ -80	CVD Drill	2.9555	14.006	19.55	0.15	2.87
A2-M-4	AWJ -80	CVD Drill	2.2945	12.5405	16.15	-0.78	3.66
A2-L-1	AWJ -80	CVD Drill	3.9865	19.38	21.45	-0.04	2.19
A2-L-2	AWJ -80	CVD Drill	2.714	14.9915	18.4165	-0.32	2.77
A2-L-3	AWJ -80	CVD Drill	2.8015	15.025	21.0665	-0.59	3.52
A2-L-4	AWJ -80	CVD Drill	4.7755	25.84	38.18	-0.43	3.23
B2-H-1	CVD Endmill	CVD Drill	0.203	1.543	1.7	-0.14	3.1
B2-H-2	CVD Endmill	CVD Drill	0.4385	3.0845	5.8665	-0.64	4.433
B2-H-3	CVD Endmill	CVD Drill	2.0775	11.086	16.85	-1.25	4.77
B2-H-4	CVD Endmill	CVD Drill	0.481	2.952	4.95	0.61	4.78
B2-M-1	CVD Endmill	CVD Drill	0.6795	3.9945	4.55	0.3	2.87
B2-M-2	CVD Endmill	CVD Drill	0.5355	4.2055	6.1	-0.66	5.29
B2-M-3	CVD Endmill	CVD Drill	0.754	7.928	17.6	0.28	3.16
B2-L-1	CVD Endmill	CVD Drill	0.563	4.0025	5.633	-0.2	3.58
B2-L-2	CVD Endmill	CVD Drill	0.492	3.762	5.85	-0.03	4.39
B2-L-3	CVD Endmill	CVD Drill	0.3485	2.508	4.283	-0.43	2.36

Table 7.4 Surface Finish Data of Test Specimens (Longitudinal)

Phase II - Fatigue Testing Specimens - Data Summary						
Specimen Name	Hole	Surface Finish (T) - R_a	Surface Finish (T) - R_z	Surface Finish (T) - R_t	Surface Finish (T) - R_{sk}	Surface Finish (T) - R_{ku}
A1-H-2		1.02	6.274	10.365	-0.51	5.35
A1-H-3		1.1905	7.117	12.15	-1.02	6.47
A1-H-4		709	4.062	5.2	-0.23	3.02
A1-M-1		1.214	6.79	10	0.39	3.63
A1-M-2		1.59	8.7105	11.1	-0.21	3.2
A1-M-3		1.2055	6.2635	9.783	0.38	3.72
A1-L-1		0.6	3.969	6.933	-1.4	8
A1-L-2		0.768	4.4935	7.333	-0.58	5.14
A1-L-3		0.7	4.554	7.783	0.19	6.17
B1-H-1		3.542	18.822	30.665	0	4.13
B1-H-2		1.13	5.8625	13.65	-1.45	8.29
B1-H-3		0.6395	3.9085	6.2665	-0.7	3.98
B1-M-1		1.762	10.3545	16.333	0.38	4.49
B1-M-2		0.6855	4.22	8.883	-0.74	4.056
B1-M-3		2.3295	13.069	18.85	0.48	3.67
B1-L-1		0.85	5.2205	12.2165	-0.726	4.216
B1-L-2		2.492	12.0175	20.683	-0.86	5.33
B1-L-3		0.371	2.3715	3.1665	-0.9	4.25
B1-L-4		1.092	6.326	18.683	-0.53	3.72
A2-H-3	CVD Drill	1.074	6.211	7.3665	0.5	3.26
A2-H-4	CVD Drill	1.3465	7.397	14.683	-0.6	6.5
A2-M-1	CVD Drill	0.679	3.788	4.733	0.213	2.79
A2-M-2	CVD Drill	0.8605	5.53	7.833	-0.59	4.5
A2-M-3	CVD Drill	0.9735	6.036	8.15	-0.43	4.16
A2-M-4	CVD Drill	1.288	7.5395	9.9165	0.3	3.5
A2-L-1	CVD Drill	0.7745	4.6925	7.2165	-0.82	5.35
A2-L-2	CVD Drill	0.9445	5.062	8.083	0.53	4.24
A2-L-3	CVD Drill	1.327	7.866	11.8165	-0.87	4.45
A2-L-4	CVD Drill	2.934	13.7685	26.433	-1.15	5.61
B2-H-1	CVD Drill	1.149	6.209	8.75	-0.65	3.59
B2-H-2	CVD Drill	0.611	3.9465	6.6	-0.98	6.51
B2-H-3	CVD Drill	0.717	4.3515	6.15	-1.07	4.95
B2-H-4	CVD Drill	0.531	3.0845	4.85	-0.66	4.17
B2-M-1	CVD Drill	0	0	0	0	0
B2-M-2	CVD Drill	0.5435	3.15	5.03	0.04	3.78
B2-M-3	CVD Drill	0.657	4.1465	6.883	-0.446	2.156
B2-L-1	CVD Drill	0.771	5.9825	10.15	-0.446	3.113
B2-L-2	CVD Drill	0.5745	3.5195	5.1	-0.44	3.85
B2-L-3	CVD Drill	0.8505	5.58	12.9165	-0.763	4.7

Table 7.5 Surface Finish Data of Test Specimens (Transverse)

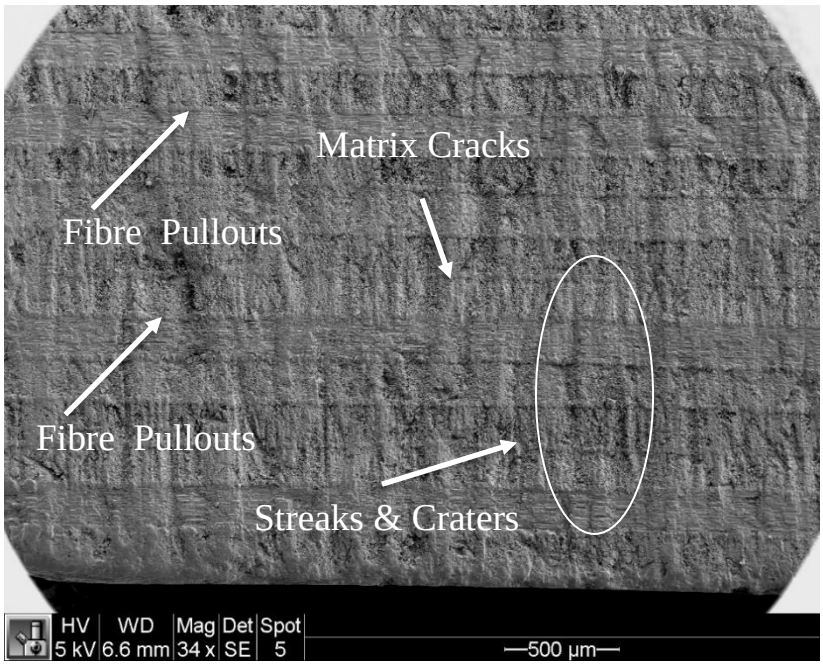

Figure 7.6 SEM of AWJ (80 Grit) Trimmed Surface

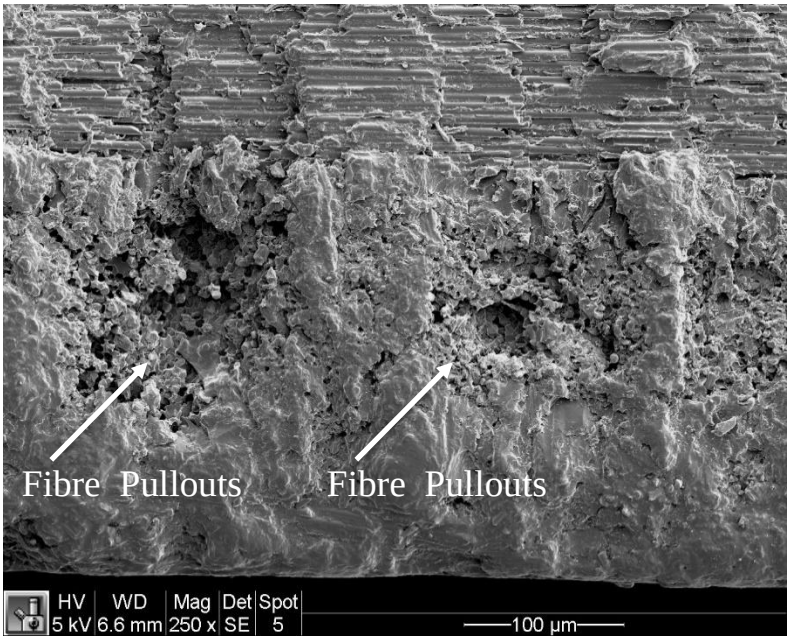

Figure 7.7 SEM of AWJ (80 Grit) Trimmed Surface

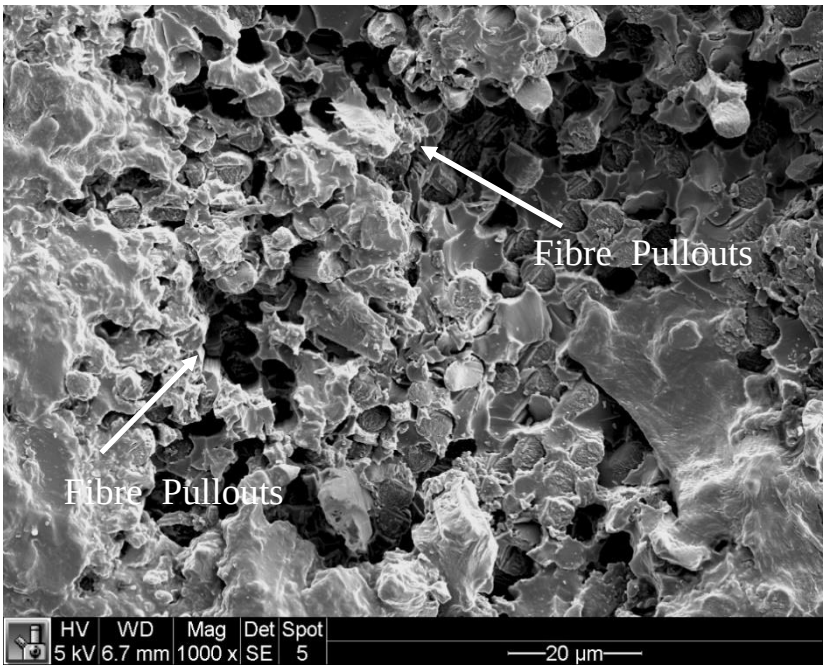

Figure 7.8 SEM of AWJ (80 Grit) Trimmed Surface

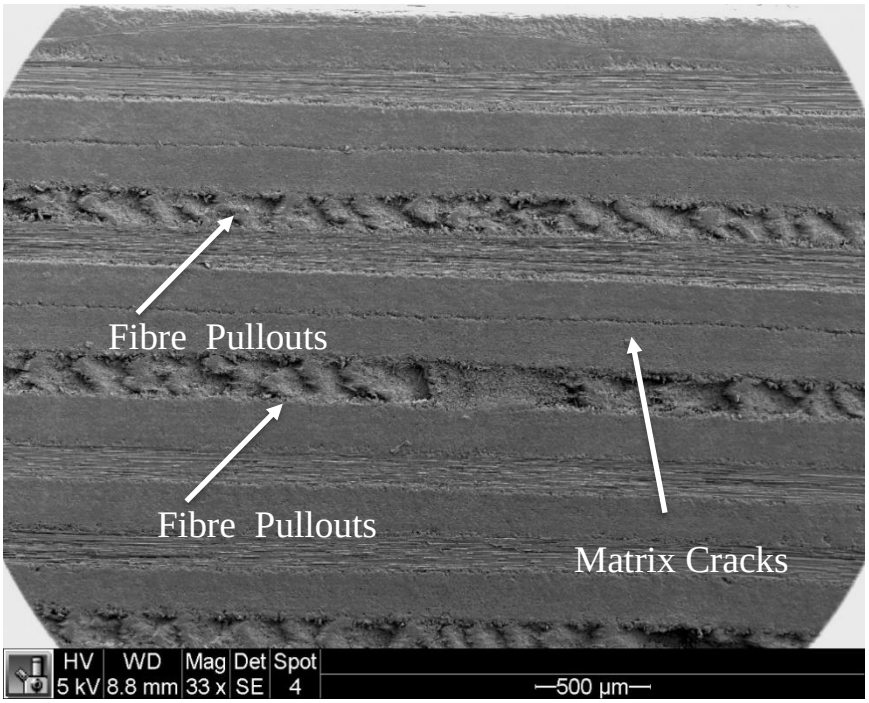

Figure 7.9 SEM of CVD Diamond Coated Endmill Trimmed Surface

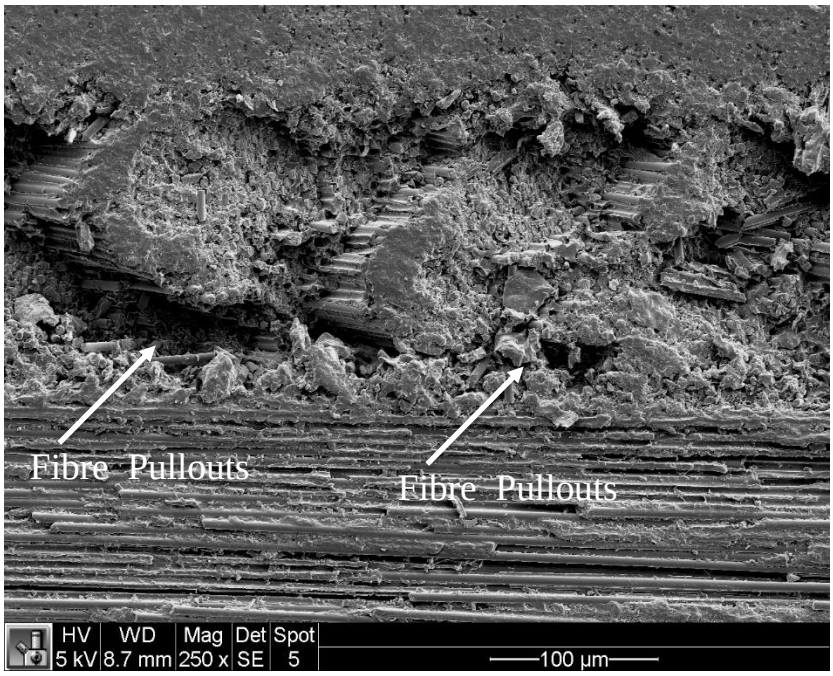

Figure 7.10 SEM of CVD Diamond Coated Endmill Trimmed Surface

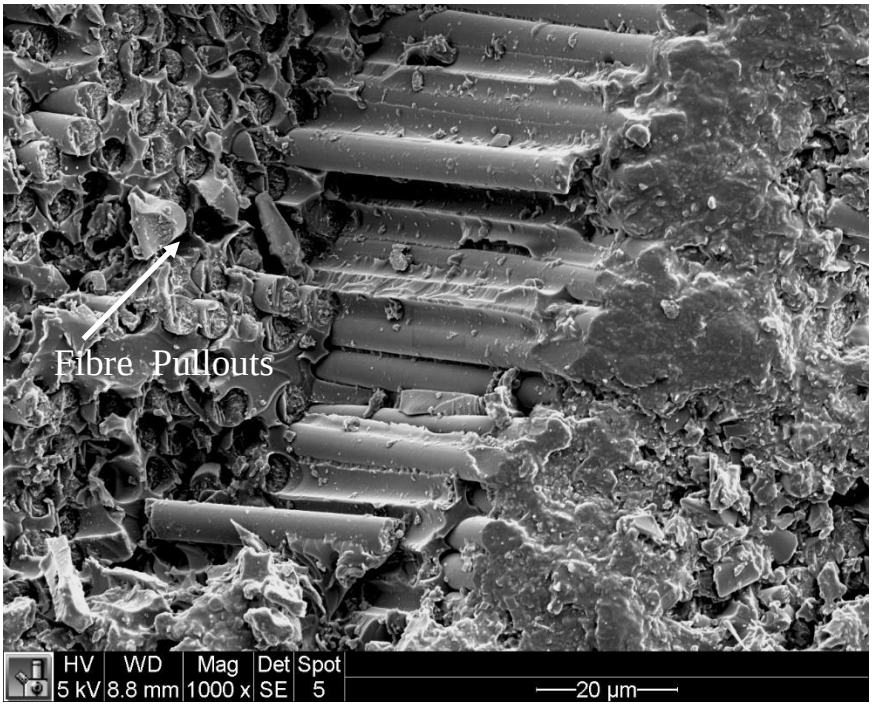

Figure 7.11 SEM of CVD Diamond Coated Endmill Trimmed Surface

7.3.4 Observations from Surface Finish data and SEMs of Trimmed Edges

The following observations were documented with the analysis of the SEMs of the trimmed edges of the test specimens.

a) CVD Endmill trimmed specimens showed a higher density of fibre pullouts
b) In both AWJ and CVD endmill trimmed specimens, fibre pullouts were predominant in the 45 degree plies
c) Delaminations were observed in both trimmed specimens but more in AWJ trimmed specimens at the exit edge
d) Generally, the surface finish data in the longitudinal direction showed smoother readings in the CVD Diamond Coated Endmill trimmed specimens
e) Surface finish data in the Transverse direction showed smoother readings in the AWJ trimmed specimens

7.3.5 Drilled Holes – Surface Finish Data

Table 7.6 shows the surface finish readings documented for a CVD Drill used to drill hole at a drilling feedrate of 508 mm/min

Phase II - Fatigue Testing Specimens - Data Summary					
Specimen Name	Surface Finish - R_a	Surface Finish - R_z	Surface Finish - R_t	Surface Finish - R_{sk}	Surface Finish - R_{ku}
CVD Hole	0.638	6.168	8.39	0.11	3.63

Table 7.6 Surface Finish Data for CVD Drilled hole

7.3.6 Drilled Holes – SEMs

Figures 7.12 through 7.14 show SEMs of CVD drilled holes

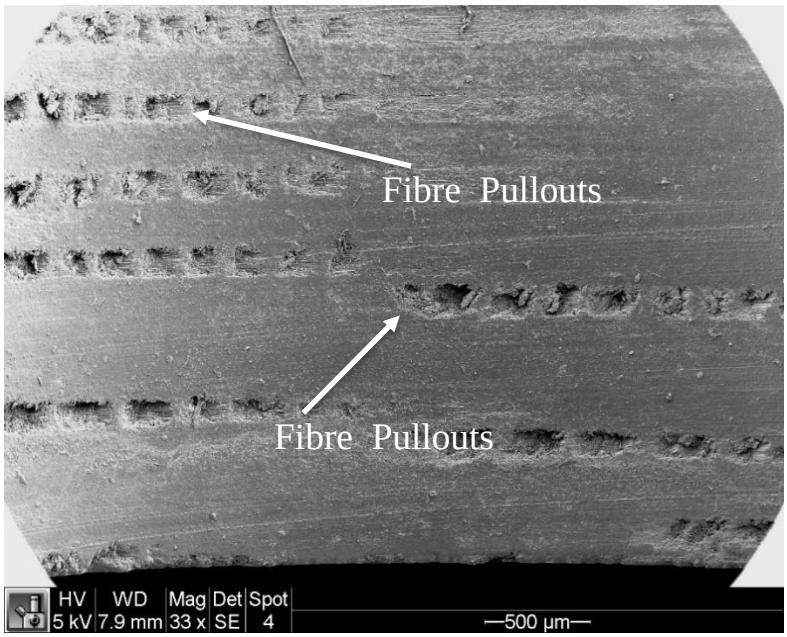

Figure 7.12 SEM of CVD Drilled Hole

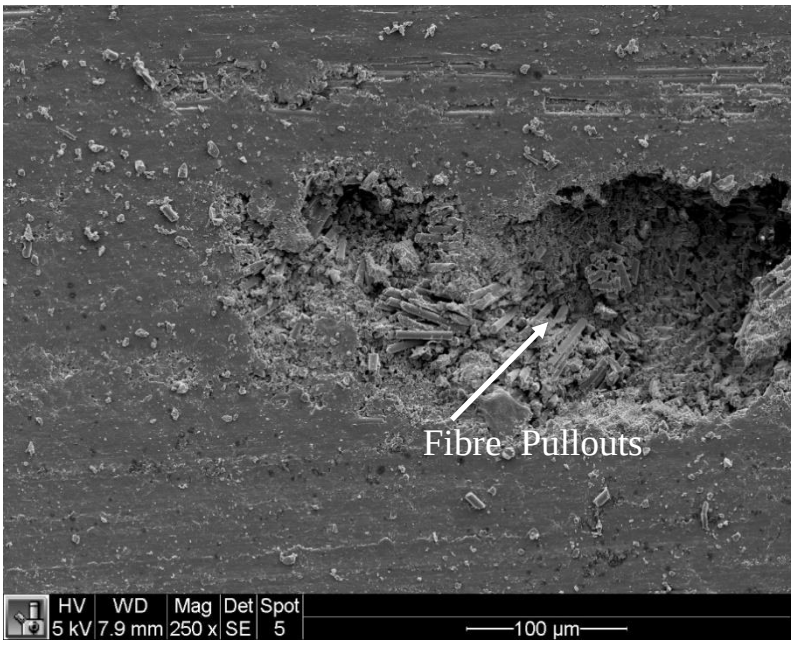

Figure 7.13 SEM of CVD Drilled Hole

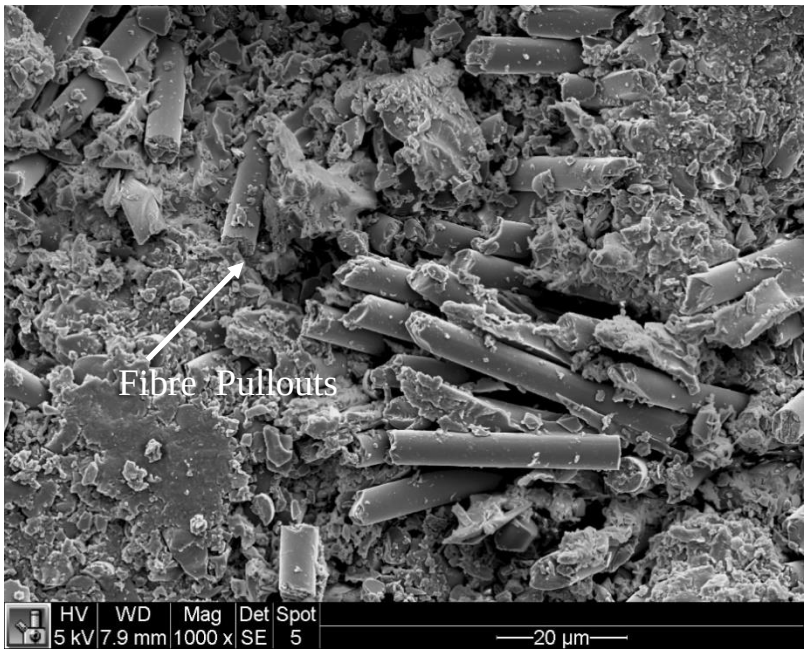

Figure 7.14 SEM of CVD Drilled Hole

7.3.7 Observations from Surface Finish data and SEMs of CVD Drilled holes

The following observations were documented with the analysis of the SEMs of the CVD drilled holes in the test specimen

a) Fibre pullouts density was consistent through the complete depth of the hole
b) Overall Fibre pullouts were localized in the 45 degree plies
c) Fibre pullouts are not completely around the circumference in the plies. This is attributed to simultaneous rotation and feed of the drill which results in a changing contact angle of the cutting edge with the 45 degree plies
d) Delaminations were noticed but were few in number

7.3.8 Fatigue Test Loads and their derivations

Based on test results from static mechanical testing as documented in chapter 6, fatigue test loads were derived for unnotched and notched specimen testing as follows:

Unnotched Testing

a) High Load Testing - An approximate average of failure loads between various tensile specimens was established for AWJ Trimmed and CVD Diamond Coated Endmill Trimmed specimens was established around 87000 N. A sample was tested at 80000 N and failed at less than 30,000 cycles for the high load/stress testing specimens. So, the fatigue test load was lowered to 77844 N (17500 lbf) for the high load specimens. This translated to approximately 89% of the average tensile failure loads.
b) Medium Load Testing – With single sample testing, the medium test load was established at 73396 N (16500 lbf). This translated to approximately 81.5% of the average tensile failure loads.
c) Low Load Testing – With single sample testing, the low test load was established at 68947 N (15500 lbf). This translated to approximately 76% of the average tensile failure loads.

For all of the unnotched specimen testing, the stress ratio for tension-tension testing was 10% (R=0.1). The test frequency used was 5Hz. Table 7.7 shows the loads and stresses used for testing of unnotched specimens.

Specimen Name	Trim	Test Load (Max) (N)	Test Load (Min) (N)	Max Stress (Mpa)	Test Frequency
A1-H-2	AWJ -80	77844	7784	679.1	5 Hz
A1-H-3	AWJ -80	77844	7784	679.1	5 Hz
A1-H-4	AWJ -80	77844	7784	679.1	5 Hz
A1-M-1	AWJ -80	73396	7339	636.24	5 Hz
A1-M-2	AWJ -80	73396	7339	636.24	5 Hz
A1-M-3	AWJ -80	73396	7339	636.24	5 Hz
A1-L-1	AWJ -80	68947	6894	600.32	5 Hz
A1-L-2	AWJ -80	68947	6894	600.32	5 Hz
A1-L-3	AWJ -80	68947	6894	600.32	5 Hz
B1-H-1	CVD Endmill	77844	7784	679.1	5 Hz
B1-H-2	CVD Endmill	77844	7784	679.1	5 Hz
B1-H-3	CVD Endmill	77844	7784	679.1	5 Hz
B1-M-1	CVD Endmill	73396	7339	636.24	5 Hz
B1-M-2	CVD Endmill	73396	7339	636.24	5 Hz
B1-M-3	CVD Endmill	73396	7339	636.24	5 Hz
B1-L-1	CVD Endmill	68947	6894	600.32	5 Hz
B1-L-2	CVD Endmill	68947	6894	600.32	5 Hz
B1-L-3	CVD Endmill	68947	6894	600.32	5 Hz
B1-L-4	CVD Endmill	68947	6894	600.32	5 Hz

Table 7.7 Test Loads & Stresses for Unnotched Fatigue Testing

Notched Testing

a) High Load Testing - An approximate average of failure loads between various open hole tensile specimens was established for AWJ Trimmed and CVD Diamond Coated Endmill Trimmed specimens was established around 58000 N. Two specimens were tested at lower loads before establishing the fatigue test load at 55603 N (12500 lbf) for the high load specimens. This translated to approximately 95% of the average open hole tensile failure loads.
b) Medium Load Testing – With single sample testing, the medium test load was established at 51115 N (11500 lbf). This translated to approximately 87% of the average open hole tensile failure loads.
c) Low Load Testing – With single sample testing, the low test load was established at 46706 N (10500 lbf). This translated to approximately 76% of the average tensile failure loads.

For all of the unnotched specimen testing, the stress ratio for tension-tension testing was 10% (R=0.1). The test frequency used was 7Hz. Table 7.8 shows the loads and stresses used for testing of unnotched specimens.

Specimen Name	Trim	Hole	Test Load (Max) (N)	Test Load (Min) (N)	Max Stress (Mpa)	Test Frequency
A2-H-3	AWJ -80	CVD Drill	55603	5560	484.2	7 Hz
A2-H-4	AWJ -80	CVD Drill	55603	5560	484.2	7 Hz
A2-M-1	AWJ -80	CVD Drill	51155	5115	444.7	7 Hz
A2-M-2	AWJ -80	CVD Drill	51155	5115	444.7	7 Hz
A2-M-3	AWJ -80	CVD Drill	51155	5115	444.7	7 Hz
A2-M-4	AWJ -80	CVD Drill	51155	5115	444.7	7 Hz
A2-L-1	AWJ -80	CVD Drill	46706	4670	406.65	7 Hz
A2-L-2	AWJ -80	CVD Drill	46706	4670	406.65	7 Hz
A2-L-3	AWJ -80	CVD Drill	46706	4670	406.65	7 Hz
A2-L-4	AWJ -80	CVD Drill	46706	4670	406.65	7 Hz
B2-H-1	CVD Endmill	CVD Drill	55603	5560	484,2	7 Hz
B2-H-2	CVD Endmill	CVD Drill	55603	5560	484.2	7 Hz
B2-H-3	CVD Endmill	CVD Drill	55603	5560	484,2	7 Hz
B2-H-4	CVD Endmill	CVD Drill	55603	5560	484.2	7 Hz
B2-M-1	CVD Endmill	CVD Drill	51155	5115	444.7	7 Hz
B2-M-2	CVD Endmill	CVD Drill	51155	5115	444.7	7 Hz
B2-M-3	CVD Endmill	CVD Drill	51155	5115	444.7	7 Hz
B2-L-1	CVD Endmill	CVD Drill	46706	4670	406.65	7 Hz
B2-L-2	CVD Endmill	CVD Drill	46706	4670	406.65	7 Hz
B2-L-3	CVD Endmill	CVD Drill	46706	4670	406.65	7 Hz

Table 7.8 Test Loads & Stresses for Notched Fatigue Testing

7.3.9 Types of Data Collected

During Fatigue Cycle testing the following data sets were recorded and collected for each test specimen

1) Number of cycles tested
2) Force (recorded in lbf and converted to Newtons)
3) Displacement (recorded in inches and converted to mm)
4) Compliance (recorded in mil/kip and converted to mm/N)
5) Baseline Compliance (recorded in mil/kip and converted to mm/N)
6) % Compliance change (recorded in mil/kip and converted to mm/N)
7) Strain gauge 1 (microstrain recorded)
8) Strain gauge 2 (microstrain recorded)
9) Poisson's ratio
10) Command Frequency
11) Total time in minutes
12) Running time in minutes

Still photos with zoom in features were taken by 2 advanced digital cameras mounted to view the forward and Aft side of each test specimen. Data collection for all data sets including recording of damage evolution with cameras was conducted by stopping the testing at regular cycling intervals. All data collection including photo micrographs were recorded in an automated mode with data acquisition software programmed to conduct data collection at following intervals:

a) For high loads data was collected at the following intervals
    a. 100 cycles
    b. 1000 cycles
    c. Interval of 1K cycles till 10K cycles
    d. After 10K cycles intervals of 5K cycles till failure
b) For medium loads data was collected at the following intervals
    a. 100 cycles
    b. 1000 cycles
    c. Interval of 5K cycles till 10K cycles after which intervals of 10K till 100K cycles
    d. After 100K cycles, interval of 25K cycles till failure
c) For low loads data was collected at the following intervals

a. 100 cycles
b. 1000 cycles
c. Interval of 5K cycles till 10K cycles after which intervals of 10K till 100K cycles
d. After 100K cycles, interval of 25K cycles till failure

7.4 Fatigue Cycles Testing Data Review

Data collected during fatigue cycle testing was reviewed per unnotched and notched test specimens categorized into high, medium and low load testing conducted. All test specimens other than those that reached 1,000,010 cycles were tested to failure. Damage initiation and propagation for each test specimen was documented through phot micrographs as well as change in compliance of the test specimen.

7.4.1 Unnotched Test Specimens Data Review

All unnotched test specimens were tested at a frequency of 5 Hz.

7.4.1.1 High Load Test Specimen Data Review

For the high load test specimens, specimen # A1-H-1 was used to derive the test load condition. The following samples were tested for AWJ trimmed specimens.

A1 – H – 2

A1 – H – 3

A1 – H – 4

For CVD Diamond Coated Endmill Trimmed specimens, the following samples were tested.

B1 – H – 1

B1 – H – 2

B1 – H – 3

Prior to testing the following surface finish parameters were recorded for each sample in both longitudinal and transverse directions

R_a , R_z , R_t , R_{sk} , R_{ku}

Table 7.9 shows the fatigue cycles to failure for each of the high load specimens along with the load applied and stress as well as % change in compliance.

Tables 7.4 and 7.5 documented earlier in this chapter show the surface finish data documented in the longitudinal and transverse direction.

Specimen Name	Trim	Fatigue Cycles	Test Load (Max) (N)	Test Load (Min) (N)	Max Stress (Mpa)	Test Frequency	Compliance
A1-H-2	AWJ -80	32369	77844	7784	679.1	5 Hz	12.80%
A1-H-3	AWJ -80	34635	77844	7784	679.1	5 Hz	9.76%
A1-H-4	AWJ -80	31995	77844	7784	679.1	5 Hz	25.54%
B1-H-1	CVD Endmill	42045	77844	7784	679.1	5 Hz	28.26%
B1-H-2	CVD Endmill	45555	77844	7784	679.1	5 Hz	17.10%
B1-H-3	CVD Endmill	46800	77844	7784	679.1	5 Hz	13.93%

Table 7.9 Fatigue Cycles/Loads/Stress & % Compliance Change for Unnotched High Loading Testing

As shown in the above table, the test specimens in both cases for AWJ and CVD Endmill trimmed that has the lowest % compliance change (magnitude of damage) lasted slightly higher during fatigue cycle testing at high loads. This was observed in the case of high loads as damage progressed the effects of cyclic loading with high loads had accelerated ultimate failure.

Damage Propagation in AWJ trimmed specimens- To compare the damage propagation % compliance change was plotted for each AWJ high load specimen and the percentage damage at 20K cycles was compared. Figures 7.15 through 7.23 show the % compliance change for each high load AWJ test specimen along with a photo micrograph depicting the damage at 20K cycles.

It was observed that the lower progression of % compliance change (damage occurred) resulted in an increase in fatigue cycles to failure.

In all cases damage started as separation of plies (delamination) as shown in the figures. The initiation of damage was localized at the 45 degree plies (also the sites of fibre pullouts). Once damage started progressing, ultimate failure occurred due to the splitting apart of the laminate.

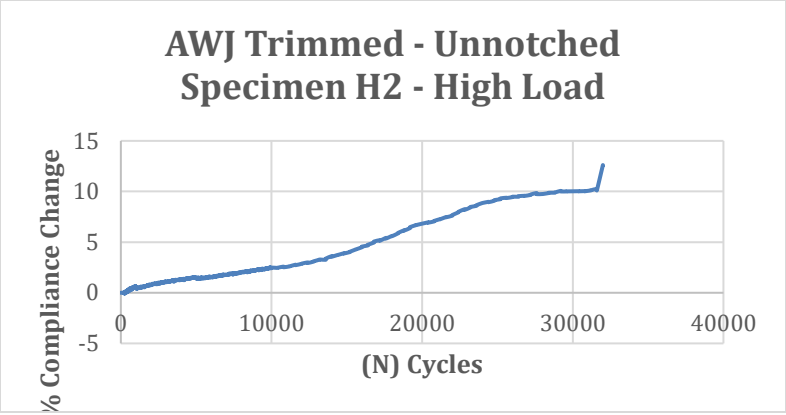

Figure 7.15 Percent Compliance Change Vs. Fatigue Cycles for A1 – H – 2

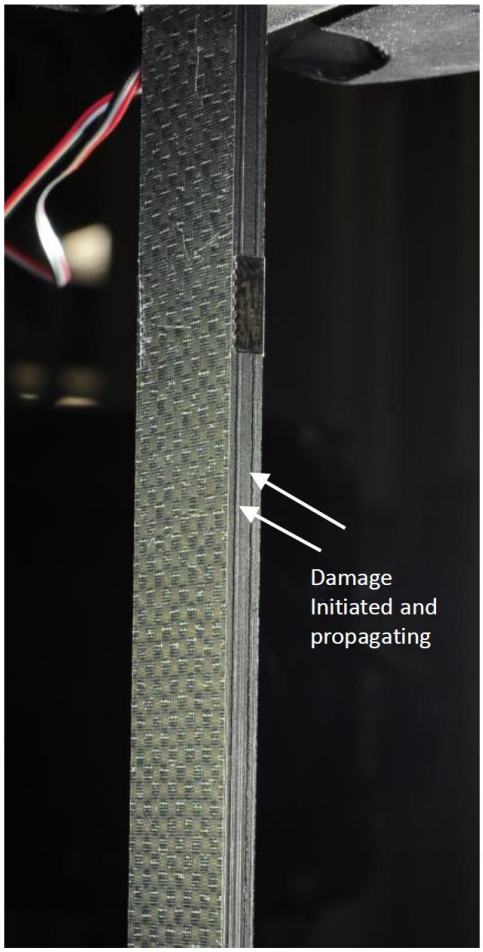

Figure 7.16 Damage at 20K Cycles, 7.49%, Test Specimen

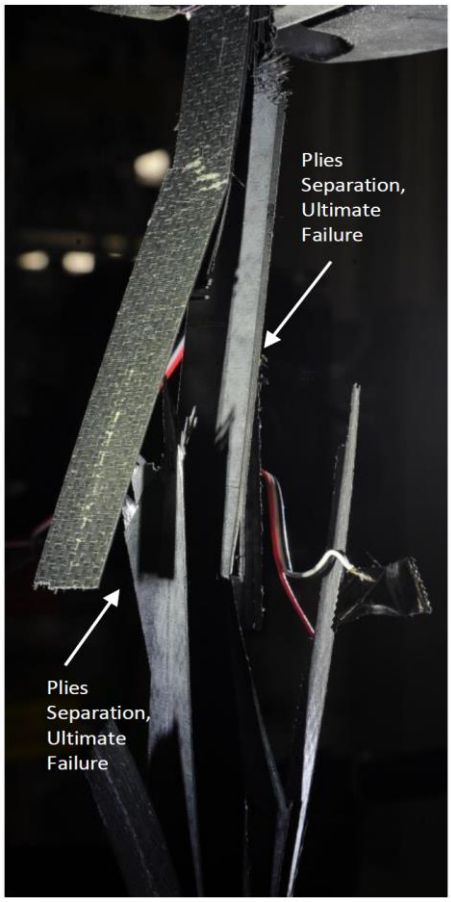

Figure 7.17 Damage (12.8%) & Ultimate Failure at 32369 Cycles A1 – H – 2

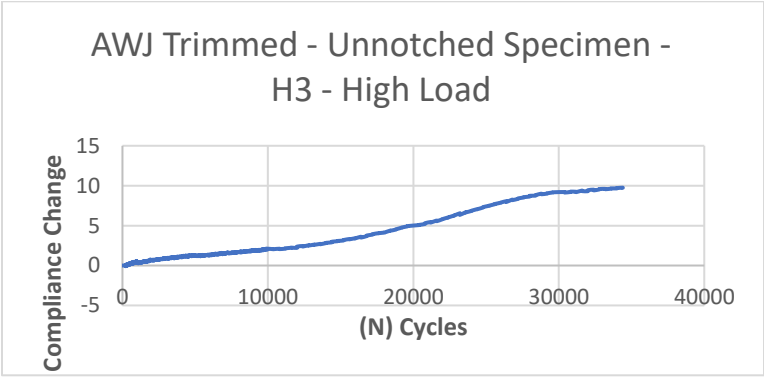

Figure 7.18 Percent Compliance Change Vs. Fatigue Cycles for A1 – H – 3

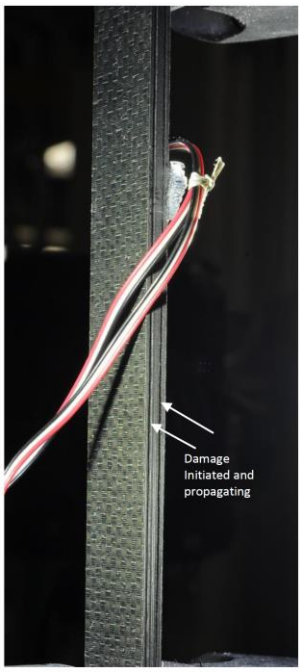

Figure 7.19 Damage at 20K Cycles, 5.64%, Test Specimen

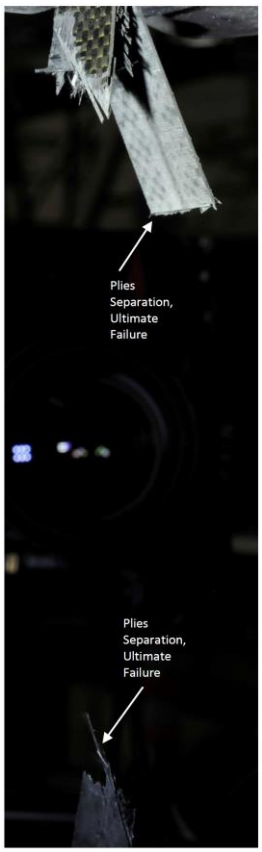

Figure 7.20 Damage (9.76%) & Ultimate Failure at 34365 Cycles A1 – H – 3

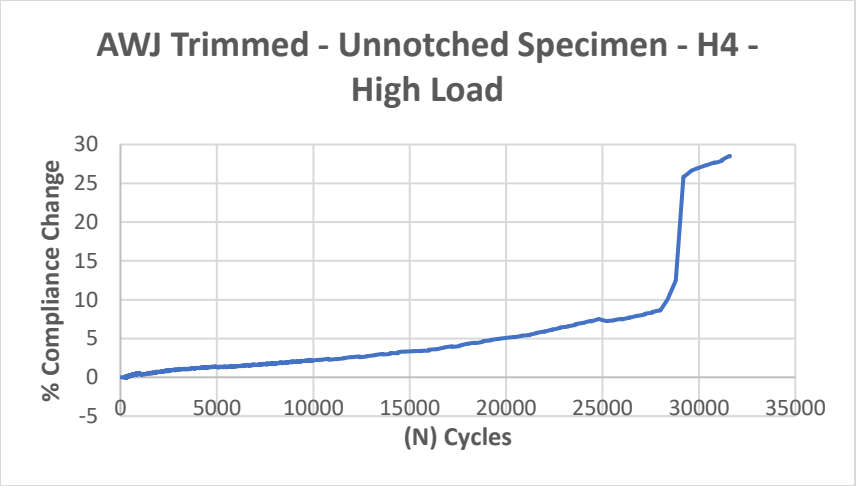

Figure 7.21 Percent Compliance Change Vs. Fatigue Cycles for A1 – H – 4

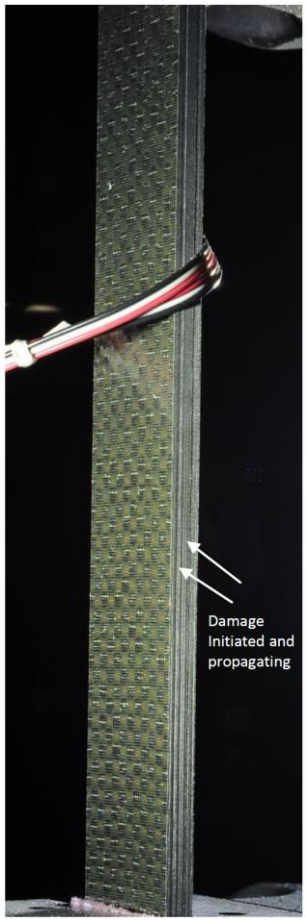

Figure 7.22 Damage at 20K Cycles, 5.76%, Test Specimen

Figure 7.23 Damage (25.54%) & Ultimate Failure at 31995 Cycles A1 – H – 4

Damage Propagation in CVD Diamond Coated Endmill trimmed specimens- To compare the damage propagation % compliance change was plotted for each CVD Diamond Coated Endmill trimmed high load specimen and the percentage damage at 20K cycles was compared. Figures 7.24 through 7.32 show the % compliance change for each high load CVD Endmill trimmed test specimen along with a photo micrograph depicting the damage at 20K cycles.

It was observed that the lower progression of % compliance change (damage occurred) resulted in an increase in fatigue cycles to failure.

In all cases damage started as separation of plies (delamination) as shown in the figures. The initiation of damage was localized at the 45 degree plies (also the sites of fibre pullouts). Once damage started progressing, ultimate failure occurred due to the splitting apart of the laminate.

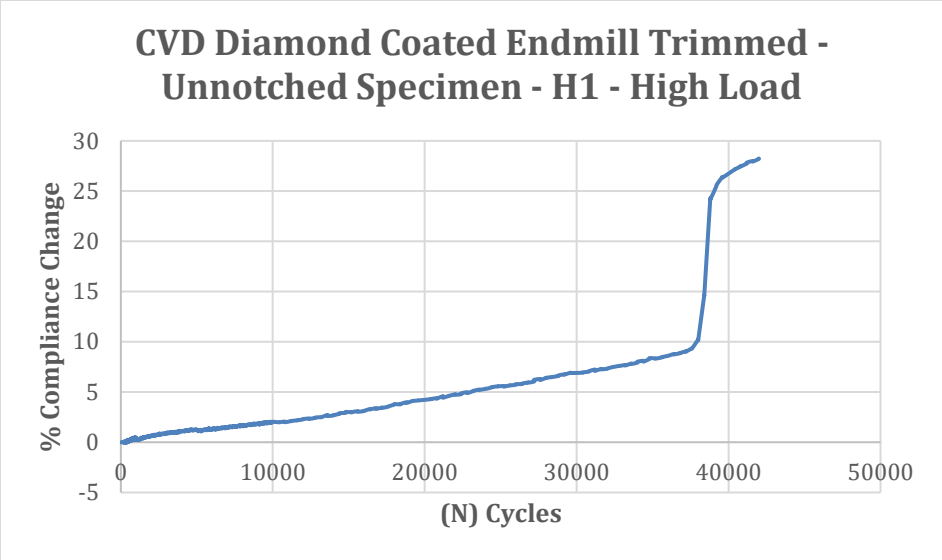

Figure 7.24 Percent Compliance Change Vs. Fatigue Cycles for B1 – H - 1

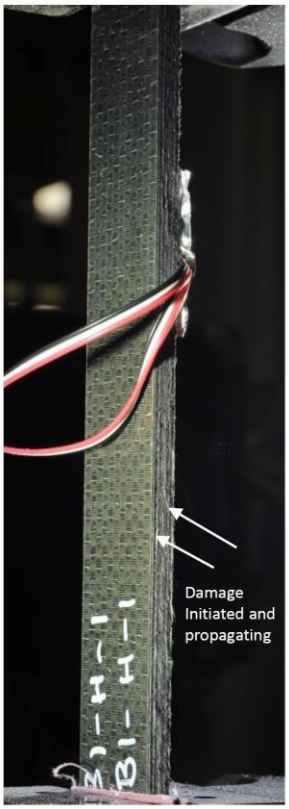

Figure 7.25 Damage at 20K Cycles, 4.37%, Test Specimen

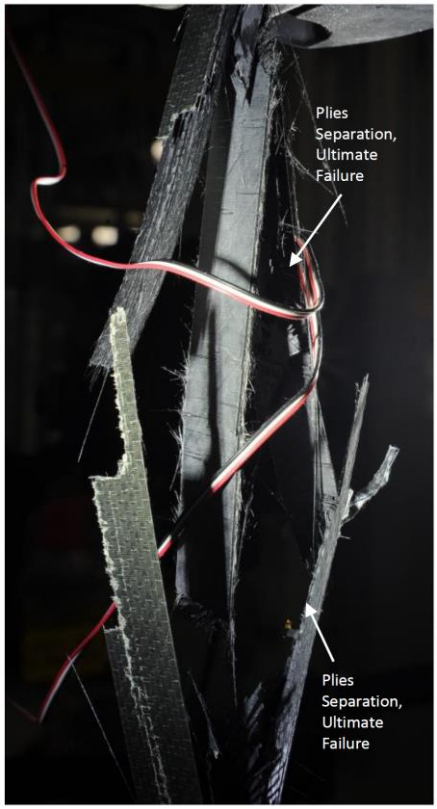

Figure 7.26 Damage (28.26%) & Ultimate Failure at 42045 Cycles

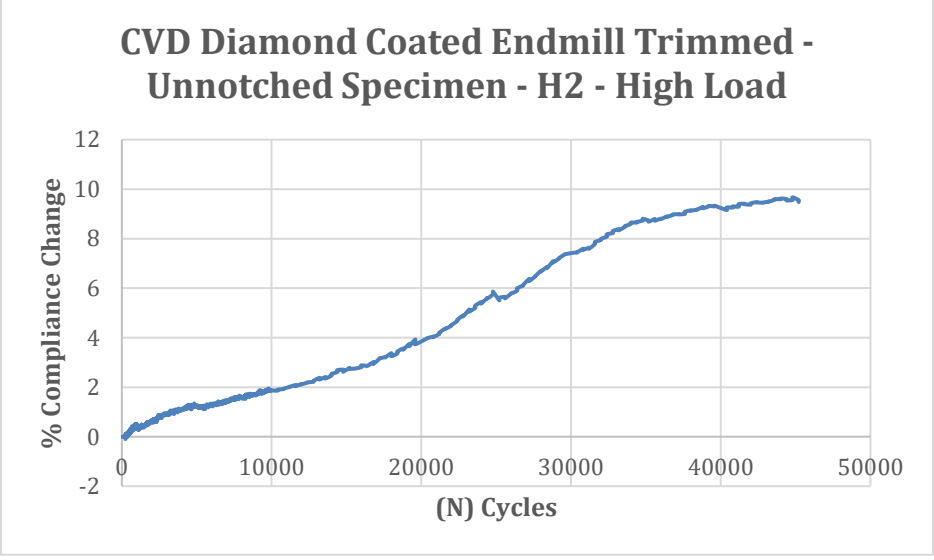

Figure 7.27 Percent Compliance Change Vs. Fatigue Cycles for B1 – H – 2

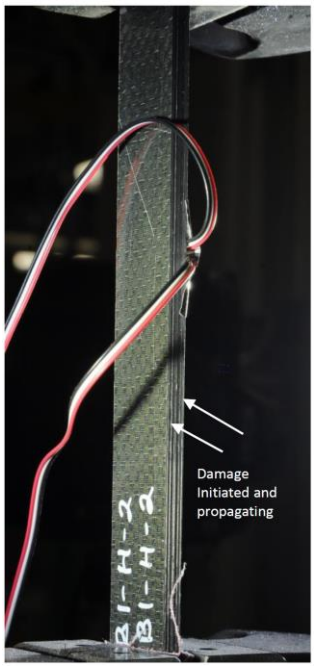

Figure 7.28 Damage at 20K Cycles, 3.92%, Test Specimen

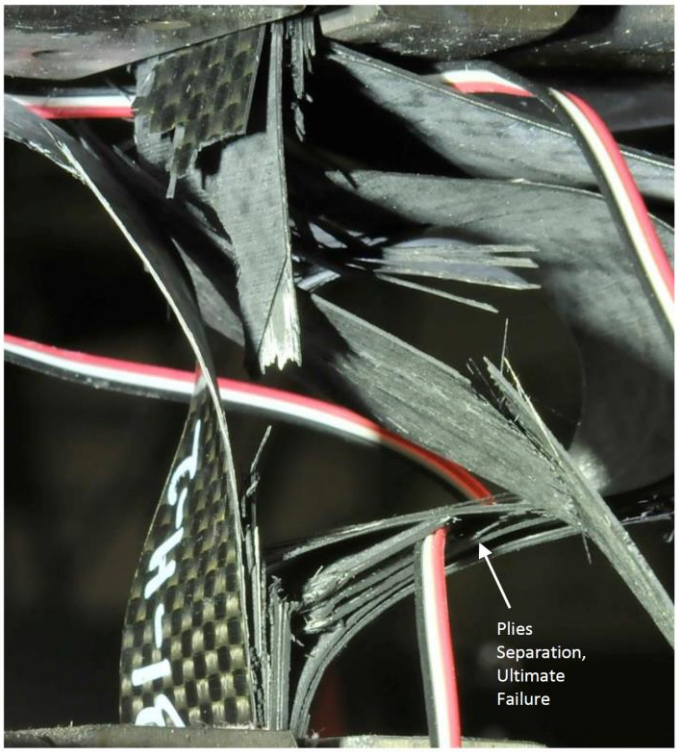

Figure 7.29 Damage (17.1%) & Ultimate Failure at 45555 Cycles

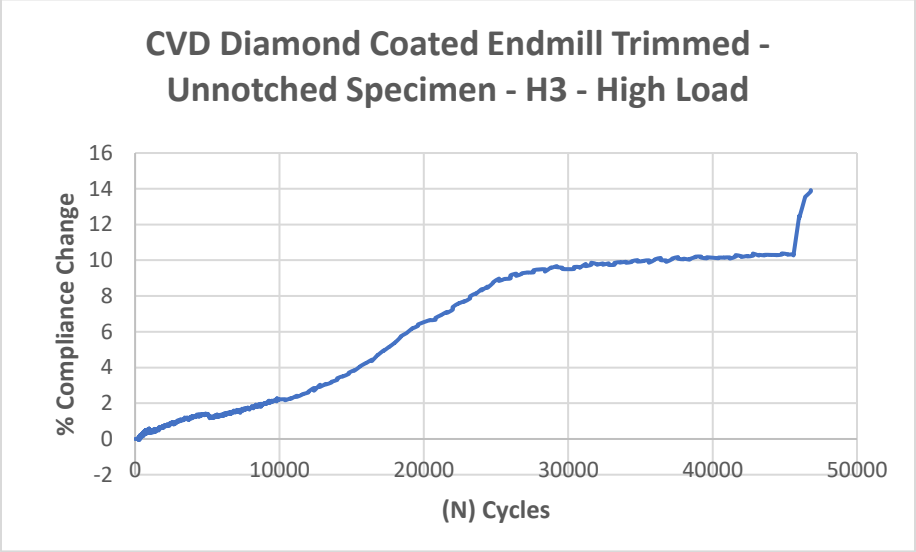

Figure 7.30 Percent Compliance Change Vs. Fatigue Cycles for B1 – H – 3

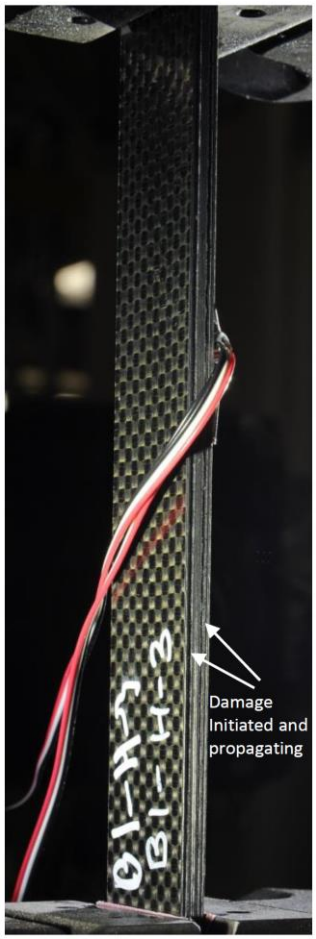

Figure 7.31 Damage at 20K Cycles, 6.65%, Test Specimen

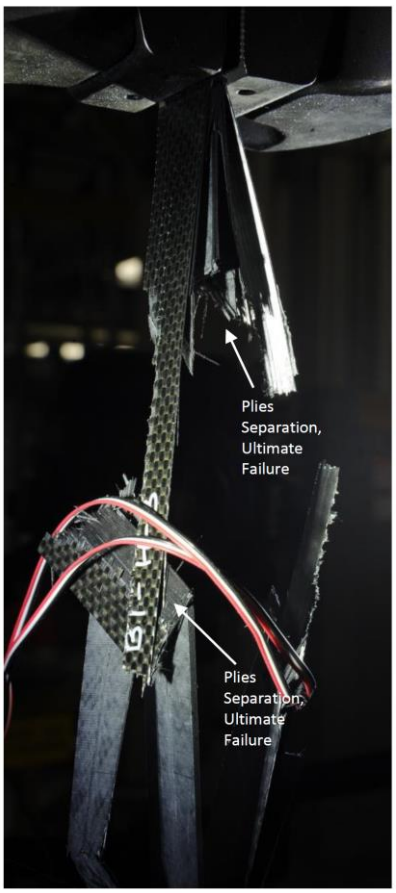

Figure 7.32 Damage (13.93%) & Ultimate Failure at 46800 Cycles

The CVD Diamond Coated Endmill Trimmed test Specimens generally had higher fatigue cycles to failure during unnotched high load testing as compared to AWJ trimmed cycles. Damage propagation in the CVD Endmill trimmed specimens was at a slower rate as compared to AWJ specimens which was contributed to a better surface finish in comparison to AWJ specimens in the longitudinal direction, the direction of applied loading.

The CVD Endmill trimmed specimens also displayed a steeper climb of the % Compliance change after certain percent damage had occurred. This was attributed to a higher density of fibre pullouts as compared to AWJ specimens. As damage progressed across the various plies, a higher number of fibre pullouts came into effective damage area thus increasing the rate of damage progress and causing a steep climb in the % Compliance change curve.

Figures 7.33, 7.34 and 7.35 show the plot of the AWJ and CVD trim compliance curves plotted to each other and versus each other.

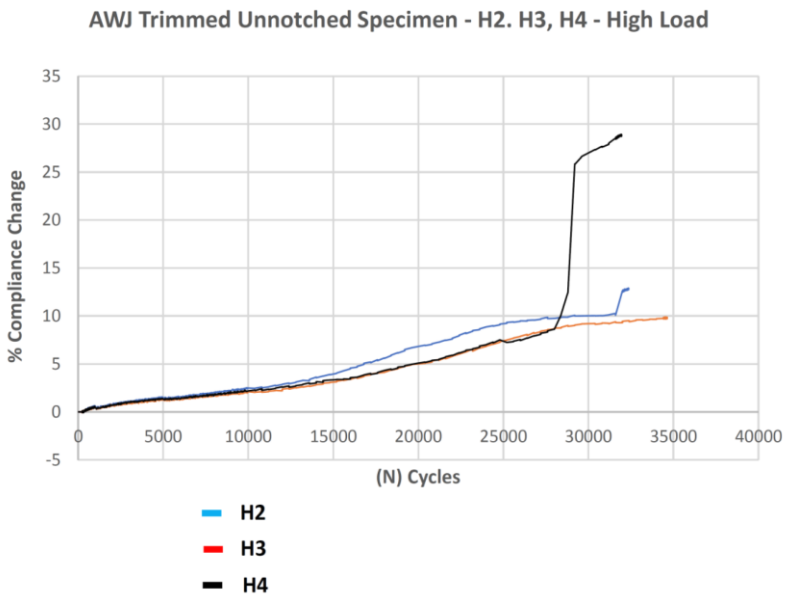

Figure 7.33 Summary Plot of AWJ High Load Percent Compliance Change Vs. Fatigues Cycles

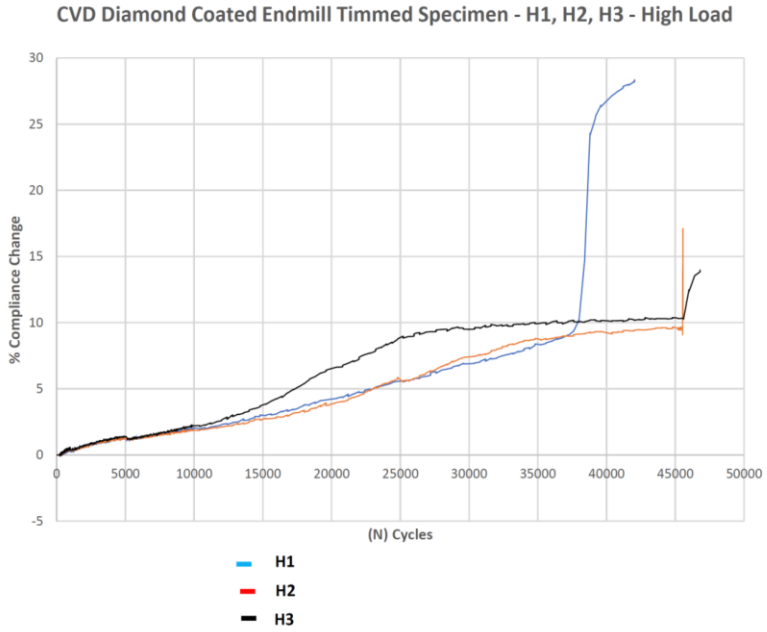

Figure 7.34 Summary Plot of CVD End Mill Trimmed High Load Percent Compliance Change Vs. Fatigues Cycles

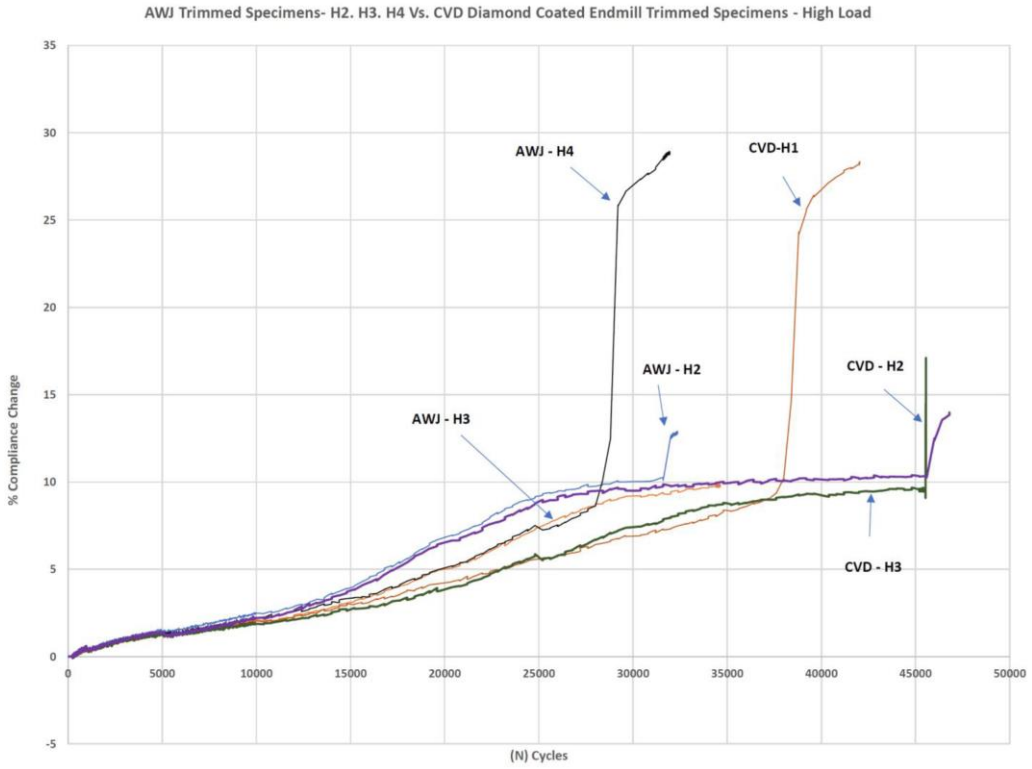

Figure 7.35 Summary Plot of AWJ Vs, CVD End Mill Trimmed High Load Percent Compliance Change Vs. Fatigues Cycles

Surface Finish Stress Concentration Factor $\left(\bar{K}_t\right)$

Surface finish profiles of all high load test specimens were used to calculate the stress concentration factor $\left(\bar{K}_t\right)$ using the formula shown in figure 7.36

$$\overline{K}_t = 1 + \eta\left(\frac{R_a}{\overline{\rho}}\right)\left(\frac{R_t}{R_z}\right) \text{ where}$$

$\eta = factor = 2(tension \,\&\, compression)$

$\overline{\rho} = notch\ root\ radius$

$R_a = average\ surface\ roughness$

$R_t = peak\ to\ valley\ height\ roughness$

$R_z = 10\ point\ roughness$

Figure 7.36 Stress Concentration Factor Calculation

Figures 7.37 through 7.42 Show the stress concentration factor determination graphically for the radius and using the formula from Figure 7.36

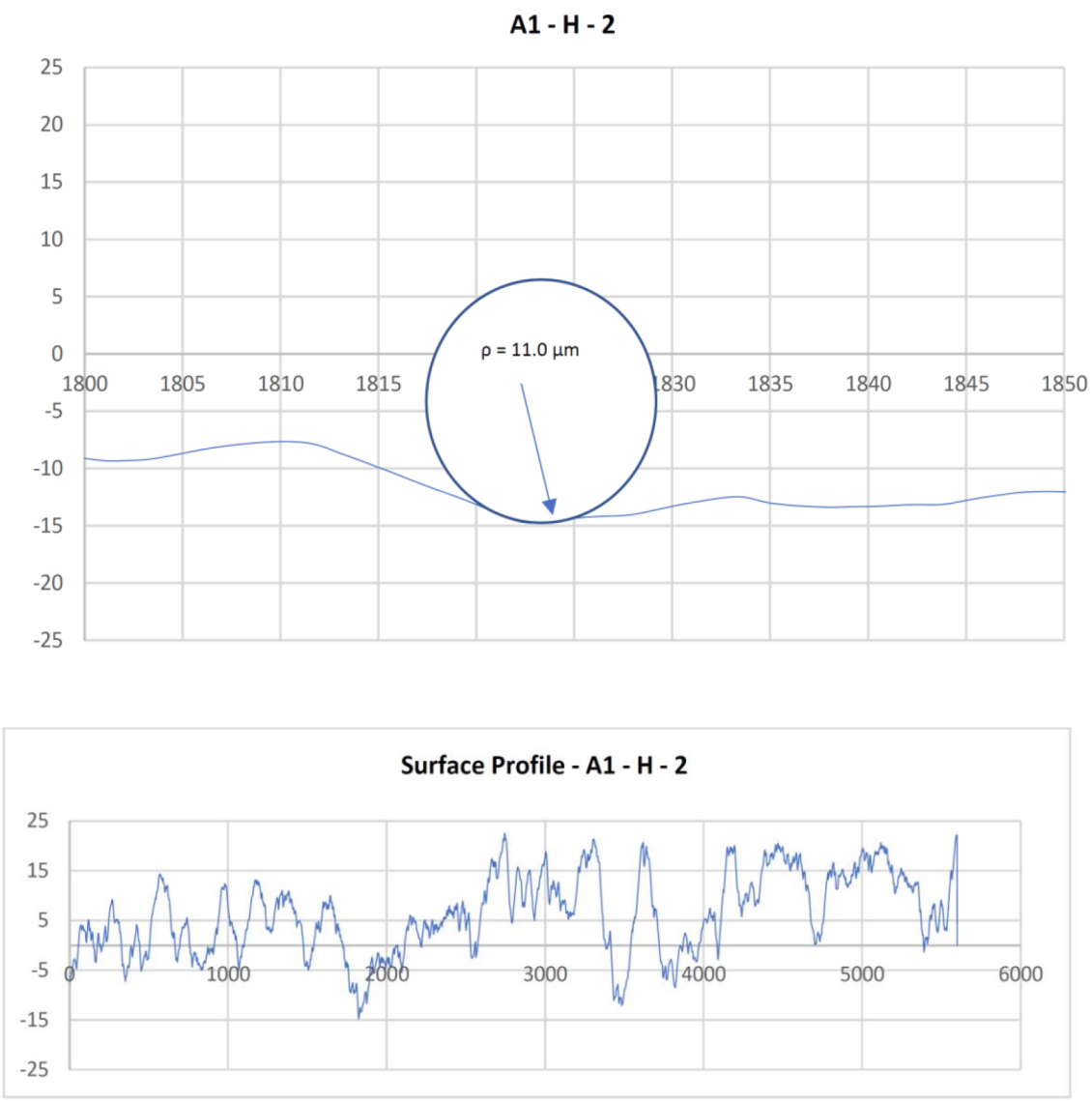

Figure 7.37 Graphical Determination of radius (ρ) from surface profile of test specimen, A1–H-2

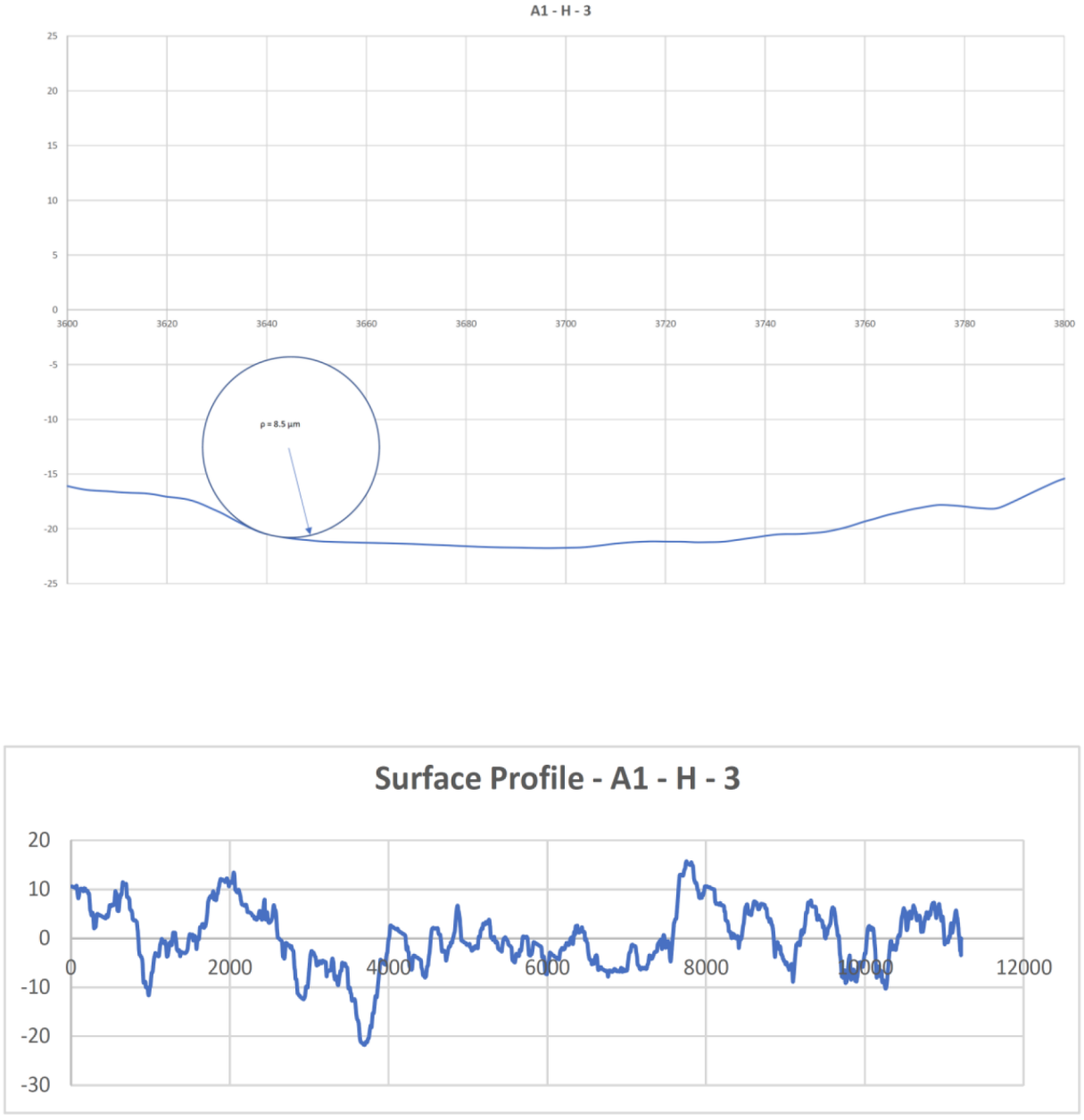

Figure 7.38 Graphical Determination of radius (ρ) from surface profile of test specimen, A1–H-3

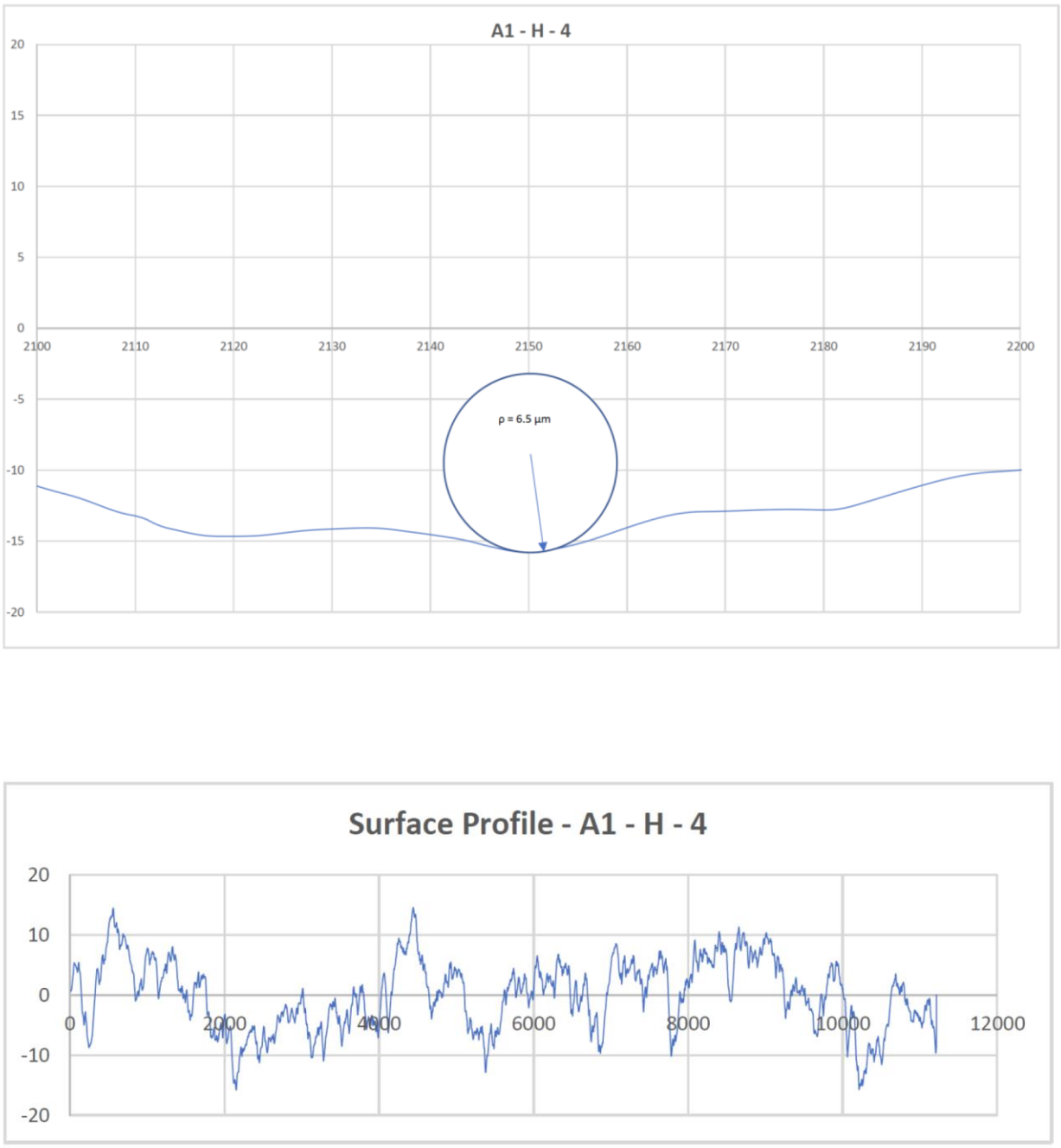

Figure 7.39 Graphical Determination of radius (ρ) from surface profile of test specimen, A1–H-4

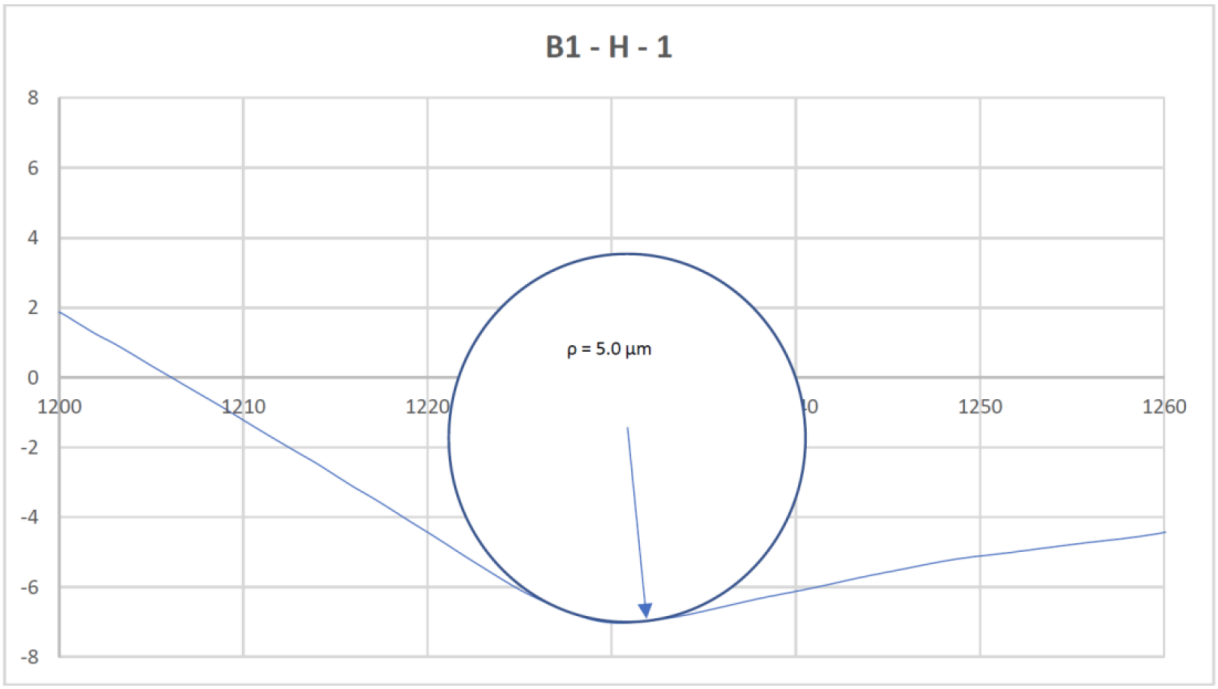

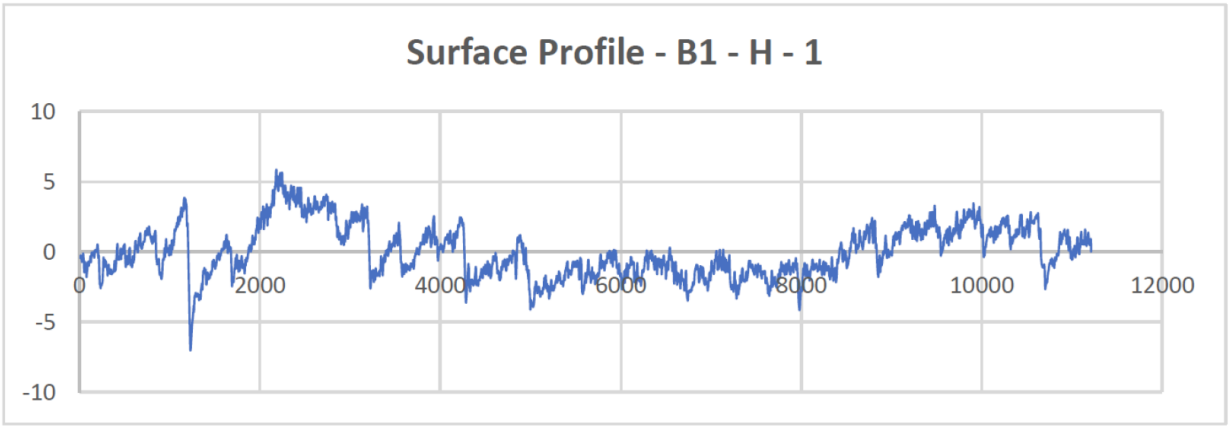

Figure 7.40 Graphical Determination of radius (ρ) from surface profile of test specimen, B1–H-1

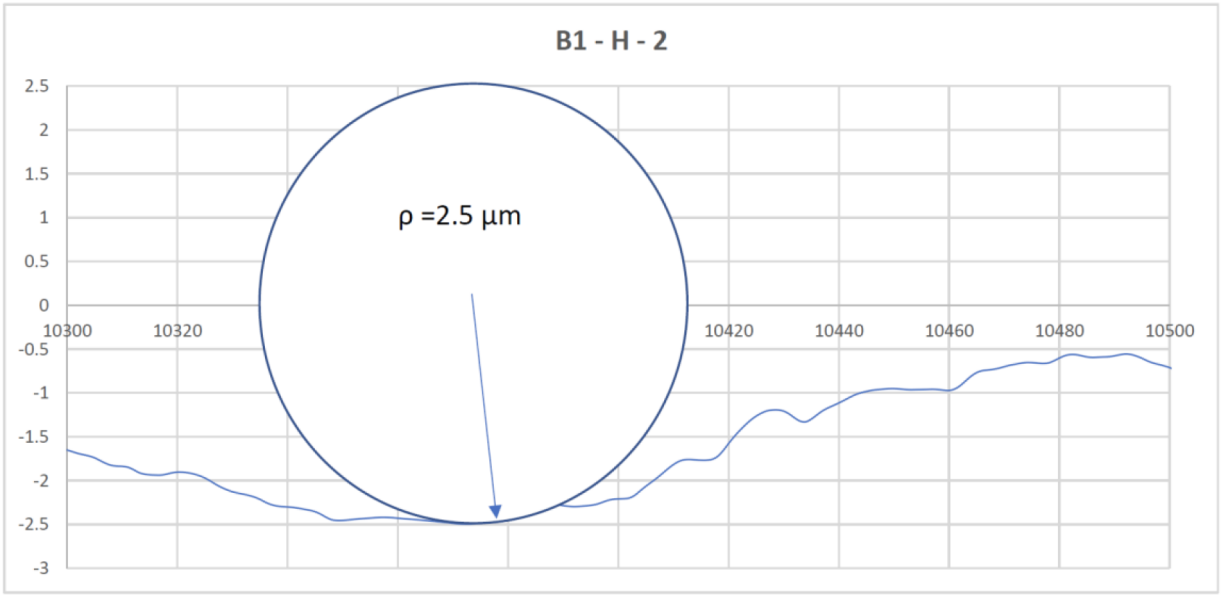

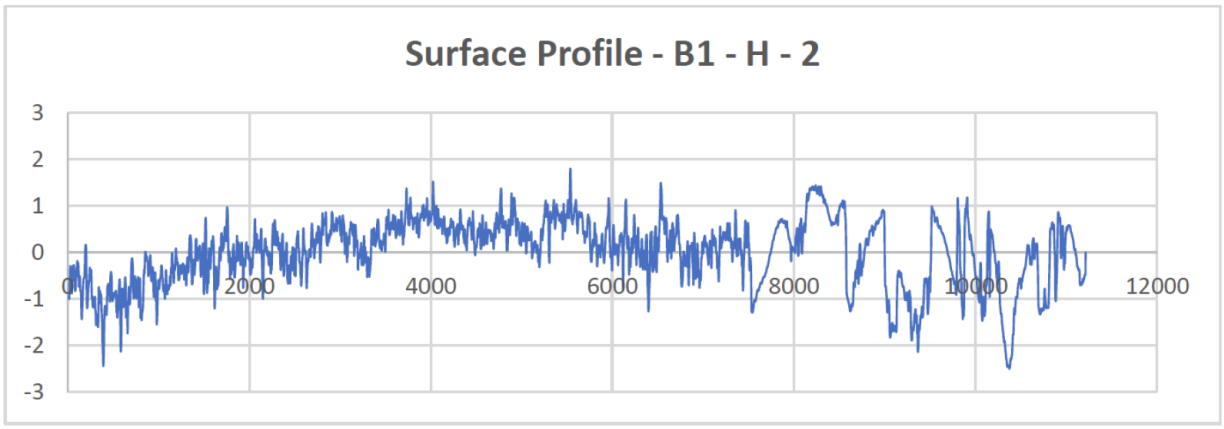

Figure 7.41 Graphical Determination of radius (ρ) from surface profile of test specimen, B1–H–2

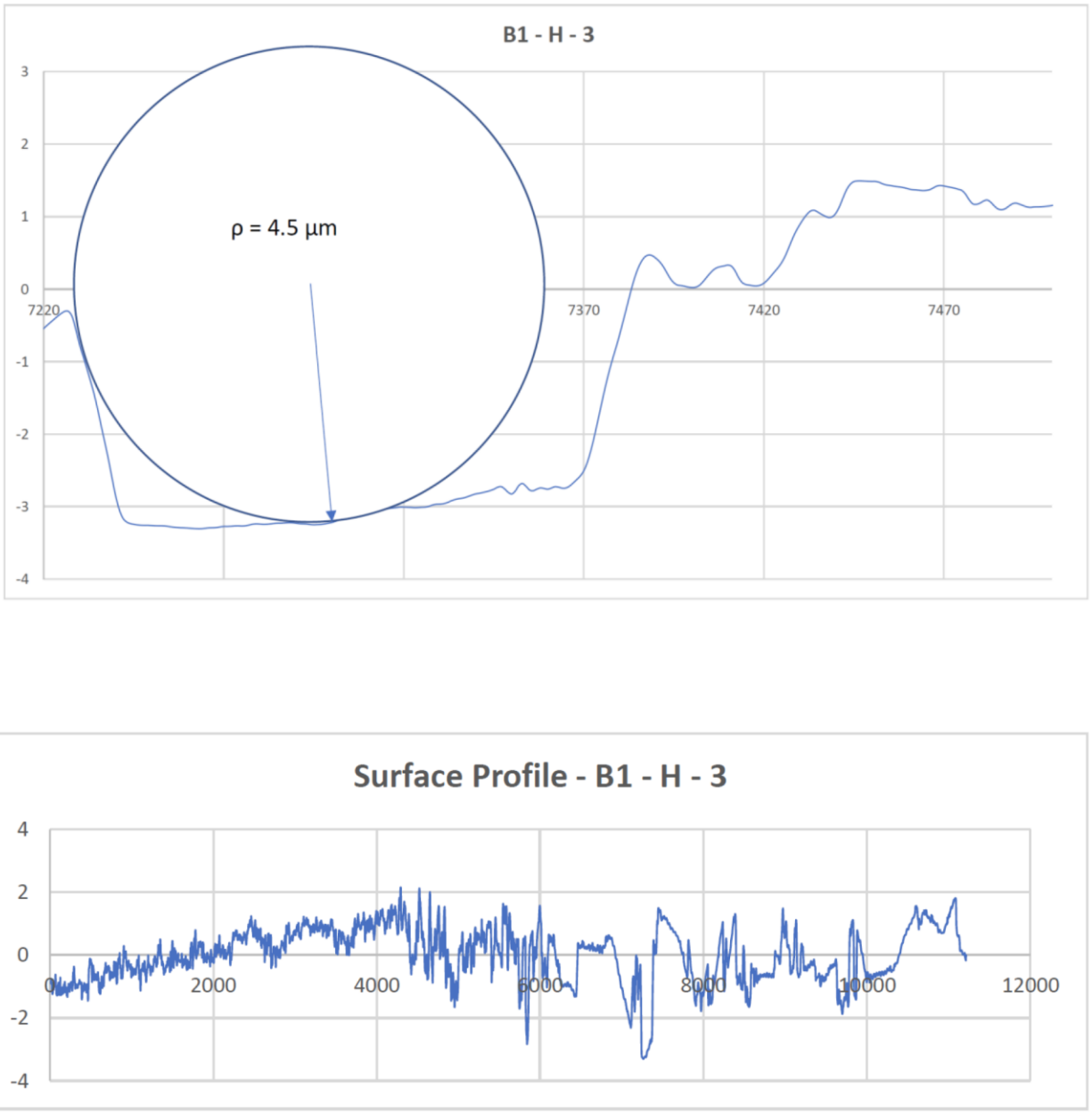

Figure 7.42 Graphical Determination of radius (ρ) from surface profile of test specimen, B1–H–3

Table 7.10 shows the calculated surface integrity stress concentration factors for unnotched high load test specimens.

Specimen Name	Surface Integrity Stress Concentration Factor
A1 – H - 2	2.14
A1 – H - 3	1.92
A1 – H - 4	2.22
B1 – H - 1	1.4
B1 – H - 2	1.35
B1 – H - 3	1.33

Table 7.10 Calculated Surface Integrity Stress Concentration Factors for Unnotched High Load Fatigue Test Specimens

Observation on Surface finish Data Vs. Fatigue Cycles – Surface finish data in the longitudinal direction was plotted against fatigue cycles and reviewed comparing AWJ trimmed specimens to CVD Diamond Coated Endmill Trimmed specimens. Figures 7.43 through 7.56 show the variation of surface finish parameters Vs. fatigue cycles for the different parameters.

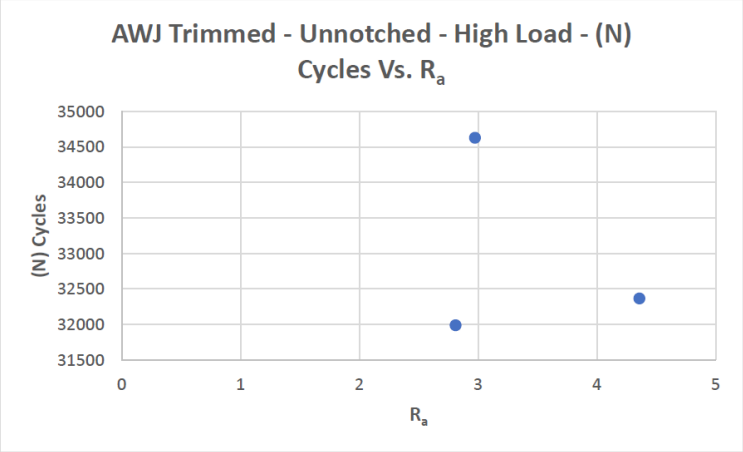

Figure 7.43 Surface Finish - R_a (longitudinal) Vs. Fatigue Cycles – AWJ Trimmed High Load Test Specimens

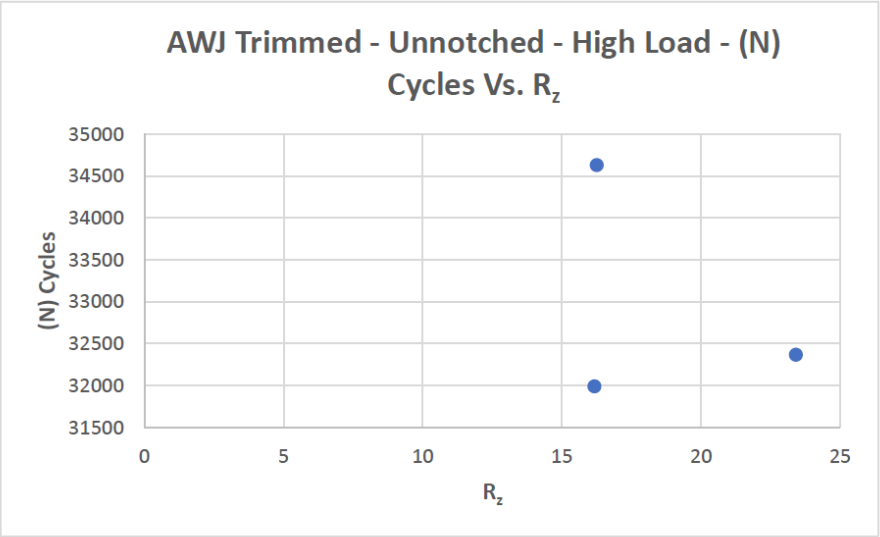

Figure 7.44 Surface Finish – R_z (longitudinal) Vs. Fatigue Cycles – AWJ Trimmed High Load Test Specimens

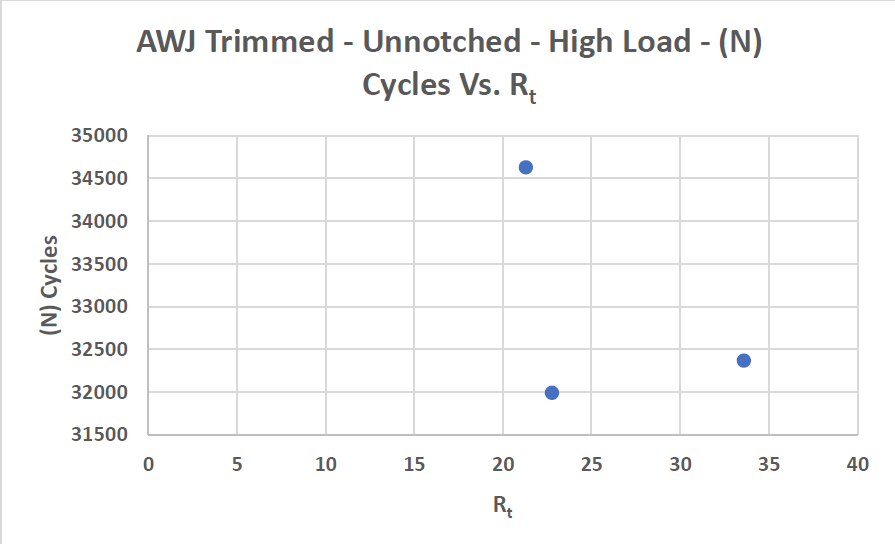

Figure 7.45 Surface Finish – R_t (longitudinal) Vs. Fatigue Cycles – AWJ Trimmed High Load Test Specimens

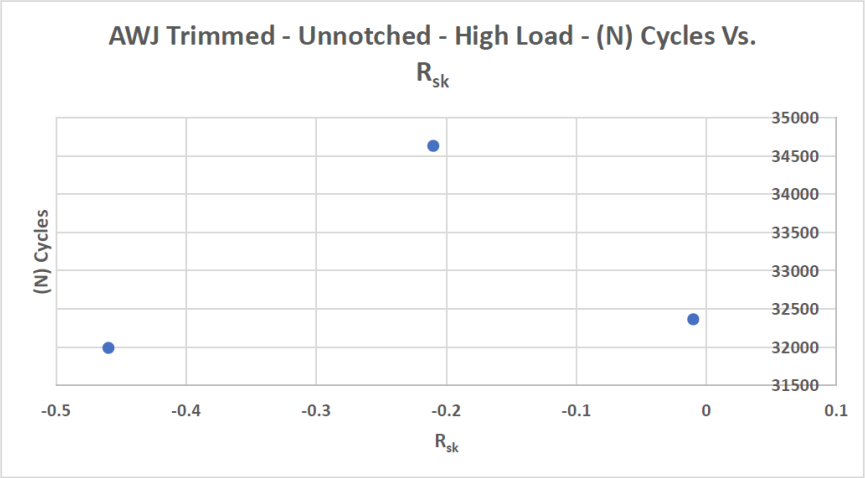

Figure 7.46 Surface Finish – R_{sk} (longitudinal) Vs. Fatigue Cycles – AWJ Trimmed High Load Test Specimens

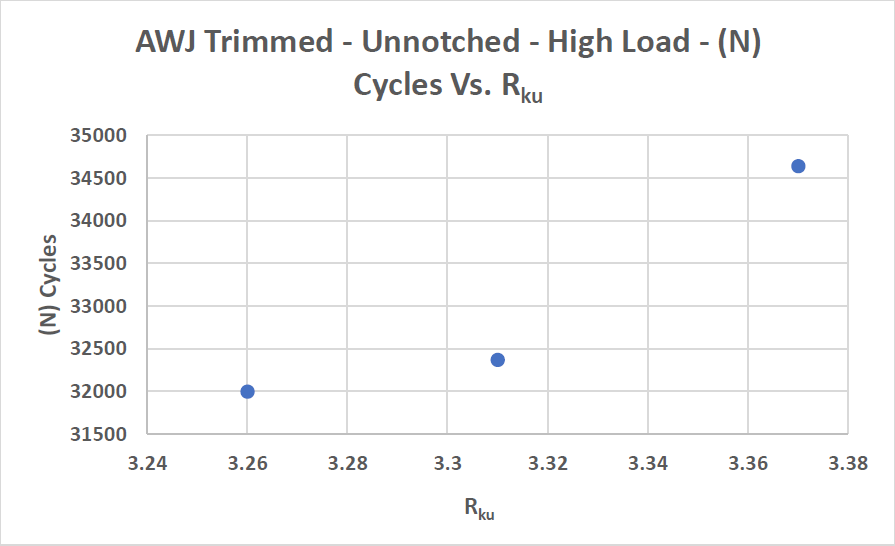

Figure 7.47 Surface Finish – R_{ku} (longitudinal) Vs. Fatigue Cycles – AWJ Trimmed High Load Test Specimens

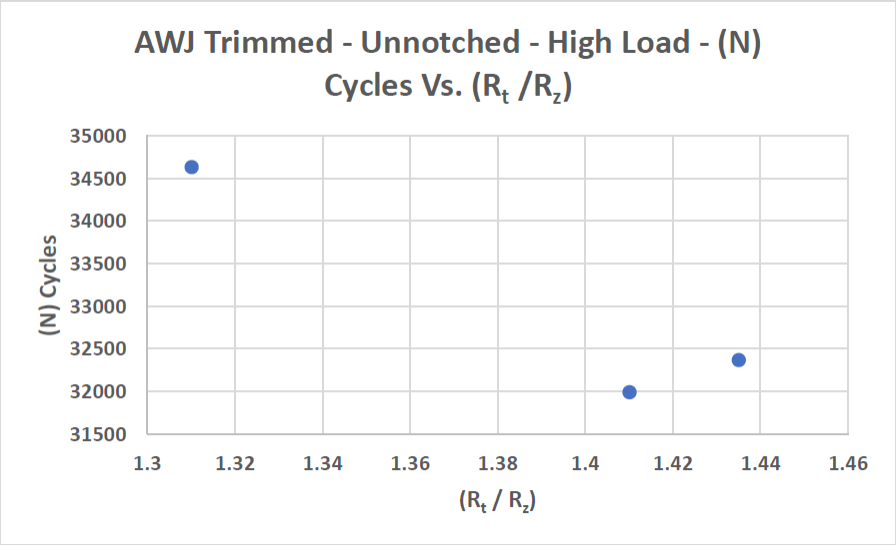

Figure 7.48 Surface Finish – (R_t/R_z) (Longitudinal) Vs. Fatigue Cycles – AWJ Trimmed High Load Test Specimens

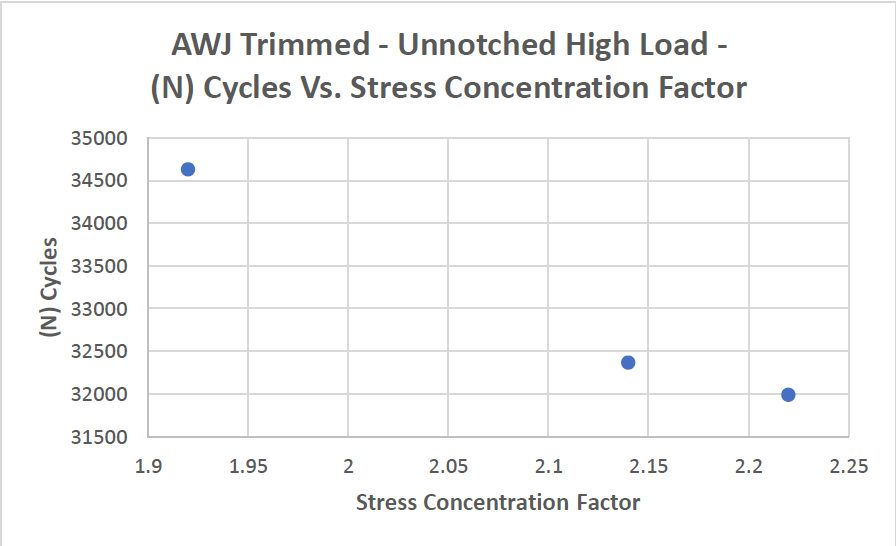

Figure 7.49 Surface Integrity Stress Concentration Factor (Longitudinal) Vs. Fatigue Cycles – AWJ Trimmed High Load Test Specimens

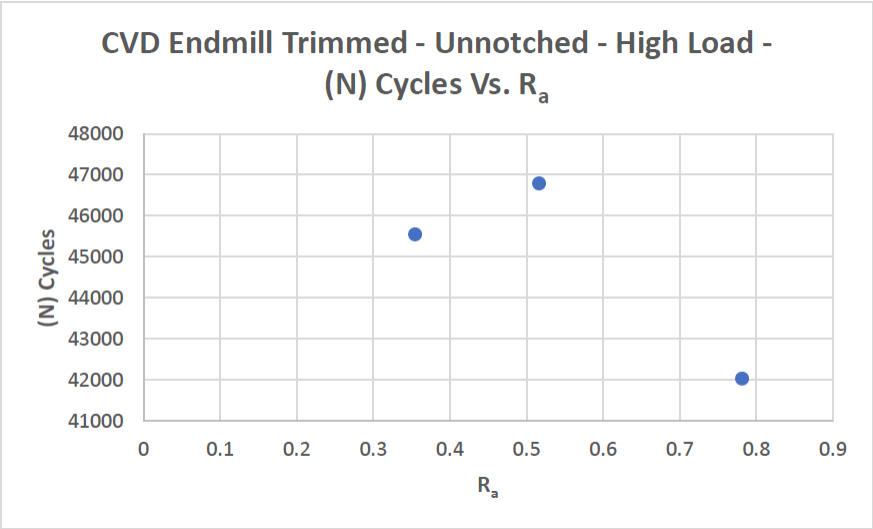

Figure 7.50 Surface Finish - R_a (longitudinal) Vs. Fatigue Cycles – CVD Endmill Trimmed High Load Test Specimens

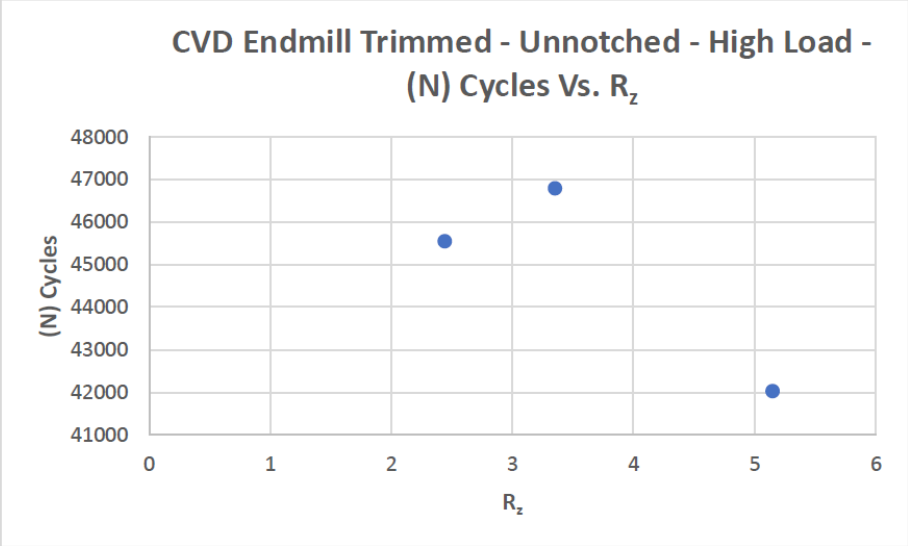

Figure 7.51 Surface Finish – R_z (longitudinal) Vs. Fatigue Cycles – CVD Endmill Trimmed High Load Test Specimens

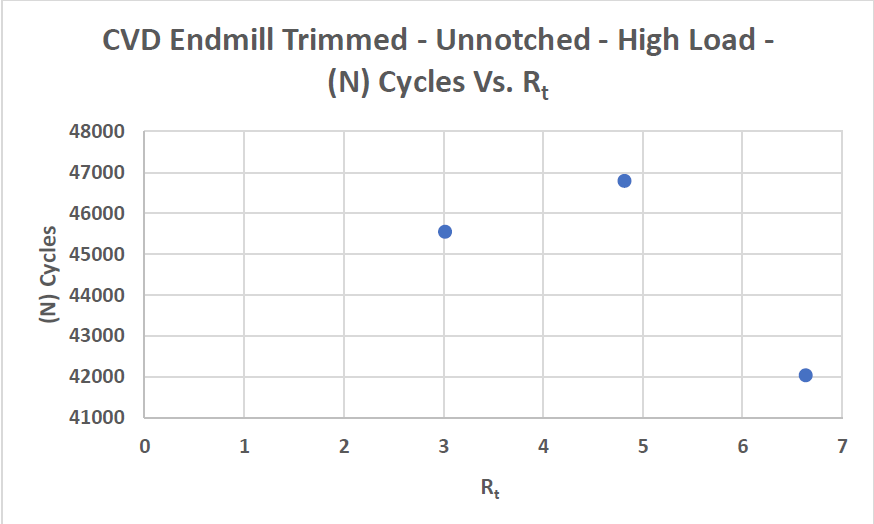

Figure 7.52 Surface Finish – R_t (longitudinal) Vs. Fatigue Cycles – CVD Endmill Trimmed High Load Test Specimens

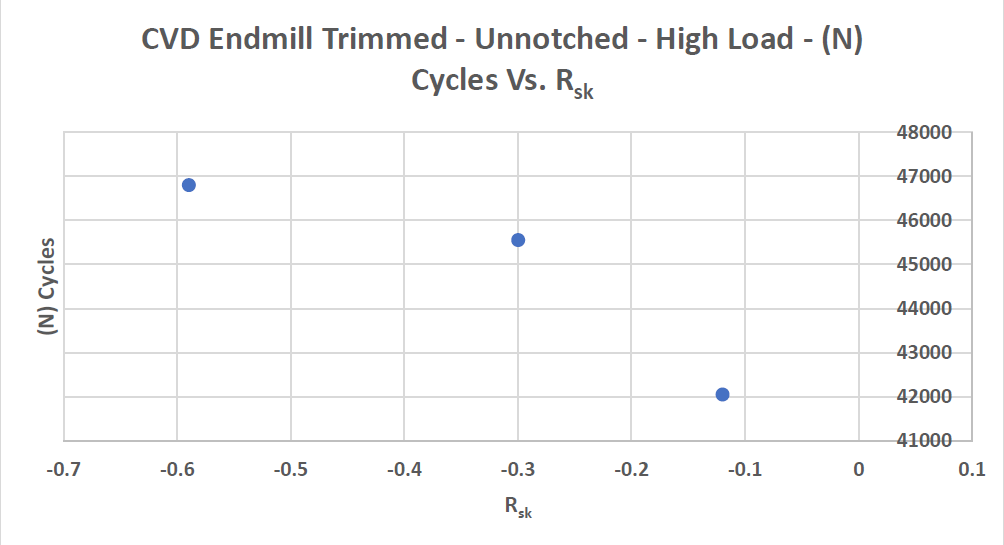

Figure 7.53 Surface Finish – R_{sk} (longitudinal) Vs. Fatigue Cycles – CVD Endmill Trimmed High Load Test Specimens

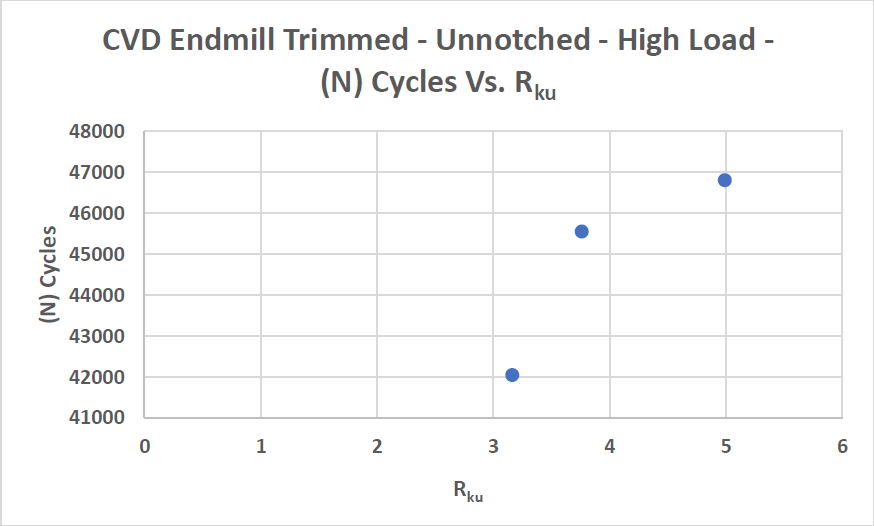

Figure 7.54 Surface Finish – R_{ku} (longitudinal) Vs. Fatigue Cycles – CVD Endmill Trimmed High Load Test Specimens

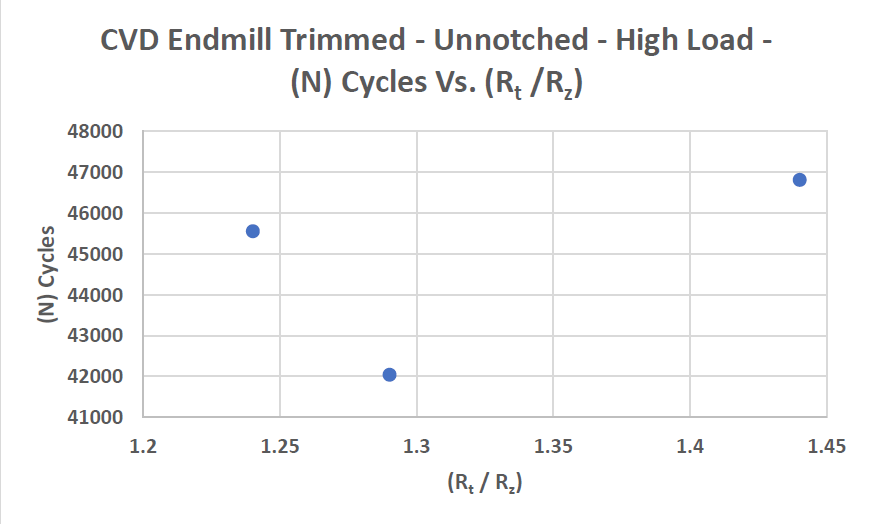

Figure 7.55 Surface Finish – (R_t/R_z) (Longitudinal) Vs. Fatigue Cycles – CVD Endmill Trimmed High Load Test Specimens

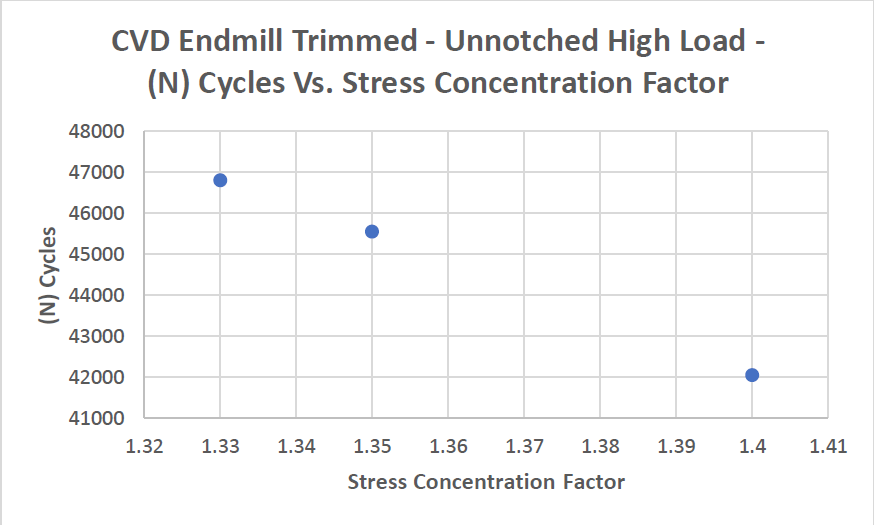

Figure 7.56 Surface Integrity Stress Concentration Factor (Longitudinal) Vs. Fatigue Cycles – CVD Endmill Trimmed High Load Test Specimens

In general, the better the surface finish in the longitudinal direction, the higher the fatigue cycles to failure. Also, the lower values of R_z (highest amplitude of Peak of profile) and lower value of R_t (maximum value of total height of profile) result in higher fatigue cycles to failure. This was observed as a general trend in the data plotted. Even though the surface finish data showed better values for the AWJ trimmed specimens in the transverse direction, the better surface finish in the longitudinal direction (direction of applied loading) for CVD Endmill trimmed specimens resulted in higher fatigue cycle failure loads for these specimens as compared to AWJ trimmed specimens.

7.4.1.2 Medium Load Test Specimen Data Review

For the medium load test specimens, the following samples were tested for AWJ trimmed specimens.

A1 – M – 1

A1 – M – 2

A1 – M – 3

For CVD Diamond Coated Endmill Trimmed specimens, the following samples were tested.

B1 – M – 1

B1 – M – 2

B1 – M – 3

Prior to testing the following surface finish parameters were recorded for each sample in both longitudinal and transverse directions

R_a , R_z , R_t , R_{sk} , R_{ku}

Table 7.11 shows the fatigue cycles to failure for each of the medium load specimens along with the load applied and stress as well as % change in compliance.

Tables 7.4 and 7.5 documented earlier in this chapter show the surface finish data documented in the longitudinal and transverse direction

Specimen Name	Trim	Fatigue Cycles	Test Load (Max) (N)	Test Load (Min) (N)	Max Stress (Mpa)	Test Frequency	Compliance
A1-M-1	AWJ -80	153480	73396	7339	636.24	5 Hz	45.34%
A1-M-2	AWJ -80	410001	73396	7339	636.24	5 Hz	27.20%
A1-M-3	AWJ -80	83375	73396	7339	636.24	5 Hz	30.07%
B1-M-1	CVD Endmill	68450	73396	7339	636.24	5 Hz	18.53%
B1-M-2	CVD Endmill	164698	73396	7339	636.24	5 Hz	32.99%
B1-M-3	CVD Endmill	161693	73396	7339	636.24	5 Hz	22.79%

Table 7.11 Fatigue Cycles/Loads/Stress & % Compliance Change for Unnotched Medium Loading Testing

As shown in the above table, the test specimens in both cases for AWJ and CVD Endmill trimmed, the % compliance change (magnitude of damage) while influencing the fatigue cycles to failure was not the sole variable with the largest impact. As medium loading and the stress associated was lower, the rate of progression of damage and ultimate failure were different as compared to high load test specimens.

Damage Propagation in AWJ trimmed specimens- To compare the damage propagation % compliance change was plotted for each AWJ medium load specimen and the percentage damage at different cycles was compared. Figures 7.57 through 7.62 show the % compliance change for test specimen A1 – M – 1 for medium load AWJ test specimen along with a photo micrograph depicting the damage at various cycles to failure.

It was observed that the lower progression of % compliance change (damage occurred) resulted in an increase in fatigue cycles to failure.

In all cases damage started as matrix cracking followed by separation of plies (delamination) as shown in the figures. The initiation of damage was localized at the 45 degree plies (also the sites of fibre pullouts). Once damage started progressing, ultimate failure occurred due to the splitting apart of the laminate.

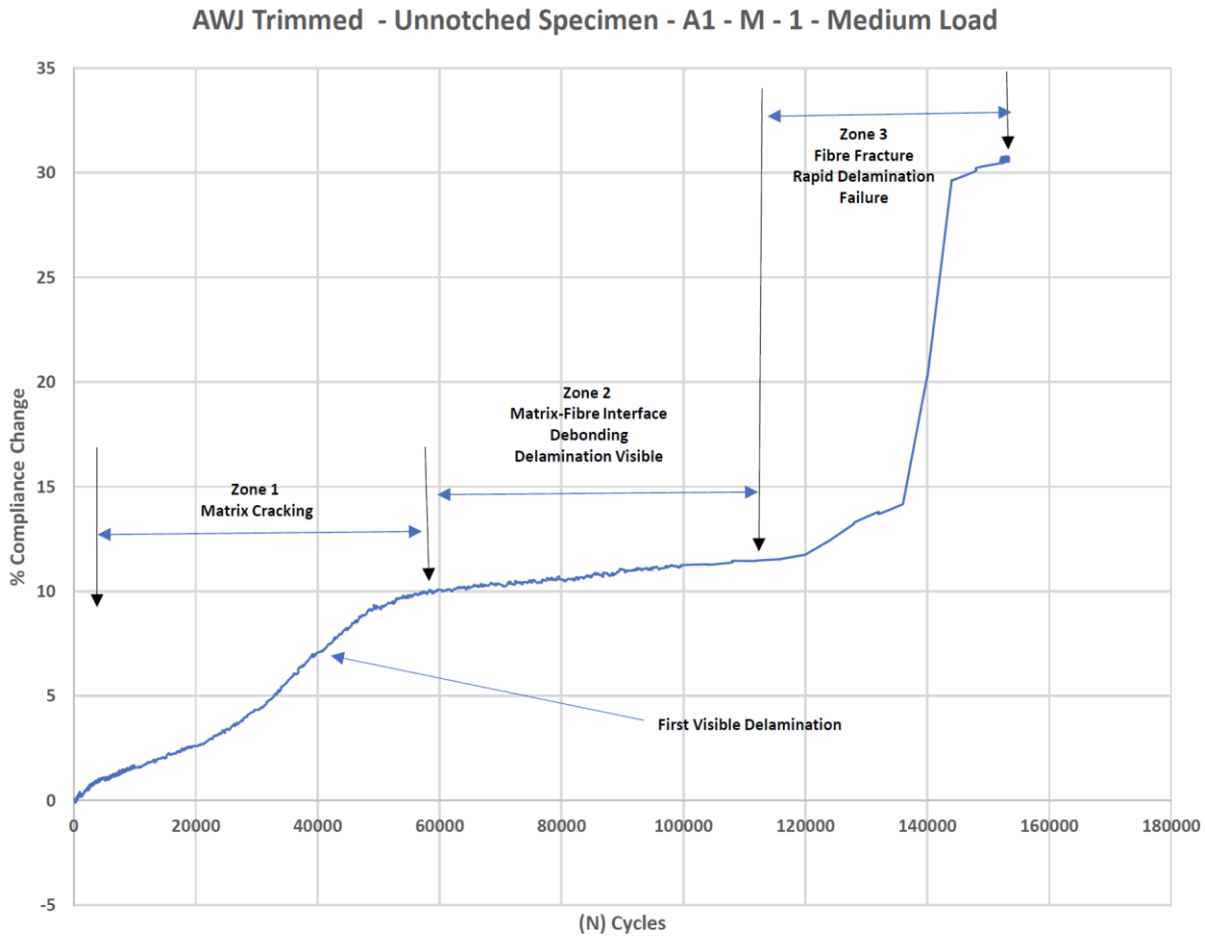

Figure 7.57 Percent Compliance Change Vs. Fatigue Cycles for A1 – M – 1

Figure 7.57 shows the zone 1 where matrix cracking takes place upto 10% compliance change around 60,000 cycles. Matrix-Fibre interface debonding occurs with visible delamination and fibres carry the load individually with reduced load transfer and zone 2 goes up to 12% compliance change and 110,000 cycles. In zone 3, fibre fracture starts with rapid delamination and increased % compliance change from 12% to over 30% and from 110,000 cycles to 153,399 cycles with failure.

Figure 7.58 through 7.62 show the damage progression from start of cycling to failure for test specimen A1 – M – 1

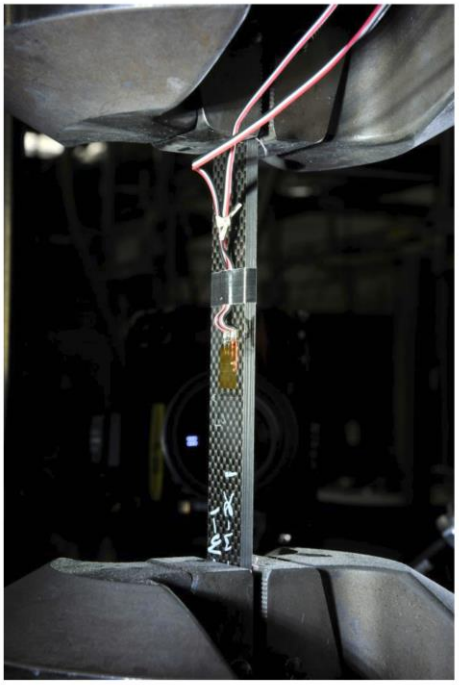

(A1-M-1) at N = 1 Cycles

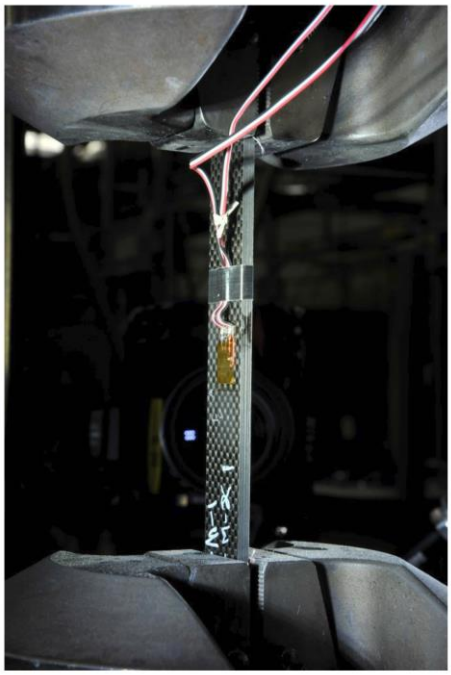

(A1-M-1) at N = 100 Cycles

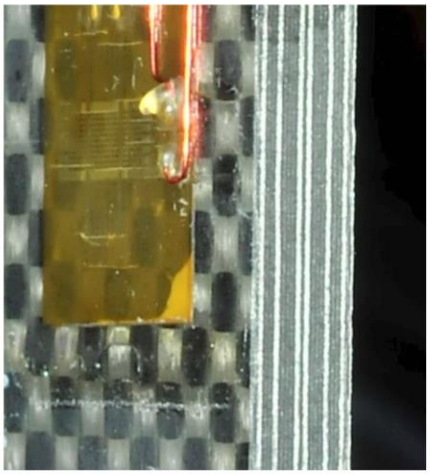

(A1-M-1) at N = 1000 Cycles
Magnified View – Matrix Cracking
No Delamination

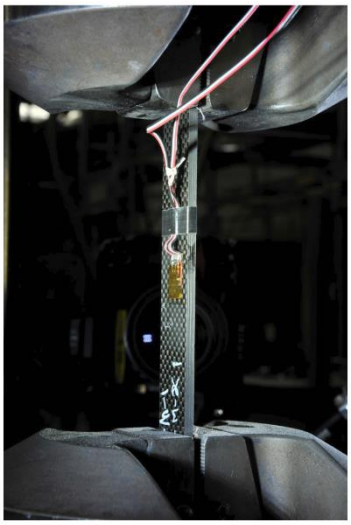

(A1-M-1) at N = 5000 Cycles

Figure 7.58 Damage Progression in (A1 – M – 1) Test specimen to 5000 Cycles

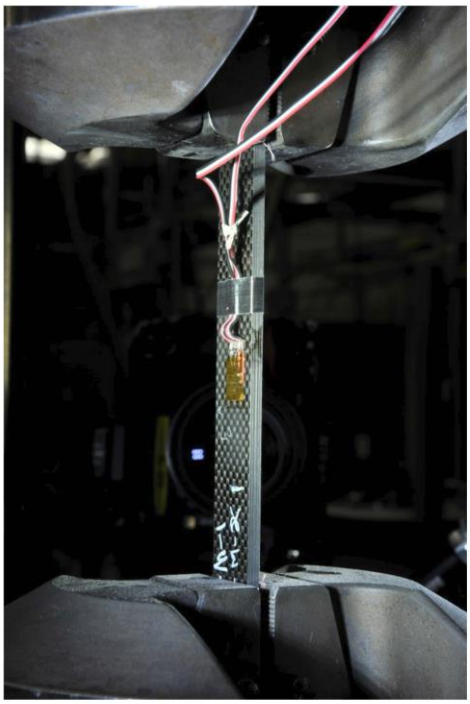

(A1-M-1) at N = 10000 Cycles

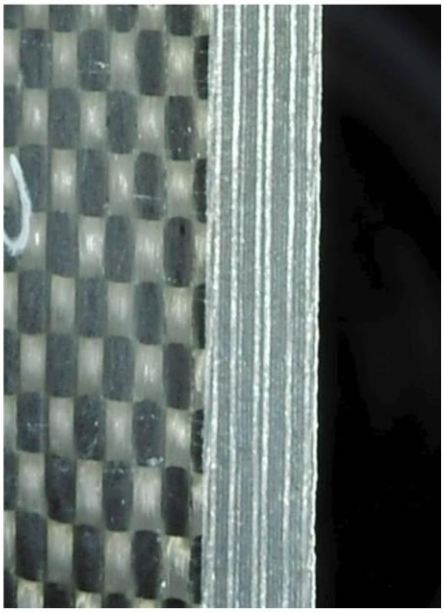

(A1-M-1) at N = 20000 Cycles
Magnified View – Matrix Cracking
No Delamination

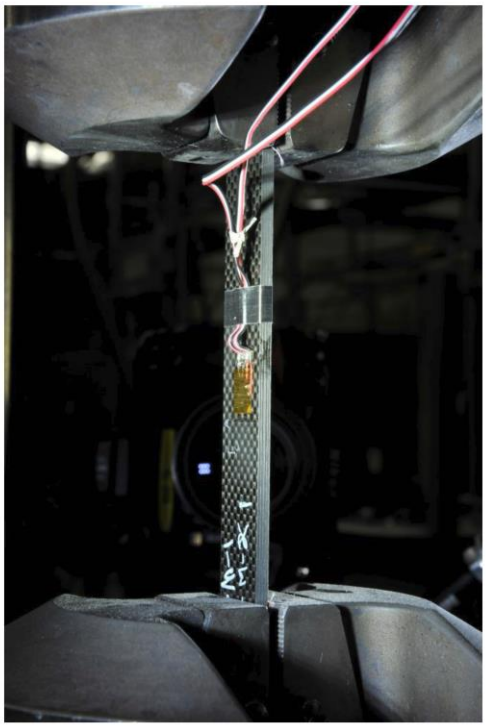

(A1-M-1) at N = 30000 Cycles

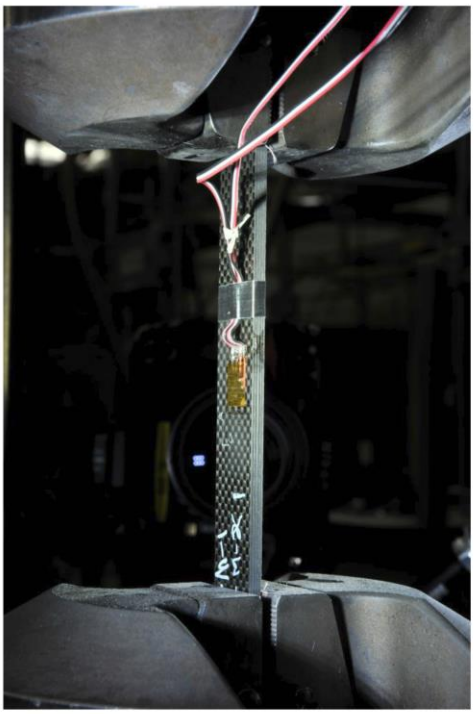

(A1-M-1) at N = 40000 Cycles

Figure 7.59 Damage Progression in (A1 – M – 1) Test specimen to 40000 Cycles

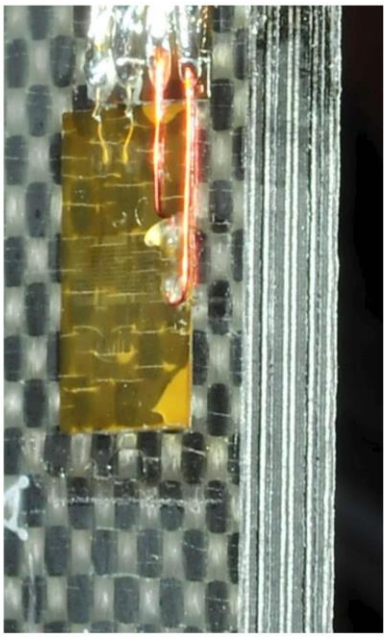

(A1-M-1) at N = 50000 Cycles
Magnified View – Showing
Delamination Started

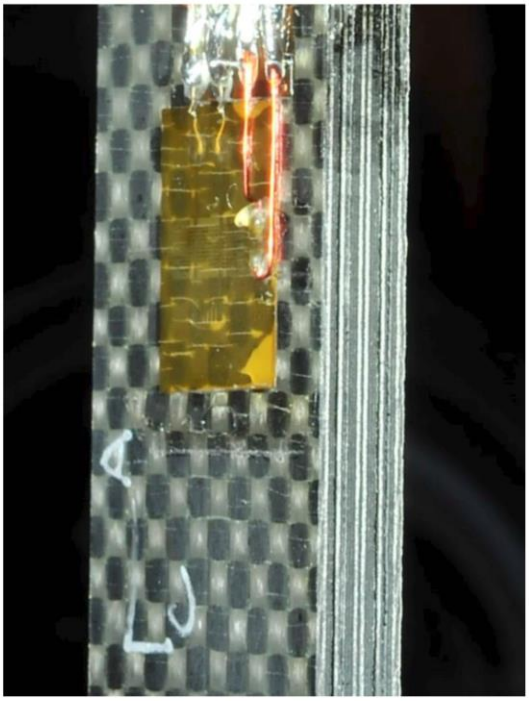

(A1-M-1) at N = 60000 Cycles

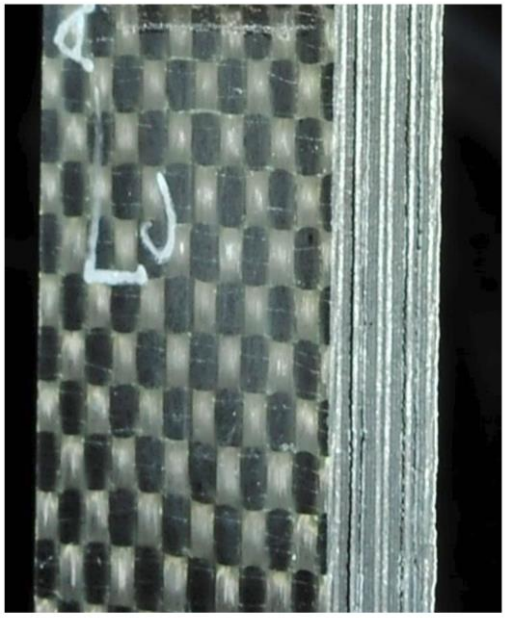

(A1-M-1) at N = 70000 Cycles

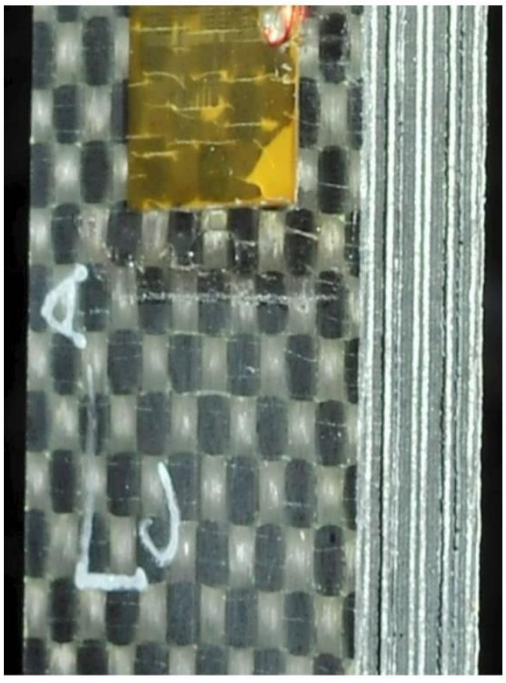

(A1-M-1) at N = 80000 Cycles

Figure 7.60 Damage Progression in (A1 – M – 1) Test specimen to 80000 Cycles

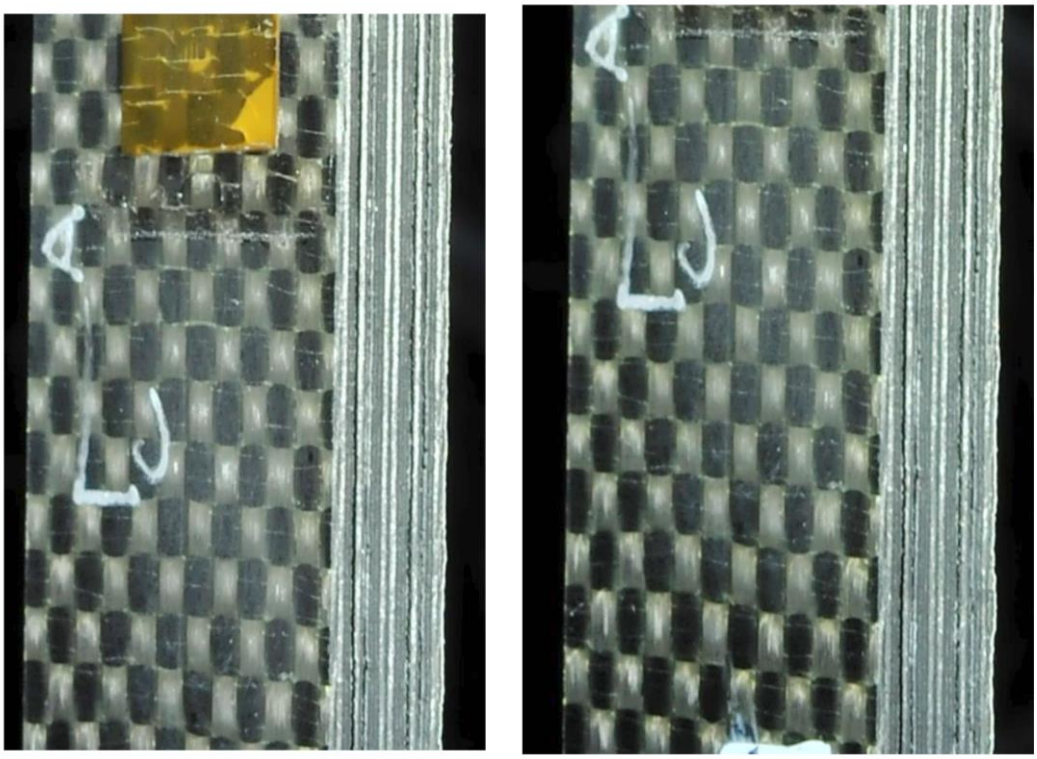

(A1-M-1) at N = 90000 Cycles

(A1-M-1) at N = 100000 Cycles

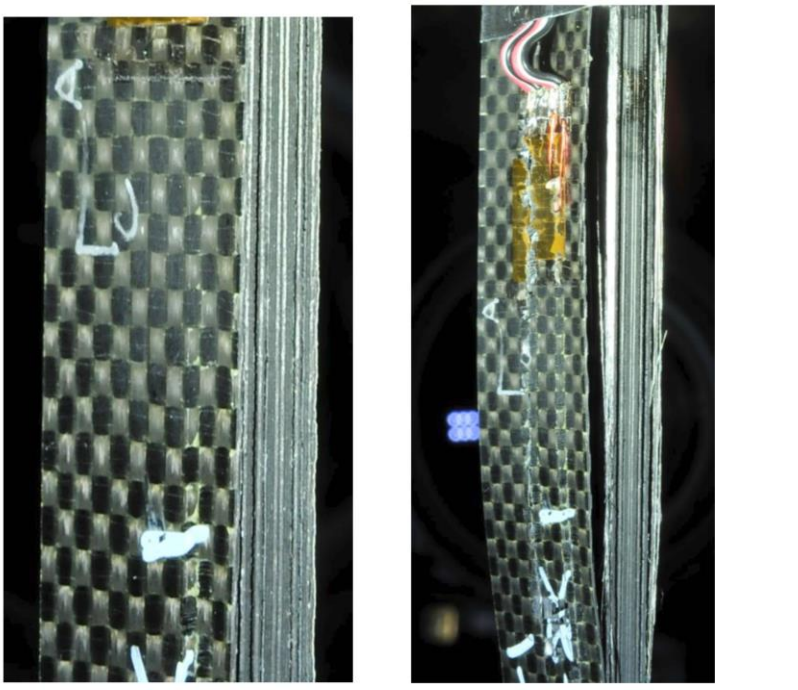

(A1-M-1) at N = 125000 Cycles

(A1-M-1) at N = 150000 Cycles

Figure 7.61 Damage Progression in (A1 – M – 1) Test specimen to 150000 Cycles

(A1-M-1) at Failure at 153,399 Cycles

Figure 7.62 Damage Progression in (A1 – M – 1) Test specimen to Failure at 153,399 Cycles

For the remaining (A1 – M – 2) & (A1 – M -3) test specimens, the damage progression to failure are documented in pictures in Appendix C of this work. Figures 7.63 through 7.75 show the % compliance change versus fatigue cycles along with damage at 50,000 cycles and at failure for both test specimens.

From figure 7.63 it is observed that in zone 1 there is matrix cracking upto 10% compliance change and 100,000 cycles. Matrix-Fibre interface debonding occurs and there is visible delmination in zone 2. Fibres carry the load invidually with reduced load transferand zone 2 extends upto 14% compliance change and 300,000 cycles. In zone 3 fibre fracture starts with rapid delmination and increased % compliance change from 14% to over 27% and from 310,000 cycles to 410,001 cycles with failure.

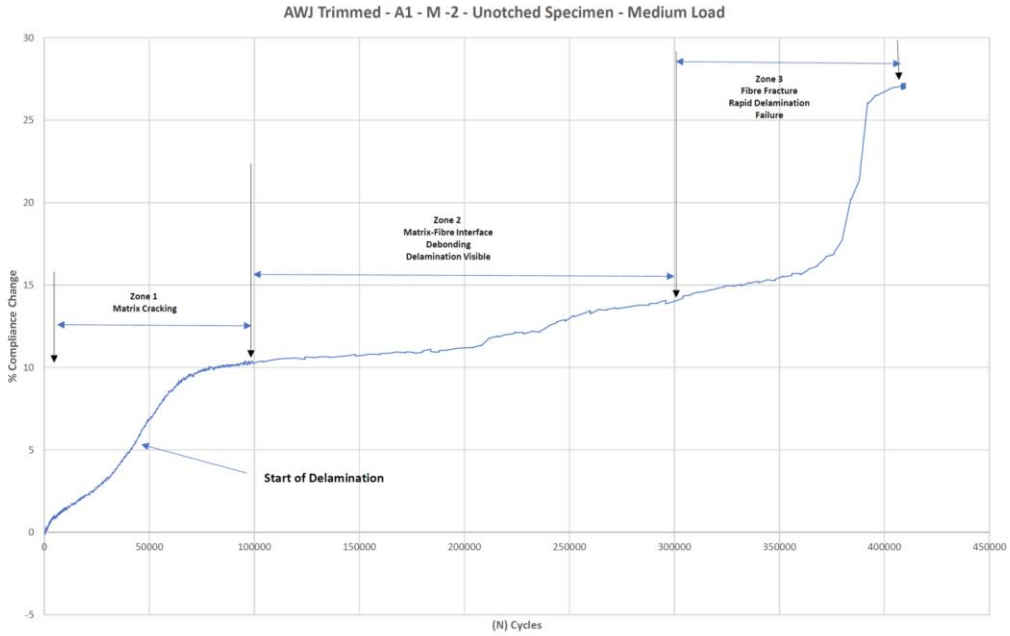

Figure 7.63 Percent Compliance Change Vs. Fatigue Cycles for (A1 – M – 2)

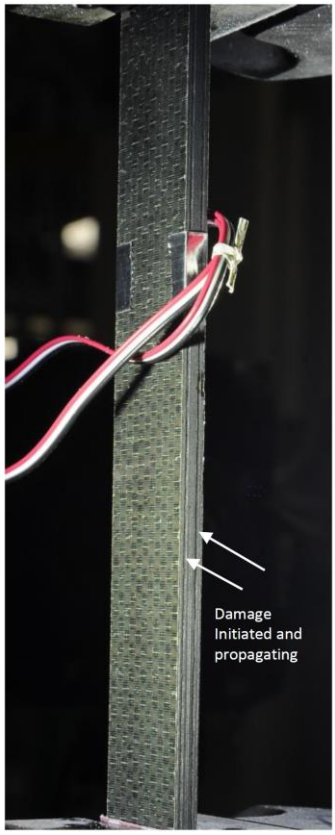

Figure 7.64 Damage at 50K Cycles, 6.9%, Test Specimen

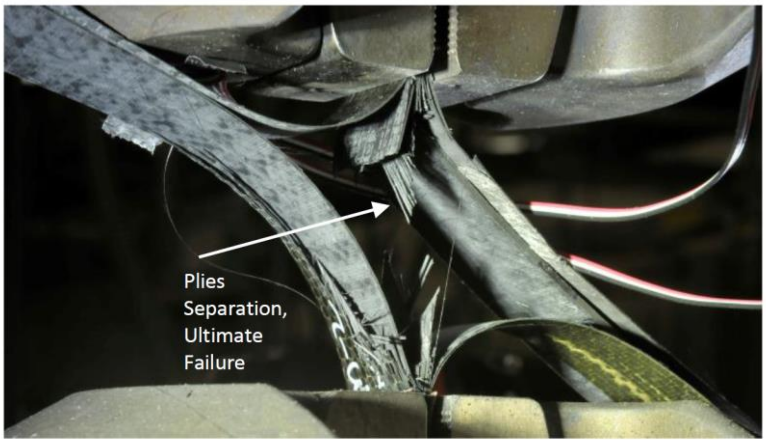

\

Figure 7.65 Damage (27.2%) & Ultimate Failure at 410001 Cycles

From figure 7.66 it is observed that in zone 1 there is matrix cracking upto 9% compliance change and 40,000 cycles. Matrix-Fibre interface debonding occurs and there is visible delmination in zone 2. Fibres carry the load invidually with reduced load transferand zone 2 extends upto 12% compliance change and 80,000 cycles. In zone 3 fibre fracture starts with rapid delmination and increased % compliance change from 12% to over 30% and from 80,000 cycles to 83,375 cycles with failure.

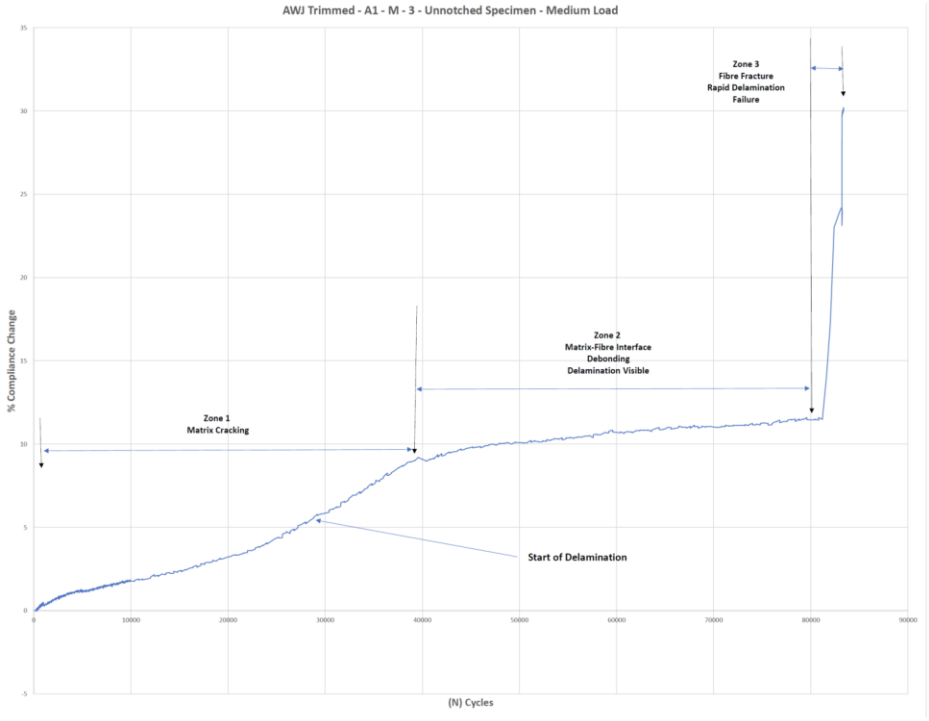

Figure 7.66 Percent Compliance Change Vs. Fatigue Cycles for (A1 – M – 3)

Figure 7.67 Damage at 50K Cycles, 10.13%, Test

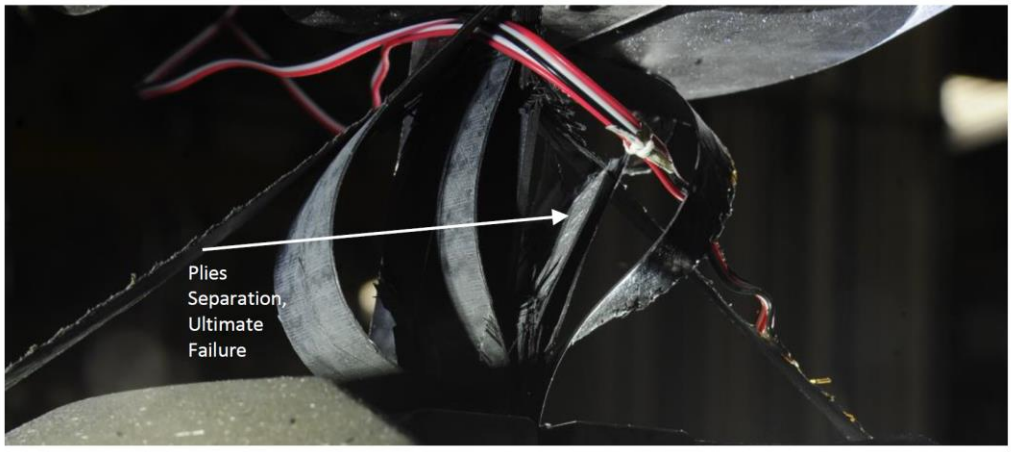

Figure 7.68 Damage (30.07%) & Ultimate Failure at 83375 Cycles

Damage Propagation in CVD Diamond Coated Endmill trimmed specimens- To compare the damage propagation % compliance change was plotted for each CVD Diamond Coated Endmill trimmed medium load specimen and the percentage damage was compared for specimens (B1 – M – 1), (B1 – M – 2) & (B1- M – 3) at 50K cycles. Figures 7.69 through 7.71 show the % compliance change for (B1 – M – 1) test specimen along with a photo micrograph depicting the damage at 50K cycles and at failure.

In all cases damage started as matrix cracking followed by separation of plies (delamination) as shown in the figures. The initiation of damage was localized at the 45 degree plies (also the sites of fibre pullouts). Once damage started progressing, ultimate failure occurred due to the splitting apart of the laminate.

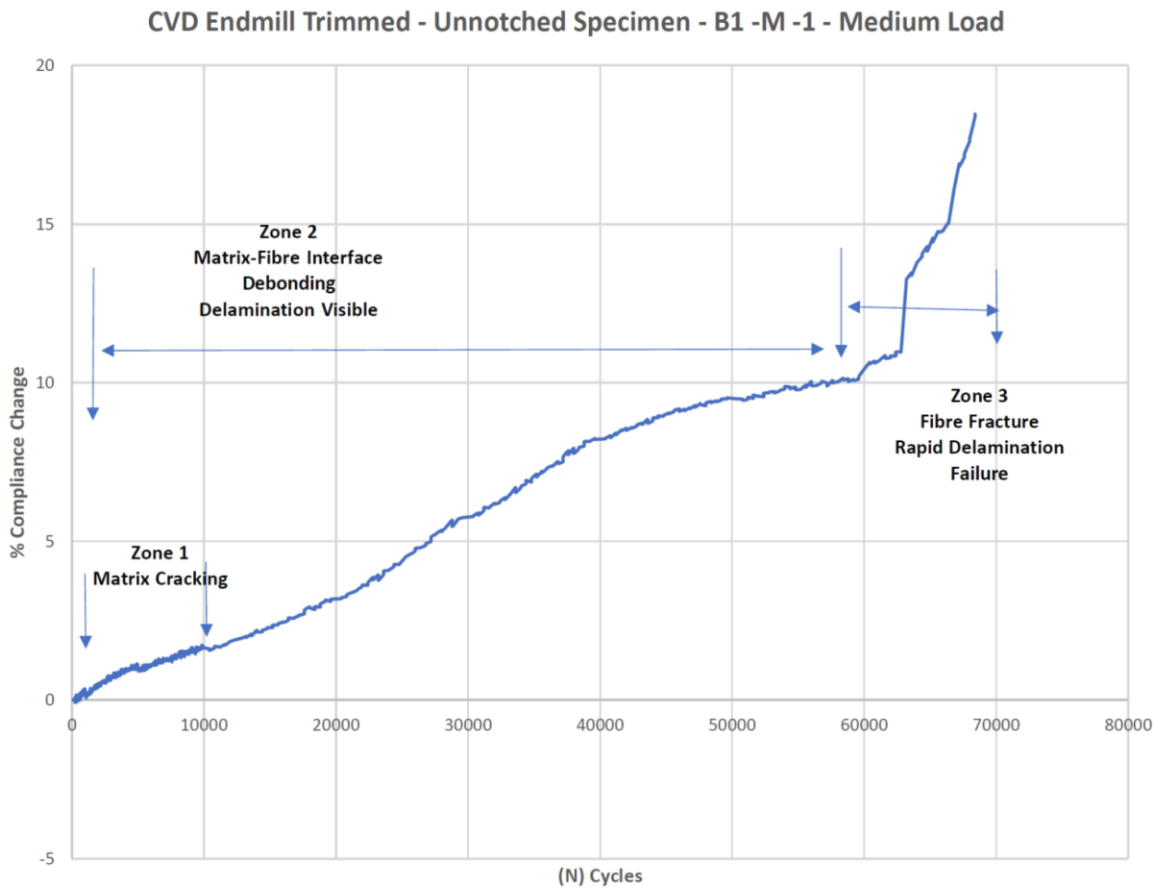

Figure 7.69 Percent Compliance Change Vs. Fatigue Cycles for (B1 – M – 1)

From figure 7.69 it is oserved that in zone 1 there is matrix cracking upto 2.5% compliance change and 10,000 cycles. It was also oberved that at the start of the fatigue cyclles testing, the test specimens had visible delaminations present from the machining processes which contributed to eraly failure of the specimen in fatigue testing. Matrix-Fibre interface debonding occurs and there is visible delmination in zone 2. Fibres carry the load invidually with reduced load transfer and zone 2 extends upto 10% compliance change and 60,000 cycles. In zone 3 fibre fracture starts with rapid delmination and increased % compliance change from 10% to over 18% and from 60,000 cycles to 68,450 cycles with failure.

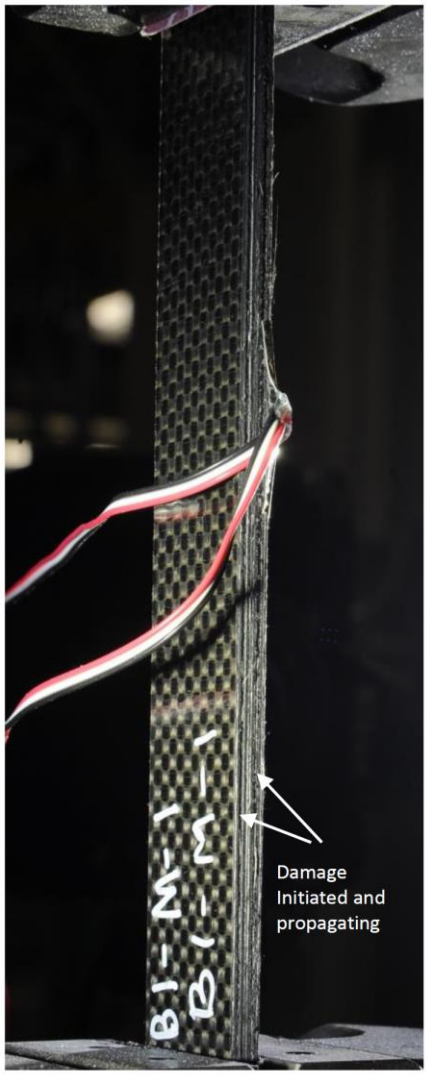

Figure 7.70 Damage at 50K Cycles, 9.48%, Test Specimen

Figure 7.71 Damage (18.53%) & Ultimate Failure at 68450 Cycles

From figure 7.72 it is observed that in zone 1 there is matrix cracking upto 10% compliance change and 60,000 cycles. Matrix-Fibre interface debonding occurs and there is visible delmination in zone 2. Fibres carry the load invidually with reduced load transferand zone 2 extends upto 11% compliance change and 105,000 cycles. In zone 3 fibre fracture starts with rapid delmination and increased % compliance change from 11% to over 32% and from 105,000 cycles to 164,698 cycles with failure.Figures 7.73 and 7.74 show the progress of damage at 50K cycles and failure.

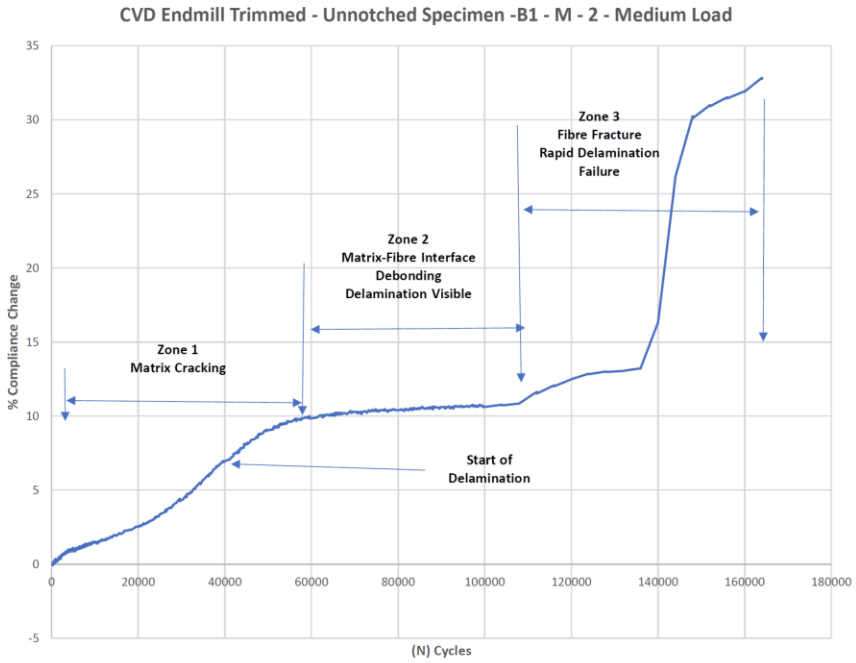

Figure 7.72 Percent Compliance Change Vs. Fatigue Cycles for B1 – M – 2

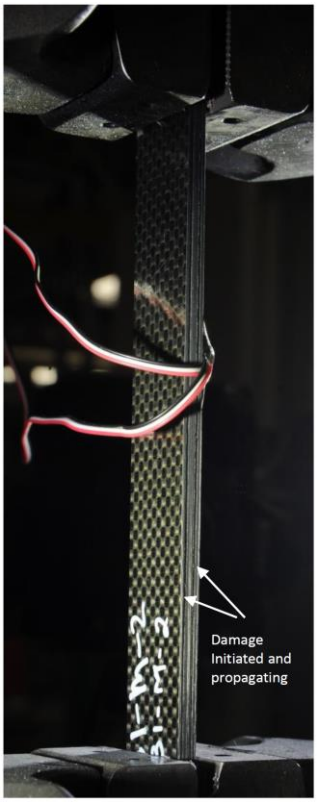

Figure 7.73 Damage at 50K Cycles, 9.09%, Test Specimen

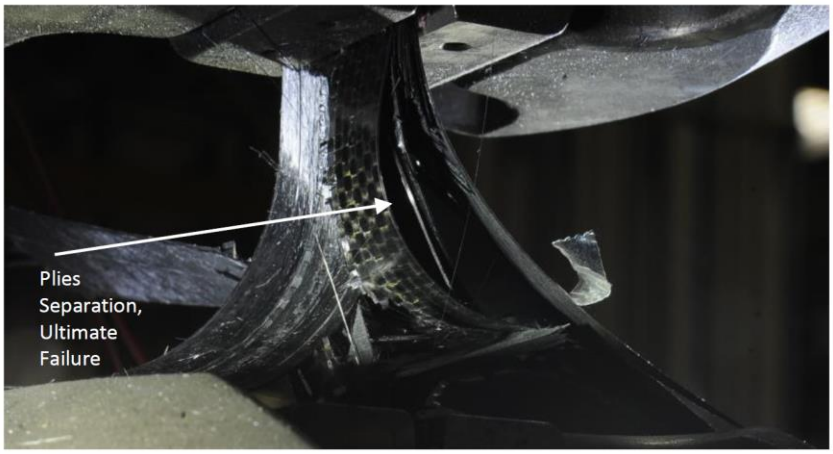

Figure 7.74 Damage (32.99%) & Ultimate Failure at 164698 Cycles

From figure 7.75 it is observed that in zone 1 there is matrix cracking upto 10% compliance change and 60,000 cycles. Matrix-Fibre interface debonding occurs and there is visible delmination in zone 2. Fibres carry the load invidually with reduced load transferand zone 2 extends upto 11% compliance change and 120,000 cycles. In zone 3 fibre fracture starts with rapid delmination and increased % compliance change from 11% to over 22% and from 120,000 cycles to 161,693 cycles with failure.Figures 7.76 and 7.77 show the progress of damage at 50K cycles and failure.

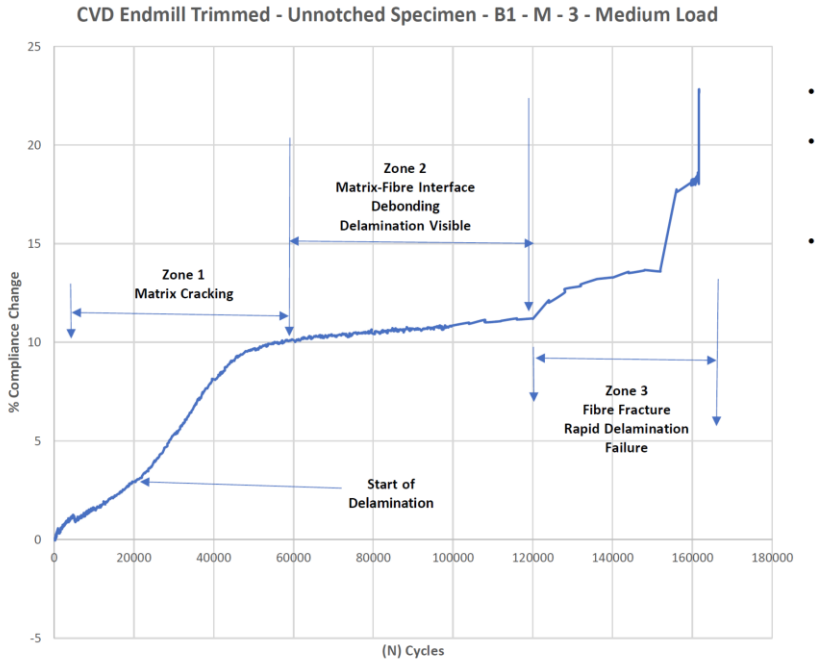

Figure 7.75 Percent Compliance Change Vs. Fatigue Cycles for (B1 – M – 3)

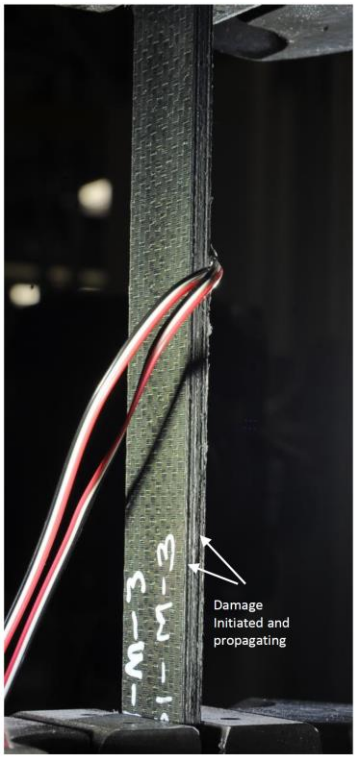

Figure 7.76 Damage at 50K Cycles, 9.69%, Test Specimen

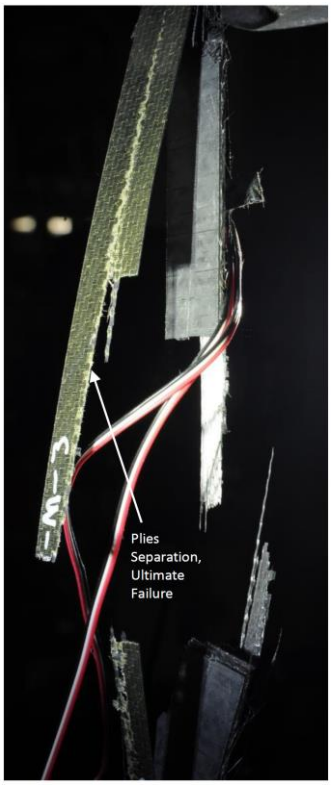

Figure 7.77 Damage (22.79%) & Ultimate Failure at 161693 Cycles

The CVD Diamond Coated Endmill Trimmed test Specimens generally had fatigue cycle failures that were closer to each other than the AWJ trimmed surface. At medium load conditions, the % Compliance change curves were similar for both AWJ trimmed and CVD Endmill trimmed specimens.

Both types of trimmed specimens also displayed a steeper climb of the % Compliance change after certain percent damage had occurred.

Figures 7.78 through 7.80 show the plots of various AWJ and CVD specimens % compliance change Vs. Fatigue cycles with respect to each other.

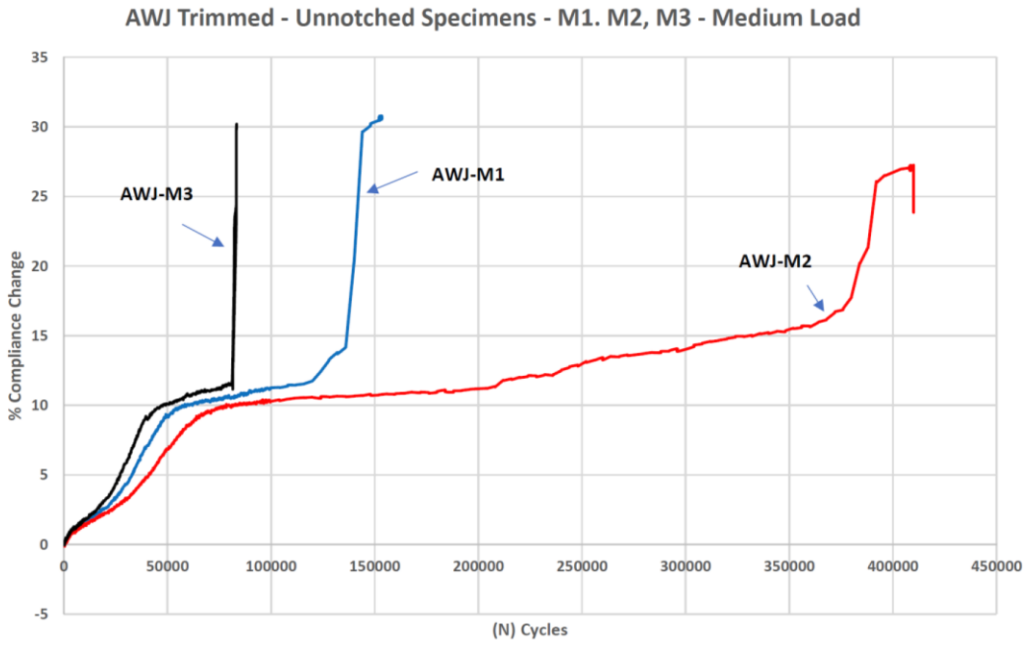

Figure 7.78 Summary Plot of AWJ Medium Load Percent Compliance Change Vs. Fatigues Cycles

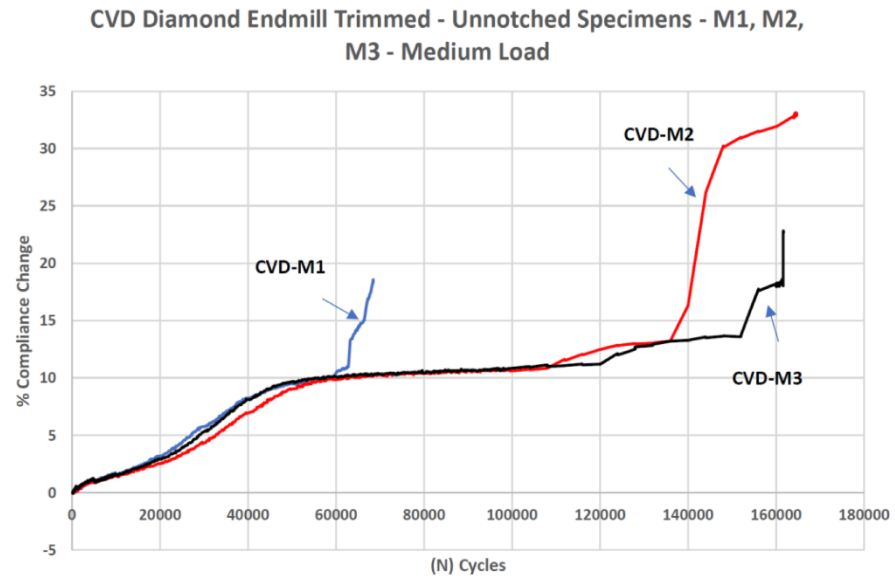

Figure 7.79 Summary Plot of CVD Endmill Trimmed Medium Load Percent Compliance Change Vs. Fatigues Cycles

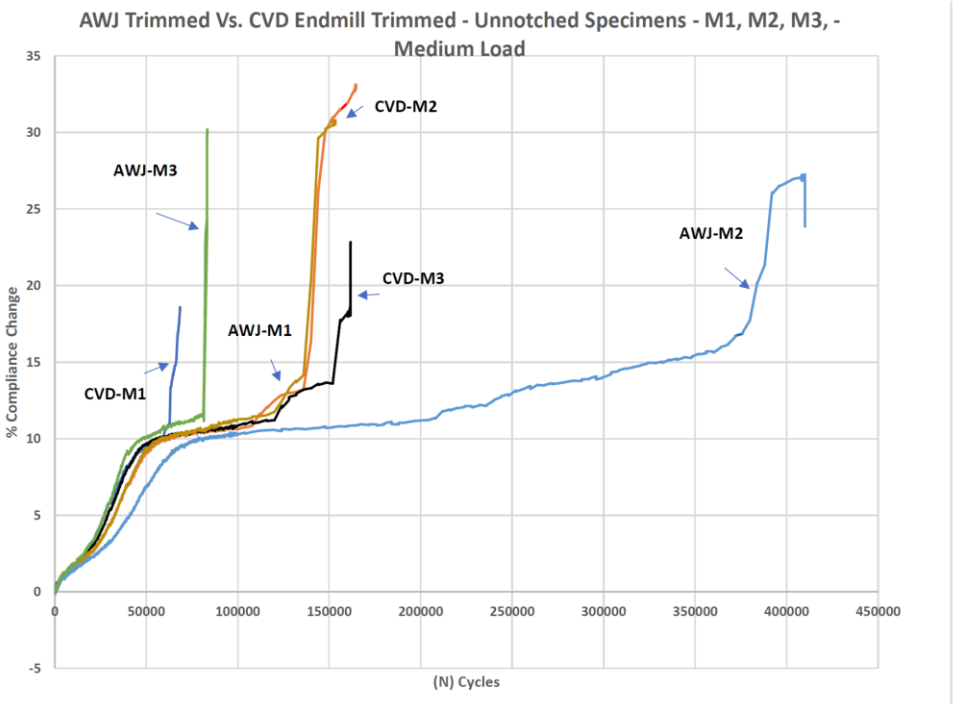

Figure 7.80 Summary Plot of AWJ Trimmed Vs. CVD Endmill Trimmed Specimens Medium Load Percent Compliance Change Vs. Fatigues Cycles

Surface Finish Stress Concentration Factor $\left(\bar{K}_t\right)$

Surface finish profiles of all high load test specimens were used to calculate the stress concentration factor $\left(\bar{K}_t\right)$ using the formula shown in figure 7.36

Figures 7.81 through 7.86 Show the stress concentration factor determination graphically for the radius and using the formula from Figure 7.36

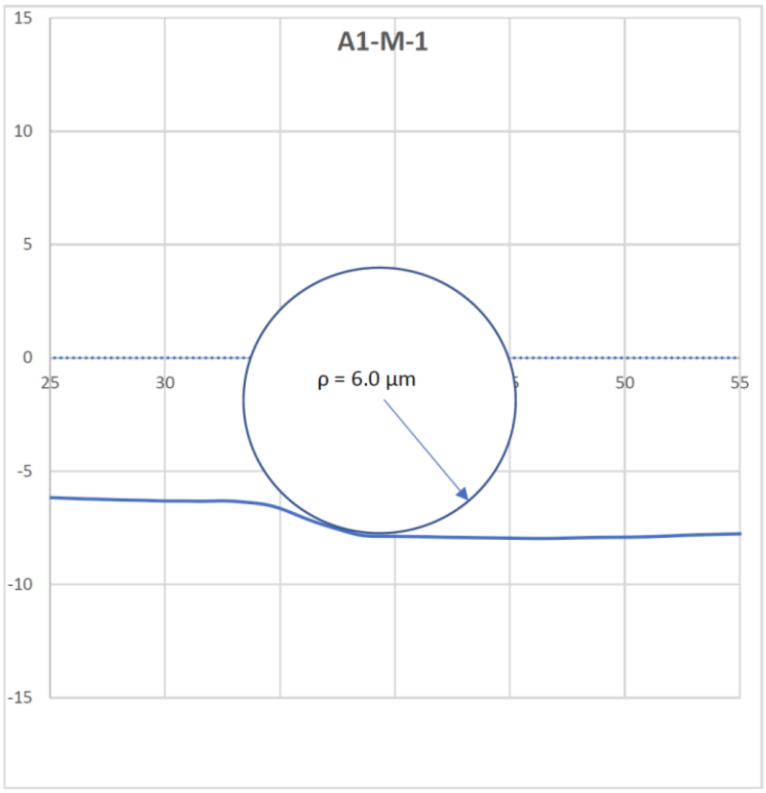

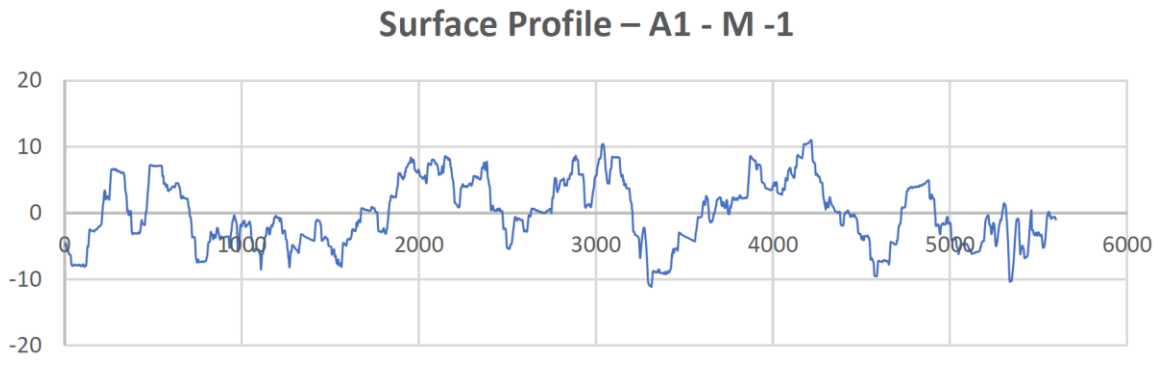

Figure 7.81 Graphical Determination of radius (ρ) from surface profile of test specimen A1–M-1

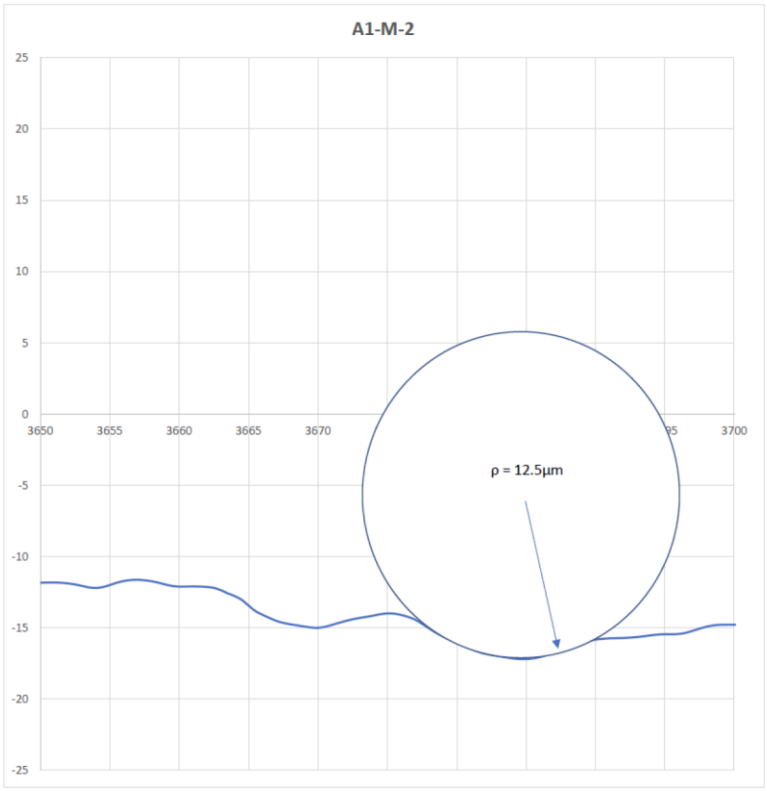

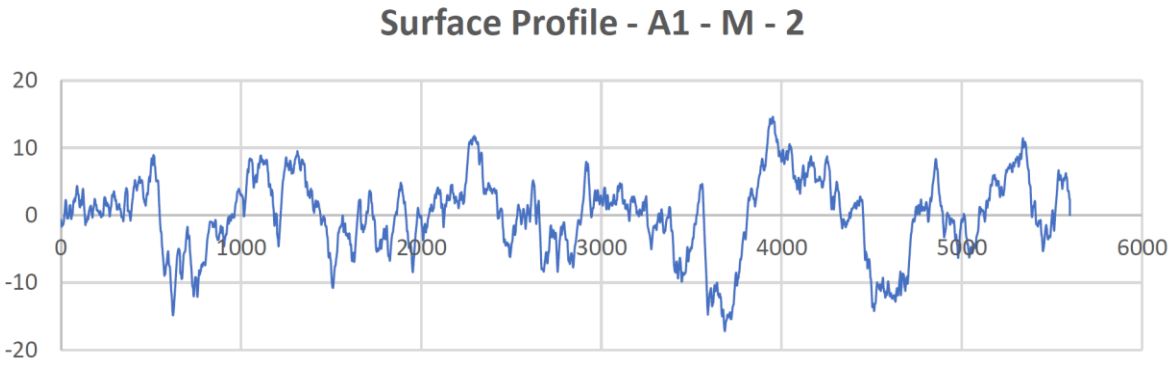

Figure 7.82 Graphical Determination of radius (ρ) from surface profile of test specimen A1–M–2

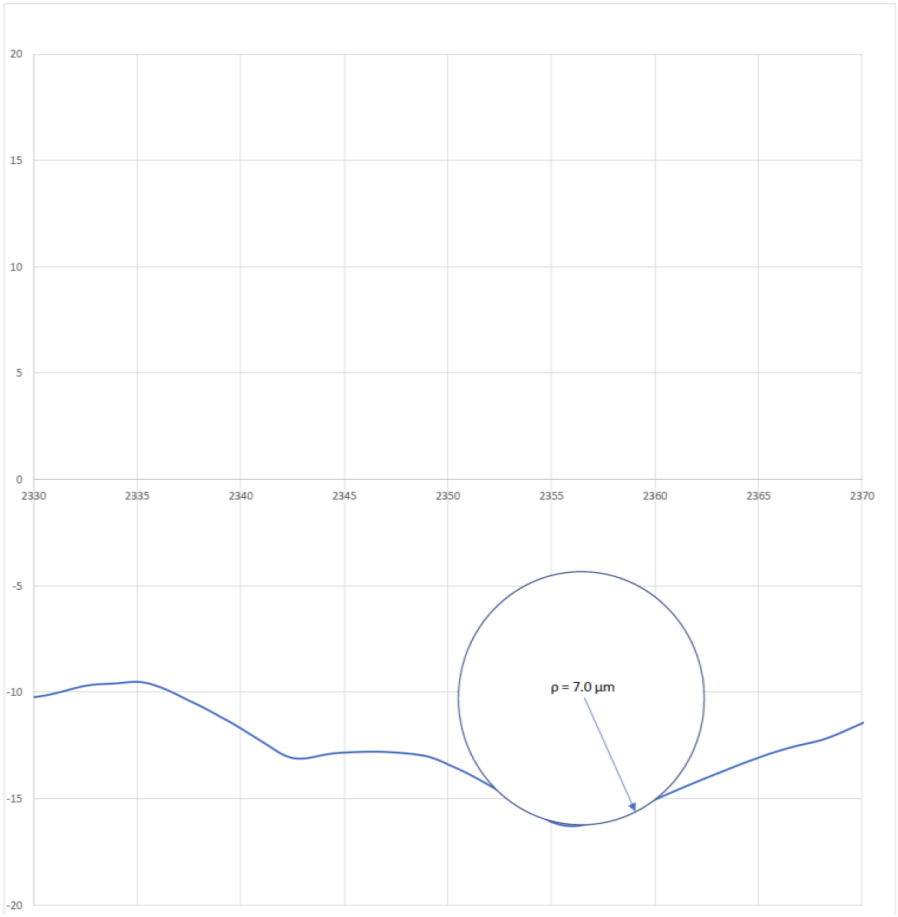

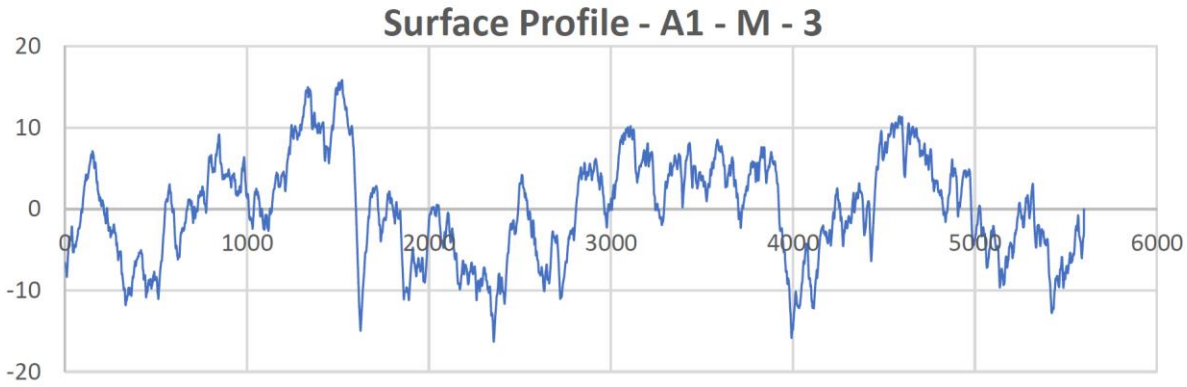

Figure 7.83 Graphical Determination of radius (ρ) from surface profile of test specimen A1–M–3

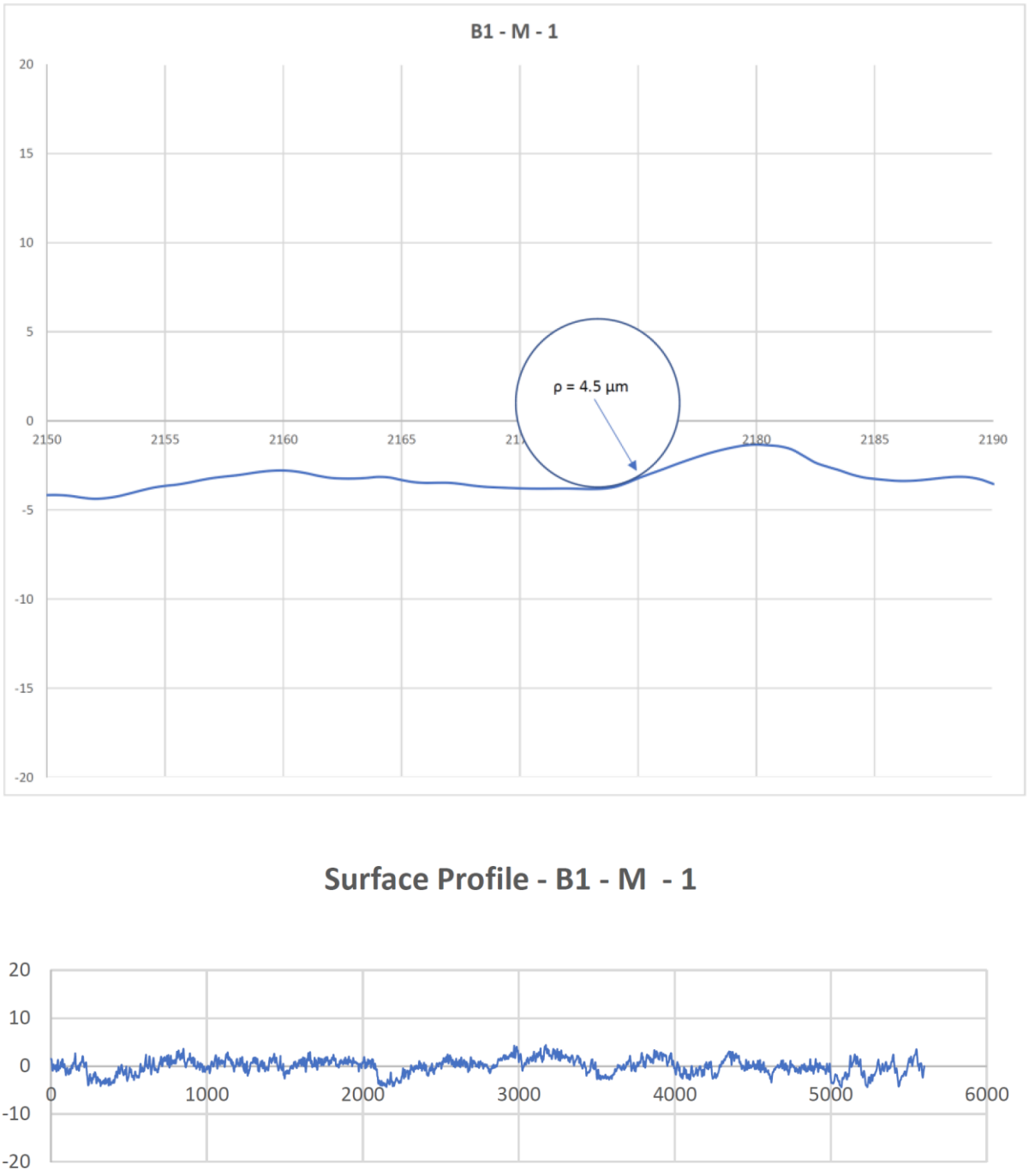

Figure 7.84 Graphical Determination of radius (ρ) from surface profile of test specimen B1–M 1

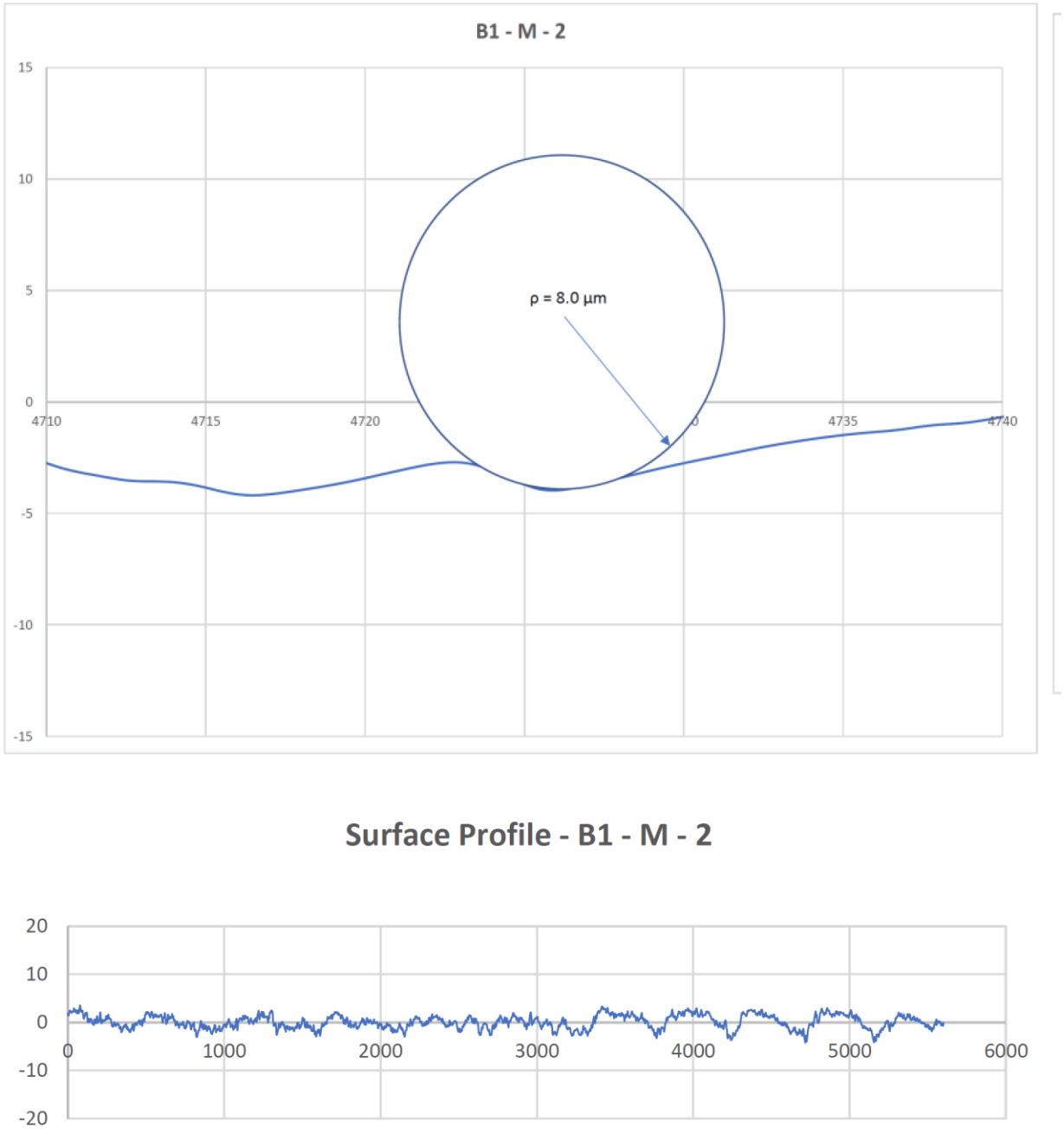

Figure 7.85 Graphical Determination of radius (ρ) from surface profile of test specimen B1–M-2

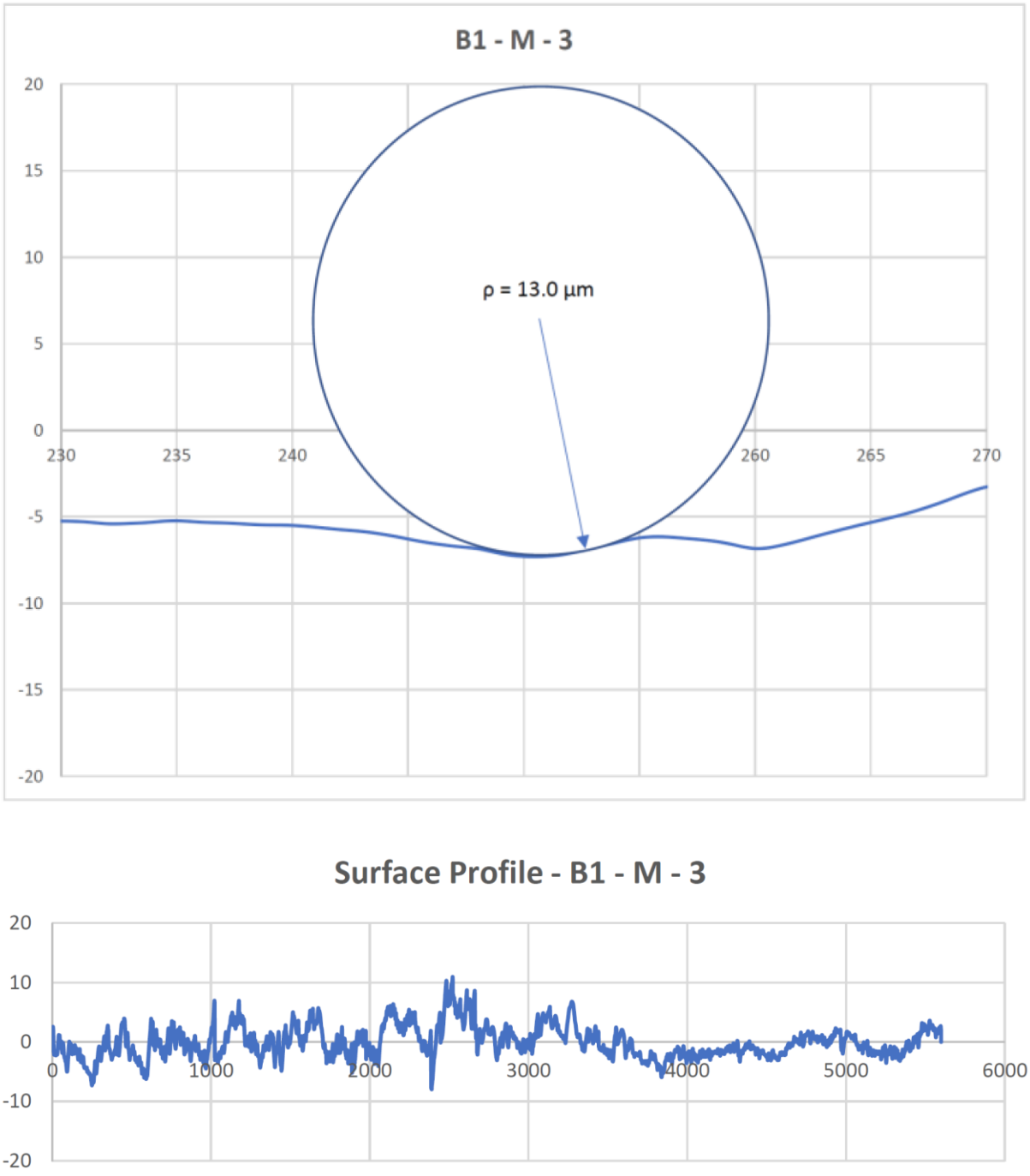

Figure 7.86 Graphical Determination of radius (ρ) from surface profile of test specimen B1–M- 3

Table 7.12 shows the calculated surface integrity stress concentration factors for medium load test specimens.

Specimen Name	Surface Integrity Stress Concentration Factor
A1 – M - 1	1.87
A1 – M - 2	1.64
A1 – M - 3	2.29
B1 – M - 1	1.43
B1 – M - 2	1.31
B1 – M - 3	1.39

Table 7.12 Calculated Surface Integrity Stress Concentration factors for Medium Load Test Specimens

Observation on Surface finish Data Vs. Fatigue Cycles – Surface finish data in the longitudinal direction was plotted against fatigue cycles and reviewed comparing AWJ trimmed specimens to CVD Diamond Coated Endmill Trimmed specimens. Figures 7.87 through 7.100 show the variation of surface finish parameters Vs. fatigue cycles for the different parameters.

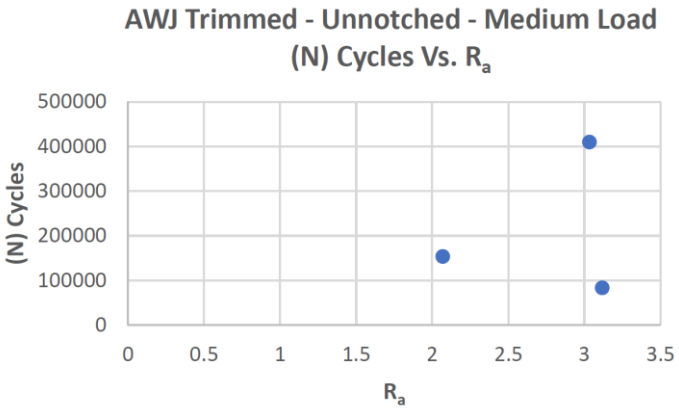

Figure 7.87 Surface Finish - R_a (longitudinal) Vs. Fatigue Cycles – AWJ Trimmed Medium Load Specimens

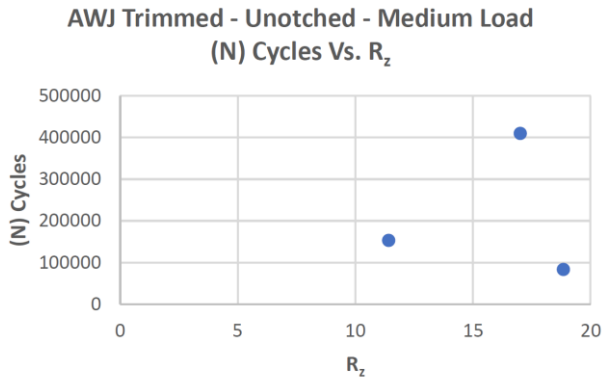

Figure 7.88 Surface Finish – R_z (longitudinal) Vs. Fatigue Cycles – AWJ Trimmed Medium Load Test Specimens

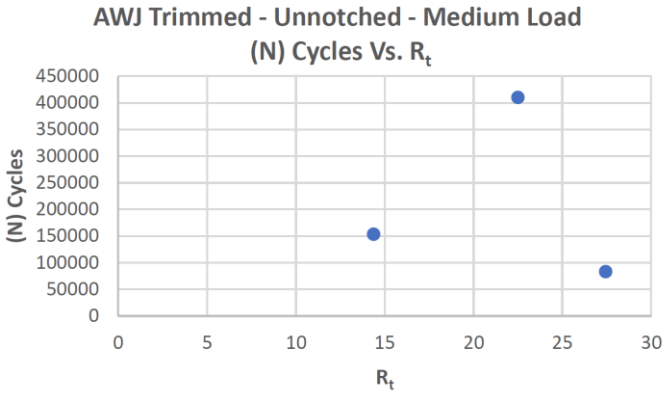

Figure 7.89 Surface Finish – R_t (longitudinal) Vs. Fatigue Cycles – AWJ trimmed Medium Load Test Specimens

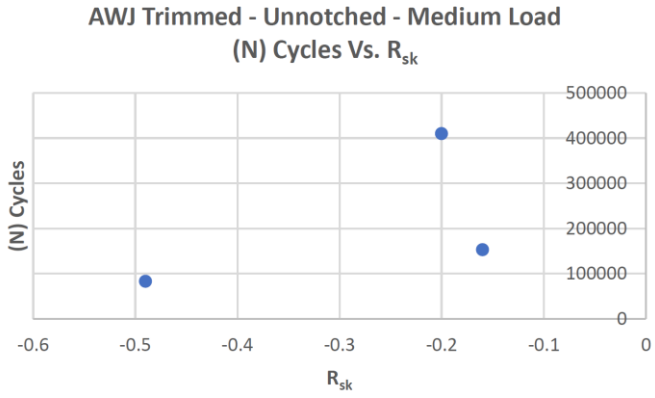

Figure 7.90 Surface Finish – R_{sk} (longitudinal) Vs. Fatigue Cycles – AWJ Trimmed Medium Load Test Specimens

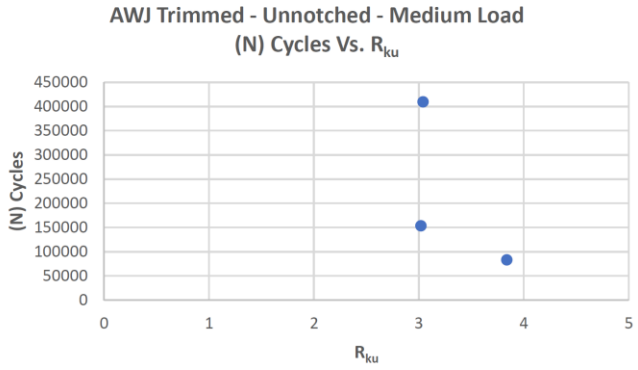

Figure 7.91 Surface Finish – R_{ku} (longitudinal) Vs. Fatigue Cycles – AWJ Trimmed Medium Load Test Specimens

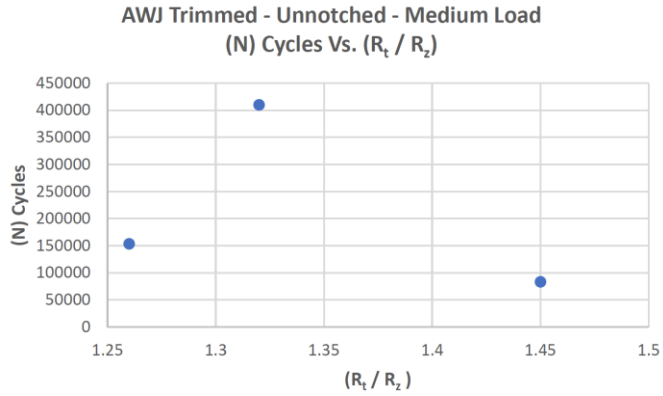

Figure 7.92 Surface Finish – (R_t/R_z) (Longitudinal) Vs. Fatigue Cycles – AWJ Trimmed Medium Load Test Specimens

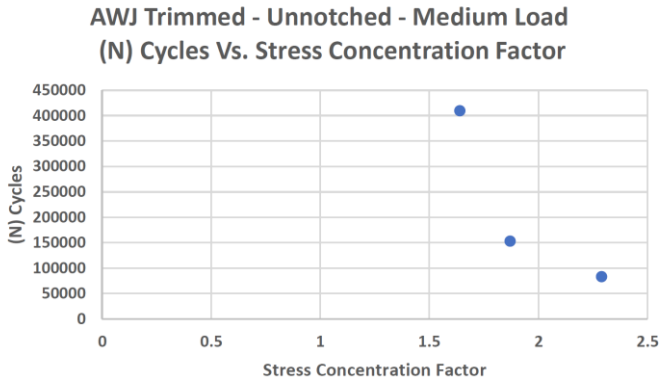

Figure 7.93 Surface Integrity Stress Concentration Factor (Longitudinal) Vs. Fatigue Cycles – AWJ Trimmed Medium Load Test Specimens

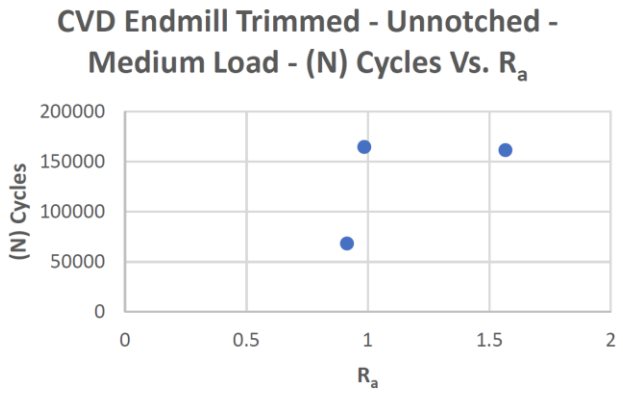

Figure 7.94 Surface Finish - R_a (longitudinal) Vs. Fatigue Cycles – CVD Endmill Trimmed Medium Load Specimens

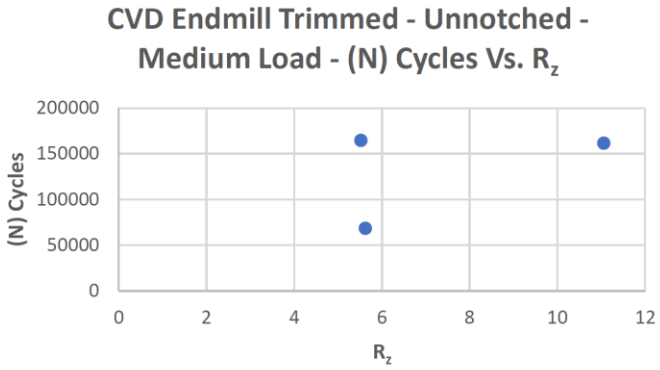

Figure 7.95 Surface Finish – R_z (longitudinal) Vs. Fatigue Cycles – CVD Endmill Trimmed Medium Load Test Specimens

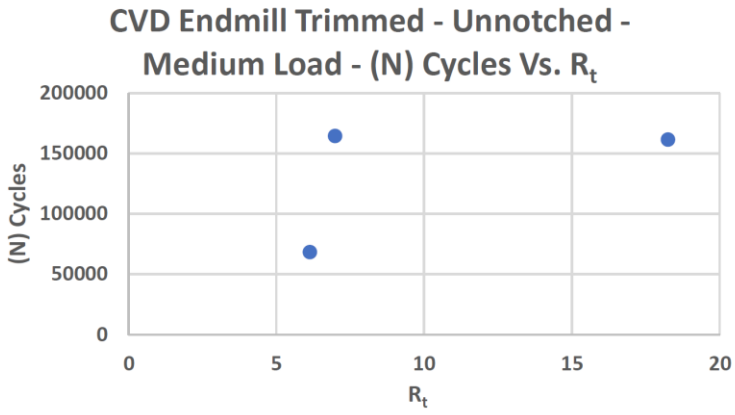

Figure 7.96 Surface Finish – R_t (longitudinal) Vs. Fatigue Cycles – CVD Endmill trimmed Medium Load Test Specimens

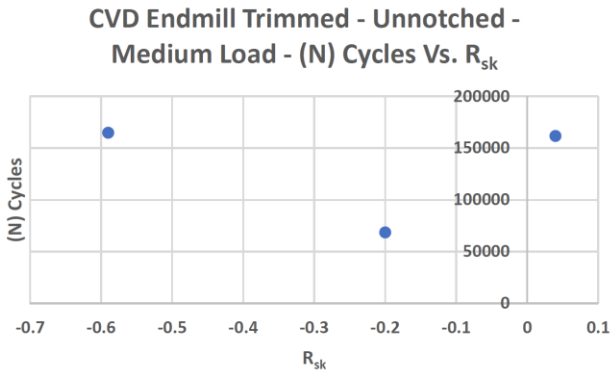

Figure 7.97 Surface Finish – R_{sk} (longitudinal) Vs. Fatigue Cycles –CVD Endmill Trimmed Medium Load Test Specimens

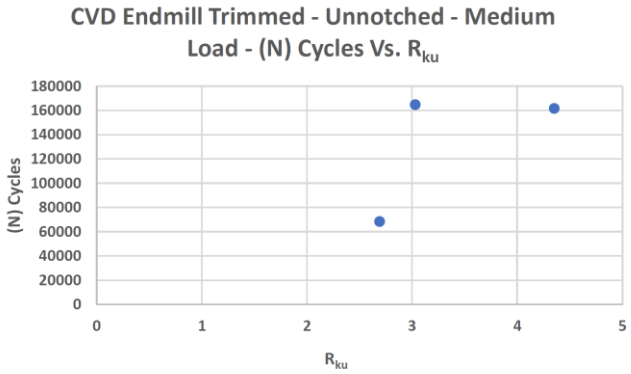

Figure 7.98 Surface Finish – R_{ku} (longitudinal) Vs. Fatigue Cycles – CVD Endmill Trimmed Medium Load Test Specimens

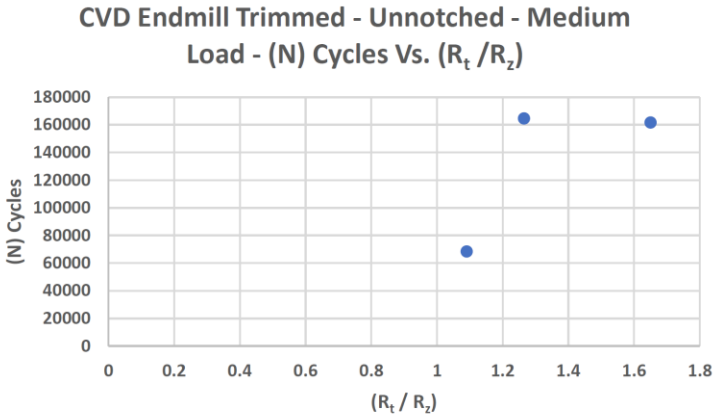

Figure 7.99 Surface Finish – (R_t/R_z) (Longitudinal) Vs. Fatigue Cycles – CVD Endmill Trimmed Medium Load Test Specimens

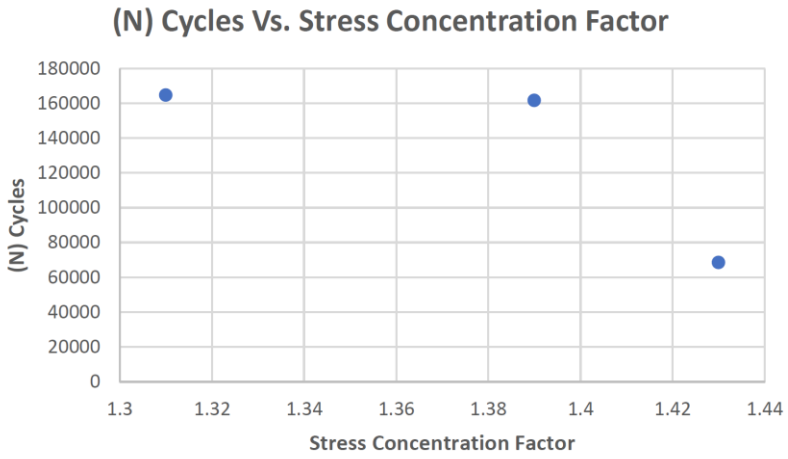

Figure 7.100 Surface Integrity Stress Concentration Factor (Longitudinal) Vs. Fatigue Cycles – CVD Endmill Trimmed Medium Load Test Specimens

It was observed that in both AWJ trimmed and CVD Endmill trimmed specimens, the surfaces with negative skew values had higher fatigue cycles to failure. The negative skew meant less amount of peaks in the profile which translates to lower count of stress risers resulting in higher fatigue cycles to failure.

For AWJ trimmed specimens the magnitude of differences in surface finish data had a bigger impact to fatigue cycles count than it did in the case of CVD Endmill trimmed surfaces.

In all cases damage started as matrix cracking followed by separation of plies (delamination) as shown in the figures. The initiation of damage was localized at the 45 degree plies (also the sites of fibre pullouts). Once damage started progressing, ultimate failure occurred due to the splitting apart of the laminate.

The damage progress for all medium load test specimens was documented with photos taken during fatigue testing and are published in the Appendix C of this work.

7.4.1.3 Low Load Test Specimen Data Review

For the low load test specimens, the following samples were tested for AWJ trimmed specimens.

A1 – L – 1

A1 – L – 2

A1 – L – 3

For CVD Diamond Coated Endmill Trimmed specimens, the following samples were tested.

B1 – L – 1

B1 – L – 2

B1 – L – 3

B1 – L - 4

Prior to testing the following surface finish parameters were recorded for each sample in both longitudinal and transverse directions

R_a , R_z , R_t , R_{sk} , R_{ku}

Table 7.13 shows the fatigue cycles to failure for each of the low load specimens along with the load applied and stress as well as % change in compliance.

Tables 7.4 and 7.5 documented earlier in this chapter show the surface finish data documented in the longitudinal and transverse direction

Specimen Name	Trim	Fatigue Cycles	Test Load (Max) (N)	Test Load (Min) (N)	Max Stress (Mpa)	Test Frequency	Compliance
A1-L-1	AWJ -80	556687	68947	6894	600.32	5 Hz	25.29%
A1-L-2	AWJ -80	487732	68947	6894	600.32	5 Hz	26.43%
A1-L-3	AWJ -80	722803	68947	6894	600.32	5 Hz	31.49%
B1-L-1	CVD Endmill	296778	68947	6894	600.32	5 Hz	30.46%
B1-L-2	CVD Endmill	76783	68947	6894	600.32	5 Hz	11.64%
B1-L-3	CVD Endmill	562123	68947	6894	600.32	5 Hz	31.06%
B1-L-4	CVD Endmill	805926	68947	6894	600.32	5 Hz	30.95%

Table 7.13 Fatigue Cycles/Loads/Stress & % Compliance Change for Unnotched Low Loading Testing

Damage Propagation in AWJ trimmed specimens- To compare the damage propagation % compliance change was plotted for each AWJ low load specimen and the percentage damage at 200K cycles was compared. Figures 7.101 through 7.109 show the % compliance change for each low load AWJ test specimen along with a photo micrograph depicting the damage at 200K cycles.

It was observed that the lower progression of % compliance change (damage occurred) resulted in an increase in fatigue cycles to failure.

In all cases damage started as matrix cracking followed by separation of plies (delamination) as shown in the figures. The initiation of damage was localized at the 45 degree plies (also the sites

of fibre pullouts). Once damage started progressing, ultimate failure occurred due to the splitting apart of the laminate.

The variation of the compliance surves in comparison to high load and medium load specimens is that the rate of % compliance change in zone 2 of the compliance curves is slower in low load fatigue cycle testing. This is explained in detailed in the fatigue modeling discussion in Chapter 8 of this research.

Figures 7.101 through 7.109 show the compliance curves as well as the damage progress documented at 200K cycles and at failure for the unnotched low load test specimens. The progress of damage is slow in low load testing as shown in the compliance curves.

The pattern of damage progress si similar to other testing s conducted for high and medium loadings. In stage 1 there is matrix cracking followed by matrix fibre interfacial debonding in stage 2. In stage 3 there is fibre fracture, delamination and ultimate splitting of plies and failure of laminate. The low loading conditions resulted in some test specimens achieving over 800K cycles of fatigue life.

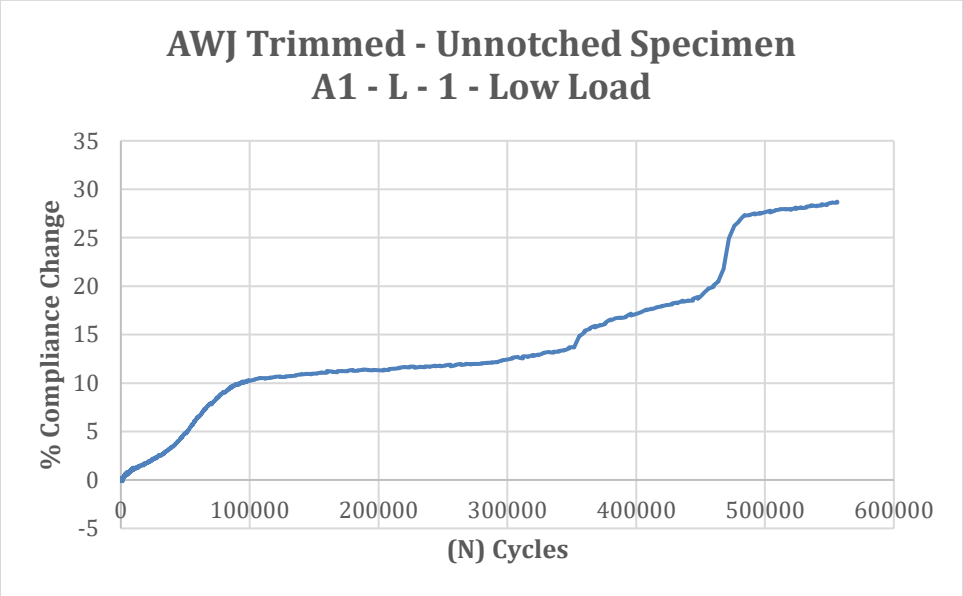

Figure 7.101 Percent Compliance Change Vs. Fatigue Cycles for (A1 – L – 1)

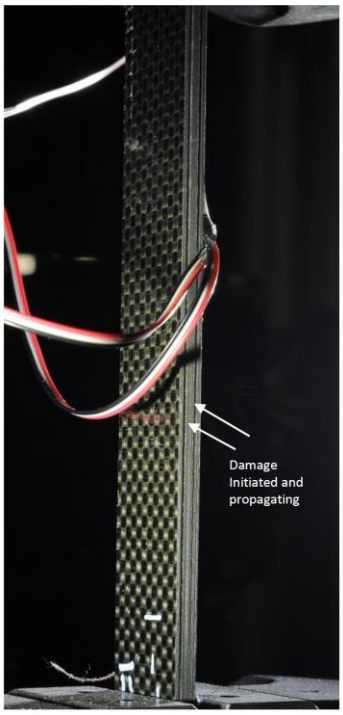

Figure 7.102 Damage at 200K Cycles, 11.67%, Test

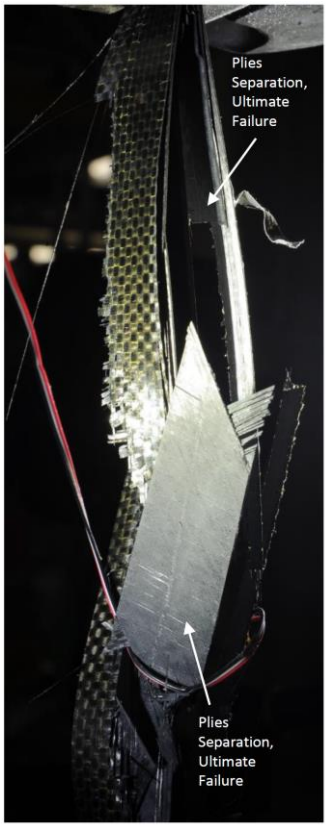

Figure 7.103 Damage (25.29%) & Ultimate Failure at 556687 Cycles

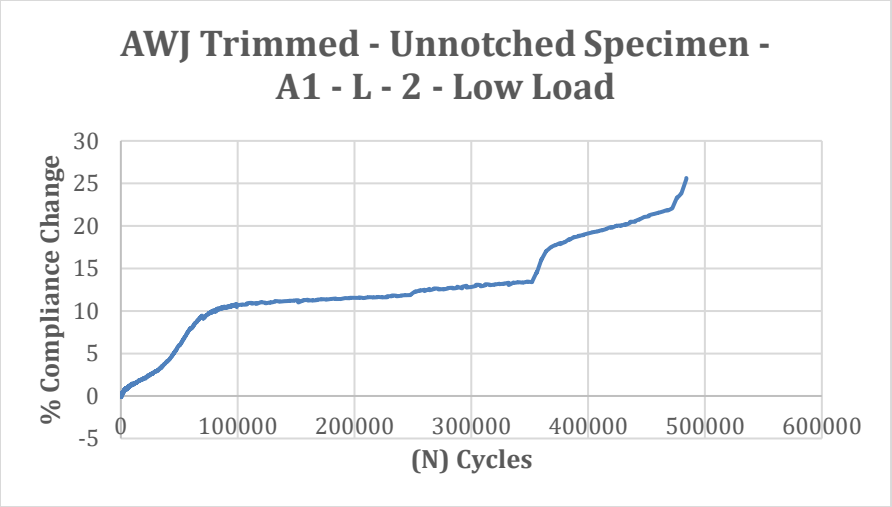

Figure 7.104 Percent Compliance Change Vs. Fatigue Cycles for (A1 – L – 2)

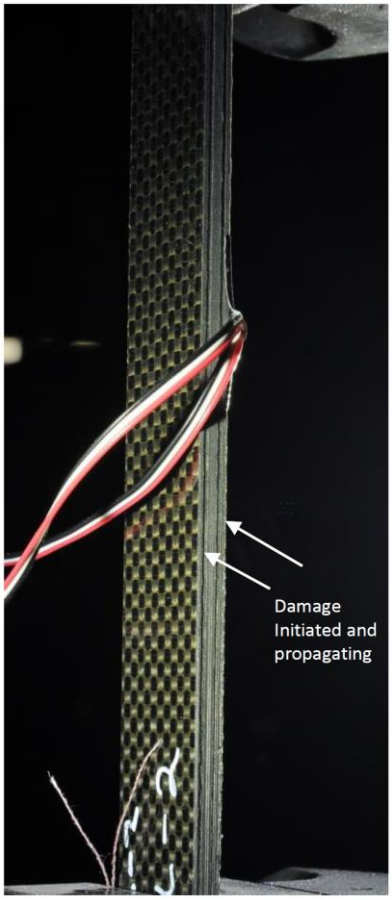

Figure 7.105 Damage at 200K Cycles, 11.49%, Test

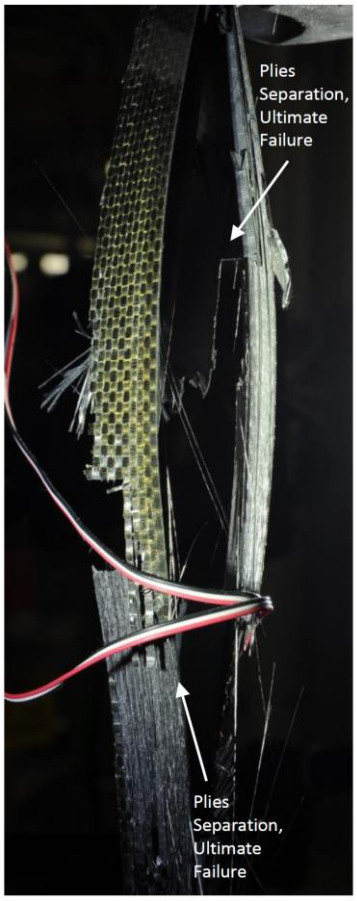

Figure 7.106 Damage (26.43%) & Ultimate Failure at 487732 Cycles

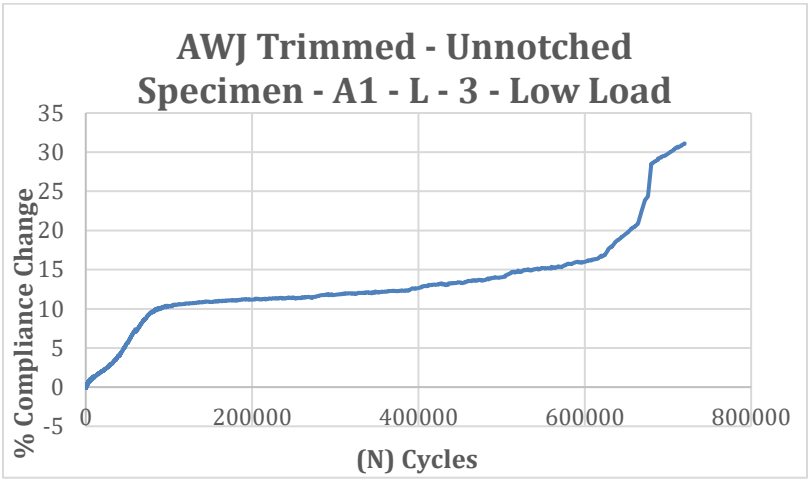

Figure 7.107 Percent Compliance Change Vs. Fatigue Cycles for (A1 – L – 3)

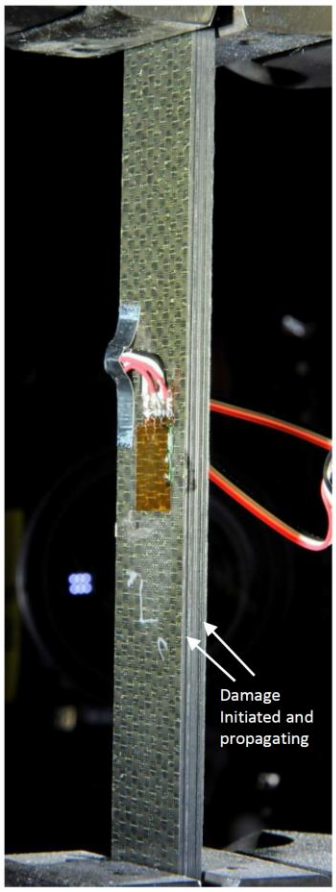

Figure 7.108 Damage at 200K Cycles, 11.22%, Test Specimen (A1 – L – 2)

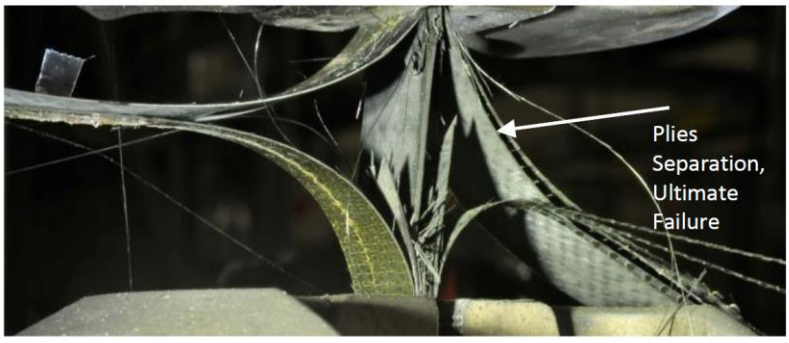

Figure 7.109 Damage (31.49%) & Ultimate Failure at 722803 Cycles

Damage Propagation in CVD Diamond Coated Endmill trimmed specimens- To compare the damage propagation % compliance change was plotted for each CVD Diamond Coated Endmill trimmed low load specimen and the percentage damage at 200K cycles was compared or 50K cycles if specimen failed at less than 200K cycles. Figures 7.110 through 7.121 show the % compliance change for each low load CVD Endmill trimmed test specimen along with a photo micrograph depicting the damage at 200K or 50Kcycles.

In all cases damage started as matrix cracking followed by separation of plies (delamination) as shown in the figures. The initiation of damage was localized at the 45 degree plies (also the sites of fibre pullouts). Once damage started progressing, ultimate failure occurred due to the splitting apart of the laminate.

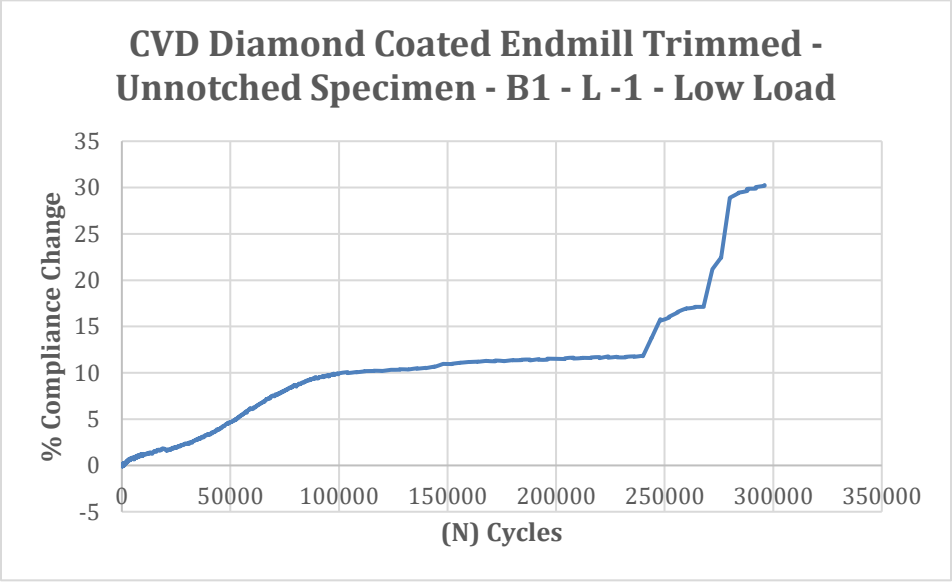

Figure 7.110 Percent Compliance Change Vs. Fatigue Cycles for (B1 – L – 1)

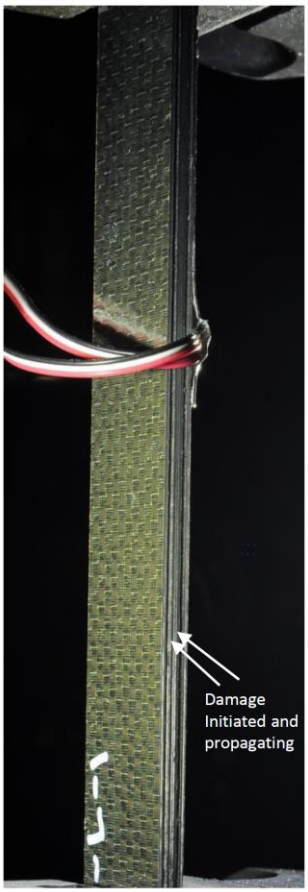

Figure 7.111 Damage at 200K Cycles, 11.53%, Test

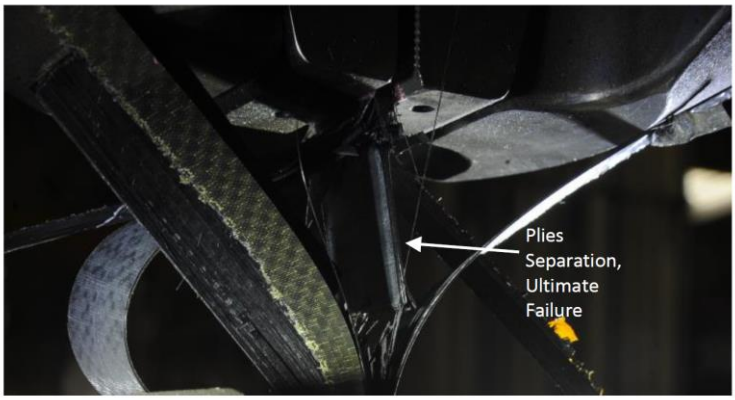

Figure 7.112 Damage (30.46%) & Ultimate Failure at 296778 Cycles

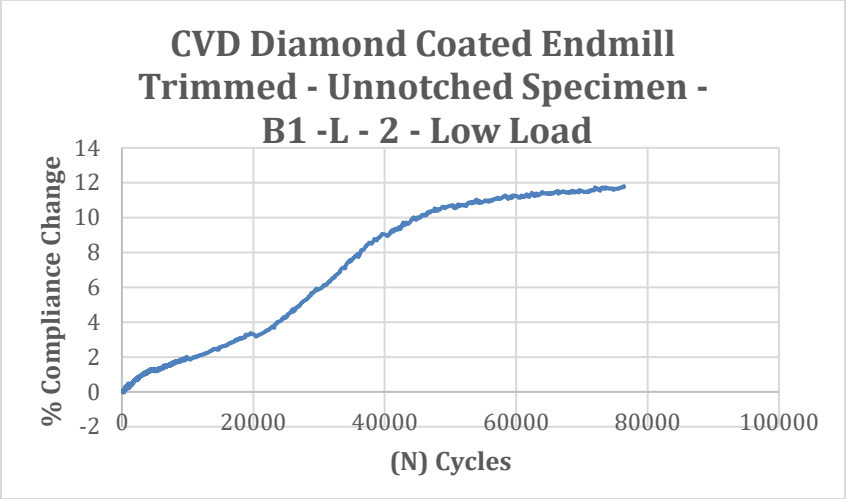

Figure 7.113 Percent Compliance Change Vs. Fatigue Cycles for (B1 – L – 2)

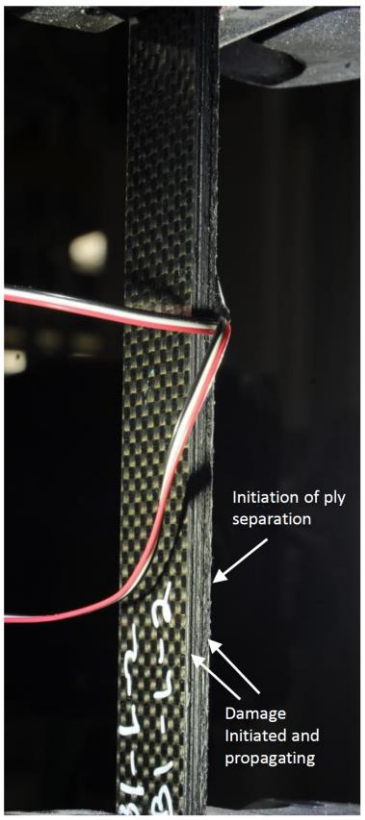

Figure 7.114 Damage at 50K Cycles, 10.68%, Test

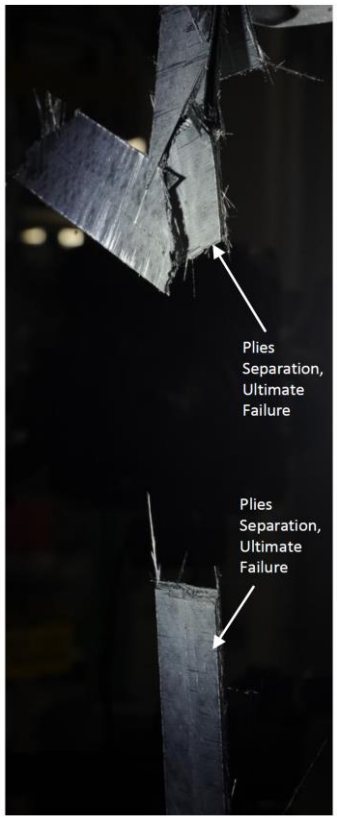

Figure 7.115 Damage (11.64%) & Ultimate Failure at 76783 Cycles

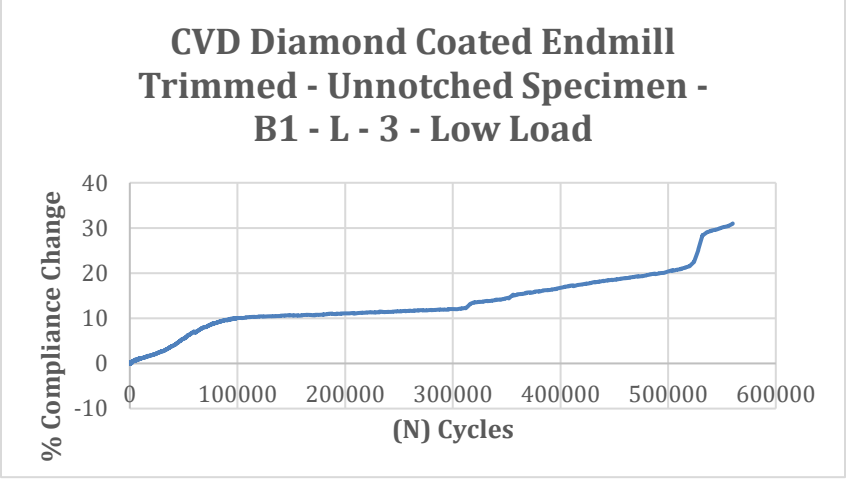

Figure 7.116 Percent Compliance Change Vs. Fatigue Cycles for (B1 – L – 3)

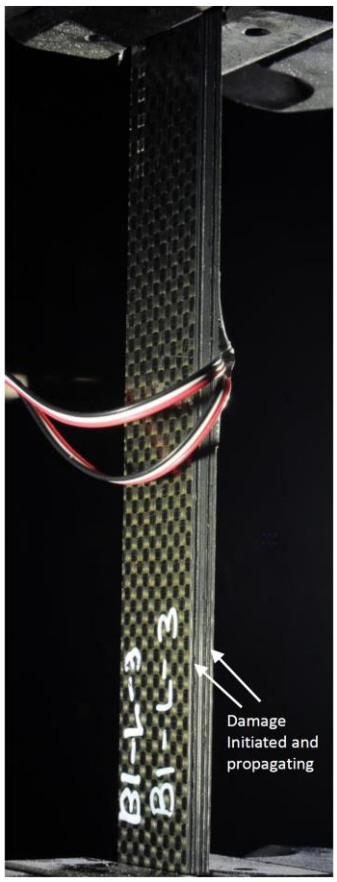

Figure 7.117 Damage at 200K Cycles, 11.07%, Test

Figure 7.118 Damage (31.06%) & Ultimate Failure at 562123 Cycles

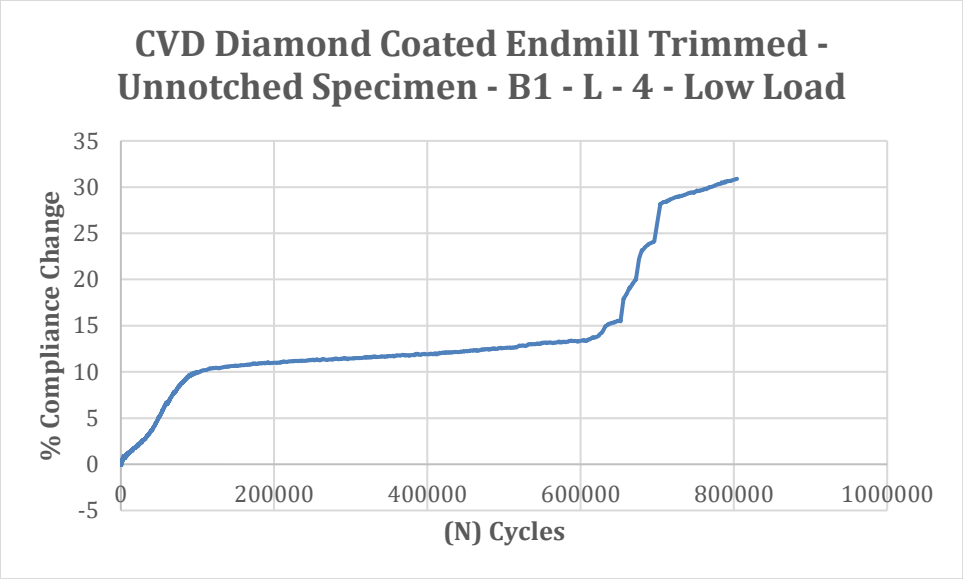

Figure 7.119 Percent Compliance Change Vs. Fatigue Cycles for (B1 – L – 4)

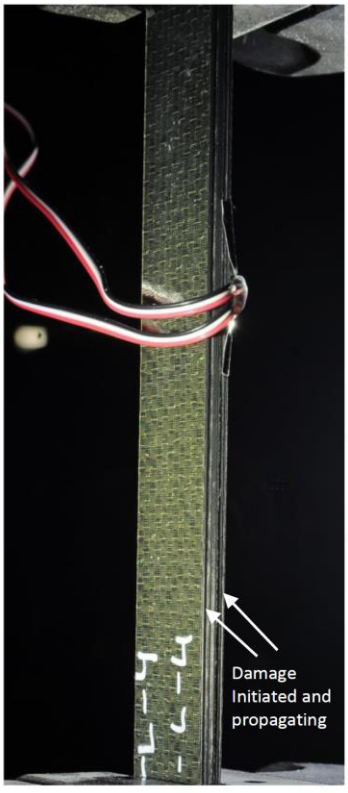

Figure 7.120 Damage at 200K Cycles, 10.99%, Test

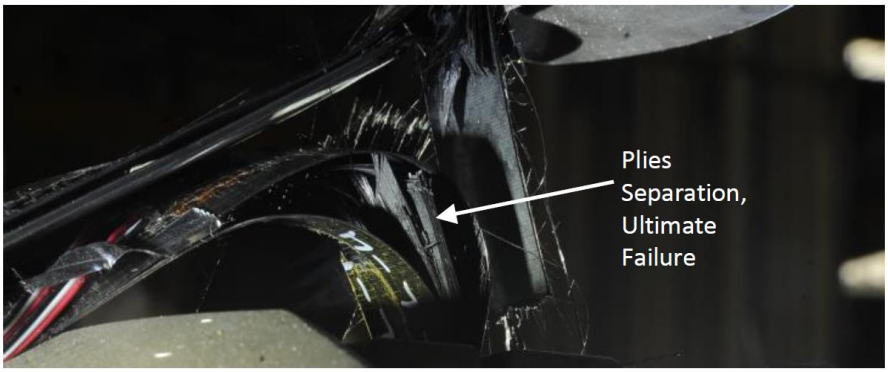

Figure 7.121 Damage (30.95%) & Ultimate Failure at 805926 Cycles

In all cases of AWJ trimmed and CVD Endmill trimmed specimens except one, the fatigue cycles to failure were higher than 250K cycles for low load testing. For test specimen number B1 – L – 2, the failure cycles were only 76783 cycles. These low fatigue cycles were attributed to the initiation of delamination at the outer edge plies during the test specimen trimming processes which ultimately led to rapid progression of damage through the laminate resulting in ultimate failure at low fatigue cycles count.

Figures 7.122 through 7.124 show the plots of various AWJ and CVD specimens % compliance change Vs. Fatigue cycles with respect to each other.

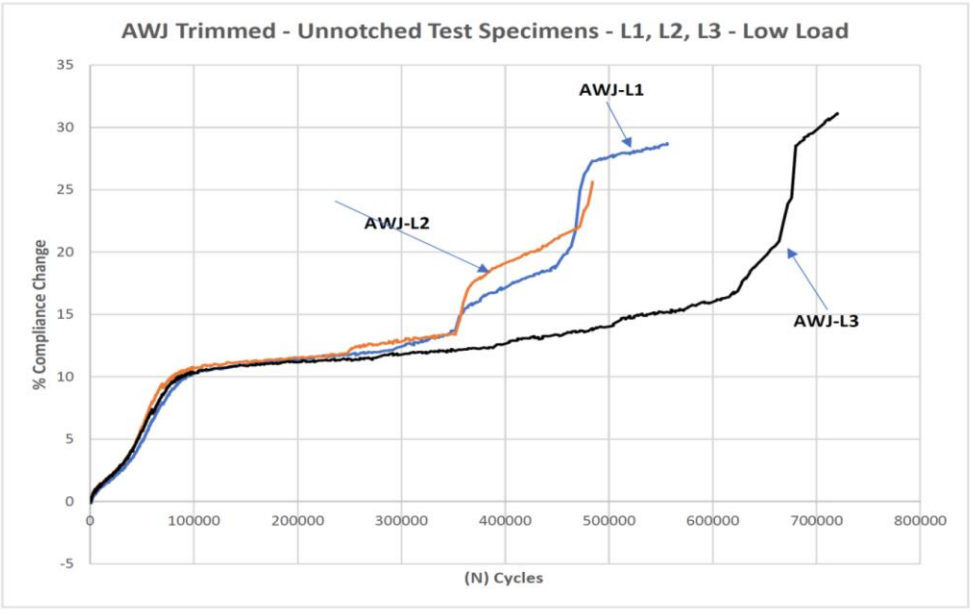

Figure 7.122 Summary Plot of AWJ Low Load Percent Compliance Change Vs. Fatigues Cycles

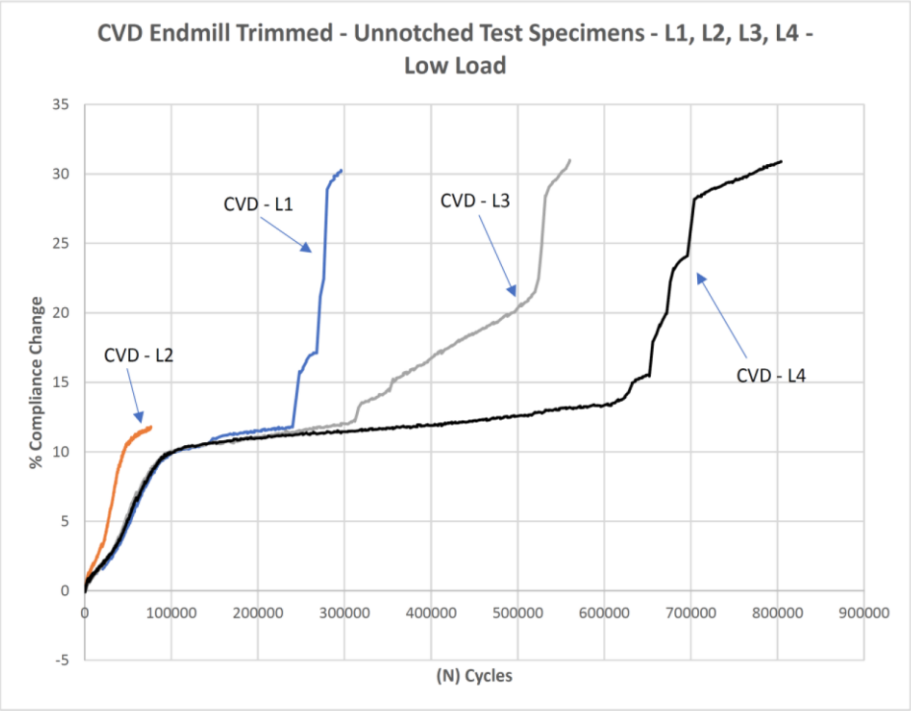

Figure 7.123 Summary Plot of CVD Endmill Trimmed Low Load Percent Compliance Change Vs. Fatigues Cycles

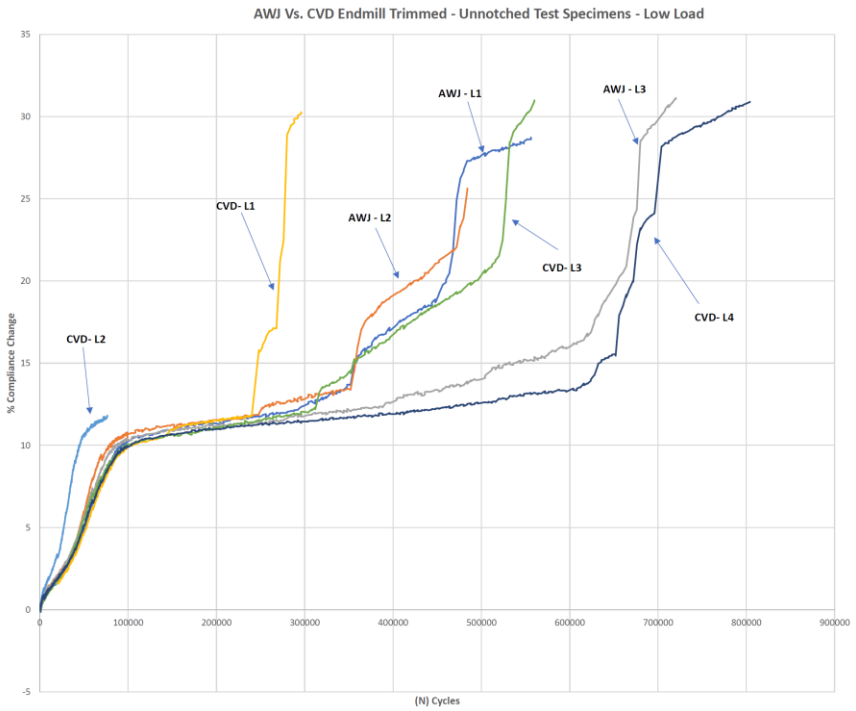

Figure 7.124 Summary Plot of AWJ Vs. CVD Endmill Trimmed Low Load Percent Compliance Change Vs. Fatigues Cycles

Surface Finish Stress Concentration Factor $\left(\bar{K}_t\right)$

Surface finish profiles of all high load test specimens were used to calculate the stress concentration factor $\left(\bar{K}_t\right)$ using the formula shown in figure 7.36

Figures 7.125 through 7.130 Show the stress concentration factor determination graphically for the radius and using the formula from Figure 7.36

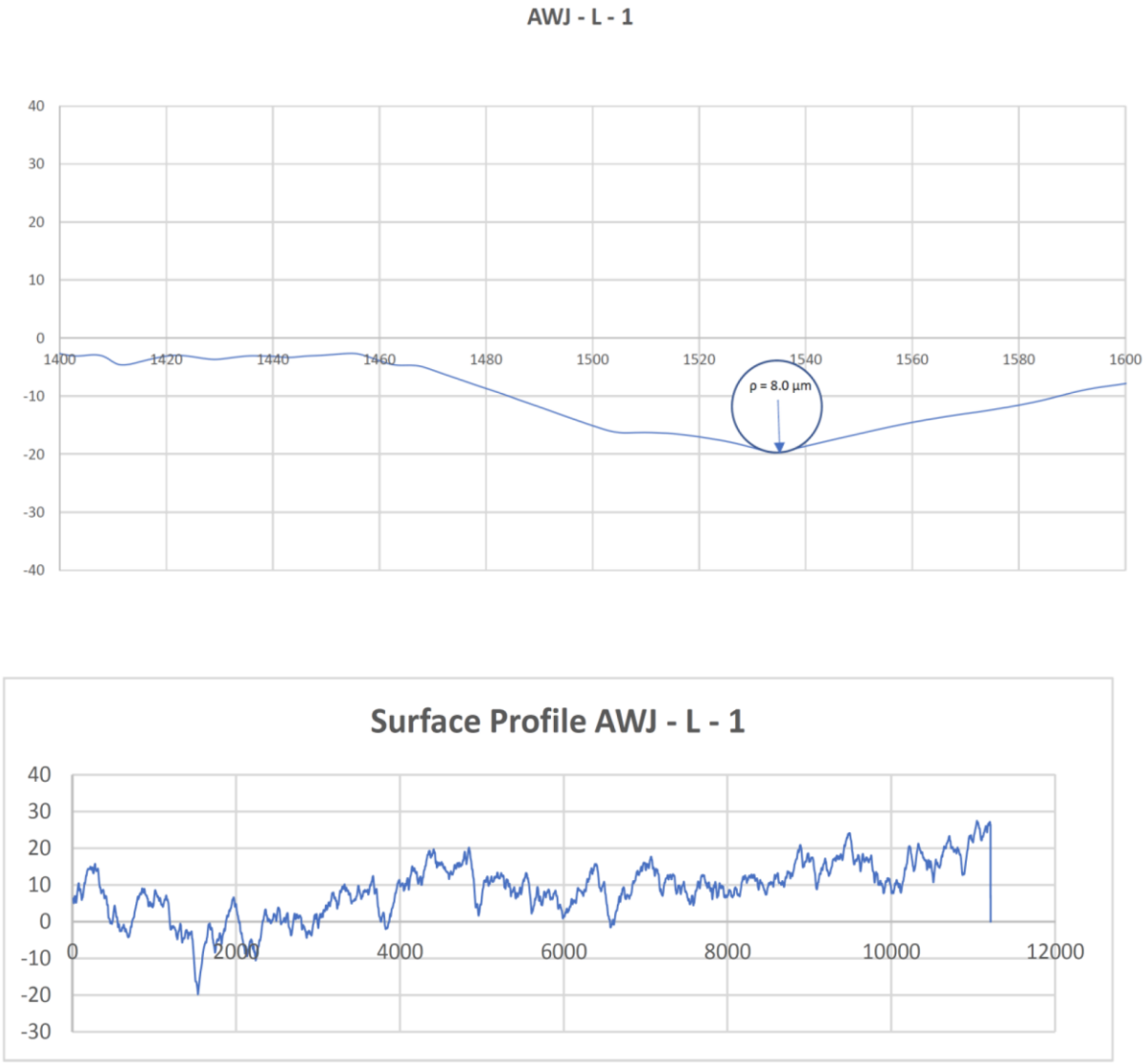

Figure 7.125 Graphical Determination of radius (ρ) from surface profile of test specimen A1-L–1

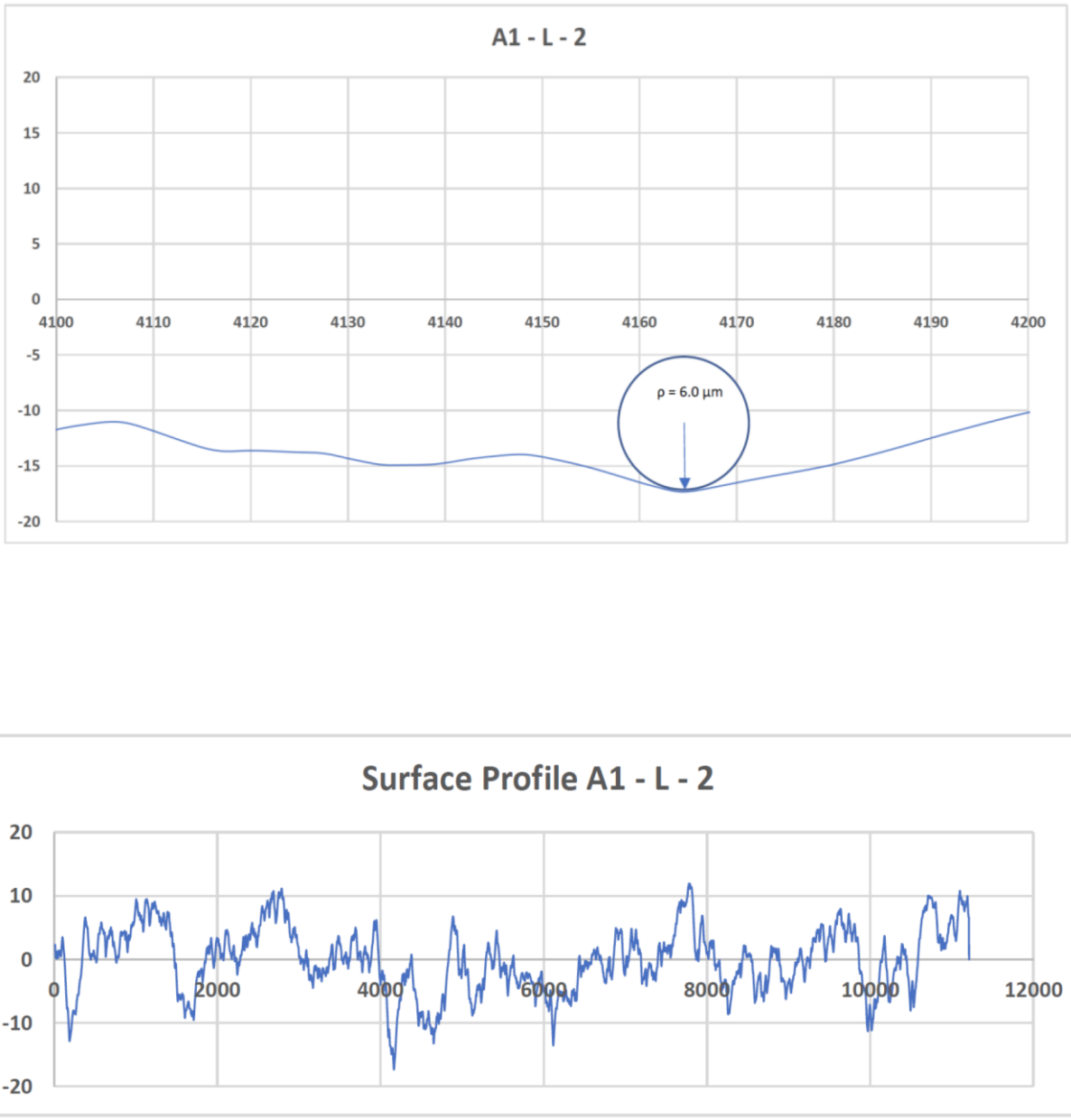

Figure 7.126 Graphical Determination of radius (ρ) from surface profile of specimen A1–L–2

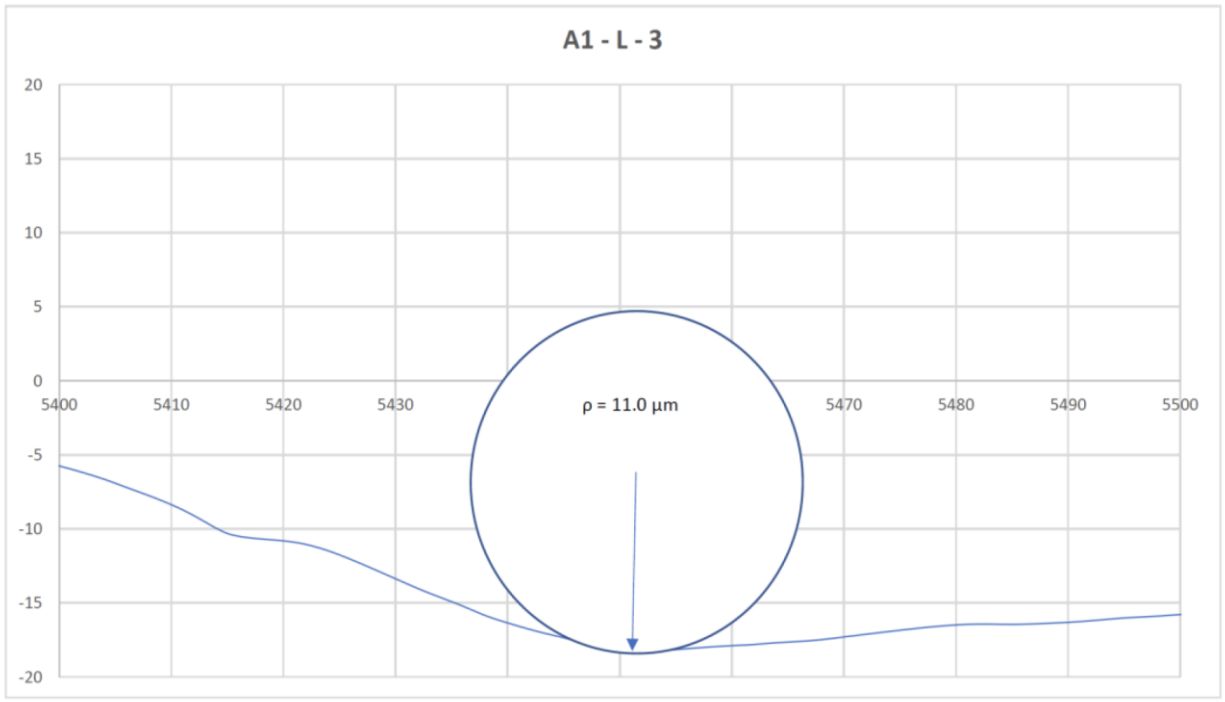

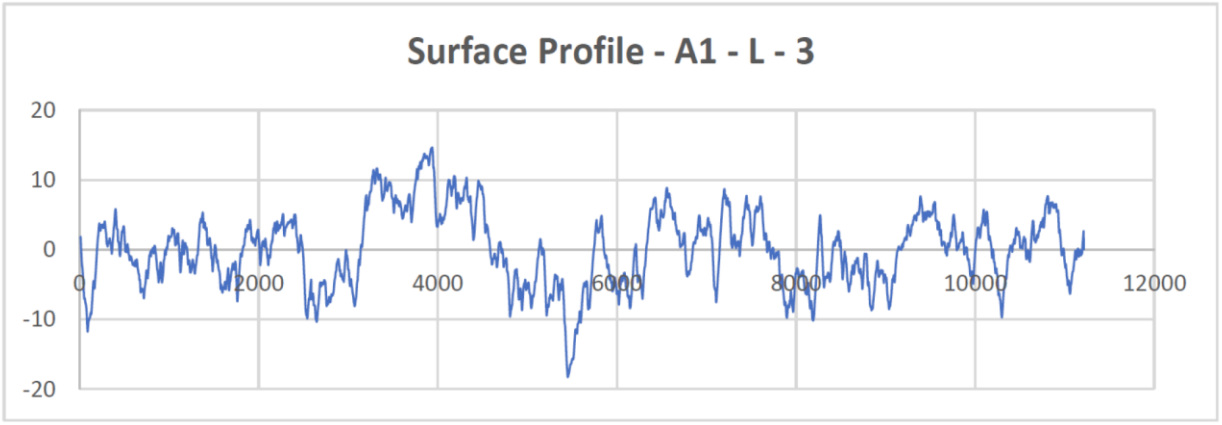

Figure 7.127 Graphical Determination of radius (ρ) from surface profile of specimen A1 – L – 3

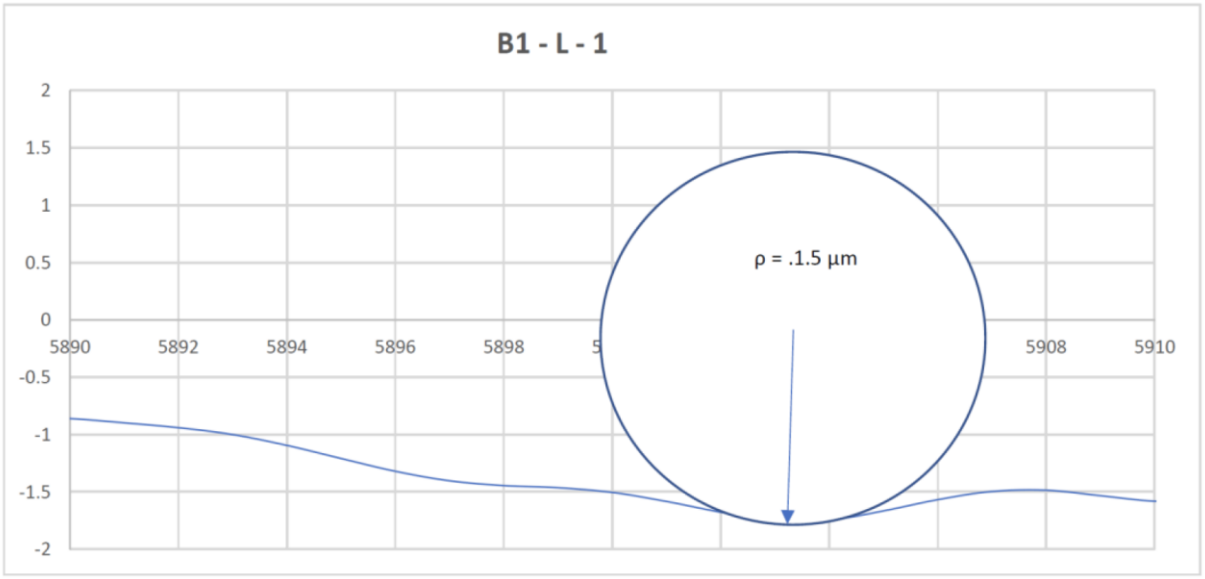

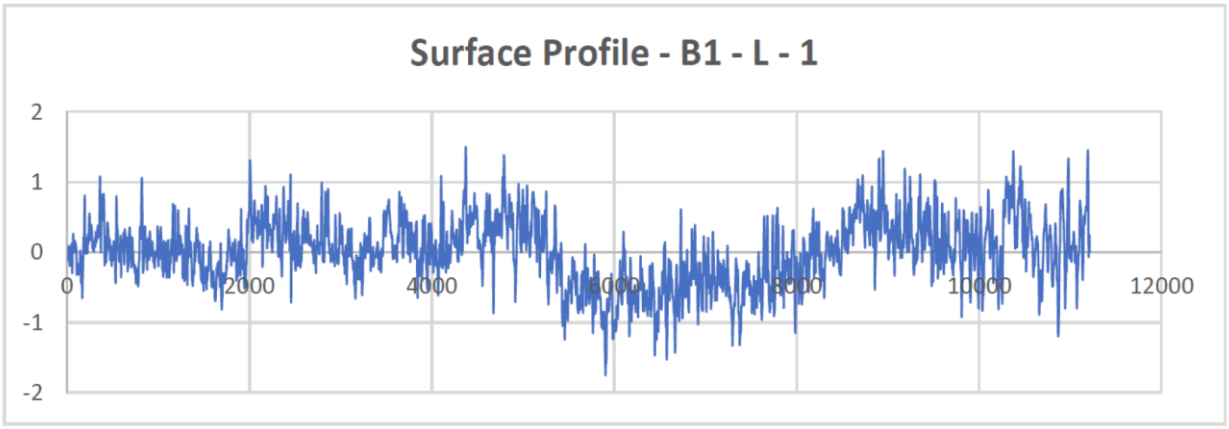

Figure 7.128 Graphical Determination of radius (ρ) from surface profile of specimen B1 – L – 1

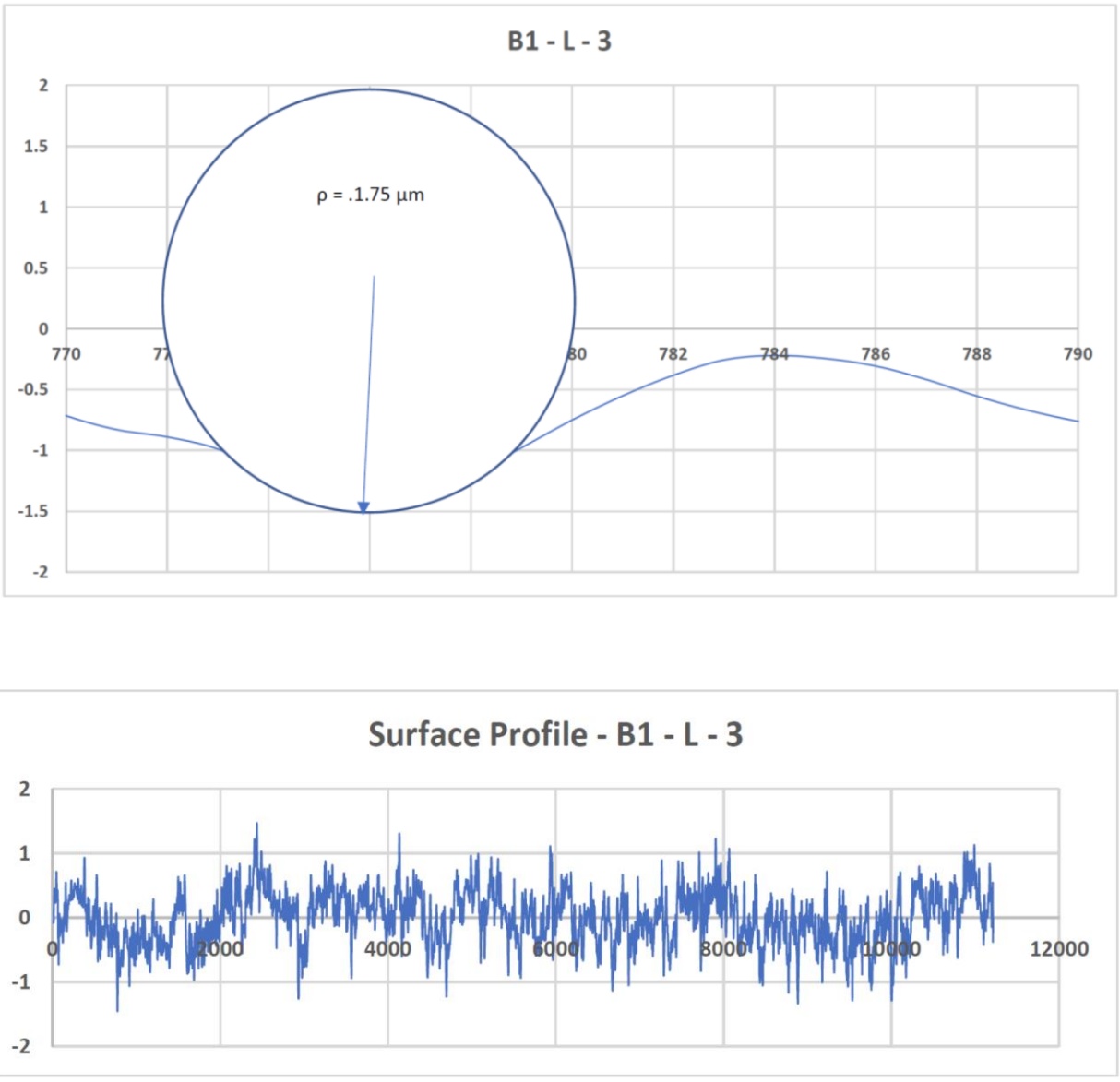

Figure 7.129 Graphical Determination of radius (ρ) from surface profile of specimen B1 – L – 3

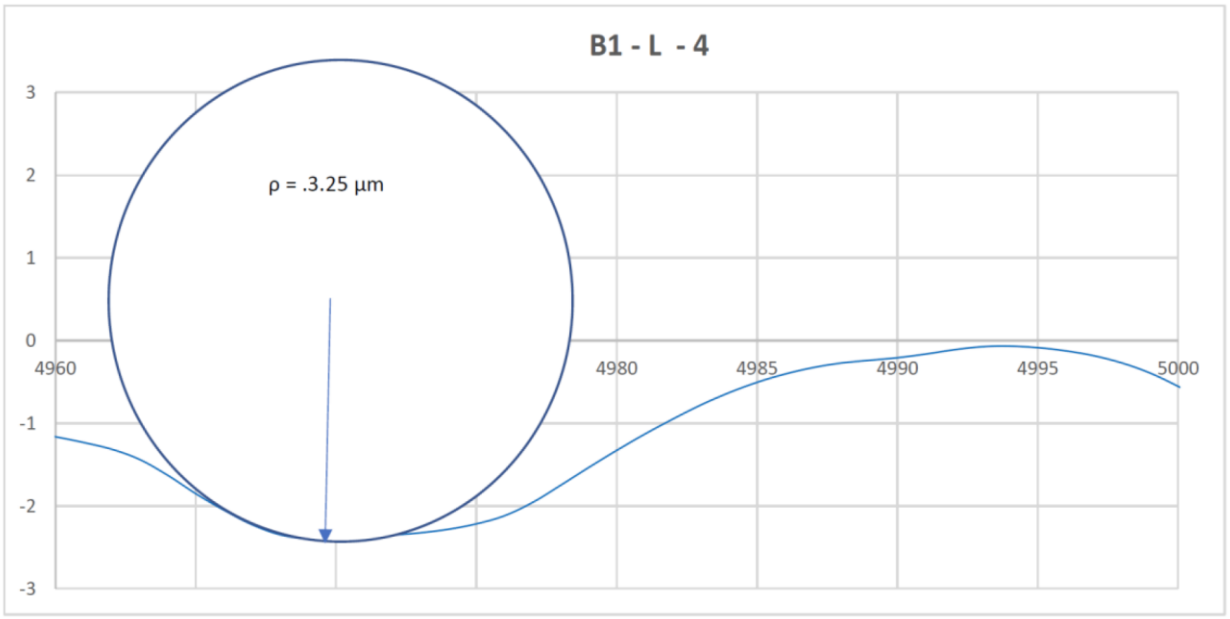

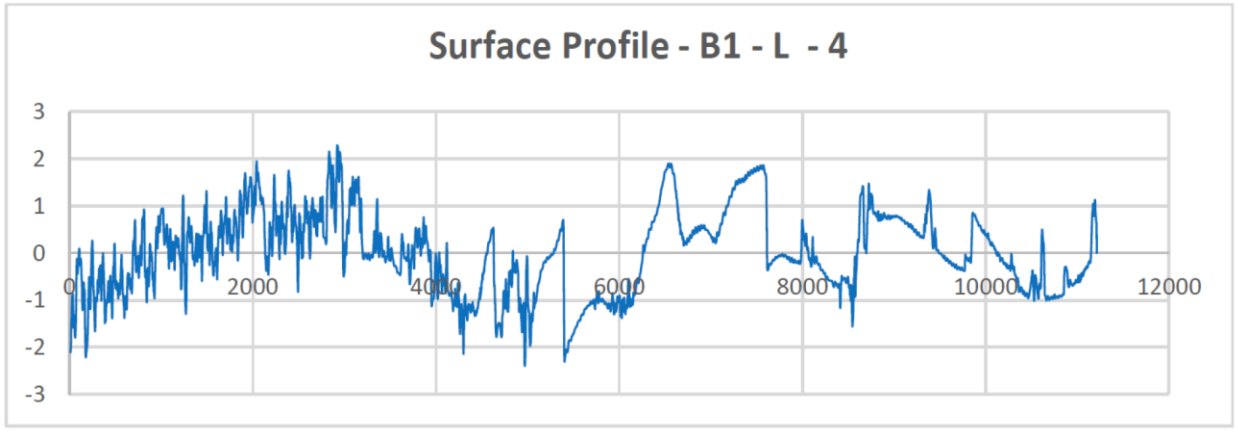

Figure 7.130 Graphical Determination of radius (ρ) from surface profile of specimen B1 – L – 4

Table 7.14 shows the calculated values for the surface integrity stress concentration factor calculated for various low load test specimens.

Specimen Name	Surface Integrity Stress Concentration Factor
A1 – L - 1	1.8
A1 – L - 2	2.2
A1 – L - 3	1.68
B1 – L - 1	1.8
B1 – L - 3	1.36
B1 – L - 4	1.32

Table 7.14 Calculated Surface Integrity Stress Concentration Factor for Low Load Test Specimens

Observation on Surface finish Data Vs. Fatigue Cycles – Surface finish data in the longitudinal direction was plotted against fatigue cycles and reviewed comparing AWJ trimmed specimens to CVD Diamond Coated Endmill Trimmed specimens. Figures 7.131 through 7.144 show the variation of surface finish parameters Vs. fatigue cycles for the different parameters.

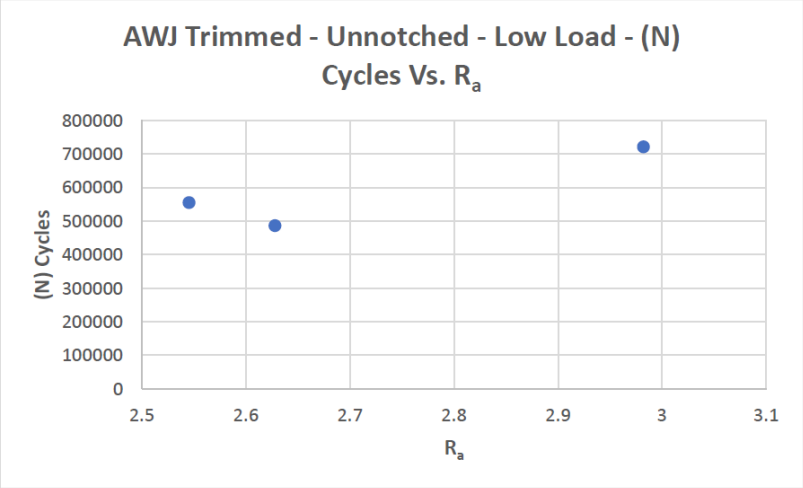

Figure 7.131 Surface Finish - R_a (longitudinal) Vs. Fatigue Cycles – AWJ Trimmed Low Load Specimens

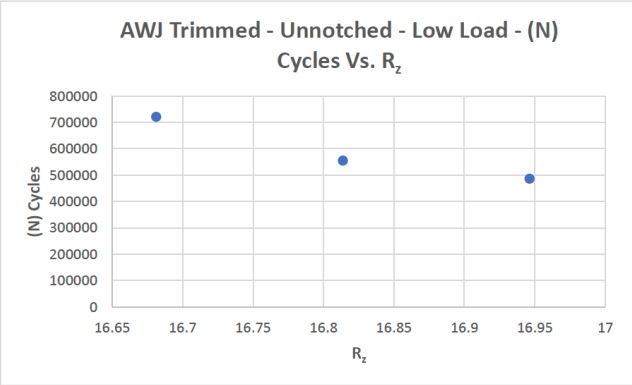

Figure 7.132 Surface Finish – R_z (longitudinal) Vs. Fatigue Cycles – AWJ Trimmed Low Load Test Specimens

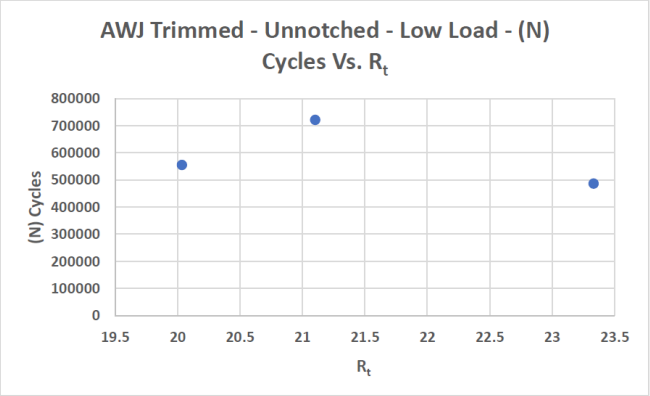

Figure 7.133 Surface Finish – R_t (longitudinal) Vs. Fatigue Cycles – AWJ trimmed Low Load Test Specimens

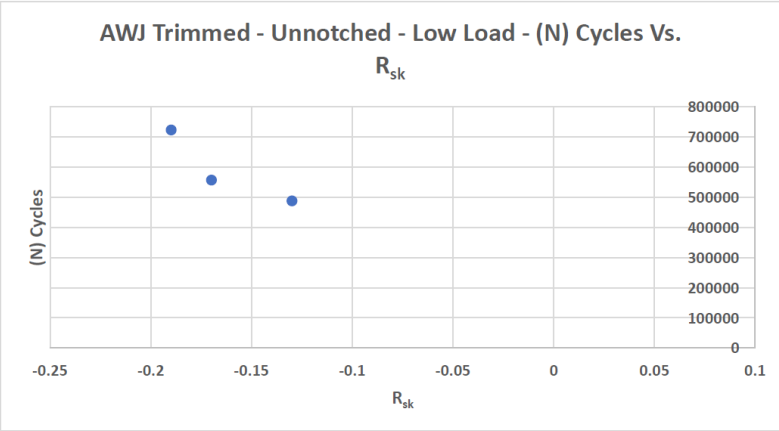

Figure 7.134 Surface Finish – R_{sk} (longitudinal) Vs. Fatigue Cycles – AWJ Trimmed Low Load Test Specimens

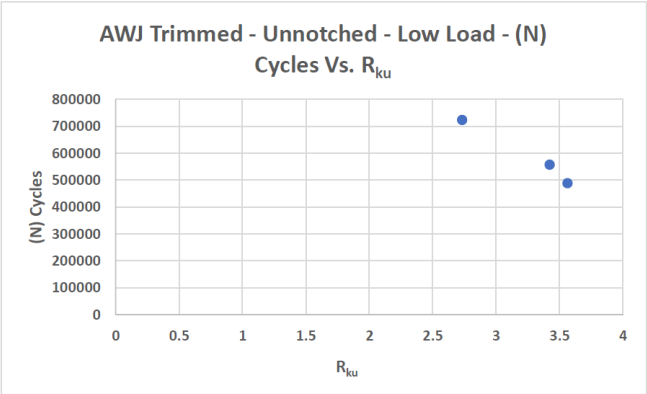

Figure 7.135 Surface Finish – R_{ku} (longitudinal) Vs. Fatigue Cycles – AWJ Trimmed Low Load Test Specimens

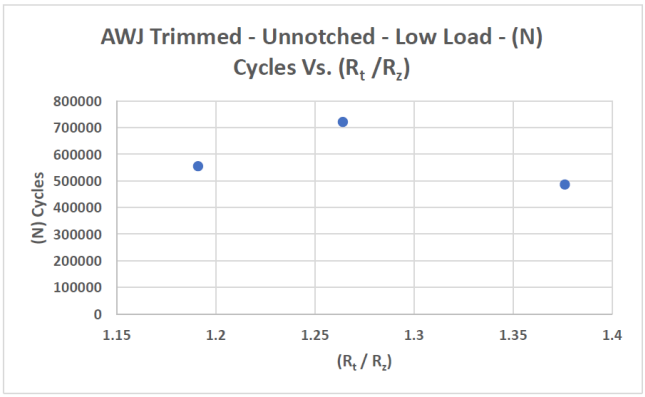

Figure 7.136 Surface Finish – (R_t/R_z) (Longitudinal) Vs. Fatigue Cycles – AWJ Trimmed Low Load Test Specimens

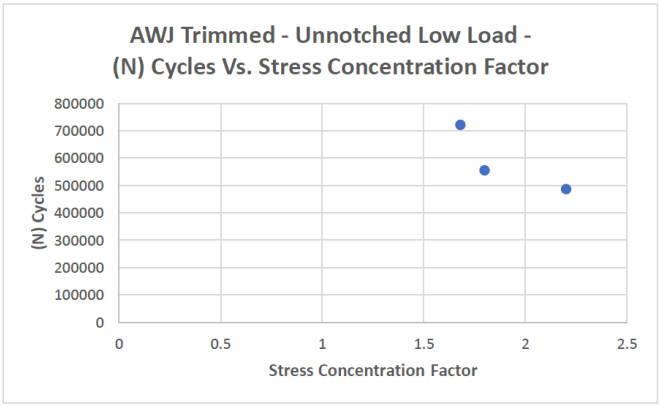

Figure 7.137 Surface Integrity Stress Concentration Factor (Longitudinal) Vs. Fatigue Cycles – AWJ Trimmed Low Load Test Specimens

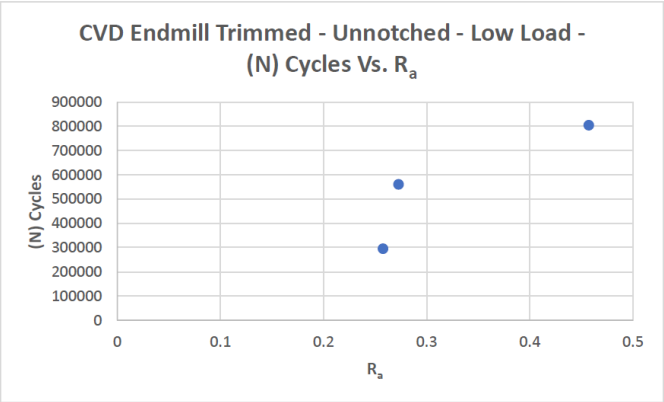

Figure 7.138 Surface Finish - R_a (longitudinal) Vs. Fatigue Cycles – AWJ Trimmed Low Load Specimens

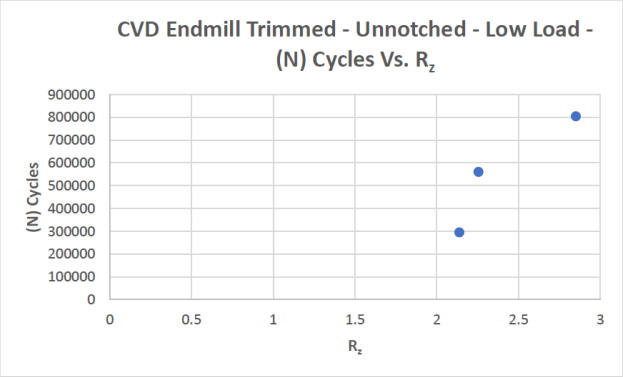

Figure 7.139 Surface Finish – R_z (longitudinal) Vs. Fatigue Cycles – CVD Endmill Trimmed Low Load Test Specimens

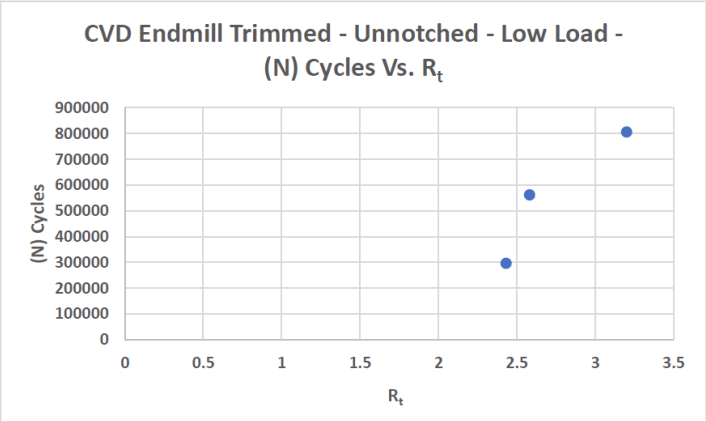

Figure 7.140 Surface Finish – R_t (longitudinal) Vs. Fatigue Cycles – CVD Endmill trimmed Low Load Test Specimens

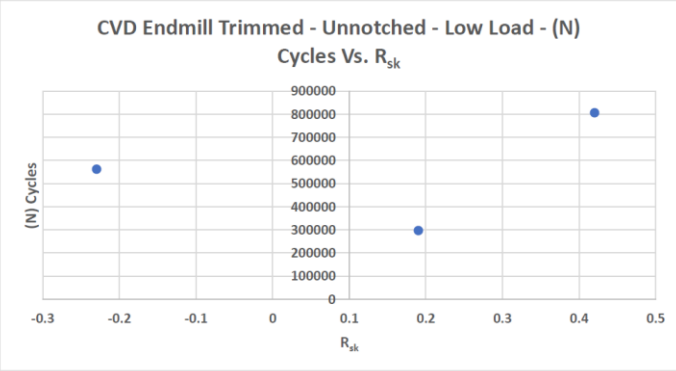

Figure 7.141 Surface Finish – R_{sk} (longitudinal) Vs. Fatigue Cycles – CVD Endmill Trimmed Low Load Test Specimens

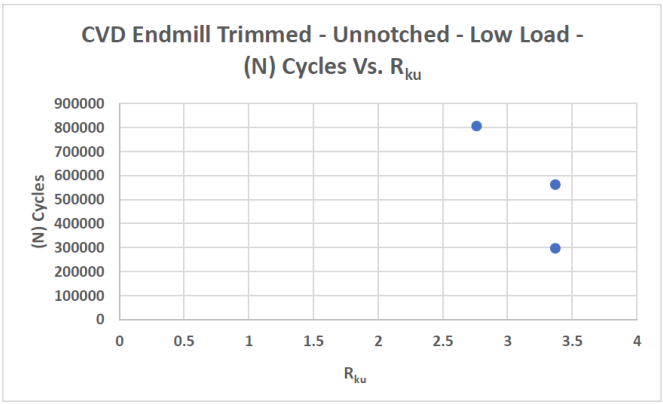

Figure 7.142 Surface Finish – R_{ku} (longitudinal) Vs. Fatigue Cycles –CVD Endmill Trimmed Low Load Test Specimens

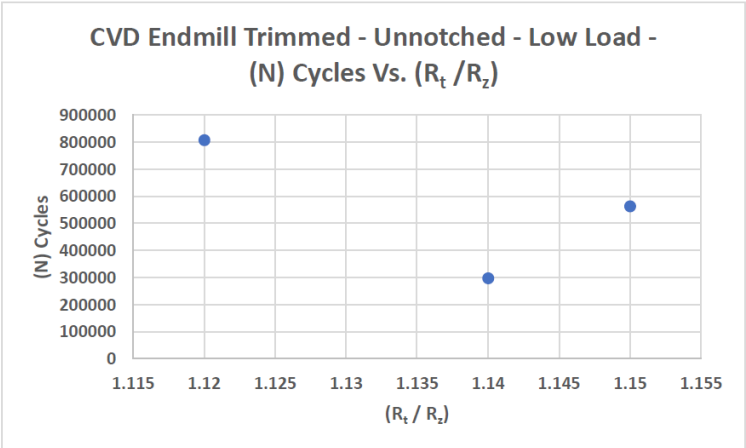

Figure 7.143 Surface Finish – (R_t/R_z) (Longitudinal) Vs. Fatigue Cycles –CVD Endmill Trimmed Low Load Test Specimens

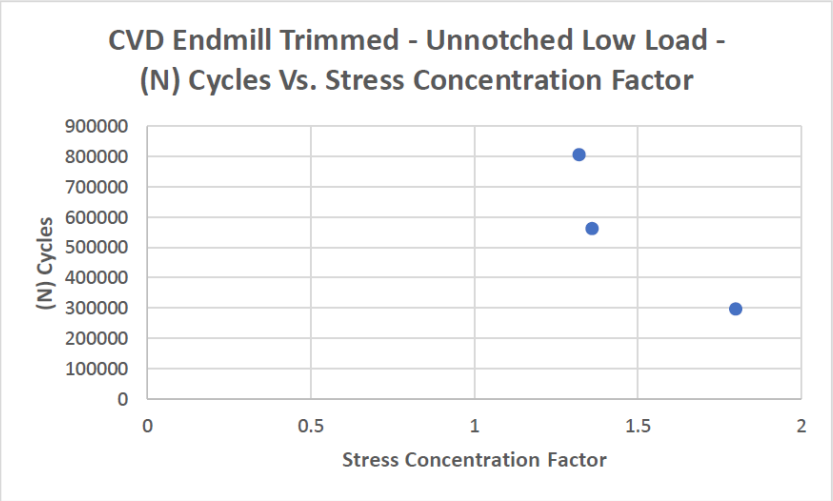

Figure 7.144 Surface Integrity Stress Concentration Factor (Longitudinal) Vs. Fatigue Cycles – CVD Endmill Trimmed Low Load Test Specimens

It was observed that in both AWJ trimmed and CVD Endmill trimmed specimens, the surface finish data when better resulted in high fatigue cycles to failure.

In the case of test specimen B1 – L – 2, the surface finish data indicated a rougher profile in both longitudinal and transverse direction. It also had damage present after the machining process. These higher values of data pointed to higher surface peaks and valleys resulting in higher count of damage initiation sites as well as preexisting damage from trimming operation. The result was an rapid damage progress at beginning of testing. This ultimately led to failure at low cycles for this test specimen.

7.4.2 Notched Test Specimens Data Review

All notched test specimens were tested at a frequency of 7 Hz. Notched specimens had a hole in the centre representing a notch for testing.

7.4.2.1 High Load Test Specimen Data Review

For the high load test specimens, specimens # A2 – H - 1 and A2 – H – 2 were used to derive the test load condition. The following samples were tested for AWJ trimmed specimens.

A2 – H – 3

A2 – H – 4

A1 – H – 4

For CVD Diamond Coated Endmill Trimmed specimens, the following samples were tested.

B2 – H – 1

B2 – H – 2

B2 – H – 3

B2 – H - 4

Prior to testing the following surface finish parameters were recorded for each sample in both longitudinal and transverse directions

R_a , R_z , R_t , R_{sk} , R_{ku}

Table 7.15 shows the fatigue cycles to failure for each of the high load specimens along with the load applied and stress as well as % change in compliance.

Tables 7.4 and 7.5 documented earlier in this chapter show the surface finish data documented in the longitudinal and transverse direction.

Specimen Name	Trim	Hole	Fatigue Cycles	Test Load (Max) (N)	Test Load (Min) (N)	Max Stress (Mpa)	Test Frequency	Compliance
A2-H-3	AWJ -80	CVD Drill	178298	55603	5560	484.2	7 Hz	36.61%
A2-H-4	AWJ -80	CVD Drill	153058	55603	5560	484.2	7 Hz	32.59%
B2-H-1	CVD Endmill	CVD Drill	162095	55603	5560	484,2	7 Hz	37.52%
B2-H-2	CVD Endmill	CVD Drill	123091	55603	5560	484.2	7 Hz	32.23%
B2-H-3	CVD Endmill	CVD Drill	92663	55603	5560	484,2	7 Hz	15.71%
B2-H-4	CVD Endmill	CVD Drill	111447	55603	5560	484.2	7 Hz	26.24%

Table 7.15 Fatigue Cycles/Loads/Stress & % Compliance Change for Notched High Loading Testing

Damage Propagation in AWJ trimmed specimens- To compare the damage propagation % compliance change was plotted for each AWJ high load specimen and the percentage damage at 80K cycles was compared. Figures 7.145 through 7.150 show the % compliance change for each high load AWJ test specimen along with a photo micrograph depicting the damage at 80K cycles and at failure.

In all cases damage started matrix cracking followed by matrix fibre interface debonding and then delamination as shown in the figures. The initiation of damage was localized at the 45 degree plies (also the sites of fibre pullouts). These sites were both at the edges as well as in the

hole. Once damage started progressing, ultimate failure occurred due to delamination in the edges and through the hole.

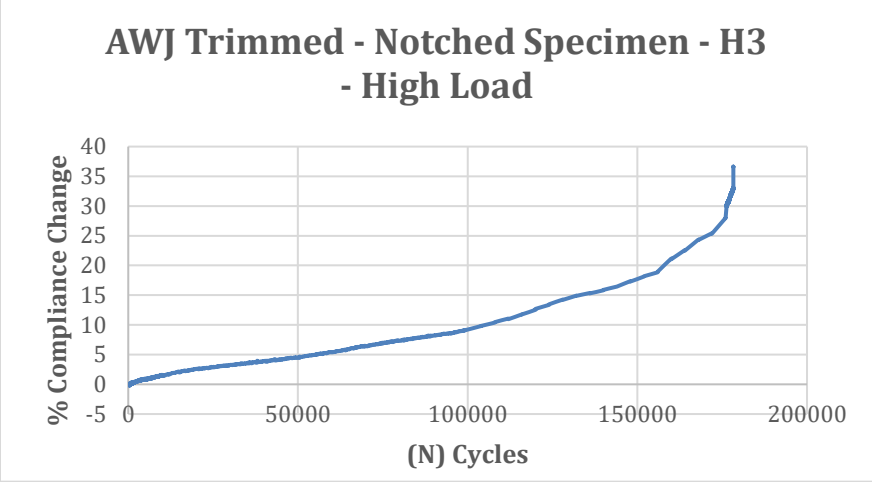

Figure 7.145 Percent Compliance Change Vs. Fatigue Cycles for A2 – H – 3

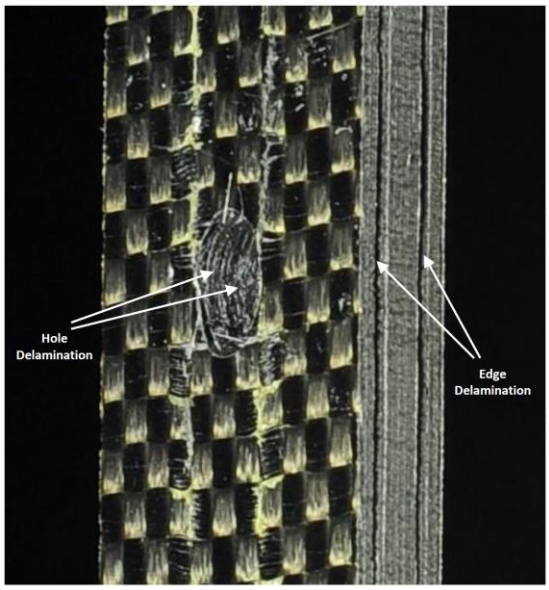

Figure 7.146 Damage at 80K Cycles, 7.40%, Test Specimen A2

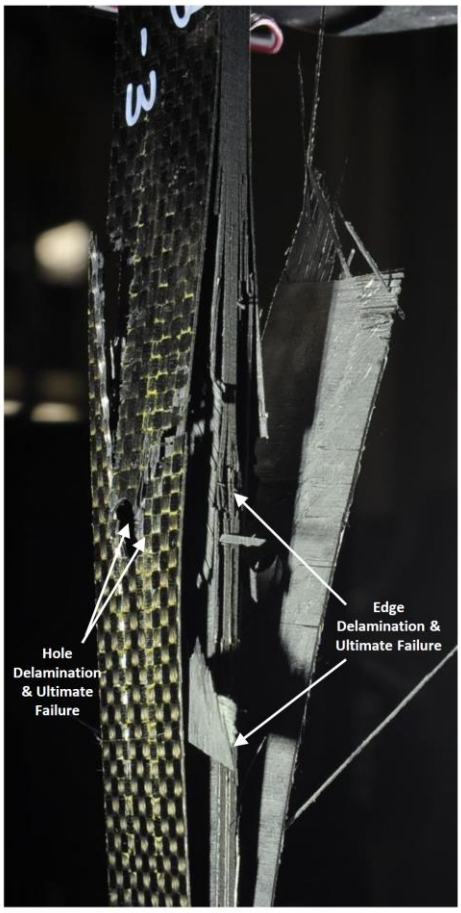

Figure 7.147 Damage (36.61%) & Ultimate Failure at 178298 Cycles, Test Specimen A2 – H - 3

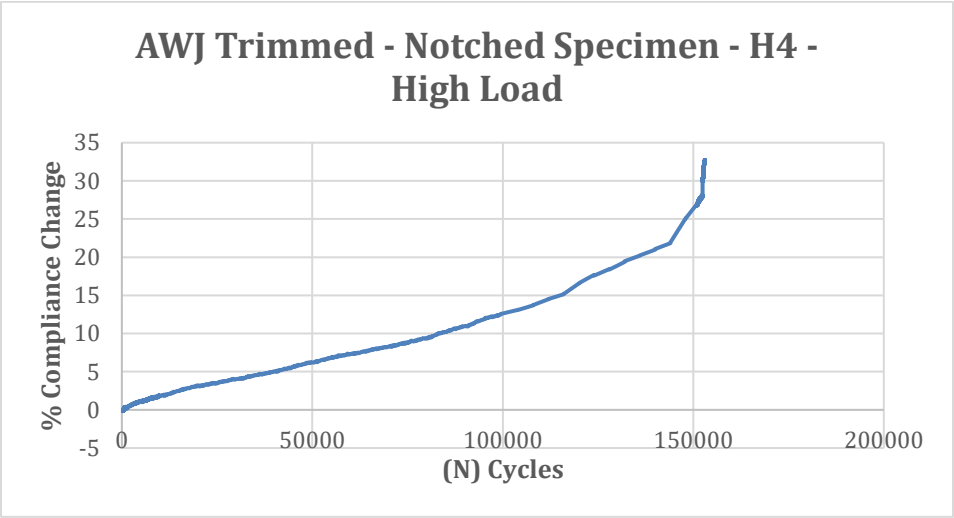

Figure 7.148 Percent Compliance Change Vs. Fatigue Cycles for A2 – H – 4

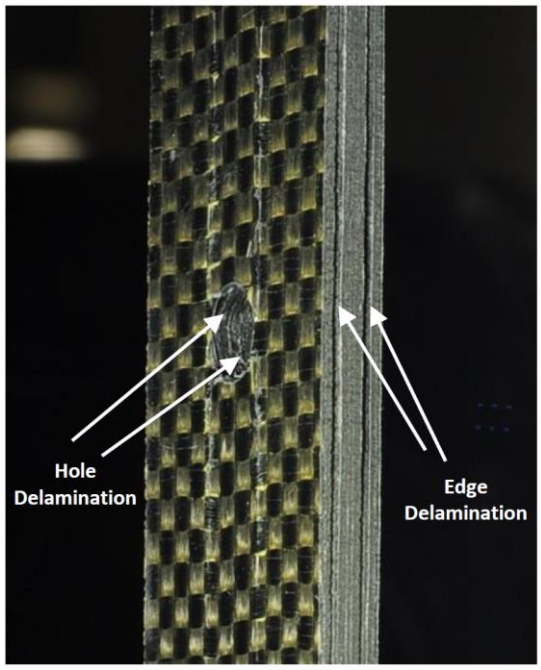

Figure 7.149 Damage at 80K Cycles, 9.44%, Test Specimen A2

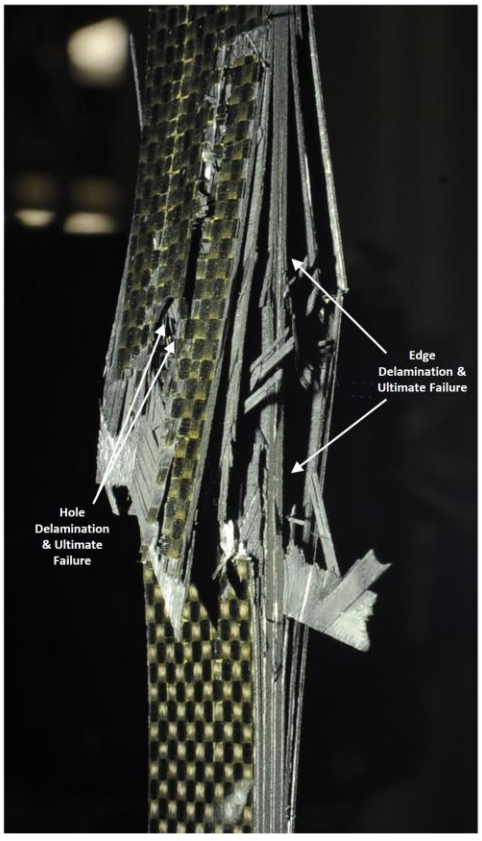

Figure 7.150 Damage (32.59%) & Ultimate Failure at 153058 Cycles, Test Specimen A2 – H - 4

Damage Propagation in CVD Diamond Coated Endmill trimmed specimens- To compare the damage propagation % compliance change was plotted for each CVD Diamond Coated Endmill trimmed high load specimen and the percentage damage at 80K cycles was compared. Figures 7.151 through 7.118 show the % compliance change for each high load CVD endmill trimmed test specimen along with a photo micrograph depicting the damage at 80K cycles and at failure. In all cases damage started as matrix cracking followed by matrix fibre interface debonding and by delamination as shown in the figures. The initiation of damage was localized at the 45 degree plies (also the sites of fibre pullouts). These sites were both at the edges as well as in the hole. Once damage started progressing, ultimate failure occurred due to delamination in the edges and through the hole.

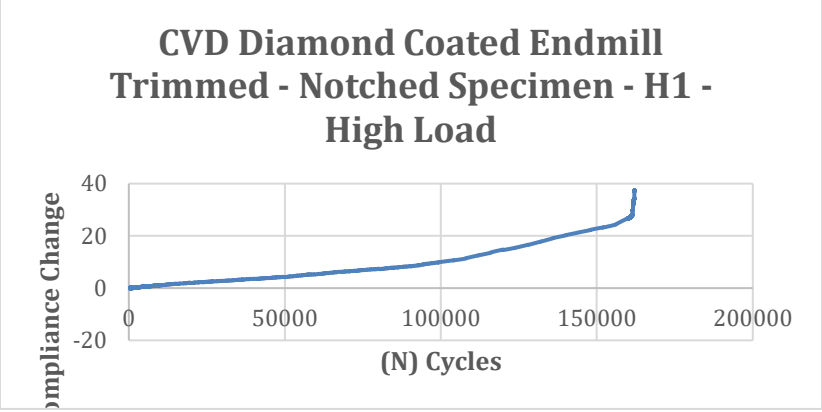

Figure 7.151 Percent Compliance Change Vs. Fatigue Cycles for B2 – H – 1

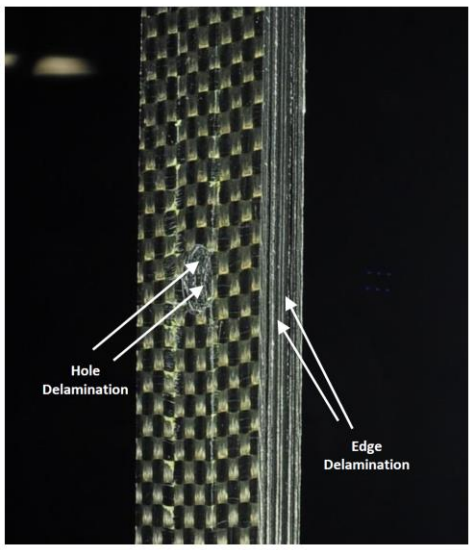

Figure 7.152 Damage at 80K Cycles, 7.33%, Test Specimen B2 – H - 1

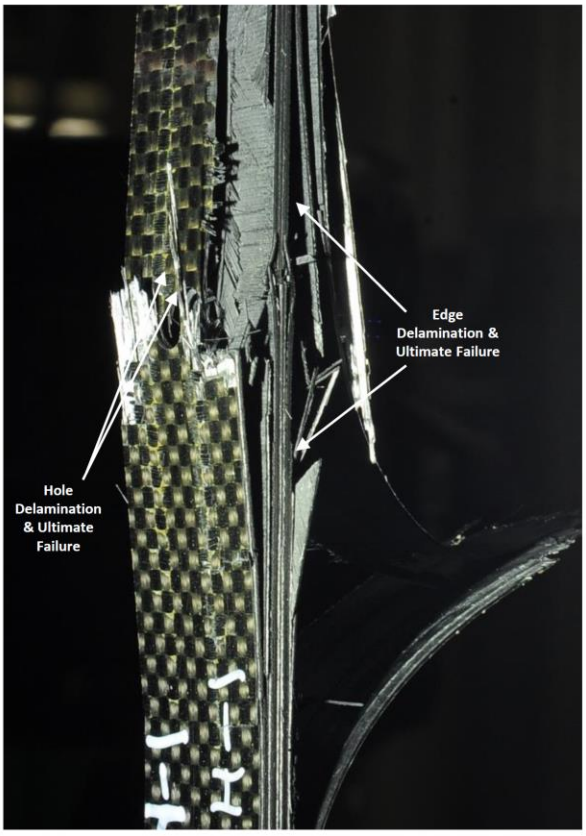

Figure 7.153 Damage (37.52%) & Ultimate Failure at 162095 Cycles, Test

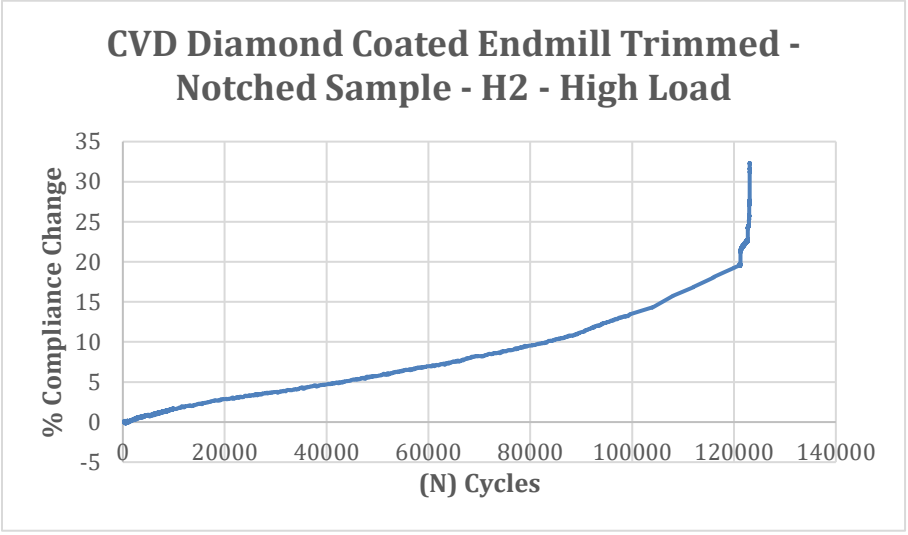

Figure 7.154 Percent Compliance Change Vs. Fatigue Cycles for B2 – H – 2

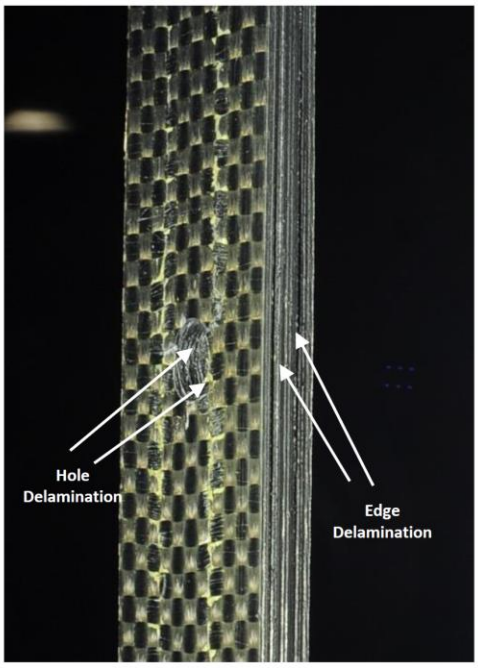

Figure 7.155 Damage at 80K Cycles, 10.62%, Test Specimen B2

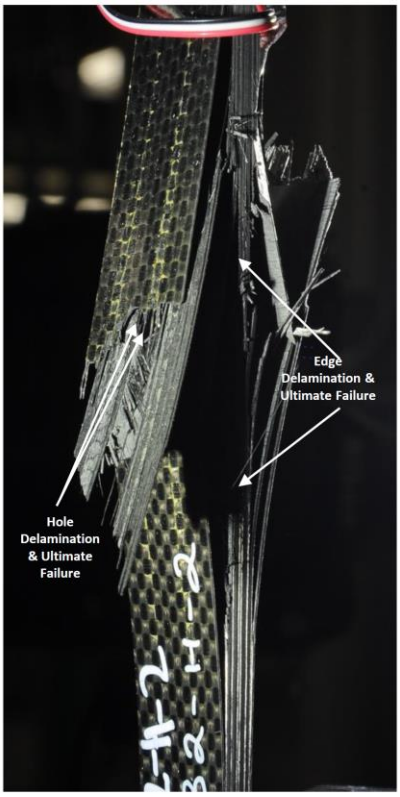

Figure 7.156 Damage (32.23%) & Ultimate Failure at 123091 Cycles, Test

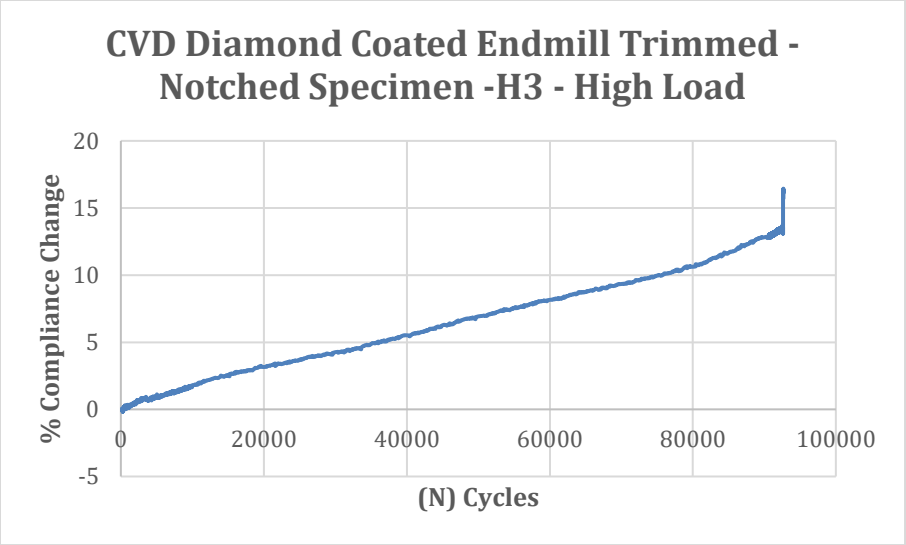

Figure 7.157 Percent Compliance Change Vs. Fatigue Cycles for B2 – H – 3

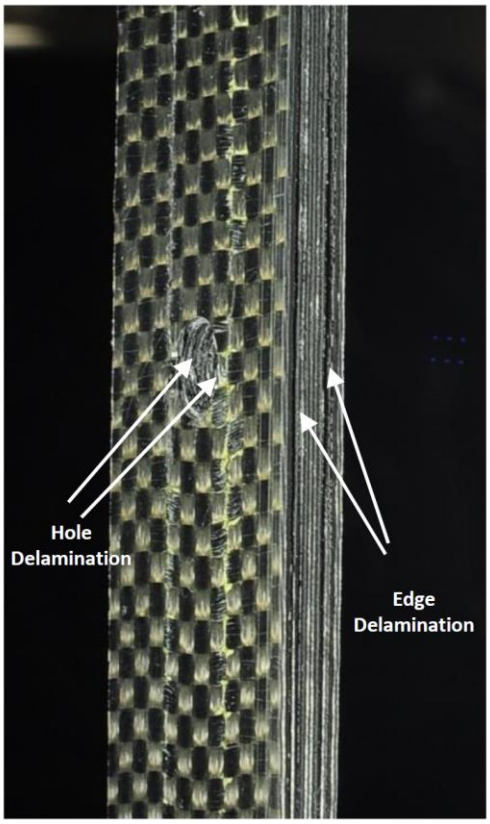

Figure 7.158 Damage at 80K Cycles, 10.63%, Test Specimen B2

Figure 7.159 Damage (15.71%) & Ultimate Failure at 92663 Cycles, Test Specimen

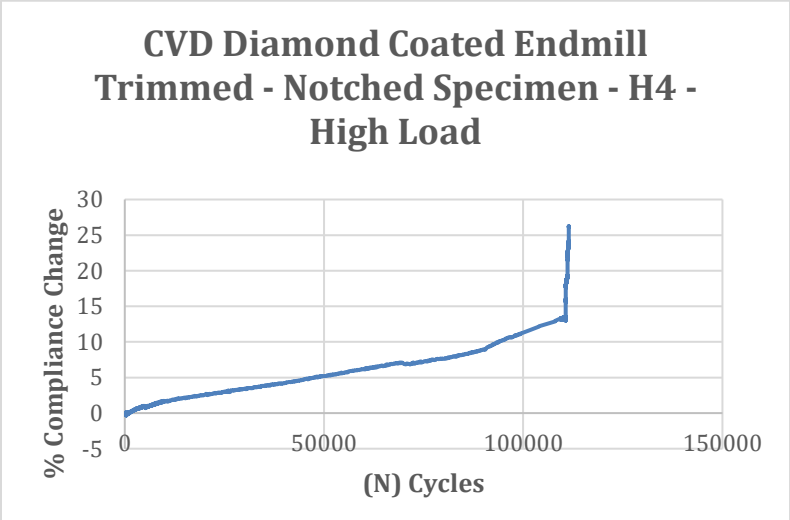

Figure 7.160 Percent Compliance Change Vs. Fatigue Cycles for B2 – H – 4

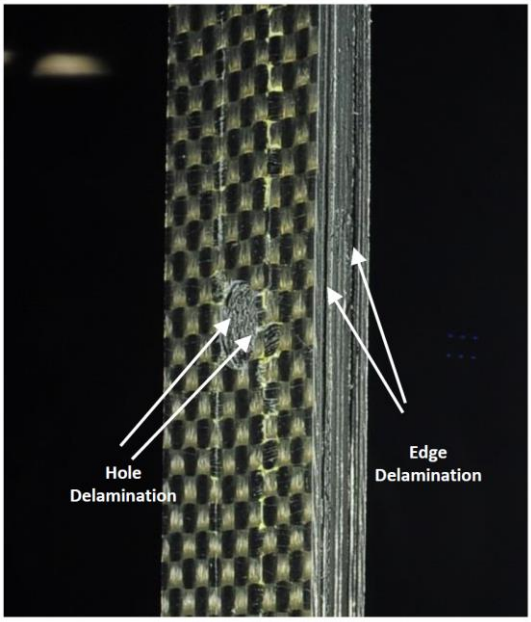

Figure 7.161 Damage at 80K Cycles, 7.81%, Test Specimen B2

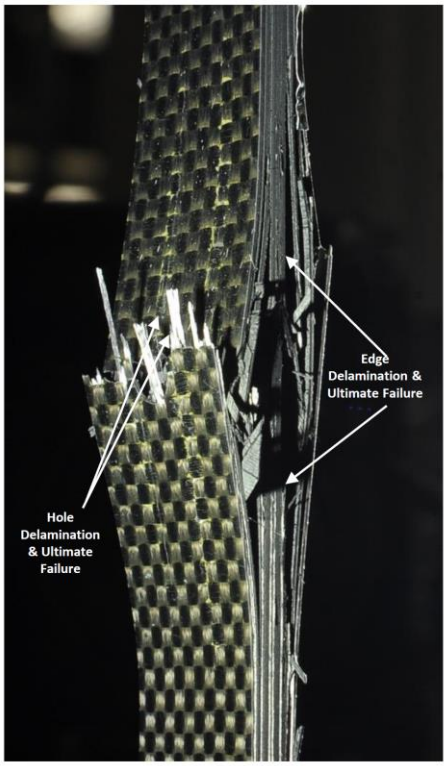

Figure 7.162 Damage (26.24%) & Ultimate Failure at 111447 Cycles, Test

Figures 7.163 through 7.165 show the combined plots of % Compliance change Vs. Cycles for the AWJ trimmed and CVD endmill trimmed specimens.

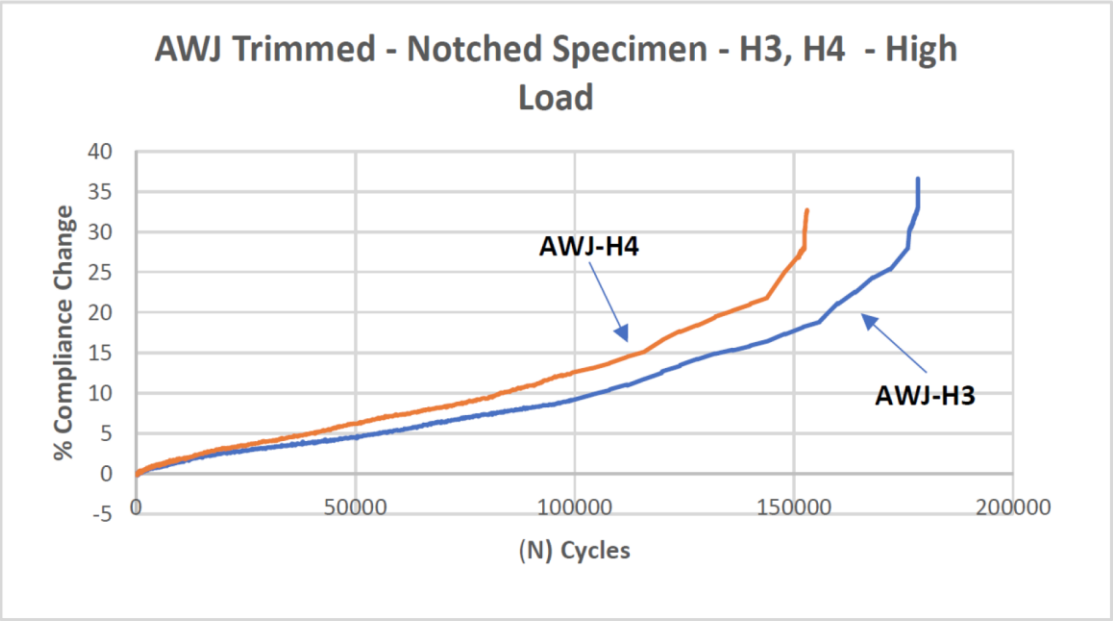

Figure 7.163 Summary Plot of % Compliance Change Vs. (N) Cycles for AWJ Trimmed Test Specimens – High Load

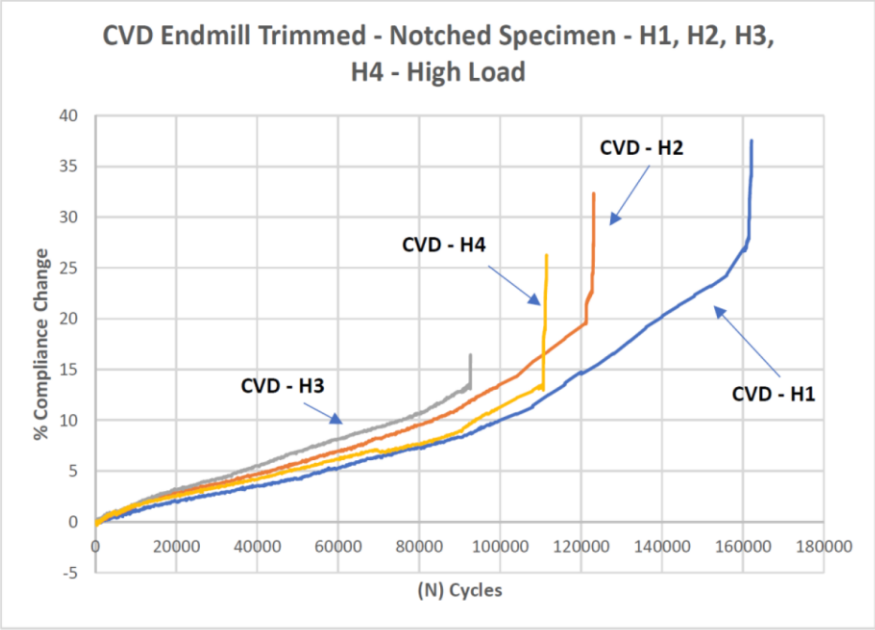

Figure 7.164 Summary Plot of % Compliance Change Vs. (N) Cycles for CVD Endmill Trimmed Test Specimens – High Load

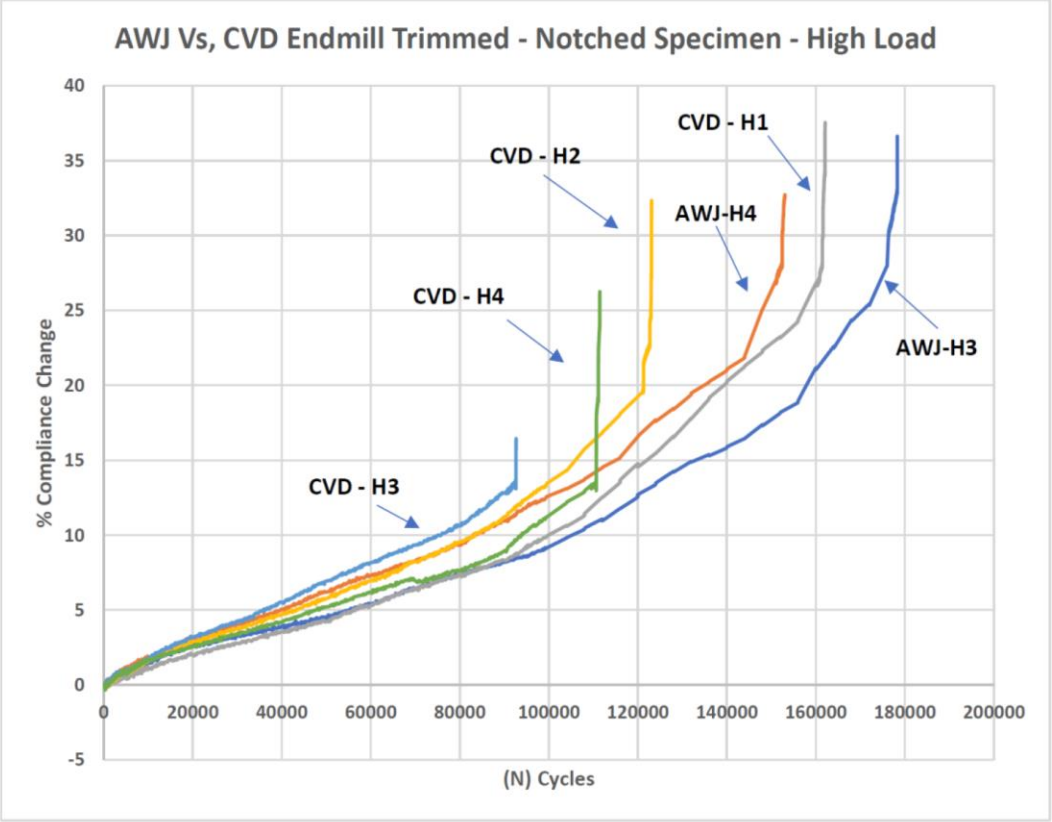

Figure 7.165 Summary of AWJ Vs. CVD Endmill Trimmed Plots of % Compliance Change Vs. (N) Cycles Test Specimens – High Load

Surface Finish Stress Concentration Factor $\left(\bar{K}_t\right)$

Surface finish profiles of all high load test specimens were used to calculate the stress concentration factor $\left(\bar{K}_t\right)$ using the formula shown in figure 7.36

Figures 7.166 through 7.170 Show the stress concentration factor determination graphically for the radius and using the formula from Figure 7.36

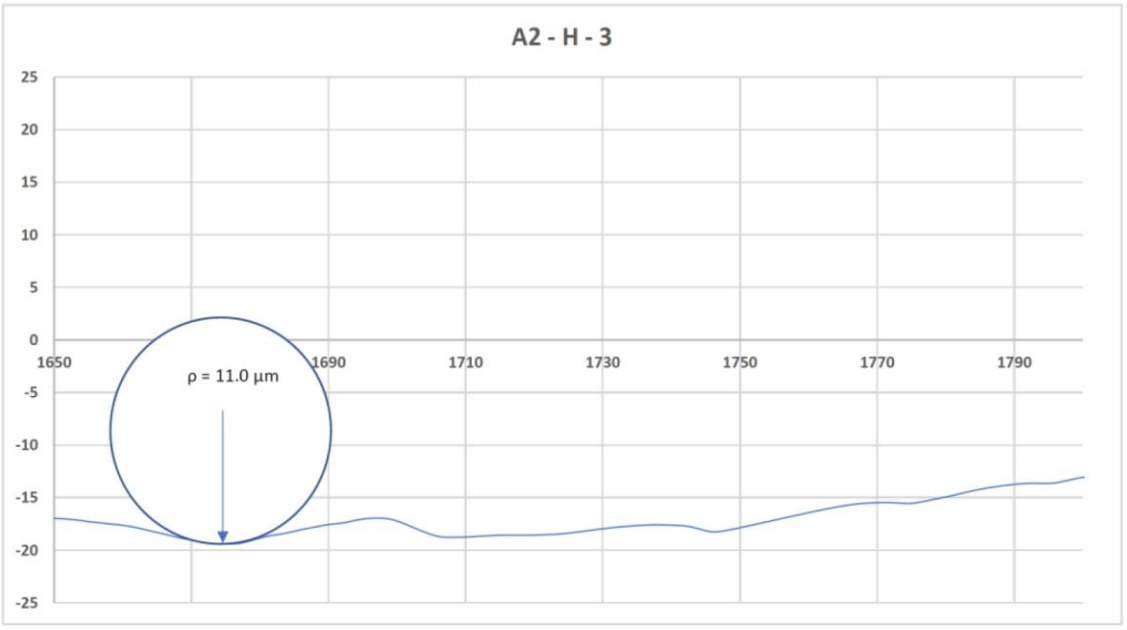

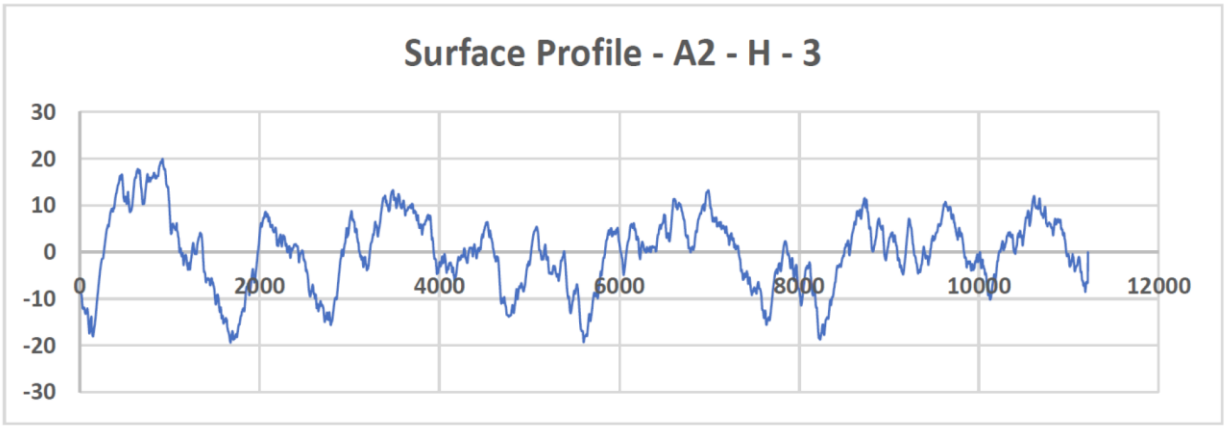

Figure 7.166 Graphical Determination of radius (ρ) from surface profile of specimen A2 – H – 3

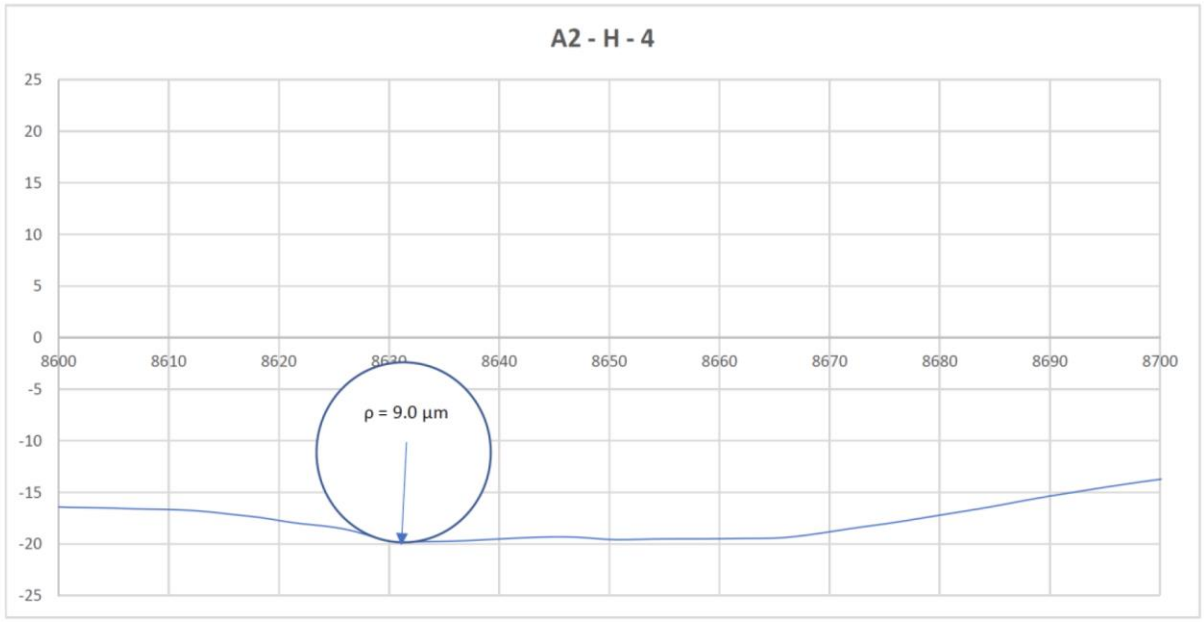

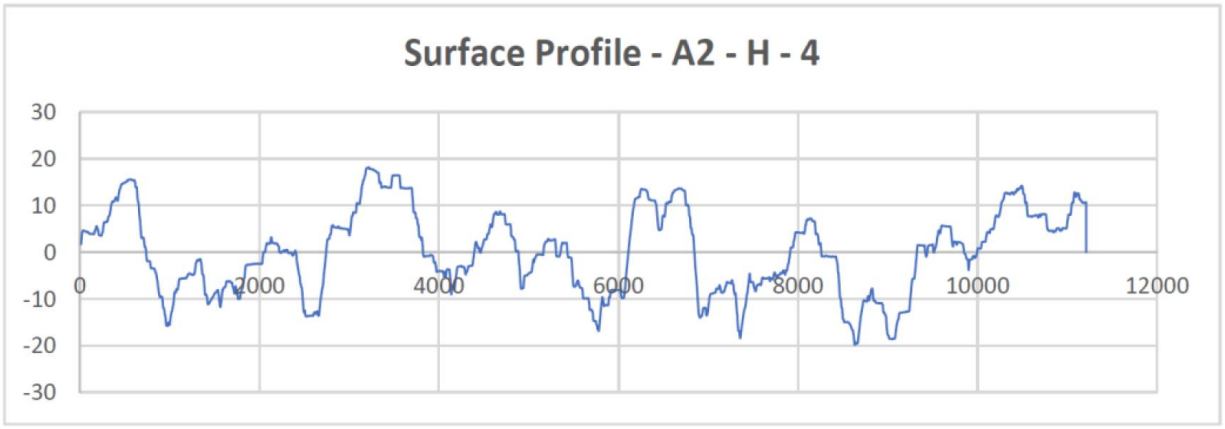

Figure 7.167 Graphical Determination of radius (ρ) from surface profile of specimen A2 – H – 4

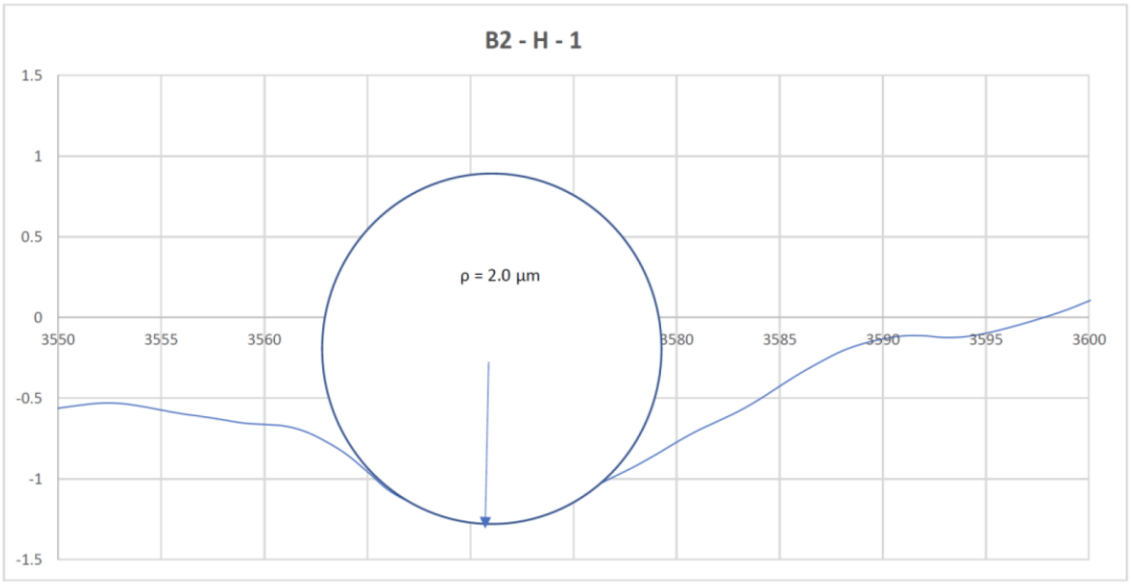

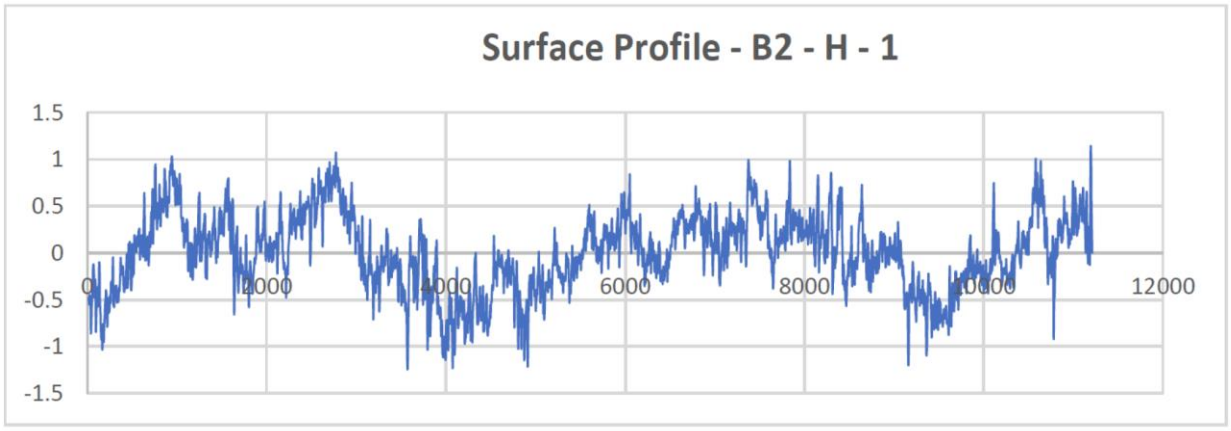

Figure 7.168 Graphical Determination of radius (ρ) from surface profile of specimen B2 – H – 1

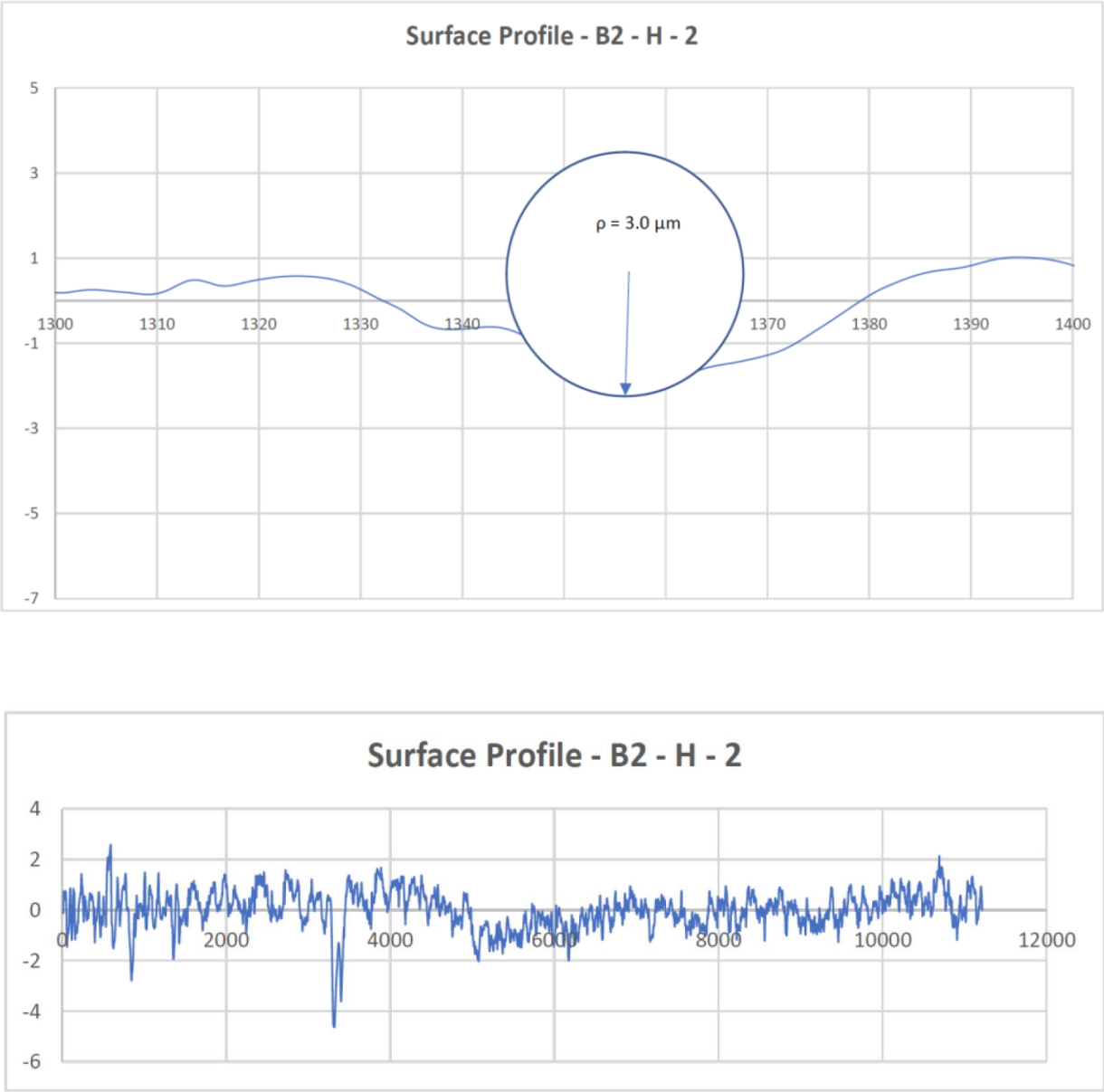

Figure 7.169 Graphical Determination of radius (ρ) from surface profile of specimen B2 – H – 2

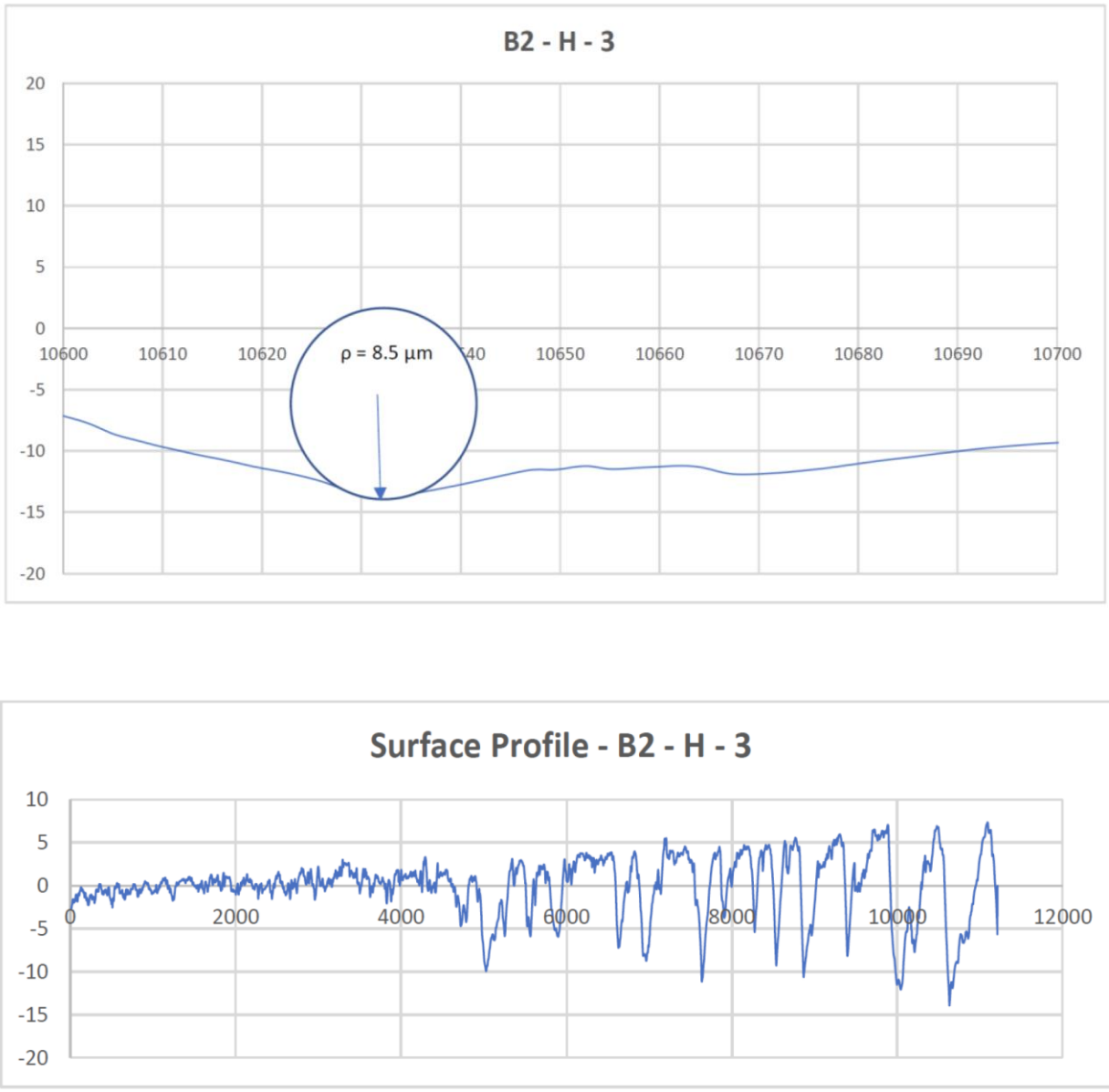

Figure 7.170 Graphical Determination of radius (ρ) from surface profile of specimen B2 – H – 3

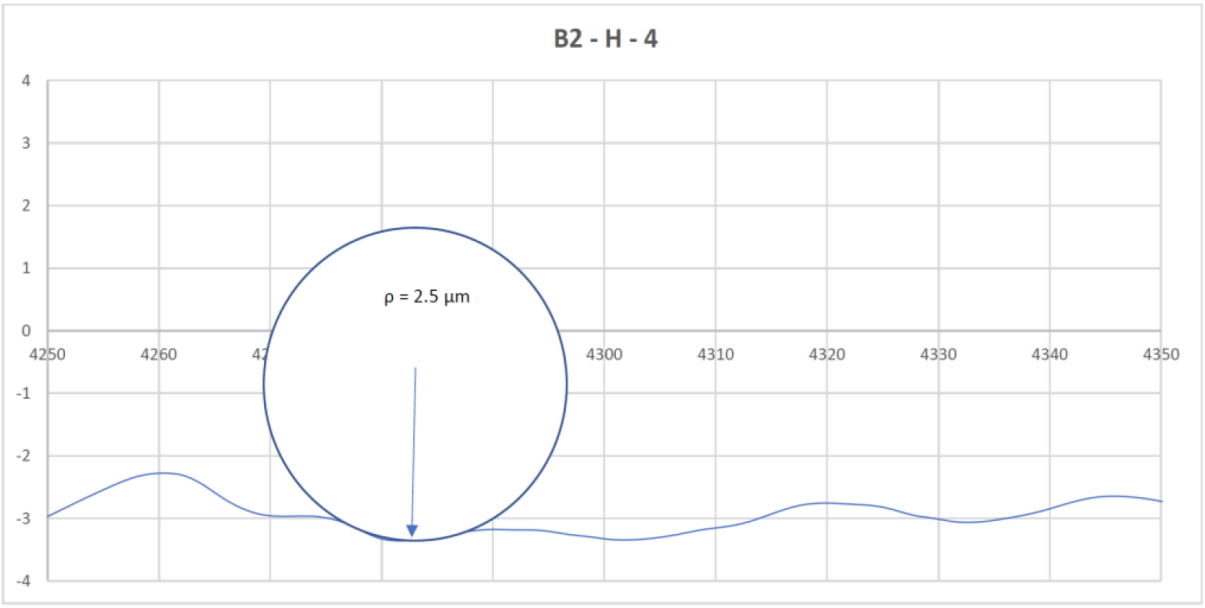

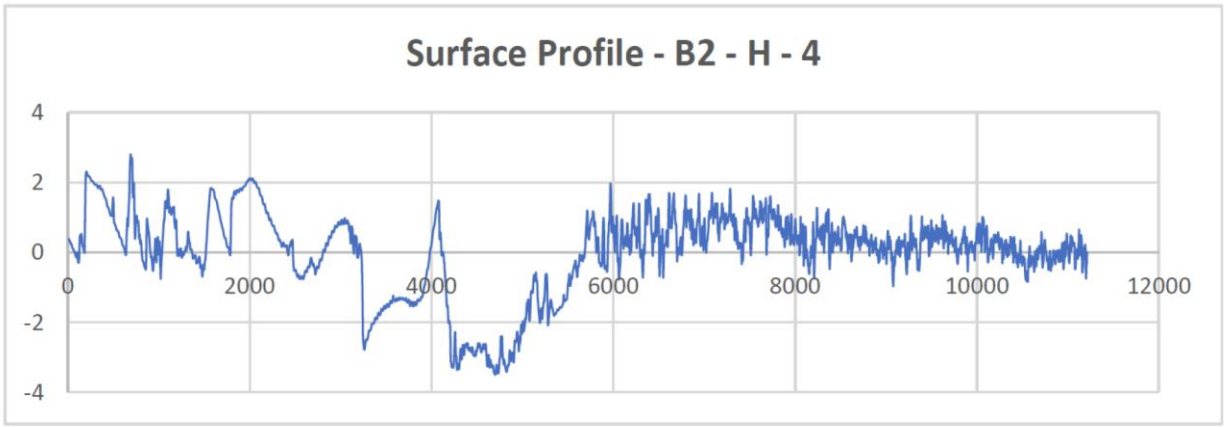

Figure 7.171 Graphical Determination of radius (ρ) from surface profile of specimen B2 – H – 4

Table 7.16 shows the calculates surface integrity stress concentration factor for Notched specimens high load testing.

Specimen Name	Surface Integrity Stress Concentration Factor
A2 – H - 3	1.89
A2 – H - 4	2.1
B2 – H - 1	1.2
B2 – H - 2	1.56
B2 – H - 3	1.74
B2 – H - 4	1.64

Table 7.16 Calculated Surface Integrity Stress Concentration Factor for Notched Specimens – High Load Testing

Observation on Surface finish Data Vs. Fatigue Cycles – Surface finish data in the longitudinal direction was plotted against fatigue cycles and reviewed comparing AWJ trimmed specimens to CVD Diamond Coated Endmill Trimmed specimens. Figures 7.172 through 7.185 show the variation of surface finish parameters Vs. fatigue cycles for the different parameters.

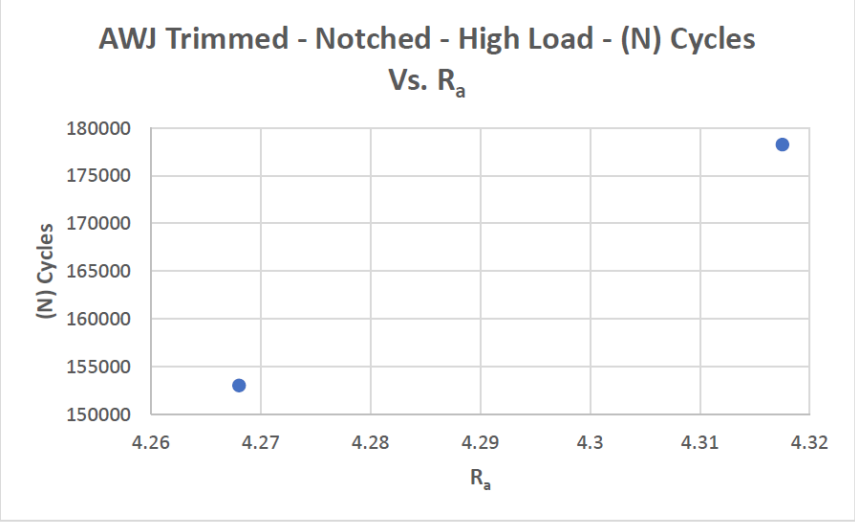

Figure 7.172 Surface Finish - R_a (longitudinal) Vs. Fatigue Cycles – AWJ Trimmed – Notched High Load Specimens

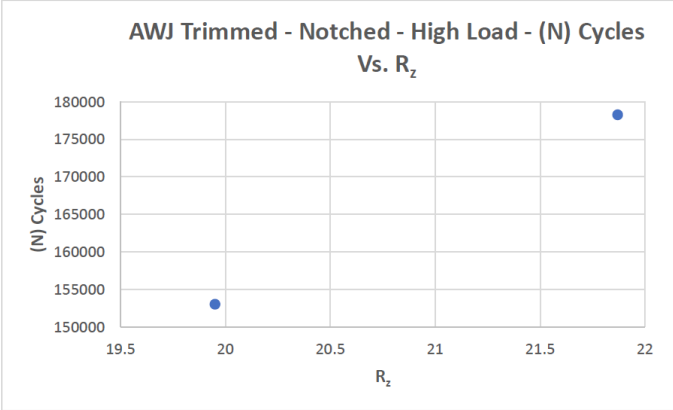

Figure 7.173 Surface Finish – R_z (longitudinal) Vs. Fatigue Cycles – AWJ Trimmed - Notched – High Load Test Specimens

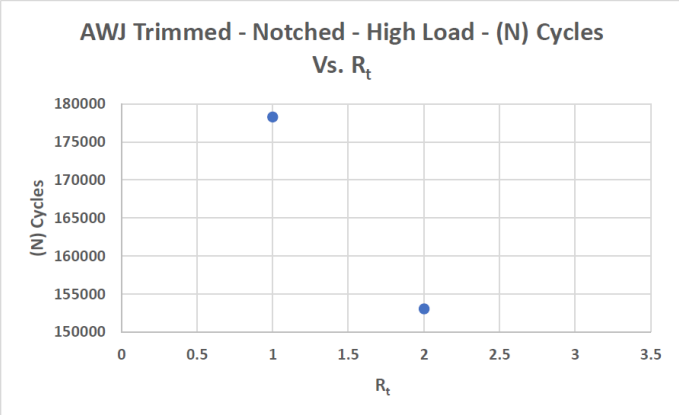

Figure 7.174 Surface Finish – R_t (longitudinal) Vs. Fatigue Cycles – AWJ trimmed – Notched - High Load Test Specimens

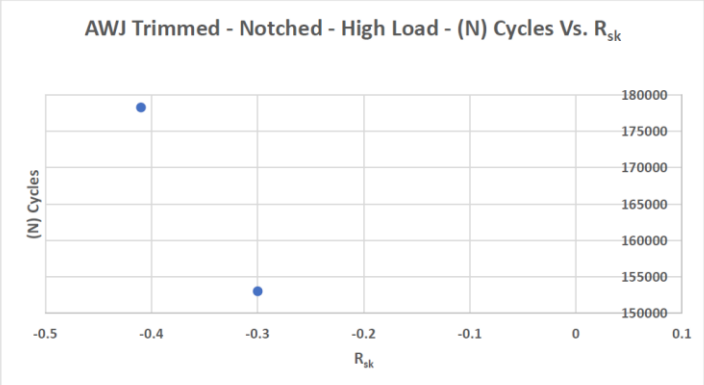

Figure 7.175 Surface Finish – R_{sk} (longitudinal) Vs. Fatigue Cycles – AWJ Trimmed – Notched High Load Test Specimens

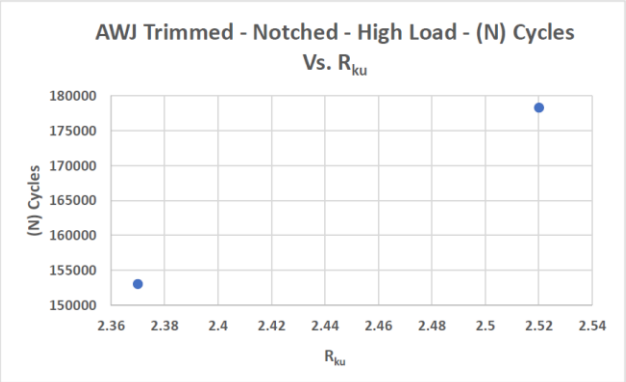

Figure 7.176 Surface Finish – R_{ku} (longitudinal) Vs. Fatigue Cycles – AWJ Trimmed – Notched High Load Test Specimens

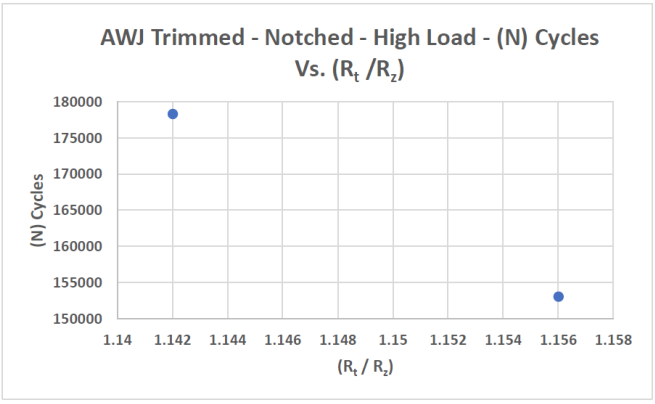

Figure 7.177 Surface Finish – (R_t/R_z) (Longitudinal) Vs. Fatigue Cycles – AWJ Trimmed – Notched High Load Test Specimens

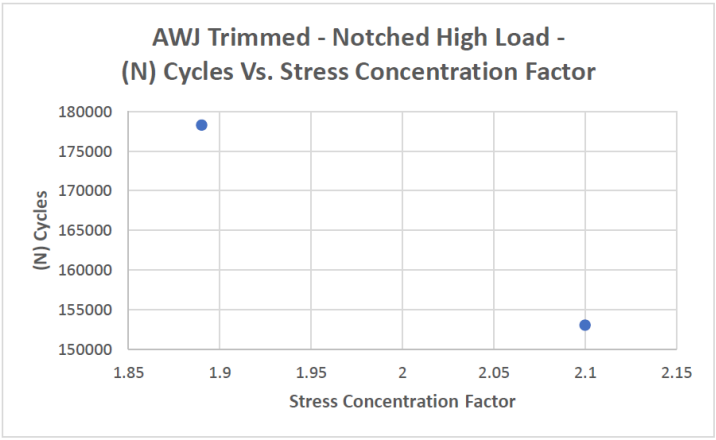

Figure 7.178 Surface Integrity Stress Concentration Factor (Longitudinal) Vs. Fatigue Cycles – AWJ Trimmed - Notched High Load Test Specimens

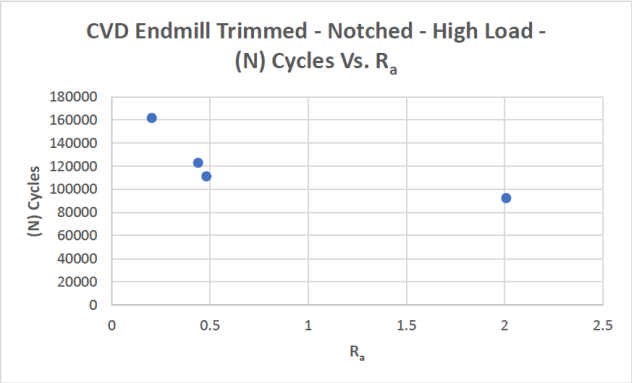

Figure 7.179 Surface Finish - R_a (longitudinal) Vs. Fatigue Cycles – CVD Endmill Trimmed – Notched High Load Specimens

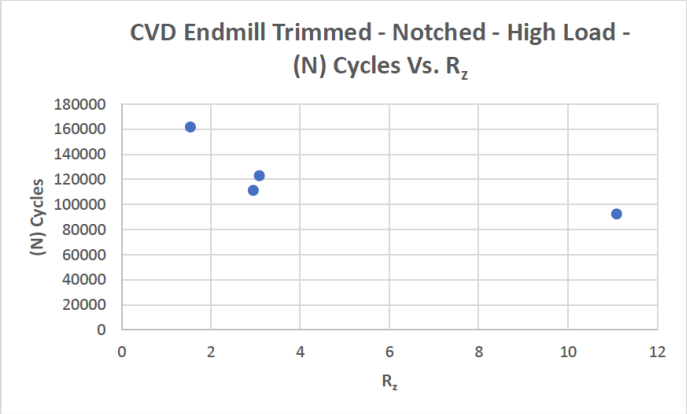

Figure 7.180 Surface Finish – R_z (longitudinal) Vs. Fatigue Cycles – CVD Endmill Trimmed - Notched – High Load Test Specimens

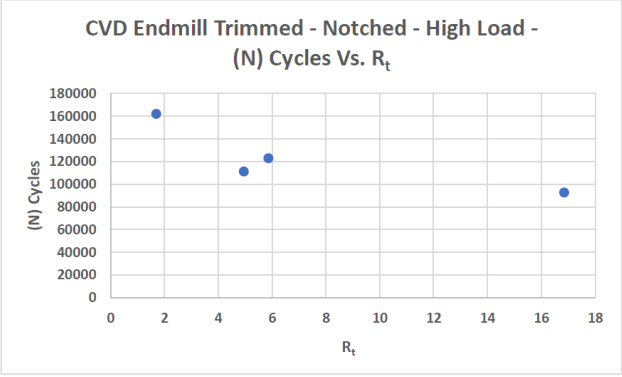

Figure 7.181 Surface Finish – R_t (longitudinal) Vs. Fatigue Cycles – CVD Endmill trimmed – Notched - High Load Test Specimens

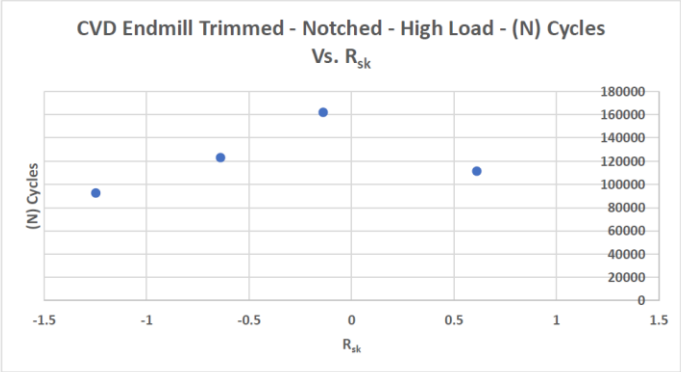

Figure 7.182 Surface Finish – R_{sk} (longitudinal) Vs. Fatigue Cycles – CVD Endmill Trimmed – Notched High Load Test Specimens

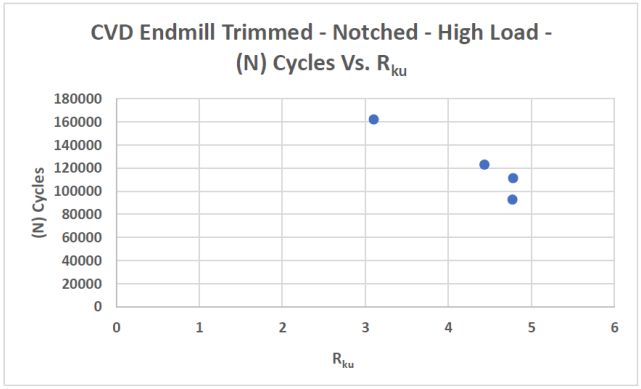

Figure 7.183 Surface Finish – R_{ku} (longitudinal) Vs. Fatigue Cycles – CVD Endmill Trimmed – Notched High Load Test Specimens

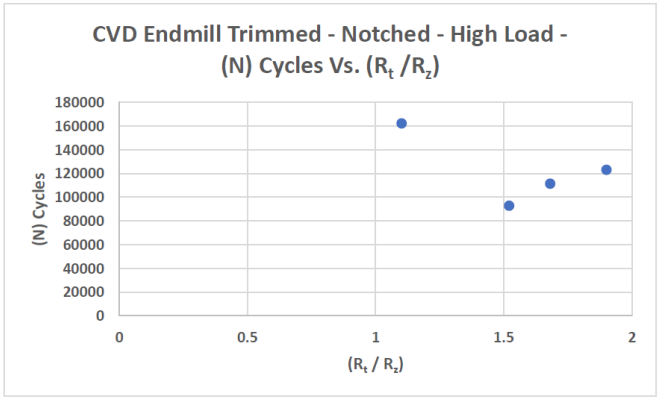

Figure 7.184 Surface Finish – (R_t/R_z) (Longitudinal) Vs. Fatigue Cycles – CVD Endmill Trimmed – Notched High Load Test Specimens

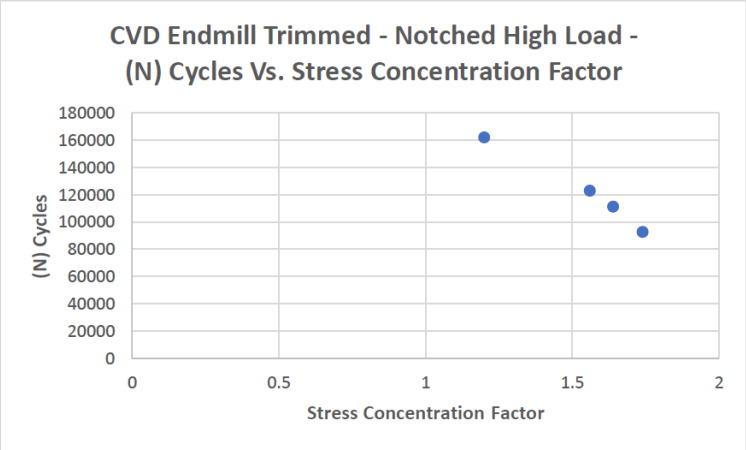

Figure 7.185 Surface Integrity Stress Concentration Factor (Longitudinal) Vs. Fatigue Cycles – CVD Endmill Trimmed - Notched High Load Test Specimens

It was observed that in the case of AWJ trimmed specimens, the better surface finish in the transverse direction contributed to higher fatigue cycles to failure. In the case of CVD Diamond Coated Endmill trimmed specimens, the specimens with better surface finish in the longitudinal direction had higher fatigue cycles to failure. Also observed was that for high loading conditions, the fatigue cycles generally were higher with improved surface finish data. In the case of specimen, B2 – H – 3, the rougher surface finish resulted in larger peaks and valleys in terms of both amplitude and frequency thus providing additional sites for damage initiation and propagation as evidenced by total delamination at edges and through the hole resulting in ultimate failure at lower fatigue cycles.

7.4.2.2 Medium Load Test Specimen Data Review

For the medium load test specimens, the following specimens were tested for AWJ trimmed specimens.

A2 – M – 1

A2 – M – 2

A2 – M – 3

A2 – M - 4

For CVD Diamond Coated Endmill Trimmed specimens, the following samples were tested.

B2 – M – 1

B2 – M – 2

B2 – M – 3

Prior to testing the following surface finish parameters were recorded for each sample in both longitudinal and transverse directions

R_a , R_z , R_t , R_{sk} , R_{ku}

Table 7.17 shows the fatigue cycles to failure for each of the medium load specimens along with the load applied and stress as well as % change in compliance.

Tables 7.4 and 7.5 documented earlier in this chapter show the surface finish data documented in the longitudinal and transverse direction.

Specimen Name	Trim	Hole	Fatigue Cycles	Test Load (Max) (N)	Test Load (Min) (N)	Max Stress (Mpa)	Test Frequency	Compliance
A2-M-1	AWJ -80	CVD Drill	495512	51155	5115	444.7	7 Hz	39.13%
A2-M-2	AWJ -80	CVD Drill	411828	51155	5115	444.7	7 Hz	32.54%
A2-M-3	AWJ -80	CVD Drill	370163	51155	5115	444.7	7 Hz	37.75%
A2-M-4	AWJ -80	CVD Drill	210389	51155	5115	444.7	7 Hz	26.86%
B2-M-1	CVD Endmill	CVD Drill	377675	51155	5115	444.7	7 Hz	40.00%
B2-M-2	CVD Endmill	CVD Drill	436382	51155	5115	444.7	7 Hz	51.05%
B2-M-3	CVD Endmill	CVD Drill	540315	51155	5115	444.7	7 Hz	43.04%

Table 7.17 Fatigue Cycles/Loads/Stress & % Compliance Change for Notched Medium Loading Testing

Damage Propagation in AWJ trimmed specimens- To compare the damage propagation % compliance change was plotted for each AWJ medium load specimen and the percentage damage at 300K cycles or 200K cycles for lower fatigue failures was compared. Figures 7.186 through 7.197 show the % compliance change for each medium load AWJ test specimen along with a photo micrograph depicting the damage at 300K or 200K cycles.

In all cases damage started as matrix cracking followed by matrix fibre interface debonding and then delamination as shown in the figures. The initiation of damage was localized at the 45 degree plies (also the sites of fibre pullouts). These sites were both at the edges as well as in the hole. Once damage started progressing, ultimate failure occurred due to delamination in the edges and through the hole.

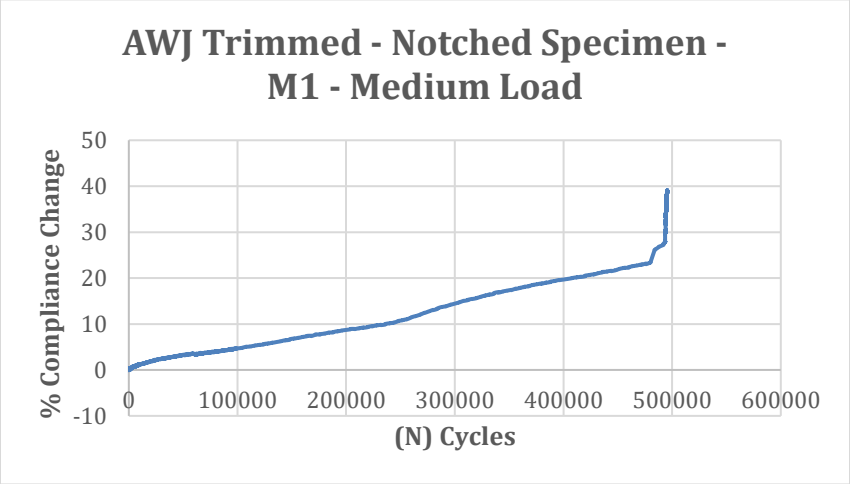

Figure 7.186 Percent Compliance Change Vs. Fatigue Cycles for A2 – M – 1

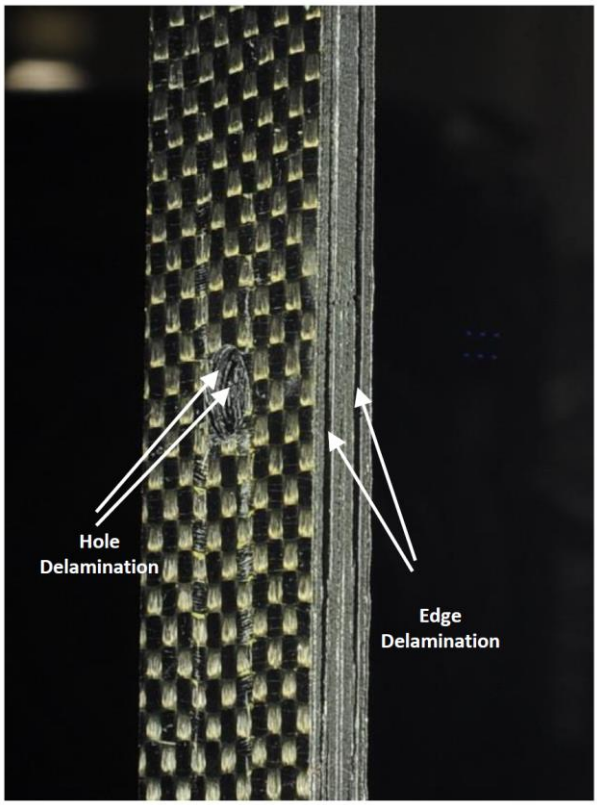

Figure 7.187 Damage at 300K Cycles, 14.47%, Test Specimen A2 – M - 1

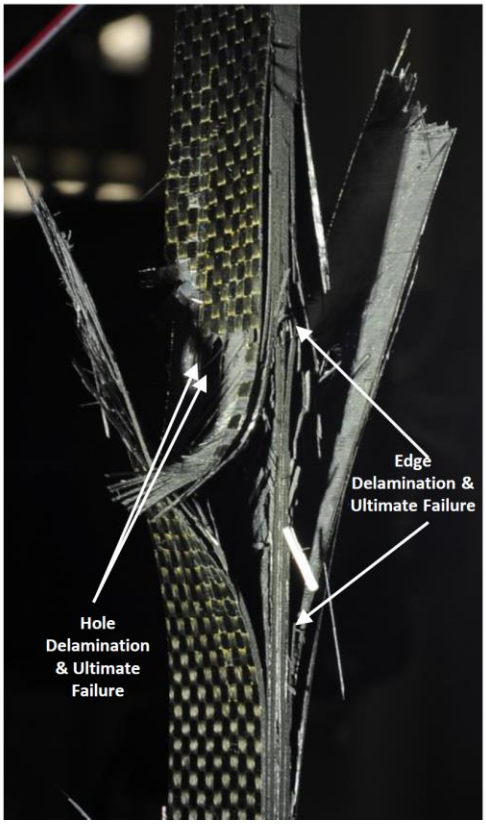

Figure 7.188 Damage (39.13%) & Ultimate Failure at 495512 Cycles, Test Specimen A2 – M - 1

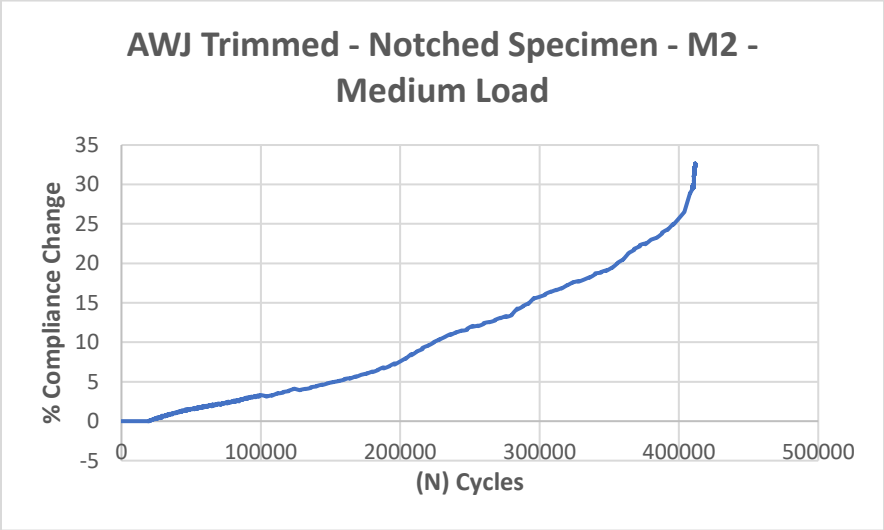

Figure 7.189 Percent Compliance Change Vs. Fatigue Cycles for A2 – M – 2

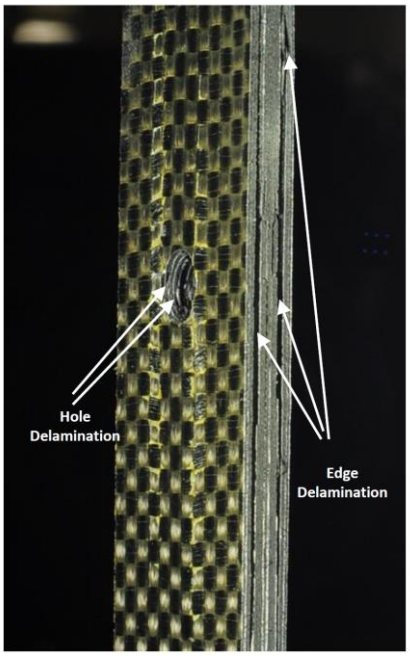

Figure 7.190 Damage at 300K Cycles, 15.83%, Test Specimen A2 – M - 2

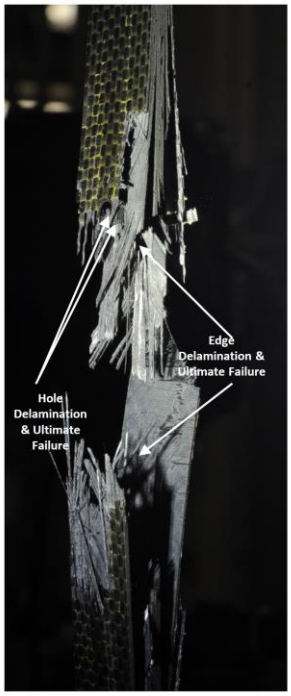

Figure 7.191 Damage (32.54%) & Ultimate Failure at 411828 Cycles, Test Specimen A2 – M - 2

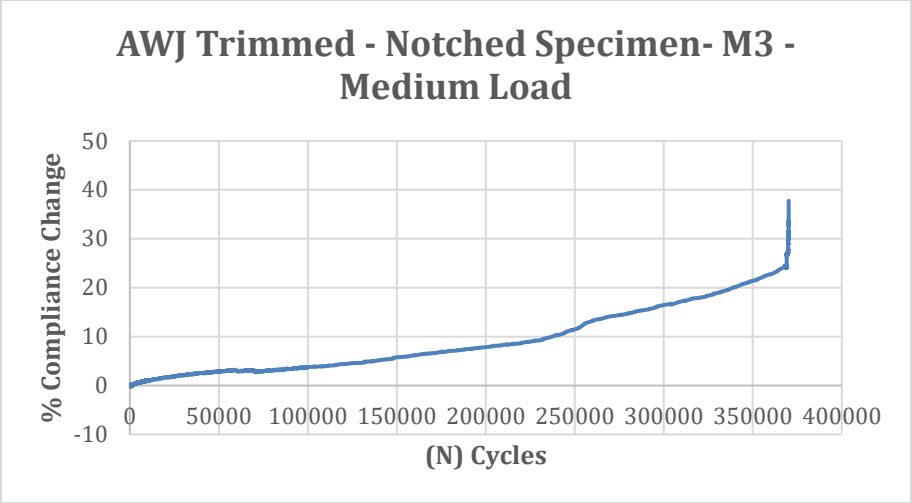

Figure 7.192 Percent Compliance Change Vs. Fatigue Cycles for A2 – M – 3

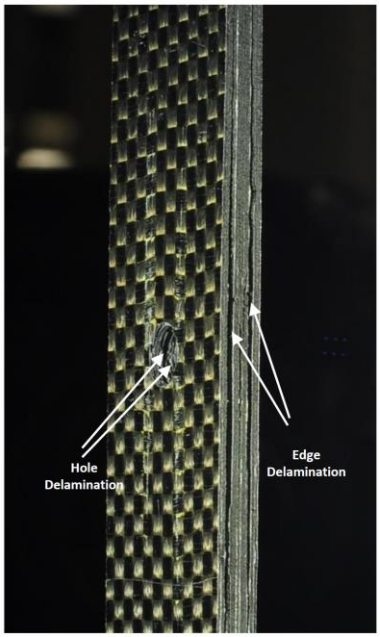

Figure 7.193 Damage at 300K Cycles, 16.24%, Test Specimen A2 – M - 3

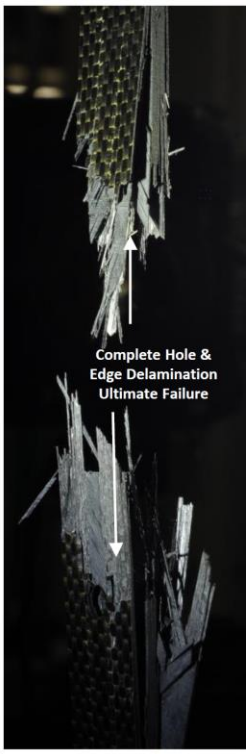

Figure 7.194 Damage (37.75%) & Ultimate Failure at 370163 Cycles, Test Specimen A2 – M - 3

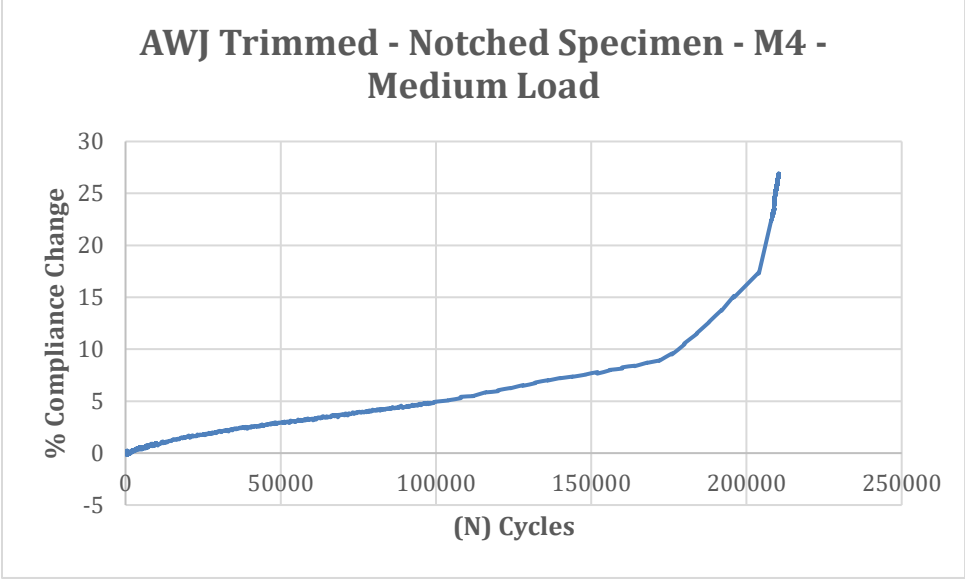

Figure 7.195 Percent Compliance Change Vs. Fatigue Cycles for A2 – M – 4

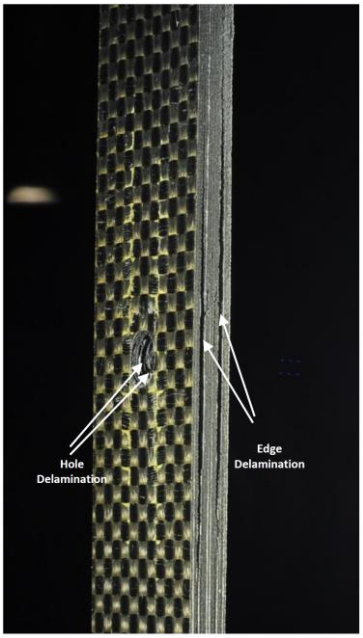

Figure 7.196 Damage at 200K Cycles, 16.39%, Test Specimen A2 – M - 4

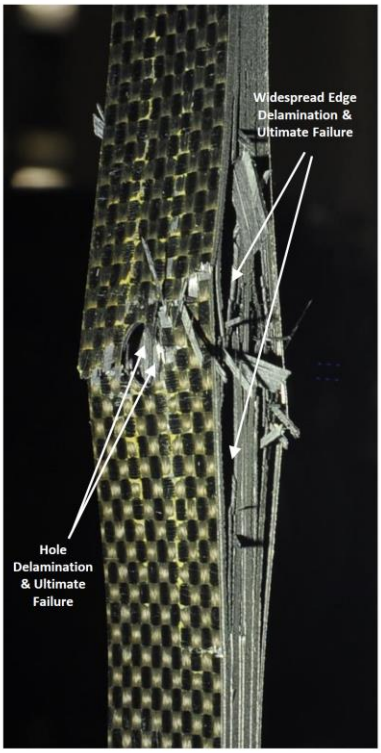

Figure 7.197 Damage (26.86%) & Ultimate Failure at 210389 Cycles, Test Specimen A2–M- 4

Damage Propagation in CVD Diamond Coated Endmill trimmed specimens- To compare the damage propagation % compliance change was plotted for each CVD Diamond Coated Endmill trimmed medium load specimen and the percentage damage at 300K cycles was compared. Figures 7.198 through 7.206 show the % compliance change for each medium load CVD endmill trimmed test specimen along with a photo micrograph depicting the damage at 300K cycles. In all cases damage started as matrix cracking followed by matrix fibre interface debonding and then delamination as shown in the figures. The initiation of damage was localized at the 45 degree plies (also the sites of fibre pullouts). These sites were both at the edges as well as in the hole. Once damage started progressing, ultimate failure occurred due to delamination in the edges and through the hole.

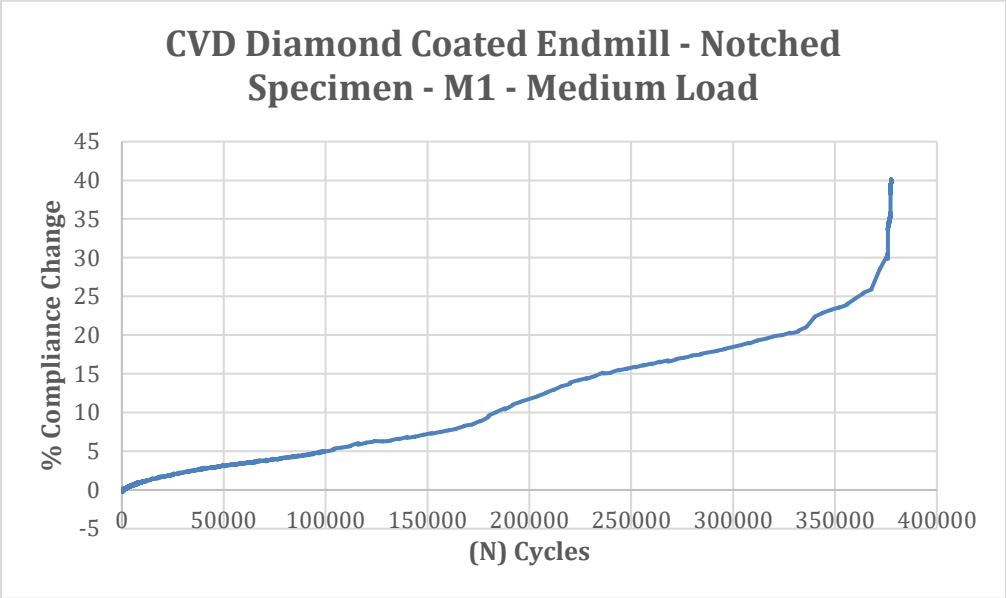

Figure 7.198 Percent Compliance Change Vs. Fatigue Cycles for B2 – M – 1

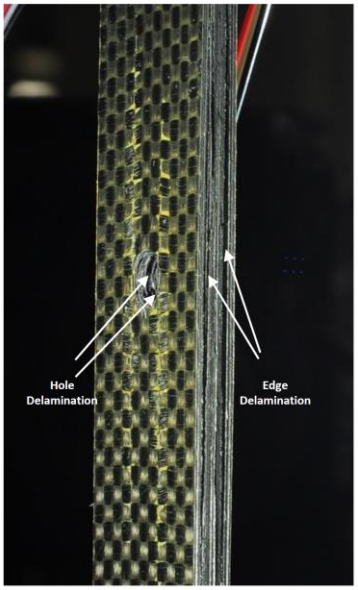

Figure 7.199 Damage at 300K Cycles, 18.49%, Test Specimen B2 – M - 1

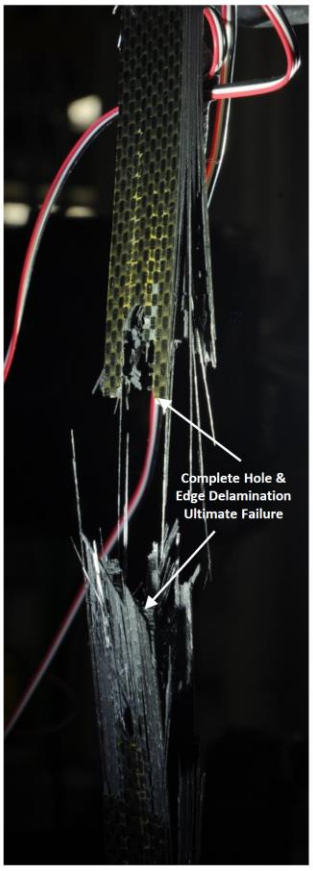

Figure 7.200 Damage (40.0%) & Ultimate Failure at 377675 Cycles, Test Specimen B2 – M - 1

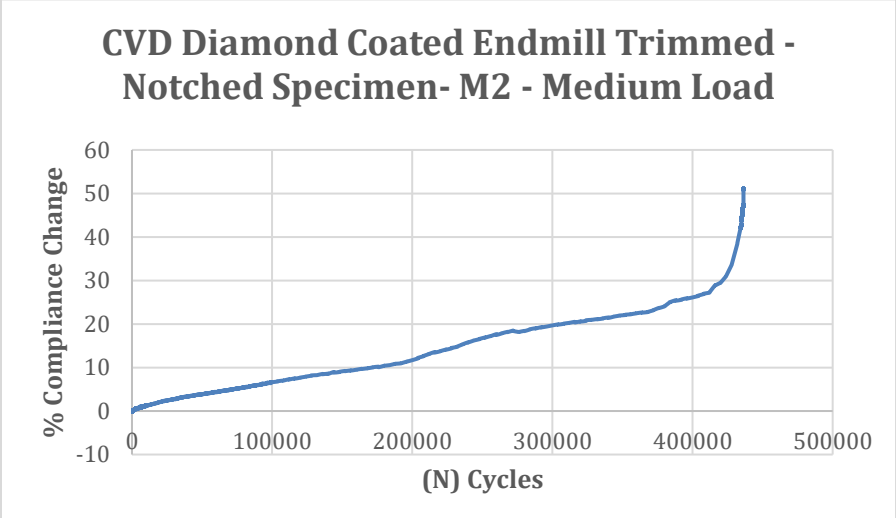

Figure 7.201 Percent Compliance Change Vs. Fatigue Cycles for B2 – M – 2

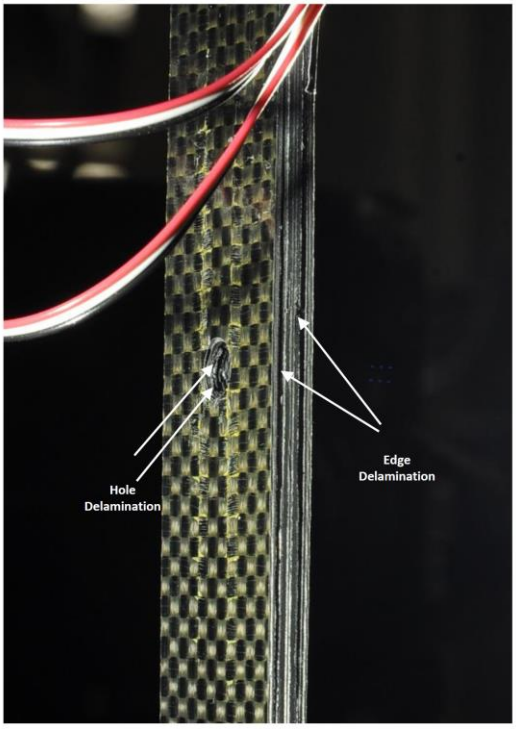

Figure 7.202 Damage at 300K Cycles, 19.71%, Test Specimen B2 – M - 2

Figure 7.203 Damage (51.05%) & Ultimate Failure at 436382 Cycles, Test Specimen B2 – M - 2

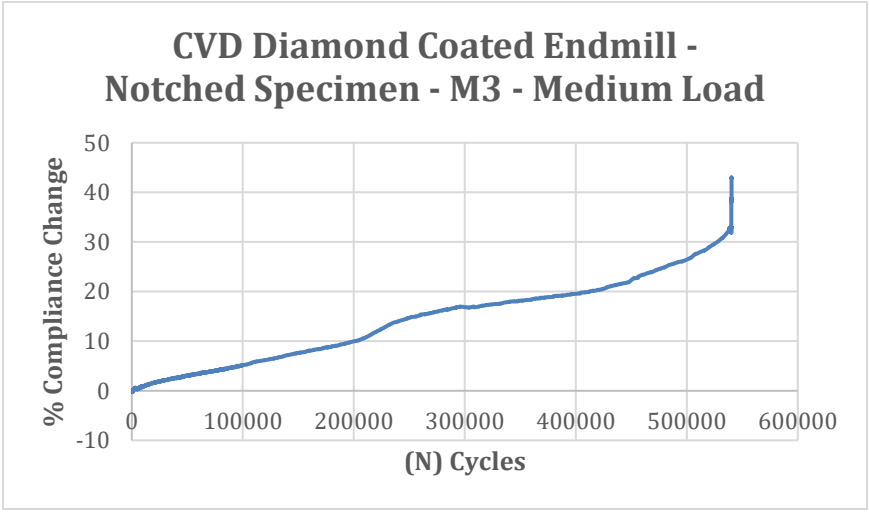

Figure 7.204 Percent Compliance Change Vs. Fatigue Cycles for B2 – M – 3

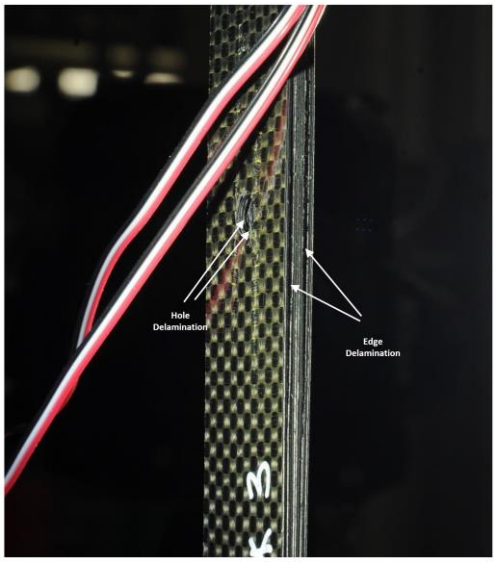

Figure 7.205 Damage at 300K Cycles, 17.07%, Test Specimen B2 – M - 3

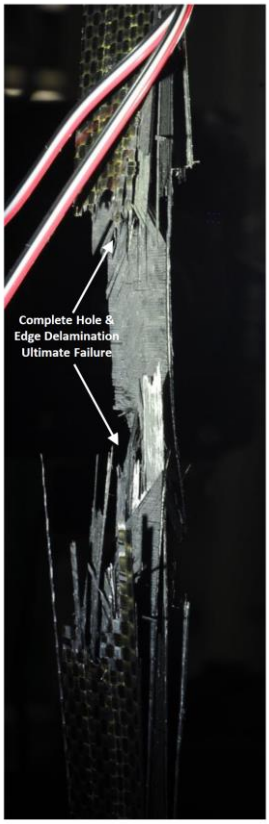

Figure 7.206 Damage (43.04%) & Ultimate Failure at 540315 Cycles, Test Specimen B2 – M - 3

Figure 7.207 through 7.209 show the summary plots of AWJ and CVD Endmill trimmed specimens of % compliance change Vs. (N) cycles.

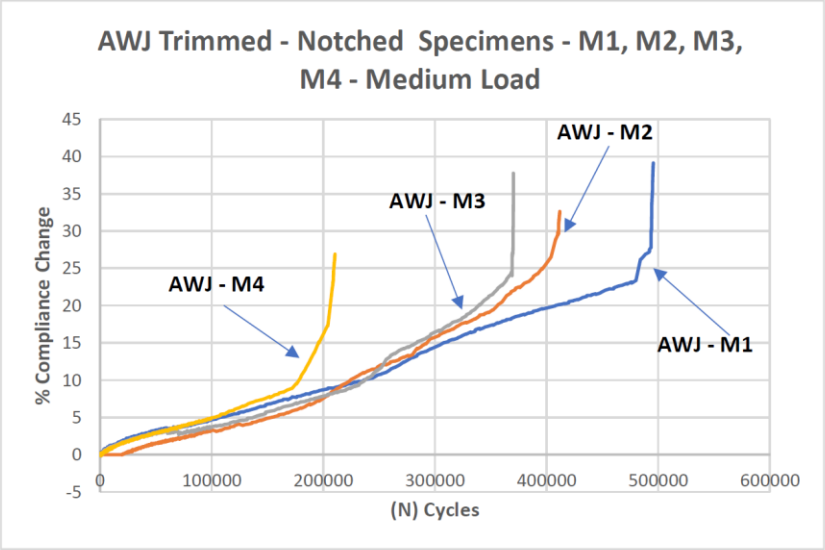

Figure 7.207 Summary Plot of % Compliance Change Vs. (N) Cycles for AWJ Trimmed Notched Specimens – Medium Load

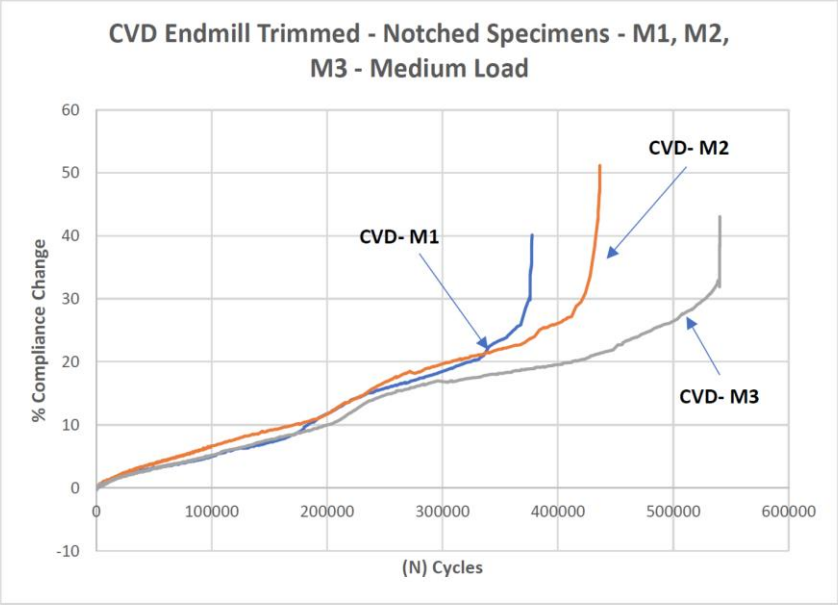

Figure 7.208 Summary Plot of % Compliance Change Vs. (N) Cycles for CVD Endmill Trimmed Notched Specimens – Medium Load

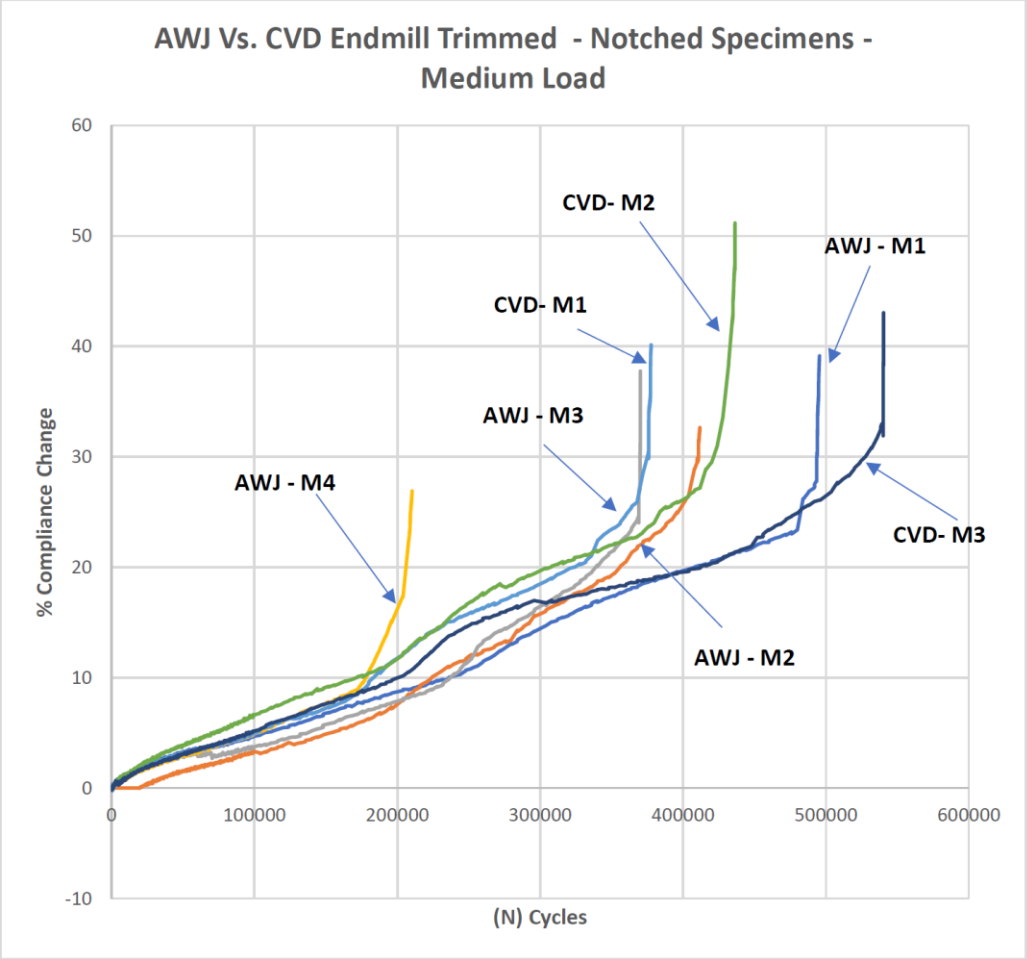

Figure 7.209 Summary Plot of AWJ Vs. CVD Endmill Trimmed of % Compliance Change Vs. (N) Cycles – Notched Specimens – Medium Load

Surface Finish Stress Concentration Factor $\left(\bar{K}_t\right)$

Surface finish profiles of all high load test specimens were used to calculate the stress concentration factor $\left(\bar{K}_t\right)$ using the formula shown in figure 7.36

Figures 7.210 through 7.216 Show the stress concentration factor determination graphically for the radius and using the formula from Figure 7.36

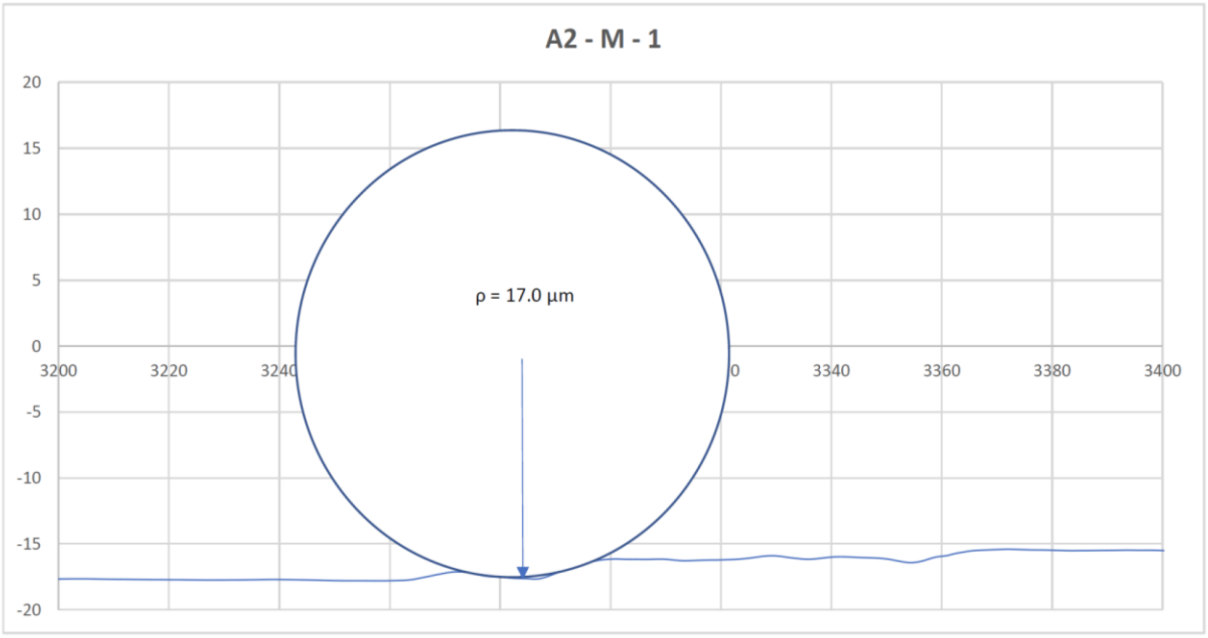

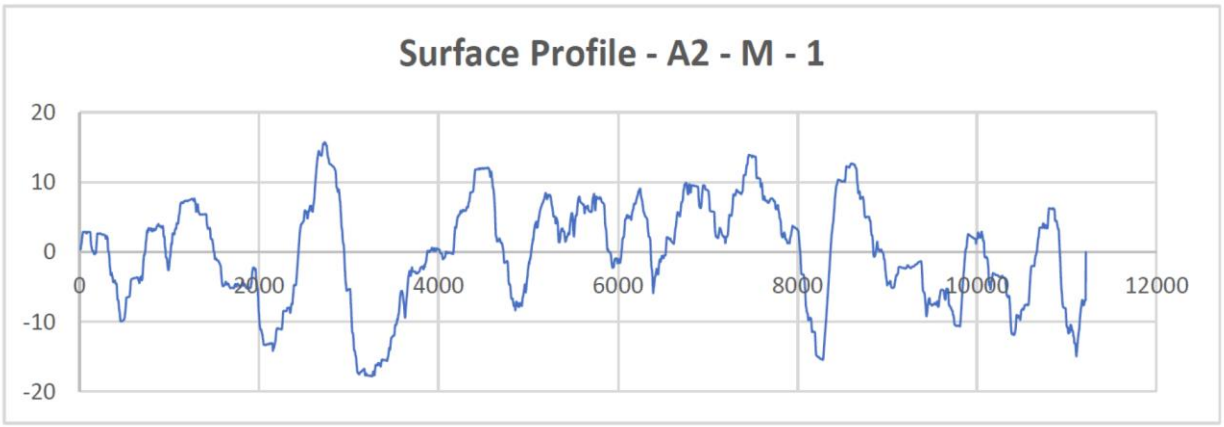

Figure 7.210 Graphical Determination of radius (ρ) from surface profile of specimen A2 – M - 1

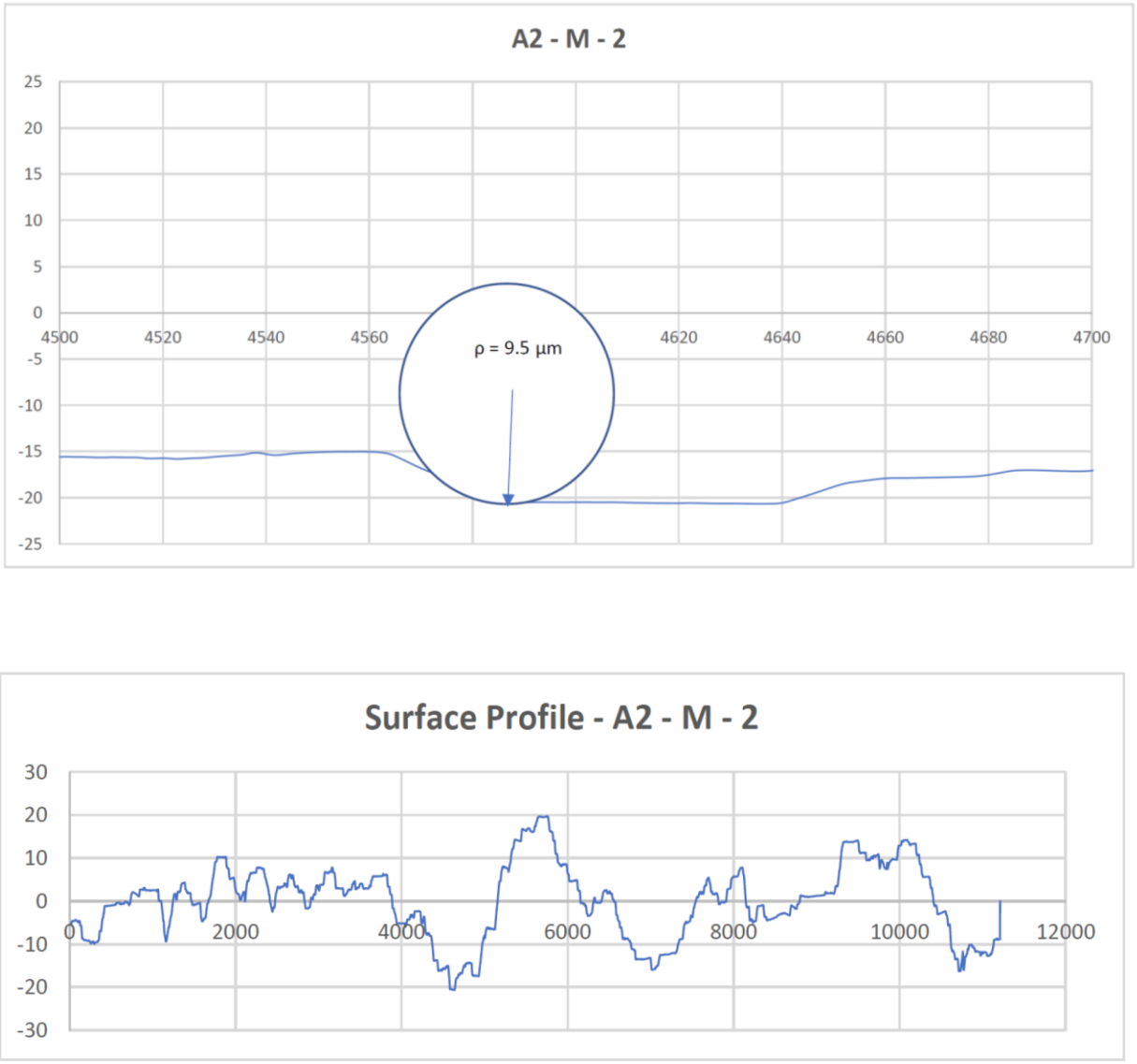

Figure 7.211 Graphical Determination of radius (ρ) from surface profile of specimen A2 – M - 2

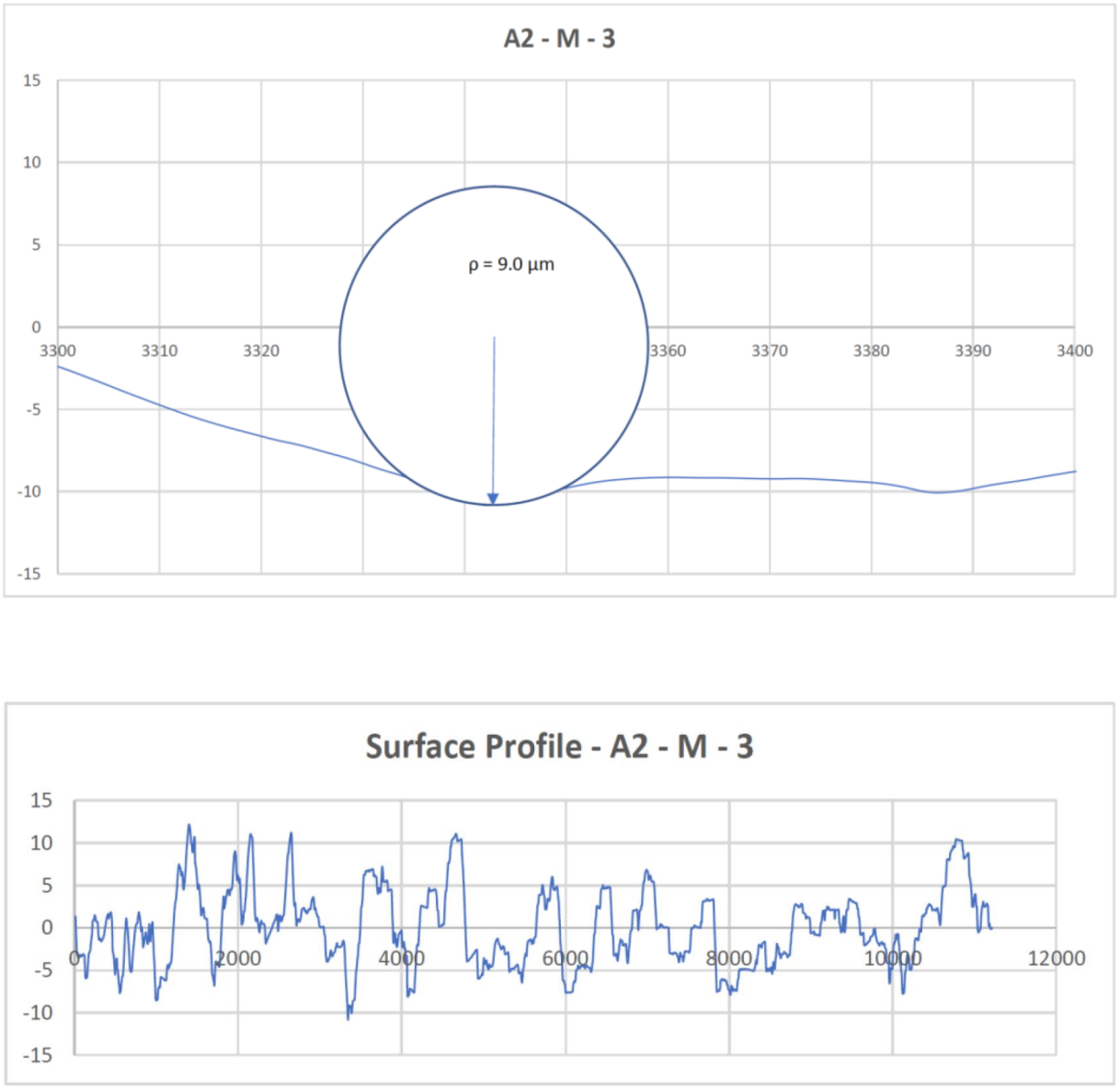

Figure 7.212 Graphical Determination of radius (ρ) from surface profile of specimen A2 – M – 3

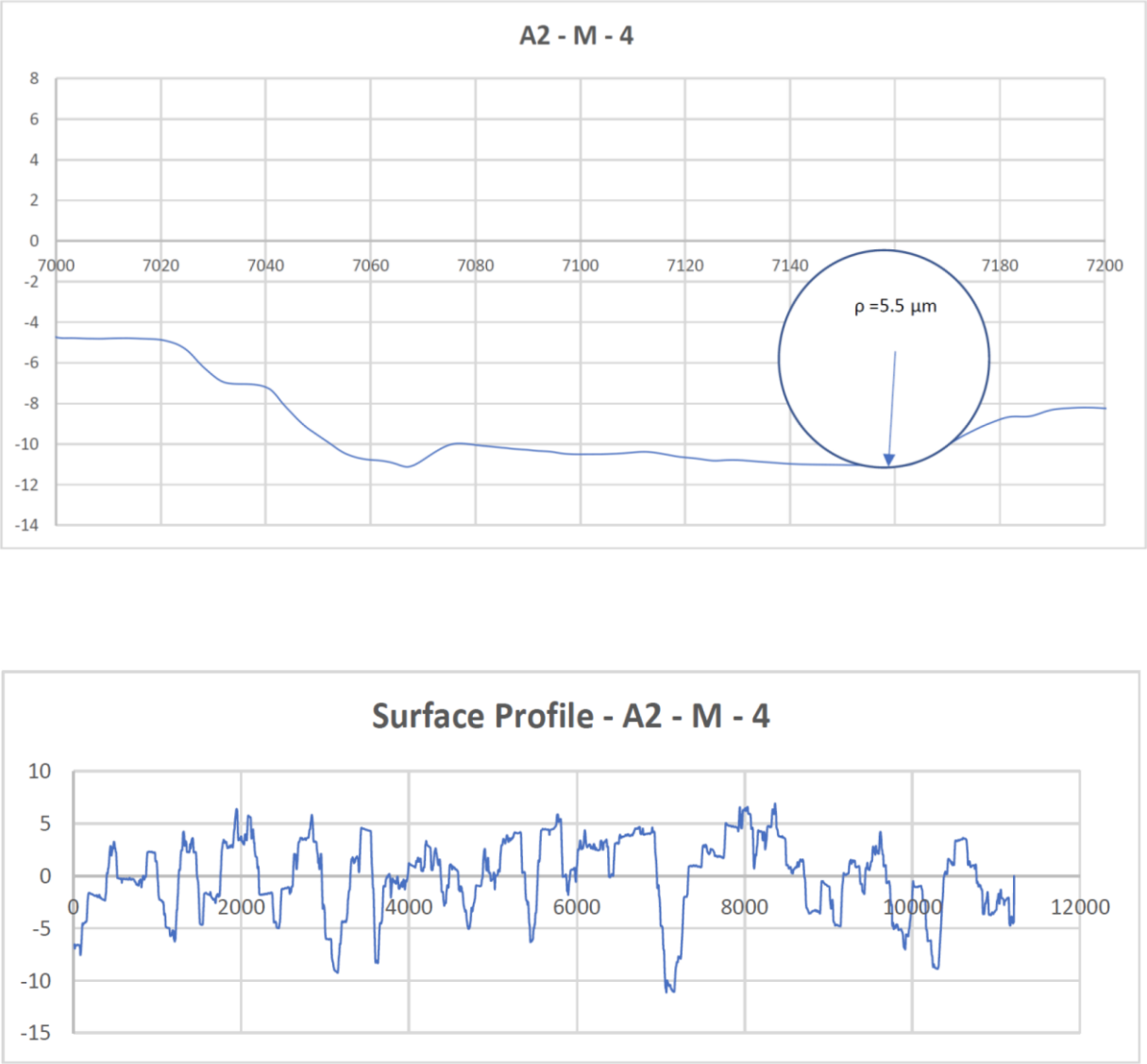

Figure 7.213 Graphical Determination of radius (ρ) from surface profile of specimen A2 – M – 4

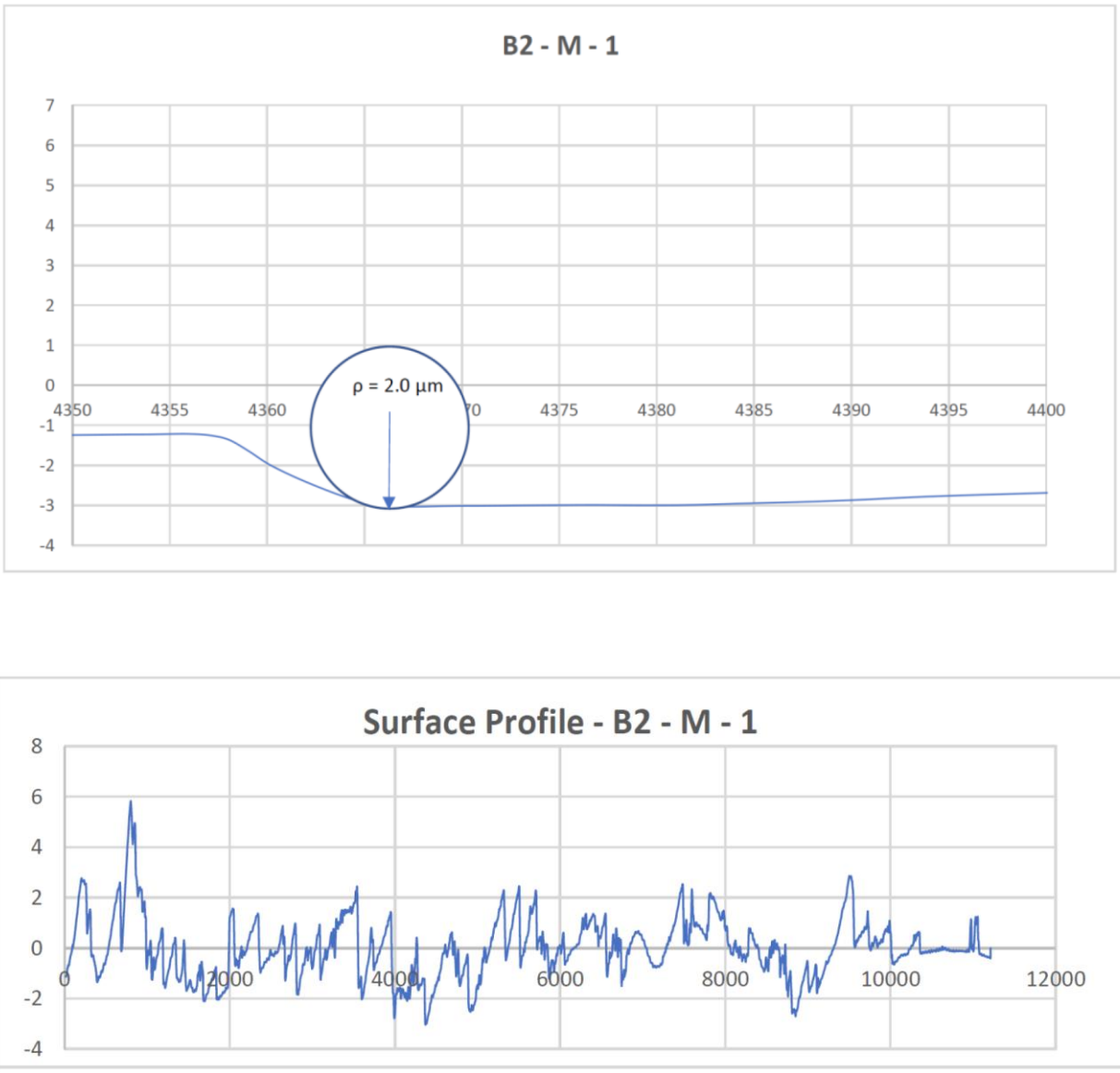

Figure 7.214 Graphical Determination of radius (ρ) from surface profile of specimen B2 – M - 1

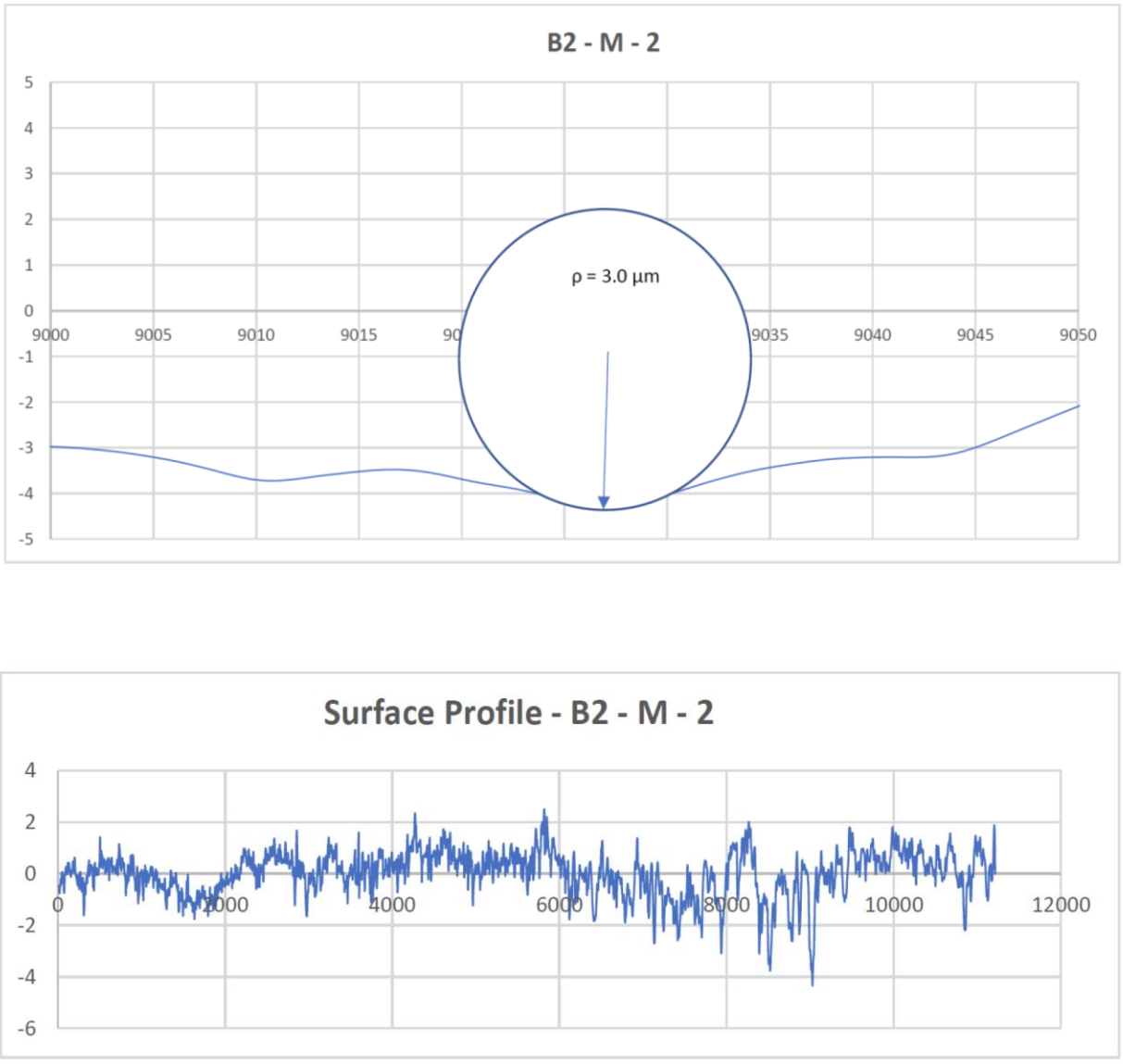

Figure 7.215 Graphical Determination of radius (ρ) from surface profile of specimen B2 – M - 2

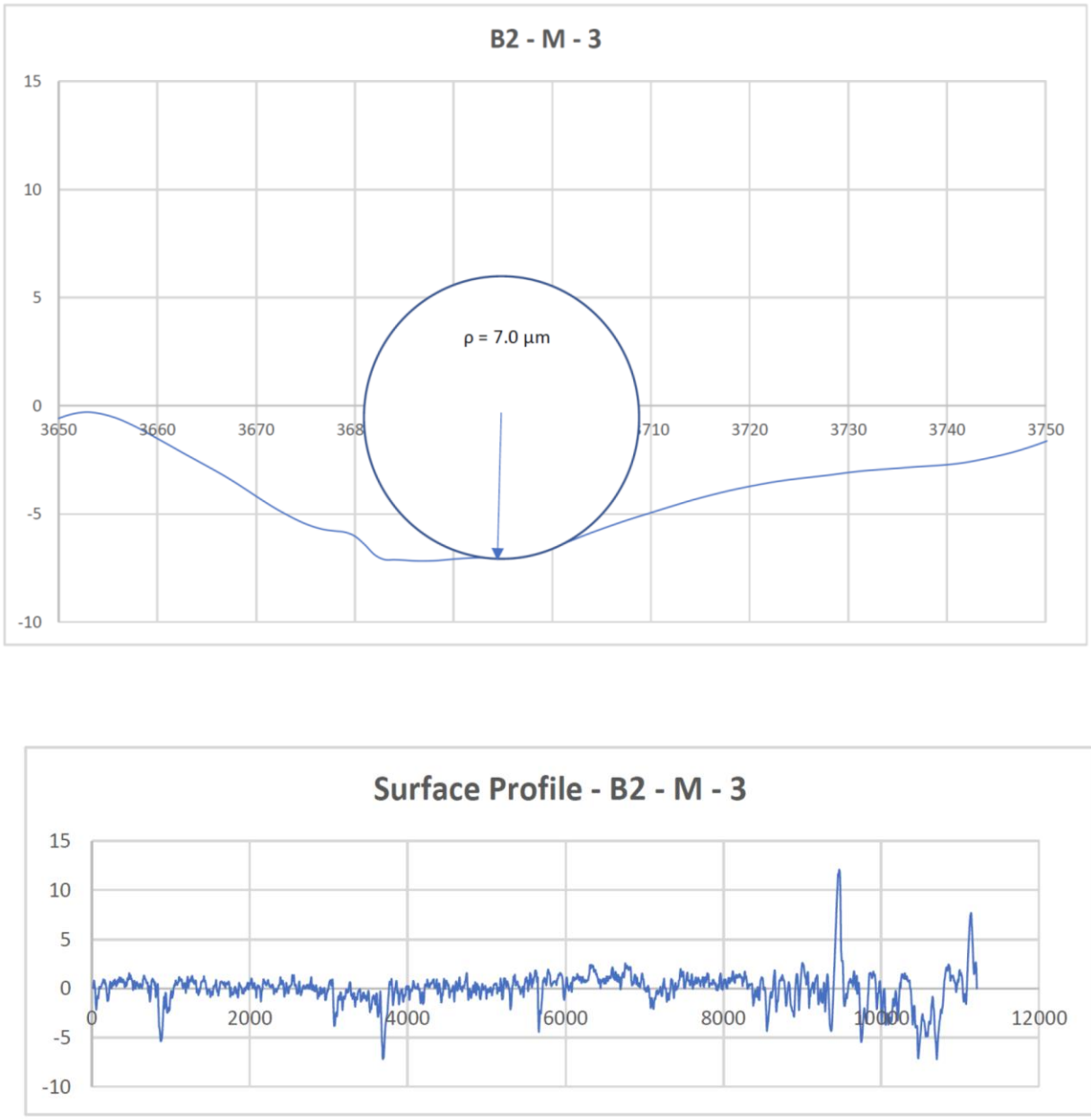

Figure 7.216 Graphical Determination of radius (ρ) from surface profile of specimen B2 – M - 3

Table 7.18 shows the calculated surface integrity stress concentration factor for Notched Specimens in medium load testing.

Specimen Name	Surface Integrity Stress Concentration Factor
A2 – M - 1	1.74
A2 – M - 2	1.81
A2 – M - 3	1.91
A2 – M - 4	2.1
B2 – M - 1	1.77
B2 – M - 2	1.52
B2 – M - 3	1.45

Table 7.18 Calculated Surface Integrity Stress Concentration Factor for Notched Specimens – Medium Load

Observation on Surface finish Data Vs. Fatigue Cycles – Surface finish data in the longitudinal direction was plotted against fatigue cycles and reviewed comparing AWJ trimmed specimens to CVD Diamond Coated Endmill Trimmed specimens. Figures 7.217 through 7.230 show the variation of surface finish parameters Vs. fatigue cycles for the different parameters

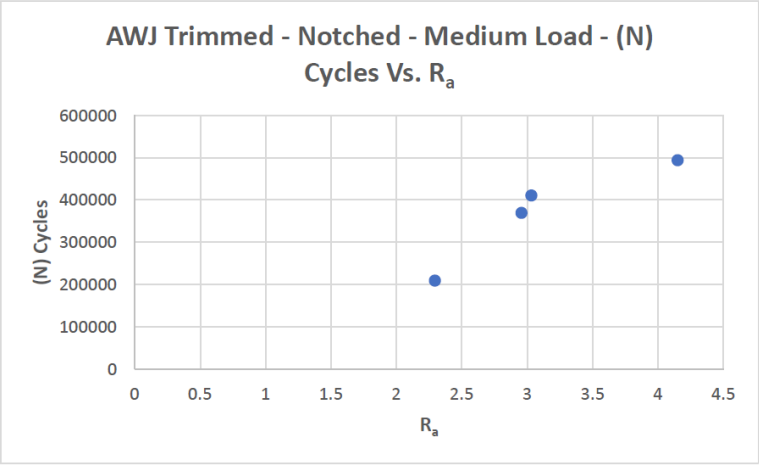

Figure 7.217 Surface Finish - R_a (longitudinal) Vs. Fatigue Cycles – AWJ Trimmed – Notched Medium Load Specimens

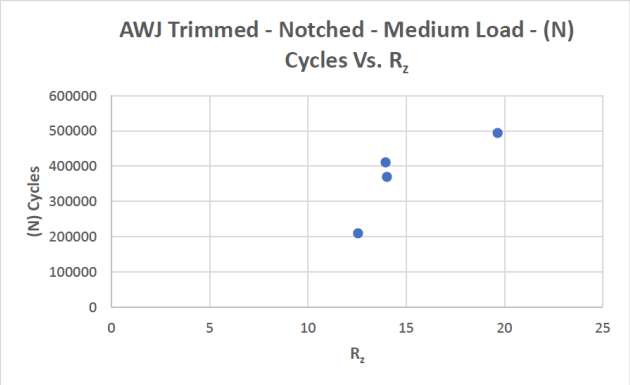

Figure 7.218 Surface Finish – R_z (longitudinal) Vs. Fatigue Cycles – AWJ Trimmed - Notched – Medium Load Test Specimens

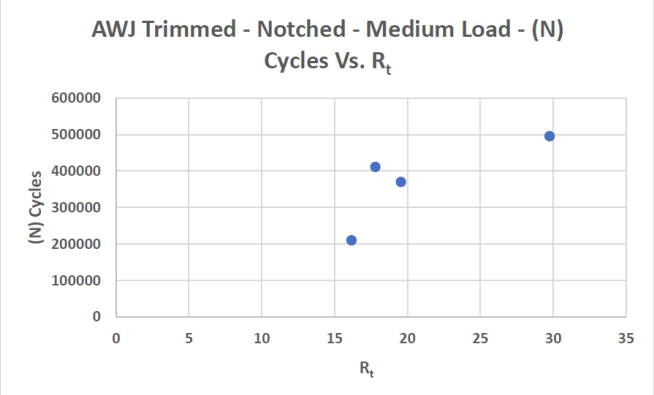

Figure 7.219 Surface Finish – R_t (longitudinal) Vs. Fatigue Cycles – AWJ trimmed – Notched - Medium Load Test Specimens

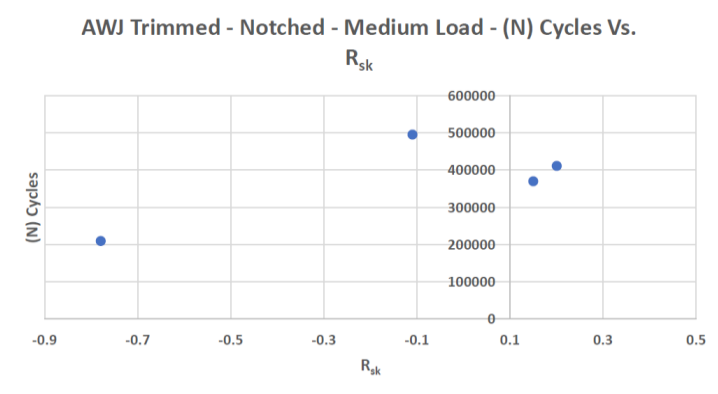

Figure 7.220 Surface Finish – R_{sk} (longitudinal) Vs. Fatigue Cycles – AWJ Trimmed – Notched Medium Load Test Specimens

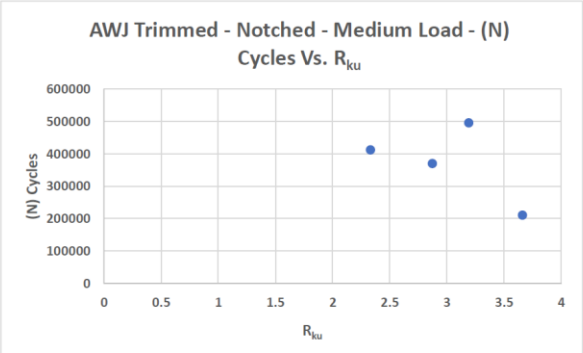

Figure 7.221 Surface Finish – R_{ku} (longitudinal) Vs. Fatigue Cycles – AWJ Trimmed – Notched Medium Load Test Specimens

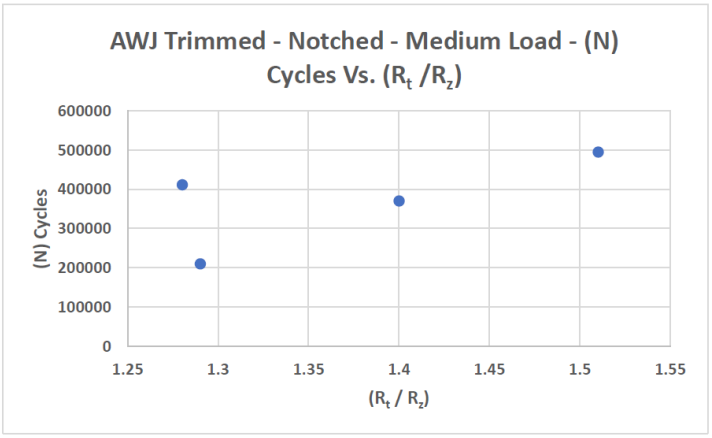

Figure 7.222 Surface Finish – (R_t/R_z) (Longitudinal) Vs. Fatigue Cycles – AWJ Trimmed – Notched Medium Load Test Specimens

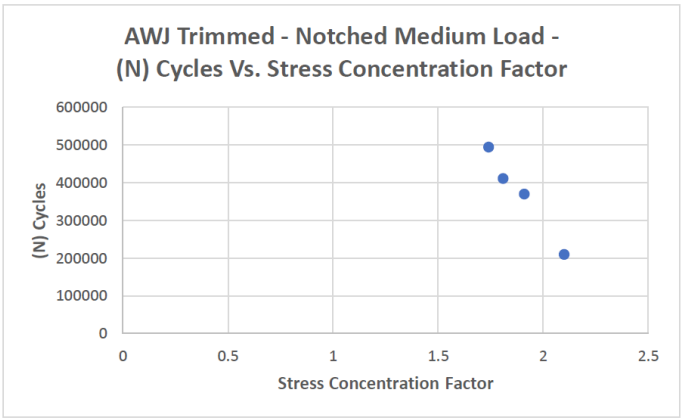

Figure 7.223 Surface Integrity Stress Concentration Factor (Longitudinal) Vs. Fatigue Cycles – AWJ Trimmed - Notched Medium Load Test Specimens

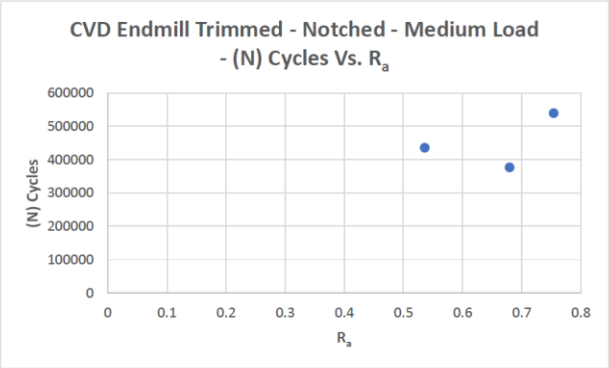

Figure 7.224 Surface Finish - R_a (longitudinal) Vs. Fatigue Cycles – CVD Endmill Trimmed – Notched Medium Load Specimens

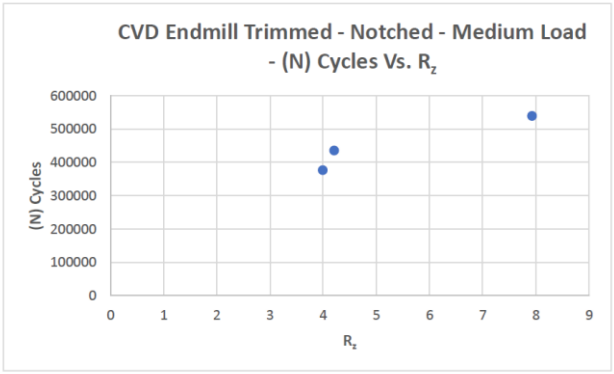

Figure 7.225 Surface Finish – R_z (longitudinal) Vs. Fatigue Cycles –CVD Endmill Trimmed - Notched – Medium Load Test Specimens

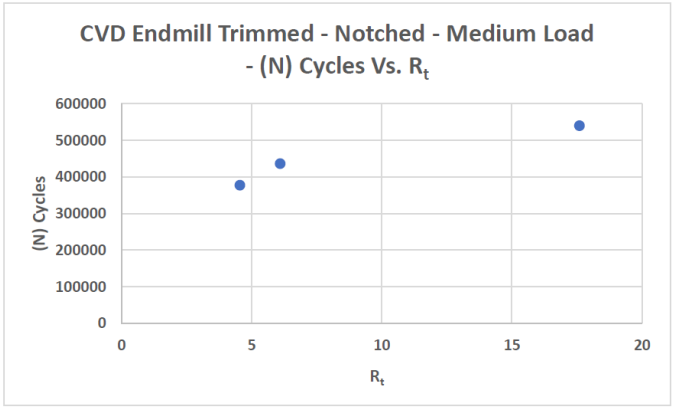

Figure 7.226 Surface Finish – R_t (longitudinal) Vs. Fatigue Cycles – CVD Endmill trimmed – Notched - Medium Load Test Specimens

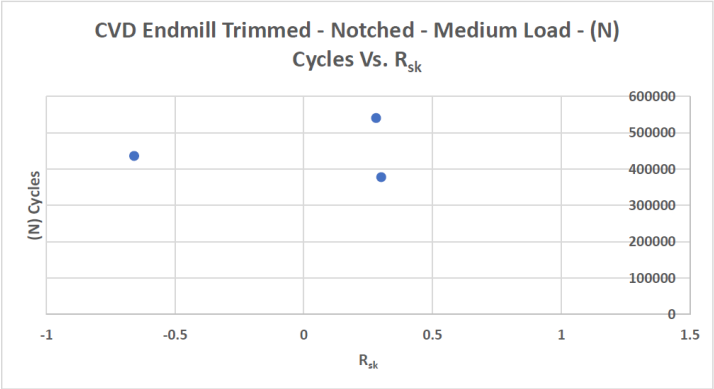

Figure 7.227 Surface Finish – R_{sk} (longitudinal) Vs. Fatigue Cycles – CVD Endmill Trimmed – Notched Medium Load Test Specimens

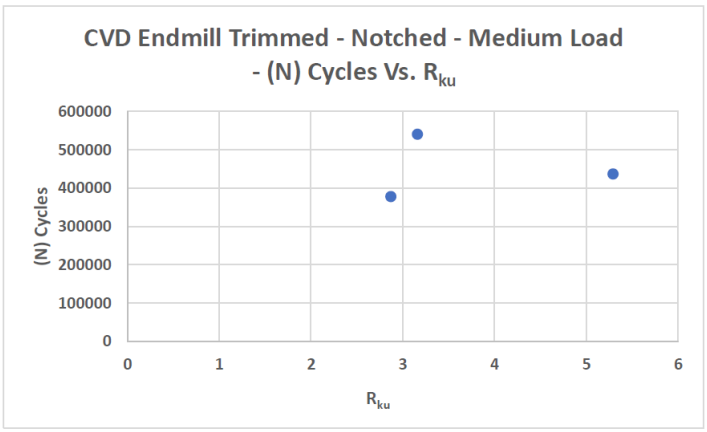

Figure 7.228 Surface Finish – R_{ku} (longitudinal) Vs. Fatigue Cycles –CVD Endmill Trimmed – Notched Medium Load Test Specimens

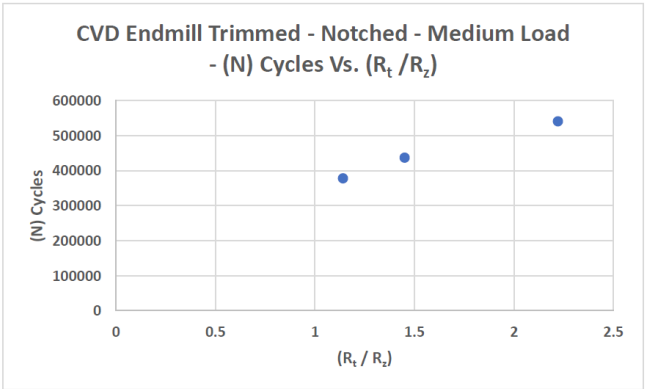

Figure 7.229 Surface Finish – (R_t/R_z) (Longitudinal) Vs. Fatigue Cycles – CVD Endmill Trimmed – Notched Medium Load Test Specimens

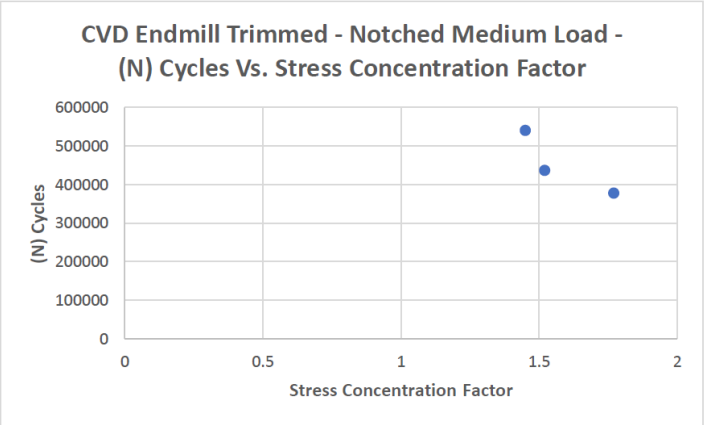

Figure 7.230 Surface Integrity Stress Concentration Factor (Longitudinal) Vs. Fatigue Cycles – CVD Endmill Trimmed - Notched Medium Load Test Specimens

It was observed that in the case of AWJ trimmed specimens, the better surface finish in the transverse direction contributed to higher fatigue cycles to failure. Also observed was that for medium loading conditions, the fatigue cycles generally were higher with improved surface finish data. The CVD Diamond Coated Endmill Trimmed test Specimens generally had fatigue cycle failures that were closer to each other than the AWJ trimmed surface. At medium load conditions, the % Compliance change curves were similar for both AWJ trimmed and CVD Endmill trimmed specimens.

In the case of AWJ specimens, the higher value of peak to valley numbers resulted in larger peaks and valleys in terms of both amplitude and frequency thus providing additional sites for damage initiation and propagation as evidenced by total delamination at edges and through the hole resulting in ultimate failure at lower fatigue cycles.

7.4.2.3 Low Load Test Specimen Data Review

For the Low Load test specimens, the following specimens were tested for AWJ trimmed specimens.

A2 – L – 1

A2 – L – 2

A2 – L – 3

A2 – L - 4

For CVD Diamond Coated Endmill Trimmed specimens, the following samples were tested.

B2 – L – 1

B2 – L – 2

B2 – L – 3

Prior to testing the following surface finish parameters were recorded for each sample in both longitudinal and transverse directions

R_a , R_z , R_t , R_{sk} , R_{ku}

Table 7.19 shows the fatigue cycles to failure for each of the medium load specimens along with the load applied and stress as well as % change in compliance.

Tables 7.4 and 7.5 documented earlier in this chapter show the surface finish data documented in the longitudinal and transverse direction.

Specimen Name	Trim	Hole	Fatigue Cycles	Test Load (Max) (N)	Test Load (Min) (N)	Max Stress (Mpa)	Test Frequency	Compliance
A2-L-1	AWJ -80	CVD Drill	546648	46706	4670	406.65	7 Hz	20.94%
A2-L-2	AWJ -80	CVD Drill	1000010	46706	4670	406.65	7 Hz	27.45%
A2-L-3	AWJ -80	CVD Drill	1000010	46706	4670	406.65	7 Hz	18.84%
A2-L-4	AWJ -80	CVD Drill	582553	46706	4670	406.65	7 Hz	52.18%
B2-L-1	CVD Endmill	CVD Drill	1000010	46706	4670	406.65	7 Hz	18.92%
B2-L-2	CVD Endmill	CVD Drill	1000010	46706	4670	406.65	7 Hz	21.16%
B2-L-3	CVD Endmill	CVD Drill	1000010	46706	4670	406.65	7 Hz	21.23%

Table 7.19 Fatigue Cycles/Loads/Stress & % Compliance Change for Notched Low Loading Testing

Damage Propagation in AWJ trimmed specimens- To compare the damage propagation % compliance change was plotted for each AWJ low load specimen and the percentage damage at 500K cycles for lower fatigue failures was compared. Figures 7.231 through 7.242 show the % compliance change for each low load AWJ test specimen along with a photo micrograph depicting the damage at 500K cycles.

In all cases damage started as matrix cracking followed by matrix fibre interface debonding and delamination as shown in the figures. The initiation of damage was localized at the 45 degree plies (also the sites of fibre pullouts). These sites were both at the edges as well as in the hole.

Once damage started progressing, ultimate failure occurred due to delamination in the edges and through the hole.

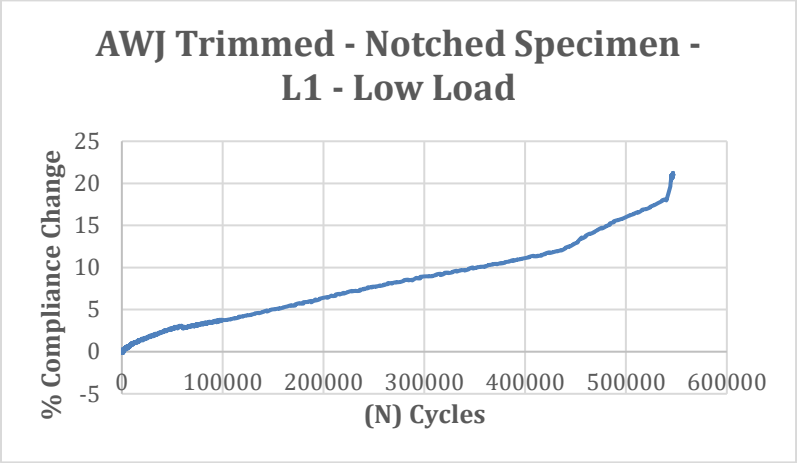

Figure 7.231 Percent Compliance Change Vs. Fatigue Cycles for A2 – L – 1

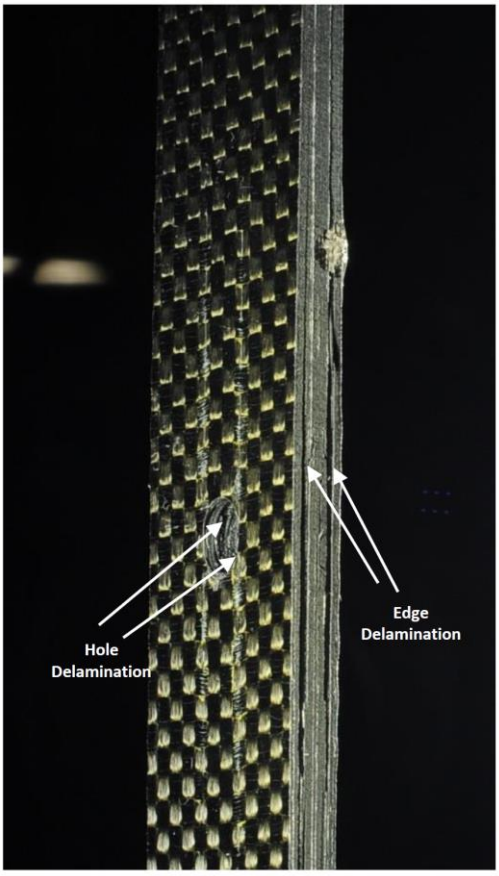

Figure 7.232 Damage at 500K Cycles, 15.94%, Test Specimen

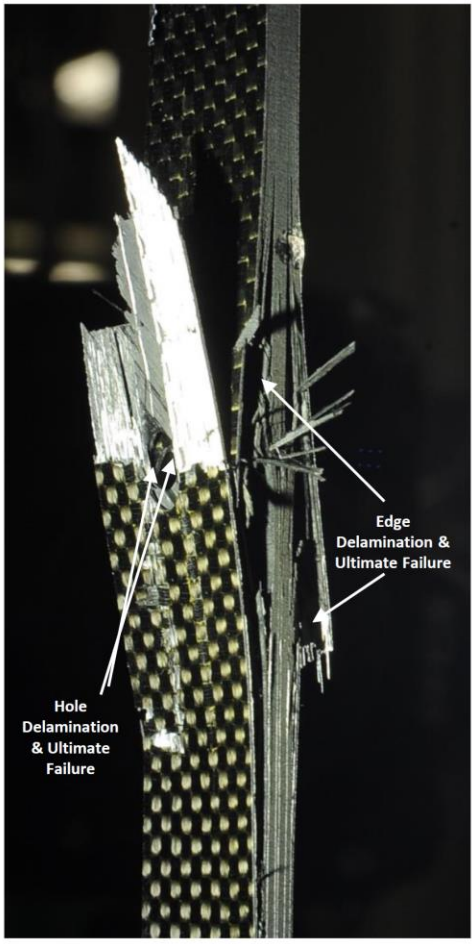

Figure 7.233 Damage (20.94%) & Ultimate Failure at 546648 Cycles, Test

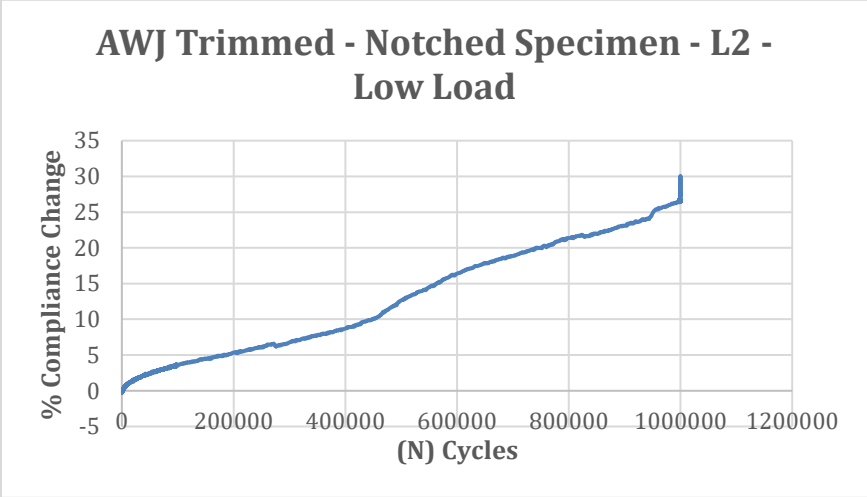

Figure 7.234 Percent Compliance Change Vs. Fatigue Cycles for A2 – L – 2

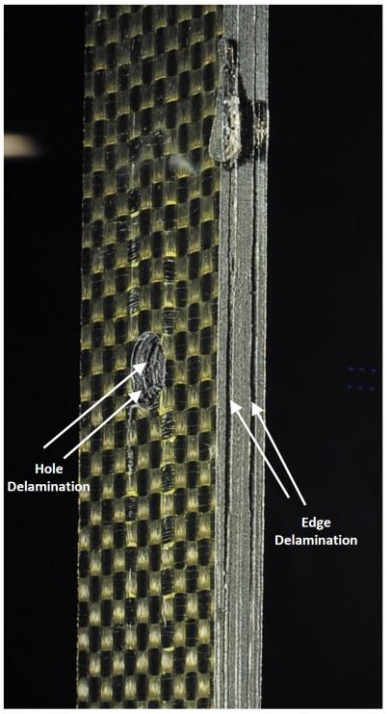

Figure 7.235 Damage at 500K Cycles, 12.61%, Test Specimen

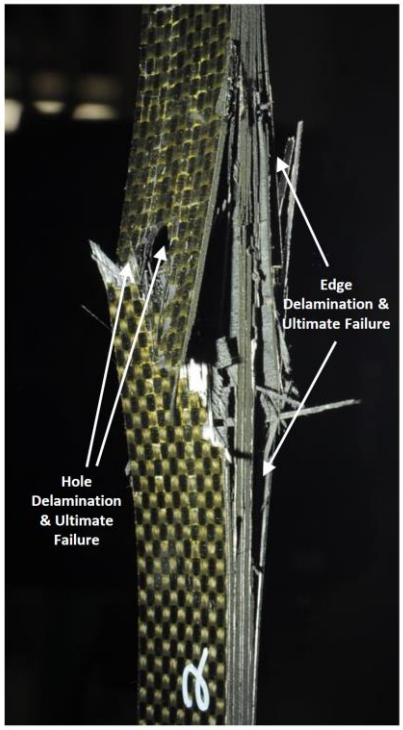

Figure 7.236 Damage (27.45%) & Ultimate Failure at 1000010 Cycles, Test

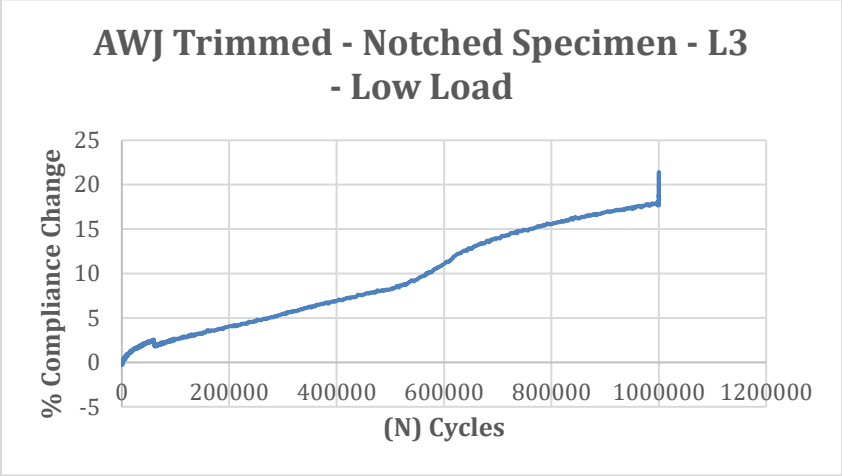

Figure 7.237 Percent Compliance Change Vs. Fatigue Cycles for A2 – L – 3

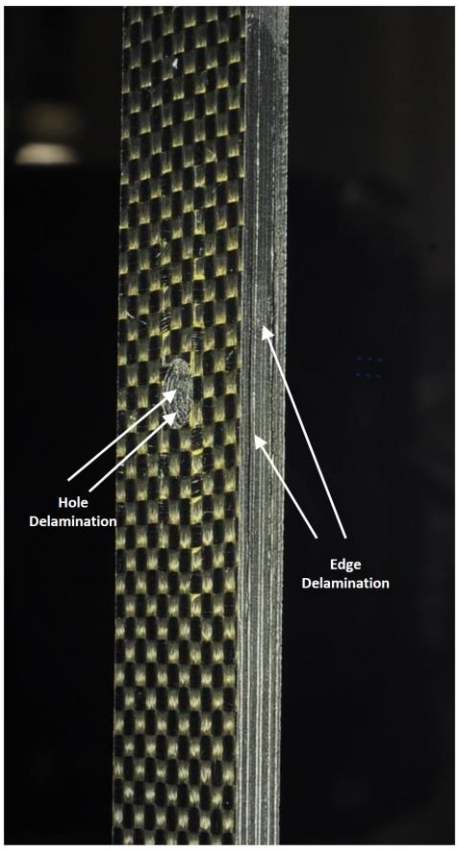

Figure 7.238 Damage at 500K Cycles, 8.29%, Test Specimen A2 – L - 3

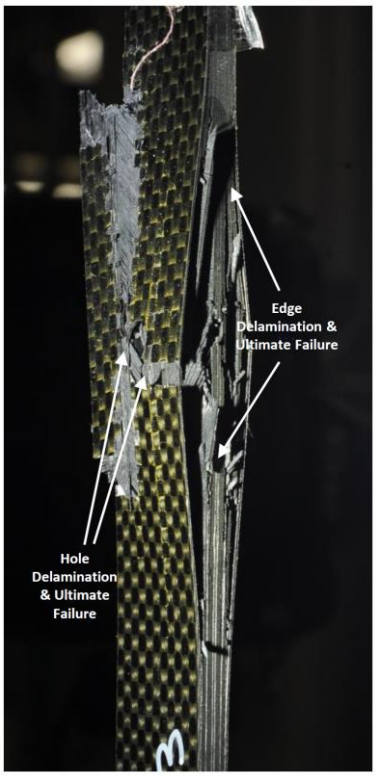

Figure 7.239 Damage (18.84%) & Ultimate Failure at 1000010 Cycles, Test

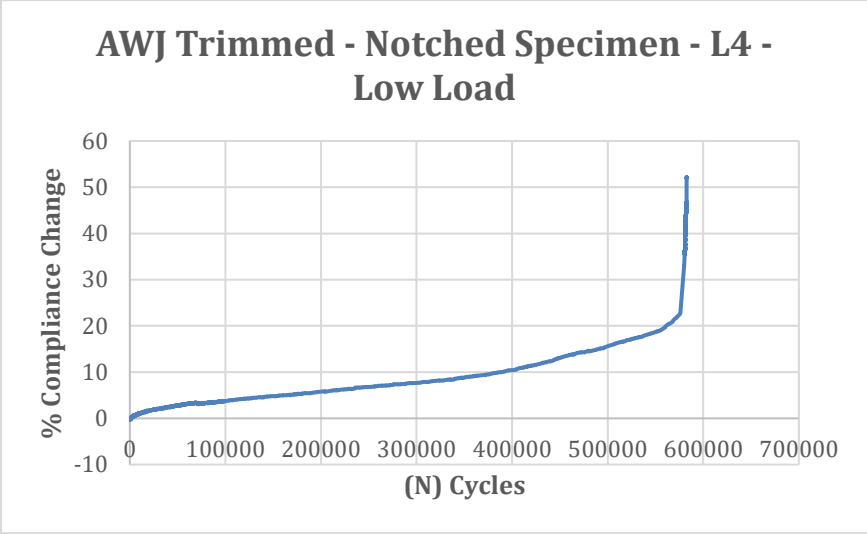

Figure 7.240 Percent Compliance Change Vs. Fatigue Cycles for A2 – L – 4

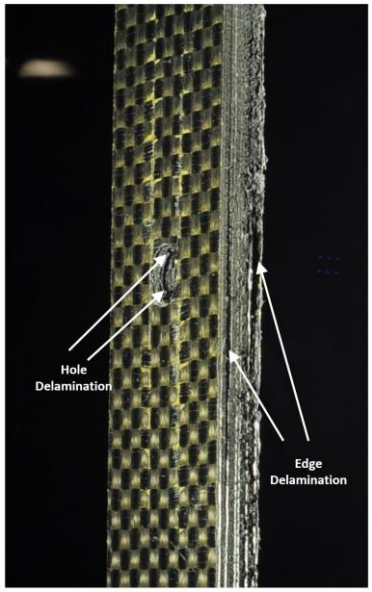

Figure 7.241 Damage at 500K Cycles, 15.84%, Test Specimen

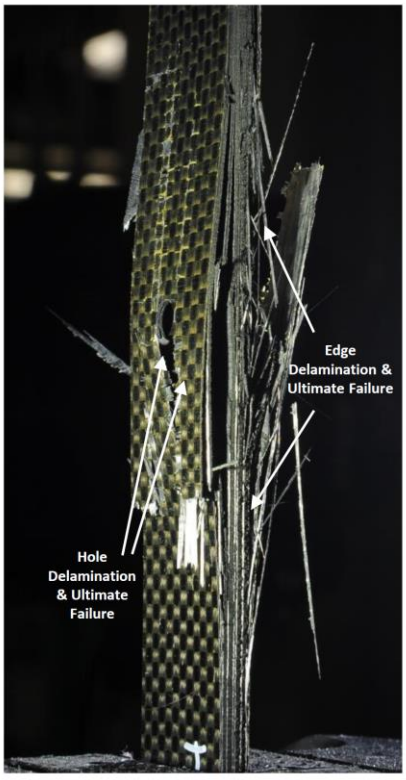

Figure 7.242 Damage (52.18%) & Ultimate Failure at 582553 Cycles, Test

Damage Propagation in CVD Diamond Coated Endmill trimmed specimens- To compare the damage propagation % compliance change was plotted for each CVD Diamond Coated Endmill trimmed low load specimen and the percentage damage at 500K cycles was compared. Figures 7.243 through 7.251 show the % compliance change for each low load CVD endmill trimmed test specimen along with a photo micrograph depicting the damage at 500K cycles.
In all cases damage started as matrix cracking followed by matrix fibre interface debonding and delamination as shown in the figures. The initiation of damage was localized at the 45 degree plies (also the sites of fibre pullouts). These sites were both at the edges as well as in the hole. Once damage started progressing, ultimate failure occurred due to delamination in the edges and through the hole.

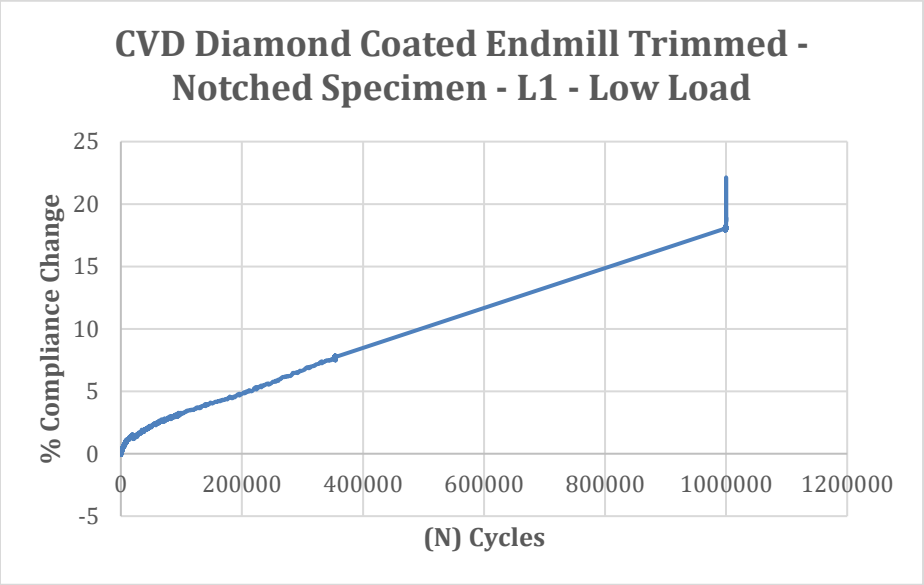

Figure 7.243 Percent Compliance Change Vs. Fatigue Cycles for B2 – L – 1

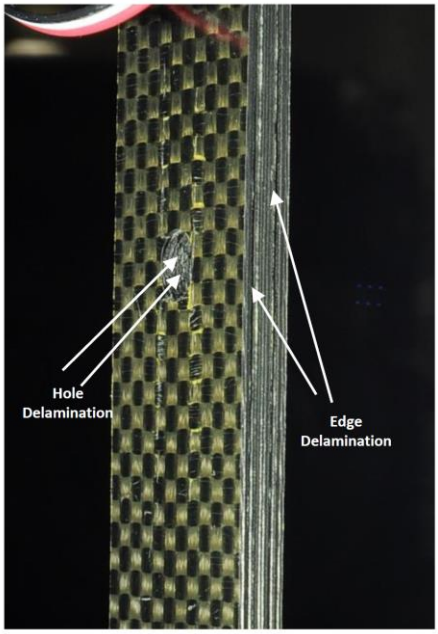

Figure 7.244 Damage at 500K Cycles, 8.98%, Test Specimen B2-L-1

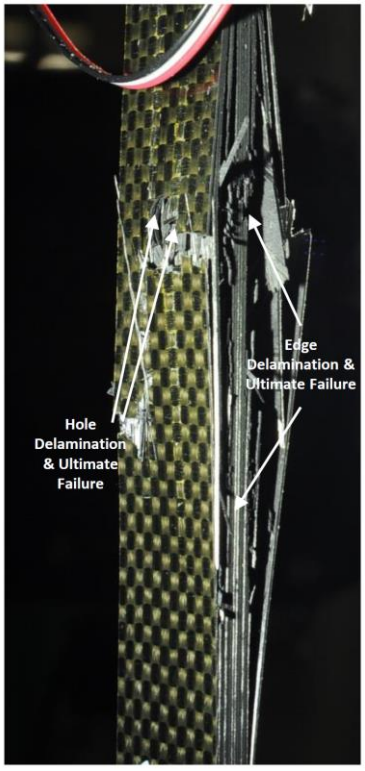

Figure 7.245 Damage (18.92%) & Ultimate Failure at 1000010 Cycles, Test Specimen B2-L-1

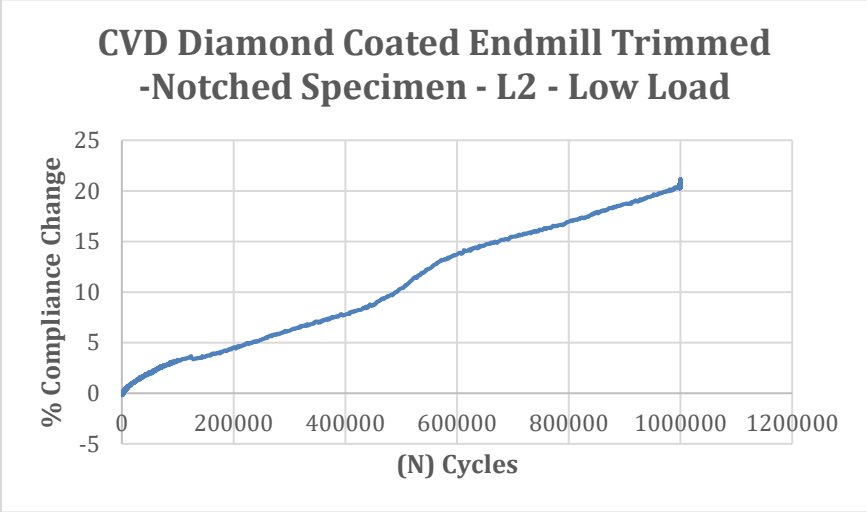

Figure 7.246 Percent Compliance Change Vs. Fatigue Cycles for B2 – L – 2

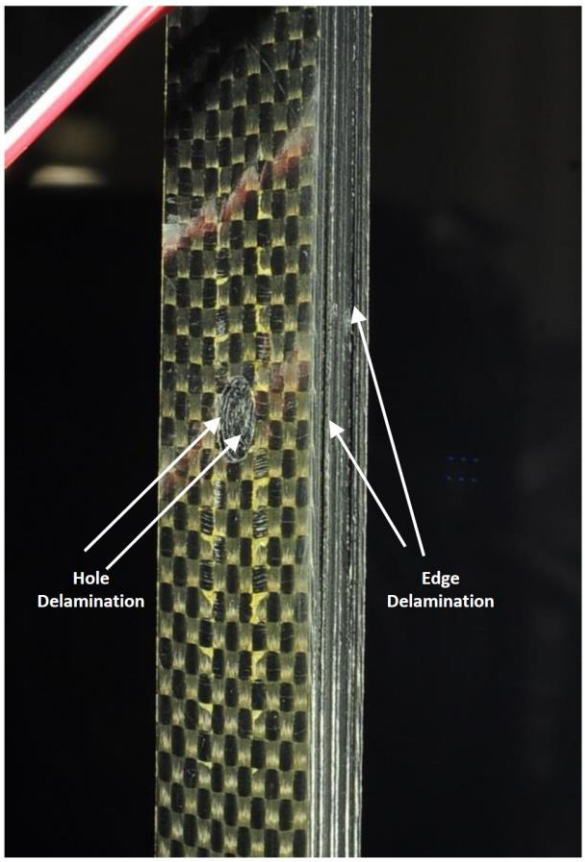

Figure 7.247 Damage at 500K Cycles, 10.29%, Test Specimen B2-L-2

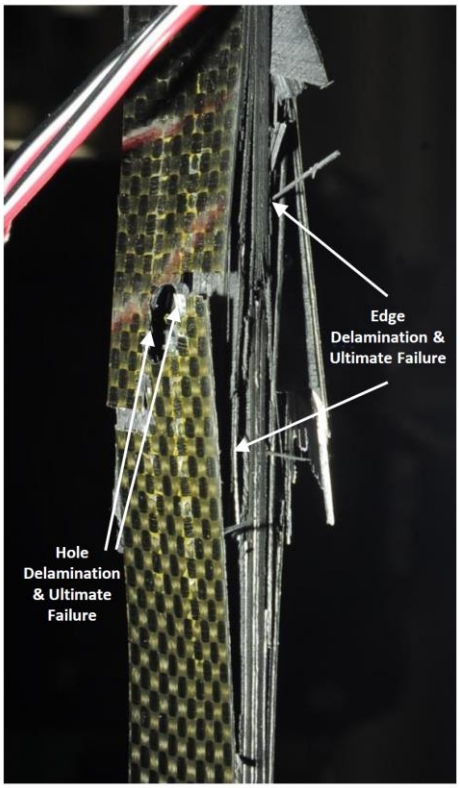

Figure 7.248 Damage (21.16%) & Ultimate Failure at 1000010 Cycles, Test Specimen B2-L-3

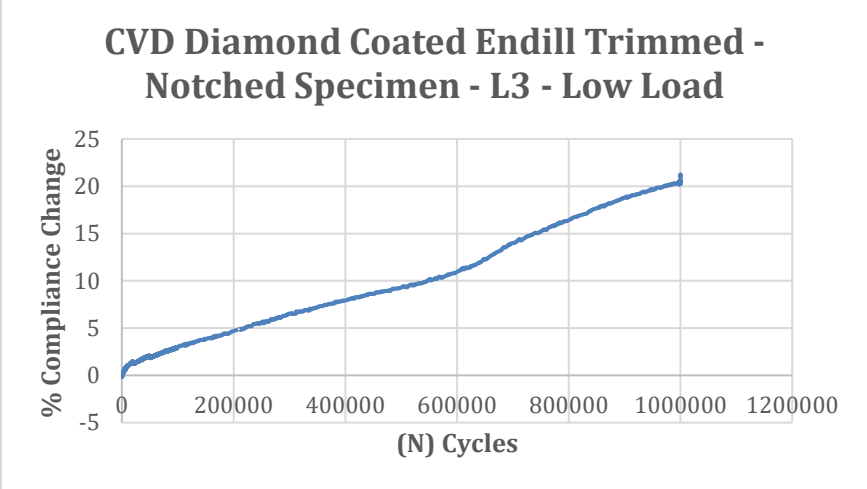

Figure 7.249 Percent Compliance Change Vs. Fatigue Cycles for B2 – L – 3

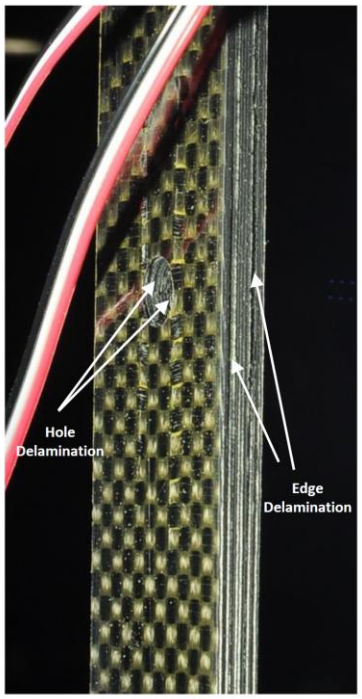

Figure 7.250 Damage at 500K Cycles, 9.27%, Test Specimen B2-L-3

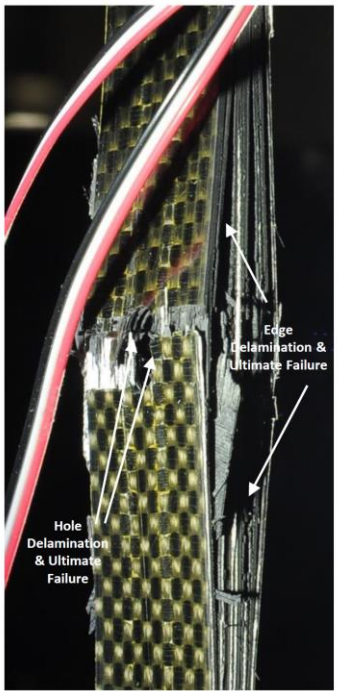

Figure 7.251 Damage (21.23%) & Ultimate Failure at 1000010 Cycles, Test Specimen B2-L-3

Figures 7.252 through 7.254 show the summary plots for % Compliance change Vs. (N) cycles for AWJ and CVD Endmill Trimmed specimens in low load testing.

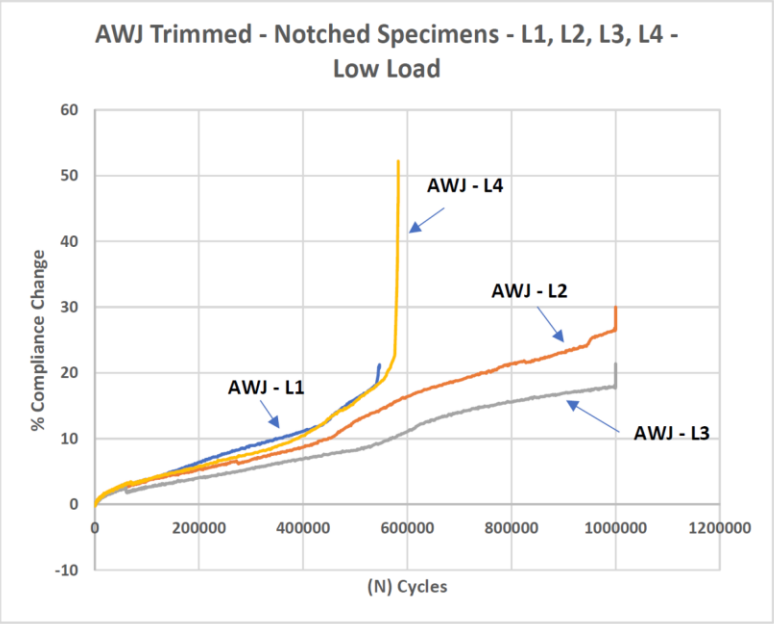

Figure 7.252 Summary Plot of % Compliance Change Vs. (N) Cycles for AWJ Trimmed Notched Specimens – Low Load

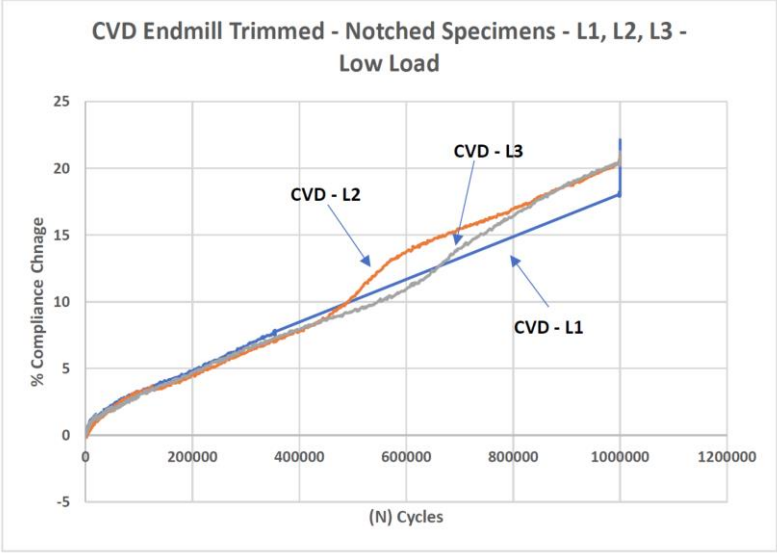

Figure 7.253 Summary Plot of % Compliance Change Vs. (N) Cycles for CVD Endmill Trimmed Notched Specimens – Low Load

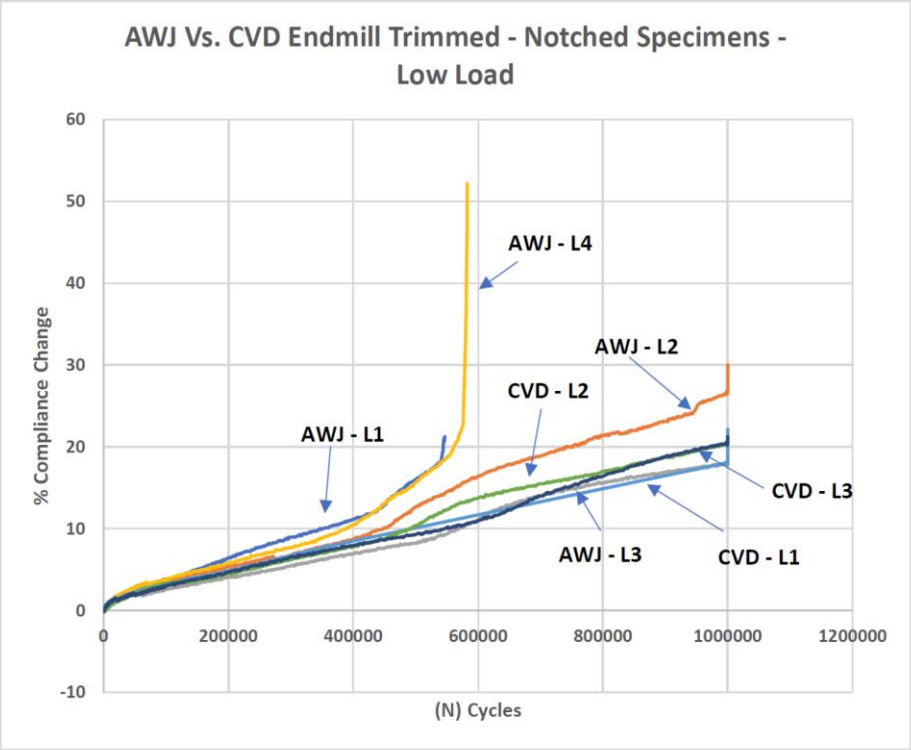

Figure 7.254 Summary Plot of % Compliance Change Vs. (N) Cycles for AWJ Vs. CVD Endmill Trimmed Notched Specimens – Low Load

Surface Finish Stress Concentration Factor $\left(\bar{K}_t\right)$

Surface finish profiles of all high load test specimens were used to calculate the stress concentration factor $\left(\bar{K}_t\right)$ using the formula shown in figure 7.36

Figures 7.255 through 7.261 Show the stress concentration factor determination graphically for the radius and using the formula from Figure 7.36

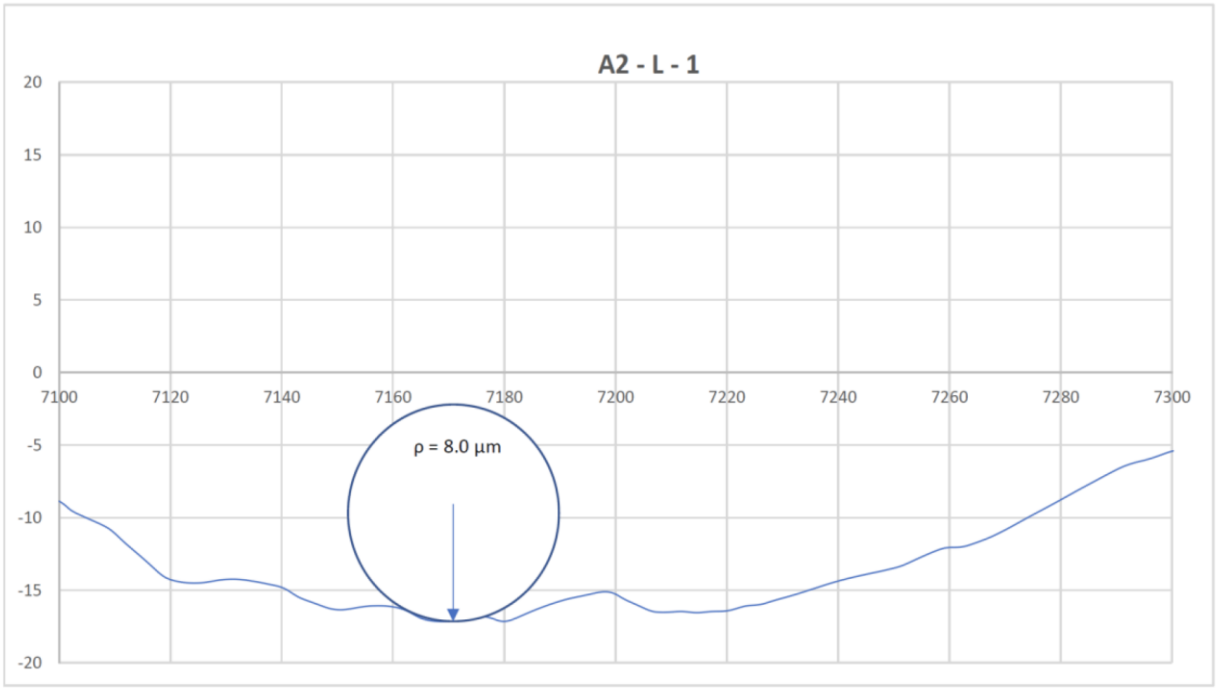

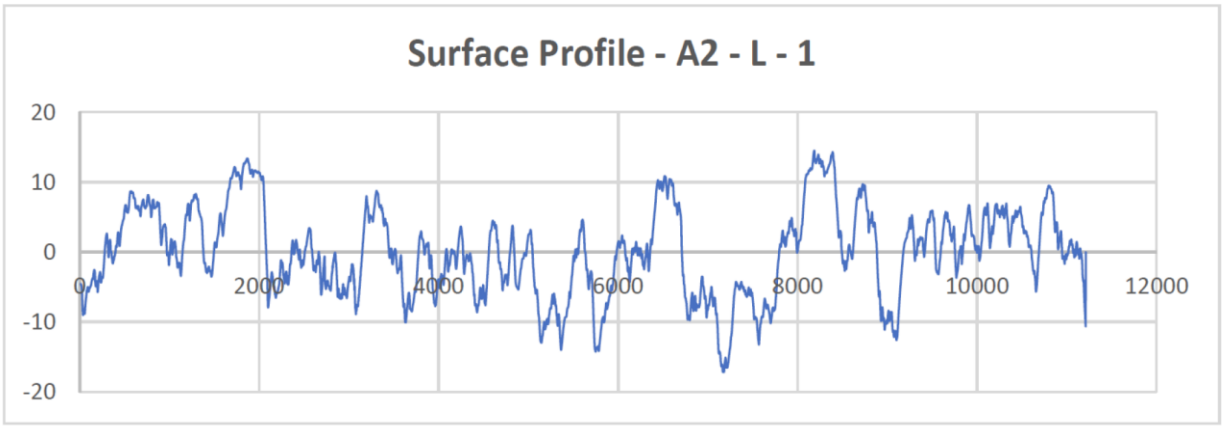

Figure 7.255 Graphical Determination of radius (ρ) from surface profile of specimen A2 – L – 1

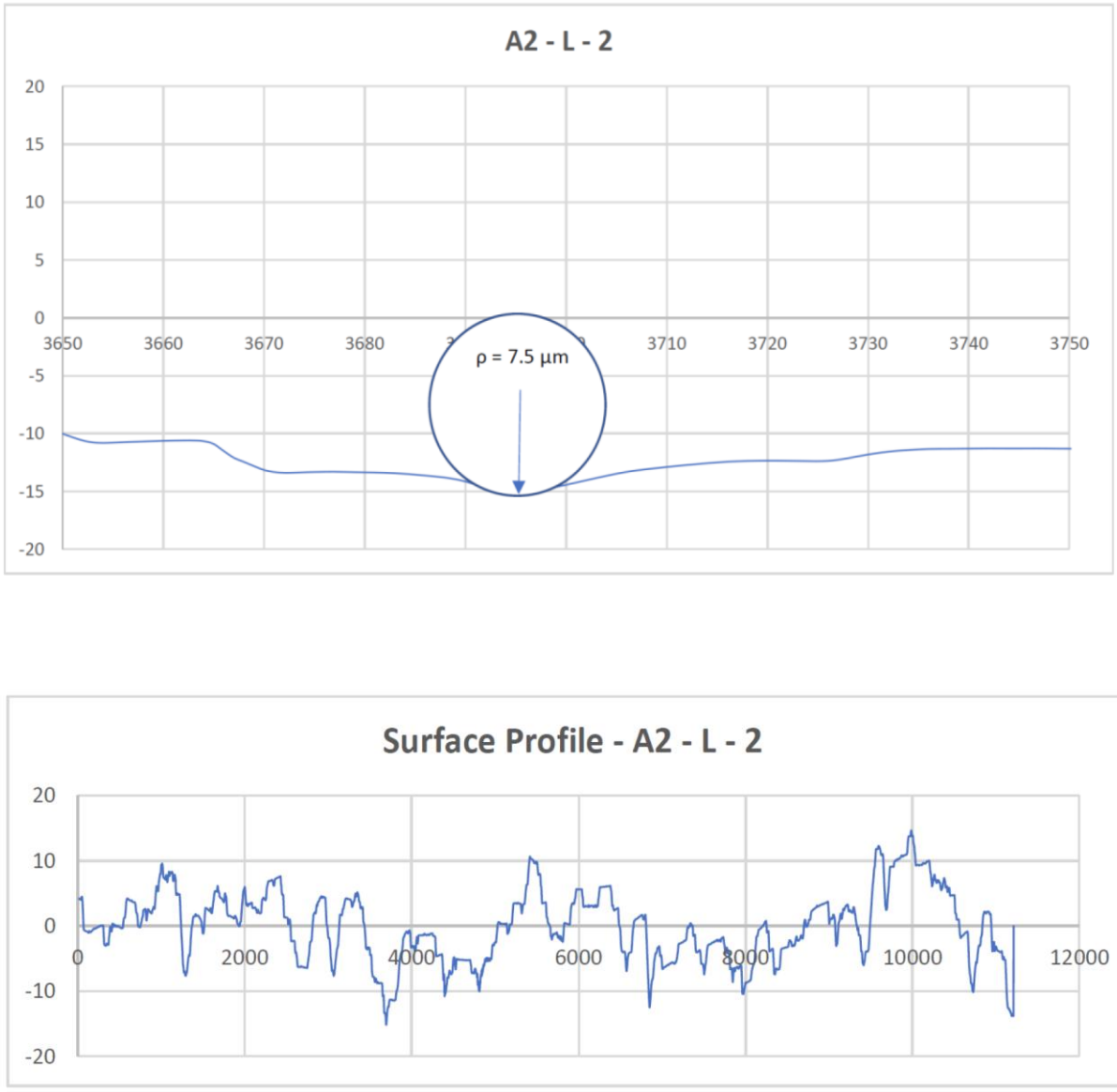

Figure 7.256 Graphical Determination of radius (ρ) from surface profile of specimen A2 – L – 2

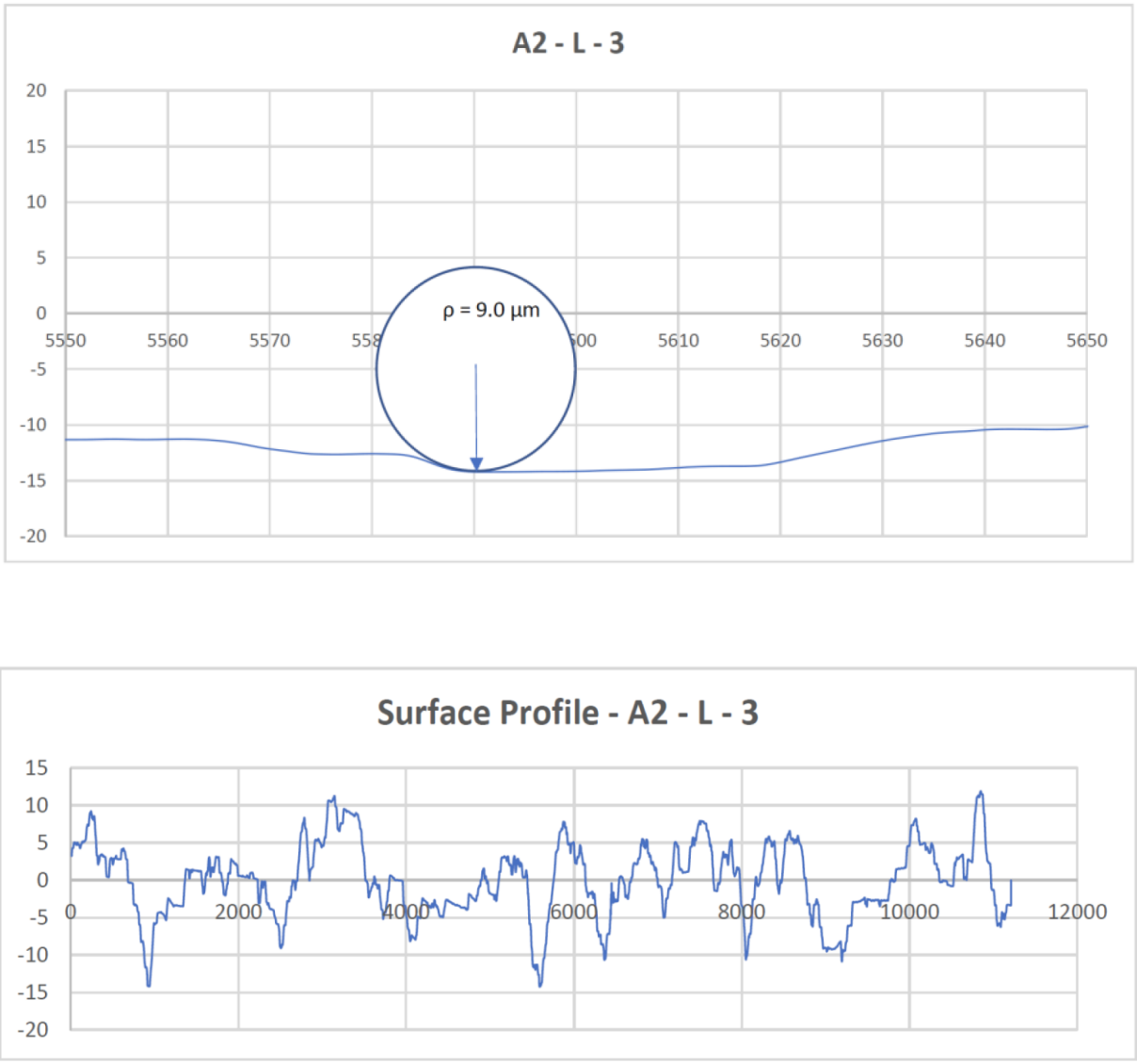

Figure 7.257 Graphical Determination of radius (ρ) from surface profile of specimen A2 – L – 3

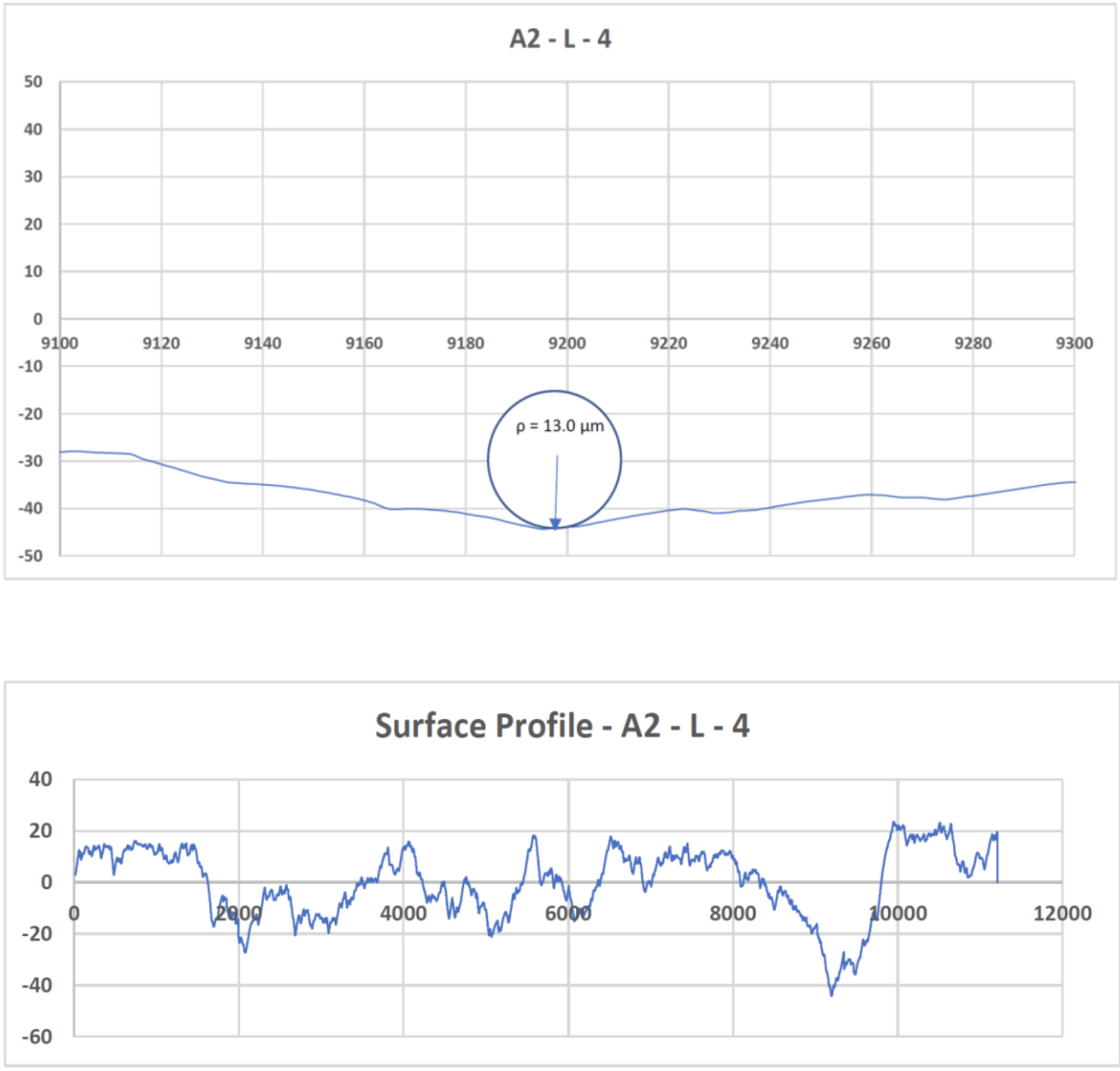

Figure 7.258 Graphical Determination of radius (ρ) from surface profile of specimen A2 – L – 4

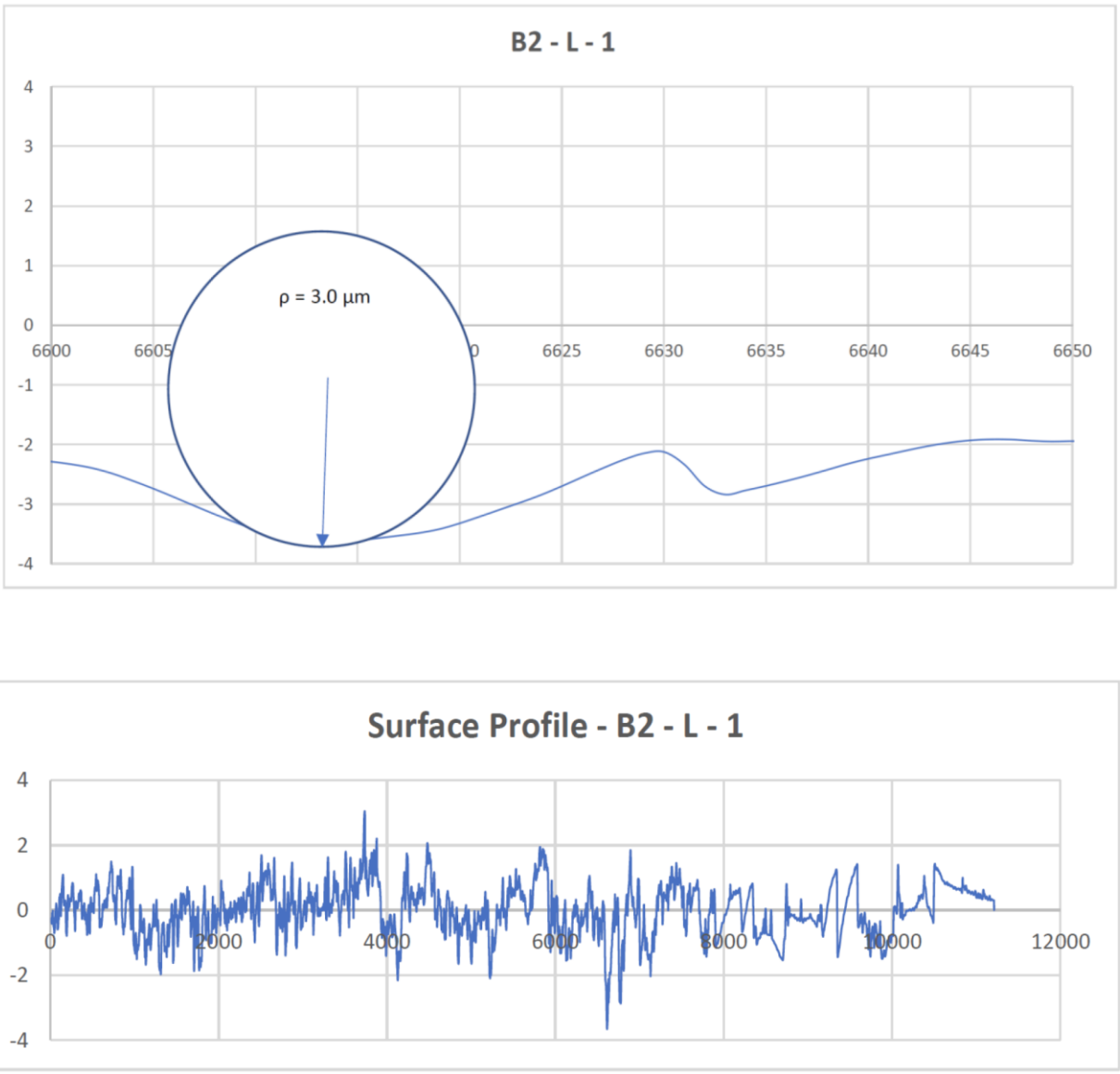

Figure 7.259 Graphical Determination of radius (ρ) from surface profile of specimen B2 – L – 1

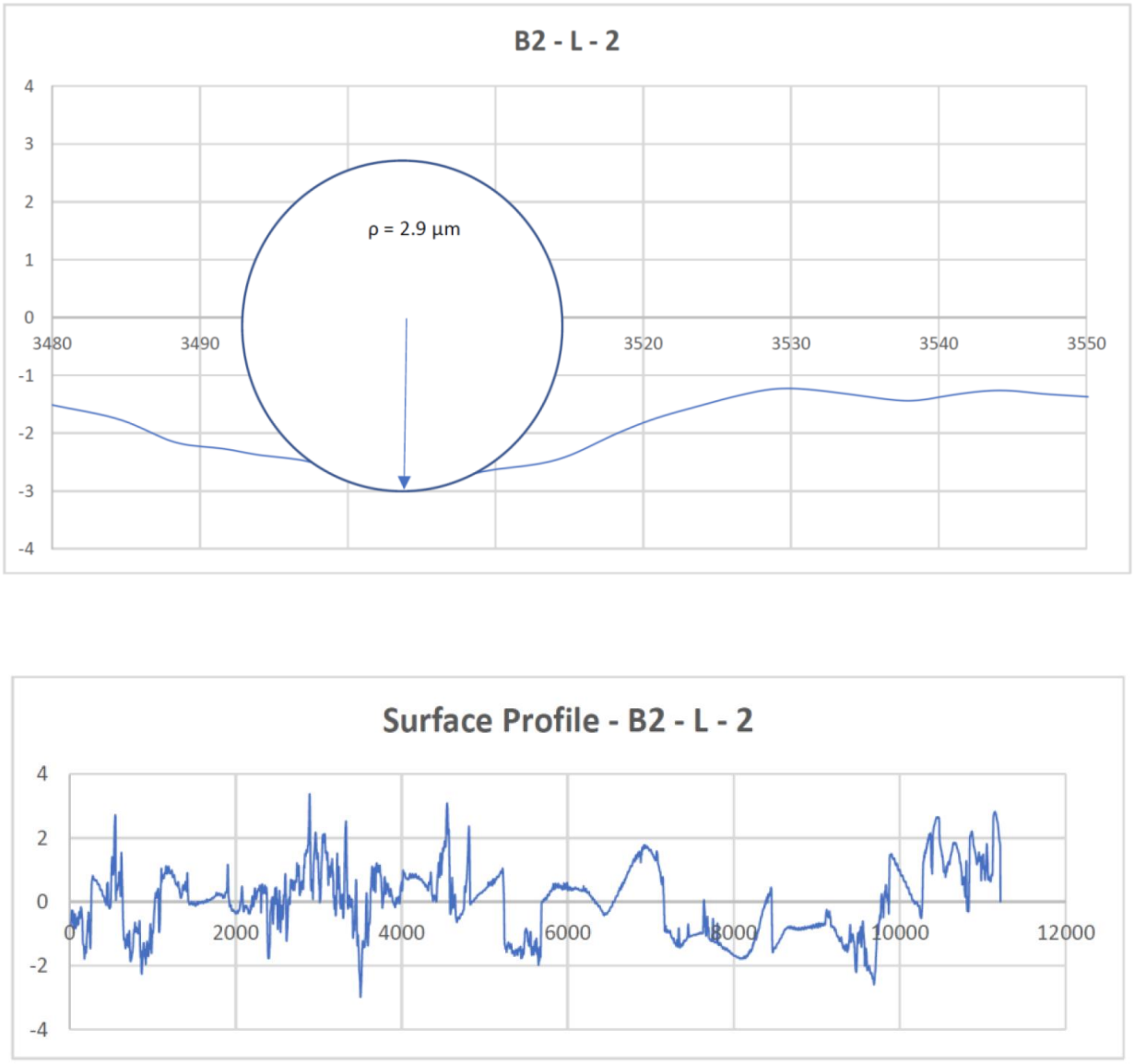

Figure 7.260 Graphical Determination of radius (ρ) from surface profile of specimen B2 – L – 2

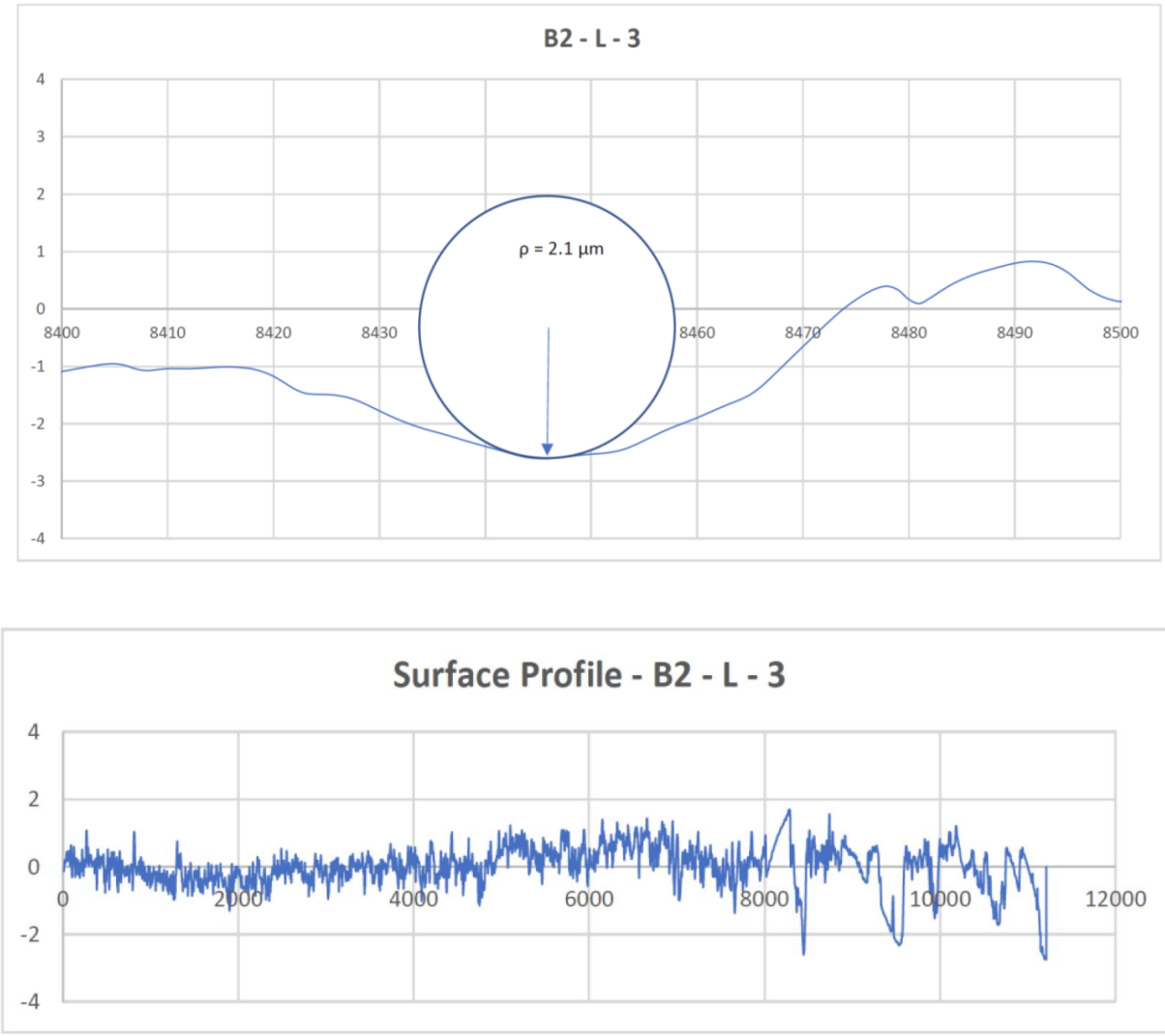

Figure 7.261 Graphical Determination of radius (ρ) from surface profile of specimen B2 – L – 3

Table 7.20 shows the calculated surface integrity stress concentration factor for Notched specimens low load testing.

Specimen Name	Surface Integrity Stress Concentration Factor
A2 – L - 1	2.1
A2 – L - 2	1.88
A2 – L - 3	1.87
A2 – L - 4	2.08
B2 – L - 1	1.53
B2 – L - 2	1.53
B2 – L - 3	1.57

Table 7.20 Calculated Surface Integrity Stress Concentration factor for Notched Specimens – Low Load Testing

Observation on Surface finish Data Vs. Fatigue Cycles – Surface finish data in the longitudinal direction was plotted against fatigue cycles and reviewed comparing AWJ trimmed specimens to CVD Diamond Coated Endmill Trimmed specimens. Figures 7.262 through 7.275 show the variation of surface finish parameters Vs. fatigue cycles for the different parameters

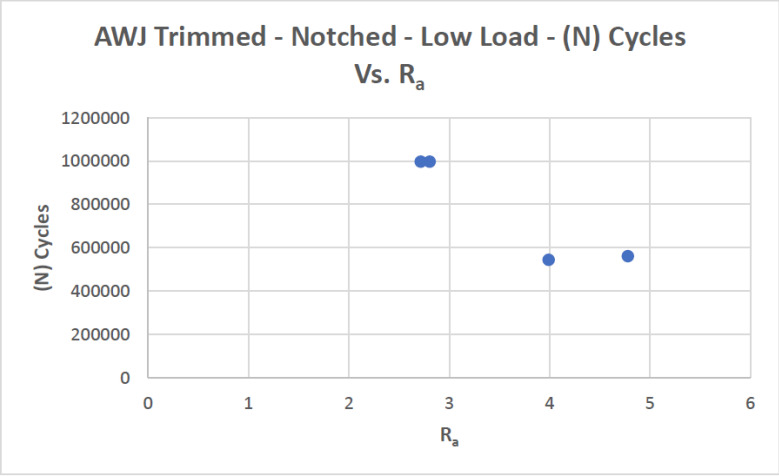

Figure 7.262 Surface Finish - R_a (longitudinal) Vs. Fatigue Cycles – AWJ Trimmed – Notched Low Load Specimens

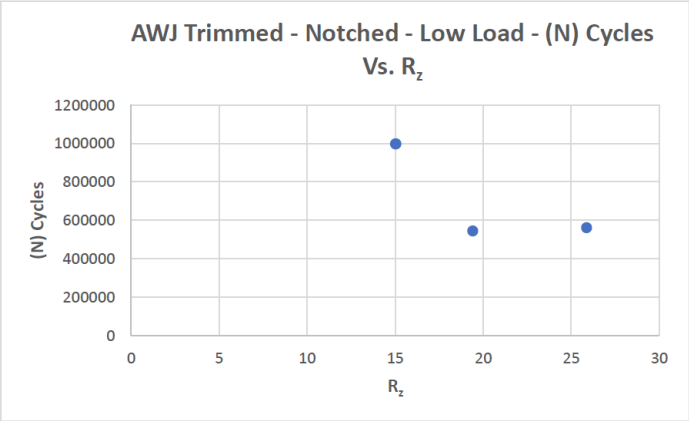

Figure 7.263 Surface Finish – R_z (longitudinal) Vs. Fatigue Cycles – AWJ Trimmed - Notched – Low Load Test Specimens

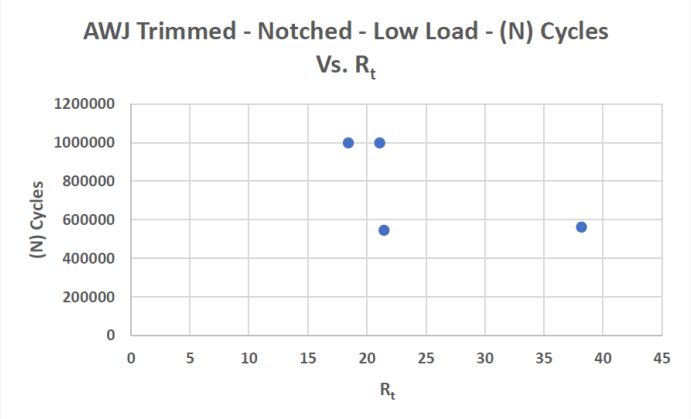

Figure 7.264 Surface Finish – R_t (longitudinal) Vs. Fatigue Cycles – AWJ trimmed – Notched – Low Load Test Specimens

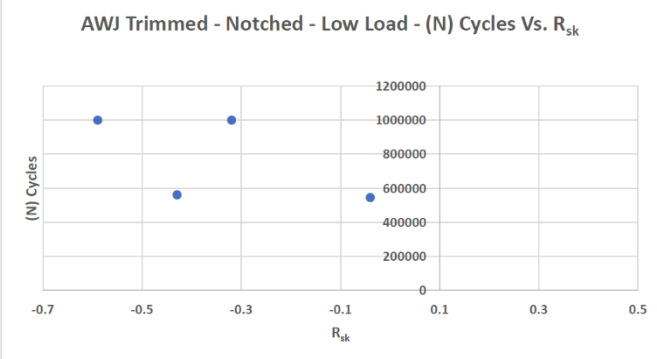

Figure 7.265 Surface Finish – R_{sk} (longitudinal) Vs. Fatigue Cycles – AWJ Trimmed – Notched Low Load Test Specimens

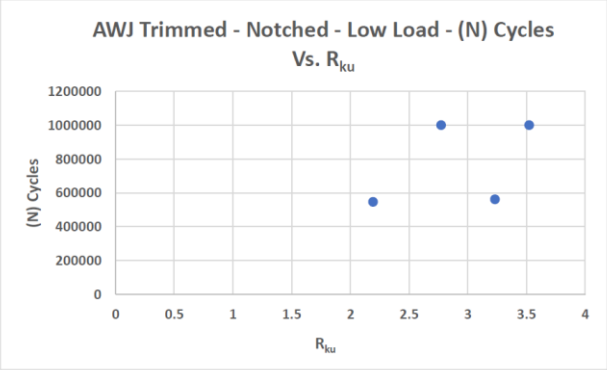

Figure 7.266 Surface Finish – R_{ku} (longitudinal) Vs. Fatigue Cycles – AWJ Trimmed – Notched Low Load Test Specimens

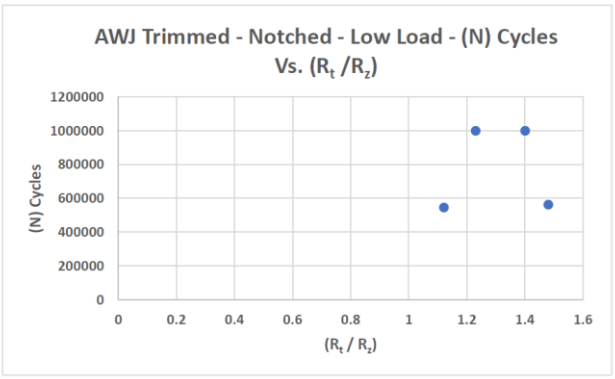

Figure 7.267 Surface Finish – (R_t/R_z) (Longitudinal) Vs. Fatigue Cycles – AWJ Trimmed – Notched Low Load Test Specimens

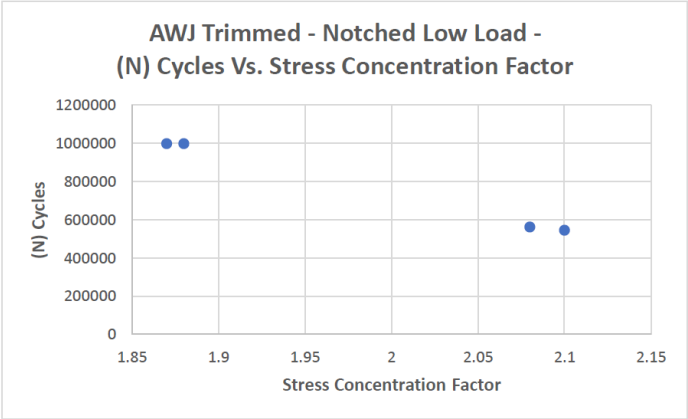

Figure 7.268 Surface Integrity Stress Concentration Factor (Longitudinal) Vs. Fatigue Cycles – AWJ Trimmed - Notched Low Load Test Specimens

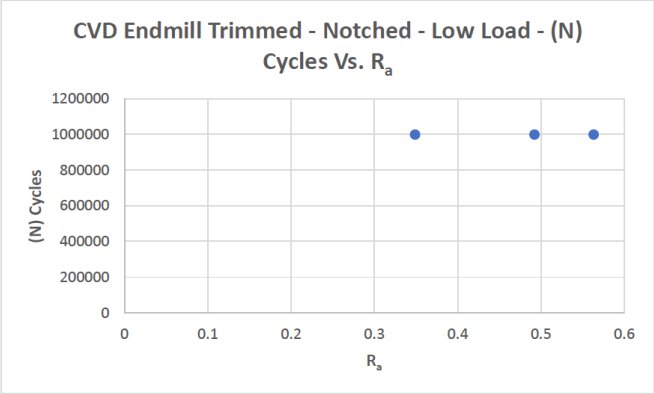

Figure 7.269 Surface Finish - R_a (longitudinal) Vs. Fatigue Cycles – CVD Endmill Trimmed – Notched Low Load Specimens

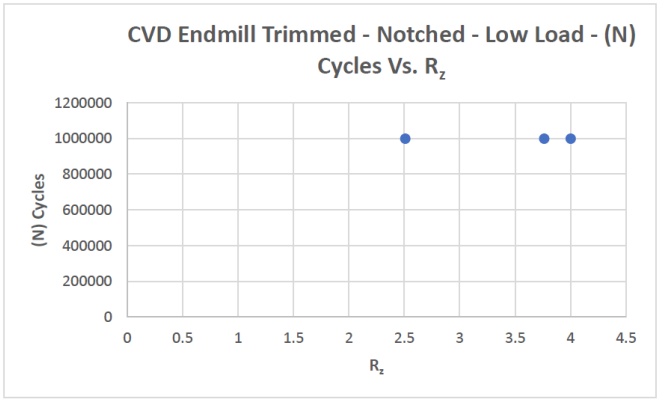

Figure 7.270 Surface Finish – R_z (longitudinal) Vs. Fatigue Cycles – CVD Endmill Trimmed - Notched – Low Load Test Specimens

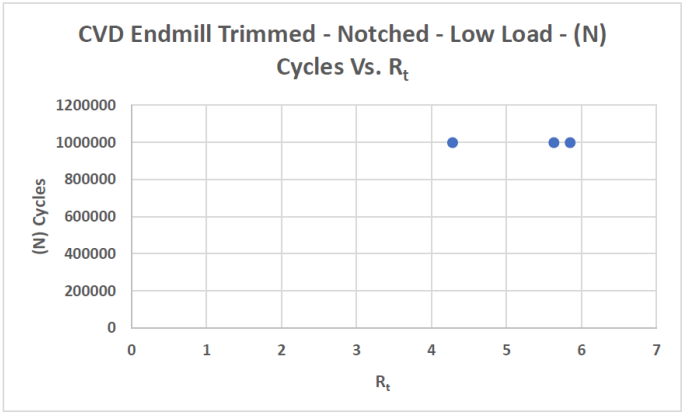

Figure 7.271 Surface Finish – R_t (longitudinal) Vs. Fatigue Cycles – CVD Endmill trimmed – Notched – Low Load Test Specimens

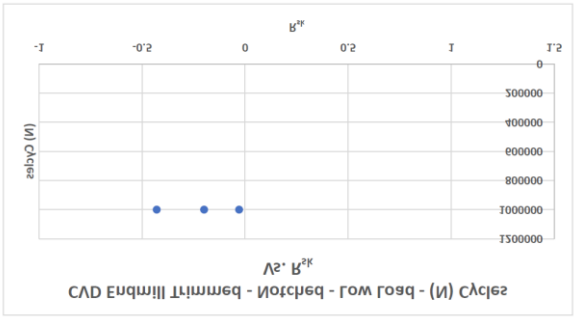

Figure 7.272 Surface Finish – R_{sk} (longitudinal) Vs. Fatigue Cycles – CVD Endmill Trimmed – Notched Low Load Test Specimens

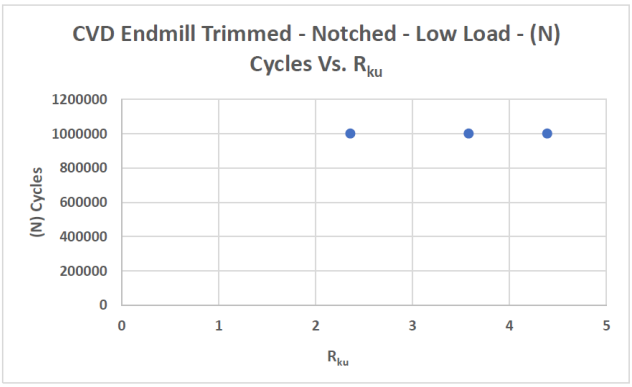

Figure 7.273 Surface Finish – R_{ku} (longitudinal) Vs. Fatigue Cycles – CVD Endmill Trimmed – Notched Low Load Test Specimens

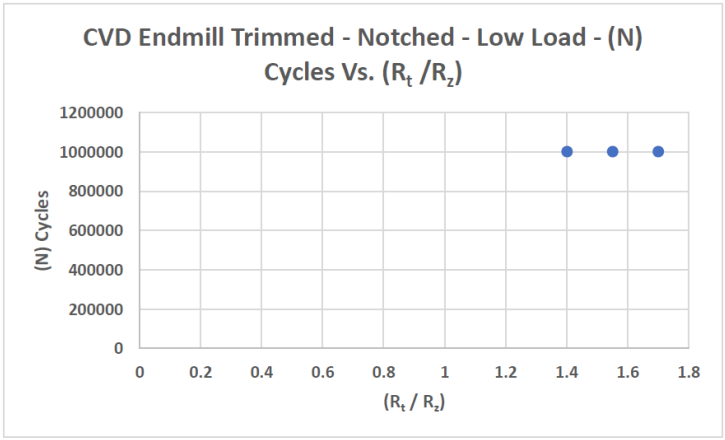

Figure 7.274 Surface Finish – (R_t/R_z) (Longitudinal) Vs. Fatigue Cycles – CVD Endmill Trimmed – Notched Low Load Test Specimens

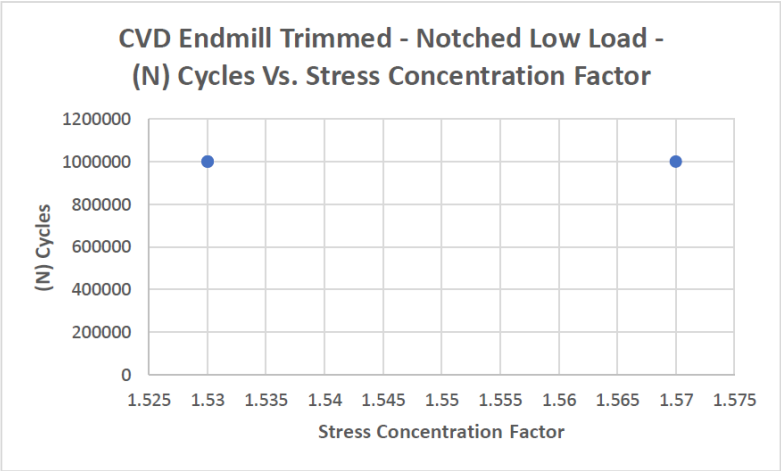

Figure 7.275 Surface Integrity Stress Concentration Factor (Longitudinal) Vs. Fatigue Cycles – CVD Endmill Trimmed - Notched Low Load Test Specimens

It was observed that in both AWJ trimmed and CVD Endmill trimmed specimens, the surface finish data when better resulted in high fatigue cycles to failure.

In the case of test specimens A2 – L – 1 and A2 – L - 4, the surface finish data indicated a rougher profile in both longitudinal and transverse direction. These higher values of data pointed to higher surface peaks and valleys resulting in higher count of damage initiation sites, the result was an initiation of delamination at lower cycles. This ultimately led to failure at low cycles for these test specimens.

7.5 Summary

The effects of surface integrity on fatigue performance and damage progression were evaluated in this chapter based on experimental study conducted on AWJ trimmed and CVD Endmill trimmed specimens. Both unnotched and notched (with hole in the centre) types of specimens were tested for evaluation of surface integrity effects on both damage progression and fatigue life from tension-tension cyclic testing.

Loading conditions for fatigue testing of both unnotched and notched specimens were categorized as high, medium and low based on percentage values of ultimate loads/stresses obtained during static testing in chapter 6 for both tension and open hole tension testing.

From a surface integrity perspective, the AWJ trimmed specimens had surface roughness values higher in the longitudinal direction in comparison to CVD Endmill trimmed specimens. In the AWJ trimmed specimens the damage observed after trimming contained streaks and craters along the direction of the Water jet axis. Matrix cracks were also present along with fibre pullouts albeit lower in density. Exit delamination was present with low occurrence of entrance delamination.

In case of CVD endmill trimmed specimens, the surface finish obtained was smoother than that obtained by AWJ trimming. Fibre pullouts were present after trimming and were higher in density in comparison to AWJ trimming. In both AWJ and CVD endmill trimming the fibre pullouts were along the 45 degree plies.

Overall the surface integrity variation between AWJ and CVD endmill trimming was in the basic differences in principles of cutting in the two processes. This resulted in differences in the surface integrity stress concentration factors calculated for the different test specimens trimmed using the 2 processes. For AWJ trimmed surfaces the surface integrity stress concentration factor varied between 1.4 and 2.5 while for CVD endmill trimmed specimens, the variation lay between 1.1 to 1.8.

When tested in the fatigue the unnotched specimens displayed the following stages of damage progression:

Stage 1 – Matrix cracking

Stage 2 – Matrix Fibre interface debonding

Stage 3 – Fibre fracture and delamination

It was observed that the damage mechanism of matrix cracking was present through all 3 stages with the highest magnitude in stage 1. From the data collected it was clear that the progress in damage is slower in stage 2 as compared to stage 1 and 3. This was a function of surface integrity and its stress concentration factor. Overall the CVD endmill trimmed specimens performed slightly better under most conditions and with consistency due to their better surface integrity and its stress concentration factor. The location of most damage initiations and progress was along the 45 degree plies due to higher concentrations of fibre pullouts.

For notched specimens the following stages of damage progression were observed:

Stage 1 – Matrix Cracking

Stage 2 – Matrix Fibre interface debonding, fibre fracture and delamination

Stage 3 – Fibre fracture and delamination

In the case of notched specimens the progress of damage was at an accelerated rate during all stages primarily due to the addition of the stress concentration factor due to the presence of a hole which complements the surface integrity stress concentration factor and causes an accelerated progression of damage and reduction in fatigue life performance. Since the same process was used to drill holes in each specimen, the effect of the drilling process was assumed to be a constant on the specimen performance and only the geometrical presence of the hole was considered as an influence on damage progress and fatigue life performance.

The progress of damage with the increased number of fatigue cycles was plotted as % compliance change Vs. (N) cycles and the rate of damage progress documented. This changing rate of damage progress influences the fatigue performance and ultimate failure and is part of analytical model discussed in chapter 8 which provides predictive modeling for damage progress and fatigue life cycles to failure.

As part of the study of damage progress the damage tolerance of both AWJ trimmed and CVD endmill trimmed specimens was studied and it was found that overall the CVD endmill trimmed specimens had a slightly lower damage tolerance performance in comparison to AWJ trimmed specimens.

Chapter 8 - Phase II Testing - Damage Progression & Fatigue Life Modeling

8.1 Phase II Fatigue Cycling

Testing data and its results were analyzed to study the damage progression in both unnotched and notched test specimens were analyzed and are summarized in this chapter. A damage progression model based on previously proposed models by other researchers is developed taking into account the surface integrity along with the varying applied stress conditions. A fatigue life predictive model is also proposed based on the damage progress model developed in this study. Both models were then validated to the test data obtained as part of this research work.

8.2 Phase II Fatigue Testing – Applied Stress Vs. (N) Cycles Data Plots

Fatigue testing was conducted and data plot for applied stress Vs. (N) cycles for all AWJ Trimmed and CVD Endmill Trimmed test specimens. Data plots were generated for both unnotched testing and notched testing specimens and are shown in figures 8.1 through 8.4

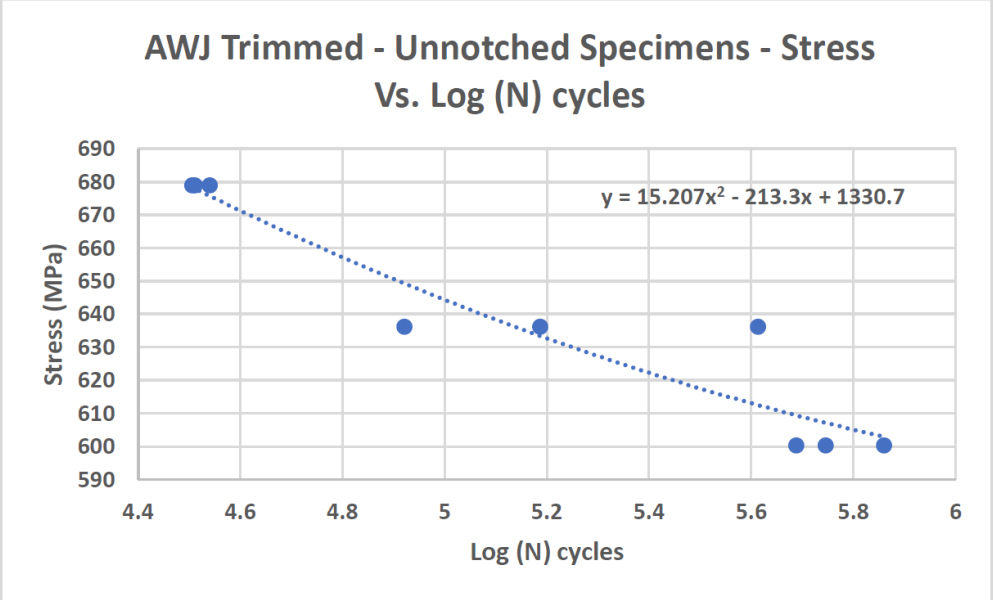

Figure 8.1 AWJ Trimmed – Unnotched Test Specimens – Stress Vs. Log (N) cycles

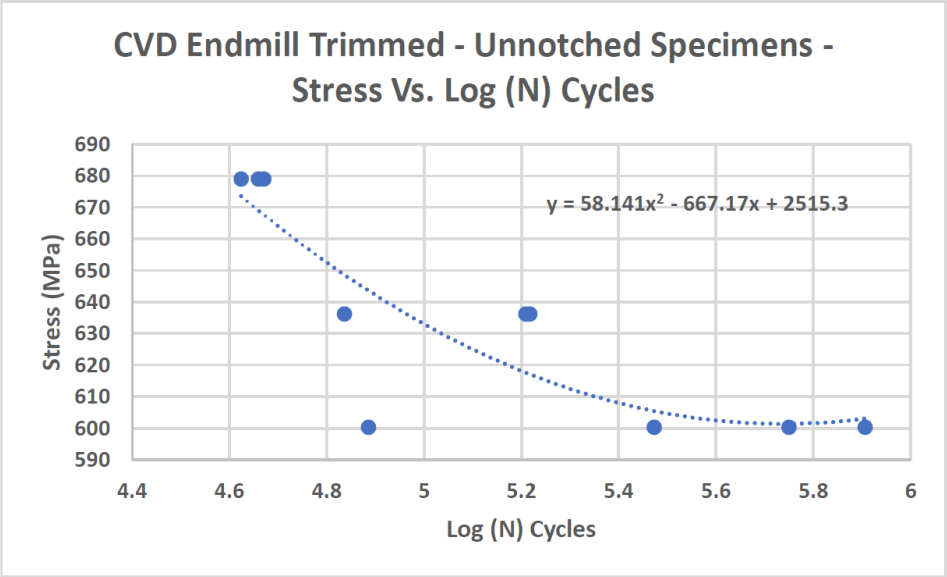

Figure 8.2 CVD Endmill Trimmed – Unnotched Test Specimens – Stress Vs. Log (N) cycles

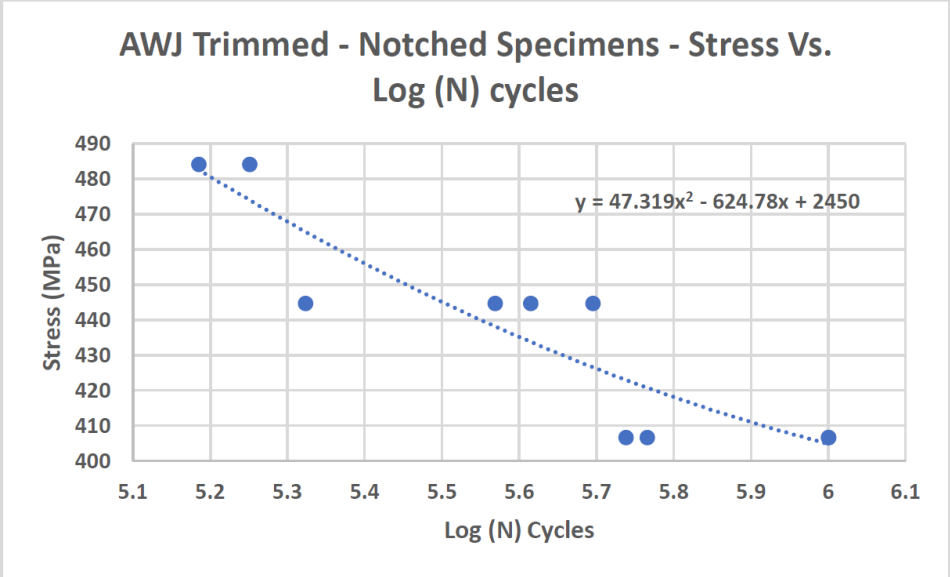

Figure 8.3 AWJ Trimmed – Notched Test Specimens – Stress Vs. Log (N) cycles

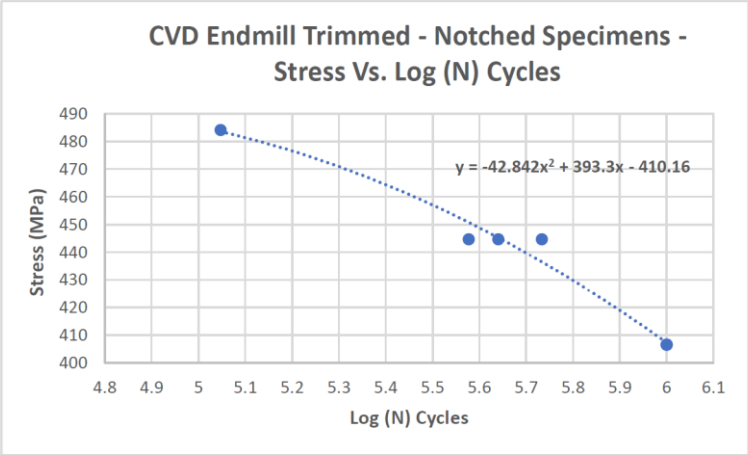

Figure 8.4 CVD Endmill Trimmed – Notched Test Specimens – Stress Vs. Log (N) cycles

8.3 Phase II Fatigue Testing –Damage Progression

Damage progression in unnotched and notched specimens was studied by analyzing the % compliance change versus (N) cycles data and plots.

8.3.1 Damage Progression in Unnotched Specimens Testing

Figure 8.5 shows a plot of damage progression Vs. (N) Cycles for an AWJ unnotched under medium loading.

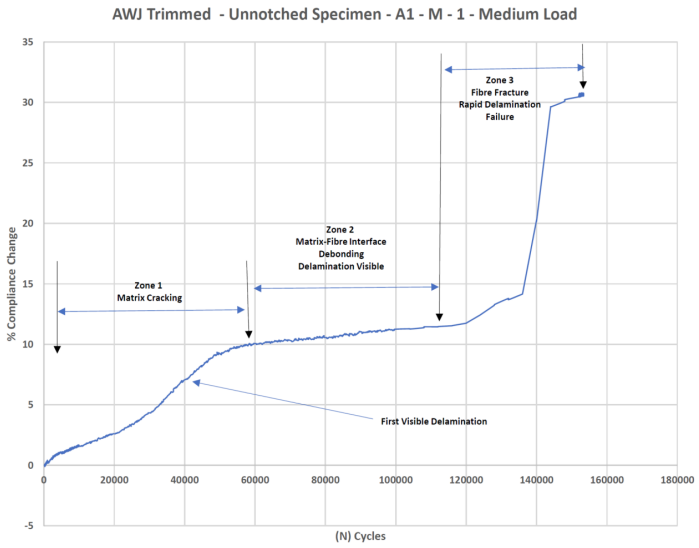

Figure 8.5 Progress of Damage in an AWJ Unnotched Test Specimen

As observed in figure 8.5 the progress of damage in unnotched test specimens is characterized into 3 zones of damage.

Zone 1 – in this zone there is initiation of matrix cracking which starts affecting the residual strength and fatigue life.

Zone 2 – in this zone there is matrix-fibre interface debonding with some delamination and a further reduction in stiffness of the laminate

Zone 3 – in this zone there is fibre fracture along with delamination leading eventually to ultimate failure.

The progress of damage from initiation to propagation and to ultimate failure is dependent on many factors. These factors include applied stress, surface integrity amongst other variables.

In zone 1, matrix cracking initiates with applied tensile loading which varies per the ratio of R = 0.1 between maximum applied stress to minimum applied stress. The variation in surface integrity between AWJ trimmed and CVD Endmill trimmed specimens is represented by the surface integrity stress concentration factor $\left(\bar{K}_t\right)$. For AWJ trimmed specimens the surface finish profile is rougher than CVD Endmill trimmed specimens. The presence of streaks and craters along the direction of water jet which is perpendicular to the load application during testing provides uneven stress distribution area s on the surface which are opportunities of sites for matrix crack initiation. For CVD Endmill trimmed specimens, the higher fibre pullout density areas provide initiation sites for matrix cracking and delamination. As matrix cracking increases, the crack formulation areas

are present both in the inter and intra ply sections of the laminate. Matrix cracks are present through the thickness of the laminate and are independent of the orientation of the fibres.

As matrix cracking density increases with the number of testing cycles and damage increases, there is debonding initiated in the fibre matrix interface. Fibre matrix interface debonding is the dominant damage mode in zone 2 and is influenced by the effective shear modulus (G_{xy}). For most test specimens, zone 2 is predominant and extends over a larger number of test cycles. The increase in damage occurs at a slower rate in zone 2. As the fibres debond from the matrix, the effective load carrying distribution changes with the individual fibres carrying the load with reduced load transfer. Delamination is initiated first mostly in the 45 degree plies and starts propagating through the laminate.

In zone 3, the damage proceeds with brittle fibre fracture occurring primarily in the 0 and 90 degree plies. As the fibres carry the load individually they fracture and the plies start to delaminate. The delamination results in plies coming apart leading to eventual failure of the laminate. In CVD specimens, zone 3 is generally of a shorter occurrence suggesting that damage tolerance is lower in CVD Endmill specimens. This attributed to the higher fibre pullout density present in these specimens due to the endmilling process.

Overall the progress of damage follows a similar path of matrix cracking to fibre matrix interface debonding and then fibre fracture along with delamination and ply separation leading to failure of laminate. This progress is similar for both AWJ and CVD Endmill trimmed specimens but the magnitude varies between the 2 due to a variation between the resultant surface integrity between the 2 different trimming processes.

Overall the CVD Endmill trimmed specimens performed slightly better than the AWJ trimmed specimens in most cases. This was attributed to a better surface integrity resulting in lower surface integrity stress concentration factor in the CVD endmill trimmed specimens.

The following sections discuss the damage progression over the cycles of testing. The data plotted is % change in compliance over the cycles of testing.

$$\% \text{ Change in Compliance} = \left[\frac{\text{Compliance - Baseline Compliance}}{\text{Baseline Compliance}} \right] \text{x } 100 \qquad 8.1$$

Where

Compliance = Compliance recoded at *n* cycles

Baseline Compliance = Compliance recorded at the application of minimum tensile stress

The % change in Compliance is effectively the damage incurred and both terms are used interchangeably going forward.

8.3.2 Damage Progression Model in Unnotched Specimens Testing

As observed from the testing and data collected the progress of damage is a function of many variables as shown below.

$$Damage = f\left[R, k, \overline{K}_t, n\right] \tag{8.2}$$

Where

$R = \frac{\sigma_{\min}}{\sigma_{\min}}$ = ratio of maximum stress to minimum stress

$k = \frac{\sigma_{app}}{\sigma_u}$ = ratio of applied stress to ultimate tensile stress

$\overline{K}_t$ = surface integrity stress concentration factor

n = number of applied fatigue cycles

Using the above relationship and a damage curve (Figure 8.6) for one of the test specimens along with the analysis of the damage curve and equation 8.1 a model was developed for the damage progression in an unnotched test specimen for both AWJ and CVD Endmilled trimmed specimens.

Table 8.1 lists the values of the various factors determined from test conditions and surface integrity of unnotched test specimens.

Type Of Loading	Specimen Number	$R = \frac{\sigma_{min}}{\sigma_{max}}$	$k = \frac{\sigma_{app}}{\sigma_u}$	$\overline{K}_t$
High	A1 – H - 2	0.1	0.89	2.14
High	A1 – H - 3	0.1	0.89	1.92
High	A1 – H - 4	0.1	0.89	2.22
High	B1 – H – 1	0.1	0.89	1.4
High	B1 – H - 2	0.1	0.89	1.35
High	B1 – H -3	0.1	0.89	1.33
Medium	A1 – M - 1	0.1	0.815	1.87
Medium	A1 – M - 2	0.1	0.815	1.64
Medium	A1 – M - 3	0.1	0.815	2.29
Medium	B1 – M - 1	0.1	0.815	1.43
Medium	B1 – M - 2	0.1	0.815	1.31
Medium	B1 – M - 3	0.1	0.815	1.39
Low	A1 – L - 1	0.1	0.76	1.8
Low	A1 – L - 2	0.1	0.76	2.2
Low	A1 – L - 3	0.1	0.76	1.68
Low	B1 – L - 1	0.1	0.76	1.8
Low	B1 – L - 3	0.1	0.76	1.36
Low	B1 – L - 4	0.1	0.76	1.32

Table 8.1 Unnotched Test Specimens, Test Variables

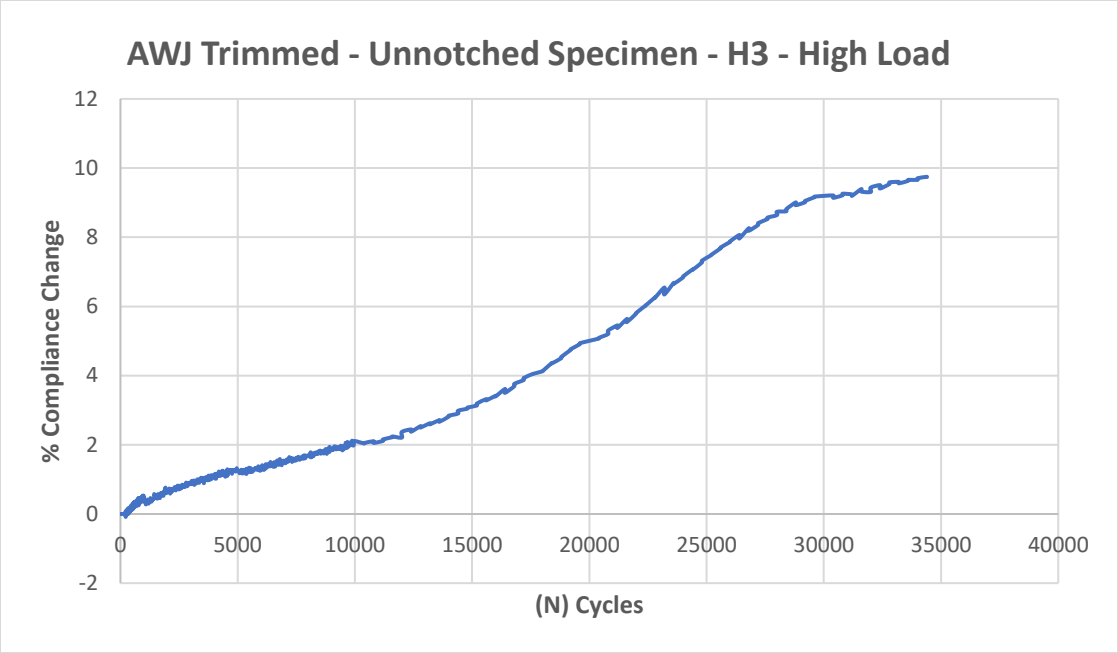

Figure 8.6 Damage curve for AWJ Unnotched High Load Test Specimen

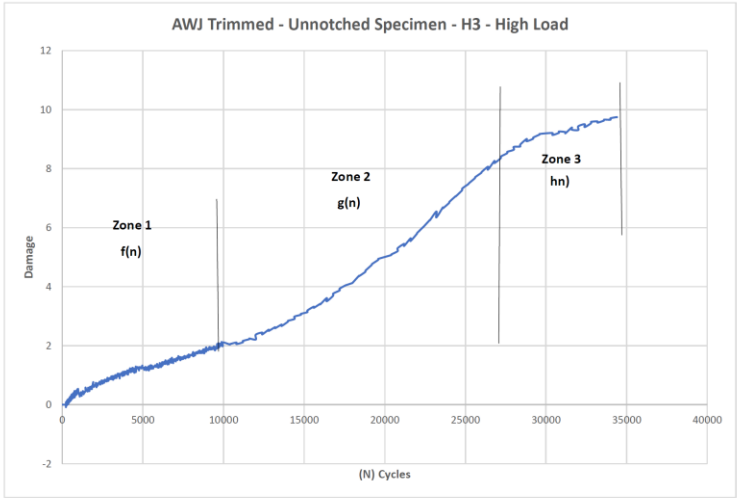

Figure 8.7 Damage Zones for AWJ Unnotched High Load Test Specimen

For the Unnotched High Load specimens, the following observations were made:

a) Zone 1 damage proceeds up to 2 – 3% damage and to less than 15000 cycles
b) Zone 2 damage proceeds at almost a 45 degree line with a fast rising slope and go up to 10% and about 25000 cycles.
c) Zone 3 damage occurs over a short region and there is not much increase in cycles as well as magnitude of damage

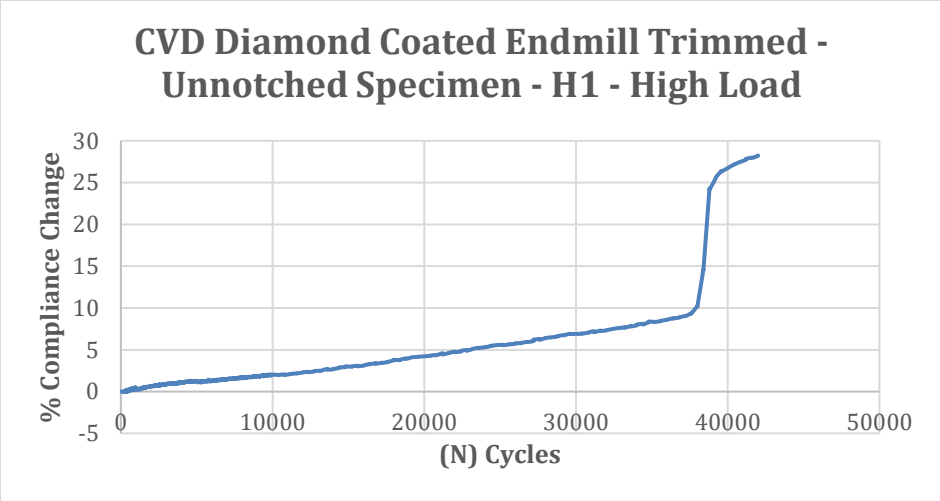

Figure 8.8 Damage Progression for a CVD Endmill Trimmed – High Load Specimen

For medium load test specimens, the following observations were made from the experimental testing.

a) Zone 1 damage proceeds up to 10% damage and to less than 60000 cycles
b) Zone 2 damage proceeds linearly with a slow rising slope and go up to 15% and above and about 140000 cycles.
c) Zone 3 damage occurs over a short region and there is not much increase in cycles as well as magnitude of damage

Figure 8.9 shows the damage progression and damage zones for an AWJ trimmed medium load specimen

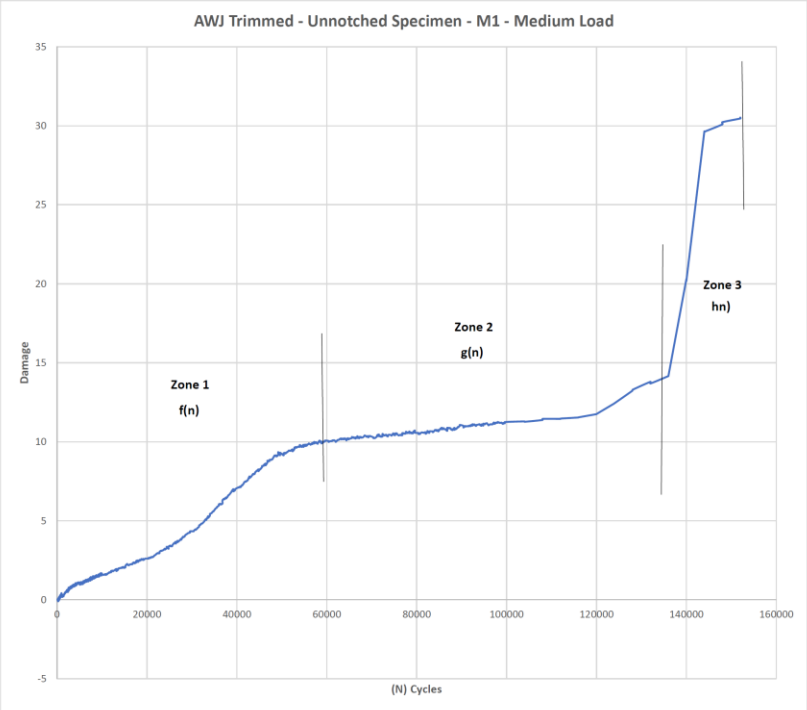

Figure 8.9 Damage zones for AWJ Trimmed Medium Load Specimen

For Low load test specimens, the following observations were made from the experimental testing.

a) Zone 1 damage proceeds up to 10% damage and to less than 100000 cycles
b) Zone 2 damage proceeds linearly with a slow rising slope and go up to 15% and about 500000 cycles.
c) Zone 3 damage occurs over a short region and there is not much increase in cycles as well as magnitude of damage

Figure 8.10 shows the damage progression and damage zones for an AWJ trimmed low load specimen

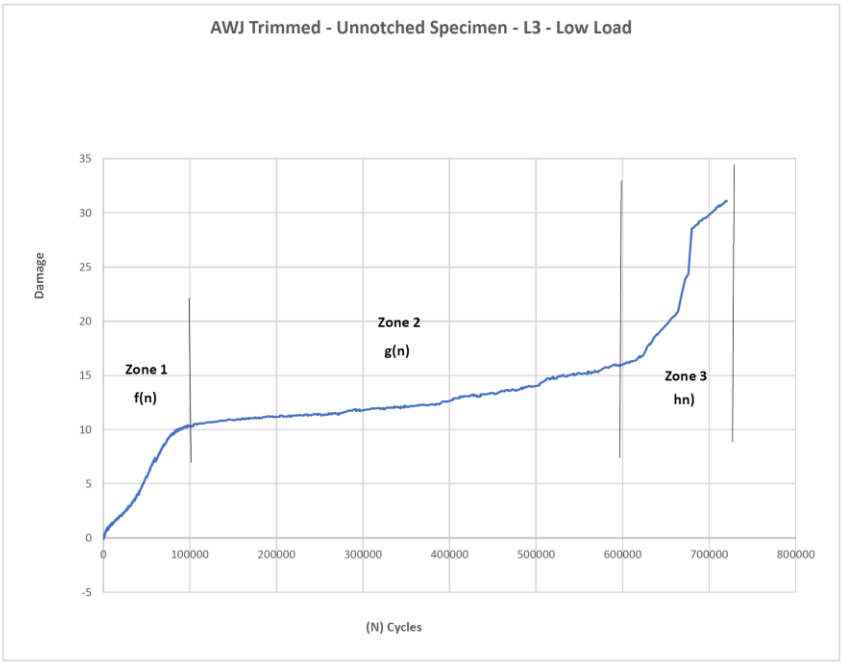

Figure 8.10 Damage zones for AWJ Trimmed Low Load Specimen

For deriving a general model for damage progress in unnotched test specimens the various curves were analyzed and a general 4^{th} degree polynomial model was derived which is shown in equation 8.3

8.4 Analytical Model for Damage Progression in Unnotched Fatigue Testing Specimens

Depending on the type of loading the damage vs. fatigue cycles curves change with the high loading curves being a lower degree polynomial to medium and low loading curves with higher degrees with higher degree polynomials with the degree of polynomials being as follows:
High load curves have a polynomial with degree of 2
Medium load curves have a polynomial with degree of 4
Low load curves have a polynomial with degree of 4

8.4.1 Unnotched High Loading Damage Vs. Fatigue Curves from Testing Vs. Analytical Modeling Curves

For high loading conditions, the analytical model curves are defined by equation 8.3

$$Damage = \alpha(n)^2 + \beta(n) \qquad 8.3$$

Where

$$\alpha = \{(k)(R)\}^{1/3}(10)^{-8}$$

$$\beta = \{\overline{K_t}\}(10)^{-4}$$

8.4.1.1 Unnotched AWJ Trimmed Specimens – Empirical Curves Vs. Analytical Modeled Curves for High Loading

Figure 8.11 shows the Damage Vs. Fatigue Cycles Curve from Testing Vs. Analytical Modeled Curve for Test specimen A1 – H - 2

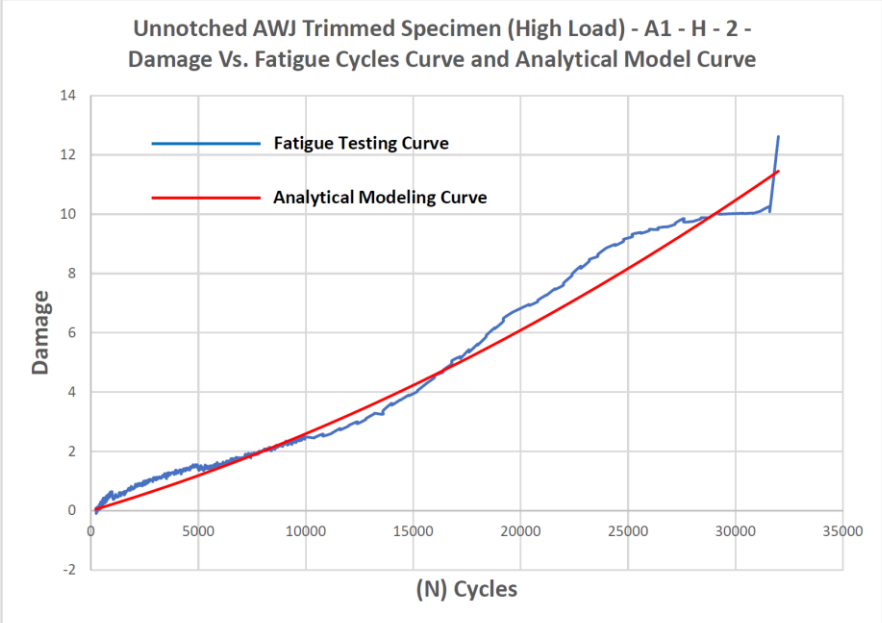

Figure 8.11 Damage Vs. Fatigue Cycles – (Test Specimen – A1 – H – 2) Testing Vs. Analytical Modeling

Figure 8.12 shows the Damage Vs. Fatigue Cycles Curve from Testing Vs. Analytical Modeled Curve for Test specimen A1 – H - 3

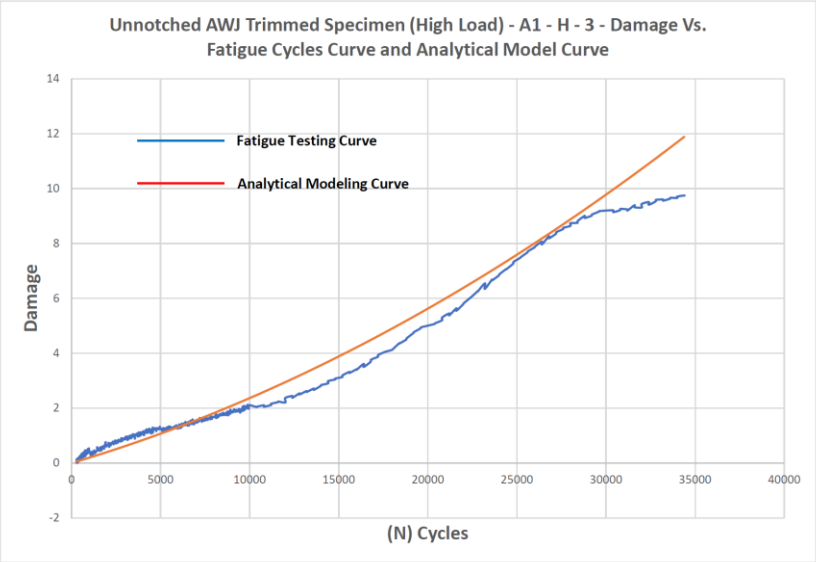

Figure 8.12 Damage Vs. Fatigue Cycles – (Test Specimen – A1 – H – 3) Testing Vs. Analytical Modeling

Figure 8.13 shows the Damage Vs. Fatigue Cycles Curve from Testing Vs. Analytical Modeled Curve for Test specimen A1 – H - 4

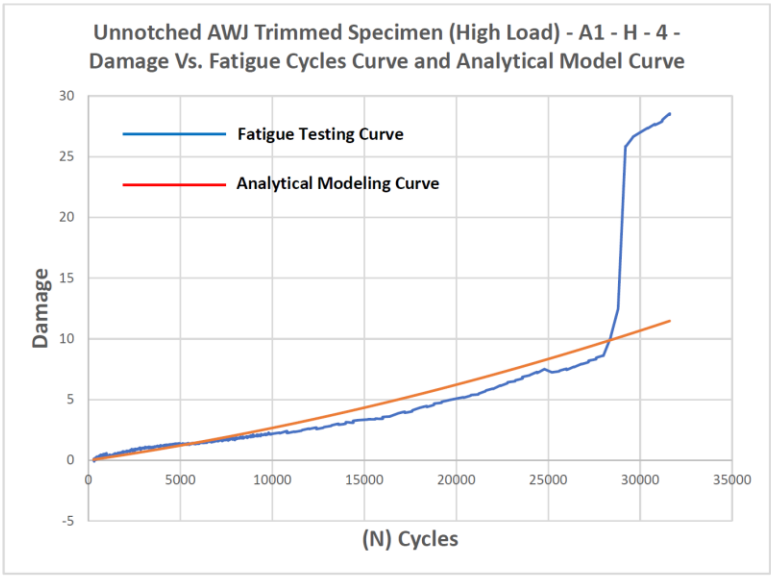

Figure 8.13 Damage Vs. Fatigue Cycles – (Test Specimen – A1 – H – 4) Testing Vs. Analytical Modeling

8.4.1.2 Unnotched CVD Endmill Trimmed Specimens – Empirical Curves Vs. Analytical Modeled Curves for High Loading

Figure 8.14 shows the Damage Vs. Fatigue Cycles Curve from Testing Vs. Analytical Modeled Curve for Test specimen B1 – H - 1

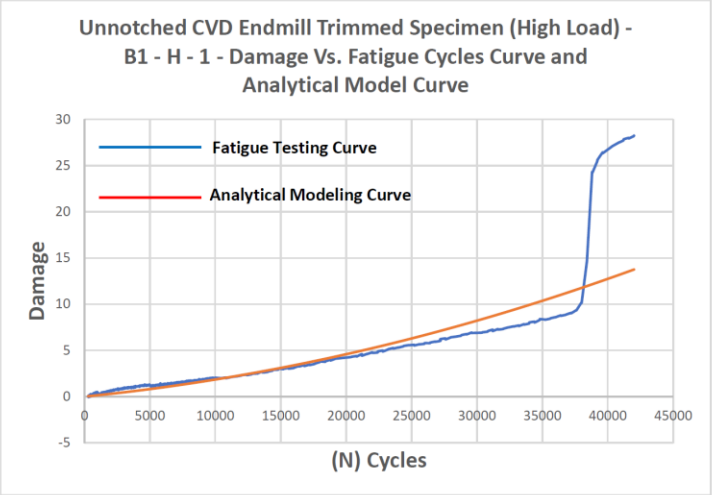

Figure 8.14 Damage Vs. Fatigue Cycles – (Test Specimen – B1 – H – 1) Testing Vs. Analytical Modeling

Figure 8.15 shows the Damage Vs. Fatigue Cycles Curve from Testing Vs. Analytical Modeled Curve for Test specimen B1 – H - 2

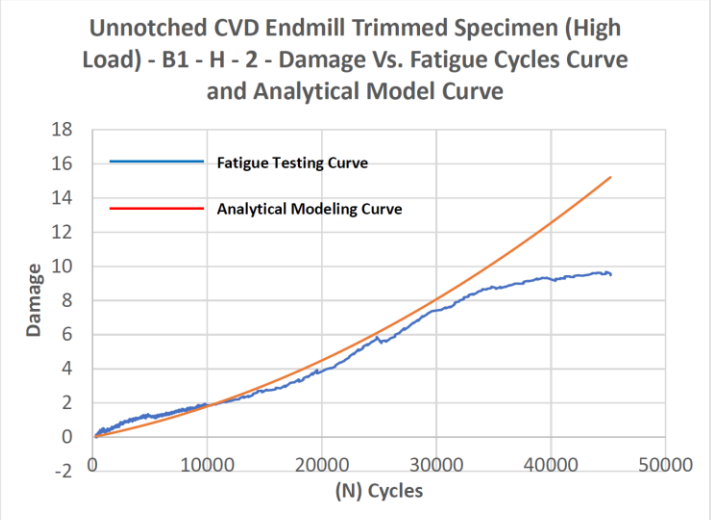

Figure 8.15 Damage Vs. Fatigue Cycles – (Test Specimen – B1 – H – 2) Testing Vs. Analytical Modeling

Figure 8.16 shows the Damage Vs. Fatigue Cycles Curve from Testing Vs. Analytical Modeled Curve for Test specimen B1 – H - 3

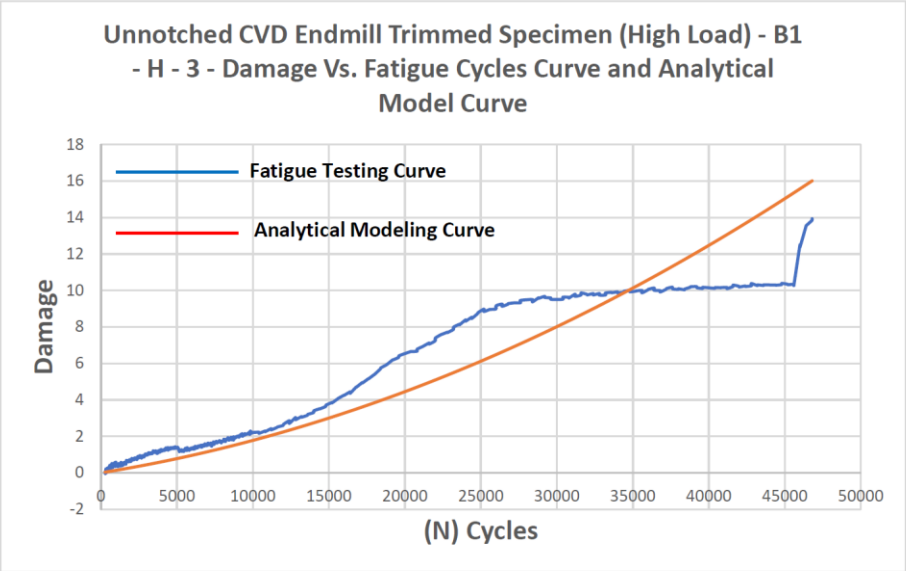

Figure 8.16 Damage Vs. Fatigue Cycles – (Test Specimen – B1 – H – 3) Testing Vs. Analytical Modeling

8.4.2 Unnotched Medium Loading Damage Vs. Fatigue Curves from Testing Vs. Analytical Modeling Curves

For medium loading conditions, the damage vs. fatigue curves are defined by equation 8.4.

$$Damage = \alpha N^4 + \beta N^3 - \delta N^2 + \lambda N \qquad 8.4$$

Where

$\alpha = \{(2)(k)(R)\}(10)^{-20}$

$\beta = (2)\{\overline{K_t}\}(10)^{-16}$

$\delta = (3.5)\{\overline{K_t}\}(10)^{-10}$

$\lambda = \{\overline{K_t}\}(10)^{-4}$

8.4.2.1 Unnotched AWJ Trimmed Specimens – Empirical Curves Vs. Analytical Modeled Curves for Medium Loading

Figure 8.17 shows the Damage Vs. Fatigue Cycles Curve from Testing Vs. Analytical Modeled Curve for Test specimen A1 – M - 1

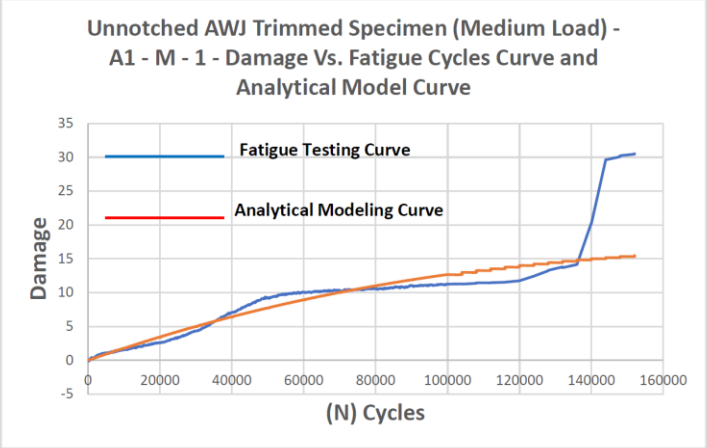

Figure 8.17 Damage Vs. Fatigue Cycles – (Test Specimen – A1 – M – 1) Testing Vs. Analytical Modeling

Figure 8.18 shows the Damage Vs. Fatigue Cycles Curve from Testing Vs. Analytical Modeled Curve for Test specimen A1 – M - 2

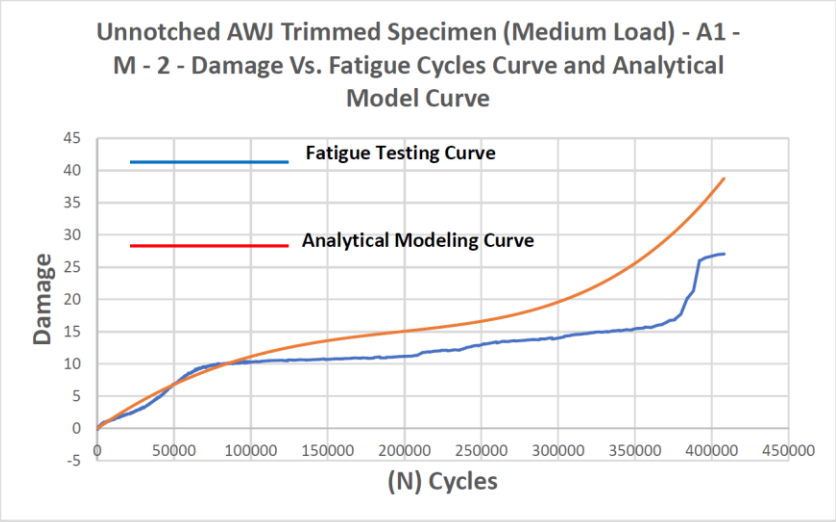

Figure 8.18 Damage Vs. Fatigue Cycles – (Test Specimen – A1 – M – 2) Testing Vs. Analytical Modeling

Figure 8.19 shows the Damage Vs. Fatigue Cycles Curve from Testing Vs. Analytical Modeled Curve for Test specimen A1 – M - 3

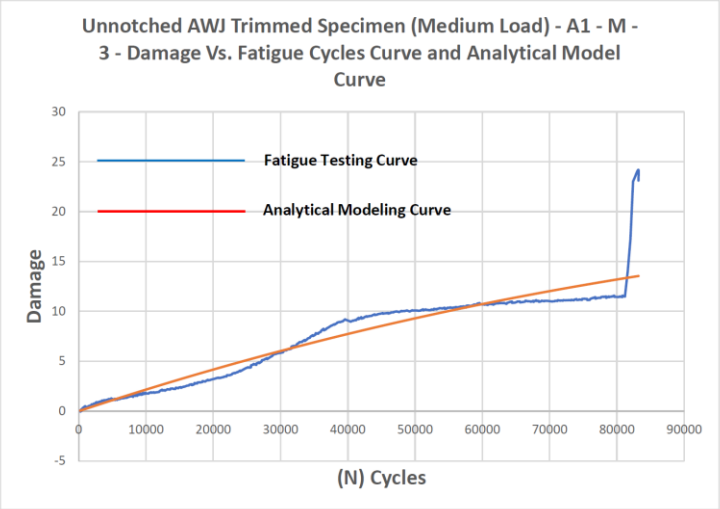

Figure 8.19 Damage Vs. Fatigue Cycles – (Test Specimen – A1 – M – 3) Testing Vs. Analytical Modeling

8.4.2.2 Unnotched CVD Endmill Trimmed Specimens – Empirical Curves Vs. Analytical Modeled Curves for Medium Loading

Figure 8.20 shows the Damage Vs. Fatigue Cycles Curve from Testing Vs. Analytical Modeled Curve for Test specimen B1 – M – 1

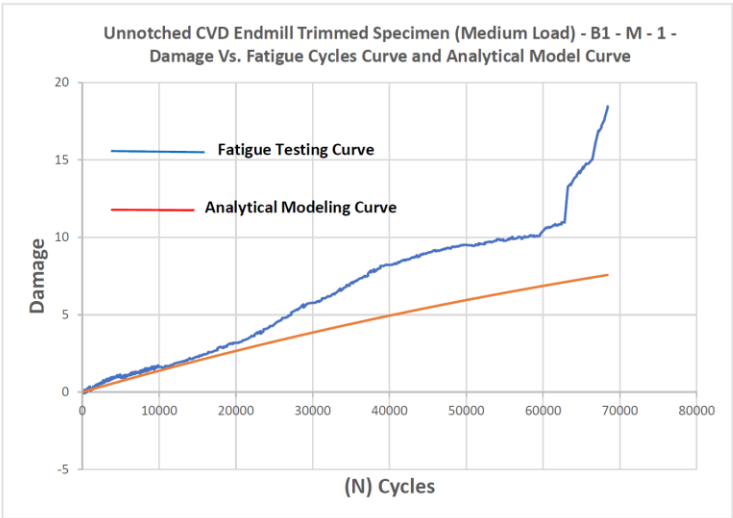

Figure 8.20 Damage Vs. Fatigue Cycles – (Test Specimen – B1 – M – 1) Testing Vs. Analytical Modeling

Figure 8.21 shows the Damage Vs. Fatigue Cycles Curve from Testing Vs. Analytical Modeled Curve for Test specimen B1 – M – 2

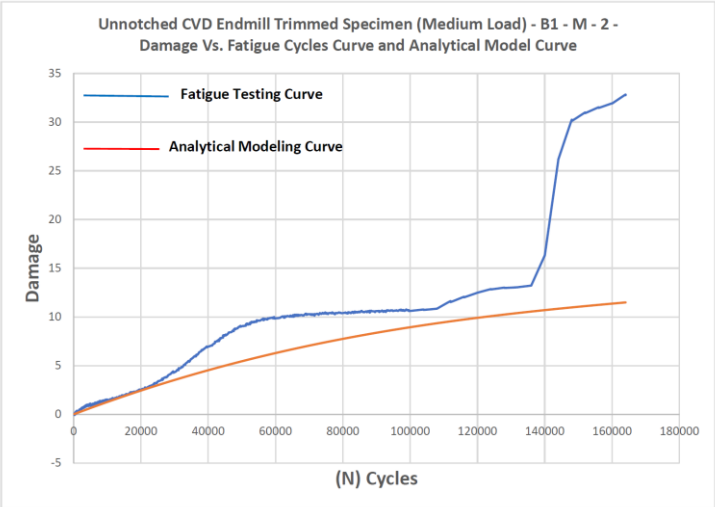

Figure 8.21 Damage Vs. Fatigue Cycles – (Test Specimen – B1 – M – 2) Testing Vs. Analytical Modeling

Figure 8.22 shows the Damage Vs. Fatigue Cycles Curve from Testing Vs. Analytical Modeled Curve for Test specimen B1 – M – 3

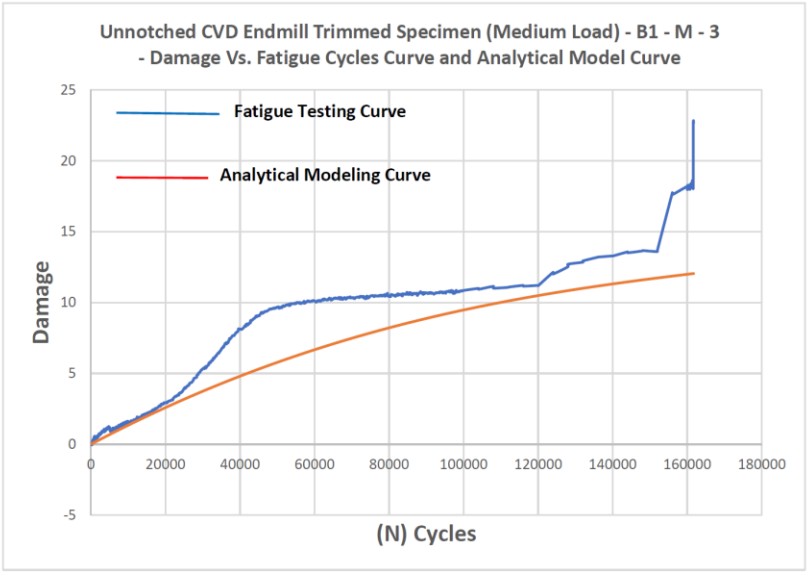

Figure 8.22 Damage Vs. Fatigue Cycles – (Test Specimen – B1 – M – 3) Testing Vs. Analytical Modeling

8.4.3 Unnotched Low Loading Damage Vs. Fatigue Curves from Testing Vs. Analytical Modeling Curves

For medium loading conditions, the damage vs. fatigue curves are defined by equation 8.5.

$$Damage = \alpha N^4 + \beta N^3 - \delta N^2 + \lambda N \qquad 8.5$$

Where

$$\alpha = \{(7)(k)(R)\}(10)^{-21}$$
$$\beta = (k)\{\overline{K_t}\}(10)^{-15}$$
$$\delta = (4.5)\{\overline{K_t}\}(10)^{-10}$$
$$\lambda = \{\overline{K_t}\}(R+1.0)(10)^{-4}$$

8.4.3.1 Unnotched AWJ Trimmed Specimens – Empirical Curves Vs. Analytical Modeled Curves for Low Loading

Figure 8.23 shows the Damage Vs. Fatigue Cycles Curve from Testing Vs. Analytical Modeled Curve for Test specimen A1 – L – 1

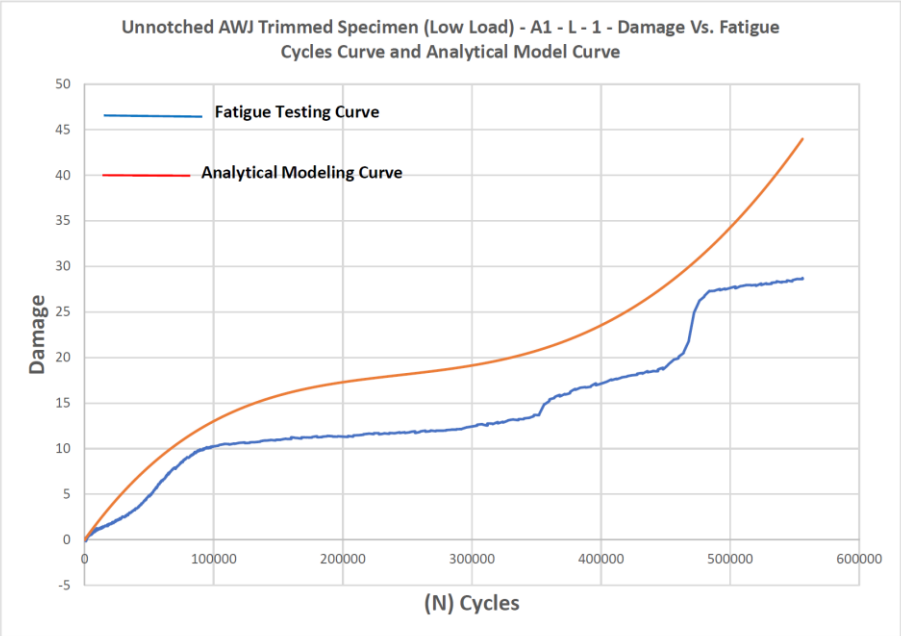

Figure 8.23 Damage Vs. Fatigue Cycles – (Test Specimen – A1 – L– 1) Testing Vs. Analytical Modeling

Figure 8.24 shows the Damage Vs. Fatigue Cycles Curve from Testing Vs. Analytical Modeled Curve for Test specimen A1 – L – 2

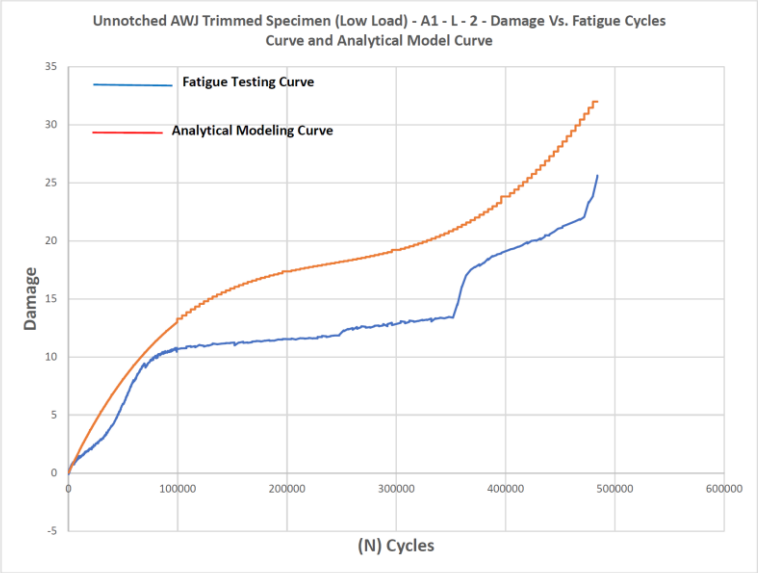

Figure 8.24 Damage Vs. Fatigue Cycles – (Test Specimen – A1 – L– 2) Testing Vs. Analytical Modeling

Figure 8.25 shows the Damage Vs. Fatigue Cycles Curve from Testing Vs. Analytical Modeled Curve for Test specimen A1 – L – 3

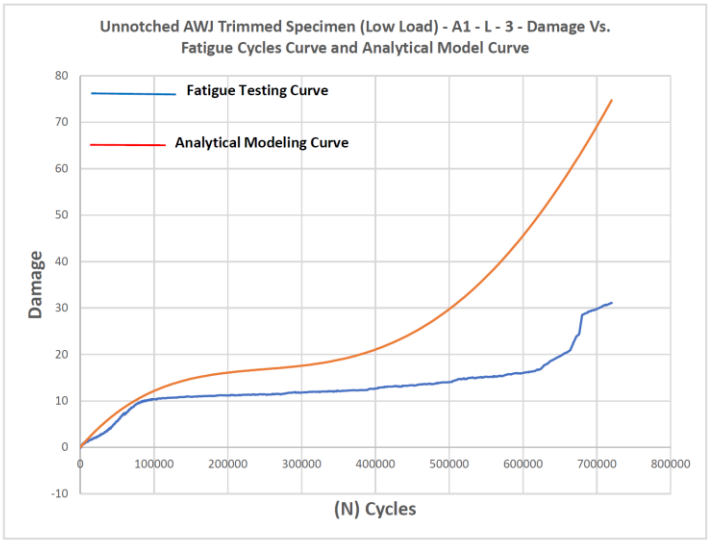

Figure 8.25 Damage Vs. Fatigue Cycles – (Test Specimen – A1 – L– 3) Testing Vs. Analytical Modeling

8.4.3.2 Unnotched CVD Endmill Trimmed Specimens – Empirical Curves Vs. Analytical Modeled Curves for Low Loading

Figure 8.26 shows the Damage Vs. Fatigue Cycles Curve from Testing Vs. Analytical Modeled Curve for Test specimen B1 – L – 1

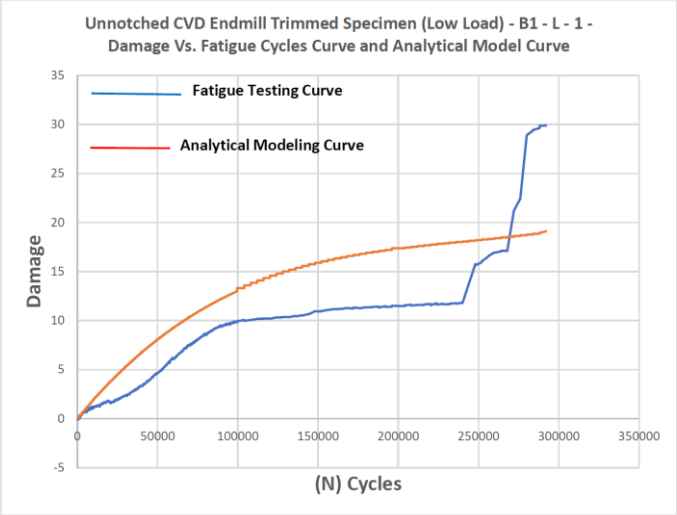

Figure 8.26 Damage Vs. Fatigue Cycles – (Test Specimen – B1 – L– 1) Testing Vs. Analytical Modeling

Figure 8.27 shows the Damage Vs. Fatigue Cycles Curve from Testing Vs. Analytical Modeled Curve for Test specimen B1 – L – 3

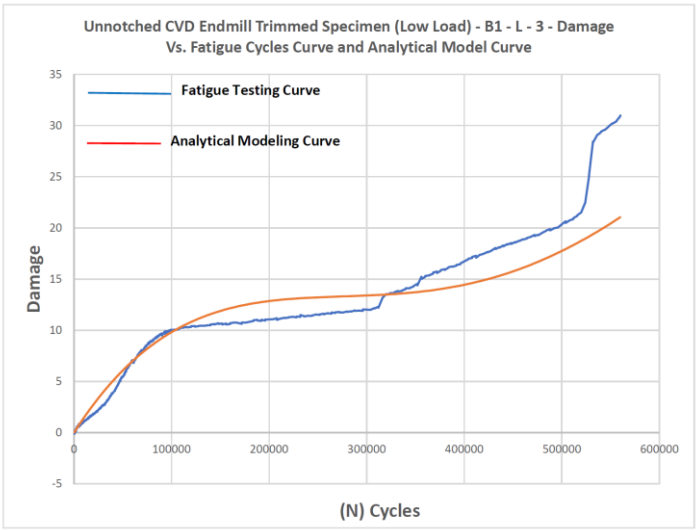

Figure 8.27 Damage Vs. Fatigue Cycles – (Test Specimen – B1 – L– 3) Testing Vs. Analytical Modeling

Figure 8.28 shows the Damage Vs. Fatigue Cycles Curve from Testing Vs. Analytical Modeled Curve for Test specimen B1 – L – 4

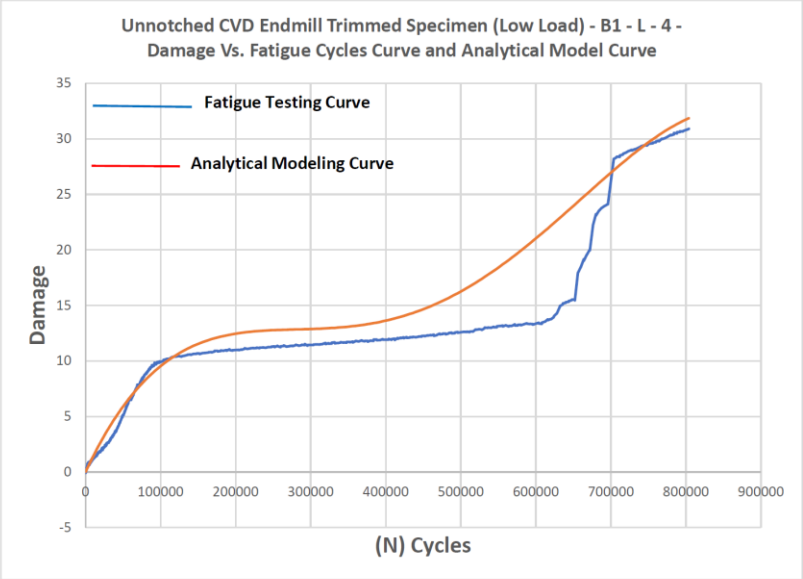

Figure 8.28 Damage Vs. Fatigue Cycles – (Test Specimen – A1 – L– 4) Testing Vs. Analytical Modeling

8.5 Analytical Model for Damage Progression in Notched Fatigue Testing Specimens

Depending on the type of loading the damage vs. fatigue cycles curves change with the high loading curves being a lower degree polynomial to medium and low loading curves with higher degrees with higher degree polynomials with the degree of polynomials being as follows:
High load curves have a polynomial with degree of 2
Medium load curves have a polynomial with degree of 3
Low load curves have a polynomial with degree of 4
The notch is represented by a hole drilled in the centre of the test specimen. The notch sensitivity factor is denoted by K_t and is assumed to have a value of 3.0 for all test conditions. The diameter of the hole is same for all test conditions and is 6.35 mm.

Table 8.2 lists the values of the various factors determined from test conditions and surface integrity of notched test specimens.

Type Of Loading	Specimen Number	$R = \frac{\sigma_{min}}{\sigma_{max}}$	$k = \frac{\sigma_{app}}{\sigma_u}$	$\overline{K}_t$	K_t
High	A2 – H - 3	0.1	0.95	1.89	3.0
High	A2 – H - 4	0.1	0.95	2.1	3.0
High	B2 – H - 1	0.1	0.95	1.2	3.0
High	B2 – H - 2	0.1	0.95	1.56	3.0
High	B2- H - 3	0.1	0.95	1.74	3.0
High	B2 – H - 4	0.1	0.95	1.64	3.0
Medium	A2 – M - 1	0.1	0.87	1.74	3.0
Medium	A2 – M - 2	0.1	0.87	1.81	3.0
Medium	A2 – M - 3	0.1	0.87	1.91	3.0
Medium	A2 – M - 4	0.1	0.87	2.1	3.0
Medium	B2 – M - 1	0.1	0.87	1.77	3.0
Medium	B2 – M - 2	0.1	0.87	1.52	3.0
Medium	B2 – M - 3	0.1	0.87	1.45	3.0
Low	A2 – L - 1	0.1	0.76	2.1	3.0
Low	A2 – L - 2	0.1	0.76	1.88	3.0
Low	A2 – L - 3	0.1	0.76	1.87	3.0
Low	A2 – L - 4	0.1	0.76	2.08	3.0
Low	B2 – L - 1	0.1	0.76	1.53	3.0
Low	B2 – L - 2	0.1	0.76	1.53	3.0
Low	B2 – L - 3	0.1	0.76	1.57	3.0

Table 8.2 Notched Test Specimens, Test Variables

8.5.1 Notched High Loading Damage Vs. Fatigue Curves from Testing Vs. Analytical Modeling Curves

For high loading conditions, the damage vs. fatigue curves are defined by equation 8.6.

$$Damage = \alpha N^2 + \beta N + C \qquad 8.6$$

Where

$$\alpha = \left\{ \frac{(K_t)^3 (R)}{k} \right\} (10)^{-10}$$

$$\beta = \left\{ (4.5)(\overline{K}_t) \right\} (10)^{-5}$$

$$C = \frac{(K_t)^2}{10}$$

8.5.1.1 Notched AWJ Trimmed Specimens – Empirical Curves Vs. Analytical Modeled Curves for High Loading

Figure 8.29 shows the Damage Vs. Fatigue Cycles Curve from Testing Vs. Analytical Modeled Curve for Test specimen A2 – H – 3

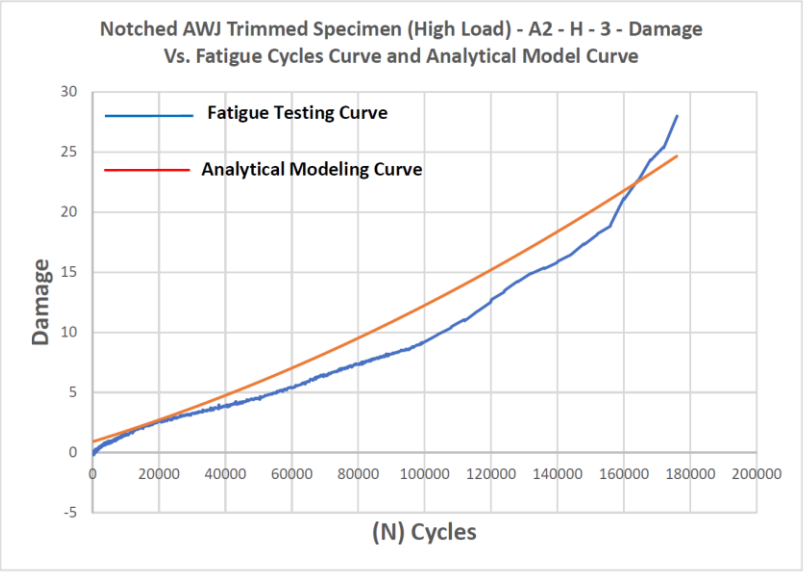

Figure 8.29 Damage Vs. Fatigue Cycles – (Test Specimen – A2 – H – 3) Testing Vs. Analytical Modeling

Figure 8.30 shows the Damage Vs. Fatigue Cycles Curve from Testing Vs. Analytical Modeled Curve for Test specimen A2 – H – 4

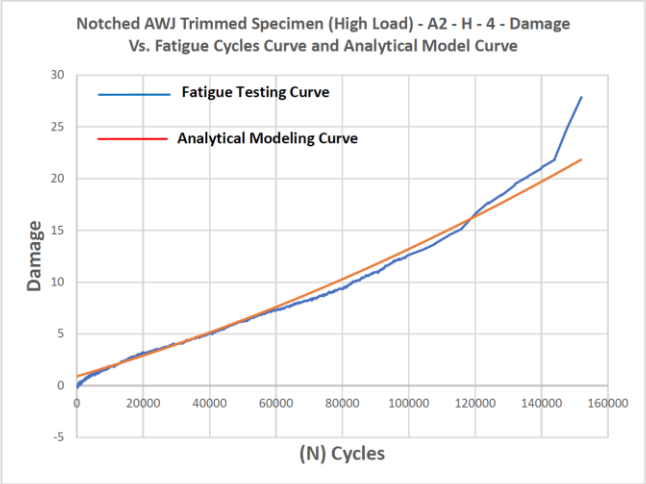

Figure 8.30 Damage Vs. Fatigue Cycles – (Test Specimen – A2 – H – 4) Testing Vs. Analytical Modeling

8.5.1.2 Notched CVD Endmill Trimmed Specimens – Empirical Curves Vs. Analytical Modeled Curves for High Loading

Figure 8.31 shows the Damage Vs. Fatigue Cycles Curve from Testing Vs. Analytical Modeled Curve for Test specimen B2 – H – 1

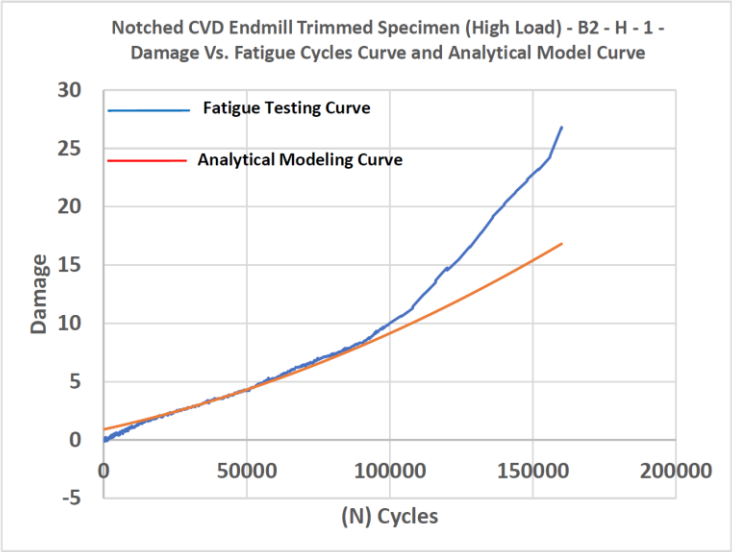

Figure 8.31 Damage Vs. Fatigue Cycles – (Test Specimen – B2 – H – 1) Testing Vs. Analytical Modeling

Figure 8.32 shows the Damage Vs. Fatigue Cycles Curve from Testing Vs. Analytical Modeled Curve for Test specimen B2 – H – 2

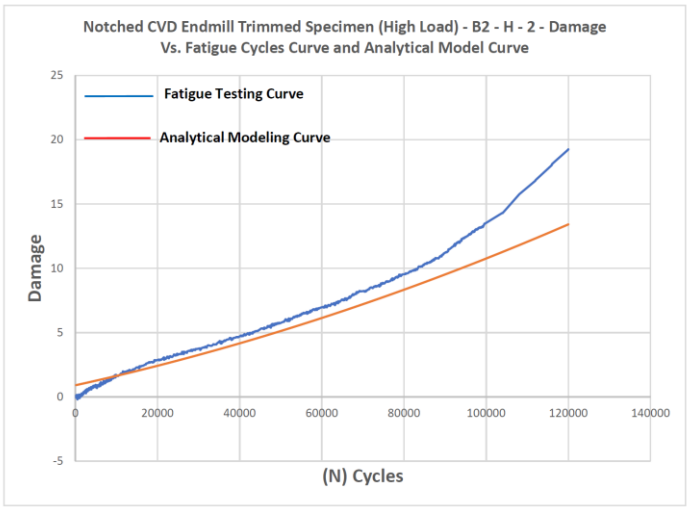

Figure 8.32 Damage Vs. Fatigue Cycles – (Test Specimen – B2 – H – 2) Testing Vs. Analytical Modeling

Figure 8.33 shows the Damage Vs. Fatigue Cycles Curve from Testing Vs. Analytical Modeled Curve for Test specimen B2 – H – 3

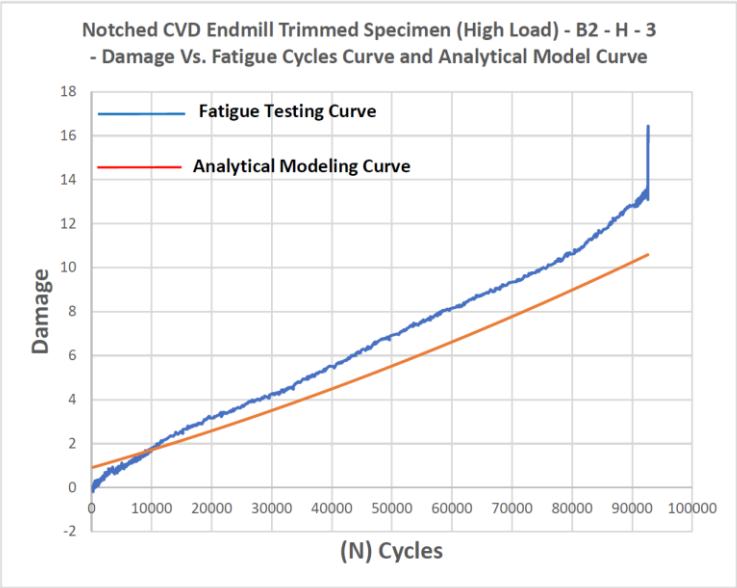

Figure 8.33 Damage Vs. Fatigue Cycles – (Test Specimen – B2 – H – 3) Testing Vs. Analytical Modeling

Figure 8.34 shows the Damage Vs. Fatigue Cycles Curve from Testing Vs. Analytical Modeled Curve for Test specimen B2 – H – 4

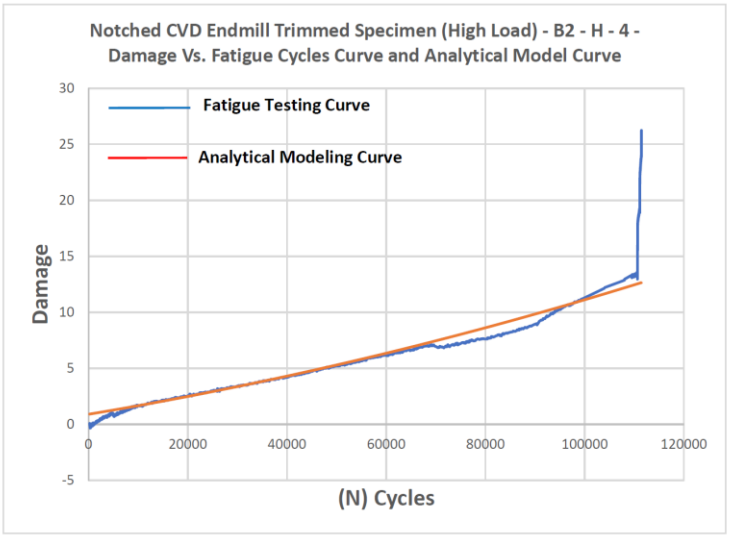

Figure 8.34 Damage Vs. Fatigue Cycles – (Test Specimen – B2 – H – 4) Testing Vs. Analytical Modeling

8.5.2 Notched Medium Loading Damage Vs. Fatigue Curves from Testing Vs. Analytical Modeling Curves

For medium loading conditions, the damage vs. fatigue curves are defined by equation 8.7

$$Damage = \alpha N^3 - \beta N^2 + \delta N \qquad 8.7$$

Where

$$\alpha = \left\{\frac{(K_t)(R)}{k}\right\}(10)^{-15}$$

$$\beta = \left\{(5)(\overline{K}_t)\right\}(10)^{-11}$$

$$\delta = \left\{\frac{(K_t)}{2}\right\}(10)^{-4}$$

8.5.2.1 Notched AWJ Trimmed Specimens – Empirical Curves Vs. Analytical Modeled Curves for Medium Loading

Figure 8.35 shows the Damage Vs. Fatigue Cycles Curve from Testing Vs. Analytical Modeled Curve for Test specimen A2 – M – 1

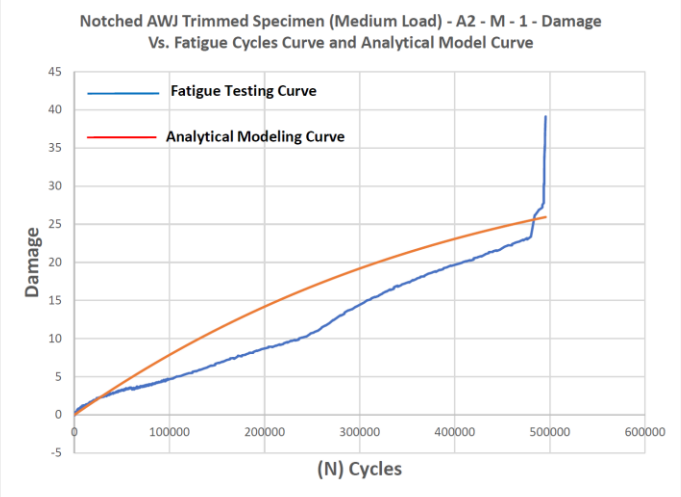

Figure 8.35 Damage Vs. Fatigue Cycles – (Test Specimen – A2 – M – 1) Testing Vs. Analytical Modeling

Figure 8.36 shows the Damage Vs. Fatigue Cycles Curve from Testing Vs. Analytical Modeled Curve for Test specimen A2 – M – 2

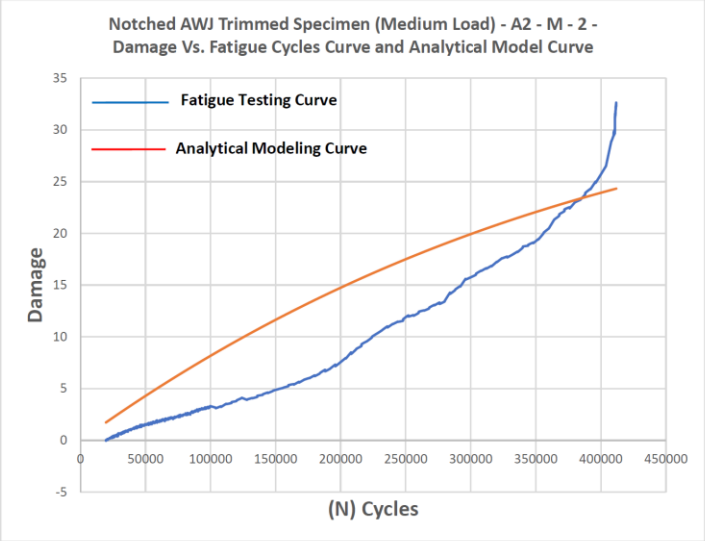

Figure 8.36 Damage Vs. Fatigue Cycles – (Test Specimen – A2 – M – 2) Testing Vs. Analytical Modeling

Figure 8.37 shows the Damage Vs. Fatigue Cycles Curve from Testing Vs. Analytical Modeled Curve for Test specimen A2 – M – 3

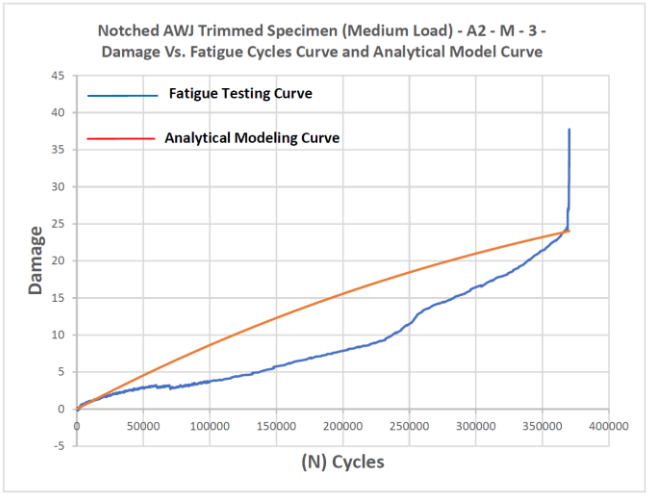

Figure 8.37 Damage Vs. Fatigue Cycles – (Test Specimen – A2 – M – 3) Testing Vs. Analytical Modeling

Figure 8.38 shows the Damage Vs. Fatigue Cycles Curve from Testing Vs. Analytical Modeled Curve for Test specimen A2 – M – 4

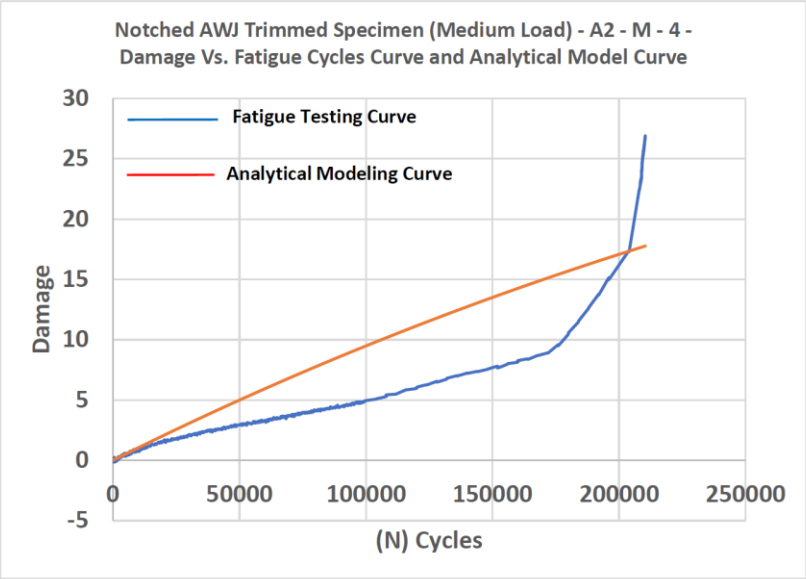

Figure 8.38 Damage Vs. Fatigue Cycles – (Test Specimen – A2 – M – 4) Testing Vs. Analytical Modeling

8.5.2.2 Notched CVD Endmill Trimmed Specimens – Empirical Curves Vs. Analytical Modeled Curves for Medium Loading

Figure 8.39 shows the Damage Vs. Fatigue Cycles Curve from Testing Vs. Analytical Modeled Curve for Test specimen B2 – M – 1

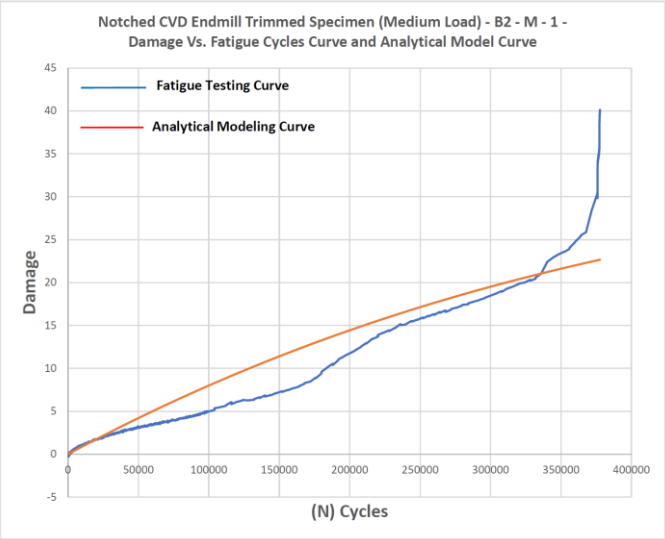

Figure 8.39 Damage Vs. Fatigue Cycles – (Test Specimen – B2 – M – 1) Testing Vs. Analytical Modeling

Figure 8.40 shows the Damage Vs. Fatigue Cycles Curve from Testing Vs. Analytical Modeled Curve for Test specimen B2 – M – 2

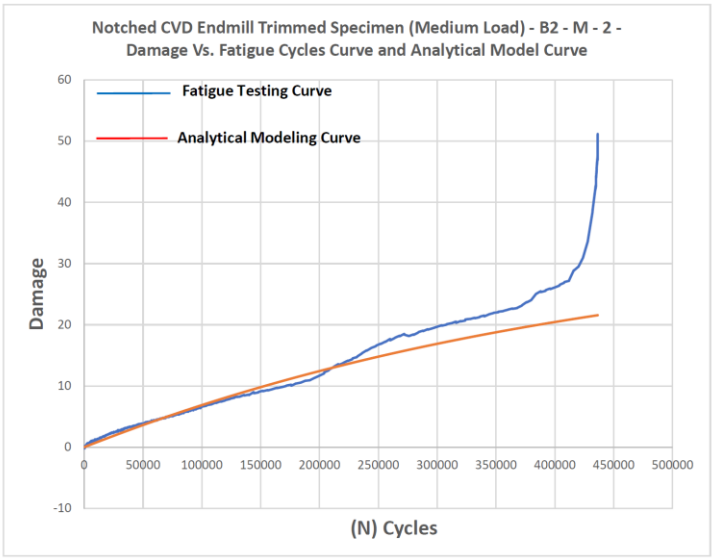

Figure 8.40 Damage Vs. Fatigue Cycles – (Test Specimen – B2 – M – 2) Testing Vs. Analytical Modeling

Figure 8.41 shows the Damage Vs. Fatigue Cycles Curve from Testing Vs. Analytical Modeled Curve for Test specimen B2 – M – 3

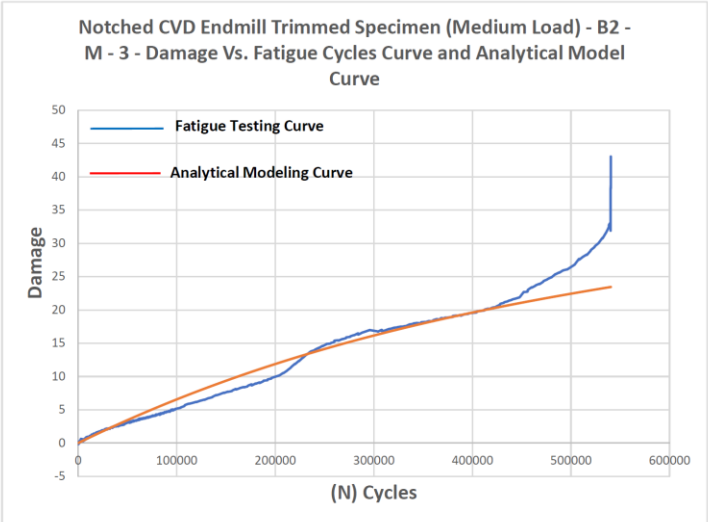

Figure 8.41 Damage Vs. Fatigue Cycles – (Test Specimen – B2 – M – 3) Testing Vs. Analytical Modeling

8.5.3 Notched Low Loading Damage Vs. Fatigue Curves from Testing Vs. Analytical Modeling Curves

For Low loading conditions, the damage vs. fatigue curves are defined by equation 8.8.

$$Damage = \alpha N^4 - \beta N^3 + \delta N^2 + \lambda N \qquad 8.8$$

Where

$$\alpha = \{(K_t)(R)(k)\}(10^{-22})$$
$$\beta = \{(K_t)(k)\}(10^{-17})$$
$$\delta = \{(1.5)(\overline{K}_t)(k)\}(10^{-11})$$
$$\lambda = \frac{\{(\overline{K}_t)(k)\}}{1.5}(10^{-5})$$

8.5.3.1 Notched AWJ Trimmed Specimens – Empirical Curves Vs. Analytical Modeled Curves for Low Loading

Figure 8.42 shows the Damage Vs. Fatigue Cycles Curve from Testing Vs. Analytical Modeled Curve for Test specimen A2 – L – 1

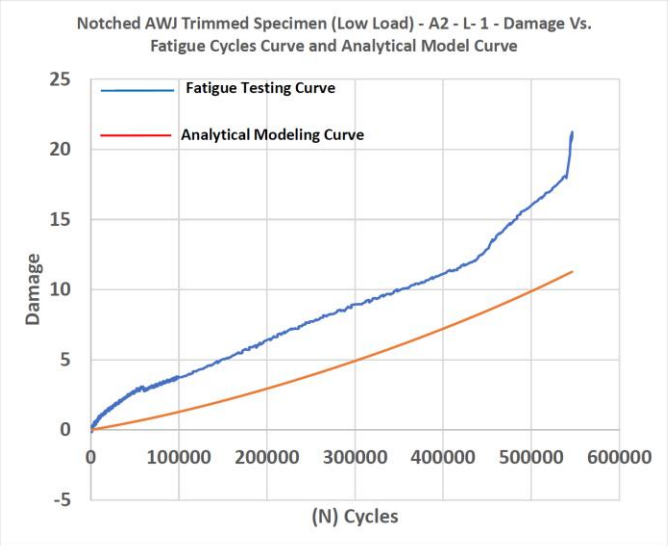

Figure 8.42 Damage Vs. Fatigue Cycles – (Test Specimen – A2 – L – 1) Testing Vs. Analytical Modeling

Figure 8.43 shows the Damage Vs. Fatigue Cycles Curve from Testing Vs. Analytical Modeled Curve for Test specimen A2 – L – 2

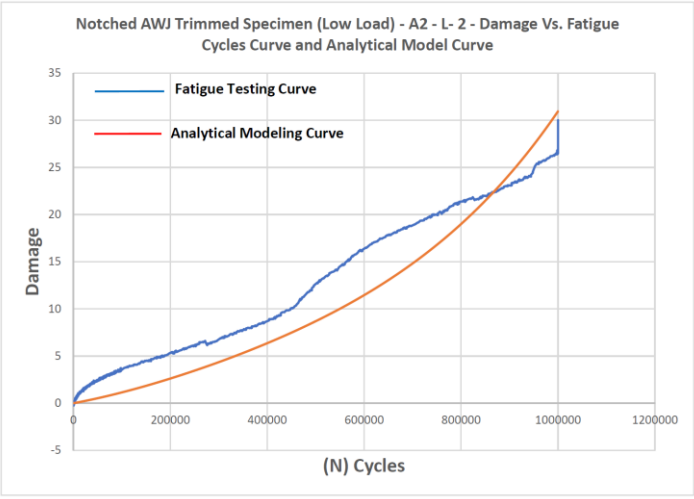

Figure 8.43 Damage Vs. Fatigue Cycles – (Test Specimen – A2 – L – 2) Testing Vs. Analytical Modeling

Figure 8.44 shows the Damage Vs. Fatigue Cycles Curve from Testing Vs. Analytical Modeled Curve for Test specimen A2 – L – 3

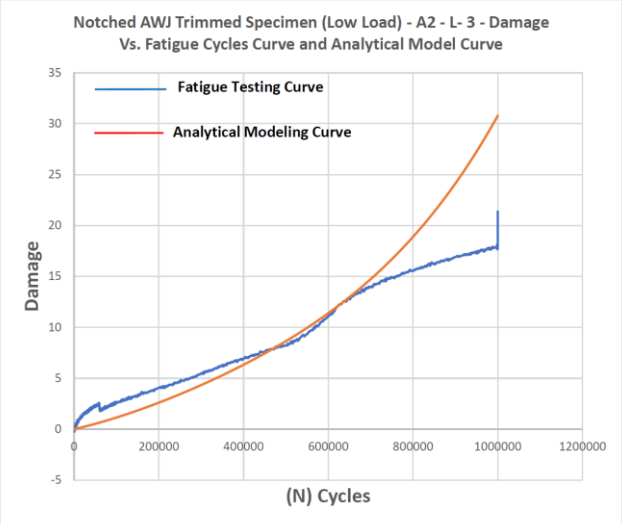

Figure 8.44 Damage Vs. Fatigue Cycles – (Test Specimen – A2 – L – 3) Testing Vs. Analytical Modeling

Figure 8.45 shows the Damage Vs. Fatigue Cycles Curve from Testing Vs. Analytical Modeled Curve for Test specimen A2 – L – 4

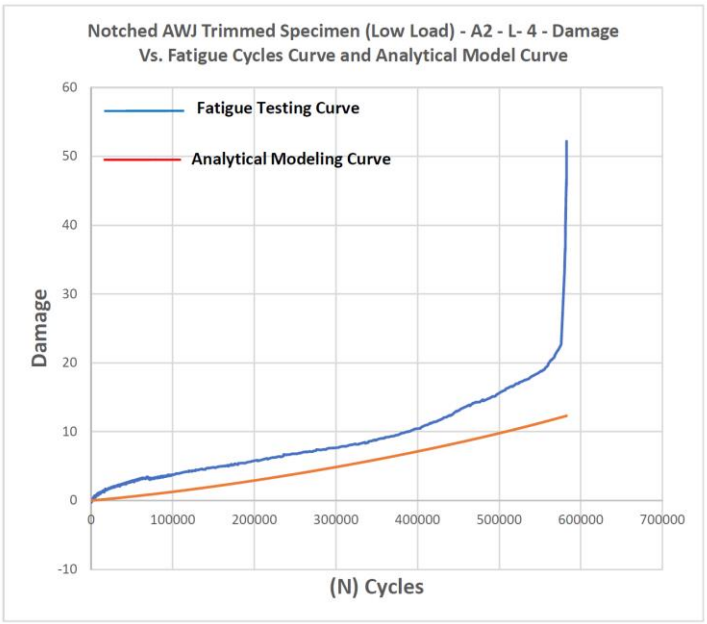

Figure 8.45 Damage Vs. Fatigue Cycles – (Test Specimen – A2 – L – 4) Testing Vs. Analytical Modeling

8.5.3.2 Notched CVD Endmill Trimmed Specimens – Empirical Curves Vs. Analytical Modeled Curves for Low Loading

Figure 8.46 shows the Damage Vs. Fatigue Cycles Curve from Testing Vs. Analytical Modeled Curve for Test specimen B2 – L – 1

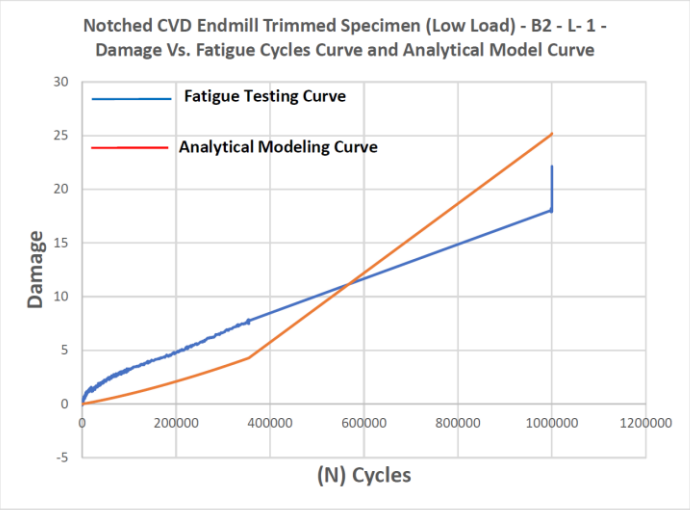

Figure 8.46 Damage Vs. Fatigue Cycles – (Test Specimen – B2 – L – 1) Testing Vs. Analytical Modeling

Figure 8.47 shows the Damage Vs. Fatigue Cycles Curve from Testing Vs. Analytical Modeled Curve for Test specimen B2 – L – 2

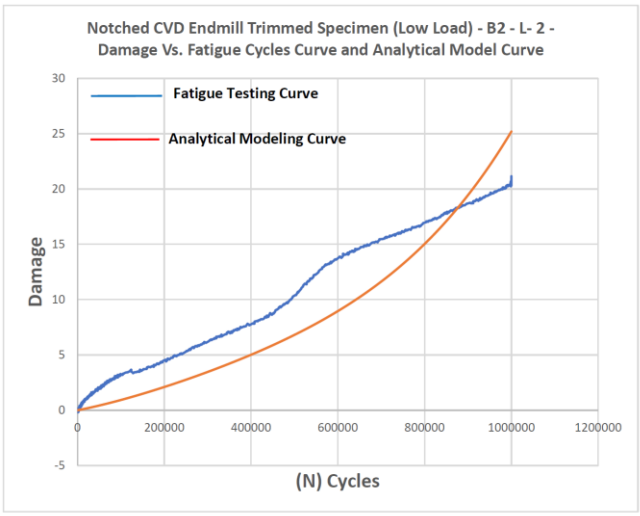

Figure 8.47 Damage Vs. Fatigue Cycles – (Test Specimen – B2 – L – 2) Testing Vs. Analytical Modeling

Figure 8.48 shows the Damage Vs. Fatigue Cycles Curve from Testing Vs. Analytical Modeled Curve for Test specimen B2 – L – 3

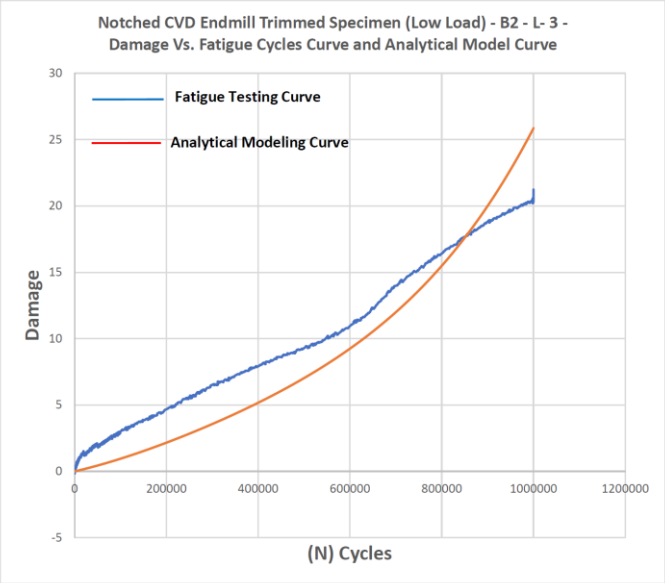

Figure 8.48 Damage Vs. Fatigue Cycles – (Test Specimen – B2 – L – 3) Testing Vs. Analytical Modeling

8.6 Discussion and Summary

As discussed previously in the chapter, the progress of damage from initiation to propagation and to ultimate failure is dependent on many factors. These factors include applied stress, surface integrity amongst other variables.

Damage includes matrix cracking, fibre matrix debonding, fibre pullouts, delamination and eventually complete failure and collapse of the laminate. Matrix cracking initiates with applied tensile loading which varies per the ratio of R = 0.1 between maximum applied stress to minimum applied stress. This is further amplified in notched specimens due to the notch sensitivity factor (K_t). The variation in surface integrity between AWJ trimmed and CVD Endmill trimmed specimens is represented by the surface integrity stress concentration factor $\left(\bar{K}_t\right)$ is a contributing factor in the fibre related damage along with delaminations and the collapse of the laminate.

The following factors contribute to the damage initiation and propagation under fatigue loading conditions.

Damage is represented as a function of the following specimen conditions and is shown in equation 8.9 and 8.10 for unnotched and notched specimens.

$$Damage = f\left[R, k, \overline{K}_t, n\right] \quad 8.9$$

$$Damage = f\left[R, k, \overline{K}_t, K_t, n\right] \quad 8.10$$

Where

$R = \frac{\sigma_{\min}}{\sigma_{\min}}$ = ratio of maximum stress to minimum stress

$k = \frac{\sigma_{app}}{\sigma_u}$ = ratio of applied stress to ultimate tensile stress

$\overline{K}_t$ = surface integrity stress concentration factor

K_t = notch sensitivity factor

n = number of applied fatigue cycles

Models for High Loading Conditions

The analytical models for high loading conditions are generally represented by a 2nd degree polynomial with the coefficients being function of the factors listed above. The primary coefficients are a function of $R = \frac{\sigma_{\min}}{\sigma_{\min}}$, $k = \frac{\sigma_{app}}{\sigma_u}$, K_t while the secondary coefficients and constant are a function of $\overline{K}_t$ and K_t.

The models in both cases of unnotched and notched specimens predict the damage closer to the damage data collected during empirical testing. The damage curves are aligned closely during the initial loading conditions but closer to failure they deviate with the analytical model predicting lower damage closer to failure. This implies that the propagation of damage at higher loads cannot be predicted well closer to failure of the laminate. This is usually not a concern as

service conditions with higher loadings are generally not utilized in most industries especially in the aerospace industry.

Models for Medium Loading Conditions

The analytical models for medium loading conditions are generally represented by a 3rd or 4th degree polynomial with the coefficients being function of the factors listed in equations 8.9 and 8.10. The primary coefficients are a function of $R = \frac{\sigma_{\min}}{\sigma_{\min}}$, $k = \frac{\sigma_{app}}{\sigma_u}$, K_t while the secondary coefficients and constant are a function of $\overline{K}_t$ and K_t.

The models in both cases of unnotched and notched specimens predict the damage closer to the damage data collected during empirical testing. The damage curves are aligned not very well closely during the initial loading conditions and they deviate with the analytical model predicting higher damage through the complete cycling process. While the models do predict higher damage at equivalent cycles, it can result in a very conservative design resulting in lower than expected economic performance. The models do predict failure closer to that observed during the empirical testing.

Models for Low Loading Conditions

The analytical models for low loading conditions are generally represented by a 4th degree polynomial with the coefficients being function of the factors listed in equations 8.9 and 8.10. The primary coefficients are a function of $R = \frac{\sigma_{\min}}{\sigma_{\min}}$, $k = \frac{\sigma_{app}}{\sigma_u}$, K_t while the secondary coefficients and constant are a function of, k, $\overline{K}_t$ and K_t.

The models in both cases of unnotched and notched specimens predict the damage slightly lower to the damage data collected during empirical testing. The damage curves are aligned not very well closely during the initial loading conditions and they deviate with the analytical model predicting lower damage through the complete cycling process. While the models do predict lower damage at equivalent cycles, it can result in an aggressive design resulting in early failures. For this reason, a factor of safety should be used coupled to the analytical model.

Alternate Modeling Approach

An alternative approach to modeling the progression of damage versus the fatigue cycles is to normalize the data at least on one of the axes. This helps bring the curves of varying loading conditions closer together with similar profiles and hence the modeling becomes stable and coincidental. Figures 8.49 through 8.52 show the plots of the data for the normalized values. Damage is plotted on the vertical axis defined as percentage change in compliance and the logarithmic values of cycles is plotted on the horizontal axis.

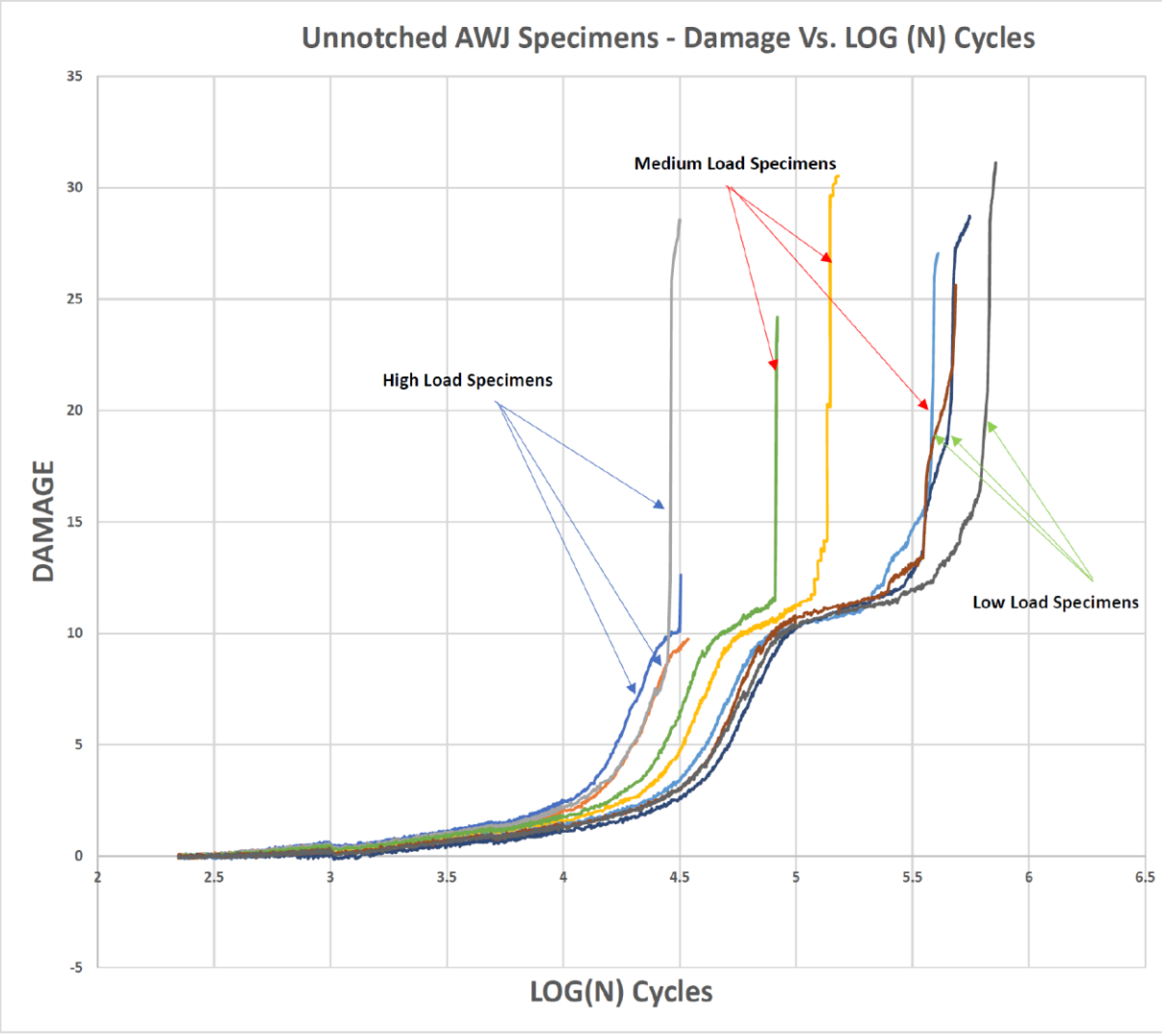

Figure 8.49 Unnotched AWJ Trimmed Specimens, Damage Vs. Log (N) Cycles

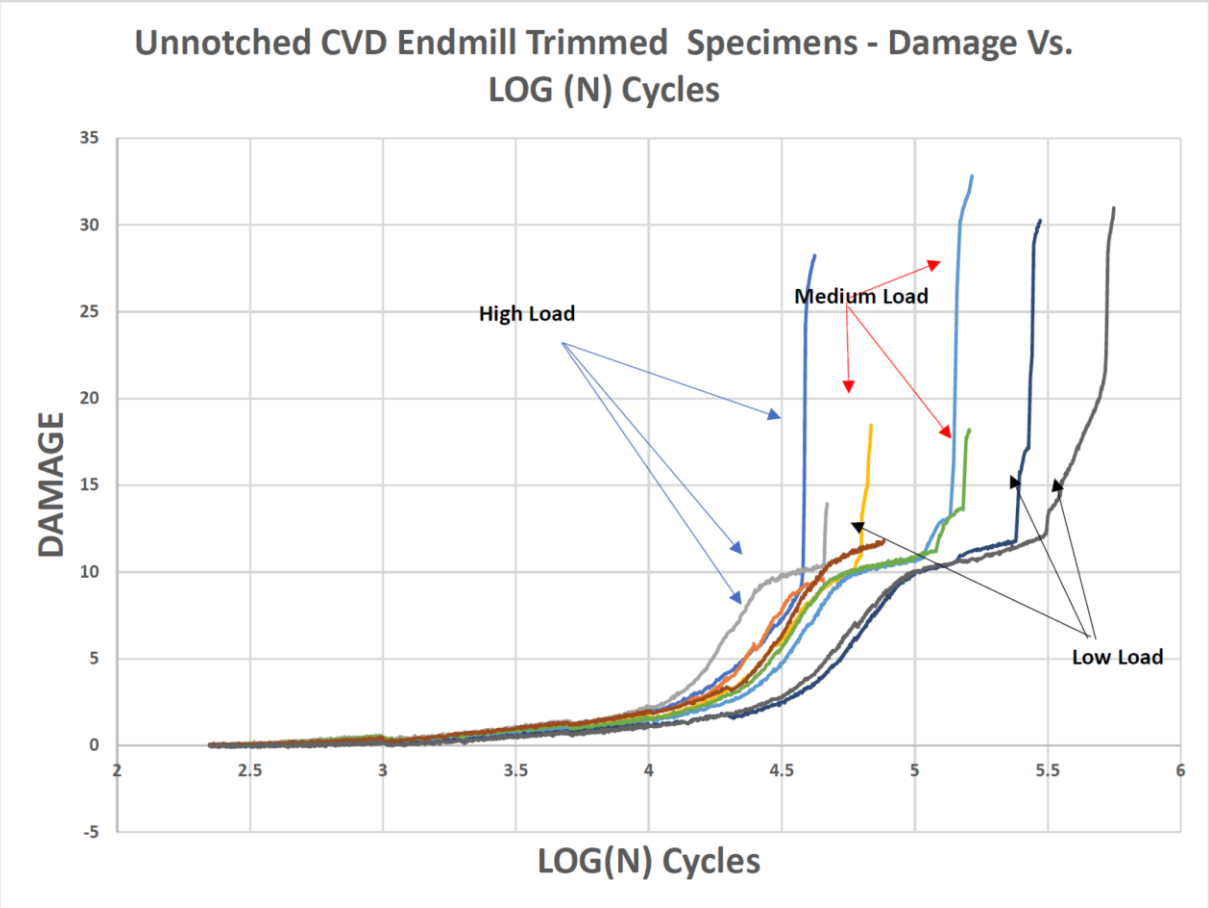

Figure 8.50 Unnotched CVD Endmill Trimmed Specimens, Damage Vs. Log (N) Cycles

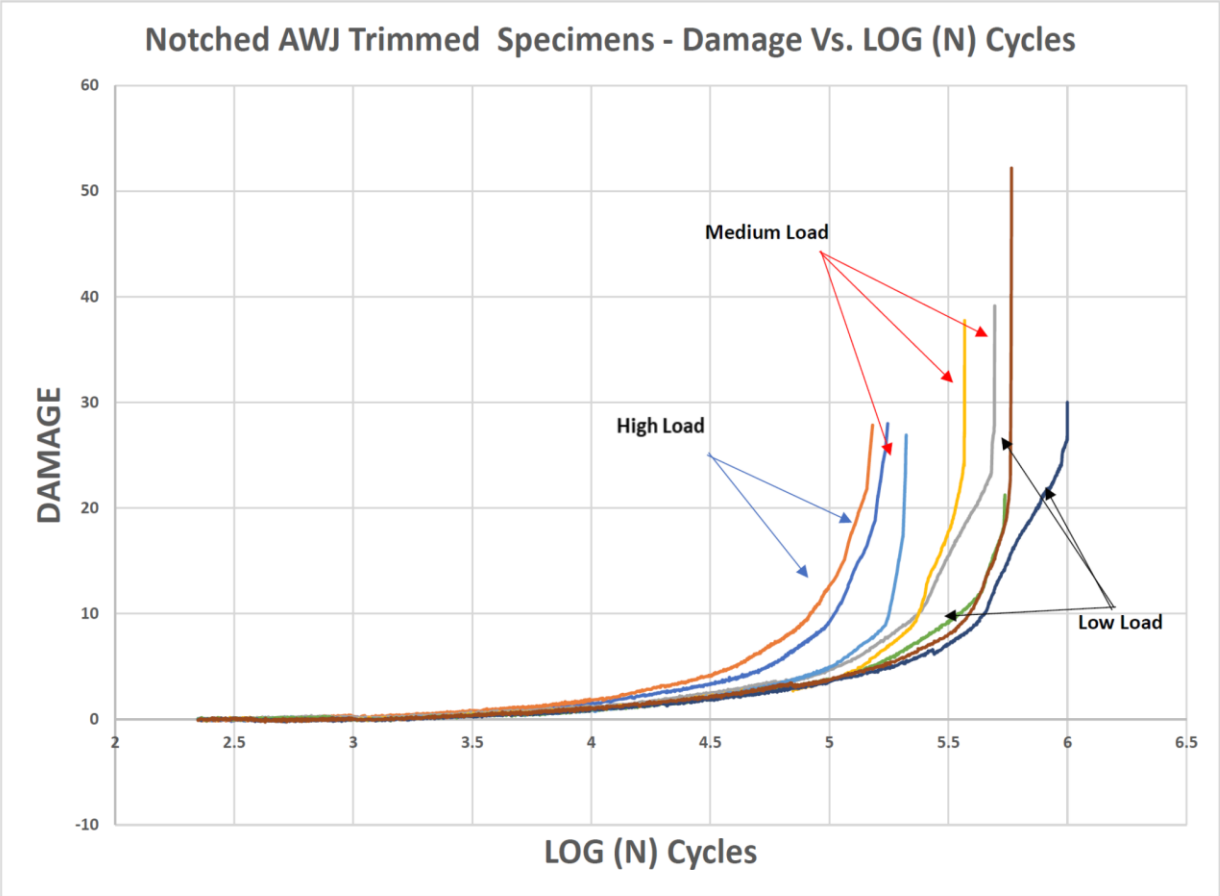

Figure 8.51 Notched AWJ Trimmed Specimens, Damage Vs. Log (N) Cycles

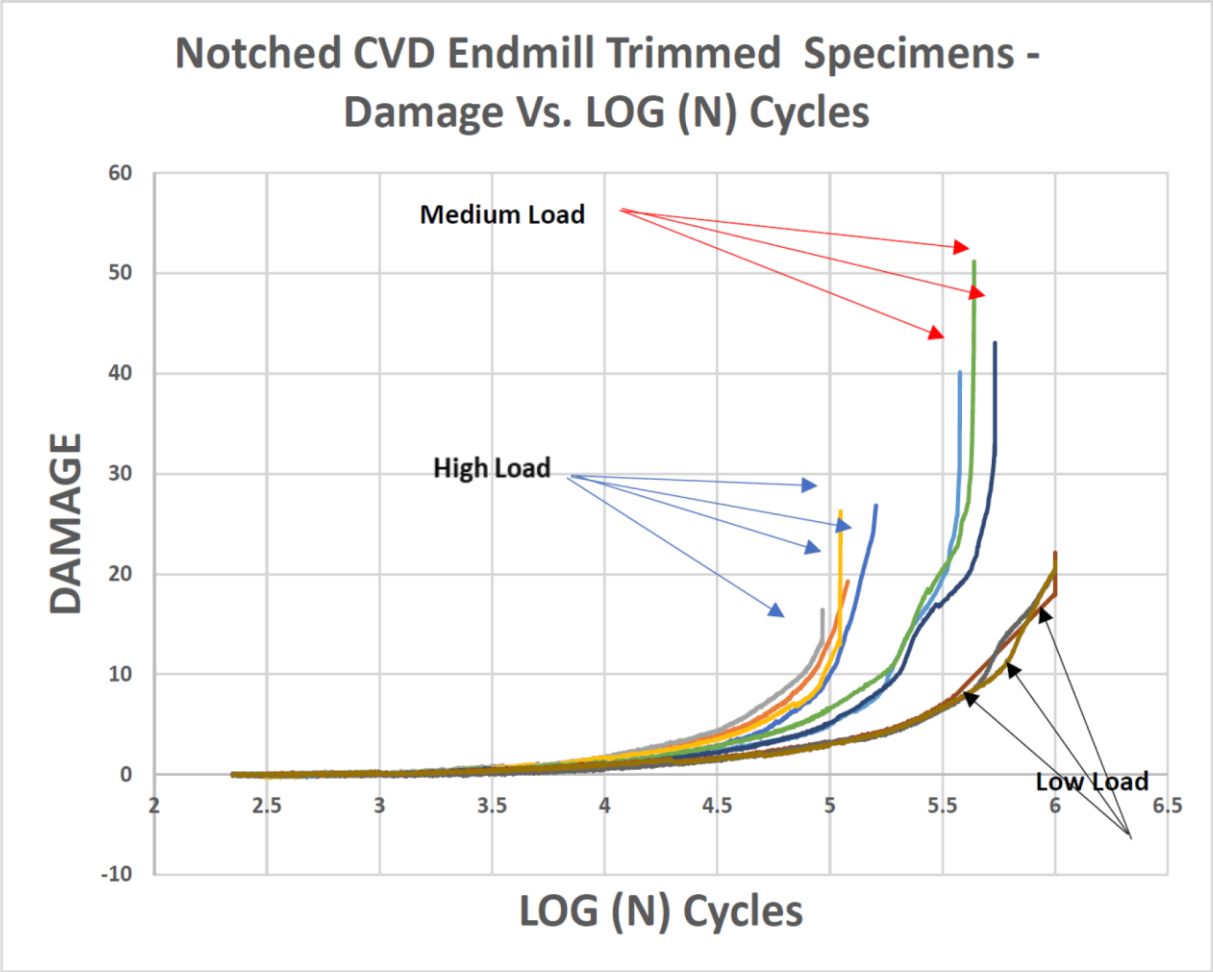

Figure 8.52 Notched CVD Endmill Trimmed Specimens, Damage Vs. Log (N) Cycles

Chapter 9 Conclusions and Recommendations

9.1 Conclusions

As part of this study literature review was made with intent to have a methodological approach to understand and explain the published research that have related surface integrity to changes in mechanical strength properties and fatigue strength. An initial study of differences in surface integrity due to machining processes with cutters and AWJ was presented along with resultant surface integrity studies due to drilling. Subsequently the limited body of research previously conducted in linkage of surface integrity effects to static and fatigue properties was reviewed.

While past work has focused on studying defects and damage in test coupons there has been a shortage of research and publications in the area of relating surface integrity of post-cure processes to strength properties and behaviour under service life conditions. Real life manufacturing processes primarily in the aerospace operations utilize edge trimming and drilling processes extensively in the final component size and shape and assembly. Fibre pullouts and delaminations are the two type of defects during these manufacturing processes whose occurrence increases the cost and schedule of usage of composite laminates while affecting the overall quality and business plan of any manufacturing operations. Fibre pullouts eventually result in delaminations and delaminations once initiated will eventually grow under fatigue loadings. Fibre pullouts can be large in size as much 1 ply (200 µm) in width and ½ ply in depth (100 µm). As part of this study the following questions were addressed.

a) What is the magnitude of the effects of machined and drilled surface integrity on stiffness/strength properties? This was answered by conducting tests on 2 different thicknesses of test laminates with a 10 ply laminate and a 22 ply thick laminate.
b) How do these initial defects from machining and drilling processes behave under service life conditions especially in terms of damage growth and propagation? This was addressed by testing the 2 types of laminates under static loadings and then the 22 ply thick laminates were tested under fatigue loadings. During the fatigue cycle testing, damage growth was recorded at a defined number of cycles period along with photography usage at each stoppage during fatigue cycling.

c) Does the damage growth and propagation change the failure loadings and fatigue life limits? These were validated during fatigue cycling testing with records of damage growth and its influence on failure loadings and fatigue life limits.
d) Can a reduced stiffness and a progressive damage model be created that uses initial defects as a starting point of failure and can then predict the damage growth and correlate it to residual strength properties and fatigue life? Various progressive damage models were developed for the 3 different types of loadings including low, medium and high loadings.

In first phase, a10 ply thick laminate was used as a screening test to understand the processes, resultant surface integrity and static mechanical testing to document the static properties.

The results from the mechanical testing of the 10 ply thick laminate provided the following observations:

1) Overall the maximum loads for a given test or loads at failure generally were slightly lower for specimens with a rougher surface finish.
2) The maximum stress at failure was also lower for specimens with a rougher surface finish.
3) For the open holes specimens both maximum load at failure and maximum stress at failure were lower as compared to specimens with no holes. This is attributed to the stress concentration factor due to the presence of notch (hole).
4) The test specimens displayed higher strength properties in Tension in all cases as the fibres that carry the load are stronger in tension versus compression.
5) For the tension properties, the effect of surface integrity did result in slight reduction in stiffness from the theoretical calculated stiffness.
6) Both the AWJ trimming and Endmill Trimming processes resulted in tension strength close to each other even though the surface roughness values were different between the 2 processes. This effectively pointed to the surface integrity factor has having a dominant effect versus surface roughness.

The damage progress mechanism constituted initial brittle nature in terms of matrix cracking. Once matrix cracking progresses, it starts with the debonding of the matrix-fibre interface. This

mechanism is first inter-ply due to the shear modulus effect and soon it progress to intra-ply with initiation of delamination and first ply failure. As the fibres debond from the matrix, load transfer reduces with individual fibres carrying the load. This eventually results in fibre fracture with ply separation and eventual failure.

The initial screening testing of all the 10 ply thick specimens led to some observations on the effects of surface integrity on the strength of CFRP laminates. Initial screening data showed a trend in reduction in stiffness and strength due to surface integrity effects. The screening testing pointed in the direction of the magnitude of the correlation between surface integrity and stiffness/strength of the laminates.

The maximum loads under tension vary based on the processes used for edge trimming as well as the drilling processes used. As expected between the AWJ trimmed and the endmill trimmed specimens, the surface integrity variance between the two results in a difference in the maximum tensile loads. It is noted that the open hole tension specimens failed at lower tensile loads than the normal tension specimens as expected. This is contributed to the notch sensitivity factor.

The maximum stress under compression vary based on the processes used for edge trimming as well as the drilling processes used. As expected between the AWJ trimmed and the endmill trimmed specimens, the surface integrity variance between the two results in a difference in the maximum compressive stress. It is noted that the open hole compression specimens failed at lower stress than the normal compression specimens as expected also due to the notch sensitivity factor. The maximum stress under compression vary based on the processes used for edge trimming as well as the drilling processes used.

The initiation of damage and its progress followed a common path in all types of testing. Initiation starts as matrix cracking in all specimens with the initiation load being an action of the type of trimming process used (AWJ Vs. Endmilling and the resultant surface integrity of the trimmed specimen. The AWJ specimens had a lower load for matrix cracking initiation but displayed slower progress of damage in comparison to endmilled trimmed specimens. The AWJ specimens also displayed larger amount of damage at failure loads. The endmilled specimens failed at slightly higher loads and showed higher amounts of delamination and ply failure at ultimate failure. Damage tolerance was also lower in the case of endmilled specimens. In all test specimens, matrix cracking damage initiated at the free edge surfaces. The transition of damage from matrix cracking to delamination occurred over a larger spread of applied loads in AWJ specimens in tension and

transition from matrix cracking to buckling in compression specimens also occurred over a larger spread of applied loads in AWJ specimens.

For testing of specimens with open holes the drilled holes had damage start at lower loads for lower feedrate as compared to the higher feedrate. This was attributed to the longer contact time of the drill in the hole which contributed to the matrix cracking initiation. The PCD specimens had slightly higher damage as compared to the CVD drilled holes. This was contributed to larger magnitude of delamination at the bottom surface of the hole attributed to the drill point. The progress of damage was similar in all specimens with matrix cracking being the dominant mode of damage initially. The transition of damage from matrix cracking to delamination followed a similar pattern for all PCD and CVD drilled hole specimens. Damage tolerance of CVD specimens is slightly lower in comparison to PCD drilled specimens. For both PCD and CVD drilled hole specimens, the damage tolerance is lower in specimens drilled at higher feedrates. All specimens displayed a sudden increase in damage showing the progression of damage from hole to across the width of the laminate. Ply damage across the hole for all specimens displayed a similar path of progression.

The effects of surface integrity on fatigue performance and damage progression were evaluated based on experimental study conducted on AWJ trimmed and CVD Endmill trimmed specimens. Both unnotched and notched (with hole in the centre) types of specimens were tested for evaluation of surface integrity effects on both damage progression and fatigue life from tension-tension cyclic testing.

Loading conditions for fatigue testing of both unnotched and notched specimens were categorized as high, medium and low based on percentage values of ultimate loads/stresses obtained during previous static testing for both tension and open hole tension testing.

From a surface integrity perspective, the AWJ trimmed specimens had surface roughness values higher in the longitudinal direction in comparison to CVD Endmill trimmed specimens. In the AWJ trimmed specimens the damage observed after trimming contained streaks and craters along the direction of the Water jet axis. Matrix cracks were also present along with fibre pullouts albeit lower in density. Exit delamination was present with low occurrence of entrance delamination.

In case of CVD endmill trimmed specimens, the surface finish obtained was smoother than that obtained by AWJ trimming. Fibre pullouts were present after trimming and were higher in density

in comparison to AWJ trimming. In both AWJ and CVD endmill trimming the fibre pullouts were along the 45 degree plies.

Overall the surface integrity variation between AWJ and CVD endmill trimming was in the basic differences in principles of cutting in the two processes. This resulted in differences in the surface integrity stress concentration factors calculated for the different test specimens trimmed using the 2 processes. For AWJ trimmed surfaces the surface integrity stress concentration factor varied between 1.4 and 2.5 while for CVD endmill trimmed specimens, the variation lay between 1.1 to 1.8.

When tested in the fatigue the unnotched specimens displayed the following stages of damage progression:

Stage 1 – Matrix cracking

Stage 2 – Matrix Fibre interface debonding

Stage 3 – Fibre fracture and delamination

It was observed that the damage mechanism of matrix cracking was present through all 3 stages with the highest magnitude in stage 1. From the data collected it was clear that the progress in damage is slower in stage 2 as compared to stage 1 and 3. This was a function of surface integrity and its stress concentration factor. Overall the CVD endmill trimmed specimens performed slightly better under most conditions and with consistency due to their better surface integrity and its stress concentration factor. The location of most damage initiations and progress was along the 45 degree plies due to higher concentrations of fibre pullouts.

For notched specimens the following stages of damage progression were observed:

Stage 1 – Matrix Cracking

Stage 2 – Matrix Fibre interface debonding, fibre fracture and delamination

Stage 3 – Fibre fracture and delamination

In the case of notched specimens, the progress of damage was at an accelerated rate during all stages primarily due to the addition of the stress concentration factor due to the presence of a hole which complements the surface integrity stress concentration factor and causes an accelerated progression of damage and reduction in fatigue life performance. Since the same process was used to drill holes in each specimen, the effect of the drilling process was assumed to be a constant on the specimen performance and only the geometrical presence of the hole was considered as an influence on damage progress and fatigue life performance.

The progress of damage with the increased number of fatigue cycles was plotted as % compliance change Vs. (N) cycles and the rate of damage progress documented. This changing rate of damage progress influences the fatigue performance and ultimate failure and is part of analytical models derived in this study which provide predictive modeling for damage progress and fatigue life cycles to failure.

As part of the study of damage progress the damage tolerance of both AWJ trimmed and CVD endmill trimmed specimens was studied and it was found that overall the CVD endmill trimmed specimens had a slightly lower damage tolerance performance in comparison to AWJ trimmed specimens.

The progress of damage from initiation to propagation and to ultimate failure is dependent on many factors. These factors include applied stress, surface integrity amongst other variables. Damage includes matrix cracking, fibre matrix debonding, fibre pullouts, delamination and eventually complete failure and collapse of the laminate. Matrix cracking initiates with applied tensile loading which varies per the ratio of R = 0.1 between maximum applied stress to minimum applied stress. This is further amplified in notched specimens due to the notch sensitivity factor (K_t). The variation in surface integrity between AWJ trimmed and CVD Endmill trimmed specimens is represented by the surface integrity stress concentration factor $\left(\overline{K}_t\right)$ is a contributing factor in the fibre related damage along with delaminations and the collapse of the laminate.

The following factors contribute to the damage initiation and propagation under fatigue loading conditions.

Damage is represented as a function of the following specimen conditions and is shown in equation 9.1and 9.2 for unnotched and notched specimens.

$$Damage = f\left[R, k, \overline{K}_t, n\right] \qquad 9.1$$

$$Damage = f\left[R, k, \overline{K}_t, K_t, n\right] \qquad 9.2$$

Where

$R = \frac{\sigma_{\min}}{\sigma_{\min}}$ = ratio of maximum stress to minimum stress

$k = \frac{\sigma_{app}}{\sigma_u}$ = ratio of applied stress to ultimate tensile stress

$\overline{K}_t$ = surface integrity stress concentration factor

K_t = notch sensitivity factor

n = number of applied fatigue cycles

The models in both cases of unnotched and notched specimens under high loading predicted the damage closer to the damage data collected during empirical testing. The damage curves were aligned closely during the initial loading conditions but closer to failure they deviated with the analytical model predicting lower damage closer to failure.

The models in both cases of unnotched and notched specimens under medium loading predicted the damage closer to the damage data collected during empirical testing. The damage curves were aligned not very well closely during the initial loading conditions and they deviated with the analytical model predicting higher damage through the complete cycling process. conservative design resulting in

The models in both cases of unnotched and notched specimens under low loading predicted the damage slightly lower to the damage data collected during empirical testing. The damage curves were aligned not very well closely during the initial loading conditions and they deviated with the analytical model predicting lower damage through the complete cycling process.

The major conclusions of this research point in the direction of surface integrity contributing to lowering of both the static properties as well as the fatigue strength. The progress of damage is accelerated due to the variance in surface integrity based on different processes used for trimming and drilling operations. While the stress concentration factor in notched specimens influences the static strength properties, in fatigue testing its effects are more concentrated in the damage initiations and progress through the surface of the hole across the thickness of the

laminate. For unnotched and notched specimens, the fatigue strength is influenced by surface integrity concentration factor $\overline{K}_t$.

9.2 Future Research Recommendations

Future researchers should focus their research on laminates belonging into the categories of laminates with number of plies greater than 24 and less than 75. Static properties to be tested should also include bolted specimens. New types of laminates of the 3-D printed type should also be included in future studies. The surface integrity factors that influence the static properties should be documented and their effects on static properties be studied for thicker laminates along with 3-D printed laminates.

For fatigue studies the damage prediction models need to be further refined so as to accurately predict damage tolerance and failure strengths while integrating the effects of surface integrity on the fatigue specimens.

It is also recommended that analytical models be created for the prediction of surface integrity for various machining operations for a variety of laminates. These models then should be used to predict both static properties as well as fatigue properties, damage initiation, progression and eventual failure.

Based on these models, a complete analytical approach to deigning the laminates can be developed which predicts theoretical strengths to post cure surface integrity effects, static properties along with fatigue strength of a manufactured laminate in theory.

Chapter 10 - BIBLIOGRAPHY

[1] Daniel, I. & Ishai, O. Engineering Mechanics of Composite Materials, 2006.

[2] Jones, R. Mechanics of Composite Materials, 1999.

[3] Ramulu, M. Machining of Composite Materials, *ME 599 Class Notes, University of Washington, 2009.*

[4] Gordon, S. & Hillery, M. A Review of the Cutting of Composite Materials, *Proceedings of the Institution of Mechanical Engineers, Part L: Journal of Materials Design and Applications,* 2003.

[5] Komanduri, R. Machining Fiber Reinforced Plastics, *Mechanical Engineering, 115(4), 58-64, 1993.*

[6] Koplev, A., Lystrup, A. & Vorm, T. Cutting Process, Chips and Cutting Forces in Machining CFRP, *Composites, 14(4), 371–376, 1983.*

[7] Hocheng, H., Puw, H. & Huang, Y. Preliminary Study on Milling of Unidirectional Carbon-Fibre Reinforced Plastics. *Composites Mfg, 4(2), 103–108.*

[8] Bhatnagar, N., Ramakrishnan, N., Naik, H. & Komanduri, R. On the Machining of Fiber-Reinforced Plastic (FRP) Composite Laminates. *Int. Journal of Machine Tools & Manufacture, 35(5), 701– 716, 1995.*

[9] Iosipescu, N. New Accurate Procedure for Single Shear Testing of Metals. *J. Mater., 2(3), 597, 1967.*

[10] Arola, D, Ramulu, M. & Wang, D. Chip Formation in Orthogonal Trimming of Unidirectional Graphite/Epoxy Composite, *Composites Part A, 27A, 121-133, 1996.*

[11] Wang. D, Ramulu, M. & Arola, D. "Orthogonal Cutting Mechanisms of Graphite/Epoxy Composite. Part I: Unidirectional Laminate", *International Journal of Machine Tools & Manufacture. Vol. 35, No. 12, 1623-1638, 1995.*

[12] Jahangir, S., Ramulu, M. & Koshy, P. Machining of Ceramics and Composites, *Marcel Dekker Inc., 1999.*

[13] Hashish, M. Cutting with Abrasive-Water Jets, *Mechanical Engineering, 60-66, March 1984.*

[14] Hashish, M. Visualization of the Abrasive-Water Jet Cutting Process, *Experimental Mechanics, 159-169, June 1988.*

[15] Hashish, M. Water Jet Machining of Advanced Composites, *Materials and Manufacturing Processes, Volume 1096), 11290-1152, 1995.*

[16] IIT, Water Jet and Abrasive Water Jet Machining, *Lesson, Version 2 ME, IIT Kharagpur*

[17] Ramulu, M. & Arola, D. Water Jet and Abrasive Water Jet Cutting of Unidirectional Graphite/Epoxy Composite, *Composites, Volume 24, Number 4, 299-308, 1993.*

[18] Arola, D. The Influence of Net Shape Machining on the Surface Integrity of Metals and Fibre Reinforced Plastics, *University of Washington, 1996.*

[19] Shyha, I., Aspinwall, D., Soo, S. & Bradley, S. Drill Geometry and Operating Effects When Cutting Small Diameter Holes in CFRP, *International Journal of Machine Tools & Manufacture, 49, 1008-1014, 2009.*

[20] Palanikumar, K., Rubio, J., Abrao, A., Correia, A. & Davim, J. Influence of Drill Point Angle in High Speed Drilling of Glass Fibre Reinforced Plastics, *Journal of Composite Materials, Vol. 42, No 24, 2585-2597, 2008.*

[21] Capello, E. & Tagliaferri, V. Drilling Damage of GFRP and Residual Mechanical Behaviour – Part I: Drilling Damage Generation, *Journal of Composites Technology & Research, American Society for Testing and Materials, 2001.*

[22] Persson, E., Eriksson, I. & Zackrisson, L. Effects of Hole Machining Defects on Strength and Fatigue Life of Composite Laminates, *Composites Part A, 28A, 141-151, 1997.*

[23] Metcut Research Associates. Surface Technology, *Machining Data Handbook, 18-1 to 18-136, 1980.*

[24] Neuber, H. Kerbsannungsleshre, *Springer-Verlag, Berlin, Germany, 159-163, 1958.*

[25] Arola, D & Ramulu, M. An Examination of the Effects from Surface Texture on the Strength of Fibre-Reinforced Plastics, *Journal of Composite Materials, 33(2), 101-186, 1999.*

[26] Nusimer, R. & Whitney, J. Uniaxial Failure of Composite Laminates Containing Stress Concentrations, *Fracture Mechanics of Composites, ASTM, STP 593, 117-142, 1975.*

[27] Whitney, J. & Nuismer, R. Stress Fracture Criteria for Laminated Composites Containing Stress Concentrations, *Journal of Composite Materials, Vol 8(3), 253-265, 1974.*

[28] Cruse, T. Tensile Strength of Notched Composites, *Journal of Composite Materials, Vol 7 (2), 218-229, 1973.*

[29] Mar, J. & Lin, K. Fracture of Boron/Aluminium Composites with Discontinuities, *Journal of Composite Materials, Vol 11 (4), 405-421, 1977.*

[30] Durao, L., Magalhaes, A., Marques, A. & Tavares, J. Damage Assessment of Drilled Hybrid Composite Laminates.

[31] Ramulu, M., Influence of Cutting Direction and Fibre Orientation on Damage Mechanisms during Composite Laminates Drilling, *University of Washington, 2011.*

[32] Mohan, N., Kulkarni, S. & Ramachandra, A. Delamination Analysis in Drilling Process of

Glass Fibre Reinforced Plastic (GFRP) Composite Materials, *Journal of Materials Processing Technology, 186, 265-271, 2007.*

[33] Davim, J. & Reis, P. Study of Delamination in Drilling of Carbon Fibre Reinforced Plastics (CFRP) using Design Experiments, *Composite Structures, 59, 481-487, 2003.*

[34] Shanmugam, D., Nguyen, T. & Wang, J. A Study of Delamination on Graphite/Epoxy Composites in Abrasive Waterjet Machining, *Composites: Part A, 39, 923-929, 2008.*

[35] Capello, E. & Tagliaferri, V. Drilling Damage of GFRP and Residual Mechanical Behaviour – Part II: Static & Cyclic Bearing Loads, *Journal of Composites Technology & Research, American Society for Testing and Materials, 2001.*

[36] Rao, B., Rudramoorthy, R., Srinivas, S. & Rao, B. Effect of Drilling Induced Damage on Notched Tensile and Pin Bearing Strengths of Woven GFR-Epoxy Composites, *Materials Science and Engineering A, 472, 347-352, 2008.*

[37] Wisnom, M. & Hallett, S. The Role of Delamination in Strength, Failure Mechanism and Hole Size Effect in Open Hole Tests on Quasi-Isotropic Laminates, *Composites: Part A, 40, 335-342, 2009.*

[38] Arola, D. & Ramulu, M. Net-Shape Machining and the Process-Dependent Failure of Fibre-Reinforced Plastics Under Static Loads, *Journal of Composites Technology & Research, Vol. 20, No. 4, 210-220, 1998.*

[39] Ramulu, M. & Colligan, K. Edge Finishing and Delamination Effects Induced During Abrasive WaterJet Machining on the Compression Strength of a Graphite/Epoxy Composite, *ASME International Mechanical Engineering Congress & Exposition, 2005.*

[40] Ghidossi, P., Mansori, M. & Pierron, F. Edge Machining Effects on the Failure of Polymer Matrix Composite Coupons, *Composites: Part A 35, 989-999, 2004.*

[41] Ghidossi, P., Mansori, M. & Pierron, F. Influence of Specimen Preparation by Machining on the Failure of Polymer Matrix Off-Axis Tensile Coupons, *Composites Science and Technology, 66, 1857-1872, 2006.*

[42] Eriksen, E. The Influence of Surface Roughness on the Mechanical Strength Properties of Machined Short-Fibre Reinforced Thermoplastics, *Composites Science and Technology, 60, 107-113, 2000.*

[43] Tagliaferri, V., Caprino, G. & Diterlizzi, A. Effect of Drilling Parameters on the Finish and Mechanical Properties of GFRP Composites, *International Journal of Machine Tools & Manufacture, Vol 30, No 1, 77-84, 1990.*

[44] Langella, A & Durante, M. Comparison of Tensile Strength of Composite Material Elements with Drilled and Moulded-In-Holes, *Applied Composites Materials, 15, 227-239, 2008.*

[45] Zitoune, R., Crouzeix, F., Collombet, F., Tamine, T. & Grunevald, Y-H, Behaviour of

Composite Plates with Drilled and Moulded Hole under Tensile Load, *Composite Structures, 2011.*

[46] Haddad, M., Zitoune, R., Bougherara, H., Eyma, F., & Castanie, B. Study of trimming damages of CFRP structures in function of the machining processes and their impact on the mechanical behavior, *Composites Part B 57, 136-143, 2013*

[47] Harris, B. Fatigue in Composites, Science and Technology of the Fatigue Response of Fibre-Reinforced Plastics, *CRC Press, 2000.*

[48] Reifsnider, K. & Case, S. Damage Tolerance and Durability of Material Systems, *Wiley Interscience, 2002.*

[49] Jamison, R., Schulte, K., Reifsnider, K. & Stinchcomb, W., Characterization and Analysis of Damage Mechanisms in Tension-Tension Fatigue of Graphite/Epoxy Laminates, *Effects of Defects in Composite Materials, ASTM STP 836, American Society for Testing and Materials, 21-55, 1984.*

[50] Plumtree, A. & Shi, L. Fatigue Damage Evolution in Off-Axis Unidirectional CFRP, *International Journal of Fatigue, 24, 155-159, 2002.*

[51] Beghini, M, Betini, L. & Forte, P. Experimental Investigation on the Influence of Crack Front Fibre Orientation on Fatigue Delamination Growth Rate under Mode II, *Composites Science & Technology, 66, 240-247, 2006.*

[52] Pearson-Nixon, O.J. & Hellet, S.R. An investigation into the damage development and residual strengths of open-hole specimens in fatigue, *Composites Part A 69, 266-278, 2015.*

[53] Montesano, J., Bougherara, H. & Fawaz, Z. Influence of drilling and abrasive water jet induced damage on the performance of carbon fabric/epoxy plates with holes, *Composites Structures 163, 257-266, 2017.*

[54] Saleem, M., Toubal, L., Zitoune, R' & Bougherara, H. Investigating the effect of machining processes on the mechanical behaviour of composite plates with circular holes, *Composites Part A 55, 169-177, 2013*

[55] Venkatachalam, S., Mohiddin, S. M., and Murthy, M. Determination of damage evolution in CFRP subjected to cyclic loading using DIC, *Fatigue and Fracture of engineering materials and structures, 41, 1412-1425, 2018*

[56] Ansari Alam, T., Singh, K. K. and Azam, M. S. Fatigure damage analysis of fibre-reinforced polymer composites – A review, *Journal of Reinforced Plastics & Composites, Vol. 37(9) 636-654, 2018*

[57] Xiao, Y. & Ishikawa, T. Bearing Strength and Failure Behaviour of Bolted Composite Joints (part I: Experimental Investigation), *Composites Science & Technology, 65, 1022-1031, 2005.*

[58] Seike, S., Takao, Y., Wang, W. & Matsubara, T. Fatigue and Static Damage of a Pinned Joint in CFRP, *AIAA Structural Dynamics and Materials Conference, AIAA 2007-2409, 2007.*

[59] Degrieck, J. & Paepegem, W. Fatigue damage modeling of fibre-reinforced composite materials: Review, *Applied Mechanics Review, Vol 54, no 4, July 2001.*

[60] Wicaksono, S. & Chai, G. B. A review of advances in fatigue and life prediction of fibre-reinforced composites, *Journal of Materials: Design and Applications, 227(3) 179-195, 2012*

[61] Bak, B., Sarrodo, C., Turon, A. & Costa, J. Delamination under fatigue Loads in composite laminates: A review on the observed phenomenology and computational methods, *Applied mechanics Revie, Vol 66, 2014*

[62] Shirazi, A. & Farahani-Varvani, A. A stiffness degradation based fatigue model for FRP composites of (0/θ) laminate systems, *Applied composite Materials, 2009*

[63] Senthilnathan, K., Hiremath, C. P., Naik, N. K., Guha, A. & Tewari, A. Microstructural damage dependent stiffness prediction of unidirectional CFRP composite under cyclic loading, *Composites: Part A, 100, 118-127, 2017*

[64] Whitworth, H. A., A stiffness degradation model for composite laminates under fatigue loading, *Composite Structures, Vol 40, No. 2., 95-101, 1998*

[65] Dahlen, C. & Springer, G. Delamination Growth in Composites Under Cyclic Loads, *Journal of Composite Materials, 28, 732-781, 1994.*

[66] Dahlen, C. & Springer, G. Delamination Growth in Composites Under Cyclic Loads, *Journal of Composite Materials, 28, 732-781, 1994.*

[67] Henaff-Gardin C, Lafarie-Frenot M & Goupillaud I. Prediction of Cracking Evolution Under Uniaxial Fatigue Loading in Cross-Ply Composite Laminates, *International Conference on Fatigue of Composites: Proceedings, Paris, France, 189–196, 1997*

[68] Reifsnider, K, The Critical Element Model: A Modeling Philosophy, *Engineering Fracture Mechanics,* 25, 739–749, *1986.*

[69] Diao, X., Ye, L. & Mai, Y. A Statistical Model of Residual Strength and Fatigue Life of Composite Laminates, *Composites Science & Technology,* 54, 329–336, *1995.*

[70] Subramanian, S., Reifsnider, K. & Stinchcomb, W. A Cumulative Damage Model to Predict the Fatigue Life of Composite Laminates including the Effect of a Fibre-Matrix Interphase, *International Journal of Fatigue,* 17, 343–351, *1995.*

[71] Pearson-Nixon, O.J., Hallet, S.R., Harper, P.W. & Kawashita, L.F. Damage development in open-hole composite specimens in fatigue. Part 2: Numerical Modelling, *Composite Structures 196, 890-898, 2013.*

[72] Shokrieh, M. M. & Behrooz-Taheri, F. Progressive fatigue damage modeling of Cross-Ply laminates, I: Modeling Strategy, *Journal of Composite Materials, Vol. 44, No 10./2010*

[73] Behrooz-Taheri, F., Shokrieh, M. M. & Lessard, L. B., Progressive fatigue damage modeling of Cross-Ply Laminates, II: Experimental Evaluation, *Journal of Composite Materials, Vol. 44, No 10./2010*

[74] Lin, K. Classical Lamination Theory, *Lecture Notes, University Of Washington, 2008.*

[75] Laminator Software, *Laminator.net, 2011*

[76] Boeing CFRP Laminate Standard Specification

Appendix A

A1.1 Surface Profiles of Static Tension Testing Specimens

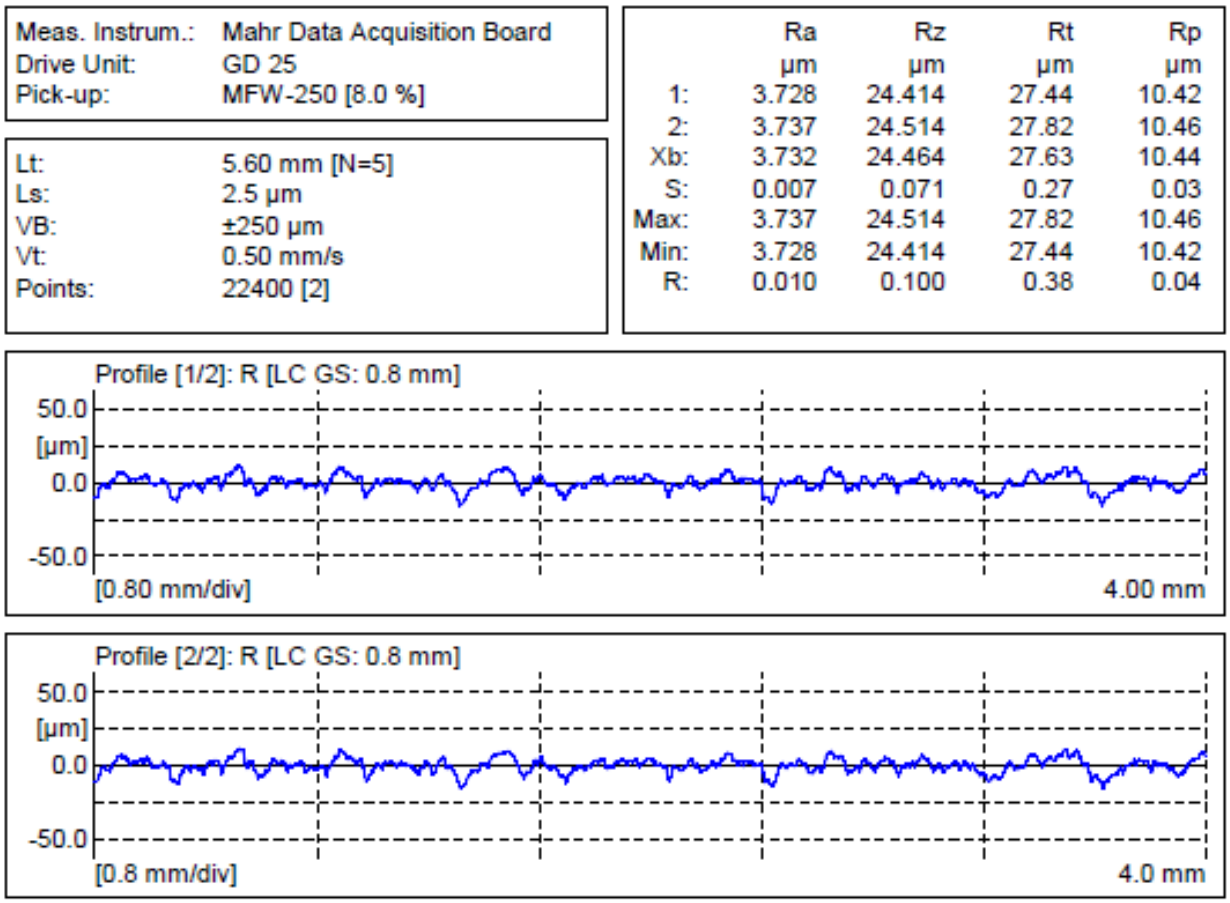

Figure A1. 1 Surface Profile (longitudinal) of Tension Test Specimen # 1 – AWJ (80 Grit)

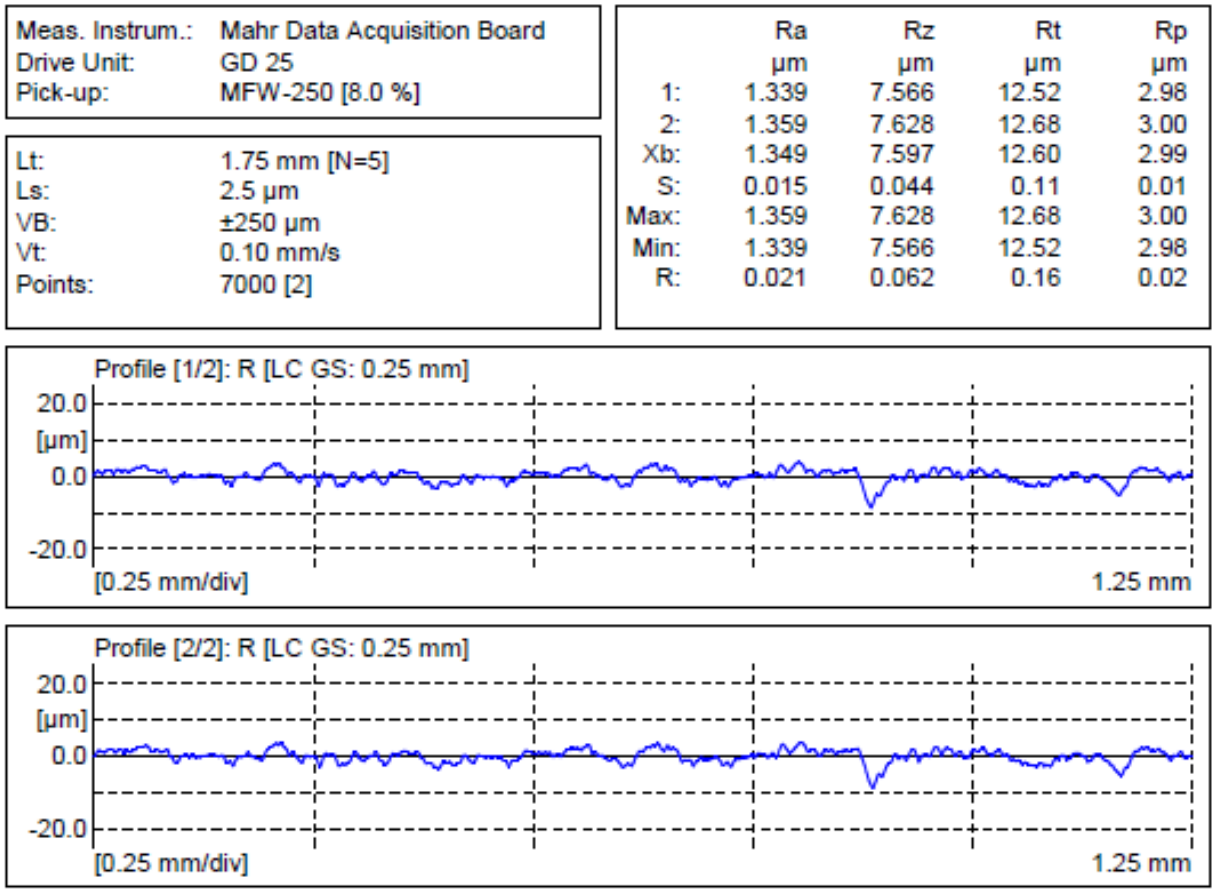

Figure A1. 2 Surface Profile (transverse) of Tension Test Specimen # 2 – AWJ (80 Grit)

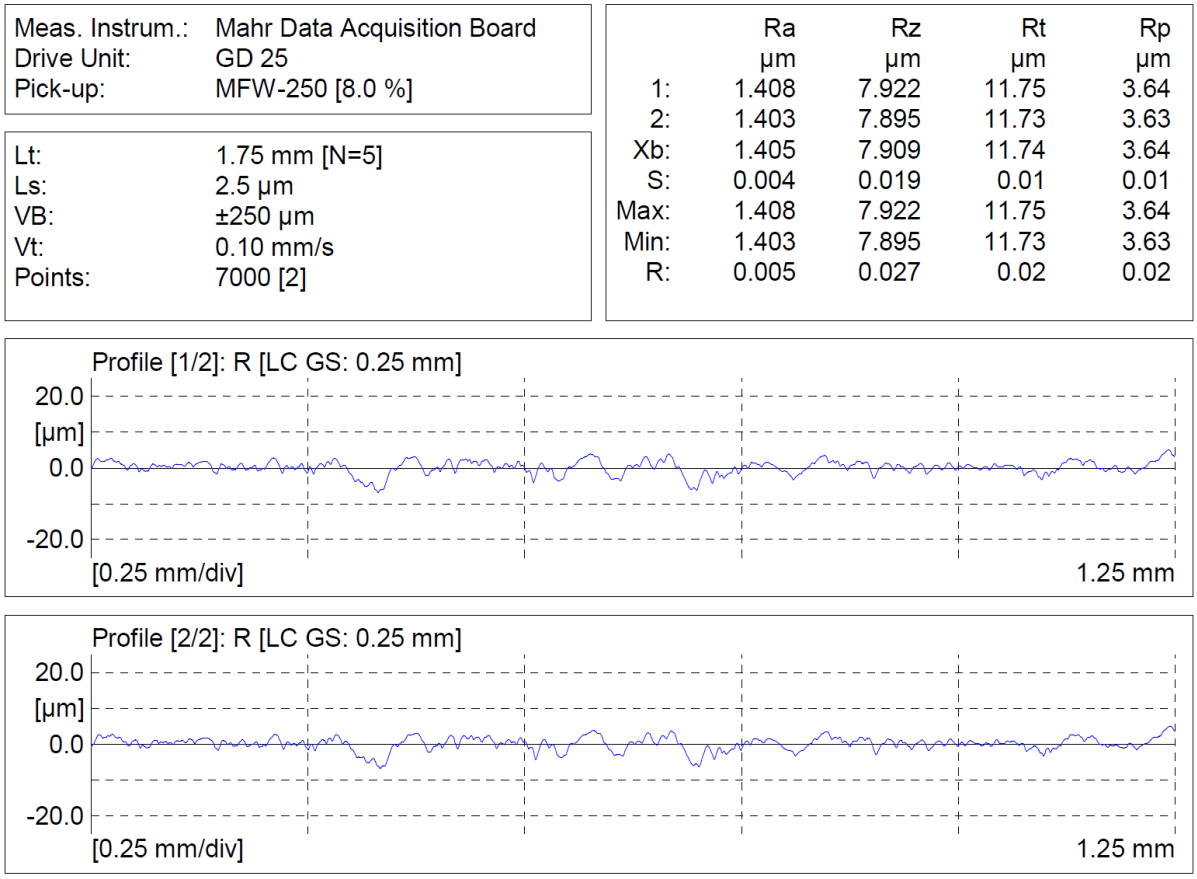

Figure A1. 3 Surface Profile (transverse) of Tension Test Specimen # 3 – AWJ (80 Grit)

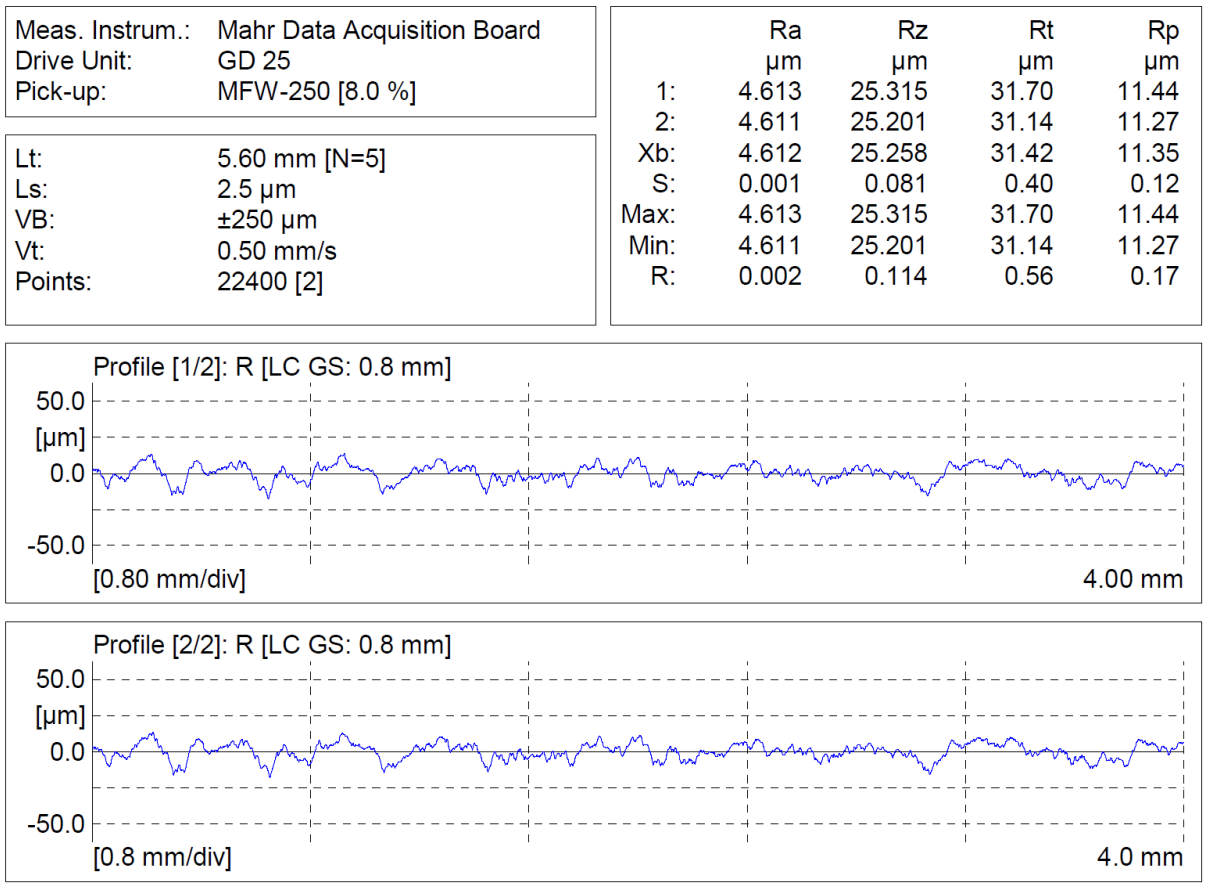

Figure A1. 4 Surface Profile (longitudinal) of Tension Test Specimen # 4 – AWJ (80 Grit)

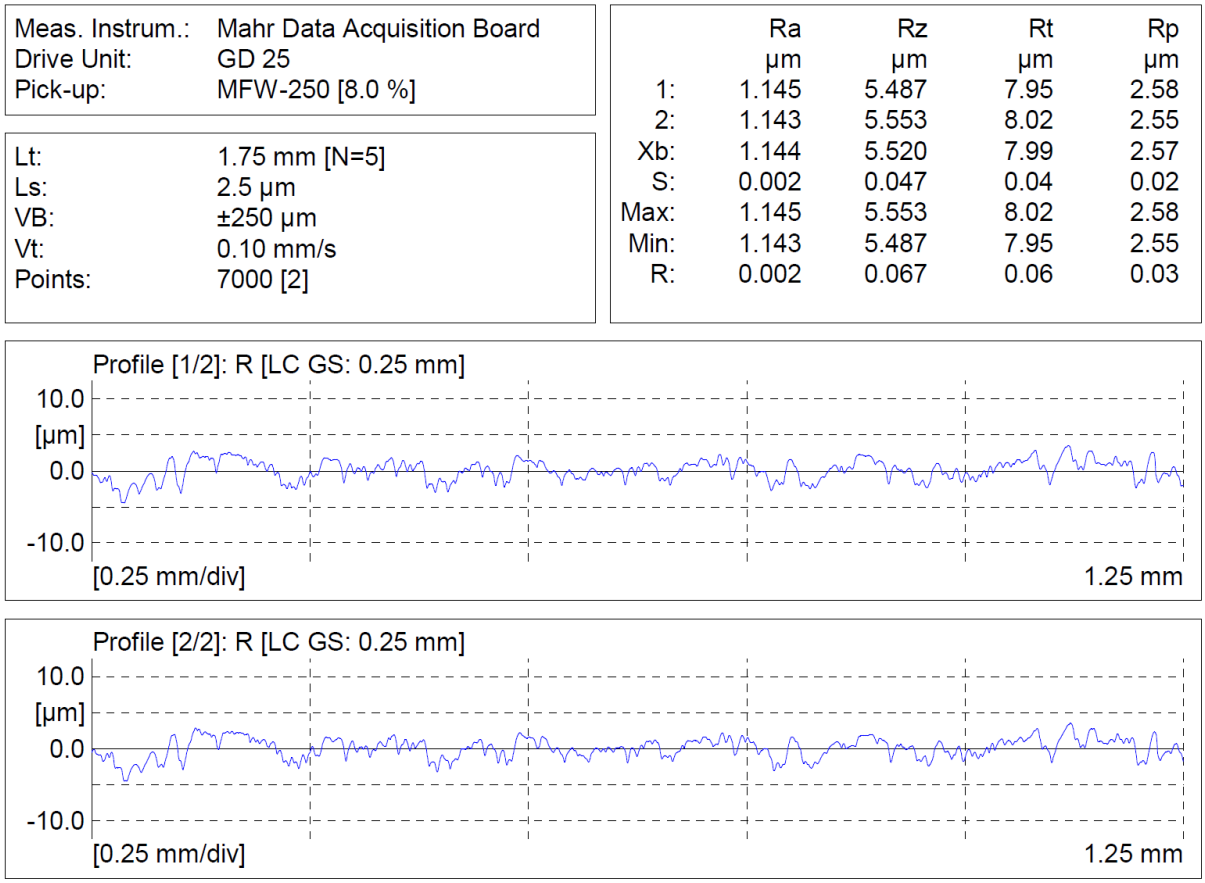

Figure A1. 5 Surface Profile (transverse) of Tension Test Specimen # 4 – AWJ (80 Grit)

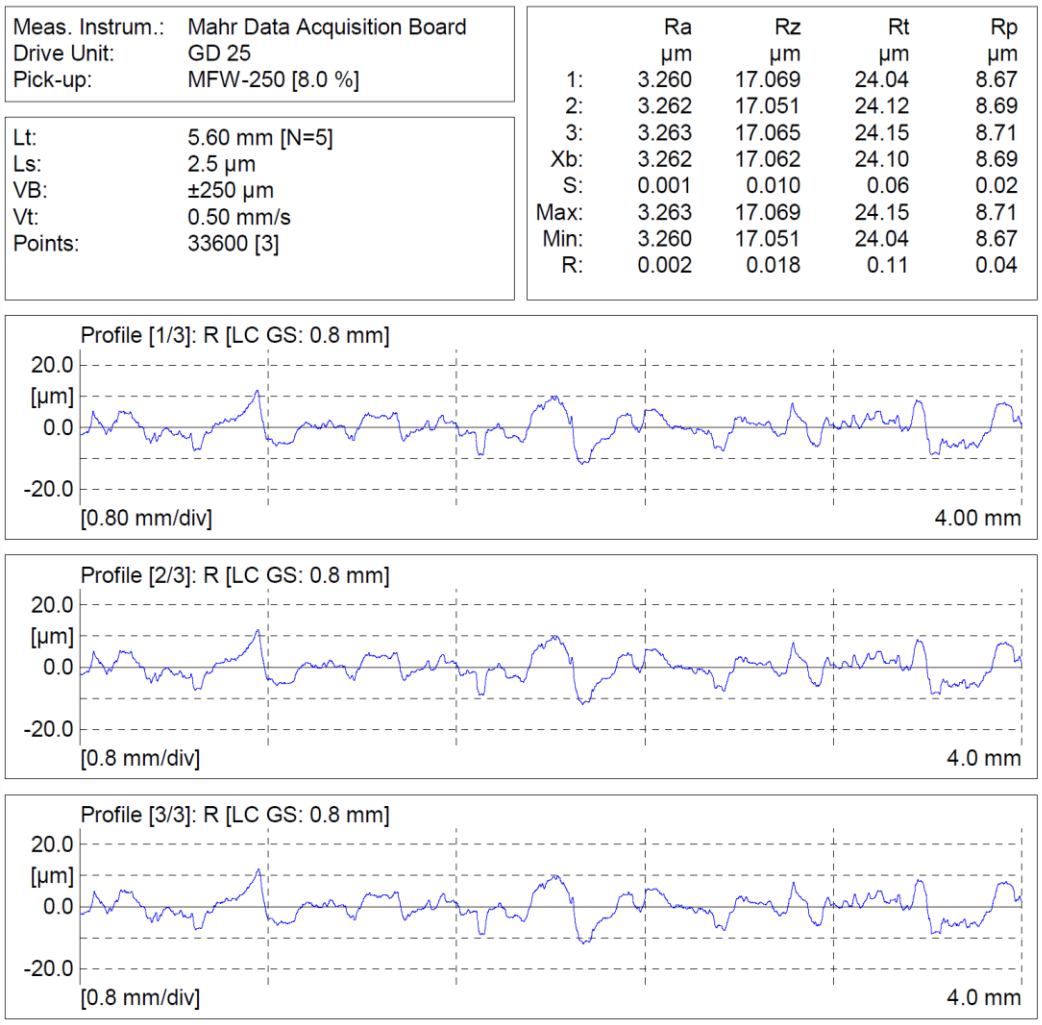

Figure A1. 6 Surface Profile (longitudinal) of Tension Test Specimen # 5 – AWJ (80 Grit)

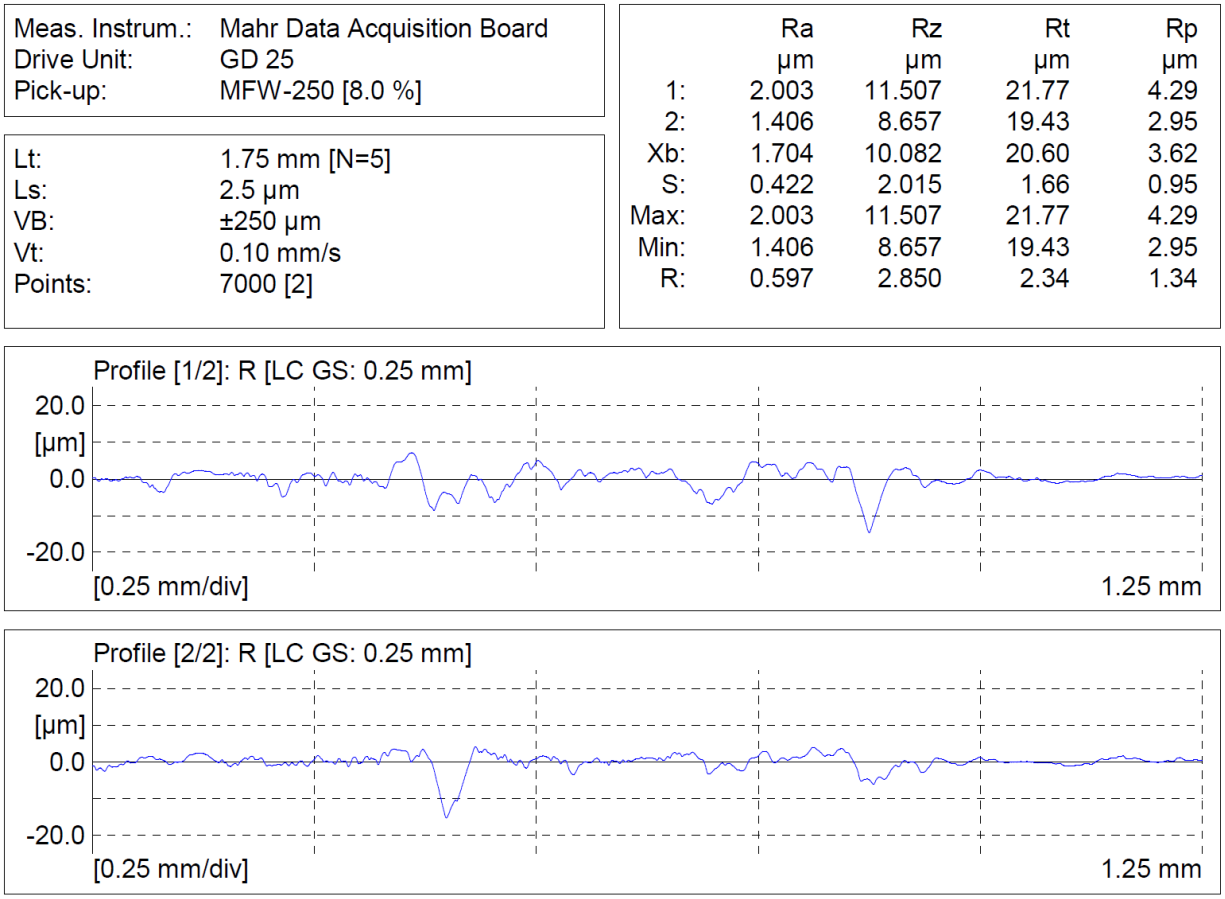

Figure A1. 7 Surface Profile (transverse) of Tension Test Specimen # 5 – AWJ (80 Grit)

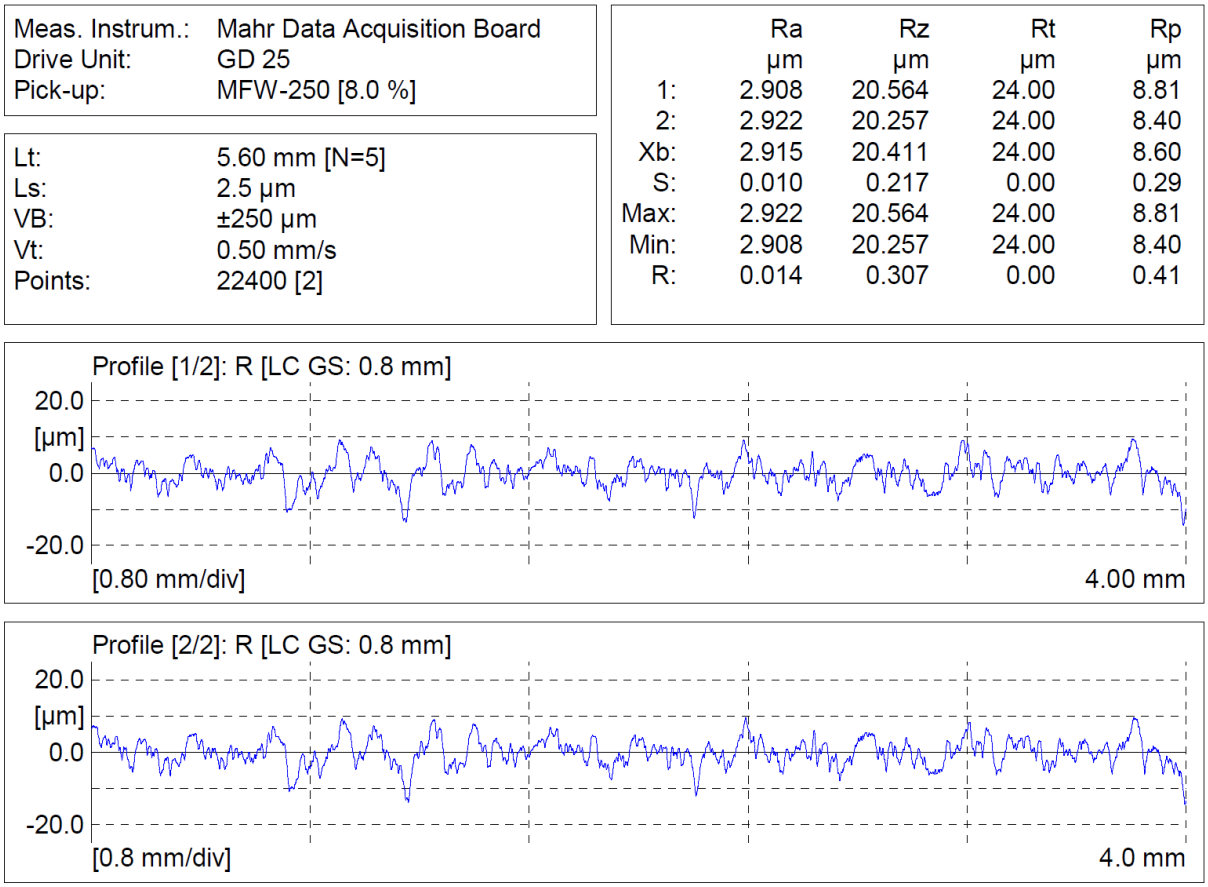

Figure A1. 8 Surface Profile (longitudinal) of Tension Test Specimen # 1 – AWJ (120 Grit)

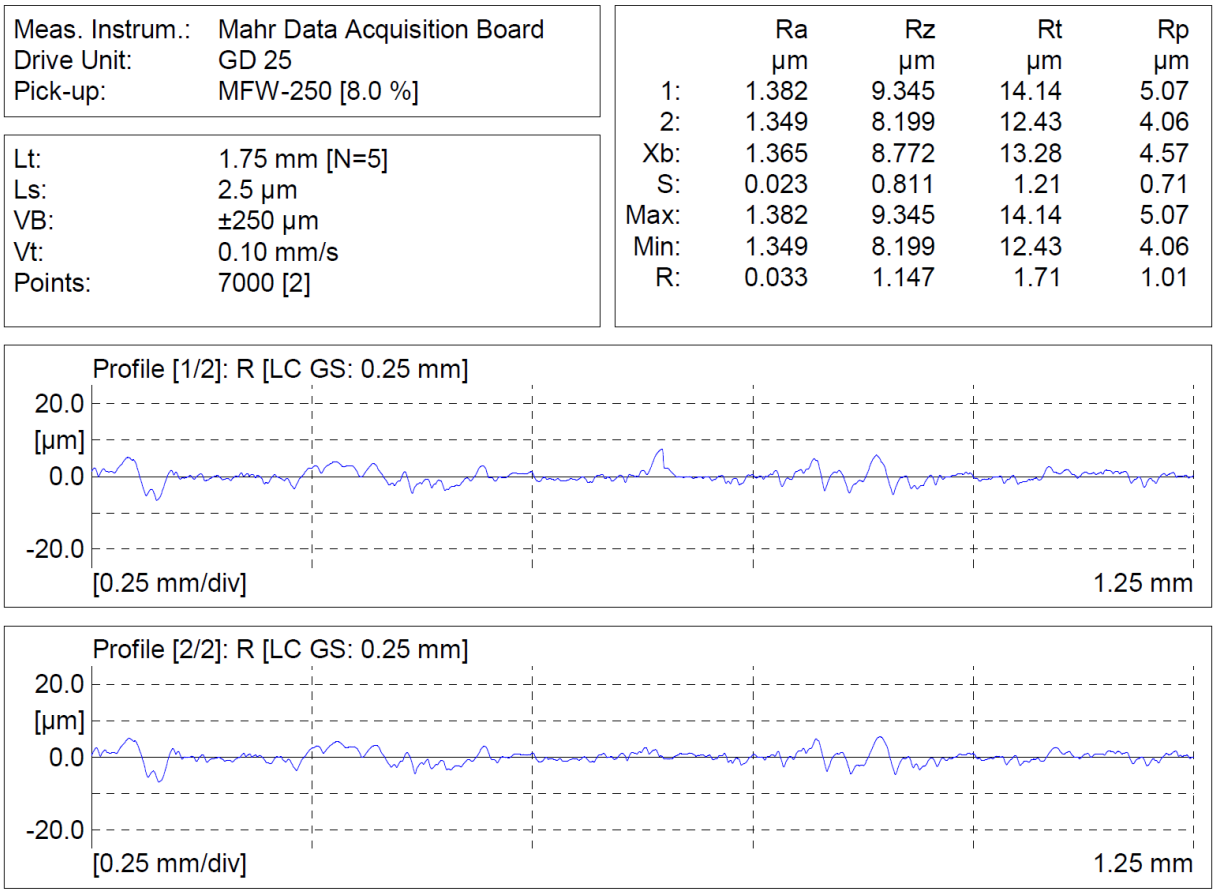

Figure A1. 9 Surface Profile (transverse) of Tension Test Specimen # 1 – AWJ (120 Grit)

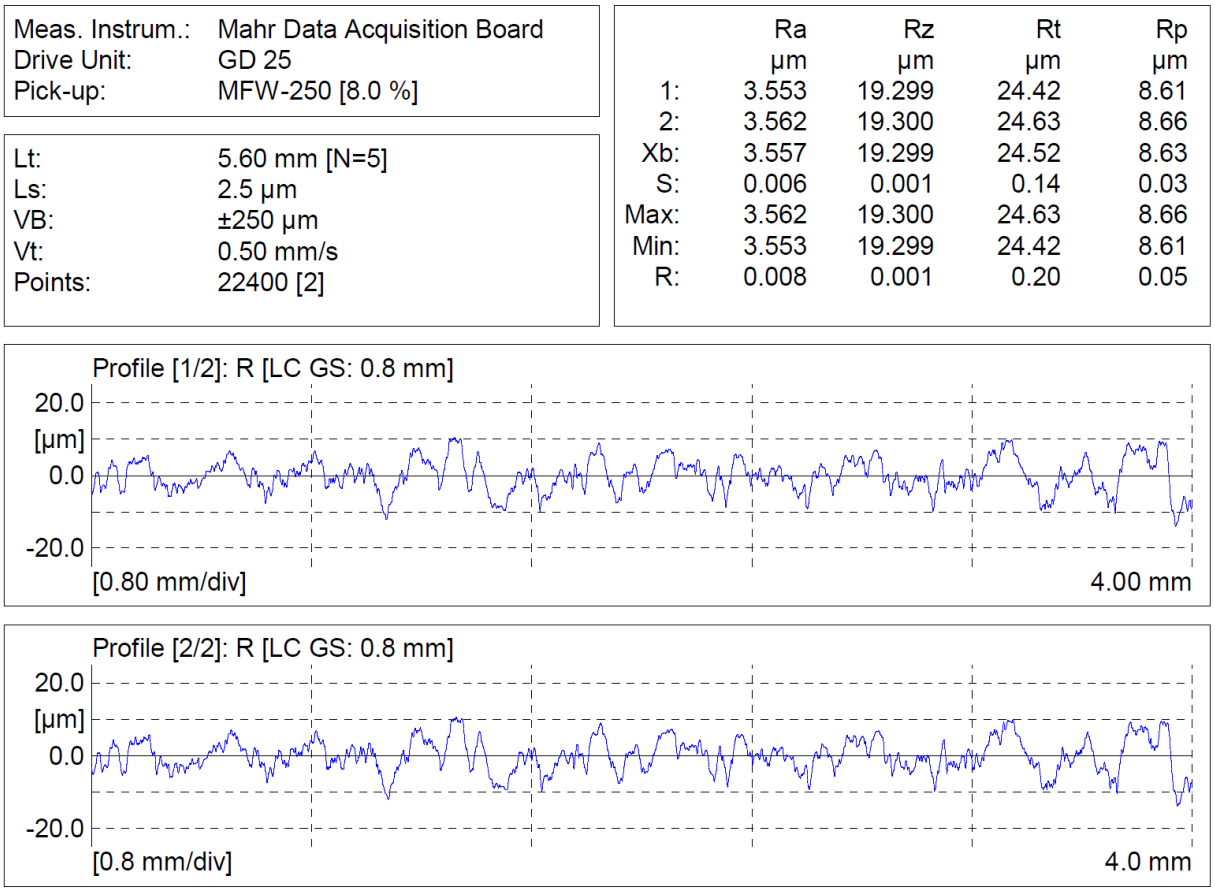

Figure A1. 10 Surface Profile (longitudinal) of Tension Test Specimen # 2 – AWJ (120 Grit)

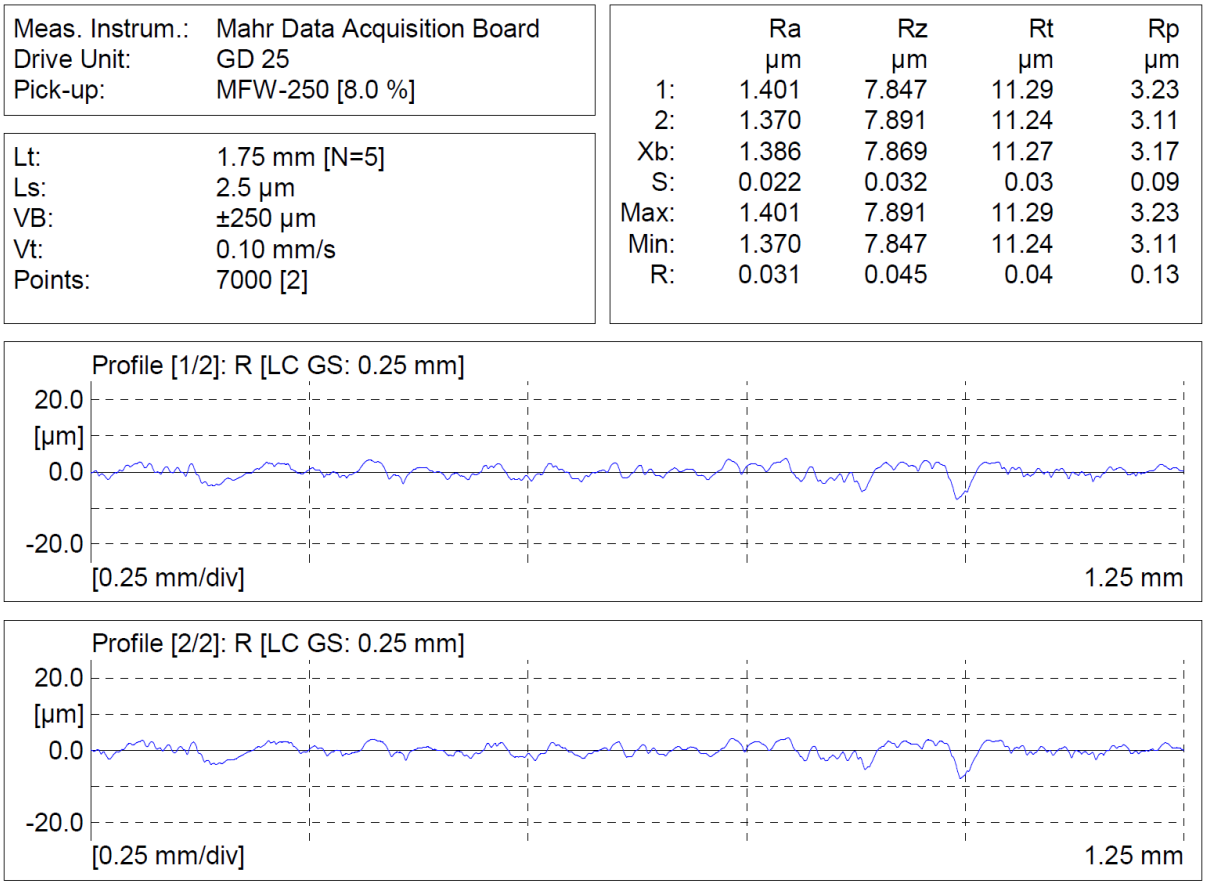

Figure A1. 11 Surface Profile (transverse) of Tension Test Specimen # 2 – AWJ (120 Grit)

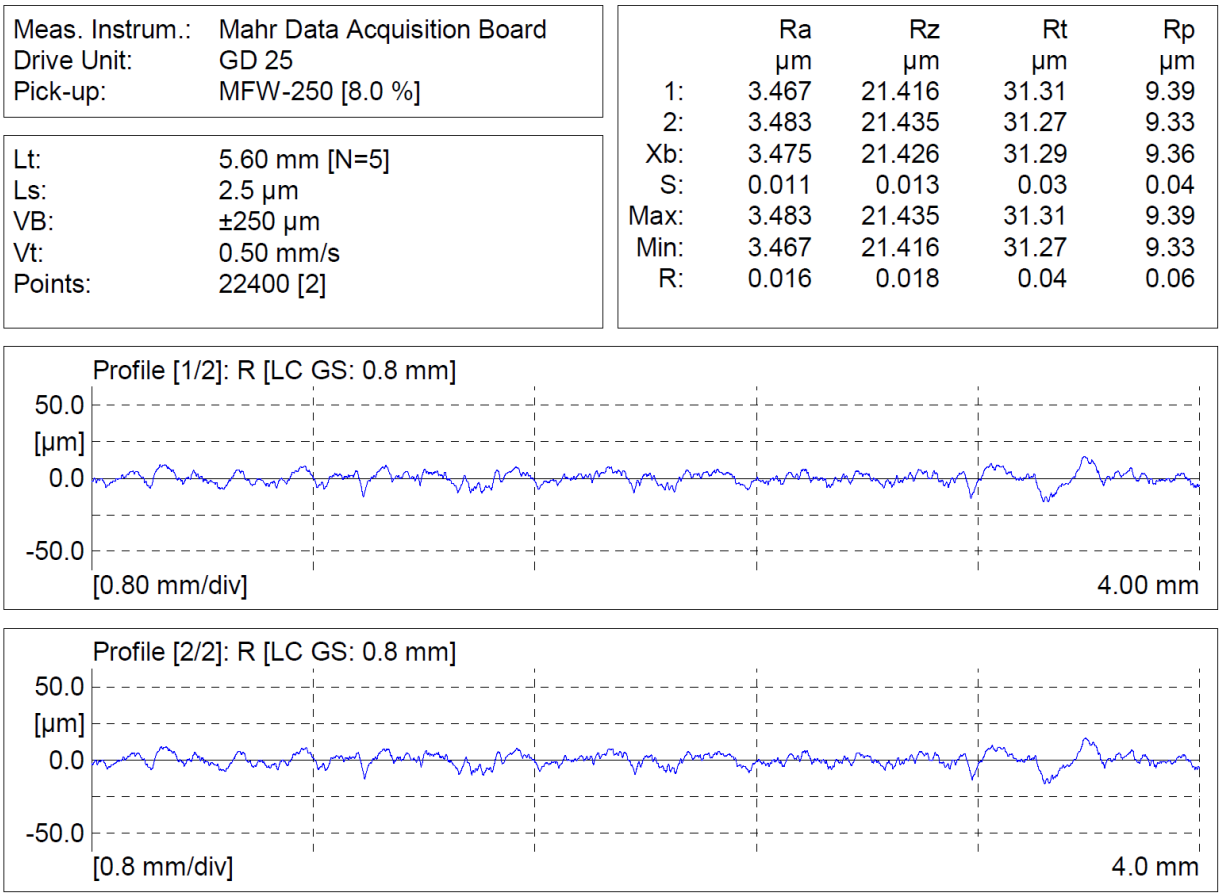

Figure A1. 12 Surface Profile (longitudinal) of Tension Test Specimen # 3 – AWJ (120 Grit)

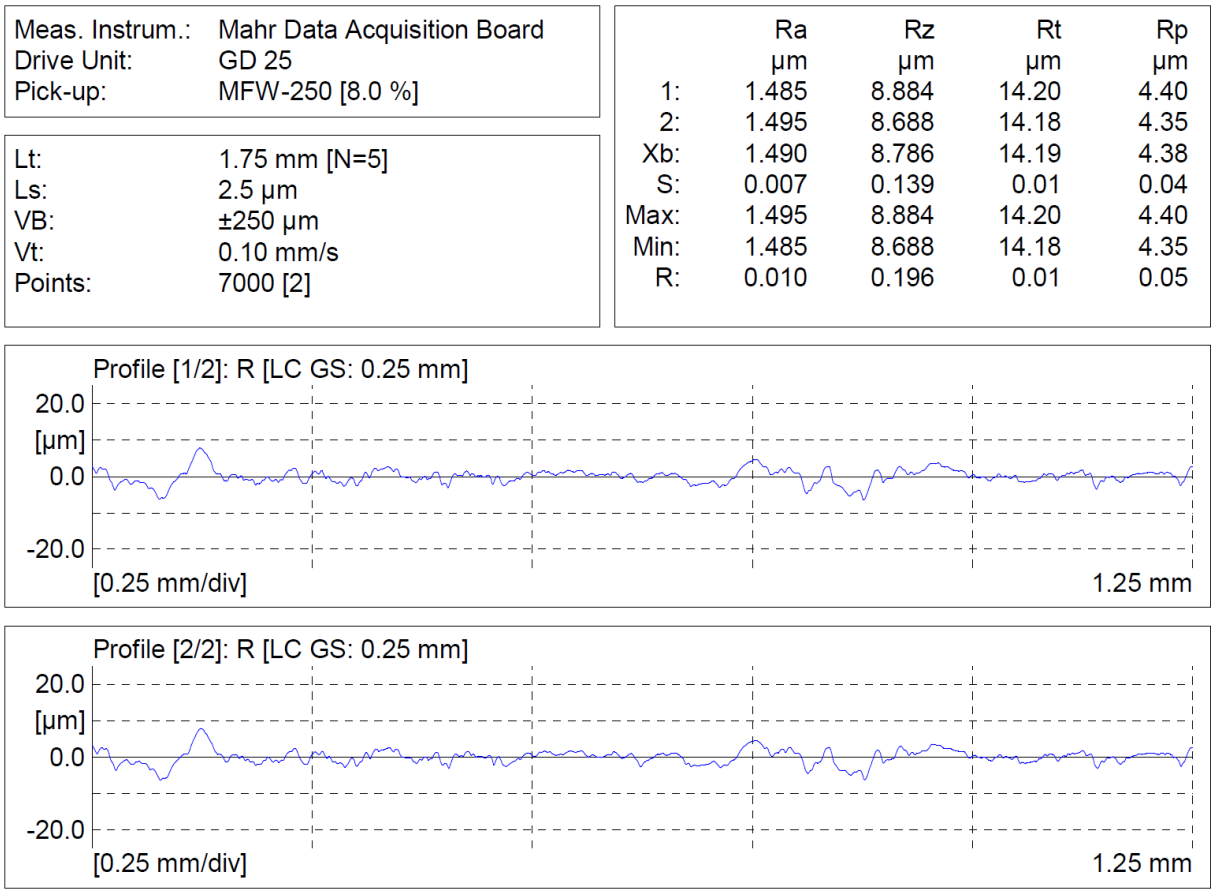

Figure A1. 13 Surface Profile (transverse) of Tension Test Specimen # 3 – AWJ (120 Grit)

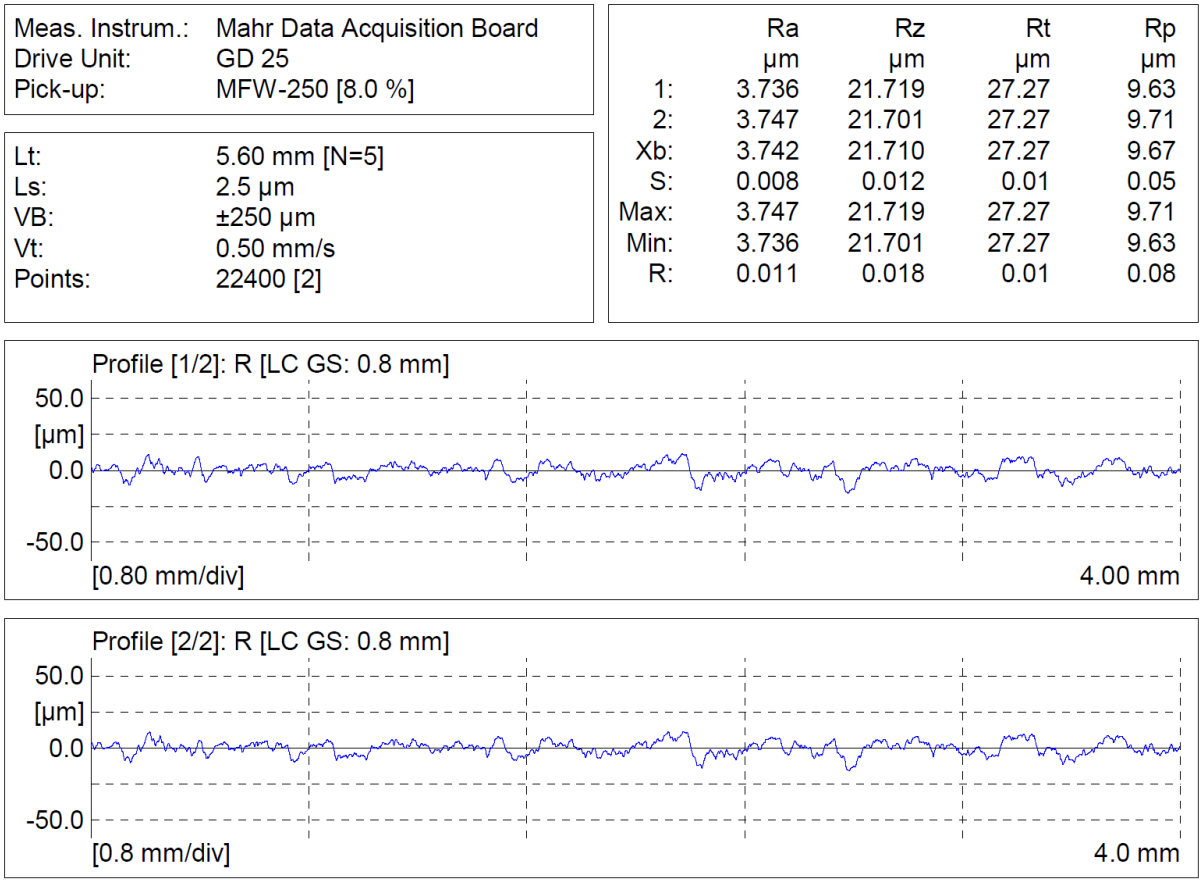

Figure A1. 14 Surface Profile (longitudinal) of Tension Test Specimen # 4 – AWJ (120 Grit)

Meas. Instrum.:	Mahr Data Acquisition Board
Drive Unit:	GD 25
Pick-up:	MFW-250 [8.0 %]

Lt:	1.75 mm [N=5]
Ls:	2.5 µm
VB:	±250 µm
Vt:	0.10 mm/s
Points:	7000 [2]

	Ra	Rz	Rt	Rp
	µm	µm	µm	µm
1:	1.377	7.692	10.38	3.26
2:	1.376	7.672	10.41	3.24
Xb:	1.376	7.682	10.40	3.25
S:	0.000	0.014	0.02	0.01
Max:	1.377	7.692	10.41	3.26
Min:	1.376	7.672	10.38	3.24
R:	0.000	0.020	0.03	0.02

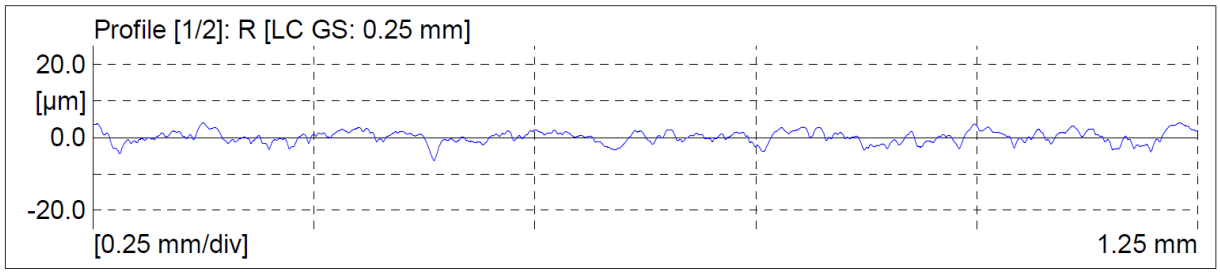

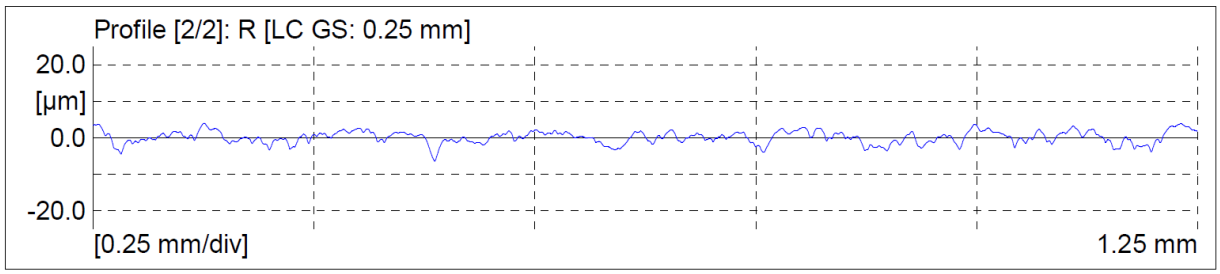

Figure A1. 15 Surface Profile (transverse) of Tension Test Specimen # 4 – AWJ (120 Grit)

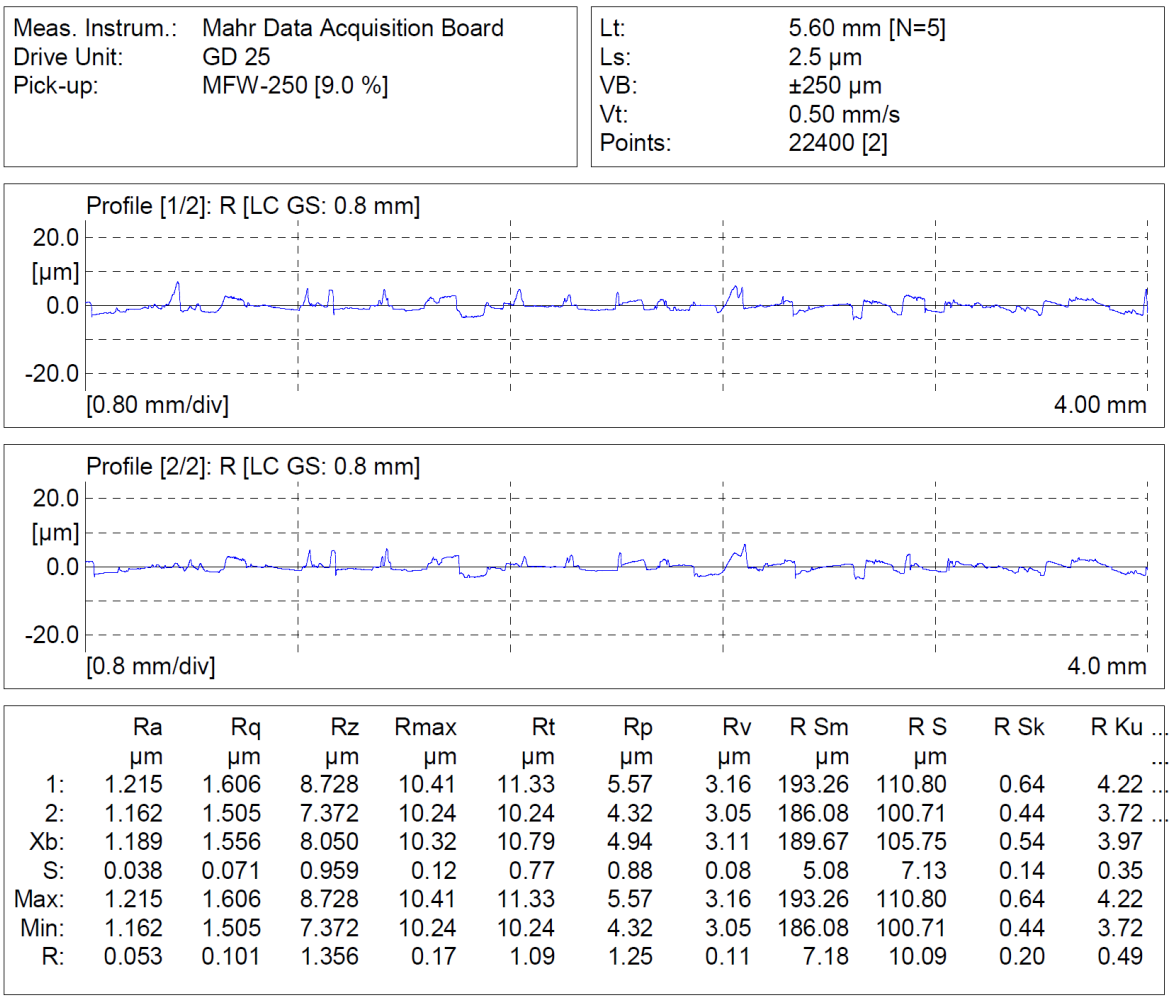

	Ra	Rq	Rz	Rmax	Rt	Rp	Rv	R Sm	R S	R Sk	R Ku ...
	µm	µm	µm	µm	µm	µm	µm	µm	µm		...
1:	1.215	1.606	8.728	10.41	11.33	5.57	3.16	193.26	110.80	0.64	4.22 ...
2:	1.162	1.505	7.372	10.24	10.24	4.32	3.05	186.08	100.71	0.44	3.72 ...
Xb:	1.189	1.556	8.050	10.32	10.79	4.94	3.11	189.67	105.75	0.54	3.97
S:	0.038	0.071	0.959	0.12	0.77	0.88	0.08	5.08	7.13	0.14	0.35
Max:	1.215	1.606	8.728	10.41	11.33	5.57	3.16	193.26	110.80	0.64	4.22
Min:	1.162	1.505	7.372	10.24	10.24	4.32	3.05	186.08	100.71	0.44	3.72
R:	0.053	0.101	1.356	0.17	1.09	1.25	0.11	7.18	10.09	0.20	0.49

Figure A1. 16 Surface Profile (longitudinal) of CVD Endmill Trimmed Tension Test Specimen # 2

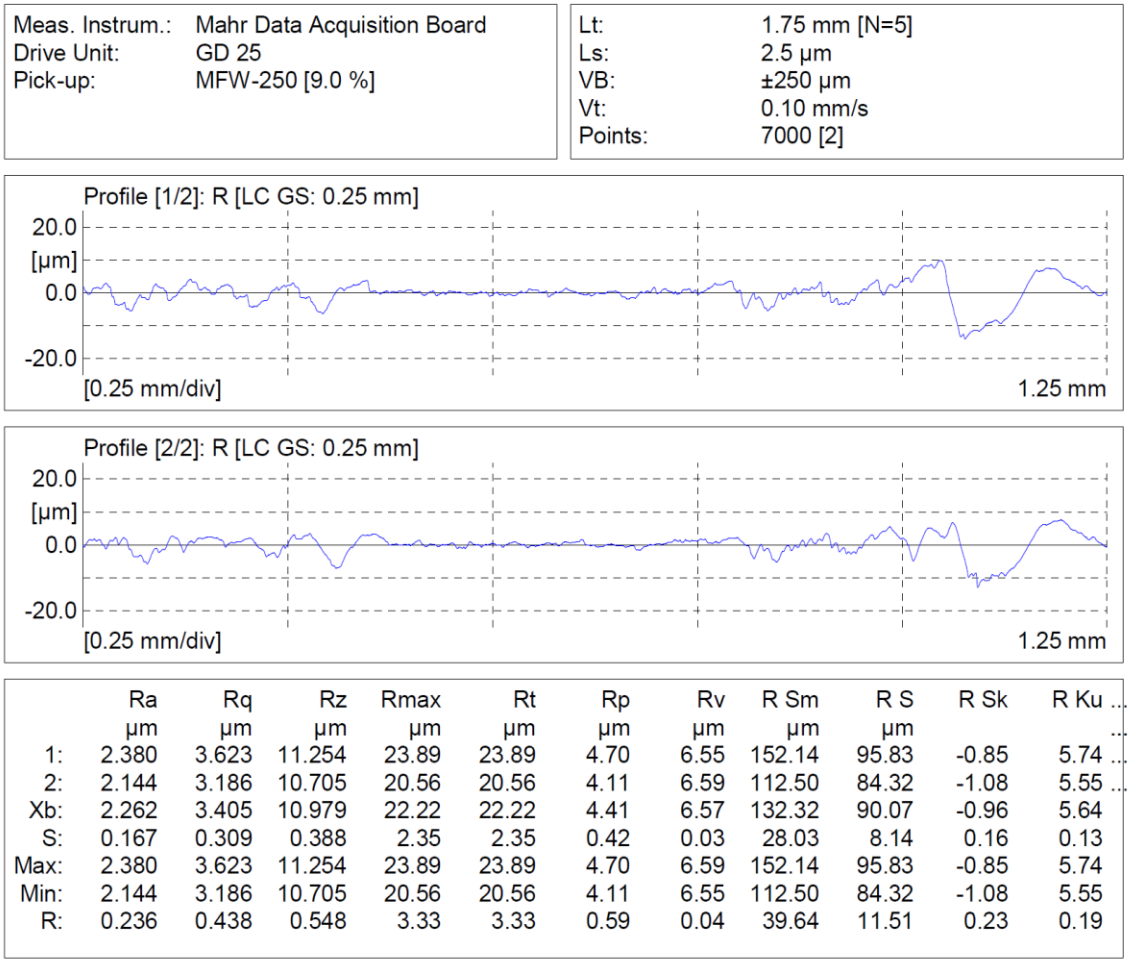

	Ra µm	Rq µm	Rz µm	Rmax µm	Rt µm	Rp µm	Rv µm	R Sm µm	R S µm	R Sk	R Ku ...
1:	2.380	3.623	11.254	23.89	23.89	4.70	6.55	152.14	95.83	-0.85	5.74 ...
2:	2.144	3.186	10.705	20.56	20.56	4.11	6.59	112.50	84.32	-1.08	5.55 ...
Xb:	2.262	3.405	10.979	22.22	22.22	4.41	6.57	132.32	90.07	-0.96	5.64
S:	0.167	0.309	0.388	2.35	2.35	0.42	0.03	28.03	8.14	0.16	0.13
Max:	2.380	3.623	11.254	23.89	23.89	4.70	6.59	152.14	95.83	-0.85	5.74
Min:	2.144	3.186	10.705	20.56	20.56	4.11	6.55	112.50	84.32	-1.08	5.55
R:	0.236	0.438	0.548	3.33	3.33	0.59	0.04	39.64	11.51	0.23	0.19

Figure A1. 17 Surface Profile (transverse) of CVD Endmill Trimmed Tension Test Specimen # 2

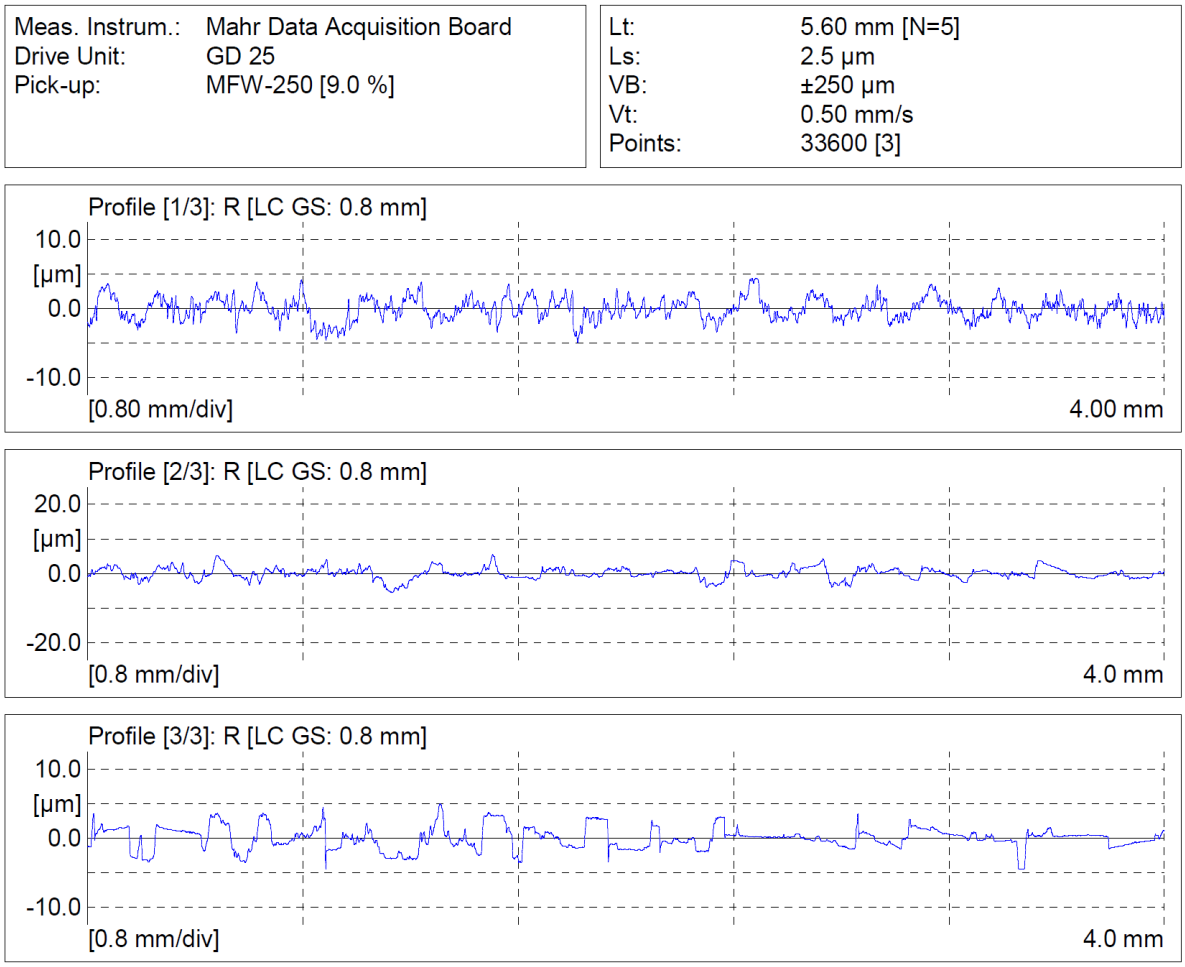

Figure A1. 18 Surface Profile (longitudinal) of CVD Endmill Trimmed Tension Test Specimen # 3

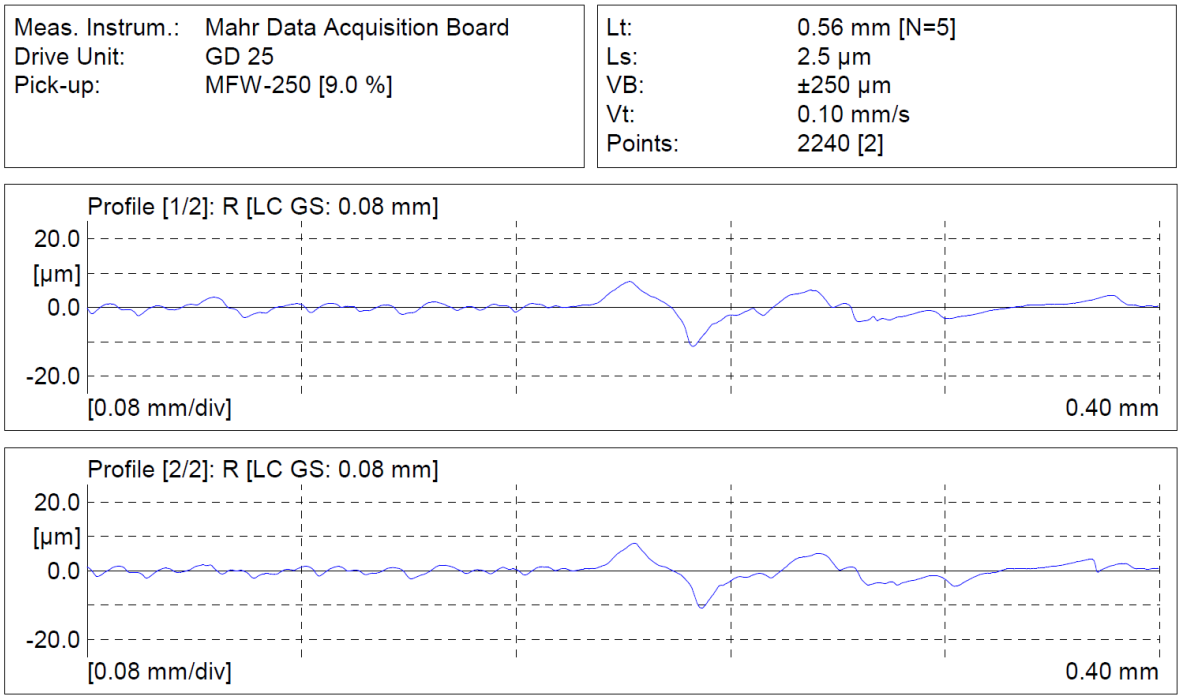

	Ra µm	Rq µm	Rz µm	Rmax µm	Rt µm	Rp µm	Rv µm	R Sm µm	R S µm	R Sk	R Ku	R Mr ... %	R Mr ... % ...
1:	1.755	2.542	8.885	18.91	18.91	4.13	4.75	50.29	41.61	-0.65	6.52	8.50	13.25 ...
2:	1.699	2.485	8.775	18.96	18.96	3.98	4.80	38.44	40.33	-0.54	6.51	7.75	10.75 ...
Xb:	1.727	2.514	8.830	18.93	18.93	4.05	4.78	44.37	40.97	-0.60	6.52	8.13	12.00
S:	0.040	0.041	0.078	0.03	0.03	0.11	0.03	8.37	0.90	0.08	0.00	0.53	1.77
Max:	1.755	2.542	8.885	18.96	18.96	4.13	4.80	50.29	41.61	-0.54	6.52	8.50	13.25
Min:	1.699	2.485	8.775	18.91	18.91	3.98	4.75	38.44	40.33	-0.65	6.51	7.75	10.75
R:	0.056	0.058	0.110	0.05	0.05	0.16	0.05	11.84	1.28	0.11	0.00	0.75	2.50

Figure A1. 19 Surface Profile (transverse) of CVD Endmill Trimmed Tension Test Specimen # 3

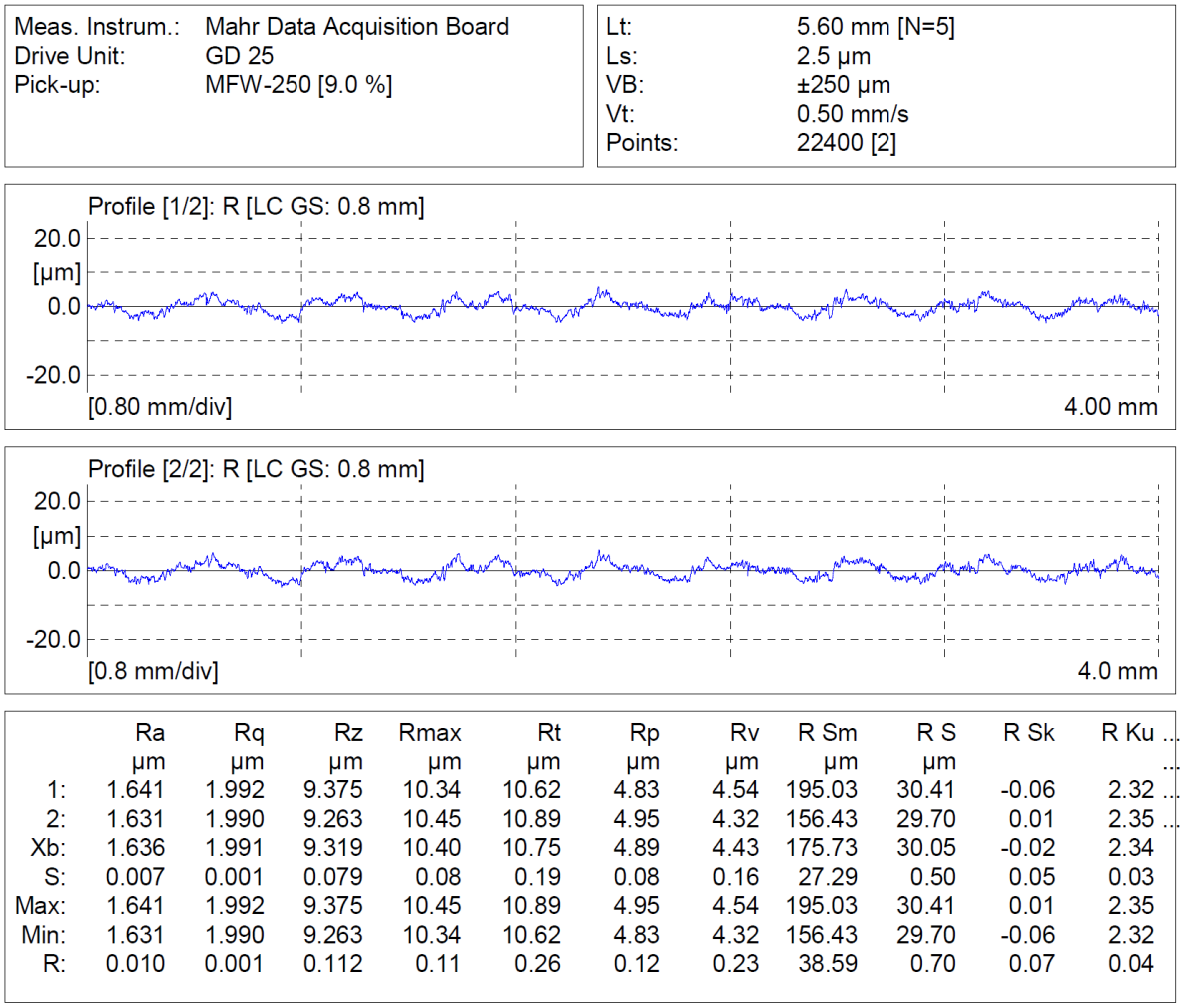

	Ra	Rq	Rz	Rmax	Rt	Rp	Rv	R Sm	R S	R Sk	R Ku ...
	µm	µm	µm	µm	µm	µm	µm	µm	µm		...
1:	1.641	1.992	9.375	10.34	10.62	4.83	4.54	195.03	30.41	-0.06	2.32 ...
2:	1.631	1.990	9.263	10.45	10.89	4.95	4.32	156.43	29.70	0.01	2.35 ...
Xb:	1.636	1.991	9.319	10.40	10.75	4.89	4.43	175.73	30.05	-0.02	2.34
S:	0.007	0.001	0.079	0.08	0.19	0.08	0.16	27.29	0.50	0.05	0.03
Max:	1.641	1.992	9.375	10.45	10.89	4.95	4.54	195.03	30.41	0.01	2.35
Min:	1.631	1.990	9.263	10.34	10.62	4.83	4.32	156.43	29.70	-0.06	2.32
R:	0.010	0.001	0.112	0.11	0.26	0.12	0.23	38.59	0.70	0.07	0.04

Figure A1. 20 Surface Profile (longitudinal) of CVD Endmill Trimmed Tension Test Specimen # 4

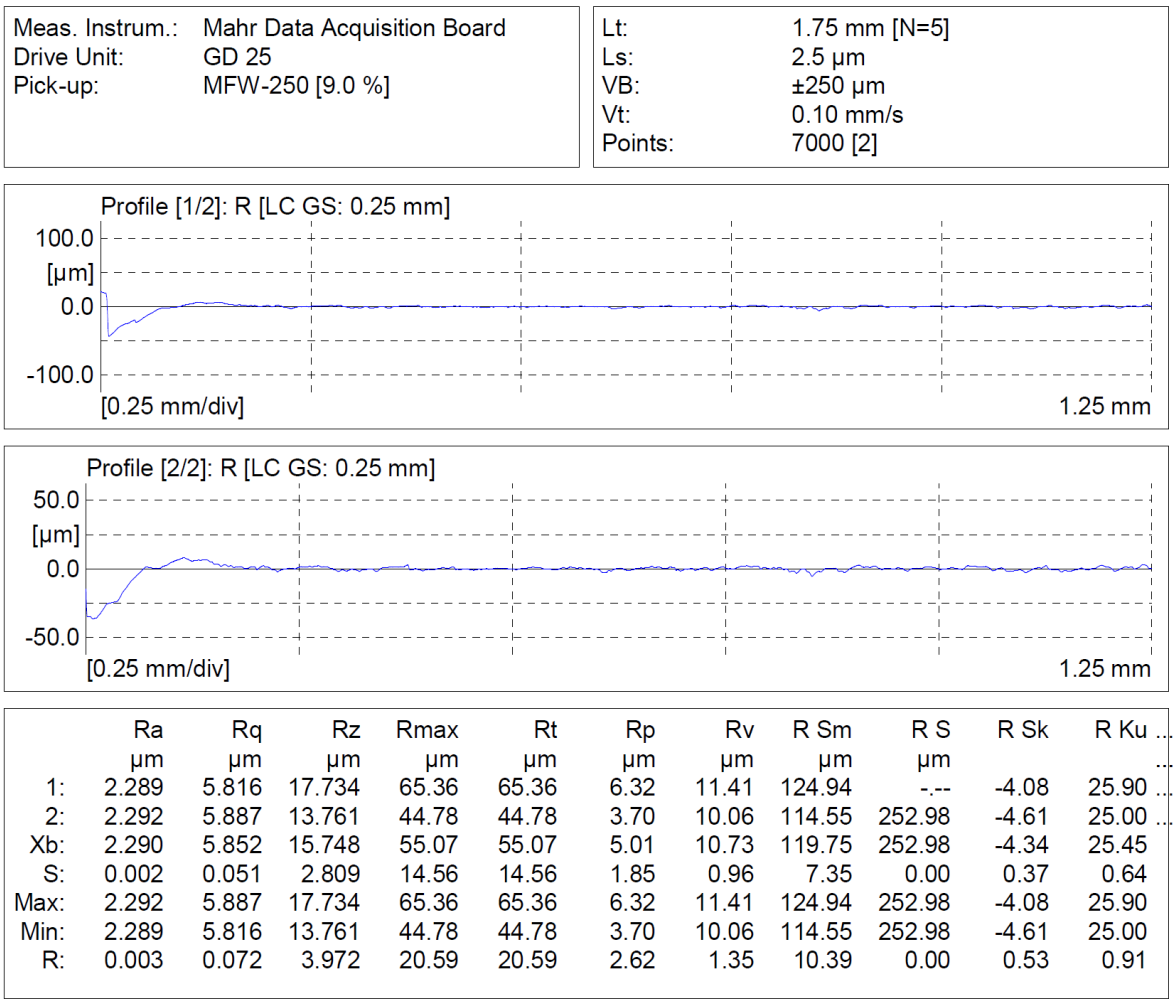

	Ra	Rq	Rz	Rmax	Rt	Rp	Rv	R Sm	R S	R Sk	R Ku ...
	µm	µm	µm	µm	µm	µm	µm	µm	µm		...
1:	2.289	5.816	17.734	65.36	65.36	6.32	11.41	124.94	-.--	-4.08	25.90 ...
2:	2.292	5.887	13.761	44.78	44.78	3.70	10.06	114.55	252.98	-4.61	25.00 ...
Xb:	2.290	5.852	15.748	55.07	55.07	5.01	10.73	119.75	252.98	-4.34	25.45
S:	0.002	0.051	2.809	14.56	14.56	1.85	0.96	7.35	0.00	0.37	0.64
Max:	2.292	5.887	17.734	65.36	65.36	6.32	11.41	124.94	252.98	-4.08	25.90
Min:	2.289	5.816	13.761	44.78	44.78	3.70	10.06	114.55	252.98	-4.61	25.00
R:	0.003	0.072	3.972	20.59	20.59	2.62	1.35	10.39	0.00	0.53	0.91

Figure A1. 21 Surface Profile (transverse) of CVD Endmill Trimmed Tension Test Specimen # 4

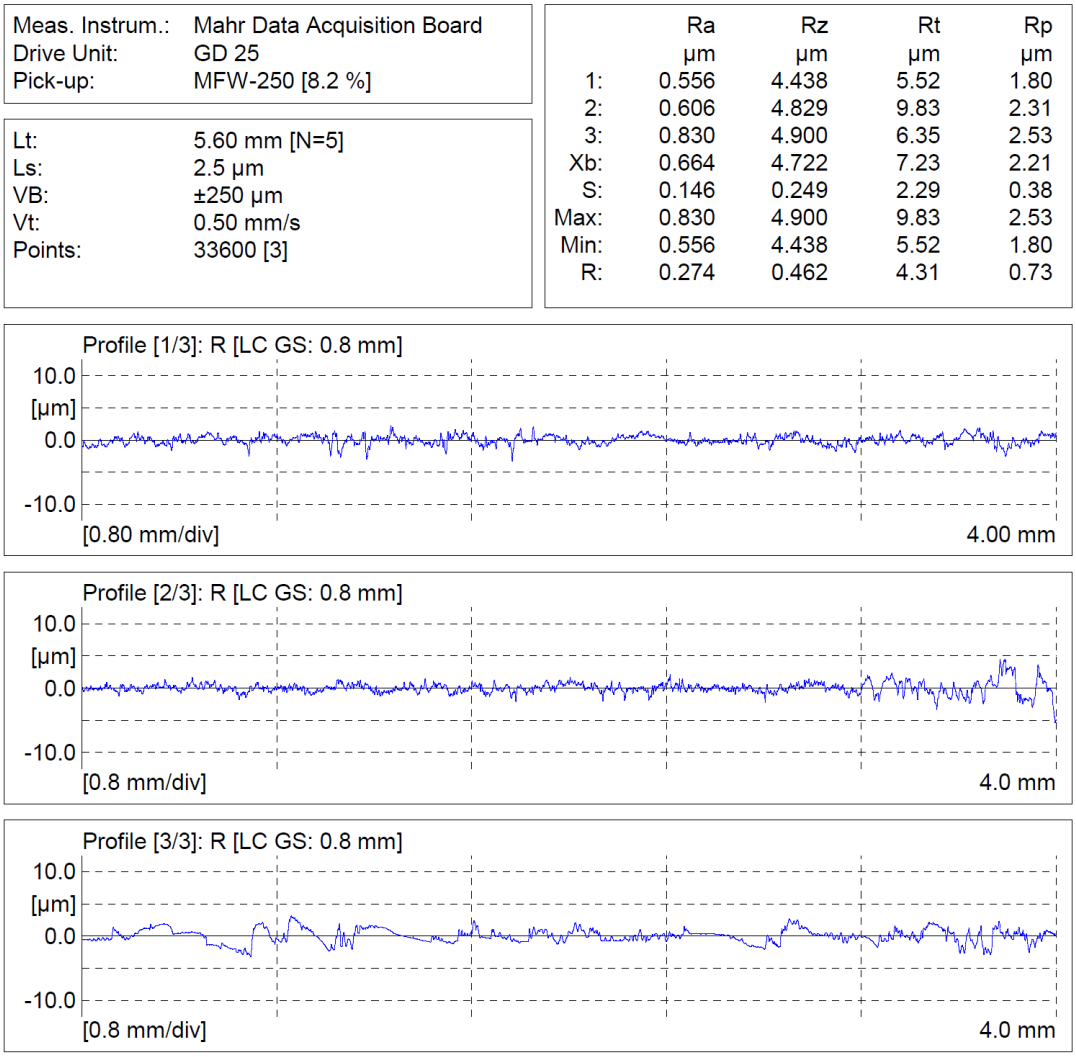

Figure A1. 22 Surface Profile (longitudinal) of PCD Endmill Trimmed Tension Test Specimen # 1

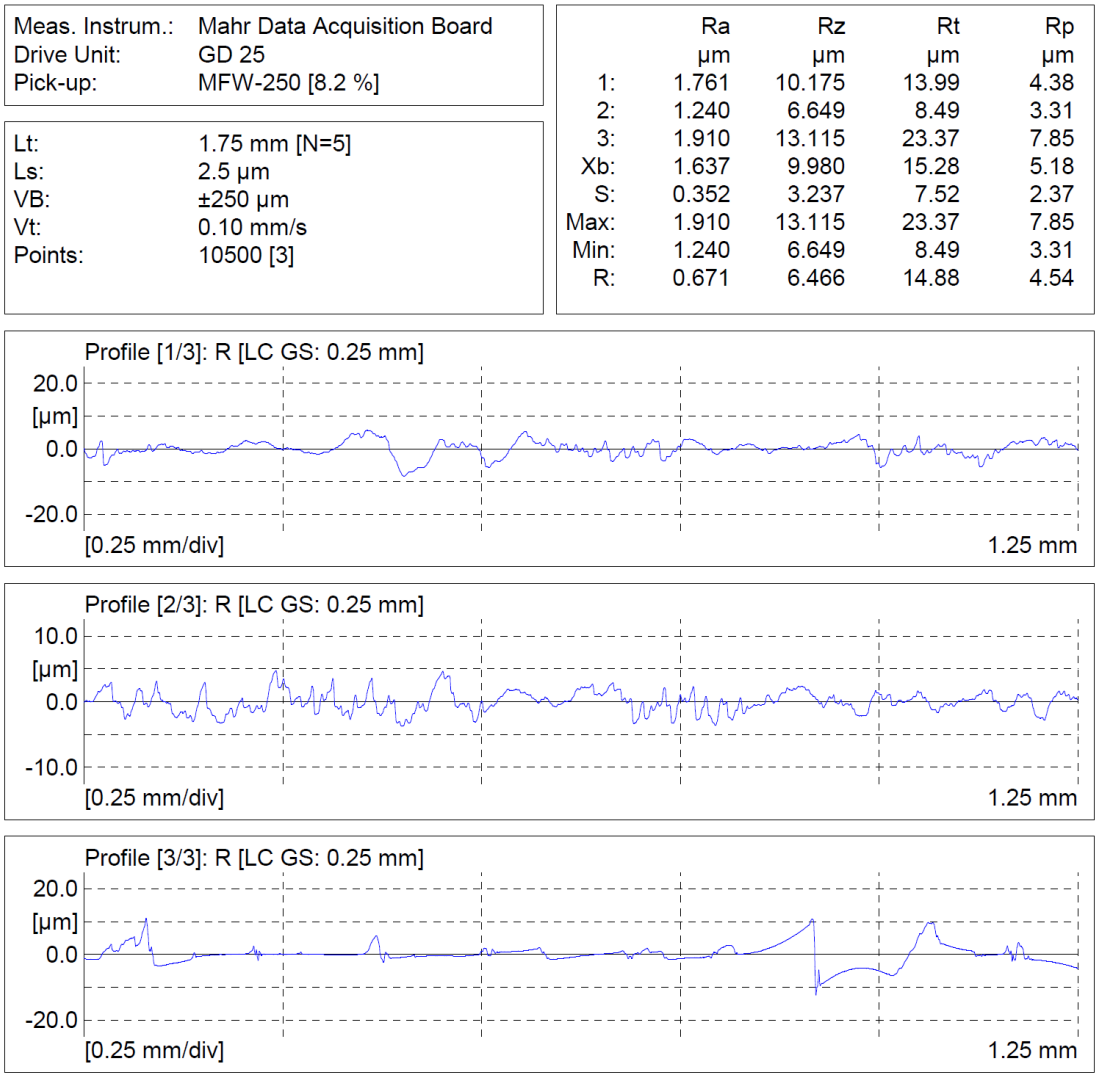

Figure A1. 23 Surface Profile (transverse) of PCD Endmill Trimmed Tension Test Specimen # 1

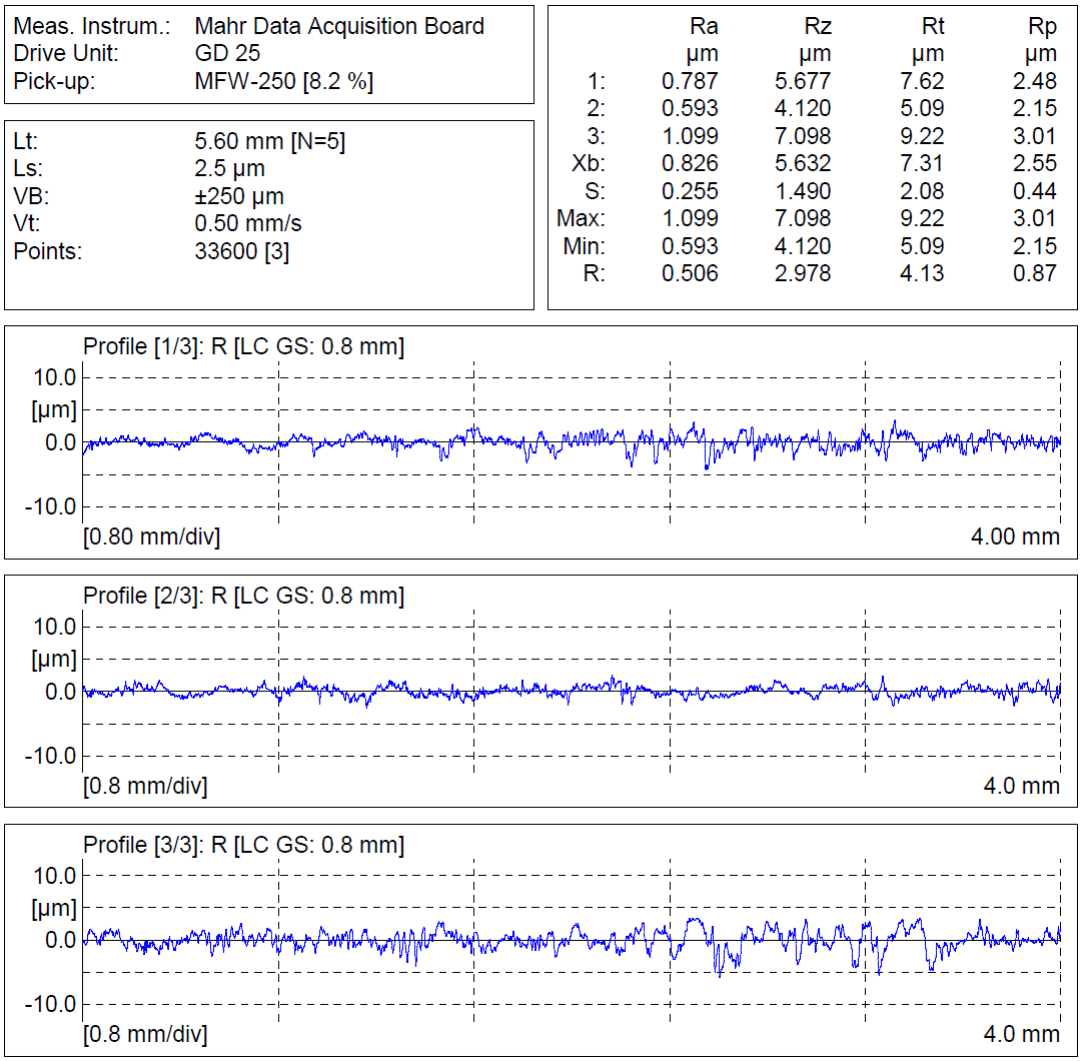

Figure A1. 24 Surface Profile (longitudinal) of PCD Endmill Trimmed Tension Test Specimen # 2

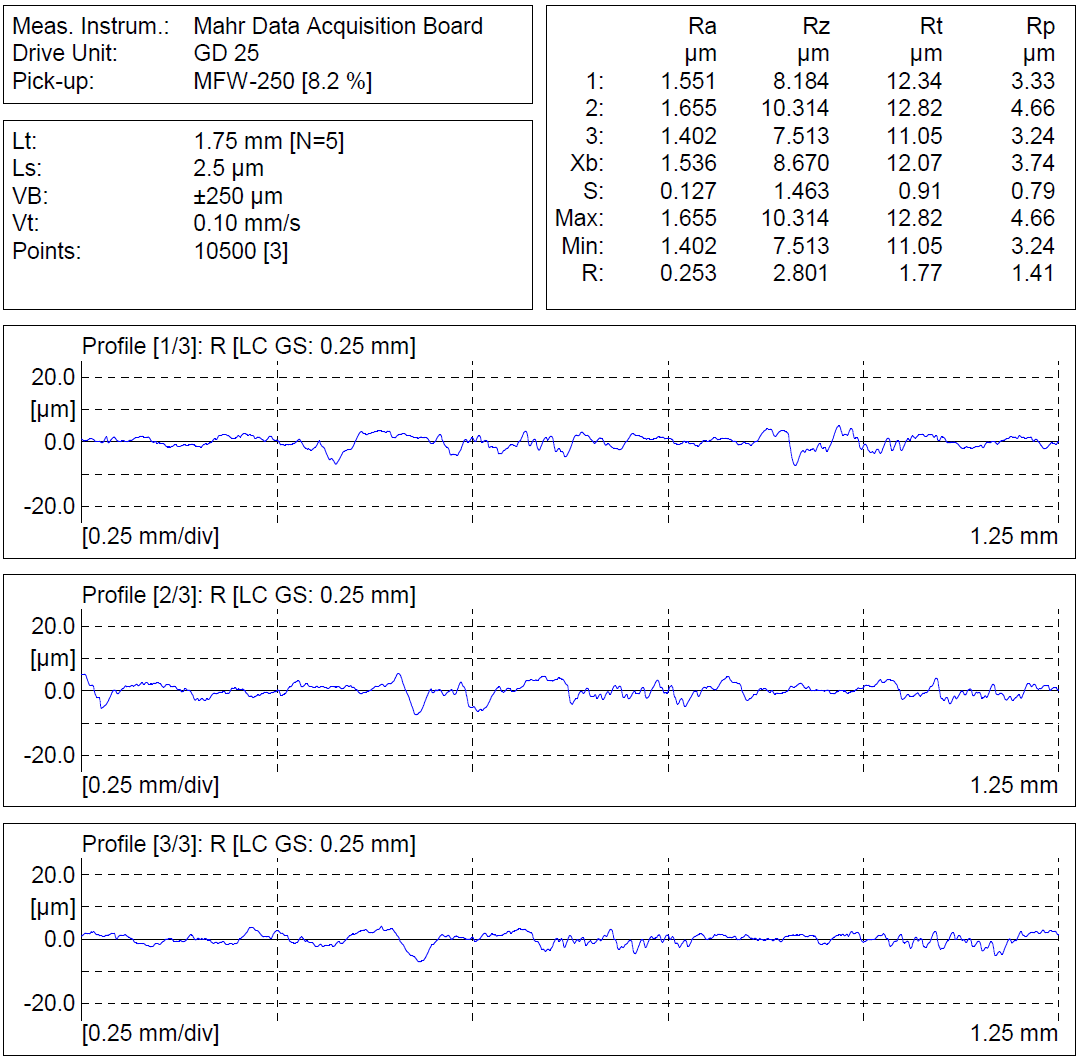

Figure A1. 25 Surface Profile (transverse) of PCD Endmill Trimmed Tension Test Specimen # 2

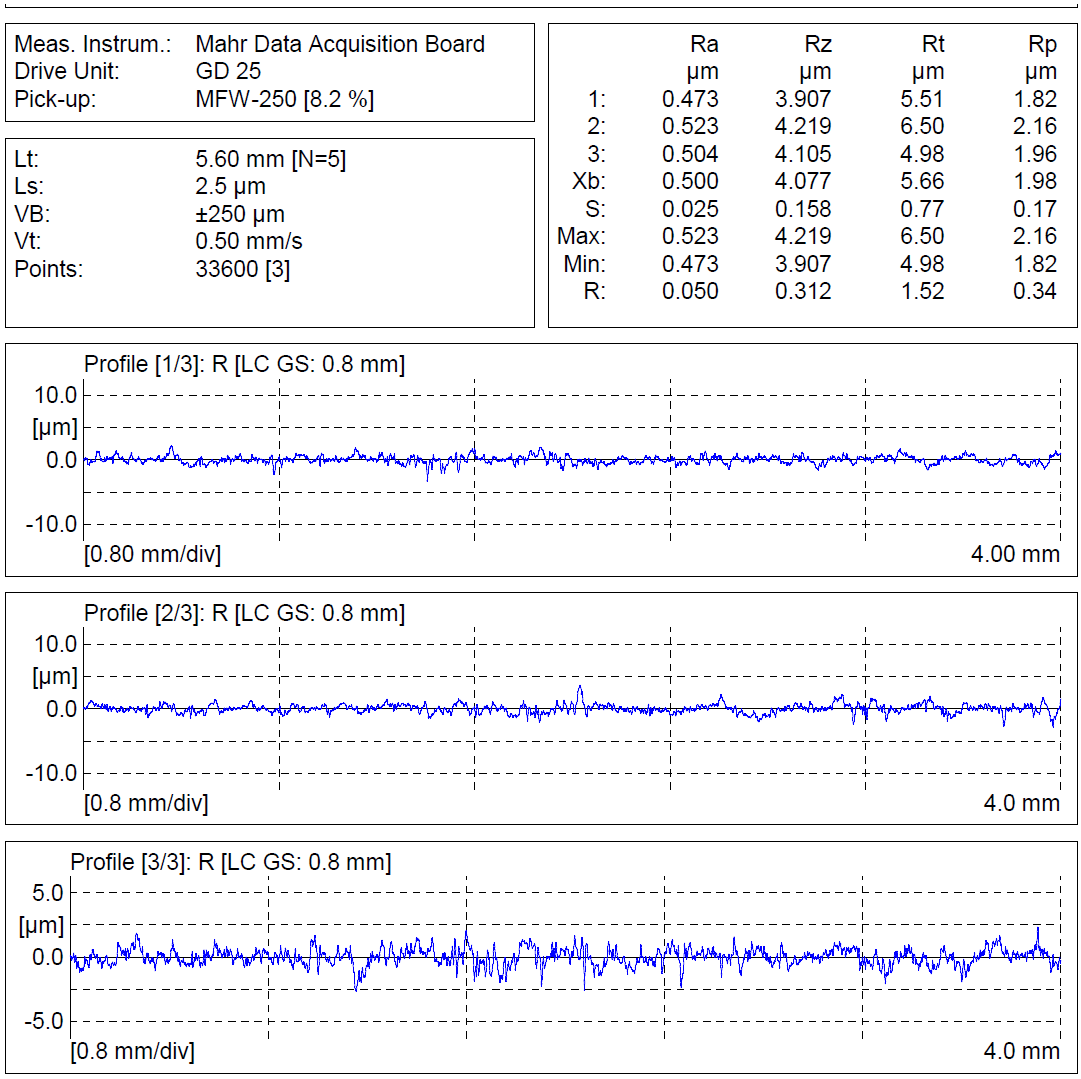

Figure A1. 26 Surface Profile (longitudinal) of PCD Endmill Trimmed Tension Test Specimen # 3

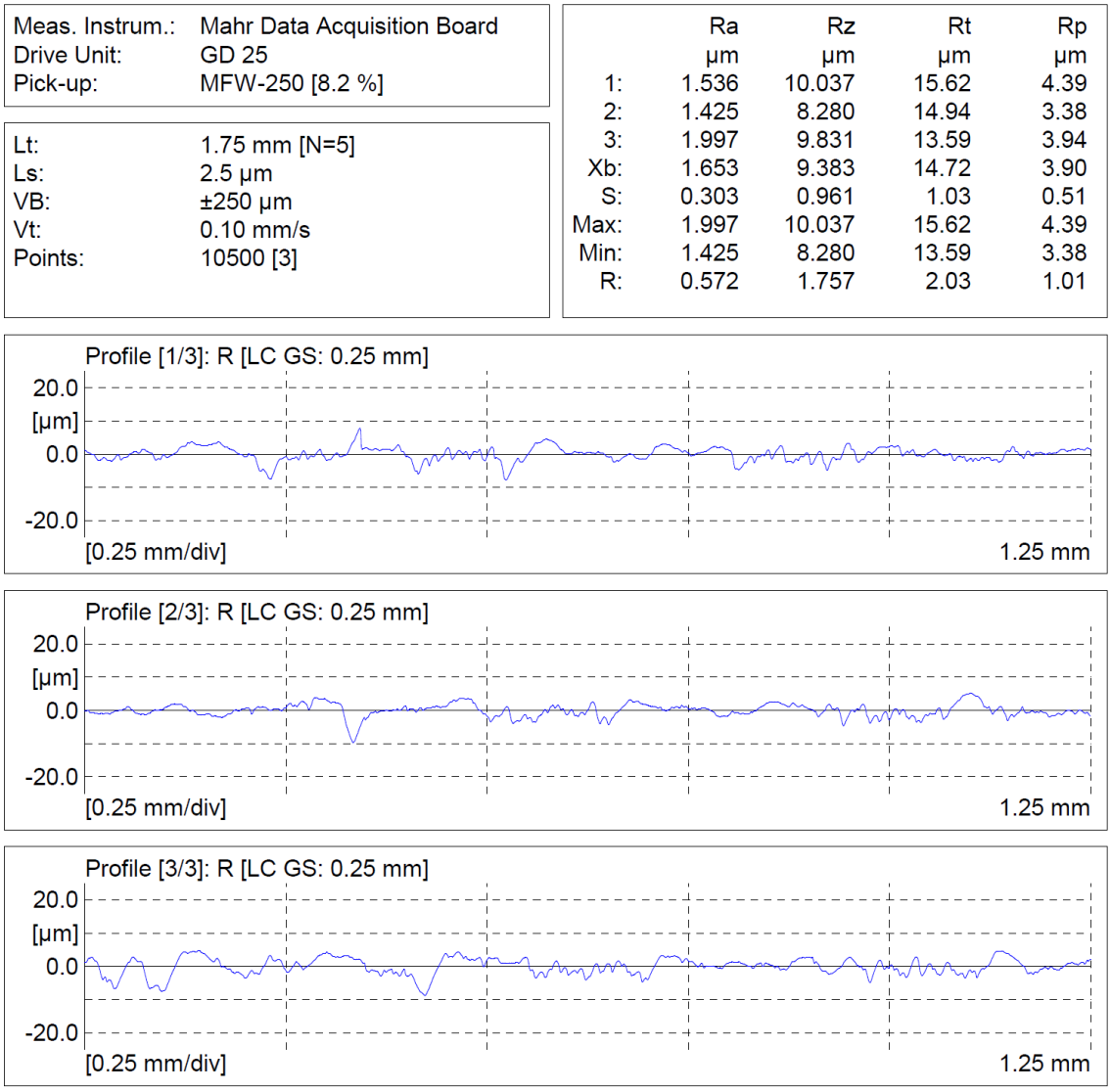

Figure A1. 27 Surface Profile (transverse) of PCD Endmill Trimmed Tension Test Specimen # 3

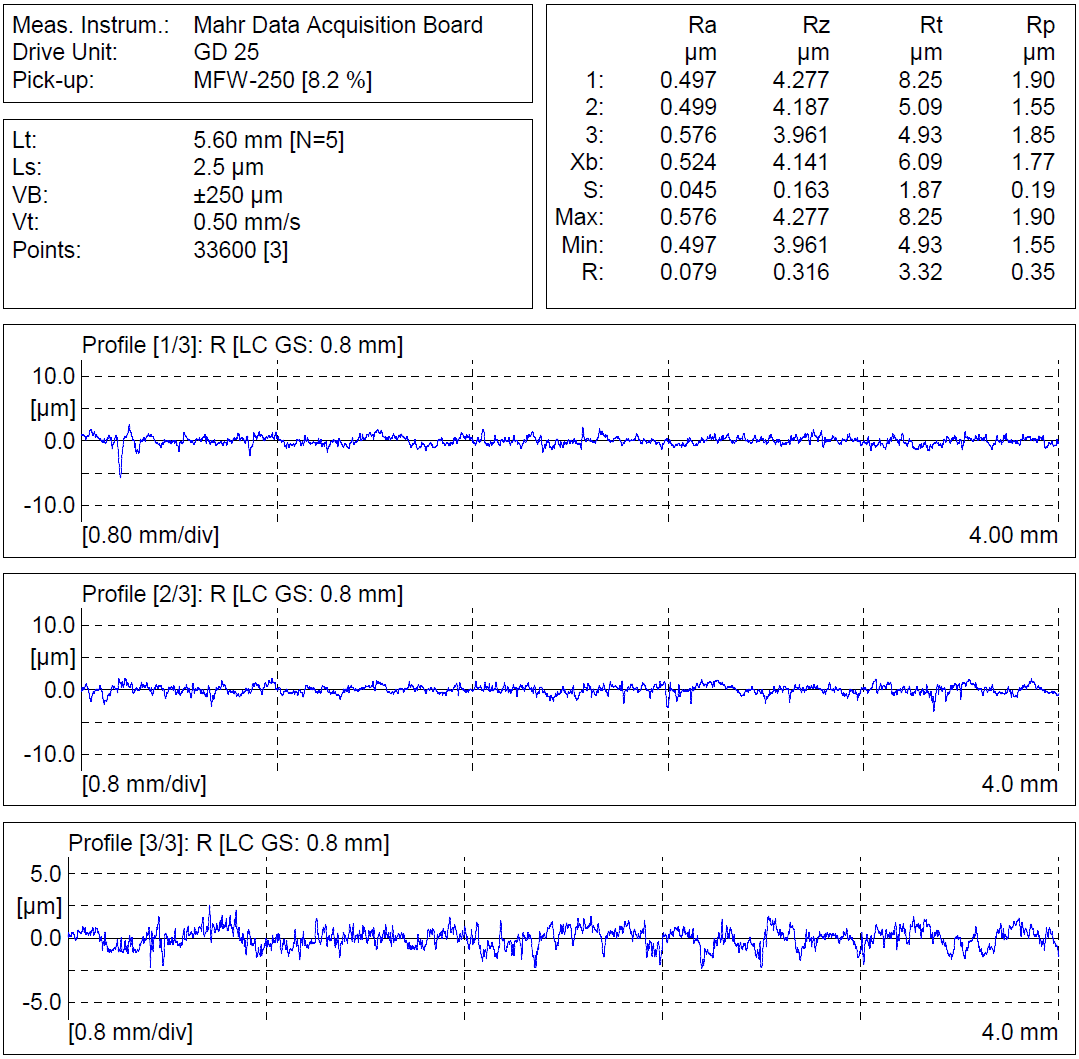

Figure A1. 28 Surface Profile (longitudinal) of PCD Endmill Trimmed Tension Test Specimen # 4

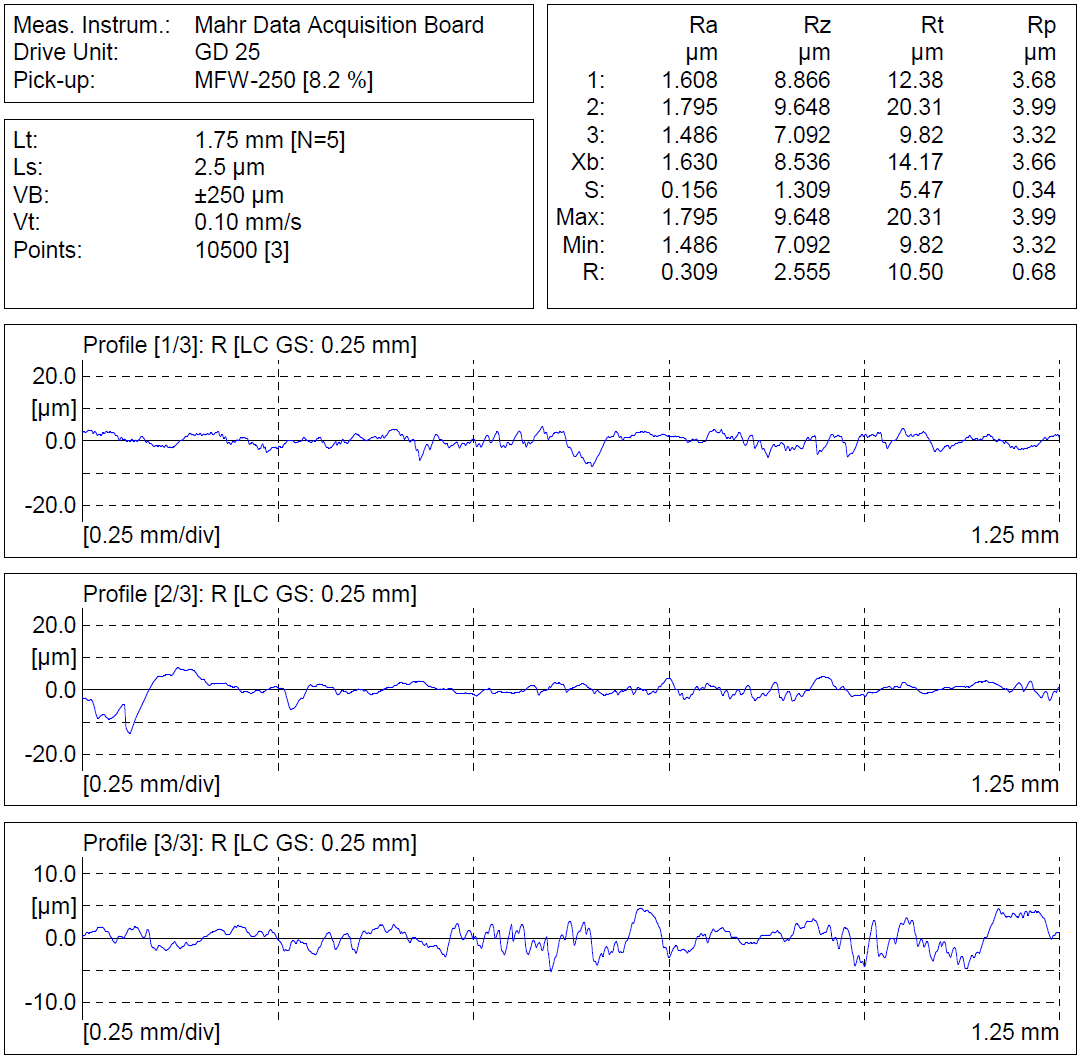

Figure A1. 29 Surface Profile (transverse) of PCD Endmill Trimmed Tension Test Specimen # 4

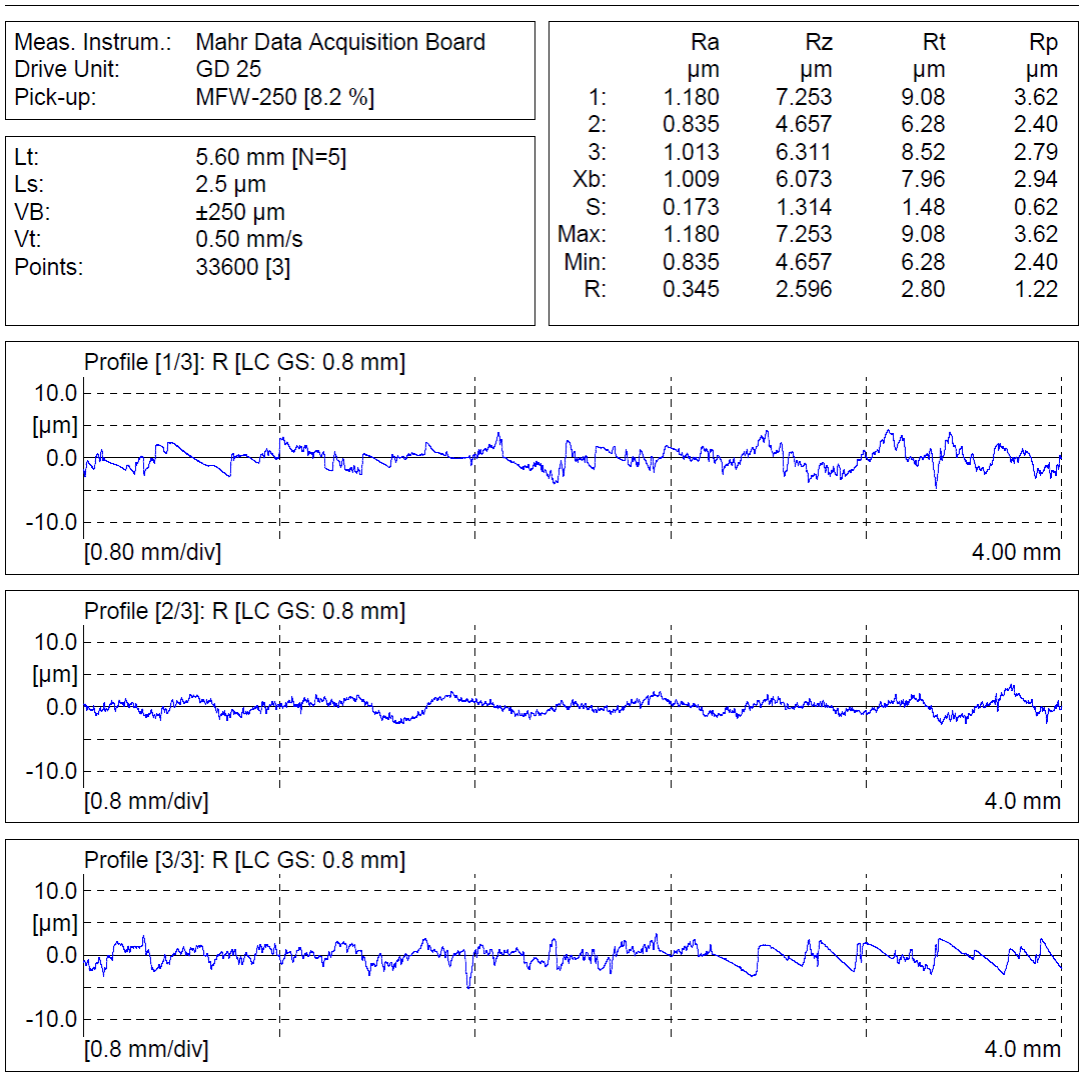

Figure A1. 30 Surface Profile (longitudinal) of PCD Endmill Trimmed Compression Test Specimen # 1

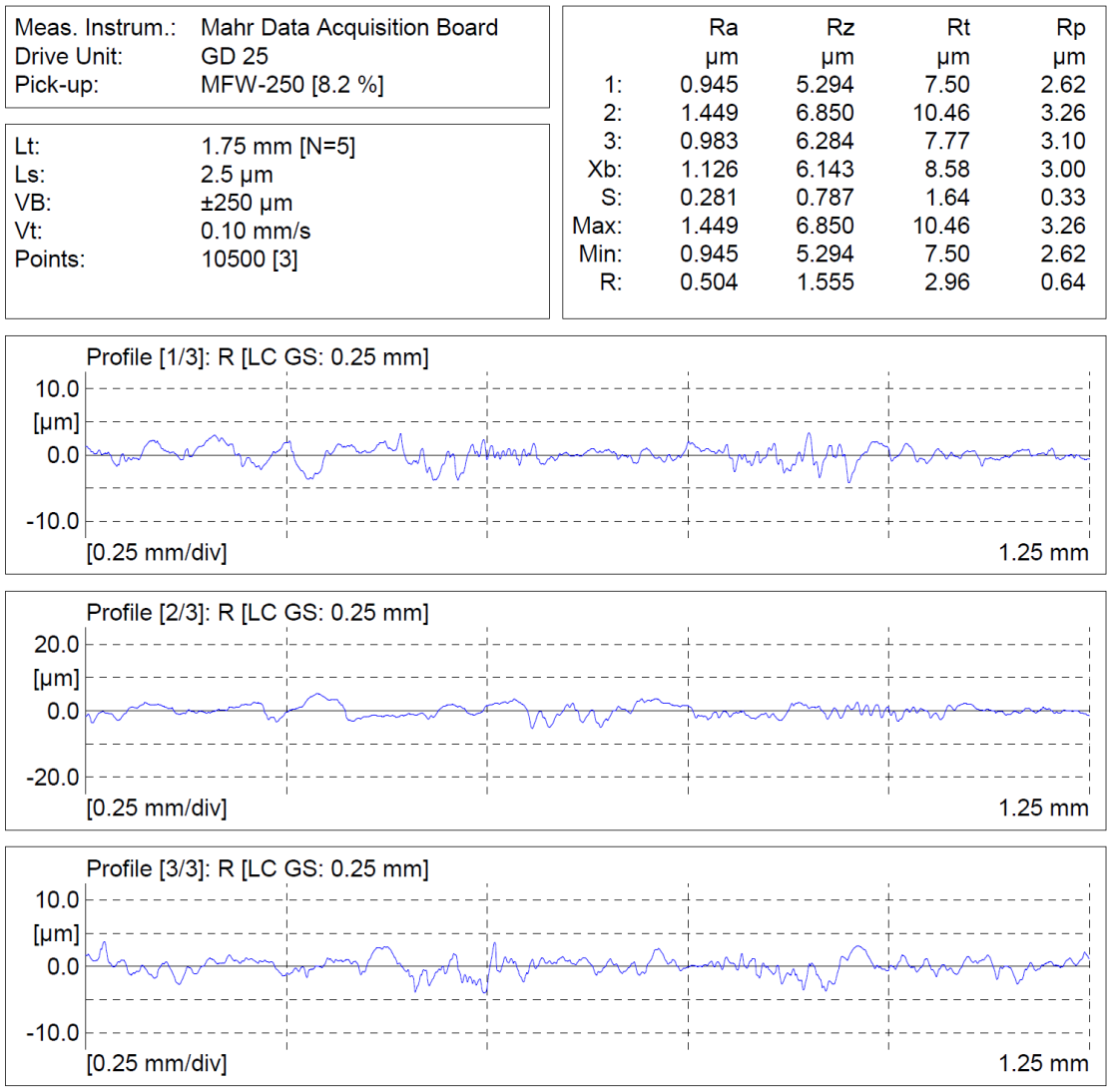

Figure A1. 31 Surface Profile (transverse) of PCD Endmill Trimmed Compression Test Specimen # 1

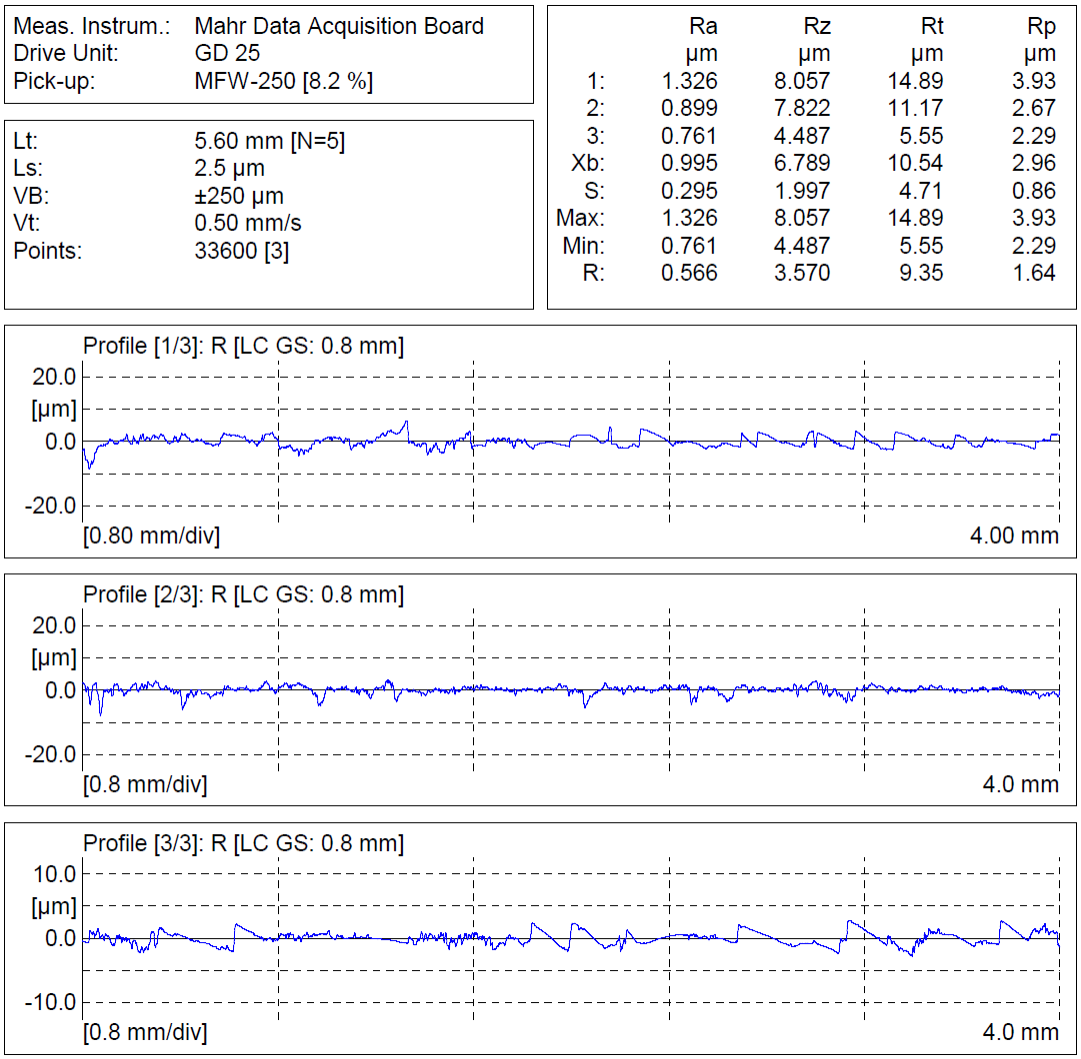

Figure A1. 32 Surface Profile (longitudinal) of PCD Endmill Trimmed Compression Test Specimen # 2

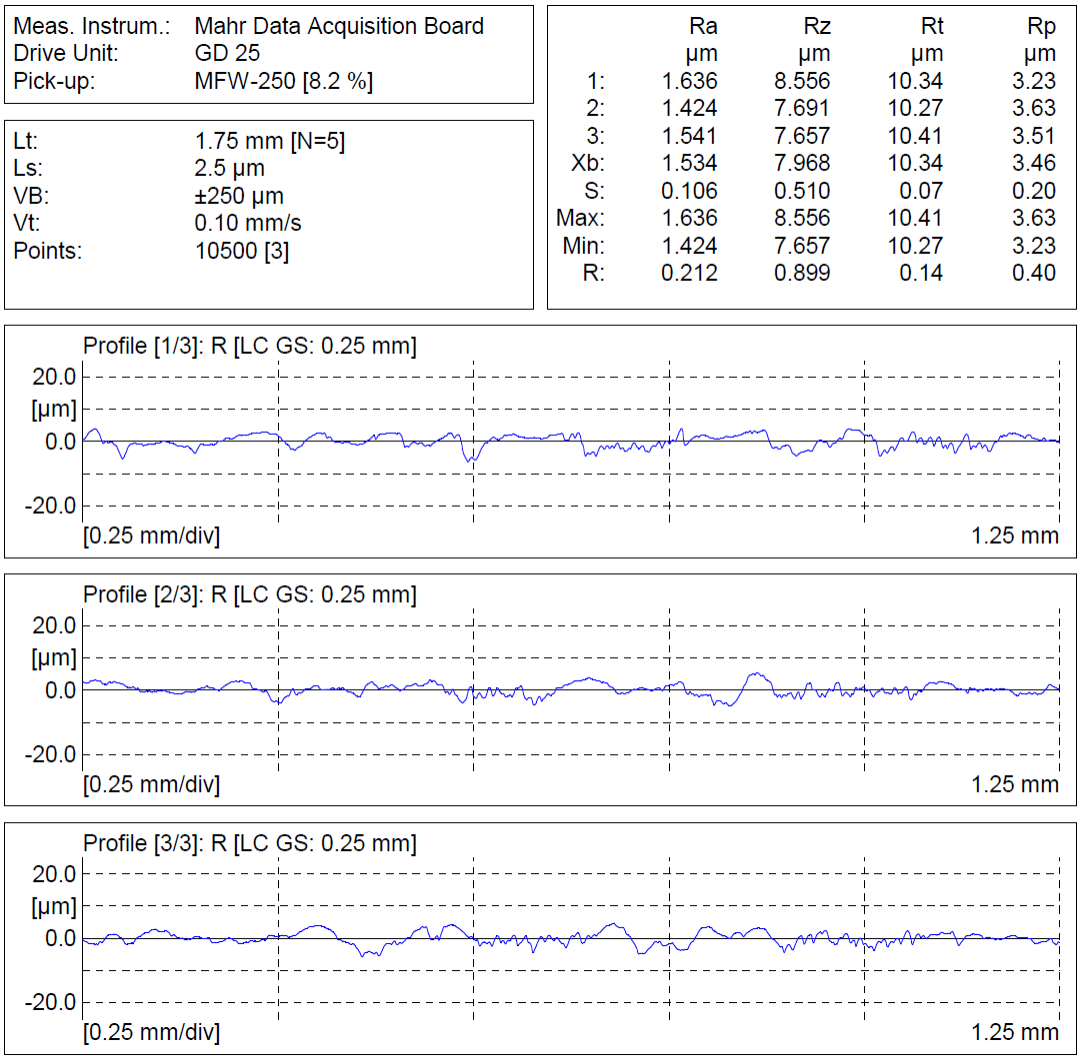

Figure A1. 33 Surface Profile (transverse) of PCD Endmill Trimmed Compression Test Specimen # 2

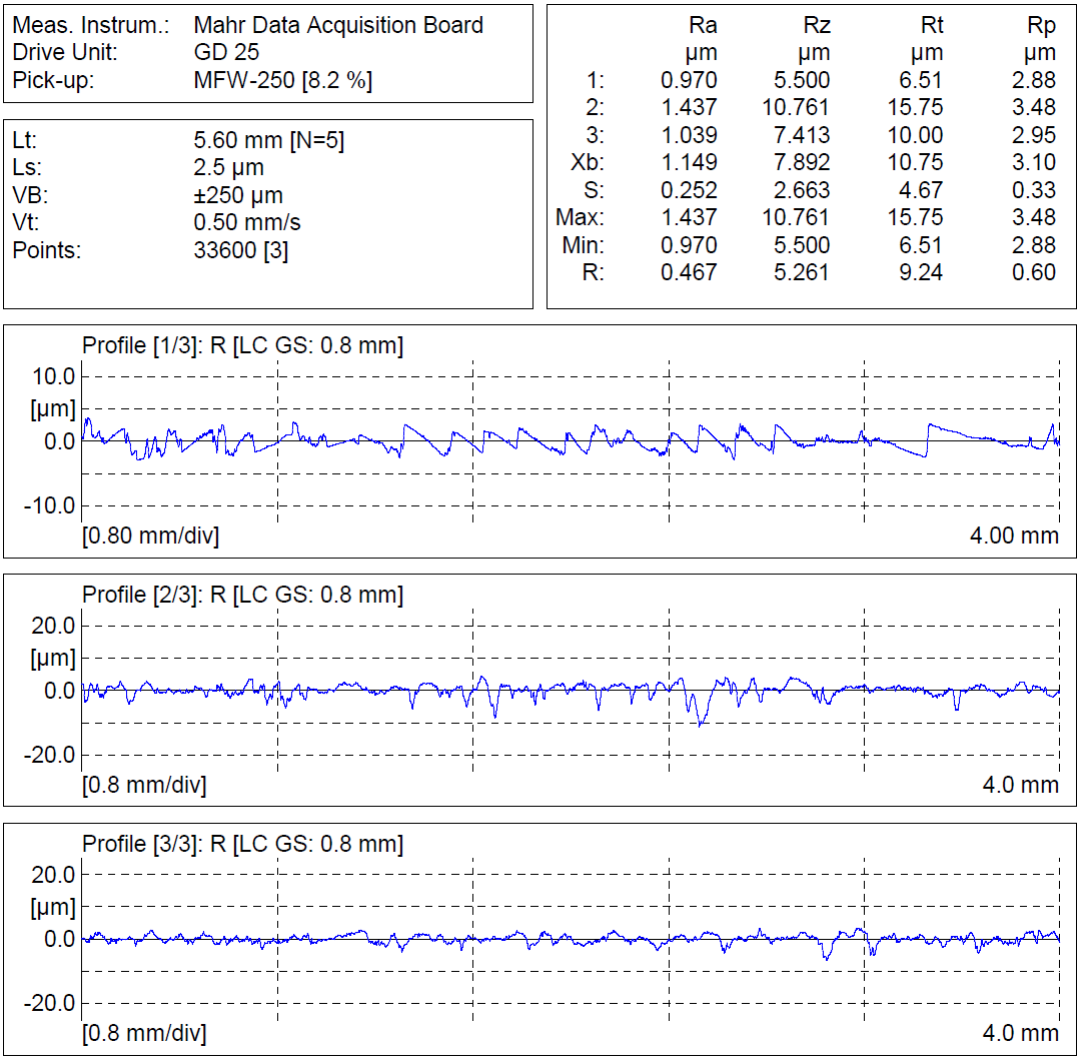

Figure A1. 34 Surface Profile (longitudinal) of PCD Endmill Trimmed Compression Test Specimen # 3

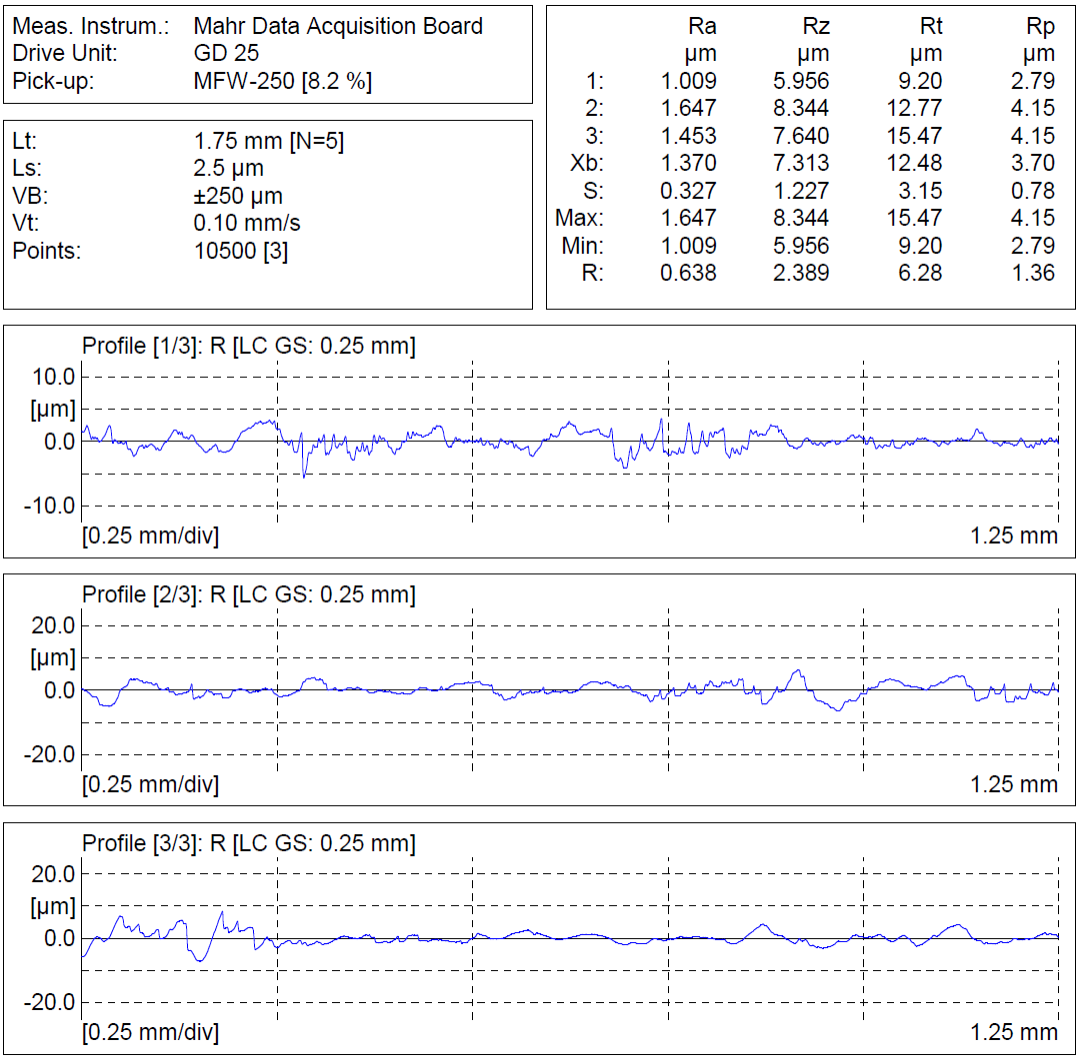

Figure A1. 35 Surface Profile (transverse) of PCD Endmill Trimmed Compression Test Specimen # 3

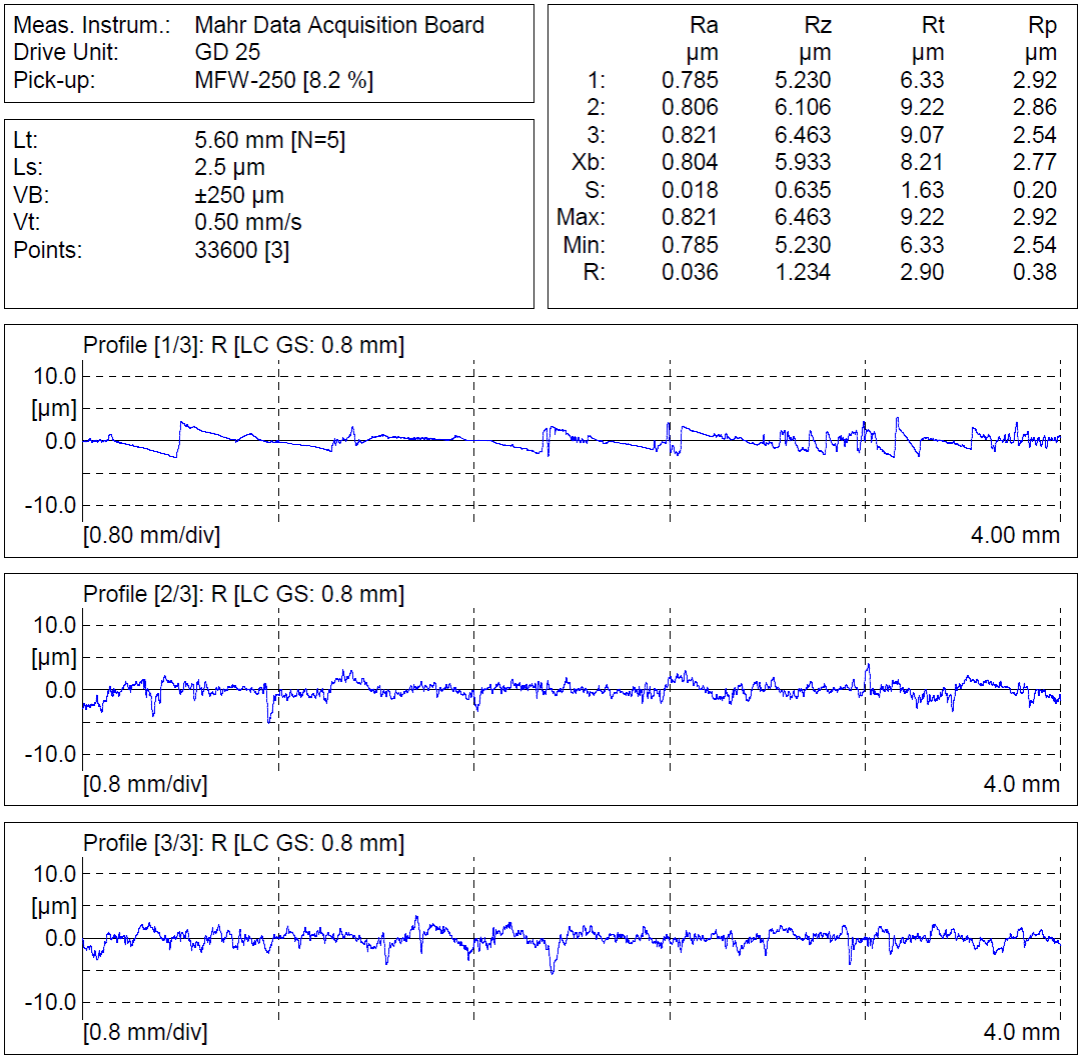

Figure A1. 36 Surface Profile (longitudinal) of PCD Endmill Trimmed Compression Test Specimen # 4

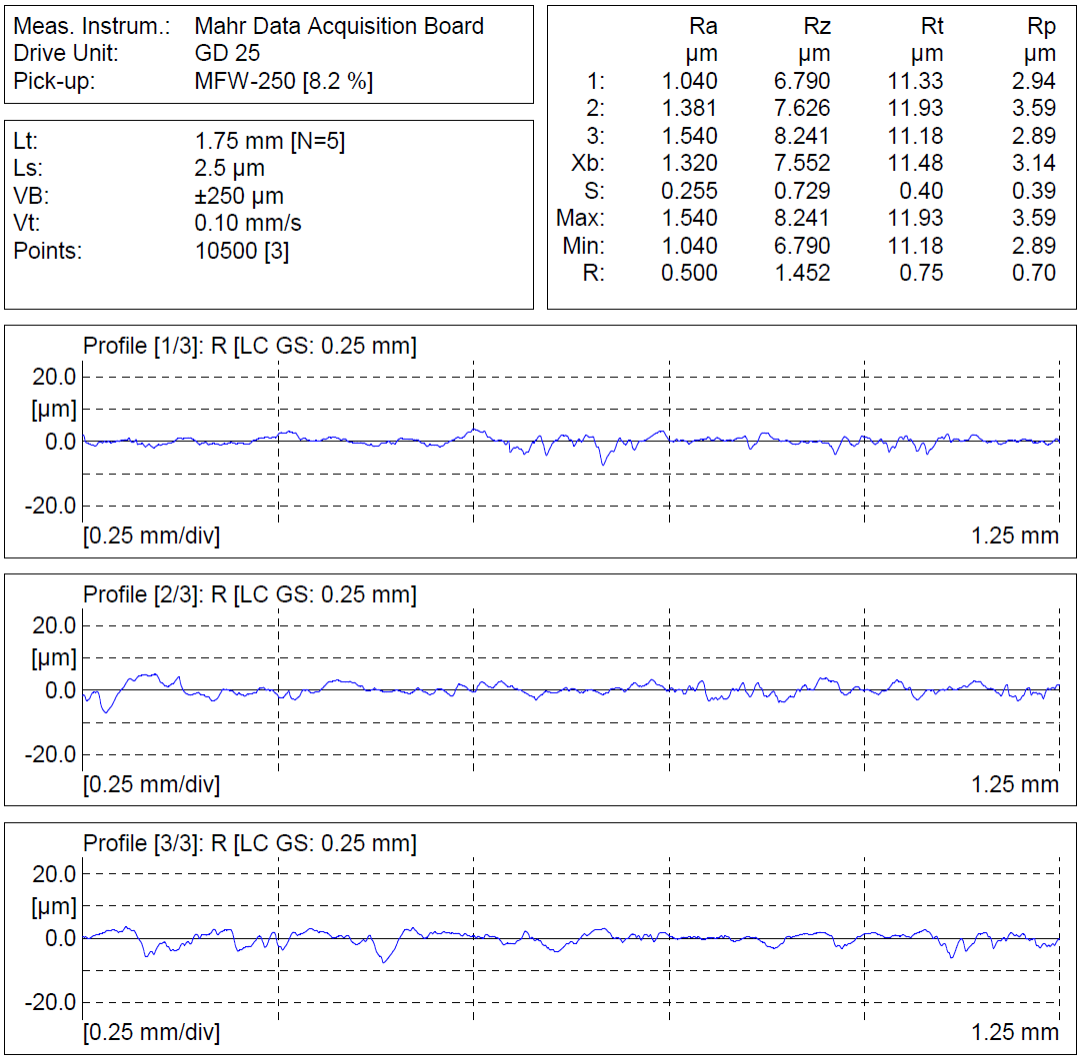

Figure A1. 37 Surface Profile (transverse) of PCD Endmill Trimmed Compression Test Specimen # 4

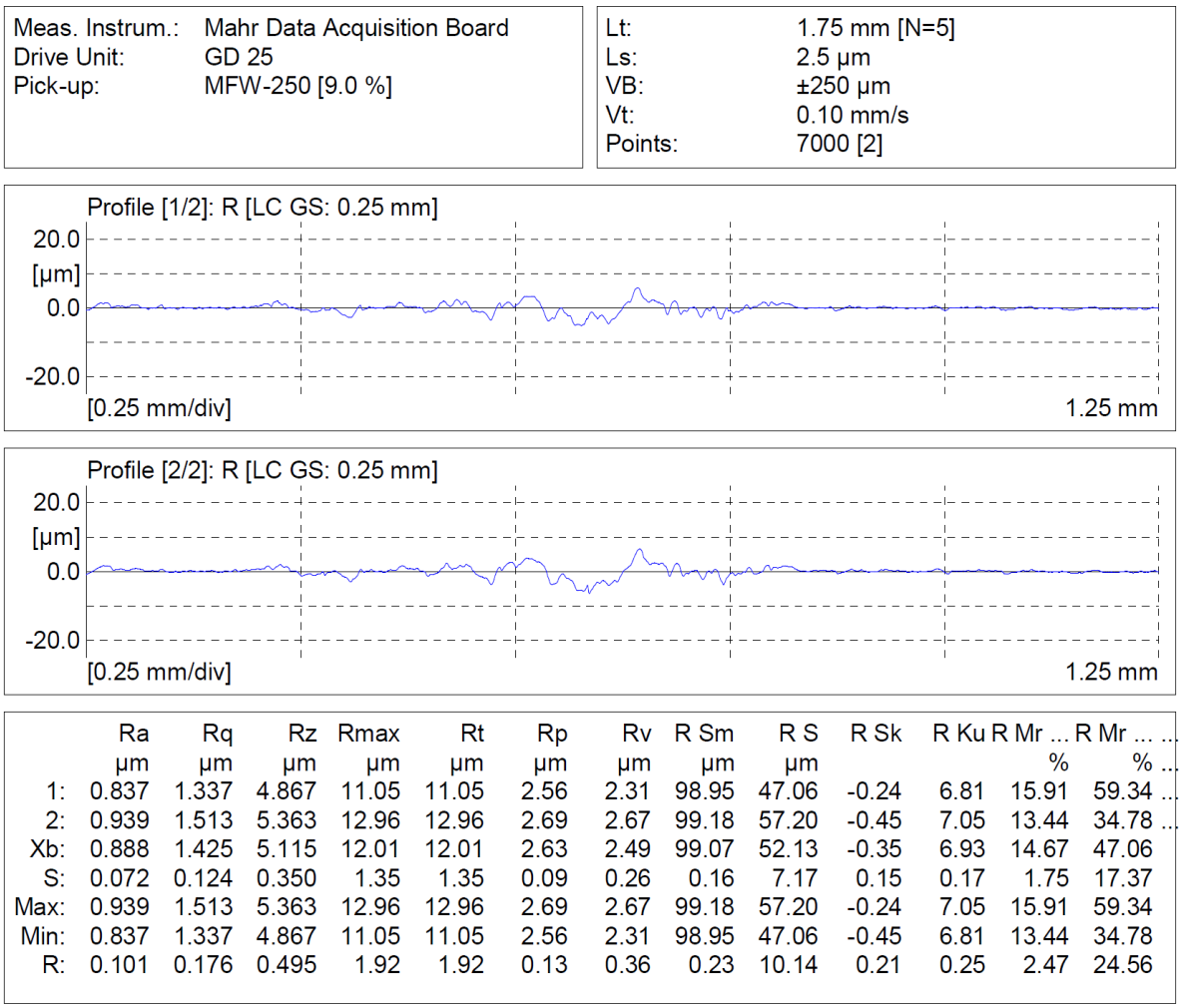

	Ra µm	Rq µm	Rz µm	Rmax µm	Rt µm	Rp µm	Rv µm	R Sm µm	R S µm	R Sk	R Ku	R Mr ... %	R Mr ... %	...
1:	0.837	1.337	4.867	11.05	11.05	2.56	2.31	98.95	47.06	-0.24	6.81	15.91	59.34	...
2:	0.939	1.513	5.363	12.96	12.96	2.69	2.67	99.18	57.20	-0.45	7.05	13.44	34.78	...
Xb:	0.888	1.425	5.115	12.01	12.01	2.63	2.49	99.07	52.13	-0.35	6.93	14.67	47.06	
S:	0.072	0.124	0.350	1.35	1.35	0.09	0.26	0.16	7.17	0.15	0.17	1.75	17.37	
Max:	0.939	1.513	5.363	12.96	12.96	2.69	2.67	99.18	57.20	-0.24	7.05	15.91	59.34	
Min:	0.837	1.337	4.867	11.05	11.05	2.56	2.31	98.95	47.06	-0.45	6.81	13.44	34.78	
R:	0.101	0.176	0.495	1.92	1.92	0.13	0.36	0.23	10.14	0.21	0.25	2.47	24.56	

Figure A1. 38 Surface Profile of CVD Drilled Hole, Feedrate 305 mm/min, Open Hole Tension Test Specimen # 1

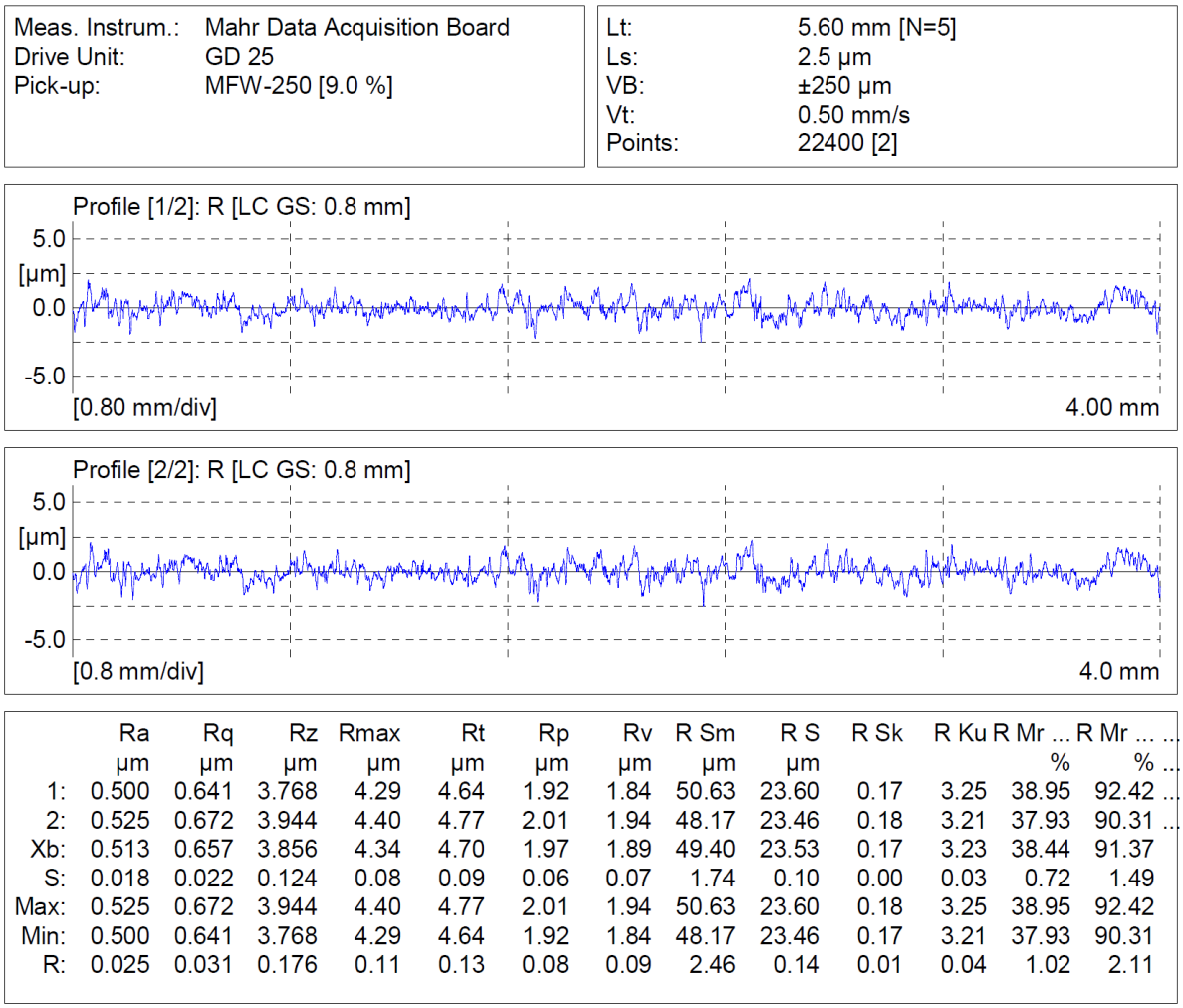

	Ra µm	Rq µm	Rz µm	Rmax µm	Rt µm	Rp µm	Rv µm	R Sm µm	R S µm	R Sk	R Ku	R Mr ... %	R Mr ... % ...
1:	0.500	0.641	3.768	4.29	4.64	1.92	1.84	50.63	23.60	0.17	3.25	38.95	92.42 ...
2:	0.525	0.672	3.944	4.40	4.77	2.01	1.94	48.17	23.46	0.18	3.21	37.93	90.31 ...
Xb:	0.513	0.657	3.856	4.34	4.70	1.97	1.89	49.40	23.53	0.17	3.23	38.44	91.37
S:	0.018	0.022	0.124	0.08	0.09	0.06	0.07	1.74	0.10	0.00	0.03	0.72	1.49
Max:	0.525	0.672	3.944	4.40	4.77	2.01	1.94	50.63	23.60	0.18	3.25	38.95	92.42
Min:	0.500	0.641	3.768	4.29	4.64	1.92	1.84	48.17	23.46	0.17	3.21	37.93	90.31
R:	0.025	0.031	0.176	0.11	0.13	0.08	0.09	2.46	0.14	0.01	0.04	1.02	2.11

Figure A1. 39 Surface Profile of CVD Drilled Hole, Feedrate 305 mm/min, PCD Endmill Trimmed Edge (longitudinal) of Open Hole Tension Test Specimen # 1

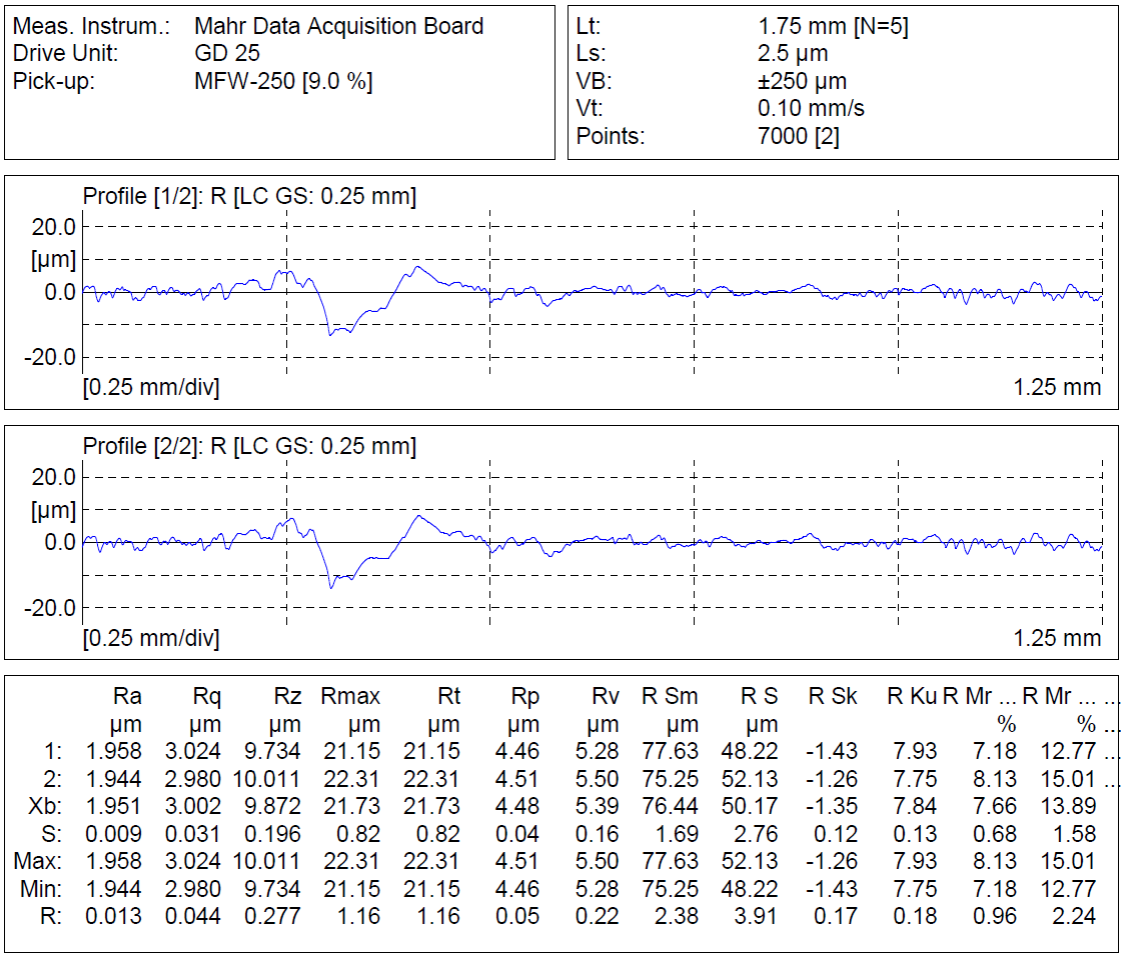

	Ra	Rq	Rz	Rmax	Rt	Rp	Rv	R Sm	R S	R Sk	R Ku	R Mr ...	R Mr ...	...
	µm	µm	µm	µm	µm	µm	µm	µm	µm			%	%	...
1:	1.958	3.024	9.734	21.15	21.15	4.46	5.28	77.63	48.22	-1.43	7.93	7.18	12.77	...
2:	1.944	2.980	10.011	22.31	22.31	4.51	5.50	75.25	52.13	-1.26	7.75	8.13	15.01	...
Xb:	1.951	3.002	9.872	21.73	21.73	4.48	5.39	76.44	50.17	-1.35	7.84	7.66	13.89	
S:	0.009	0.031	0.196	0.82	0.82	0.04	0.16	1.69	2.76	0.12	0.13	0.68	1.58	
Max:	1.958	3.024	10.011	22.31	22.31	4.51	5.50	77.63	52.13	-1.26	7.93	8.13	15.01	
Min:	1.944	2.980	9.734	21.15	21.15	4.46	5.28	75.25	48.22	-1.43	7.75	7.18	12.77	
R:	0.013	0.044	0.277	1.16	1.16	0.05	0.22	2.38	3.91	0.17	0.18	0.96	2.24	

Figure A1. 40 Surface Profile of CVD Drilled Hole, Feedrate 305 mm/min, PCD Endmill Trimmed Edge (transverse) of Open Hole Tension Test Specimen # 1

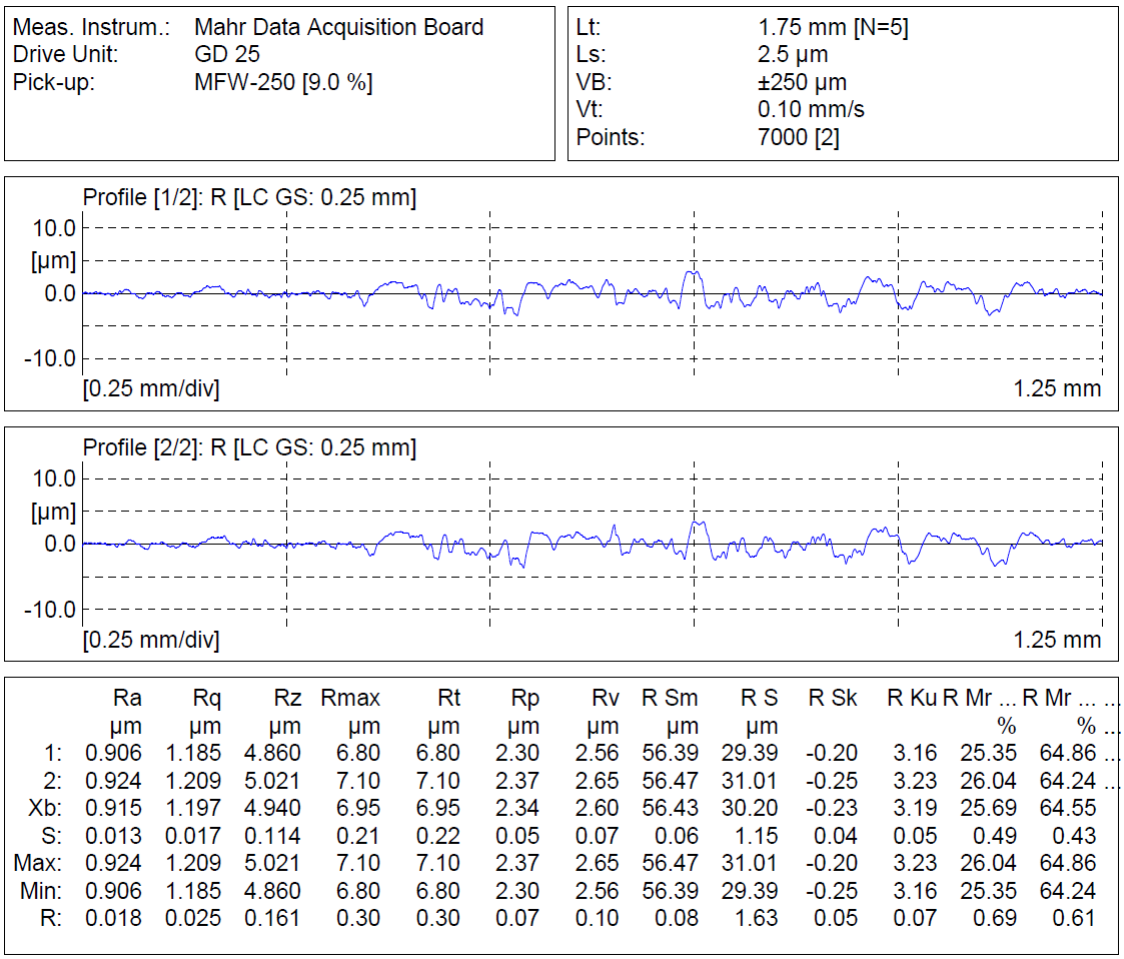

	Ra	Rq	Rz	Rmax	Rt	Rp	Rv	R Sm	R S	R Sk	R Ku	R Mr ...	R Mr ...	...
	µm	µm	µm	µm	µm	µm	µm	µm	µm			%	%	...
1:	0.906	1.185	4.860	6.80	6.80	2.30	2.56	56.39	29.39	-0.20	3.16	25.35	64.86	...
2:	0.924	1.209	5.021	7.10	7.10	2.37	2.65	56.47	31.01	-0.25	3.23	26.04	64.24	...
Xb:	0.915	1.197	4.940	6.95	6.95	2.34	2.60	56.43	30.20	-0.23	3.19	25.69	64.55	
S:	0.013	0.017	0.114	0.21	0.22	0.05	0.07	0.06	1.15	0.04	0.05	0.49	0.43	
Max:	0.924	1.209	5.021	7.10	7.10	2.37	2.65	56.47	31.01	-0.20	3.23	26.04	64.86	
Min:	0.906	1.185	4.860	6.80	6.80	2.30	2.56	56.39	29.39	-0.25	3.16	25.35	64.24	
R:	0.018	0.025	0.161	0.30	0.30	0.07	0.10	0.08	1.63	0.05	0.07	0.69	0.61	

Figure A1. 41 Surface Profile of CVD Drilled Hole, Feedrate 305 mm/min, Open Hole Tension Test Specimen # 2

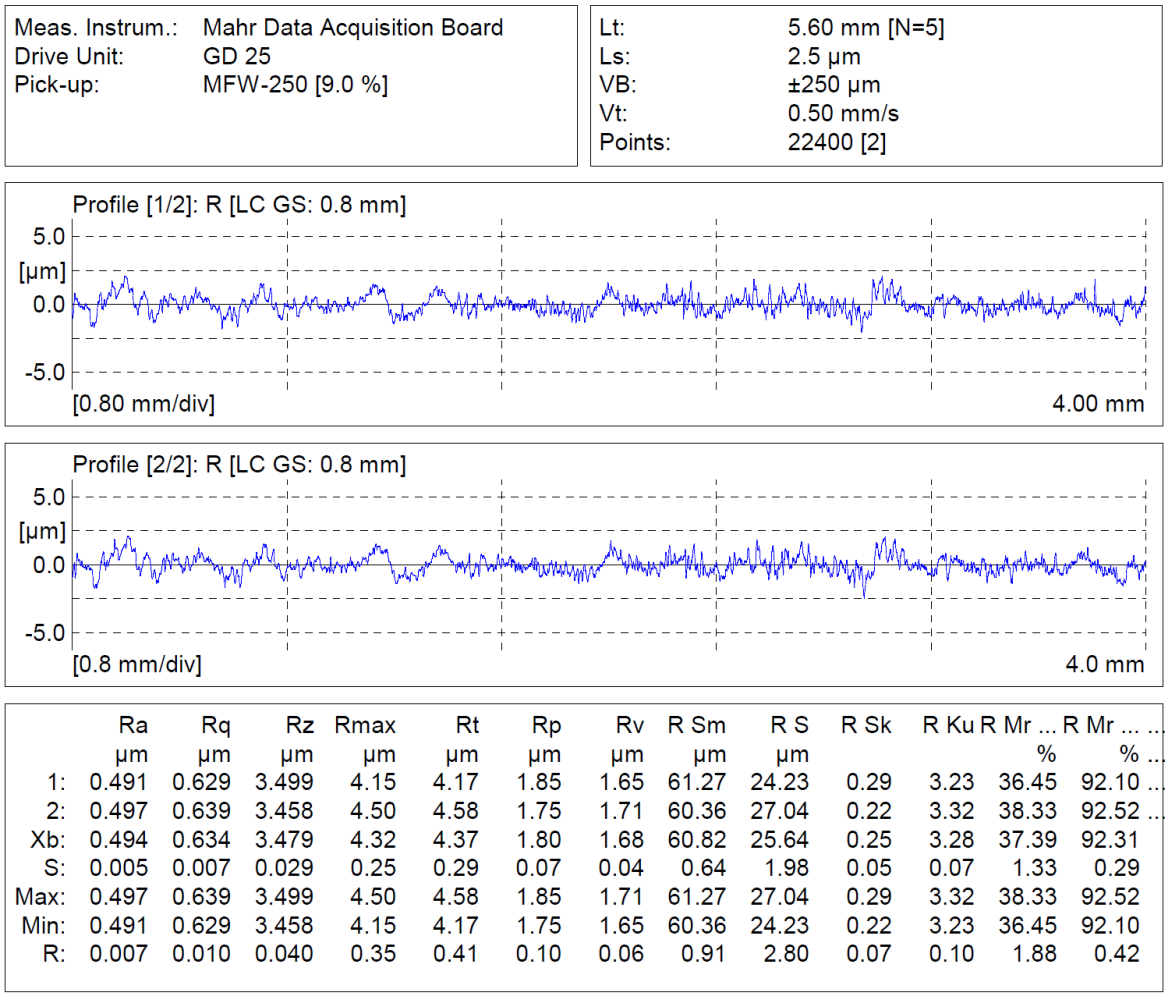

	Ra	Rq	Rz	Rmax	Rt	Rp	Rv	R Sm	R S	R Sk	R Ku	R Mr ...	R Mr ...	...
	µm	µm	µm	µm	µm	µm	µm	µm	µm			%	%	...
1:	0.491	0.629	3.499	4.15	4.17	1.85	1.65	61.27	24.23	0.29	3.23	36.45	92.10	...
2:	0.497	0.639	3.458	4.50	4.58	1.75	1.71	60.36	27.04	0.22	3.32	38.33	92.52	...
Xb:	0.494	0.634	3.479	4.32	4.37	1.80	1.68	60.82	25.64	0.25	3.28	37.39	92.31	
S:	0.005	0.007	0.029	0.25	0.29	0.07	0.04	0.64	1.98	0.05	0.07	1.33	0.29	
Max:	0.497	0.639	3.499	4.50	4.58	1.85	1.71	61.27	27.04	0.29	3.32	38.33	92.52	
Min:	0.491	0.629	3.458	4.15	4.17	1.75	1.65	60.36	24.23	0.22	3.23	36.45	92.10	
R:	0.007	0.010	0.040	0.35	0.41	0.10	0.06	0.91	2.80	0.07	0.10	1.88	0.42	

Figure A1. 42 Surface Profile of CVD Drilled Hole, Feedrate 305 mm/min, PCD Endmill Trimmed Edge (longitudinal) of Open Hole Tension Test Specimen # 2

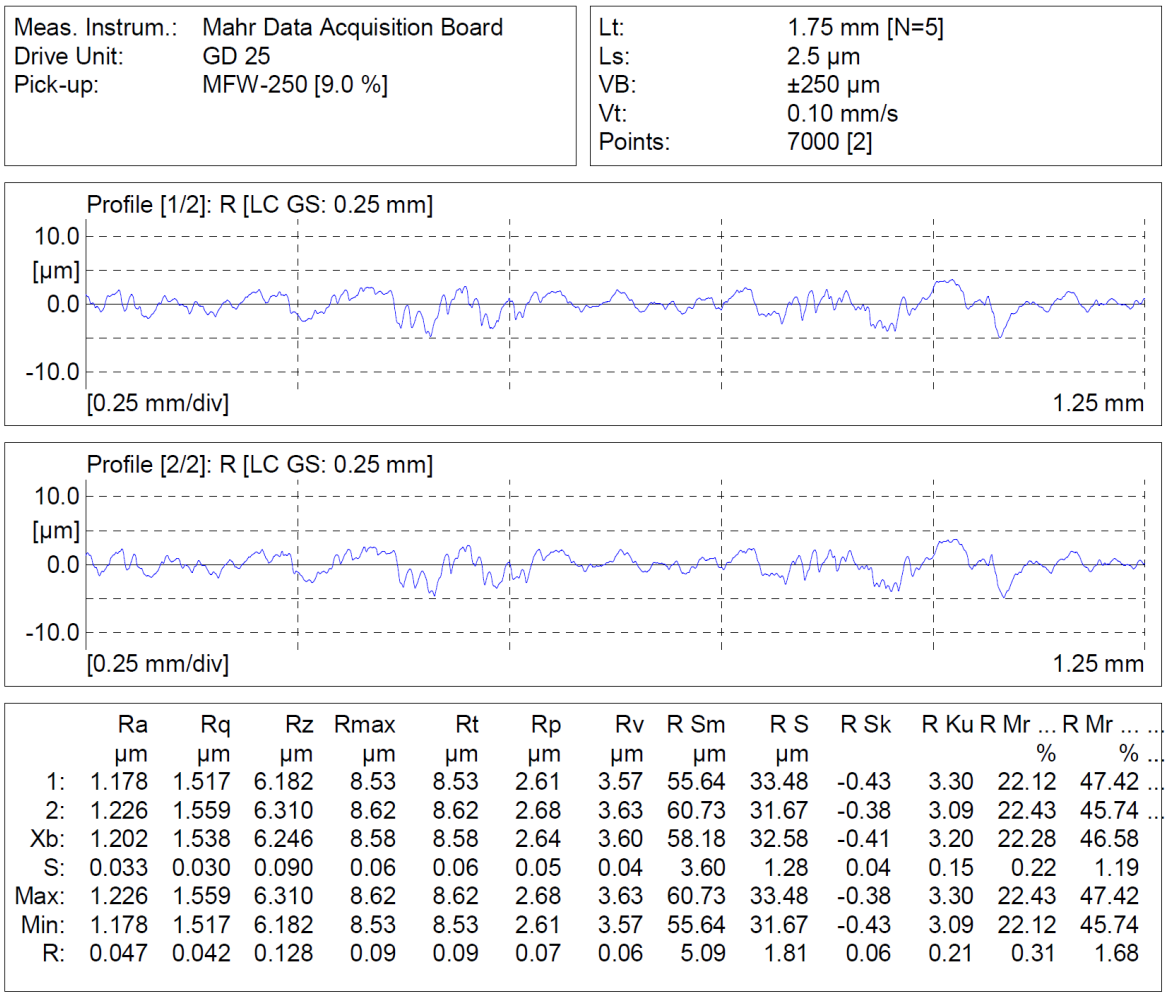

	Ra	Rq	Rz	Rmax	Rt	Rp	Rv	R Sm	R S	R Sk	R Ku	R Mr ...	R Mr ...	...
	µm	µm	µm	µm	µm	µm	µm	µm	µm			%	%	...
1:	1.178	1.517	6.182	8.53	8.53	2.61	3.57	55.64	33.48	-0.43	3.30	22.12	47.42	...
2:	1.226	1.559	6.310	8.62	8.62	2.68	3.63	60.73	31.67	-0.38	3.09	22.43	45.74	...
Xb:	1.202	1.538	6.246	8.58	8.58	2.64	3.60	58.18	32.58	-0.41	3.20	22.28	46.58	
S:	0.033	0.030	0.090	0.06	0.06	0.05	0.04	3.60	1.28	0.04	0.15	0.22	1.19	
Max:	1.226	1.559	6.310	8.62	8.62	2.68	3.63	60.73	33.48	-0.38	3.30	22.43	47.42	
Min:	1.178	1.517	6.182	8.53	8.53	2.61	3.57	55.64	31.67	-0.43	3.09	22.12	45.74	
R:	0.047	0.042	0.128	0.09	0.09	0.07	0.06	5.09	1.81	0.06	0.21	0.31	1.68	

Figure A1. 43 Surface Profile of CVD Drilled Hole, Feedrate 305 mm/min, PCD Endmill Trimmed Edge (transverse) of Open Hole Tension Test Specimen # 2

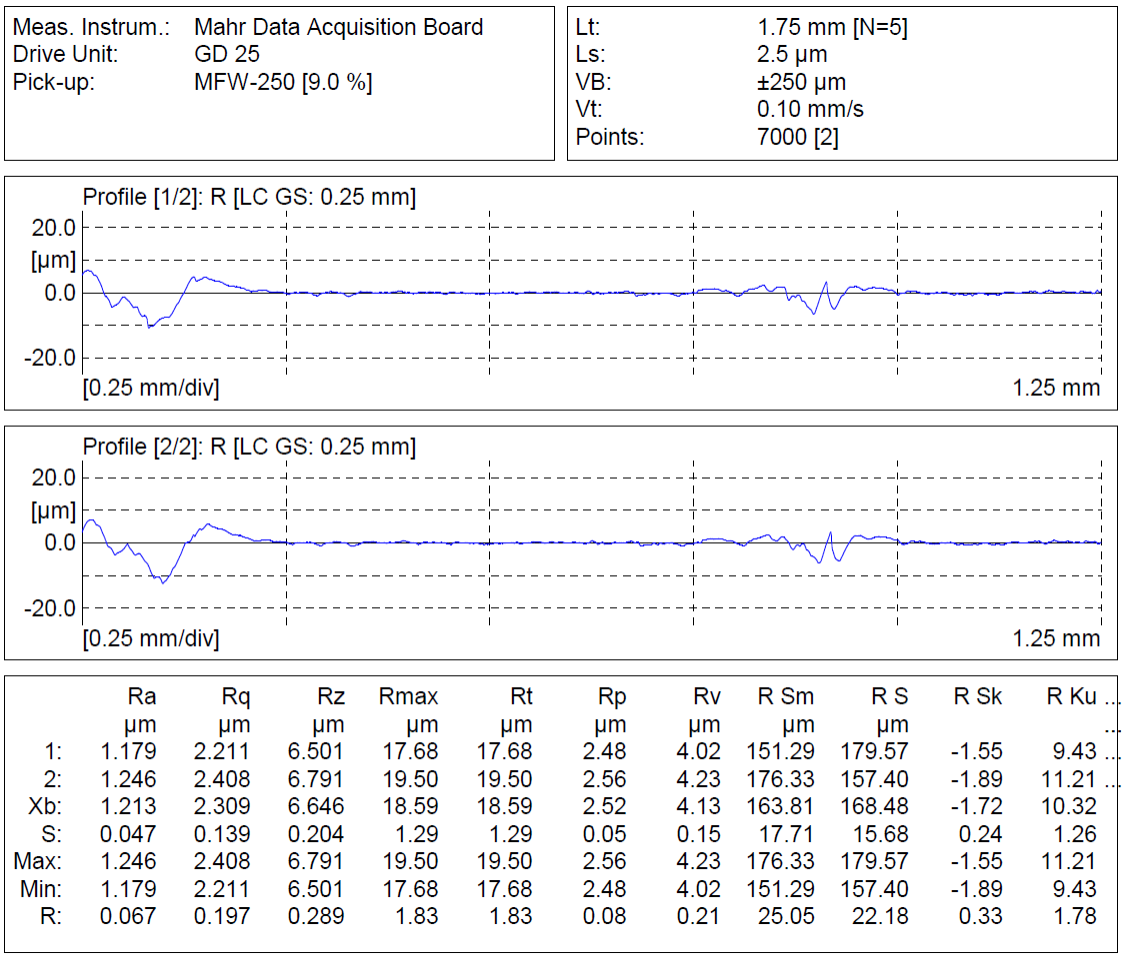

	Ra µm	Rq µm	Rz µm	Rmax µm	Rt µm	Rp µm	Rv µm	R Sm µm	R S µm	R Sk	R Ku ...
1:	1.179	2.211	6.501	17.68	17.68	2.48	4.02	151.29	179.57	-1.55	9.43 ...
2:	1.246	2.408	6.791	19.50	19.50	2.56	4.23	176.33	157.40	-1.89	11.21 ...
Xb:	1.213	2.309	6.646	18.59	18.59	2.52	4.13	163.81	168.48	-1.72	10.32
S:	0.047	0.139	0.204	1.29	1.29	0.05	0.15	17.71	15.68	0.24	1.26
Max:	1.246	2.408	6.791	19.50	19.50	2.56	4.23	176.33	179.57	-1.55	11.21
Min:	1.179	2.211	6.501	17.68	17.68	2.48	4.02	151.29	157.40	-1.89	9.43
R:	0.067	0.197	0.289	1.83	1.83	0.08	0.21	25.05	22.18	0.33	1.78

Figure A1. 44 Surface Profile of CVD Drilled Hole, Feedrate 305 mm/min, Open Hole Tension Test Specimen # 3

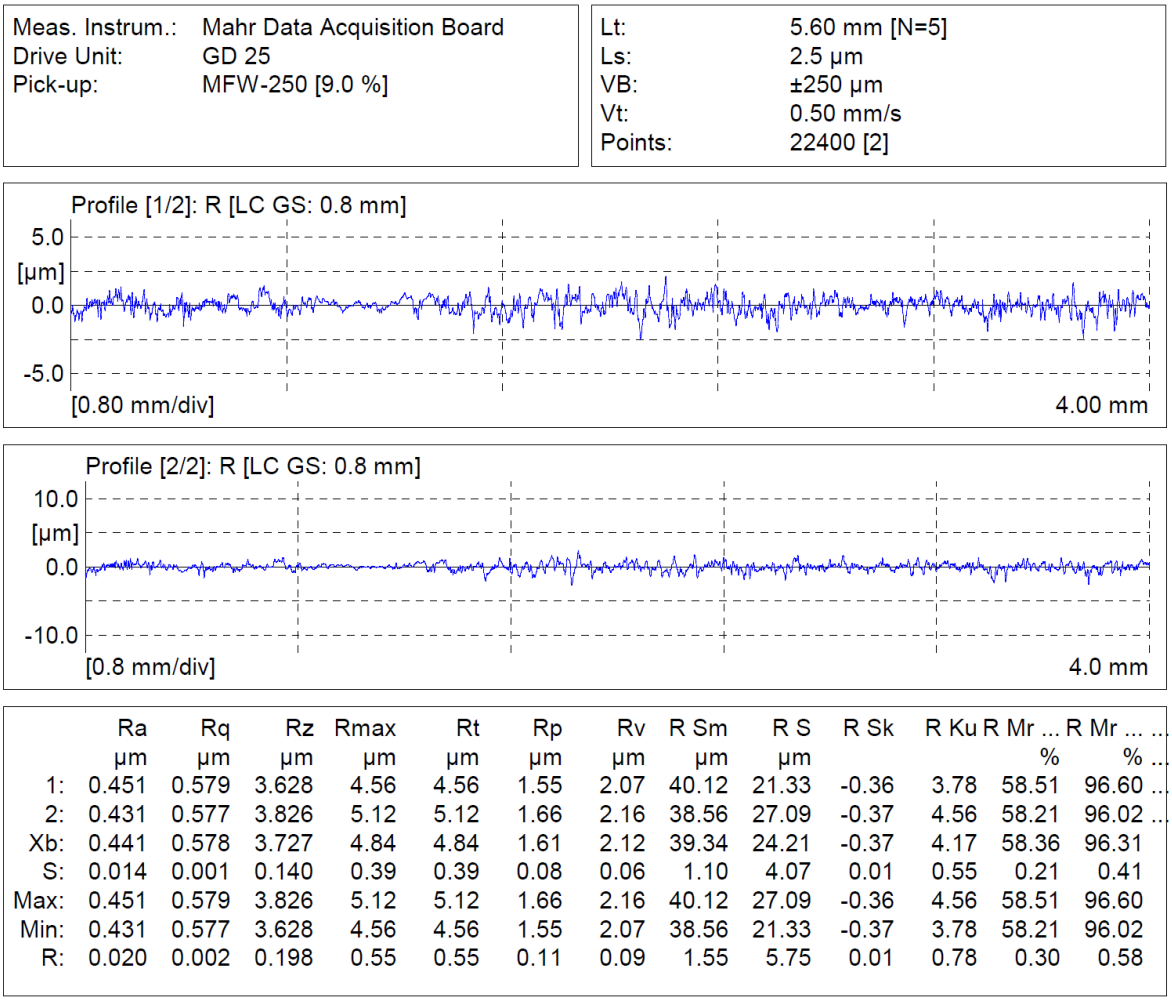

	Ra	Rq	Rz	Rmax	Rt	Rp	Rv	R Sm	R S	R Sk	R Ku	R Mr ...	R Mr ...	...
	µm	µm	µm	µm	µm	µm	µm	µm	µm			%	%	...
1:	0.451	0.579	3.628	4.56	4.56	1.55	2.07	40.12	21.33	-0.36	3.78	58.51	96.60	...
2:	0.431	0.577	3.826	5.12	5.12	1.66	2.16	38.56	27.09	-0.37	4.56	58.21	96.02	...
Xb:	0.441	0.578	3.727	4.84	4.84	1.61	2.12	39.34	24.21	-0.37	4.17	58.36	96.31	
S:	0.014	0.001	0.140	0.39	0.39	0.08	0.06	1.10	4.07	0.01	0.55	0.21	0.41	
Max:	0.451	0.579	3.826	5.12	5.12	1.66	2.16	40.12	27.09	-0.36	4.56	58.51	96.60	
Min:	0.431	0.577	3.628	4.56	4.56	1.55	2.07	38.56	21.33	-0.37	3.78	58.21	96.02	
R:	0.020	0.002	0.198	0.55	0.55	0.11	0.09	1.55	5.75	0.01	0.78	0.30	0.58	

Figure A1. 45 Surface Profile of CVD Drilled Hole, Feedrate 305 mm/min, PCD Endmill Trimmed Edge (longitudinal) of Open Hole Tension Test Specimen # 3

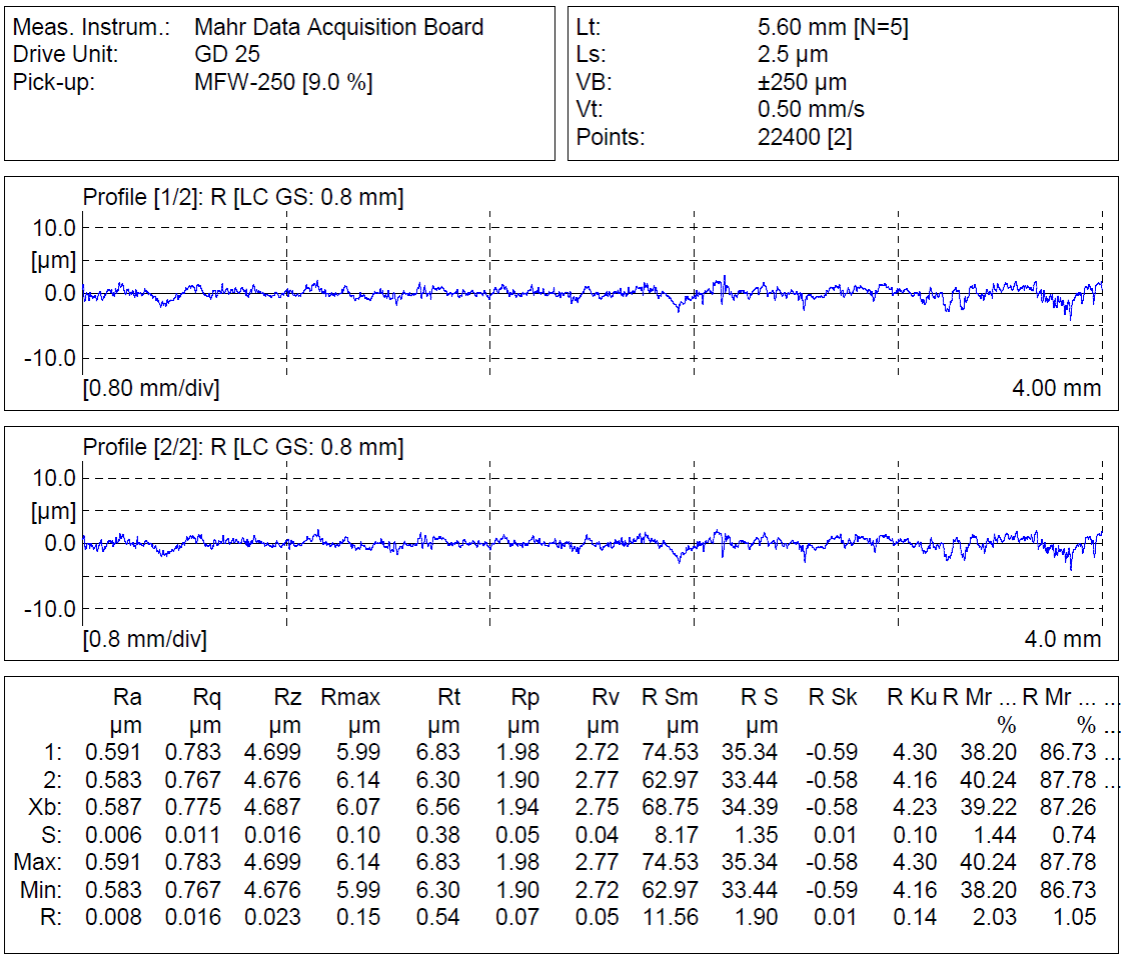

	Ra µm	Rq µm	Rz µm	Rmax µm	Rt µm	Rp µm	Rv µm	R Sm µm	R S µm	R Sk	R Ku	R Mr ... %	R Mr ... % ...
1:	0.591	0.783	4.699	5.99	6.83	1.98	2.72	74.53	35.34	-0.59	4.30	38.20	86.73 ...
2:	0.583	0.767	4.676	6.14	6.30	1.90	2.77	62.97	33.44	-0.58	4.16	40.24	87.78 ...
Xb:	0.587	0.775	4.687	6.07	6.56	1.94	2.75	68.75	34.39	-0.58	4.23	39.22	87.26
S:	0.006	0.011	0.016	0.10	0.38	0.05	0.04	8.17	1.35	0.01	0.10	1.44	0.74
Max:	0.591	0.783	4.699	6.14	6.83	1.98	2.77	74.53	35.34	-0.58	4.30	40.24	87.78
Min:	0.583	0.767	4.676	5.99	6.30	1.90	2.72	62.97	33.44	-0.59	4.16	38.20	86.73
R:	0.008	0.016	0.023	0.15	0.54	0.07	0.05	11.56	1.90	0.01	0.14	2.03	1.05

Figure A1. 46 Surface Profile of CVD Drilled Hole, Feedrate 305 mm/min, PCD Endmill Trimmed Edge (transverse) of Open Hole Tension Test Specimen # 3

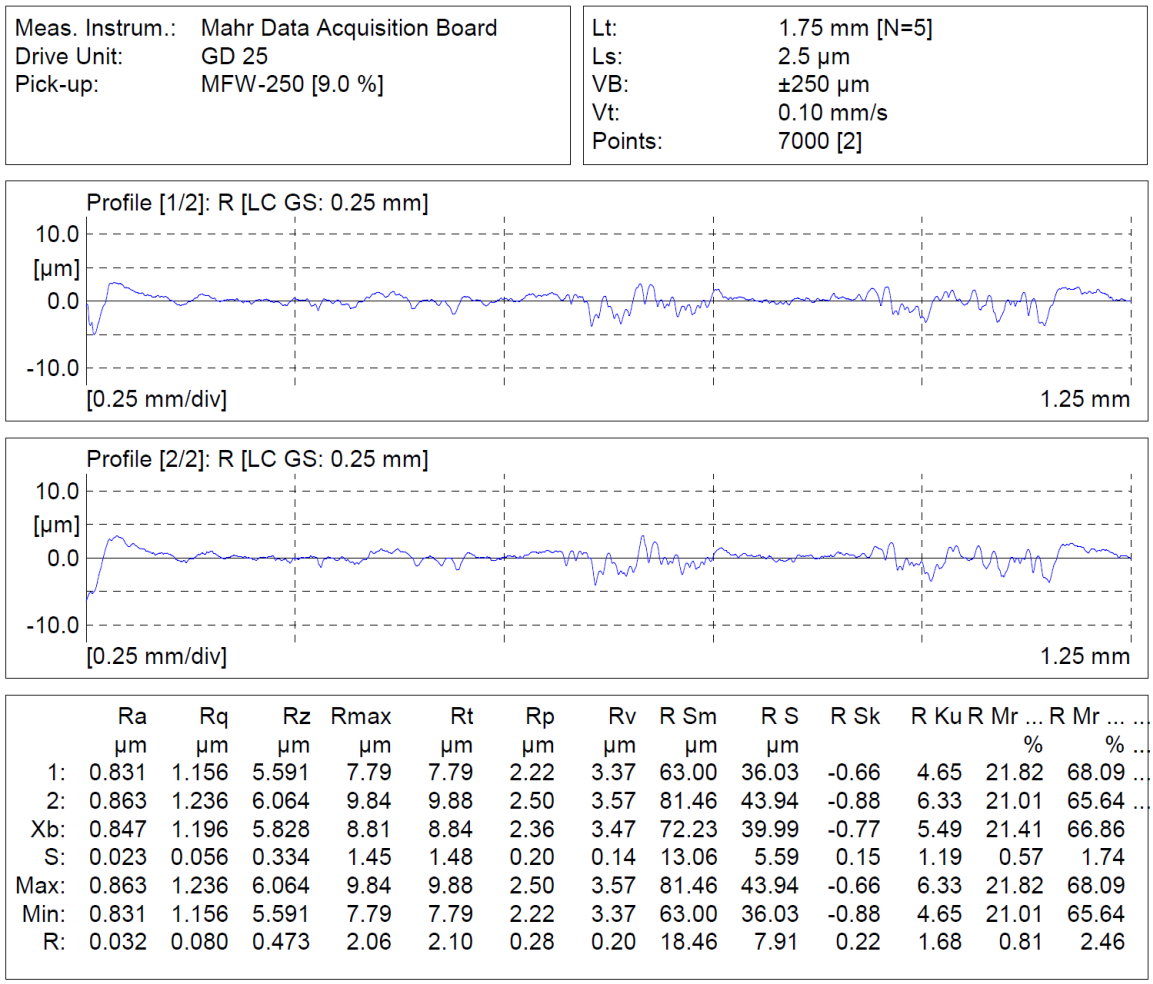

	Ra	Rq	Rz	Rmax	Rt	Rp	Rv	R Sm	R S	R Sk	R Ku	R Mr ...	R Mr ...	...
	µm	µm	µm	µm	µm	µm	µm	µm	µm			%	%	...
1:	0.831	1.156	5.591	7.79	7.79	2.22	3.37	63.00	36.03	-0.66	4.65	21.82	68.09	...
2:	0.863	1.236	6.064	9.84	9.88	2.50	3.57	81.46	43.94	-0.88	6.33	21.01	65.64	...
Xb:	0.847	1.196	5.828	8.81	8.84	2.36	3.47	72.23	39.99	-0.77	5.49	21.41	66.86	
S:	0.023	0.056	0.334	1.45	1.48	0.20	0.14	13.06	5.59	0.15	1.19	0.57	1.74	
Max:	0.863	1.236	6.064	9.84	9.88	2.50	3.57	81.46	43.94	-0.66	6.33	21.82	68.09	
Min:	0.831	1.156	5.591	7.79	7.79	2.22	3.37	63.00	36.03	-0.88	4.65	21.01	65.64	
R:	0.032	0.080	0.473	2.06	2.10	0.28	0.20	18.46	7.91	0.22	1.68	0.81	2.46	

Figure A1. 47 Surface Profile of CVD Drilled Hole, Feedrate 305 mm/min, Open Hole Tension Test Specimen # 4

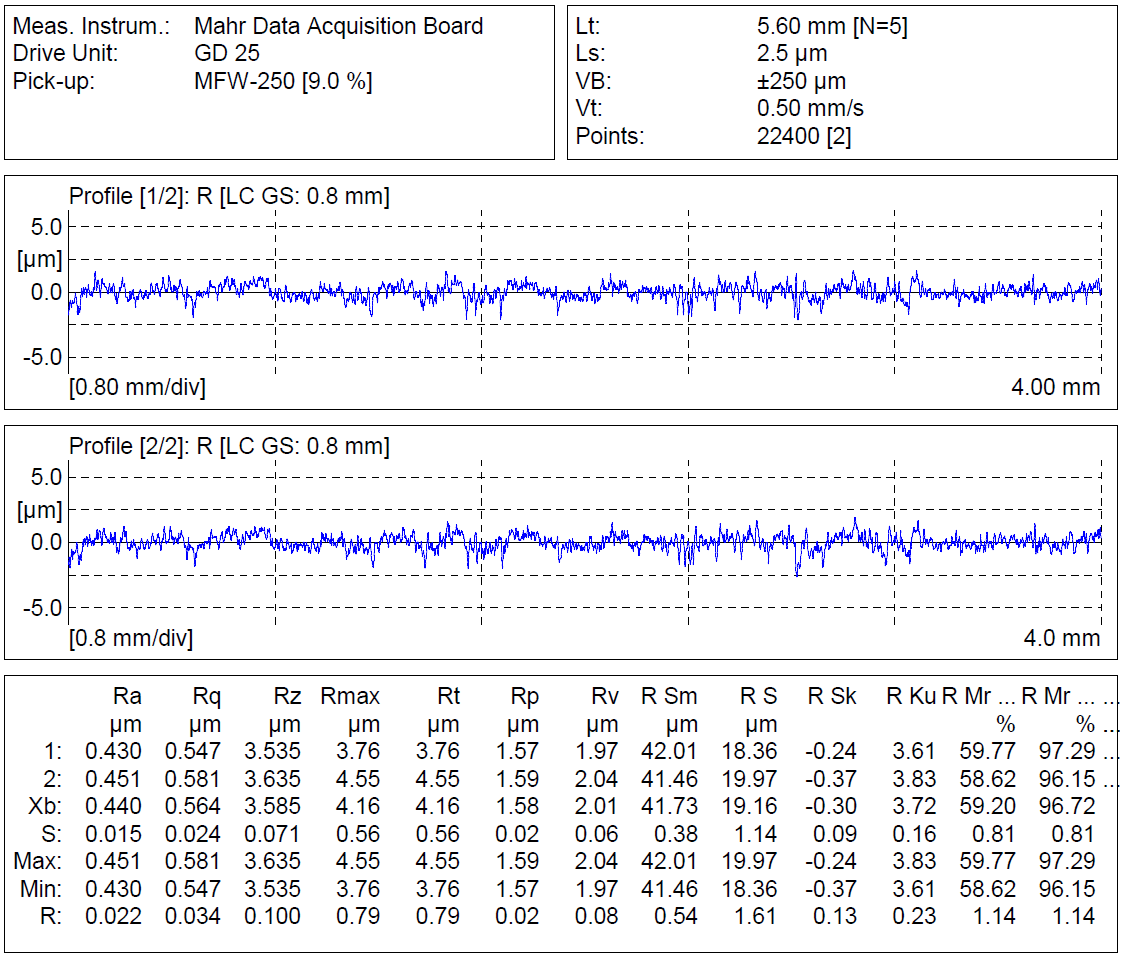

	Ra µm	Rq µm	Rz µm	Rmax µm	Rt µm	Rp µm	Rv µm	R Sm µm	R S µm	R Sk	R Ku	R Mr ... %	R Mr ... % ...
1:	0.430	0.547	3.535	3.76	3.76	1.57	1.97	42.01	18.36	-0.24	3.61	59.77	97.29 ...
2:	0.451	0.581	3.635	4.55	4.55	1.59	2.04	41.46	19.97	-0.37	3.83	58.62	96.15 ...
Xb:	0.440	0.564	3.585	4.16	4.16	1.58	2.01	41.73	19.16	-0.30	3.72	59.20	96.72
S:	0.015	0.024	0.071	0.56	0.56	0.02	0.06	0.38	1.14	0.09	0.16	0.81	0.81
Max:	0.451	0.581	3.635	4.55	4.55	1.59	2.04	42.01	19.97	-0.24	3.83	59.77	97.29
Min:	0.430	0.547	3.535	3.76	3.76	1.57	1.97	41.46	18.36	-0.37	3.61	58.62	96.15
R:	0.022	0.034	0.100	0.79	0.79	0.02	0.08	0.54	1.61	0.13	0.23	1.14	1.14

Figure A1. 48 Surface Profile of CVD Drilled Hole, Feedrate 305 mm/min, PCD Endmill Trimmed Edge (longitudinal) of Open Hole Tension Test Specimen # 4

Meas. Instrum.:	Mahr Data Acquisition Board	Lt:	1.75 mm [N=5]
Drive Unit:	GD 25	Ls:	2.5 µm
Pick-up:	MFW-250 [9.0 %]	VB:	±250 µm
		Vt:	0.10 mm/s
		Points:	7000 [2]

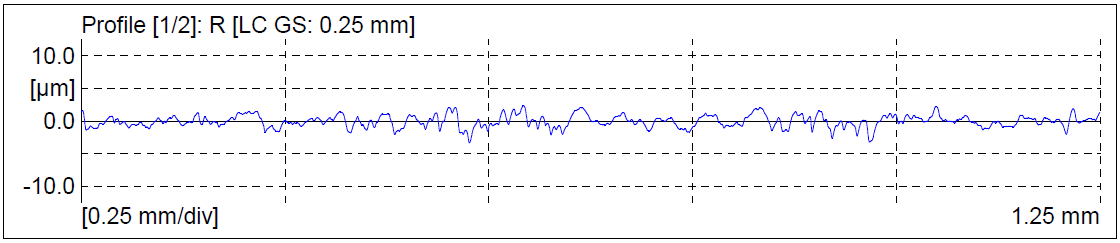

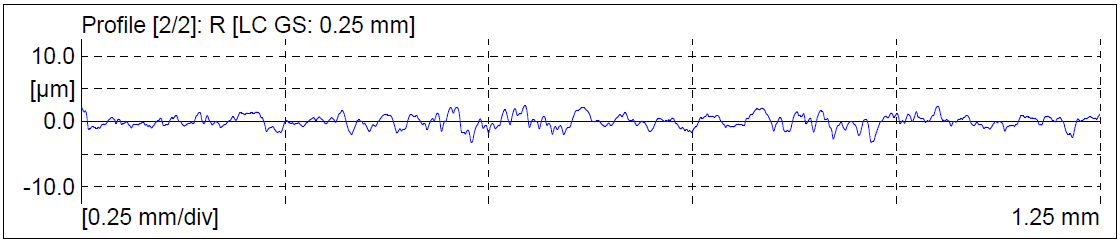

	Ra µm	Rq µm	Rz µm	Rmax µm	Rt µm	Rp µm	Rv µm	R Sm µm	R S µm	R Sk	R Ku	R Mr ... %	R Mr ... %	...
1:	0.724	0.922	4.531	5.42	5.69	2.09	2.44	43.72	24.08	-0.15	3.23	26.11	68.79	...
2:	0.752	0.950	4.760	5.41	5.67	2.25	2.51	45.65	23.27	-0.17	3.15	25.36	65.39	...
Xb:	0.738	0.936	4.646	5.41	5.68	2.17	2.47	44.69	23.68	-0.16	3.19	25.74	67.09	
S:	0.020	0.020	0.162	0.01	0.02	0.11	0.05	1.37	0.57	0.01	0.05	0.53	2.40	
Max:	0.752	0.950	4.760	5.42	5.69	2.25	2.51	45.65	24.08	-0.15	3.23	26.11	68.79	
Min:	0.724	0.922	4.531	5.41	5.67	2.09	2.44	43.72	23.27	-0.17	3.15	25.36	65.39	
R:	0.028	0.028	0.229	0.01	0.02	0.16	0.07	1.93	0.81	0.02	0.07	0.75	3.40	

Figure A1. 49 Surface Profile of CVD Drilled Hole, Feedrate 305 mm/min, PCD Endmill Trimmed Edge (transverse) of Open Hole Tension Test Specimen # 4

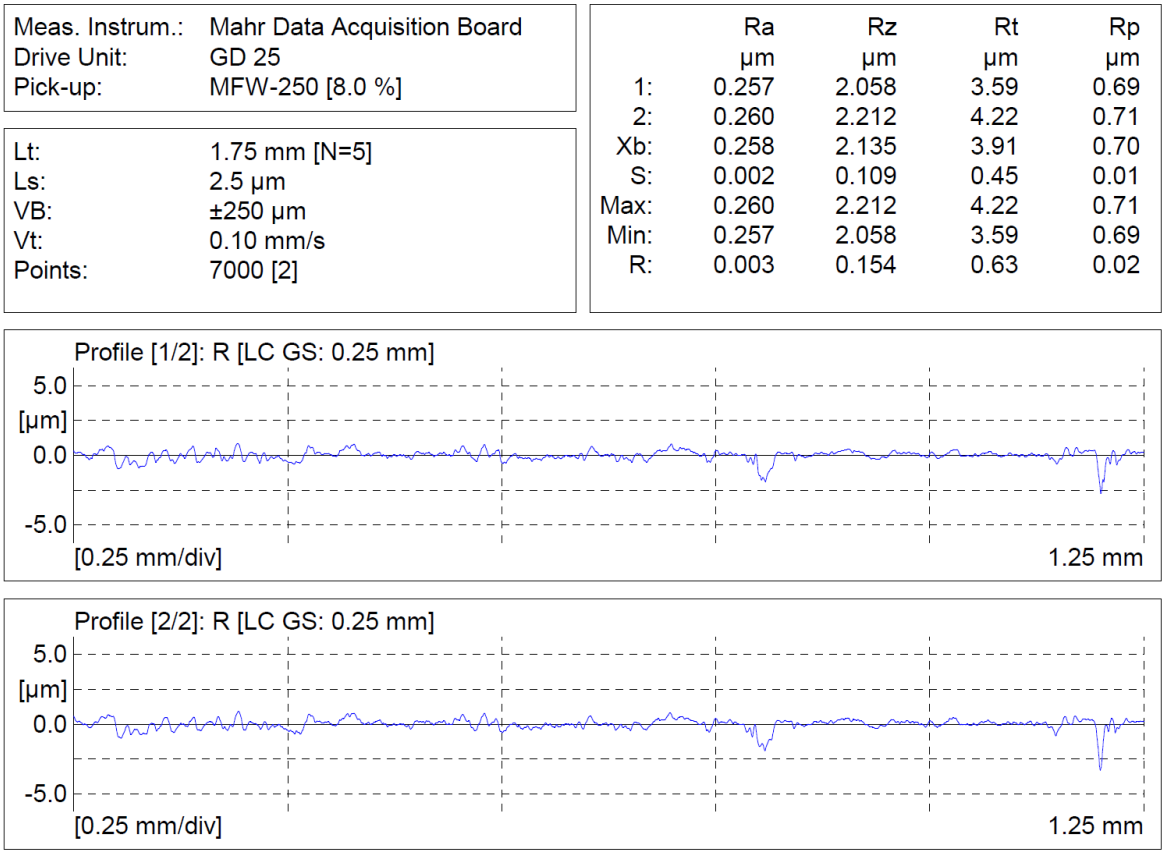

Figure A1. 50 Surface Profile of PCD Drilled Hole, Feedrate 305 mm/min, Open Hole Tension Test Specimen # 1

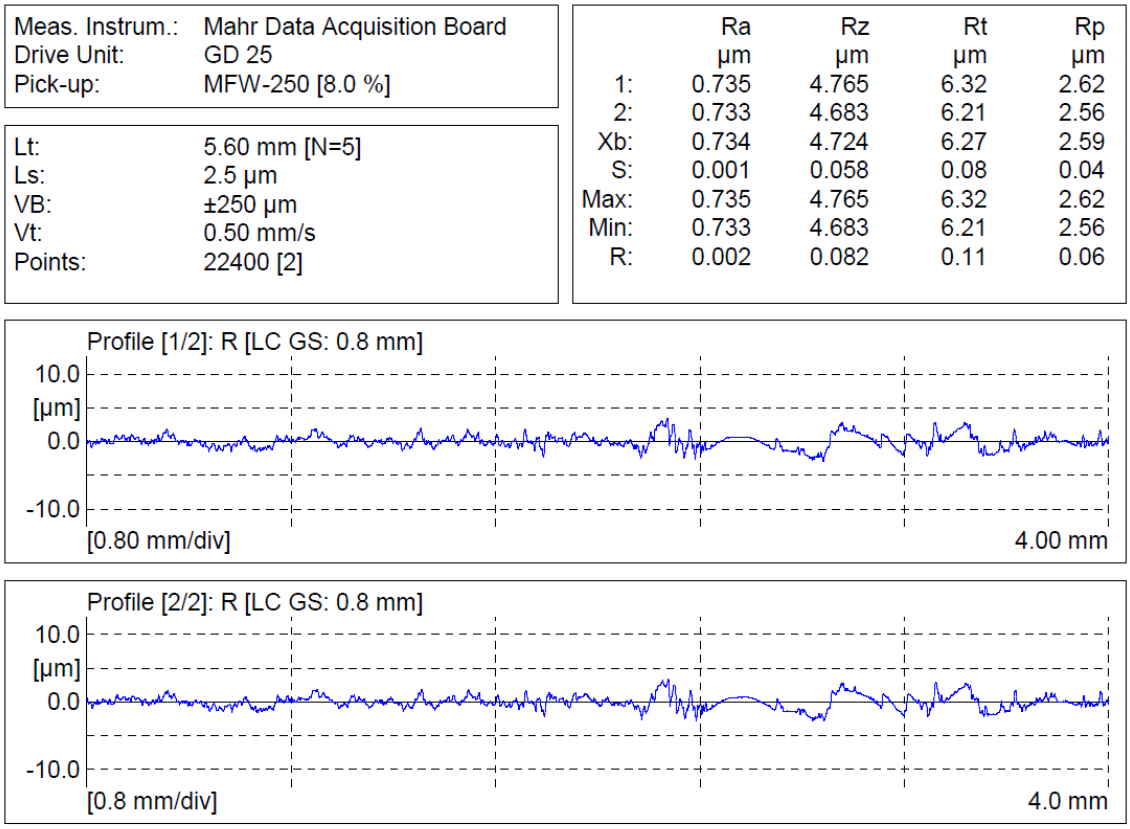

Figure A1. 51 Surface Profile of PCD Drilled Hole, Feedrate 305 mm/min, PCD Endmill Trimmed Edge (longitudinal) of Open Hole Tension Test Specimen # 1

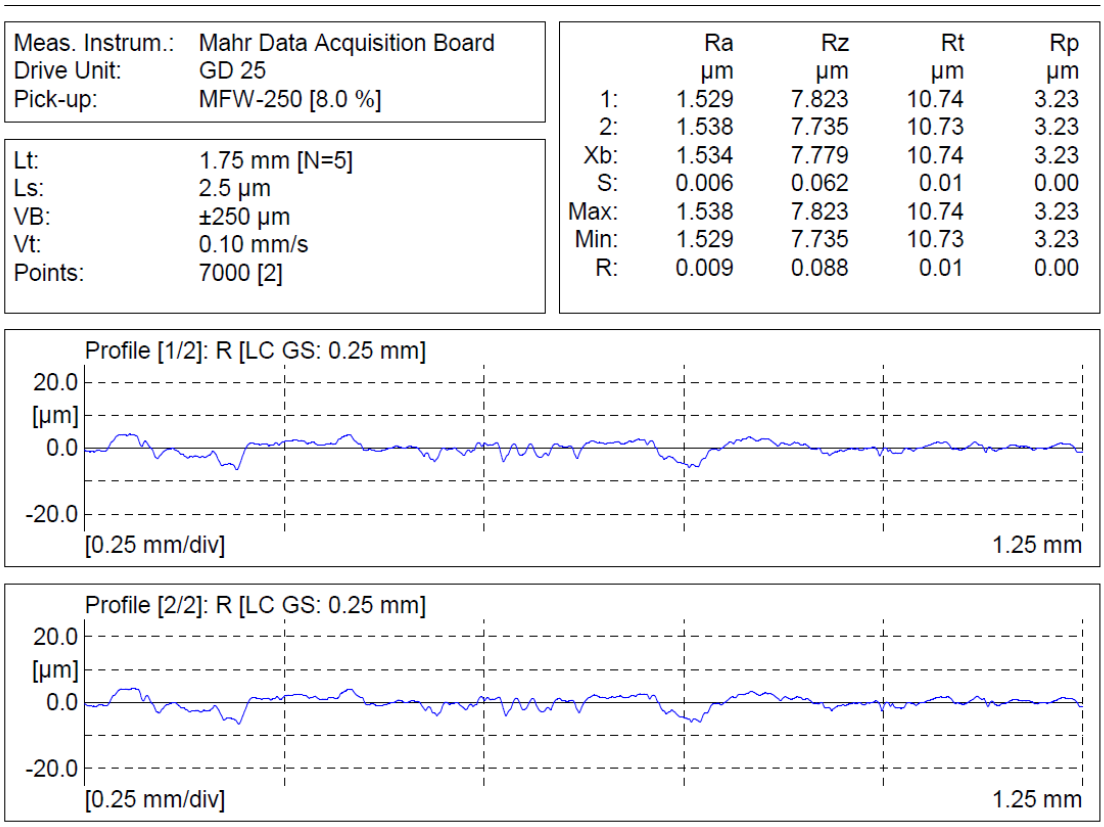

Figure A1. 52 Surface Profile of PCD Drilled Hole, Feedrate 305 mm/min, PCD Endmill Trimmed Edge (transverse) of Open Hole Tension Test Specimen # 1

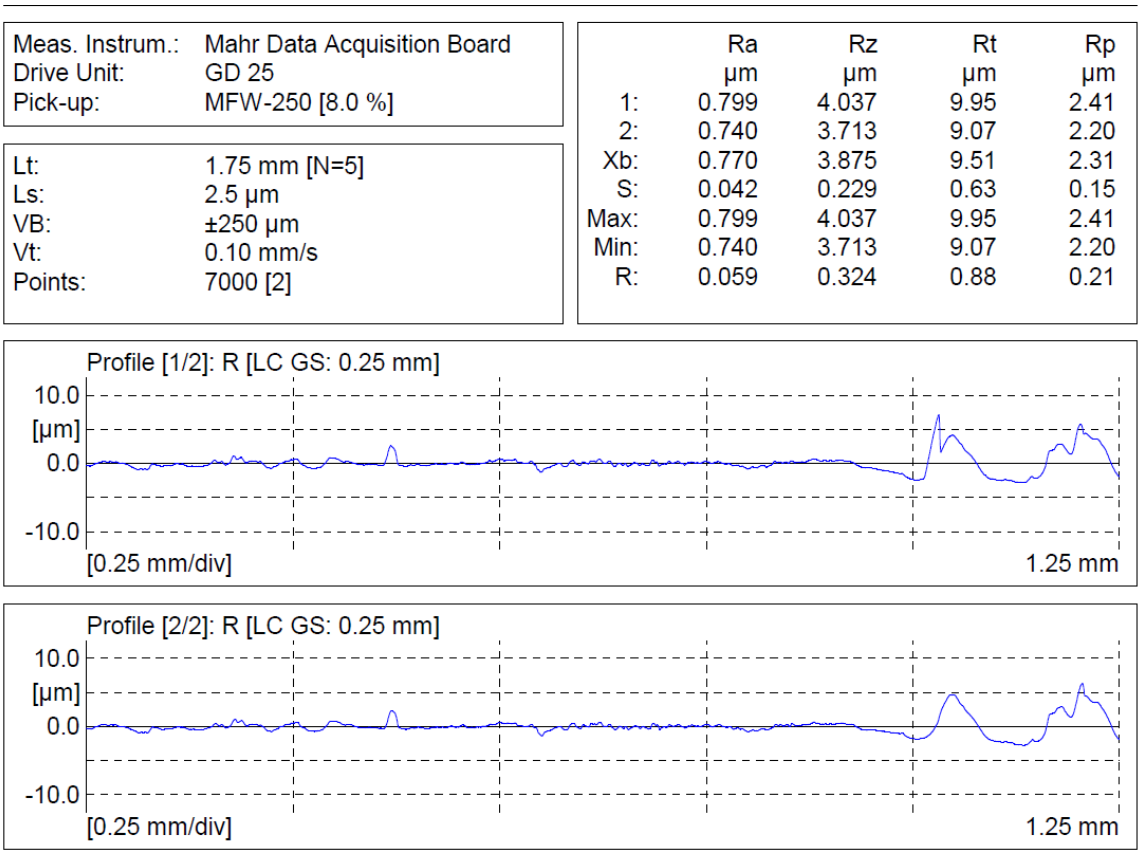

Figure A1. 53 Surface Profile of PCD Drilled Hole, Feedrate 305 mm/min, Open Hole Tension Test Specimen # 2

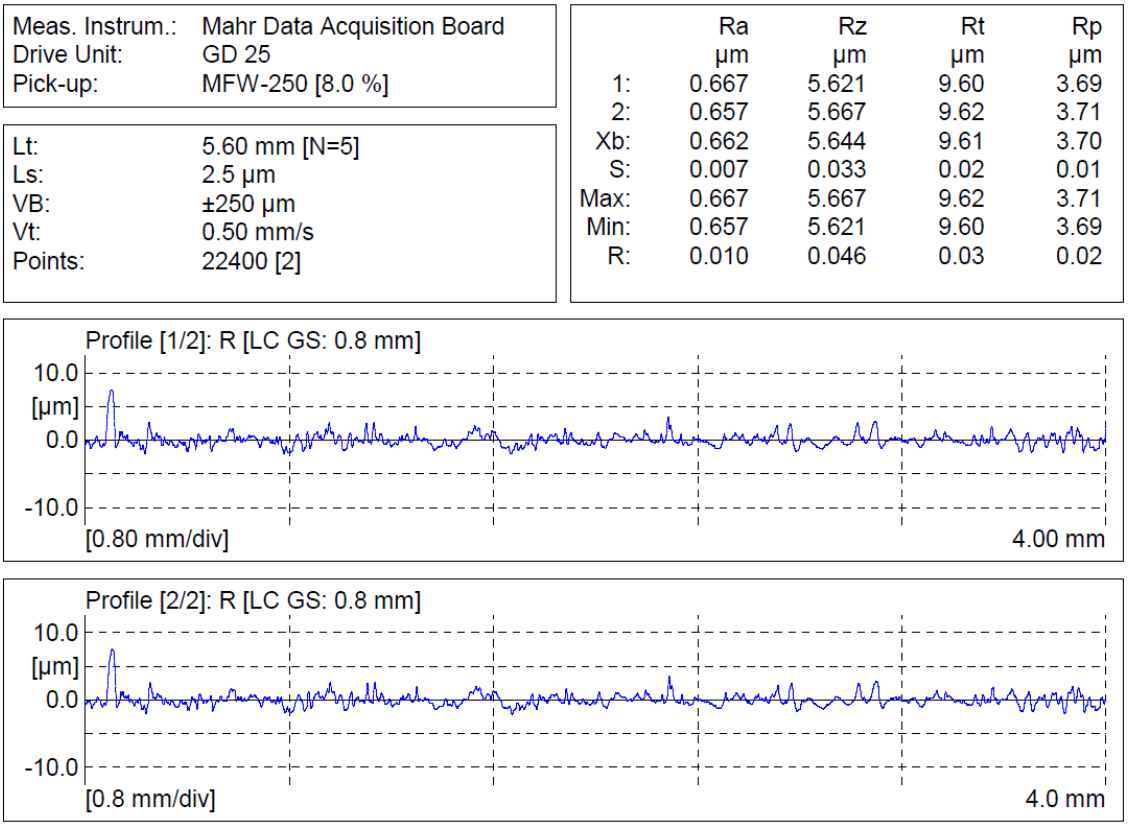

Figure A1. 54 Surface Profile of PCD Drilled Hole, Feedrate 305 mm/min, PCD Endmill Trimmed Edge (longitudinal) of Open Hole Tension Test Specimen # 2

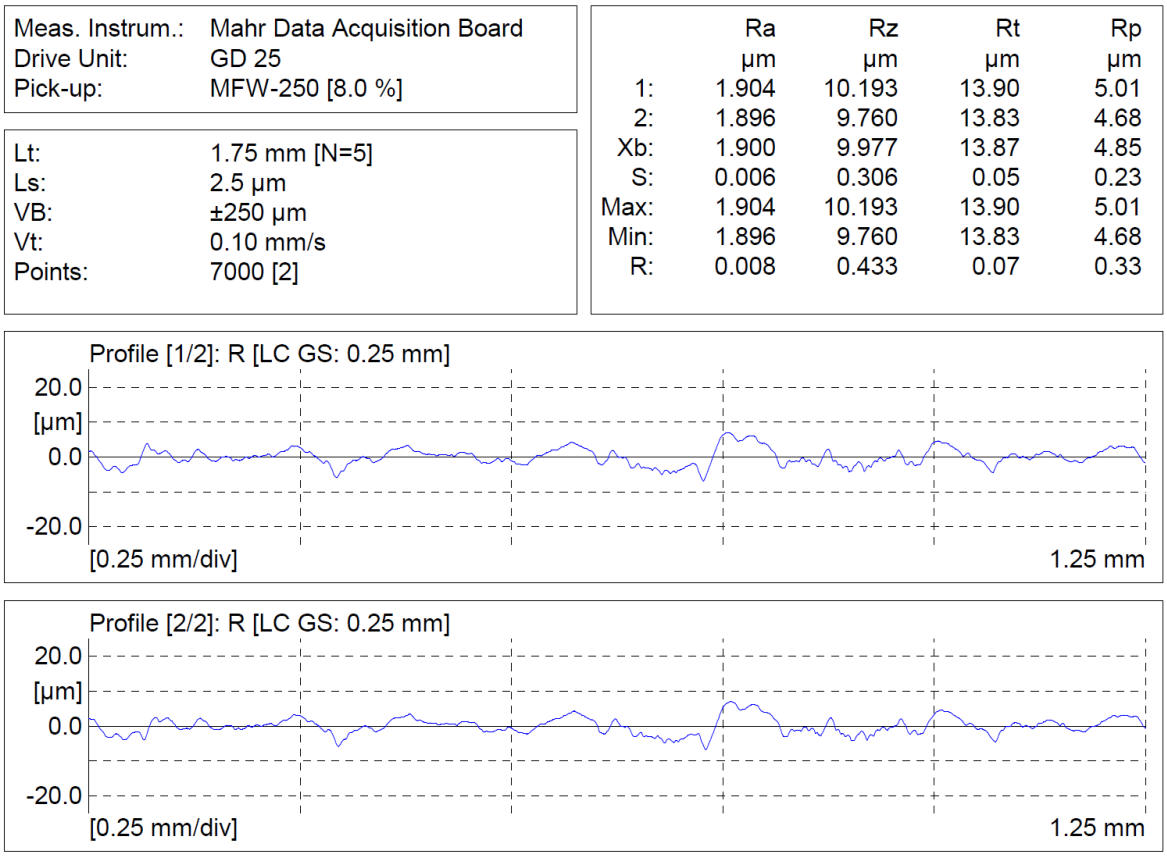

Figure A1. 55 urface Profile of PCD Drilled Hole, Feedrate 305 mm/min, PCD Endmill Trimmed Edge (transverse) of Open Hole Tension Test Specimen # 2

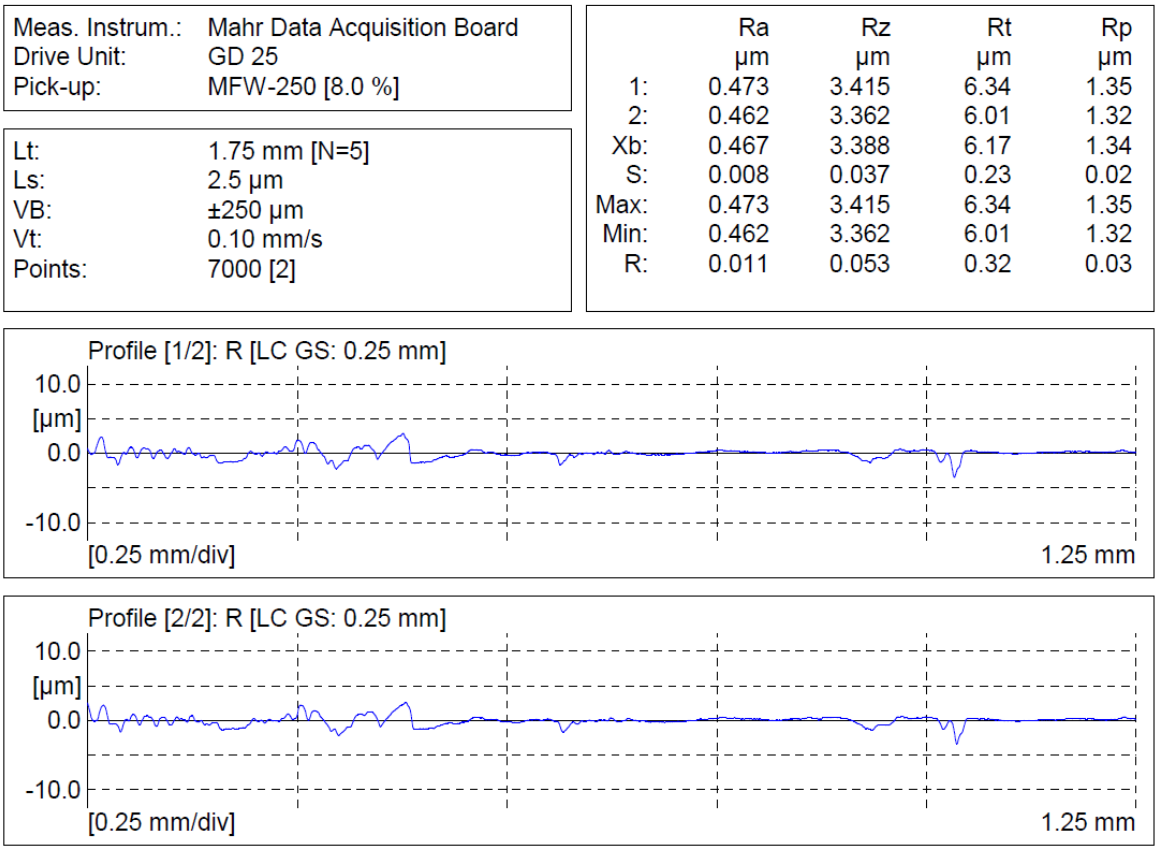

Figure A1. 56 Surface Profile of PCD Drilled Hole, Feedrate 305 mm/min, Open Hole Tension Test Specimen # 3

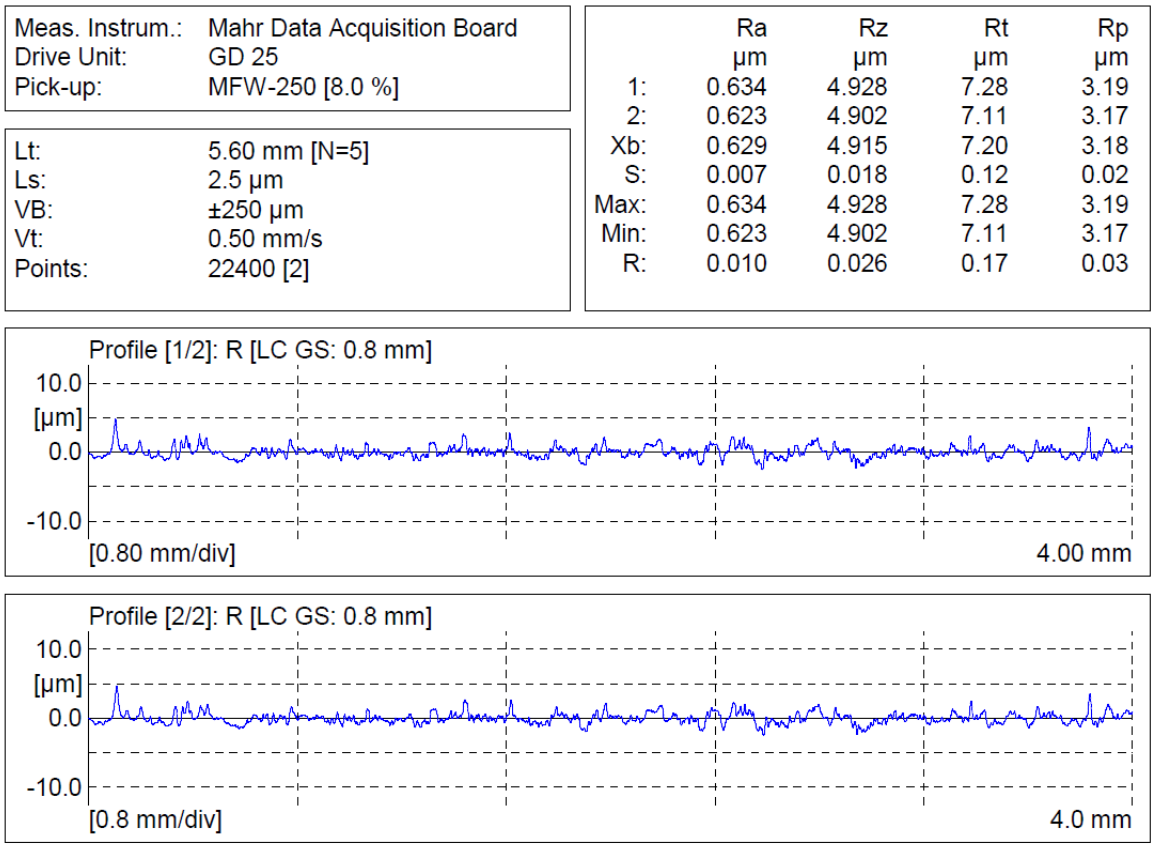

Figure A1. 57 Surface Profile of PCD Drilled Hole, Feedrate 305 mm/min, PCD Endmill Trimmed Edge (longitudinal) of Open Hole Tension Test Specimen # 3

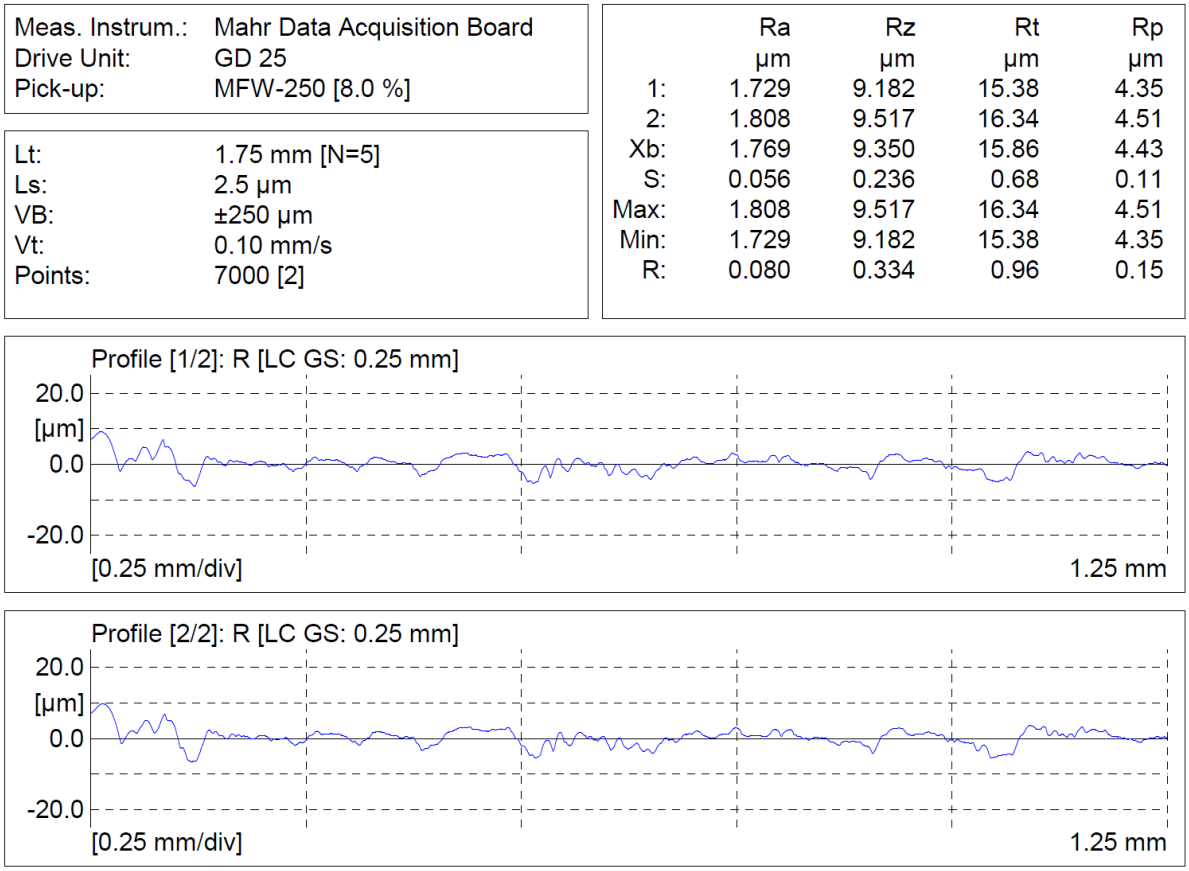

Figure A1. 58 Surface Profile of PCD Drilled Hole, Feedrate 305 mm/min, PCD Endmill Trimmed Edge (transverse) of Open Hole Tension Test Specimen # 3

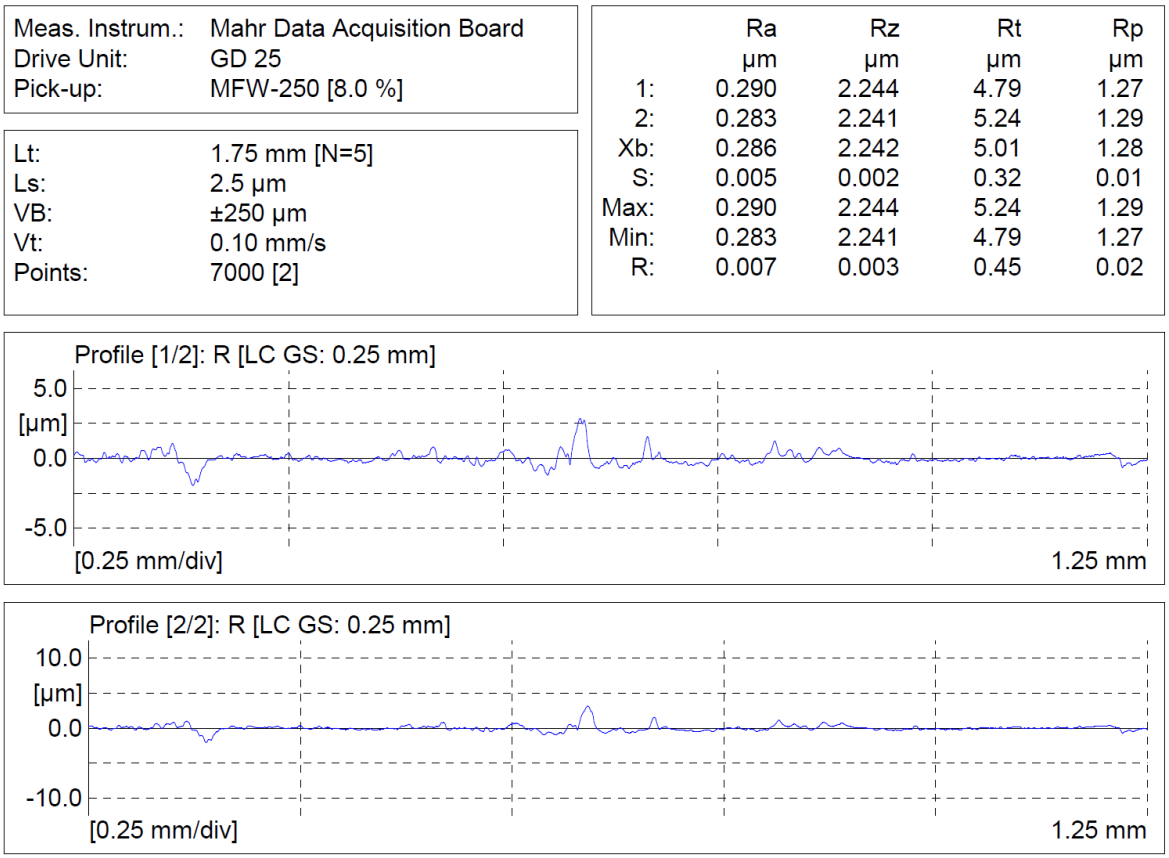

Figure A1. 59 Surface Profile of PCD Drilled Hole, Feedrate 305 mm/min, Open Hole Tension Test Specimen # 4

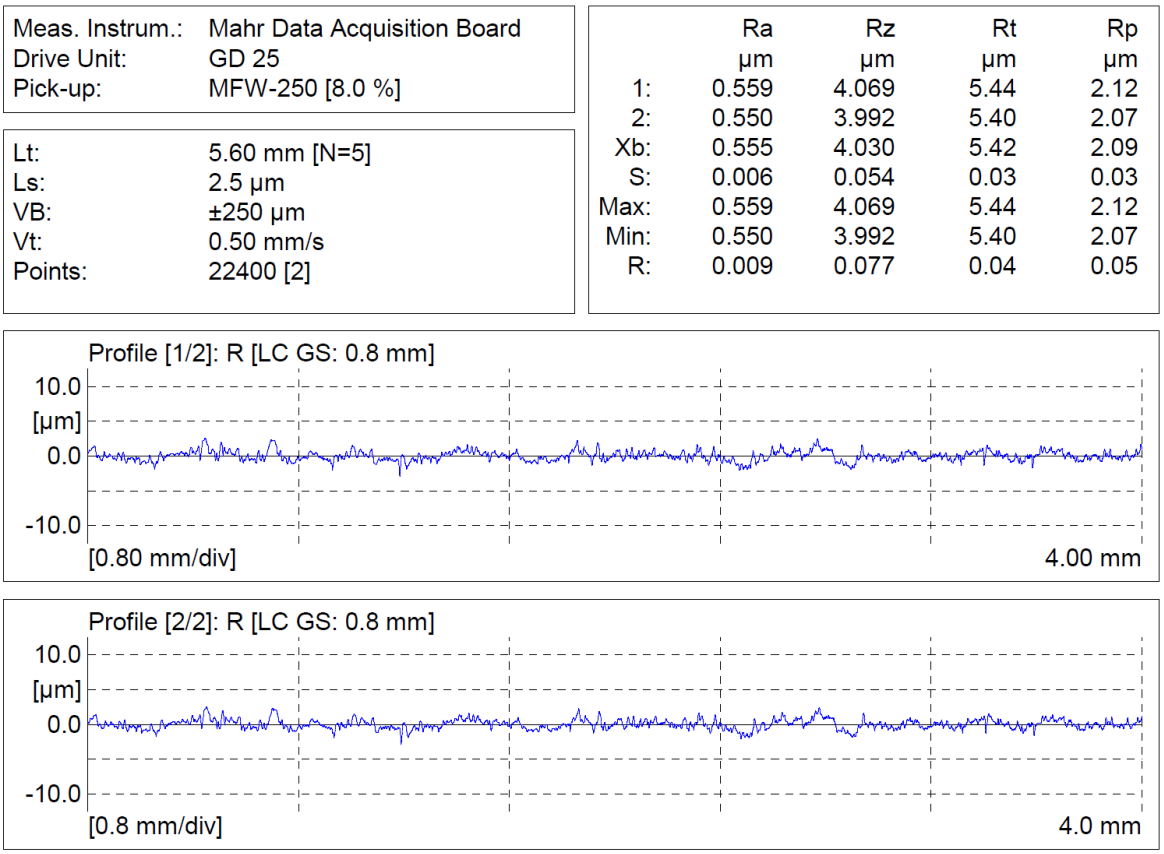

Figure A1. 60 Surface Profile of PCD Drilled Hole, Feedrate 305 mm/min, PCD Endmill Trimmed Edge (longitudinal) of Open Hole Tension Test Specimen # 4

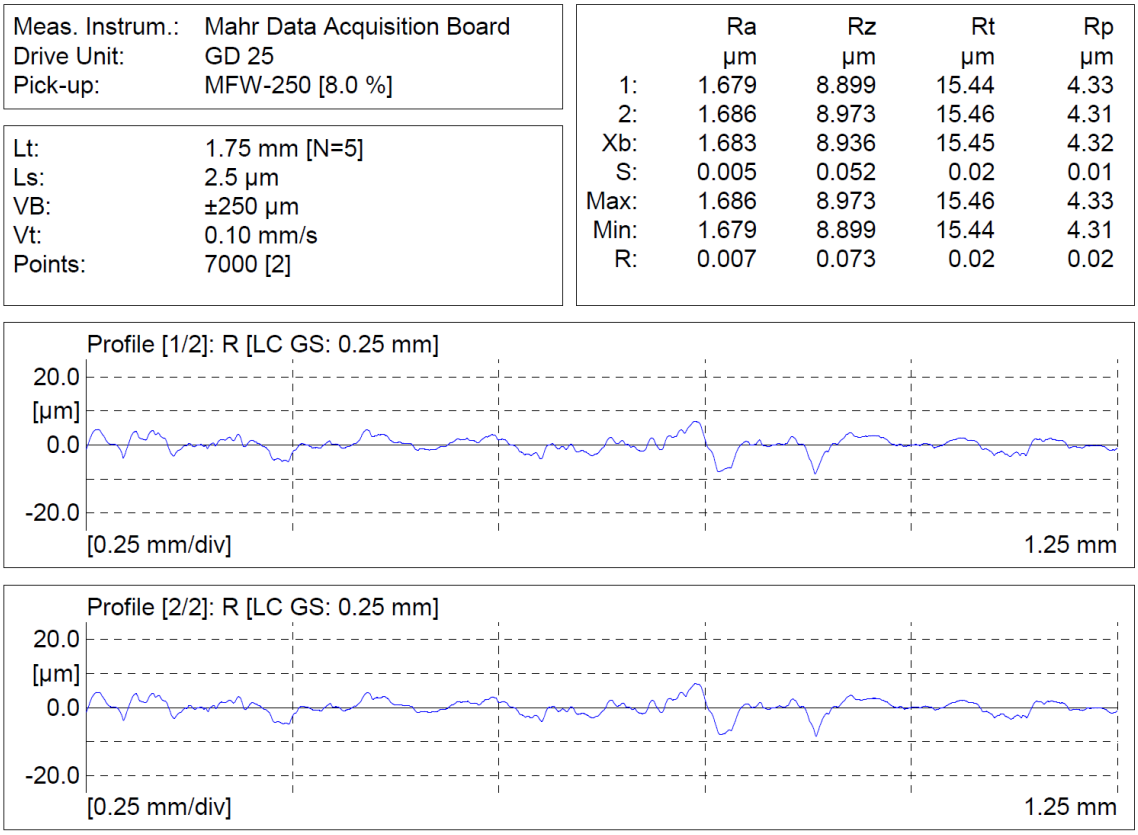

Figure A1. 61 Surface Profile of PCD Drilled Hole, Feedrate 305 mm/min, PCD Endmill Trimmed Edge (transverse) of Open Hole Tension Test Specimen # 4

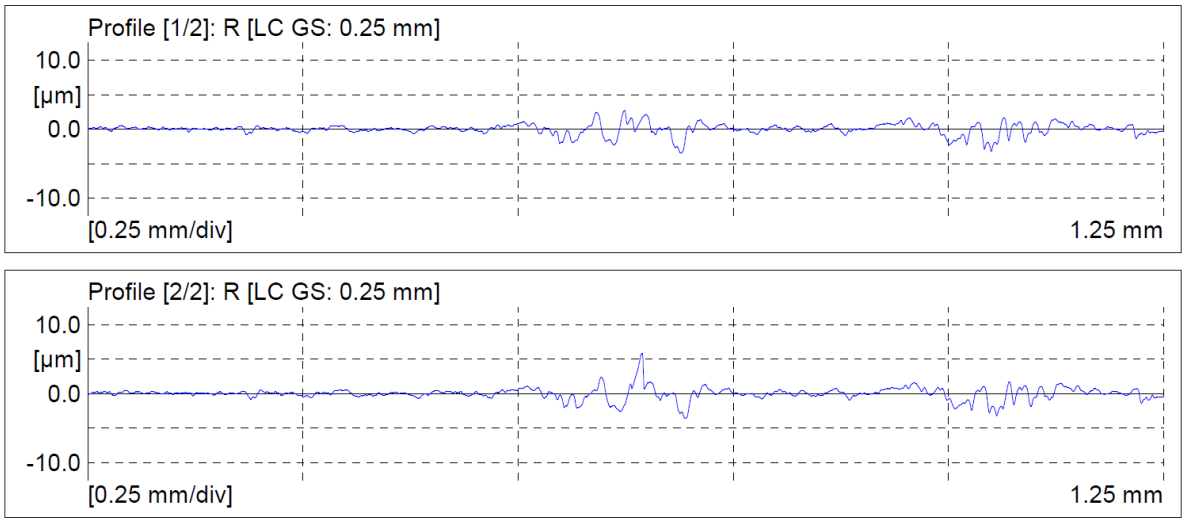

	Ra	Rq	Rz	Rmax	Rt	Rp	Rv	R Sm	R S	R Sk	R Ku	R Mr ...	R Mr ...	...
	µm	µm	µm	µm	µm	µm	µm	µm	µm			%	%	...
1:	0.528	0.790	3.489	6.22	6.22	1.47	2.02	53.25	36.67	-0.92	6.14	49.27	91.09	...
2:	0.554	0.877	3.916	9.44	9.44	2.07	1.85	52.62	46.29	0.12	10.40	46.86	90.57	...
Xb:	0.541	0.833	3.702	7.83	7.83	1.77	1.93	52.93	41.48	-0.40	8.27	48.07	90.83	
S:	0.019	0.062	0.302	2.27	2.27	0.42	0.12	0.45	6.80	0.73	3.01	1.70	0.37	
Max:	0.554	0.877	3.916	9.44	9.44	2.07	2.02	53.25	46.29	0.12	10.40	49.27	91.09	
Min:	0.528	0.790	3.489	6.22	6.22	1.47	1.85	52.62	36.67	-0.92	6.14	46.86	90.57	
R:	0.026	0.087	0.427	3.22	3.22	0.60	0.17	0.63	9.62	1.04	4.25	2.41	0.52	

Figure A1. 62 Surface Profile of CVD Drilled Hole, Feedrate 508 mm/min, Open Hole Tension Test Specimen # 1

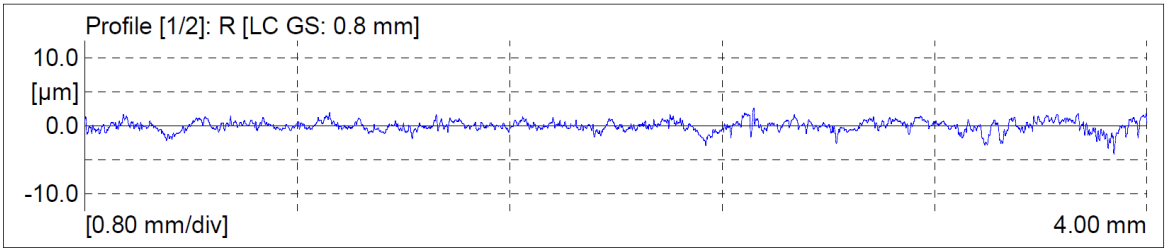

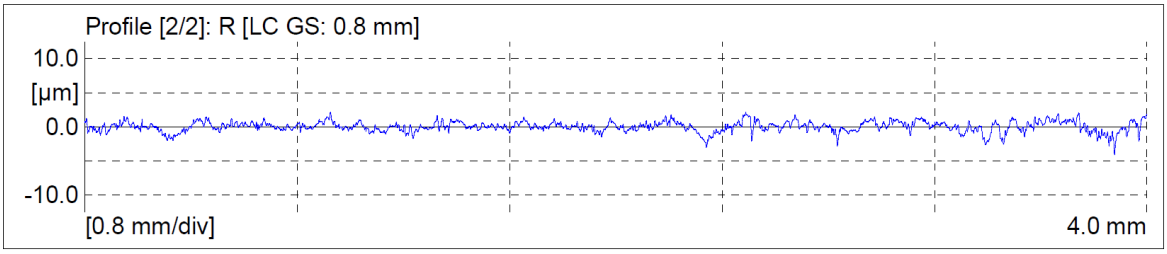

	Ra	Rq	Rz	Rmax	Rt	Rp	Rv	R Sm	R S	R Sk	R Ku	R Mr ...	R Mr ...	...
	µm	µm	µm	µm	µm	µm	µm	µm	µm			%	%	...
1:	0.591	0.783	4.699	5.99	6.83	1.98	2.72	74.53	35.34	-0.59	4.30	38.20	86.73	...
2:	0.583	0.767	4.676	6.14	6.30	1.90	2.77	62.97	33.44	-0.58	4.16	40.24	87.78	...
Xb:	0.587	0.775	4.687	6.07	6.56	1.94	2.75	68.75	34.39	-0.58	4.23	39.22	87.26	
S:	0.006	0.011	0.016	0.10	0.38	0.05	0.04	8.17	1.35	0.01	0.10	1.44	0.74	
Max:	0.591	0.783	4.699	6.14	6.83	1.98	2.77	74.53	35.34	-0.58	4.30	40.24	87.78	
Min:	0.583	0.767	4.676	5.99	6.30	1.90	2.72	62.97	33.44	-0.59	4.16	38.20	86.73	
R:	0.008	0.016	0.023	0.15	0.54	0.07	0.05	11.56	1.90	0.01	0.14	2.03	1.05	

Figure A1. 63 Surface Profile of CVD Drilled Hole, Feedrate 508 mm/min, PCD Endmill Trimmed Edge (longitudinal) of Open Hole Tension Test Specimen # 1

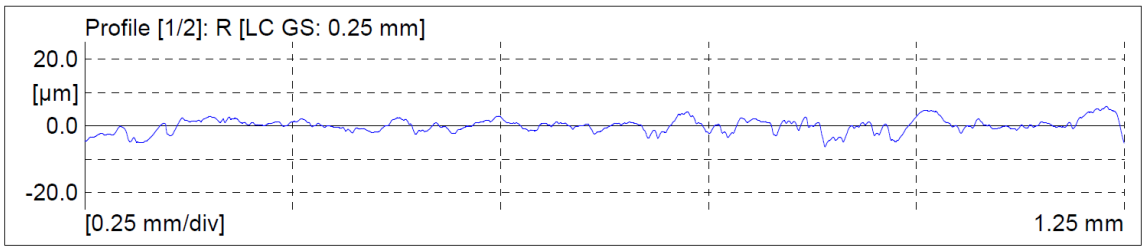

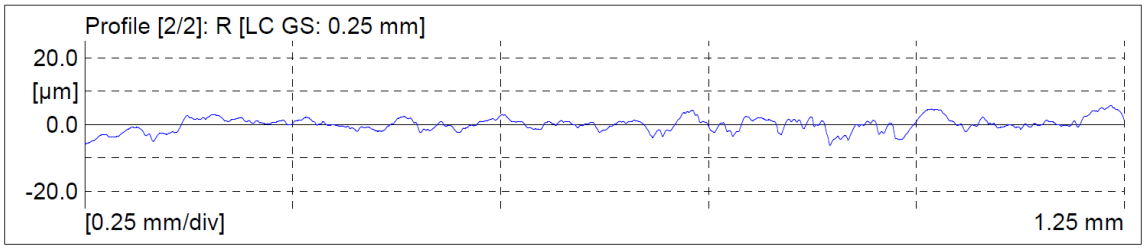

	Ra	Rq	Rz	Rmax	Rt	Rp	Rv	R Sm	R S	R Sk	R Ku	R Mr ...	R Mr ...	...
	µm	µm	µm	µm	µm	µm	µm	µm	µm			%	%	...
1:	1.562	2.055	8.237	11.00	12.14	3.71	4.53	77.11	43.92	-0.04	3.32	7.88	16.34	...
2:	1.609	2.086	7.720	8.77	12.07	3.65	4.08	79.73	47.06	-0.08	3.20	8.12	16.77	...
Xb:	1.585	2.070	7.979	9.88	12.10	3.68	4.30	78.42	45.49	-0.06	3.26	8.00	16.56	
S:	0.033	0.022	0.366	1.58	0.05	0.04	0.32	1.86	2.22	0.03	0.08	0.17	0.31	
Max:	1.609	2.086	8.237	11.00	12.14	3.71	4.53	79.73	47.06	-0.04	3.32	8.12	16.77	
Min:	1.562	2.055	7.720	8.77	12.07	3.65	4.08	77.11	43.92	-0.08	3.20	7.88	16.34	
R:	0.047	0.031	0.517	2.23	0.07	0.06	0.46	2.62	3.13	0.04	0.12	0.24	0.44	

Figure A1. 64 Surface Profile of CVD Drilled Hole, Feedrate 508 mm/min, PCD Endmill Trimmed Edge (transverse) of Open Hole Tension Test Specimen # 1

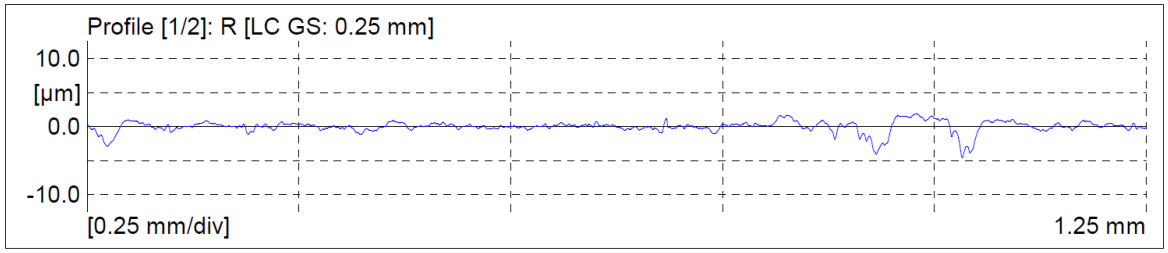

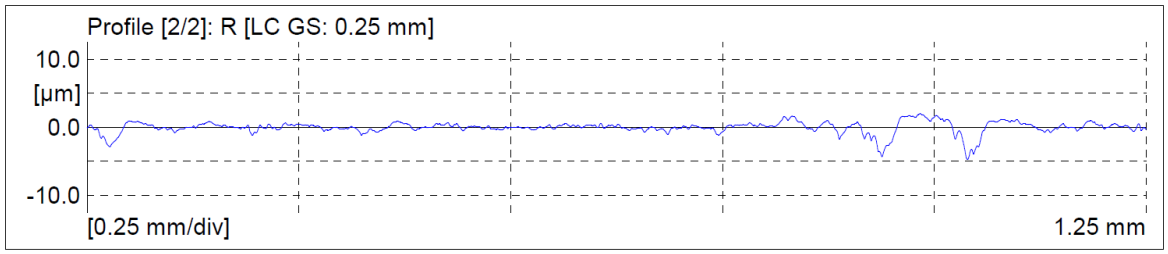

	Ra	Rq	Rz	Rmax	Rt	Rp	Rv	R Sm	R S	R Sk	R Ku	R Mr ...	R Mr ...	...
	µm	µm	µm	µm	µm	µm	µm	µm	µm			%	%	...
1:	0.550	0.864	3.978	6.00	6.49	1.23	2.74	66.28	47.46	-1.84	8.92	42.76	90.71	...
2:	0.560	0.884	4.087	6.48	6.74	1.25	2.84	79.70	54.18	-1.85	9.29	41.83	90.56	...
Xb:	0.555	0.874	4.033	6.24	6.62	1.24	2.79	72.99	50.82	-1.85	9.11	42.29	90.64	
S:	0.007	0.014	0.077	0.34	0.18	0.01	0.07	9.49	4.75	0.01	0.26	0.66	0.11	
Max:	0.560	0.884	4.087	6.48	6.74	1.25	2.84	79.70	54.18	-1.84	9.29	42.76	90.71	
Min:	0.550	0.864	3.978	6.00	6.49	1.23	2.74	66.28	47.46	-1.85	8.92	41.83	90.56	
R:	0.010	0.020	0.109	0.48	0.25	0.01	0.10	13.42	6.72	0.01	0.37	0.93	0.15	

Figure A1. 65 Surface Profile of CVD Drilled Hole, Feedrate 508 mm/min, Open Hole Tension Test Specimen # 2

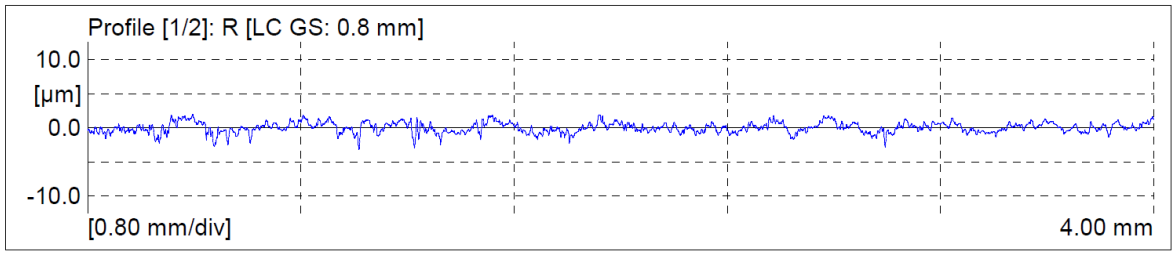

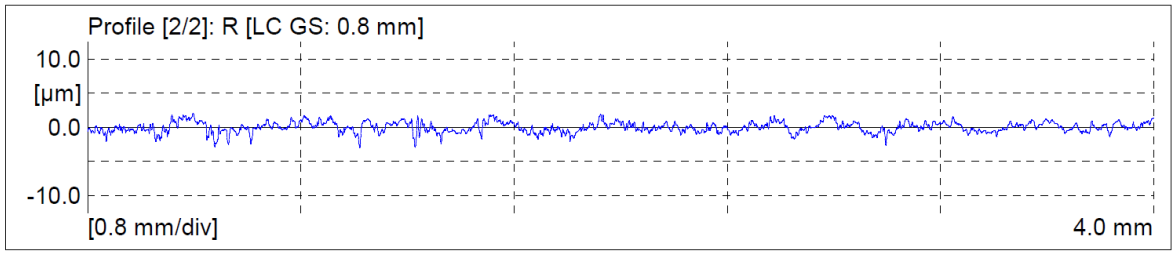

	Ra	Rq	Rz	Rmax	Rt	Rp	Rv	R Sm	R S	R Sk	R Ku	R Mr ...	R Mr ...	...
	µm	µm	µm	µm	µm	µm	µm	µm	µm			%	%	...
1:	0.609	0.764	4.321	5.04	5.17	1.84	2.48	89.12	32.90	-0.19	3.34	36.63	84.73	...
2:	0.614	0.770	4.208	4.93	5.10	1.82	2.39	79.83	32.10	-0.20	3.31	37.27	84.67	...
Xb:	0.612	0.767	4.264	4.99	5.13	1.83	2.43	84.47	32.50	-0.19	3.32	36.95	84.70	
S:	0.004	0.004	0.080	0.08	0.04	0.02	0.06	6.56	0.57	0.01	0.02	0.45	0.04	
Max:	0.614	0.770	4.321	5.04	5.17	1.84	2.48	89.12	32.90	-0.19	3.34	37.27	84.73	
Min:	0.609	0.764	4.208	4.93	5.10	1.82	2.39	79.83	32.10	-0.20	3.31	36.63	84.67	
R:	0.005	0.006	0.113	0.11	0.06	0.03	0.08	9.28	0.80	0.01	0.03	0.64	0.06	

Figure A1. 66 Surface Profile of CVD Drilled Hole, Feedrate 508 mm/min, PCD Endmill Trimmed Edge (longitudinal) of Open Hole Tension Test Specimen # 2

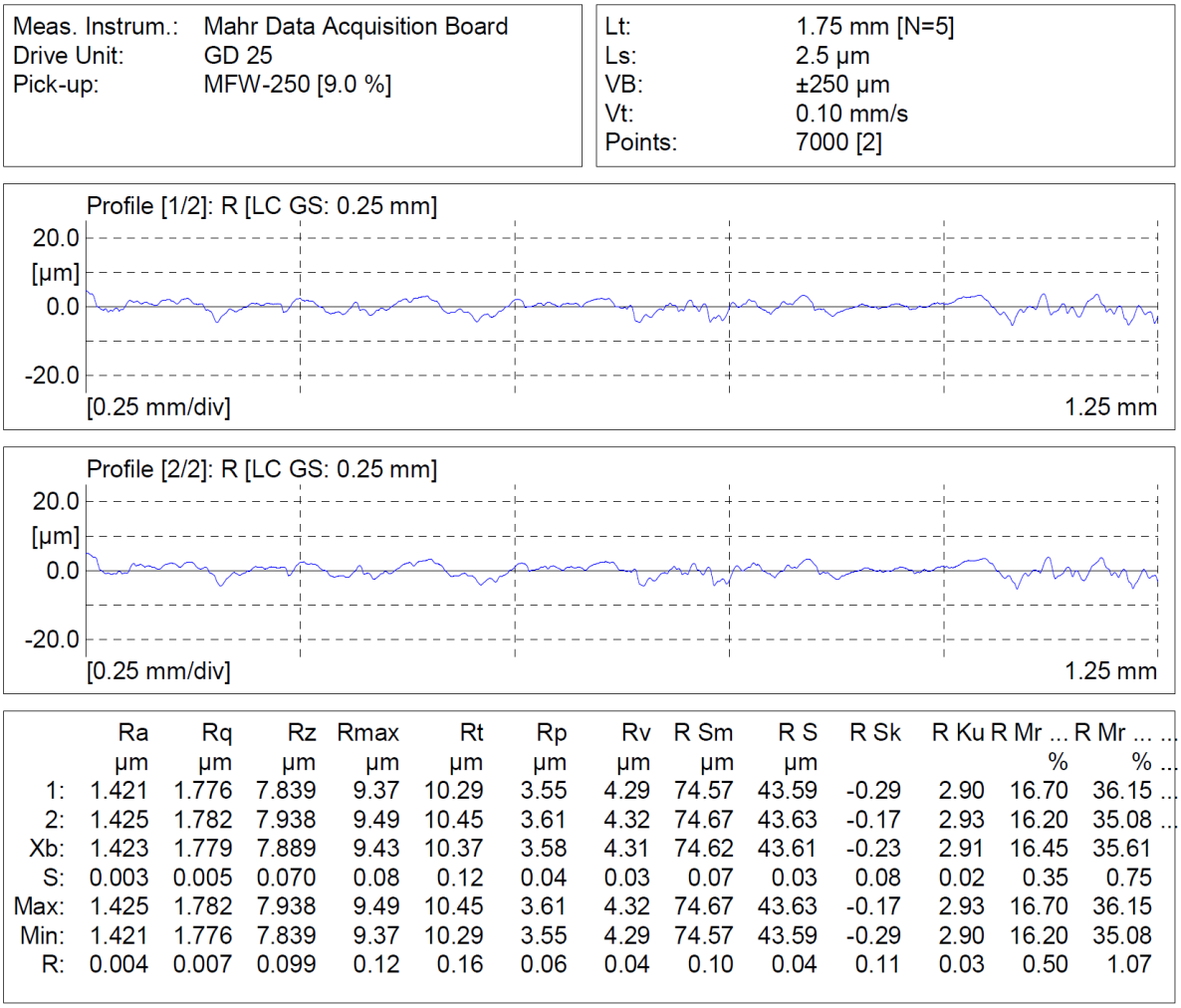

	Ra	Rq	Rz	Rmax	Rt	Rp	Rv	R Sm	R S	R Sk	R Ku	R Mr ...	R Mr ...	...
	µm	µm	µm	µm	µm	µm	µm	µm	µm			%	%	...
1:	1.421	1.776	7.839	9.37	10.29	3.55	4.29	74.57	43.59	-0.29	2.90	16.70	36.15	...
2:	1.425	1.782	7.938	9.49	10.45	3.61	4.32	74.67	43.63	-0.17	2.93	16.20	35.08	...
Xb:	1.423	1.779	7.889	9.43	10.37	3.58	4.31	74.62	43.61	-0.23	2.91	16.45	35.61	
S:	0.003	0.005	0.070	0.08	0.12	0.04	0.03	0.07	0.03	0.08	0.02	0.35	0.75	
Max:	1.425	1.782	7.938	9.49	10.45	3.61	4.32	74.67	43.63	-0.17	2.93	16.70	36.15	
Min:	1.421	1.776	7.839	9.37	10.29	3.55	4.29	74.57	43.59	-0.29	2.90	16.20	35.08	
R:	0.004	0.007	0.099	0.12	0.16	0.06	0.04	0.10	0.04	0.11	0.03	0.50	1.07	

Figure A1. 67 Surface Profile of CVD Drilled Hole, Feedrate 508 mm/min, PCD Endmill Trimmed Edge (transverse) of Open Hole Tension Test Specimen # 2

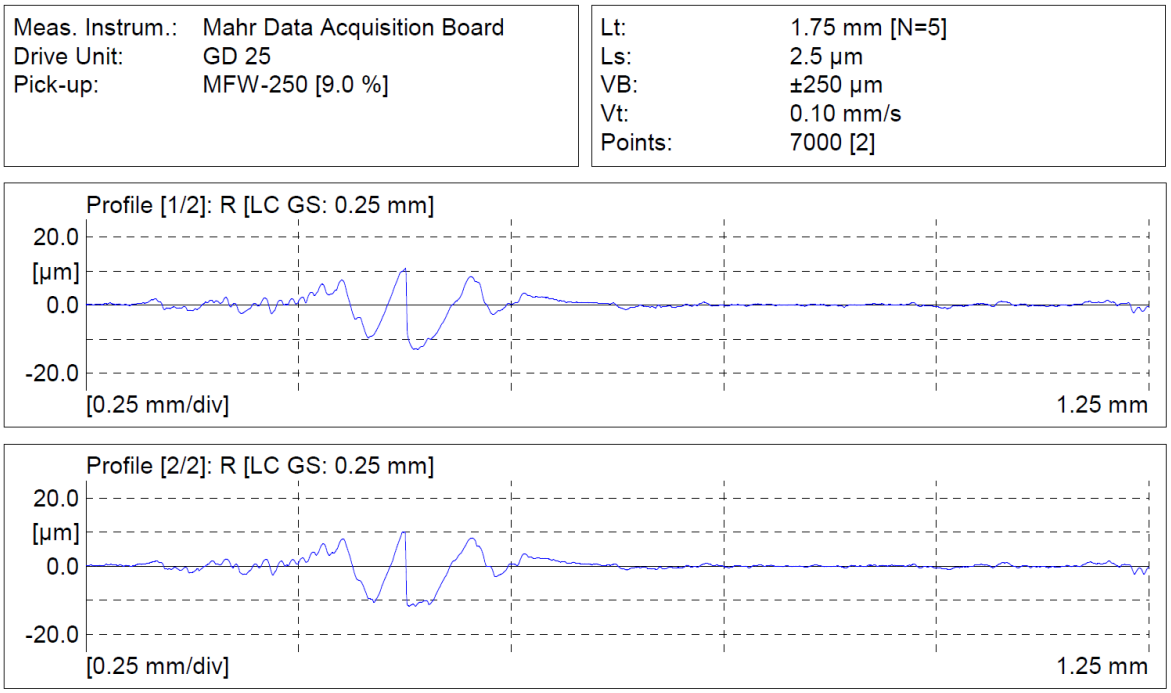

	Ra µm	Rq µm	Rz µm	Rmax µm	Rt µm	Rp µm	Rv µm	R Sm µm	R S µm	R Sk	R Ku ...
1:	1.521	2.923	7.722	23.83	23.83	3.77	3.95	133.14	148.13	-1.27	9.86 ...
2:	1.540	2.920	7.257	21.82	21.82	3.61	3.65	132.93	148.27	-1.24	8.91 ...
Xb:	1.531	2.922	7.489	22.82	22.82	3.69	3.80	133.04	148.20	-1.26	9.38
S:	0.014	0.002	0.329	1.42	1.42	0.11	0.21	0.15	0.10	0.02	0.67
Max:	1.540	2.923	7.722	23.83	23.83	3.77	3.95	133.14	148.27	-1.24	9.86
Min:	1.521	2.920	7.257	21.82	21.82	3.61	3.65	132.93	148.13	-1.27	8.91
R:	0.019	0.003	0.465	2.01	2.01	0.16	0.30	0.21	0.14	0.03	0.94

Figure A1. 68 Surface Profile of CVD Drilled Hole, Feedrate 508 mm/min, Open Hole Tension Test Specimen # 3

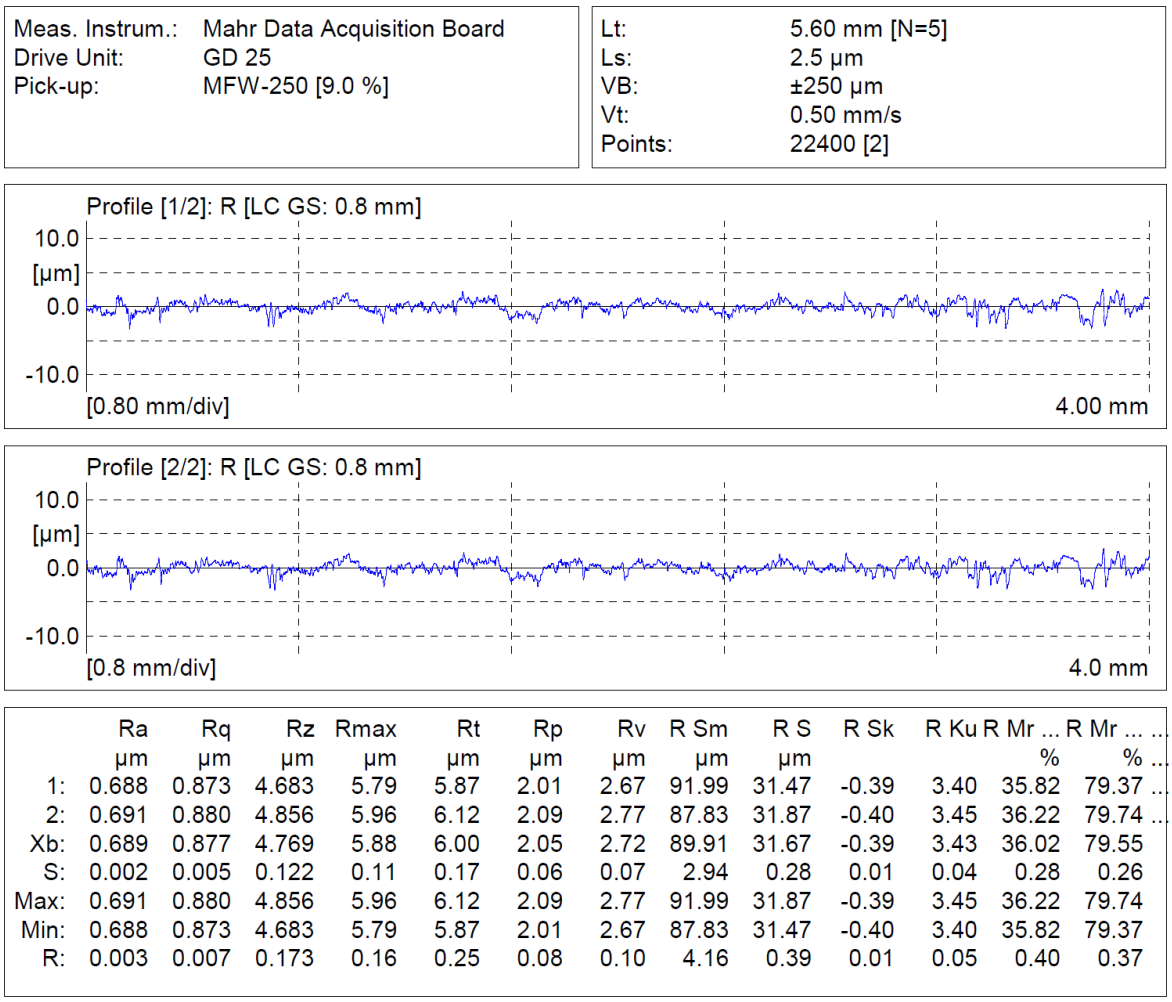

	Ra	Rq	Rz	Rmax	Rt	Rp	Rv	R Sm	R S	R Sk	R Ku	R Mr ...	R Mr ...	...
	µm	µm	µm	µm	µm	µm	µm	µm	µm			%	%	...
1:	0.688	0.873	4.683	5.79	5.87	2.01	2.67	91.99	31.47	-0.39	3.40	35.82	79.37	...
2:	0.691	0.880	4.856	5.96	6.12	2.09	2.77	87.83	31.87	-0.40	3.45	36.22	79.74	...
Xb:	0.689	0.877	4.769	5.88	6.00	2.05	2.72	89.91	31.67	-0.39	3.43	36.02	79.55	
S:	0.002	0.005	0.122	0.11	0.17	0.06	0.07	2.94	0.28	0.01	0.04	0.28	0.26	
Max:	0.691	0.880	4.856	5.96	6.12	2.09	2.77	91.99	31.87	-0.39	3.45	36.22	79.74	
Min:	0.688	0.873	4.683	5.79	5.87	2.01	2.67	87.83	31.47	-0.40	3.40	35.82	79.37	
R:	0.003	0.007	0.173	0.16	0.25	0.08	0.10	4.16	0.39	0.01	0.05	0.40	0.37	

Figure A1. 69 Surface Profile of CVD Drilled Hole, Feedrate 508 mm/min, PCD Endmill Trimmed Edge (longitudinal) of Open Hole Tension Test Specimen # 3

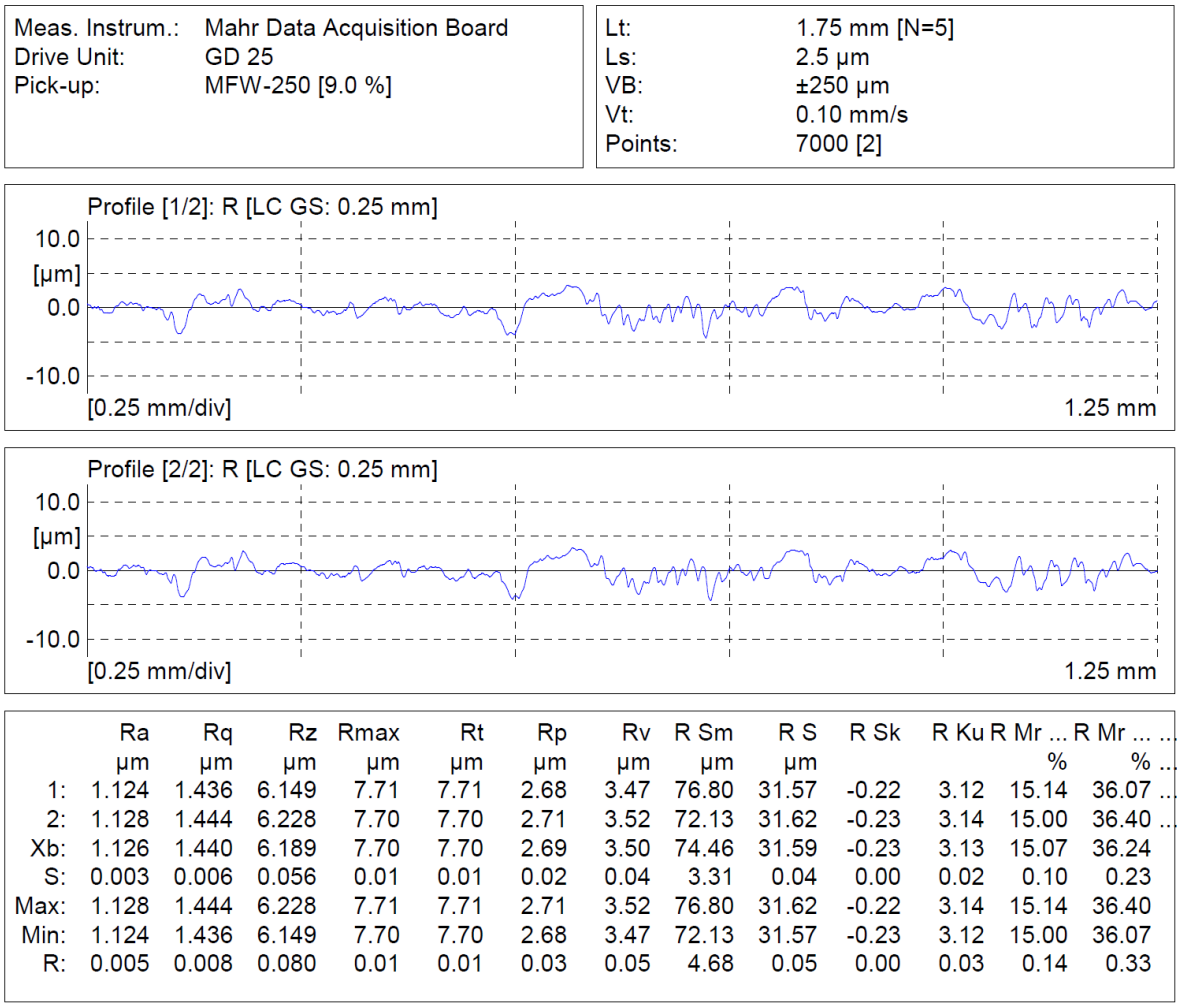

	Ra µm	Rq µm	Rz µm	Rmax µm	Rt µm	Rp µm	Rv µm	R Sm µm	R S µm	R Sk	R Ku	R Mr ... %	R Mr ... % ...
1:	1.124	1.436	6.149	7.71	7.71	2.68	3.47	76.80	31.57	-0.22	3.12	15.14	36.07 ...
2:	1.128	1.444	6.228	7.70	7.70	2.71	3.52	72.13	31.62	-0.23	3.14	15.00	36.40 ...
Xb:	1.126	1.440	6.189	7.70	7.70	2.69	3.50	74.46	31.59	-0.23	3.13	15.07	36.24
S:	0.003	0.006	0.056	0.01	0.01	0.02	0.04	3.31	0.04	0.00	0.02	0.10	0.23
Max:	1.128	1.444	6.228	7.71	7.71	2.71	3.52	76.80	31.62	-0.22	3.14	15.14	36.40
Min:	1.124	1.436	6.149	7.70	7.70	2.68	3.47	72.13	31.57	-0.23	3.12	15.00	36.07
R:	0.005	0.008	0.080	0.01	0.01	0.03	0.05	4.68	0.05	0.00	0.03	0.14	0.33

Figure A1. 70 Surface Profile of CVD Drilled Hole, Feedrate 508 mm/min, PCD Endmill Trimmed Edge (transverse) of Open Hole Tension Test Specimen # 3

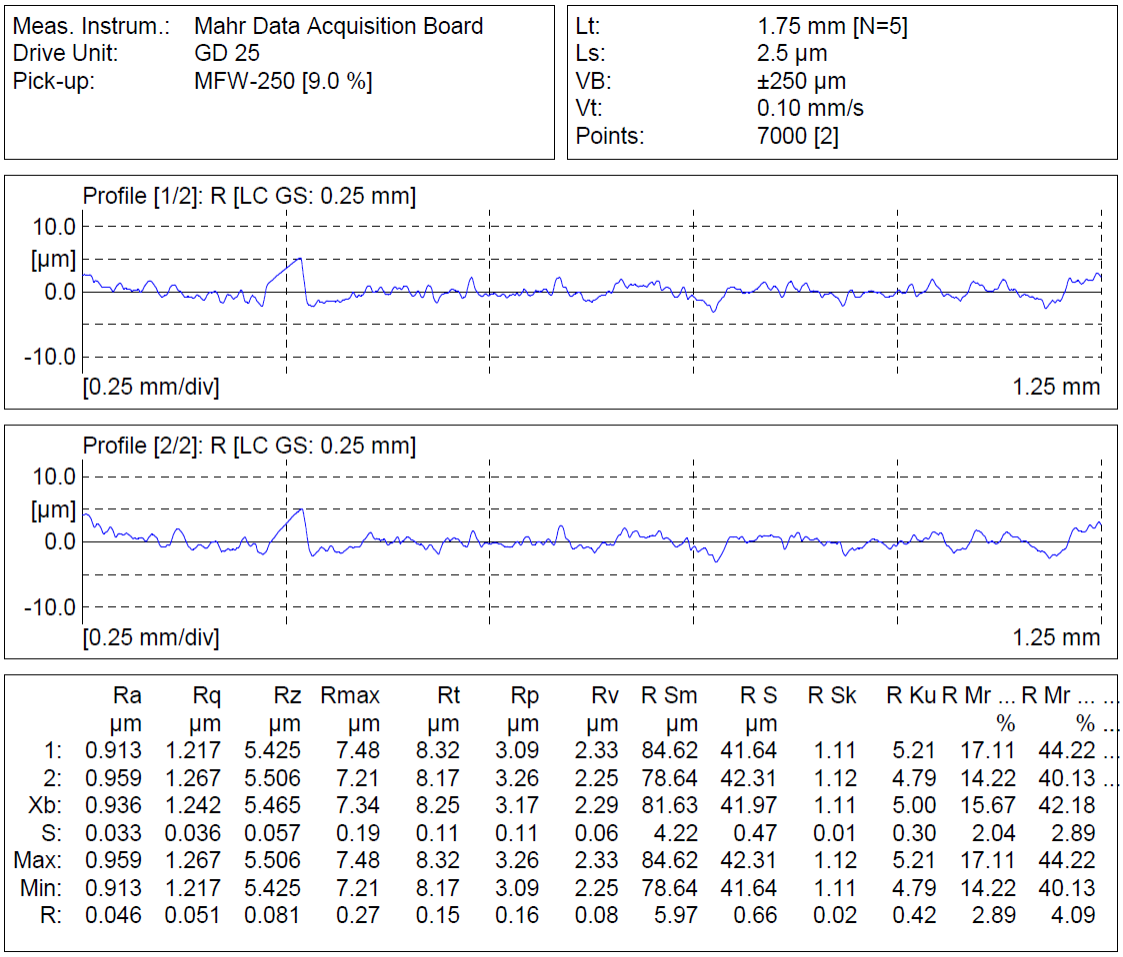

	Ra µm	Rq µm	Rz µm	Rmax µm	Rt µm	Rp µm	Rv µm	R Sm µm	R S µm	R Sk	R Ku	R Mr ... %	R Mr ... %	...
1:	0.913	1.217	5.425	7.48	8.32	3.09	2.33	84.62	41.64	1.11	5.21	17.11	44.22	...
2:	0.959	1.267	5.506	7.21	8.17	3.26	2.25	78.64	42.31	1.12	4.79	14.22	40.13	...
Xb:	0.936	1.242	5.465	7.34	8.25	3.17	2.29	81.63	41.97	1.11	5.00	15.67	42.18	
S:	0.033	0.036	0.057	0.19	0.11	0.11	0.06	4.22	0.47	0.01	0.30	2.04	2.89	
Max:	0.959	1.267	5.506	7.48	8.32	3.26	2.33	84.62	42.31	1.12	5.21	17.11	44.22	
Min:	0.913	1.217	5.425	7.21	8.17	3.09	2.25	78.64	41.64	1.11	4.79	14.22	40.13	
R:	0.046	0.051	0.081	0.27	0.15	0.16	0.08	5.97	0.66	0.02	0.42	2.89	4.09	

Figure A1. 71 Surface Profile of CVD Drilled Hole, Feedrate 508 mm/min, Open Hole Tension Test Specimen # 4

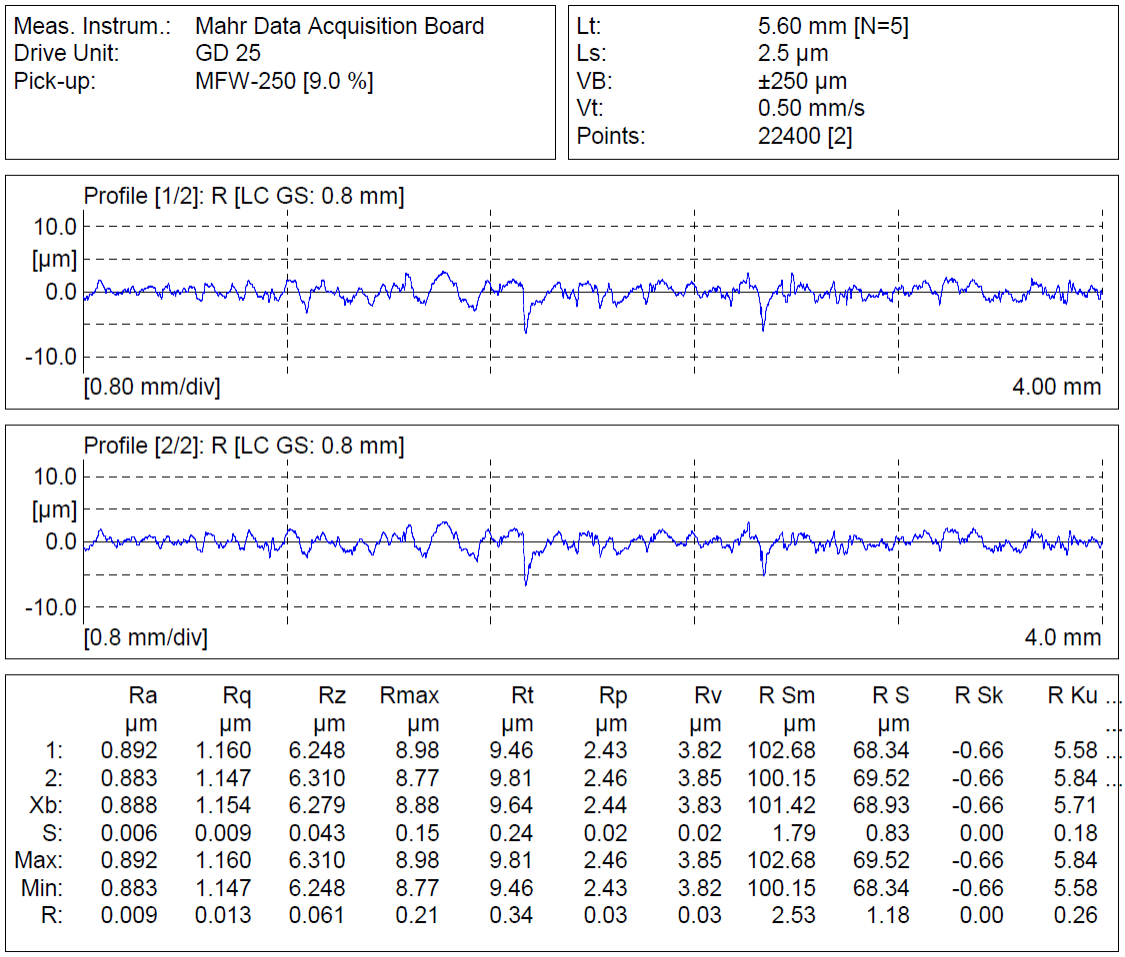

	Ra	Rq	Rz	Rmax	Rt	Rp	Rv	R Sm	R S	R Sk	R Ku ...
	µm	µm	µm	µm	µm	µm	µm	µm	µm		...
1:	0.892	1.160	6.248	8.98	9.46	2.43	3.82	102.68	68.34	-0.66	5.58 ...
2:	0.883	1.147	6.310	8.77	9.81	2.46	3.85	100.15	69.52	-0.66	5.84 ...
Xb:	0.888	1.154	6.279	8.88	9.64	2.44	3.83	101.42	68.93	-0.66	5.71
S:	0.006	0.009	0.043	0.15	0.24	0.02	0.02	1.79	0.83	0.00	0.18
Max:	0.892	1.160	6.310	8.98	9.81	2.46	3.85	102.68	69.52	-0.66	5.84
Min:	0.883	1.147	6.248	8.77	9.46	2.43	3.82	100.15	68.34	-0.66	5.58
R:	0.009	0.013	0.061	0.21	0.34	0.03	0.03	2.53	1.18	0.00	0.26

Figure A1. 72 Surface Profile of CVD Drilled Hole, Feedrate 508 mm/min, PCD Endmill Trimmed Edge (longitudinal) of Open Hole Tension Test Specimen # 4

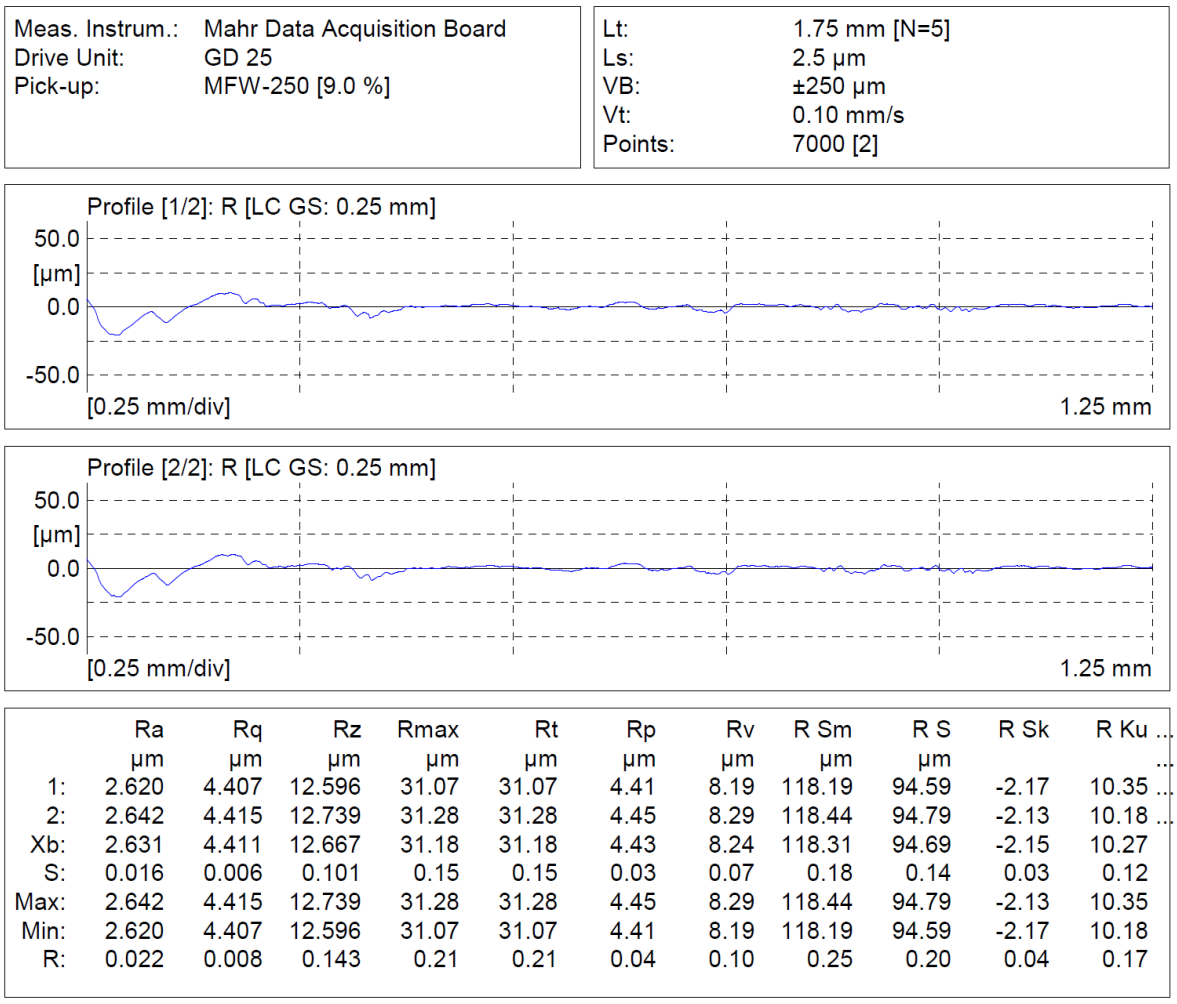

	Ra	Rq	Rz	Rmax	Rt	Rp	Rv	R Sm	R S	R Sk	R Ku ...
	µm	µm	µm	µm	µm	µm	µm	µm	µm		...
1:	2.620	4.407	12.596	31.07	31.07	4.41	8.19	118.19	94.59	-2.17	10.35 ...
2:	2.642	4.415	12.739	31.28	31.28	4.45	8.29	118.44	94.79	-2.13	10.18 ...
Xb:	2.631	4.411	12.667	31.18	31.18	4.43	8.24	118.31	94.69	-2.15	10.27
S:	0.016	0.006	0.101	0.15	0.15	0.03	0.07	0.18	0.14	0.03	0.12
Max:	2.642	4.415	12.739	31.28	31.28	4.45	8.29	118.44	94.79	-2.13	10.35
Min:	2.620	4.407	12.596	31.07	31.07	4.41	8.19	118.19	94.59	-2.17	10.18
R:	0.022	0.008	0.143	0.21	0.21	0.04	0.10	0.25	0.20	0.04	0.17

Figure A1. 73 Surface Profile of CVD Drilled Hole, Feedrate 508 mm/min, PCD Endmill Trimmed Edge (transverse) of Open Hole Tension Test Specimen # 4

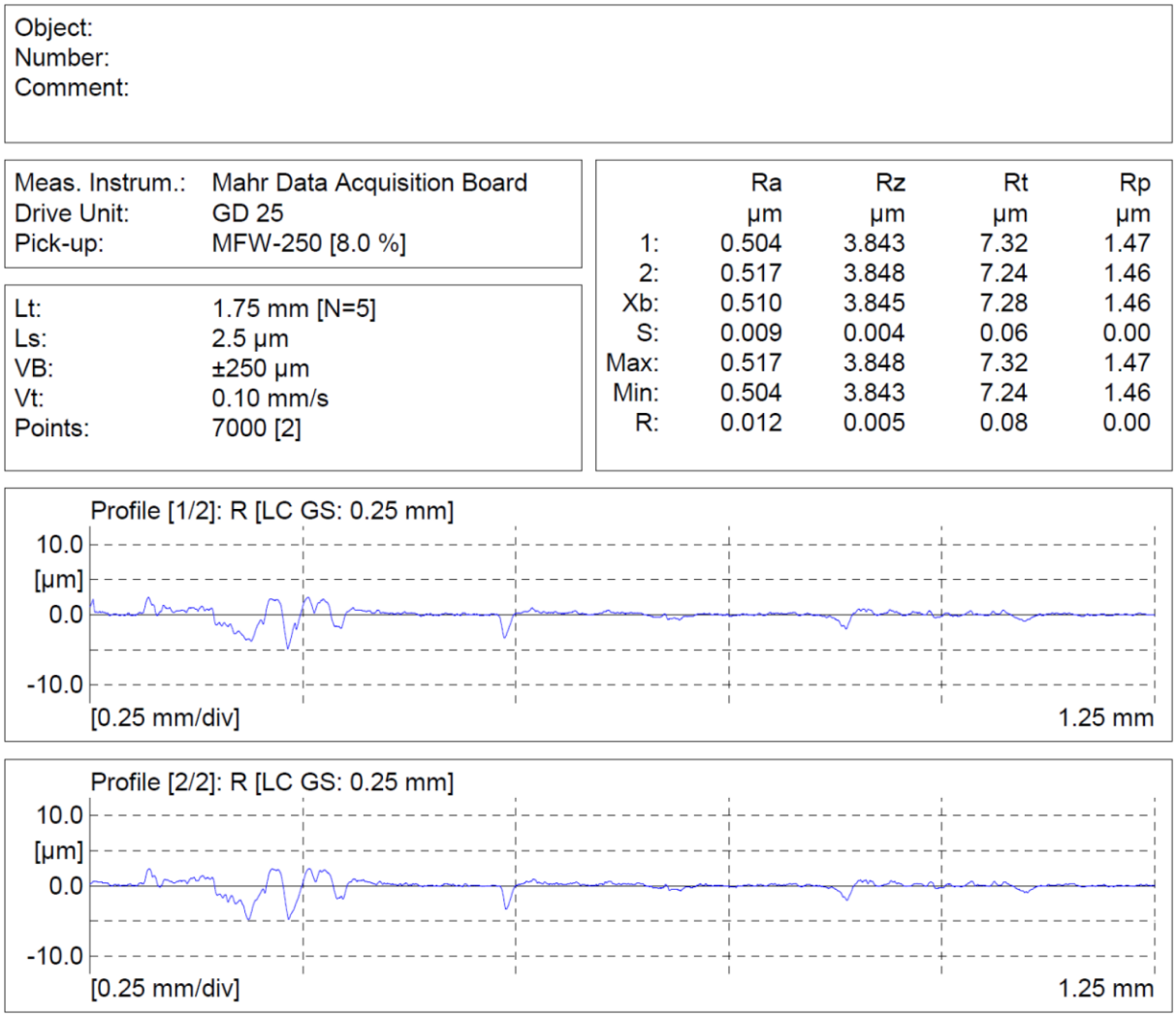

Figure A1. 74 Surface Profile of PCD Drilled Hole, Feedrate 508 mm/min, Open Hole Tension Test Specimen # 1

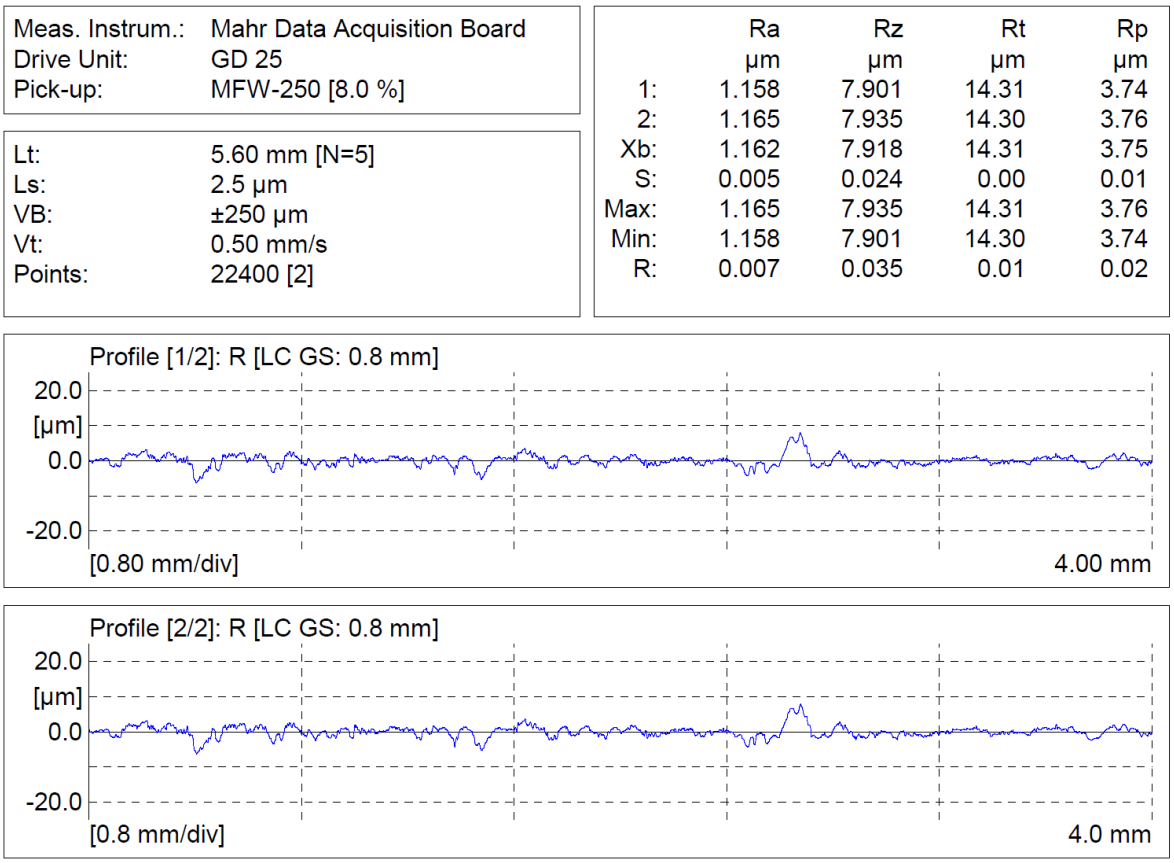

Figure A1. 75 Surface Profile of PCD Drilled Hole, Feedrate 508 mm/min, PCD Endmill Trimmed Edge (longitudinal) of Open Hole Tension Test Specimen # 1

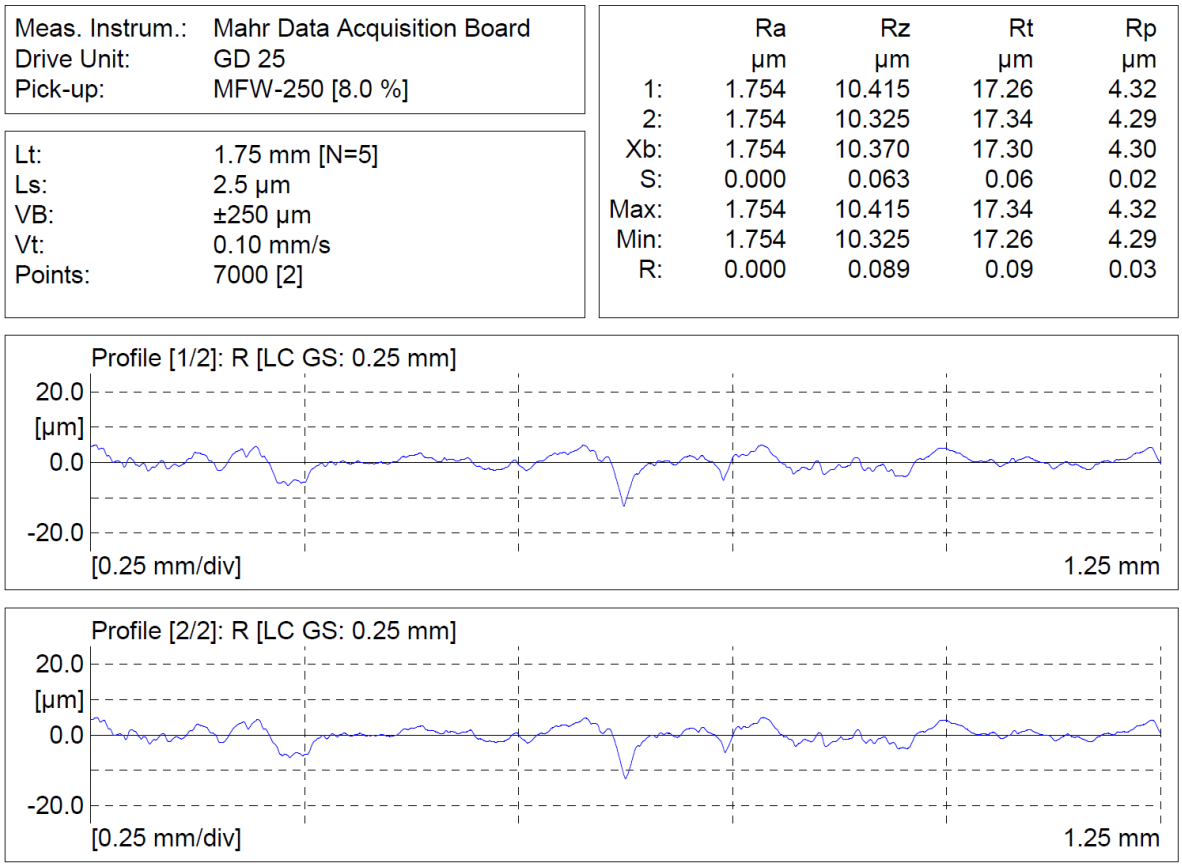

Figure A1. 76 Surface Profile of PCD Drilled Hole, Feedrate 508 mm/min, PCD Endmill Trimmed Edge (transverse) of Open Hole Tension Test Specimen # 1

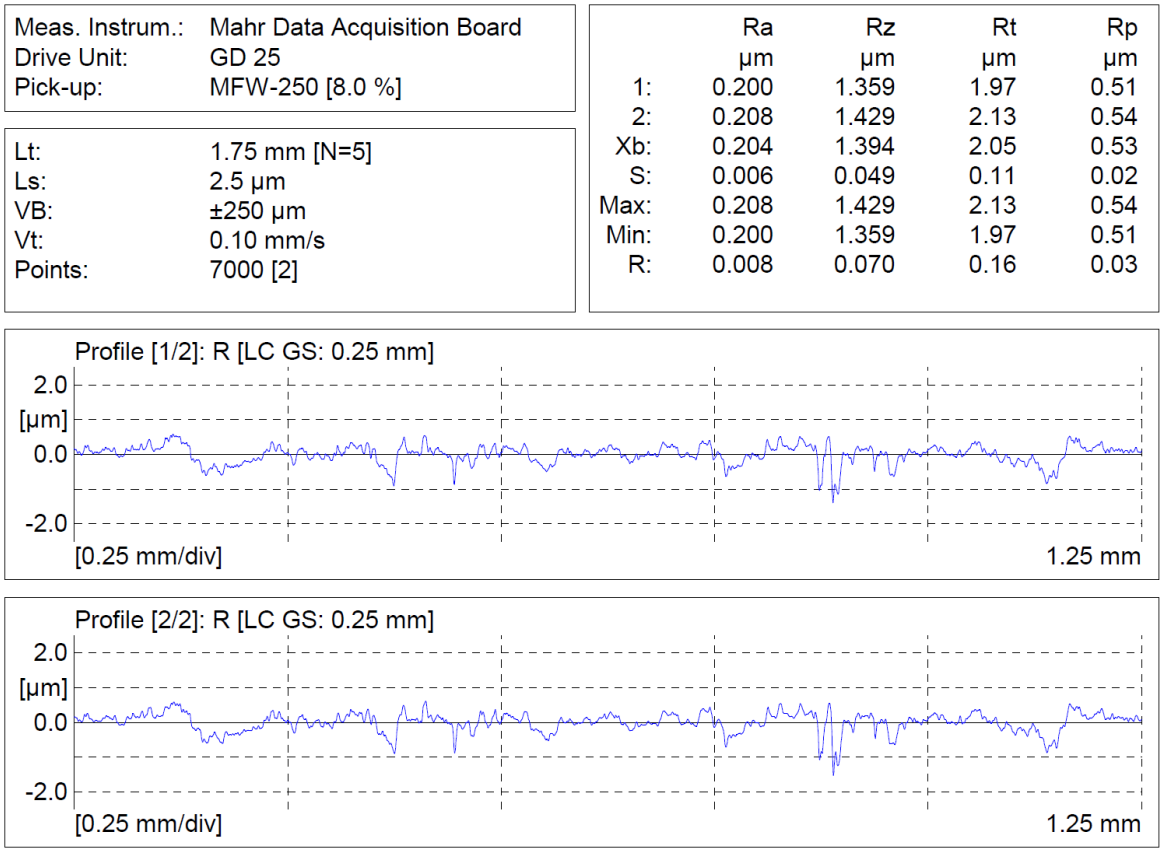

Figure A1. 77 Surface Profile of PCD Drilled Hole, Feedrate 508 mm/min, Open Hole Tension Test Specimen # 2

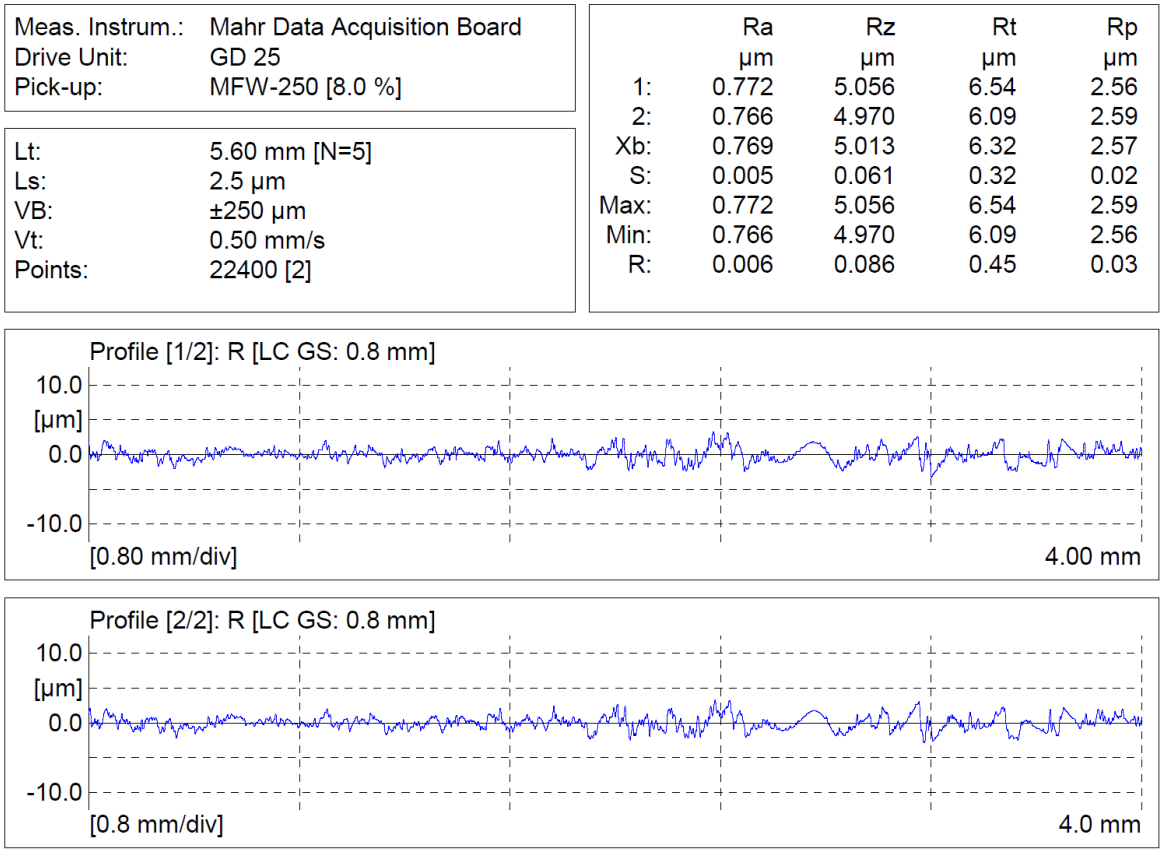

Figure A1. 78 Surface Profile of PCD Drilled Hole, Feedrate 508 mm/min, PCD Endmill Trimmed Edge (longitudinal) of Open Hole Tension Test Specimen # 2

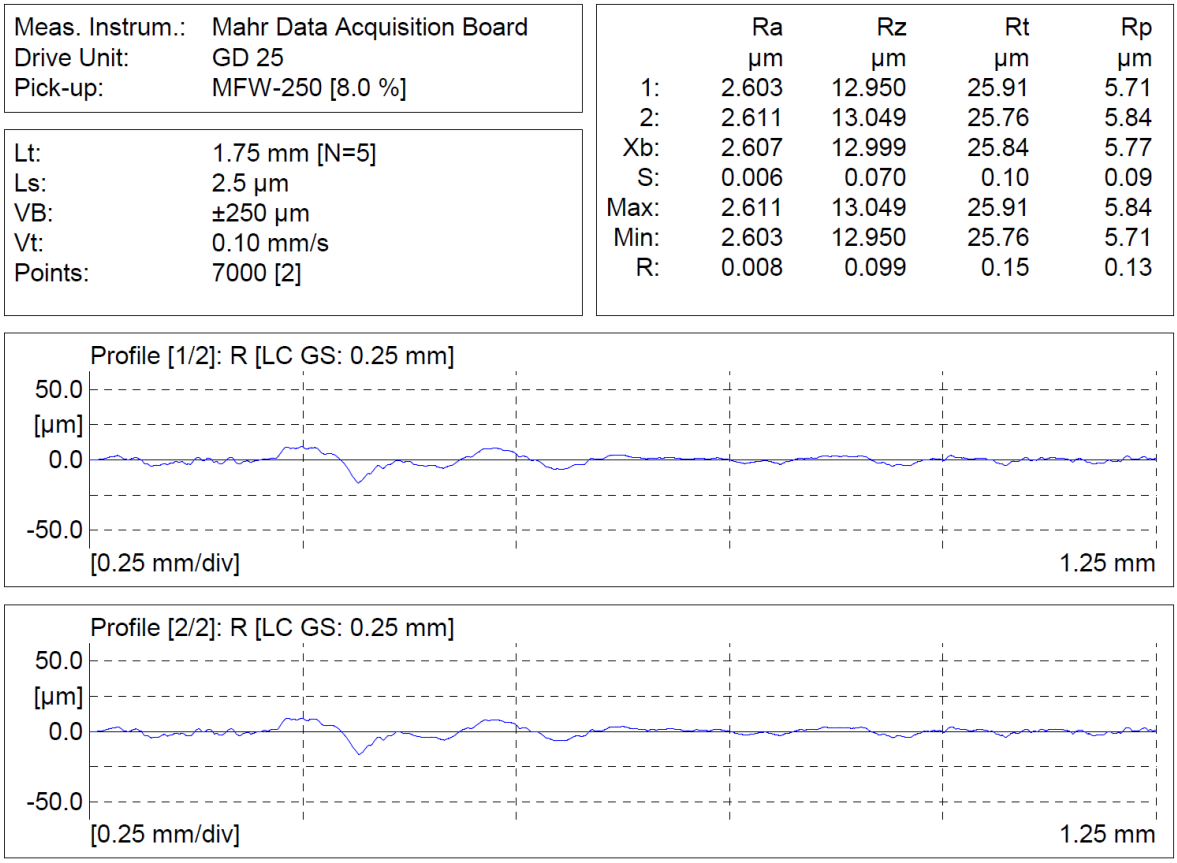

Figure A1. 79 Surface Profile of PCD Drilled Hole, Feedrate 508 mm/min, PCD Endmill Trimmed Edge (transverse) of Open Hole Tension Test Specimen # 2

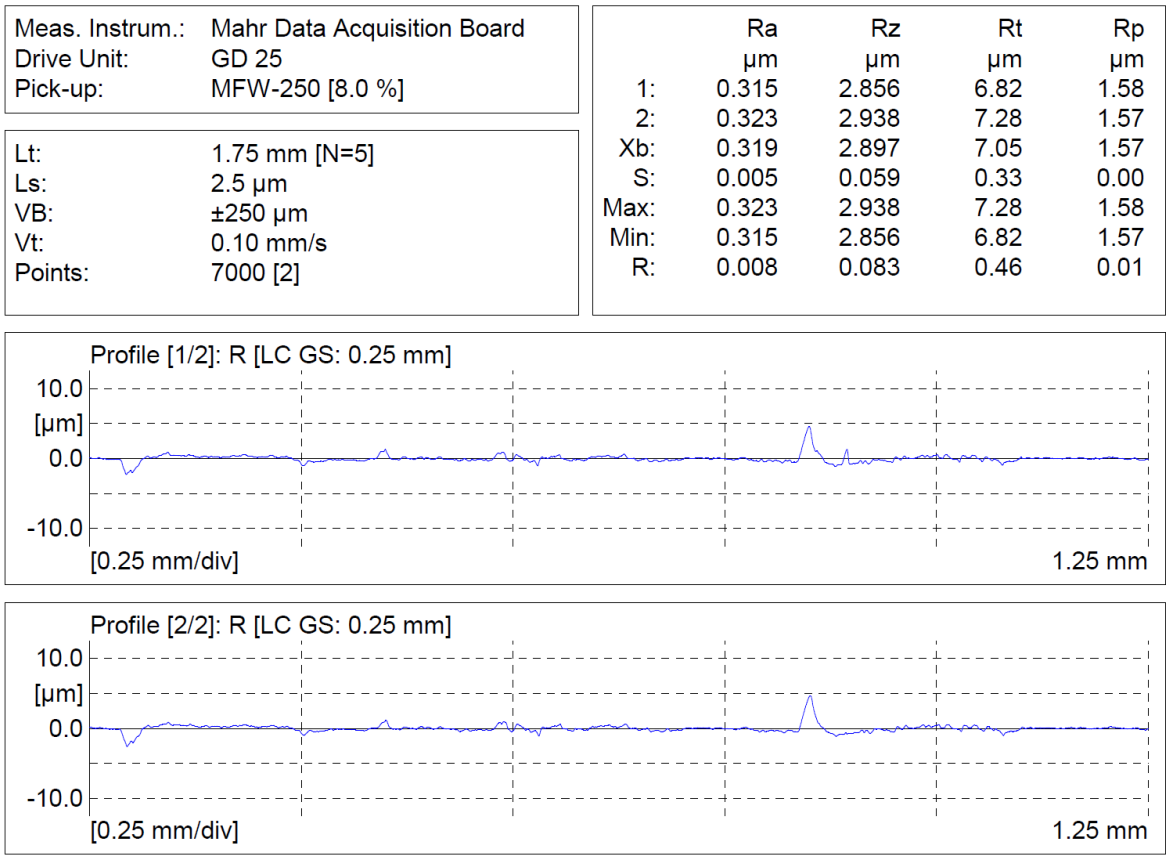

Figure A1. 80 Surface Profile of PCD Drilled Hole, Feedrate 508 mm/min, Open Hole Tension Test Specimen # 3

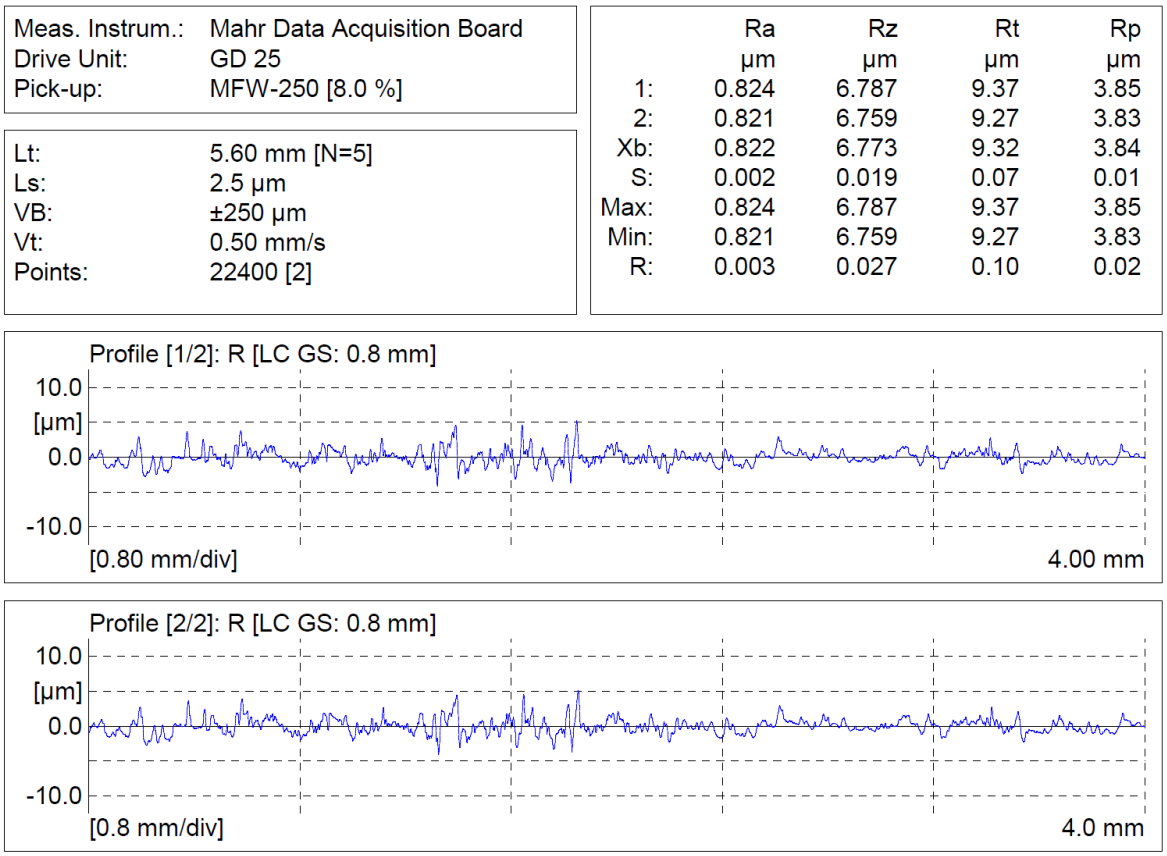

Figure A1. 81 Surface Profile of PCD Drilled Hole, Feedrate 508 mm/min, PCD Endmill Trimmed Edge (longitudinal) of Open Hole Tension Test Specimen # 3

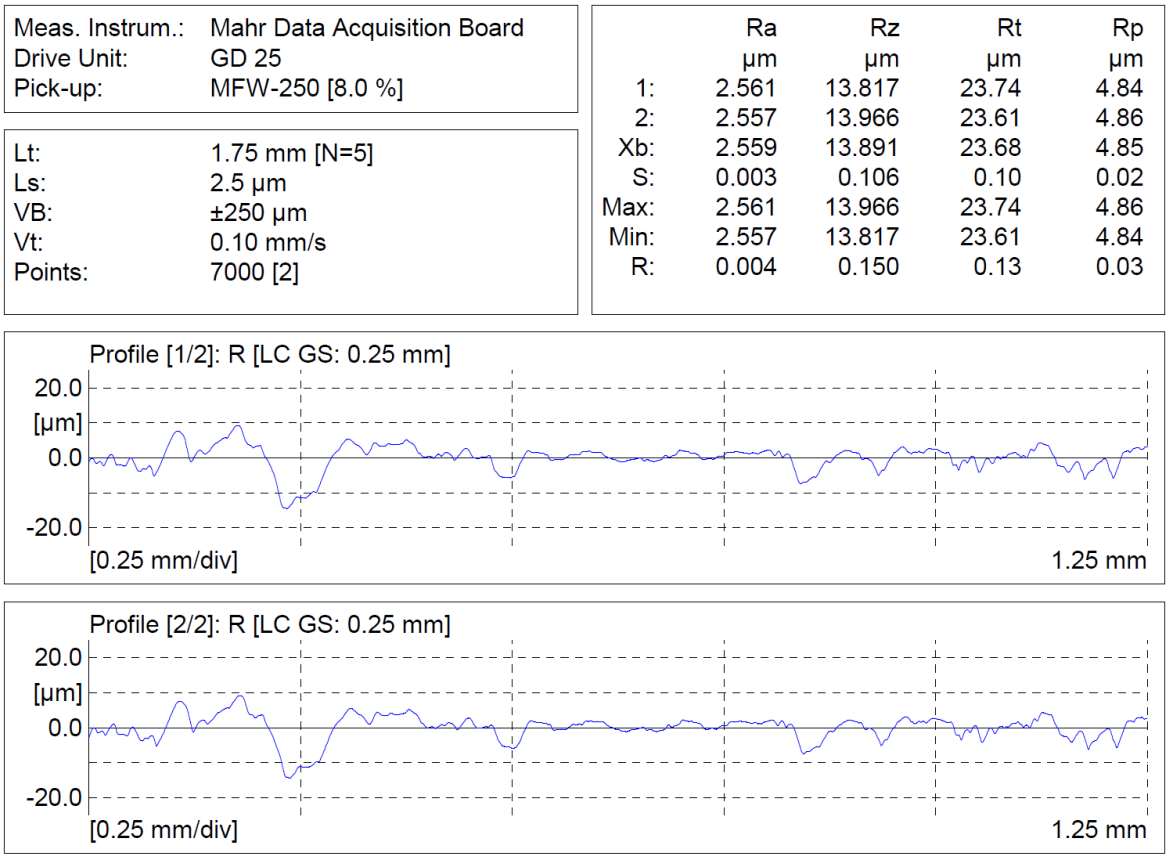

Figure A1. 82 Surface Profile of PCD Drilled Hole, Feedrate 508 mm/min, PCD Endmill Trimmed Edge (transverse) of Open Hole Tension Test Specimen # 3

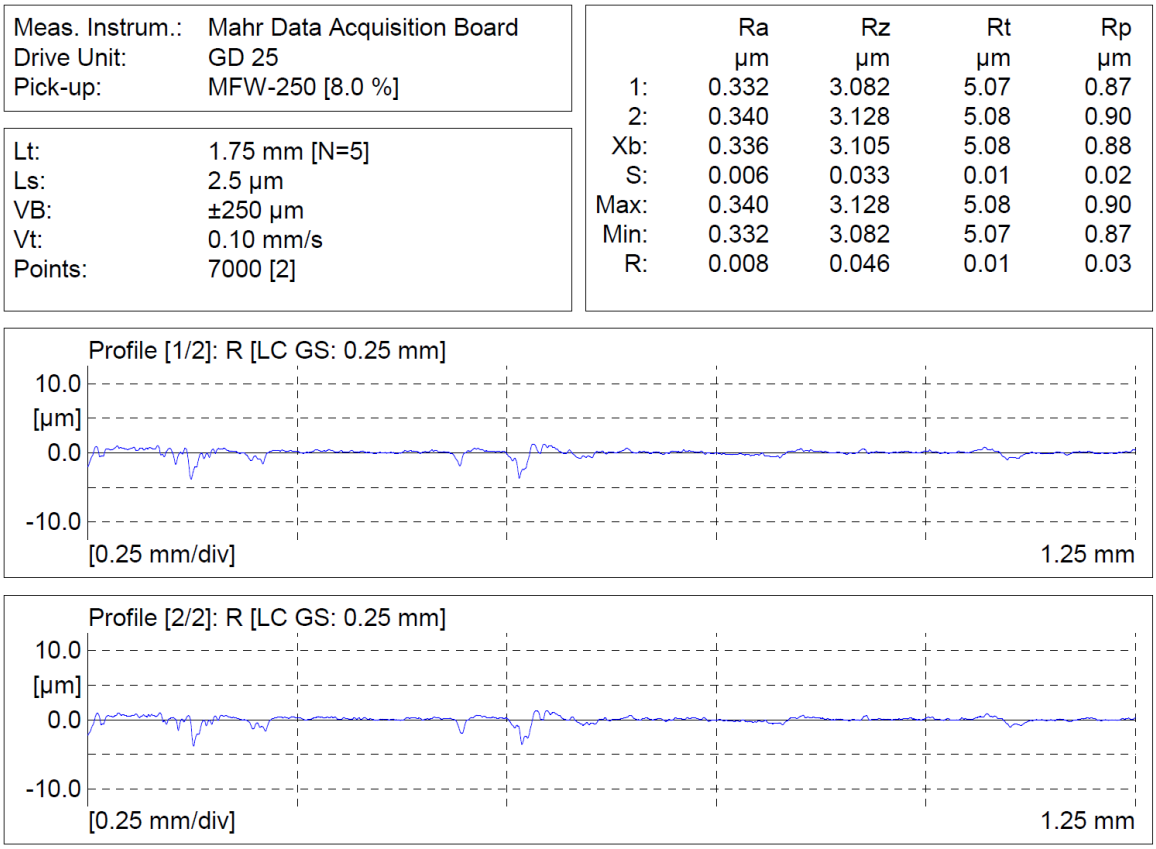

Figure A1. 83 Surface Profile of PCD Drilled Hole, Feedrate 508 mm/min, Open Hole Tension Test Specimen # 4

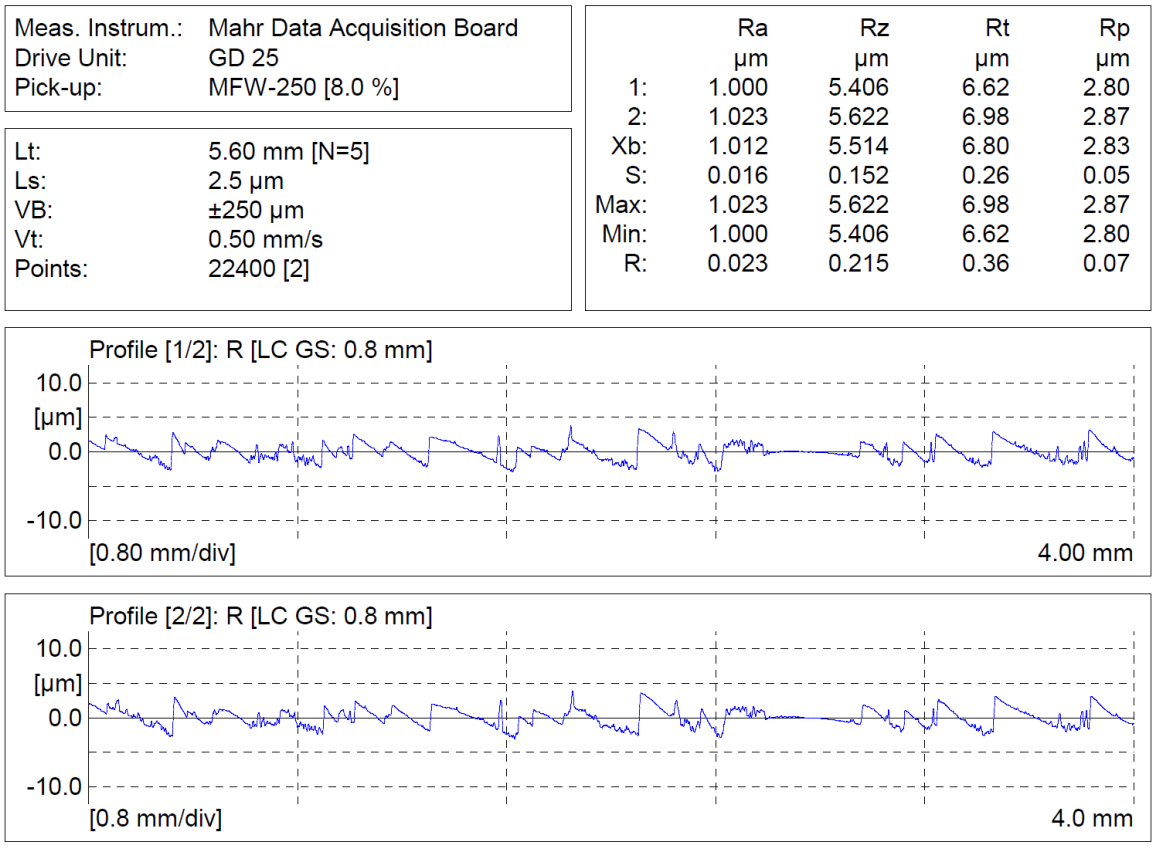

Figure A1. 84 Surface Profile of PCD Drilled Hole, Feedrate 508 mm/min, PCD Endmill Trimmed Edge (longitudinal) of Open Hole Tension Test Specimen # 4

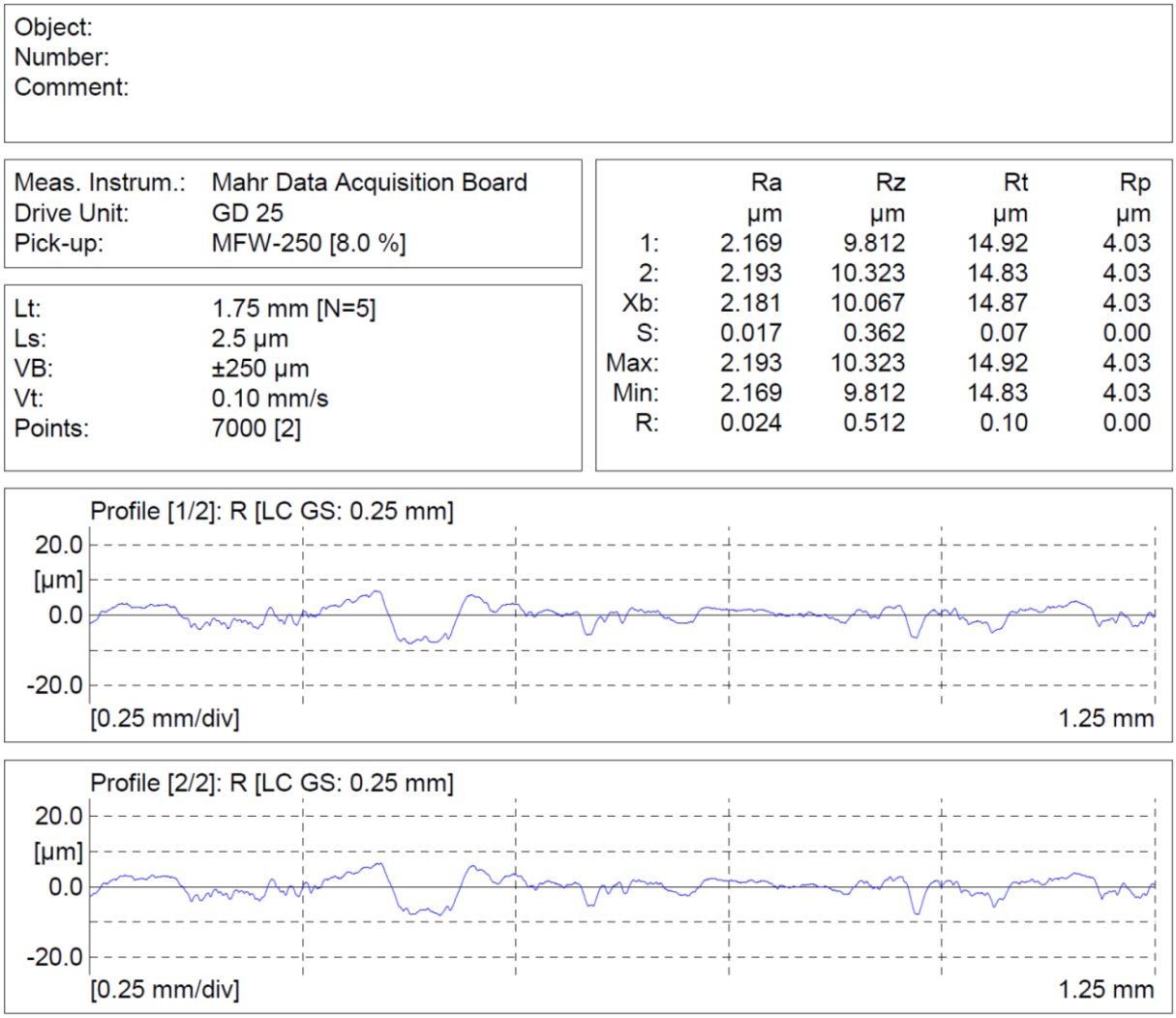

Figure A1.85 Surface Profile of PCD Drilled Hole, Feedrate 508 mm/min, PCD Endmill Trimmed Edge (transverse) of Open Hole Tension Test Specimen # 4

Appendix B

B1.1 Surface Profiles of Fatigue Testing Specimens as recorded by profilometer

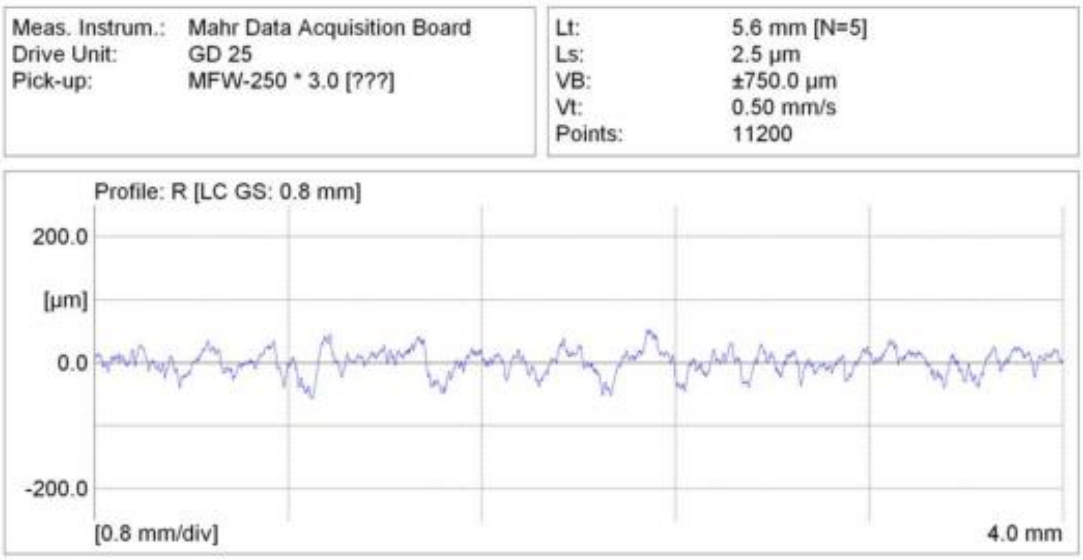

Figure B 1.53 Surface Profile (Longitudinal) of AWJ Trimmed Fatigue Test Specimen A1-H-1

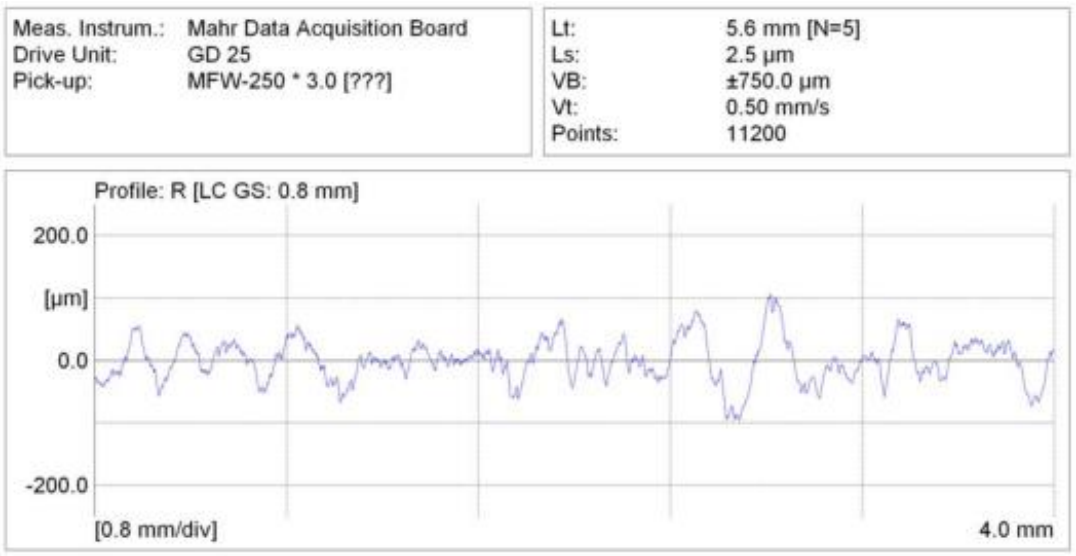

Figure B 1.54 Surface Profile (Longitudinal) of AWJ Trimmed Fatigue Test

Specimen A1-H-2

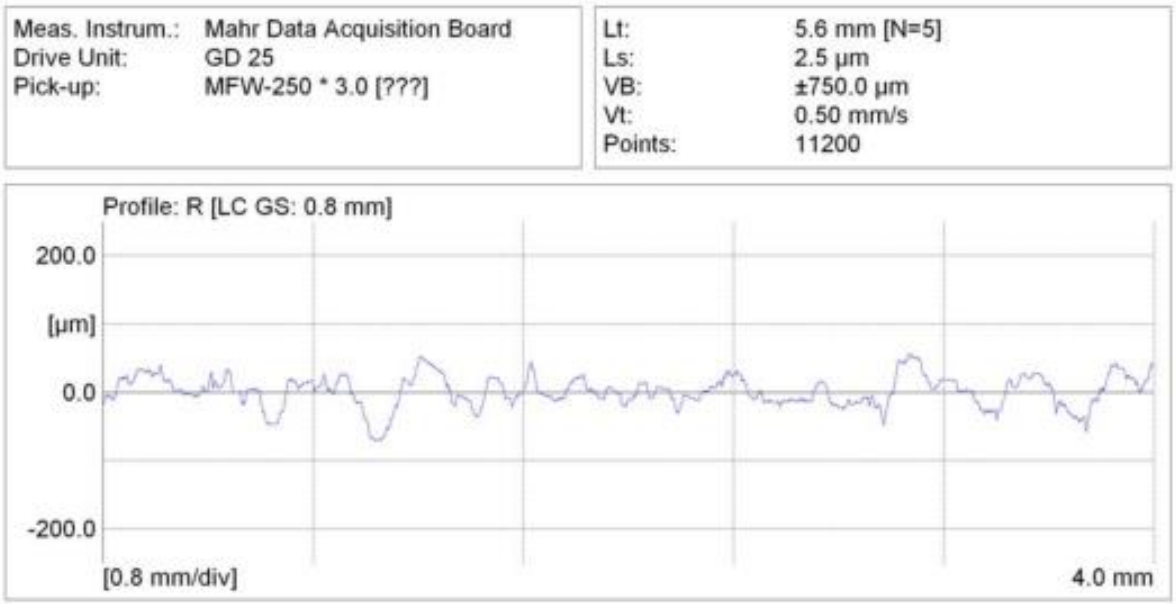

Figure B 1.55 Surface Profile (Longitudinal) of AWJ Trimmed Fatigue Test

Specimen A1-H-3

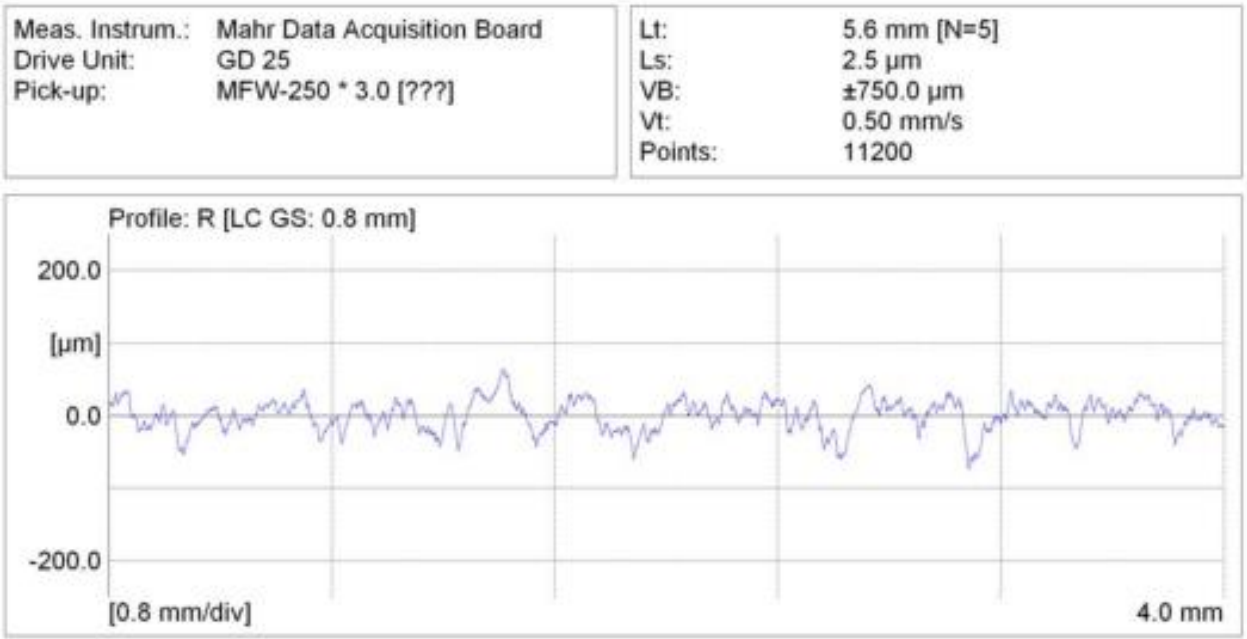

Figure B 1.56 Surface Profile (Longitudinal) of AWJ Trimmed Fatigue Test

Specimen A1-H-4

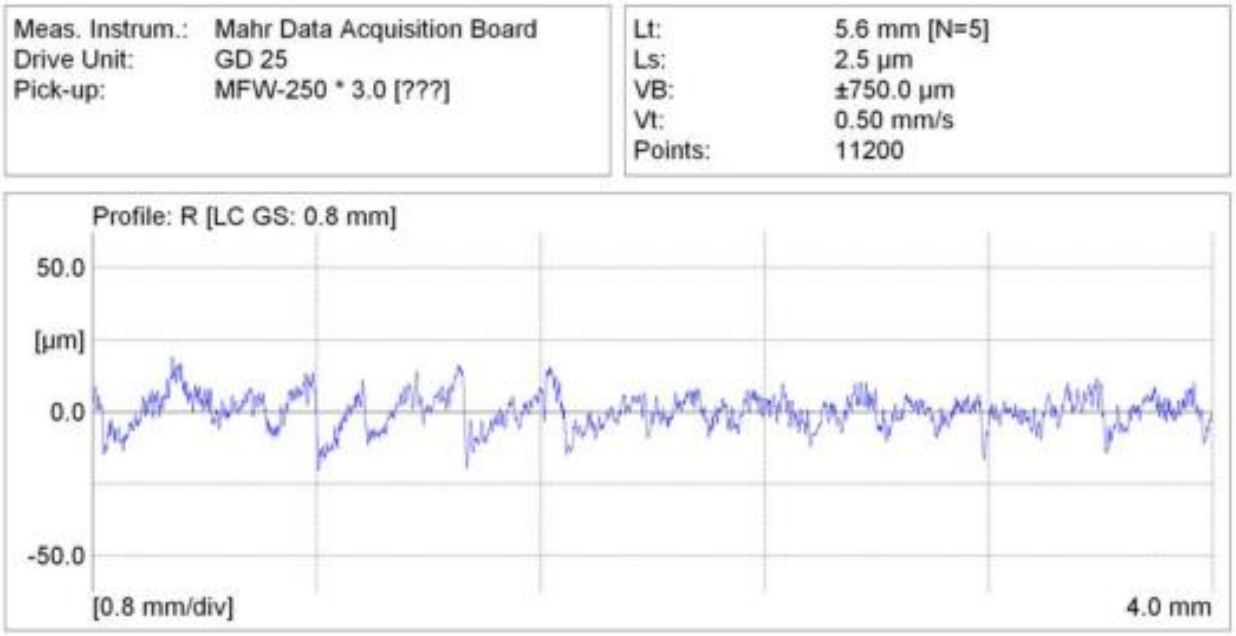

Figure B 1.57 Surface Profile (Longitudinal) of CVD Trimmed Fatigue Test

Specimen B1-H-1

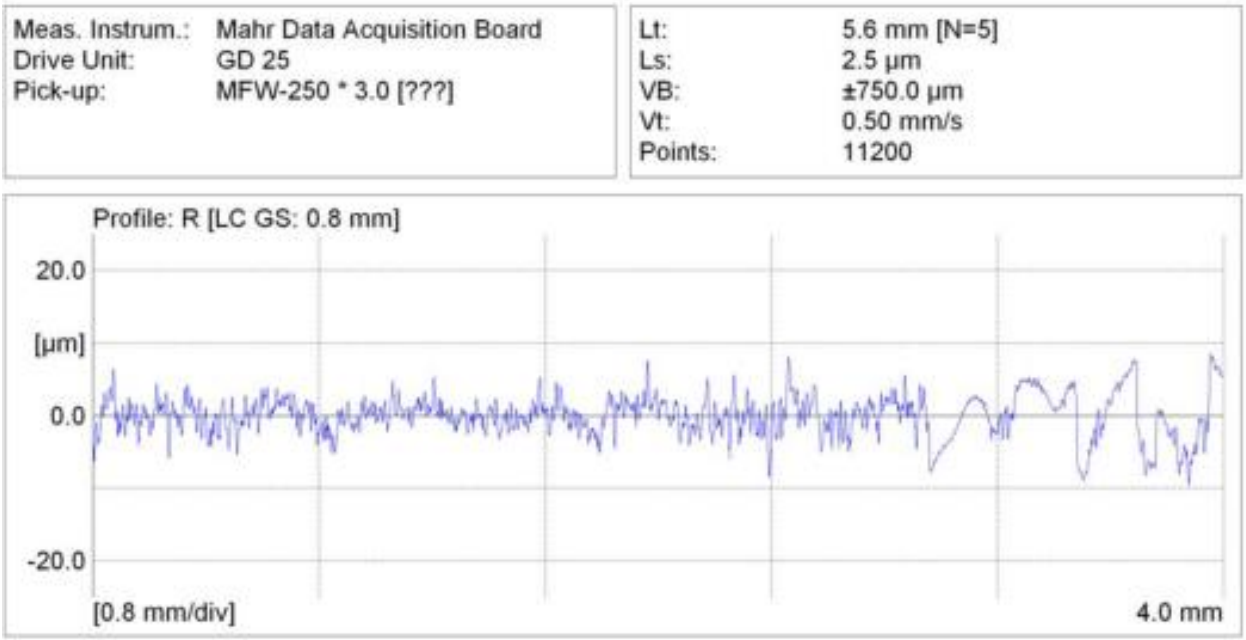

Figure B 1.58 Surface Profile (Longitudinal) of CVD Trimmed Fatigue Test

Specimen B1-H-2

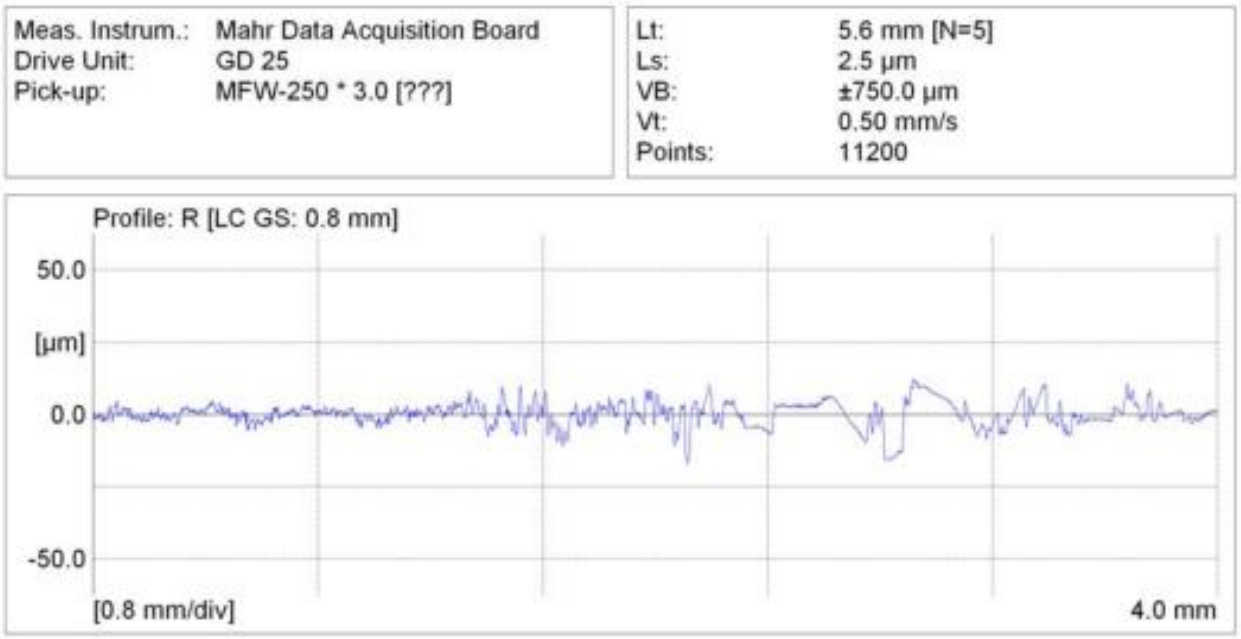

Figure B 1.59 Surface Profile (Longitudinal) of CVD Trimmed Fatigue Test

Specimen B1-H-3

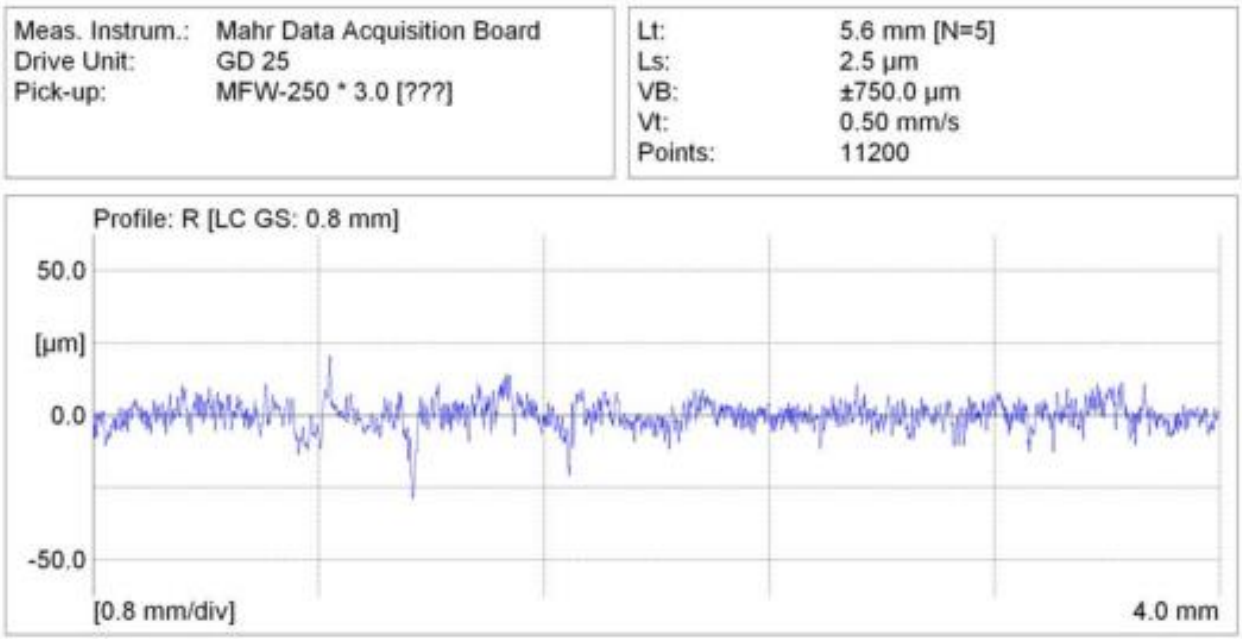

Figure B 1.60 Surface Profile (Longitudinal) of CVD Trimmed Fatigue Test

Specimen B1-H-4

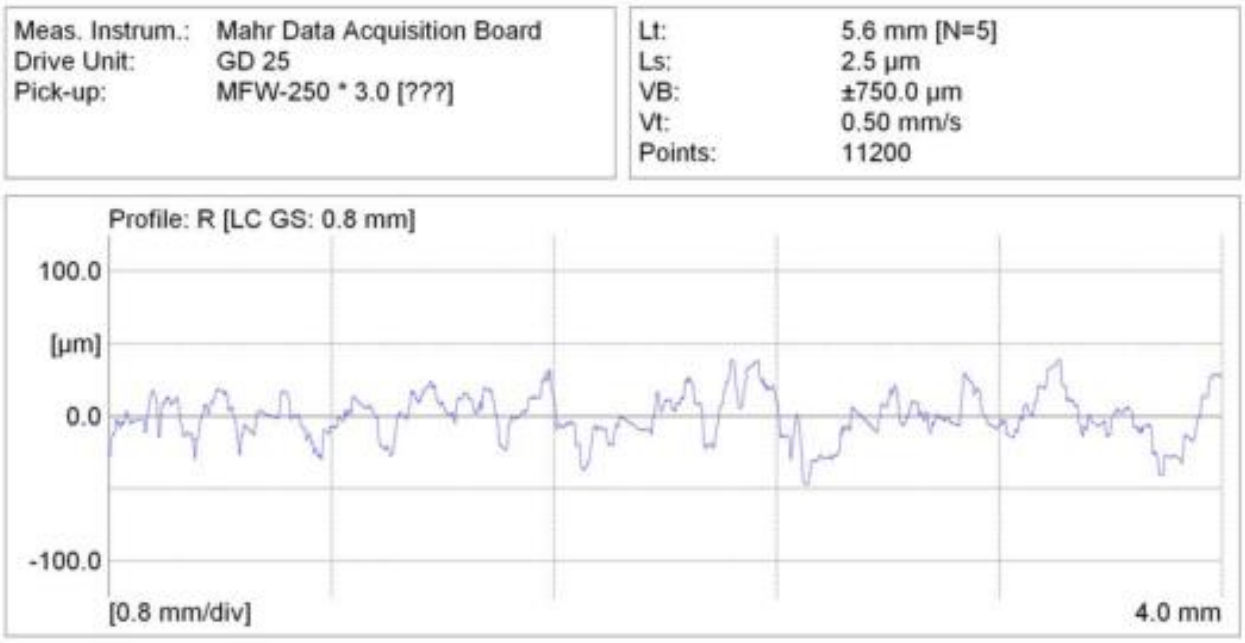

Figure B 1.61 Surface Profile (Longitudinal) of AWJ Trimmed Fatigue Test Specimen A1-M-1

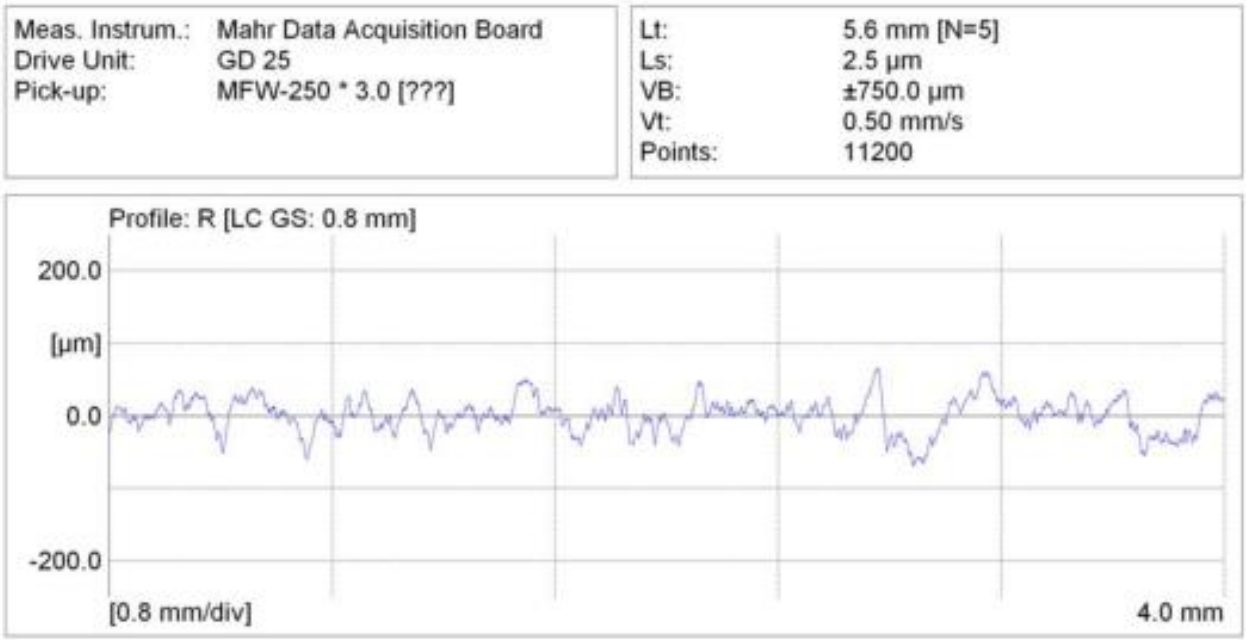

Figure B 1.62 Surface Profile (Longitudinal) of AWJ Trimmed Fatigue Test Specimen A1-M-2

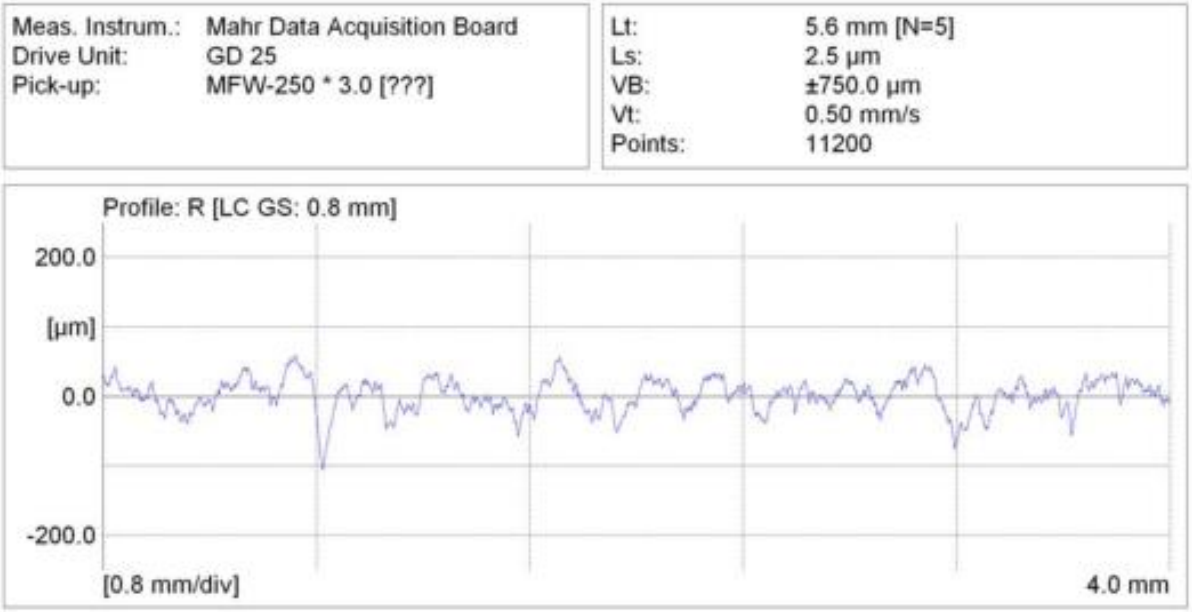

Figure B 1.63 Surface Profile (Longitudinal) of AWJ Trimmed Fatigue Test Specimen A1-M-3

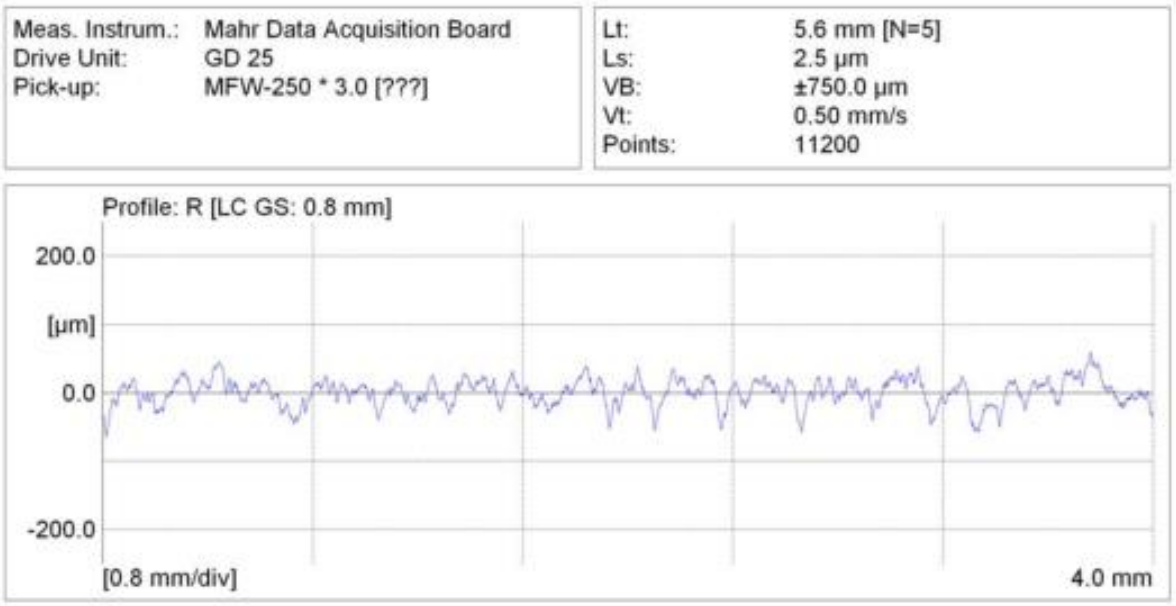

Figure B 1.64 Surface Profile (Longitudinal) of AWJ Trimmed Fatigue Test Specimen A1-M-4

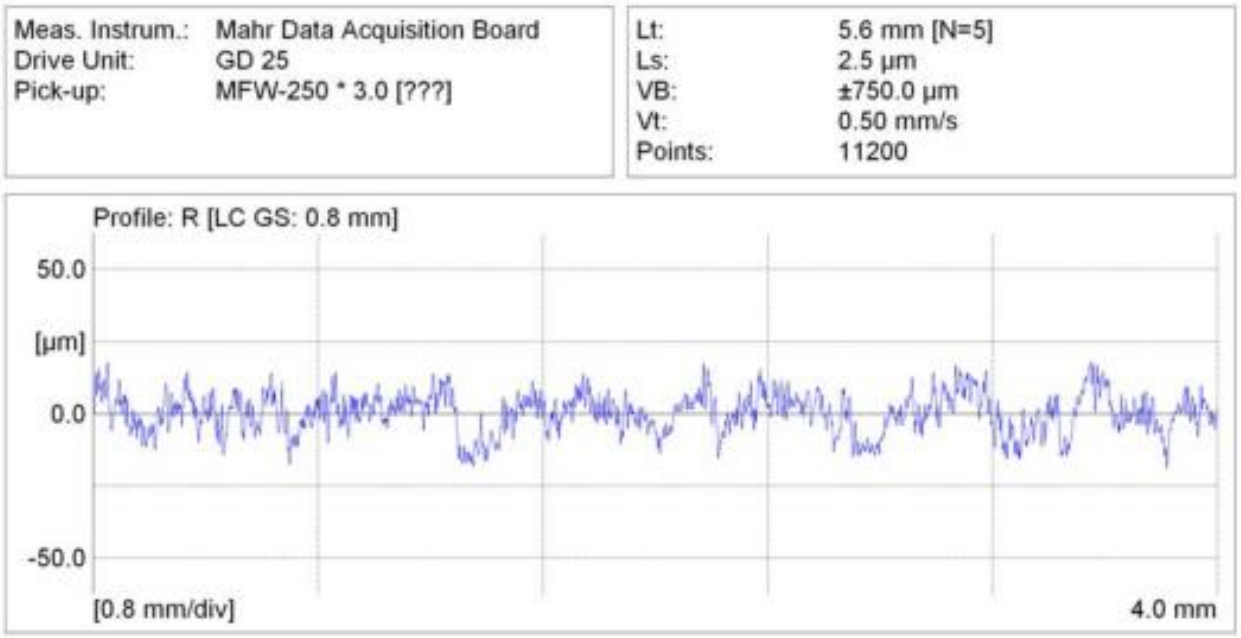

Figure B 1.65 Surface Profile (Longitudinal) of CVD Trimmed Fatigue Test Specimen B1-M-1

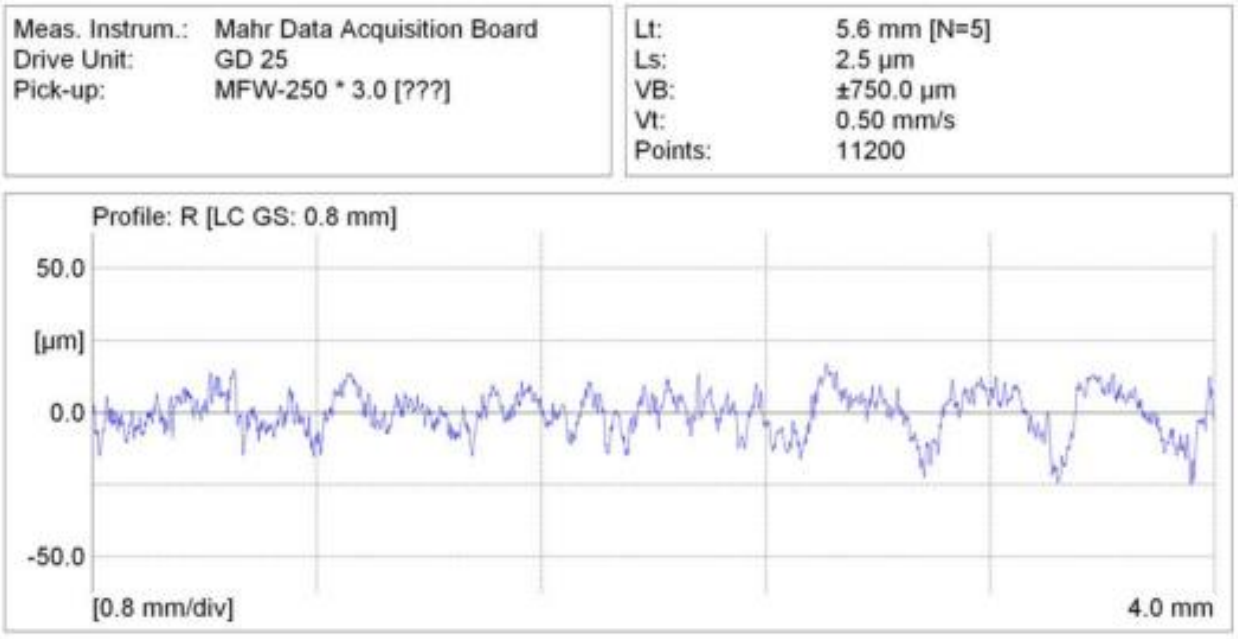

Figure B 1.66 Surface Profile (Longitudinal) of CVD Trimmed Fatigue Test Specimen B1-M-2

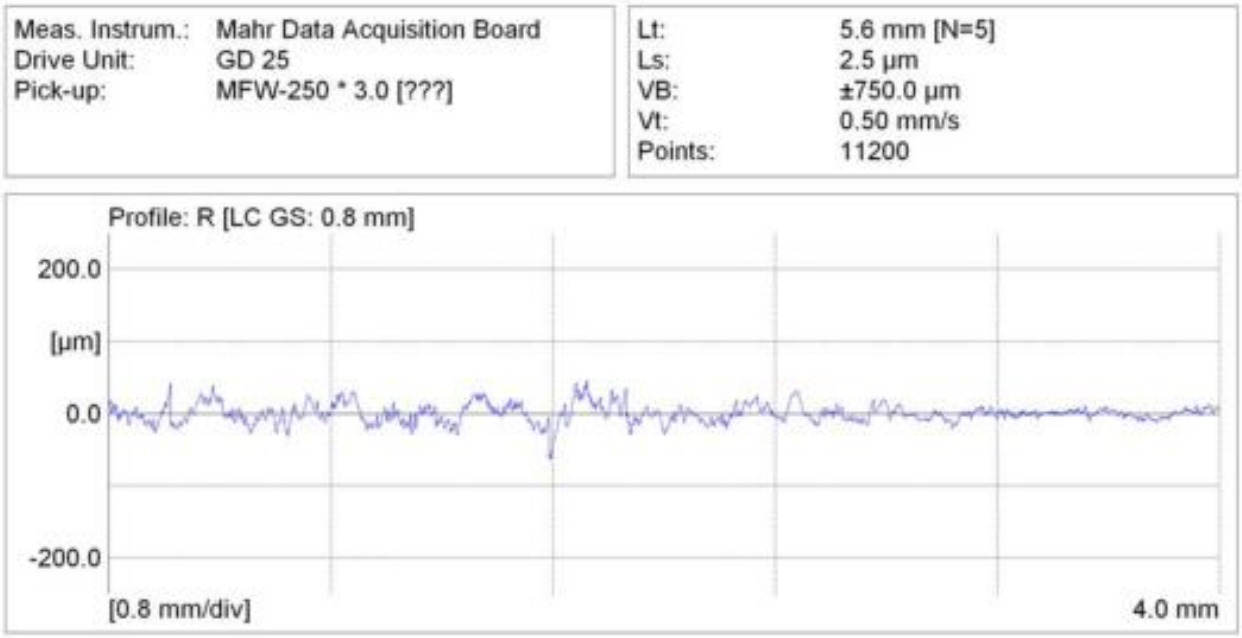

Figure B 1.67 Surface Profile (Longitudinal) of CVD Trimmed Fatigue Test Specimen B1-M-3

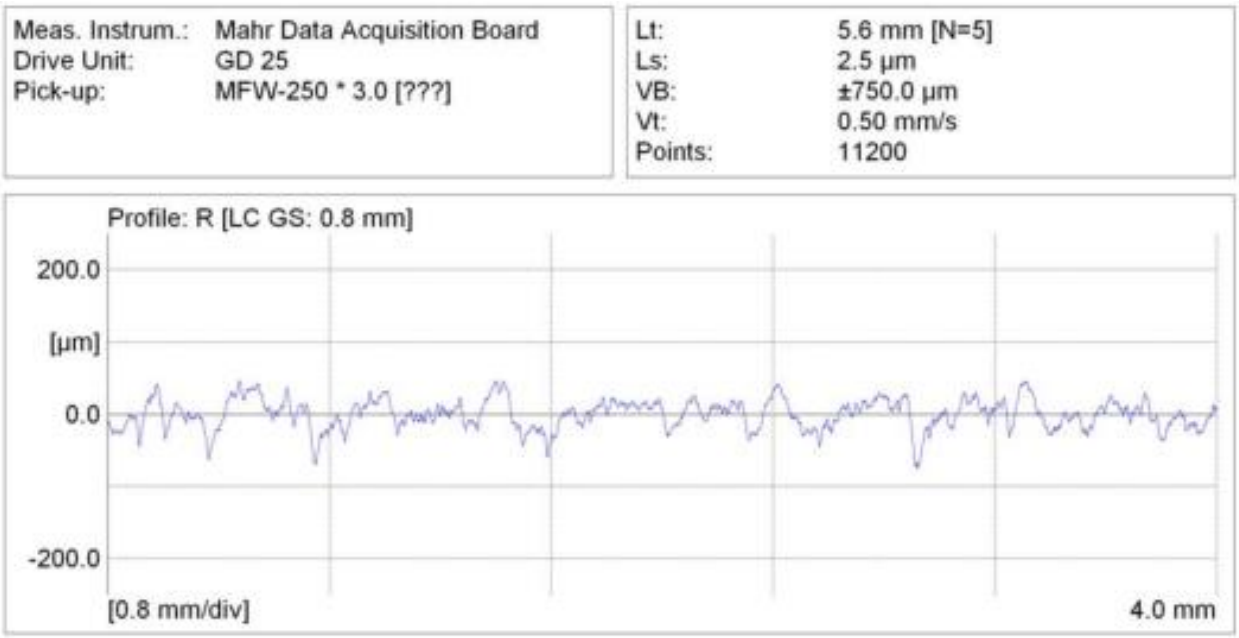

Figure B 1.16 Surface Profile (Longitudinal) of CVD Trimmed Fatigue Test Specimen B1-M-4

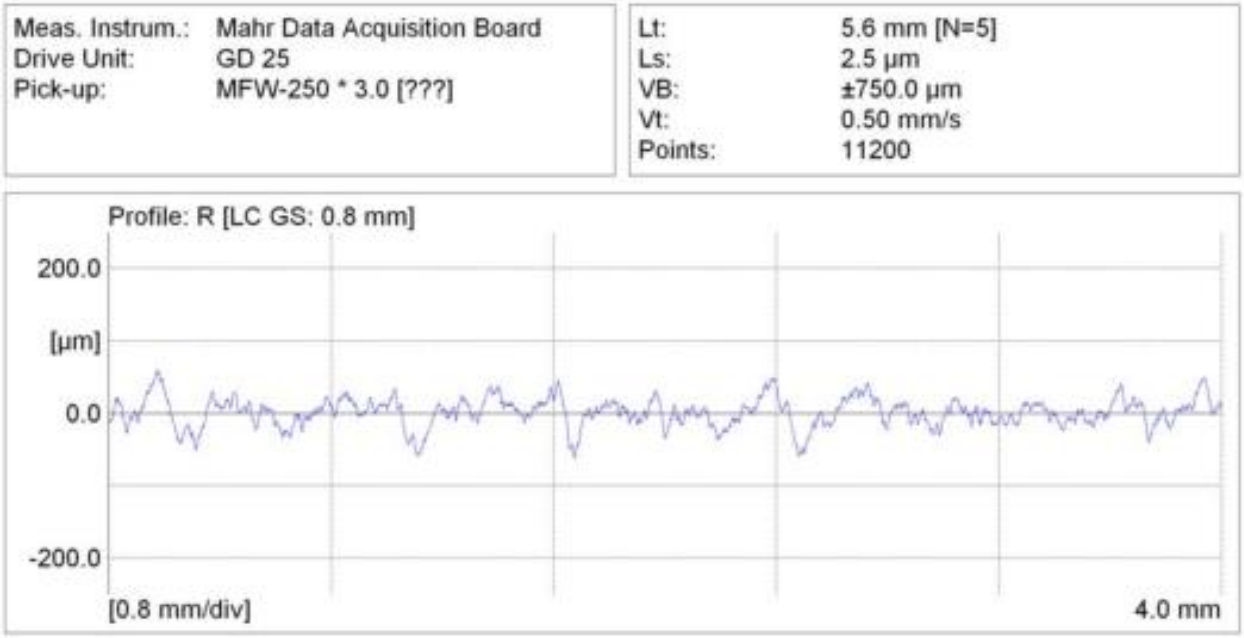

Figure B 1.68 Surface Profile (Longitudinal) of AWJ Trimmed Fatigue Test Specimen A1-L-1

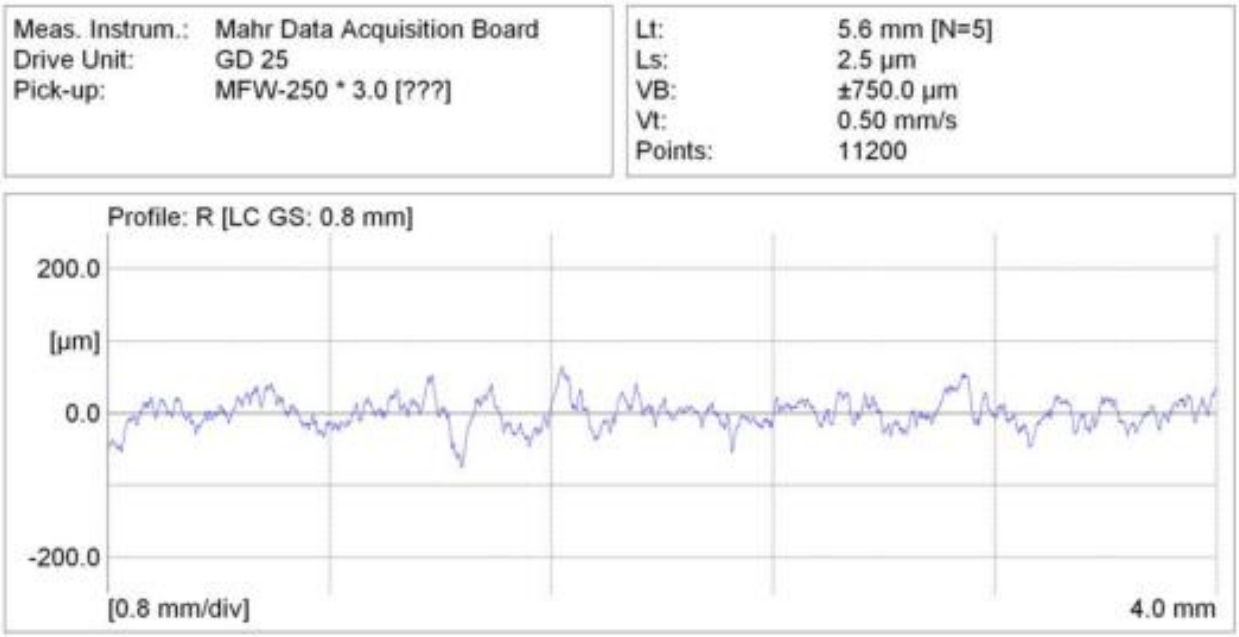

Figure B 1.69 Surface Profile (Longitudinal) of AWJ Trimmed Fatigue Test Specimen A1-L-2

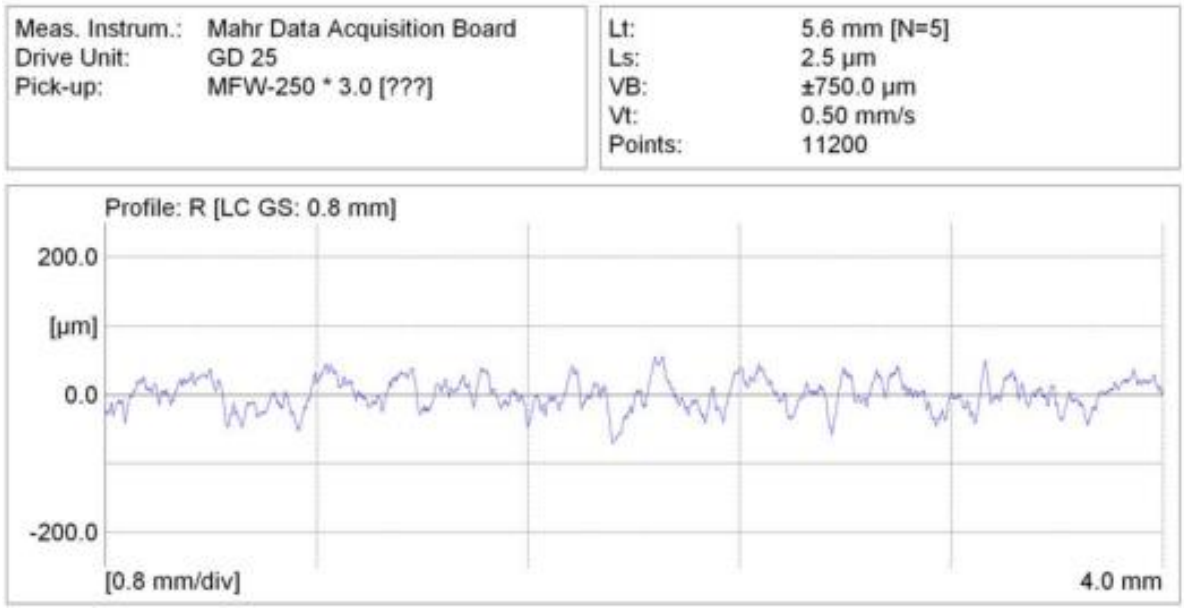

Figure B 1.70 Surface Profile (Longitudinal) of AWJ Trimmed Fatigue Test Specimen A1-L-3

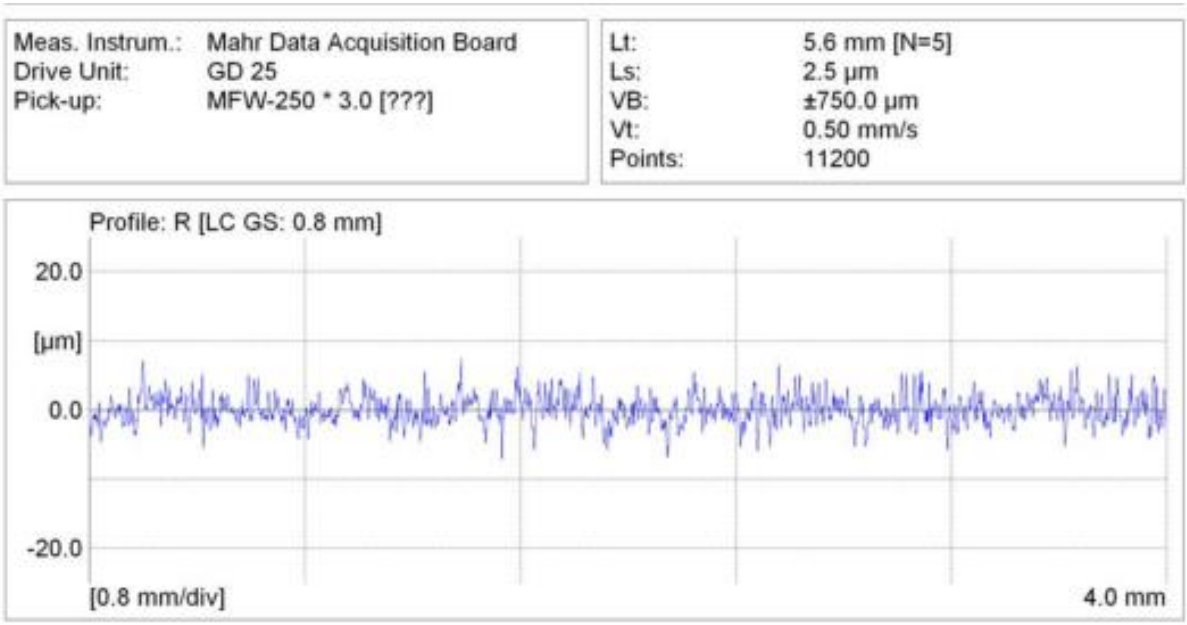

Figure B 1.71 Surface Profile (Longitudinal) of CVD Trimmed Fatigue Test Specimen B1-L-1

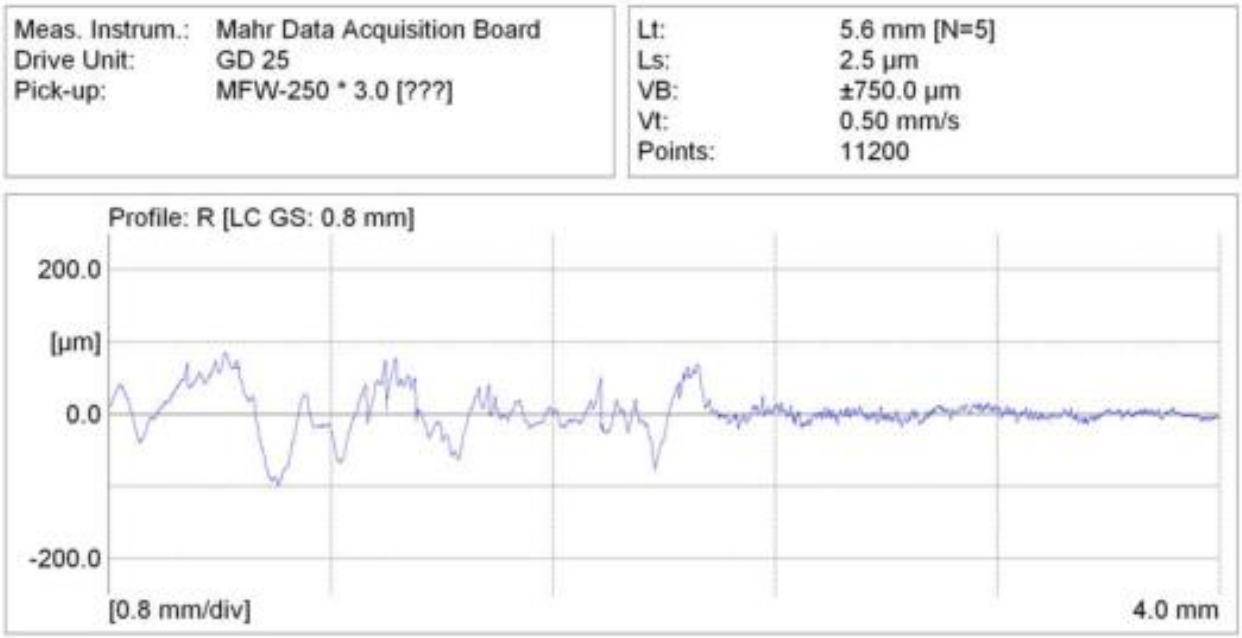

Figure B 1.72 Surface Profile (Longitudinal) of CVD Trimmed Fatigue Test Specimen B1-L-2

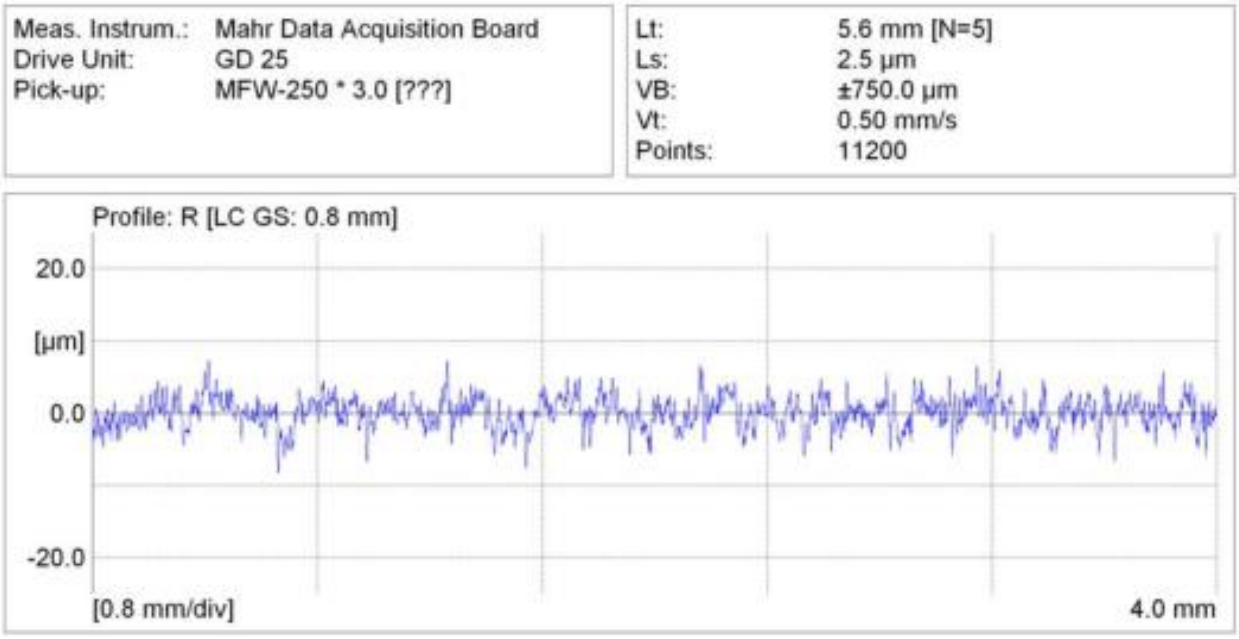

Figure B 1.73 Surface Profile (Longitudinal) of CVD Trimmed Fatigue Test Specimen B1-L-3

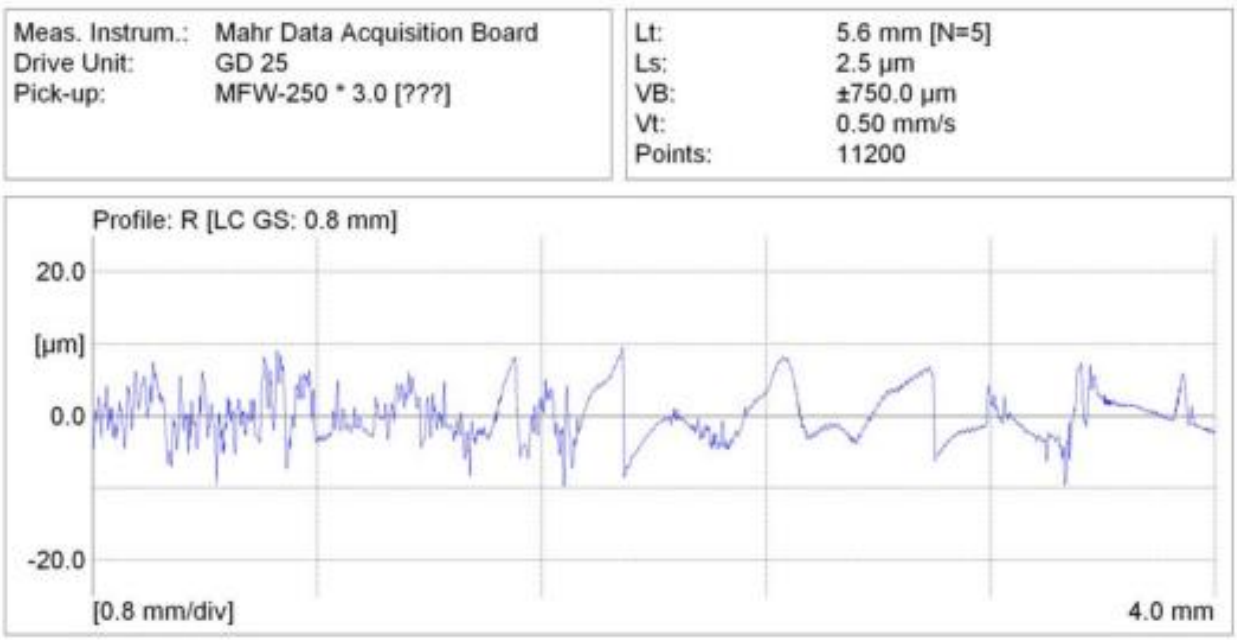

Figure B 1.74 Surface Profile (Longitudinal) of CVD Trimmed Fatigue Test Specimen B1-L-4

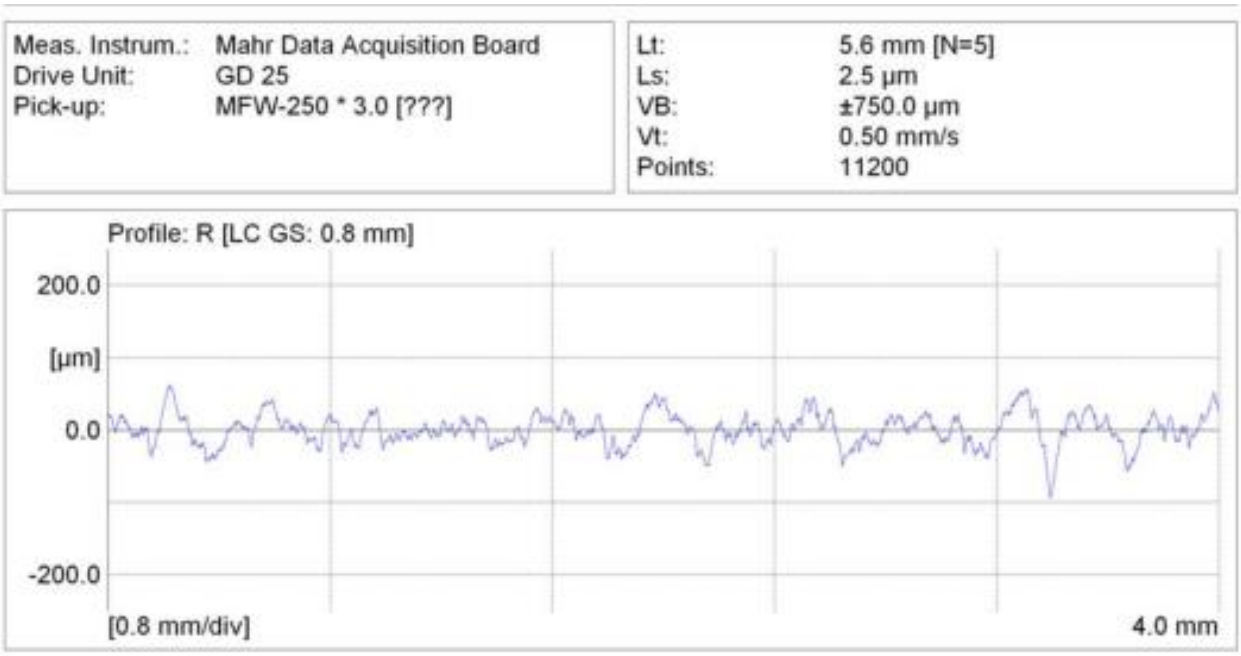

Figure B 1.75 Surface Profile (Longitudinal) of AWJ Trimmed Fatigue Test Specimen A2-H-1

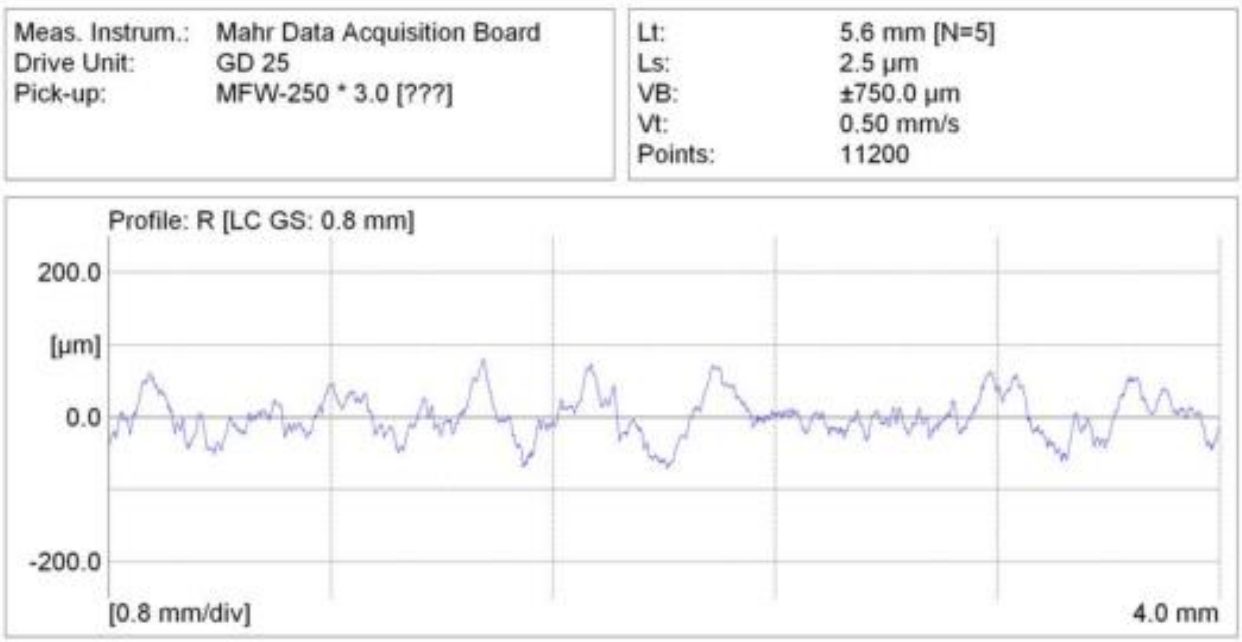

Figure B 1.76 Surface Profile (Longitudinal) of AWJ Trimmed Fatigue Test Specimen A2-H-2

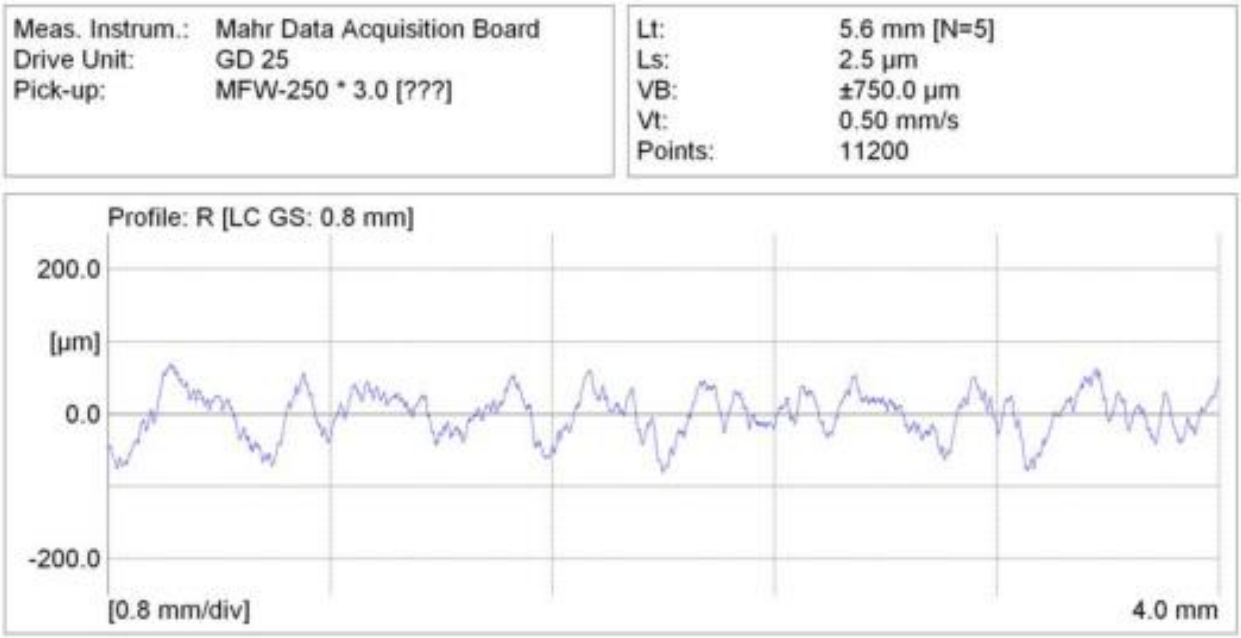

Figure B 1.77 Surface Profile (Longitudinal) of AWJ Trimmed Fatigue Test Specimen A2-H-3

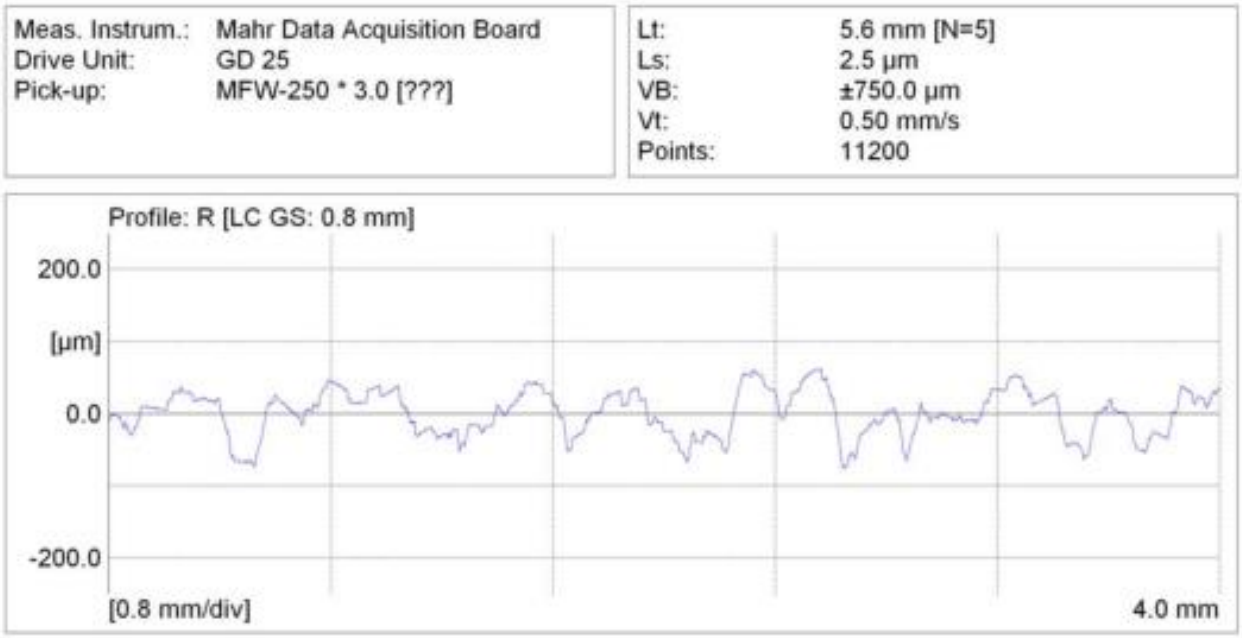

Figure B 1.78 Surface Profile (Longitudinal) of AWJ Trimmed Fatigue Test Specimen A2-H-4

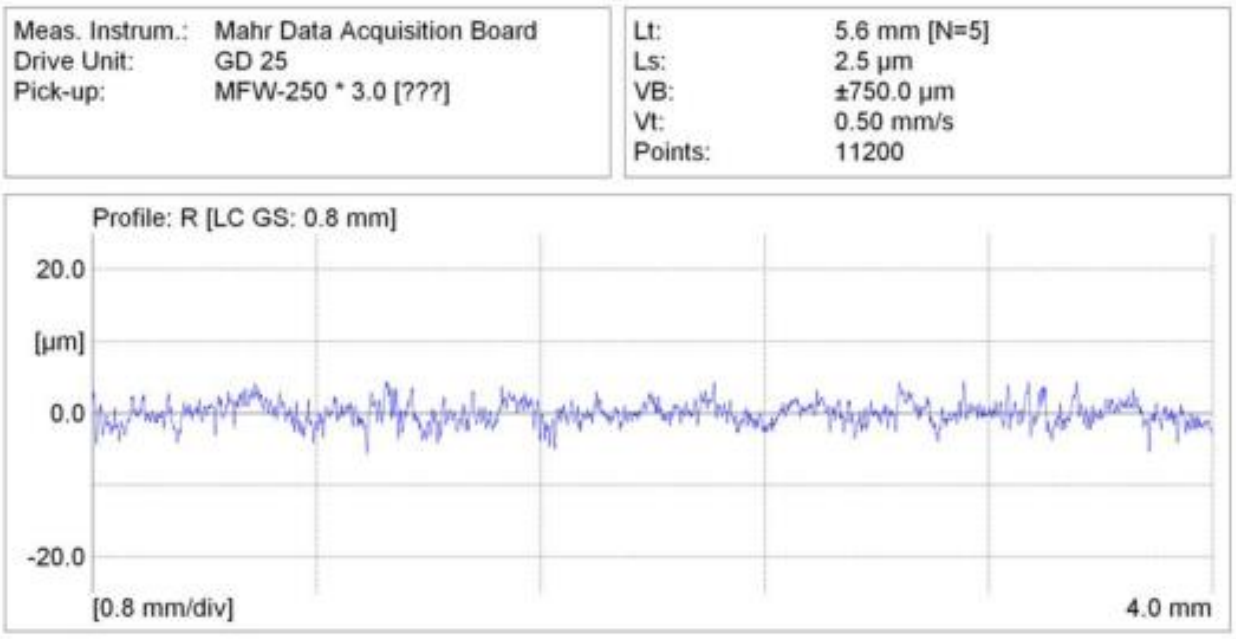

Figure B 1.79 Surface Profile (Longitudinal) of CVD Trimmed Fatigue Test Specimen B2-H-1

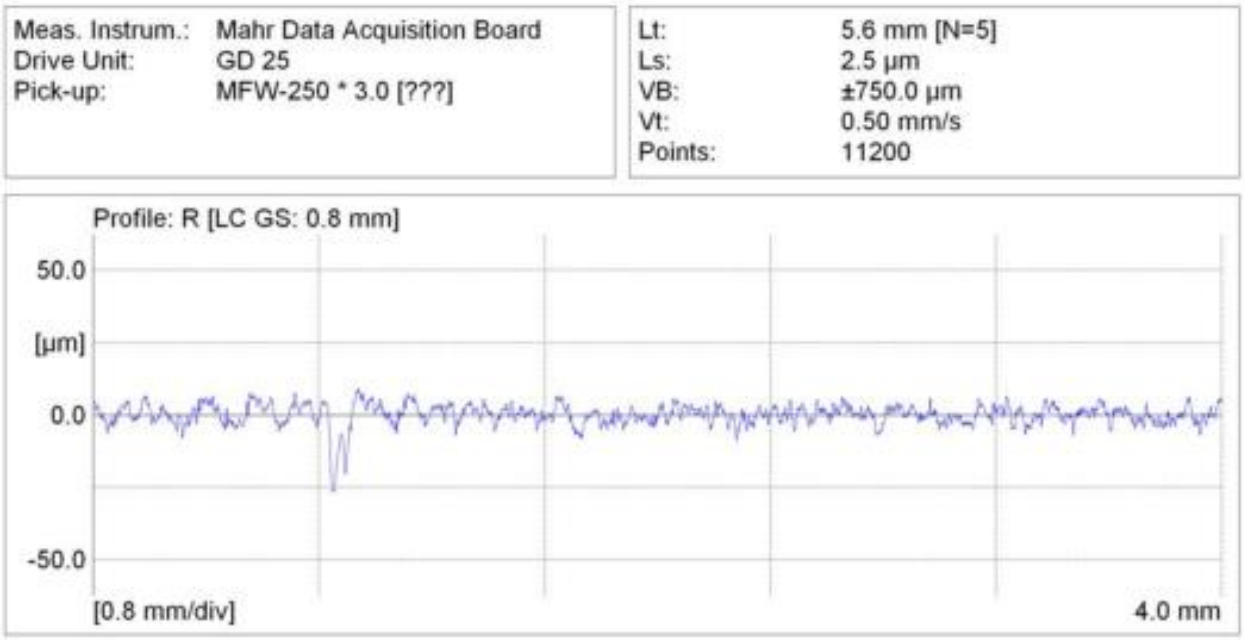

Figure B 1.80 Surface Profile (Longitudinal) of CVD Trimmed Fatigue Test Specimen B2-H-2

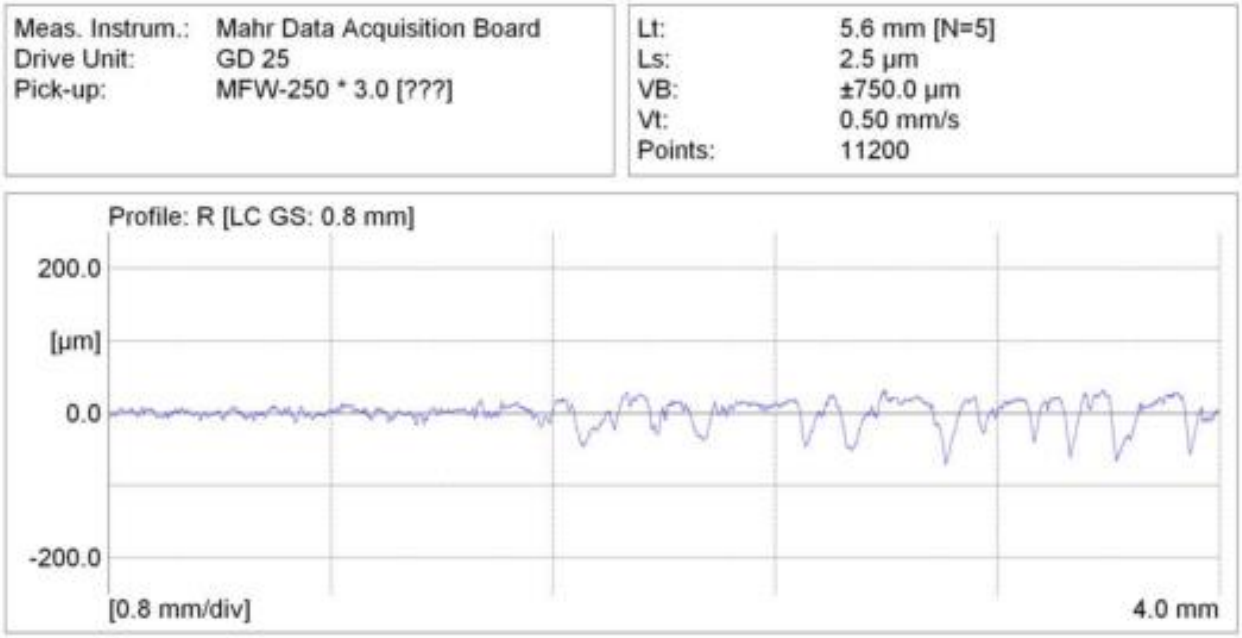

Figure B 1.81 Surface Profile (Longitudinal) of CVD Trimmed Fatigue Test Specimen B2-H-3

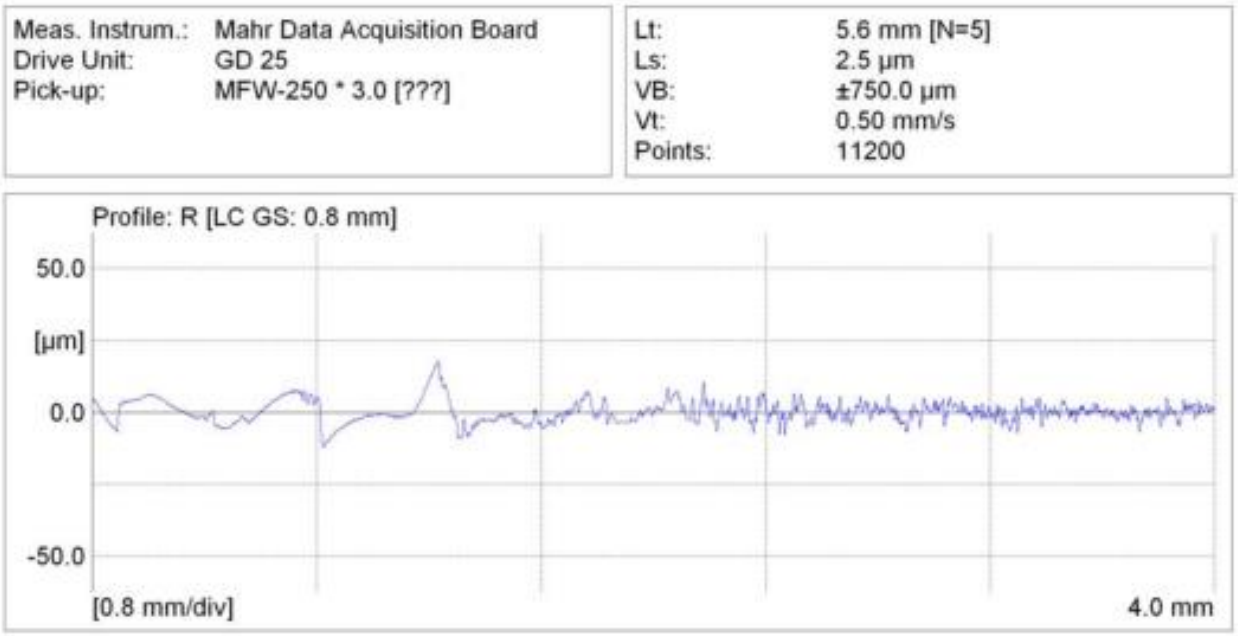

Figure B 1.82 Surface Profile (Longitudinal) of CVD Trimmed Fatigue Test Specimen B2-H-4

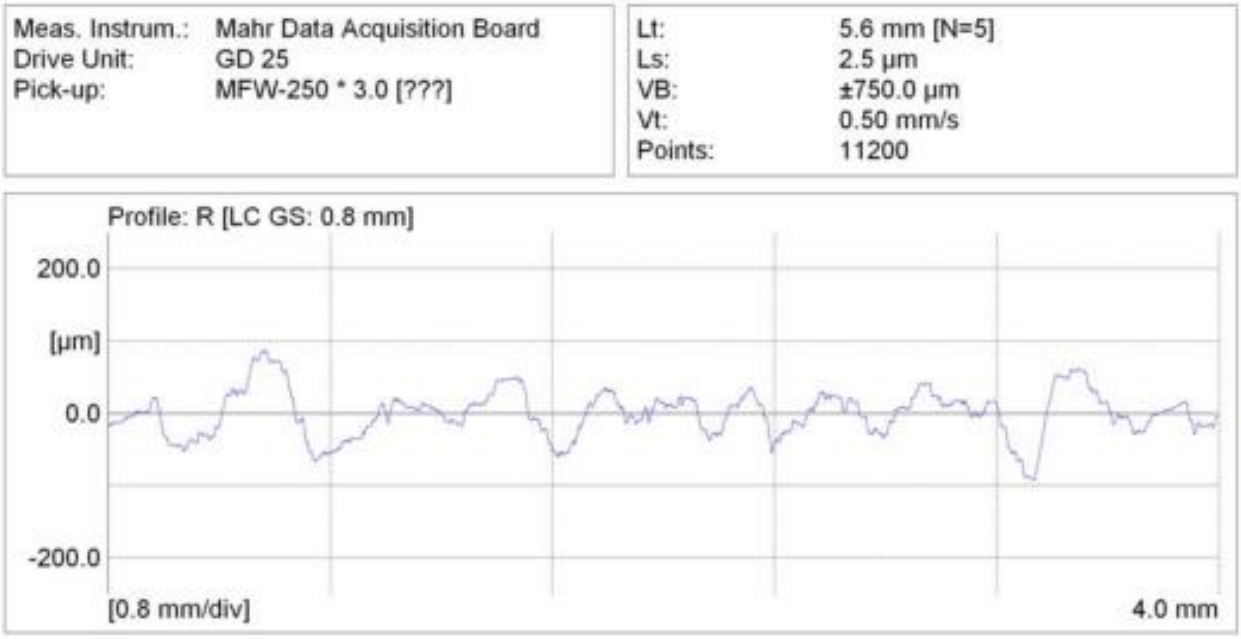

Figure B 1.83 Surface Profile (Longitudinal) of AWJ Trimmed Fatigue Test Specimen A2-M-1

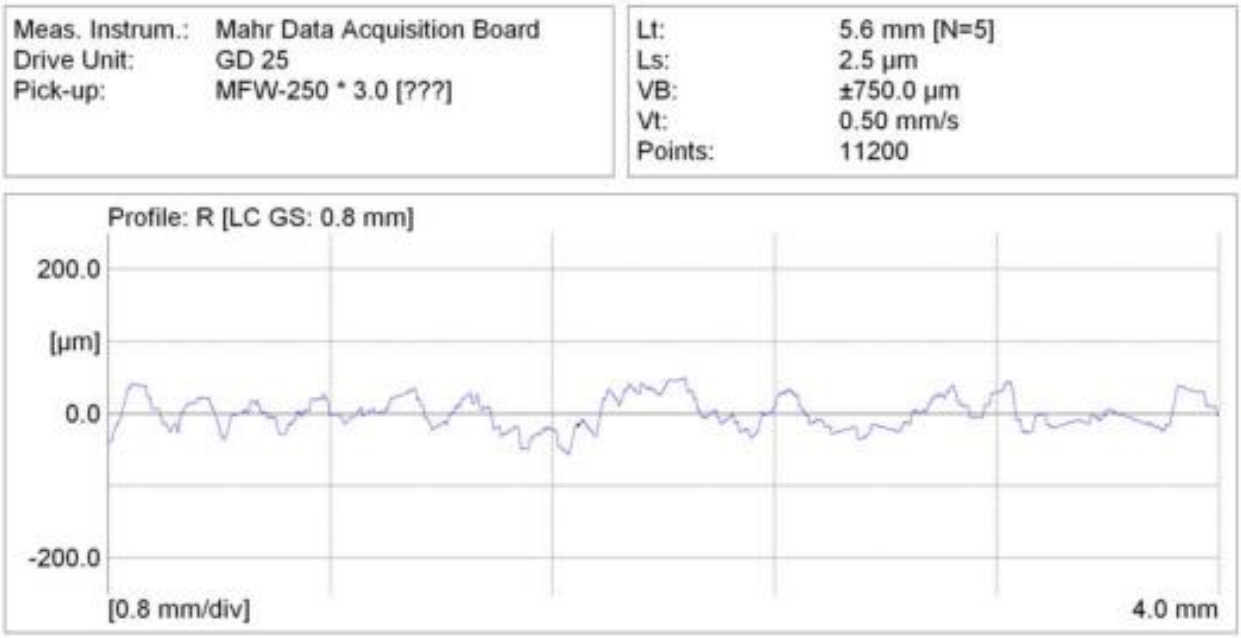

Figure B 1.84 Surface Profile (Longitudinal) of AWJ Trimmed Fatigue Test Specimen A2-M-2

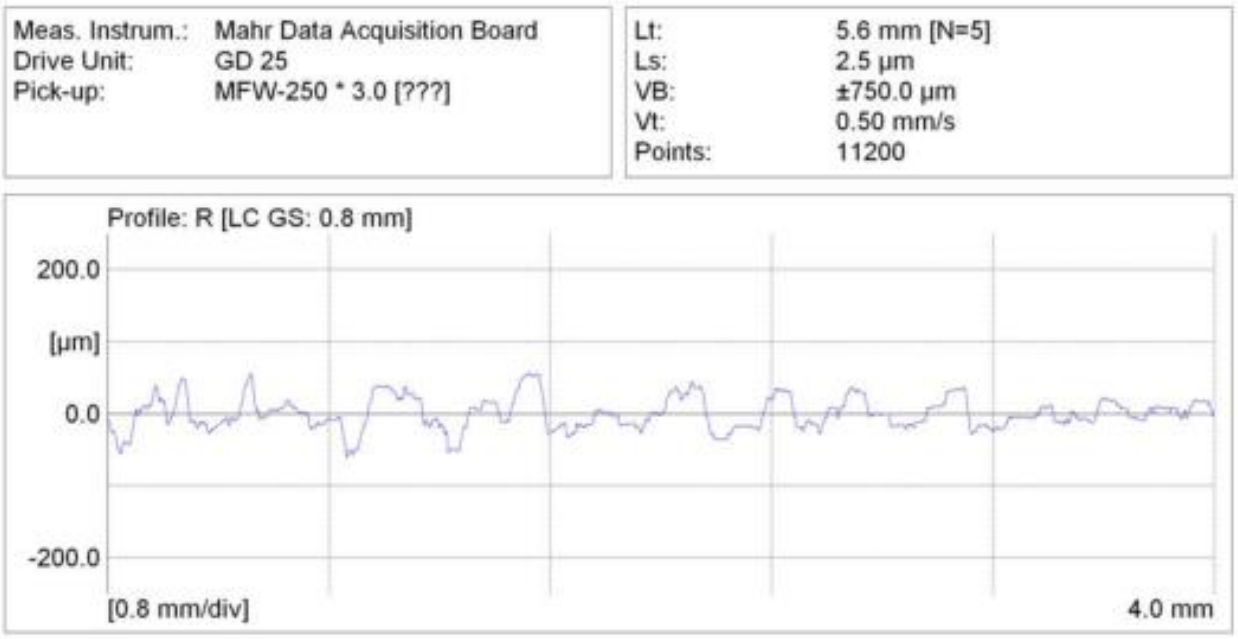

Figure B 1.85 Surface Profile (Longitudinal) of AWJ Trimmed Fatigue Test Specimen A2-M-3

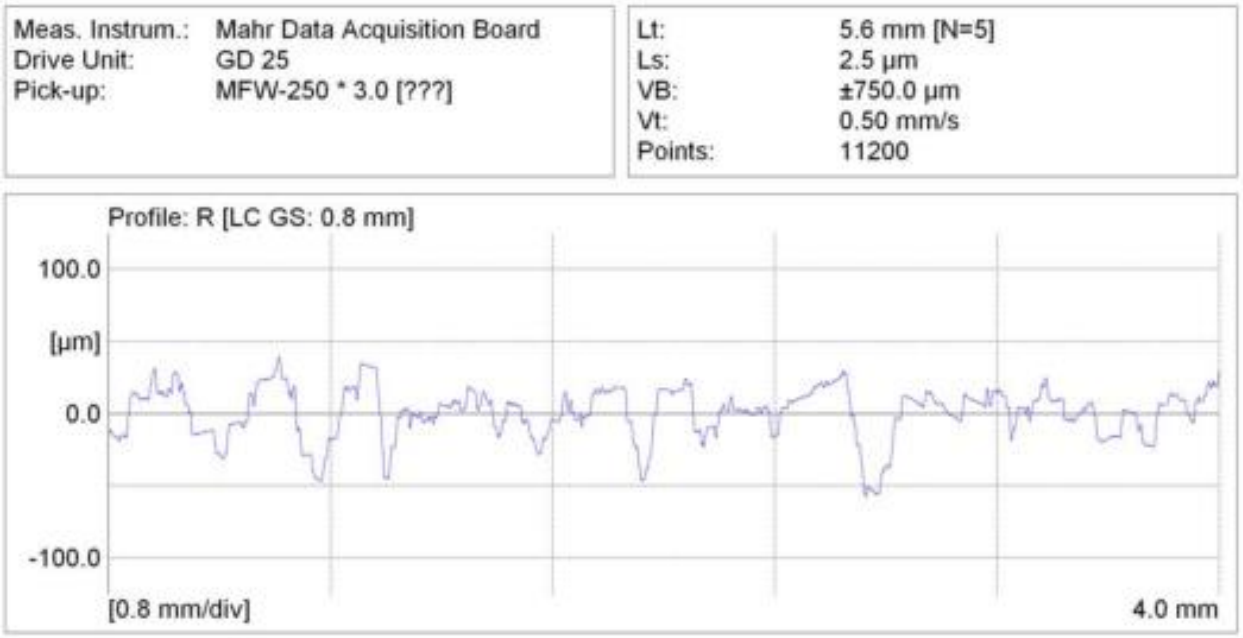

Figure B 1.86 Surface Profile (Longitudinal) of AWJ Trimmed Fatigue Test Specimen A2-M-4

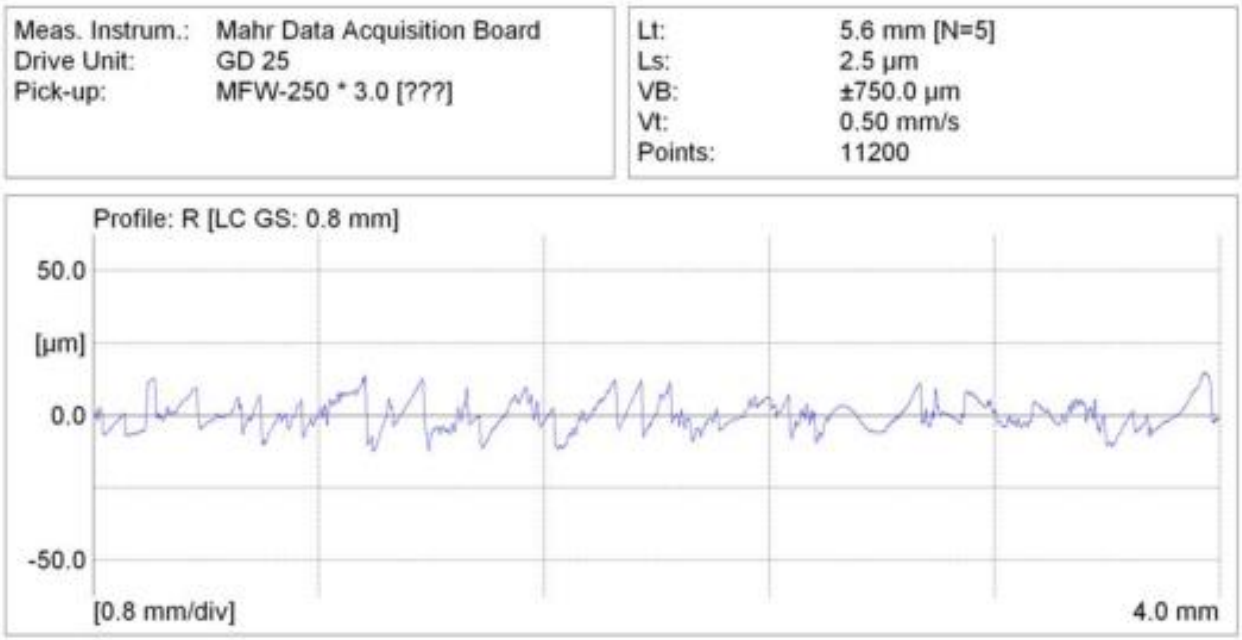

Figure B 1.87 Surface Profile (Longitudinal) of CVD Trimmed Fatigue Test Specimen B2-M-1

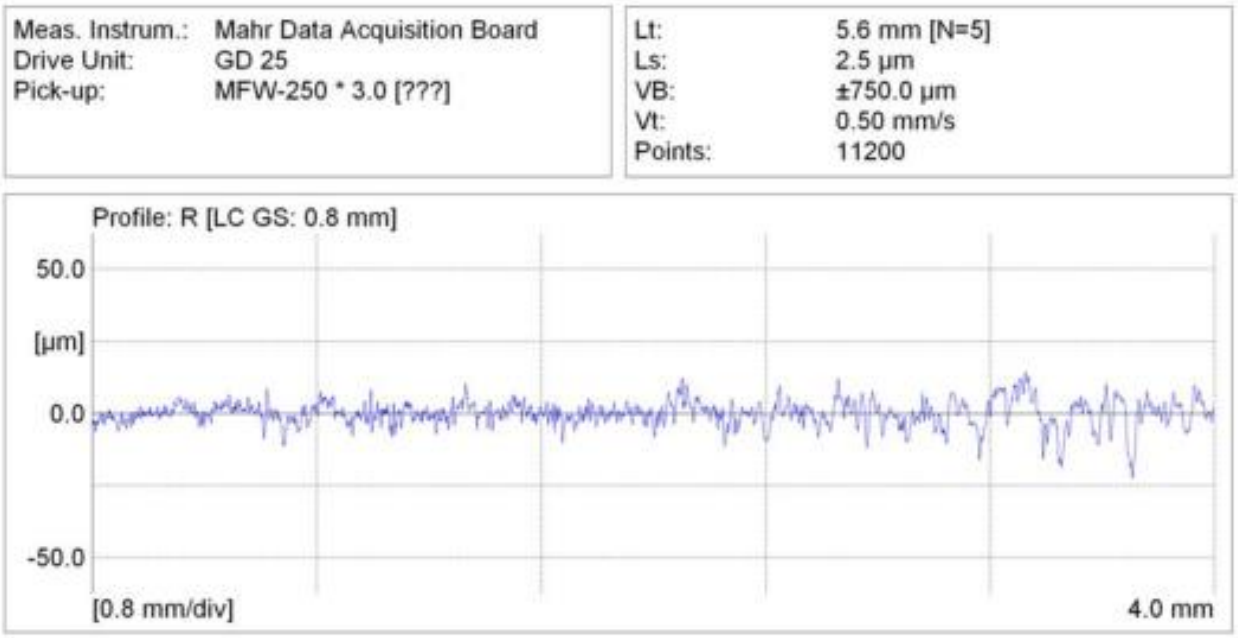

Figure B 1.88 Surface Profile (Longitudinal) of CVD Trimmed Fatigue Test Specimen B2-M-2

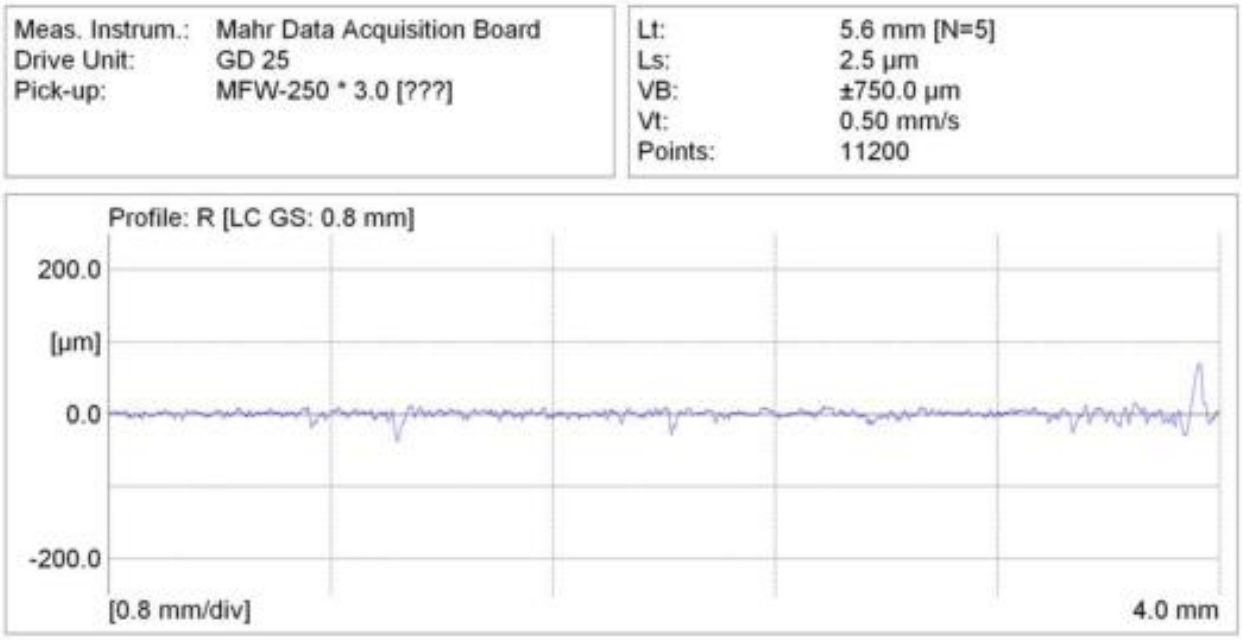

Figure B 1.89 Surface Profile (Longitudinal) of CVD Trimmed Fatigue Test Specimen B2-M-3

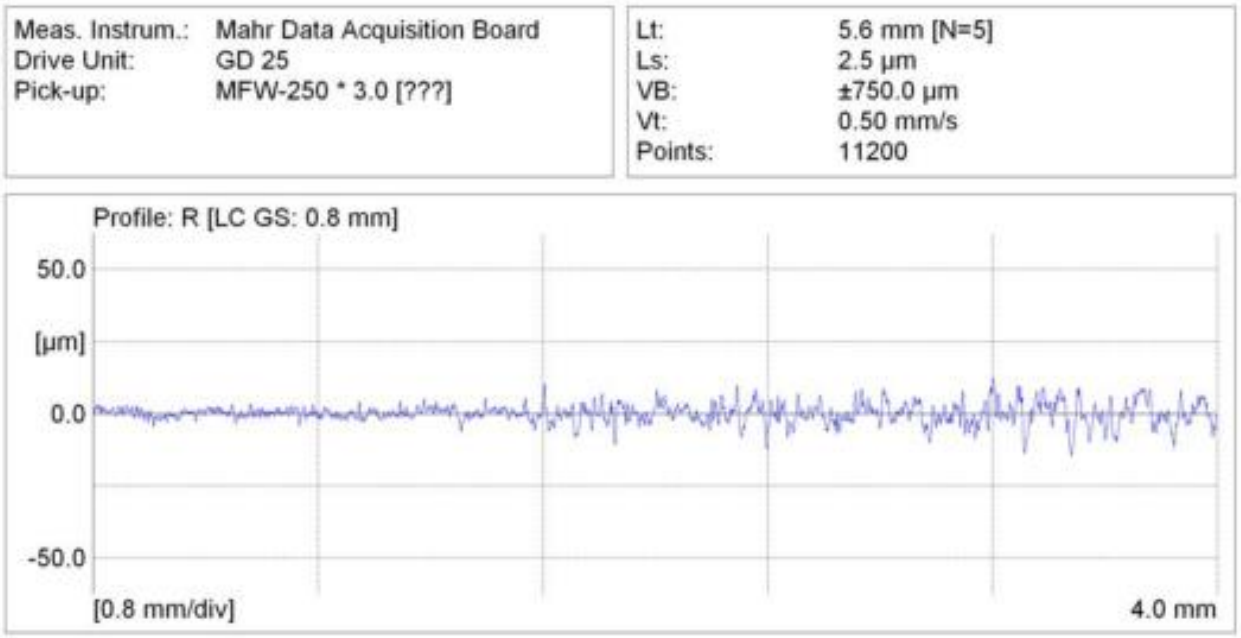

Figure B 1.90 Surface Profile (Longitudinal) of CVD Trimmed Fatigue Test Specimen B2-M-4

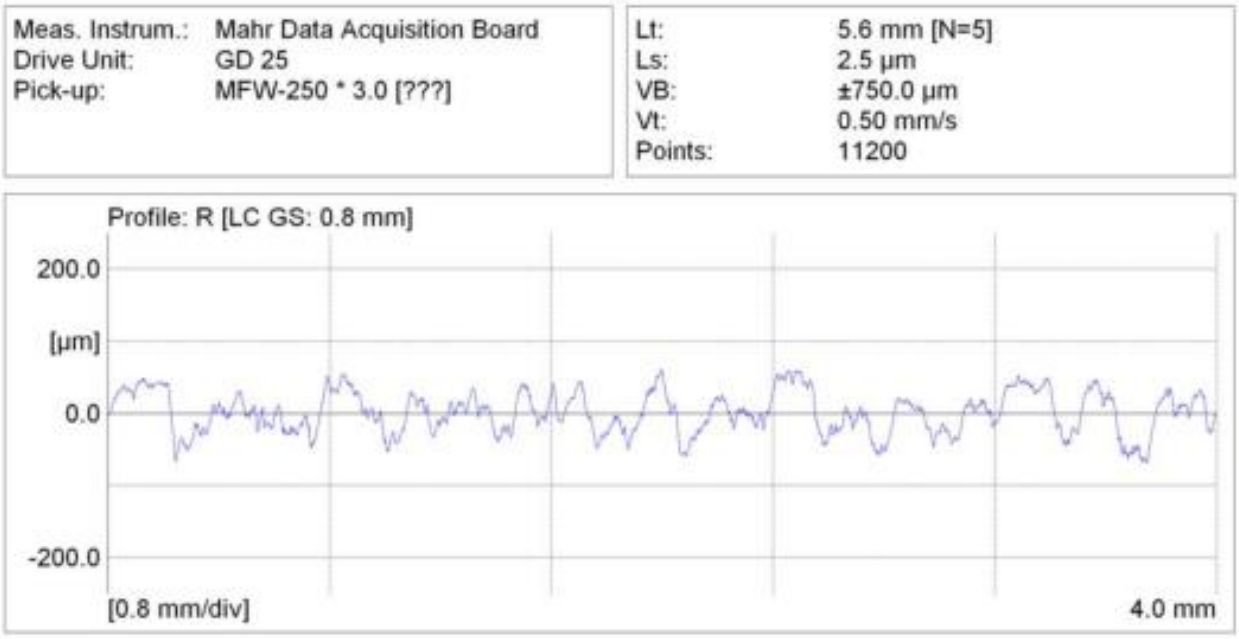

Figure B 1.91 Surface Profile (Longitudinal) of AWJ Trimmed Fatigue Test Specimen A2-L-1

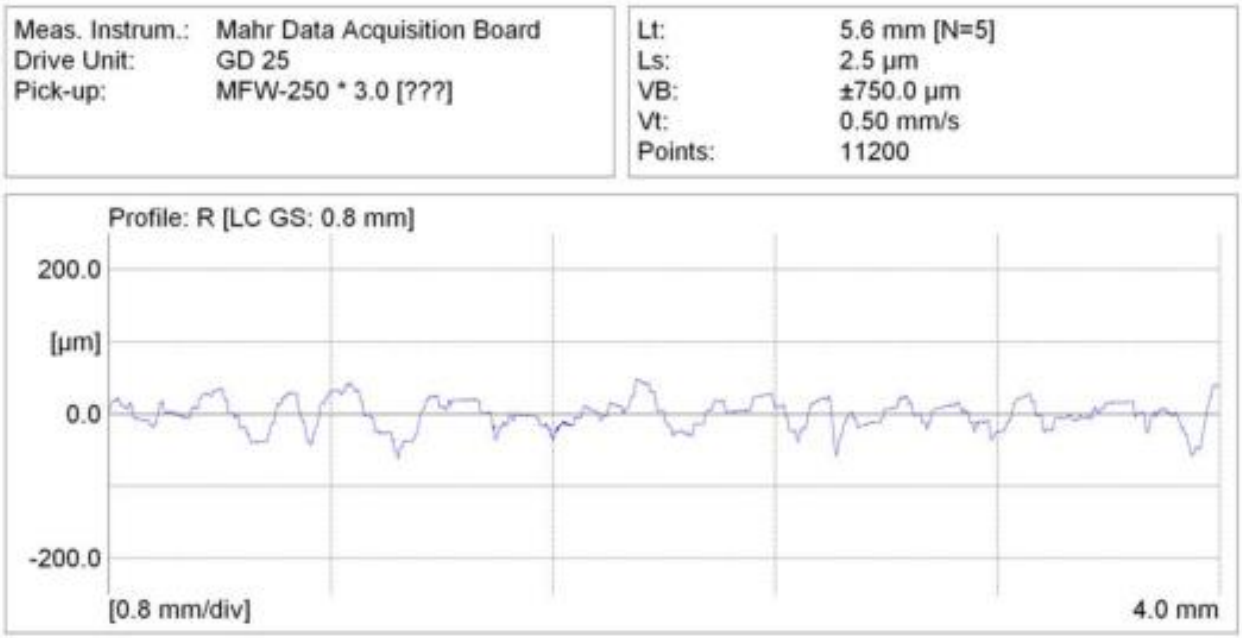

Figure B 1.92 Surface Profile (Longitudinal) of AWJ Trimmed Fatigue Test Specimen A2-L-2

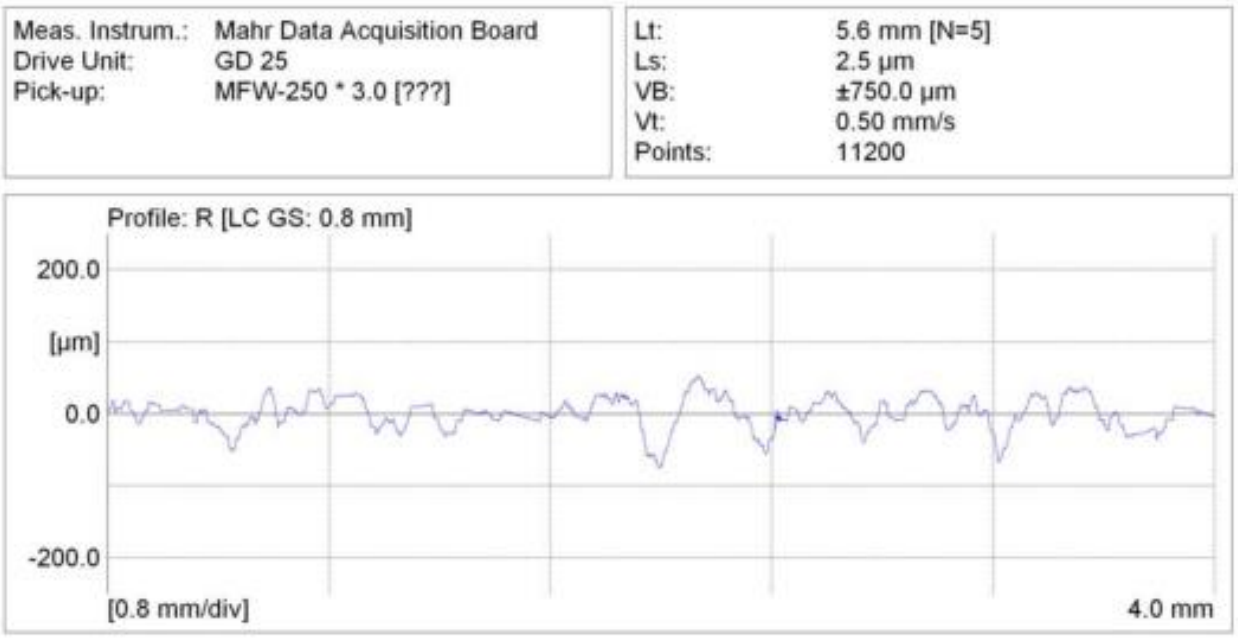

Figure B 1.93 Surface Profile (Longitudinal) of AWJ Trimmed Fatigue Test Specimen A2-L-3

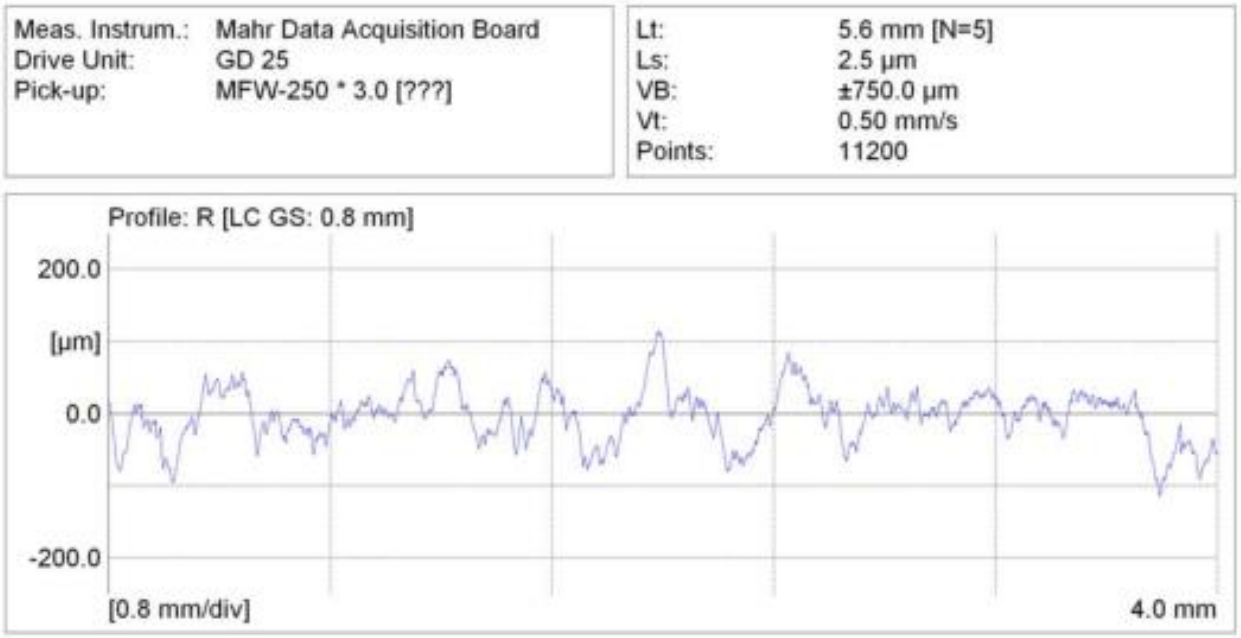

Figure B 1.94 Surface Profile (Longitudinal) of AWJ Trimmed Fatigue Test Specimen A2-L-4

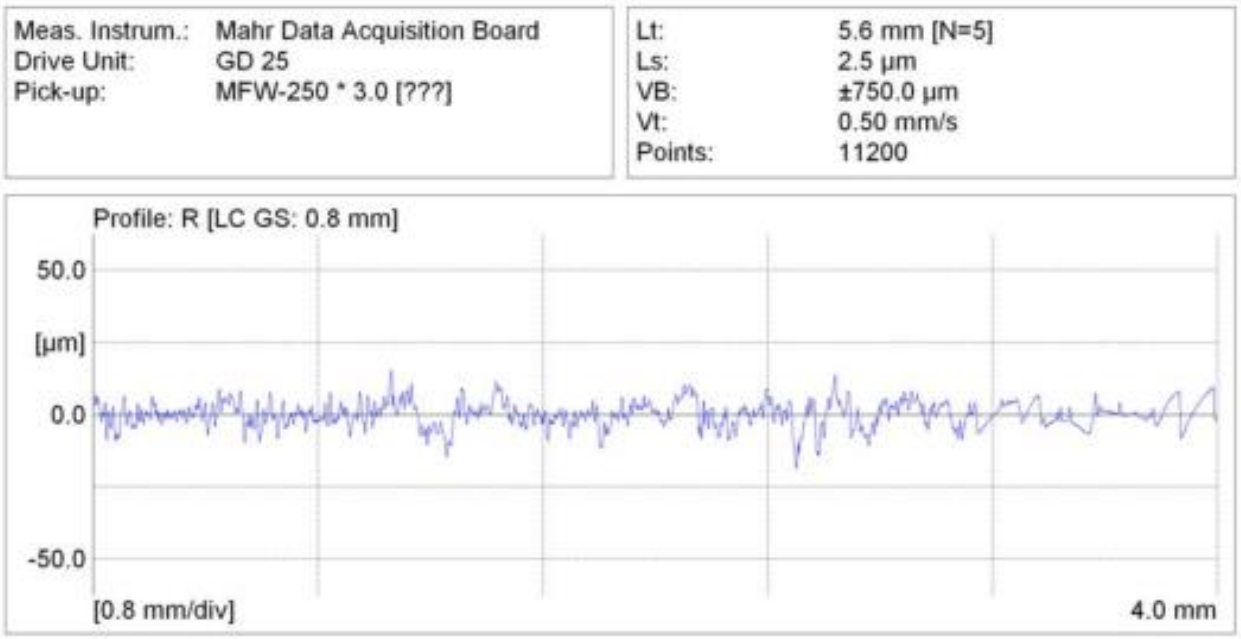

Figure B 1.95 Surface Profile (Longitudinal) of CVD Trimmed Fatigue Test Specimen B2-L-1

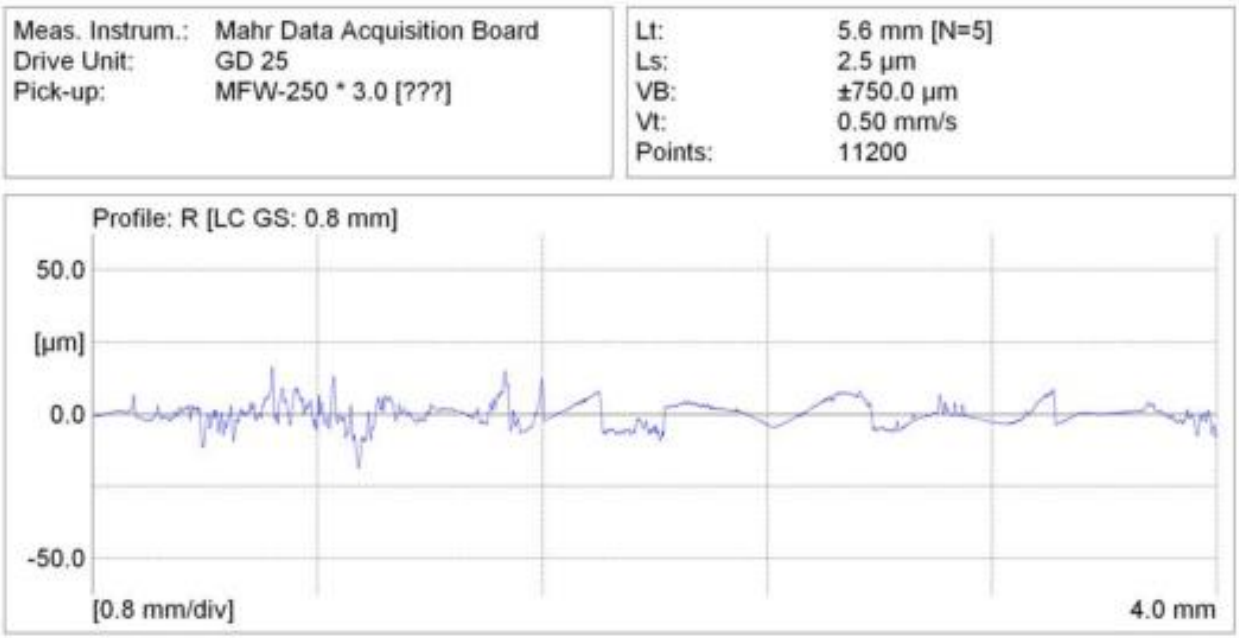

Figure B 1.96 Surface Profile (Longitudinal) of CVD Trimmed Fatigue Test Specimen B2-L-2

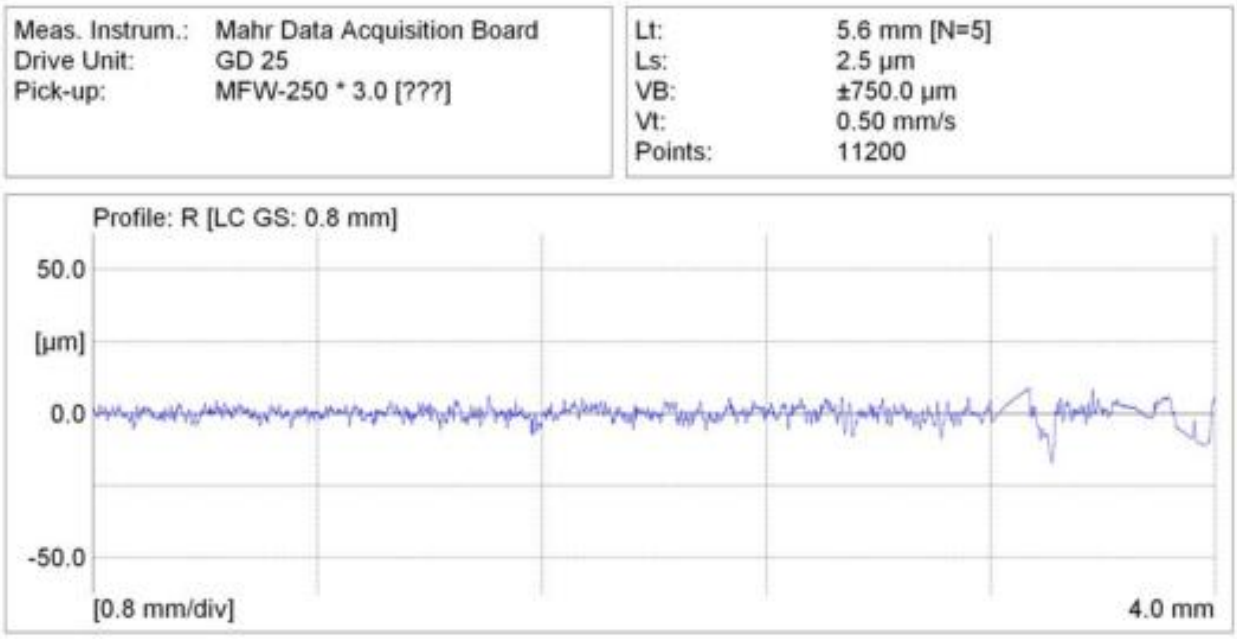

Figure B 1.97 Surface Profile (Longitudinal) of CVD Trimmed Fatigue Test Specimen B2-L-3

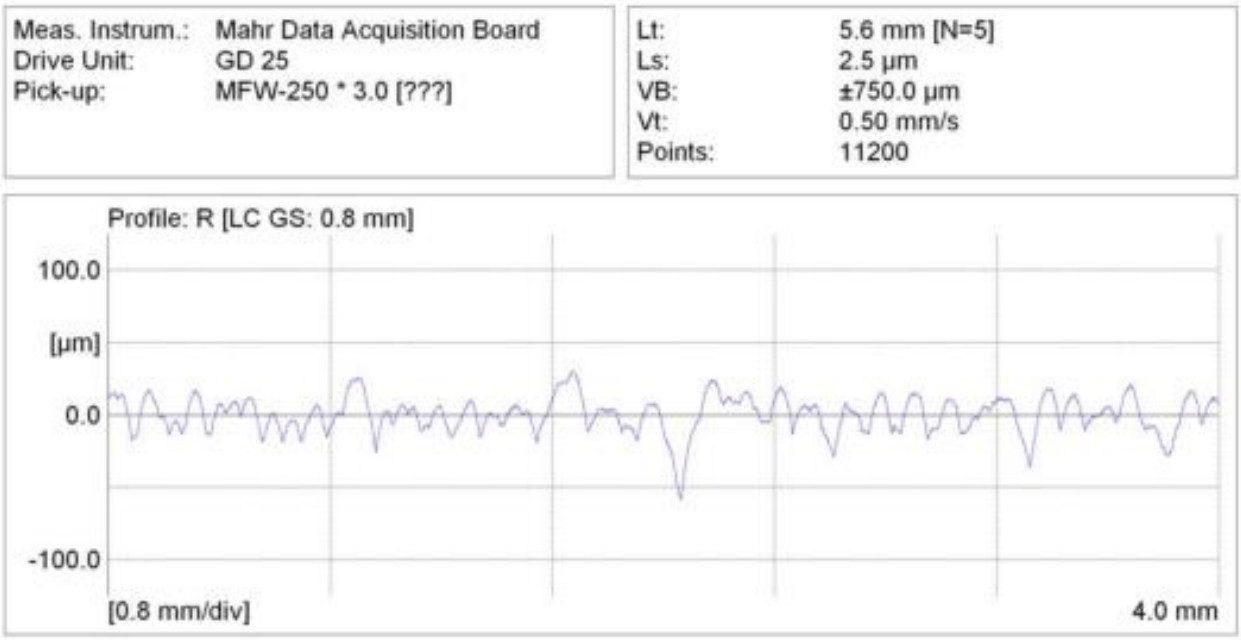

Figure B 1.98 Surface Profile (Longitudinal) of CVD Trimmed Fatigue Test Specimen B2-L-4

Appendix C

C 1.1 Photographs of Damage Progression in Fatigue Testing of Unnotched Specimens

The following pages contain photographs of the damage progression during fatigue cyclic testing of unnotched test specimens.

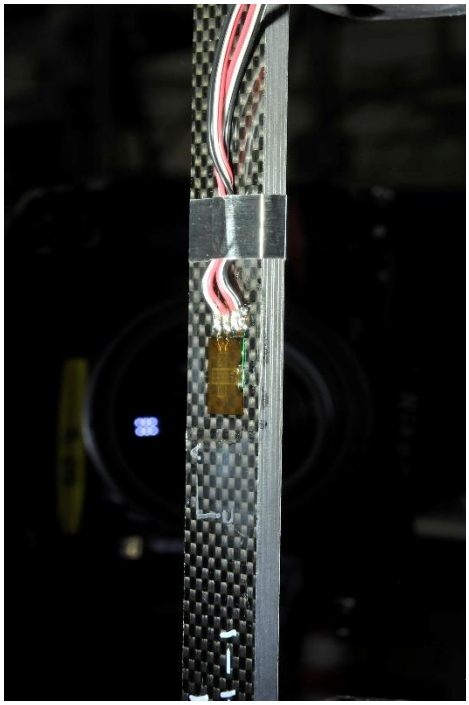

(A1-H-1) at 1 cycles

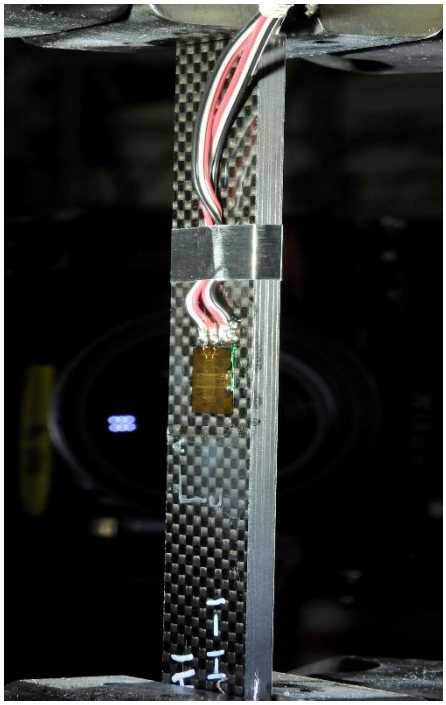

(A1-H-1) at 100 cycles

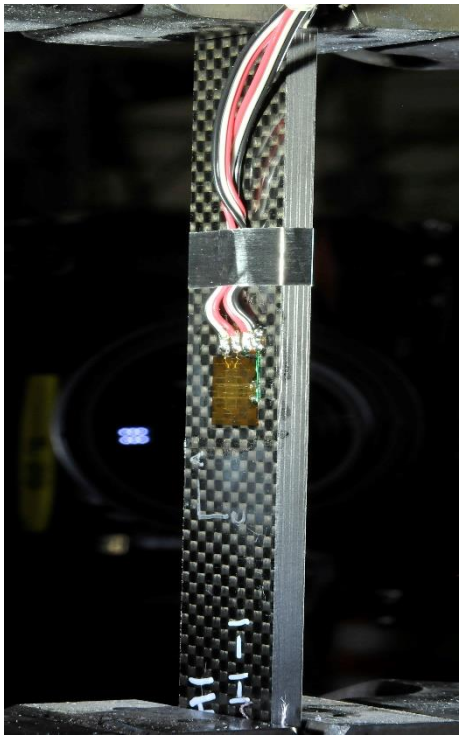

(A1-H-1) at 1K Cycles

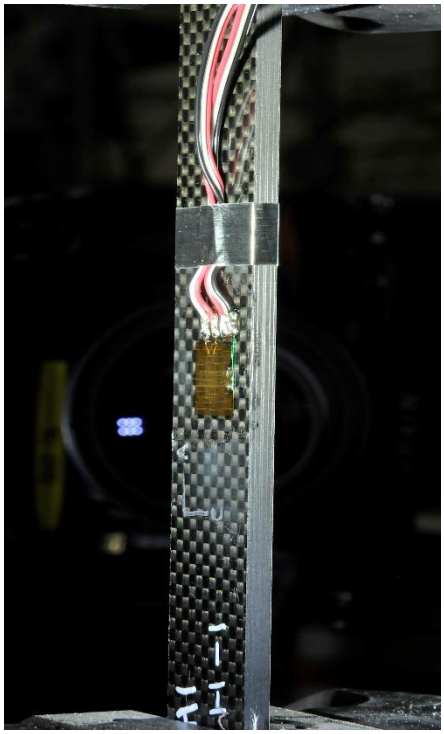

(A1-H-1) at 5K cycles

Figure C1.1 Damage Progression in (A1-H-1) Test Specimen to 5K cycles

\

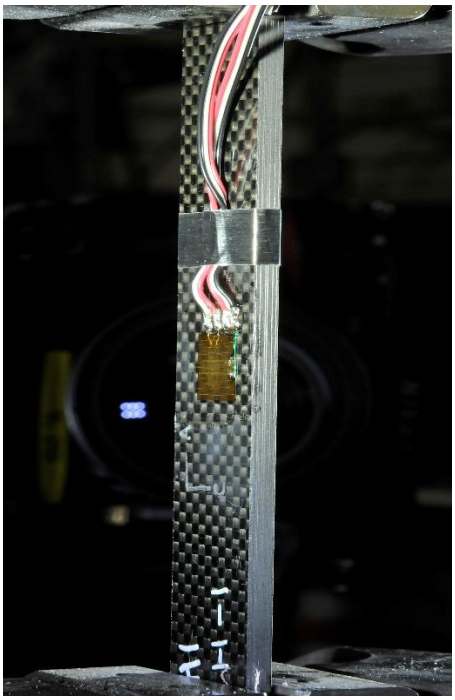

(A1-H-1) at 10K cycles

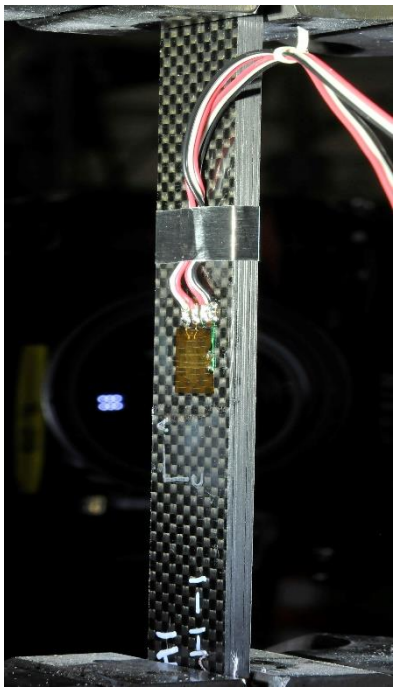

(A1-H-1) at 20K cycles

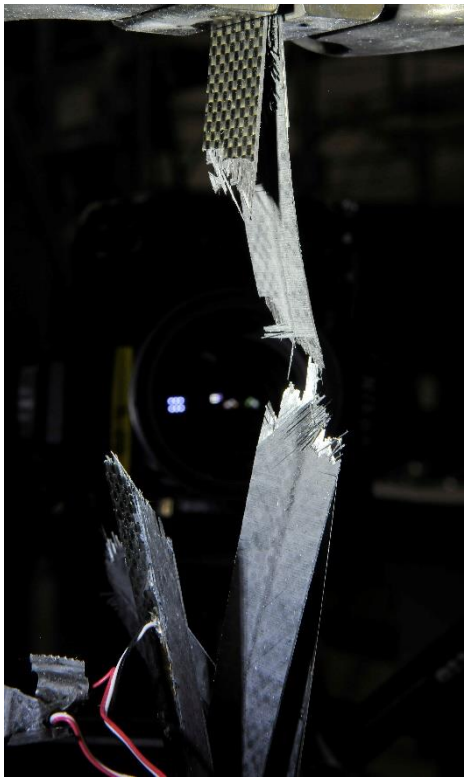

(A1-H-1) at Failure

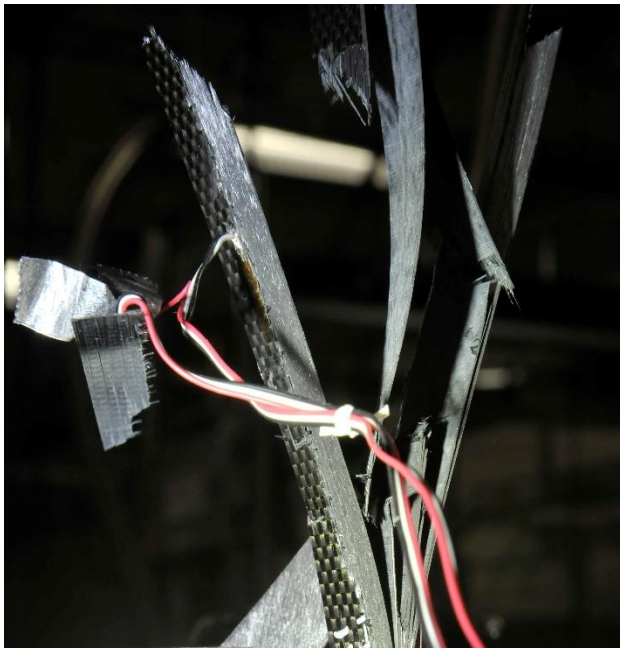

(A1-H-1) at Failure

Figure C1.2 Damage Progression in (A1-H-1) Test Specimen at Failure

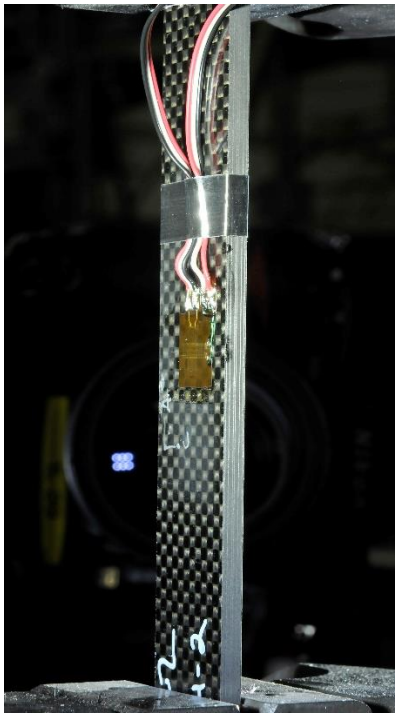

(A1-H-2) at 1 cycles

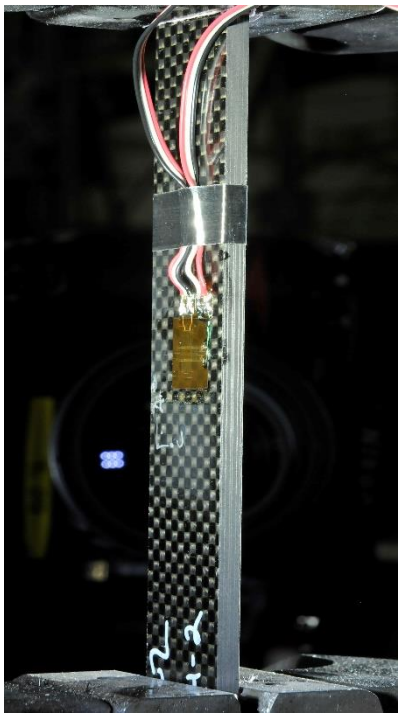

(A1-H-2) at 100 cycles

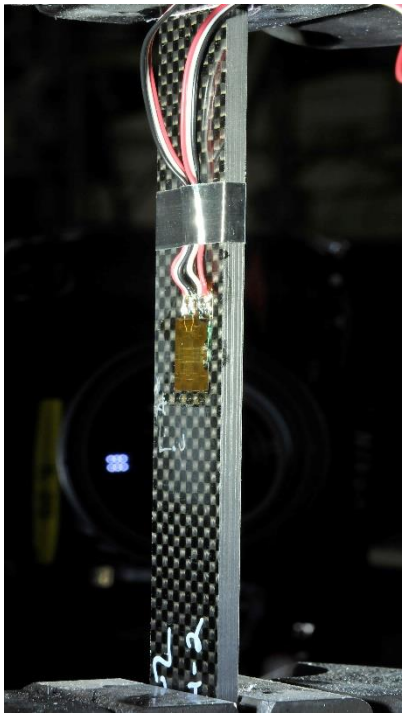

(A1-H-2) at 1K cycles

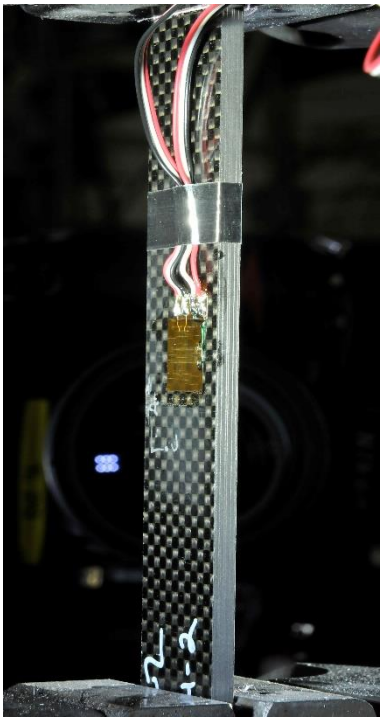

(A1-H-2) at 5K cycles

Figure C1.3 Damage Progression in (A1-H-2) Test Specimen at 5K cycles

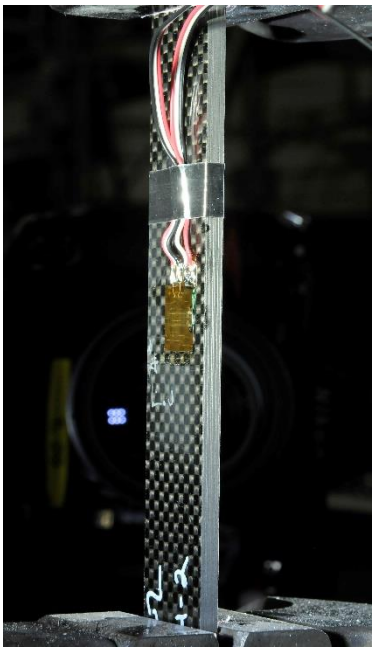

(A1-H-2) at 10K cycles

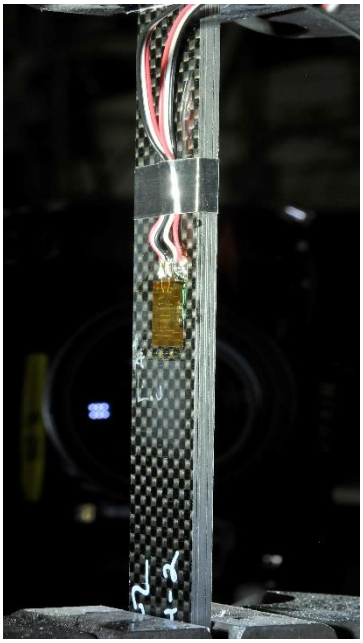

(A1-H-2) at 20K cycles

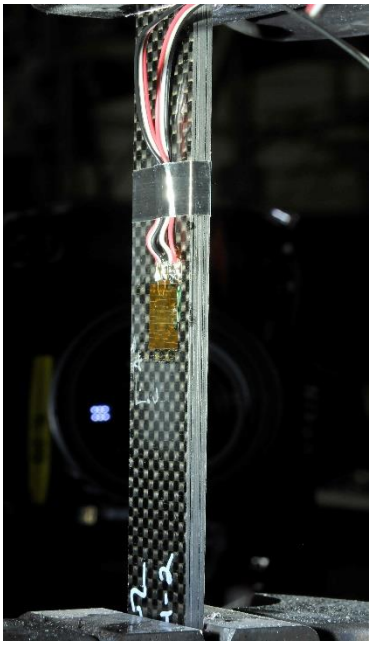

(A1-H-2) at 30K cycles

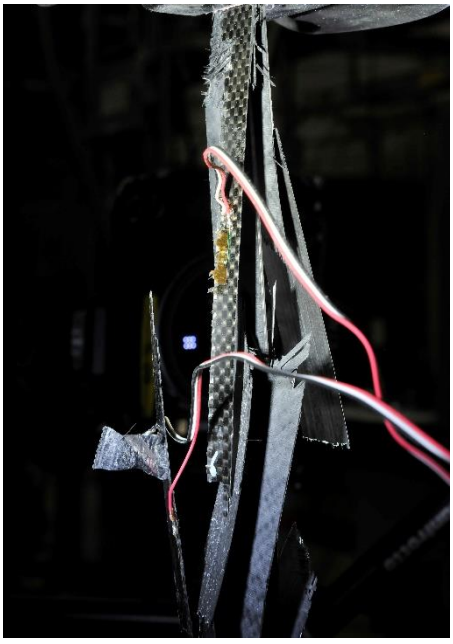

(A1-H-2) at Failure

Figure C1.4 Damage Progression in (A1-H-2) Test Specimen at Failure

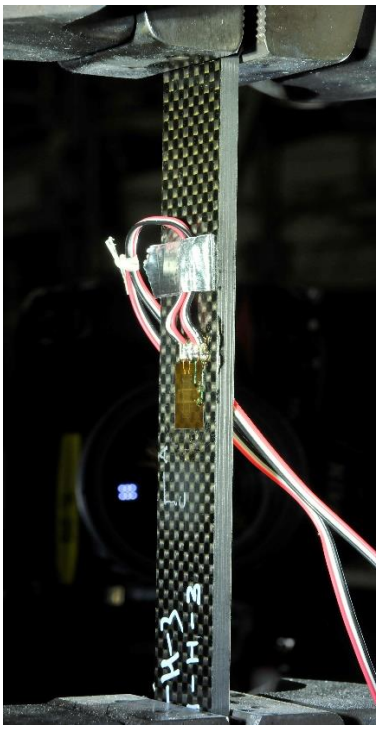

(A1-H-3) at 1 cycle

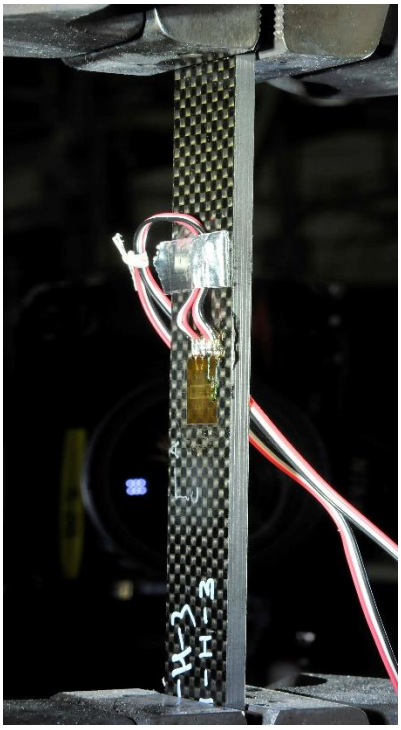

(A1-H-3) at 100 cycles

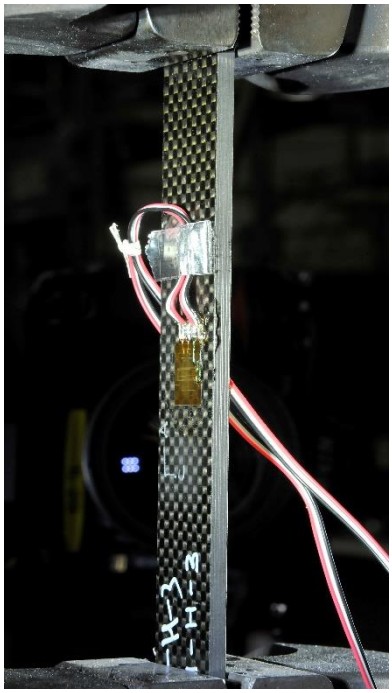

(A1-H-3) at 1K cycles

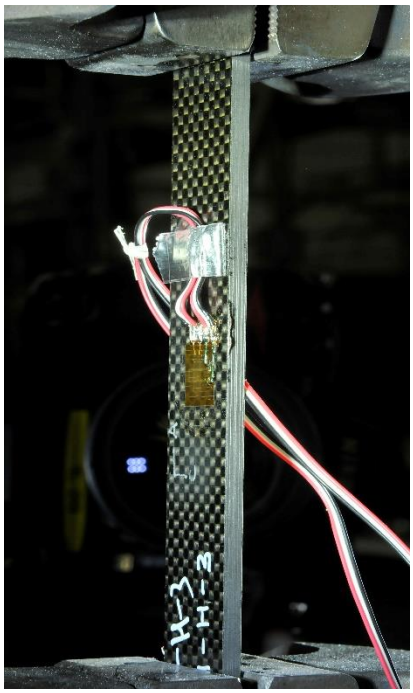

(A1-H-3) at 5K cycles

Figure C1.5 Damage Progression in (A1-H-3) Test Specimen at 5K cycles

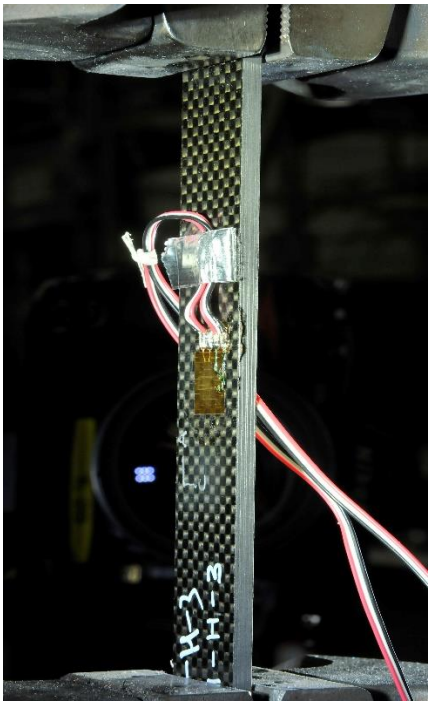

(A3-H-3) at 10K cycles

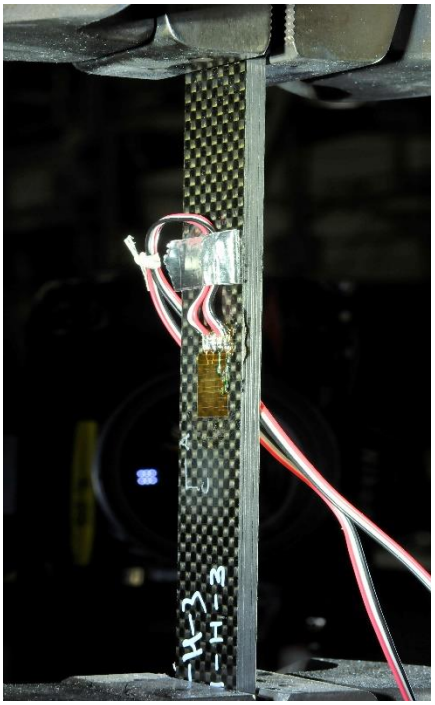

(A3-H-3) at 20K cycles

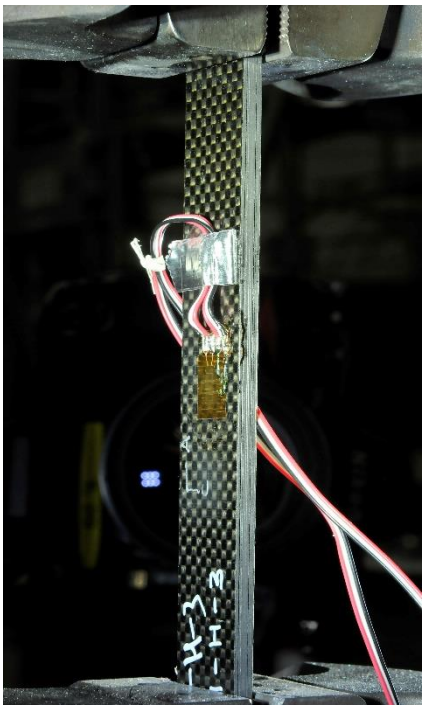

(A3-H-3) at 25K cycles

(A3-H-3) at Failure

Figure C1.6 Damage Progression in (A1-H-3) Test Specimen at Failure

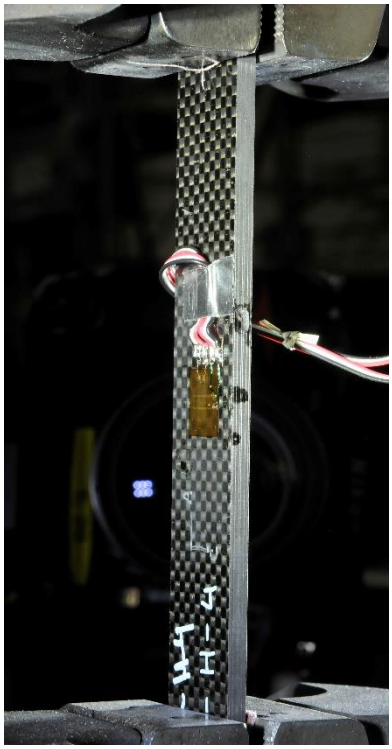

(A1-H-4) at 1 cycle

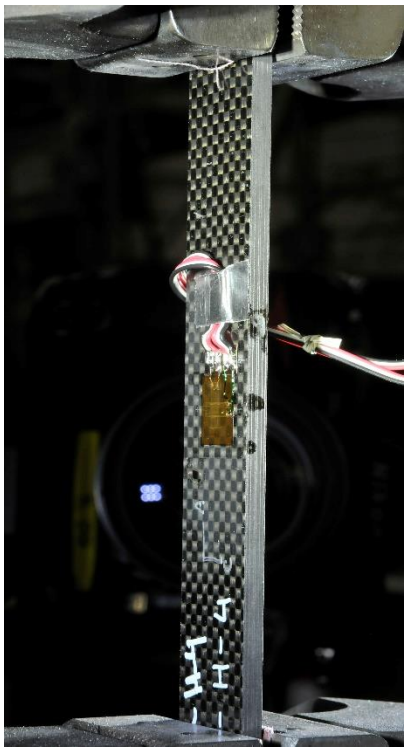

(A1-H-4) at 100 cycles

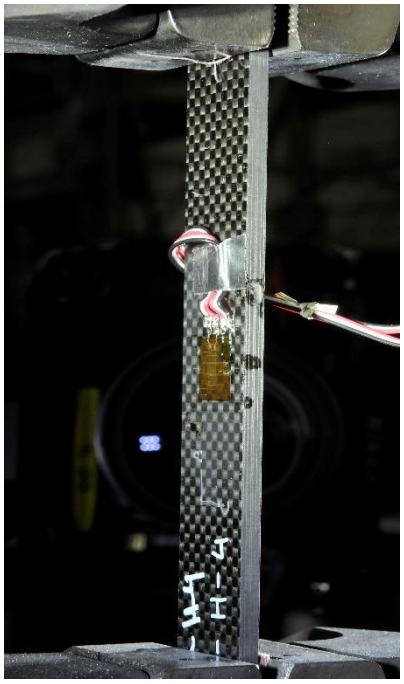

(A1-H-4) at 1K cycles

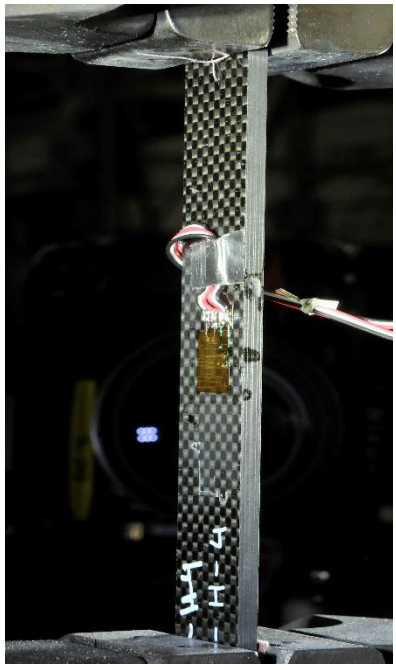

(A1-H-4) at 5K cycles

Figure C1.7 Damage Progression in (A1-H-4) Test Specimen at 5K cycles

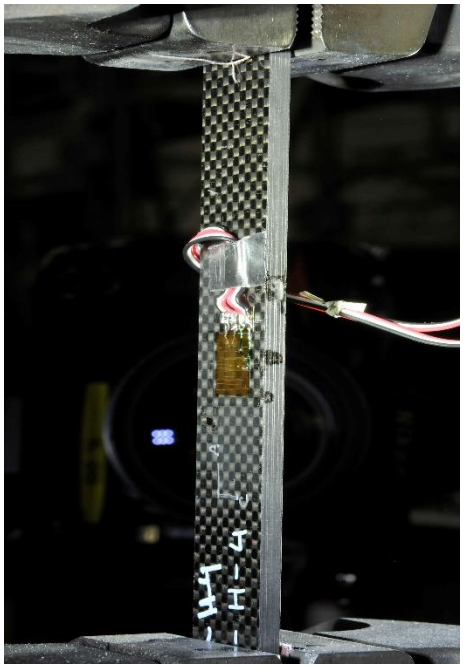

(A1-H-4) at 10K cycles

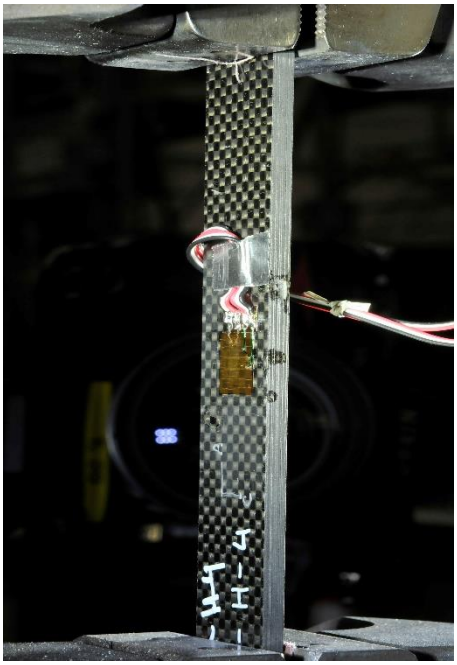

(A1-H-4) at 15K cycles

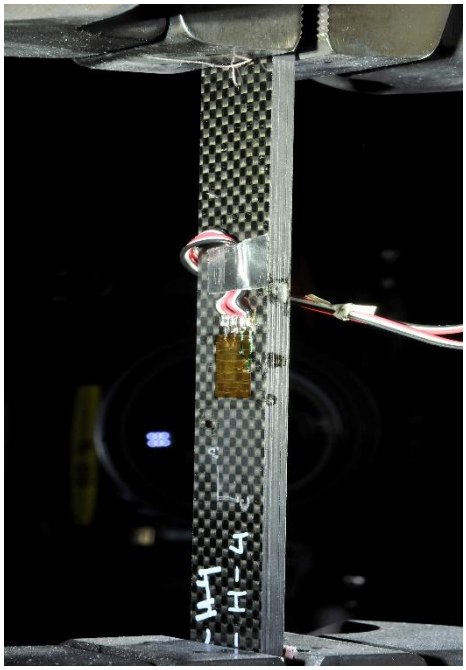

(A1-H-4) at 20K cycles

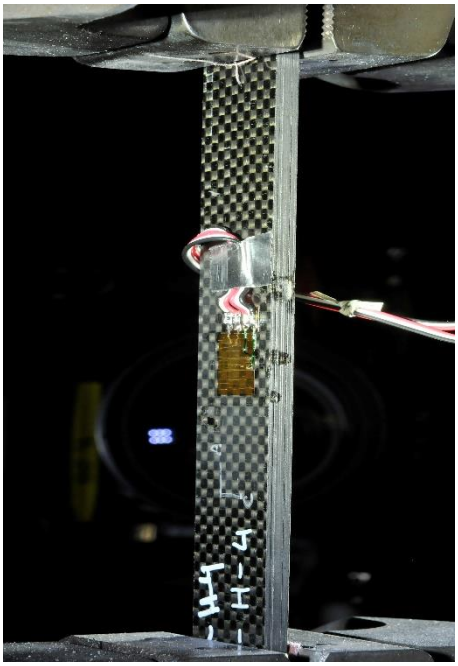

(A1-H-4) 25K cycles

Figure C1.8 Damage Progression in (A1-H-1) Test Specimen at 25K cycles

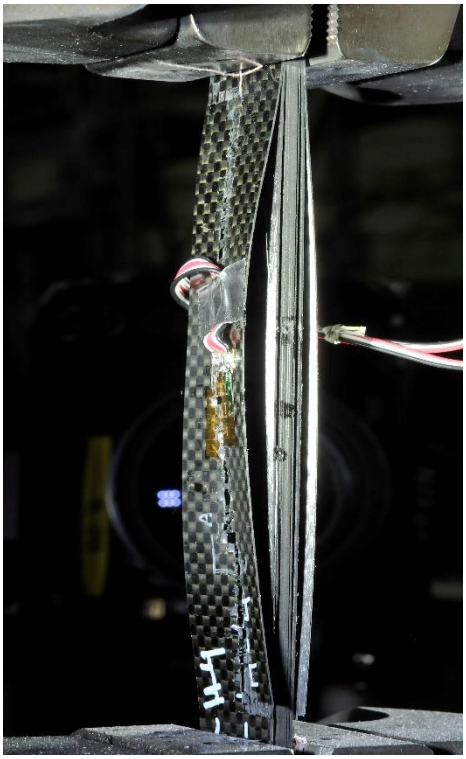

(A1-H-4) at 30K cycles

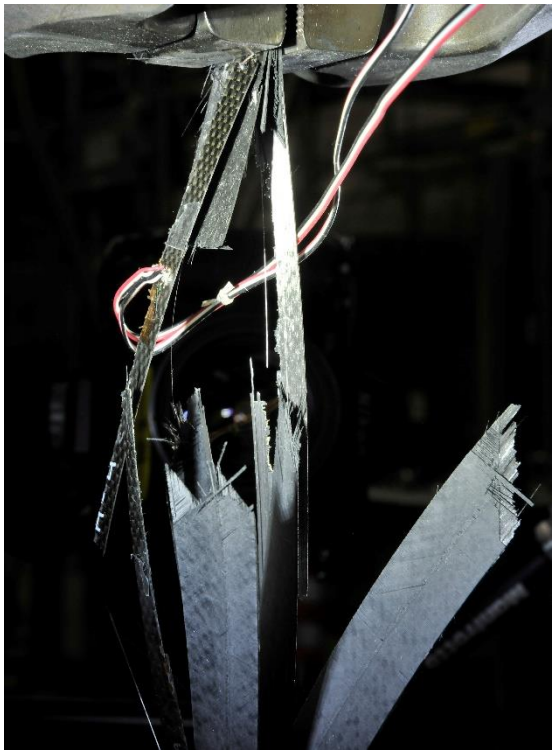

(A1-H-4) at Failure

Figure C1.9 Damage Progression in (A1-H-4) Test Specimen at Failure

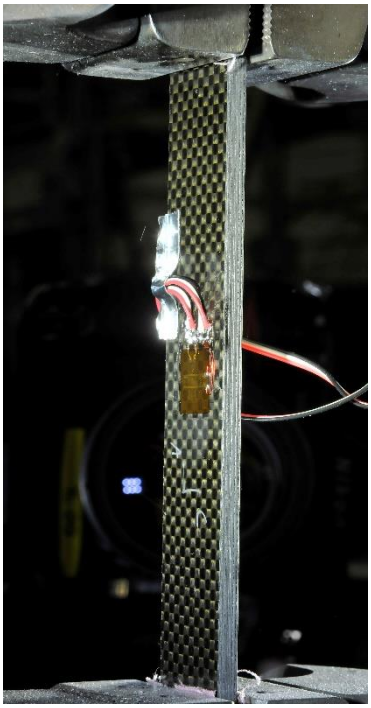

(B1-H-1) at 1 cycle

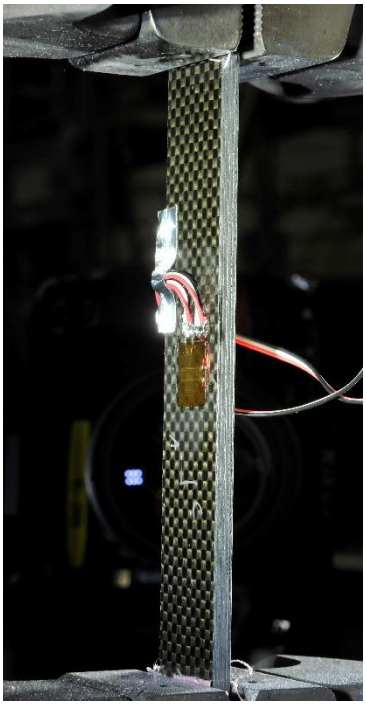

(B1-H-1) at 100 cycles

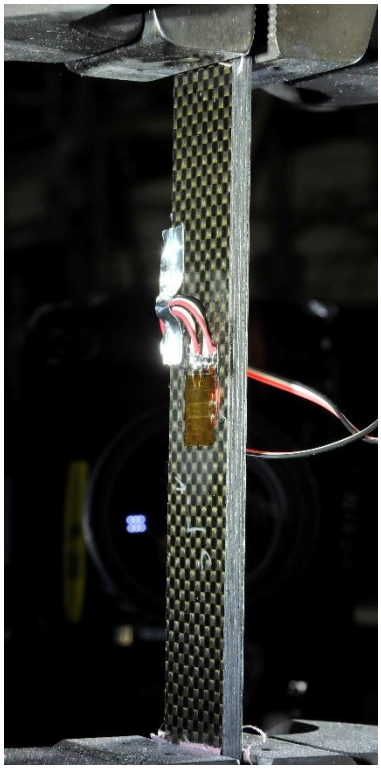

(B1-H-1) at 1K cycles

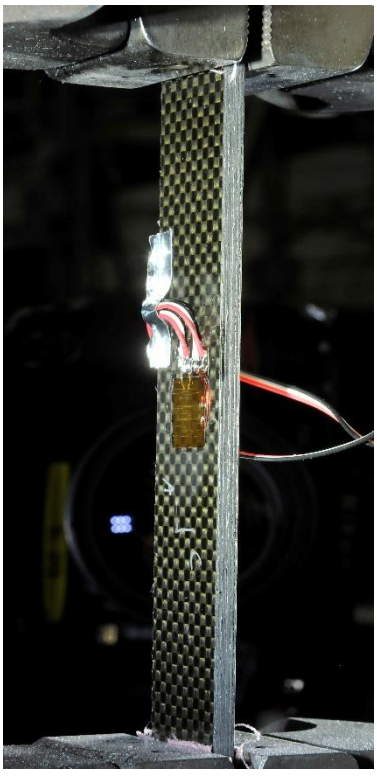

(B1-H-1) at 5K cycles

Figure C1.10 Damage Progression in (B1-H-1) Test Specimen at 5K cycles

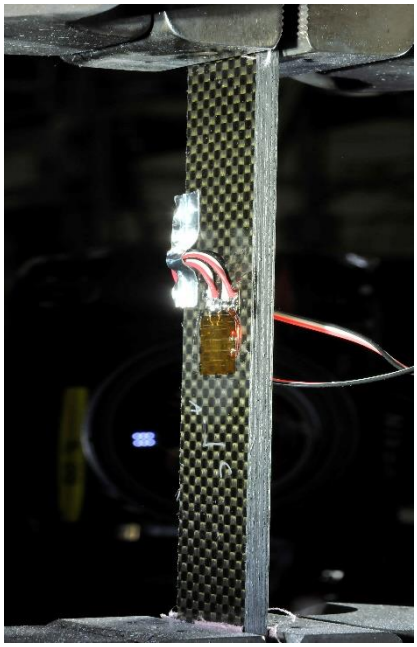

(B1-H-1) at 10K cycles

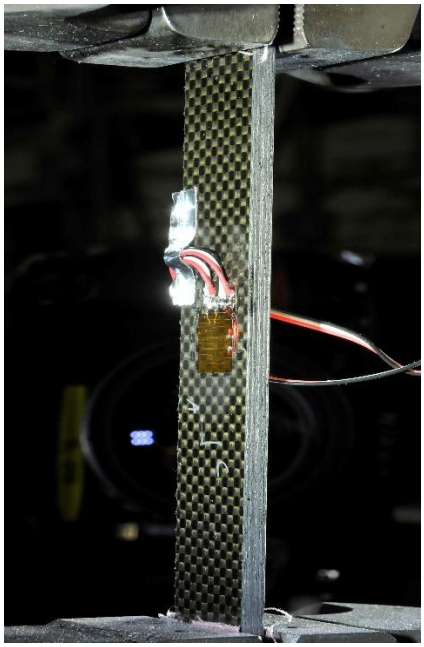

(B1-H-1) at 15K cycles

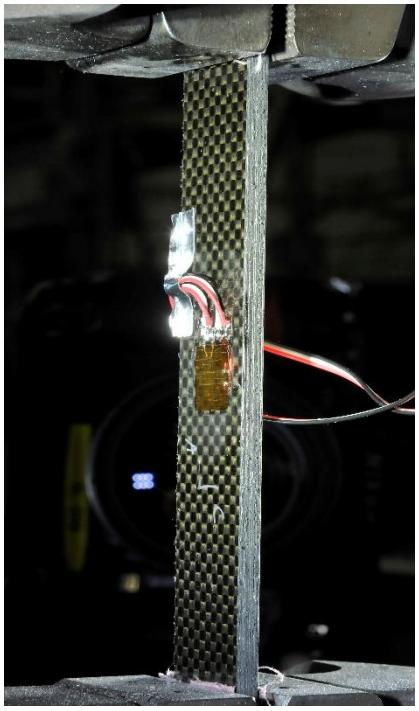

(B1-H-1) at 20K cycles

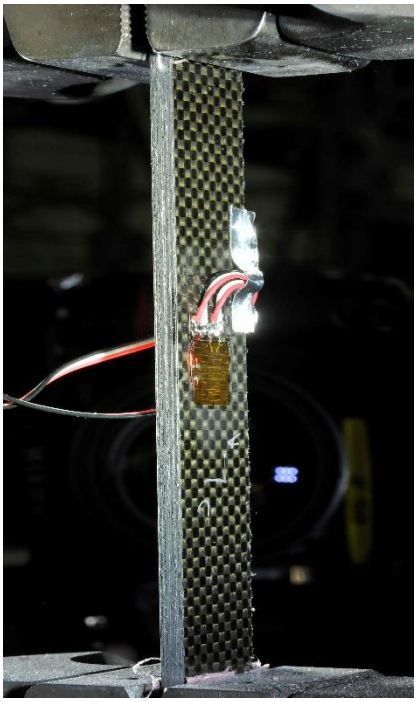

(B1-H-1) at 25K cycles

Figure C1.11 Damage Progression in (B1-H-1) Test Specimen at 25K cycles

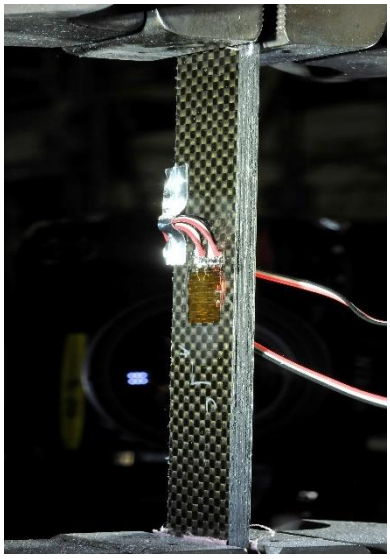

(B1-H-1) at 30K cycles

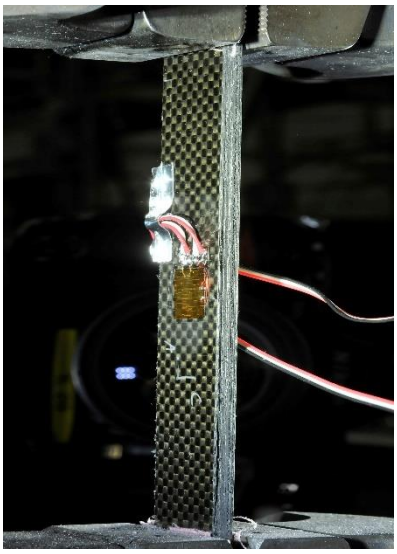

(B1-H-1) at 35K cycles

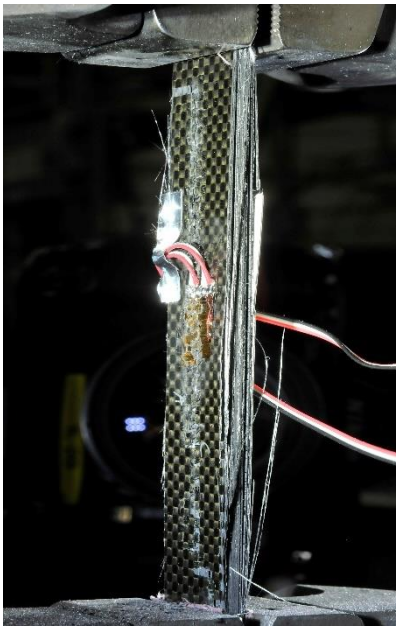

(B1-H-1) at 45K cycles

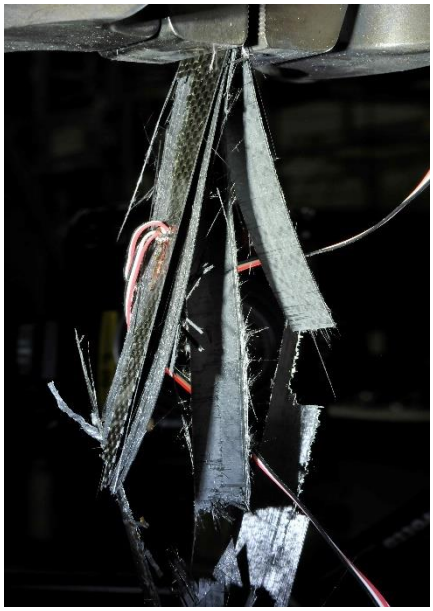

(B1-H-1) at Failure

Figure C1.12 Damage Progression in (B1-H-1) Test Specimen at Failure

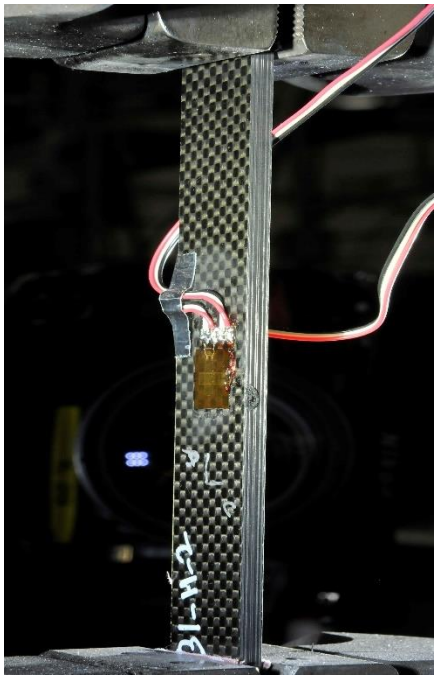

(B1-H-2) at 1 cycle

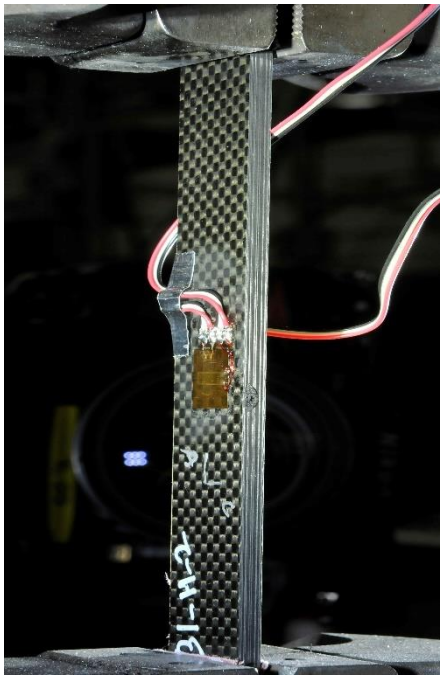

(B1-H-2) at 100 cycles

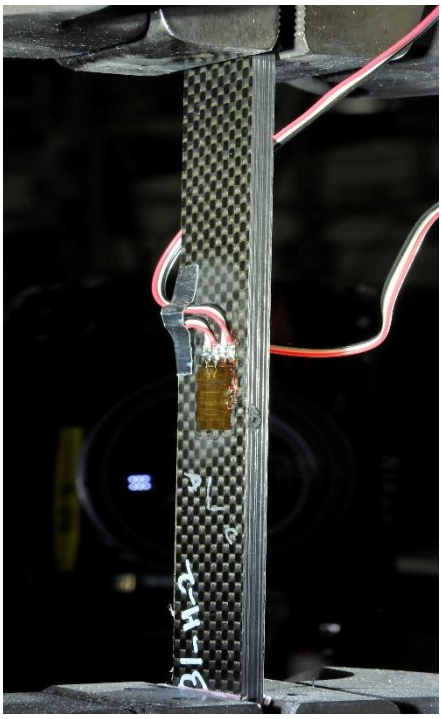

(B1-H-2) at 1K cycles

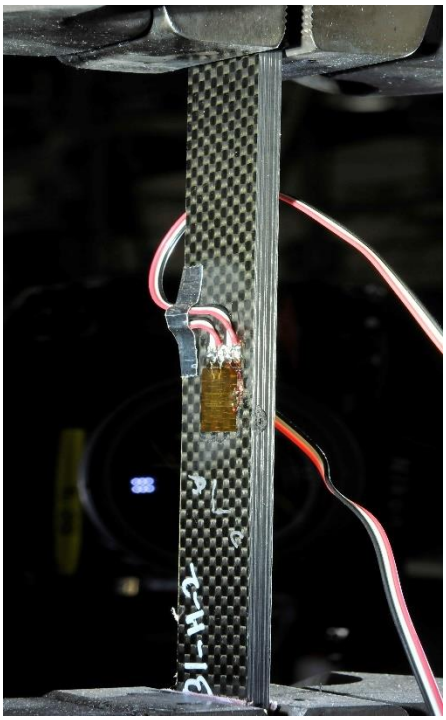

(B1-H-2) at 5K cycles

Figure C1.13 Damage Progression in (B1-H-2) Test Specimen at 5K cycles

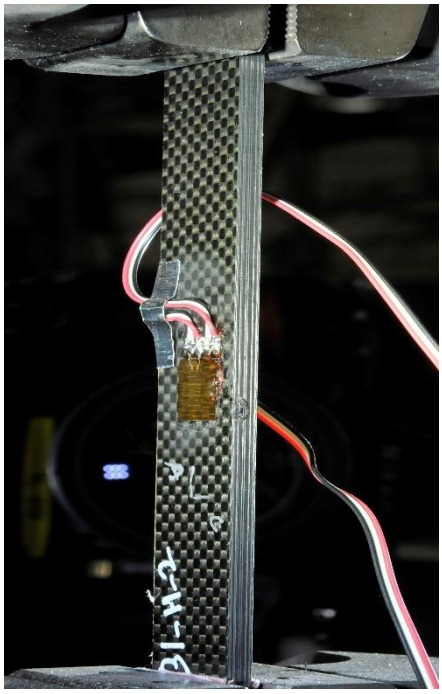

(B1-H-2) at 10K cycles

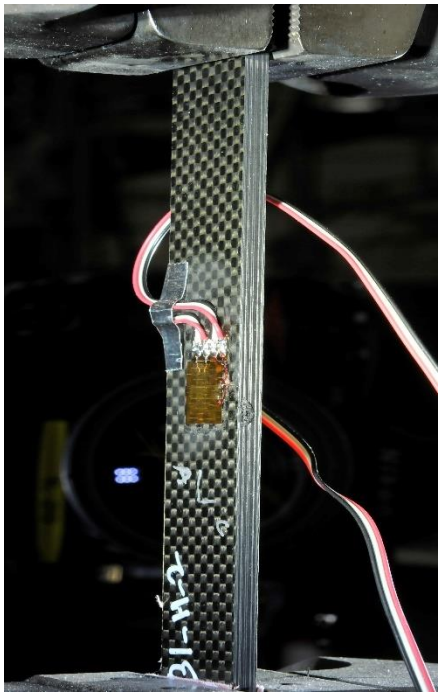

(B1-H-2) at 15K cycles

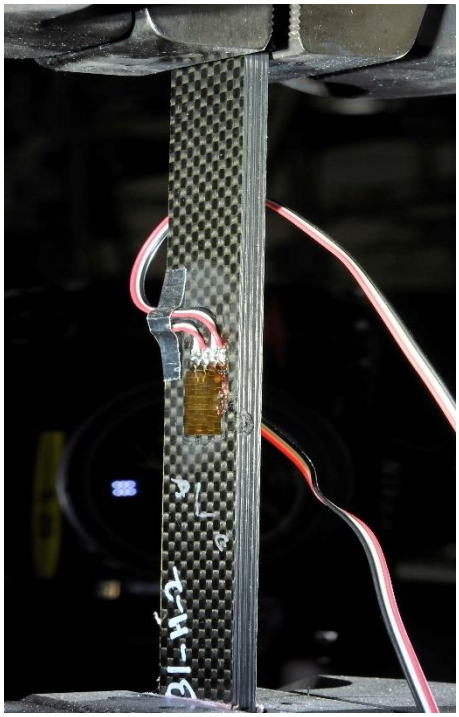

(B1-H-2) at 20K cycles

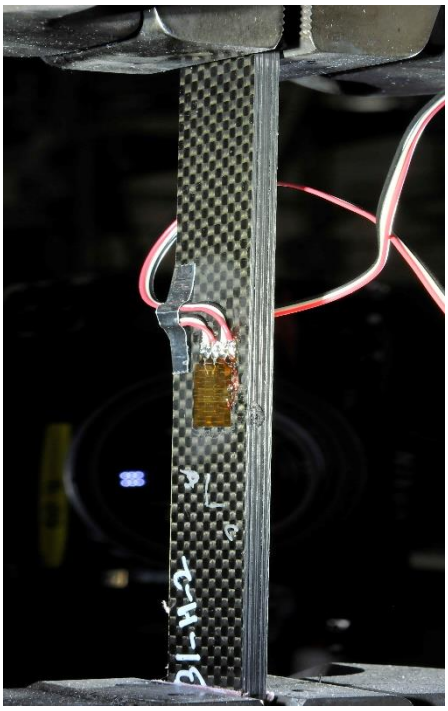

(B1-H-2) at 25K cycles

Figure C1.14 Damage Progression in (B1-H-2) Test Specimen at 25K cycles

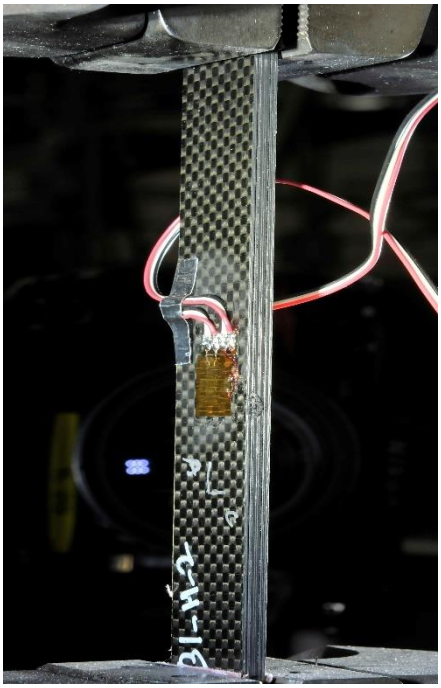

(B1-H-2) at 30K cycles

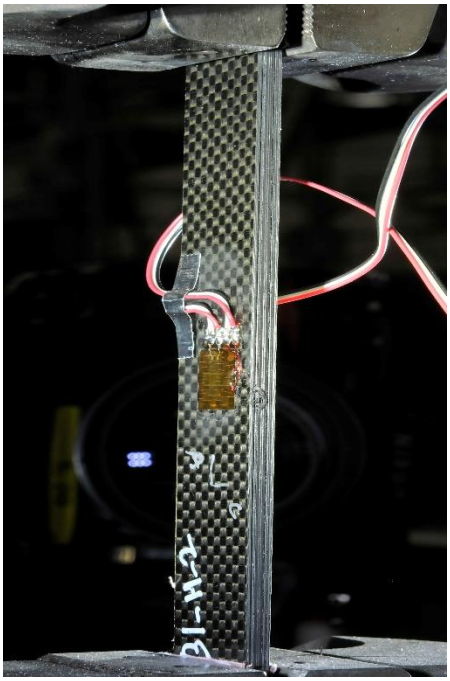

(B1-H-2) at 35K cycles

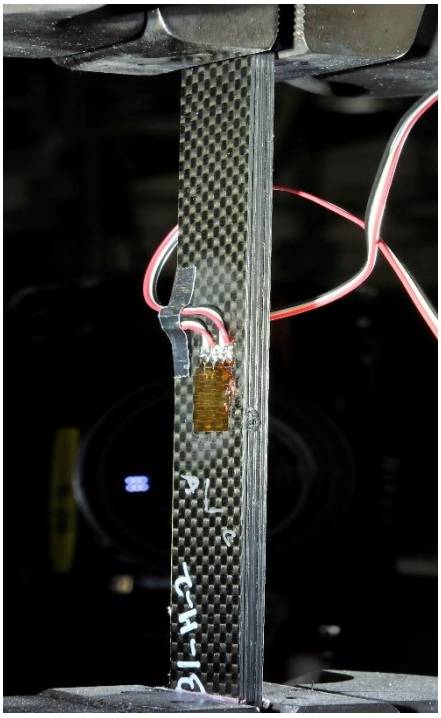

(B1-H-2) at 40K cycles

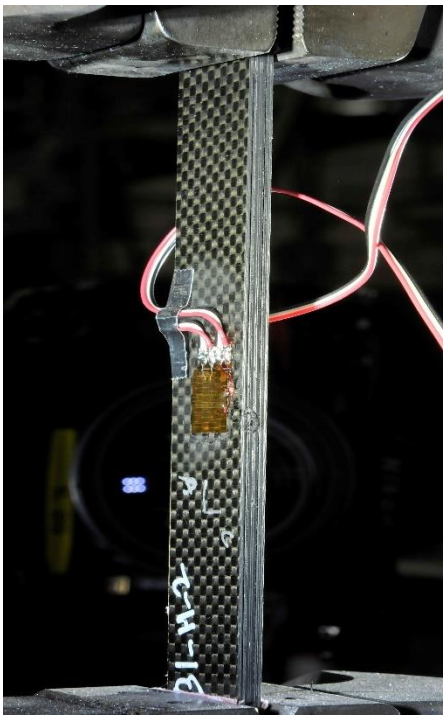

(B1-H-2) at 45K cycles

Figure C1.15 Damage Progression in (B1-H-2) Test Specimen at 45K cycles

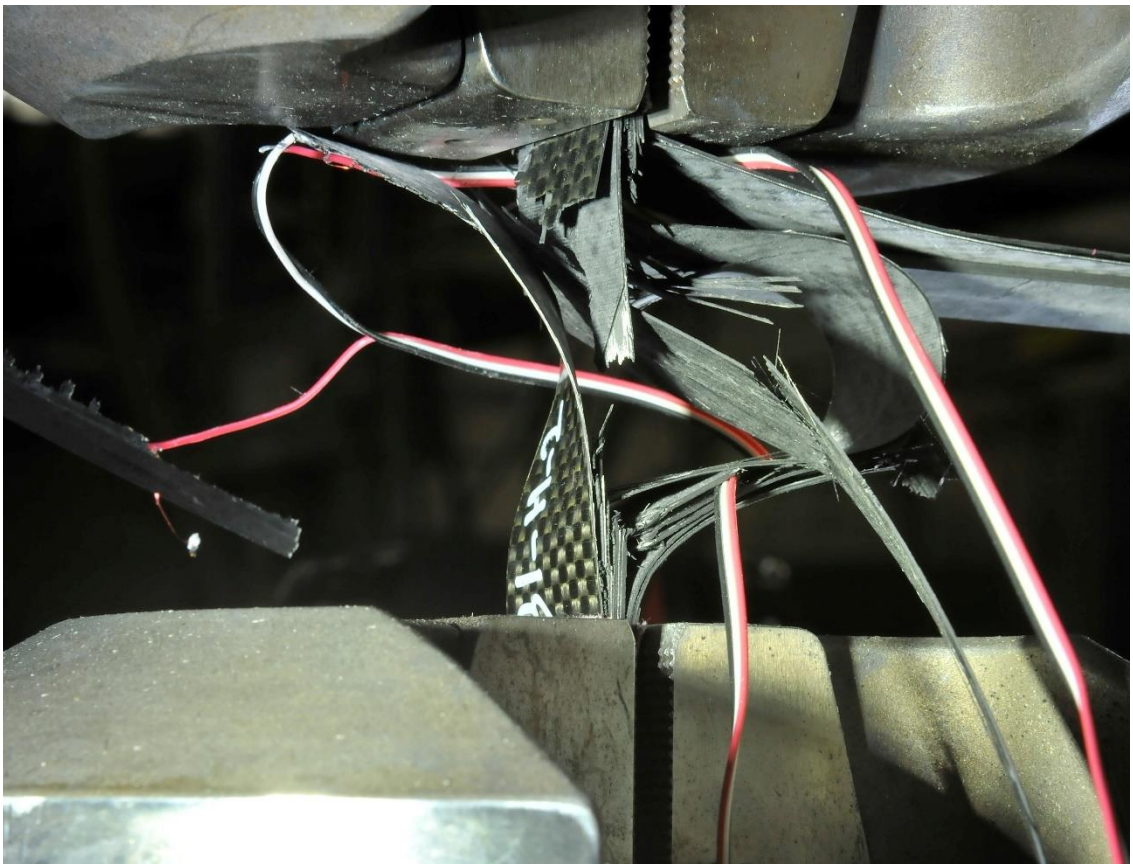

(B1-H-2) at Failure

Figure C1.16 Damage Progression in (B1-H-2) Test Specimen at Failure

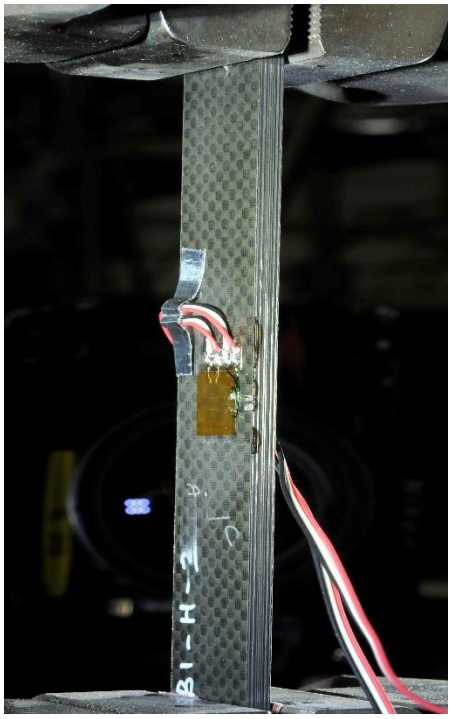

(B1-H-3) at 1 cycle

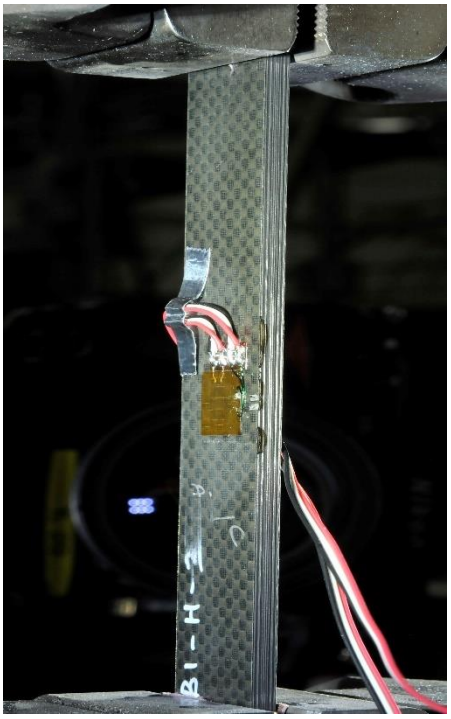

(B1-H-3) at 100 cycles

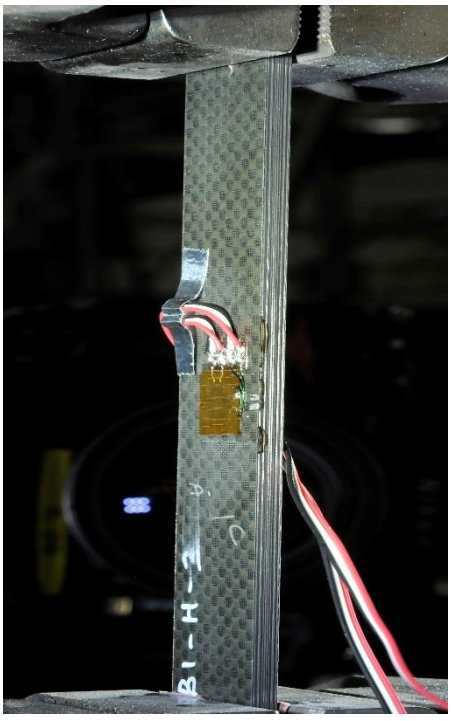

(B1-H-3) at 1K cycles

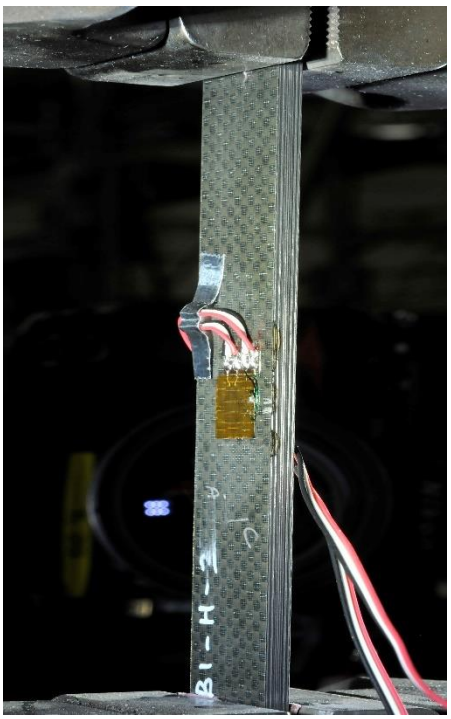

(B1-H-3) at 5K cycles

Figure C1.17 Damage Progression in (B1-H-3) Test Specimen at 5K cycles

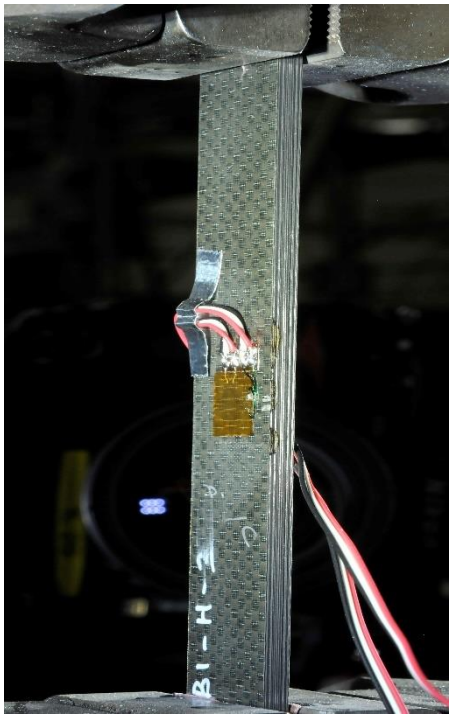

(B1-H-3) at 10K cycles

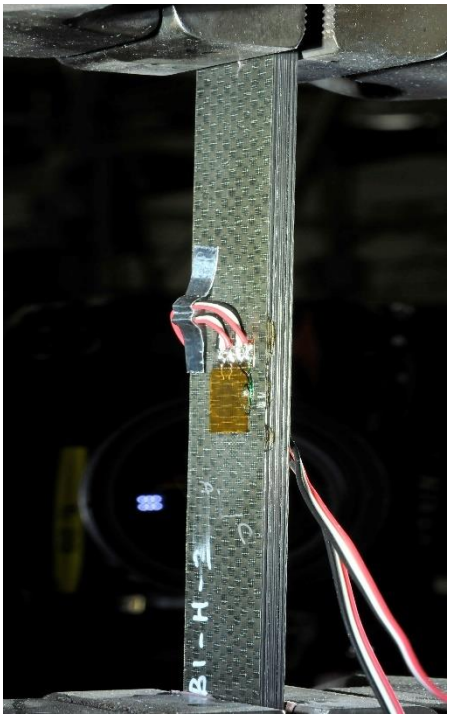

(B1-H-3) at 15K cycles

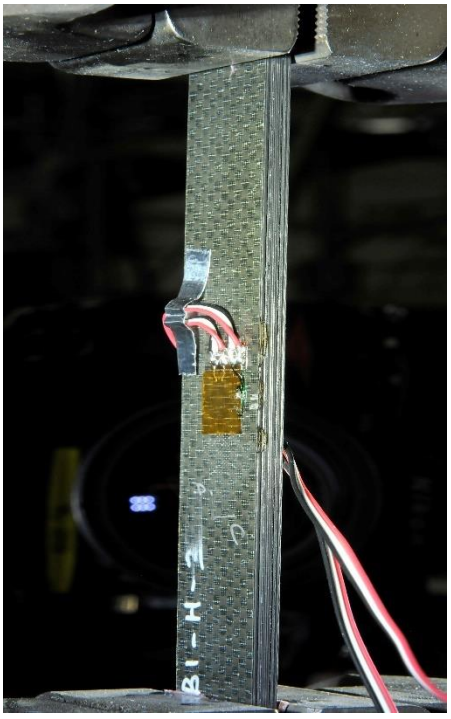

(B1-H-3) at 20K cycles

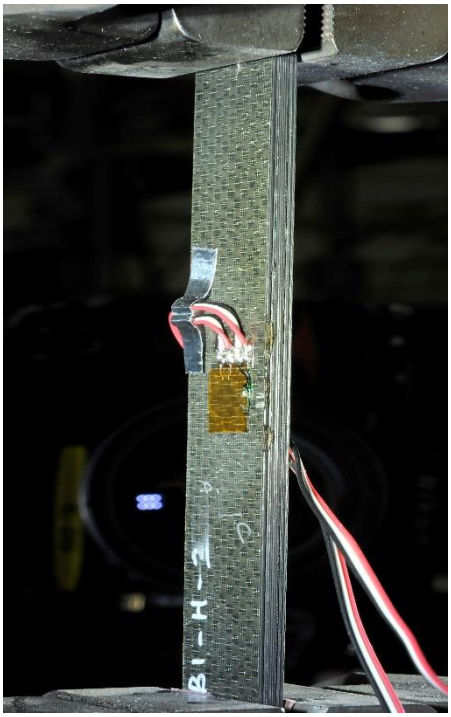

(B1-H-3) at 25K cycles

Figure C1.18 Damage Progression in (B1-H-3) Test Specimen at 25K cycles

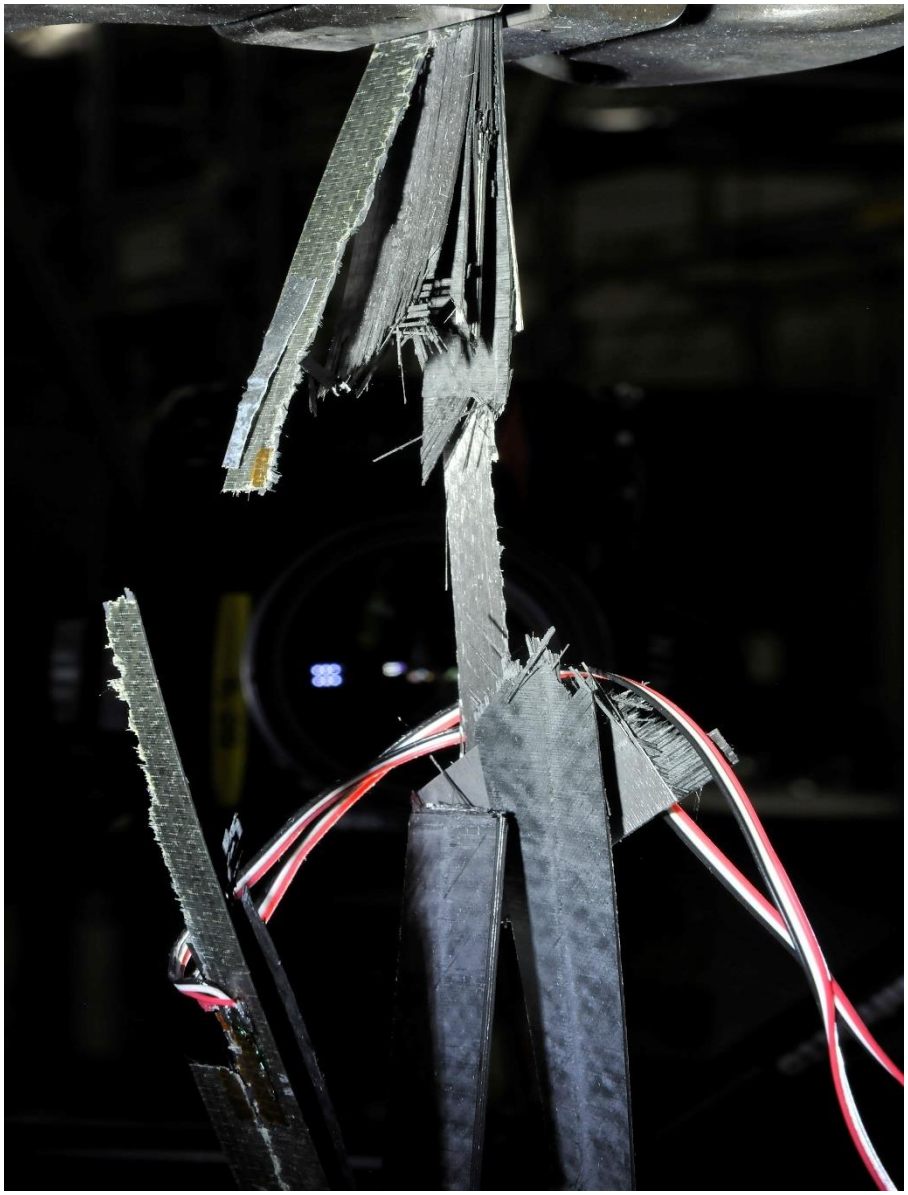

(B1-H-3) at Failure

Figure C1.19 Damage Progression in (B1-H-3) Test Specimen at Failure

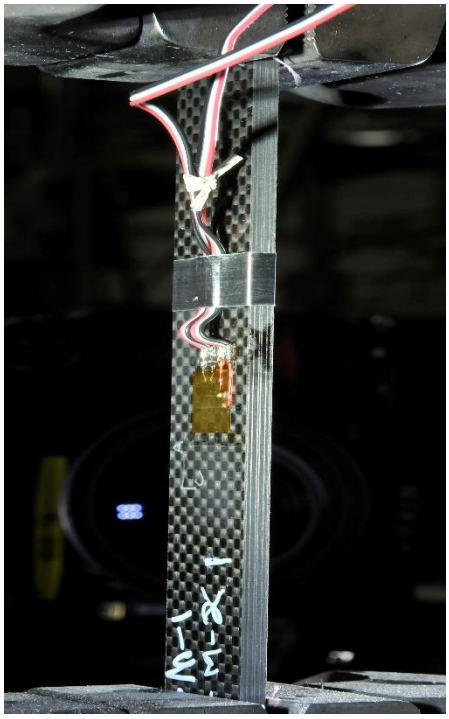

(A1-M-1) at 1 cycle

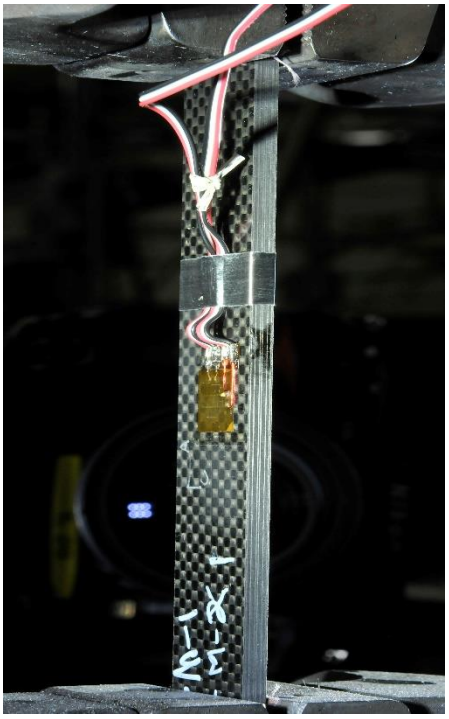

(A1-M-1) at 100 cycles

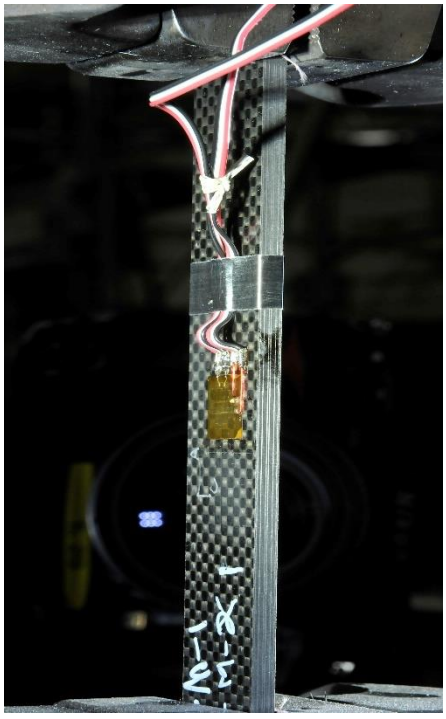

(A1-M-1) at 1K cycles

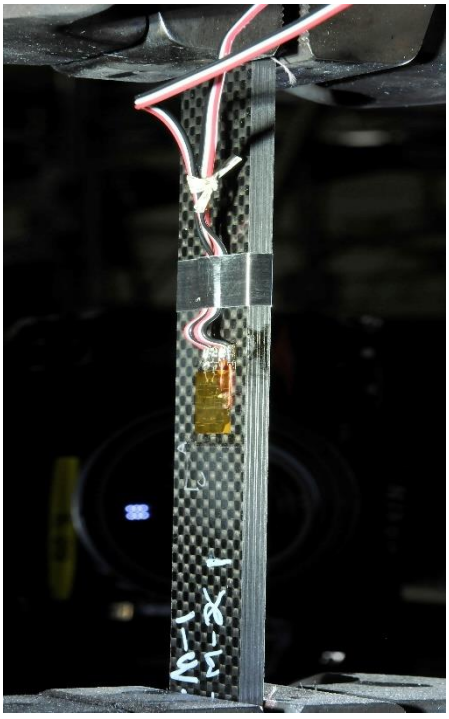

(A1-M-1) at 5K cycles

Figure C1.20 Damage Progression in (A1-M-1) Test Specimen at 5K cycles

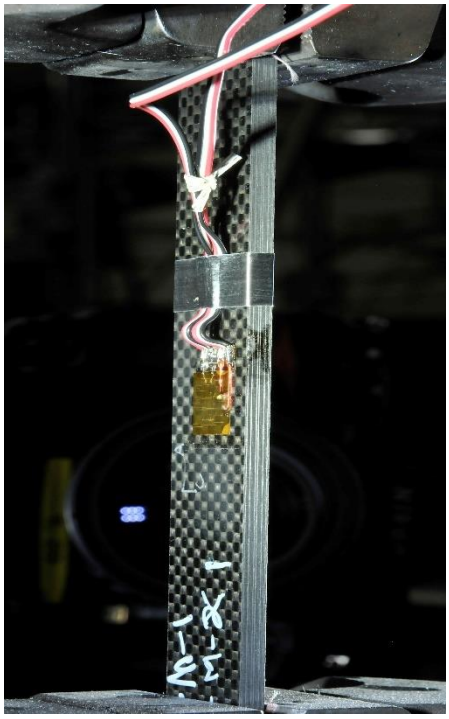

(A1-M-1) at 10K cycles

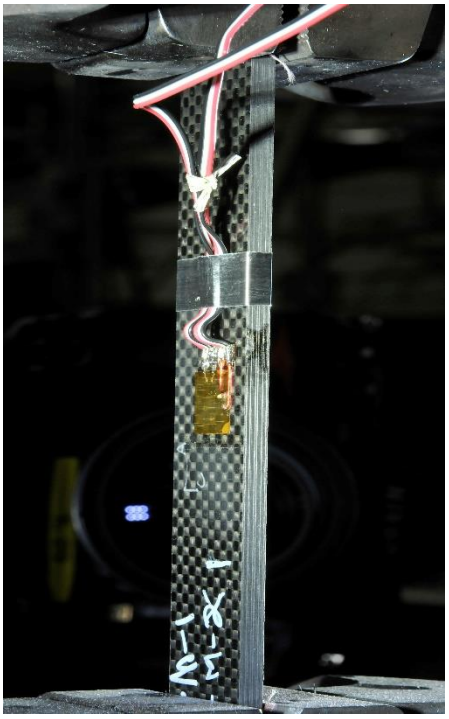

(A1-M-1) at 20K cycles

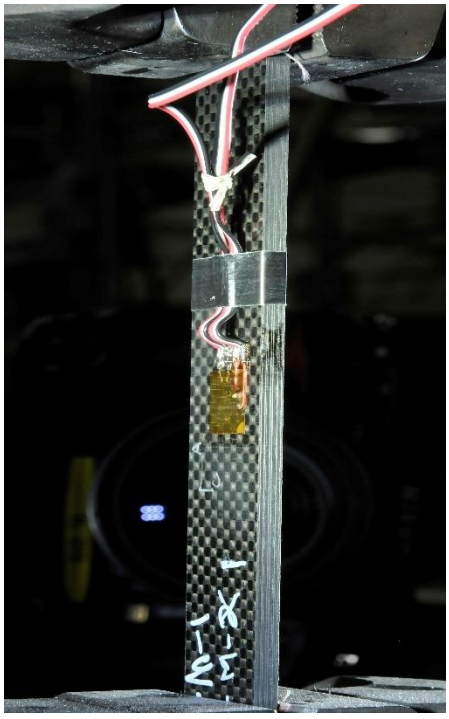

(A1-M-1) at 30K cycles

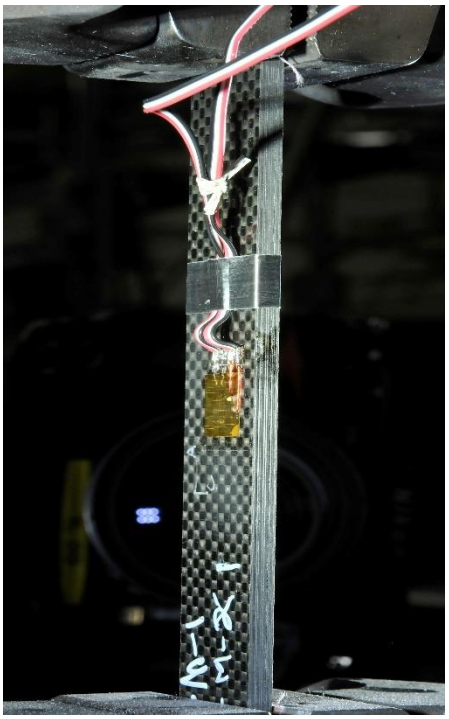

(A1-M-1) at 40K cycles

Figure C1.21 Damage Progression in (A1-M-1) Test Specimen at 40K cycles

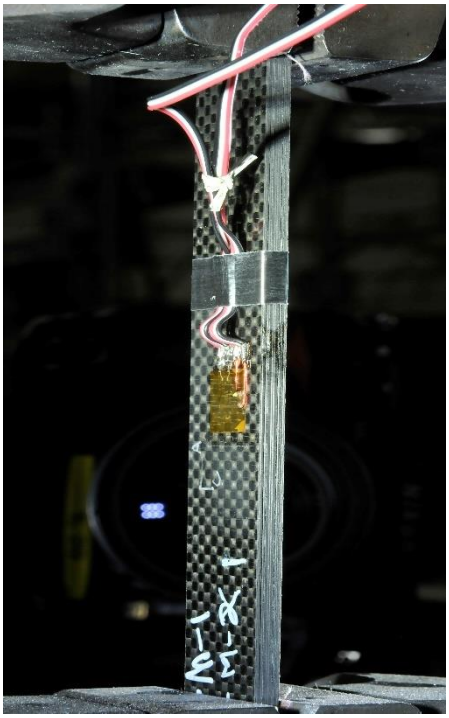

(A1-M-1) at 50K cycles

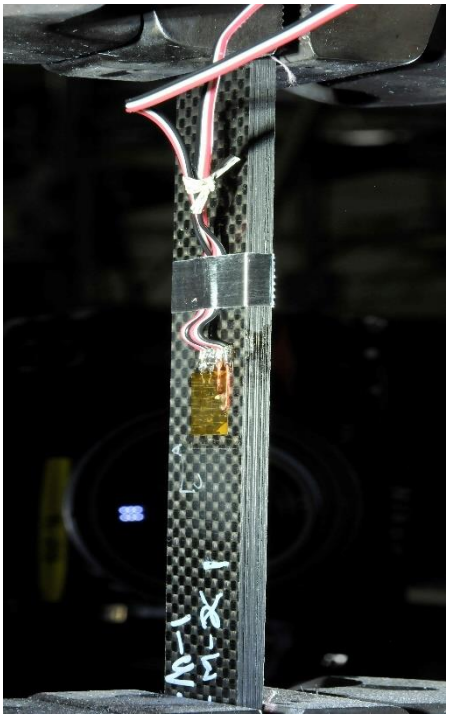

(A1-M-1) at 60K cycles

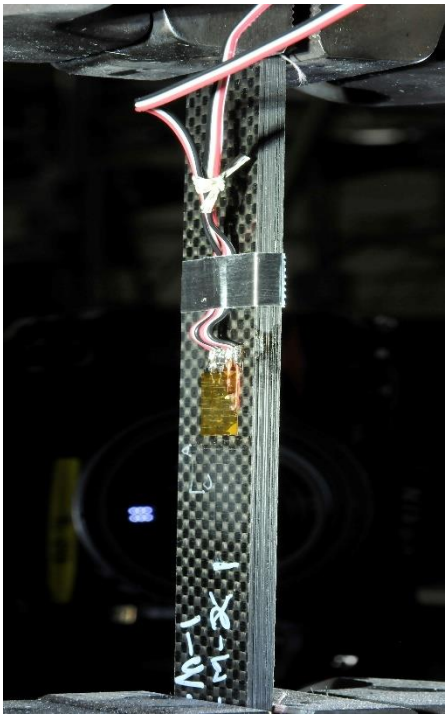

(A1-M-1) at 70K cycles

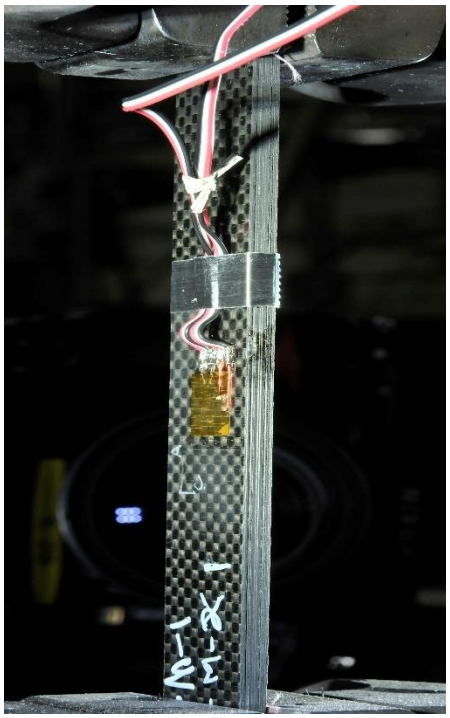

(A1-M-1) at 80K cycles

Figure C1.22 Damage Progression in (A1-M-1) Test Specimen at 80K cycles

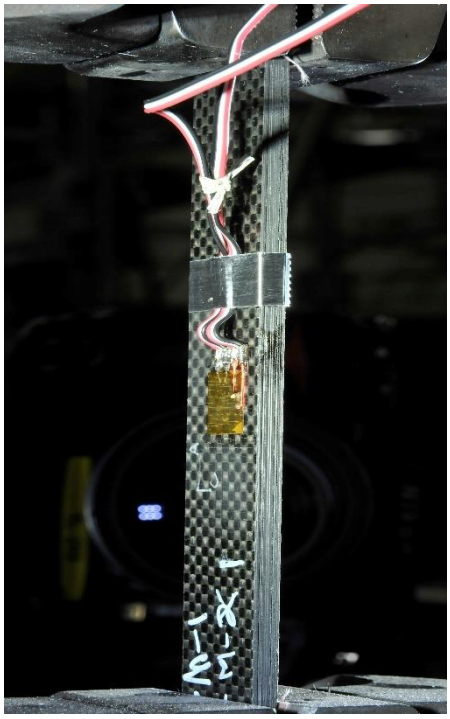

(A1-M-1) at 90K cycles

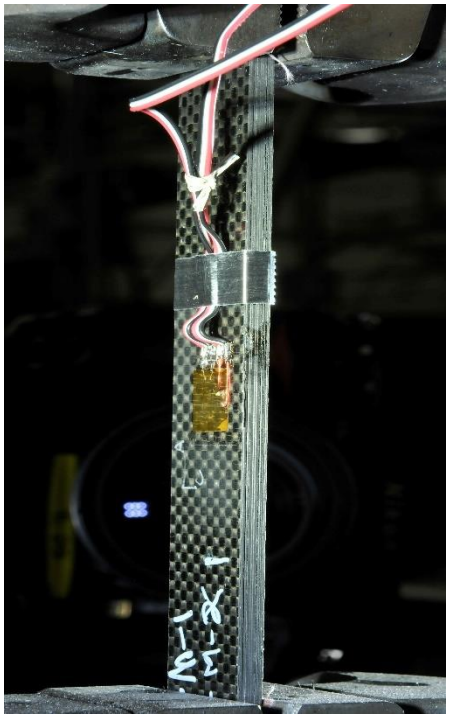

(A1-M-1) at 100K cycles

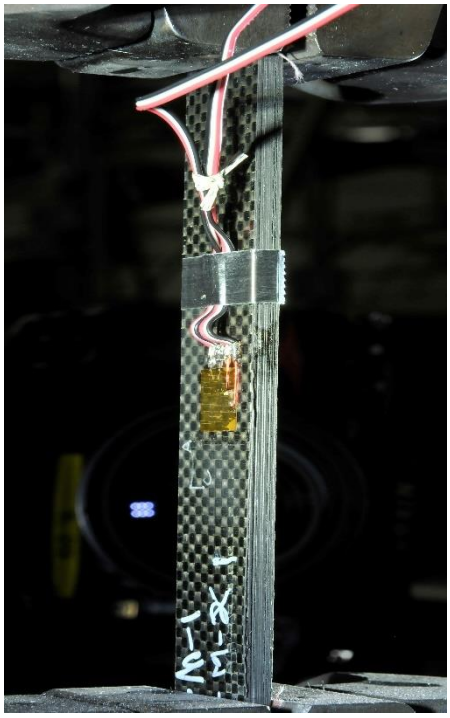

(A1-M-1) at 125K cycles

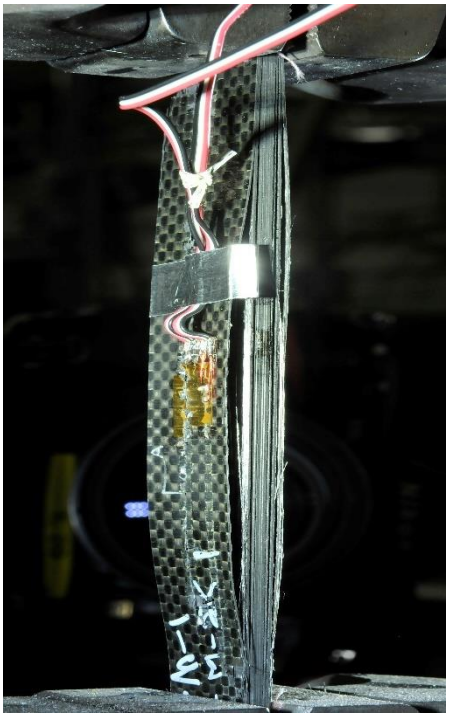

(A1-M-1) at 150K cycles

Figure C1.23 Damage Progression in (A1-M-1) Test Specimen at 150K cycles

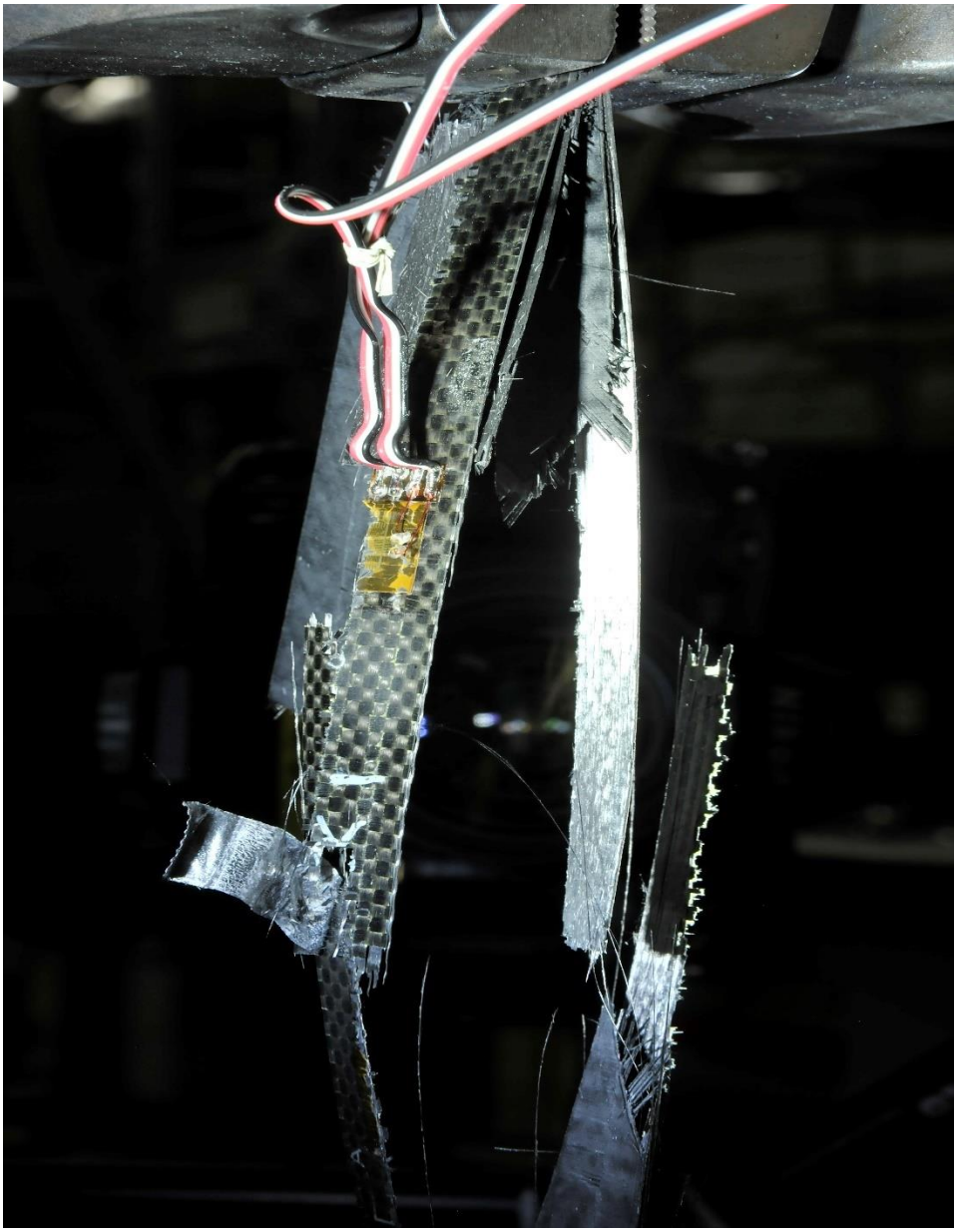

(A1-M-1) at Failure

Figure C1.24 Damage Progression in (A1-M-1) Test Specimen at Failure

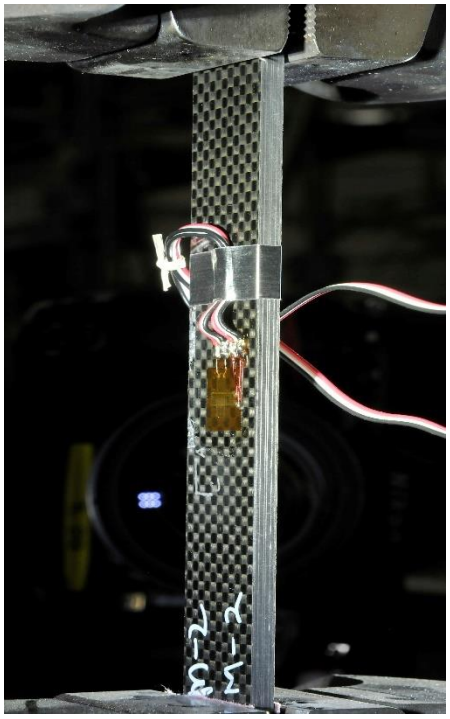

(A1-M-2) at 1 cycle

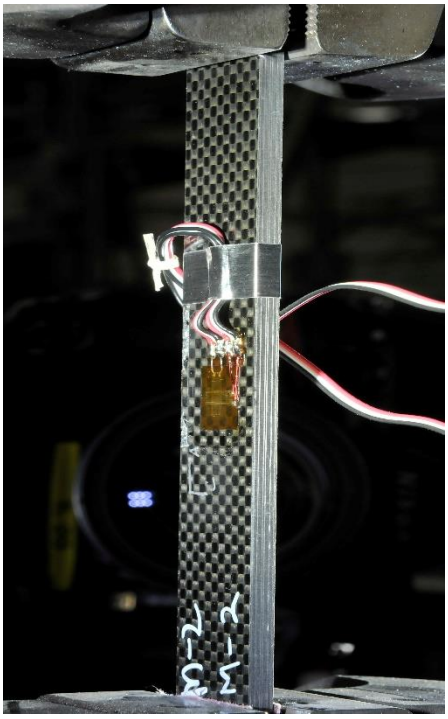

(A1-M-2) at 100 cycles

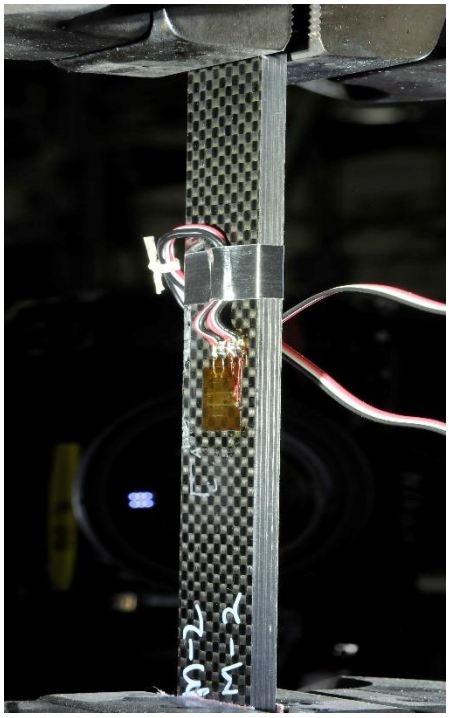

(A1-M-2) at 1K cycles

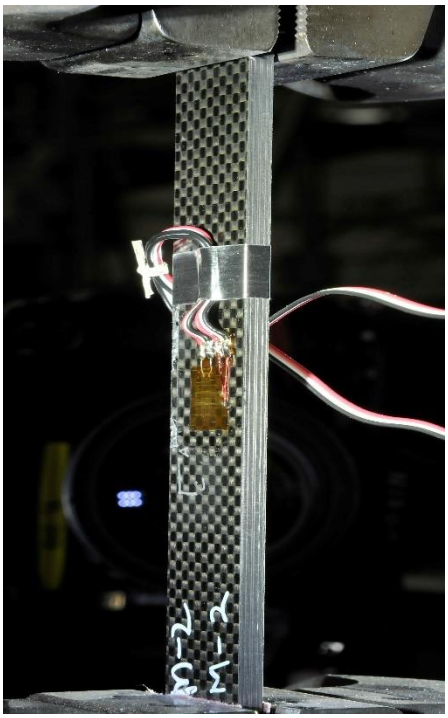

(A1-M-2) at 5K cycles

Figure C1.25 Damage Progression in (A1-M-2) Test Specimen at 5K cycles

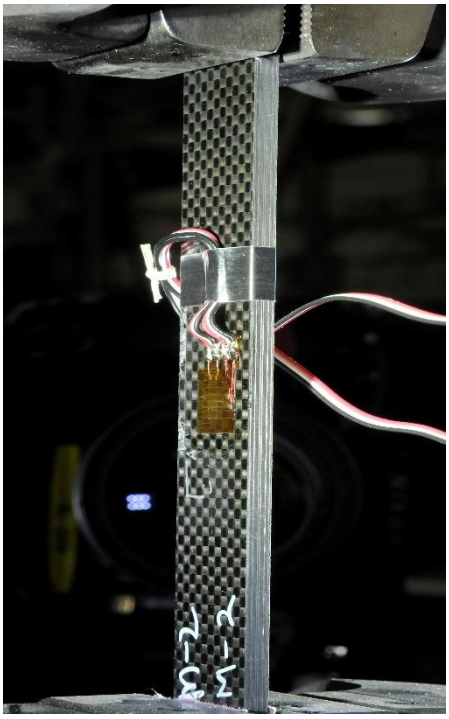

(A1-M-2) at 10K cycles

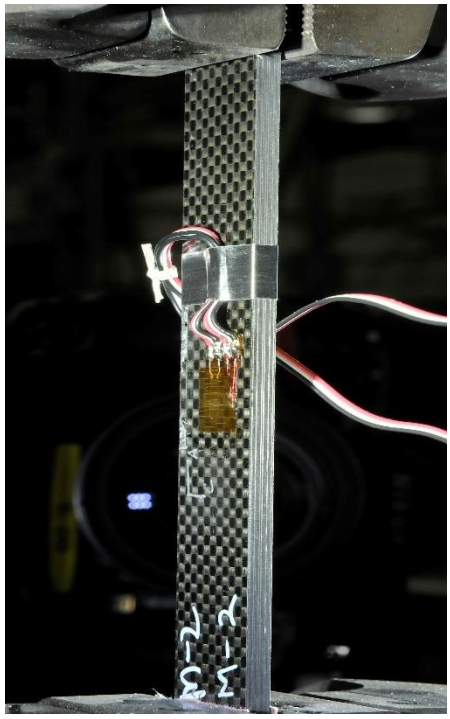

(A1-M-2) at 20K cycles

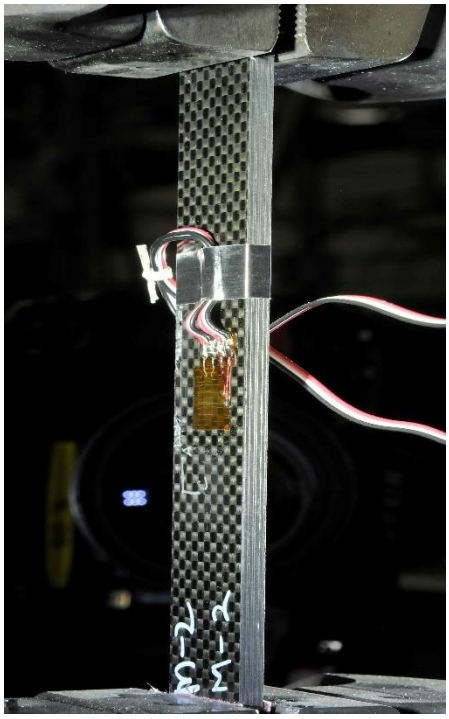

(A1-M-2) at 30K cycles

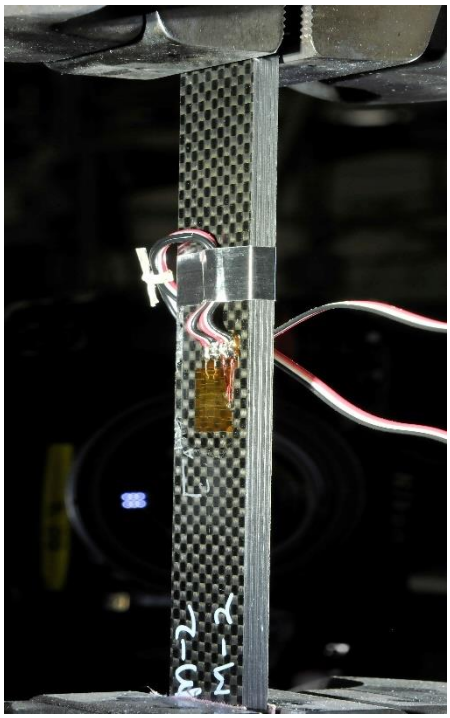

(A1-M-2) at 40K cycles

Figure C1.26 Damage Progression in (A1-M-2) Test Specimen at 40K cycles

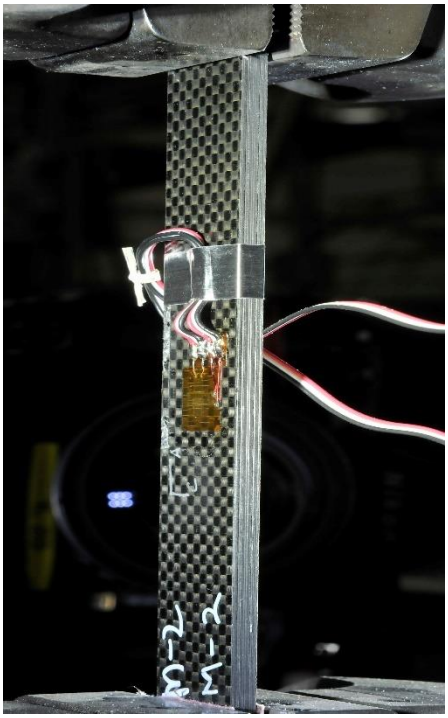

(A1-M-2) at 50K cycles

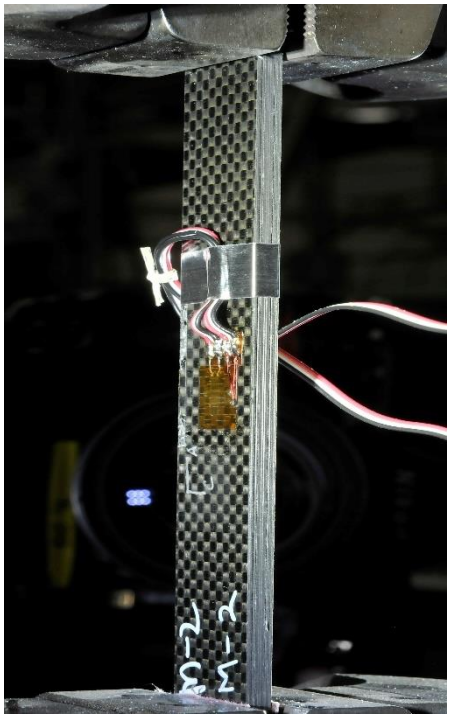

(A1-M-2) at 60K cycles

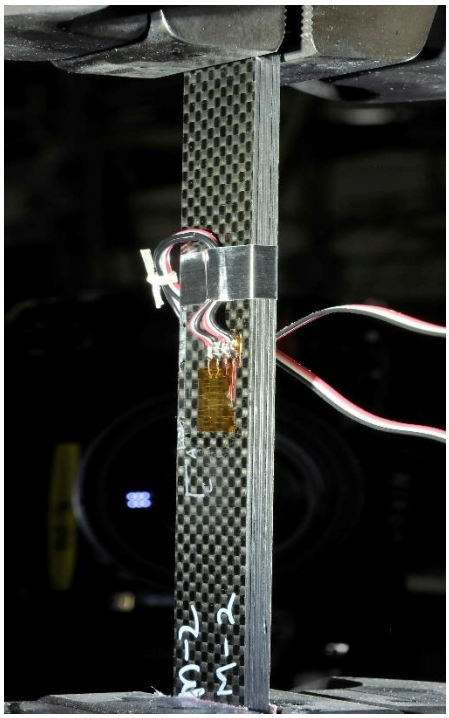

(A1-M-2) at 70K cycles

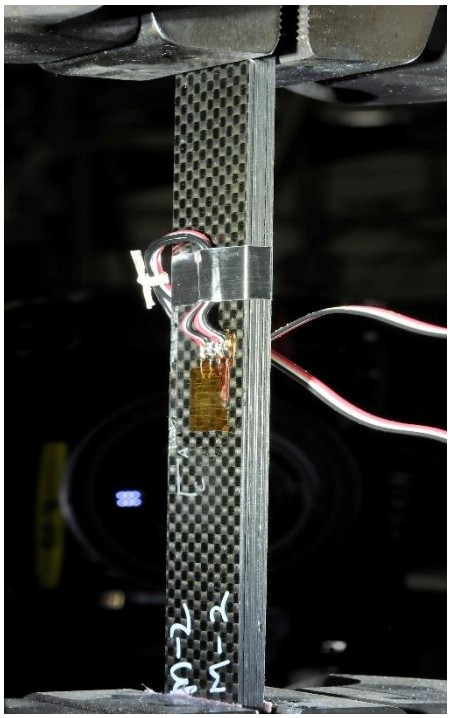

(A1-M-2) at 80K cycles

Figure C1.27 Damage Progression in (A1-M-2) Test Specimen at 80K cycles

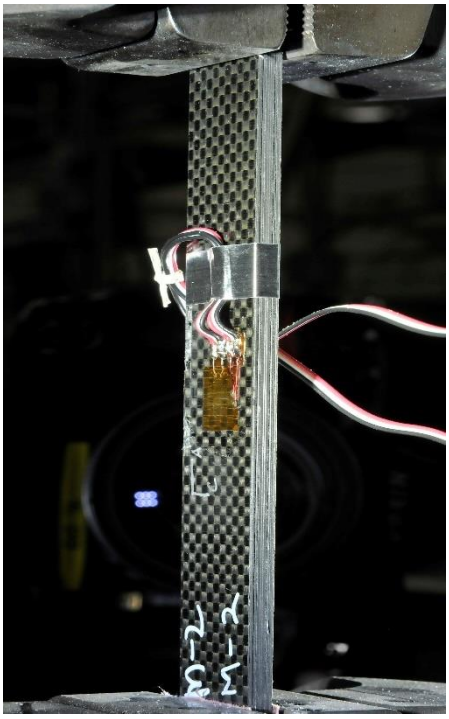

(A1-M-2) at 90K cycles

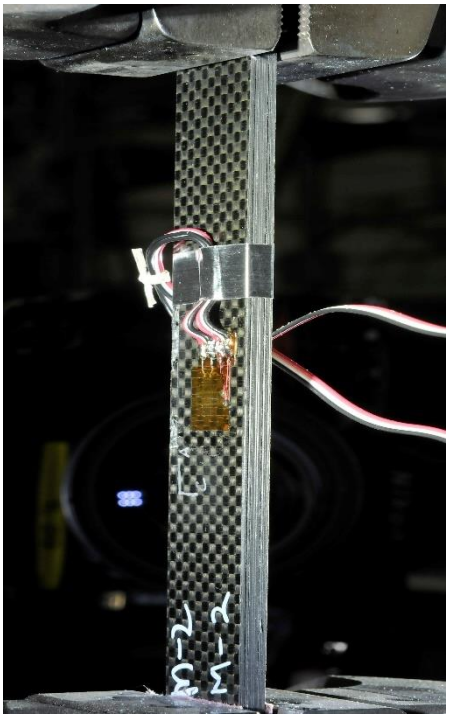

(A1-M-2) at 100K cycles

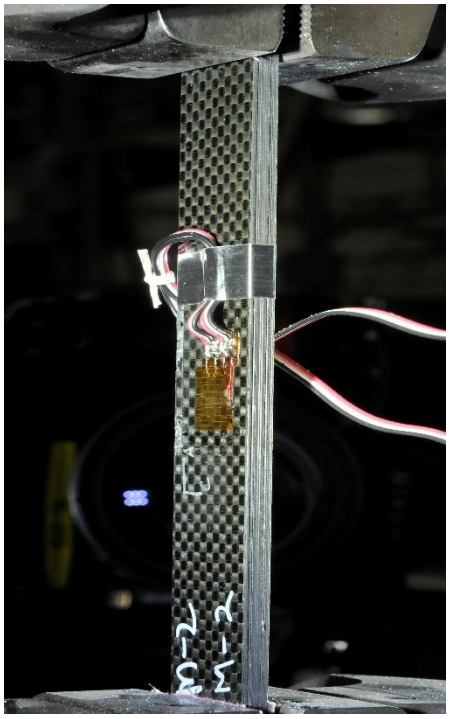

(A1-M-2) at 125K cycles

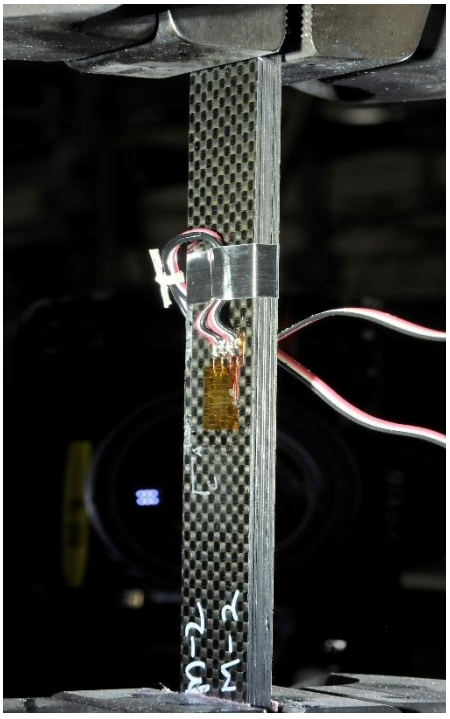

(A1-M-2) at 150K cycles

Figure C1.28 Damage Progression in (A1-M-2) Test Specimen at 150K cycles

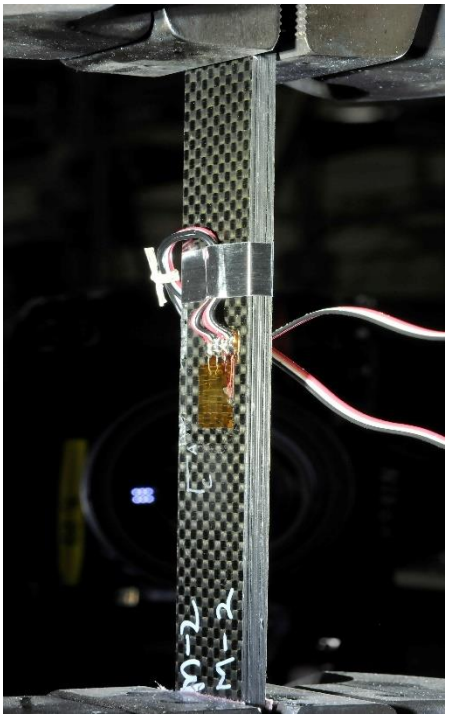

(A1-M-2) at 175K cycles

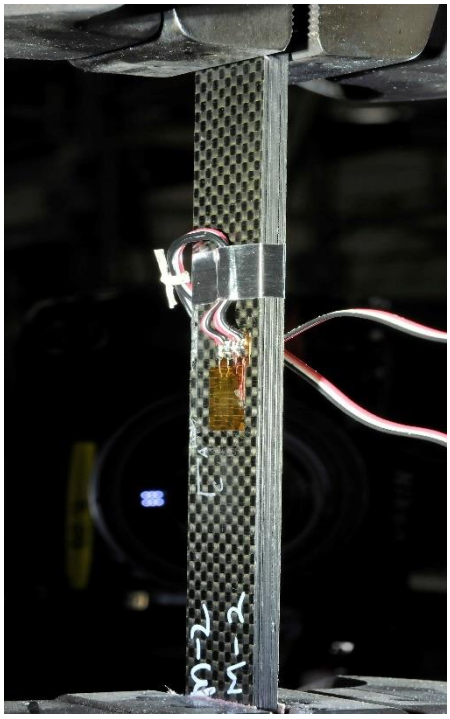

(A1-M-2) at 200K cycles

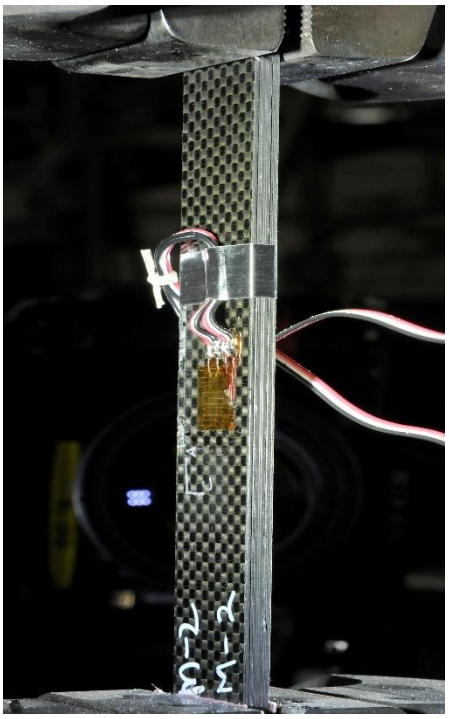

(A1-M-2) at 225K cycles

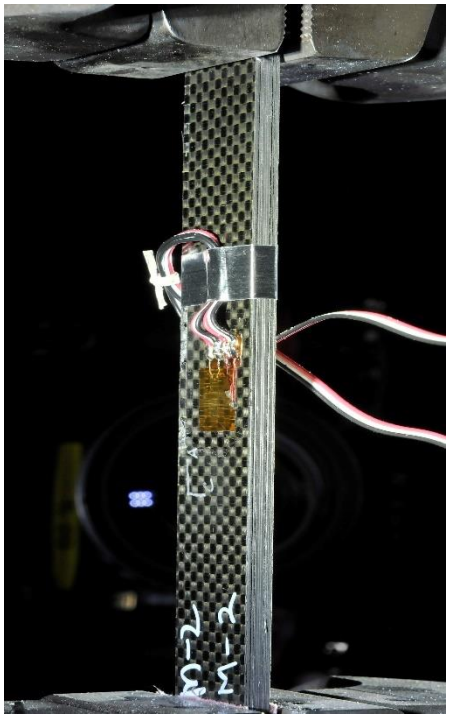

(A1-M-2) at 250K cycles

Figure C1.29 Damage Progression in (A1-M-2) Test Specimen at 250K cycles

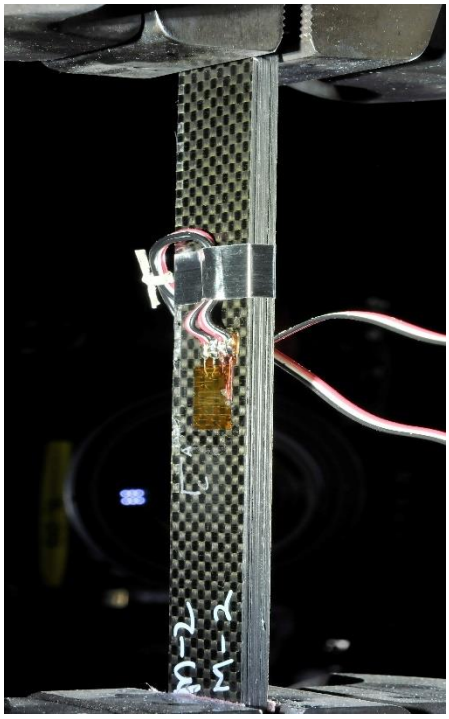

(A1-M-2) at 275K cycles

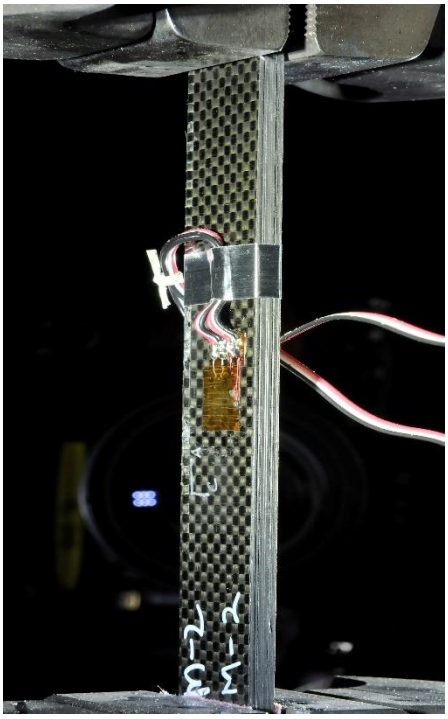

(A1-M-2) at 300K cycles

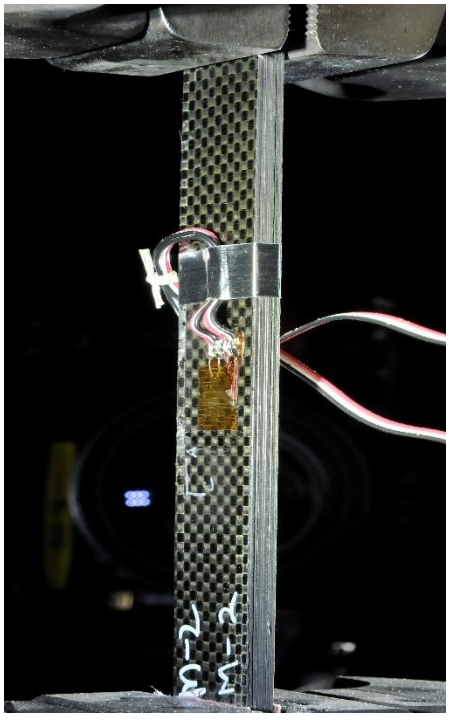

(A1-M-2) at 325K cycles

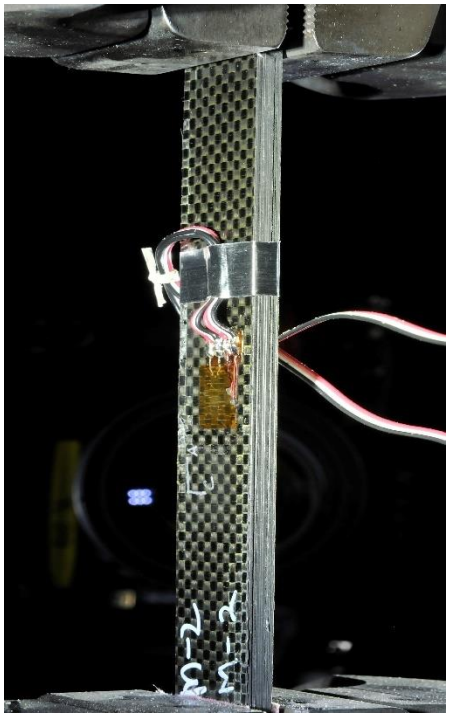

(A1-M-2) at 350K cycles

Figure C1.30 Damage Progression in (A1-M-2) Test Specimen at 350K cycles

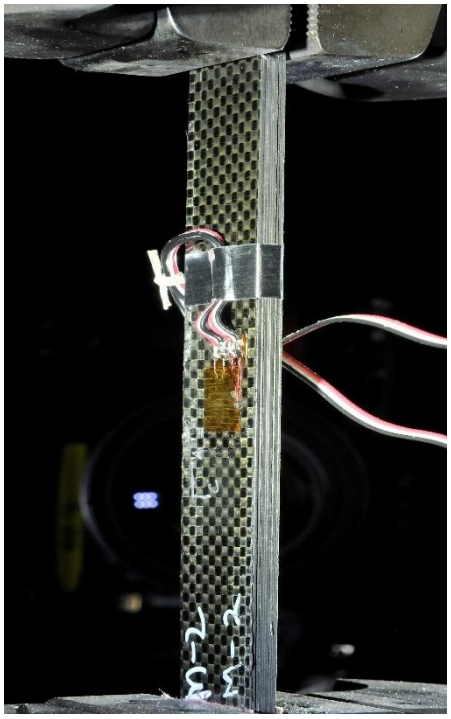

(A1-M-2) at 375K cycles

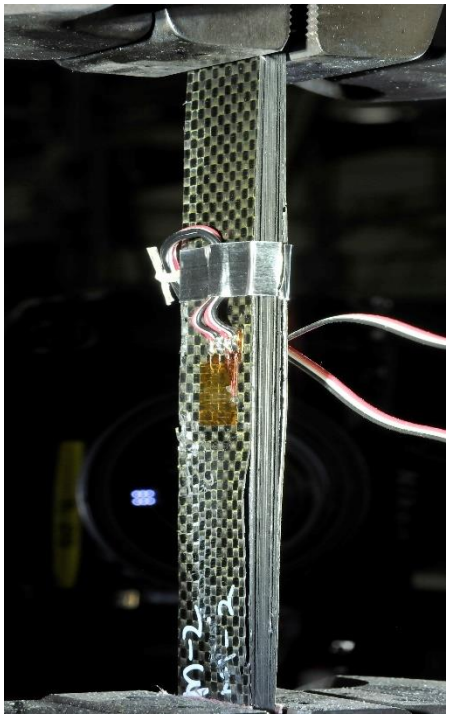

(A1-M-2) at 400K cycles

(A1-M-2) at Failure

Figure C1.31 Damage Progression in (A1-M-2) Test Specimen at Failure

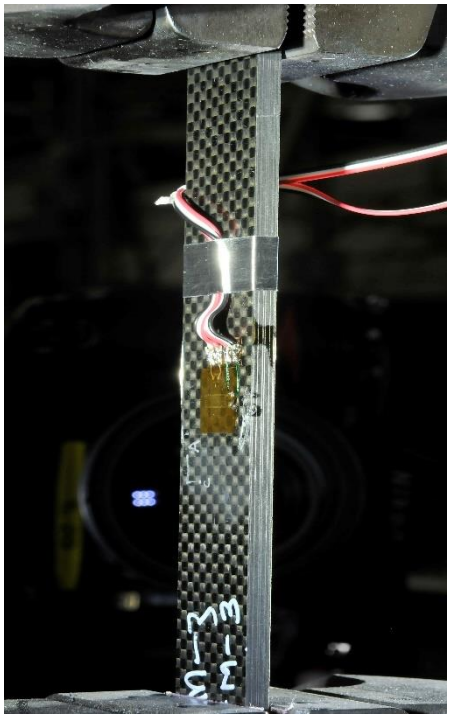

(A1-M-3) at 1 cycle

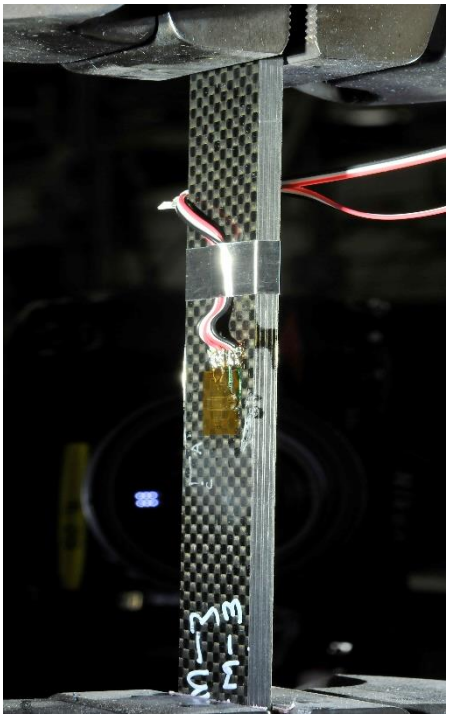

(A1-M-3) at 100 cycle

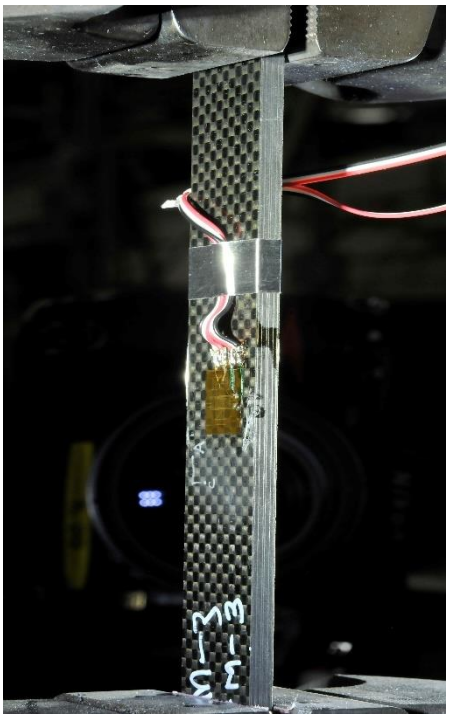

(A1-M-3) at 1K cycles

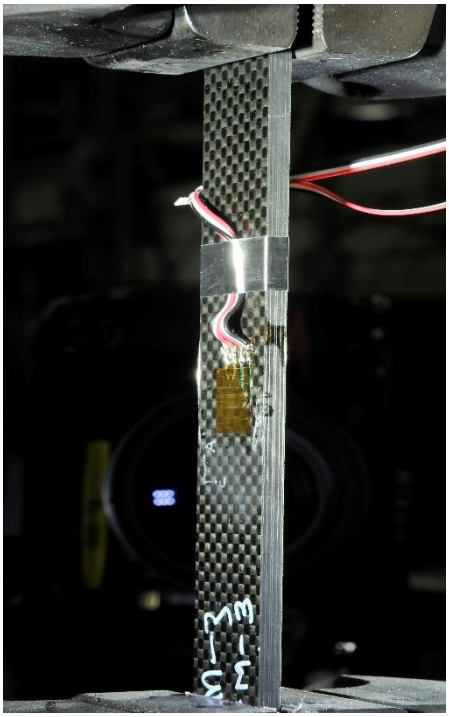

(A1-M-3) at 5K cycles

Figure C1.32 Damage Progression in (A1-M-3) Test Specimen at 5K cycles

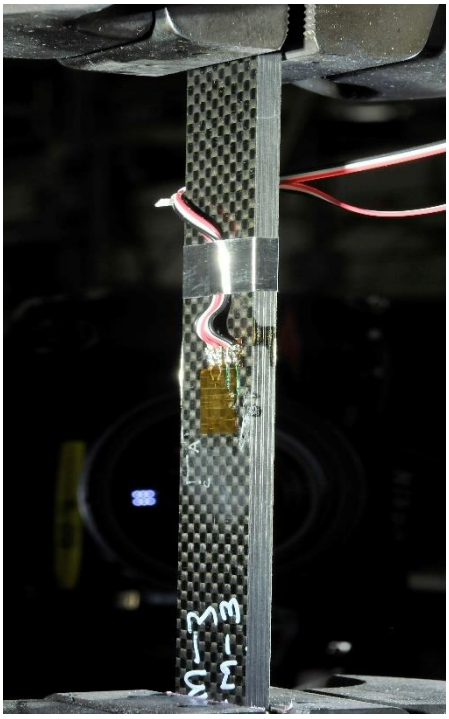

(A1-M-3) at 10K cycles

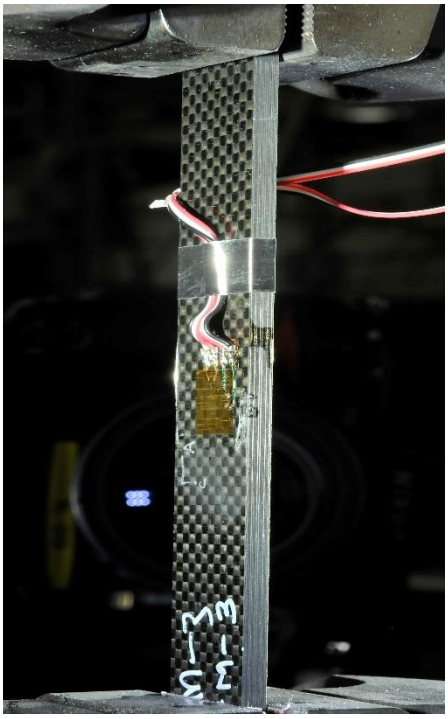

(A1-M-3) at 20K cycles

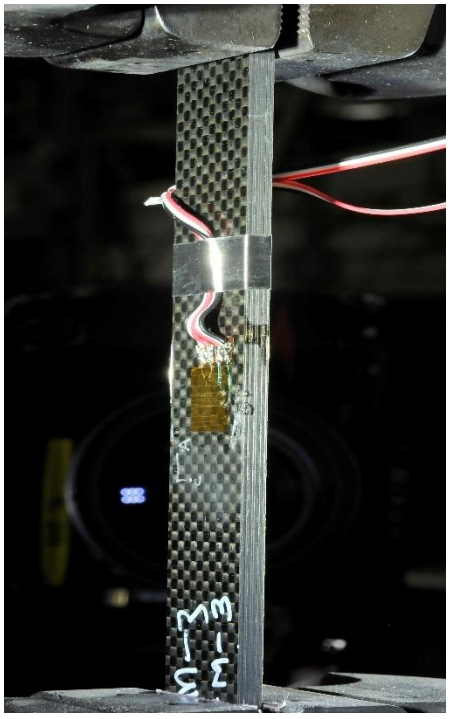

(A1-M-3) at 30K cycles

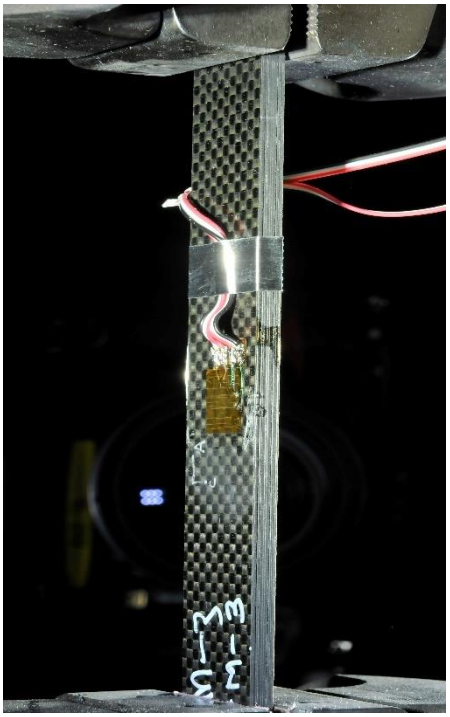

(A1-M-3) at 40K cycles

Figure C1.33 Damage Progression in (A1-M-3) Test Specimen at 40K cycles

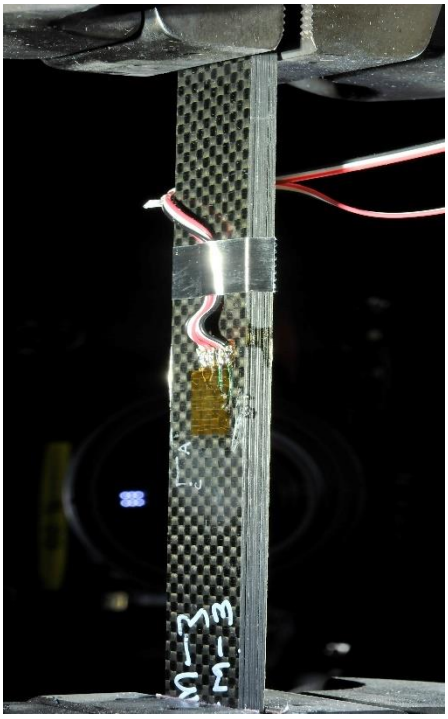

(A1-M-3) at 50K cycles

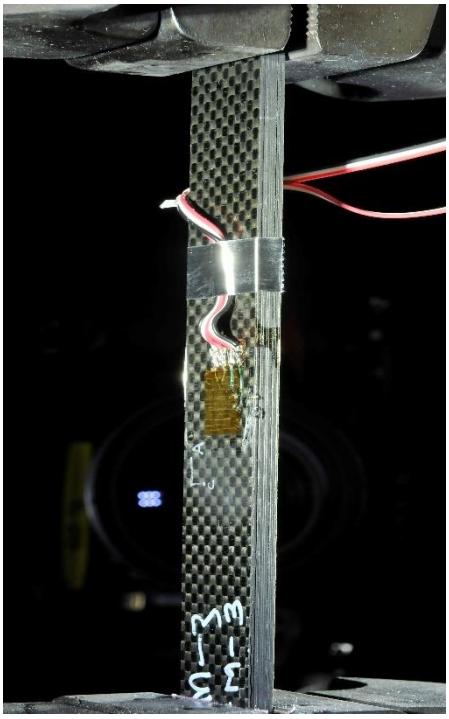

(A1-M-3) at 60K cycles

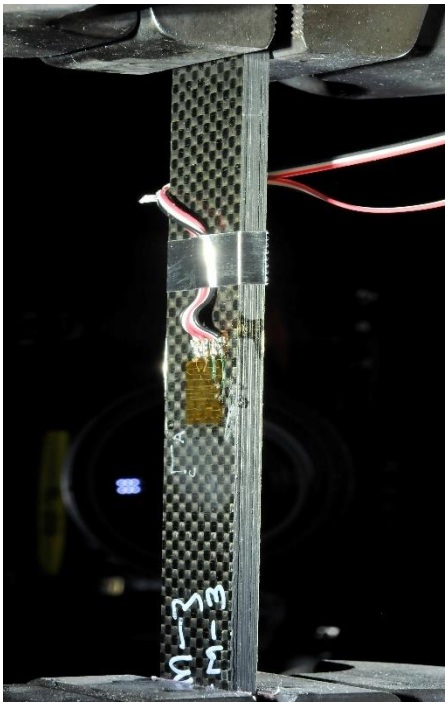

(A1-M-3) at 70K cycles

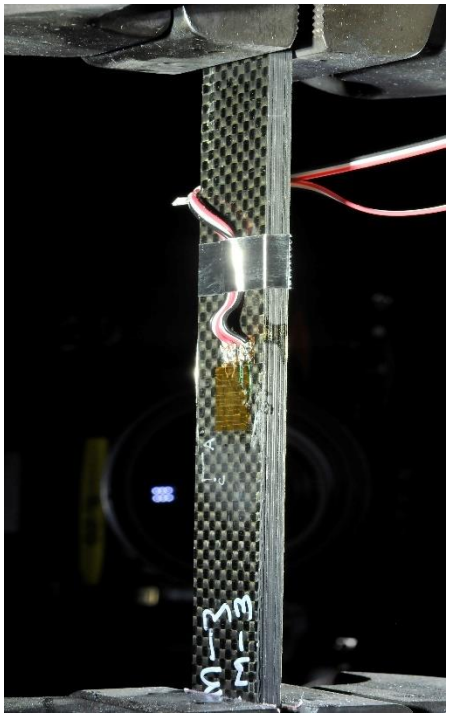

(A1-M-3) at 80K cycles

Figure C1.34 Damage Progression in (A1-M-3) Test Specimen at 80K cycles

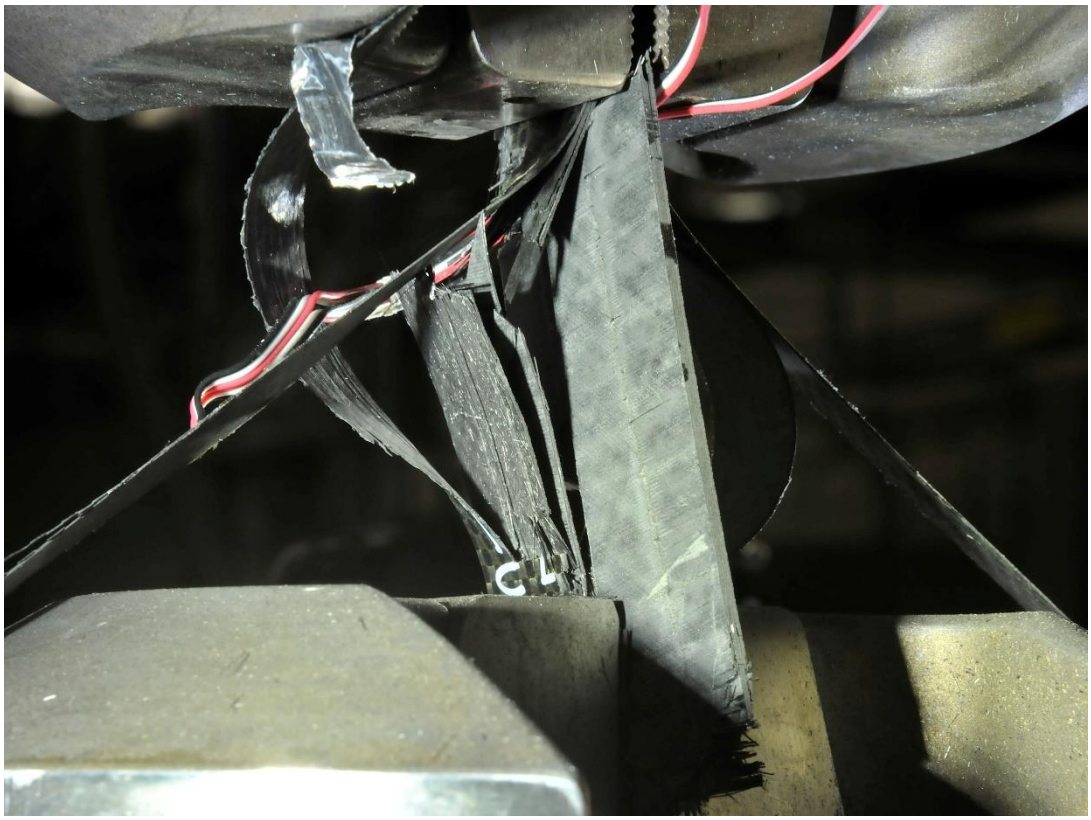

(A1-M-3) at Failure

Figure C1.35 Damage Progression in (A1-M-3) Test Specimen at Failure

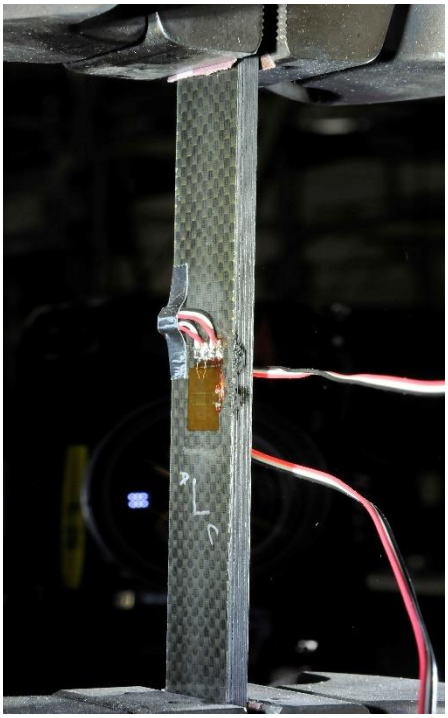

(B1-M-1) at 1 cycle

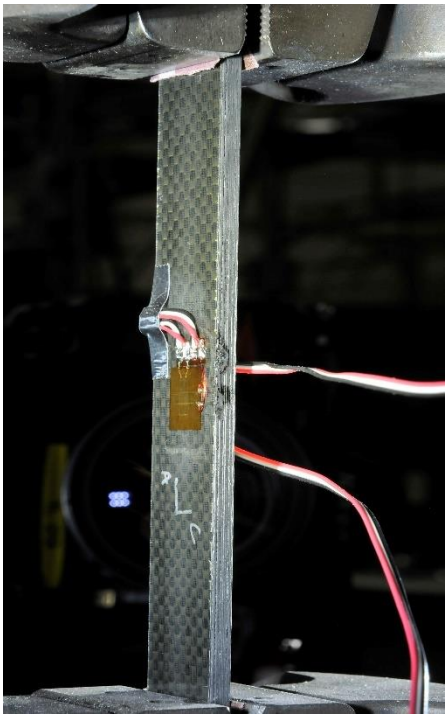

(B1-M-1) at 100 cycles

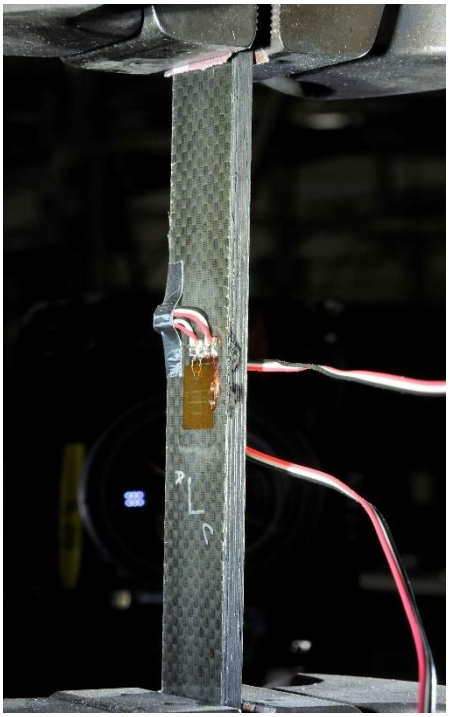

(B1-M-1) at 1K cycles

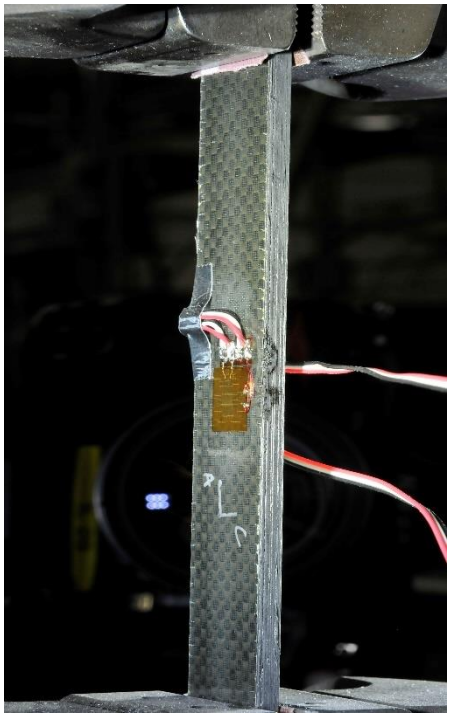

(B1-M-1) at 5K cycles

Figure C1.36 Damage Progression in (B1-M-1) Test Specimen at 5K cycles

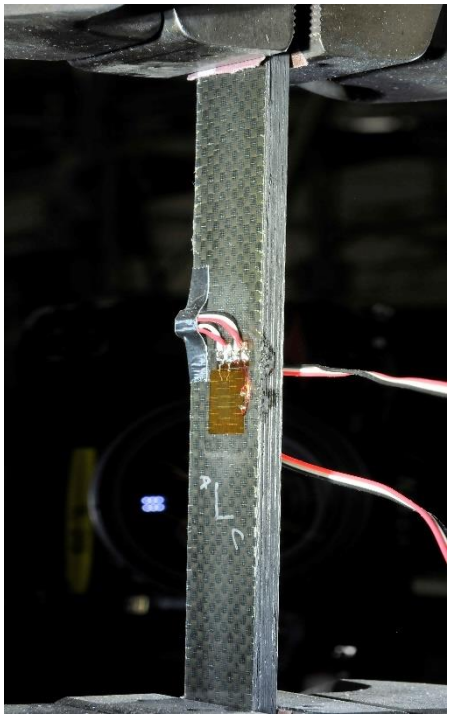

(B1-M-1) at 10K cycles

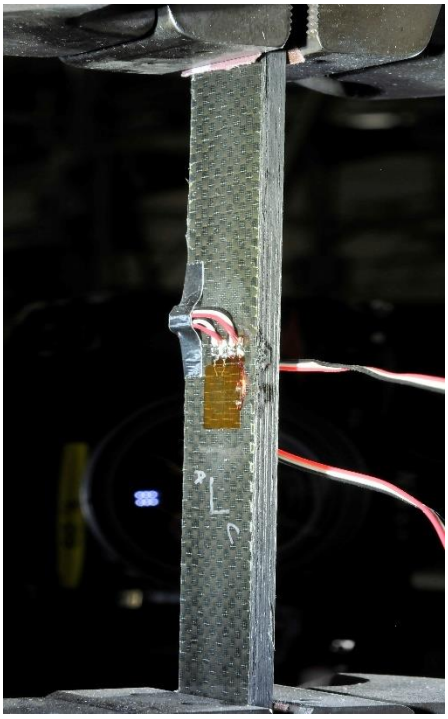

(B1-M-1) at 20K cycles

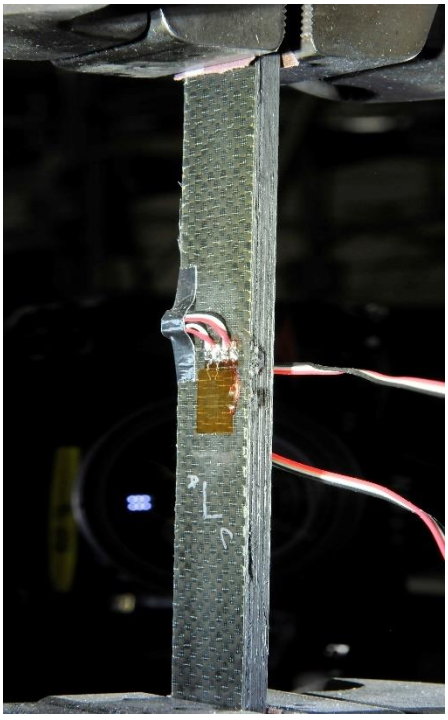

(B1-M-1) at 30K cycles

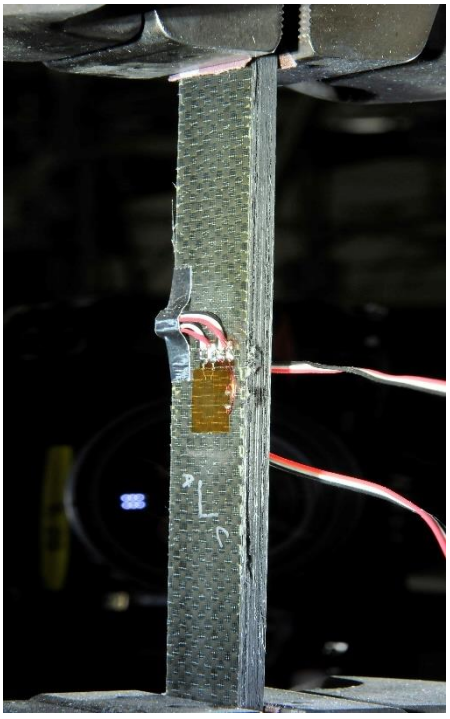

(B1-M-1) at 40K cycles

Figure C1.37 Damage Progression in (B1-M-1) Test Specimen at 40K cycles

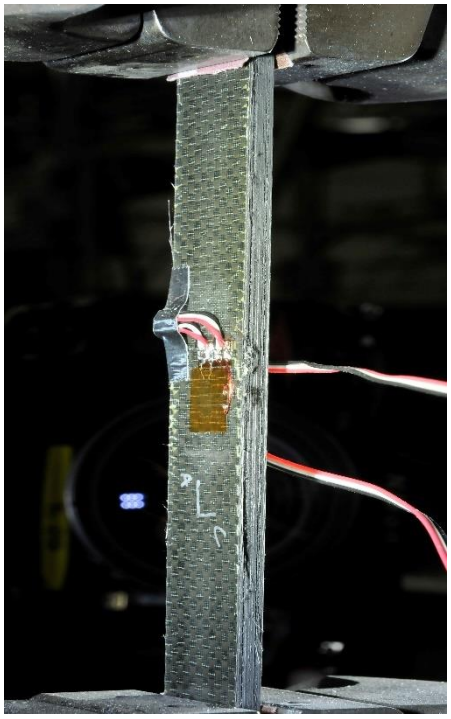

(B1-M-1) at 50K cycles

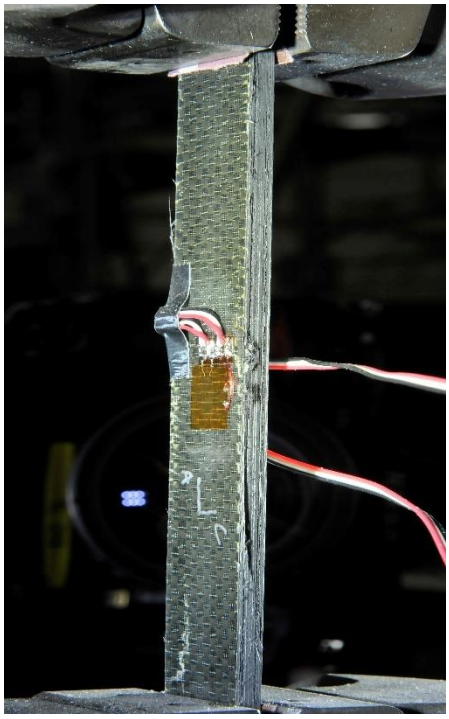

(B1-M-1) at 60K cycles

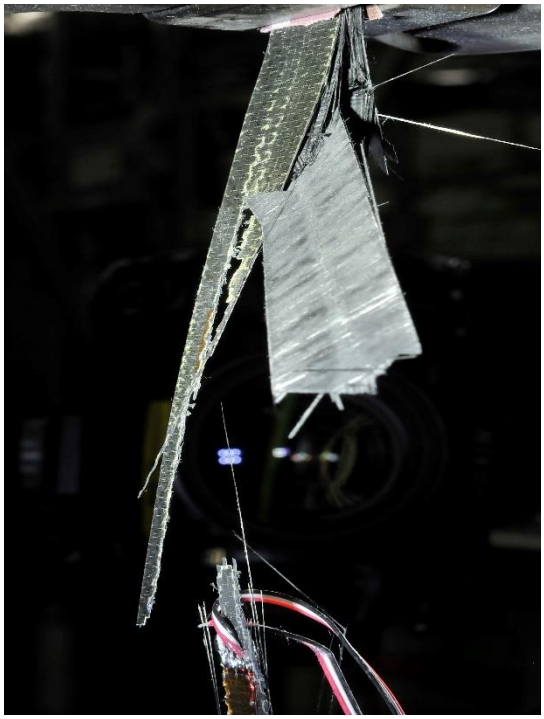

(B1-M-1) at Failure

Figure C1.38 Damage Progression in (B1-M-1) Test Specimen at Failure

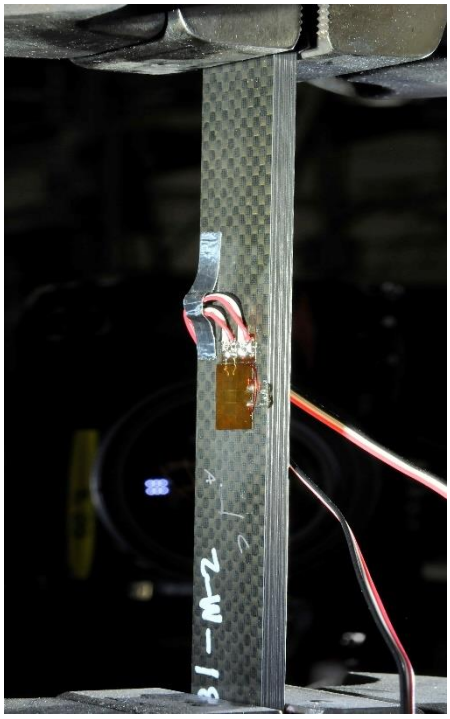

(B1-M-2) at 1 cycle

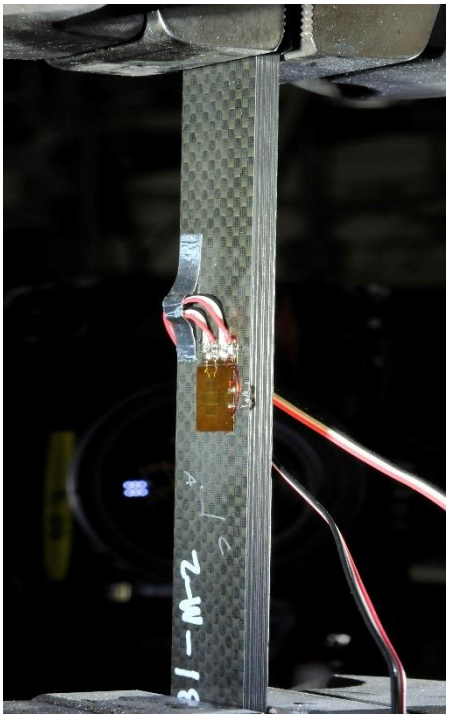

(B1-M-2) at 100 cycle

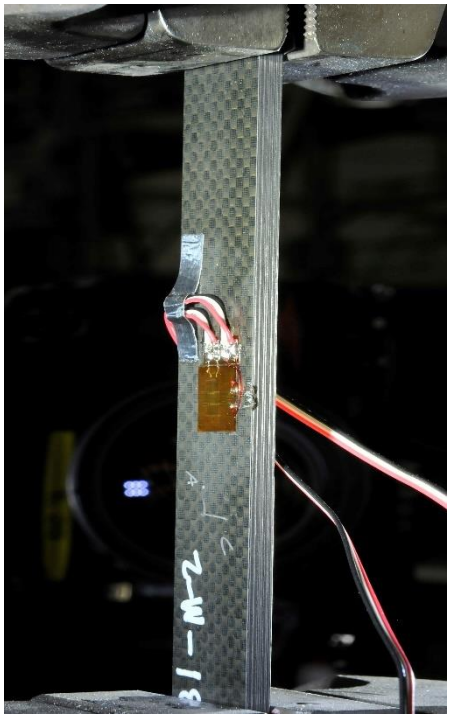

(B1-M-2) at 1K cycles

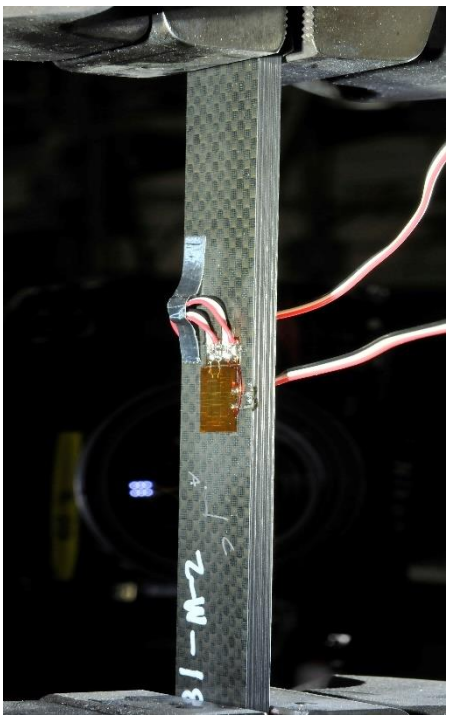

(B1-M-2) at 5K cycles

Figure C1.39 Damage Progression in (B1-M-2) Test Specimen at 5K cycles

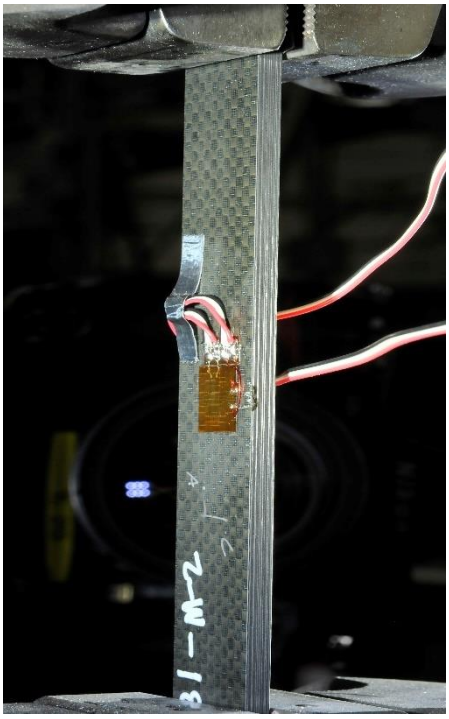

(B1-M-2) at 10K cycles

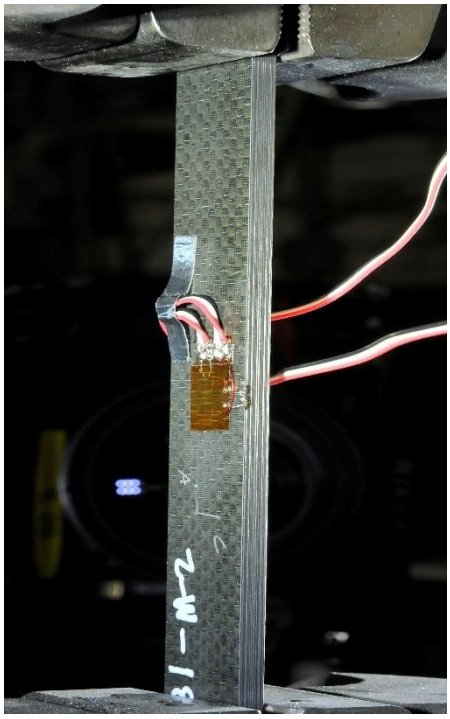

(B1-M-2) at 20K cycles

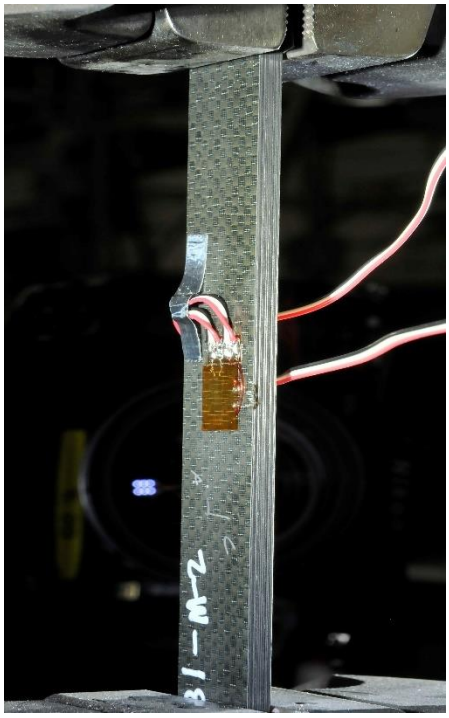

(B1-M-2) at 30K cycles

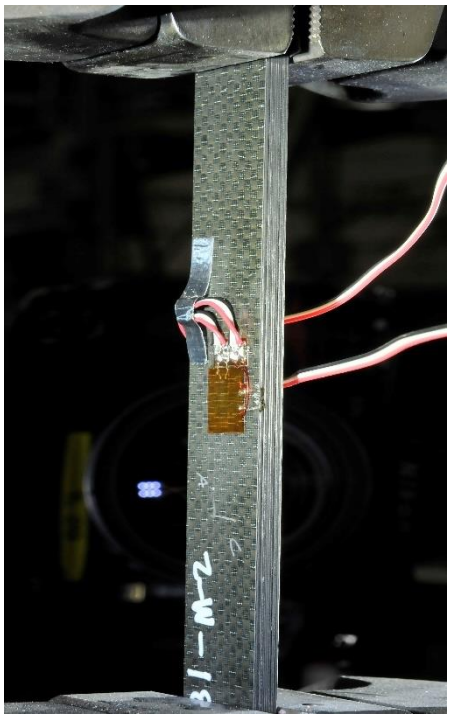

(B1-M-2) at 40K cycles

Figure C1.40 Damage Progression in (B1-M-2) Test Specimen at 40K cycles

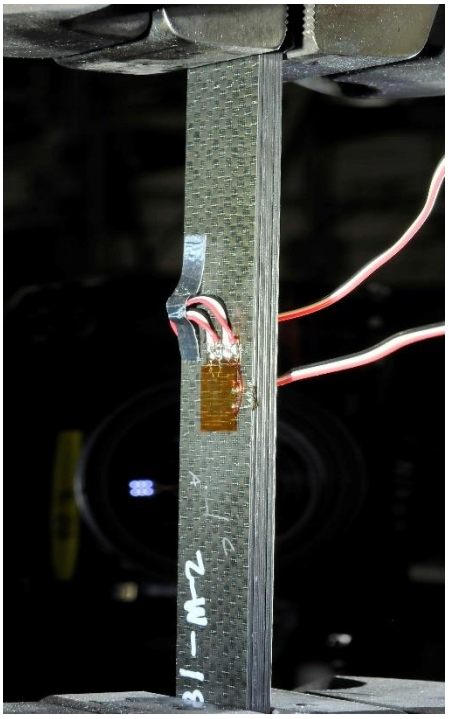

(B1-M-2) at 50K cycles

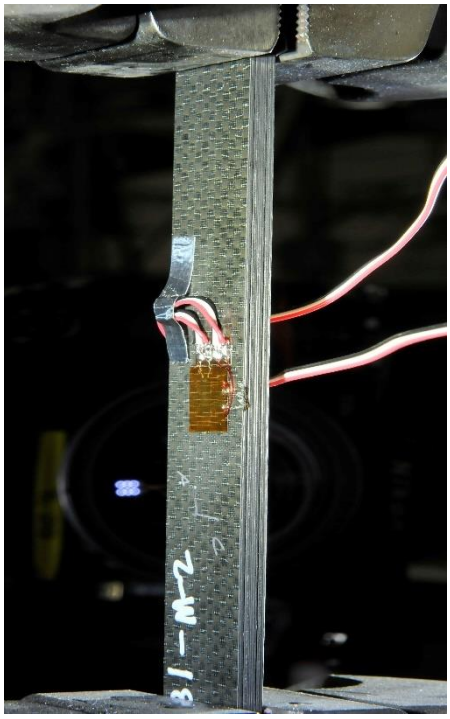

(B1-M-2) at 60K cycles

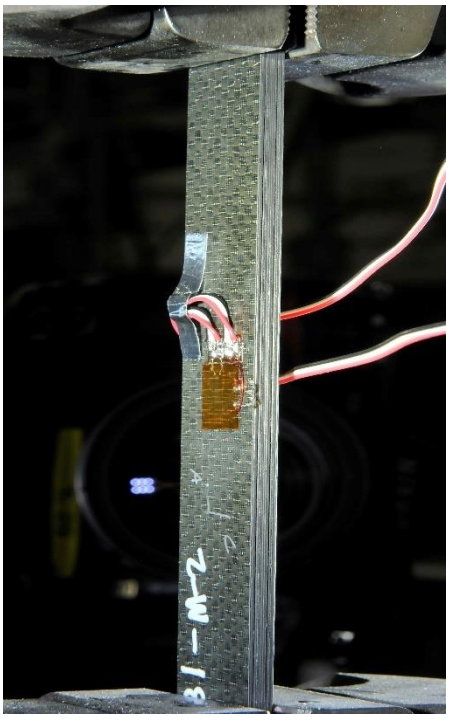

(B1-M-2) at 70K cycles

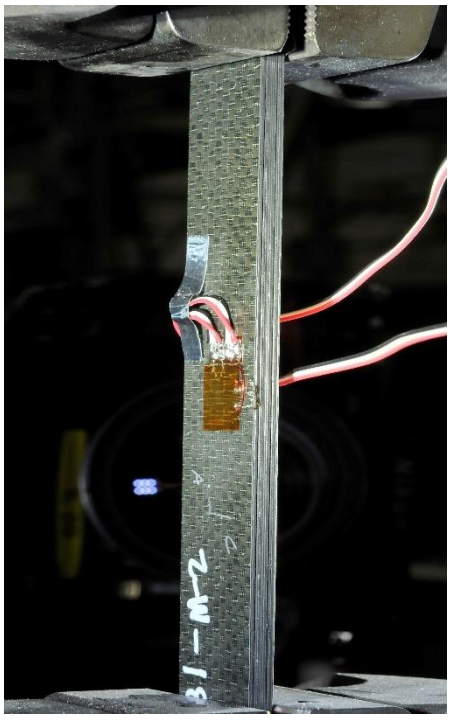

(B1-M-2) at 80K cycles

Figure C1.41 Damage Progression in (B1-M-2) Test Specimen at 80K cycles

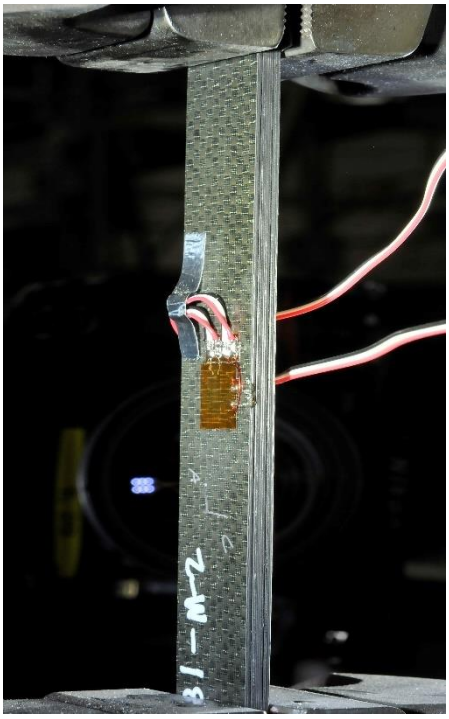

(B1-M-2) at 90K cycles

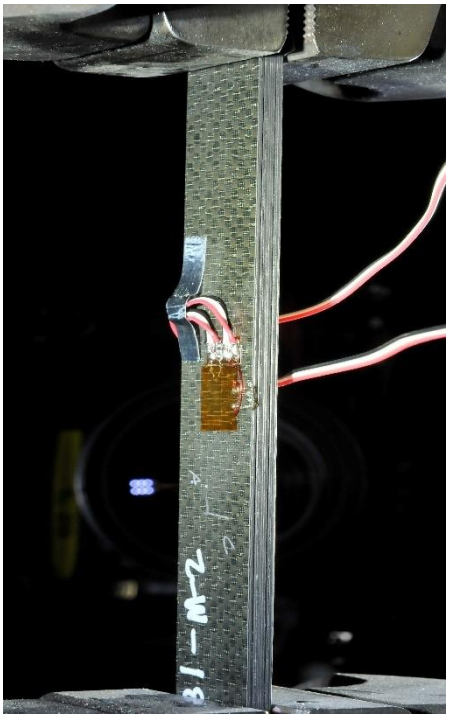

(B1-M-2) at 100K cycles

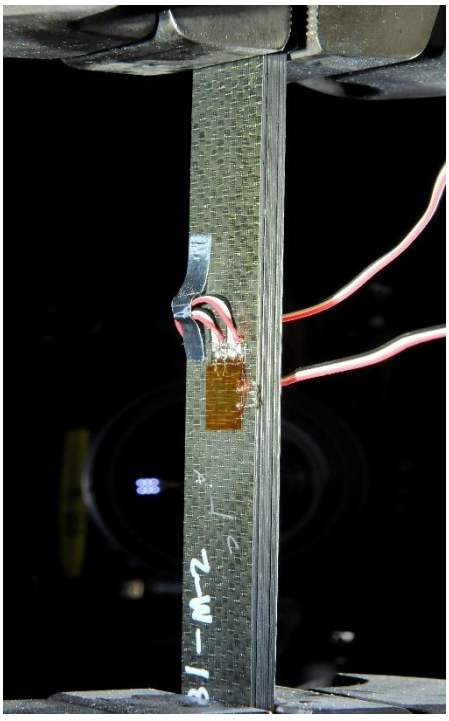

(B1-M-2) at 125K cycles

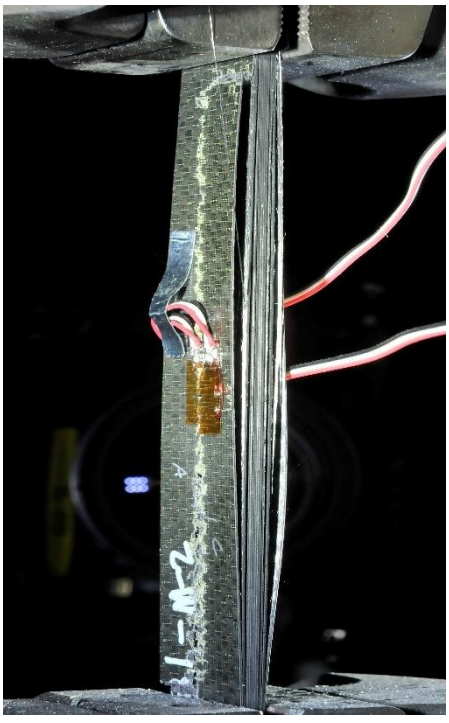

(B1-M-2) at 150K cycles

Figure C1.42 Damage Progression in (B1-M-2) Test Specimen at 150K cycles

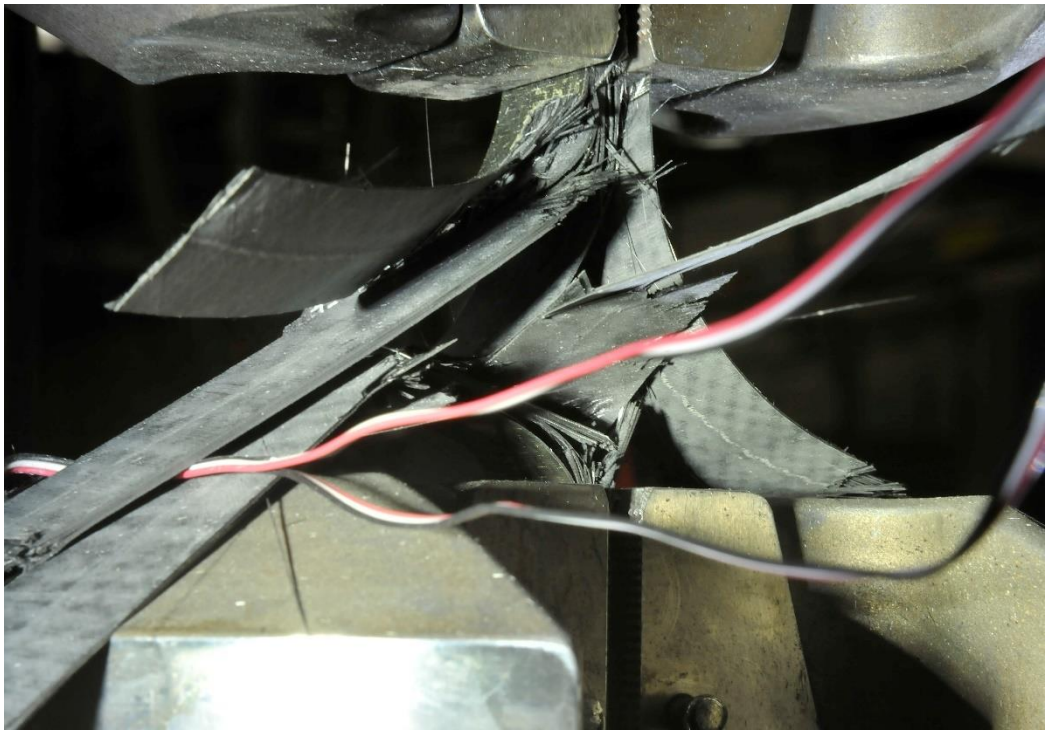

(B1-M-2) at Failure

Figure C1.43 Damage Progression in (B1-M-2) Test Specimen at Failure

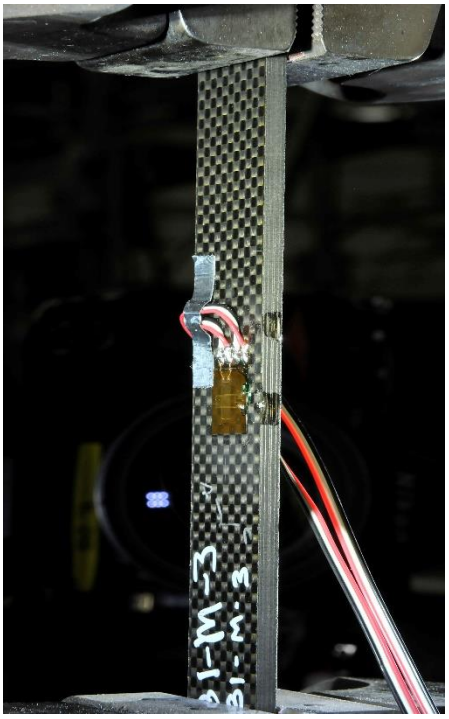

(B1-M-3) at 1 cycle

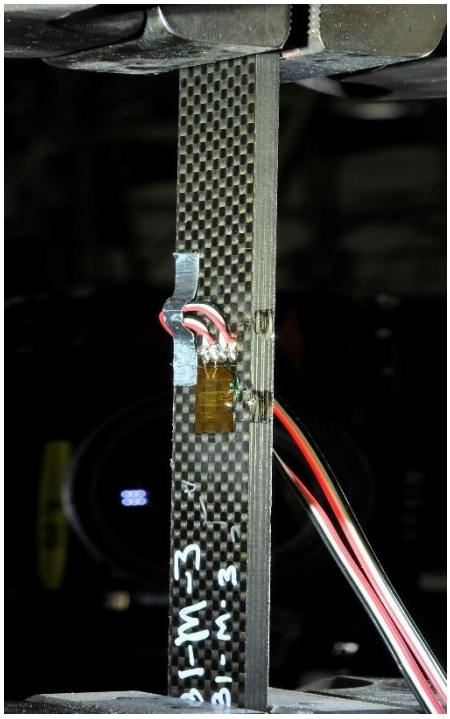

(B1-M-3) at 100 cycles

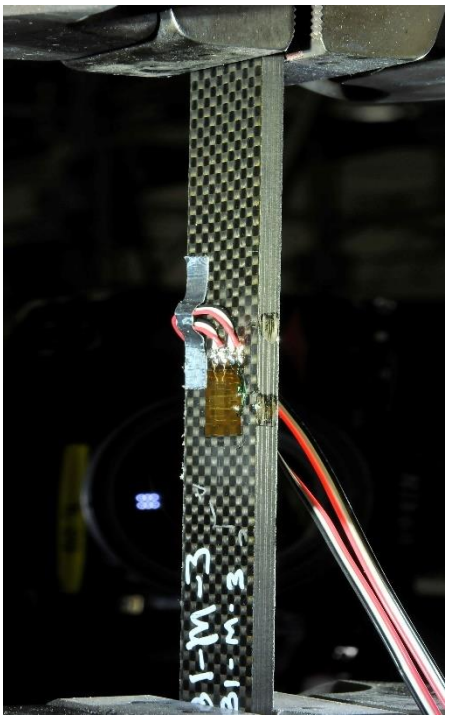

(B1-M-3) at 1K cycles

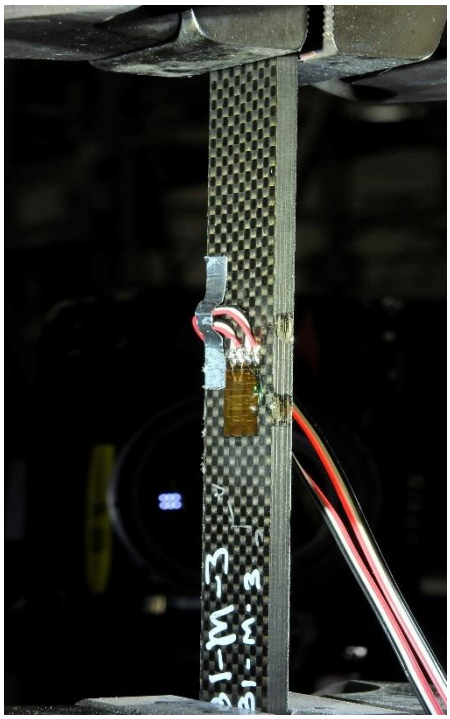

(B1-M-3) at 5K cycles

Figure C1.44 Damage Progression in (B1-M-3) Test Specimen at 5K cycles

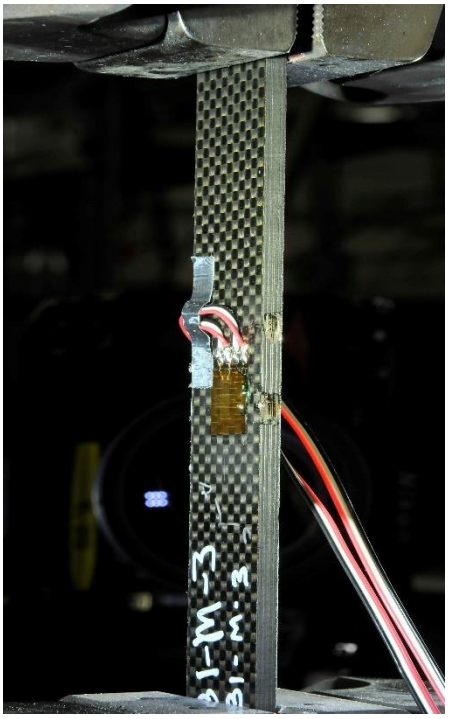

(B1-M-3) at 10K cycles

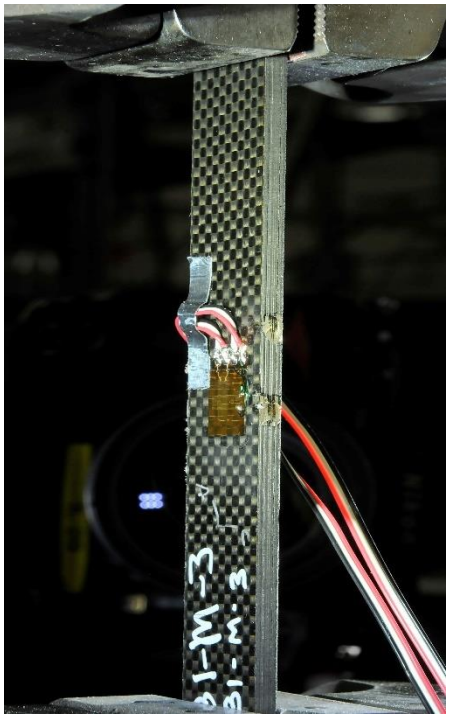

(B1-M-3) at 20K cycles

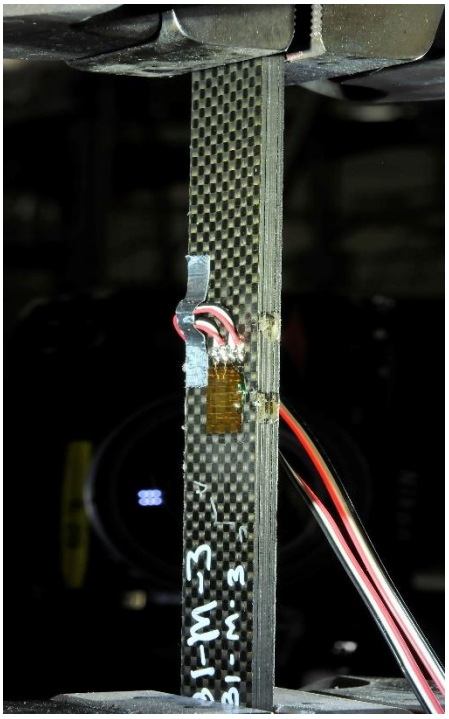

(B1-M-3) at 30K cycles

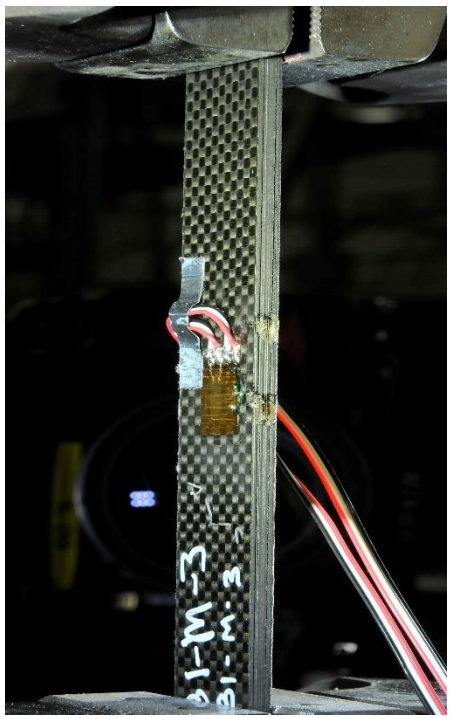

(B1-M-3) at 40K cycles

Figure C1.45 Damage Progression in (B1-M-3) Test Specimen at 40K cycles

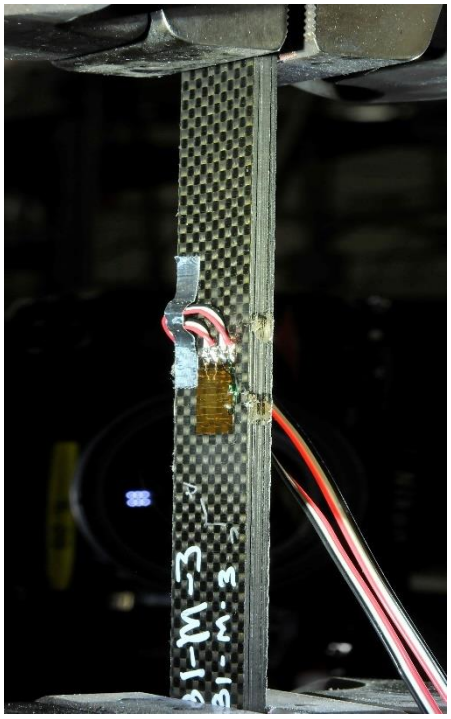

(B1-M-3) at 50K cycles

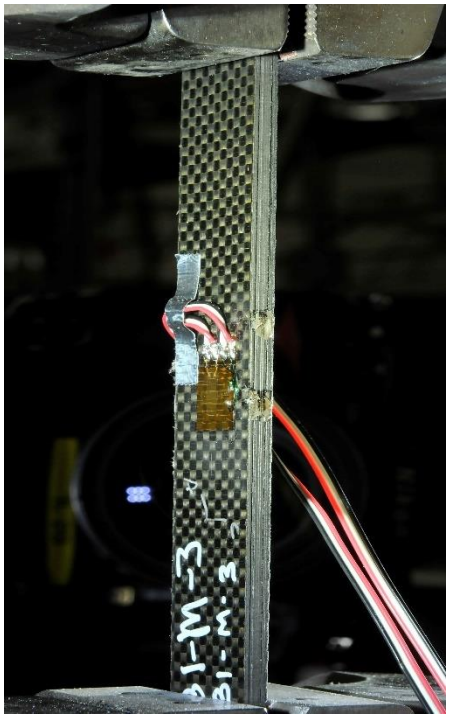

(B1-M-3) at 60K cycles

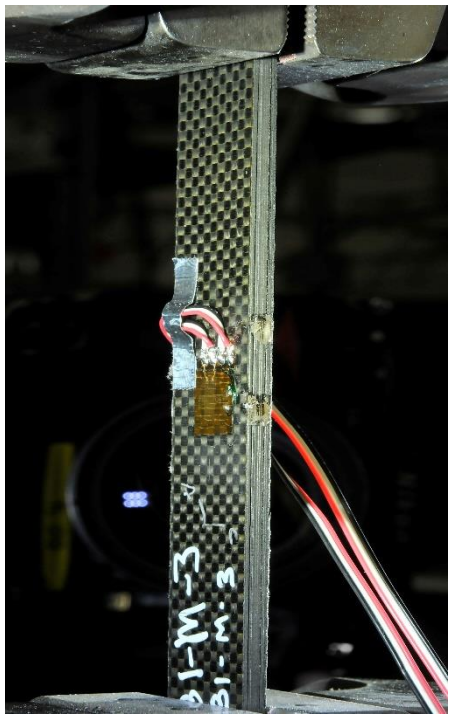

(B1-M-3) at 70K cycles

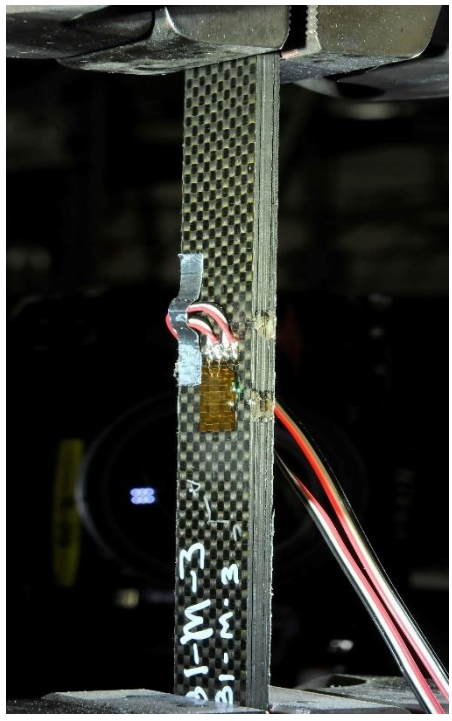

(B1-M-3) at 80K cycles

Figure C1.46 Damage Progression in (B1-M-3) Test Specimen at 80K cycles

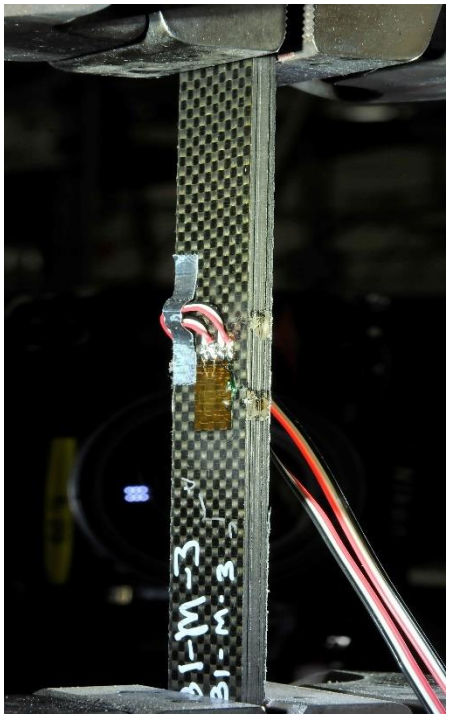

(B1-M-3) at 90K cycles

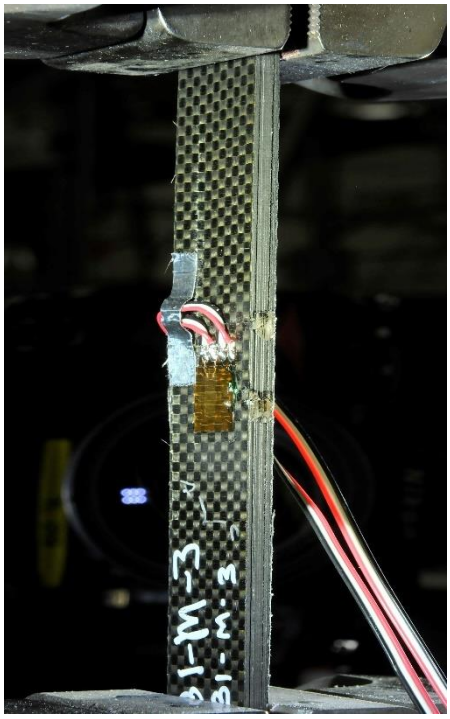

(B1-M-3) at 100K cycles

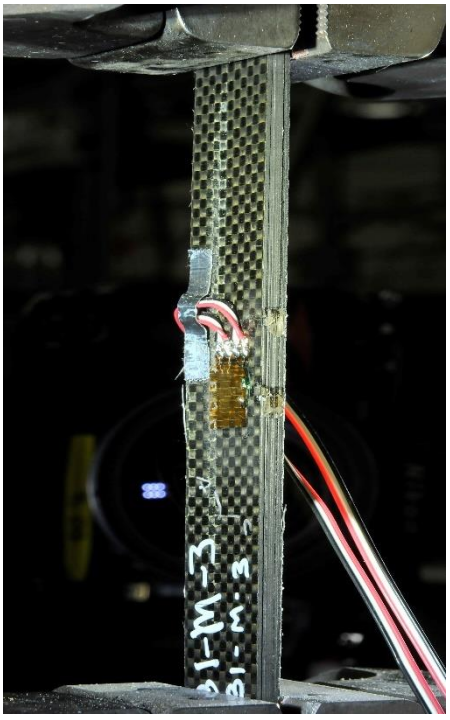

(B1-M-3) at 125K cycles

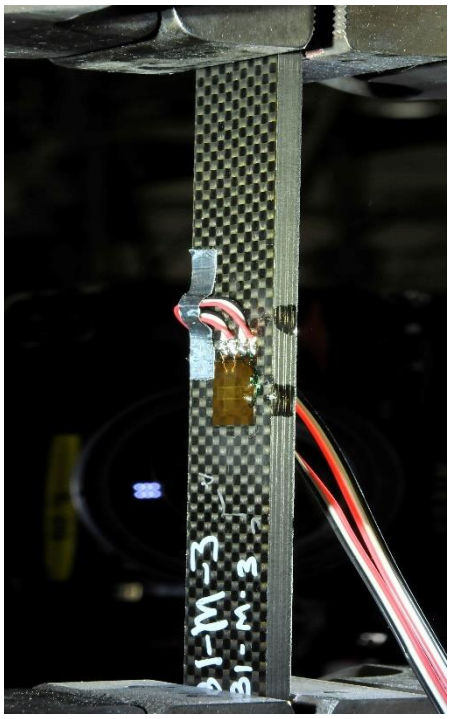

(B1-M-3) at 150K cycles

Figure C1.47 Damage Progression in (B1-M-3) Test Specimen at 150K cycles

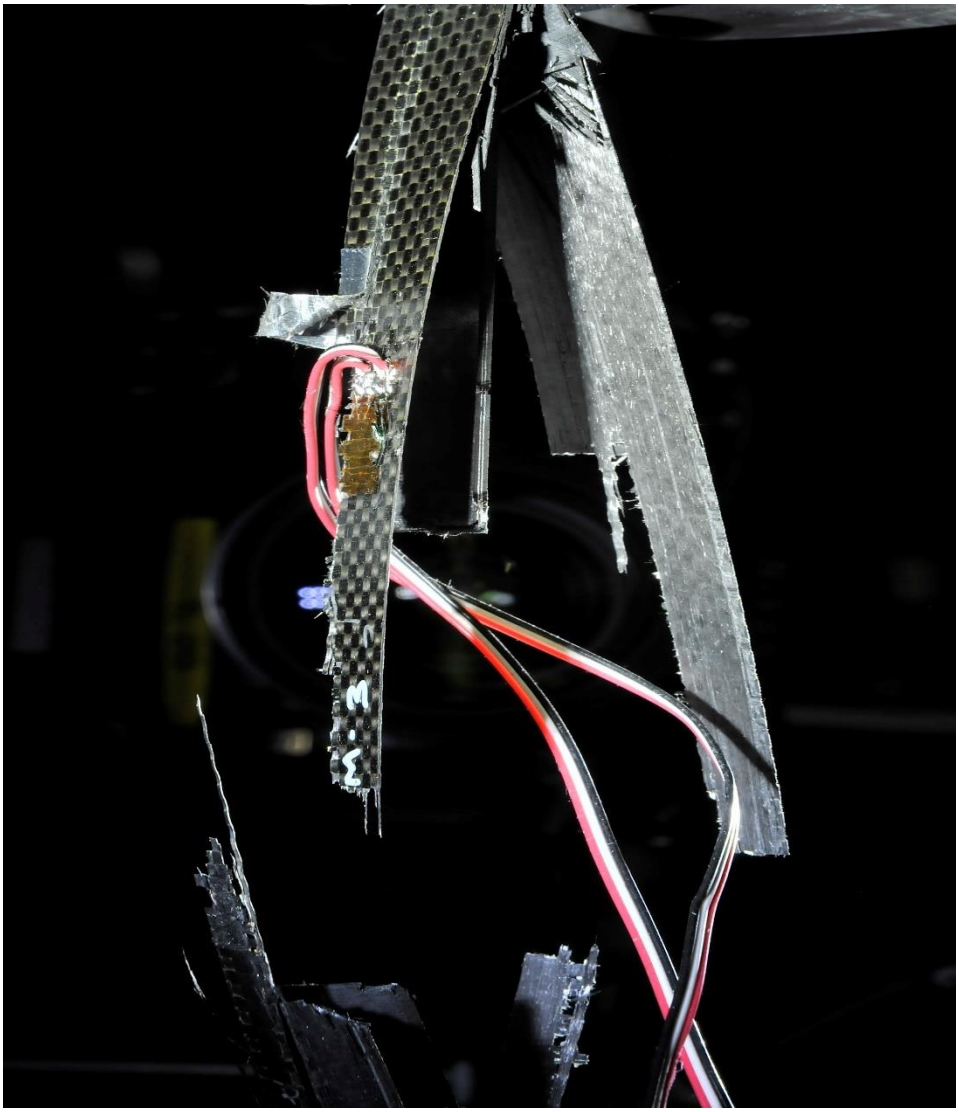

(B1-M-3) at Failure

Figure C1.48 Damage Progression in (B1-M-3) Test Specimen at Failure

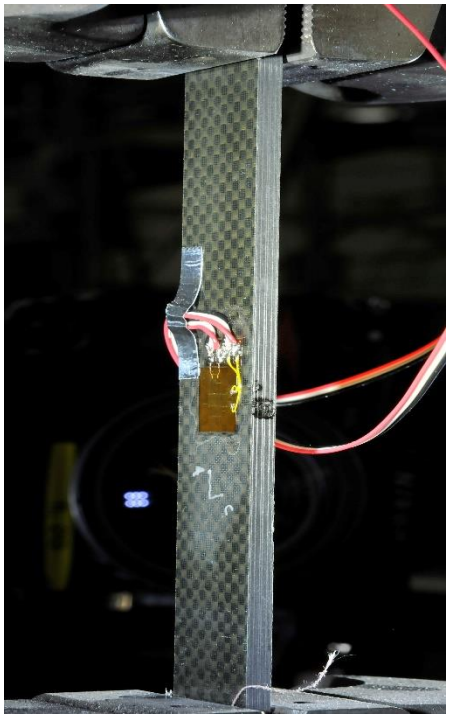

(A1-L-1) at 1 cycle

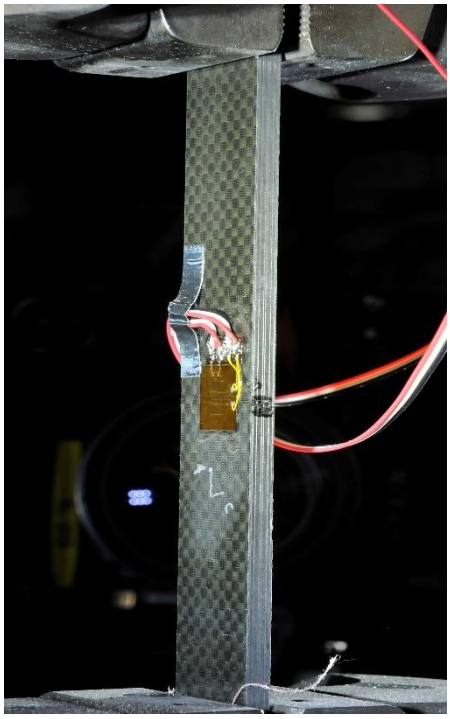

(A1-L-1) at 100 cycles

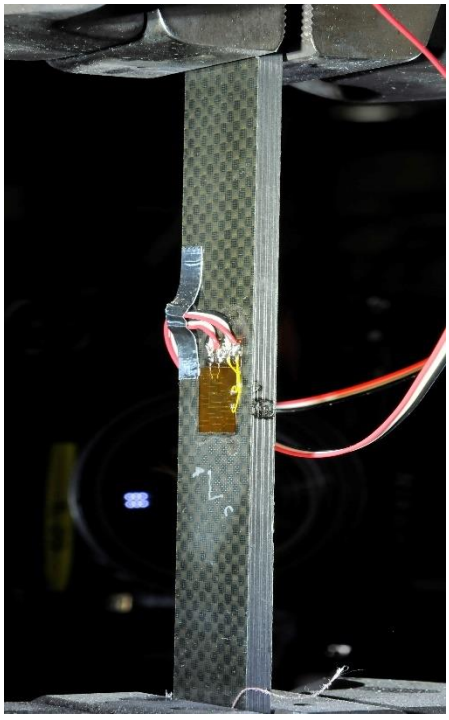

(A1-L-1) at 1K cycles

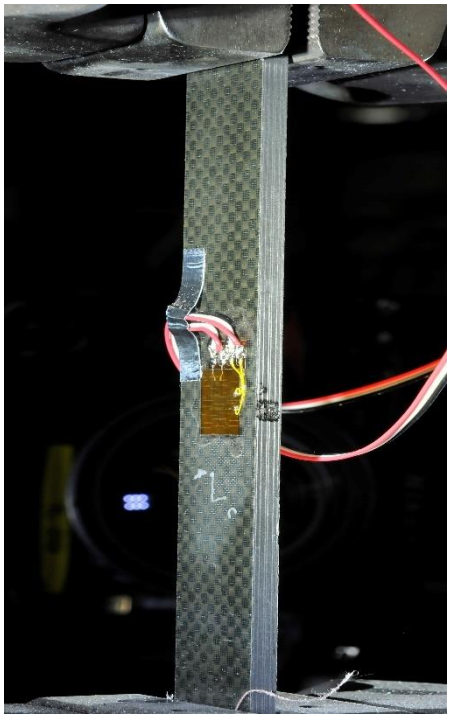

(A1-L-1) at 5K cycles

Figure C1.49 Damage Progression in (A1-L-1) Test Specimen at 5K cycles

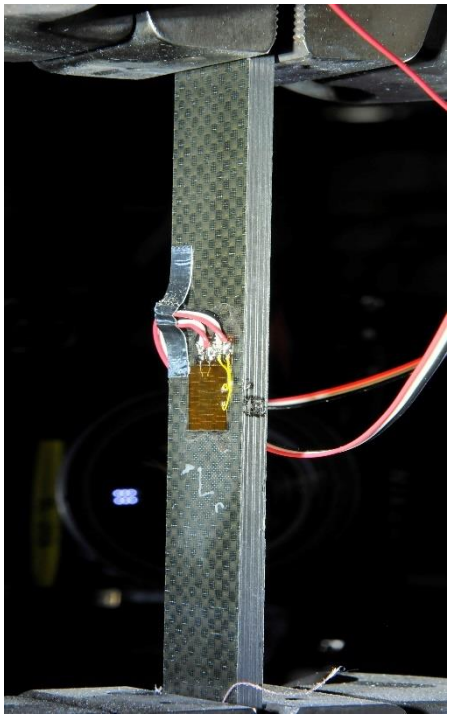

(A1-L-1) at 10K cycles

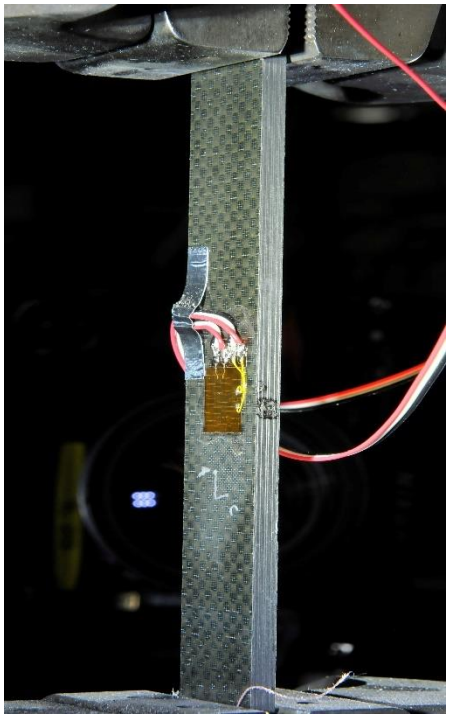

(A1-L-1) at 20K cycles

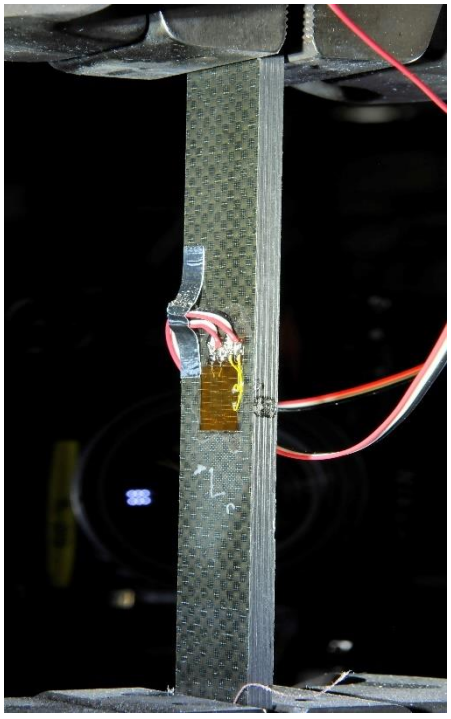

(A1-L-1) at 30K cycles

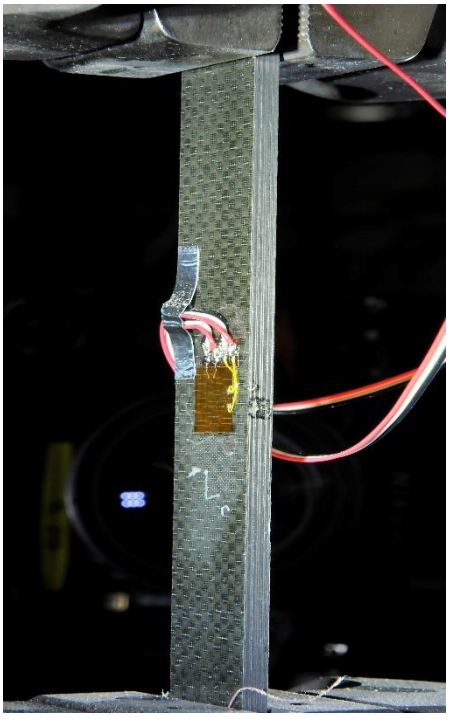

(A1-L-1) at 40K cycles

Figure C1.50 Damage Progression in (A1-L-1) Test Specimen at 40K cycles

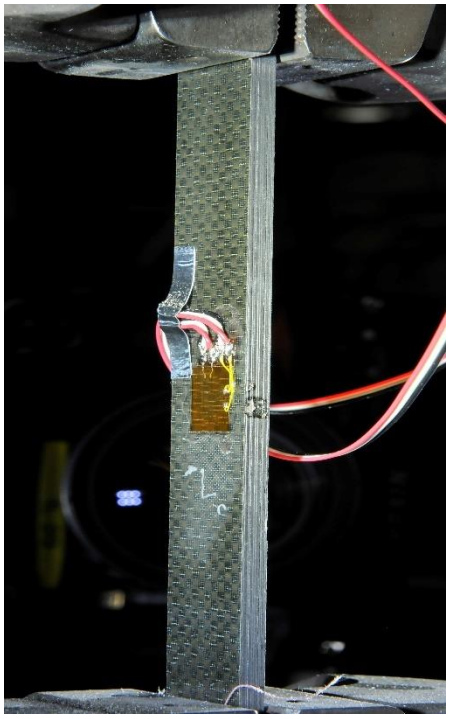

(A1-L-1) at 50K cycles

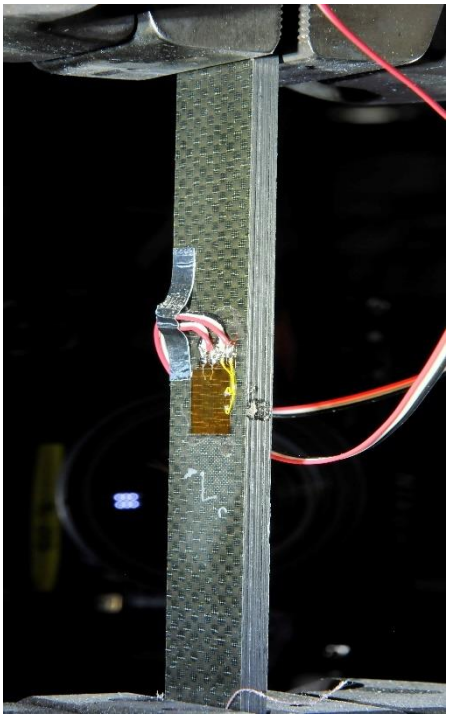

(A1-L-1) at 60K cycles

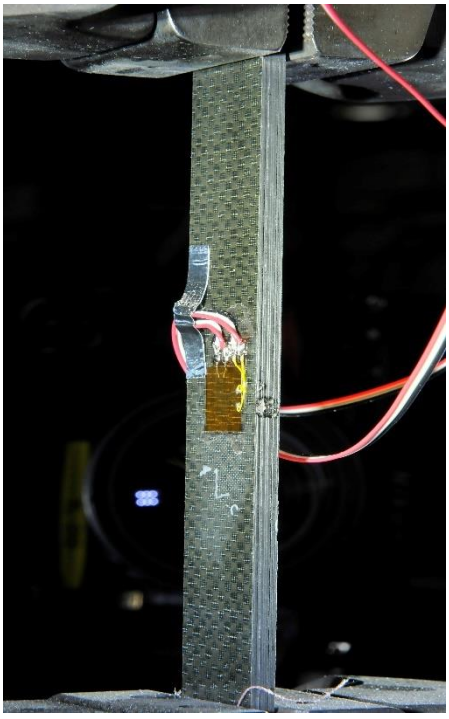

(A1-L-1) at 70K cycles

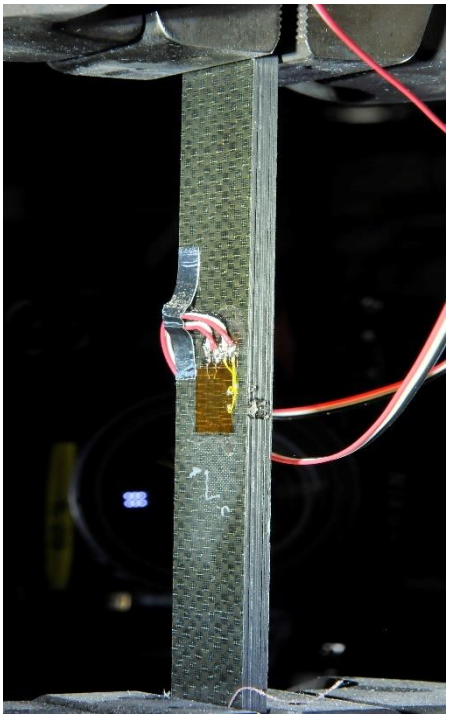

(A1-L-1) at 80K cycles

Figure C1.51 Damage Progression in (A1-L-1) Test Specimen at 80K cycles

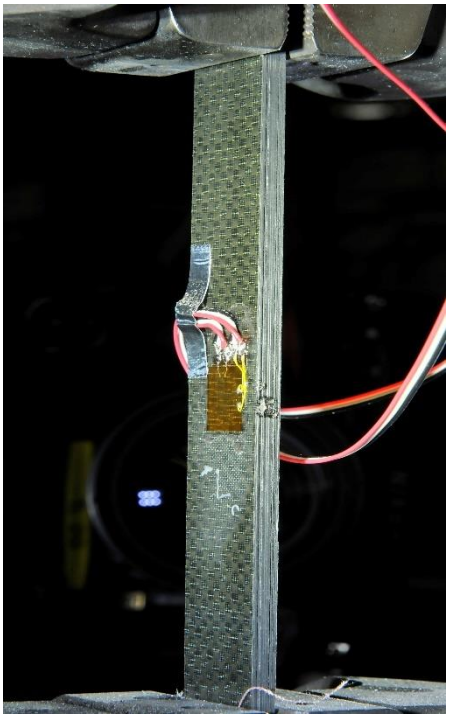

(A1-L-1) at 90K cycles

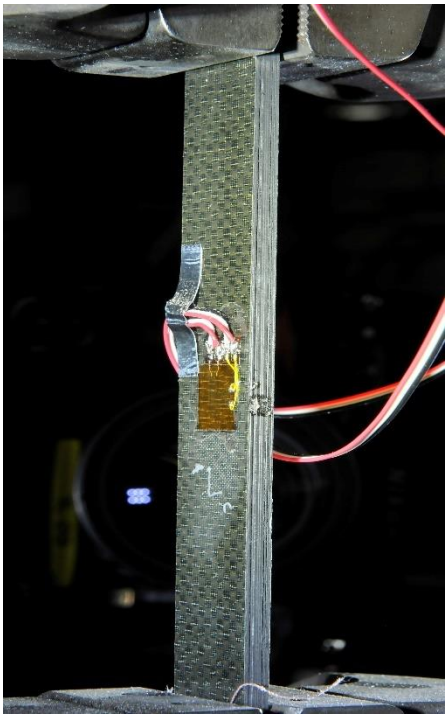

(A1-L-1) at 100K cycles

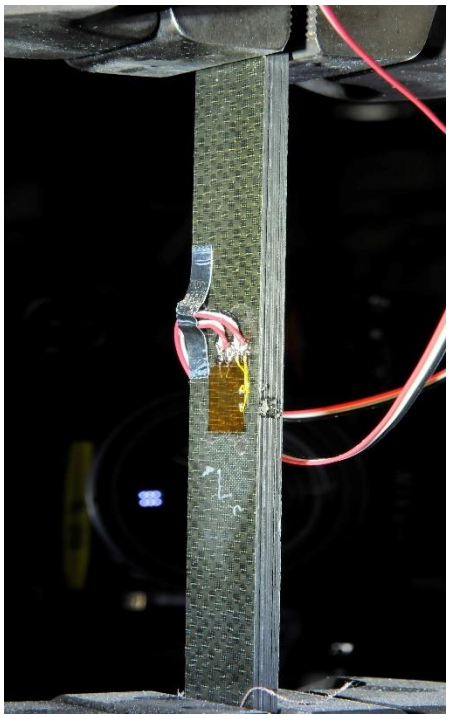

(A1-L-1) at 125K cycles

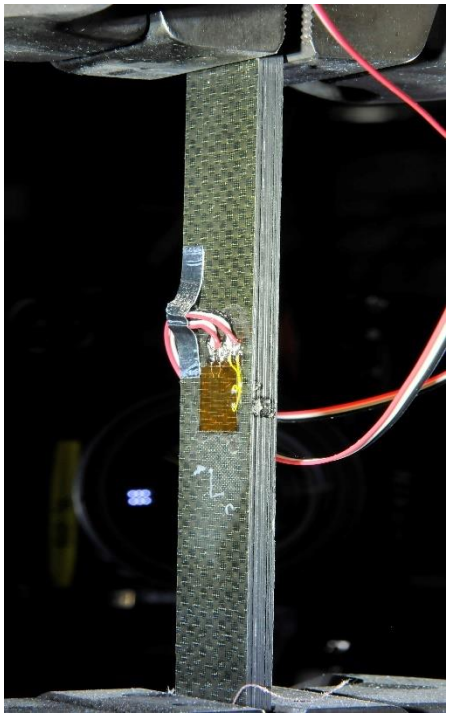

(A1-L-1) at 150K cycles

Figure C1.52 Damage Progression in (A1-L-1) Test Specimen at 150K cycles

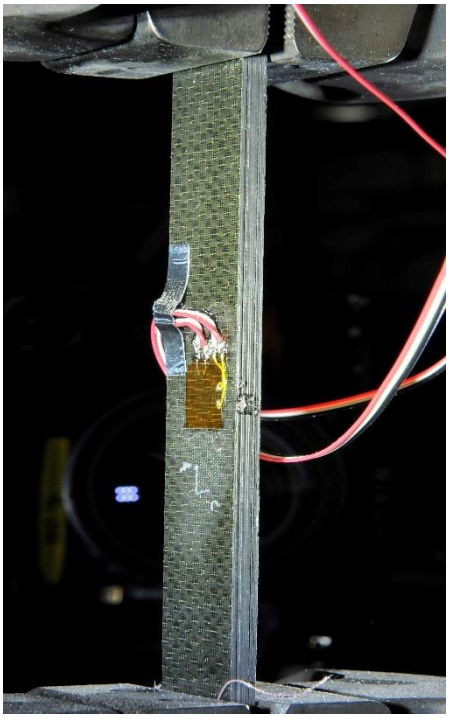

(A1-L-1) at 175K cycles

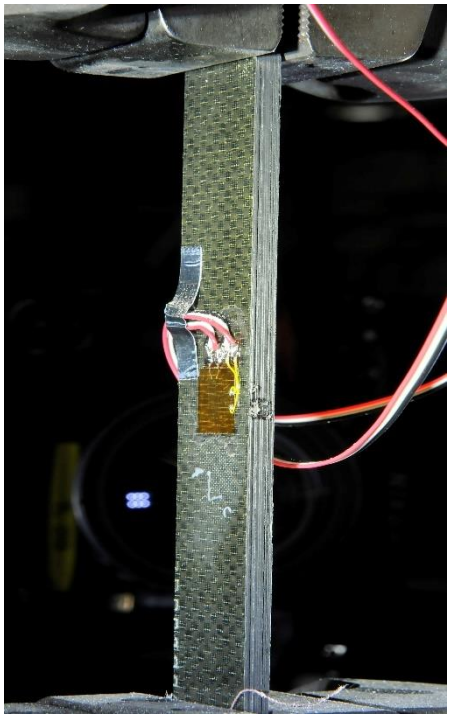

(A1-L-1) at 200K cycles

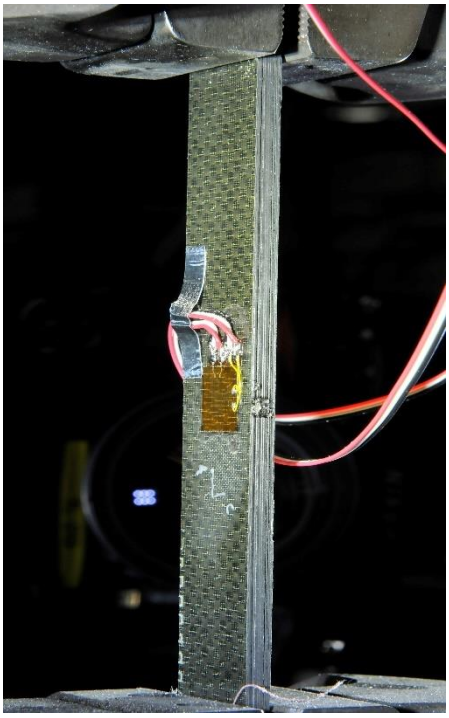

(A1-L-1) at 225K cycles

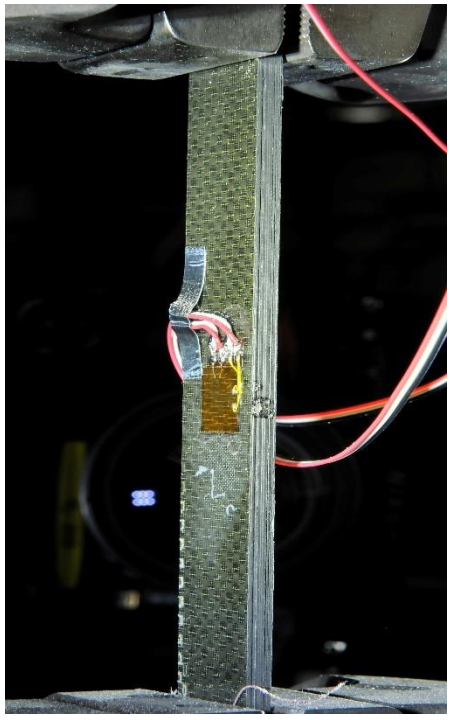

(A1-L-1) at 250K cycles

Figure C1.53 Damage Progression in (A1-L-1) Test Specimen at 250K cycles

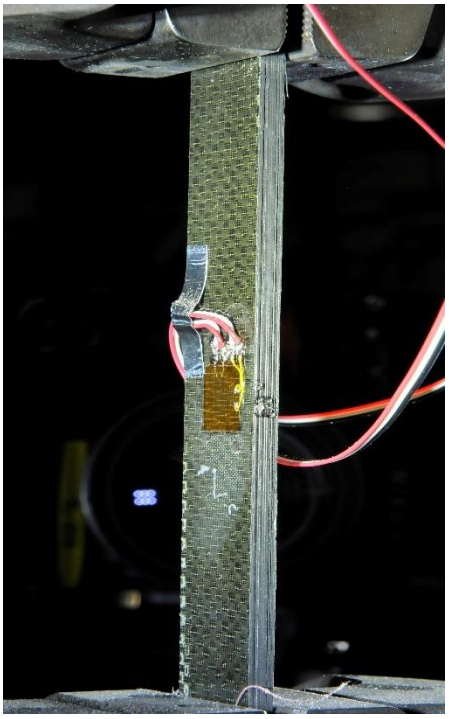

(A1-L-1) at 275K cycles

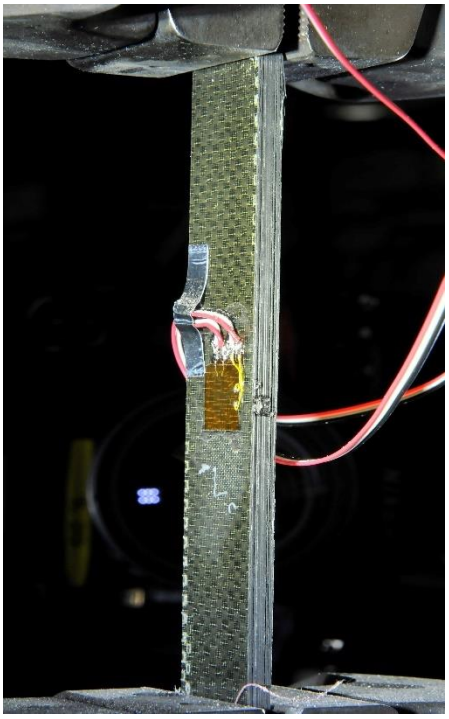

(A1-L-1) at 300K cycles

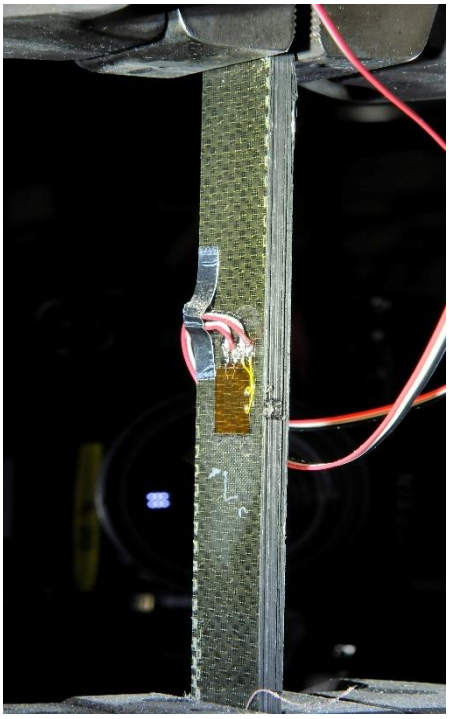

(A1-L-1) at 325K cycles

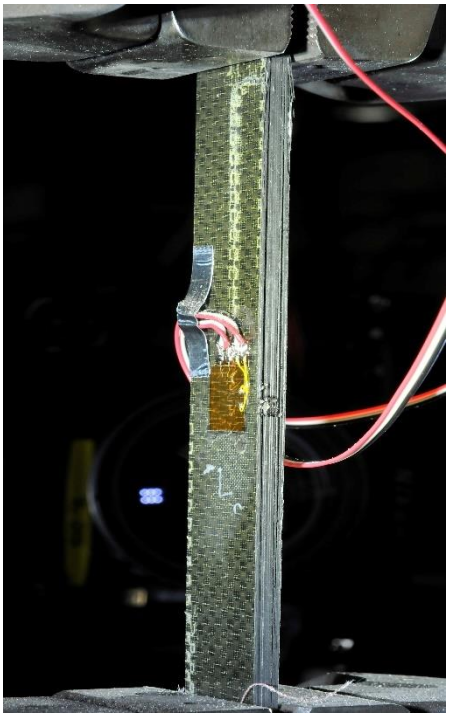

(A1-L-1) at 350K cycles

Figure C1.54 Damage Progression in (A1-L-1) Test Specimen at 350K cycles

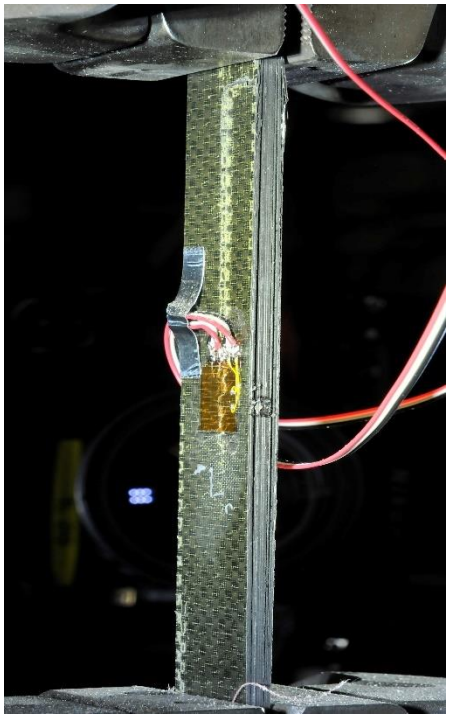

(A1-L-1) at 375K cycles

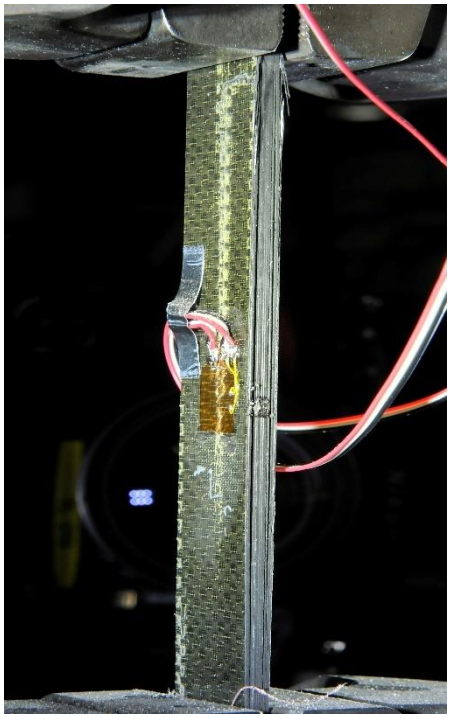

(A1-L-1) at 400K cycles

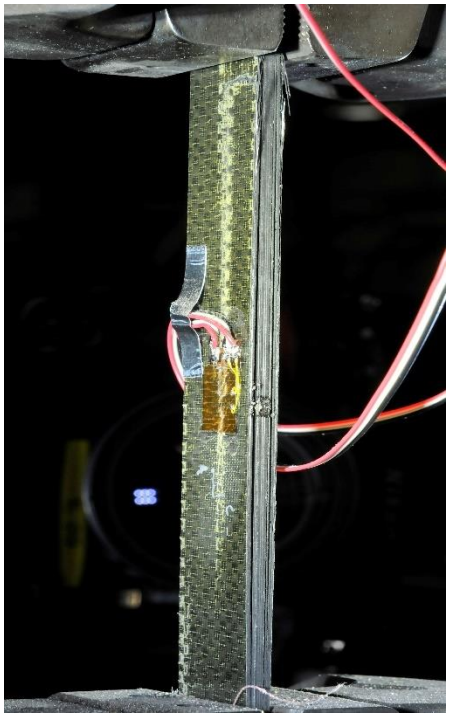

(A1-L-1) at 425K cycles

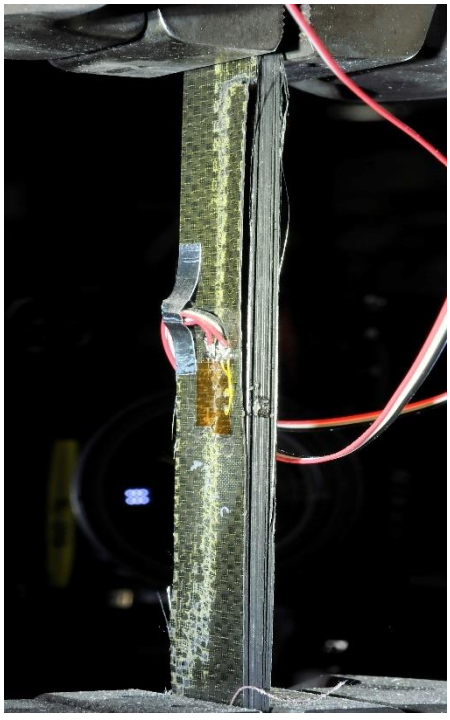

(A1-L-1) at 450K cycles

Figure C1.55 Damage Progression in (A1-L-1) Test Specimen at 450K cycles

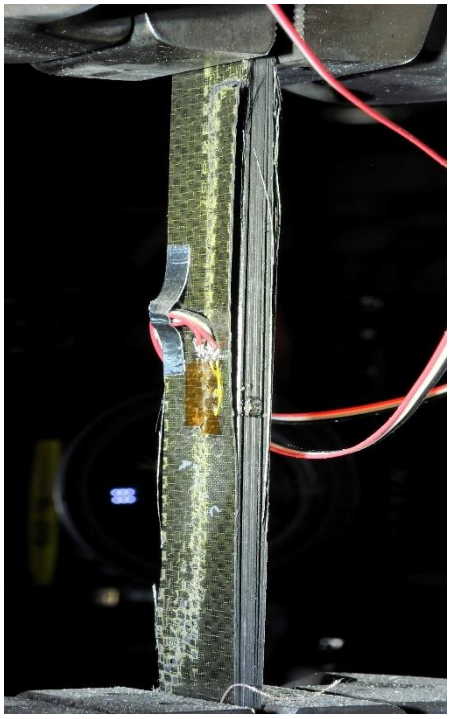

(A1-L-1) at 475K cycles

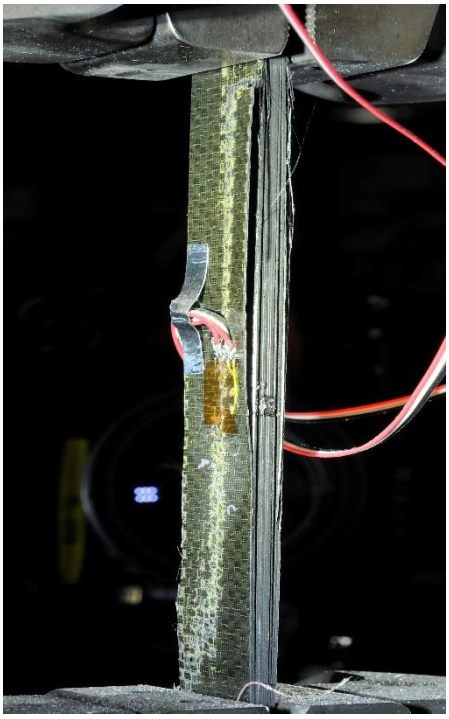

(A1-L-1) at 500K cycles

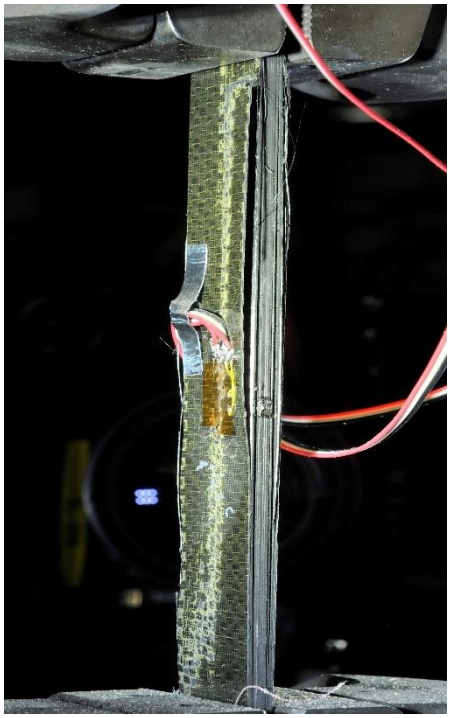

(A1-L-1) at 525K cycles

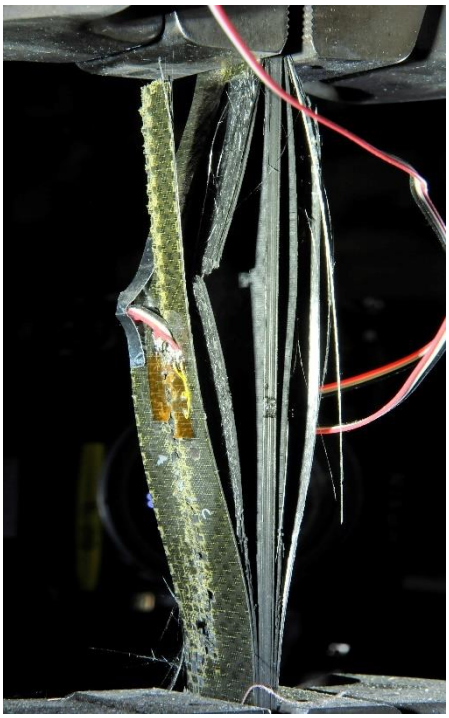

(A1-L-1) at 556680 cycles

Figure C1.56 Damage Progression in (A1-L-1) Test Specimen at 556680 cycles

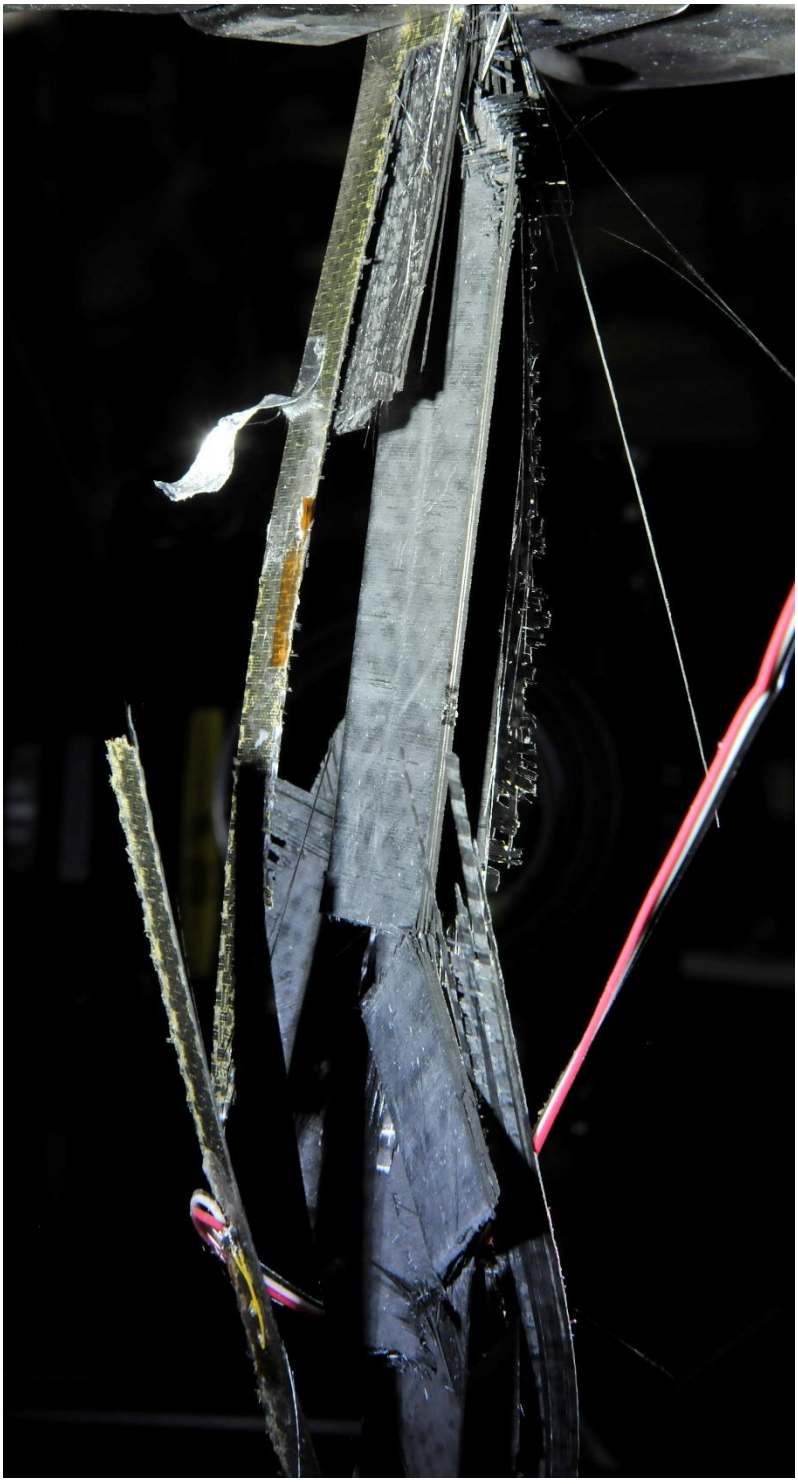

(A1-L-1) at Failure

Figure C1.57 Damage Progression in (A1-L-1) Test Specimen at Failure

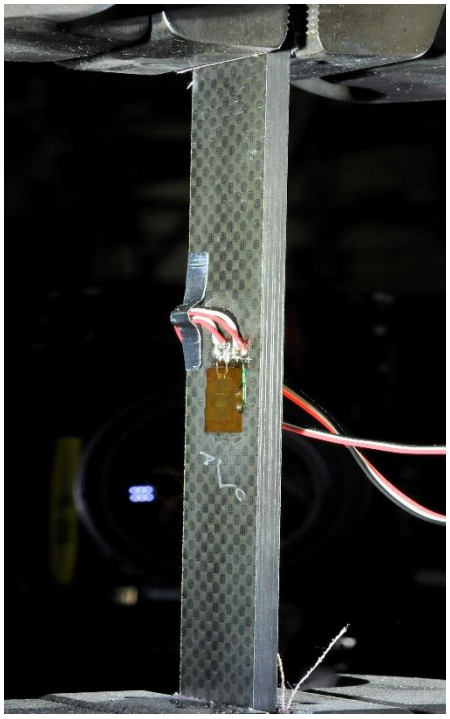

(A1-L-2) at 1 cycle

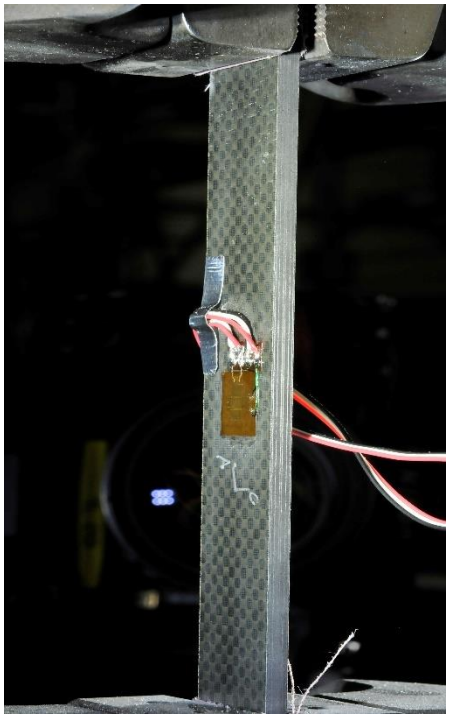

(A1-L-2) at 100 cycles

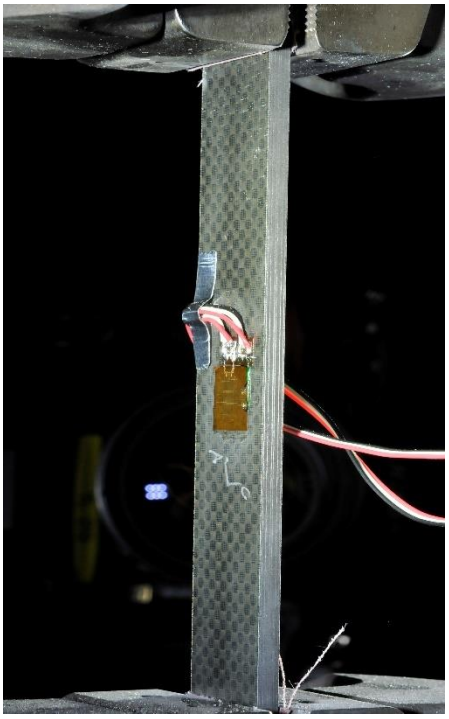

(A1-L-2) at 1K cycles

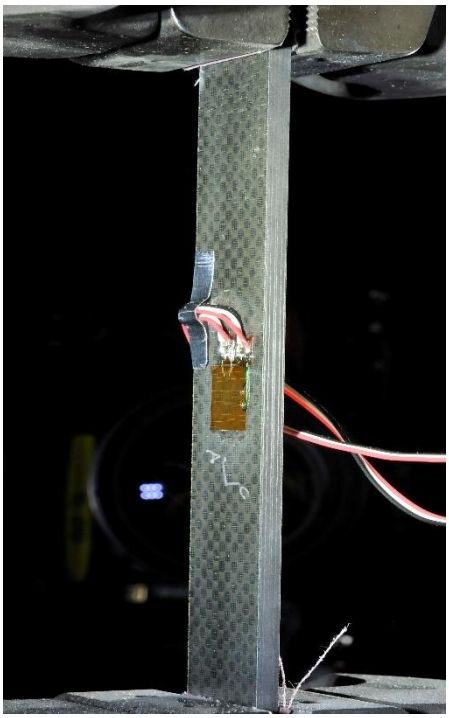

(A1-L-2) at 5K cycles

Figure C1.58 Damage Progression in (A1-L-2) Test Specimen at 5K cycles

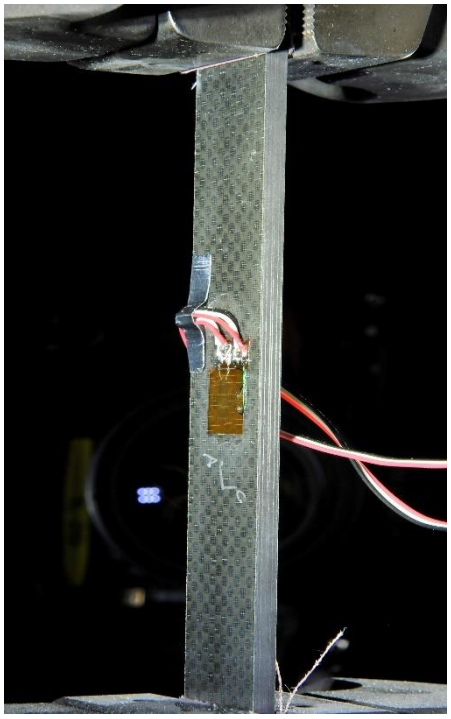

(A1-L-2) at 10K cycles

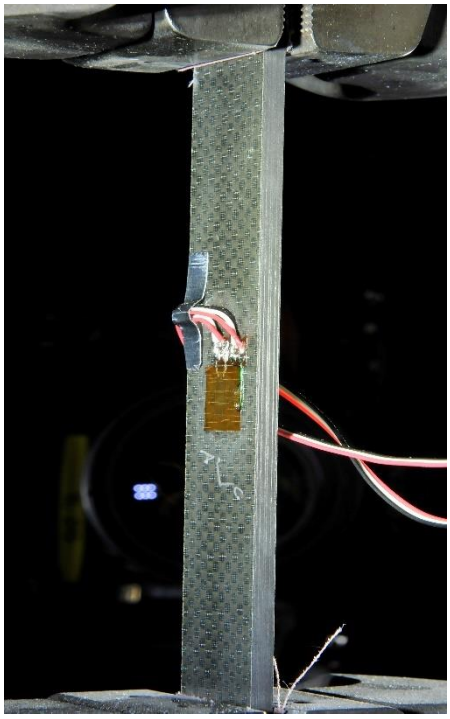

(A1-L-2) at 20K cycles

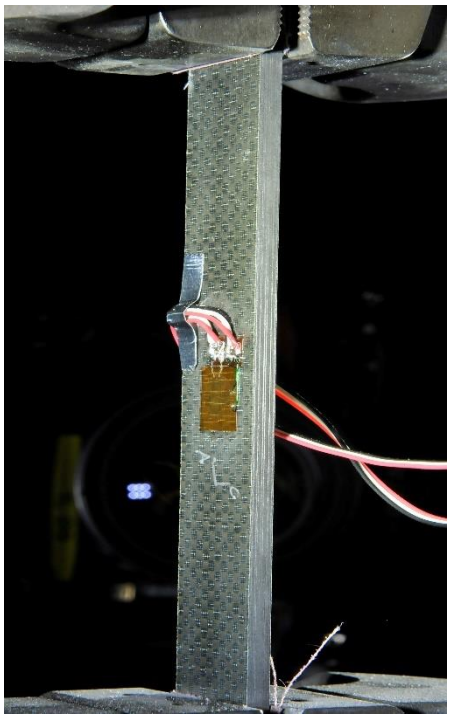

(A1-L-2) at 30K cycles

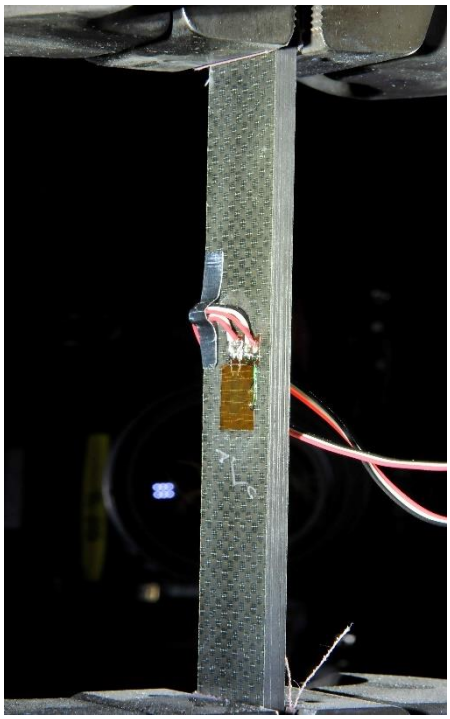

(A1-L-2) at 40K cycles

Figure C1.59 Damage Progression in (A1-L-2) Test Specimen at 40K cycles

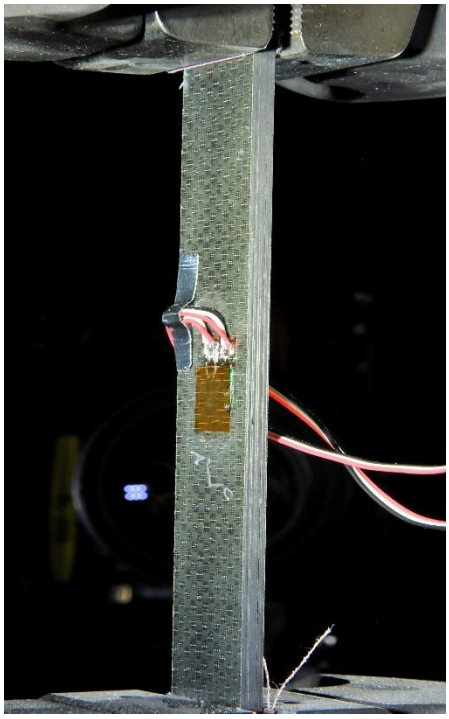

(A1-L-2) at 50K cycles

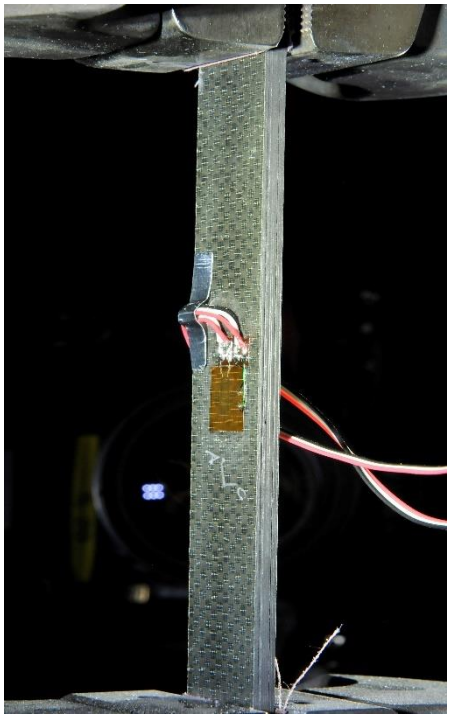

(A1-L-2) at 60K cycles

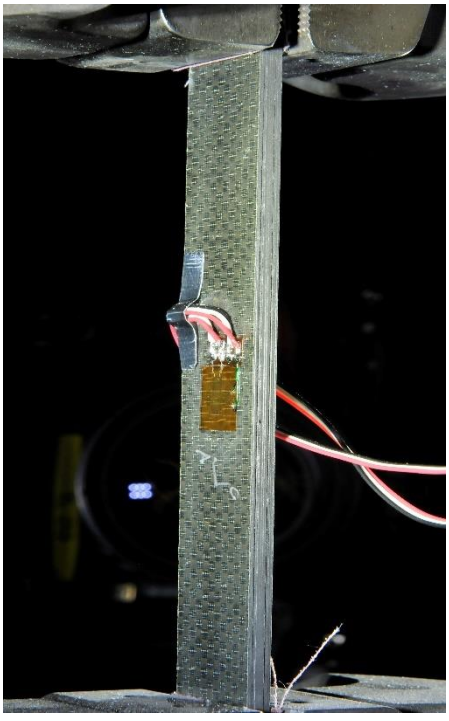

(A1-L-2) at 70K cycles

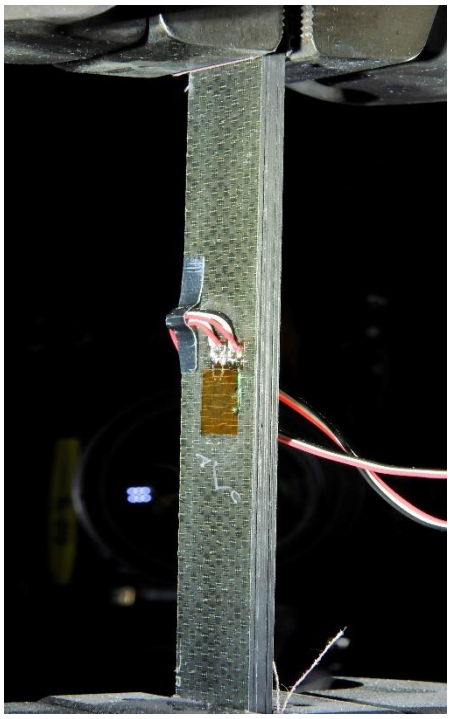

(A1-L-2) at 80K cycles

Figure C1.60 Damage Progression in (A1-L-2) Test Specimen at 80K cycles

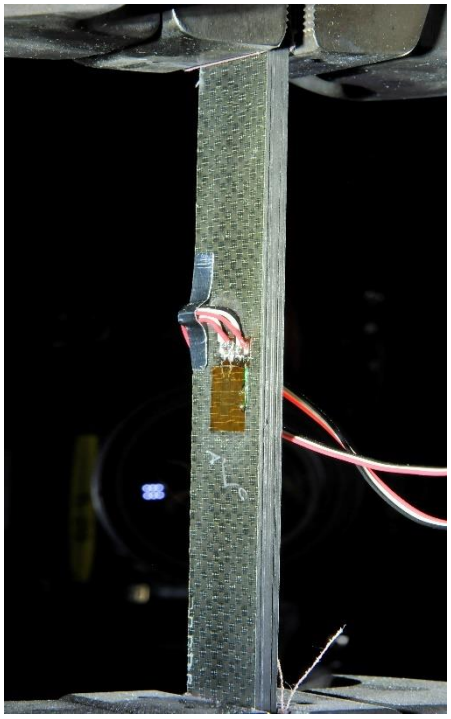

(A1-L-2) at 90K cycles

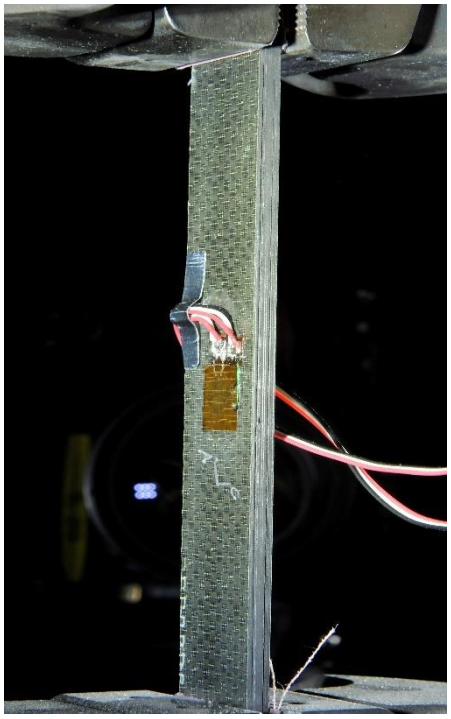

(A1-L-2) at 100K cycles

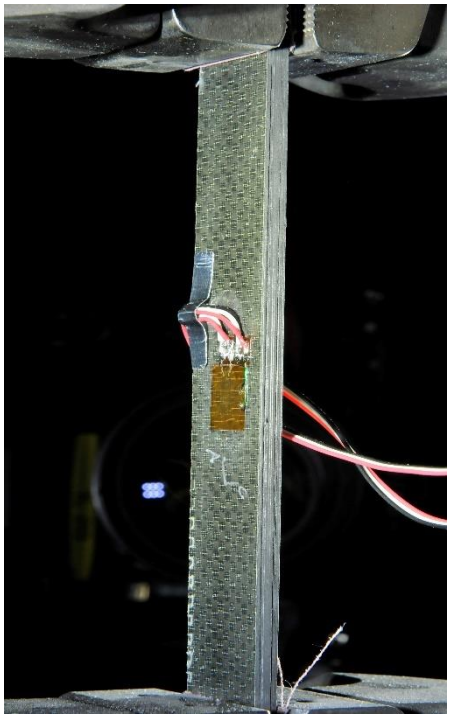

(A1-L-2) at 125K cycles

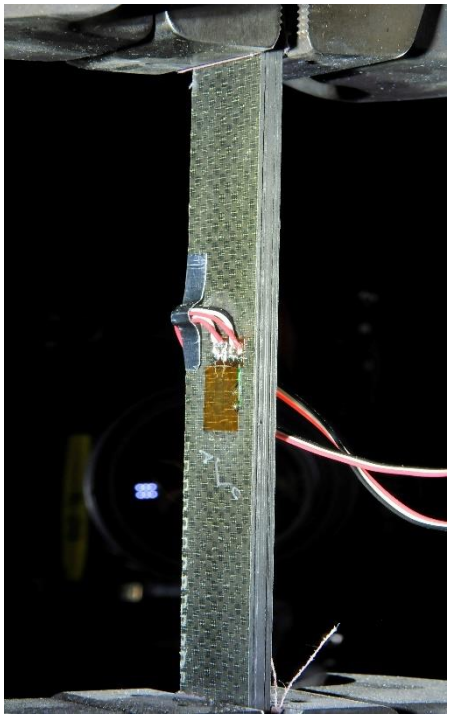

(A1-L-2) at 150K cycles

Figure C1.61 Damage Progression in (A1-L-2) Test Specimen at 150K cycles

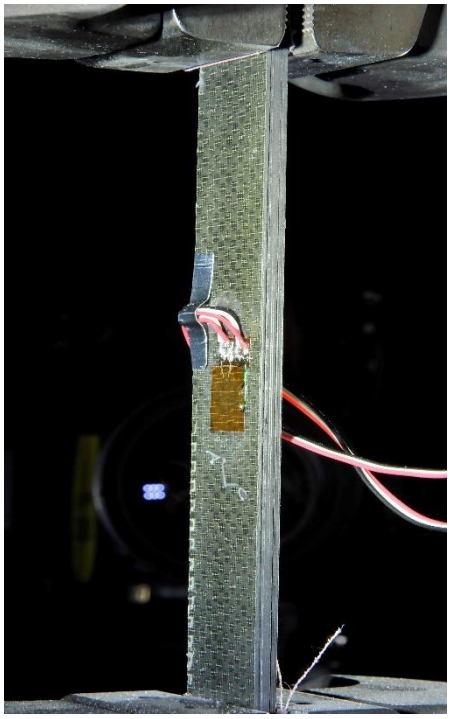

(A1-L-2) at 175K cycles

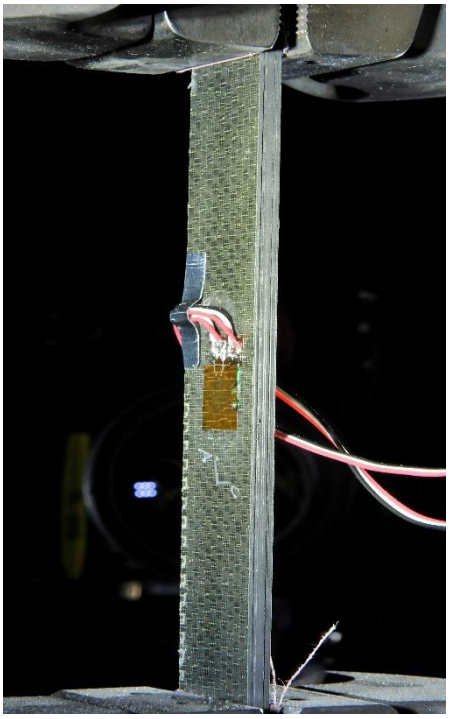

(A1-L-2) at 200K cycles

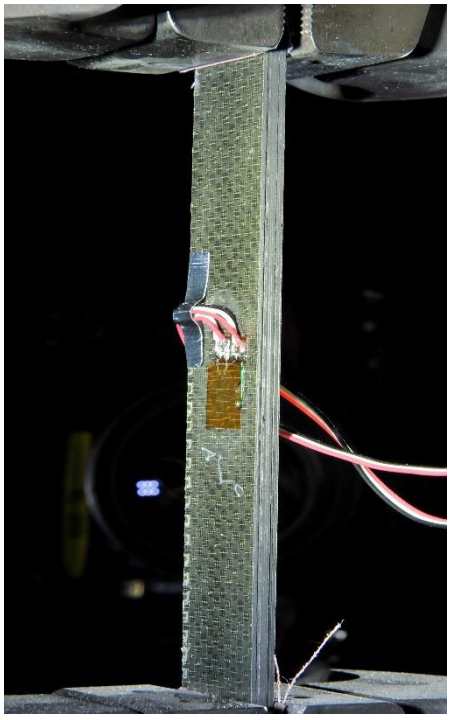

(A1-L-2) at 225K cycles

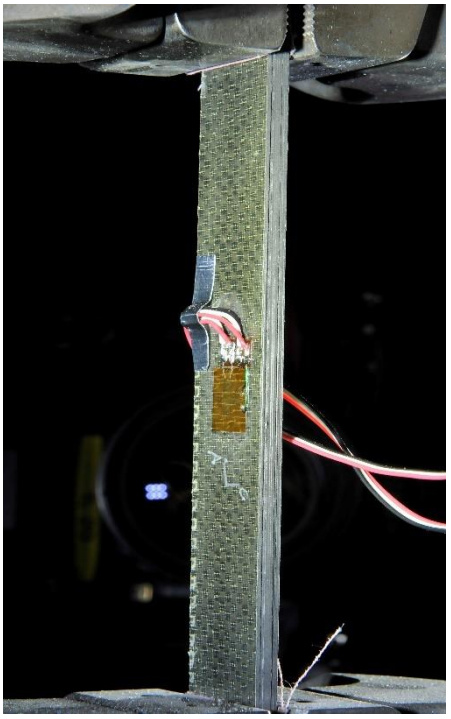

(A1-L-2) at 250K cycles

Figure C1.62 Damage Progression in (A1-L-2) Test Specimen at 250K cycles

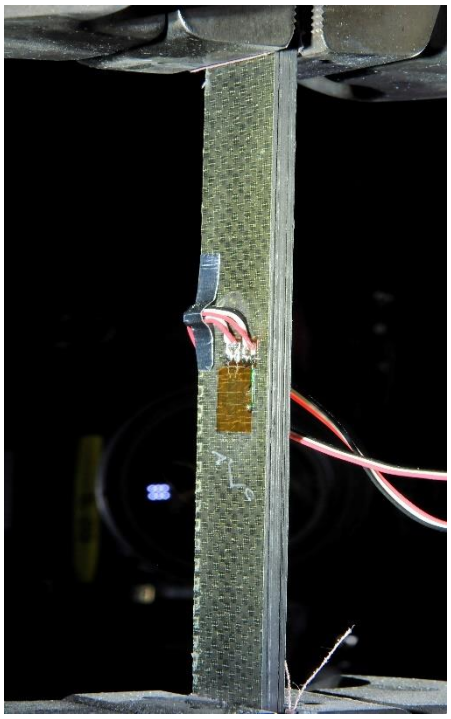

(A1-L-2) at 275K cycles

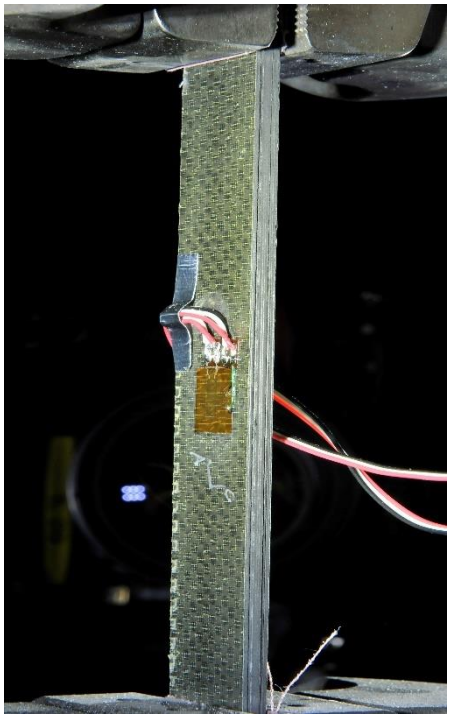

(A1-L-2) at 300K cycles

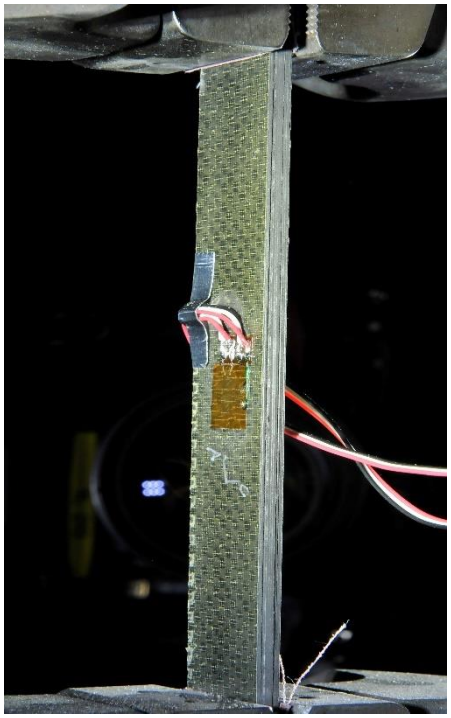

(A1-L-2) at 325K cycles

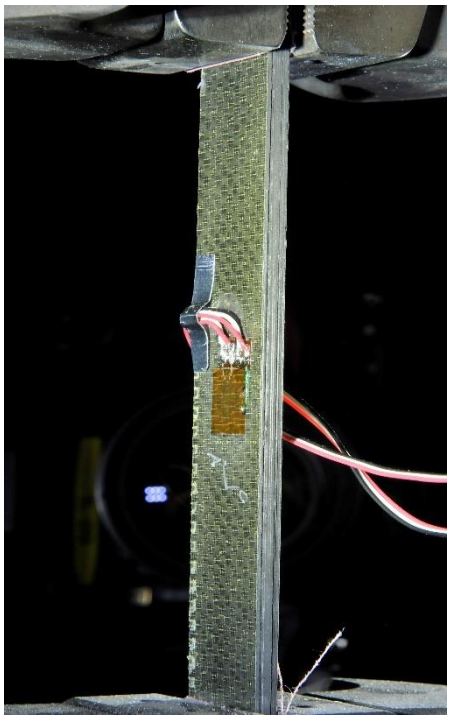

(A1-L-2) at 350K cycles

Figure C1.63 Damage Progression in (A1-L-2) Test Specimen at 350K cycles

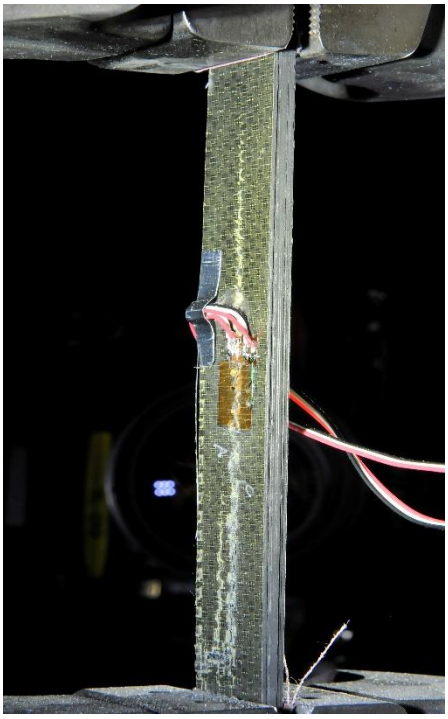

(A1-L-2) at 375K cycles

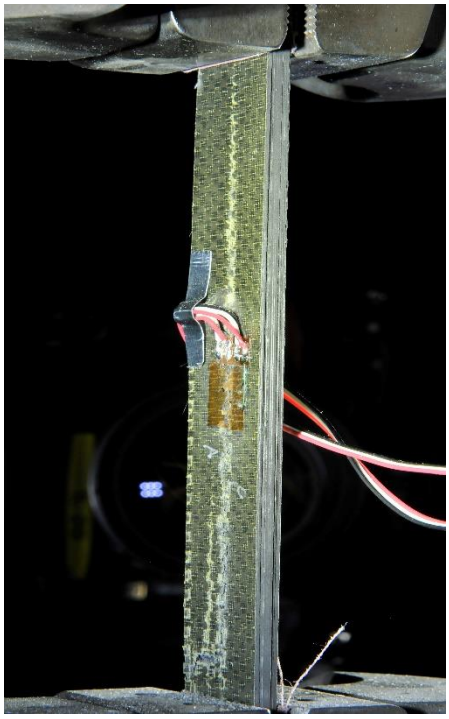

(A1-L-2) at 400K cycles

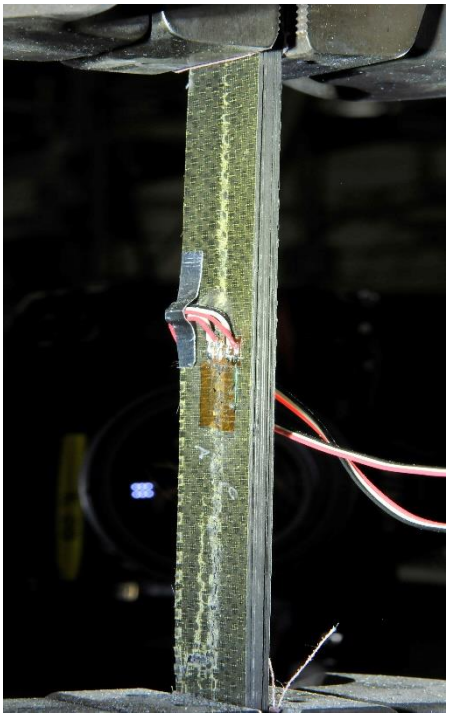

(A1-L-2) at 425K cycles

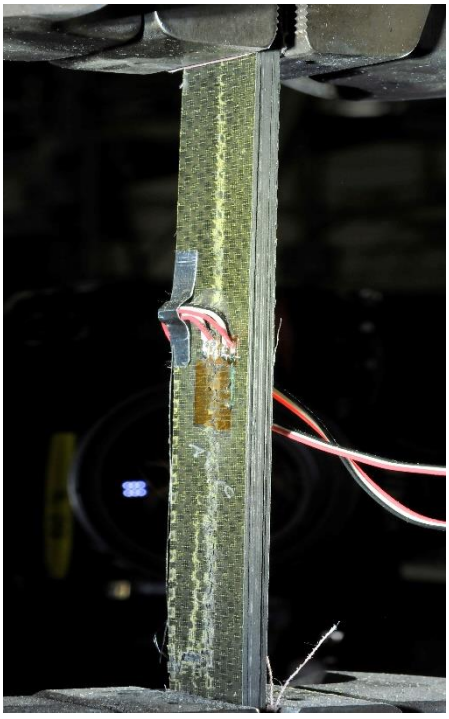

(A1-L-2) at 450K cycles

Figure C1.64 Damage Progression in (A1-L-2) Test Specimen at 450K cycles

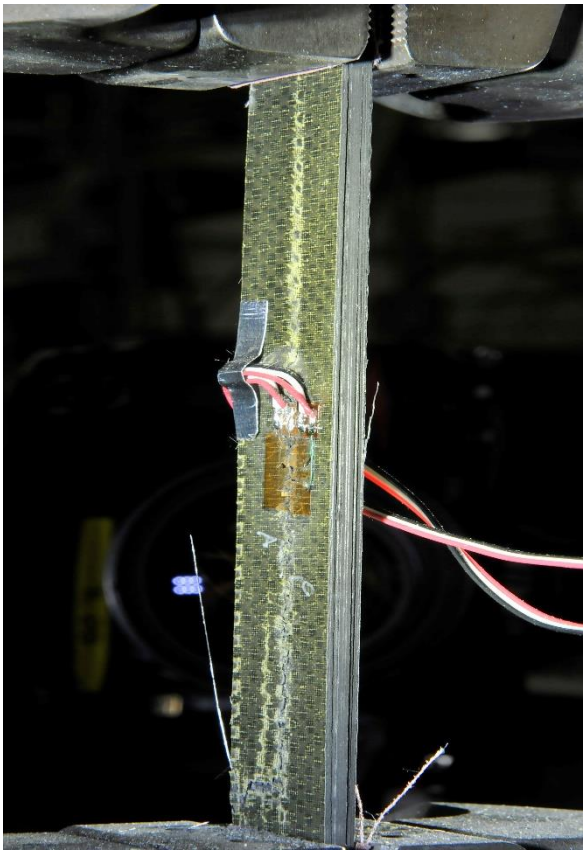

(A1-L-2) at 475K cycles

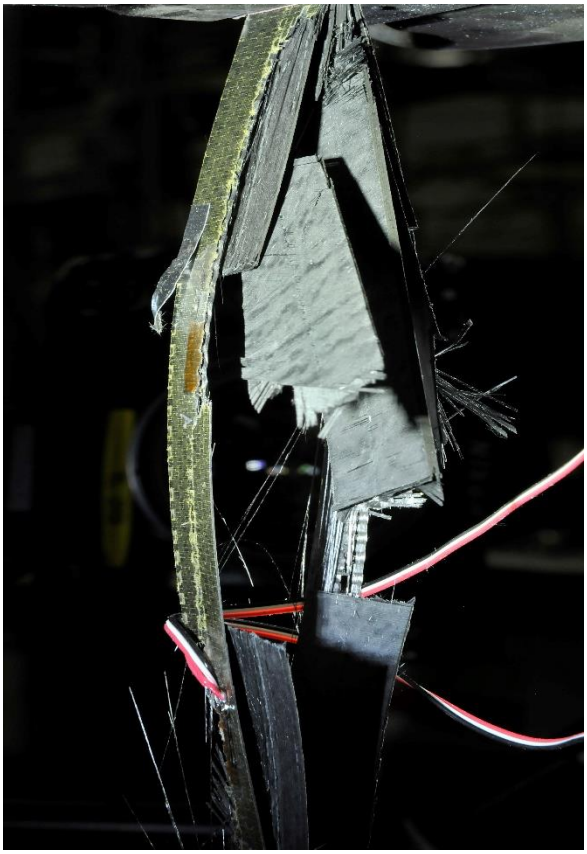

(A1-L-2) at Failure

Figure C1.65 Damage Progression in (A1-L-2) Test Specimen Failure

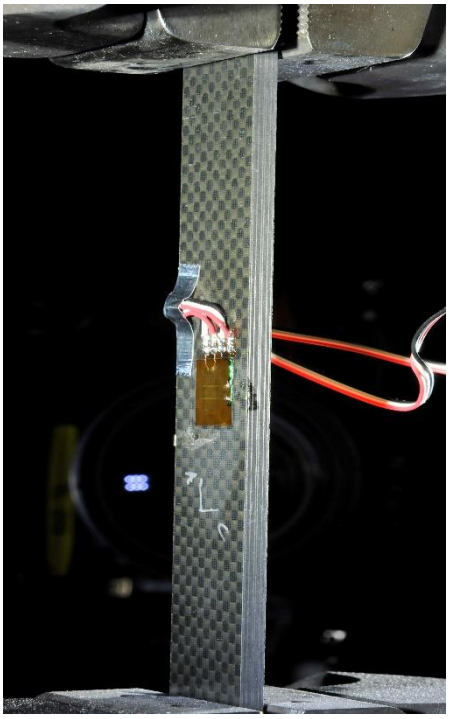

(A1-L-3) at 1 cycle

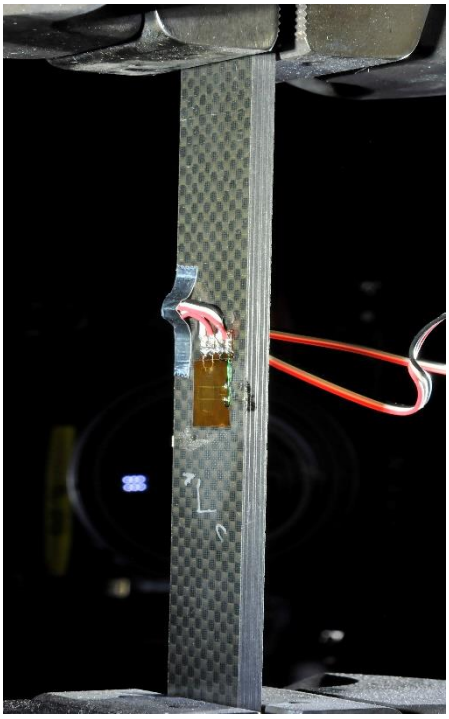

(A1-L-3) at 100 cycles

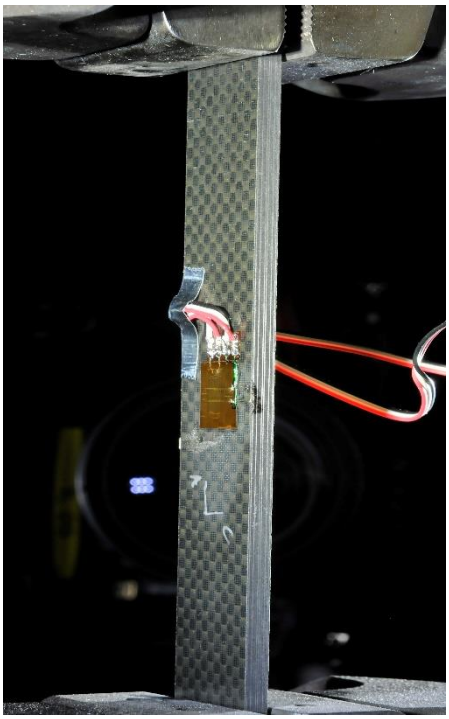

(A1-L-3) at 1K cycles

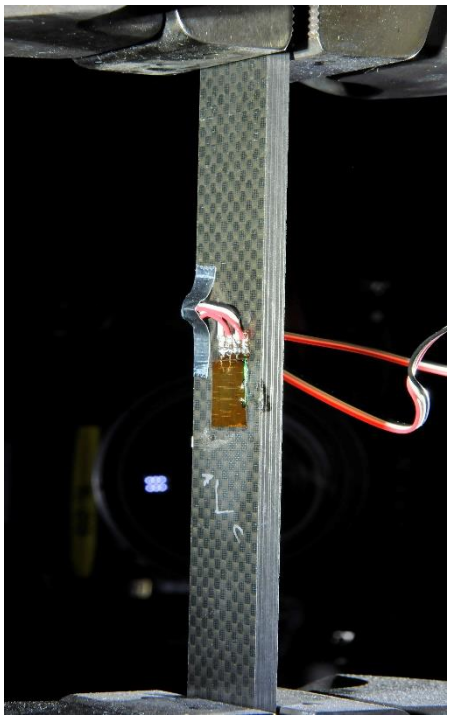

(A1-L-3) at 5K cycles

Figure C1.66 Damage Progression in (A1-L-3) Test Specimen at 5K cycles

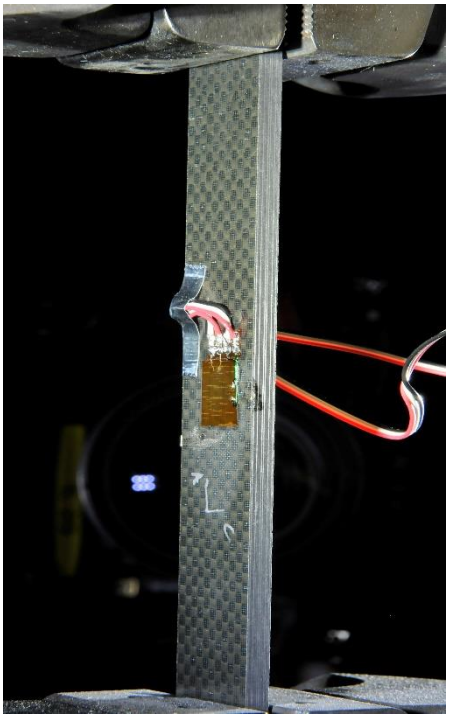

(A1-L-3) at 10K cycles

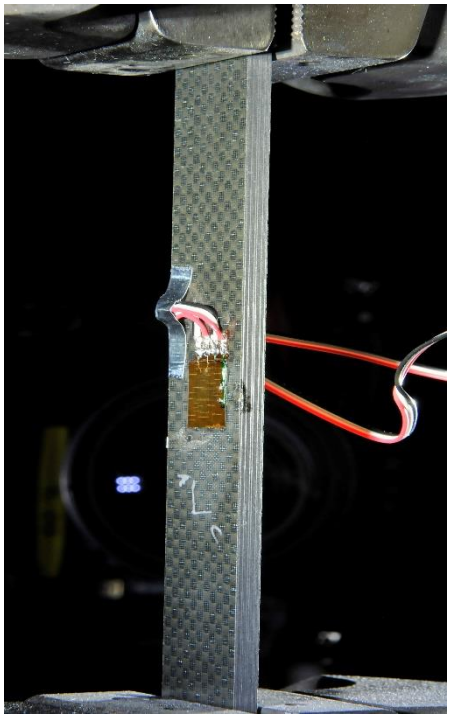

(A1-L-3) at 20K cycles

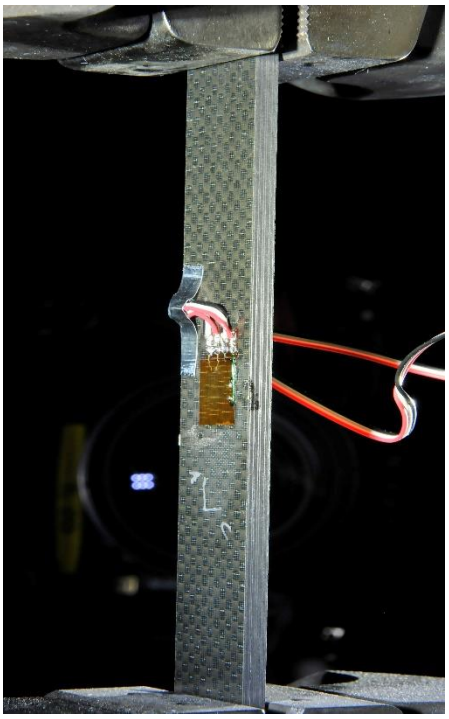

(A1-L-3) at 30K cycles

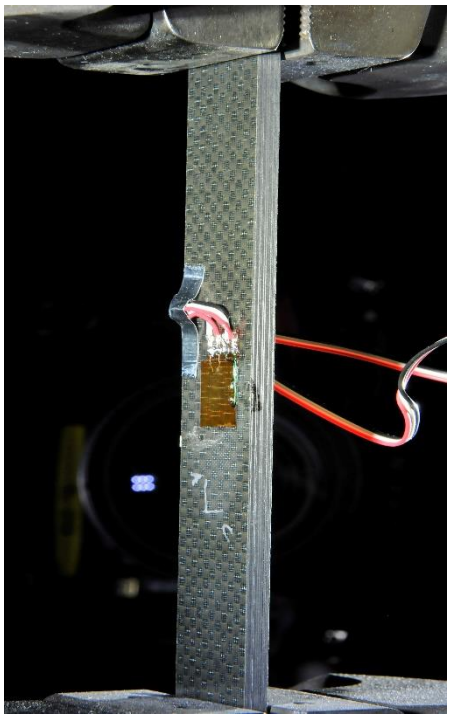

(A1-L-3) at 40K cycles

Figure C1.67 Damage Progression in (A1-L-3) Test Specimen at 40K cycles

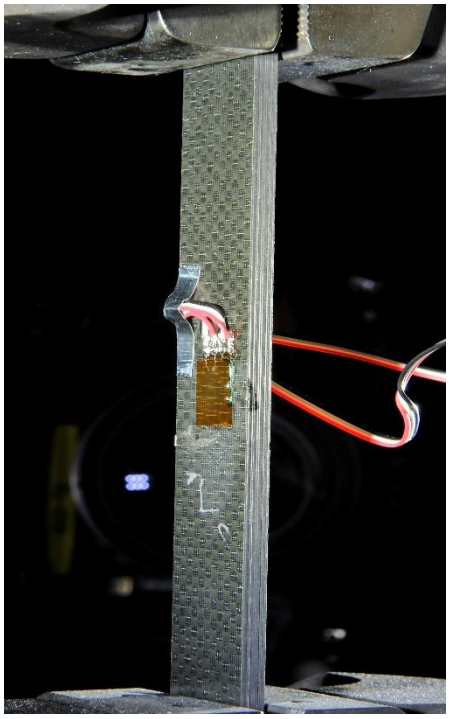

(A1-L-3) at 50K cycles

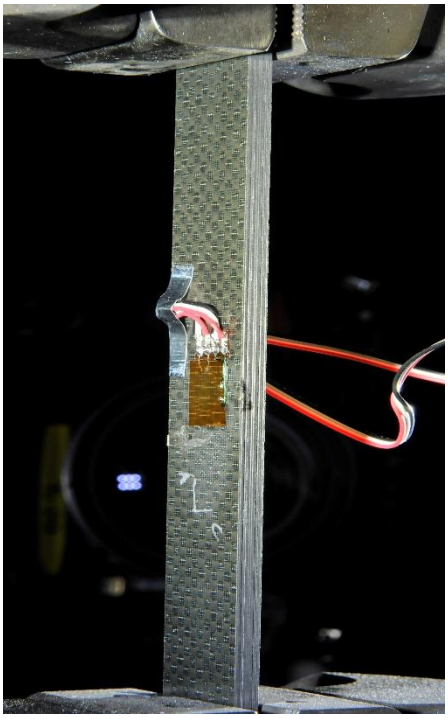

(A1-L-3) at 60K cycles

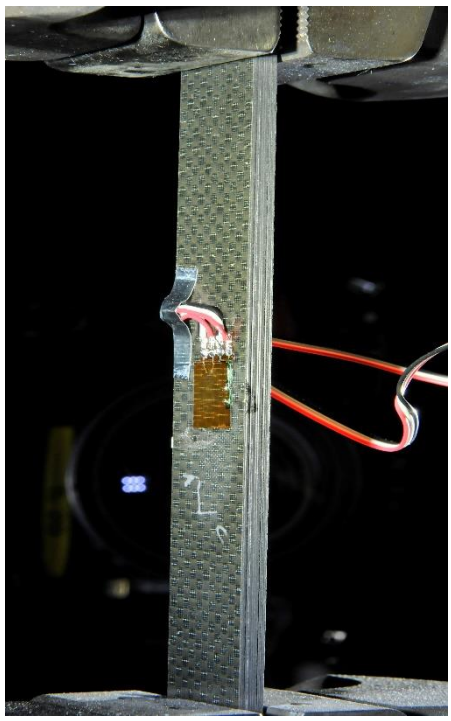

(A1-L-3) at 70K cycles

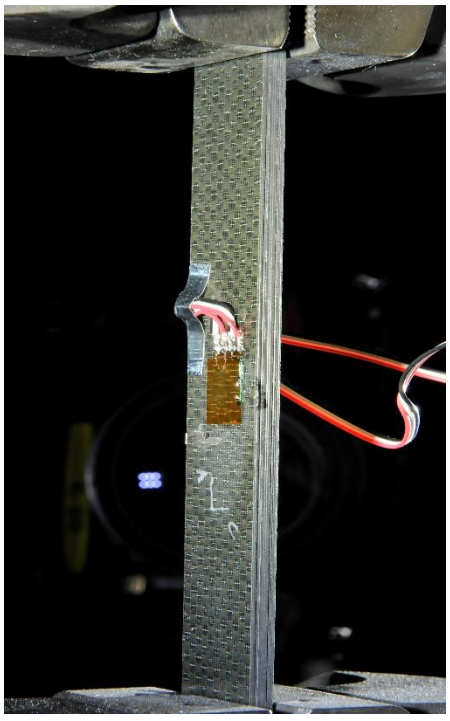

(A1-L-3) at 80K cycles

Figure C1.68 Damage Progression in (A1-L-3) Test Specimen at 80K cycles

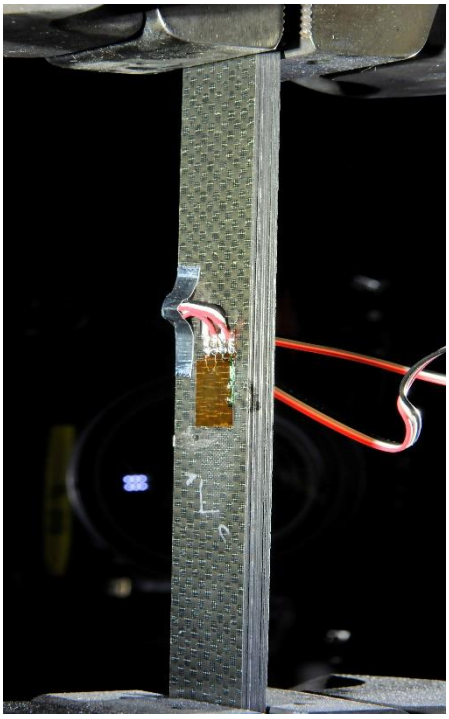

(A1-L-3) at 90K cycles

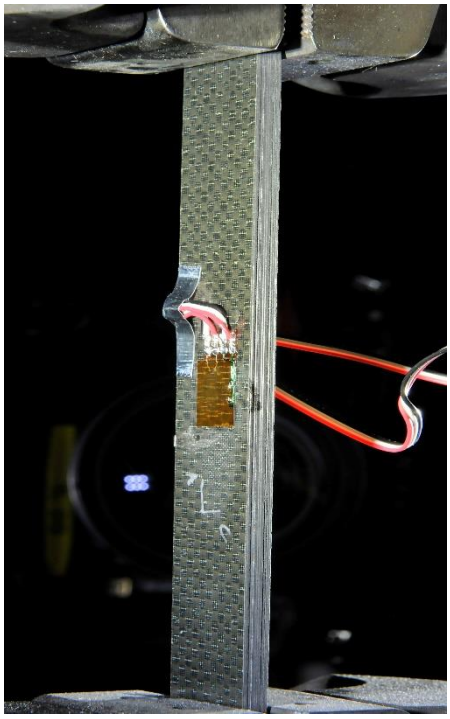

(A1-L-3) at 100K cycles

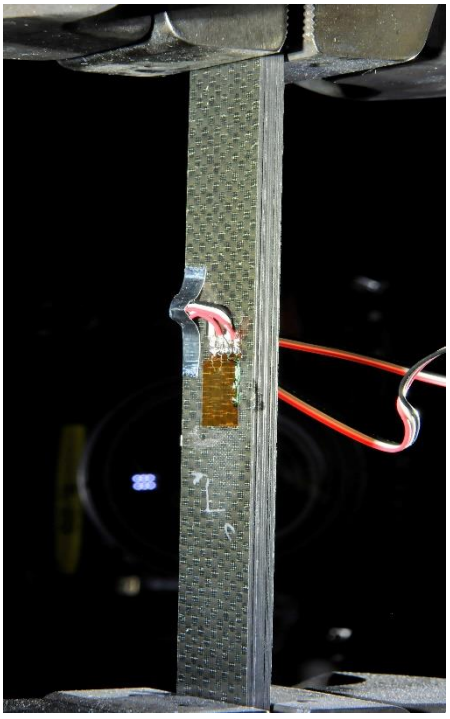

(A1-L-3) at 125K cycles

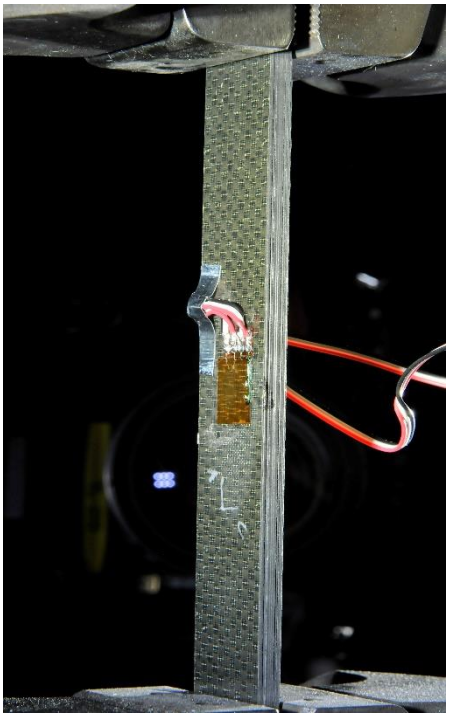

(A1-L-3) at 150K cycles

Figure C1.69 Damage Progression in (A1-L-3) Test Specimen at 150K cycles

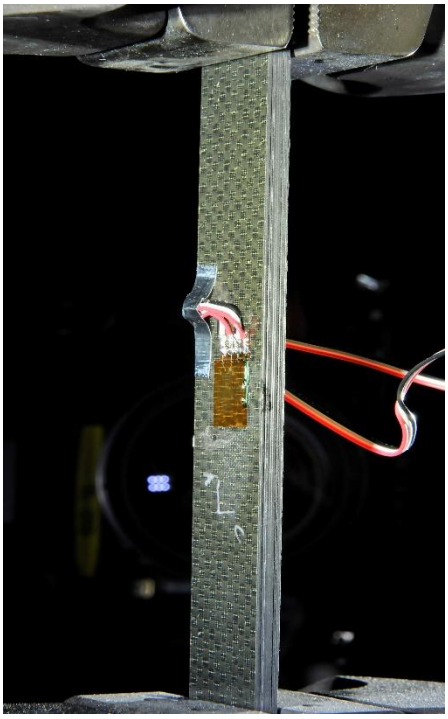

(A1-L-3) at 175K cycles

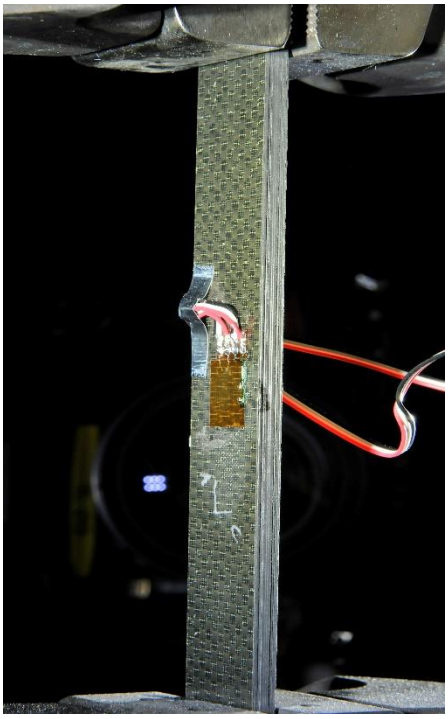

(A1-L-3) at 200K cycles

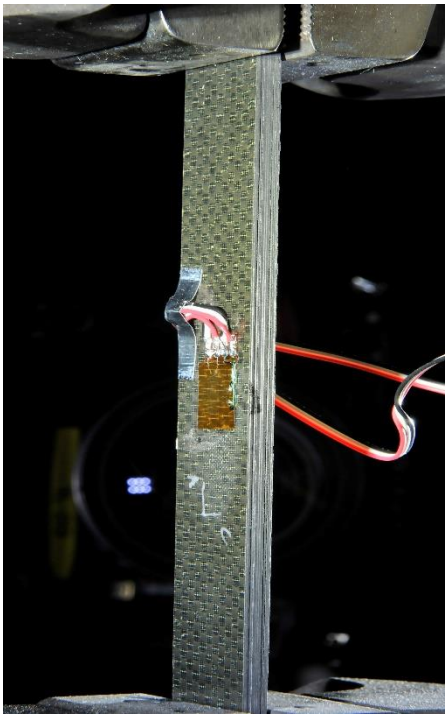

(A1-L-3) at 225K cycles

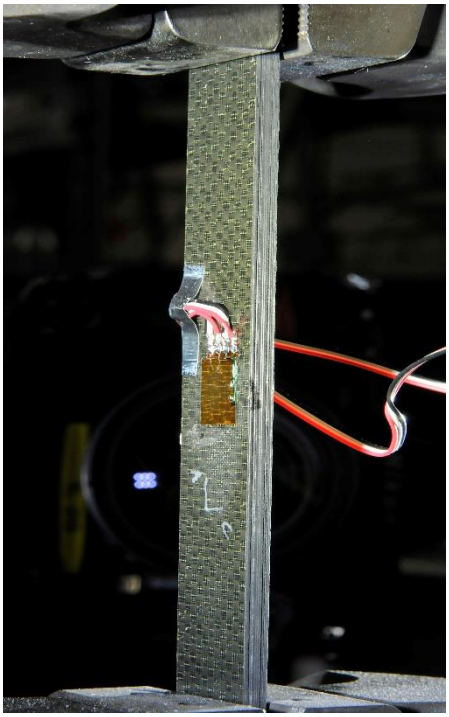

(A1-L-3) at 250K cycles

Figure C1.70 Damage Progression in (A1-L-3) Test Specimen at 250K cycles

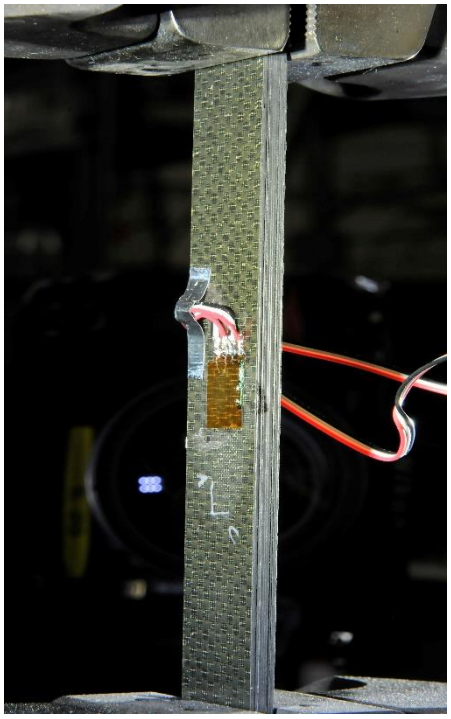

(A1-L-3) at 275K cycles

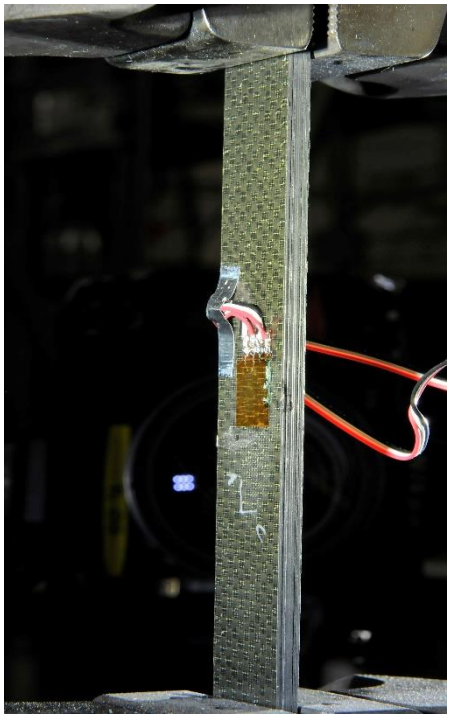

(A1-L-3) at 300K cycles

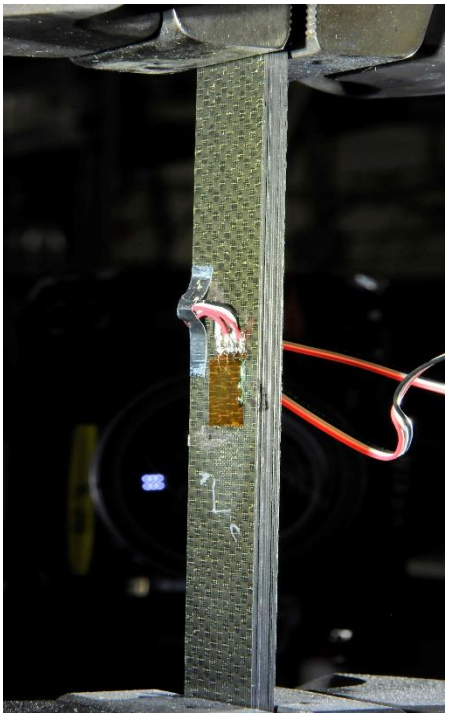

(A1-L-3) at 325K cycles

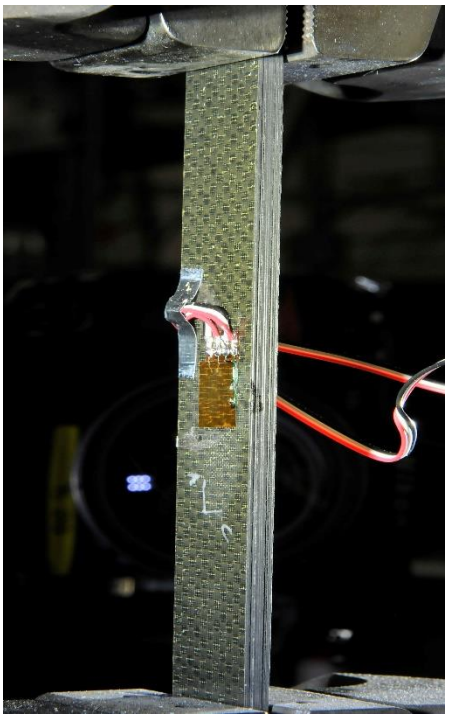

(A1-L-3) at 350K cycles

Figure C1.71 Damage Progression in (A1-L-3) Test Specimen at 350K cycles

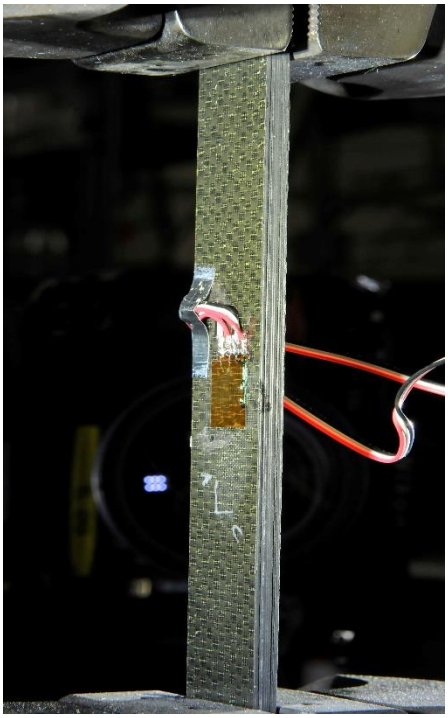

(A1-L-3) at 375K cycles

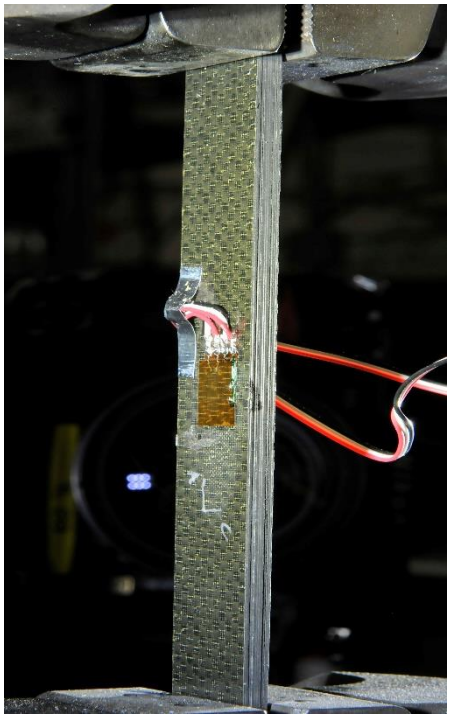

(A1-L-3) at 400K cycles

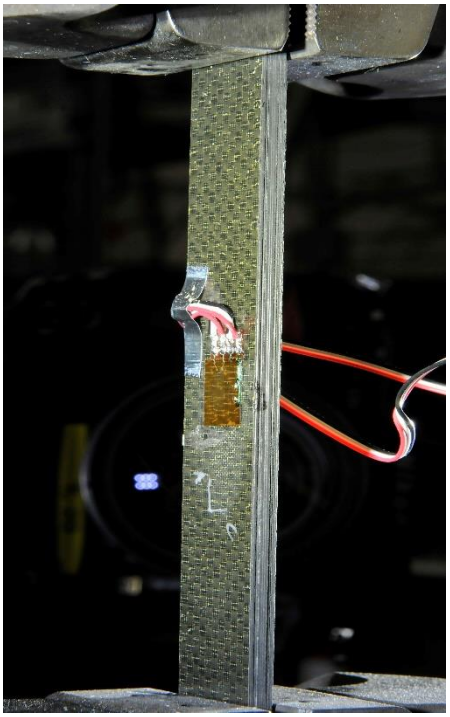

(A1-L-3) at 425K cycles

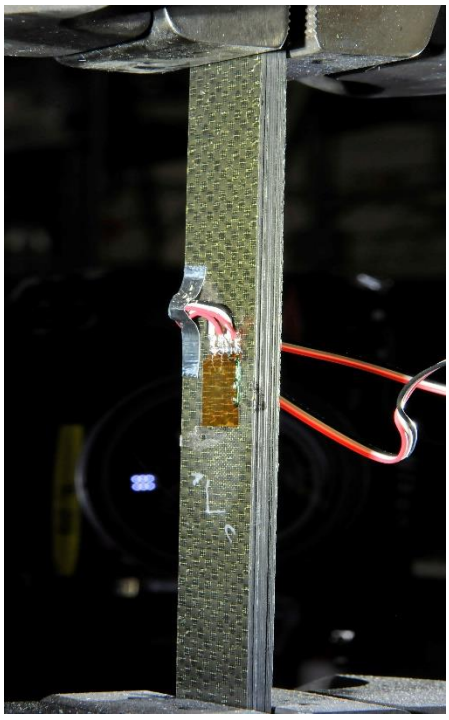

(A1-L-3) at 450K cycles

Figure C1.72 Damage Progression in (A1-L-3) Test Specimen at 450K cycles

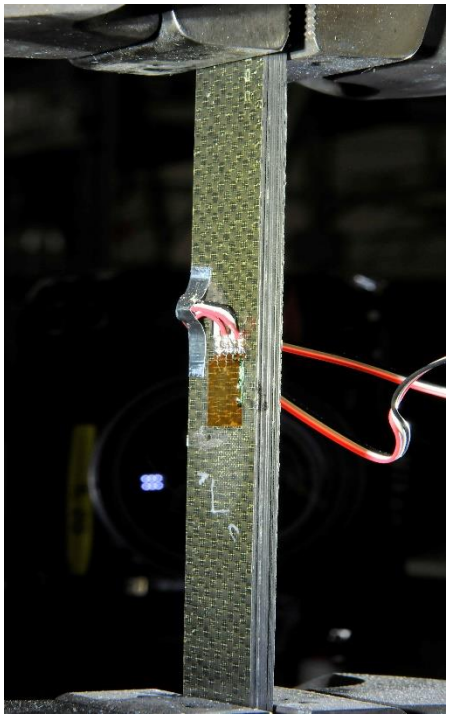

(A1-L-3) at 475K cycles

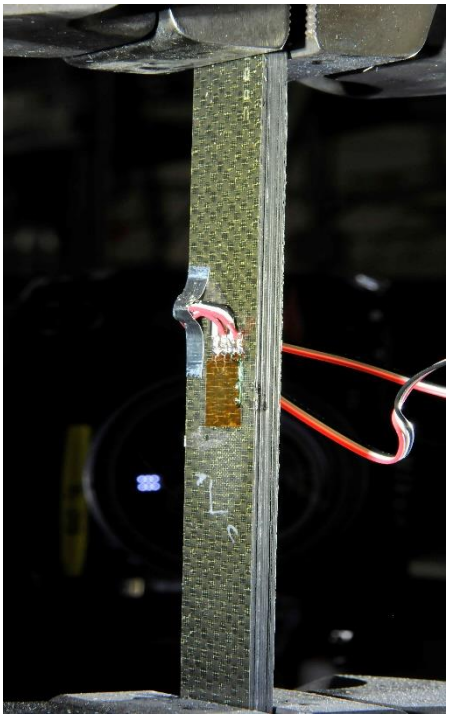

(A1-L-3) at 500K cycles

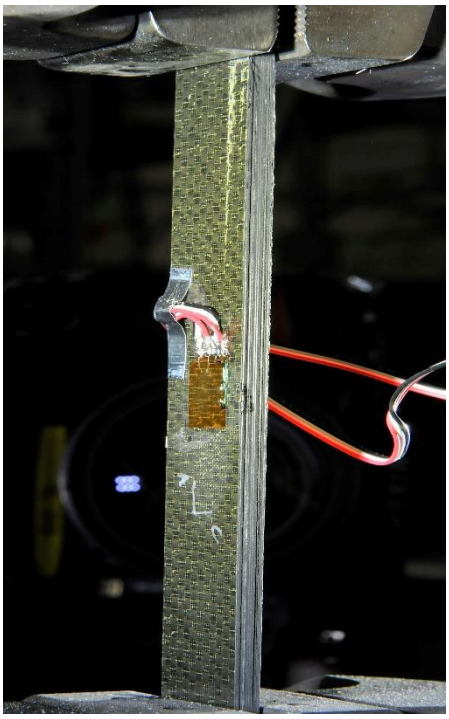

(A1-L-3) at 525K cycles

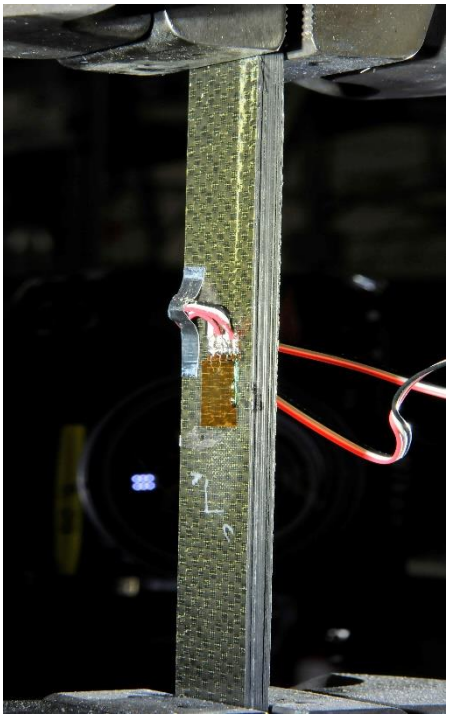

(A1-L-3) at 550K cycles

Figure C1.73 Damage Progression in (A1-L-3) Test Specimen at 550K cycles

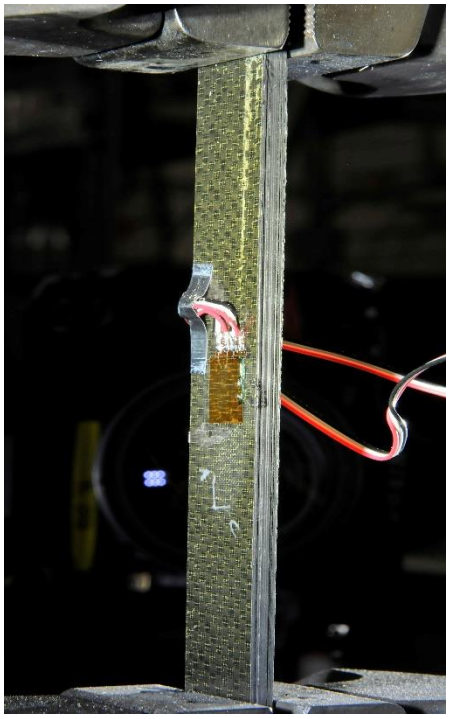

(A1-L-3) at 575K cycles

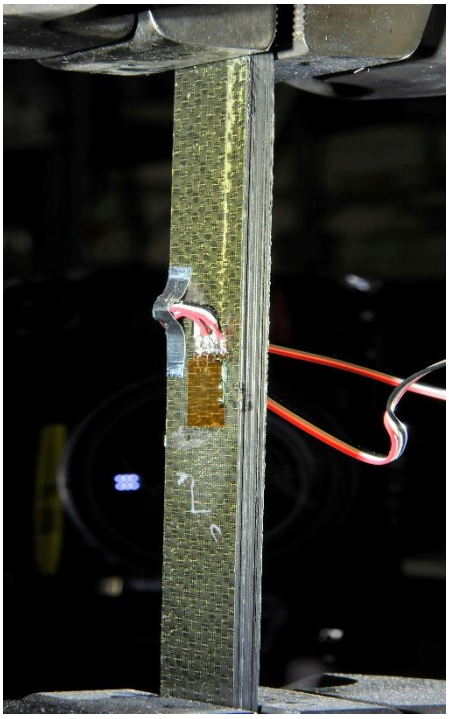

(A1-L-3) at 600K cycles

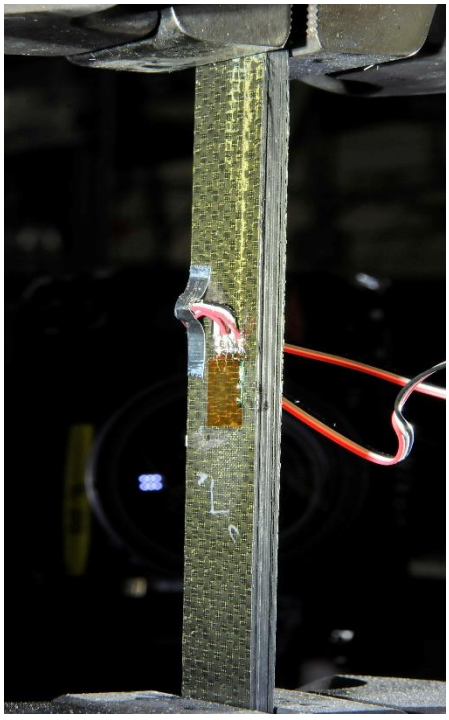

(A1-L-3) at 625K cycles

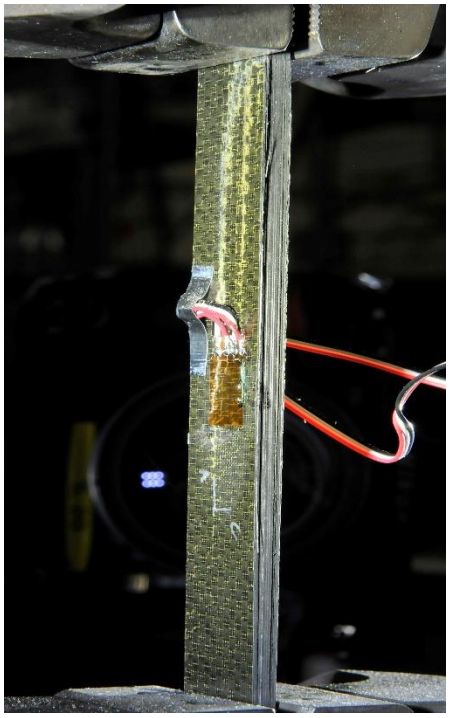

(A1-L-3) at 650K cycles

Figure C1.74 Damage Progression in (A1-L-3) Test Specimen at 650K cycles

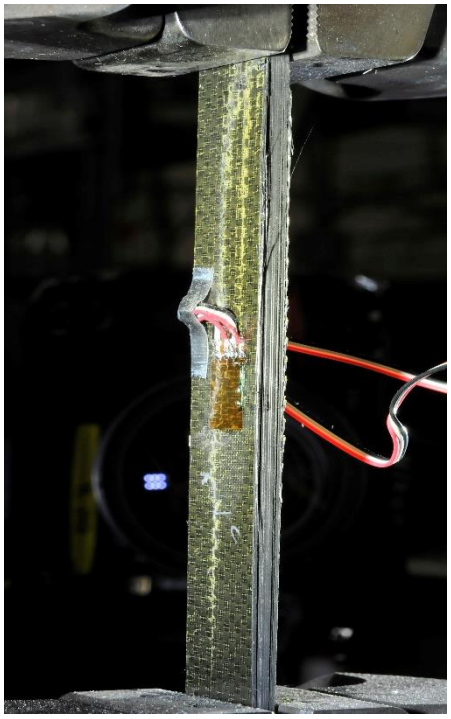

(A1-L-3) at 675K cycles

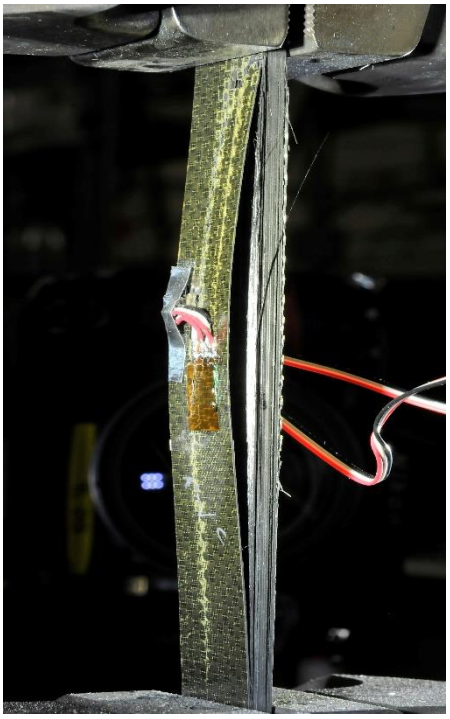

(A1-L-3) at 700K cycles

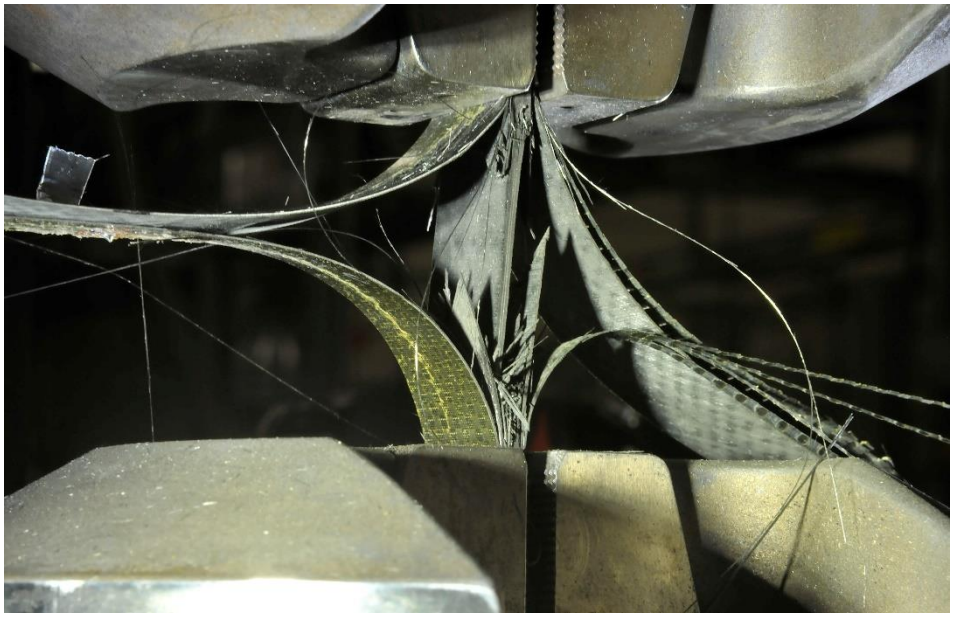

(A1-L-3) at Failure

Figure C1.75 Damage Progression in (A1-L-3) Test Specimen at Failure

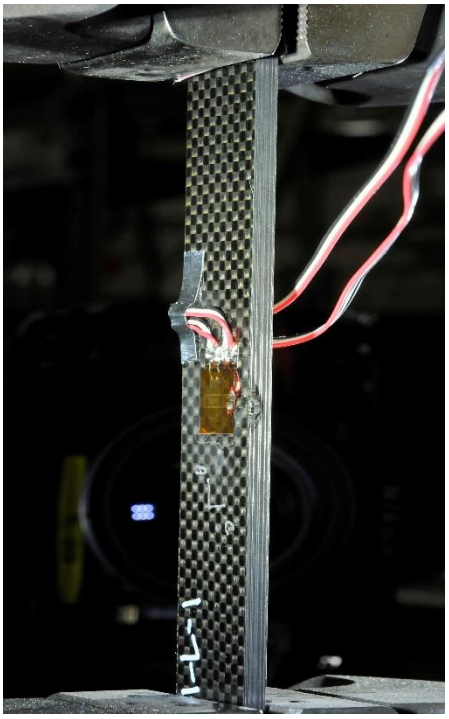

(B1-L-1) at 1 cycle

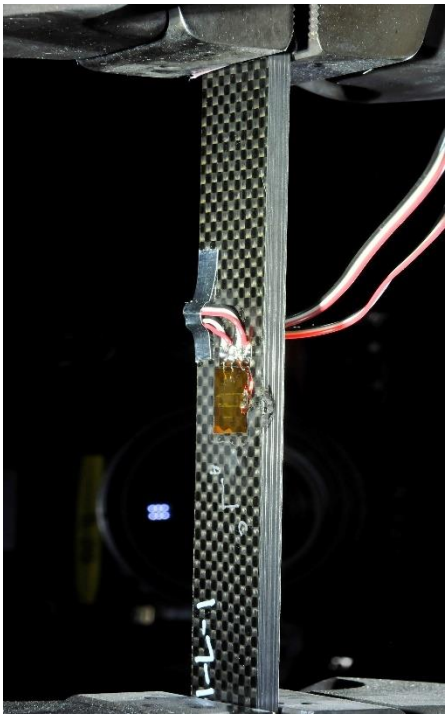

(B1-L-1) at 100 cycles

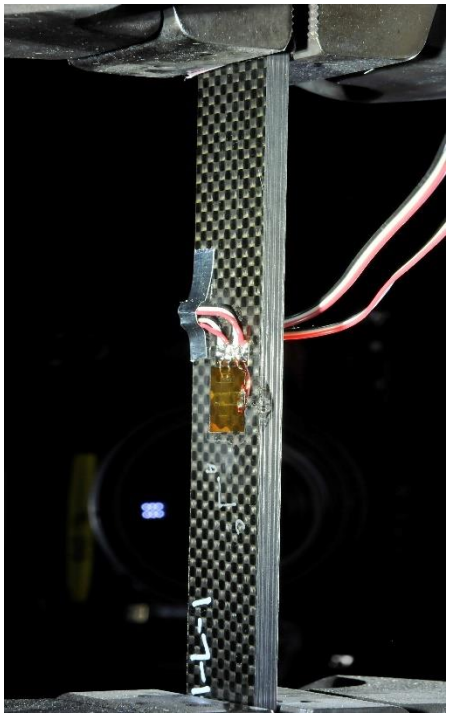

(B1-L-1) at 1K cycles

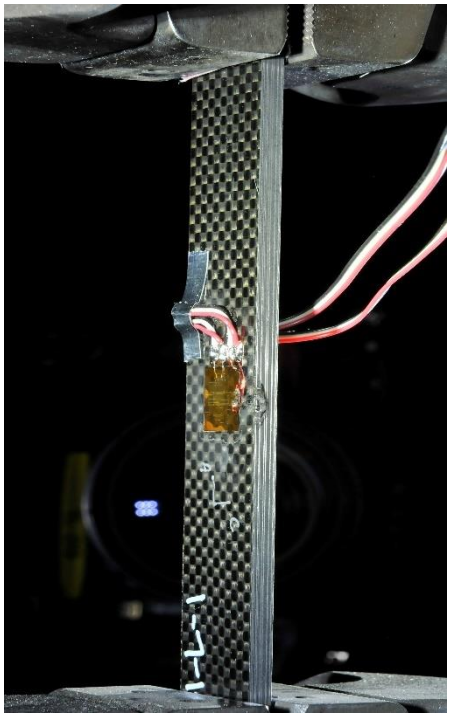

(B1-L-1) at 5K cycles

Figure C1.76 Damage Progression in (B1-L-1) Test Specimen at 5K cycles

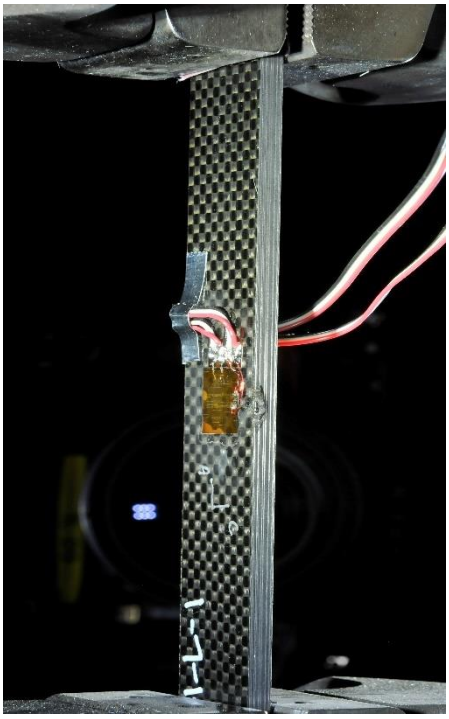

(B1-L-1) at 10K cycles

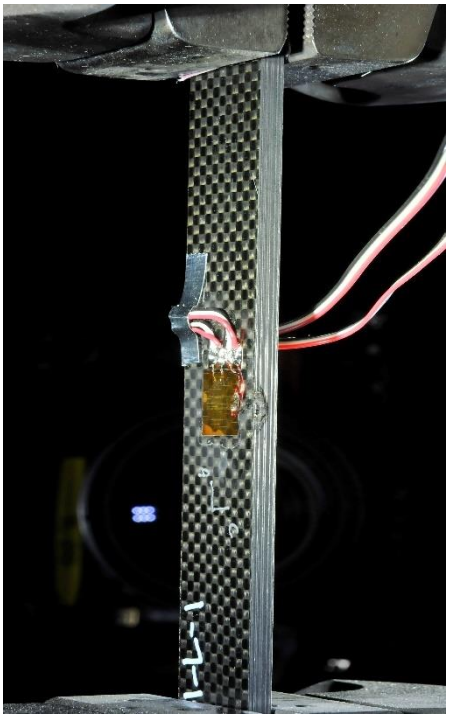

(B1-L-1) at 20K cycles

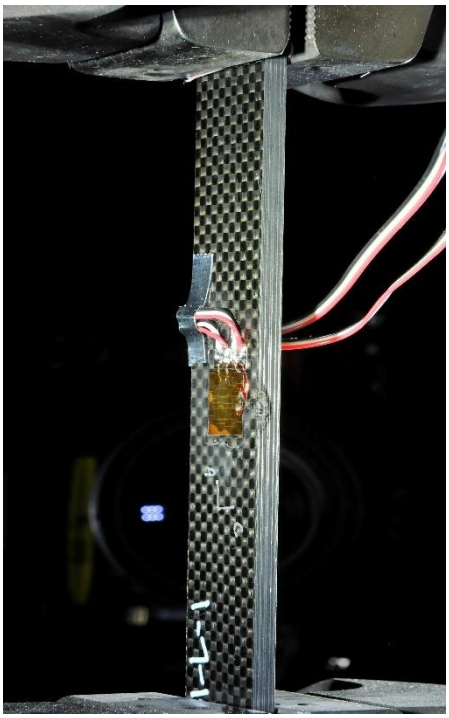

(B1-L-1) at 30K cycles

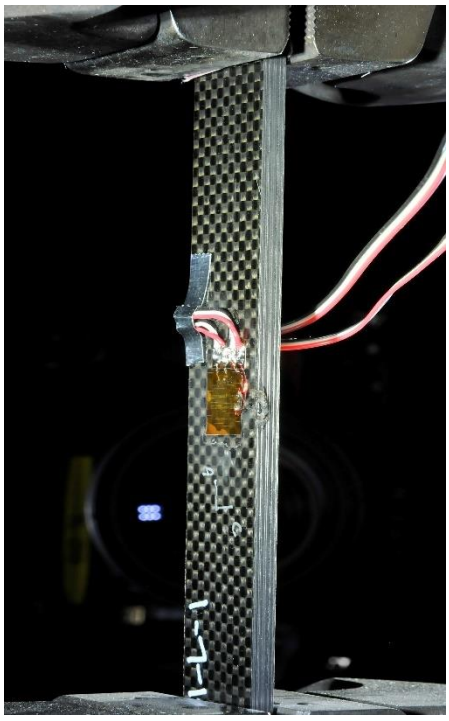

(B1-L-1) at 40K cycles

Figure C1.77 Damage Progression in (B1-L-1) Test Specimen at 40K cycles

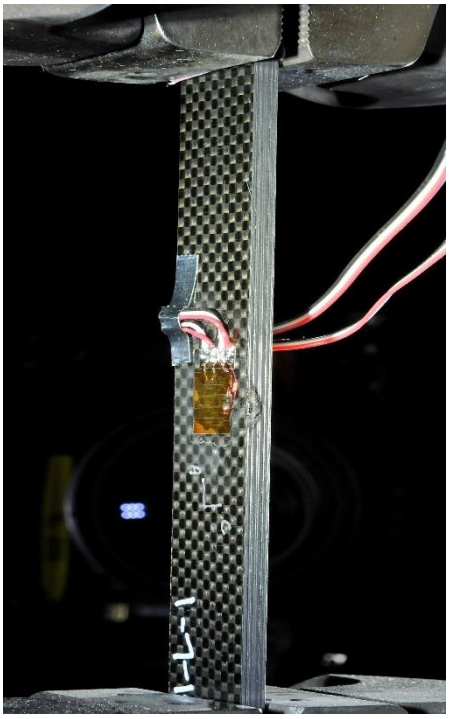

(B1-L-1) at 50K cycles

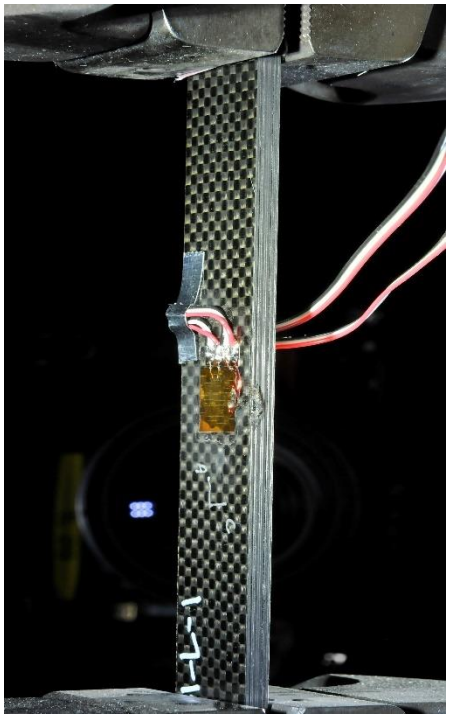

(B1-L-1) at 60K cycles

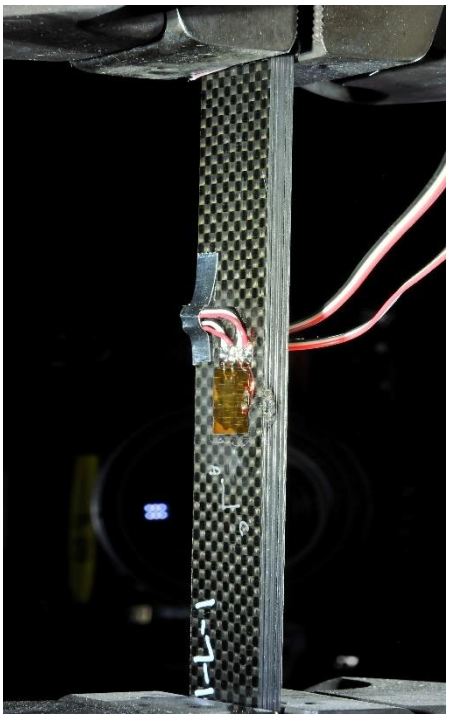

(B1-L-1) at 70K cycles

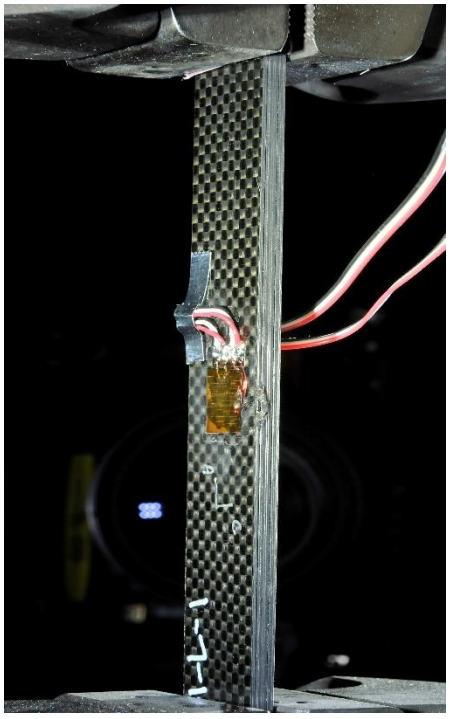

(B1-L-1) at 80K cycles

Figure C1.78 Damage Progression in (B1-L-1) Test Specimen at 80K cycles

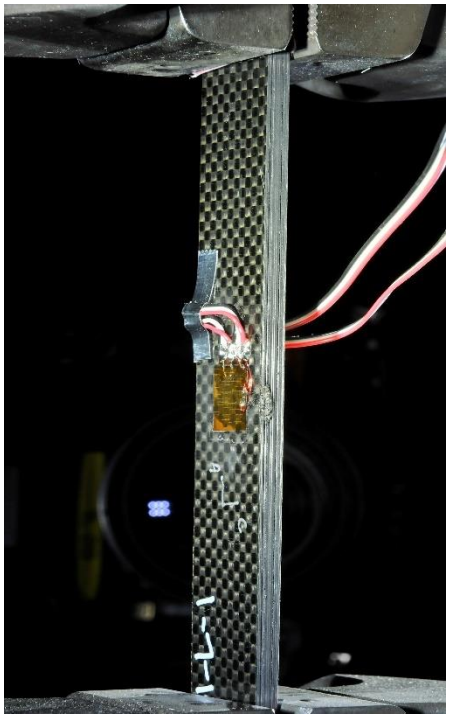

(B1-L-1) at 90K cycles

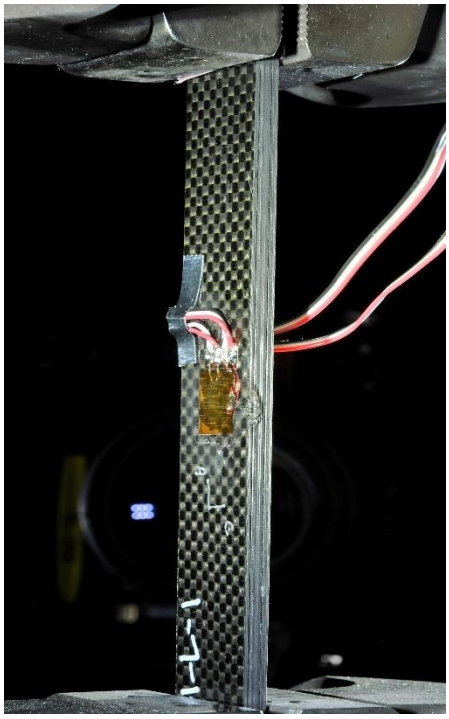

(B1-L-1) at 100K cycles

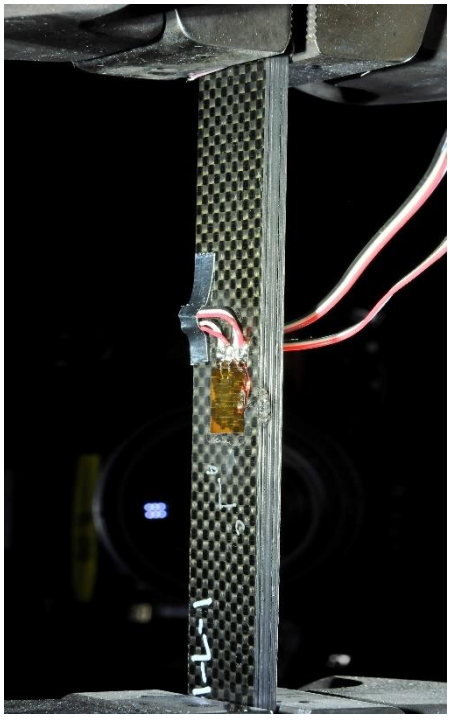

(B1-L-1) at 125K cycles

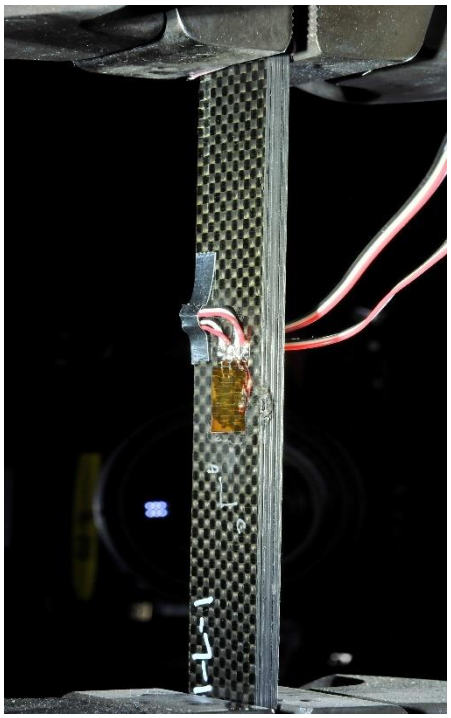

(B1-L-1) at 150K cycles

Figure C1.79 Damage Progression in (B1-L-1) Test Specimen at 150K cycles

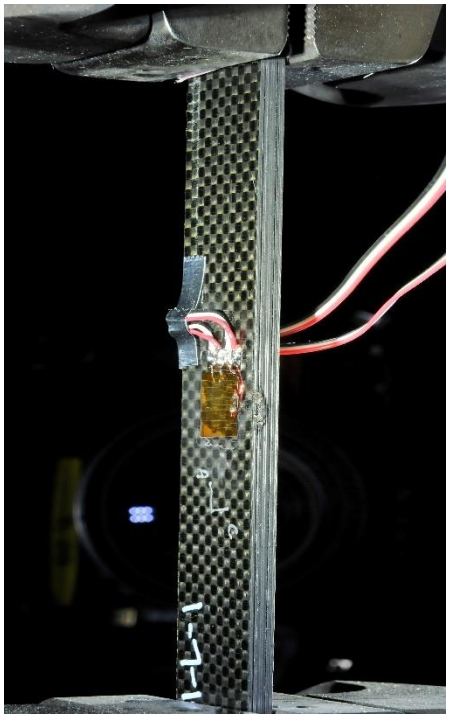
(B1-L-1) at 1750K cycles

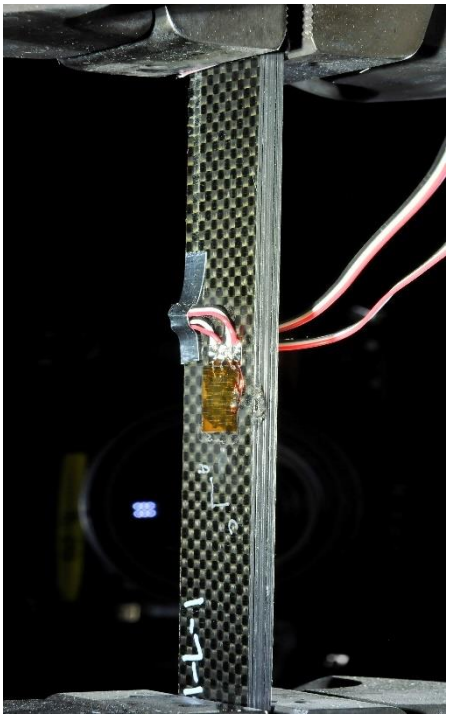
(B1-L-1) at 200K cycles

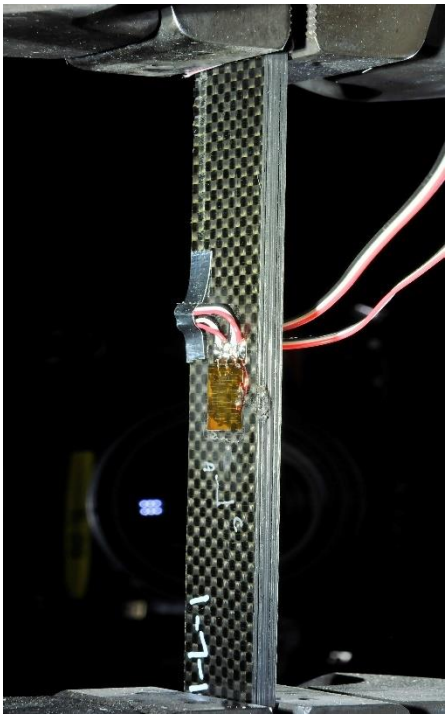
(B1-L-1) at 225K cycles

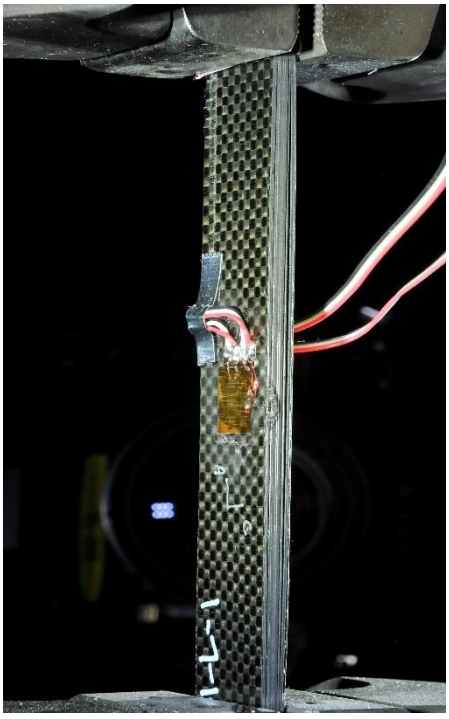
(B1-L-1) at 250K cycles

Figure C1.80 Damage Progression in (B1-L-1) Test Specimen at 250K cycles

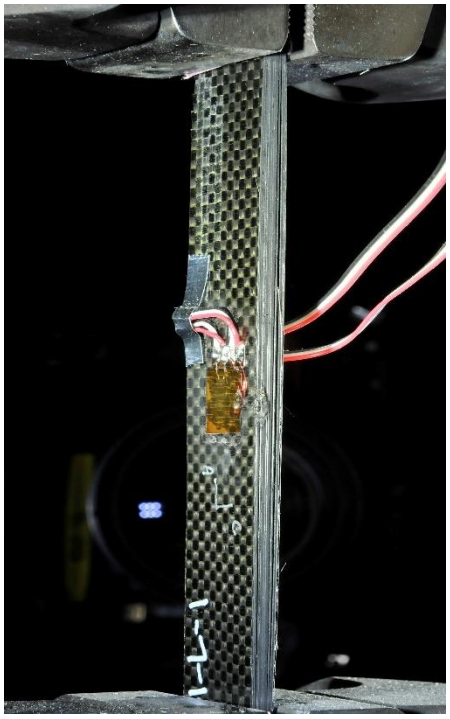

(B1-L-1) at 275K cycles

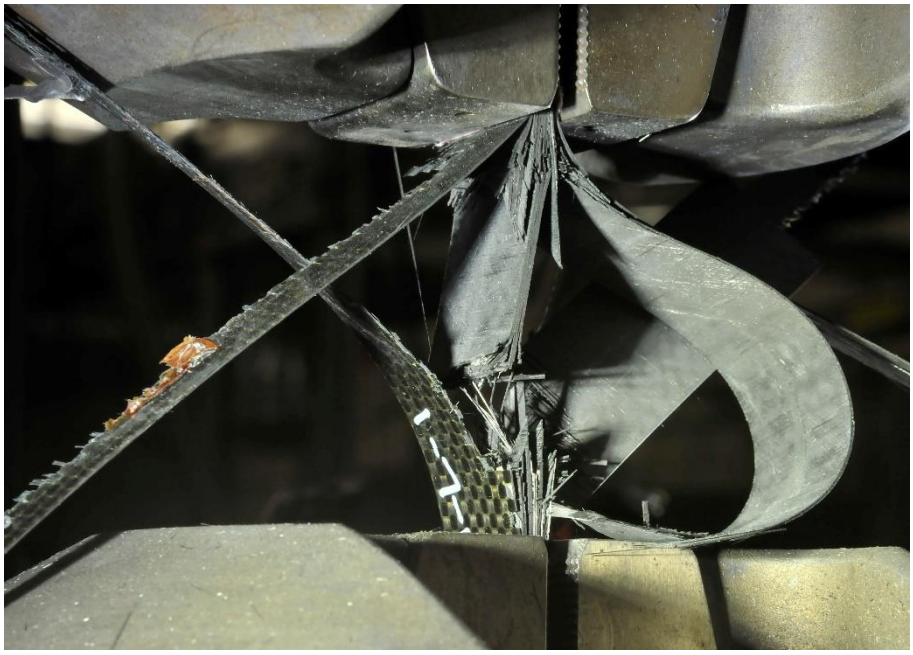

(B1-L-1) at Failure

Figure C1.81 Damage Progression in (B1-L-1) Test Specimen at Failure

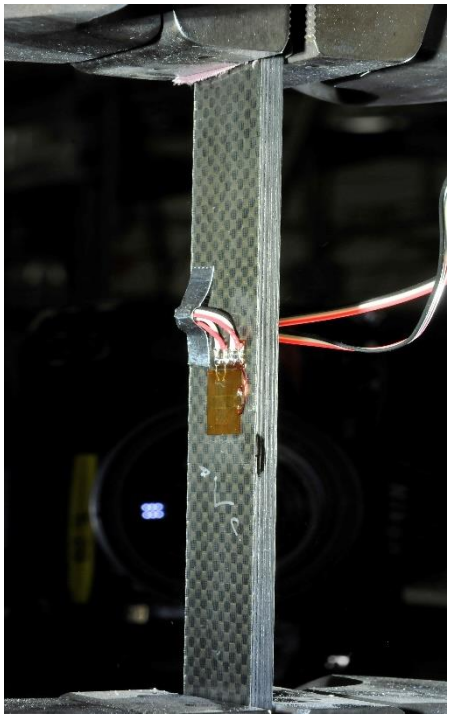

(B1-L-2) at 1 cycle

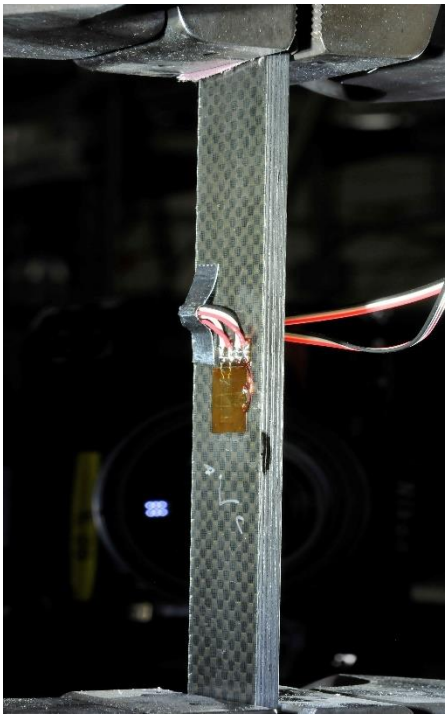

(B1-L-2) at 100 cycles

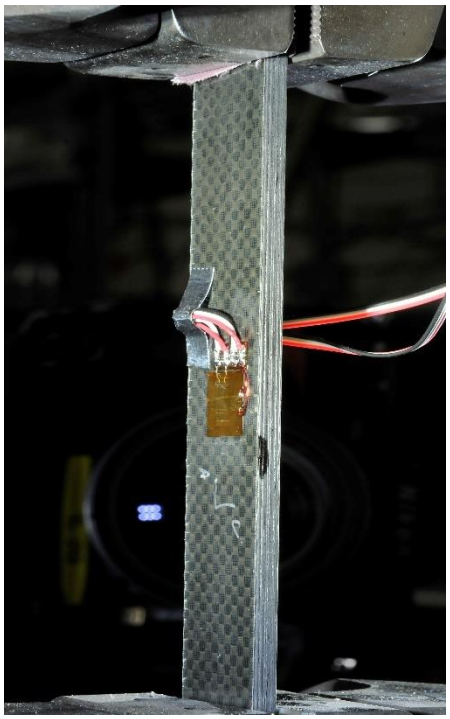

(B1-L-2) at 1K cycles

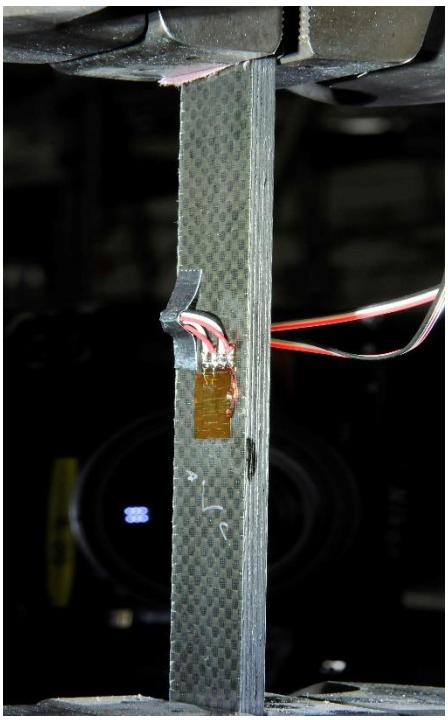

(B1-L-2) at 5K cycles

Figure C1.82 Damage Progression in (B1-L-2) Test Specimen at 5K cycles

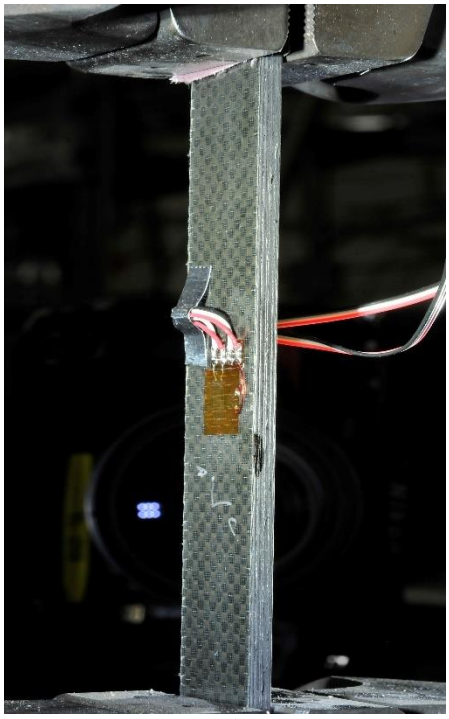

(B1-L-2) at 10K cycles

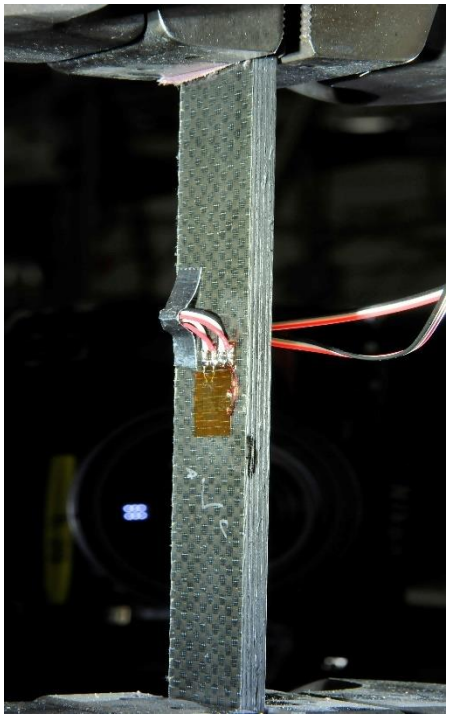

(B1-L-2) at 20K cycles

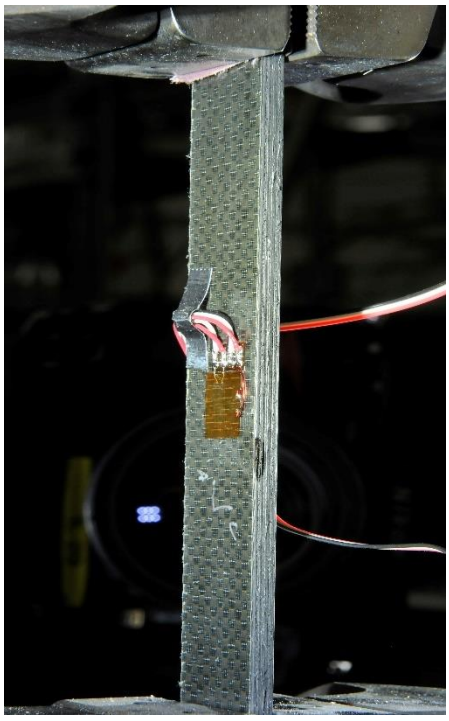

(B1-L-2) at 30K cycles

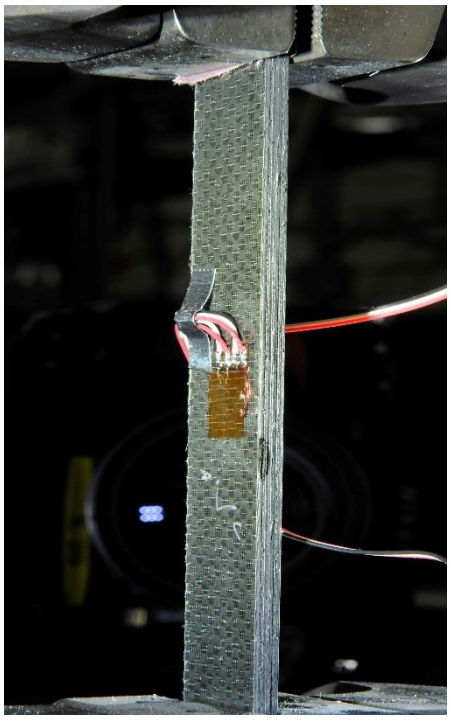

(B1-L-2) at 40K cycles

Figure C1.83 Damage Progression in (B1-L-2) Test Specimen at 40K cycles

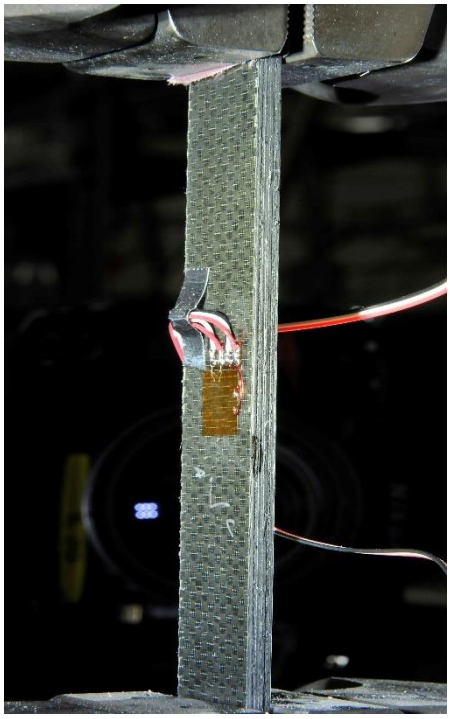

(B1-L-2) at 50K cycles

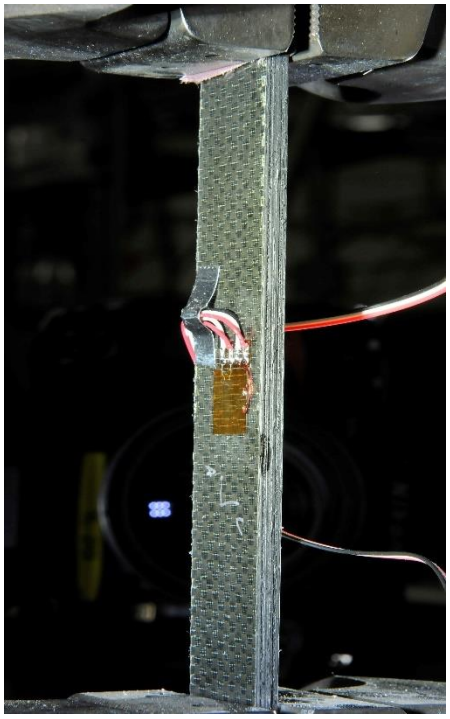

(B1-L-2) at 60K cycles

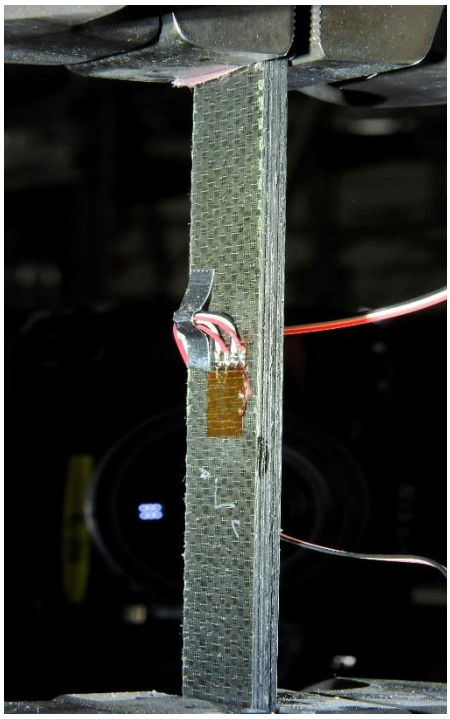

(B1-L-2) at 70K cycles

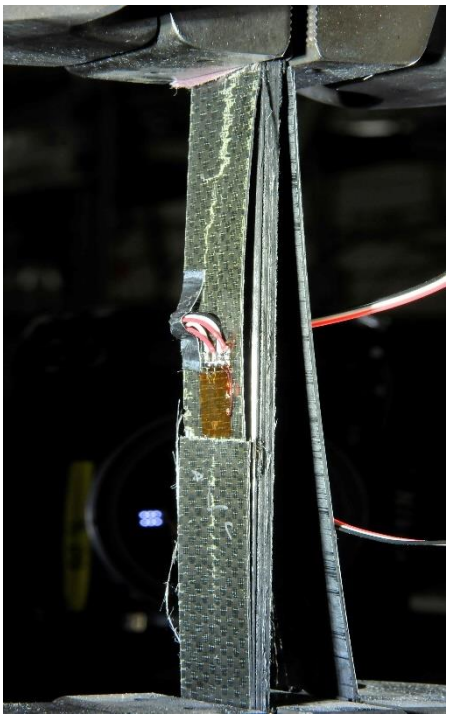

(B1-L-2) at Failure

Figure C1.84 Damage Progression in (B1-L-2) Test Specimen at Failure

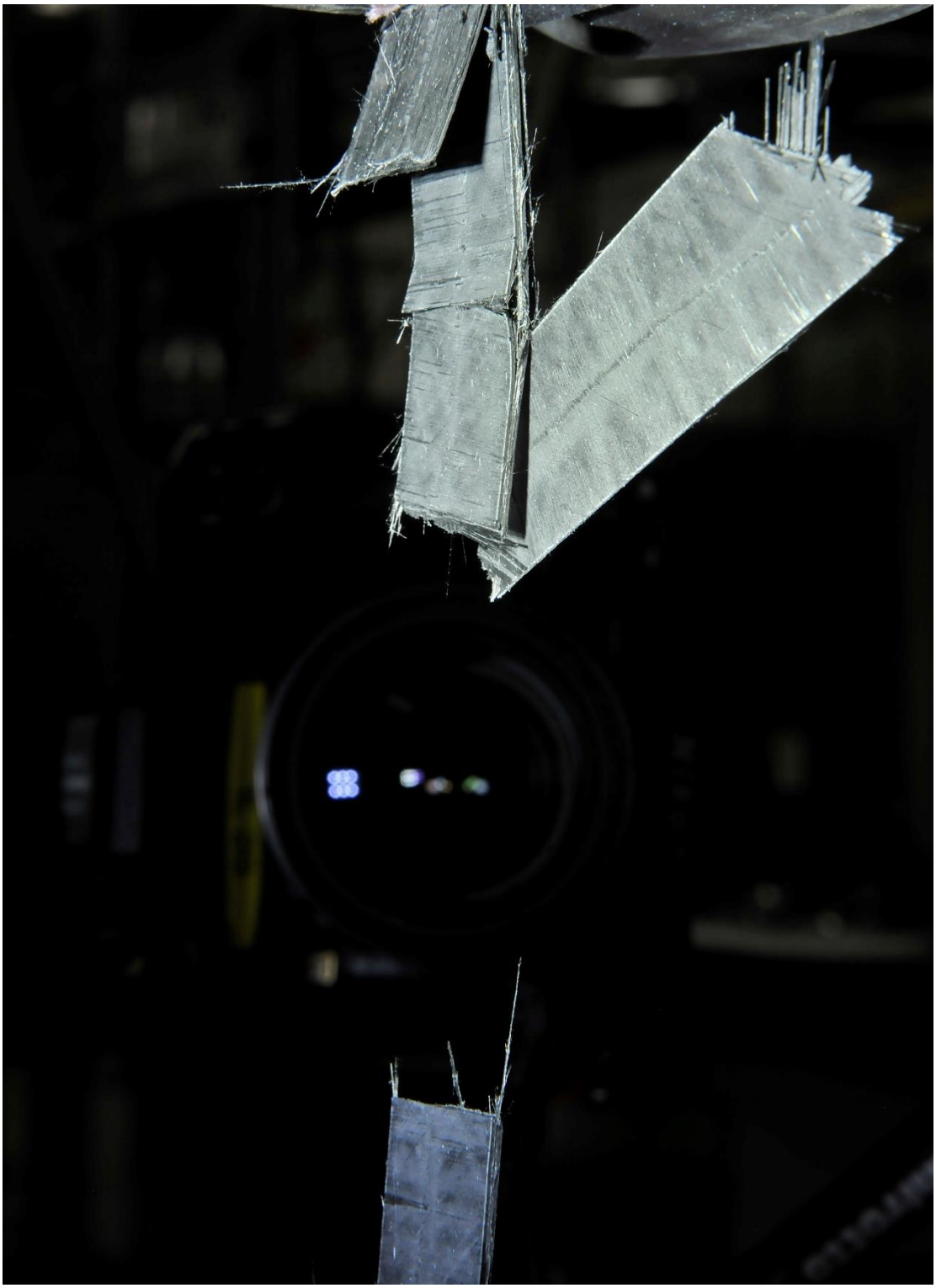

(B1-L-2) at Failure

Figure C1.85 Damage Progression in (B1-L-2) Test Specimen at Failure

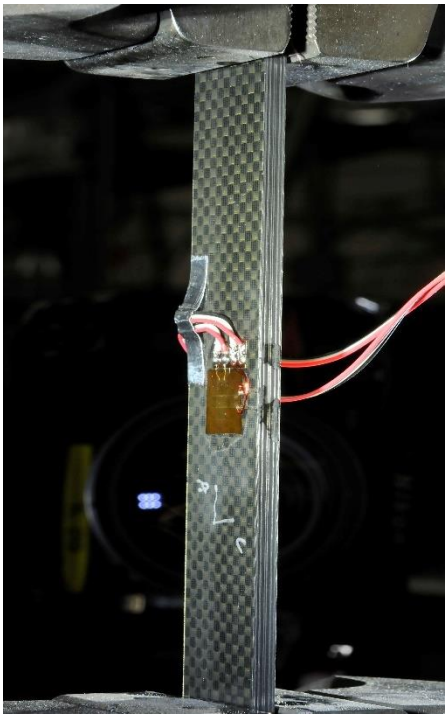

(B1-L-3) at 1 cycle

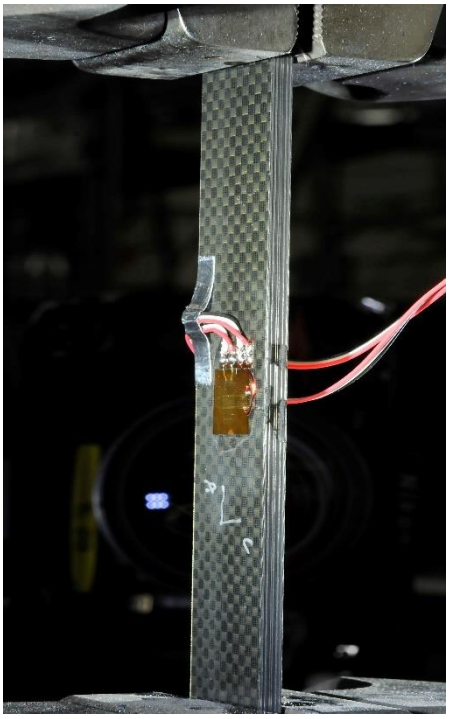

(B1-L-3) at 100 cycles

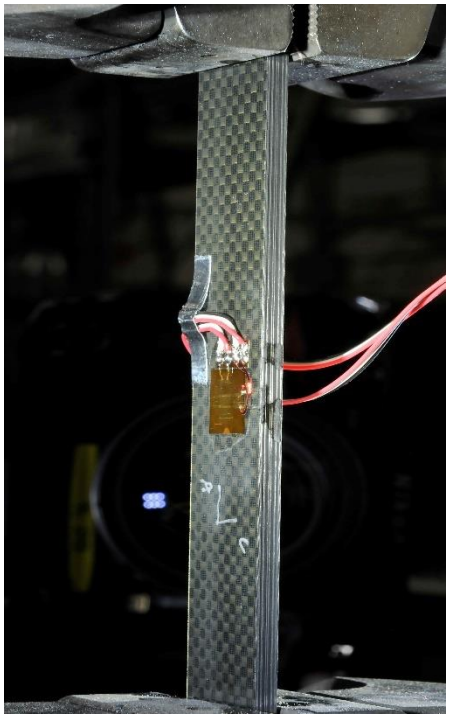

(B1-L-3) at 1K cycles

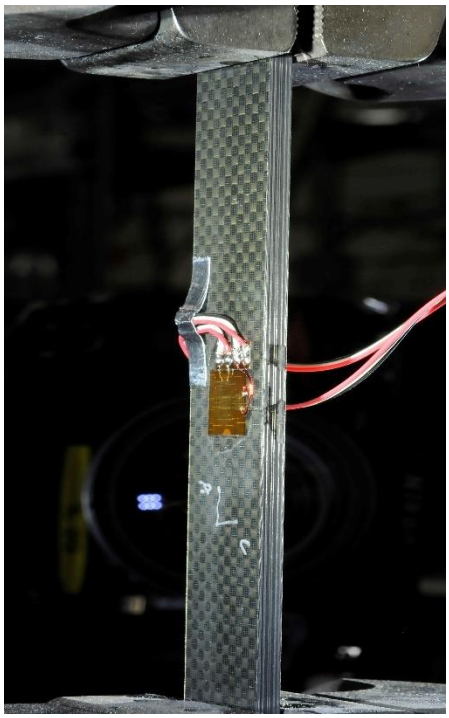

(B1-L-3) at 5K cycles

Figure C1.86 Damage Progression in (B1-L-3) Test Specimen at 5K cycles

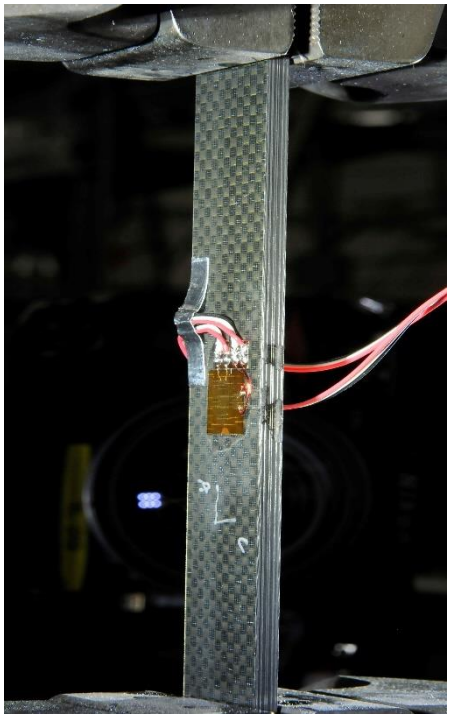

(B1-L-3) at 10K cycles

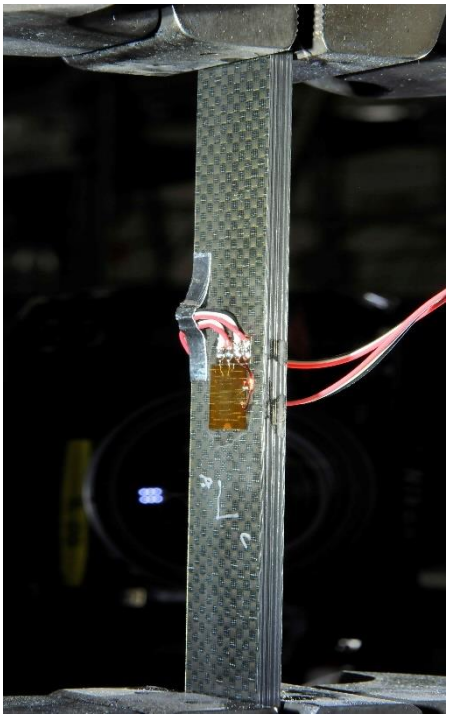

(B1-L-3) at 20K cycles

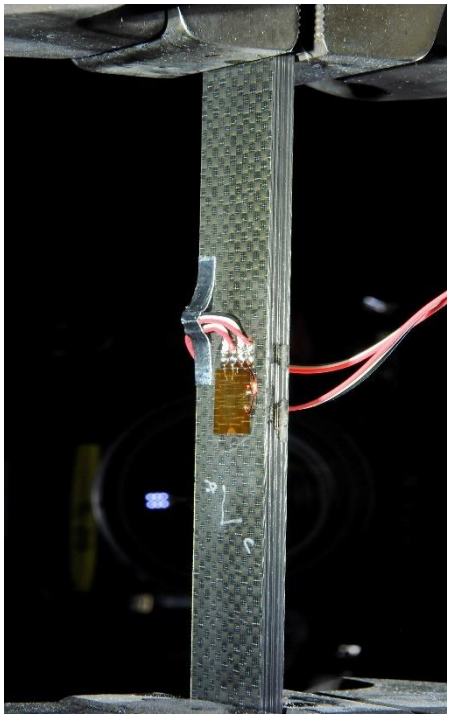

(B1-L-3) at 30K cycles

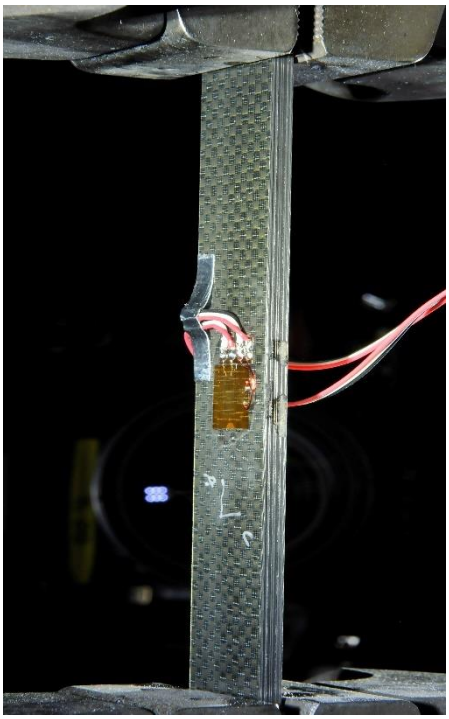

(B1-L-3) at 40K cycles

Figure C1.87 Damage Progression in (B1-L-3) Test Specimen at 40K cycles

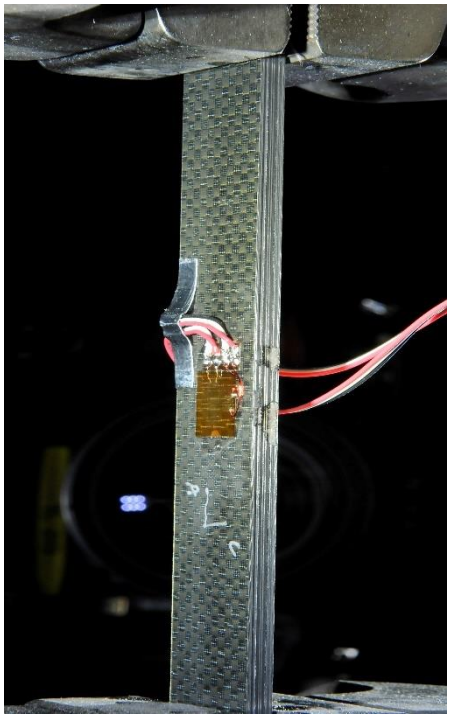

(B1-L-3) at 50K cycles

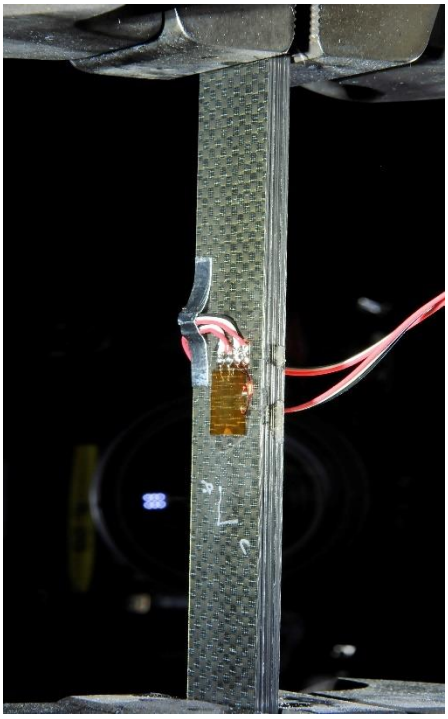

(B1-L-3) at 60K cycles

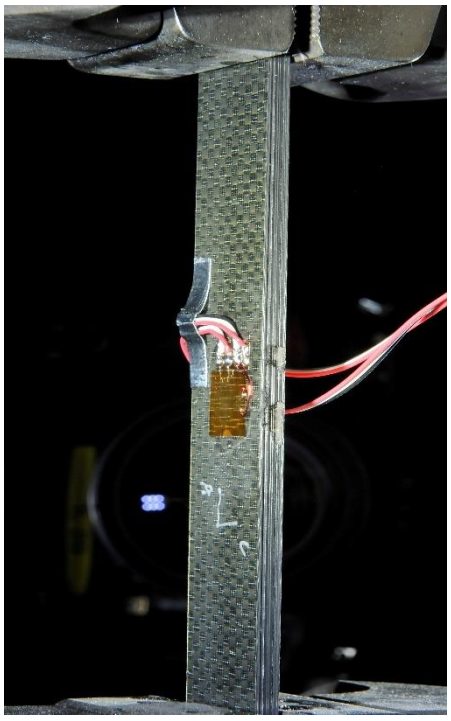

(B1-L-3) at 70K cycles

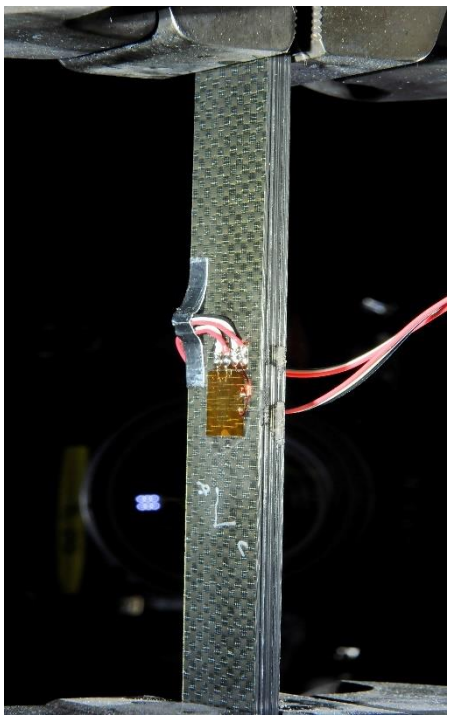

(B1-L-3) at 80K cycles

Figure C1.88 Damage Progression in (B1-L-3) Test Specimen at 80K cycles

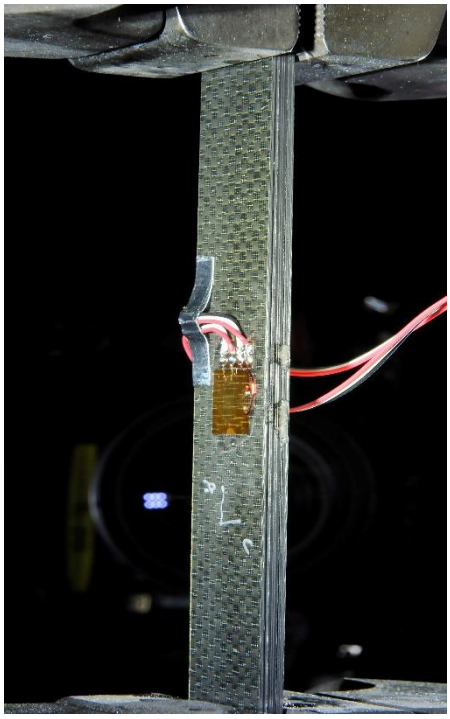

(B1-L-3) at 90K cycles

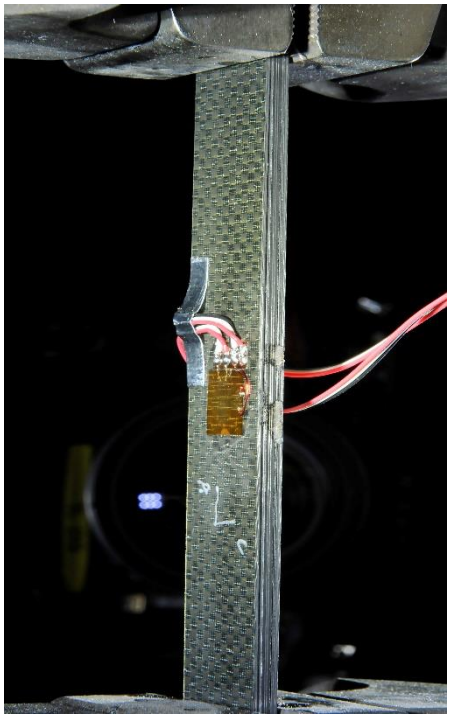

(B1-L-3) at 100K cycles

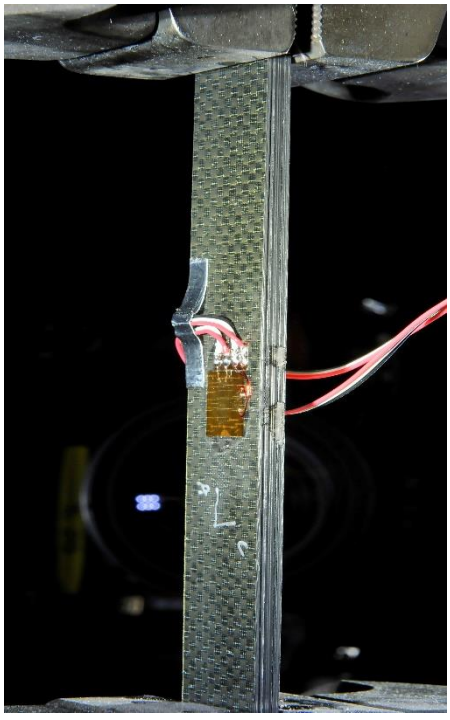

(B1-L-3) at 125K cycles

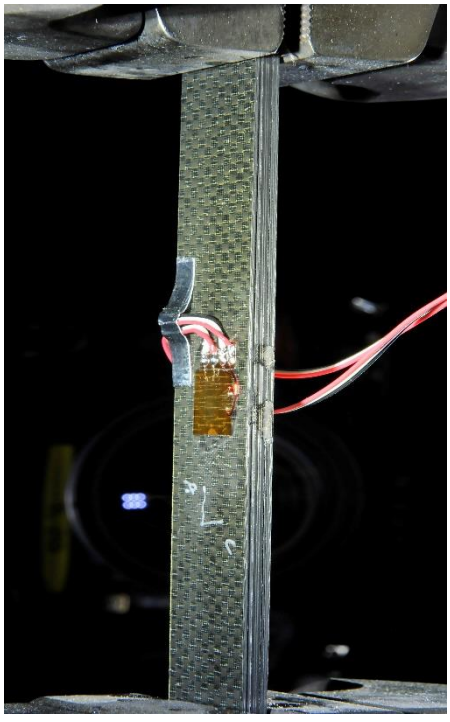

(B1-L-3) at 150K cycles

Figure C1.89 Damage Progression in (B1-L-3) Test Specimen at 150K cycles

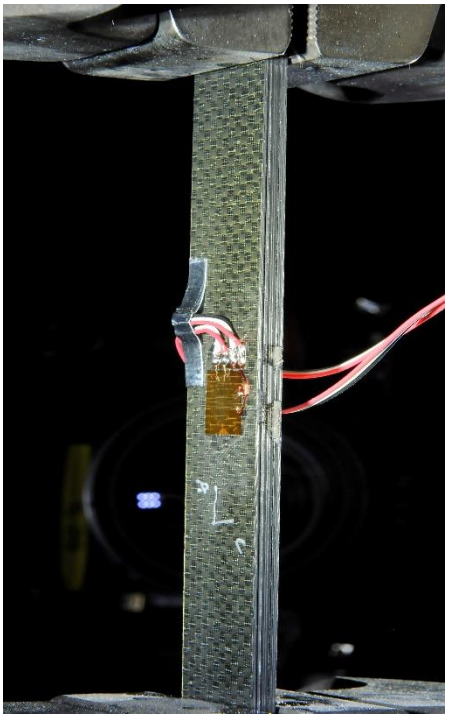

(B1-L-3) at 175K cycles

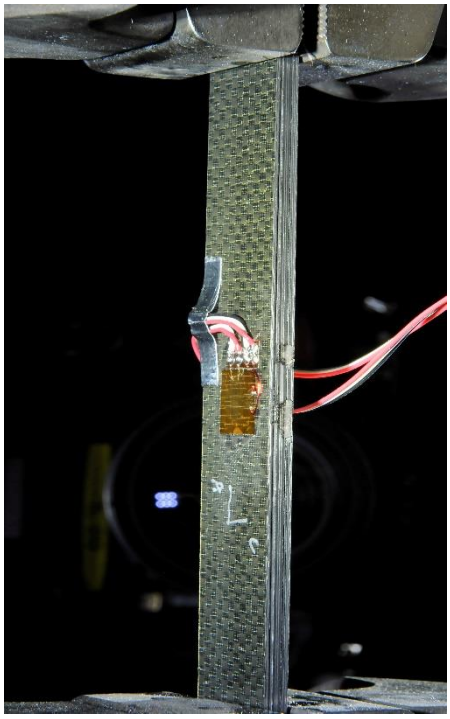

(B1-L-3) at 200K cycles

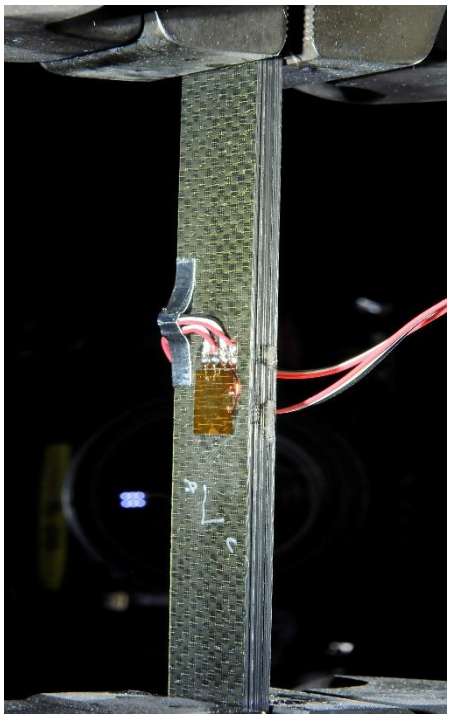

(B1-L-3) at 225K cycles

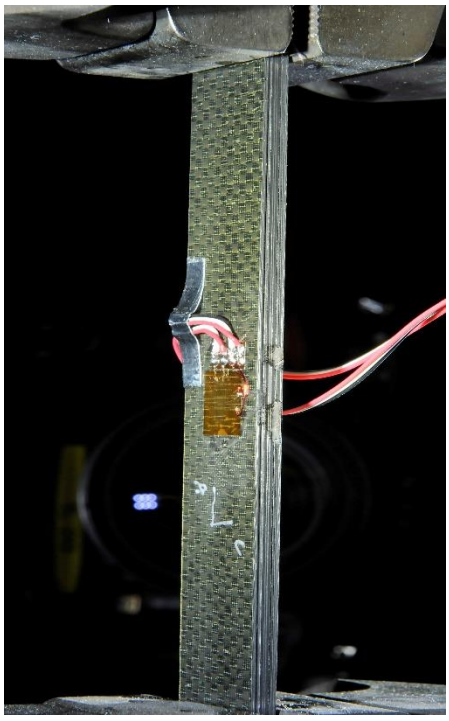

(B1-L-3) at 250K cycles

Figure C1.90 Damage Progression in (B1-L-3) Test Specimen at 250K cycles

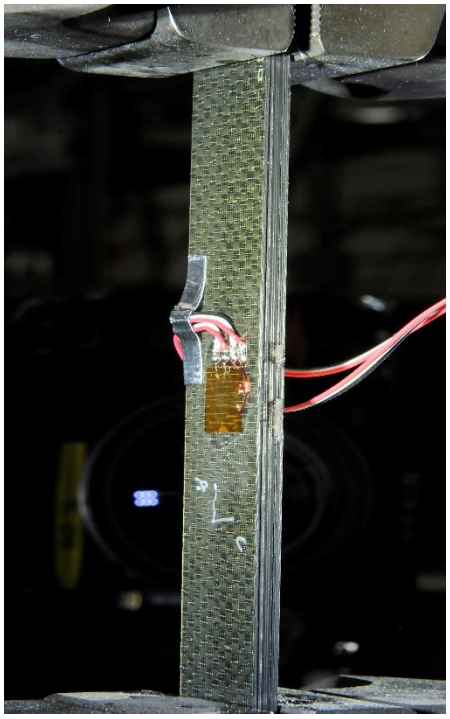

(B1-L-3) at 275K cycles

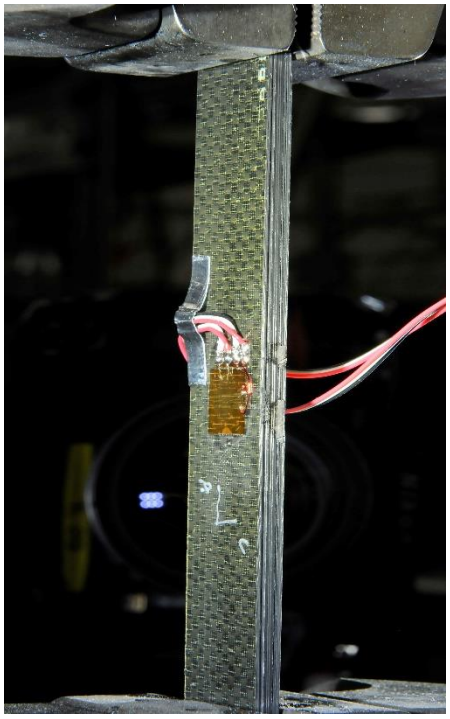

(B1-L-3) at 300K cycles

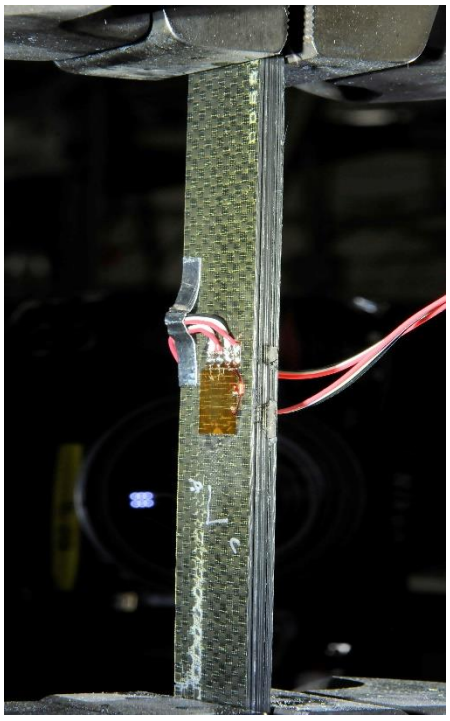

(B1-L-3) at 325K cycles

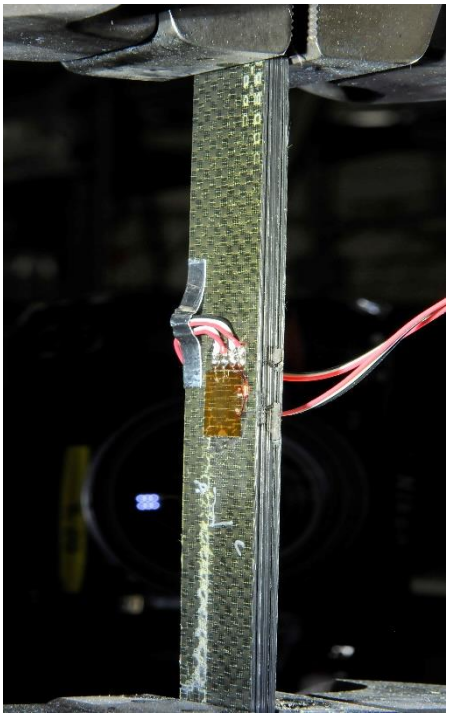

(B1-L-3) at 350K cycles

Figure C1.91 Damage Progression in (B1-L-3) Test Specimen at 350K cycles

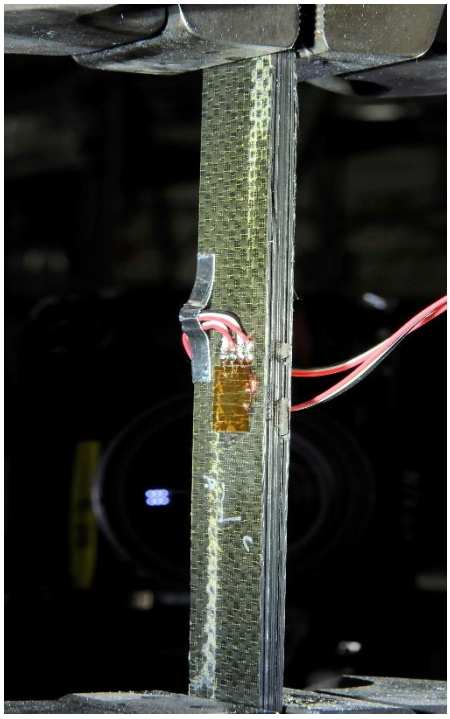

(B1-L-3) at 375K cycles

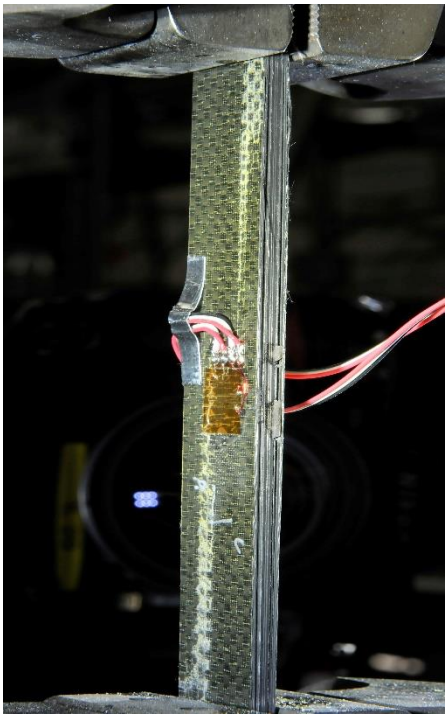

(B1-L-3) at 400K cycles

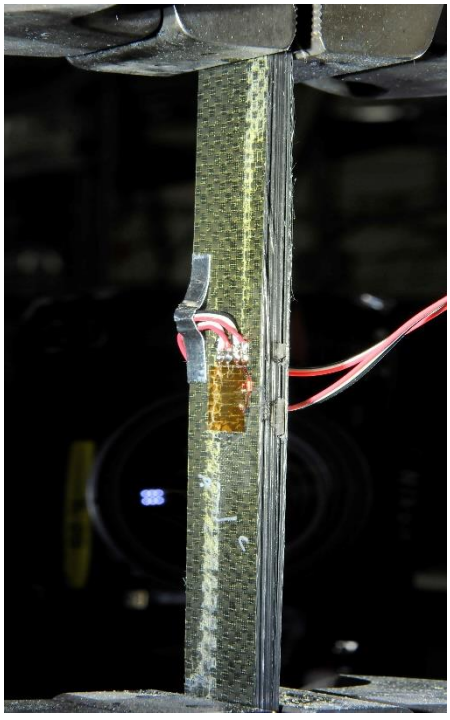

(B1-L-3) at 425K cycles

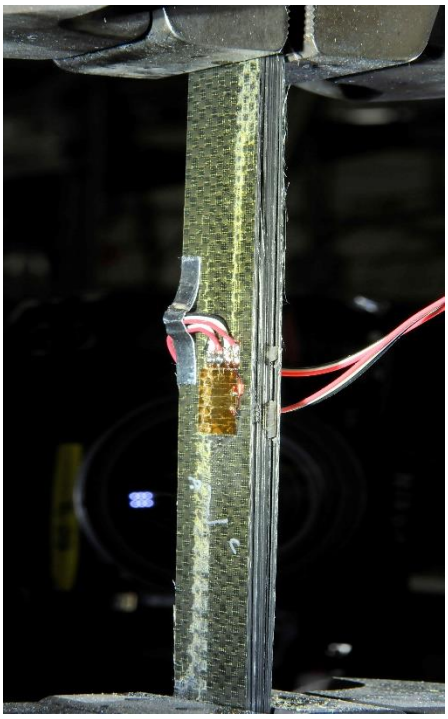

(B1-L-3) at 450K cycles

Figure C1.92 Damage Progression in (B1-L-3) Test Specimen at 450K cycles

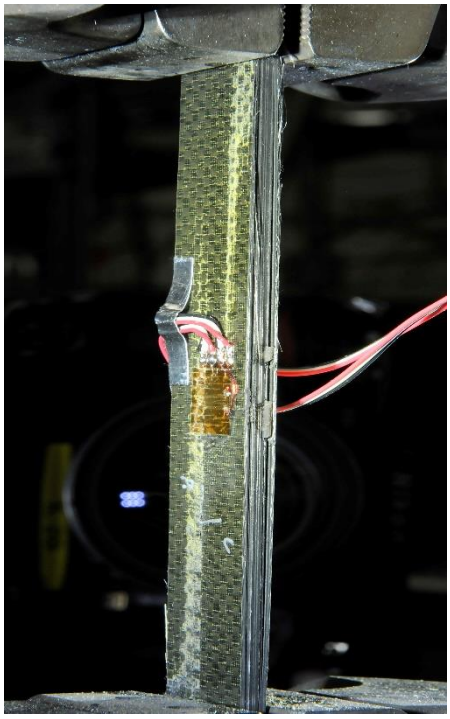

(B1-L-3) at 475K cycles

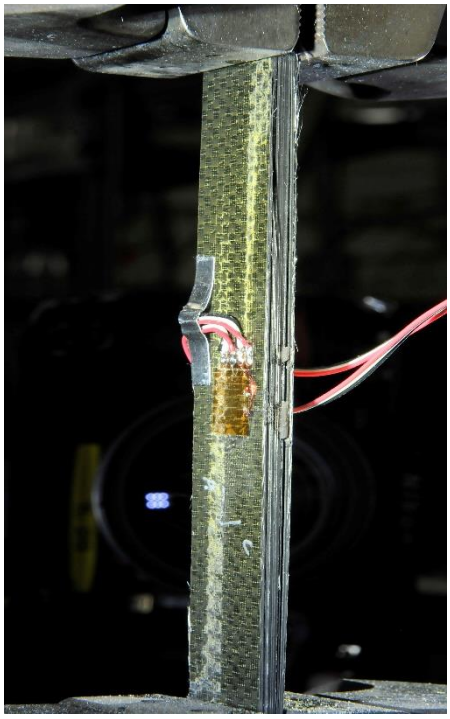

(B1-L-3) at 500K cycles

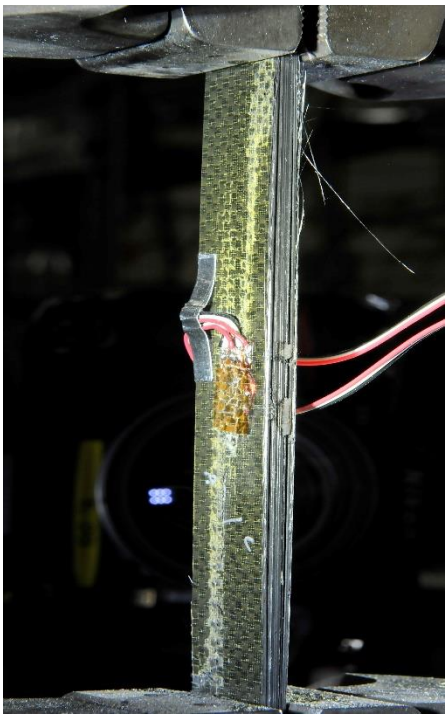

(B1-L-3) at 525K cycles

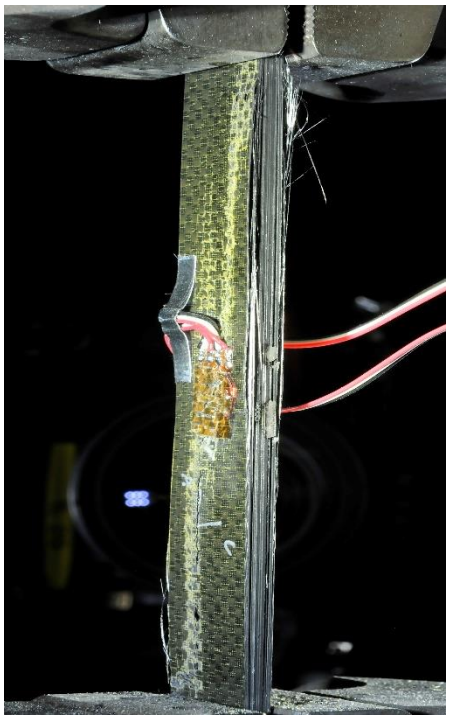

(B1-L-3) at 550K cycles

Figure C1.93 Damage Progression in (B1-L-3) Test Specimen at 550K cycles

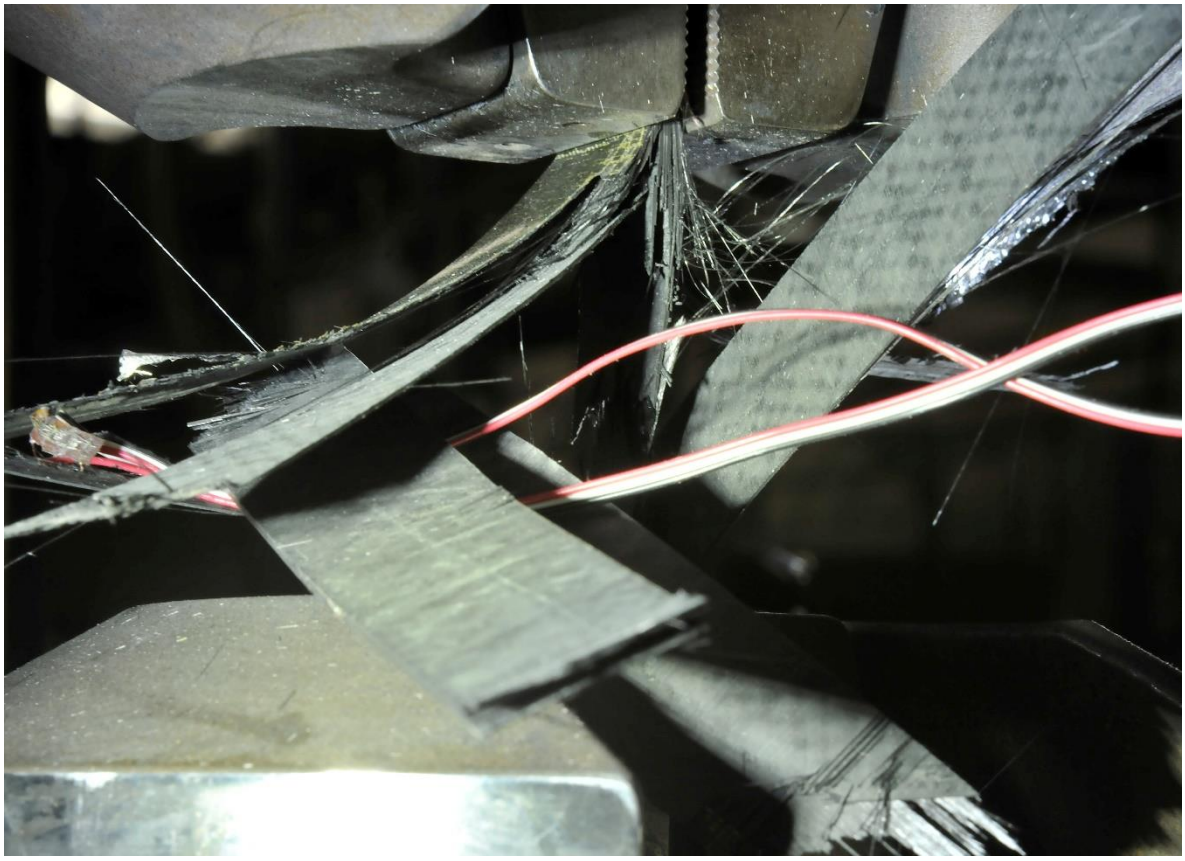

(B1-L-3) at Failure

Figure C1.94 Damage Progression in (B1-L-3) Test Specimen at Failure

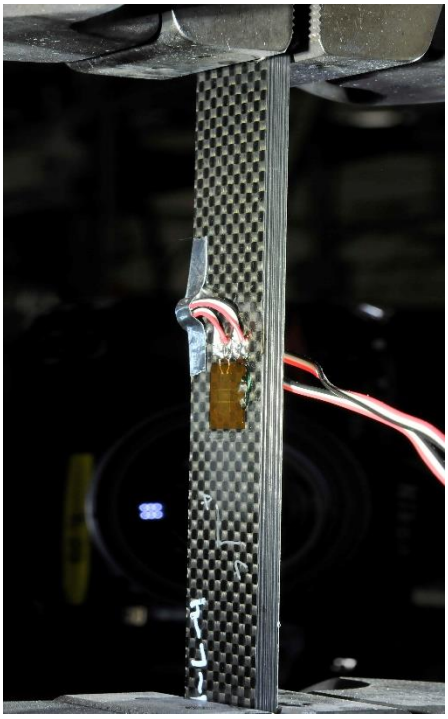

(B1-L-4) at 1 cycle

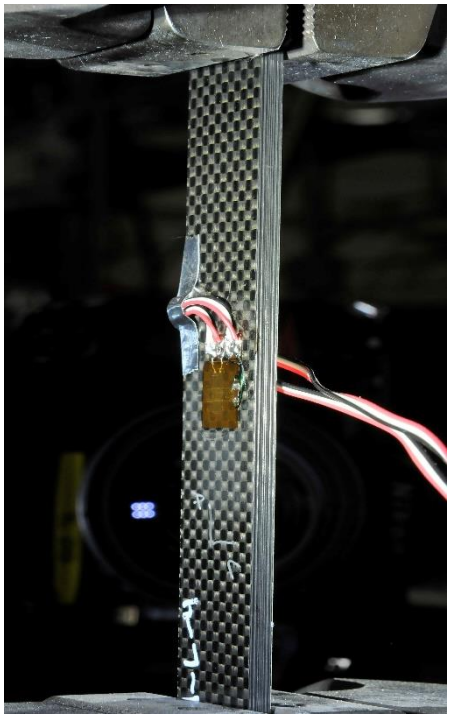

(B1-L-4) at 100 cycles

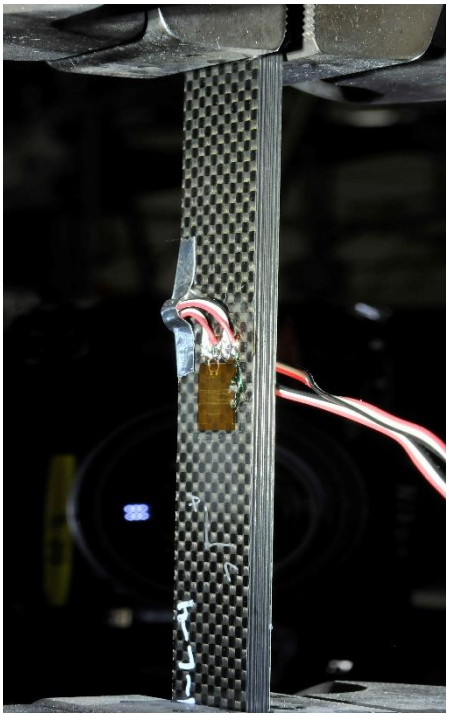

(B1-L-4) at 1K cycles

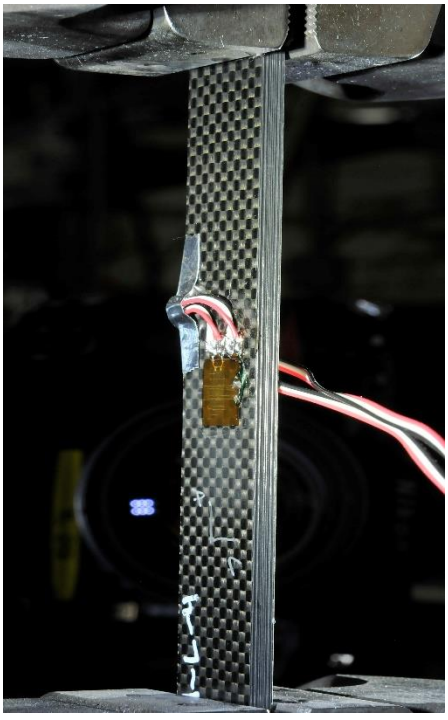

(B1-L-4) at 5K cycles

Figure C1.95 Damage Progression in (B1-L-4) Test Specimen at 5K cycles

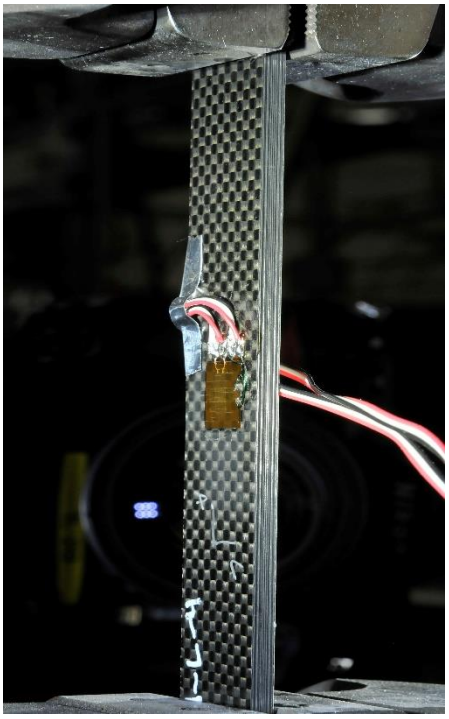

(B1-L-4) at 10K cycles

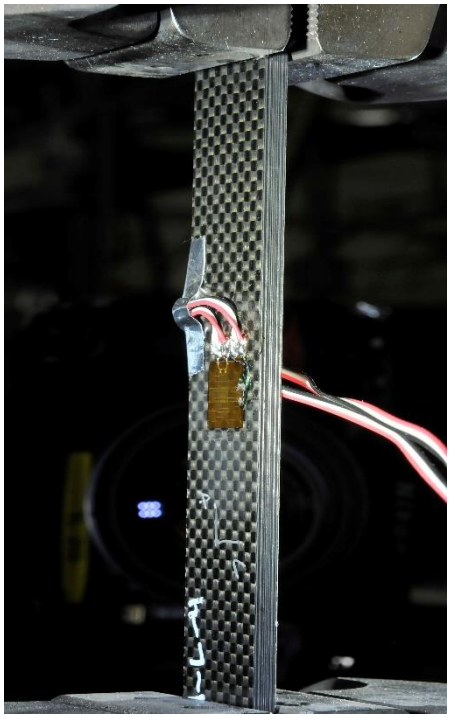

(B1-L-4) at 20K cycles

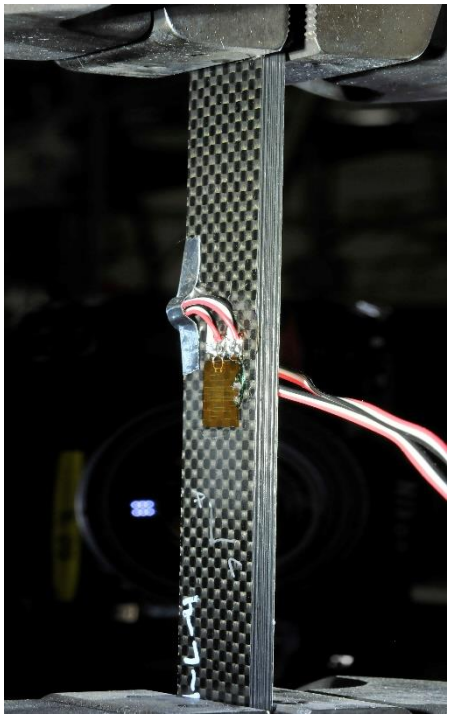

(B1-L-4) at 30K cycles

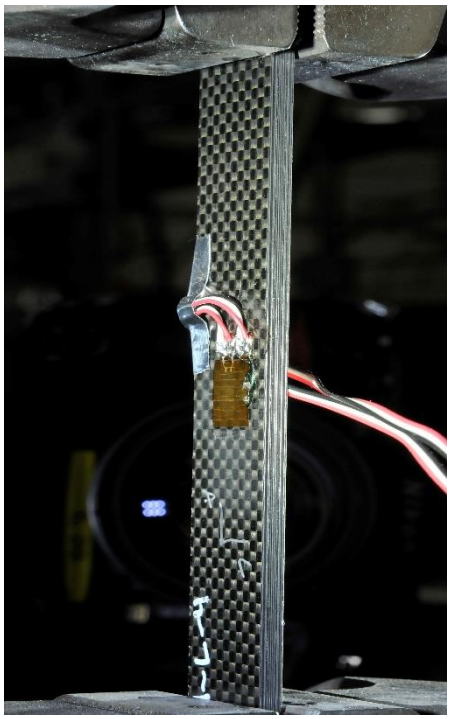

(B1-L-4) at 40K cycles

Figure C1.96 Damage Progression in (B1-L-4) Test Specimen at 40K cycles

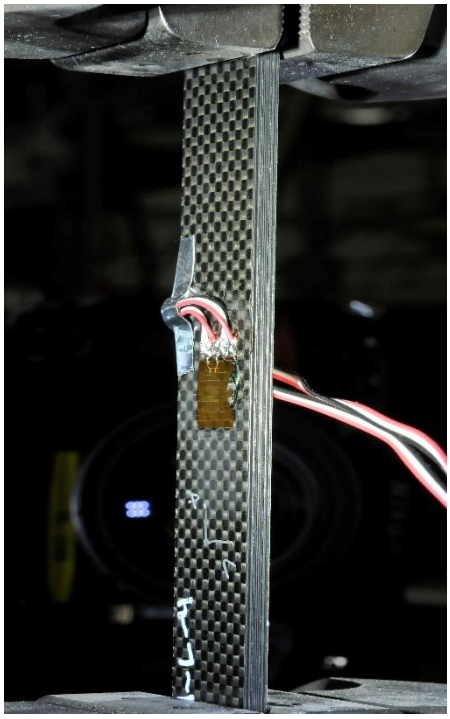

(B1-L-4) at 50K cycles

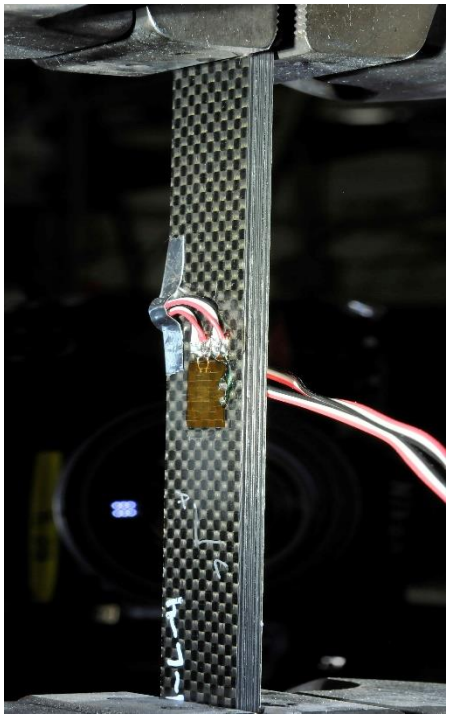

(B1-L-4) at 60K cycles

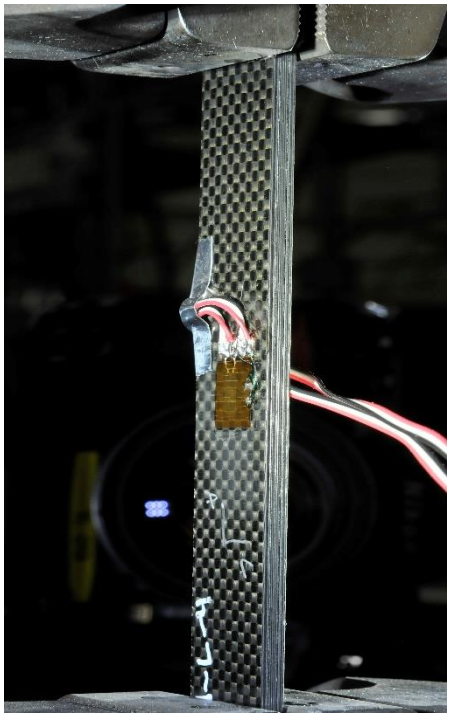

(B1-L-4) at 70K cycles

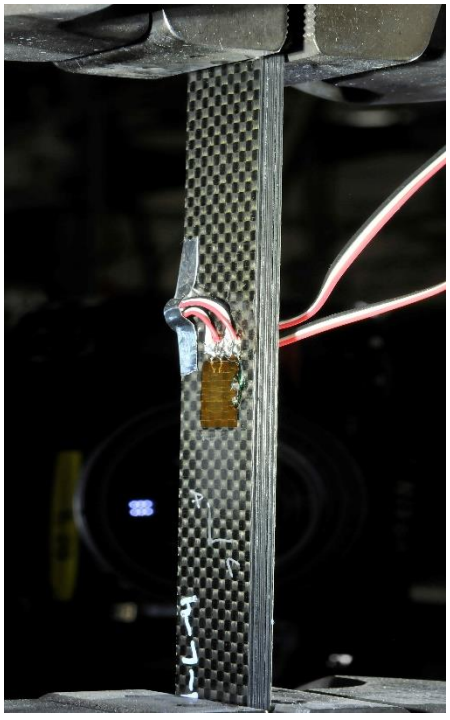

(B1-L-4) at 80K cycles

Figure C1.97 Damage Progression in (B1-L-4) Test Specimen at 80K cycles

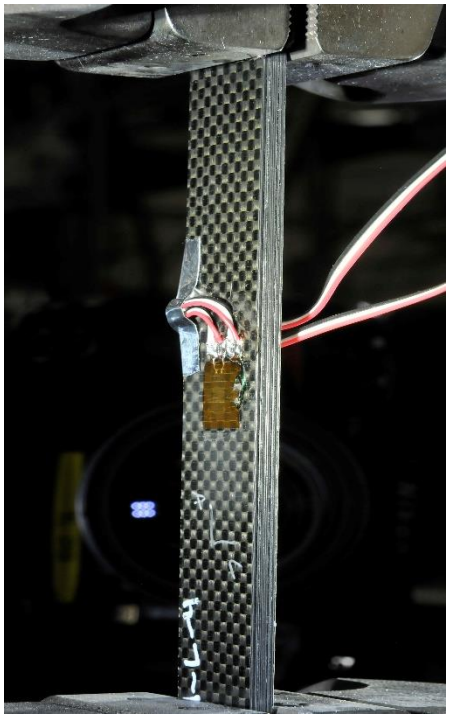

(B1-L-4) at 90K cycles

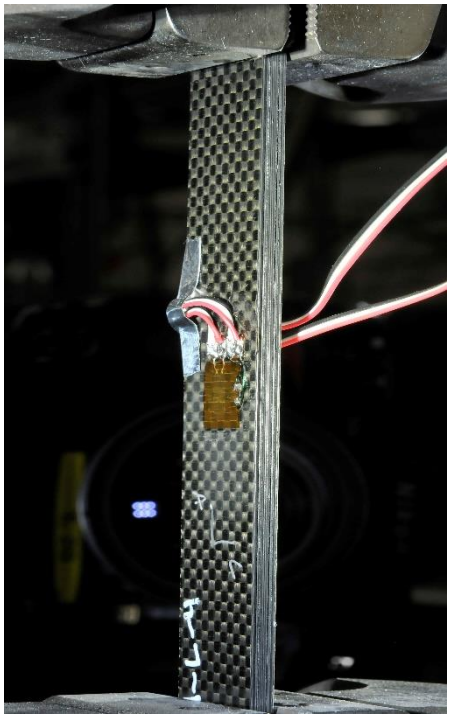

(B1-L-4) at 100K cycles

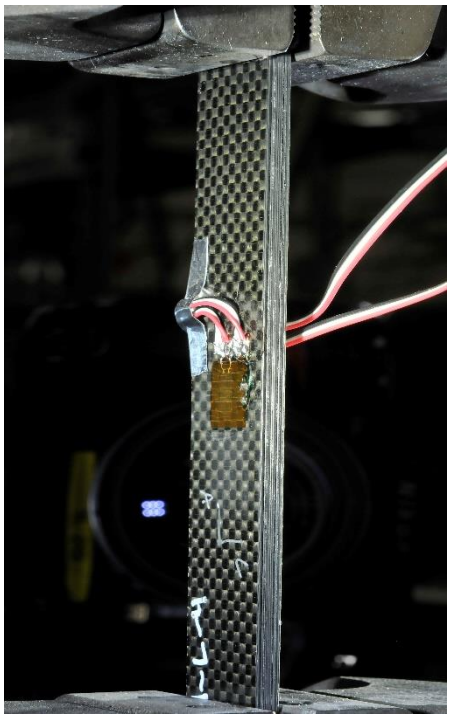

(B1-L-4) at 125K cycles

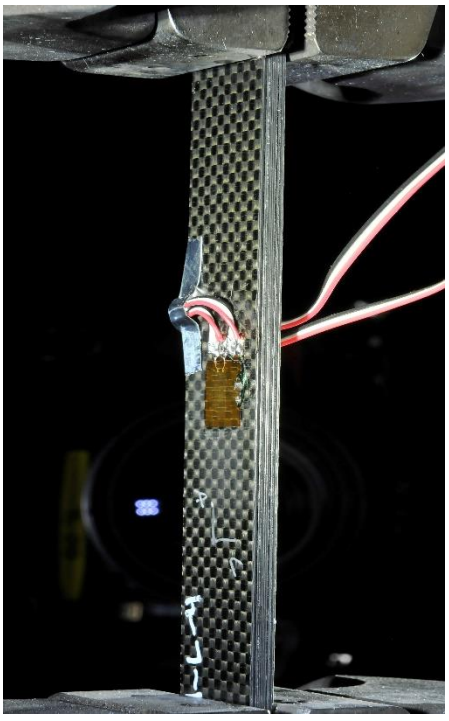

(B1-L-4) at 150K cycles

Figure C1.98 Damage Progression in (B1-L-4) Test Specimen at 150K cycles

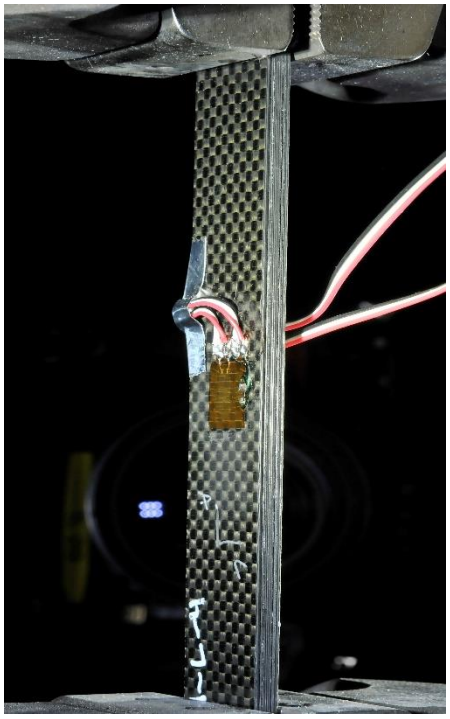

(B1-L-4) at 175K cycles

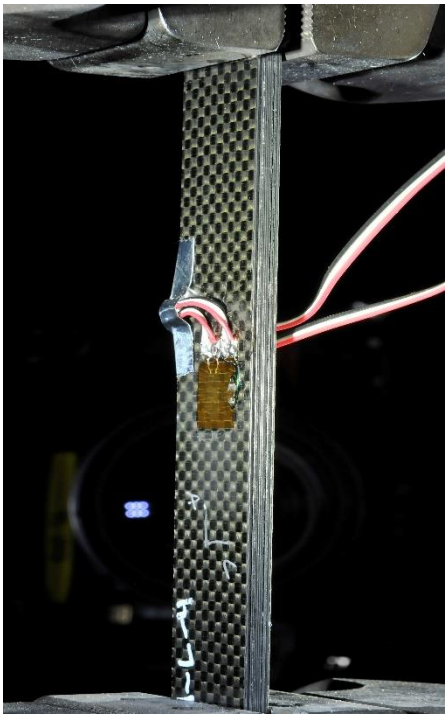

(B1-L-4) at 200K cycles

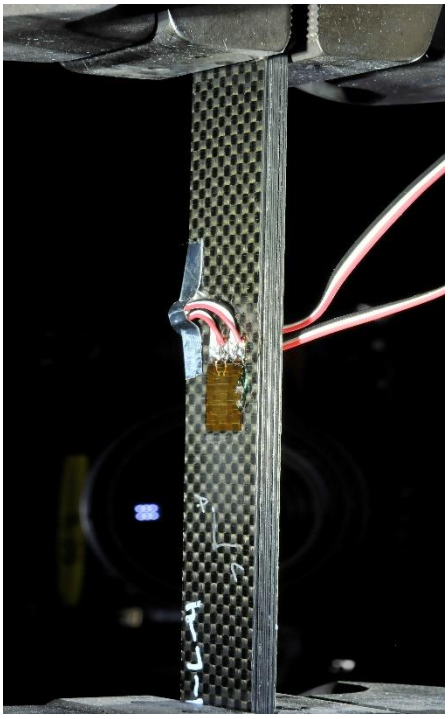

(B1-L-4) at 225K cycles

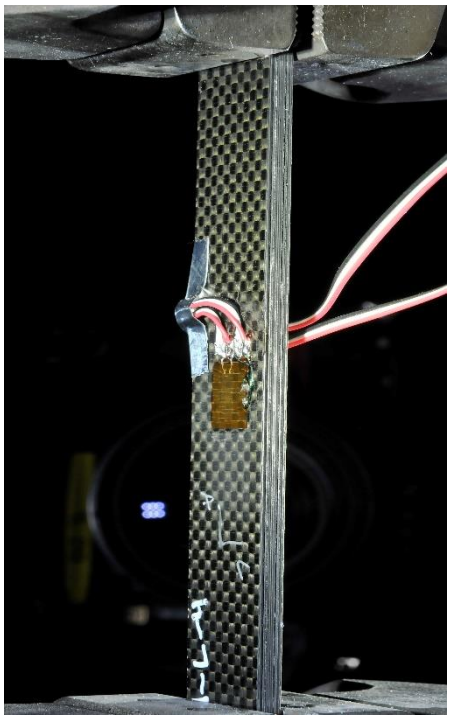

(B1-L-4) at 250K cycles

Figure C1.99 Damage Progression in (B1-L-4) Test Specimen at 250K cycles

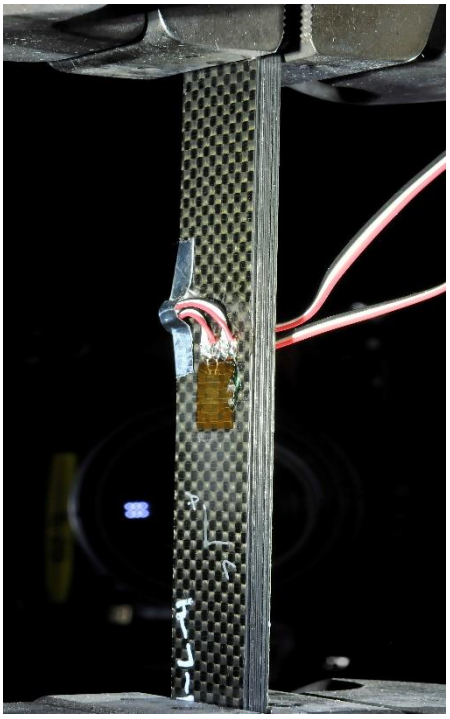

(B1-L-4) at 275K cycles

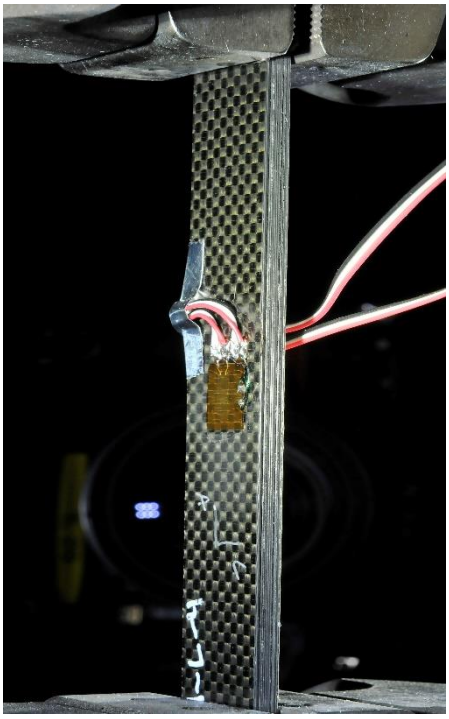

(B1-L-4) at 300K cycles

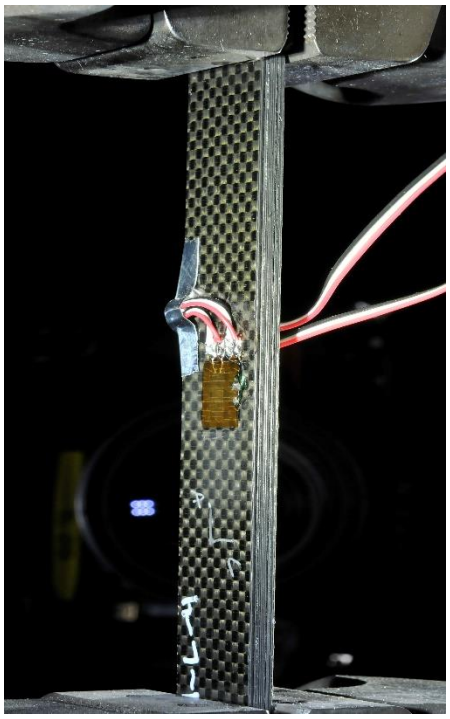

(B1-L-4) at 325K cycles

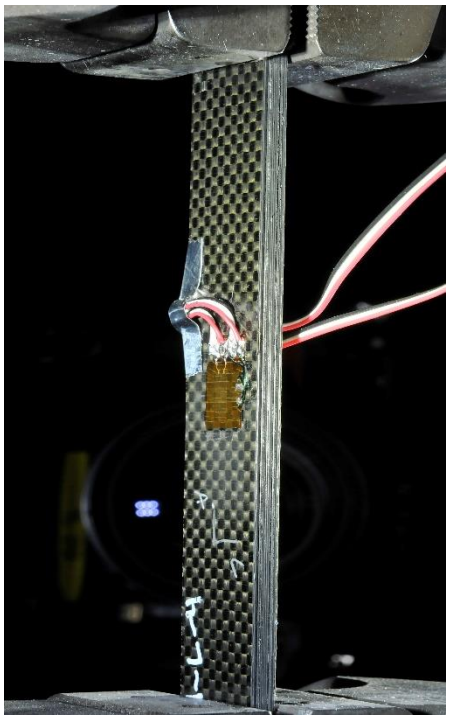

(B1-L-4) at 350K cycles

Figure C1.100 Damage Progression in (B1-L-4) Test Specimen at 350K cycles

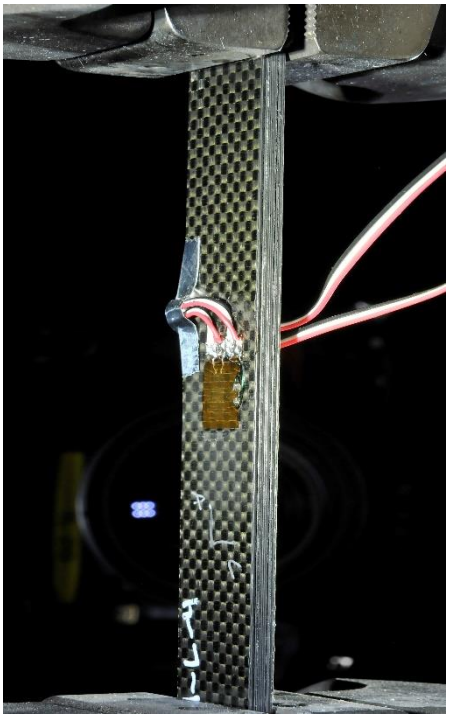

(B1-L-4) at 375K cycles

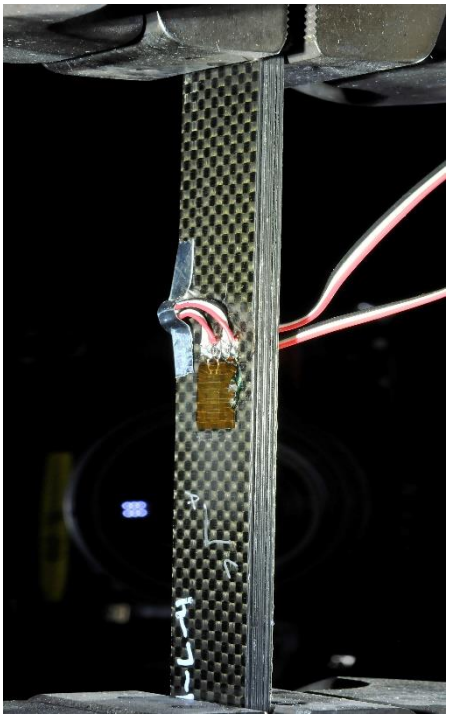

(B1-L-4) at 400K cycles

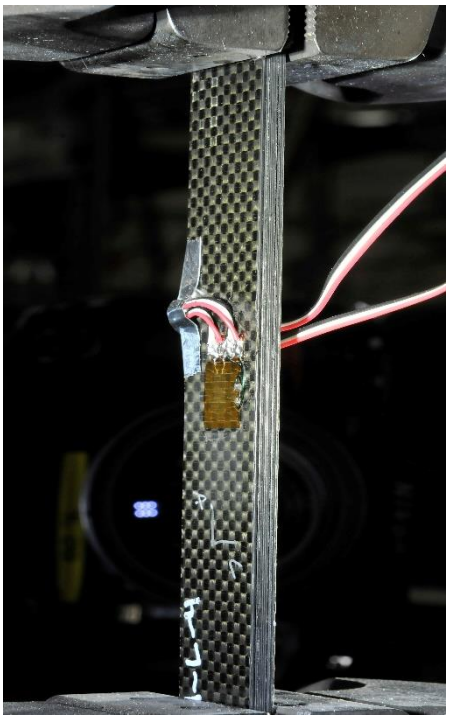

(B1-L-4) at 425K cycles

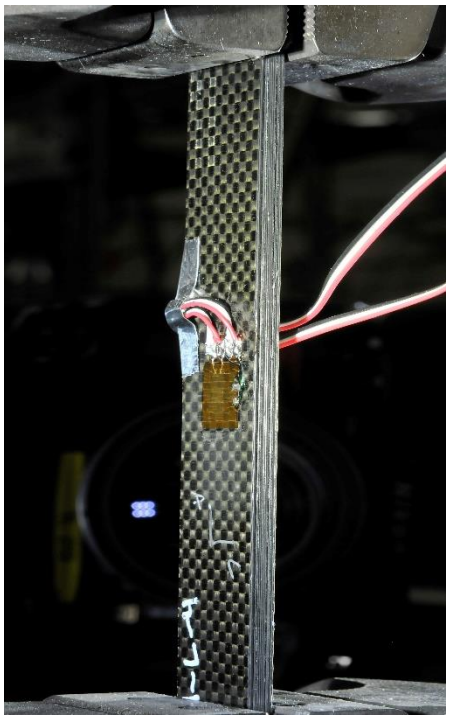

(B1-L-4) at 450K cycles

Figure C1.101 Damage Progression in (B1-L-4) Test Specimen at 450K cycles

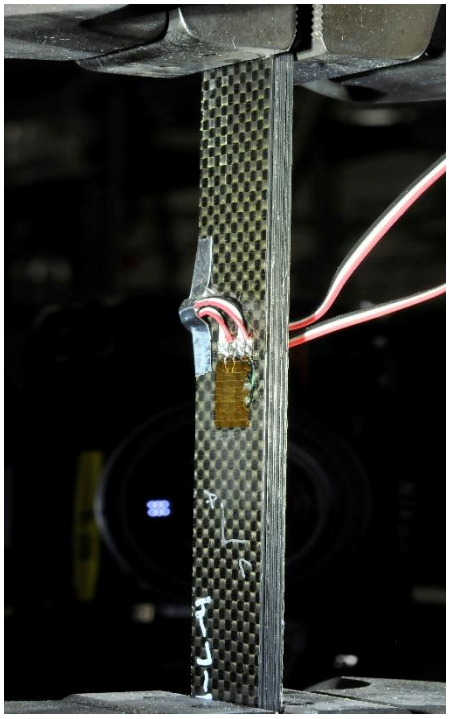

(B1-L-4) at 475K cycles

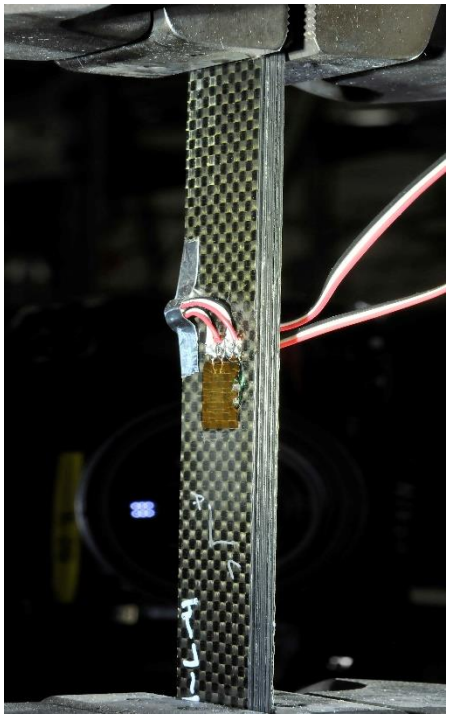

(B1-L-4) at 500K cycles

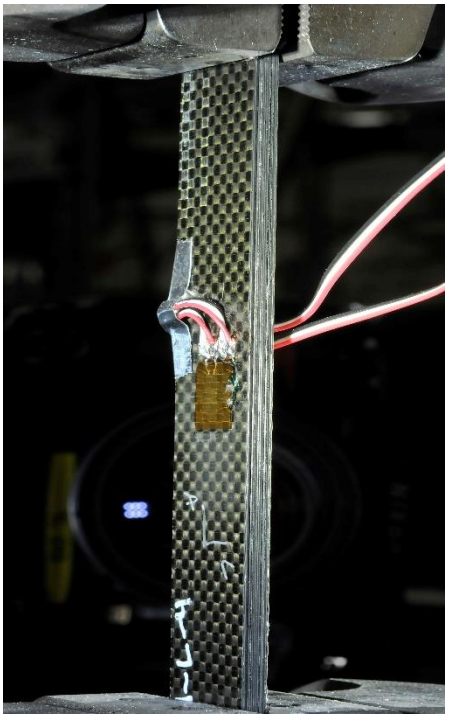

(B1-L-4) at 525K cycles

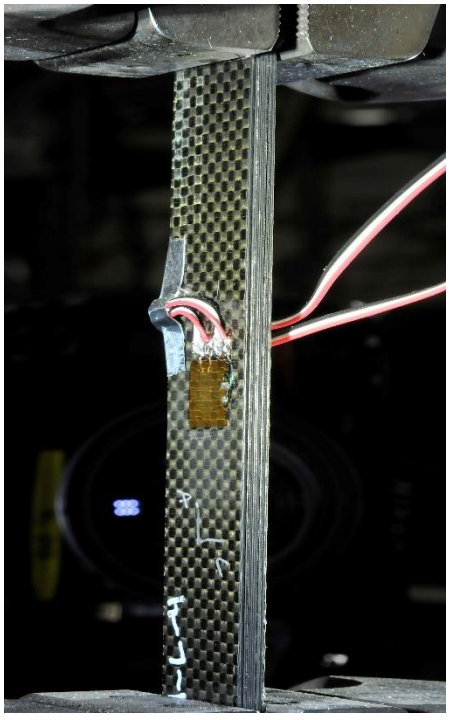

(B1-L-4) at 550K cycles

Figure C1.102 Damage Progression in (B1-L-4) Test Specimen at 550K cycles

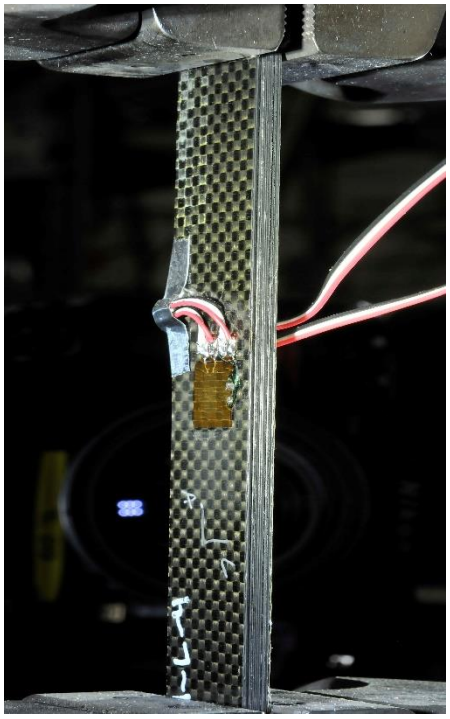

(B1-L-4) at 575K cycles

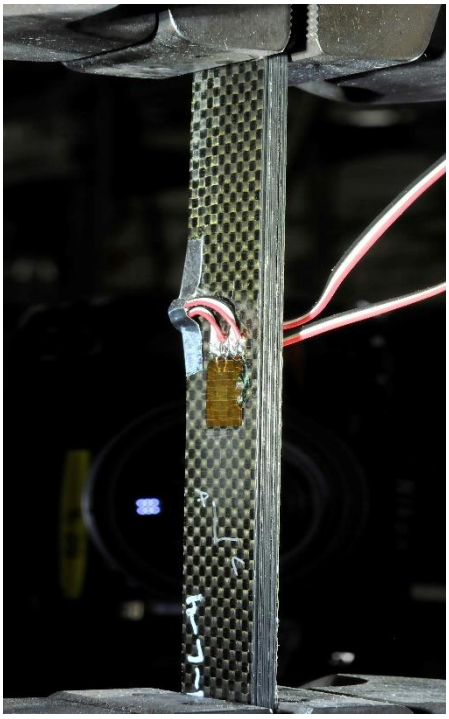

(B1-L-4) at 600K cycles

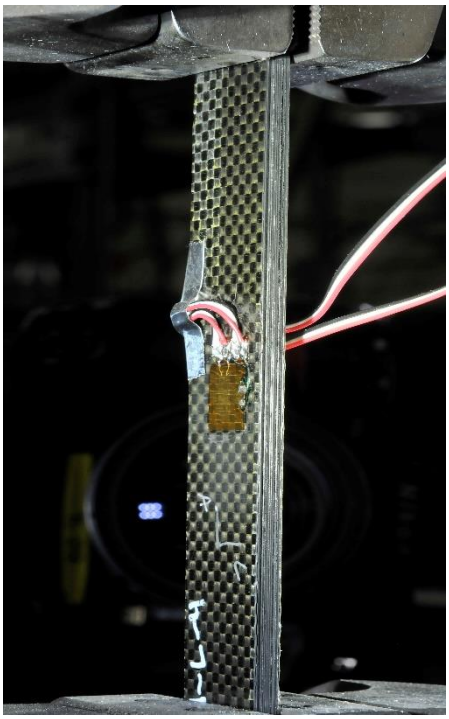

(B1-L-4) at 625K cycles

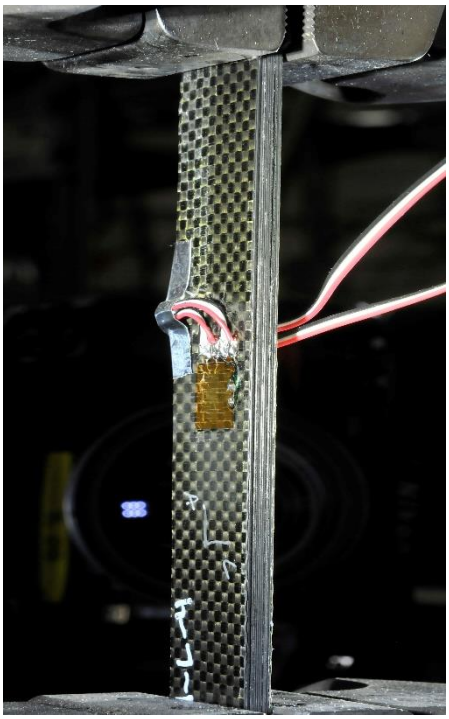

(B1-L-4) at 650K cycles

Figure C1.103 Damage Progression in (B1-L-4) Test Specimen at 650K cycles

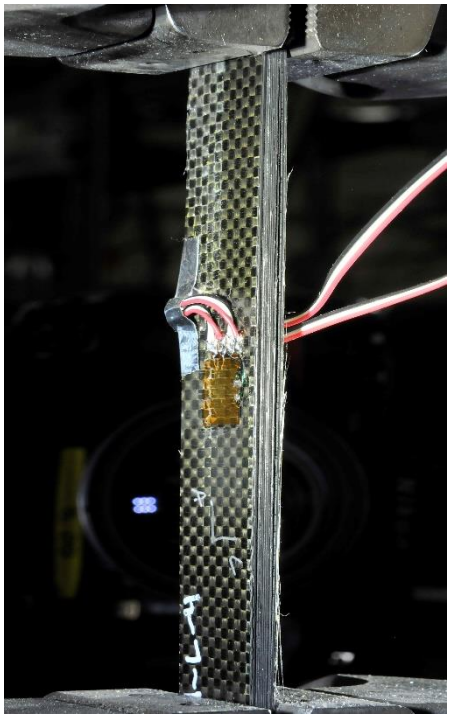

(B1-L-4) at 675K cycles

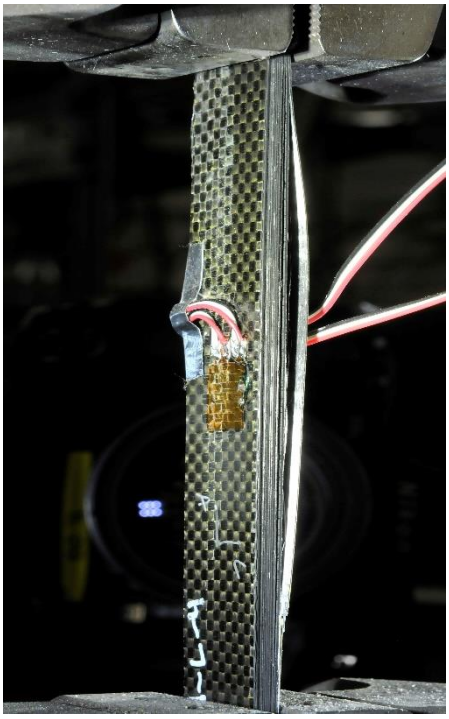

(B1-L-4) at 700K cycles

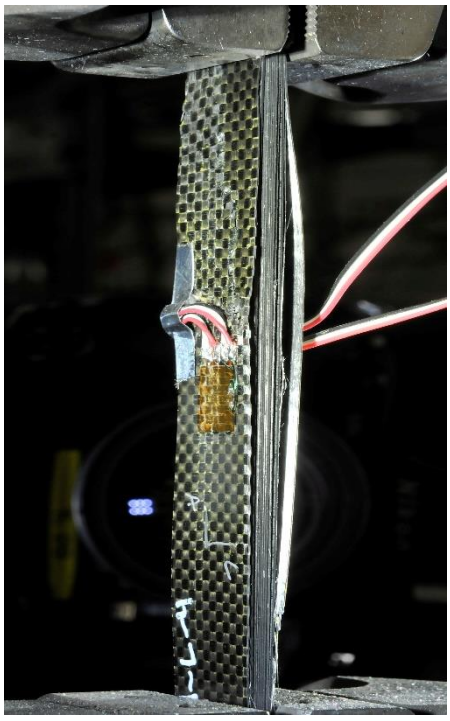

(B1-L-4) at 725K cycles

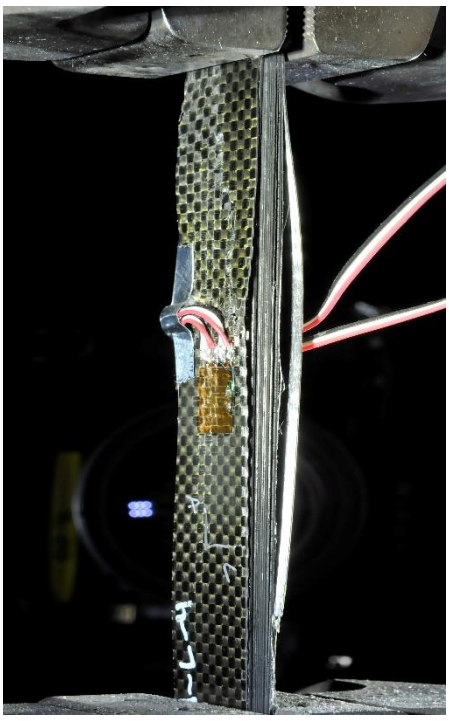

(B1-L-4) at 750K cycles

Figure C1.104 Damage Progression in (B1-L-4) Test Specimen at 750K cycles

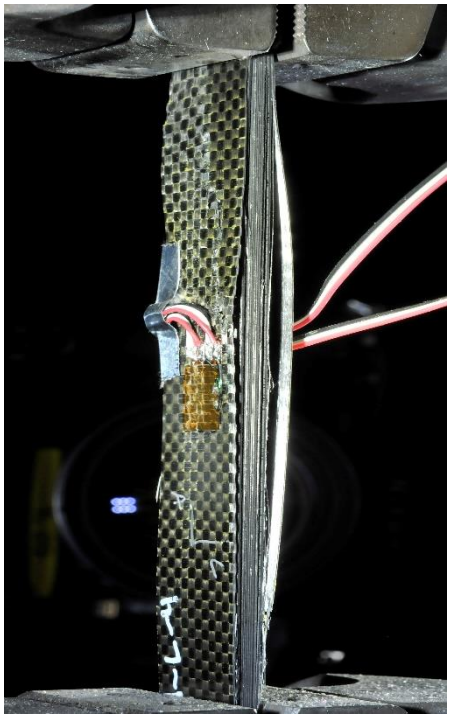

(B1-L-4) at 775K cycles

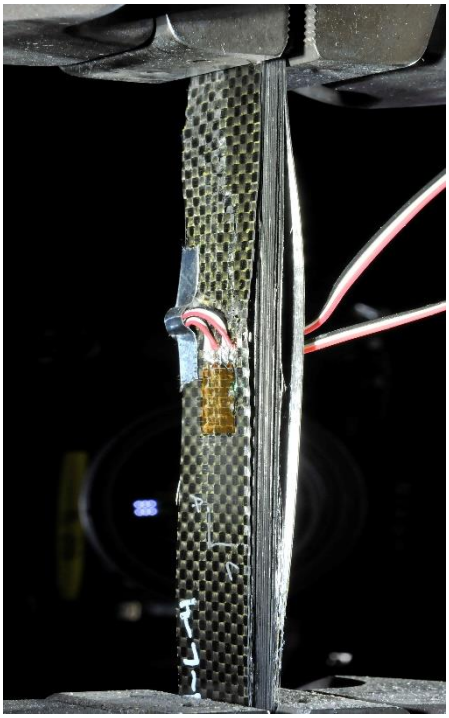

(B1-L-4) at 800K cycles

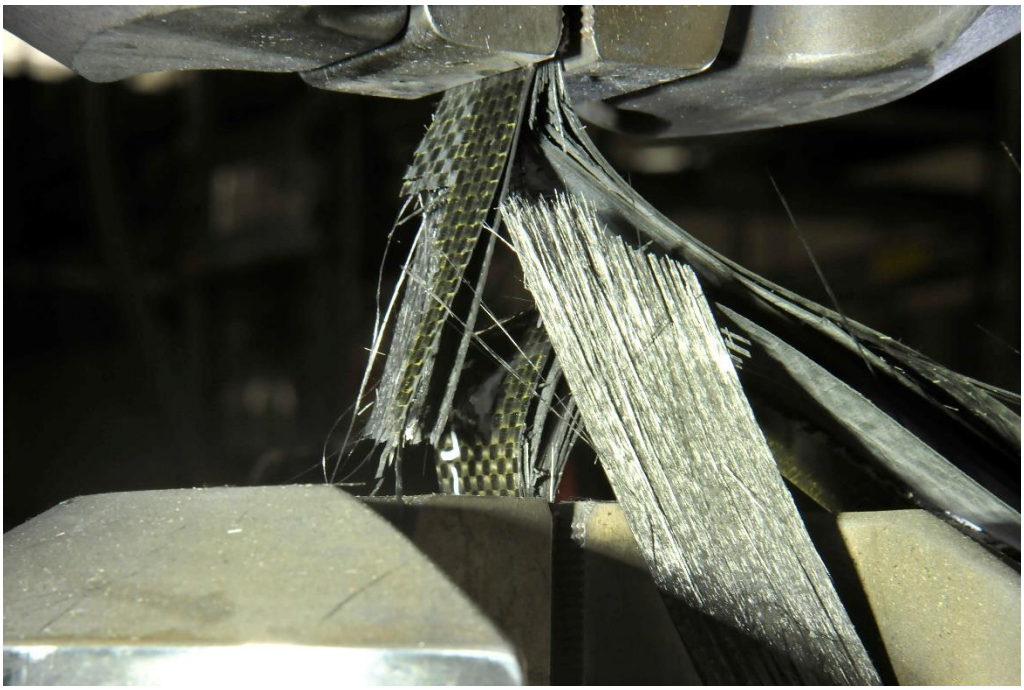

(B1-L-4) at Failure

Figure C1.105 Damage Progression in (B1-L-4) Test Specimen at Failure

C2.2 Photographs of Damage Progression in Fatigue Testing of Notched Specimens

The following pages contain photographs of the damage progression during fatigue cyclic testing of notched test specimens.

(A2-H-1) at 1 Cycle

(A2-H-1) at 100 Cycles

(A2-H-1) at 1k Cycles

(A2-H-1) at 2k Cycles

Figure C 2-1 Damage Progression in (A2-H-1) Test specimen to 2k Cycles

(A2-H-1) at 3k Cycles

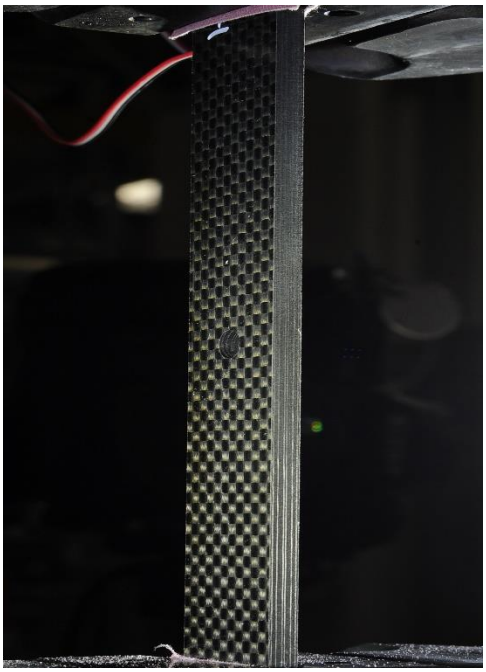

(A2-H-1) at 4k Cycles

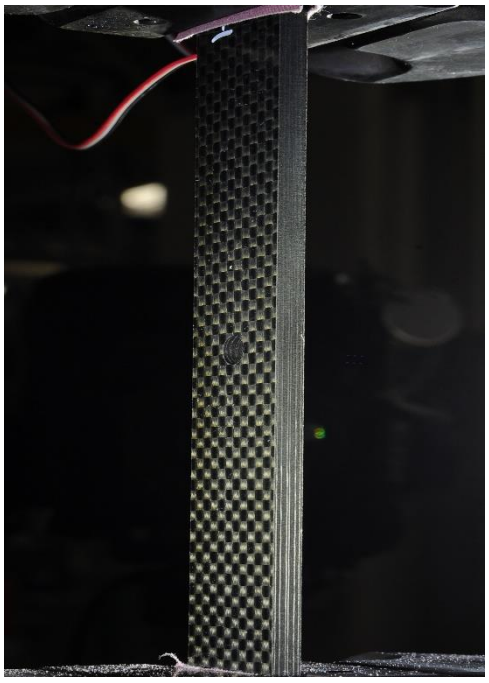

(A2-H-1) at 5k Cycles

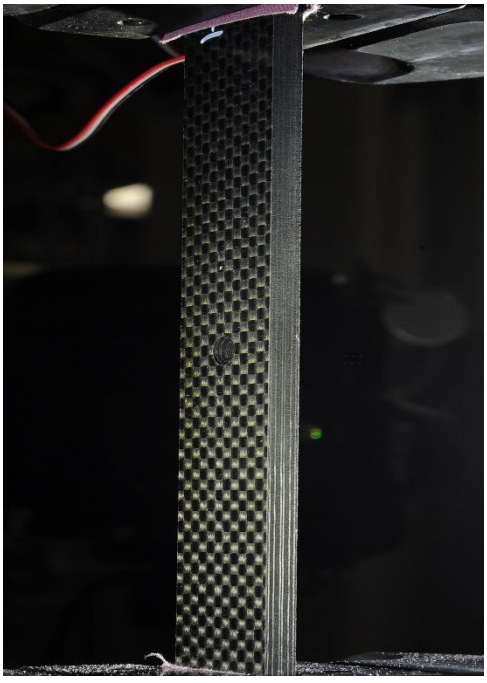

(A2-H-1) at 6k Cycles

Figure C 2-2 Damage Progression in (A2-H-1) Test specimen to 6k Cycles

(A2-H-1) at 7k Cycles

(A2-H-1) at 8k Cycles

(A2-H-1) at 9k Cycles

(A2-H-1) at 10k Cycles

Figure C 2-3 Damage Progression in (A2-H-1) Test specimen to 10k Cycles

(A2-H-1) at 15k Cycles

(A2-H-1) at 20k Cycles

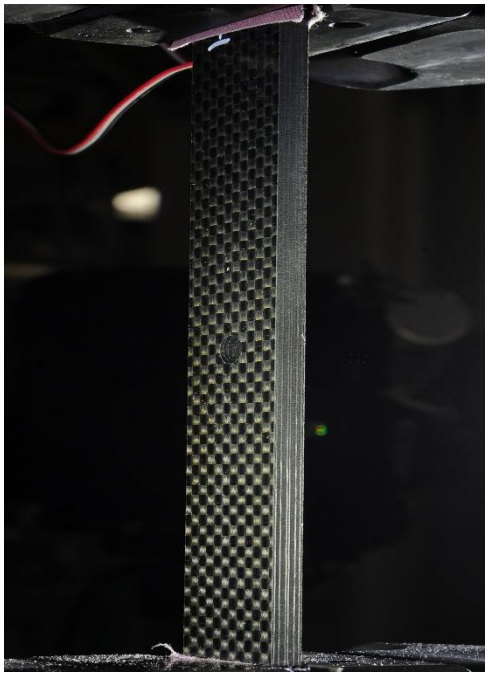

(A2-H-1) at 25k Cycles

(A2-H-1) at 30k Cycles

Figure C 2-4 Damage Progression in (A2-H-1Test specimen to 30k Cycles

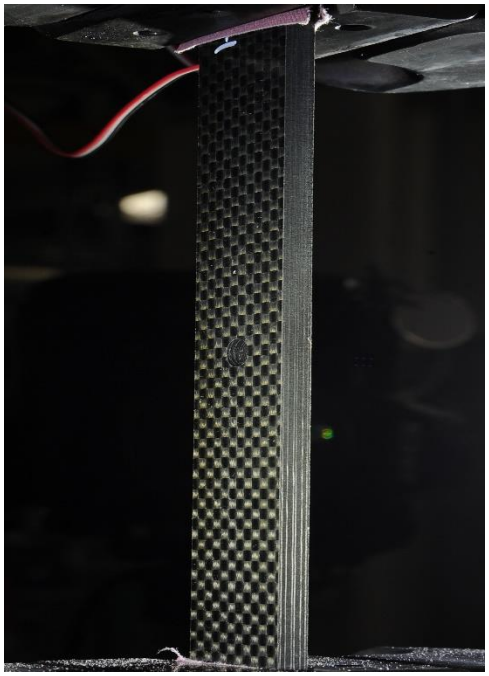

(A2-H-1) at 35k Cycles

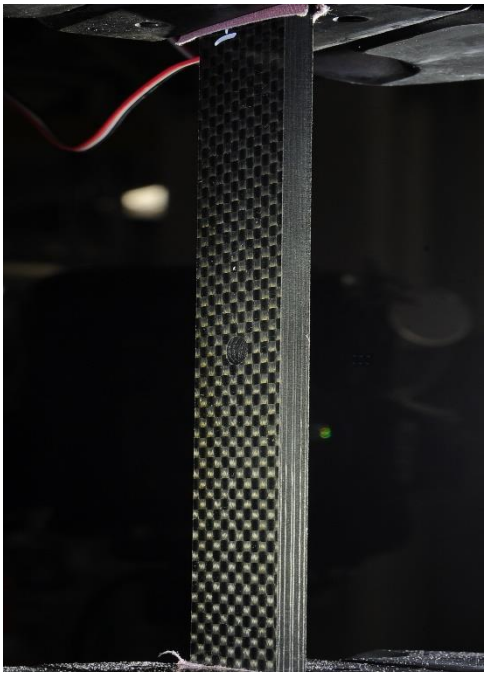

(A2-H-1) at 40k Cycles

(A2-H-1) at 45k Cycles

(A2-H-1) at 50k Cycles

Figure C 2-5 Damage Progression in (A2-H-1) Test specimen to 50k Cycles

(A2-H-1) at 55k Cycles

(A2-H-1) at 60k Cycles

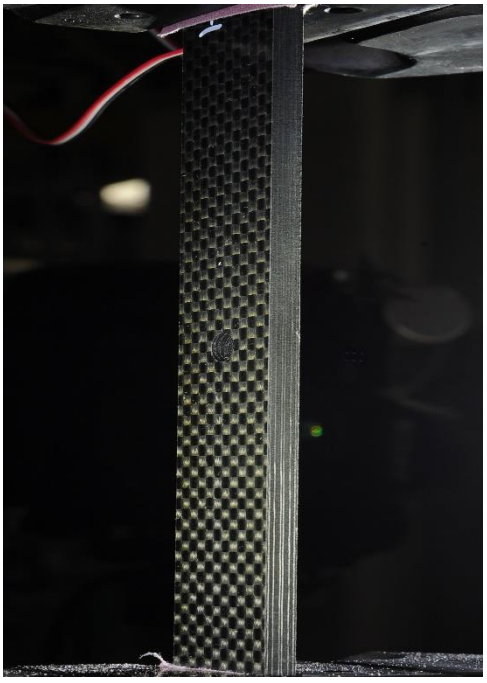

(A2-H-1) at 65k Cycles

(A2-H-1) at 70k Cycles

Figure C 2-6 Damage Progression in (A2-H-1) Test specimen to 70k Cycles

(A2-H-1) at 75k Cycles

(A2-H-1) at 80k Cycles

(A2-H-1) at 85k Cycles

(A2-H-1) at 90k Cycles

Figure C 2-7 Damage Progression in (A2-H-1) Test specimen to 90k Cycles

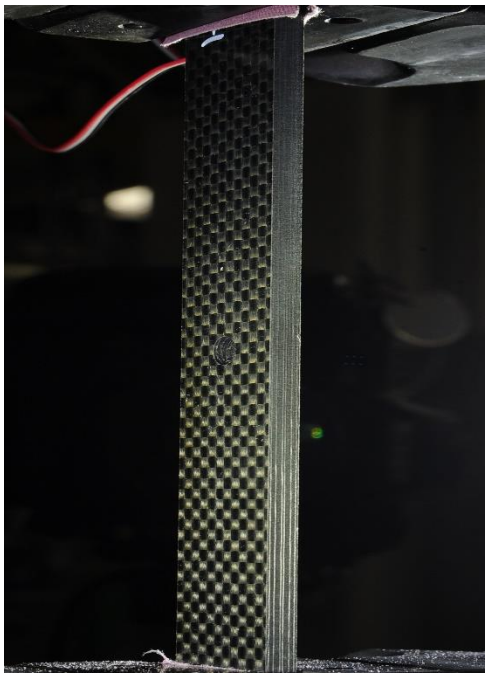

(A2-H-1) at 95k Cycles

(A2-H-1) at 100k Cycles

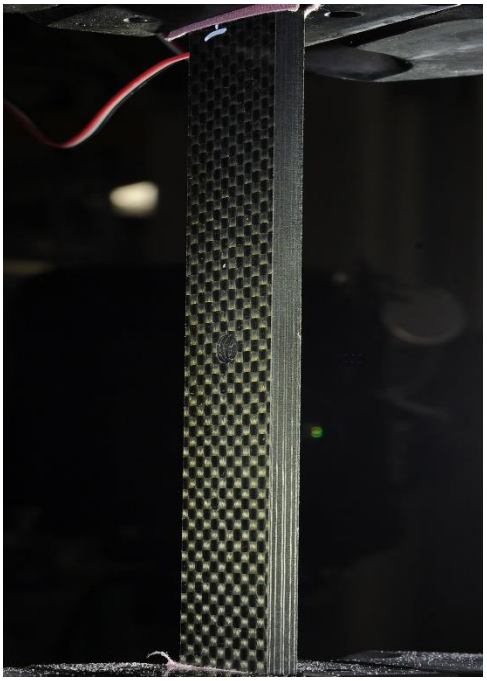

(A2-H-1) at 150k Cycles

(A2-H-1) at 200k Cycles

Figure C 2-8 Damage Progression in (A2-H-1) Test specimen to 200k Cycles

(A2-H-1) at 250k Cycles

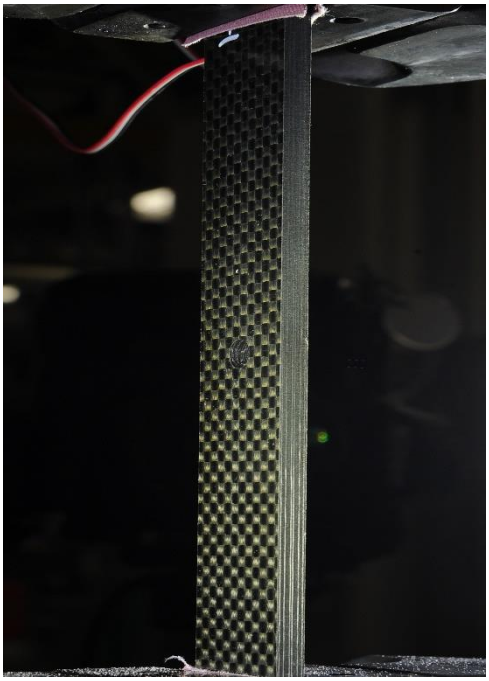

(A2-H-1) at 300k Cycles

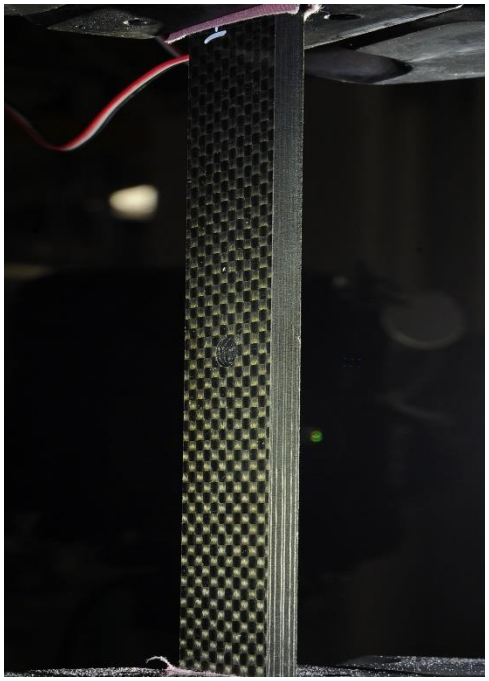

(A2-H-1) at 350k Cycles

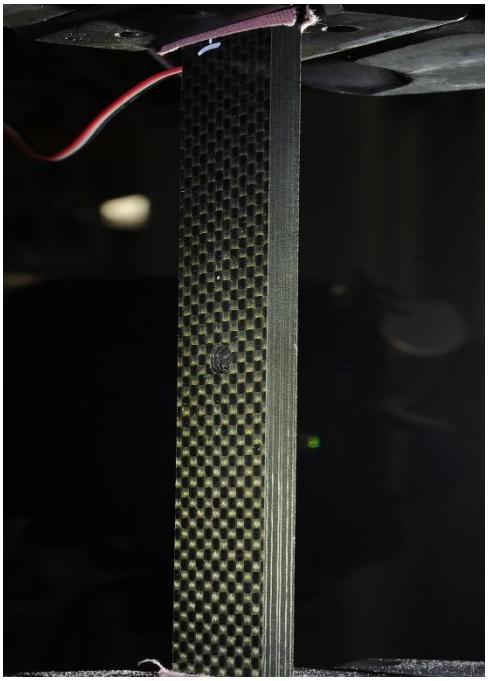

(A2-H-1) at 400k Cycles

Figure C 2-9 Damage Progression in (A2-H-1) Test specimen to 400k Cycles

(A2-H-1) at 450k Cycles

(A2-H-1) at 500k Cycles

(A2-H-1) at 550k Cycles

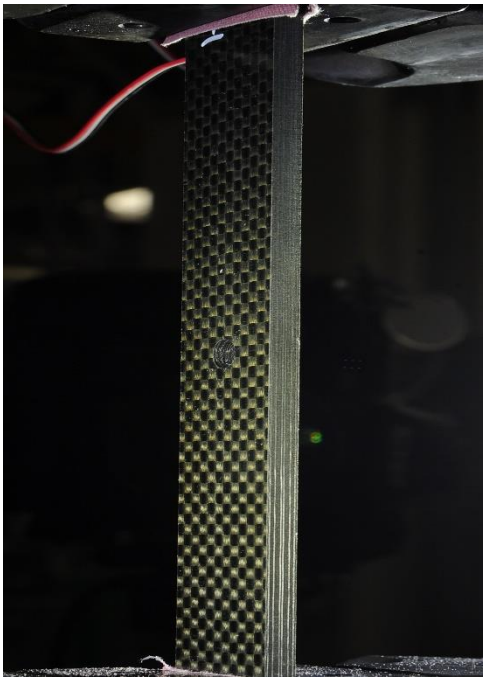

(A2-H-1) at 600k Cycles

Figure C 2-10 Damage Progression in (A2-H-1) Test specimen to 600k Cycles

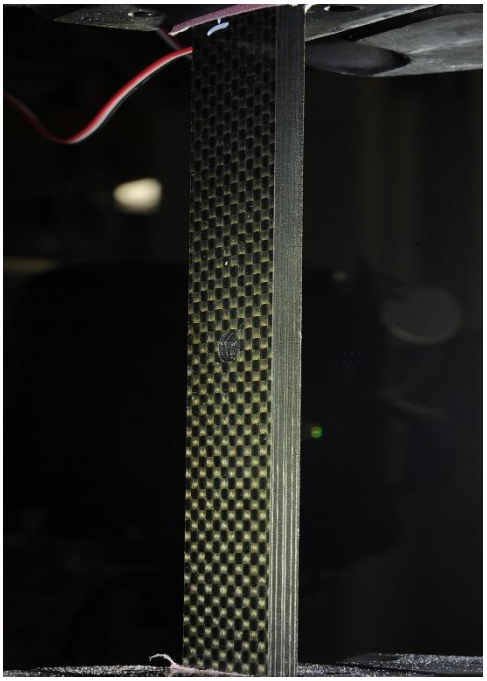

(A2-H-1) at 650k Cycles

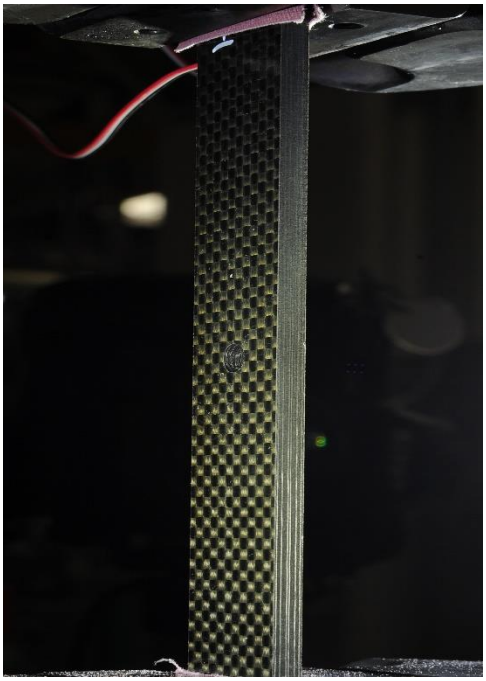

(A2-H-1) at 700k Cycles

(A2-H-1) at 750k Cycles

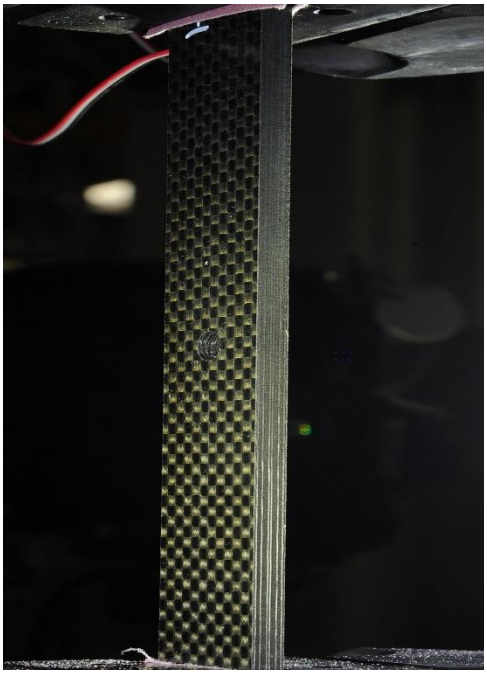

(A2-H-1) at 800k Cycles

Figure C 2-11 Damage Progression in (A2-H-1) Test specimen to 800k Cycles

(A2-H-1) at 850k Cycles

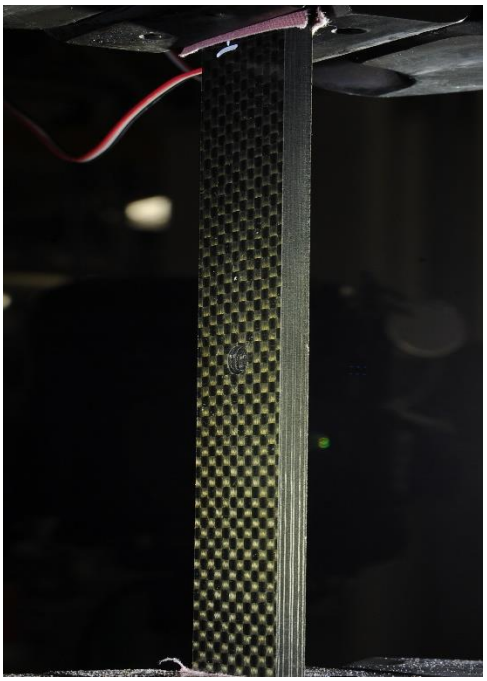

(A2-H-1) at 900k Cycles

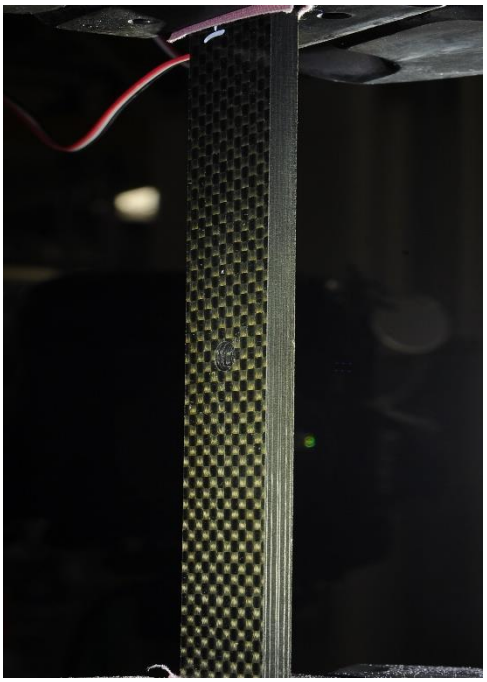

(A2-H-1) at 950k Cycles

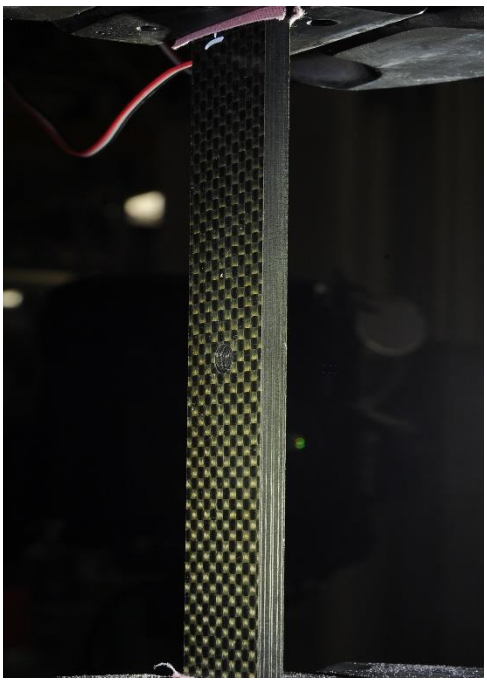

(A2-H-1) at 1000k Cycles

Figure C 2-12 Damage Progression in (A2-H-1) Test specimen to 1000k Cycles

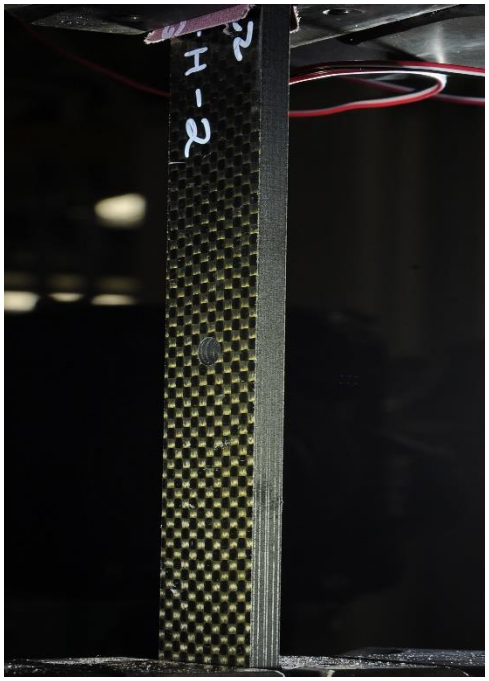

(A2-H-2) at 1 Cycle

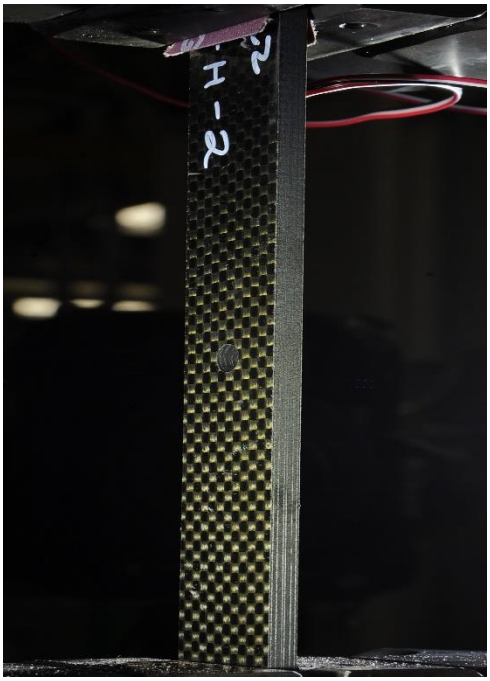

(A2-H-2) at 100 Cycles

(A2-H-2) at 1k Cycles

(A2-H-2) at 2k Cycles

Figure C 2-13 Damage Progression in (A2-H-2) Test specimen to 2k Cycles

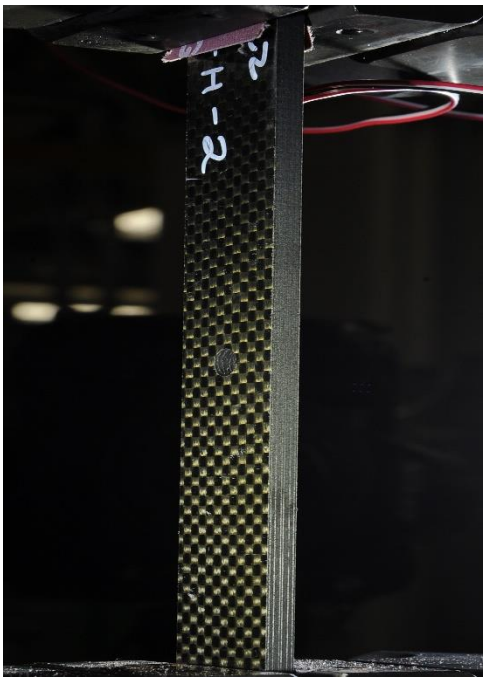

(A2-H-2) at 3k Cycles

(A2-H-2) at 4k Cycles

(A2-H-2) at 5k Cycles

(A2-H-2) at 6k Cycles

Figure C 2-14 Damage Progression in (A2-H-2) Test specimen to 6k Cycles

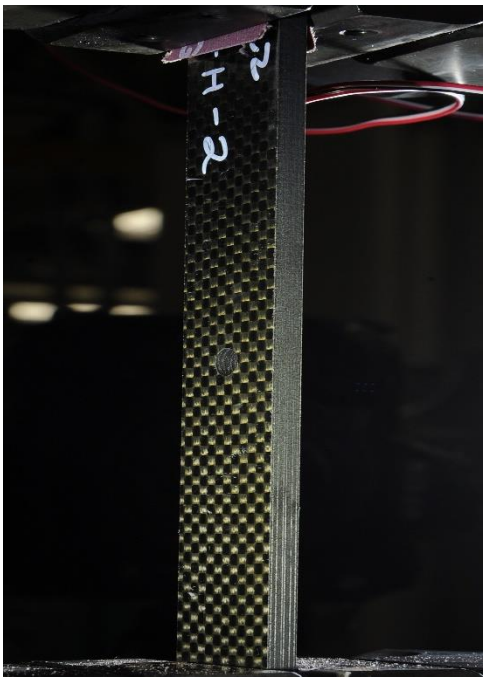

(A2-H-2) at 7k Cycles

(A2-H-2) at 8k Cycles

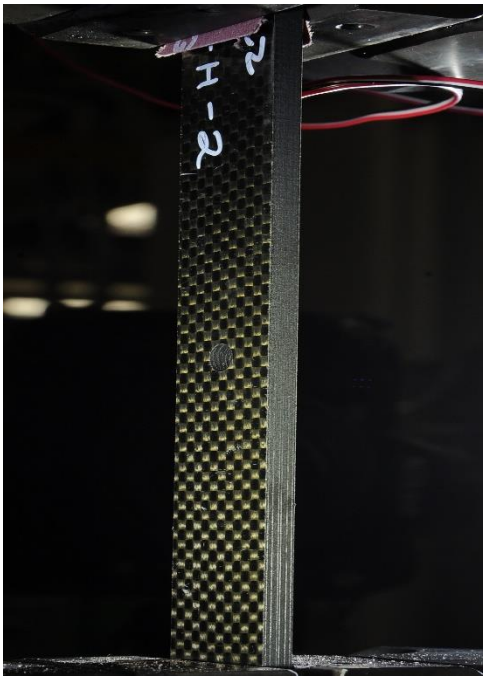

(A2-H-2) at 9k Cycles

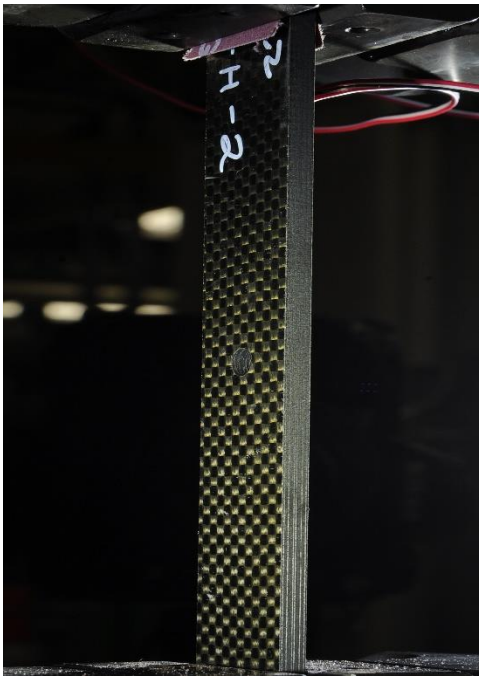

(A2-H-2) at 10k Cycles

Figure C 2-15 Damage Progression in (A2-H-2) Test specimen to 10k Cycles

(A2-H-2) at 15k Cycles

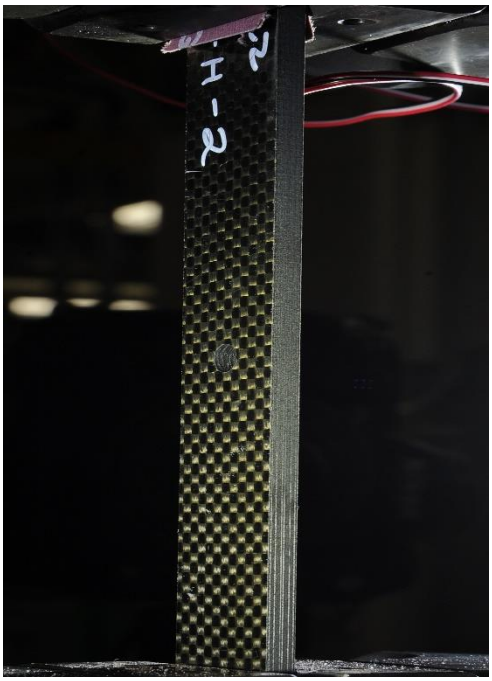

(A2-H-2) at 20k Cycles

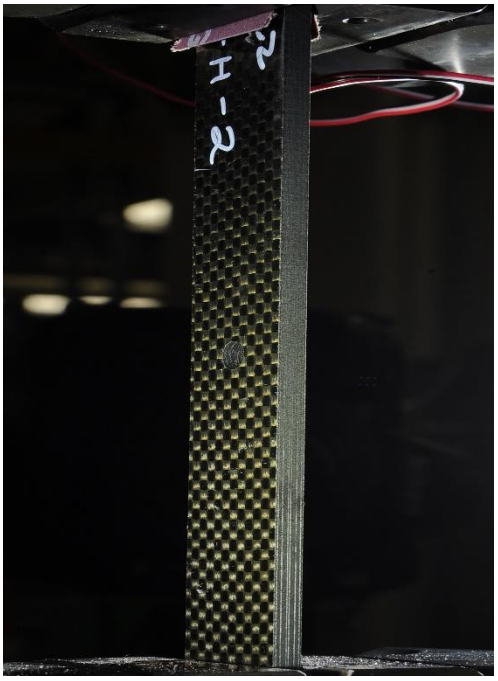

(A2-H-2) at 25k Cycles

(A2-H-2) at 30k Cycles

Figure C 2-16 Damage Progression in (A2-H-2) Test specimen to 30k Cycles

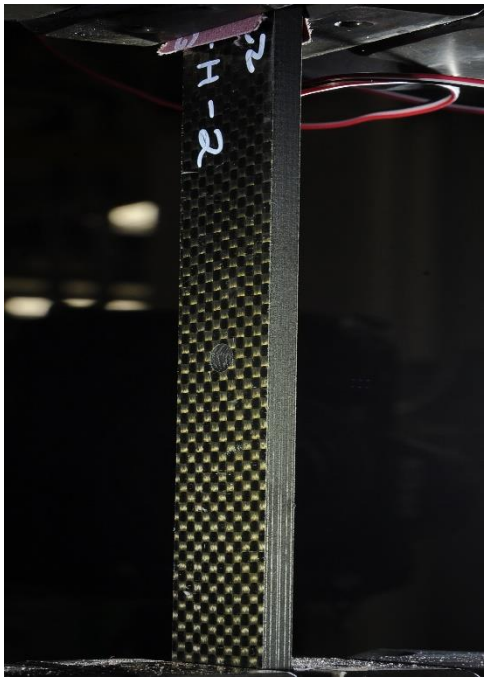

(A2-H-2) at 35k Cycles

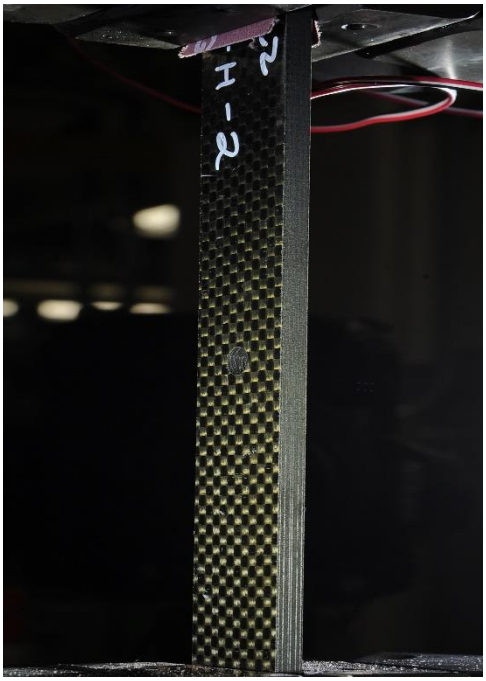

(A2-H-2) at 40k Cycles

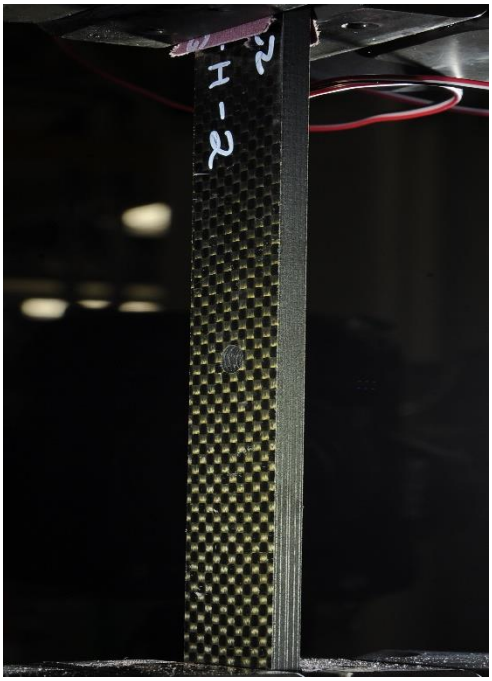

(A2-H-2) at 45k Cycles

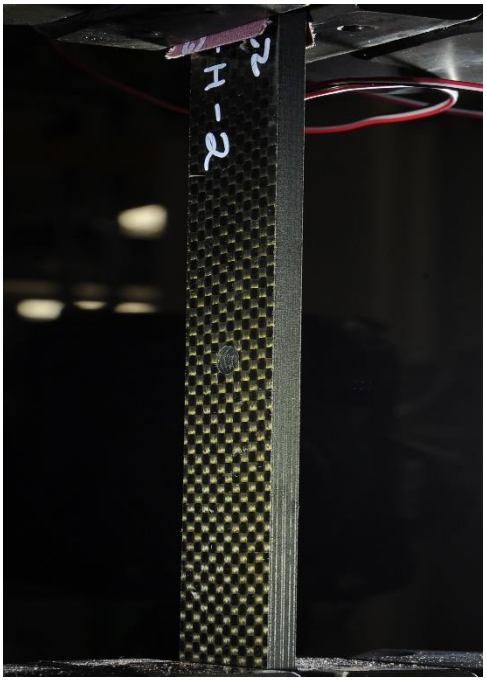

(A2-H-2) at 50k Cycles

Figure C 2-17 Damage Progression in (A2-H-2) Test specimen to 50k Cycles

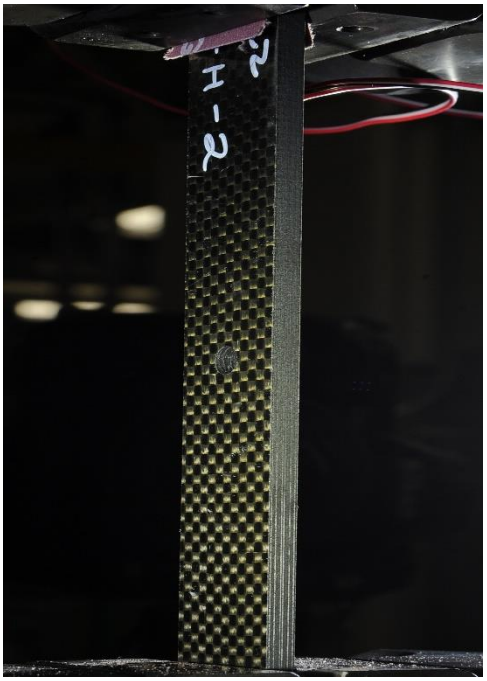

(A2-H-2) at 55k Cycles

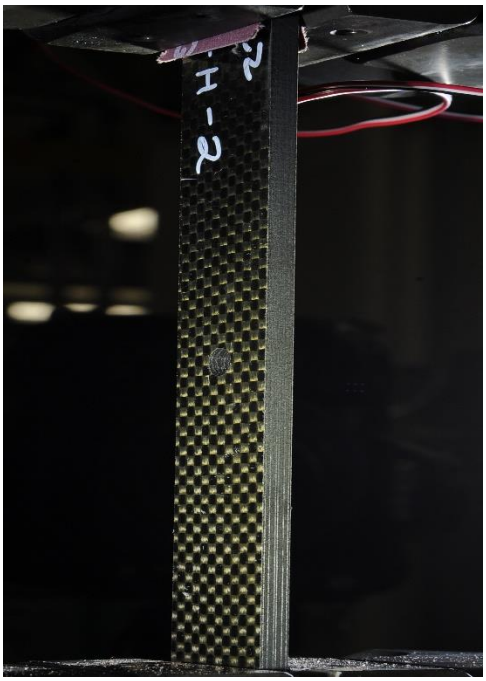

(A2-H-2) at 60k Cycles

(A2-H-2) at 65k Cycles

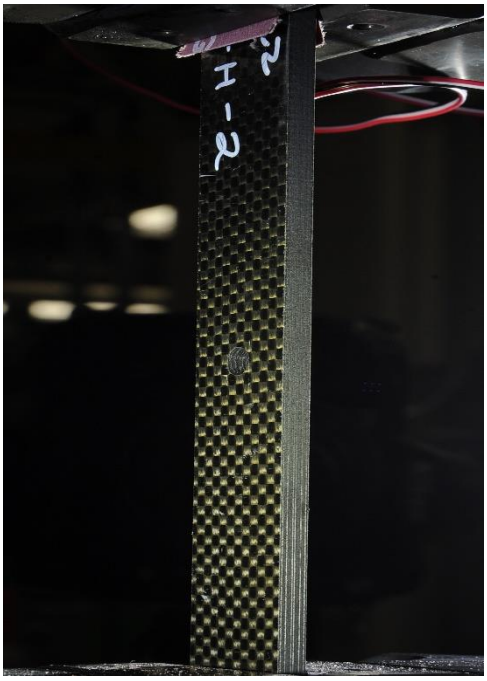

(A2-H-2) at 70k Cycles

Figure C 2-18 Damage Progression in (A2-H-2) Test specimen to 70k Cycles

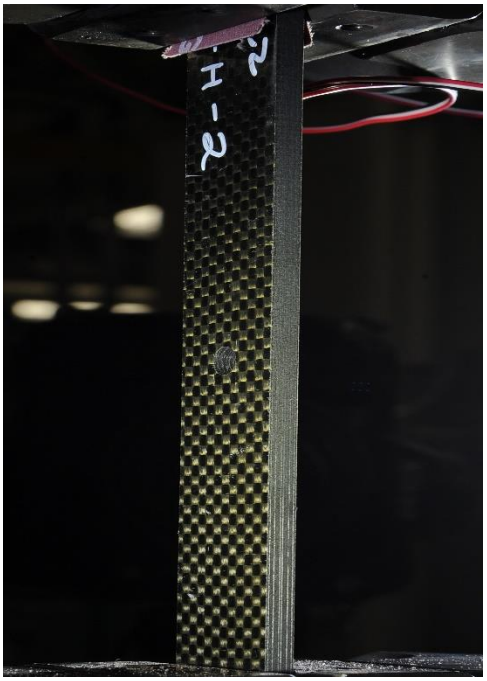

(A2-H-2) at 75k Cycles

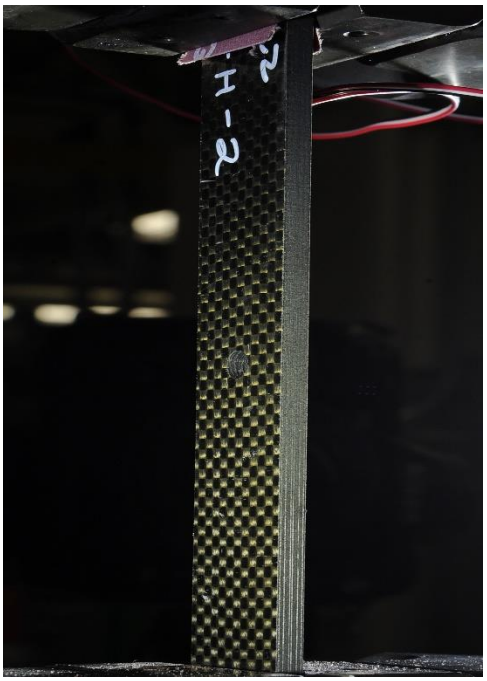

(A2-H-2) at 80k Cycles

(A2-H-2) at 85k Cycles

(A2-H-2) at 90k Cycles

Figure C 2-19 Damage Progression in (A2-H-2) Test specimen to 90k Cycles

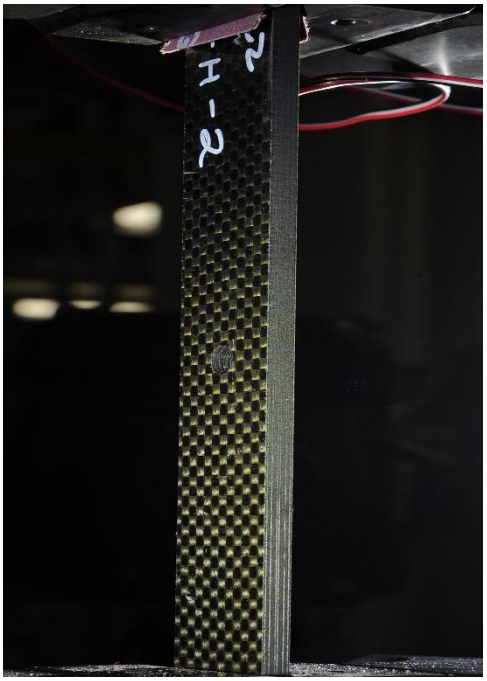

(A2-H-2) at 95k Cycles

(A2-H-2) at 100k Cycles

(A2-H-2) at 150k Cycles

(A2-H-2) at 200k Cycles

Figure C 2-20 Damage Progression in (A2-H-2) Test specimen to 200k Cycles

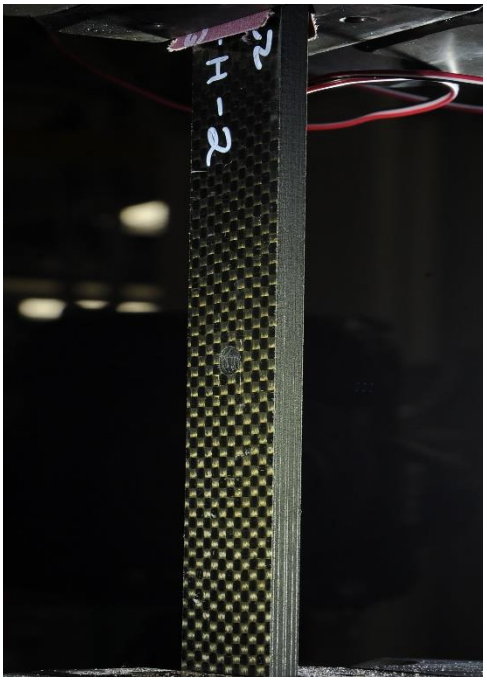

(A2-H-2) at 250k Cycles

(A2-H-2) at 300k Cycles

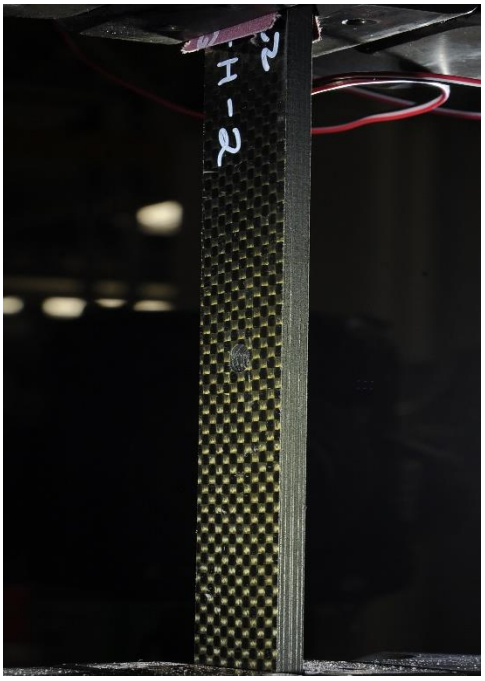

(A2-H-2) at 350k Cycles

(A2-H-2) at 400k Cycles

Figure C 2-21 Damage Progression in (A2-H-2) Test specimen to 400k Cycles

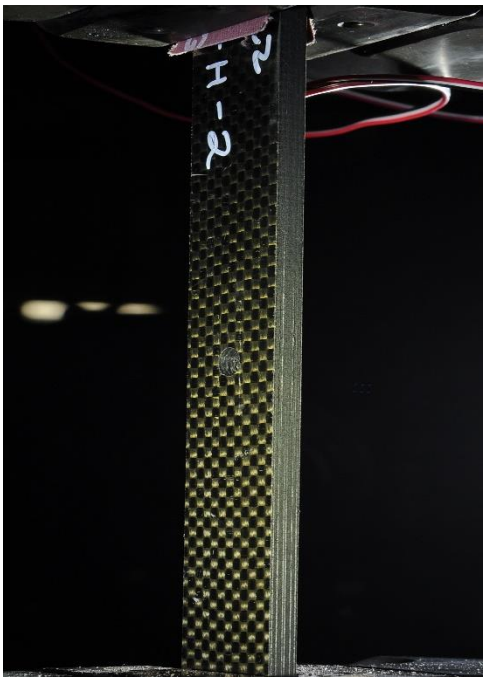

(A2-H-2) at 450k Cycles

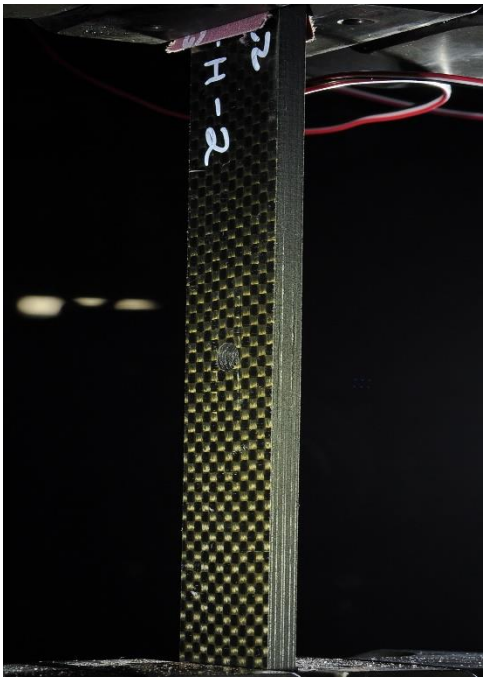

(A2-H-2) at 500k Cycles

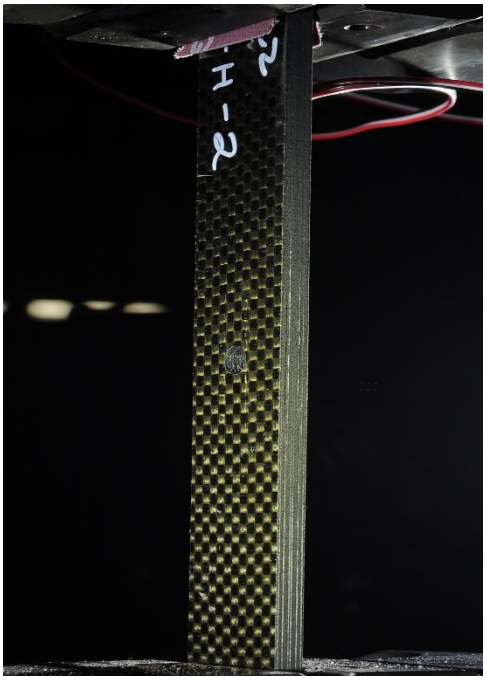

(A2-H-2) at 550k Cycles

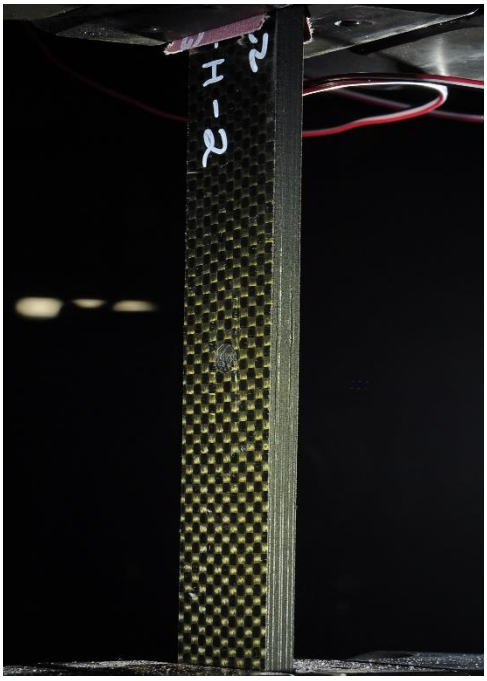

(A2-H-2) at 600k Cycles

Figure C 2-22 Damage Progression in (A2-H-2) Test specimen to 600k Cycles

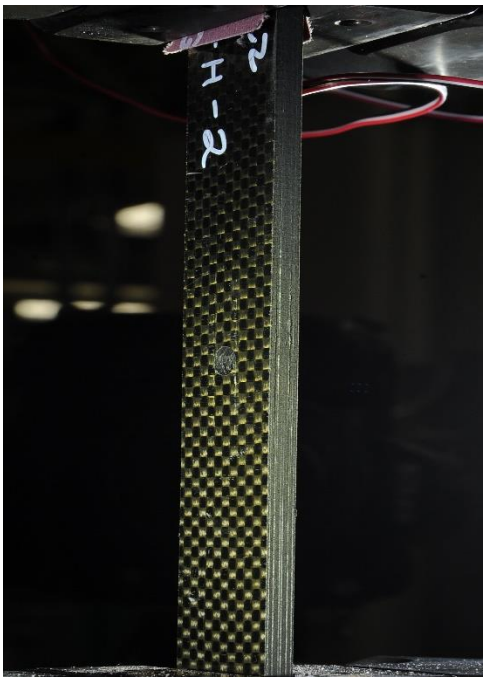

(A2-H-2) at 650k Cycles

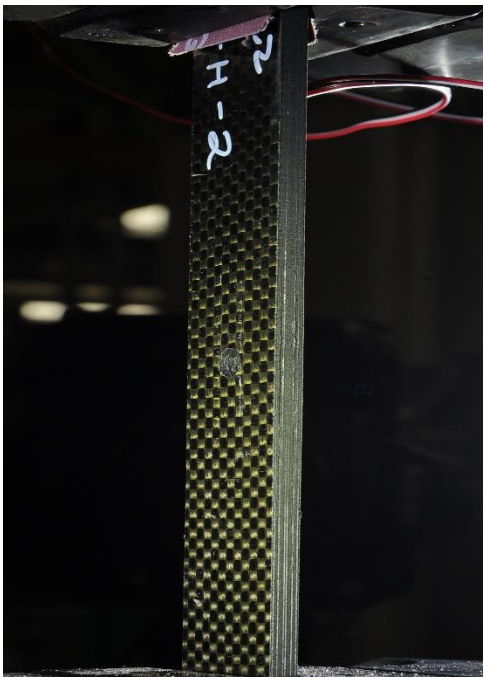

(A2-H-2) at 700k Cycles

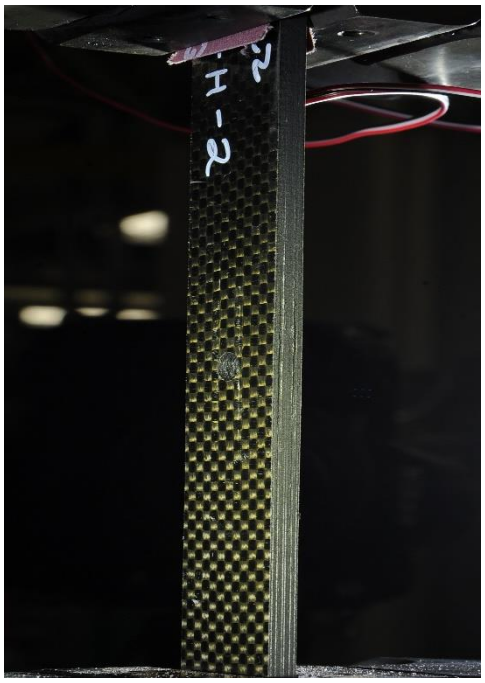

(A2-H-2) at 750k Cycles

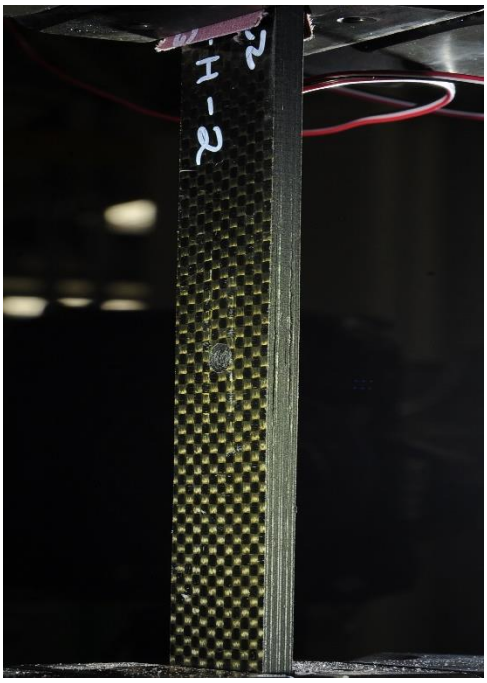

(A2-H-2) at 800k Cycles

Figure C 2-23 Damage Progression in (A2-H-2) Test specimen to 800k Cycles

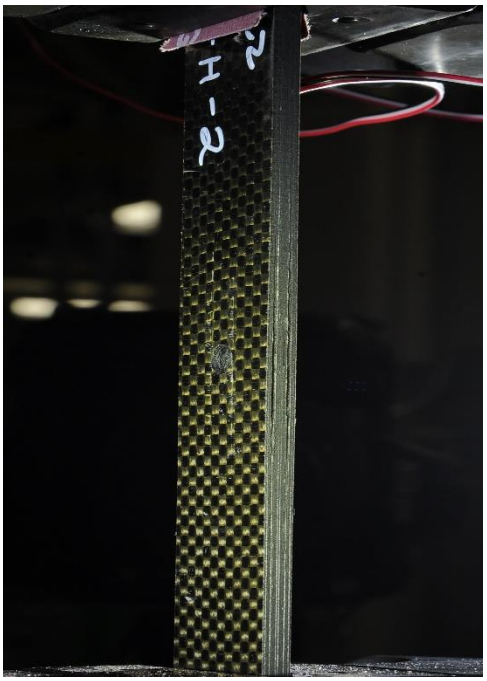

(A2-H-2) at 850k Cycles

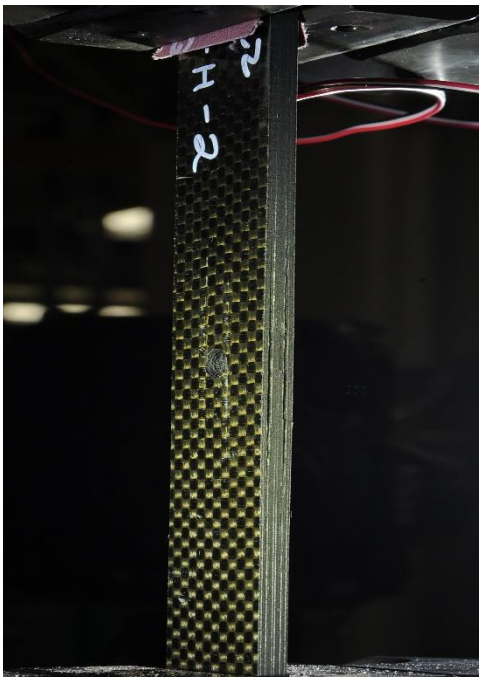

(A2-H-2) at 900k Cycles

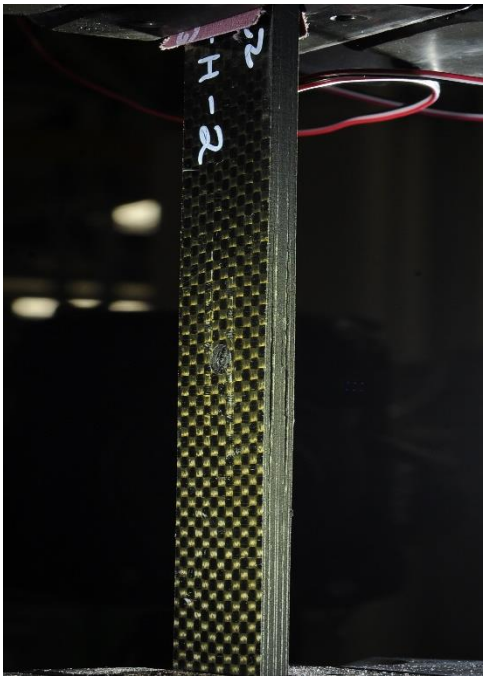

(A2-H-2) at 950k Cycles

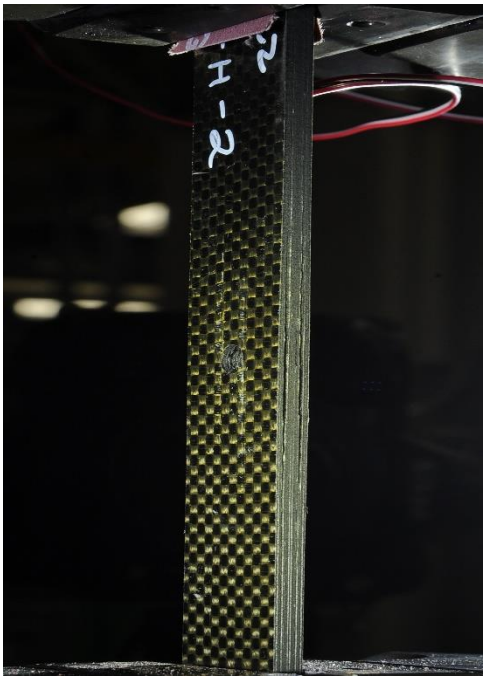

(A2-H-2) at 1000k Cycles

Figure C 2-24 Damage Progression in (A2-H-2) Test specimen to 1000k Cycles

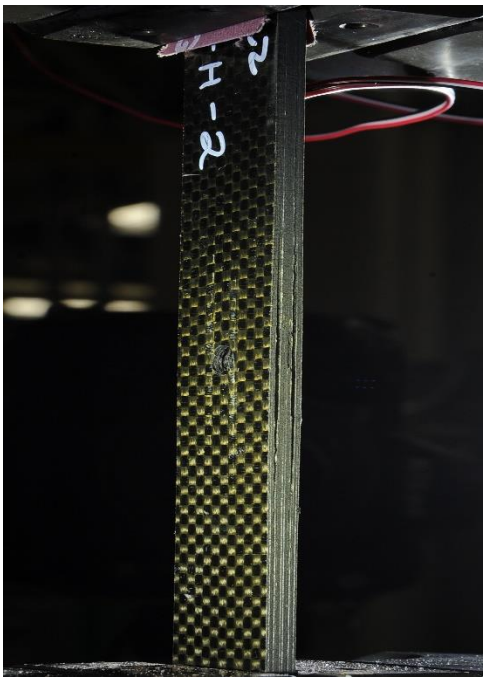

(A2-H-2) at Pre RS

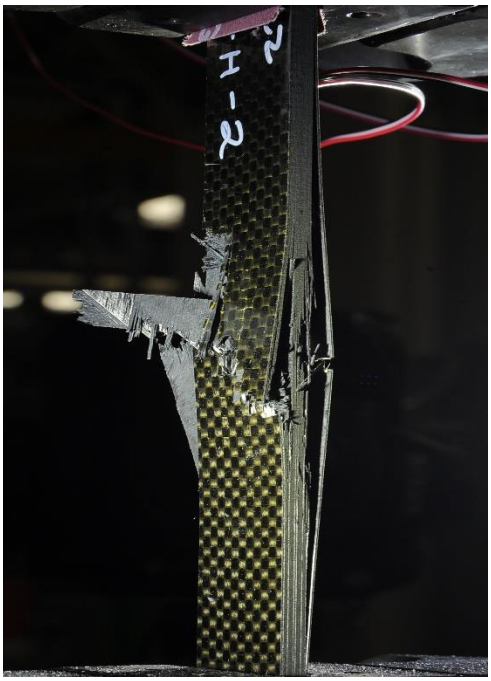

(A2-H-2) at Failure

Figure C 2-25 Damage Progression in (A2-H-2) Test specimen to Failure

(A2-H-3) at 1 Cycle

(A2-H-3) at 100 Cycles

(A2-H-3) at 1k Cycles

(A2-H-3) at 5k Cycles

Figure C 2-26 Damage Progression in (A2-H-3) Test specimen to 5k Cycles

(A2-H-3) at 10k Cycles

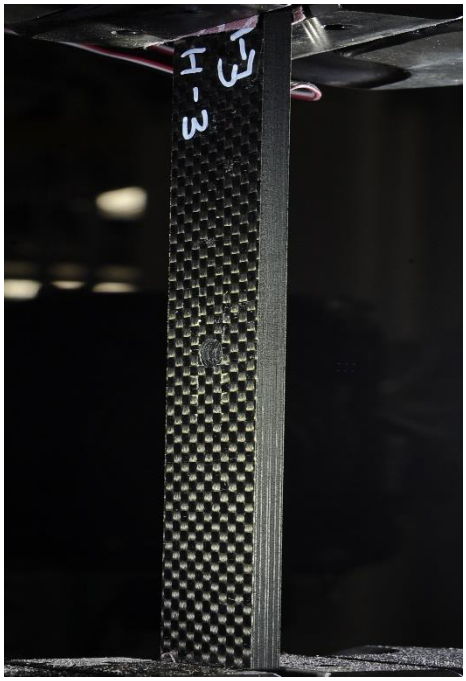

(A2-H-3) at 20k Cycles

(A2-H-3) at 30k Cycles

(A2-H-3) at 40k Cycles

Figure C 2-27 Damage Progression in (A2-H-3) Test specimen to 40k Cycles

(A2-H-3) at 50k Cycles

(A2-H-3) at 60k Cycles

(A2-H-3) at 70k Cycles

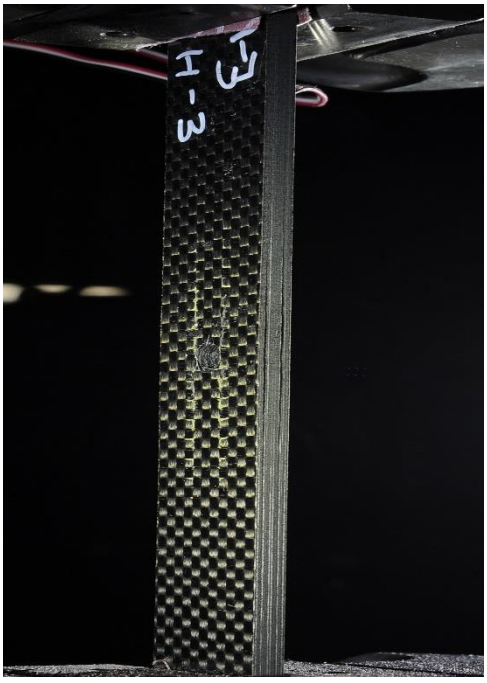

(A2-H-3) at 80k Cycles

Figure C 2-28 Damage Progression in (A2-H-3) Test specimen to 80k Cycles

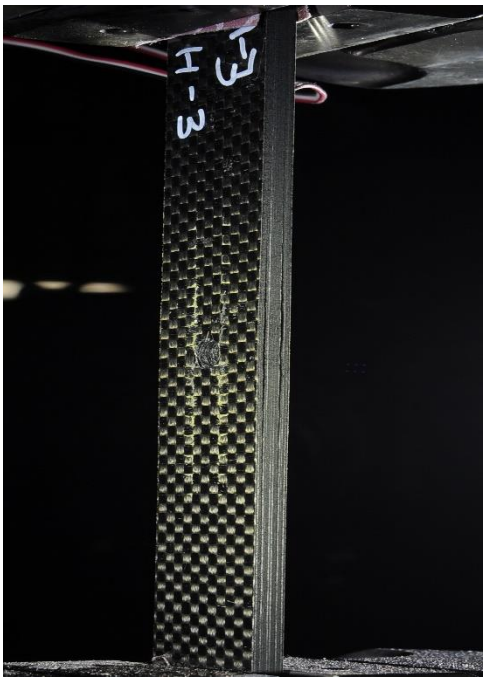

(A2-H-3) at 90k Cycles

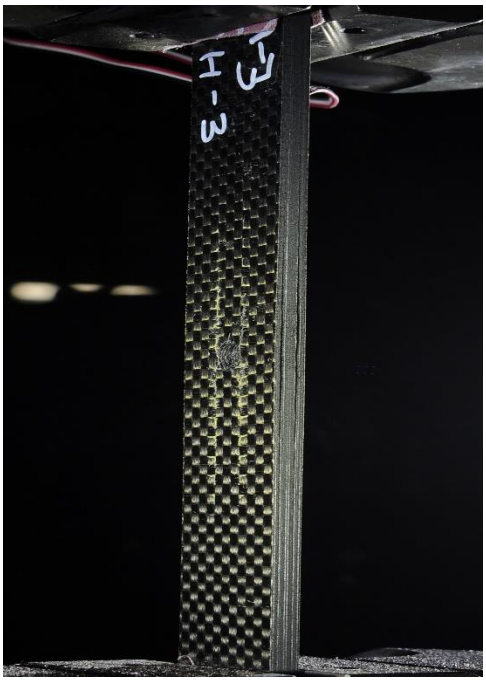

(A2-H-3) at 100k Cycles

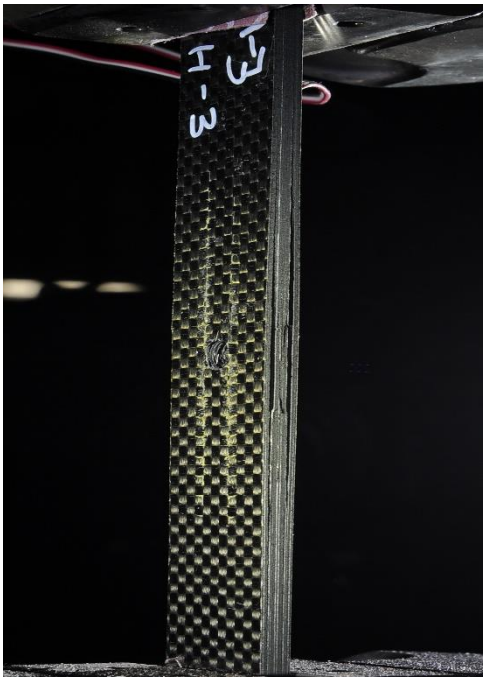

(A2-H-3) at 150k Cycles

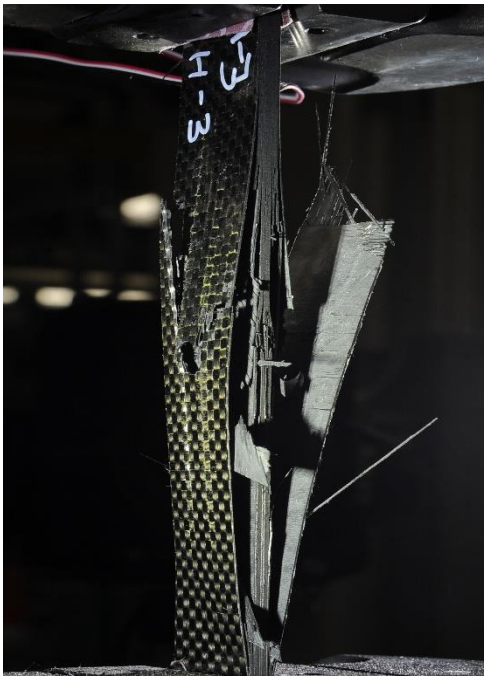

(A2-H-3) at Failure

Figure C 2-29 Damage Progression in (A2-H-3) Test specimen to Failure

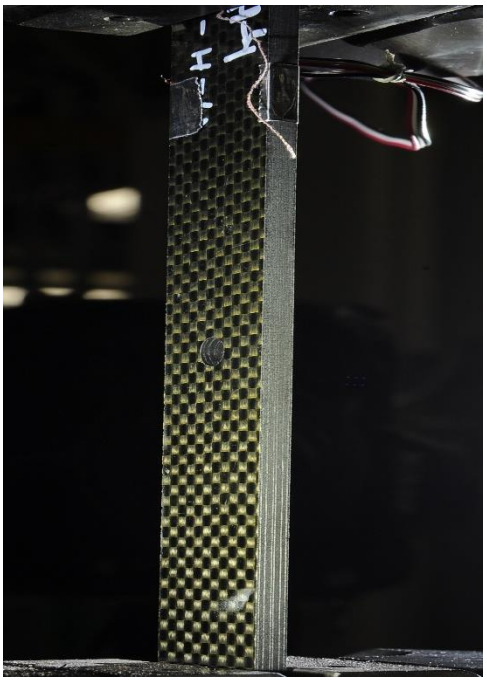

(A2-H-4) at 1 Cycle

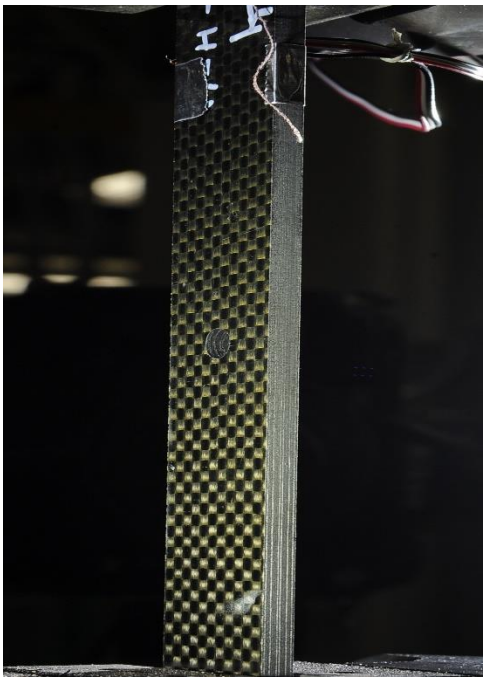

(A2-H-4) at 100 Cycles

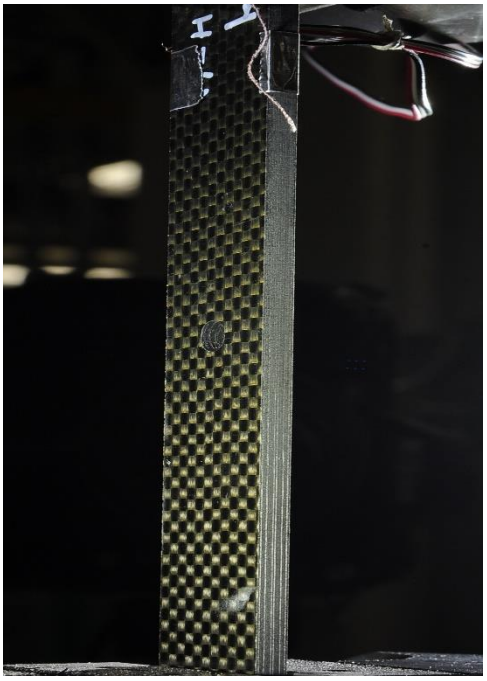

(A2-H-4) at 1k Cycles

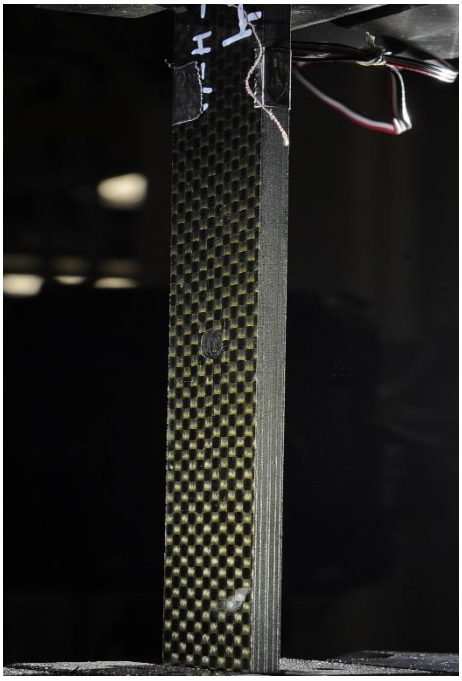

(A2-H-4) at 5k Cycles

Figure C 2-30 Damage Progression in (A2-H-4) Test specimen to 2k Cycles

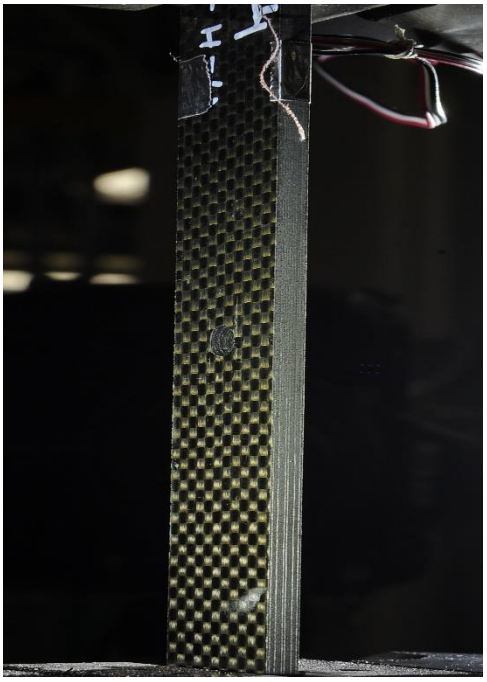

(A2-H-4) at 10k Cycles

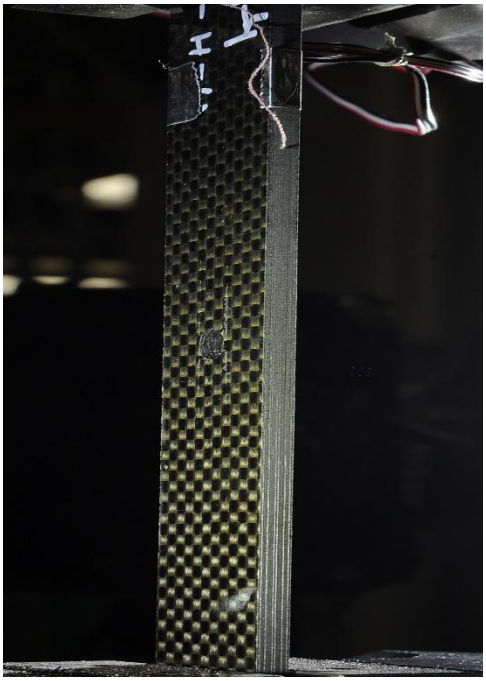

(A2-H-4) at 20k Cycles

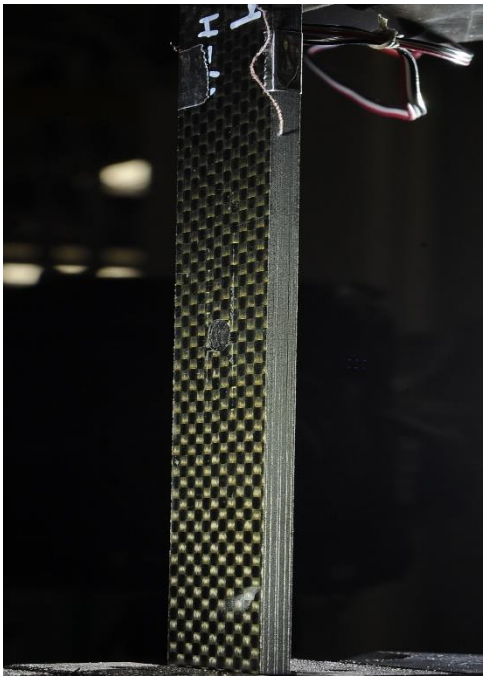

(A2-H-4) at 30k Cycles

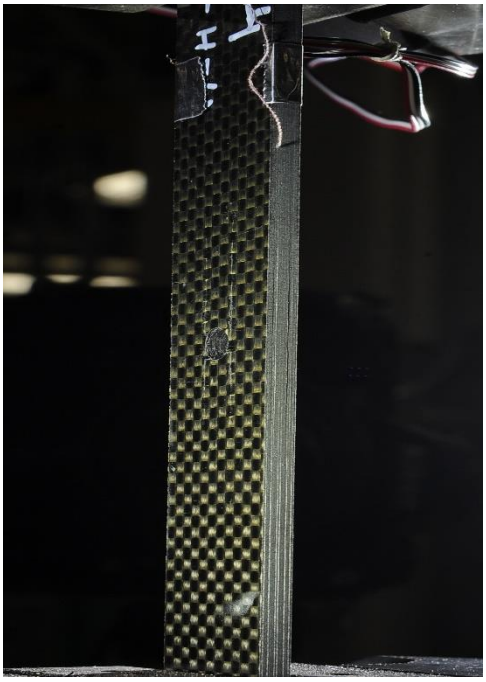

(A2-H-4) at 40k Cycles

Figure C 2-31 Damage Progression in (A2-H-4) Test specimen to 40k Cycles

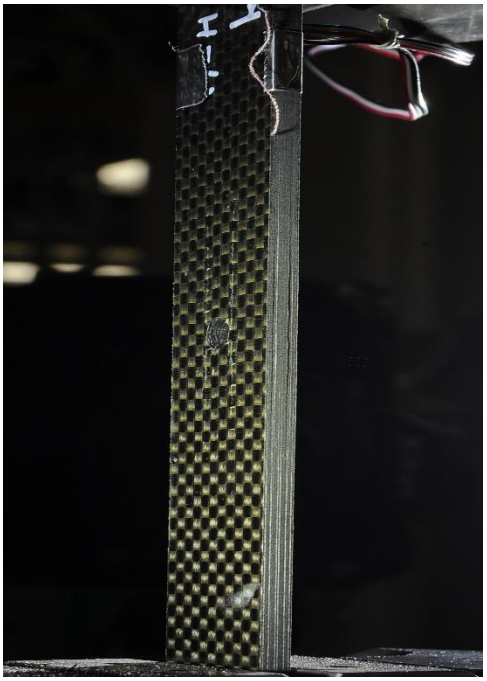

(A2-H-4) at 50k Cycles

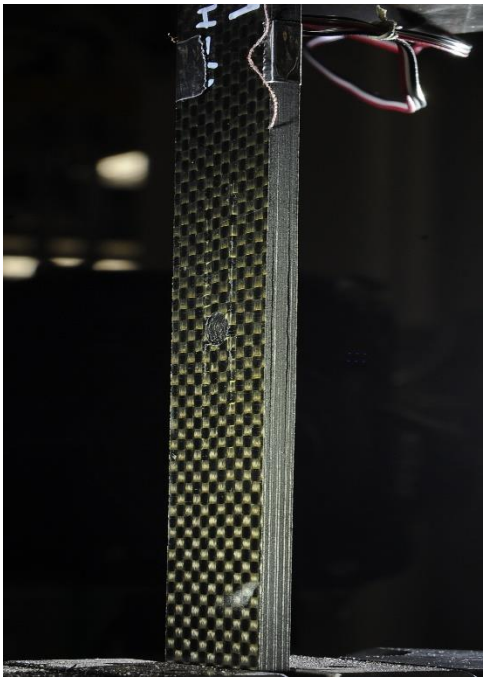

(A2-H-4) at 60k Cycles

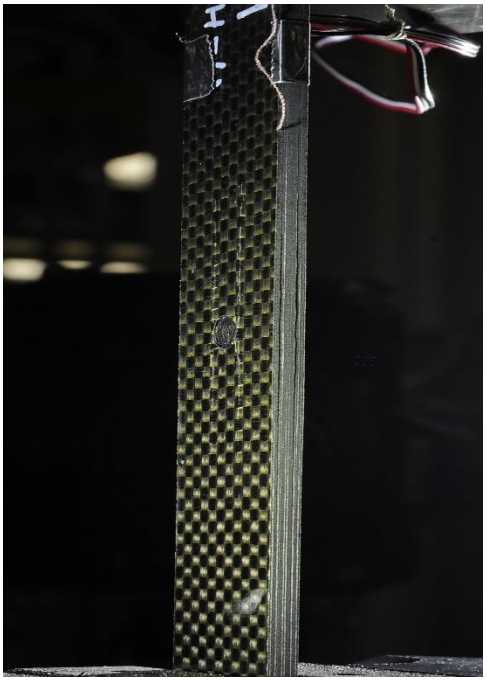

(A2-H-4) at 70k Cycles

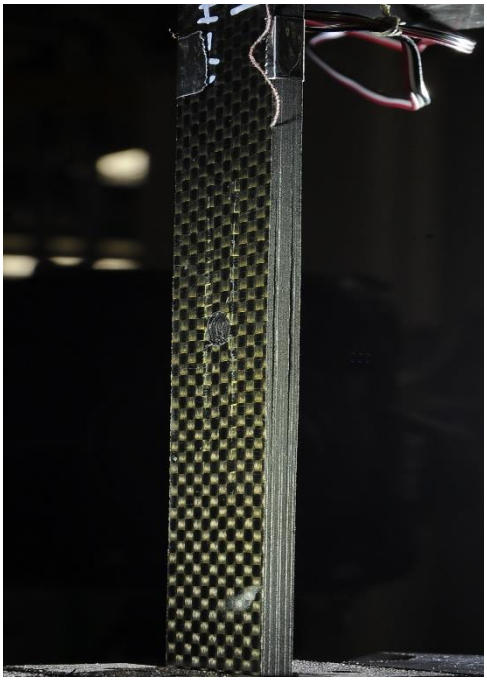

(A2-H-4) at 80k Cycles

Figure C 2-32 Damage Progression in (A2-H-4) Test specimen to 80k Cycles

(A2-H-4) at 90k Cycles

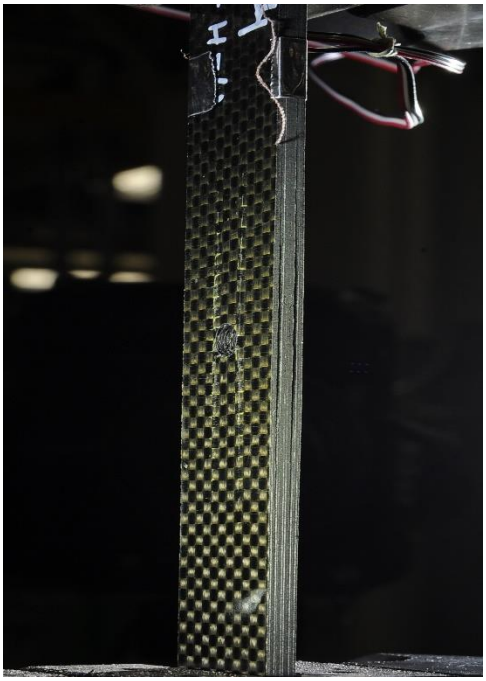

(A2-H-4) at 100k Cycles

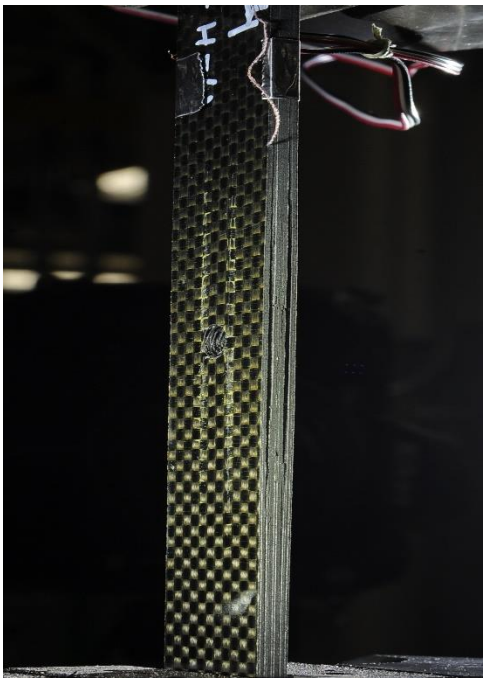

(A2-H-4) at 125k Cycles

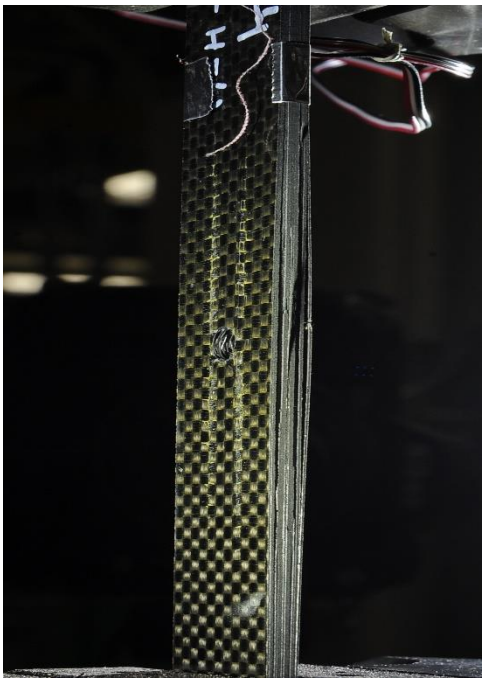

(A2-H-4) at 150k Cycles

Figure C 2-33 Damage Progression in (A2-H-4) Test specimen to 150k Cycles

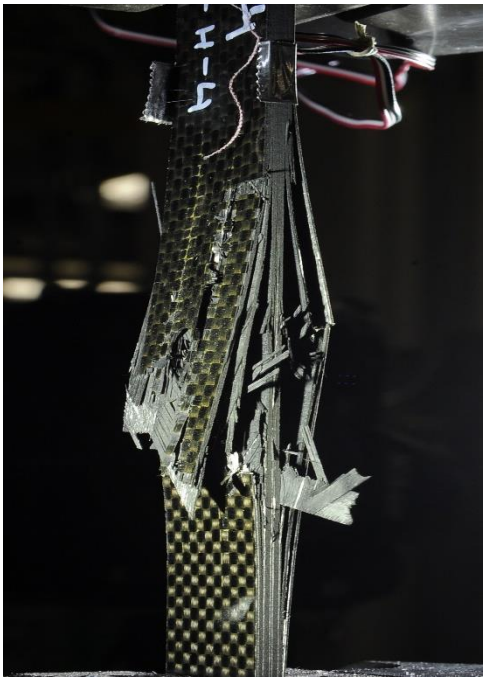

(A2-H-4) at Failure

Figure C 2-34 Damage Progression in (A2-H-4) Test specimen to Failure

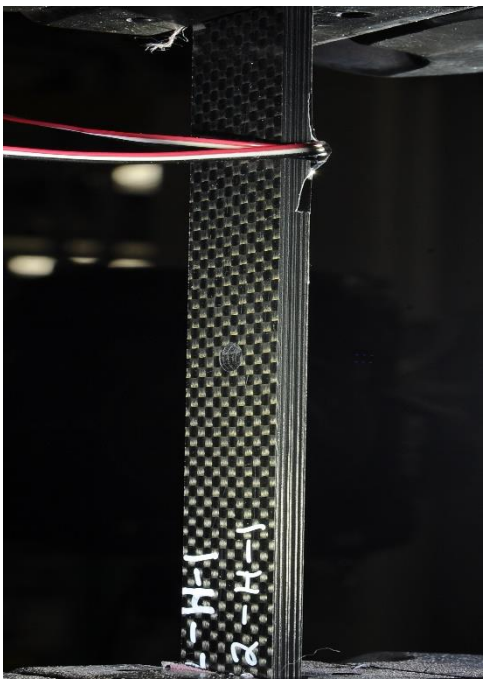

(B2-H-1) at 1 Cycle

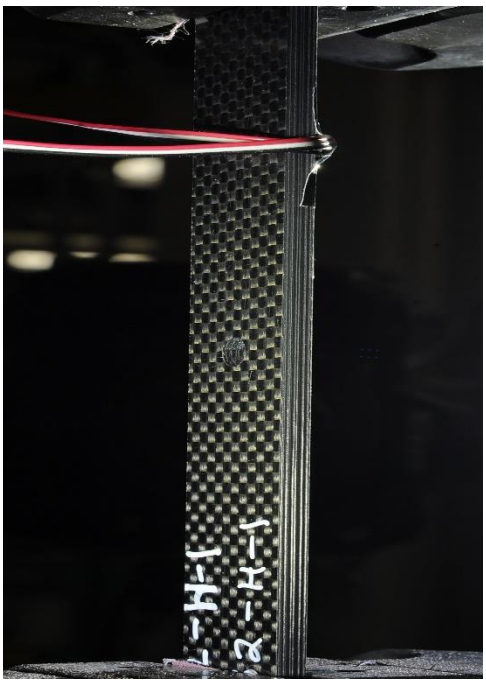

(B2-H-1) at 100 Cycles

(B2-H-1) at 1k Cycles

(B2-H-1) at 5k Cycles

Figure C 2-35 Damage Progression in (B2-H-1) Test specimen to 5k Cycles

(B2-H-1) at 10k Cycles

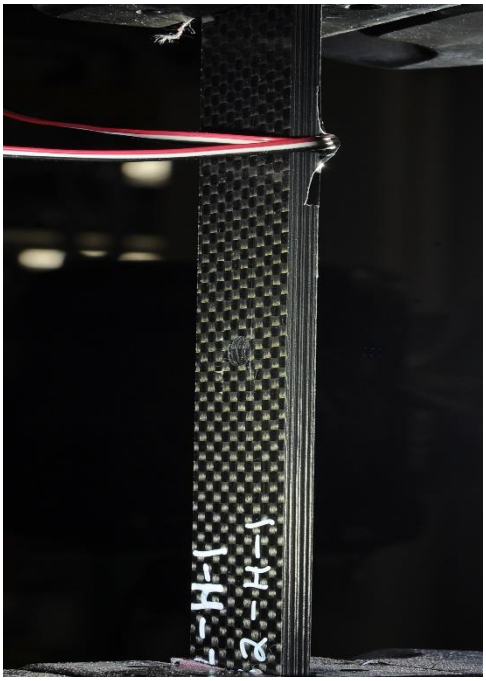

(B2-H-1) at 20k Cycles

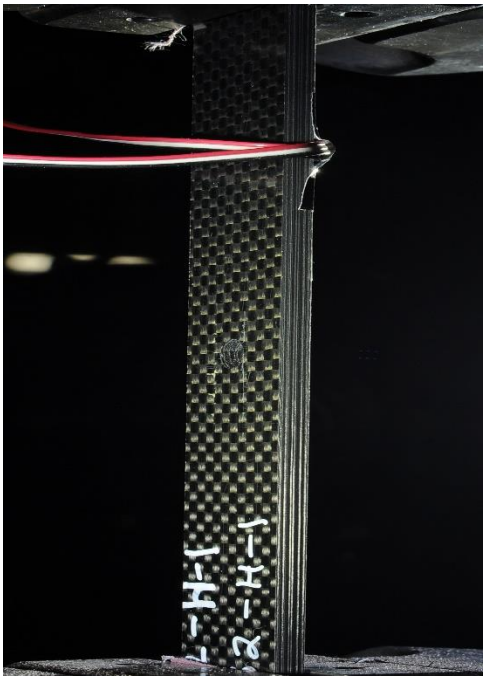

(B2-H-1) at 30k Cycles

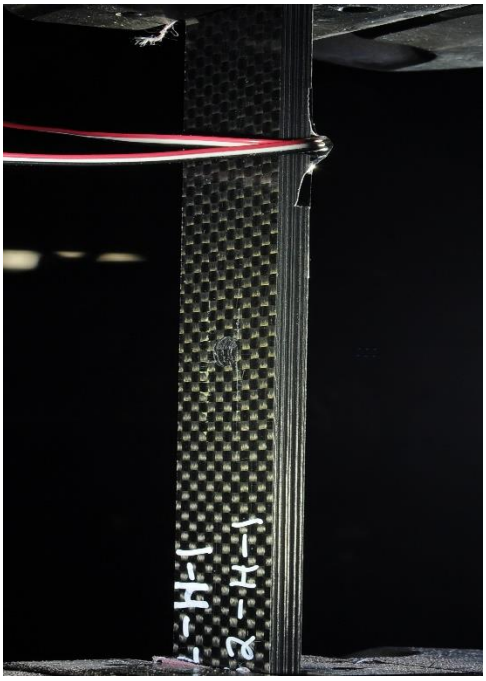

(B2-H-1) at 40k Cycles

Figure C 2-36 Damage Progression in (B2-H-1) Test specimen to 40k Cycles

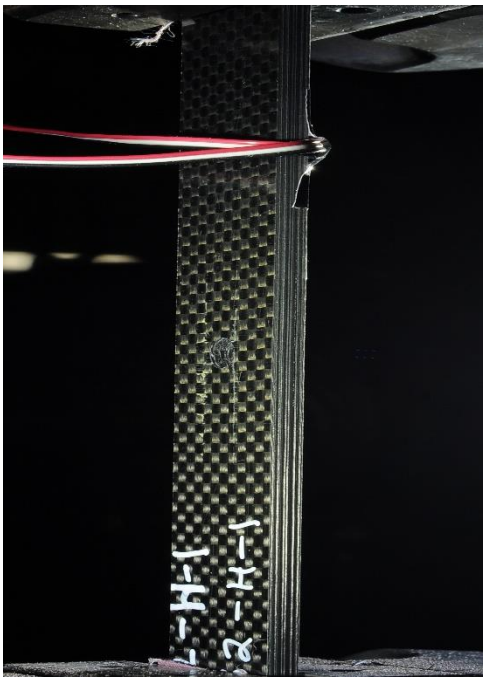

(B2-H-1) at 50k Cycles

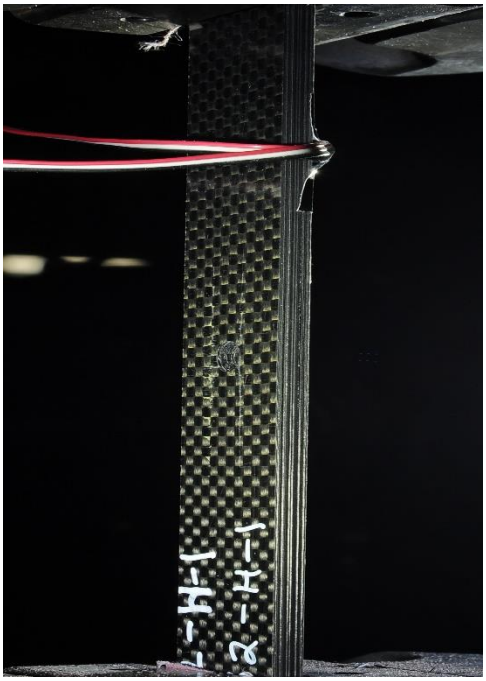

(B2-H-1) at 60k Cycles

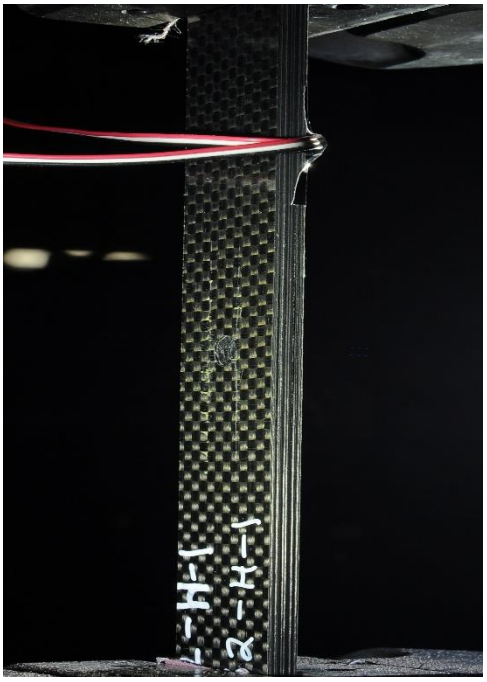

(B2-H-1) at 70k Cycles

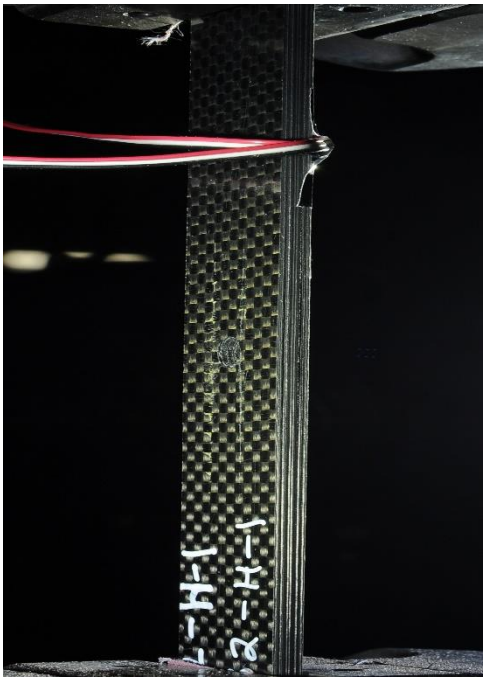

(B2-H-1) at 80k Cycles

Figure C 2-37 Damage Progression in (B2-H-1) Test specimen to 80k Cycles

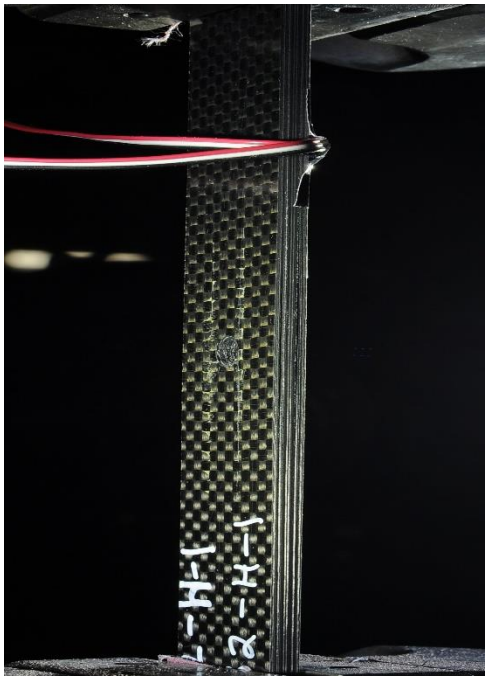

(B2-H-1) at 90k Cycles

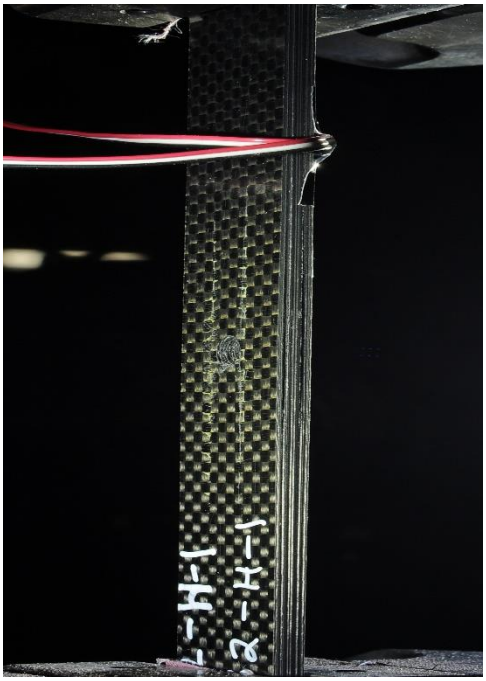

(B2-H-1) at 100k Cycles

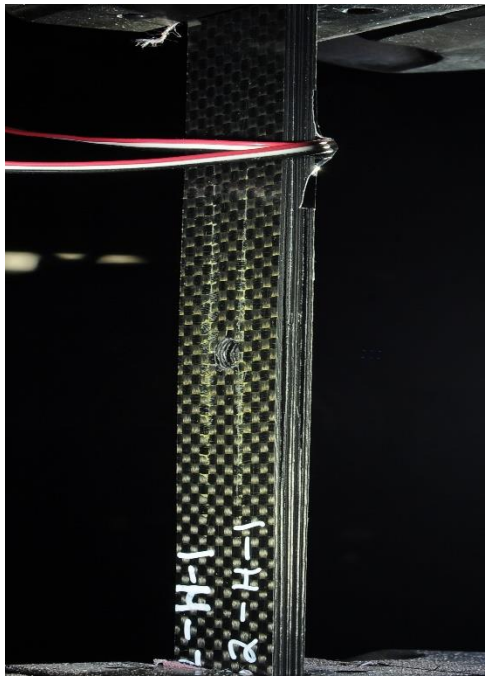

(B2-H-1) at 125k Cycles

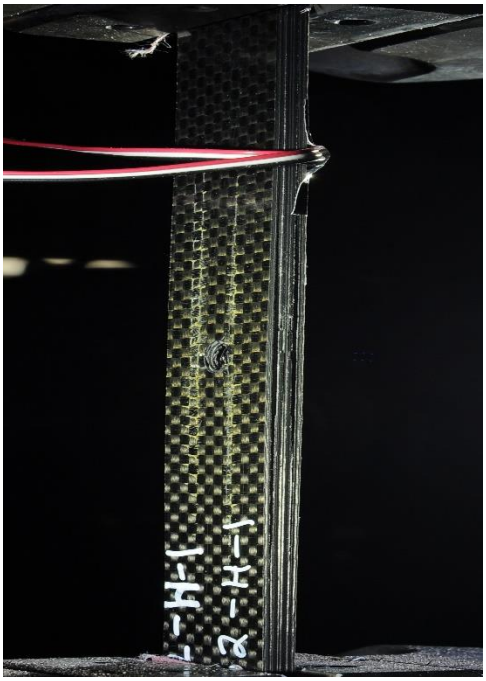

(B2-H-1) at 150k Cycles

Figure C 2-38 Damage Progression in (B2-H-1) Test specimen to 150k Cycles

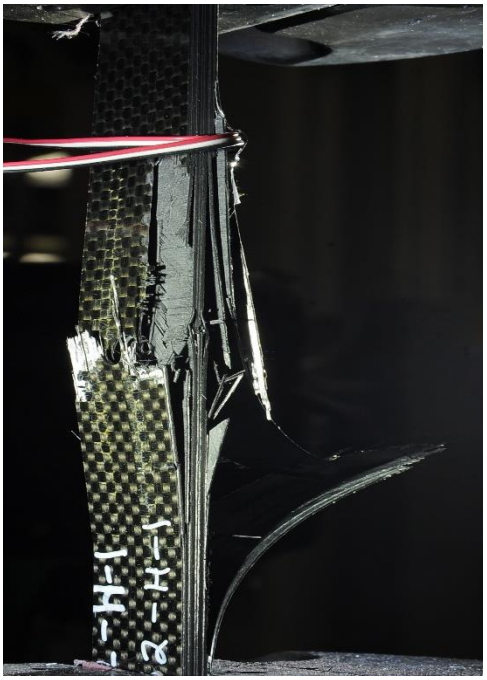

(B2-H-1) at Failure

Figure C 2-39 Damage Progression in (B2-H-1) Test specimen to Failure

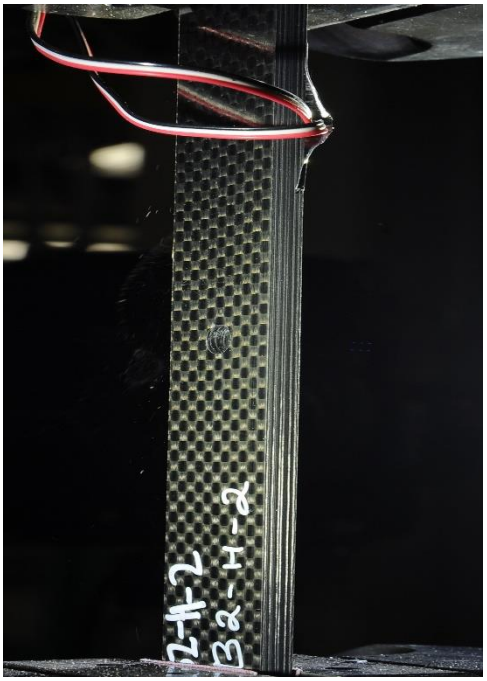

(B2-H-2) at 1 Cycle

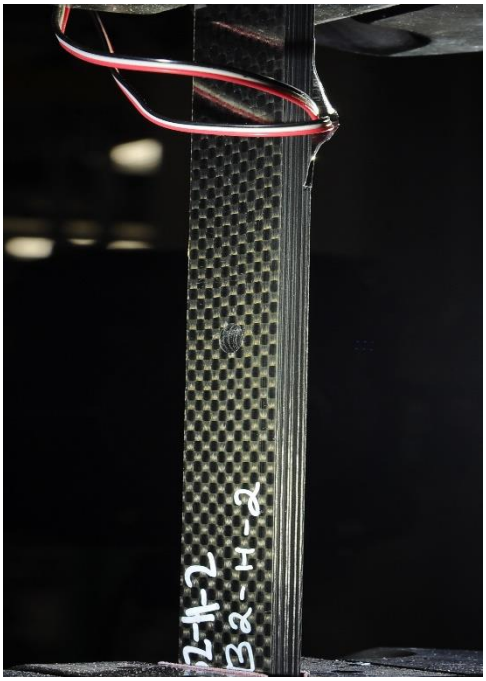

(B2-H-2) at 100 Cycles

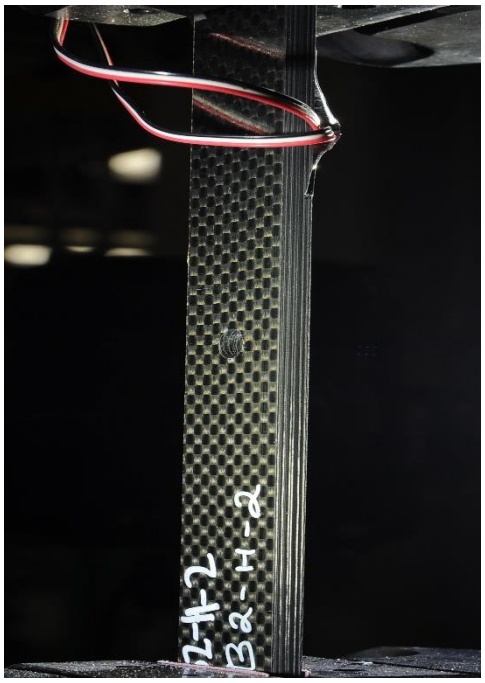

(B2-H-2) at 1k Cycles

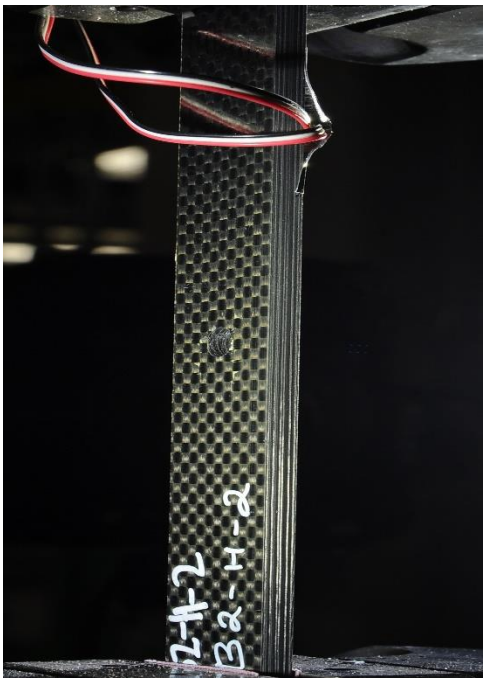

(B2-H-2) at 5k Cycles

Figure C 2-40 Damage Progression in (B2-H-2) Test specimen to 5k Cycles

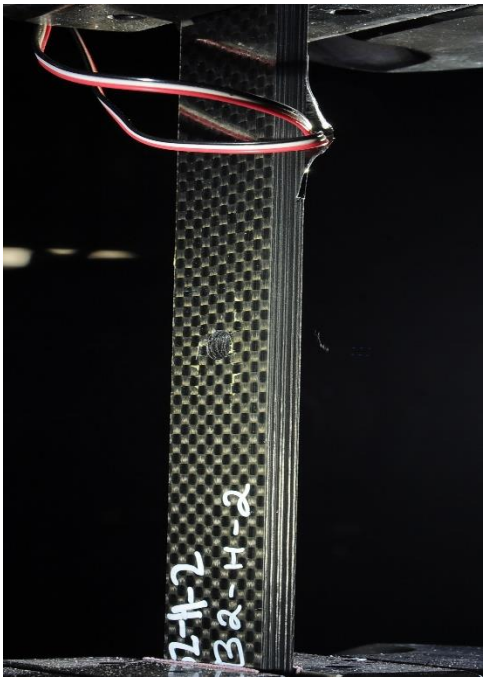

(B2-H-2) at 10k Cycles

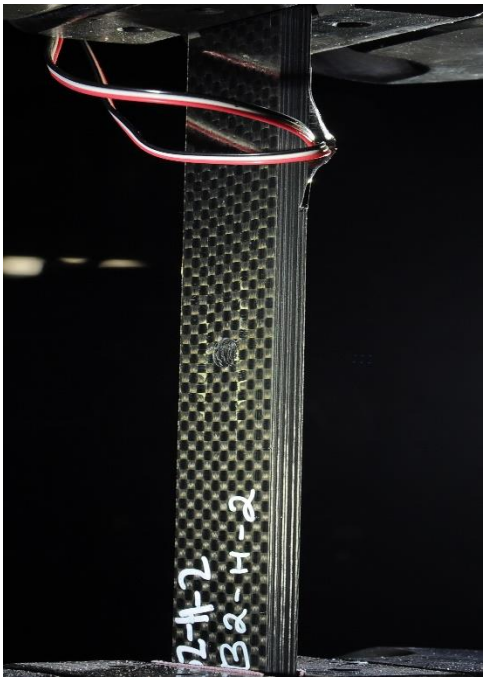

(B2-H-2) at 20k Cycles

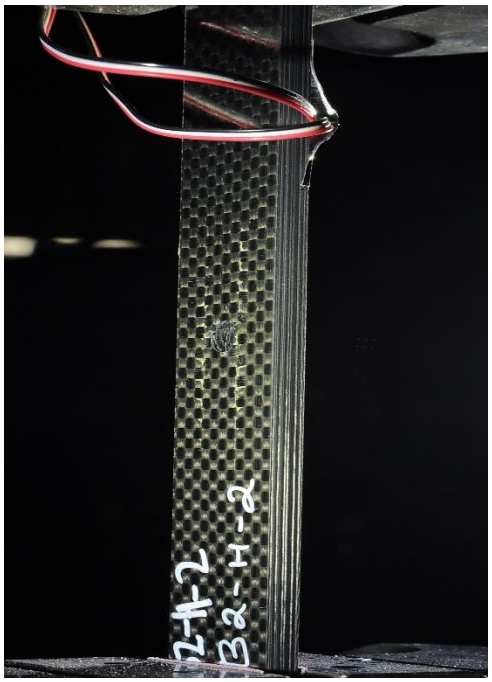

(B2-H-2) at 30k Cycles

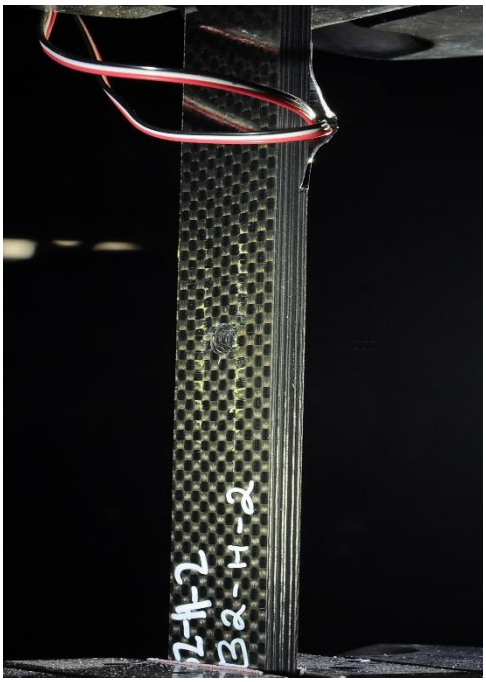

(B2-H-2) at 40k Cycles

Figure C 2-41 Damage Progression in (B2-H-2) Test specimen to 40k Cycles

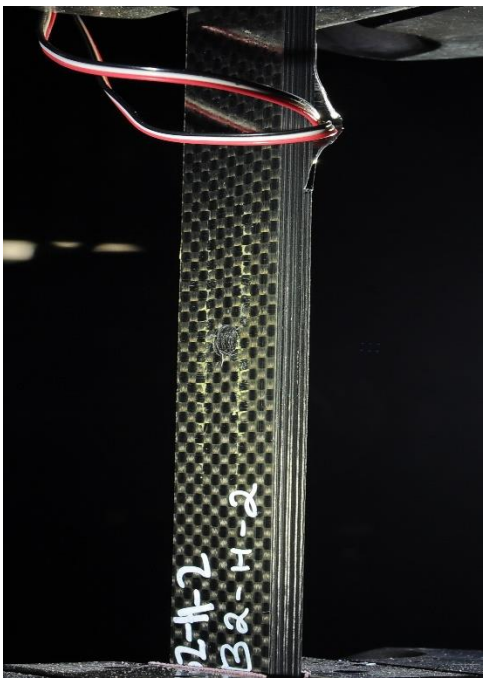

(B2-H-2) at 50k Cycles

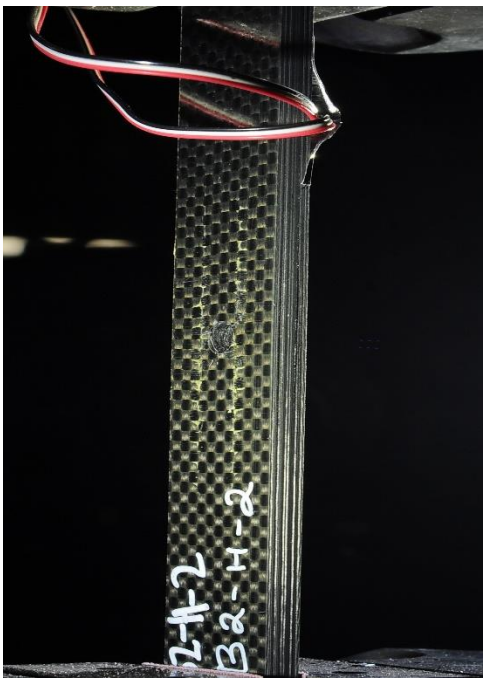

(B2-H-2) at 60k Cycles

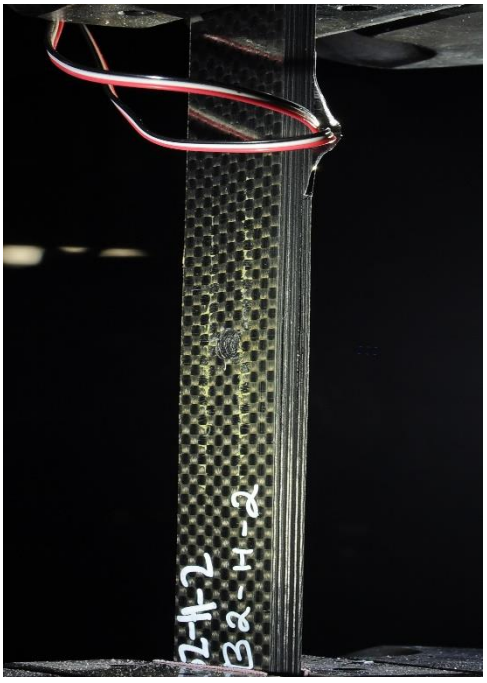

(B2-H-2) at 70k Cycles

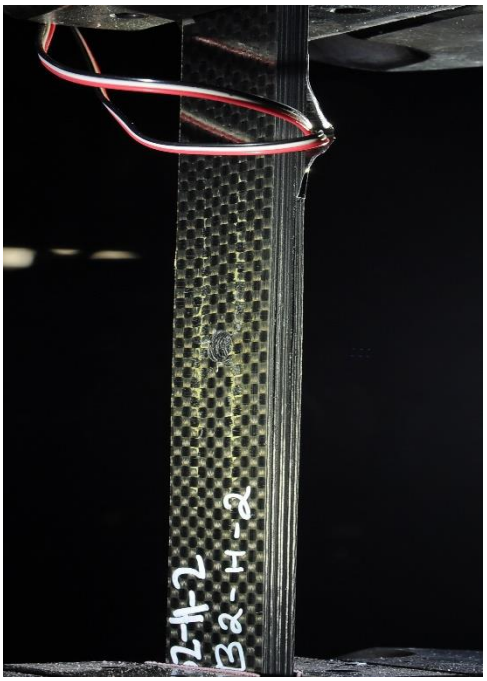

(B2-H-2) at 80k Cycles

Figure C 2-42 Damage Progression in (B2-H-2) Test specimen to 80k Cycles

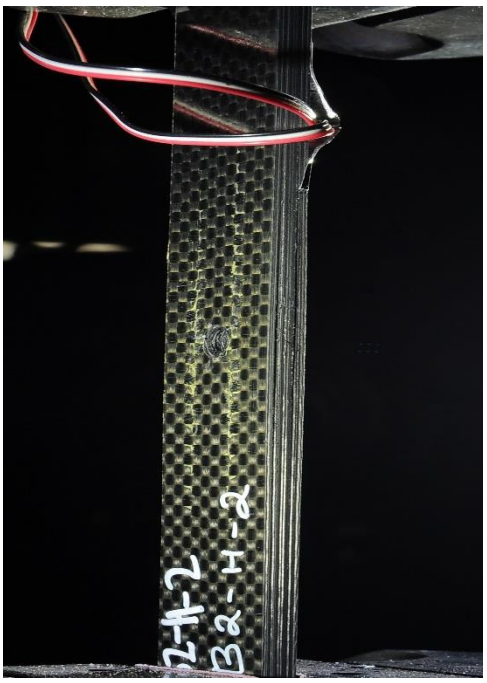

(B2-H-2) at 90k Cycles

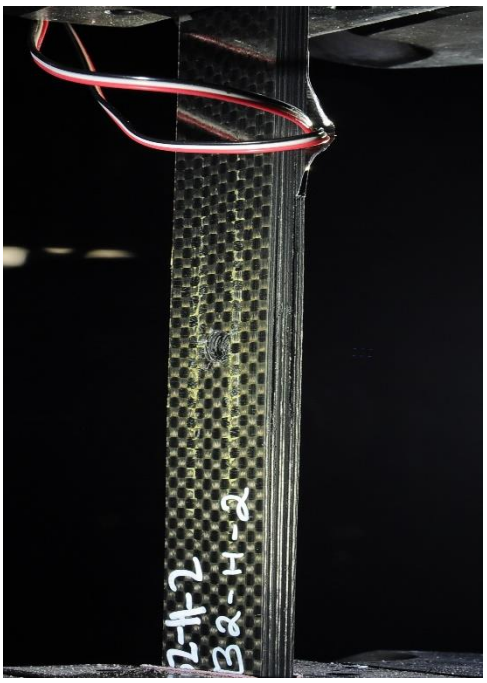

(B2-H-2) at 100k Cycles

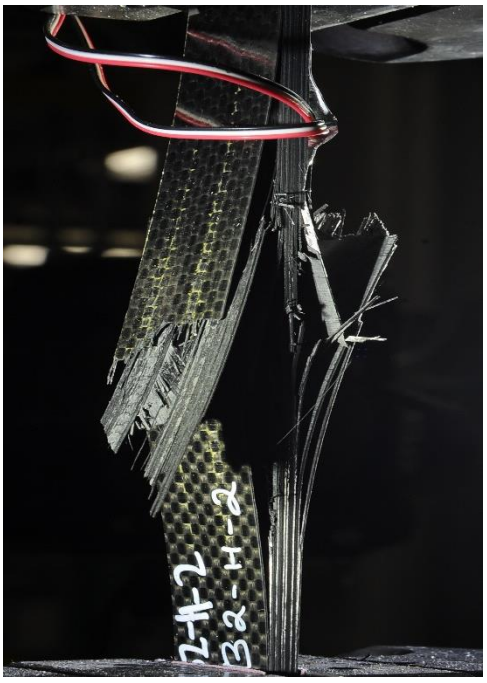

(B2-H-2) at Failure

Figure C 2-43 Damage Progression in (B2-H-2) Test specimen to Failure

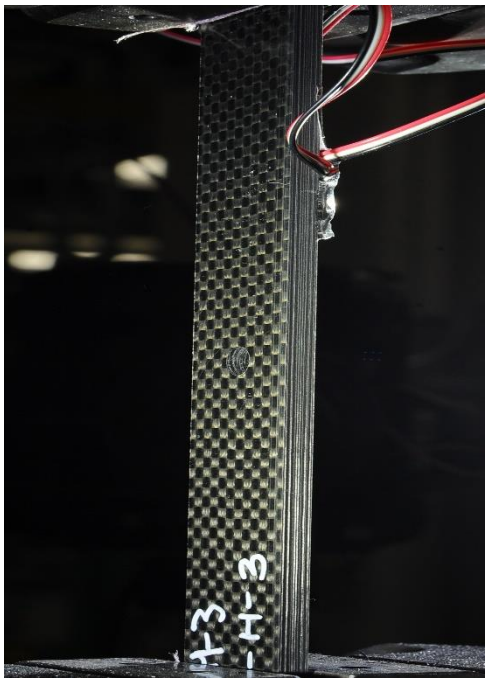

(B2-H-3) at 1 Cycle

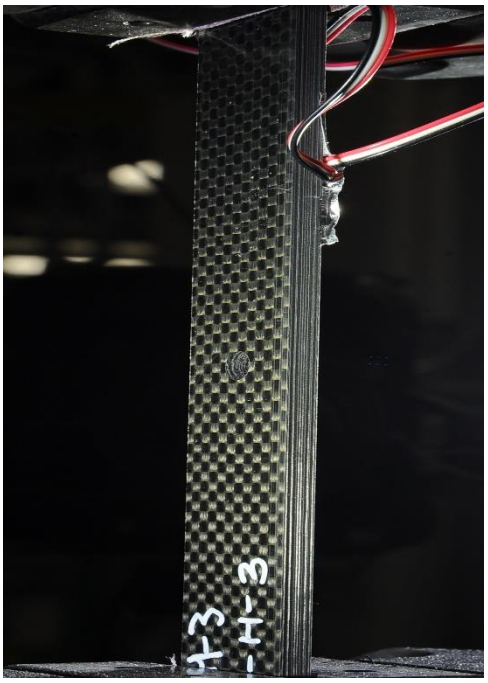

(B2-H-3) at 100 Cycles

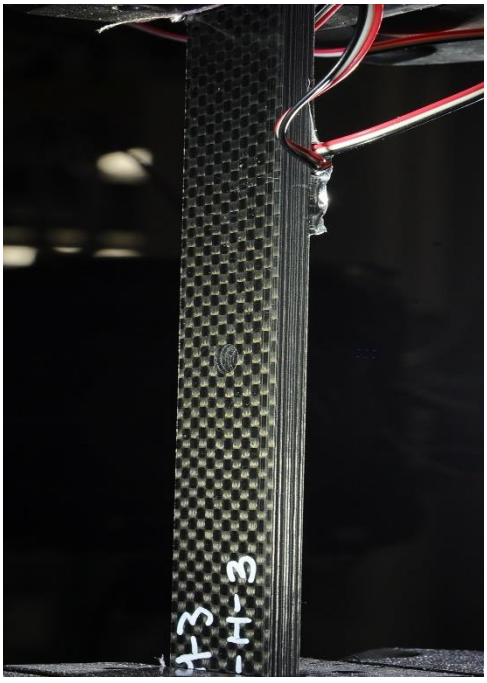

(B2-H-3) at 1k Cycles

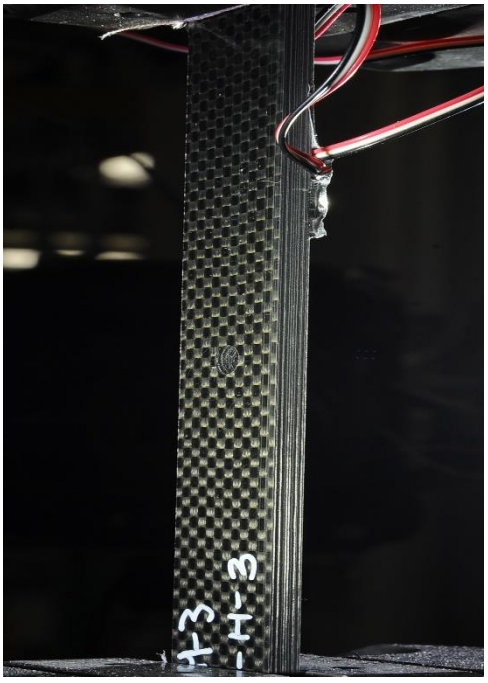

(B2-H-3) at 5k Cycles

Figure C 2-44 Damage Progression in (B2-H-3) Test specimen to 5k Cycles

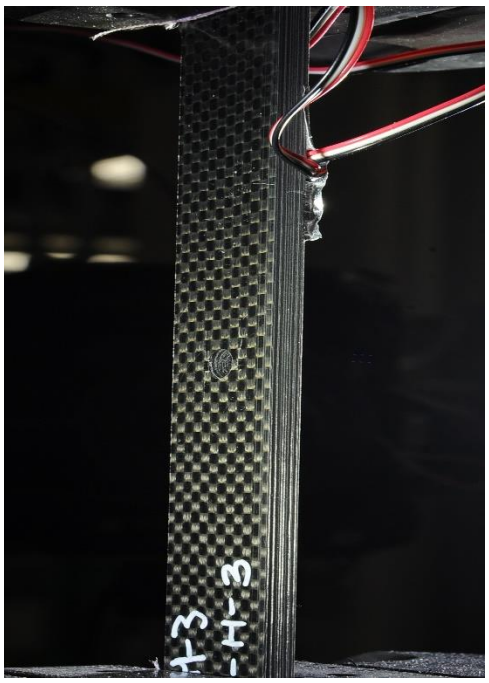

(B2-H-3) at 10k Cycles

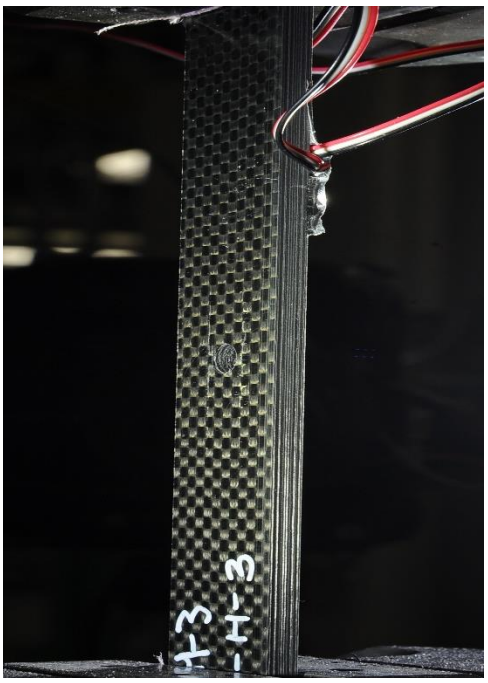

(B2-H-3) at 20k Cycles

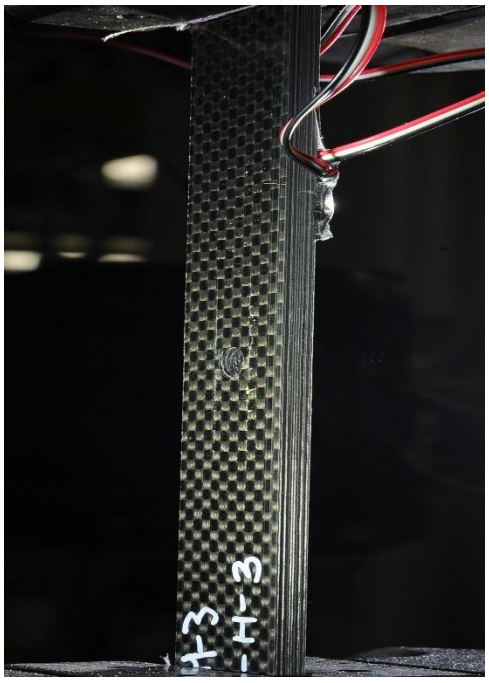

(B2-H-3) at 30k Cycles

(B2-H-3) at 40k Cycles

Figure C 2-45 Damage Progression in (B2-H-3) Test specimen to 40k Cycles

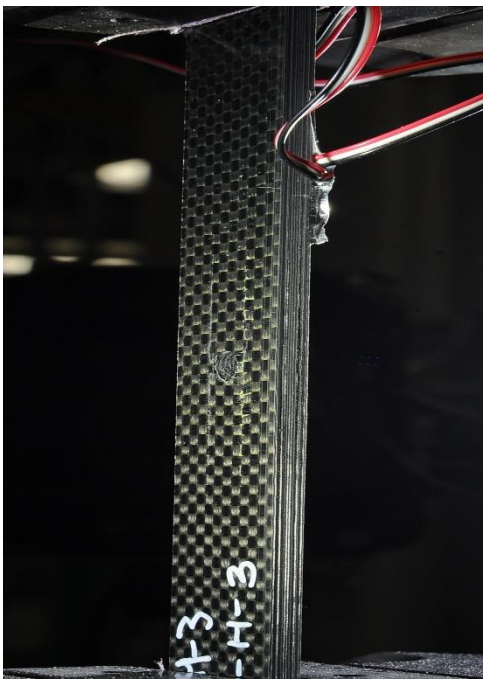

(B2-H-3) at 50k Cycles

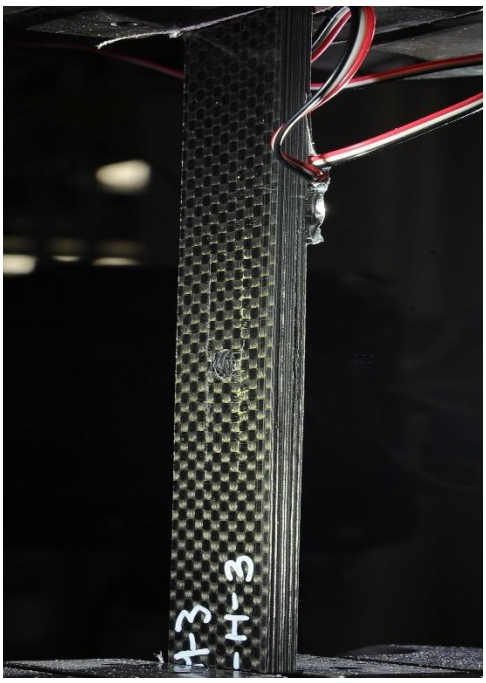

(B2-H-3) at 60k Cycles

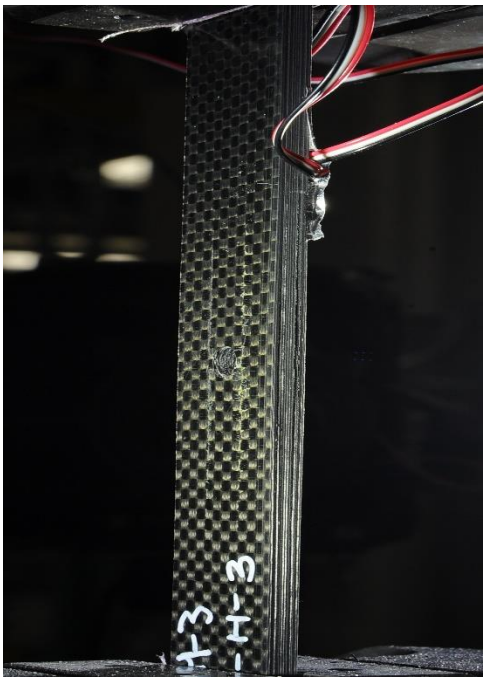

(B2-H-3) at 70k Cycles

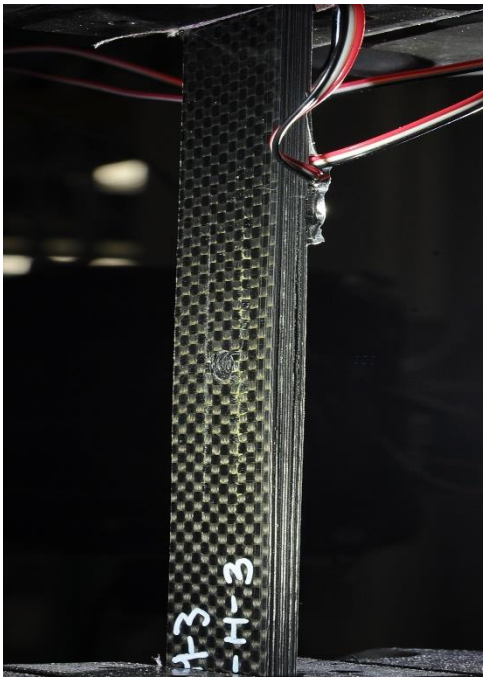

(B2-H-3) at 80k Cycles

Figure C 2-46 Damage Progression in (B2-H-3) Test specimen to 80k Cycles

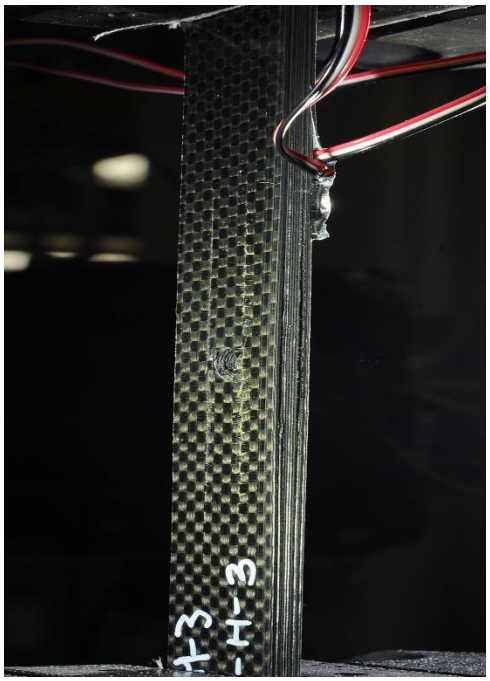

(B2-H-3) at 90k Cycles

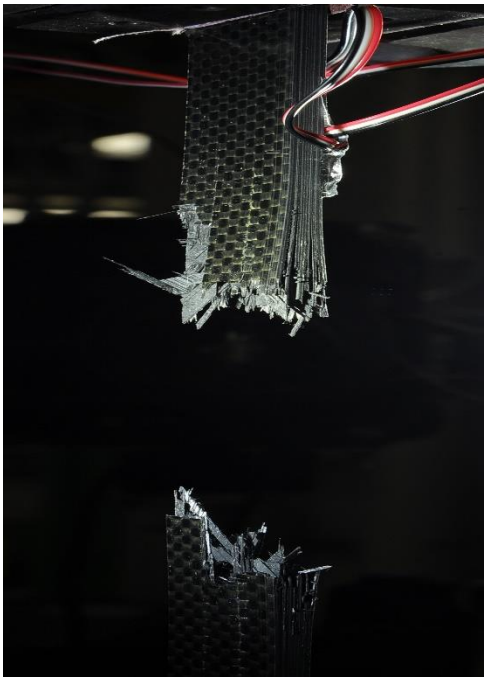

(B2-H-3) at Failure

Figure C 2-47 Damage Progression in (B2-H-3) Test specimen to Failure

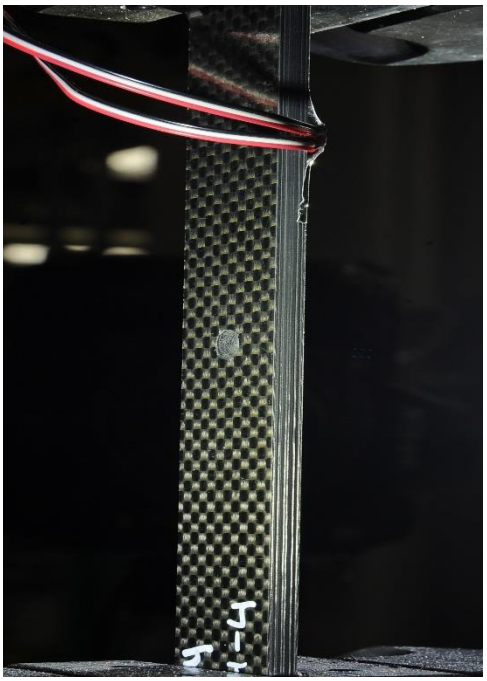

(B2-H-4) at 1 Cycle

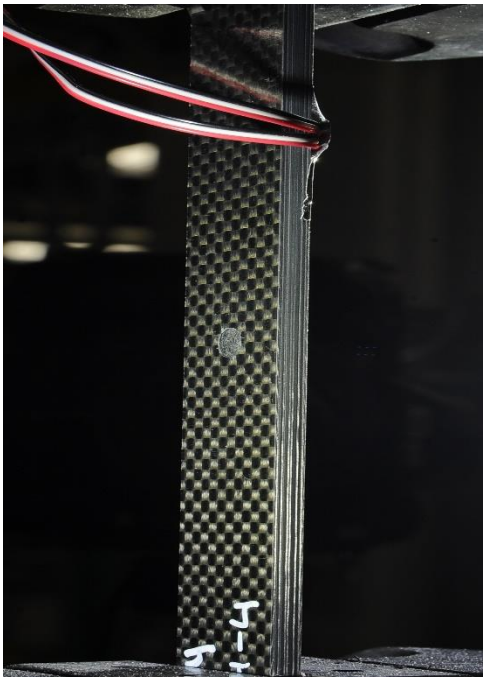

(B2-H-4) at 100 Cycles

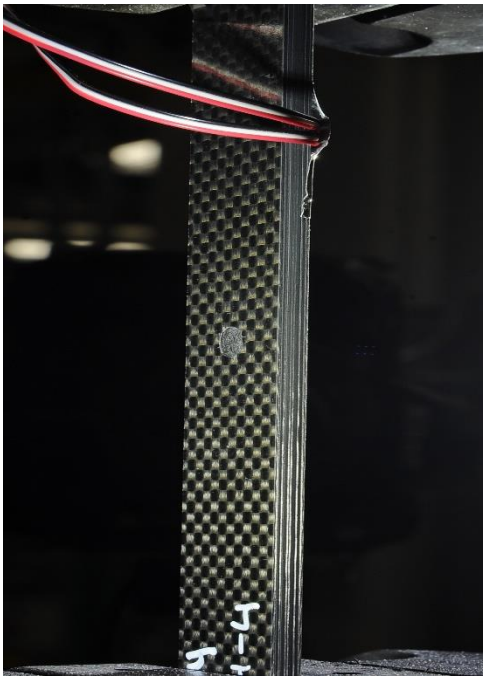

(B2-H-4) at 1k Cycles

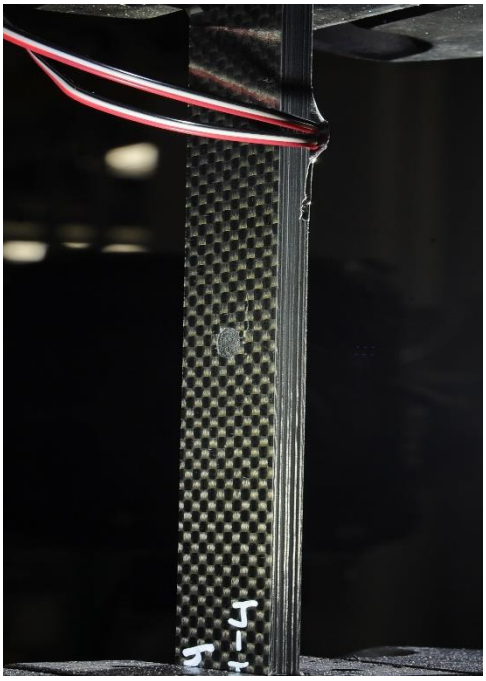

(B2-H-4) at 2k Cycles

Figure C 2-48 Damage Progression in (B2-H-4) Test specimen to 2k Cycles

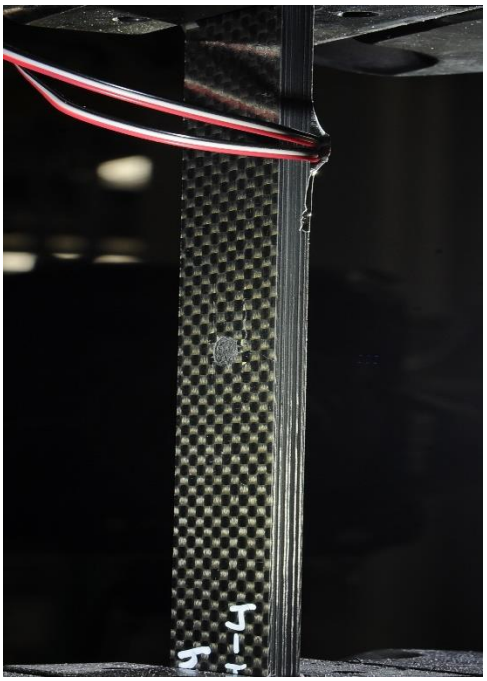

(B2-H-4) at 3k Cycles

(B2-H-4) at 4k Cycles

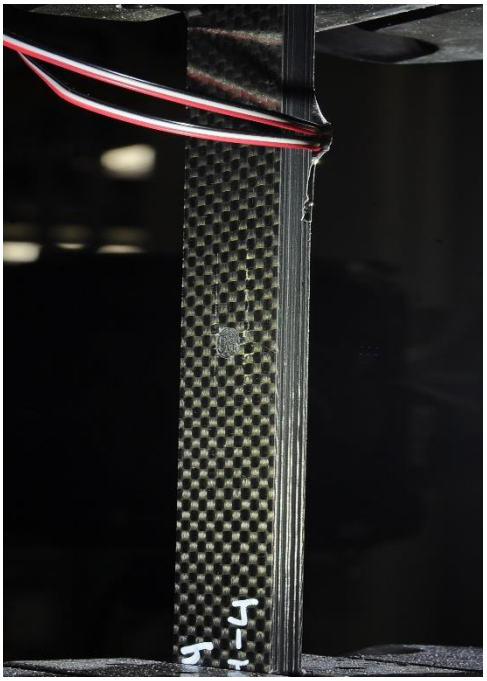

(B2-H-4) at 5k Cycles

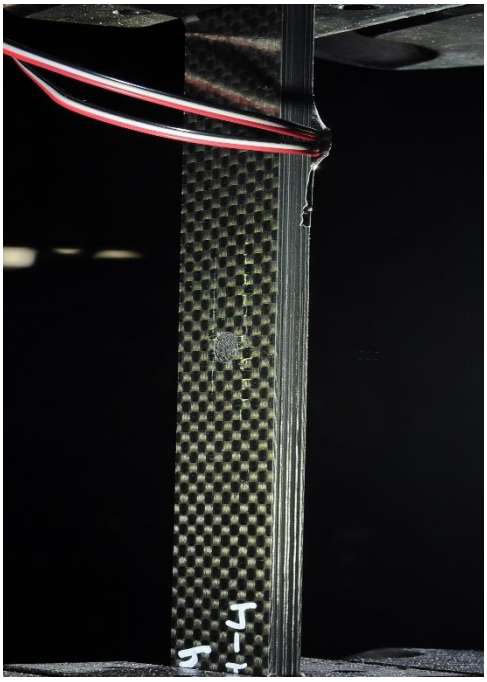

(B2-H-4) at 6k Cycles

Figure C 2-49 Damage Progression in (B2-H-4) Test specimen to 6k Cycles

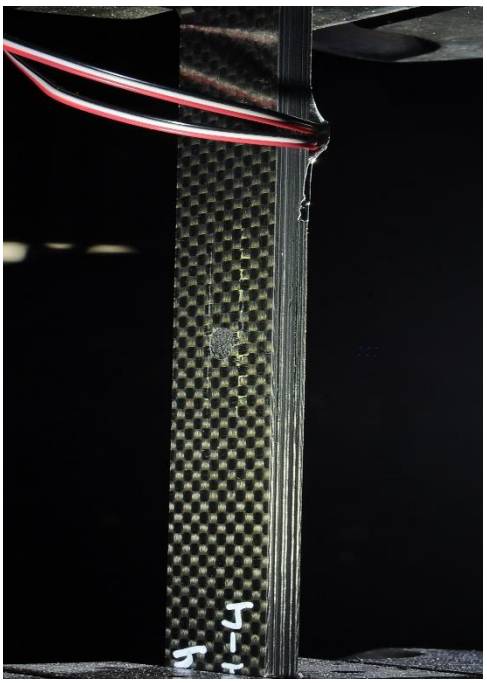

(B2-H-4) at 7k Cycles

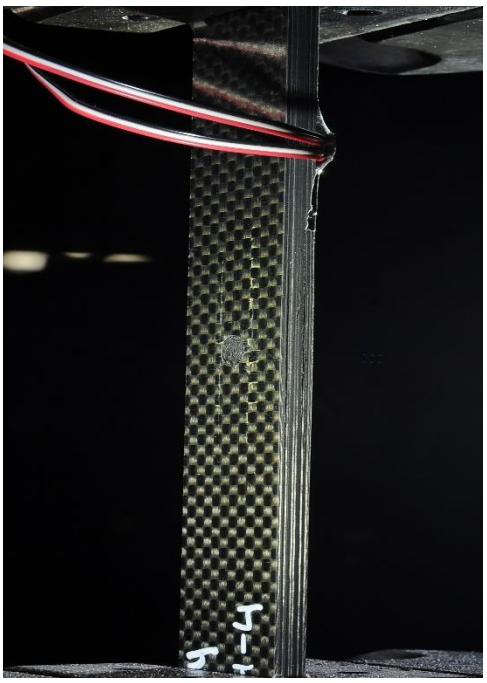

(B2-H-4) at 8k Cycles

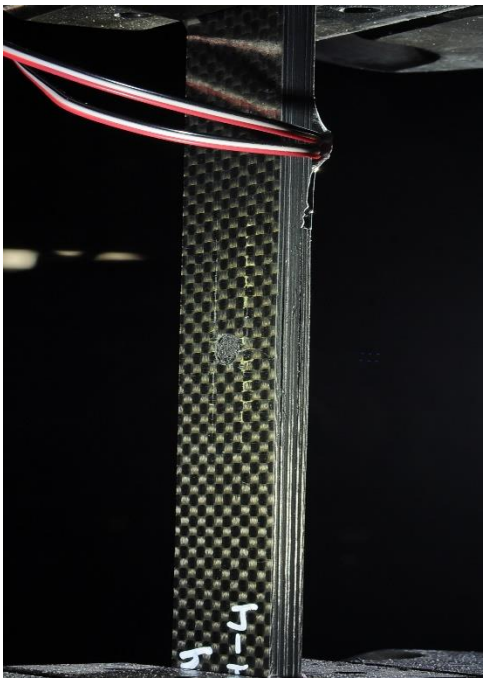

(B2-H-4) at 9k Cycles

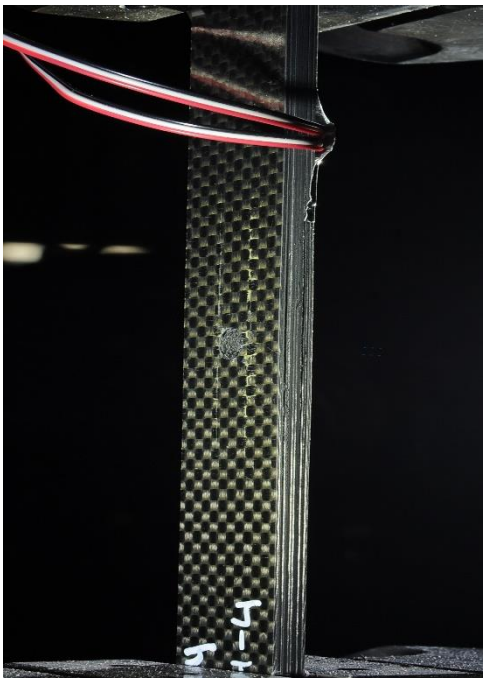

(B2-H-4) at 10k Cycles

Figure C 2-50 Damage Progression in (B2-H-4) Test specimen to 10k Cycles

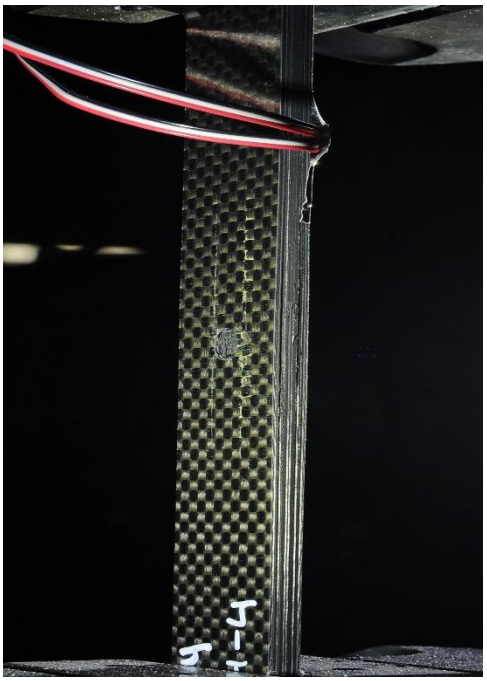

(B2-H-4) at 15k Cycles

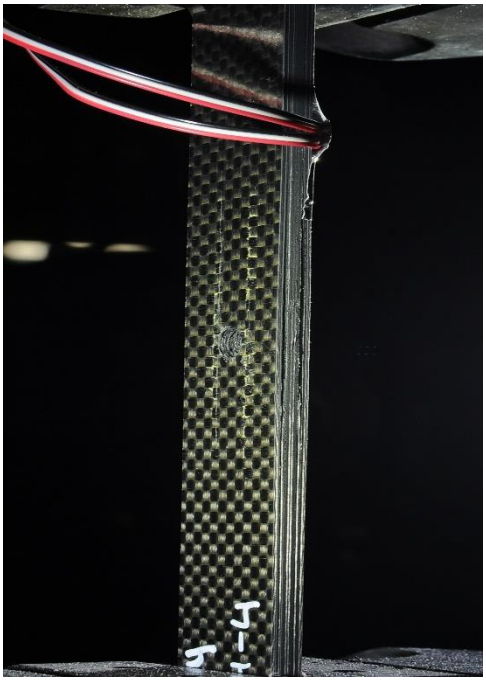

(B2-H-4) at 20k Cycles

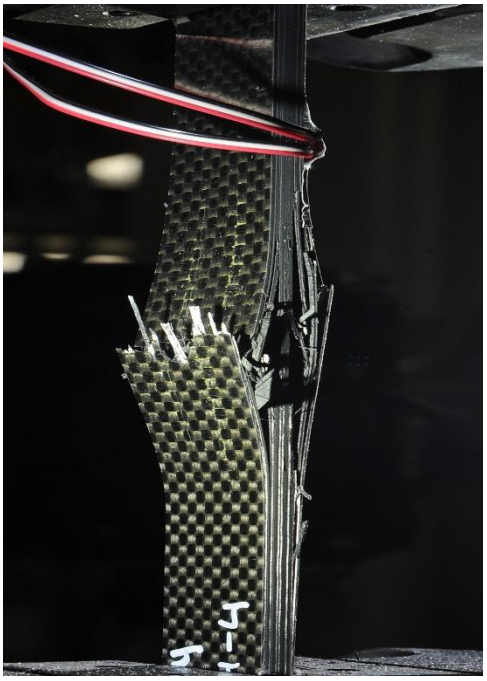

(B2-H-4) at Failure

Figure C 2-51 Damage Progression in (B2-H-4) Test specimen to Failure

(A2-M-1) at 1 Cycle

(A2-M-1) at 100 Cycles

(A2-M-1) at 1k Cycles

(A2-M-1) at 5k Cycles

Figure C 2-52 Damage Progression in (A2-M-1) Test specimen to 5k Cycles

(A2-M-1) at 10k Cycles

(A2-M-1) at 20k Cycles

(A2-M-1) at 30k Cycles

(A2-M-1) at 40k Cycles

Figure C 2-53 Damage Progression in (A2-M-1) Test specimen to 40k Cycles

(A2-M-1) at 50k Cycles

(A2-M-1) at 60k Cycles

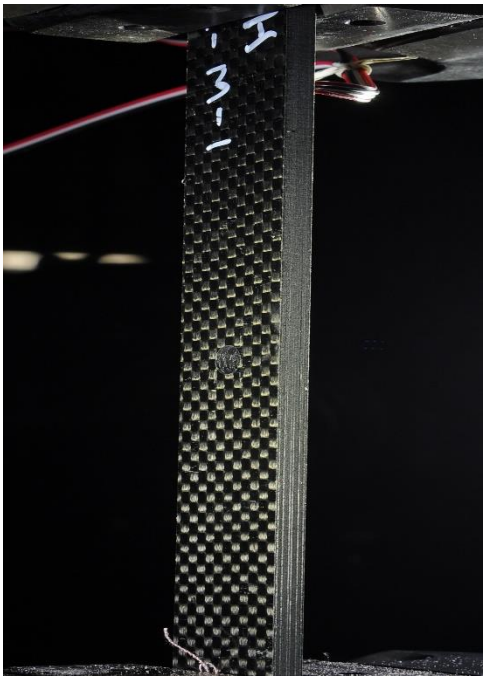

(A2-M-1) at 70k Cycles

(A2-M-1) at 80k Cycles

Figure C 2-54 Damage Progression in (A2-M-1) Test specimen to 80k Cycles

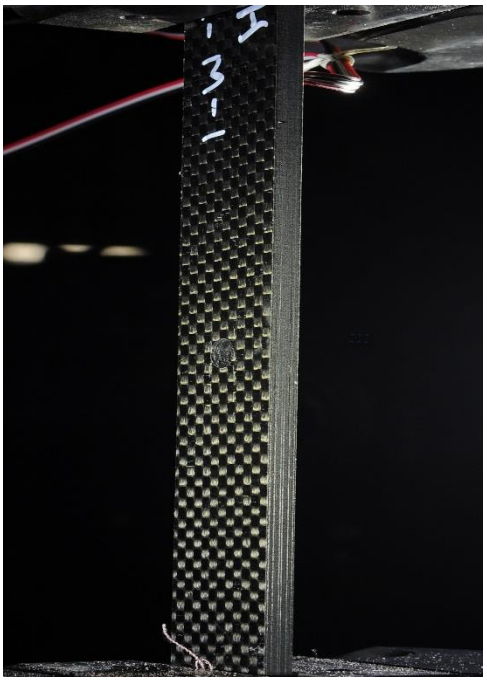

(A2-M-1) at 90k Cycles

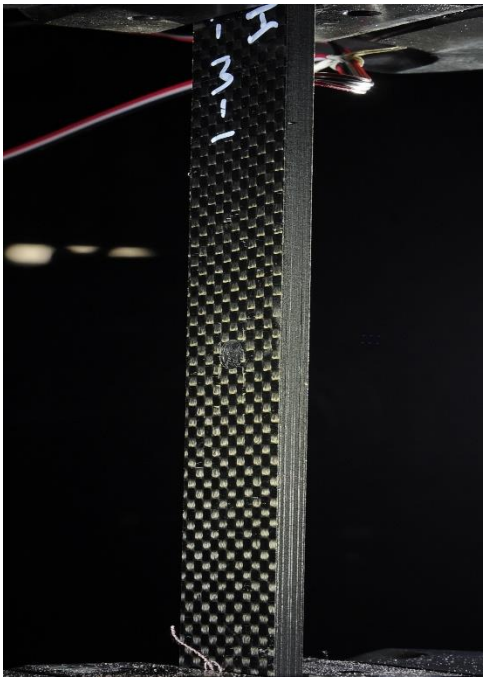

(A2-M-1) at 100k Cycles

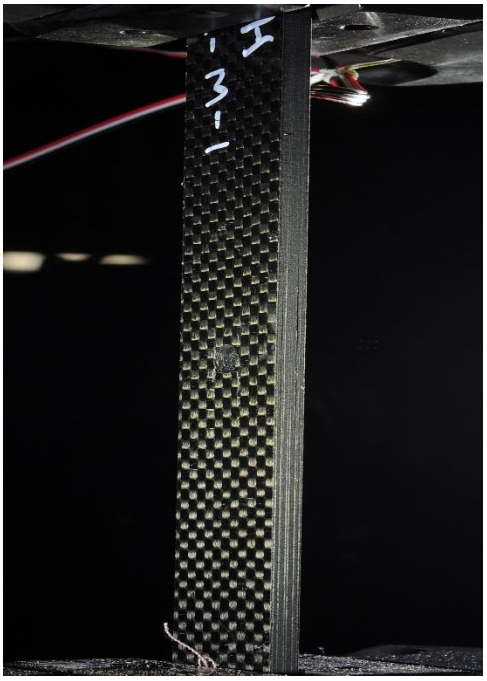

(A2-M-1) at 125k Cycles

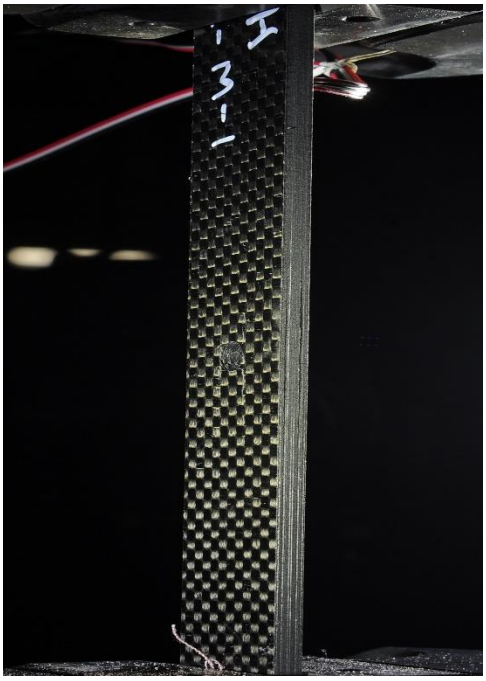

(A2-M-1) at 150k Cycles

Figure C 2-55 Damage Progression in (A2-M-1) Test specimen to 150k Cycles

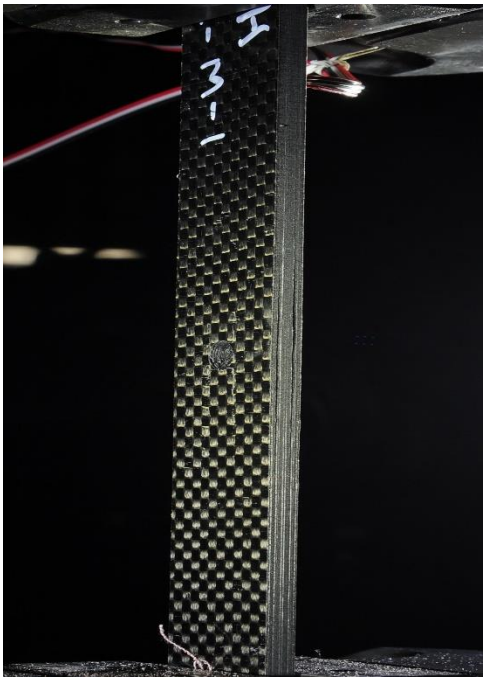

(A2-M-1) at 175k Cycles

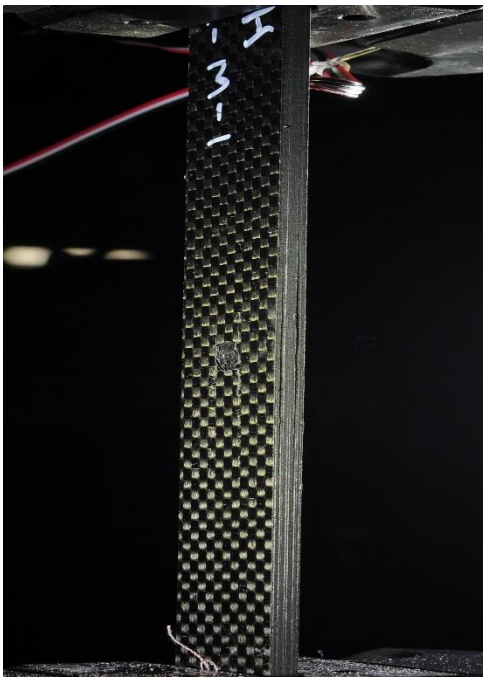

(A2-M-1) at 200k Cycles

(A2-M-1) at 225k Cycles

(A2-M-1) at 250k Cycles

Figure C 2-56 Damage Progression in (A2-M-1) Test specimen to 250k Cycles

(A2-M-1) at 275k Cycles

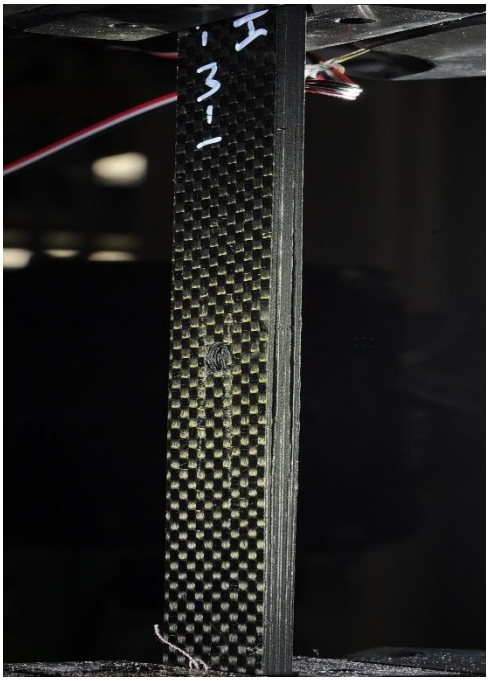

(A2-M-1) at 300k Cycles

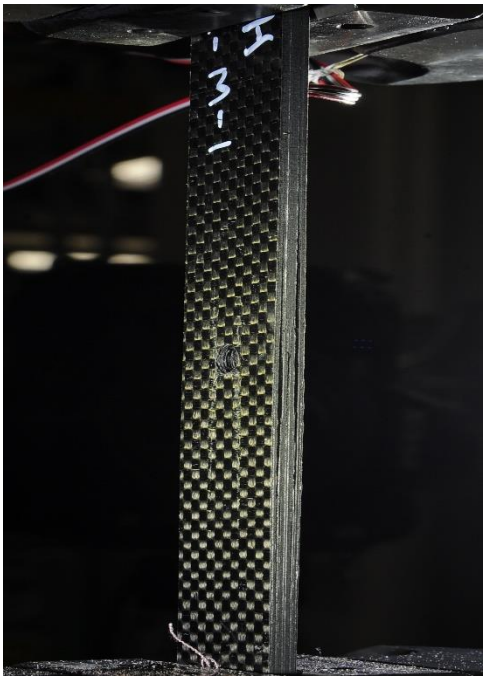

(A2-M-1) at 325k Cycles

(A2-M-1) at 350k Cycles

Figure C 2-57 Damage Progression in (A2-M-1) Test specimen to 350k Cycles

(A2-M-1) at 375k Cycles

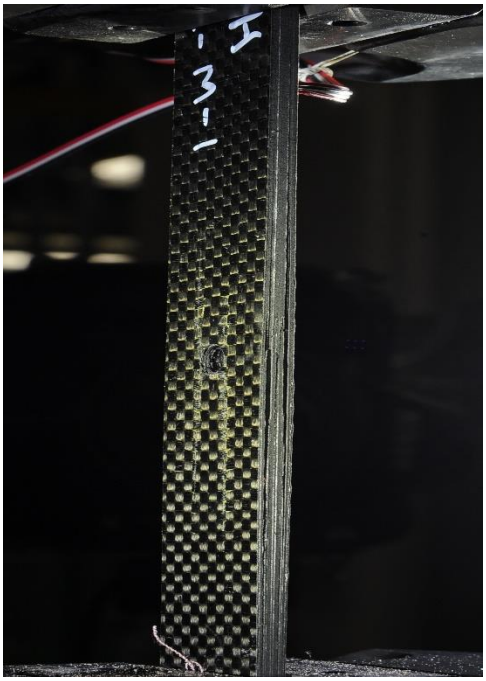

(A2-M-1) at 400k Cycles

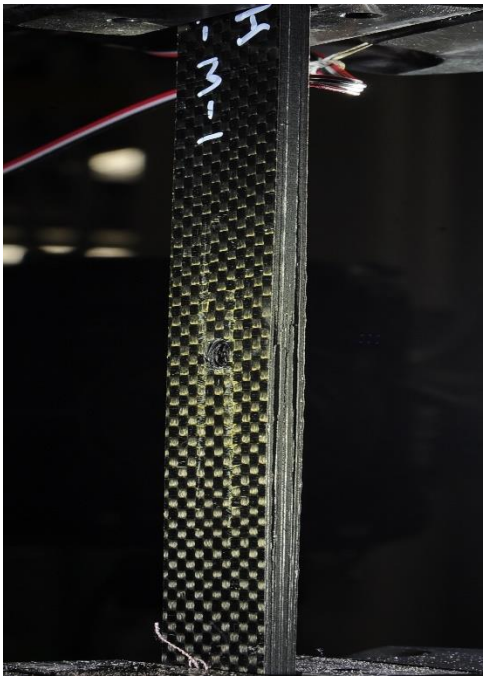

(A2-M-1) at 425k Cycles

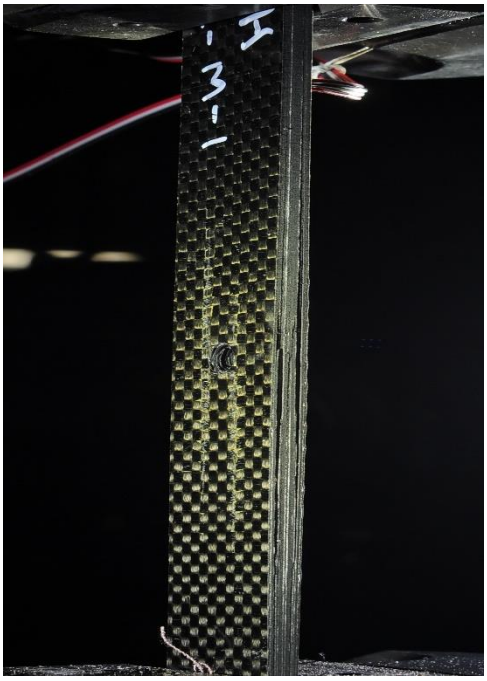

(A2-M-1) at 450k Cycles

Figure C 2-58 Damage Progression in (A2-M-1) Test specimen to 450k Cycles

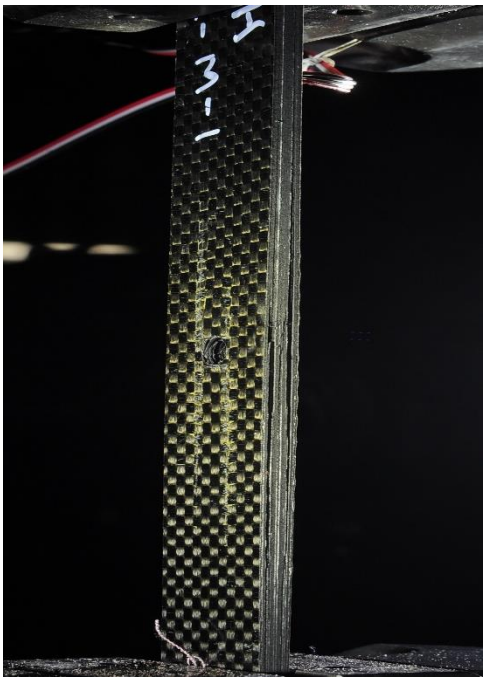

(A2-M-1) at 475k Cycles

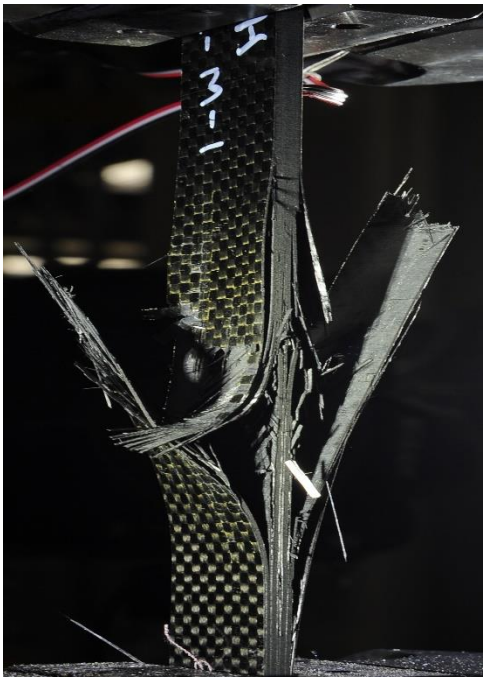

(A2-M-1) at Failure

Figure C 2-59 Damage Progression in (A2-M-1) Test specimen to Failure

(A2-M-2) at 1 Cycle

(A2-M-2) at 100 Cycles

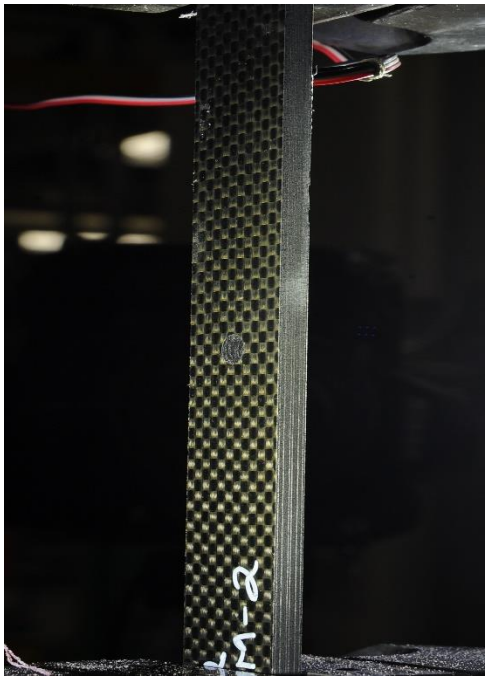

(A2-M-2) at 1k Cycles

(A2-M-2) at 5k Cycles

Figure C 2-60 Damage Progression in (A2-M-2) Test specimen to 5k cycles

(A2-M-2) at 10k Cycles

(A2-M-2) at 20k Cycles

(A2-M-2) at 30k Cycles

(A2-M-2) at 40k Cycles

Figure C 2-61 Damage Progression in (A2-M-2) Test specimen to 40k cycles

(A2-M-2) at 50k Cycles

(A2-M-2) at 60k Cycles

(A2-M-2) at 70k Cycles

(A2-M-2) at 80k Cycles

Figure C 2-62 Damage Progression in (A2-M-2) Test specimen to 80k cycles

(A2-M-2) at 90k Cycles

(A2-M-2) at 100k Cycles

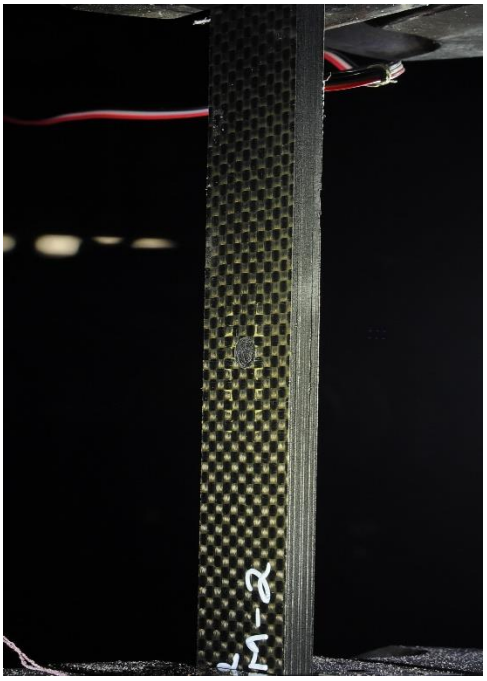

(A2-M-2) at 125k Cycles

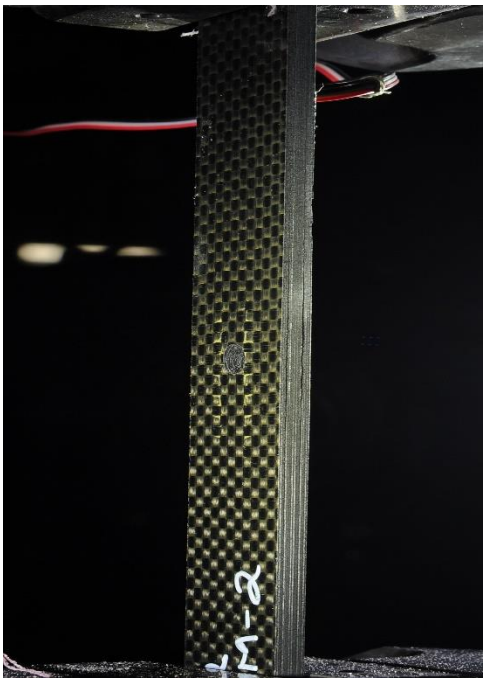

(A2-M-2) at 150k Cycles

Figure C 2-63 Damage Progression in (A2-M-2) Test specimen to 150k cycles

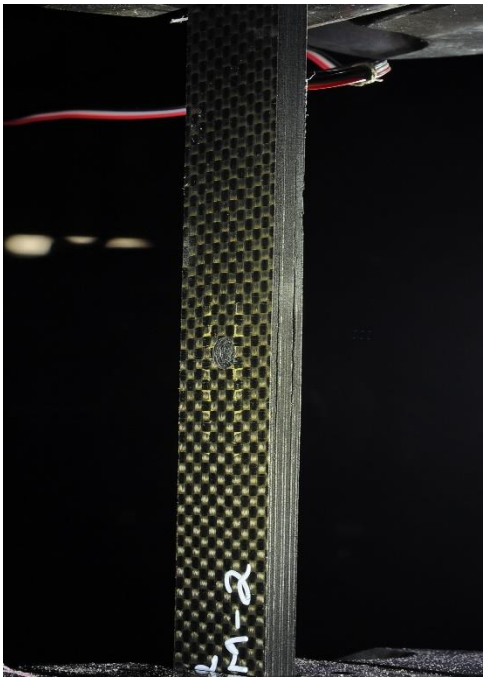

(A2-M-2) at 175k Cycles

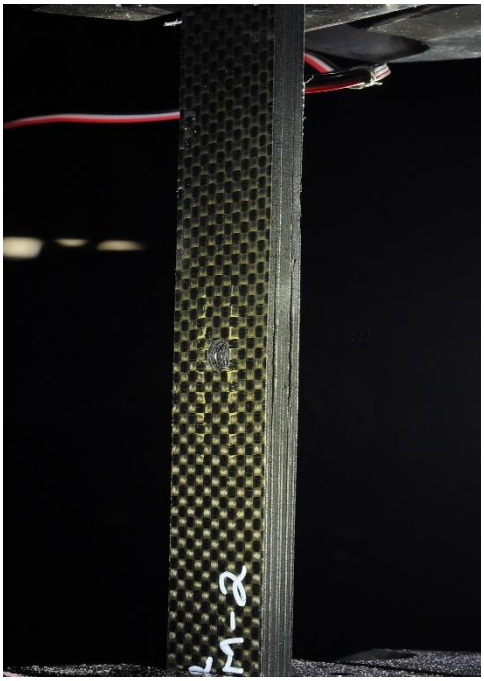

(A2-M-2) at 200k Cycles

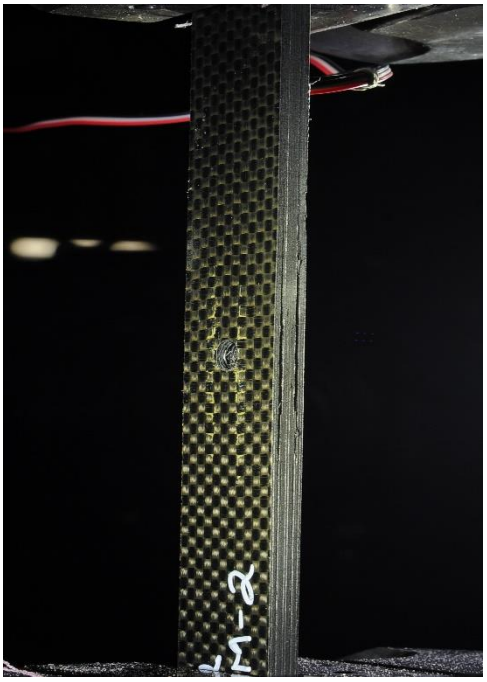

(A2-M-2) at 225k Cycles

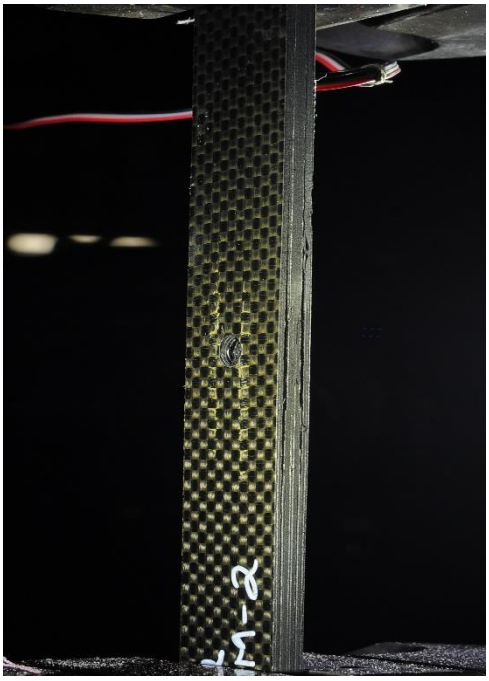

(A2-M-2) at 250k Cycles

Figure C 2-64 Damage Progression in (A2-M-2) Test specimen to 250k cycles

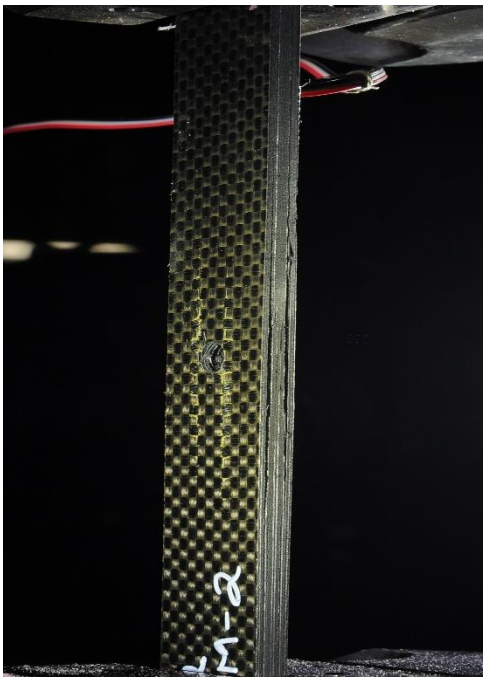

(A2-M-2) at 275k Cycles

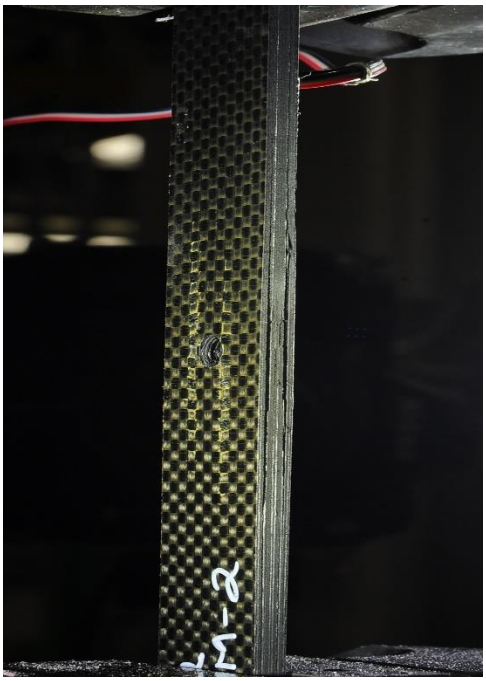

(A2-M-2) at 300k Cycles

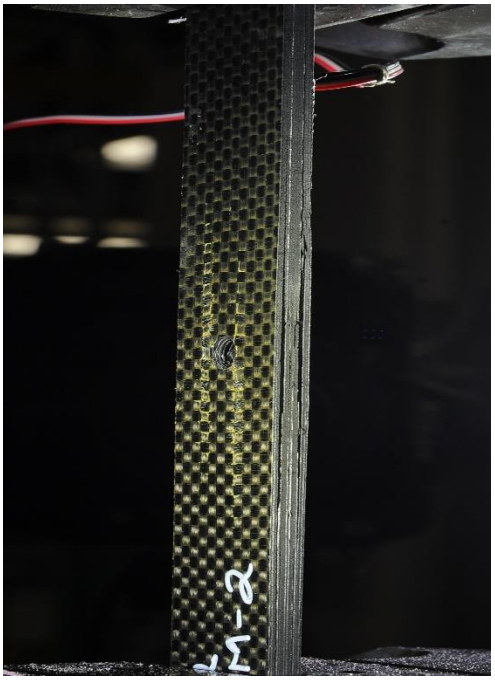

(A2-M-2) at 325k Cycles

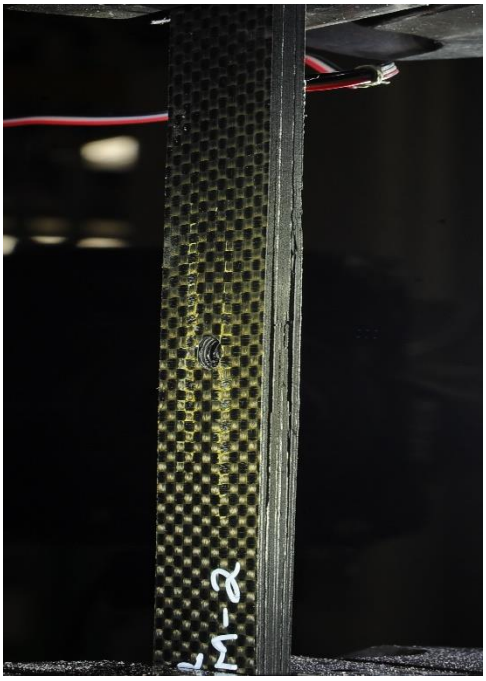

(A2-M-2) at 350k Cycles

Figure C 2-65 Damage Progression in (A2-M-2) Test specimen to 350k cycles

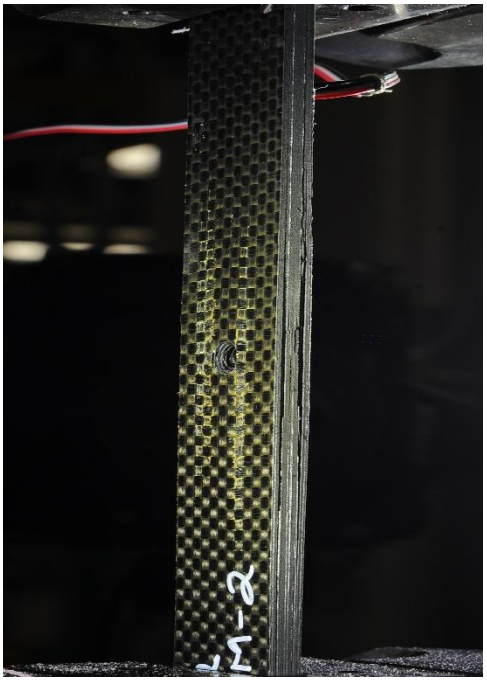

(A2-M-2) at 375k Cycles

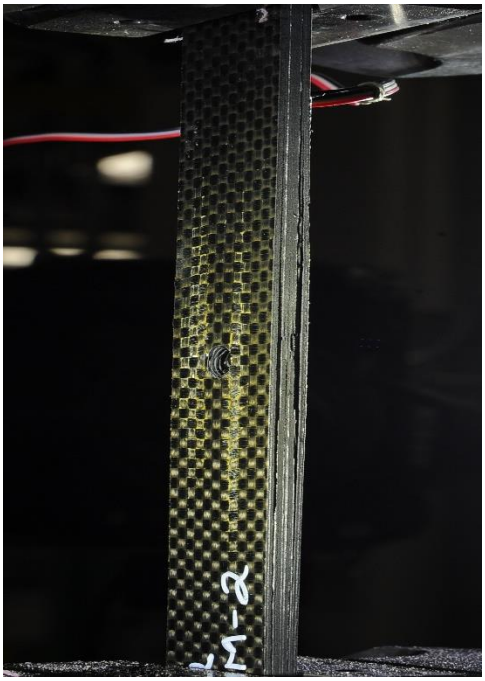

(A2-M-2) at 400k Cycles

(A2-M-2) at Failure

Figure C 2-66 Damage Progression in (A2-M-2) Test specimen to Failure

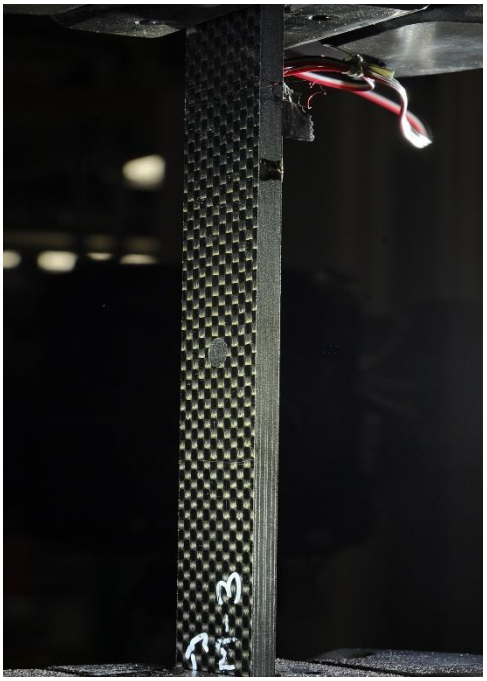

(A2-M-3) at 1 Cycle

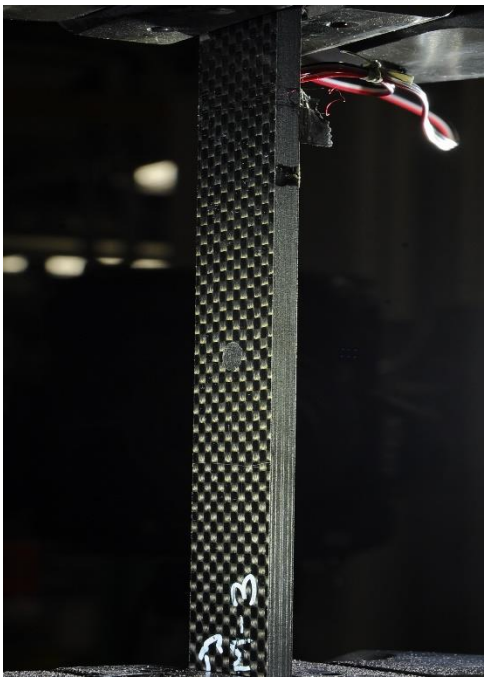

(A2-M-3) at 100 Cycles

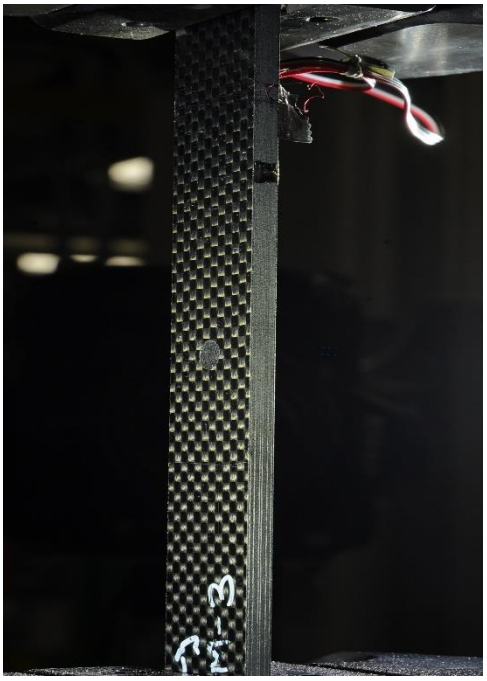

(A2-M-3) at 1k Cycles

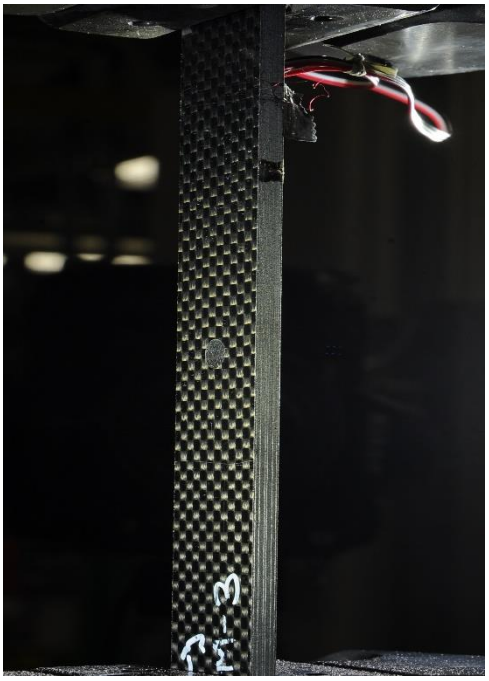

(A2-M-3) at 5k Cycles

Figure C 2-67 Damage Progression in (A2-M-3) Test specimen to 5k cycles

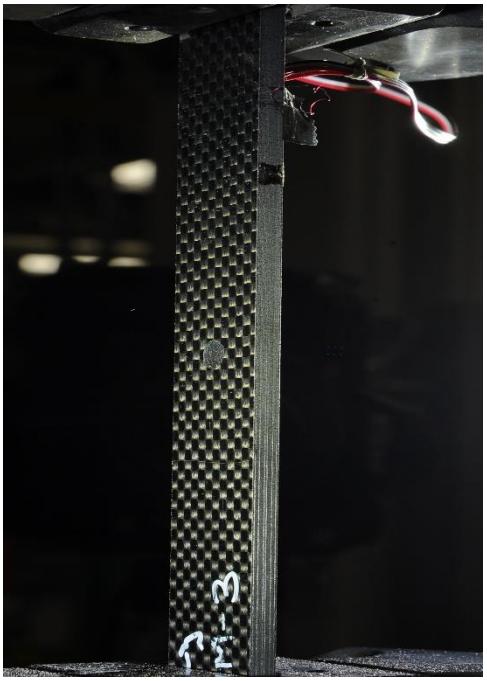

(A2-M-3) at 10k Cycles

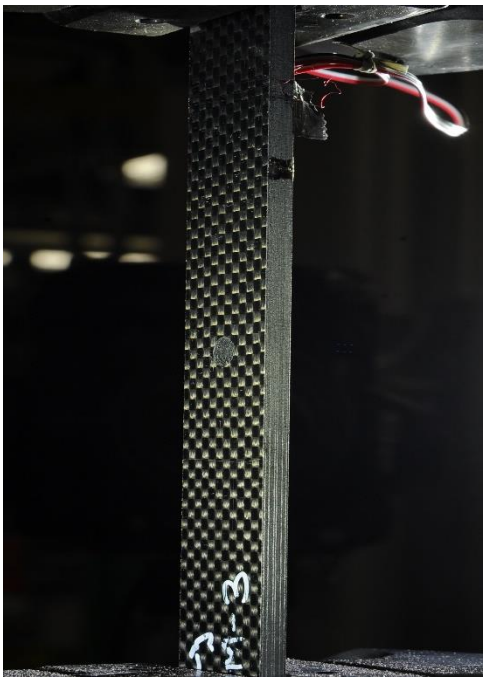

(A2-M-3) at 20k Cycles

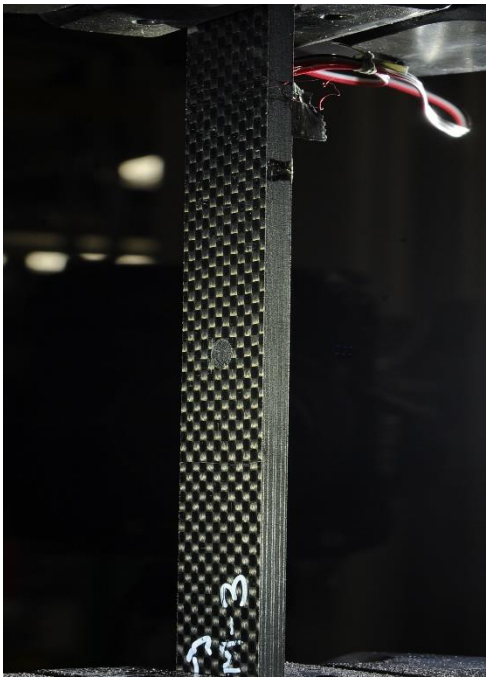

(A2-M-3) at 30k Cycles

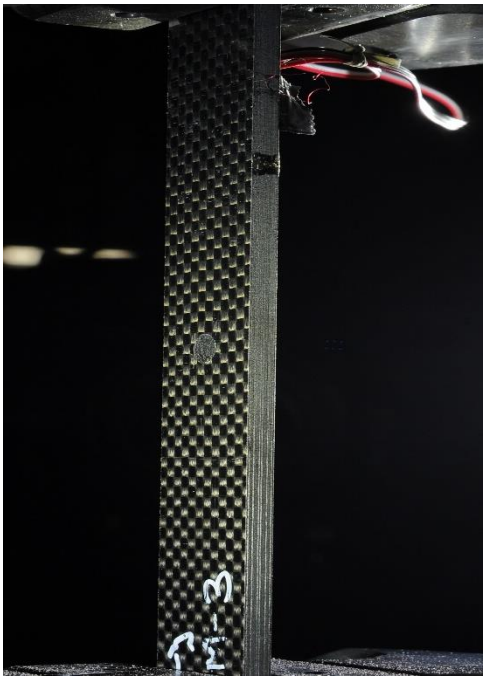

(A2-M-3) at 40k Cycles

Figure C 2-68 Damage Progression in (A2-M-3) Test specimen to 40k cycles

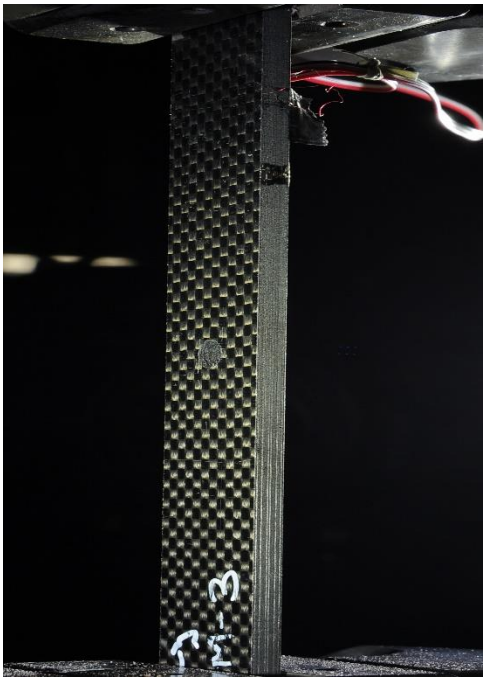

(A2-M-3) at 50k Cycles

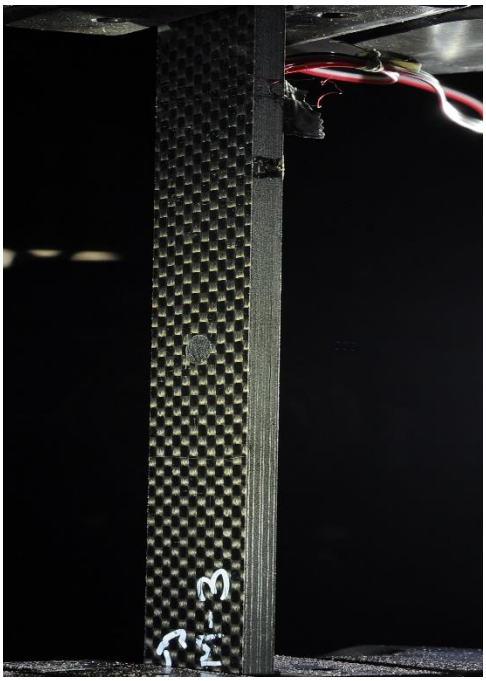

(A2-M-3) at 60k Cycles

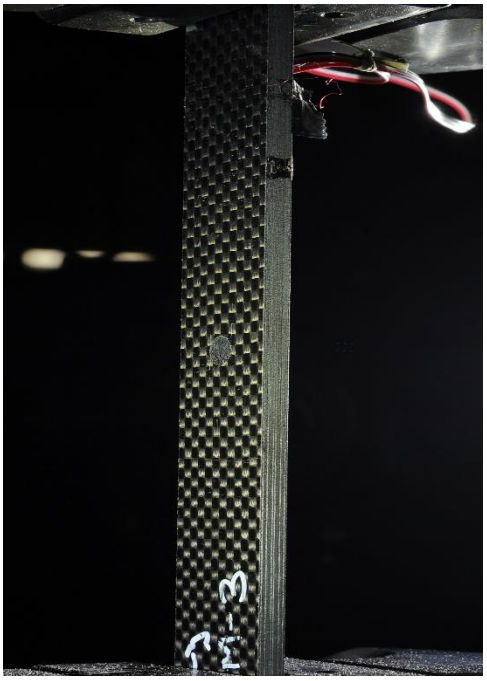

(A2-M-3) at 70k Cycles

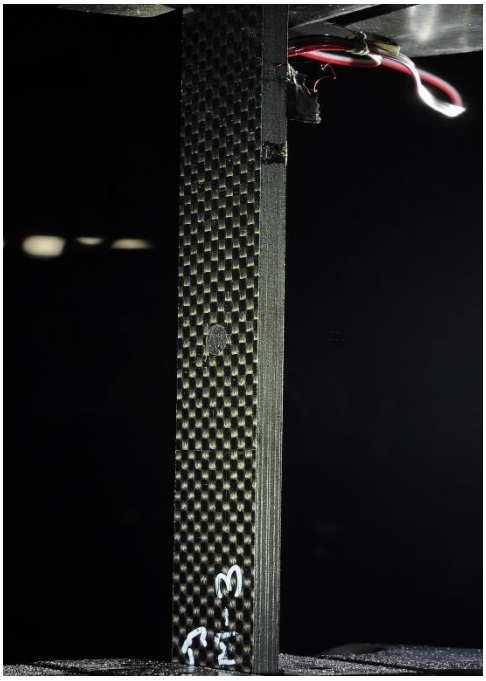

(A2-M-3) at 80k Cycles

Figure C 2-69 Damage Progression in (A2-M-3) Test specimen to 80k cycles

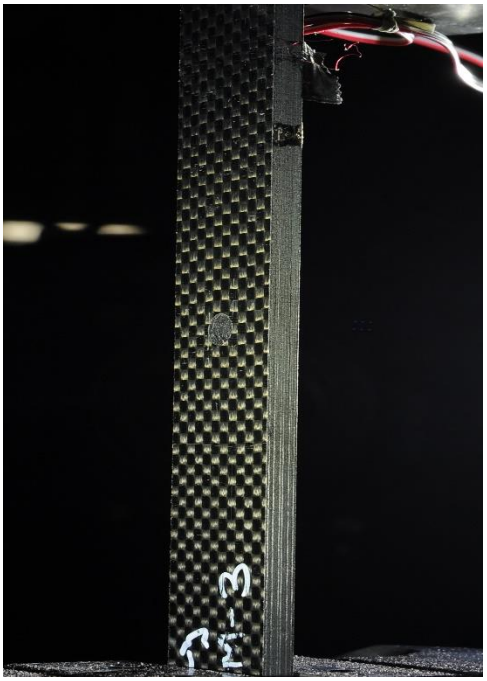

(A2-M-3) at 90k Cycles

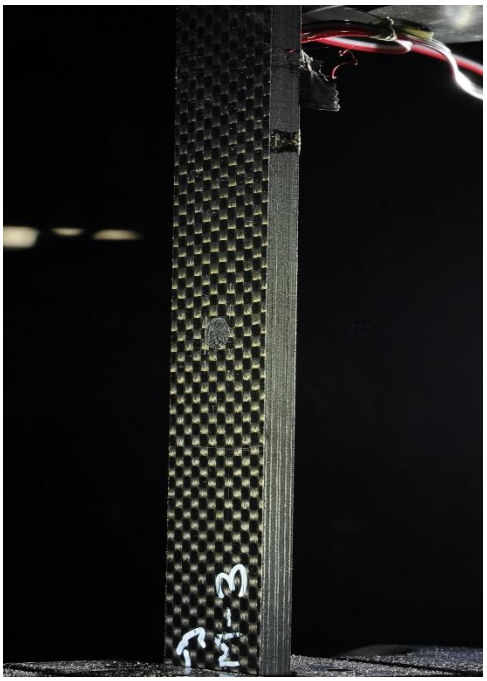

(A2-M-3) at 100k Cycles

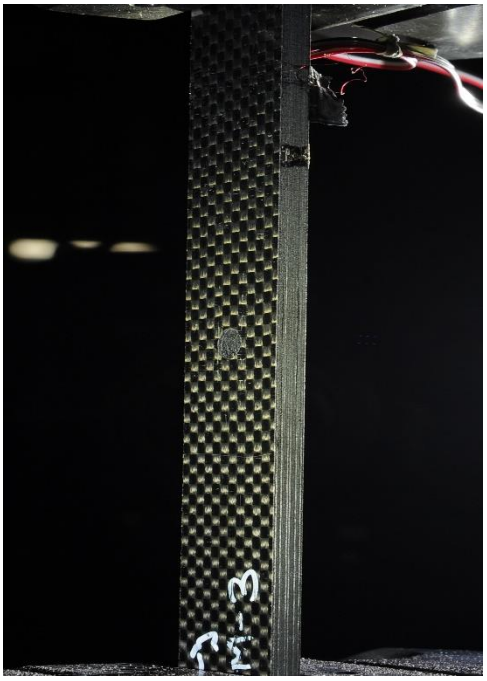

(A2-M-3) at 125k Cycles

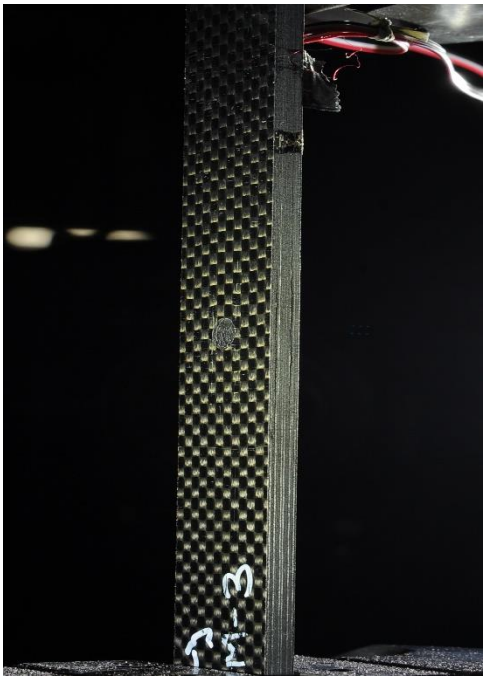

(A2-M-3) at 150k Cycles

Figure C 2-70 Damage Progression in (A2-M-3) Test specimen to 150k cycles

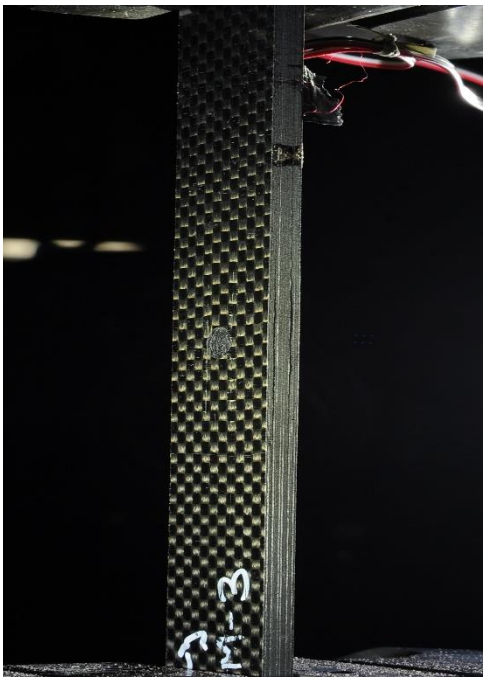

(A2-M-3) at 175k Cycles

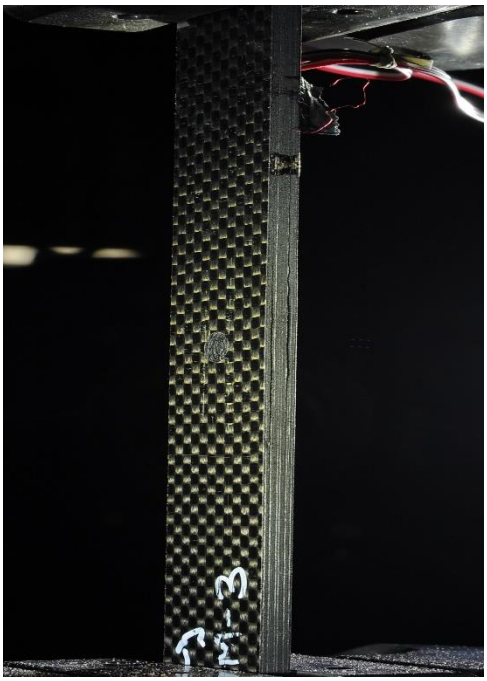

(A2-M-3) at 200k Cycles

(A2-M-3) at 225k Cycles

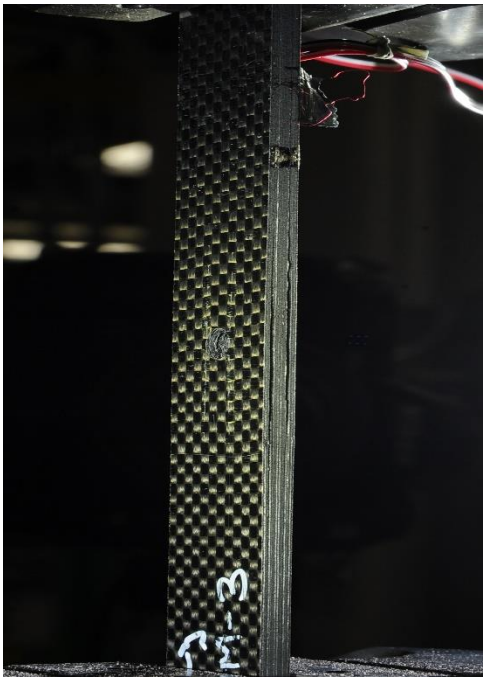

(A2-M-3) at 250k Cycles

Figure C 2-71 Damage Progression in (A2-M-3) Test specimen to 250k cycles

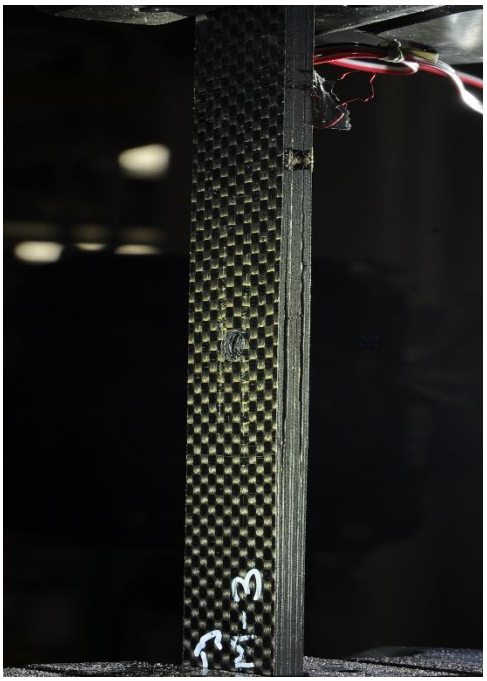

(A2-M-3) at 275k Cycles

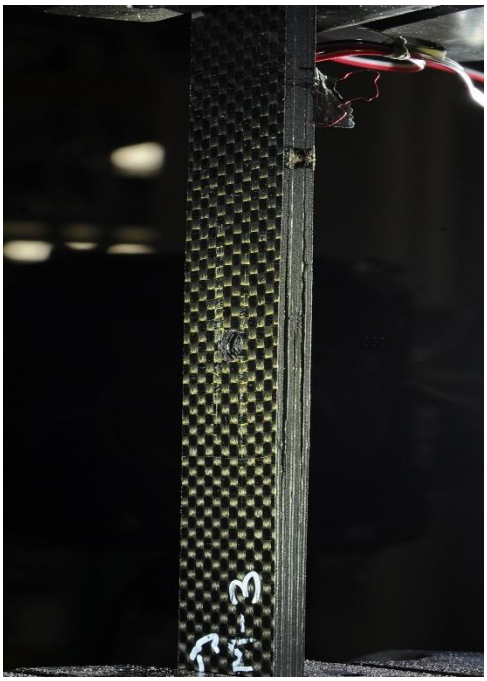

(A2-M-3) at 300k Cycles

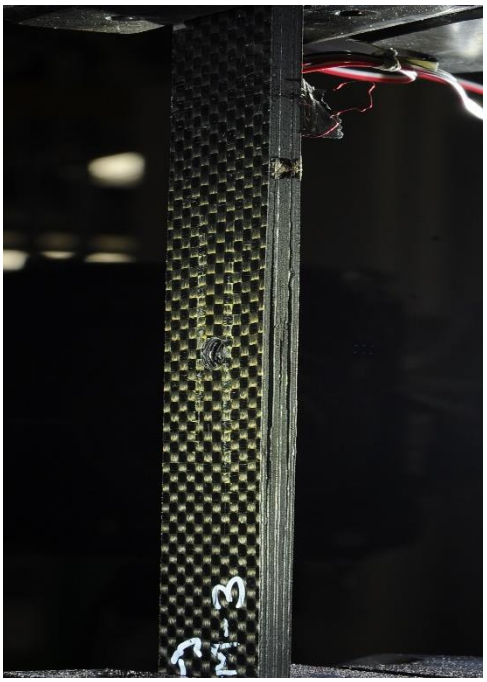

(A2-M-3) at 325k Cycles

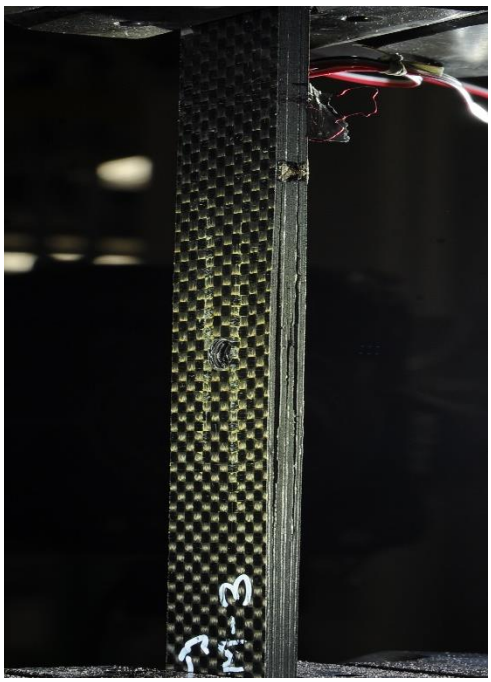

(A2-M-3) at 350k Cycles

Figure C 2-72 Damage Progression in (A2-M-3) Test specimen to 350k cycles

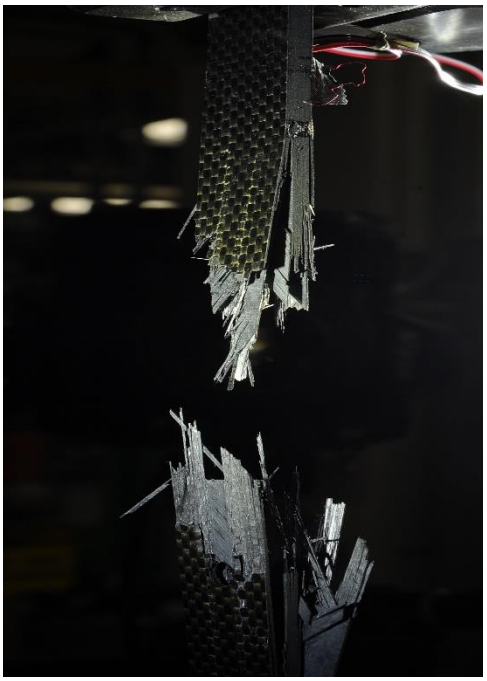

(A2-M-3) at Failure

Figure C 2-73 Damage Progression in (A2-M-3) Test specimen to Failure

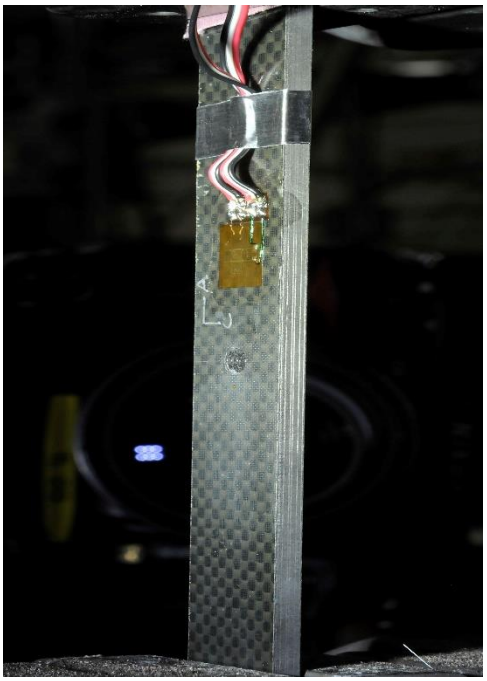

(A2-M-4) at 1 Cycle

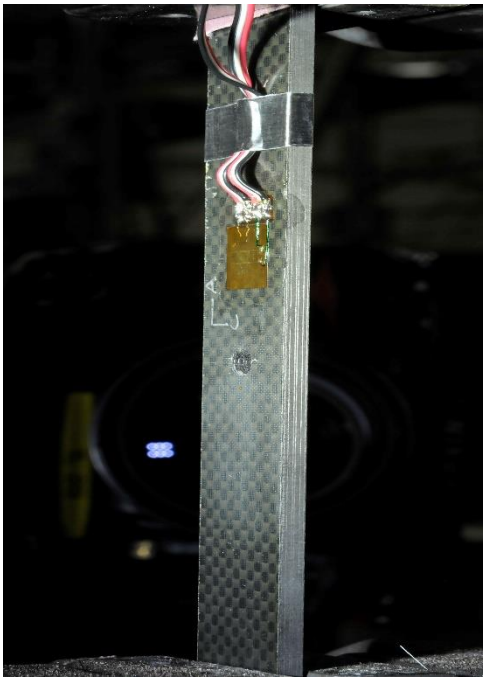

(A2-M-4) at 100 Cycles

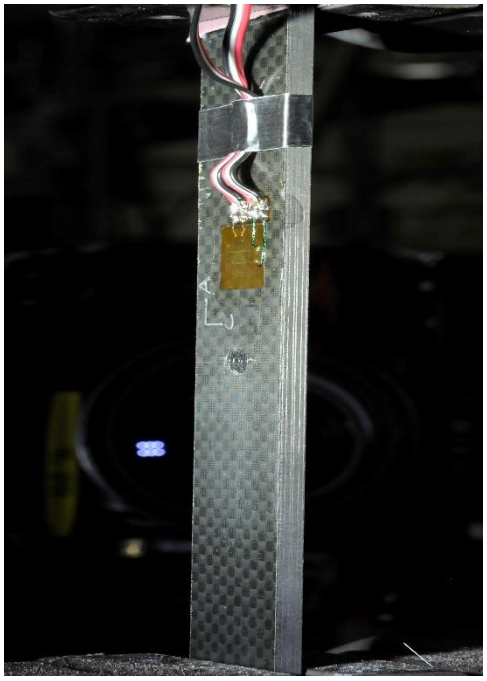

(A2-M-4) at 1k Cycles

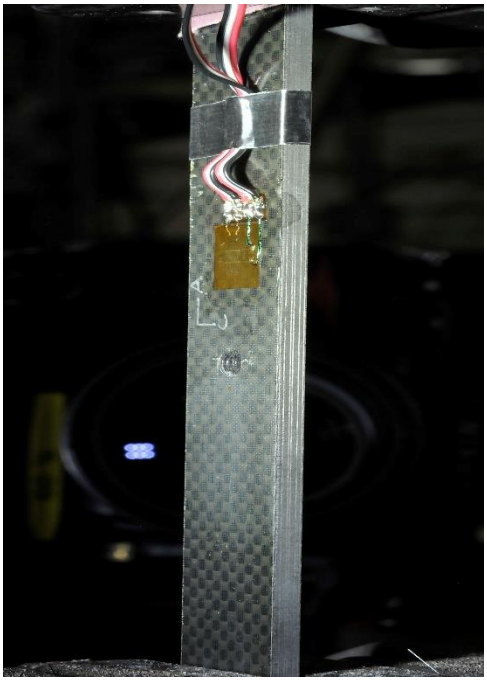

(A2-M-4) at 5k Cycles

Figure C 2-74 Damage Progression in (A2-M-4) Test specimen to 5k cycles

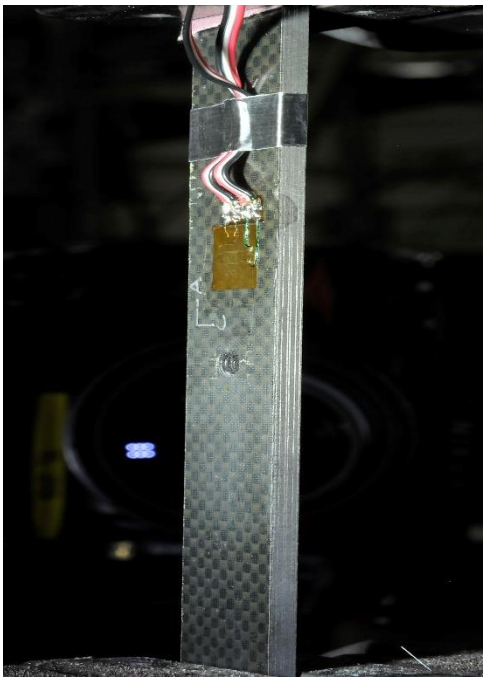

(A2-M-4) at 10k Cycles

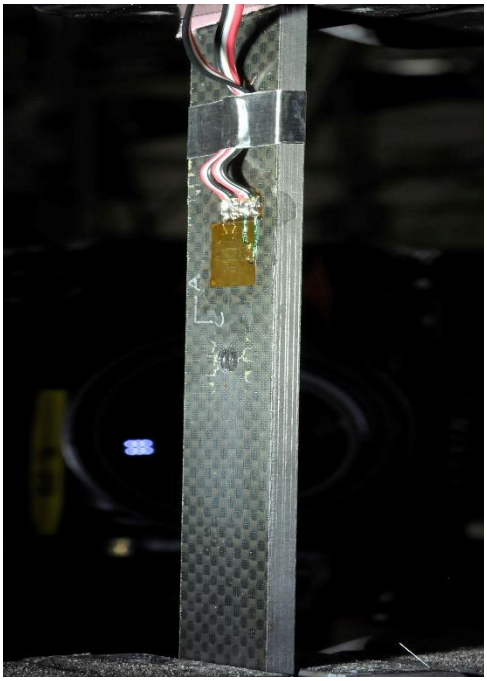

(A2-M-4) at 20k Cycles

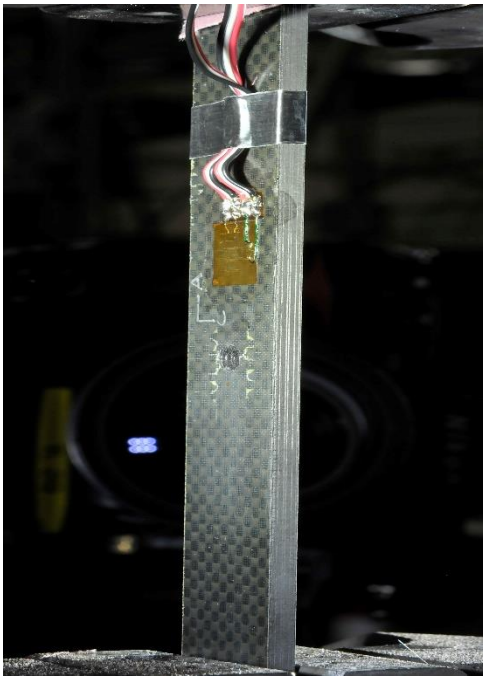

(A2-M-4) at 30k Cycles

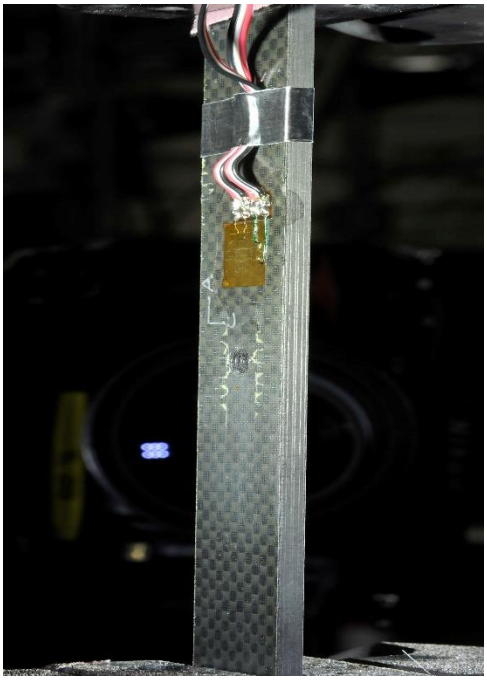

(A2-M-4) at 40k Cycles

Figure C 2-75 Damage Progression in (A2-M-4) Test specimen to 40k cycles

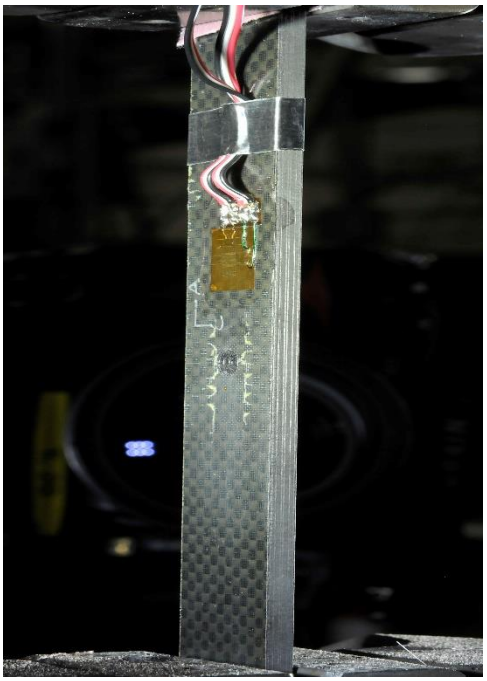

(A2-M-4) at 50k Cycles

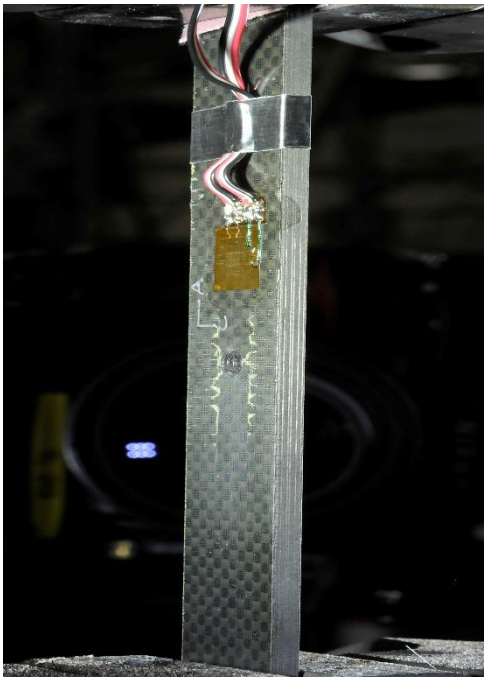

(A2-M-4) at 60k Cycles

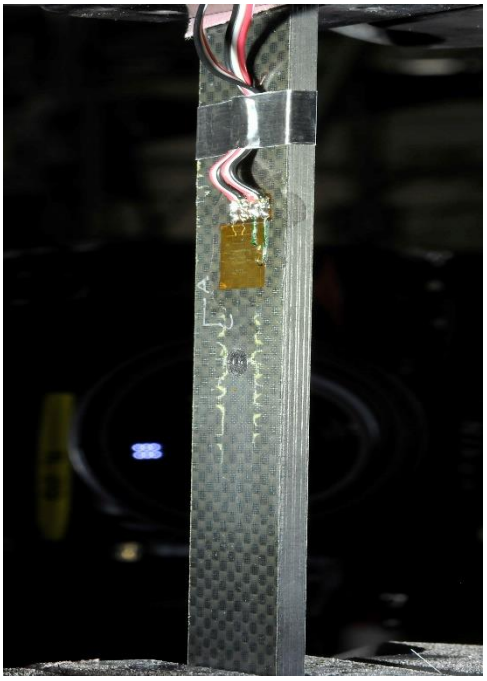

(A2-M-4) at 70k Cycles

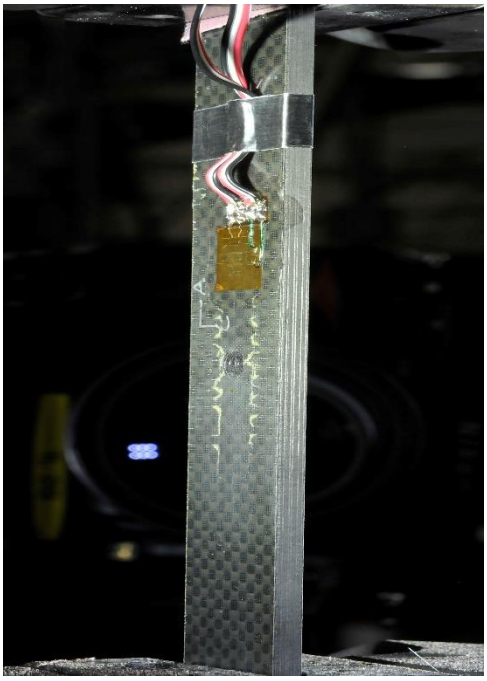

(A2-M-4) at 80k Cycles

Figure C 2-76 Damage Progression in (A2-M-4) Test specimen to 80k cycles

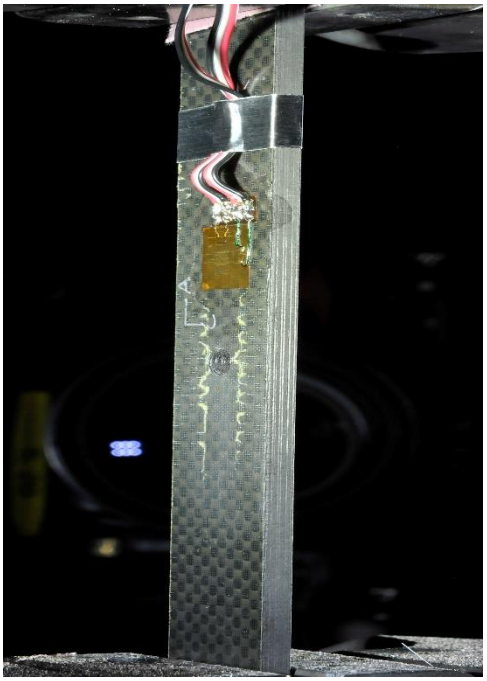

(A2-M-4) at 90k Cycles

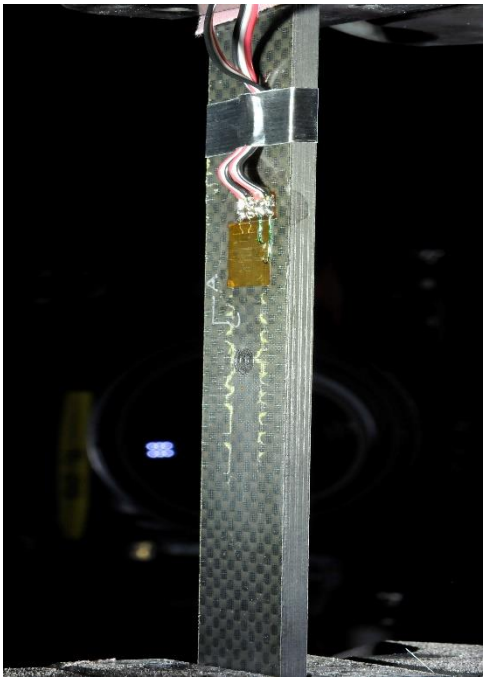

(A2-M-4) at 100k Cycles

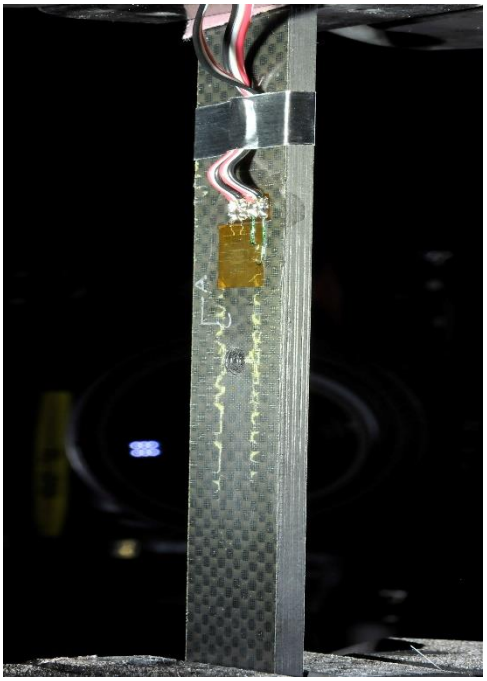

(A2-M-4) at 125k Cycles

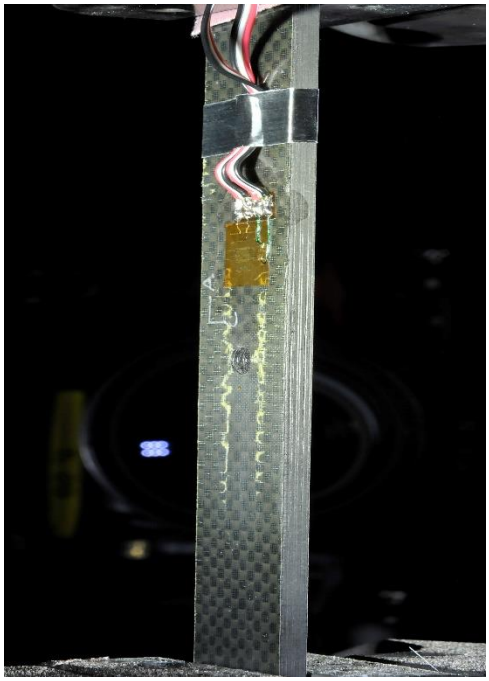

(A2-M-4) at 150k Cycles

Figure C 2-77 Damage Progression in (A2-M-4) Test specimen to 150k cycles

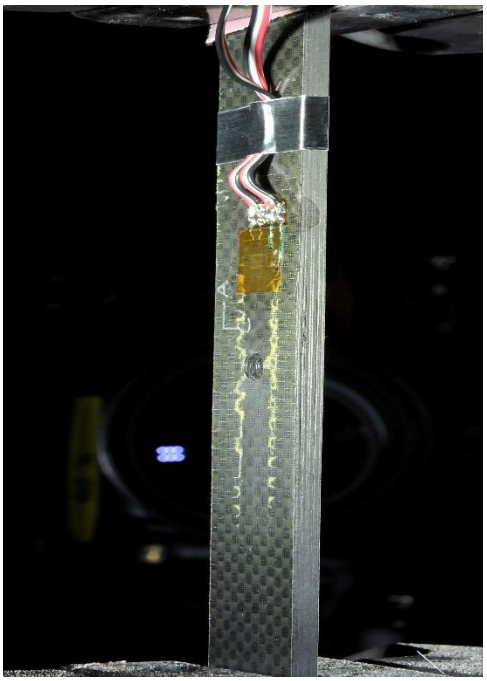

(A2-M-4) at 175k Cycles

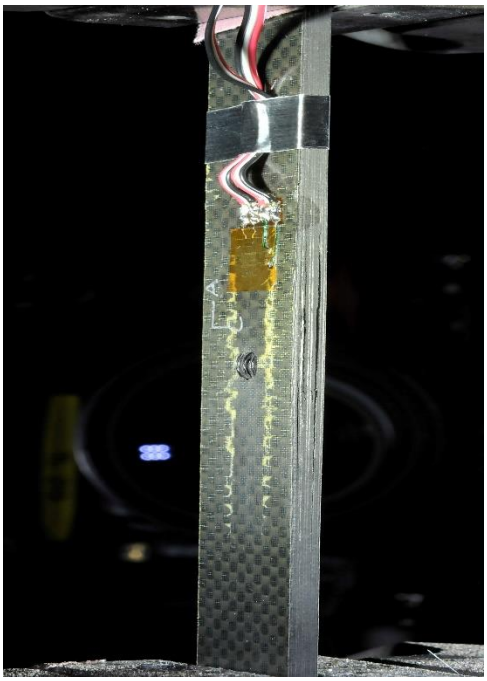

(A2-M-4) at 200k Cycles

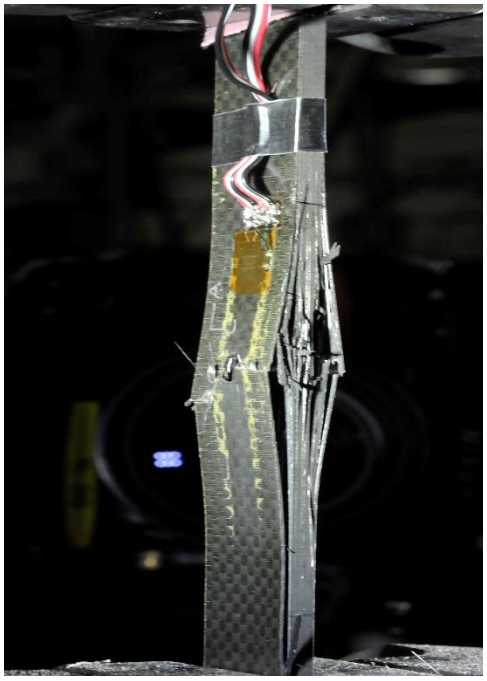

(A2-M-4) at Failure

Figure C 2-78 Damage Progression in (A2-M-4) Test specimen to Failure

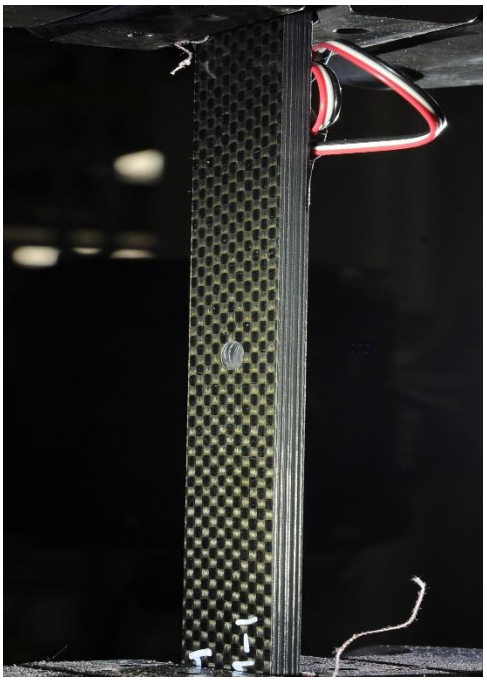

(B2-M-1) at 1 Cycle

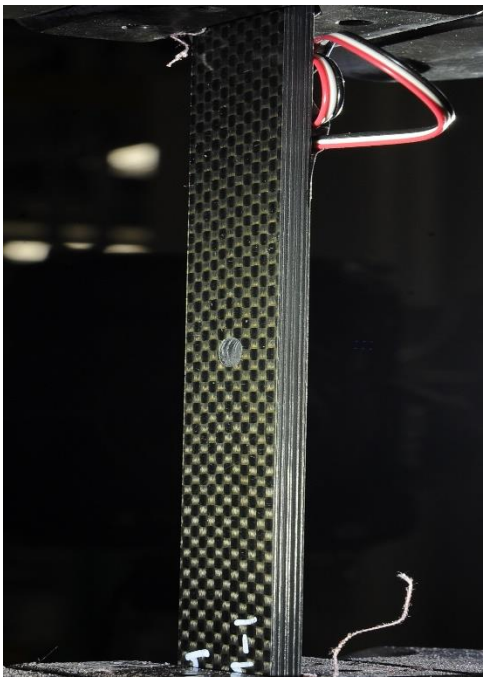

(B2-M-1) at 100 Cycles

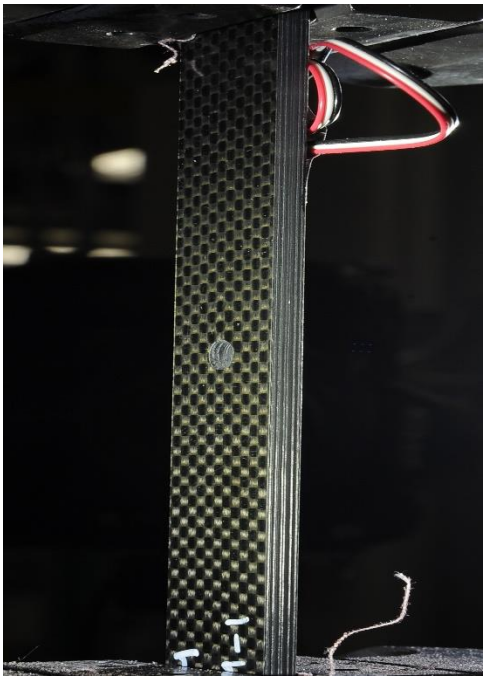

(B2-M-1) at 1k Cycles

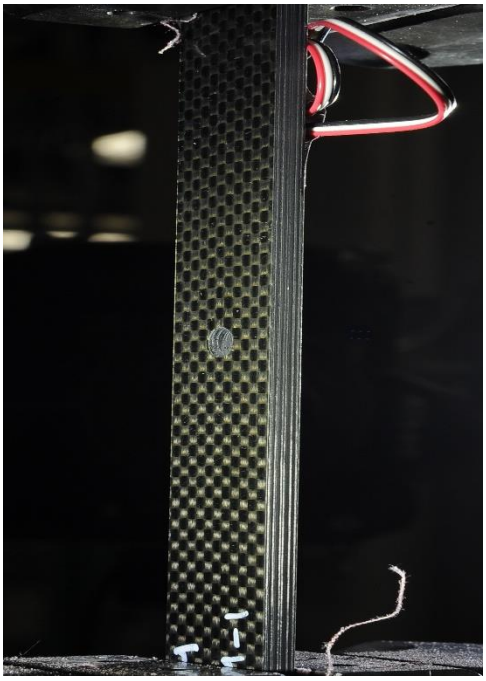

(B2-M-1) at 5k Cycles

Figure C 2-79 Damage Progression in (B2-M-1) Test specimen to 5k Cycles

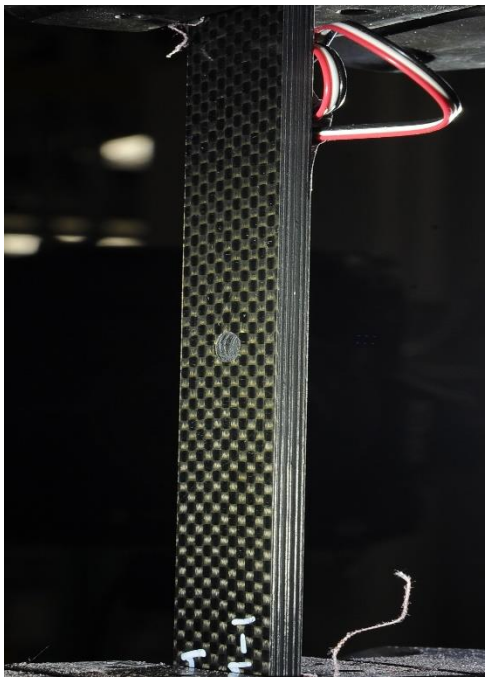

(B2-M-1) at 10k Cycles

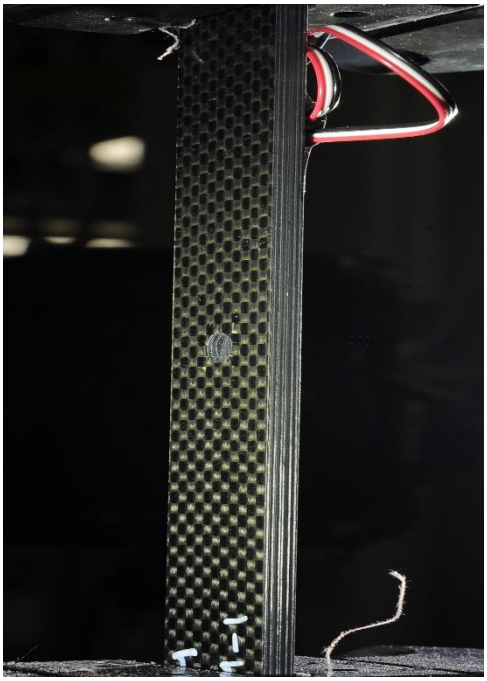

(B2-M-1) at 20k Cycles

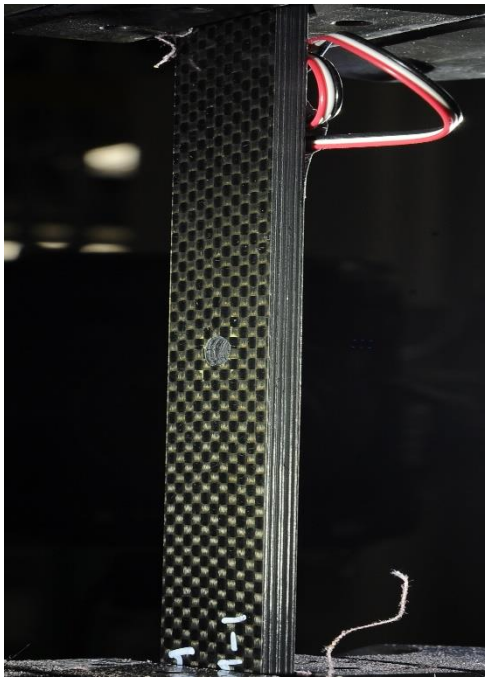

(B2-M-1) at 30k Cycles

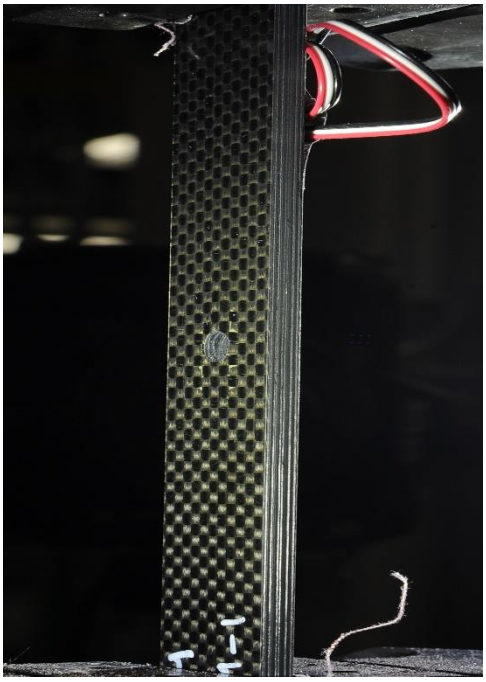

(B2-M-1) at 40k Cycles

Figure C 2-80 Damage Progression in (B2-M-1) Test specimen to 40k Cycles

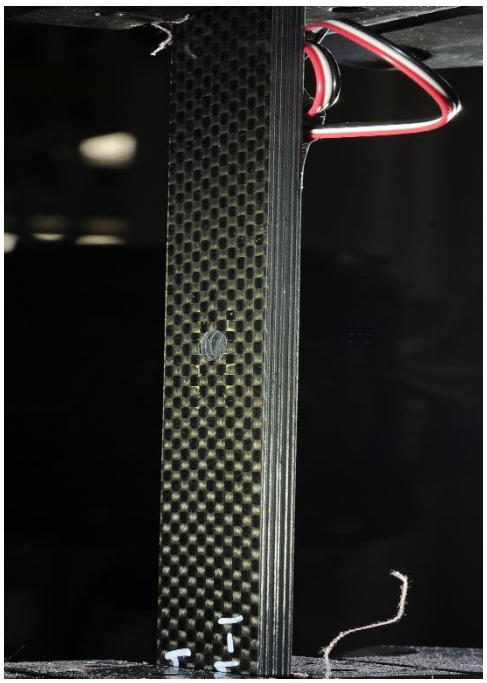

(B2-M-1) at 50k Cycles

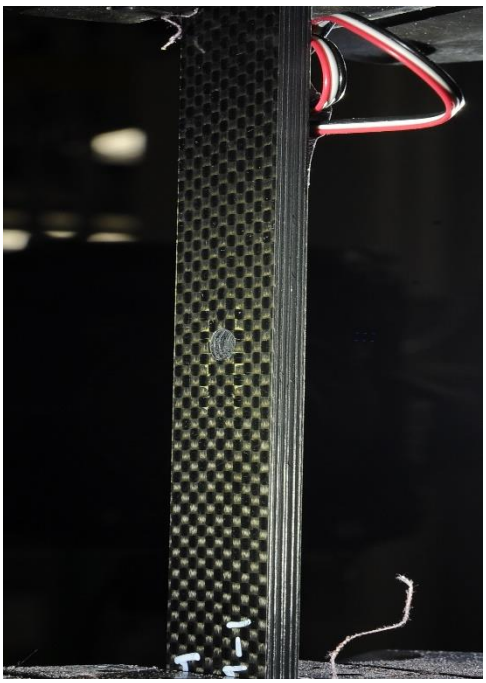

(B2-M-1) at 60k Cycles

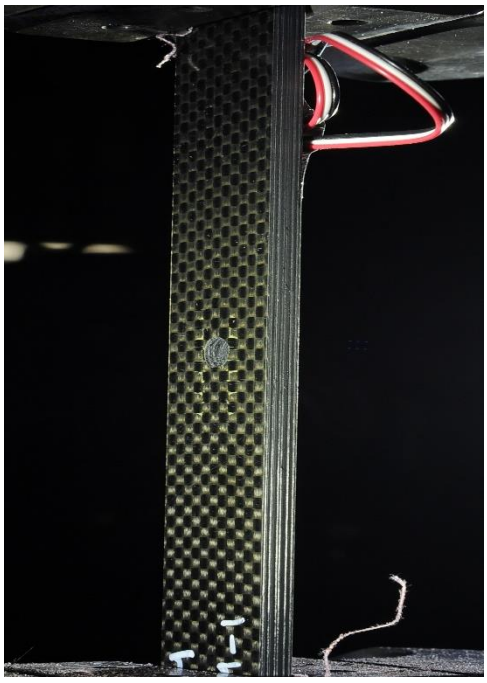

(B2-M-1) at 70k Cycles

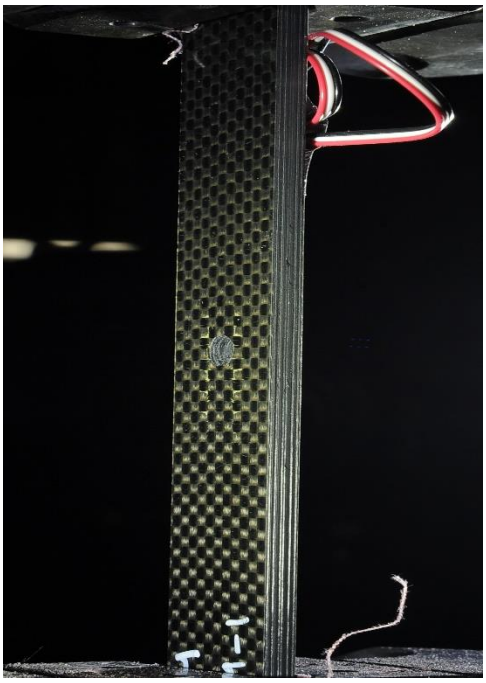

(B2-M-1) at 80k Cycles

Figure C 2-81 Damage Progression in (B2-M-1) Test specimen to 80k Cycles

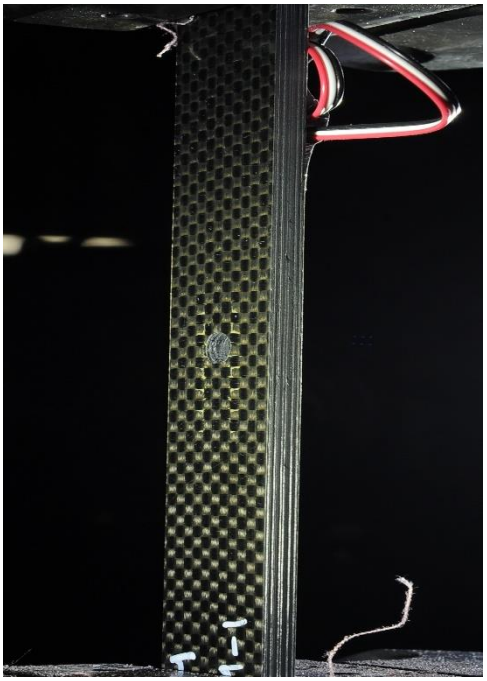

(B2-M-1) at 90k Cycles

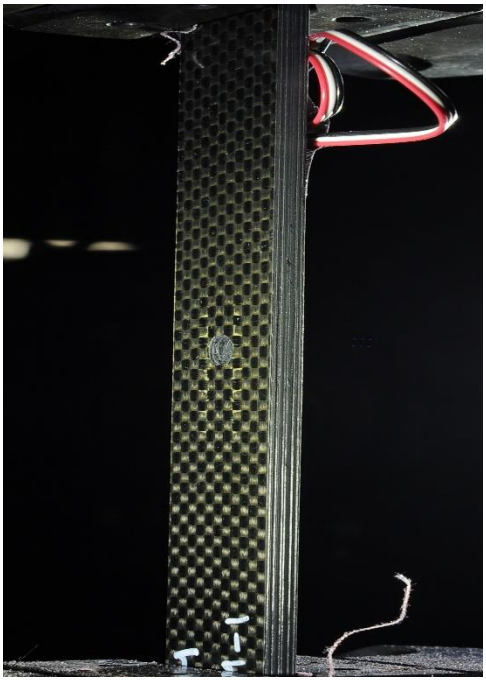

(B2-M-1) at 100k Cycles

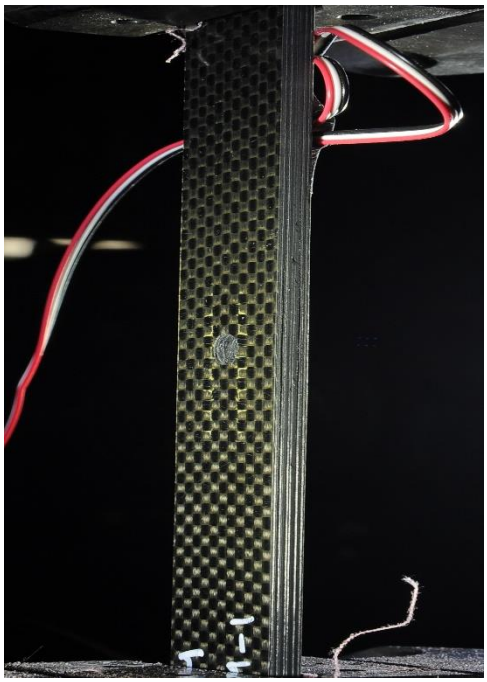

(B2-M-1) at 125k Cycles

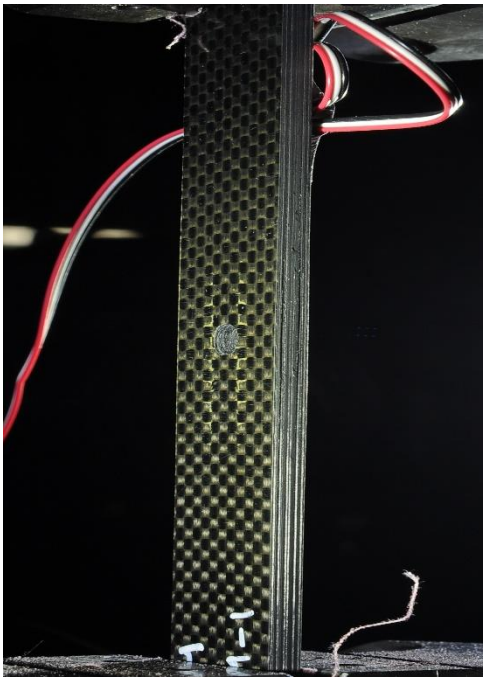

(B2-M-1) at 150k Cycles

Figure C 2-82 Damage Progression in (B2-M-1) Test specimen to 150k Cycles

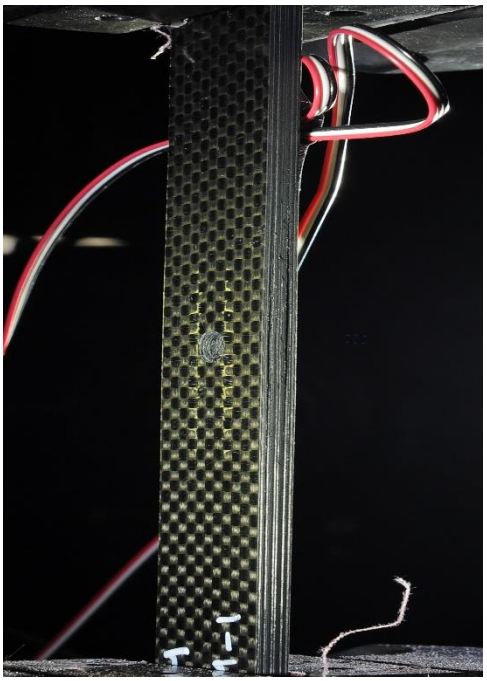

(B2-M-1) at 175k Cycles

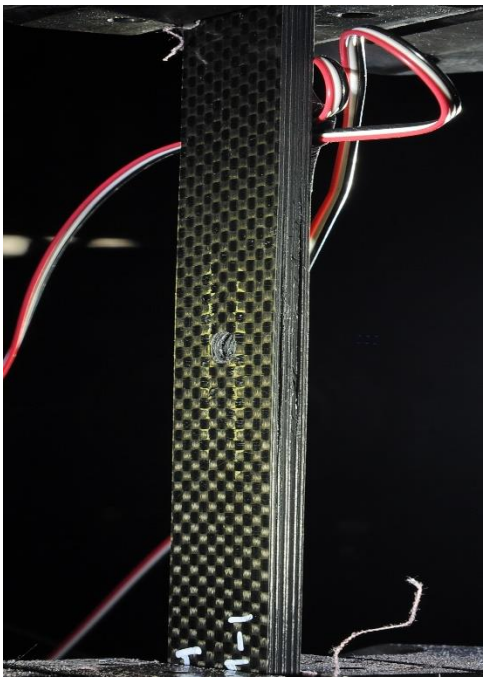

(B2-M-1) at 200k Cycles

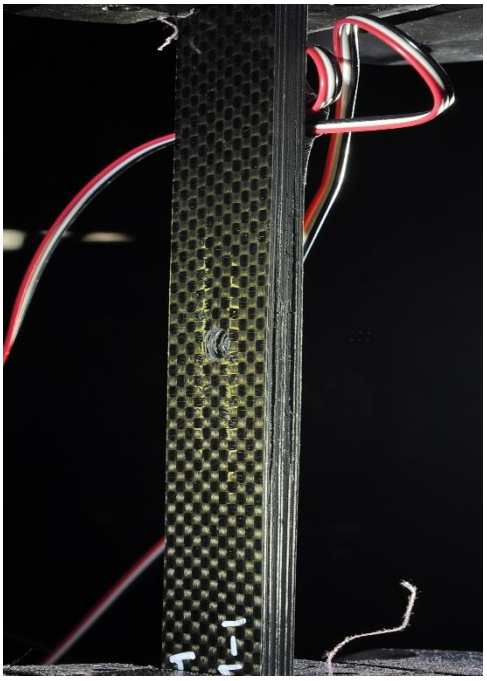

(B2-M-1) at 225k Cycles

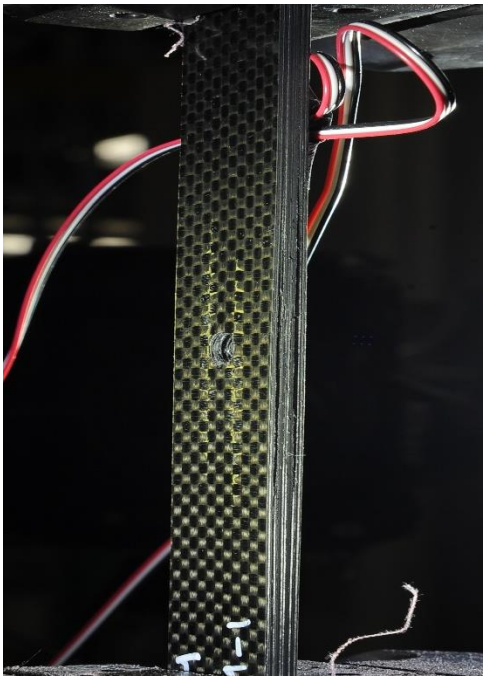

(B2-M-1) at 250k Cycles

Figure C 2-83 Damage Progression in (B2-M-1) Test specimen to 250k Cycles

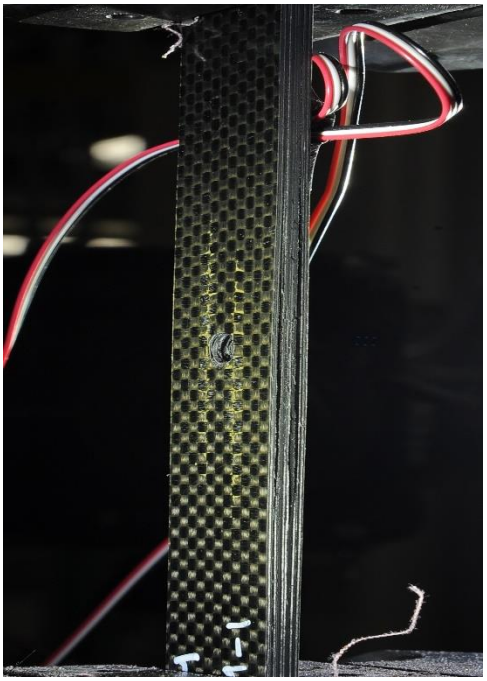

(B2-M-1) at 275k Cycles

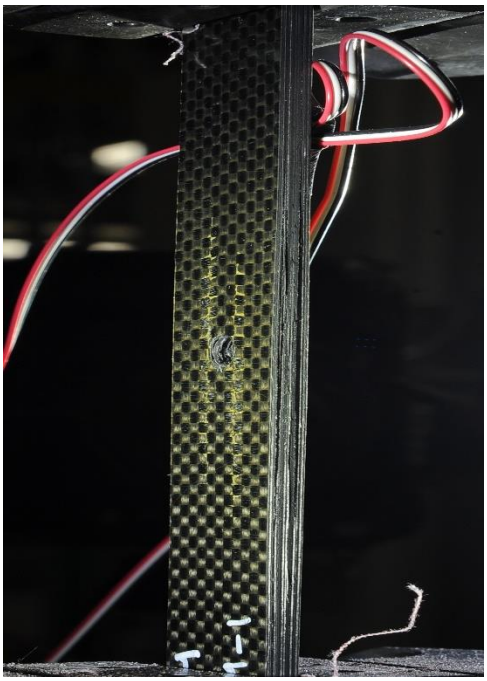

(B2-M-1) at 300k Cycles

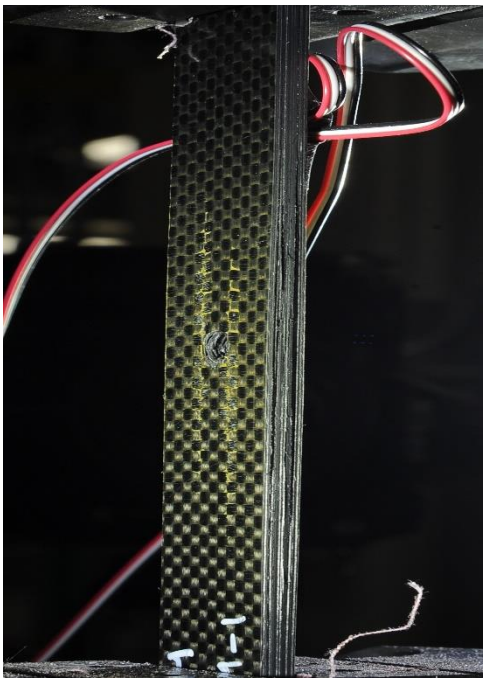

(B2-M-1) at 325k Cycles

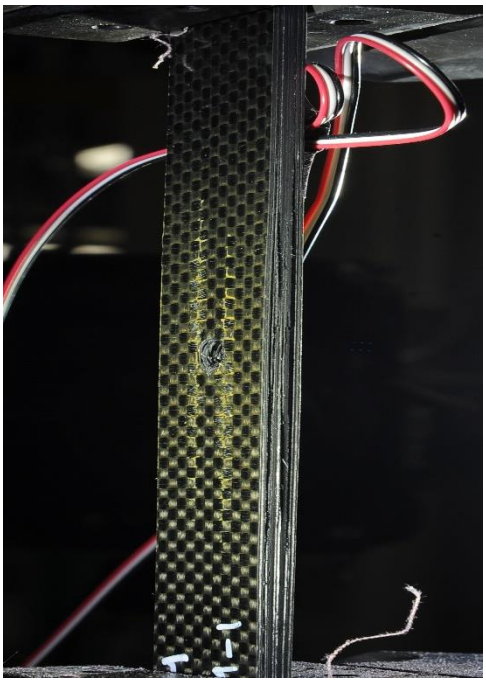

(B2-M-1) at 350k Cycles

Figure C 2-84 Damage Progression in (B2-M-1) Test specimen to 350k Cycles

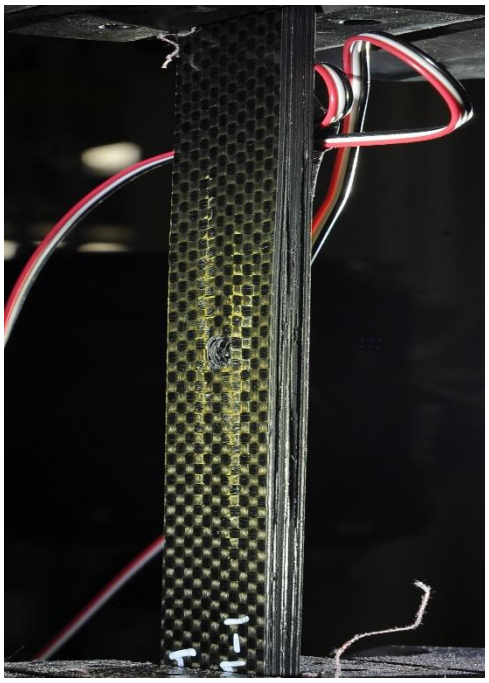

(B2-M-1) at 375k Cycles

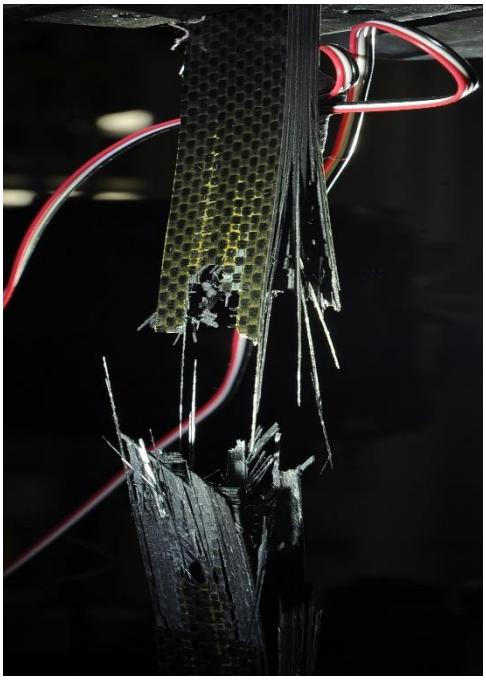

(B2-M-1) at Failure

Figure C 2-85 Damage Progression in (B2-M-1) Test specimen to Failure

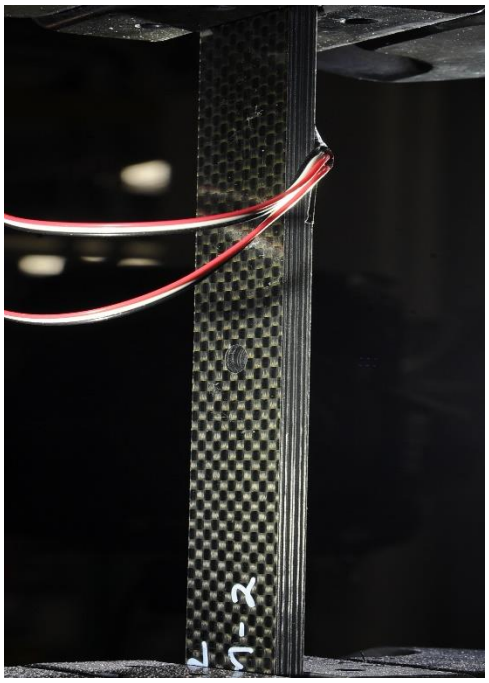

(B2-M-2) at 1 Cycle

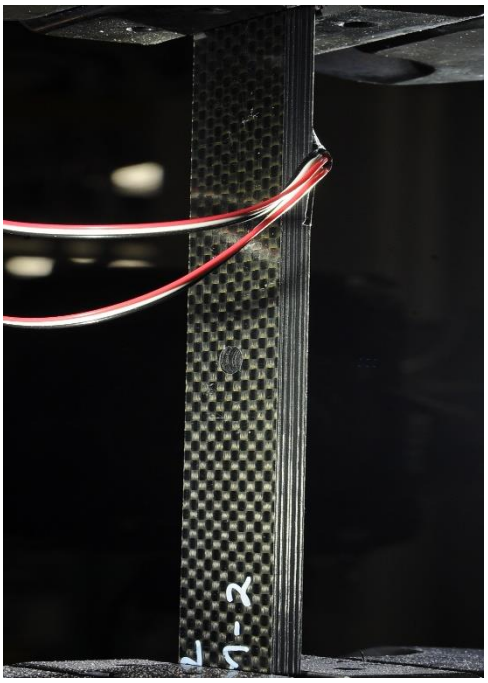

(B2-M-2) at 100 Cycles

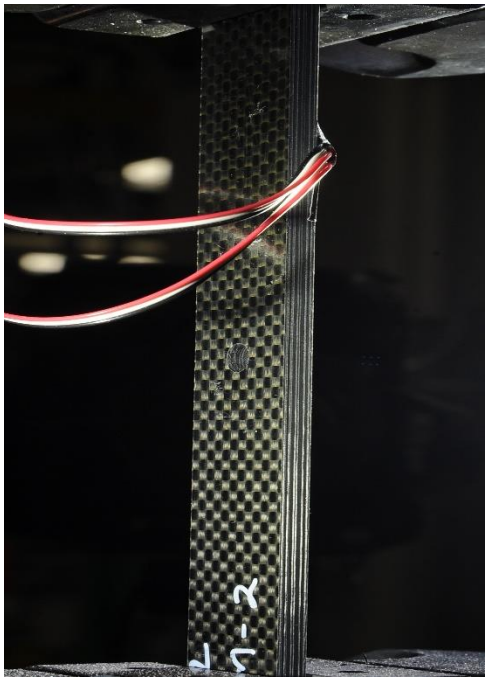

(B2-M-2) at 1k Cycles

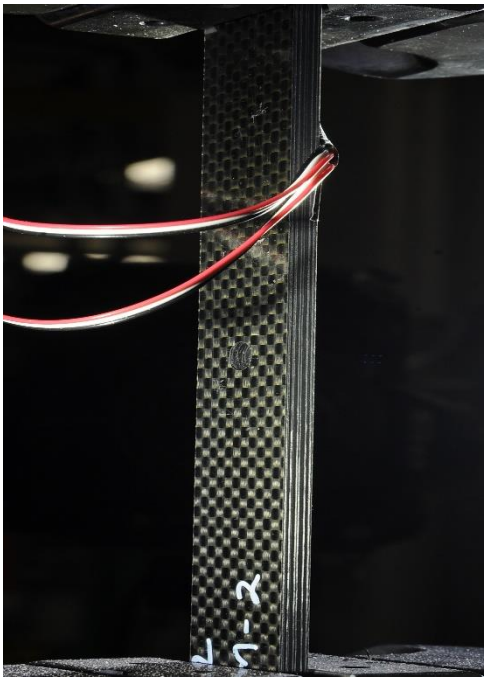

(B2-M-2) at 10k Cycles

Figure C 2-86 Damage Progression in (B2-M-2) Test specimen to 10k Cycles

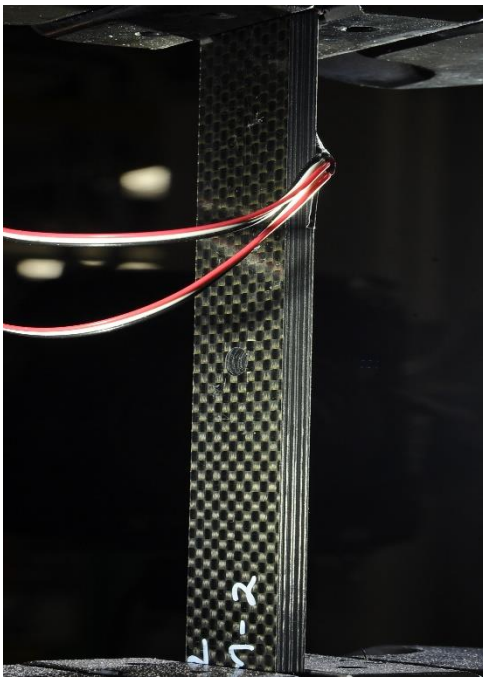

(B2-M-2) at 20k Cycles

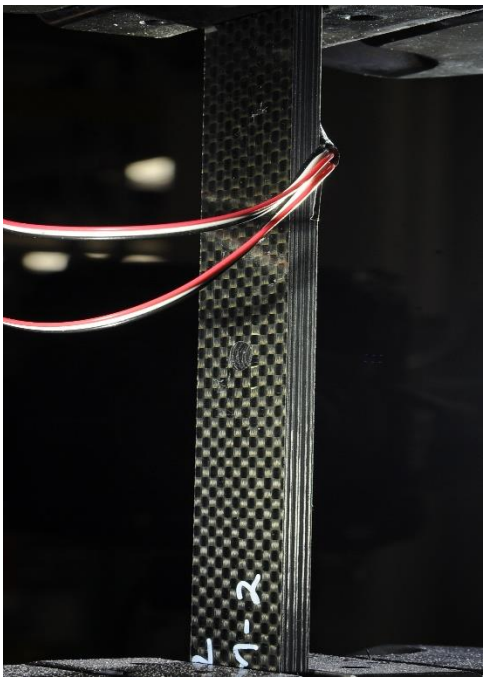

(B2-M-2) at 30k Cycles

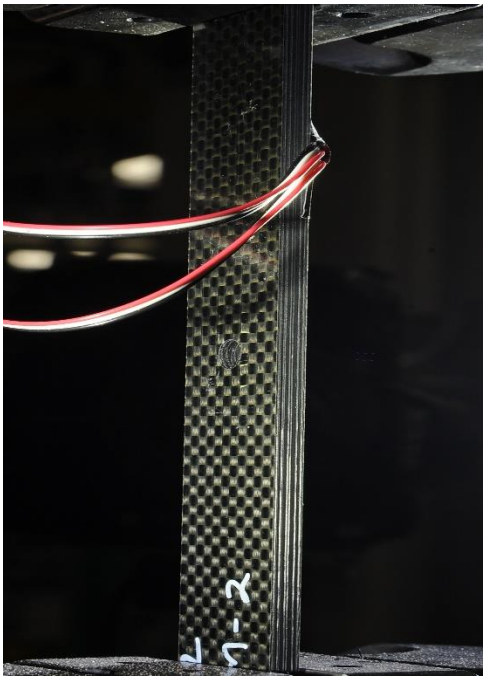

(B2-M-2) at 40k Cycles

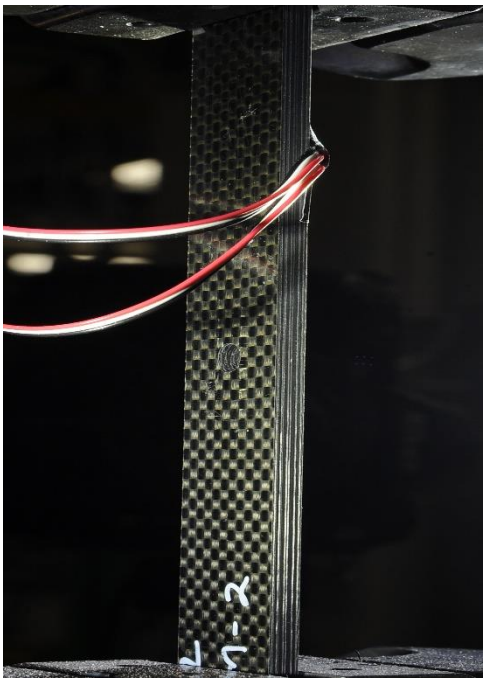

(B2-M-2) at 50k Cycles

Figure C 2-87 Damage Progression in (B2-M-2) Test specimen to 50k Cycles

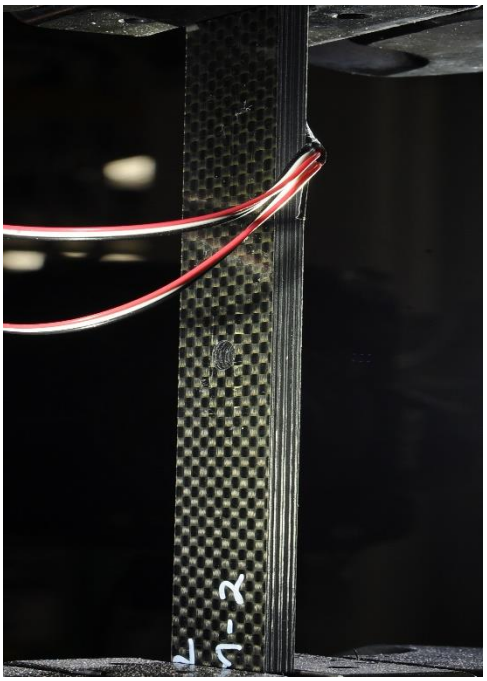

(B2-M-2) at 60k Cycles

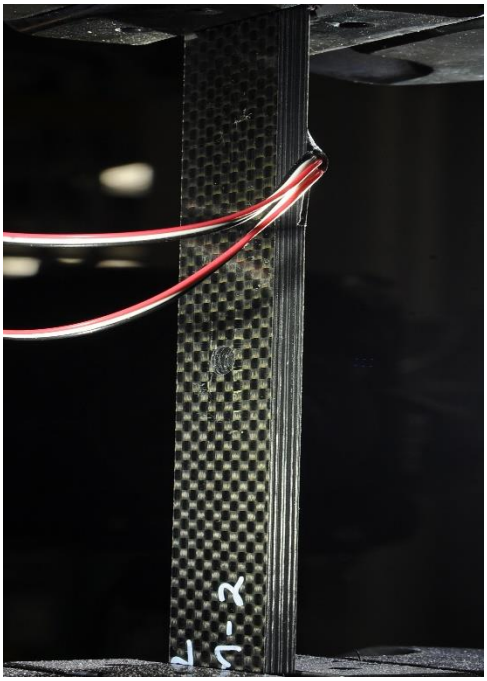

(B2-M-2) at 70k Cycles

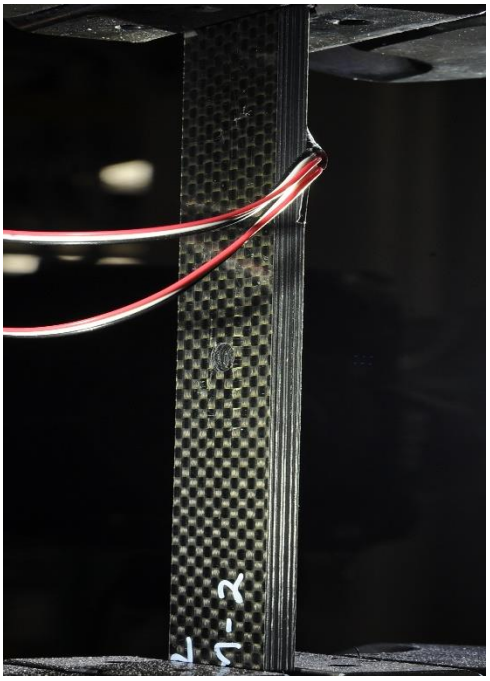

(B2-M-2) at 80k Cycles

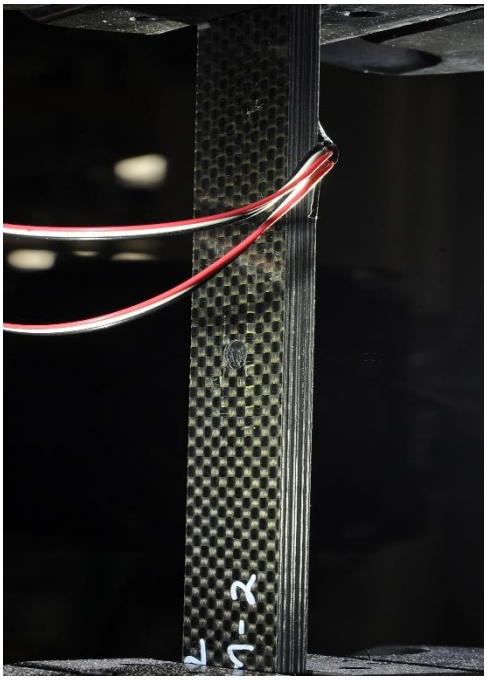

(B2-M-2) at 90k Cycles

Figure C 2-88 Damage Progression in (B2-M-2) Test specimen to 90k Cycles

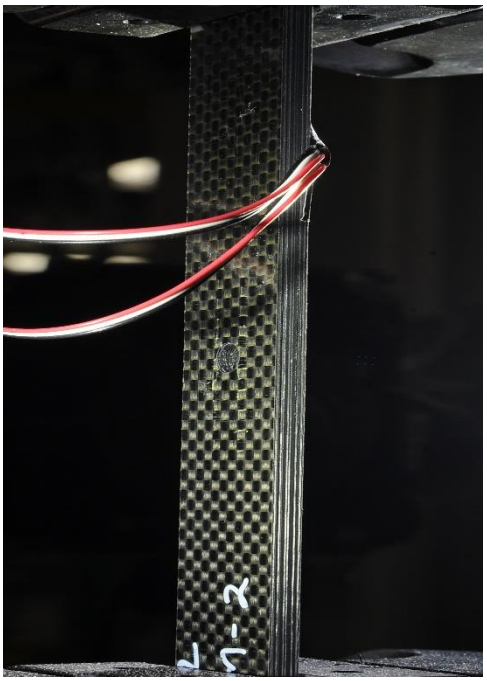

(B2-M-2) at 100k Cycles

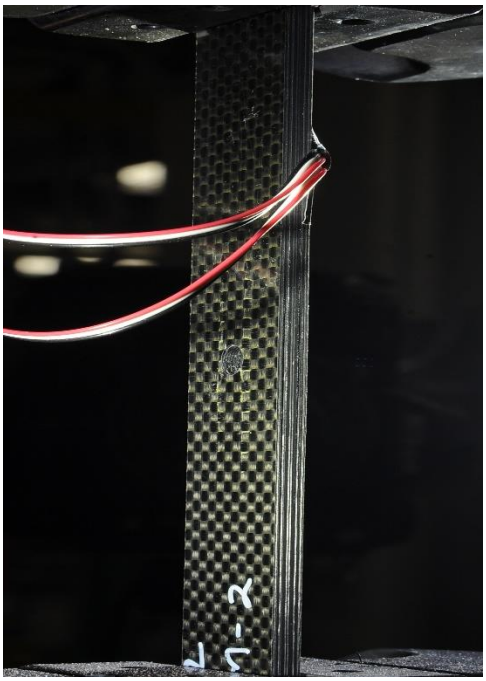

(B2-M-2) at 125k Cycles

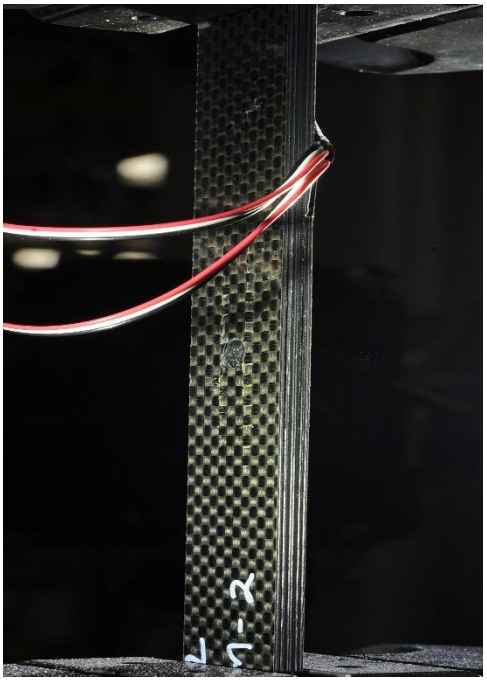

(B2-M-2) at 150k Cycles

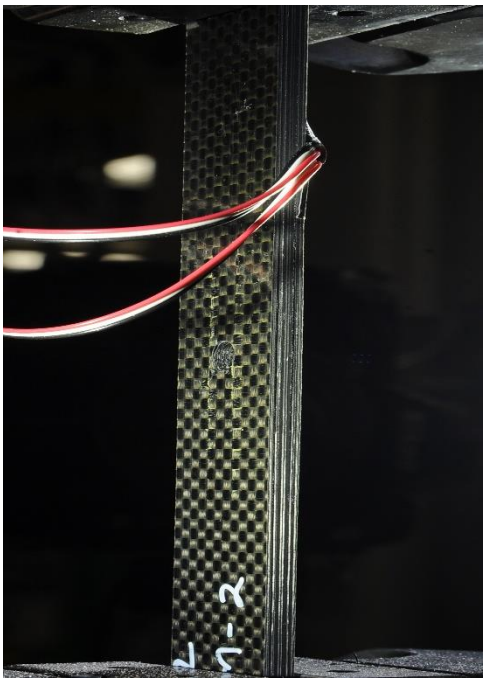

(B2-M-2) at 175k Cycles

Figure C 2-89 Damage Progression in (B2-M-2) Test specimen to 175k Cycles

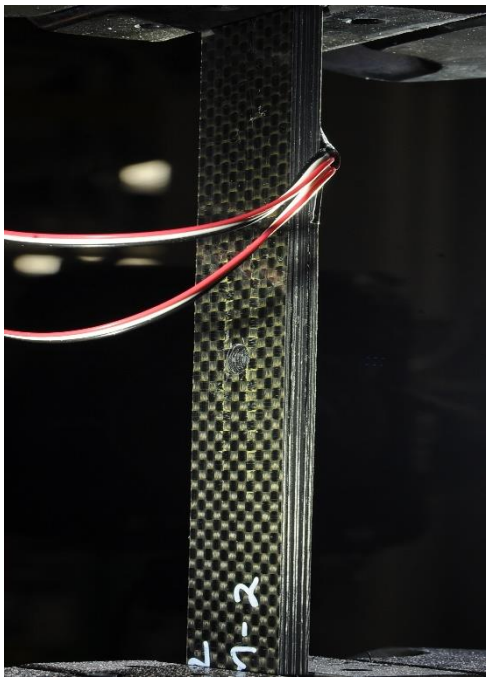

(B2-M-2) at 200k Cycles

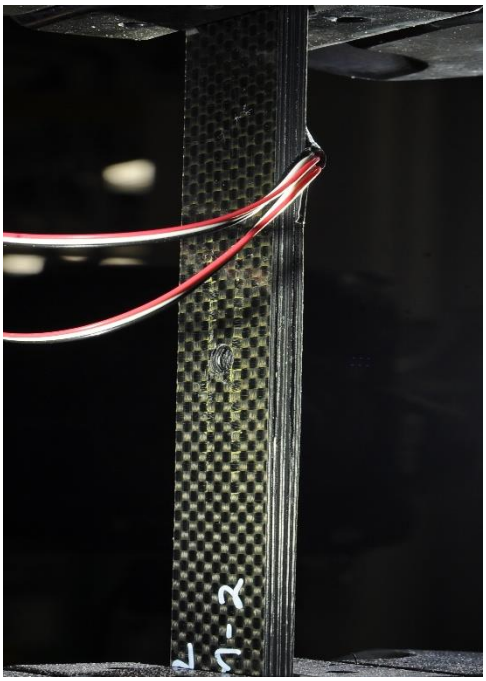

(B2-M-2) at 225k Cycles

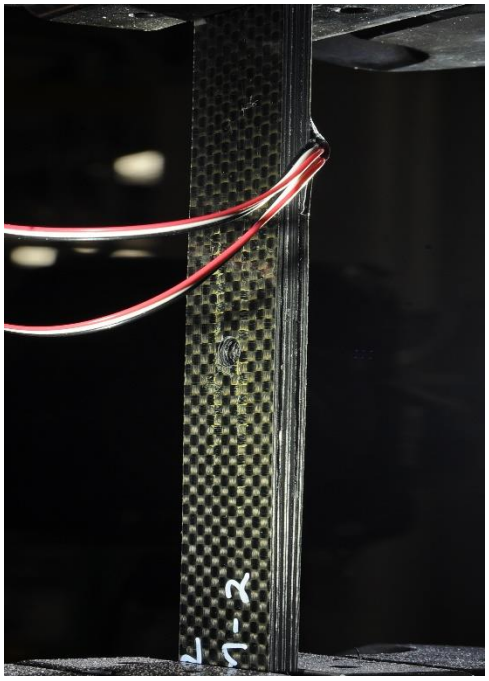

(B2-M-2) at 250k Cycles

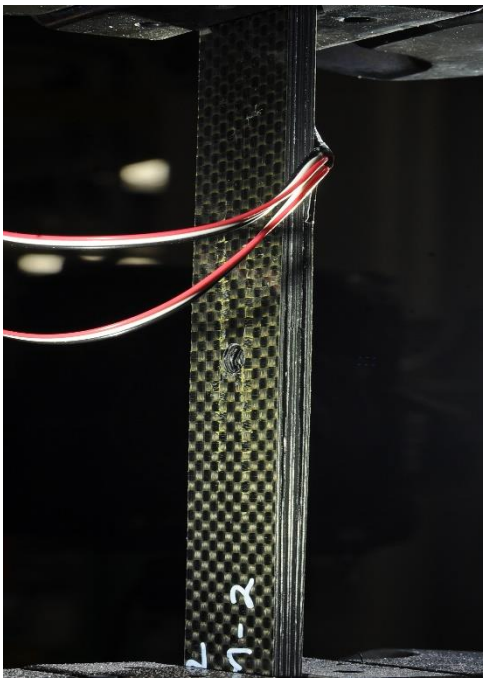

(B2-M-2) at 275k Cycles

Figure C 2-90 Damage Progression in (B2-M-2) Test specimen to 275k Cycles

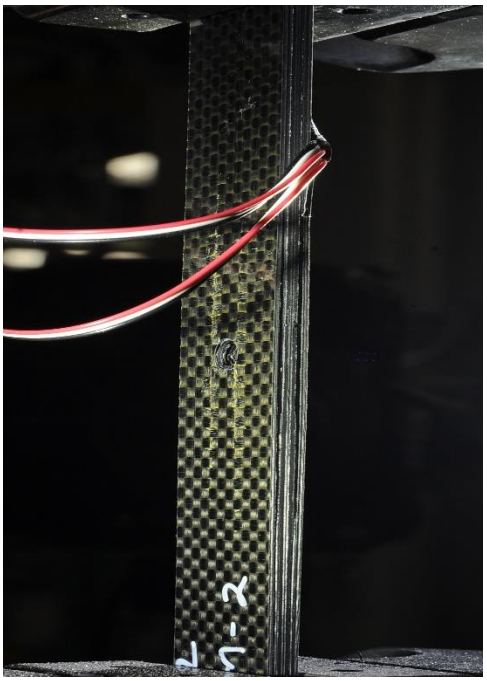

(B2-M-2) at 300k Cycles

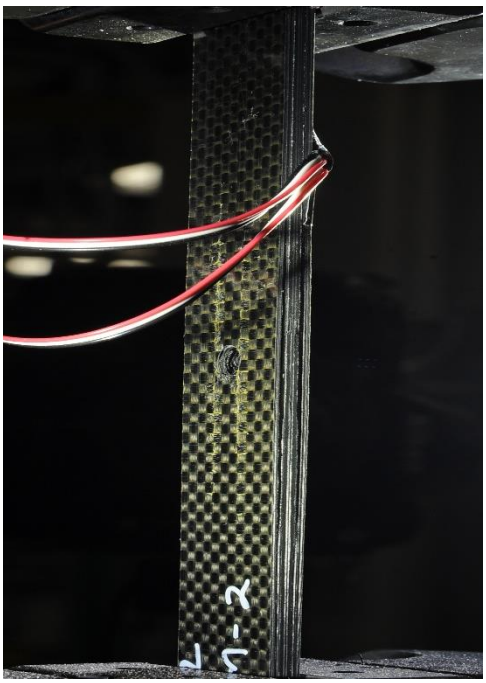

(B2-M-2) at 325k Cycles

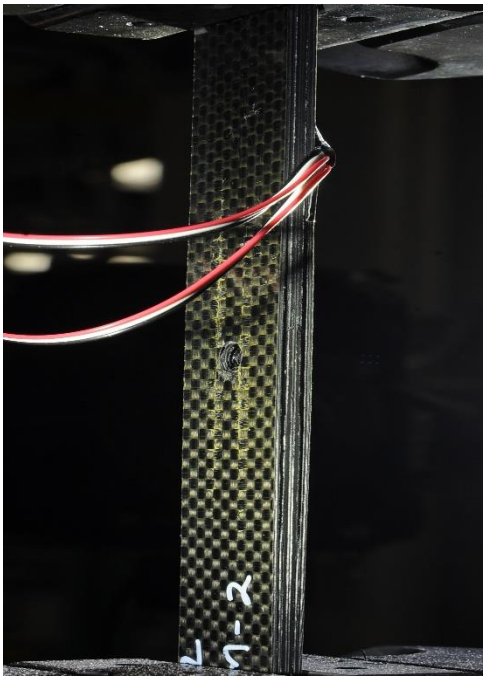

(B2-M-2) at 350k Cycles

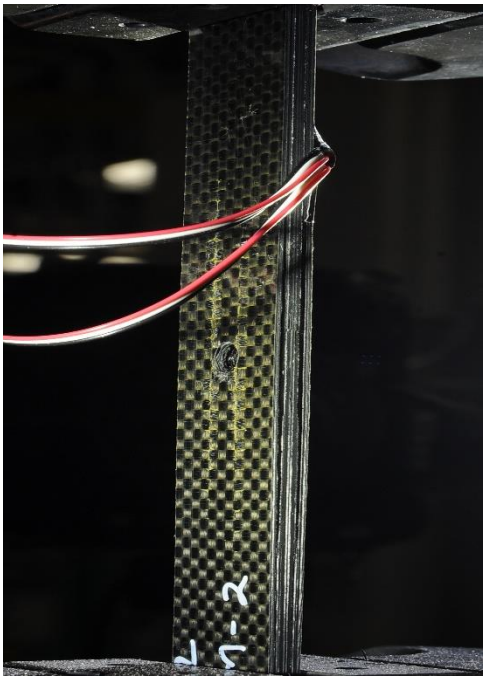

(B2-M-2) at 375k Cycles

Figure C 2-91 Damage Progression in (B2-M-2) Test specimen to 375k Cycles

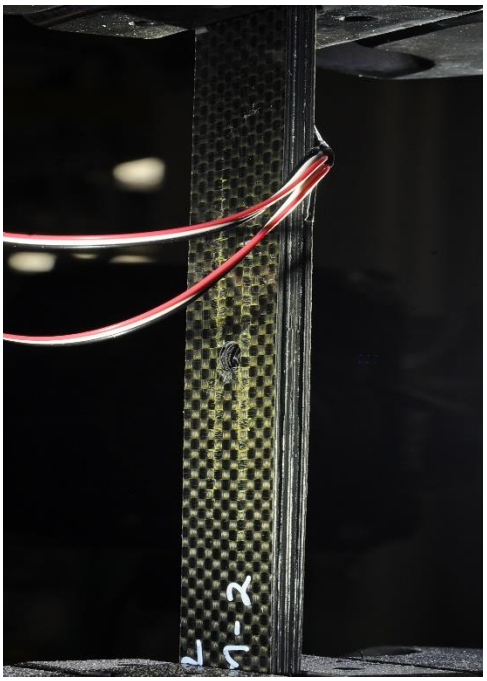

(B2-M-2) at 400k Cycles

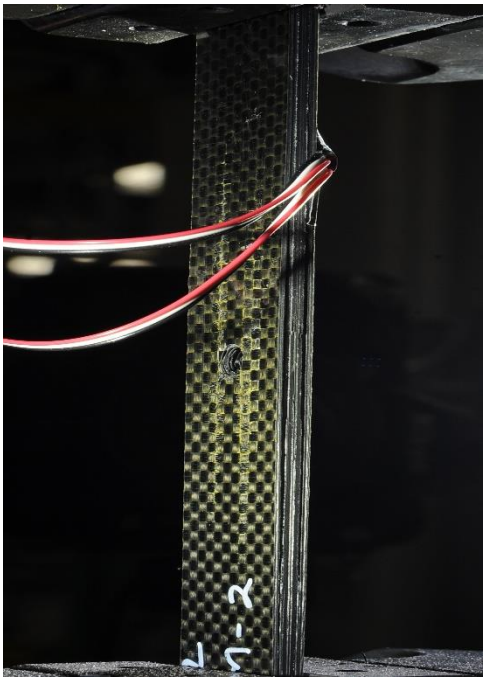

(B2-M-2) at 425k Cycles

(B2-M-2) at Failure

Figure C 2-92 Damage Progression in (B2-M-2) Test specimen to Failure

(B2-M-3) at 1 Cycle

(B2-M-3) at 100 Cycles

(B2-M-3) at 1k Cycles

(B2-M-3) at 5k Cycles

Figure C 2-93 Damage Progression in (B2-M-3) Test specimen to 5k Cycles

(B2-M-3) at 10k Cycles

(B2-M-3) at 20k Cycles

(B2-M-3) at 30k Cycles

(B2-M-3) at 40k Cycles

Figure C 2-94 Damage Progression in (B2-M-3) Test specimen to 40k Cycles

(B2-M-3) at 50k Cycles

(B2-M-3) at 60k Cycles

(B2-M-3) at 70k Cycles

(B2-M-3) at 80k Cycles

Figure C 2-95 Damage Progression in (B2-M-3) Test specimen to 80k Cycles

(B2-M-3) at 90k Cycles

(B2-M-3) at 100k Cycles

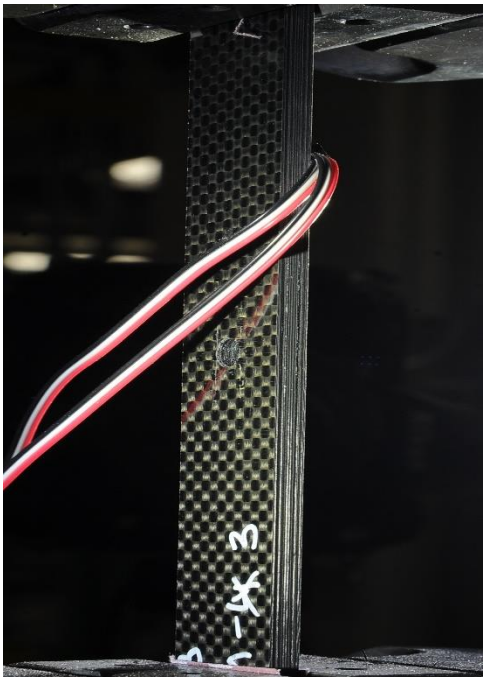

(B2-M-3) at 125k Cycles

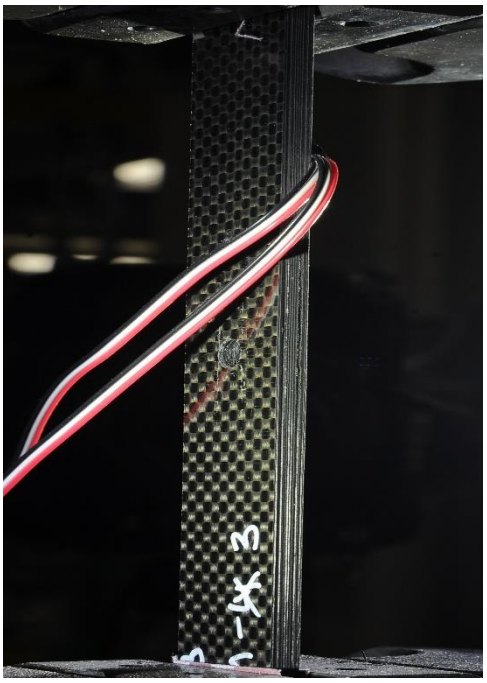

(B2-M-3) at 150k Cycles

Figure C 2-96 Damage Progression in (B2-M-3) Test specimen to 150k Cycles

(B2-M-3) at 175k Cycles

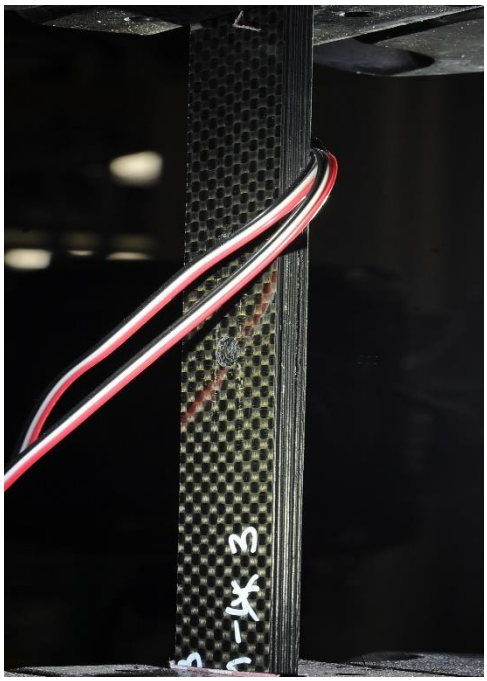

(B2-M-3) at 200k Cycles

(B2-M-3) at 225k Cycles

(B2-M-3) at 250k Cycles

Figure C 2-97 Damage Progression in (B2-M-3) Test specimen to 250k Cycles

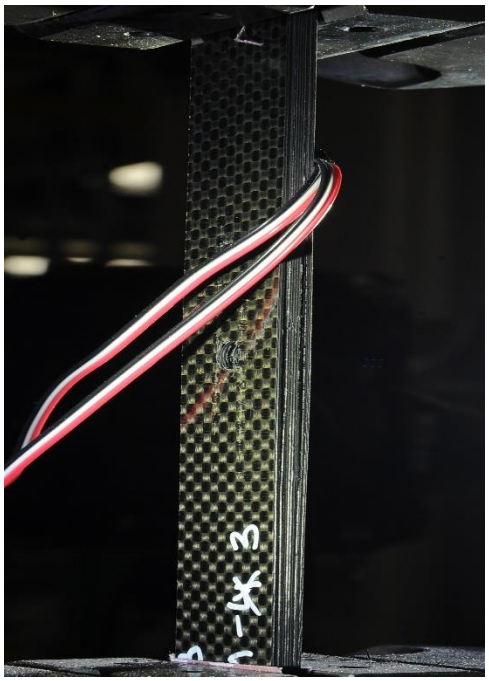

(B2-M-3) at 275k Cycles

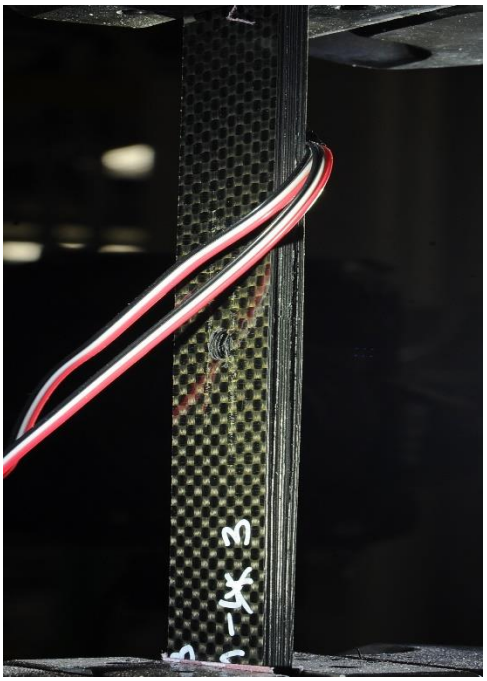

(B2-M-3) at 300k Cycles

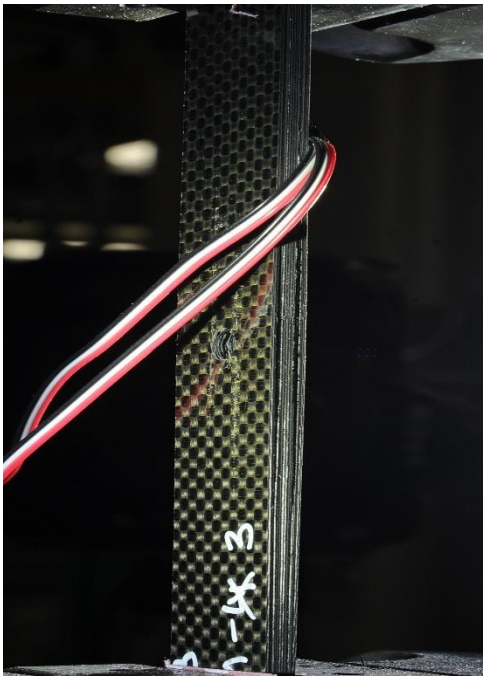

(B2-M-3) at 325k Cycles

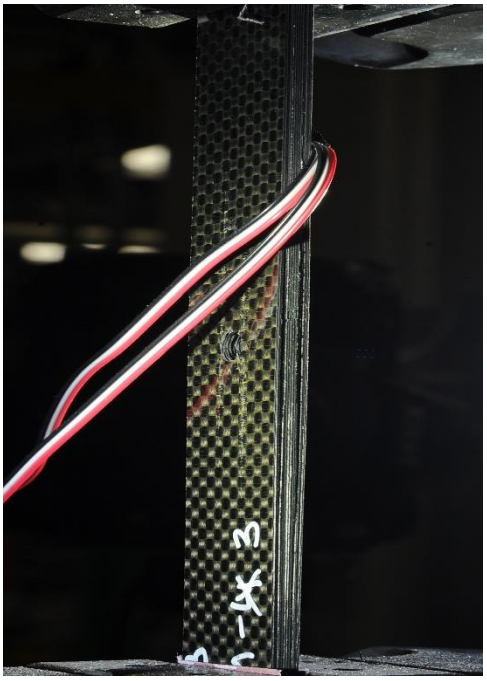

(B2-M-3) at 350k Cycles

Figure C 2-98 Damage Progression in (B2-M-3) Test specimen to 350k Cycles

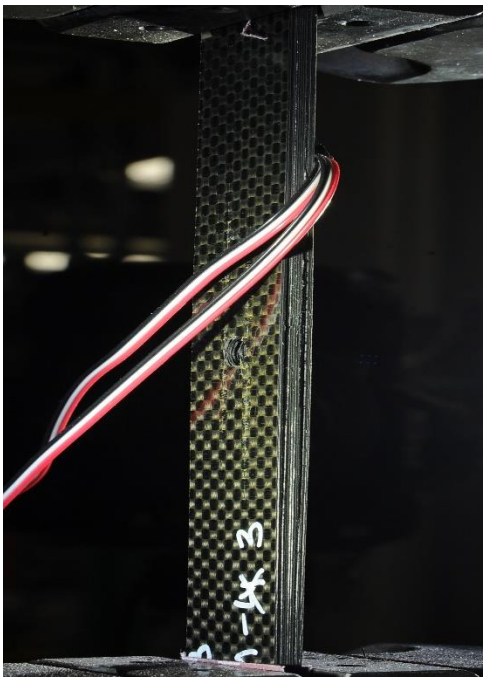

(B2-M-3) at 375k Cycles

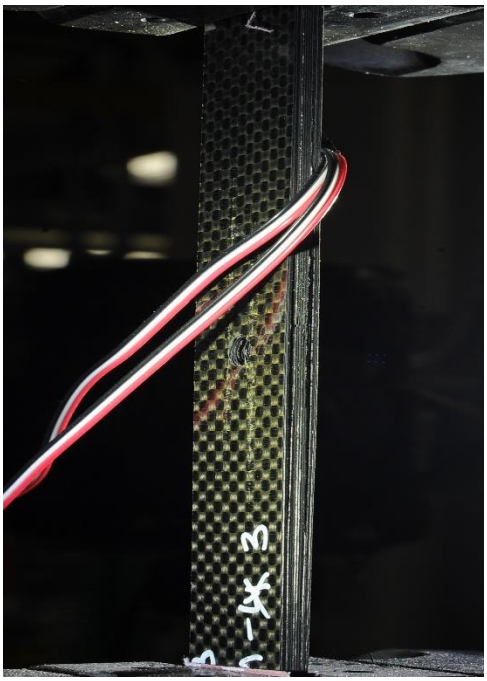

(B2-M-3) at 400k Cycles

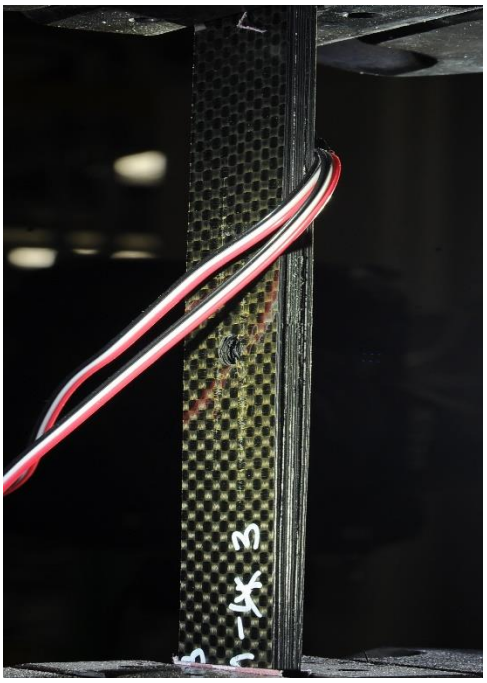

(B2-M-3) at 425k Cycles

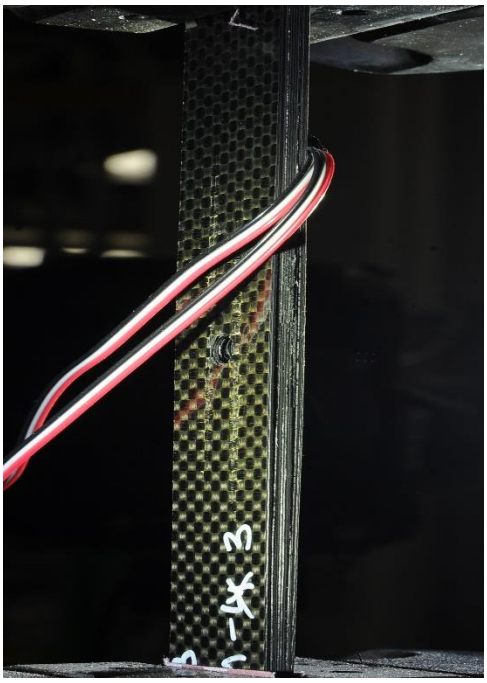

(B2-M-3) at 450k Cycles

Figure C 2-99 Damage Progression in (B2-M-3) Test specimen to 450k Cycles

(B2-M-3) at 475k Cycles

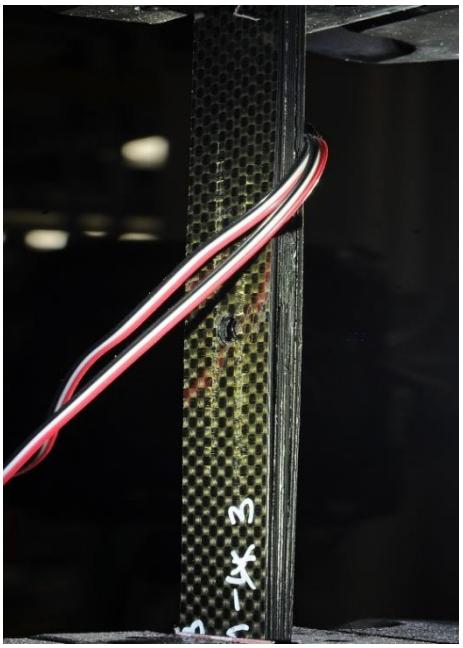

(B2-M-3) at 500k Cycles

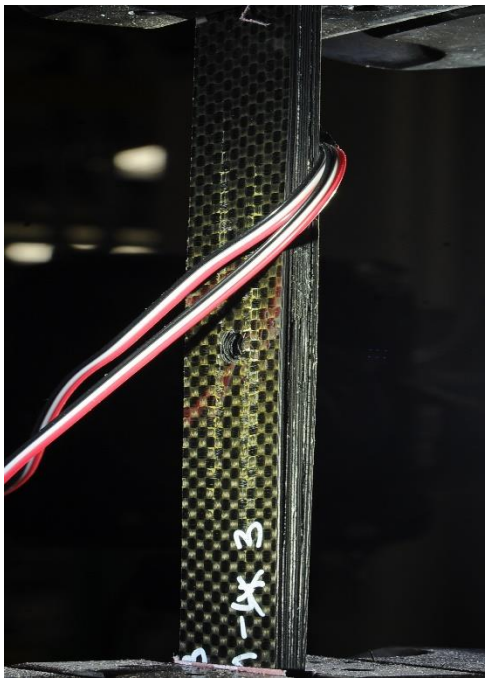

(B2-M-3) at 525k Cycles

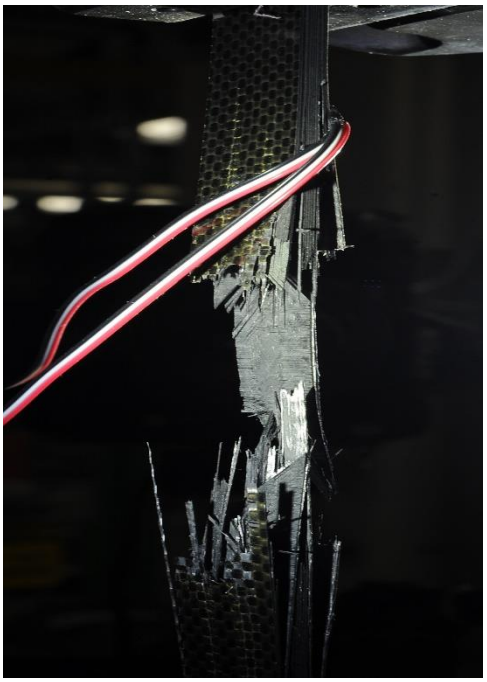

(B2-M-3) at Failure

Figure C 2-100 Damage Progression in (B2-M-3) Test specimen to Failure

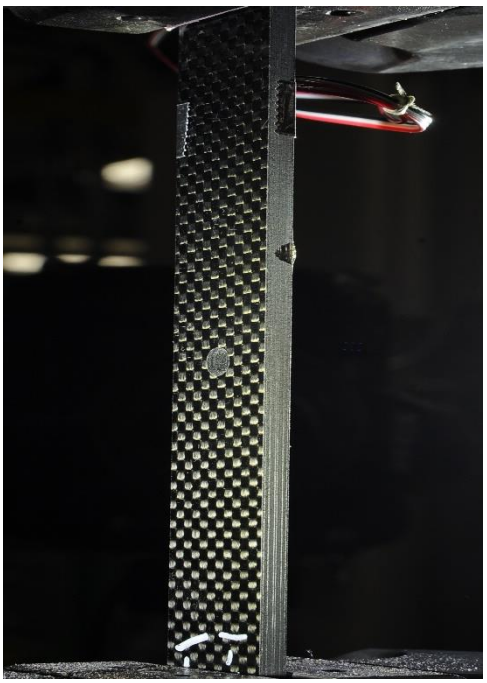

(A2-L-1) at 1 Cycle

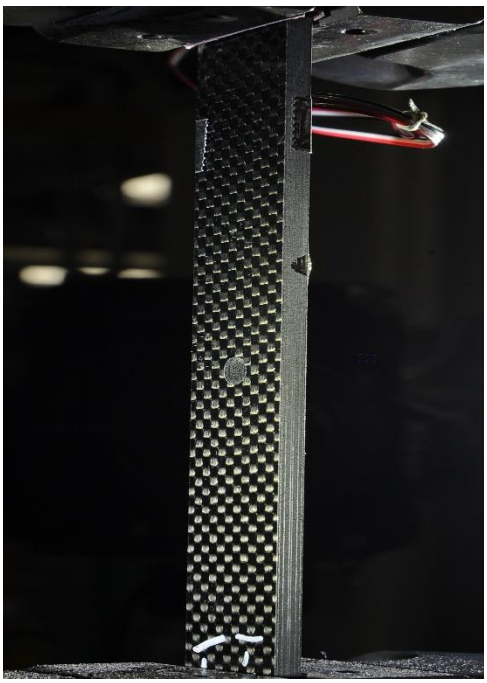

(A2-L-1) at 100 Cycles

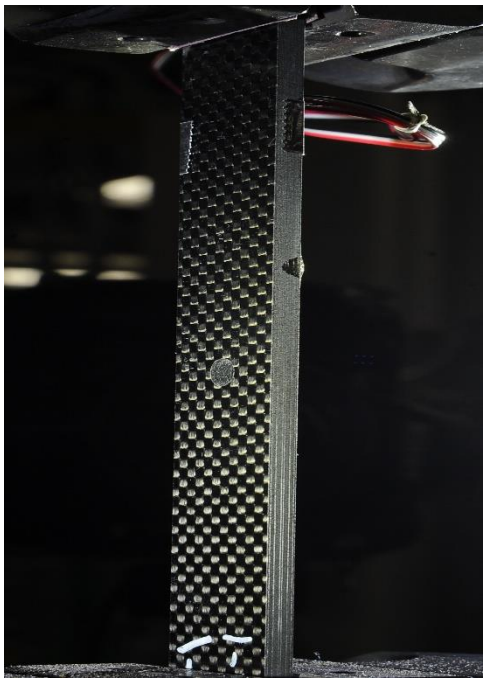

(A2-L-1) at 1k Cycles

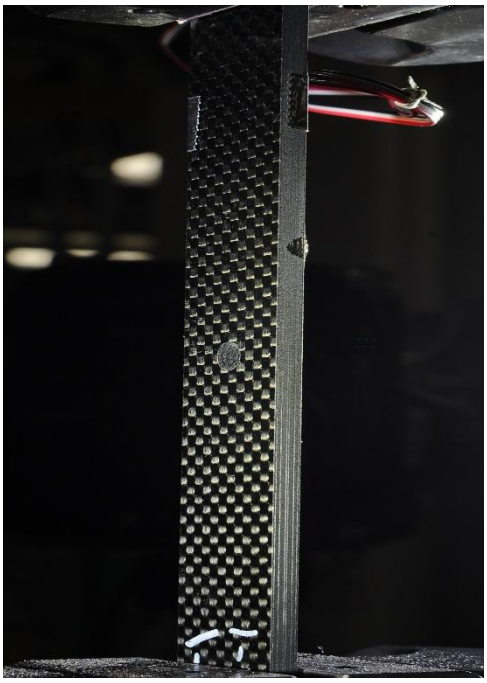

(A2-L-1) at 5k Cycles

Figure C 2-101 Damage Progression in (A2-L-1) Test specimen to 5k Cycles

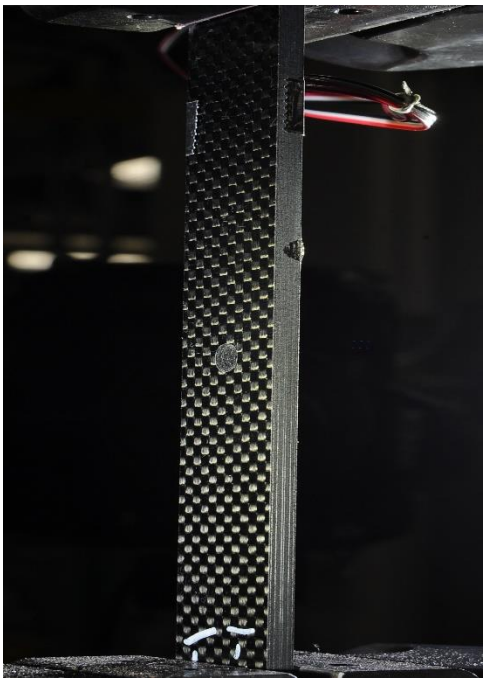

(A2-L-1) at 10k Cycles

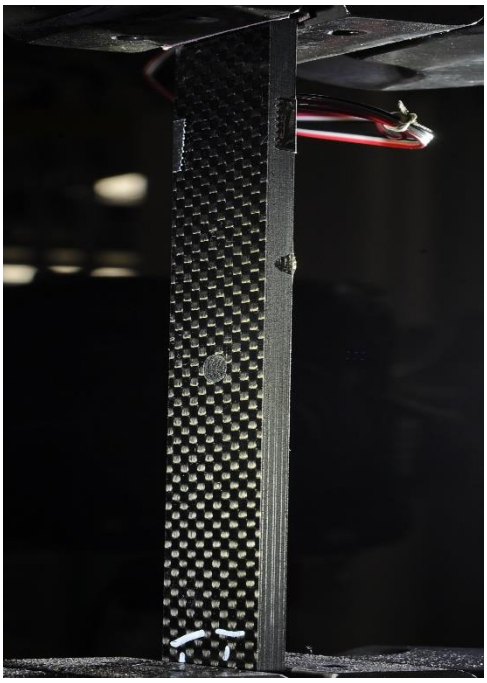

(A2-L-1) at 20k Cycles

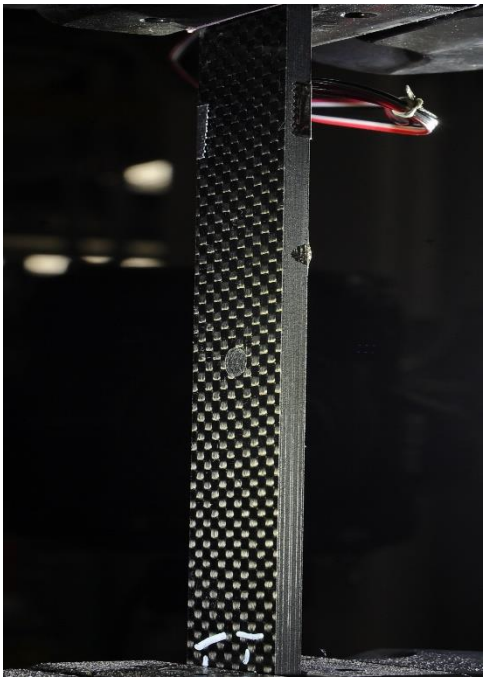

(A2-L-1) at 30k Cycles

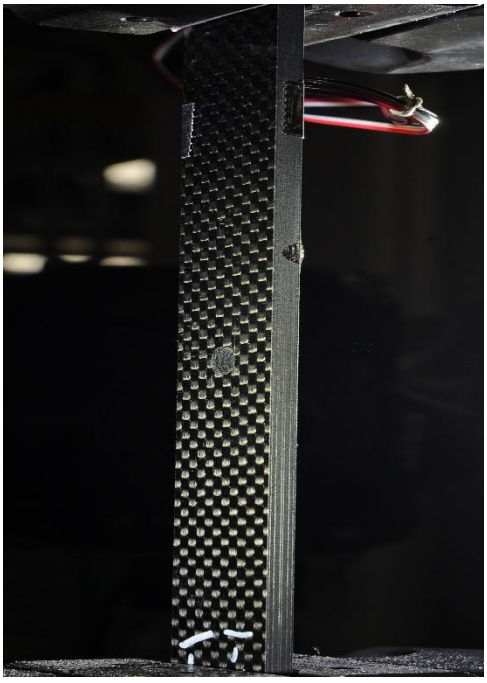

(A2-L-1) at 40k Cycles

Figure C 2-102 Damage Progression in (A2-L-1) Test specimen to 40k Cycles

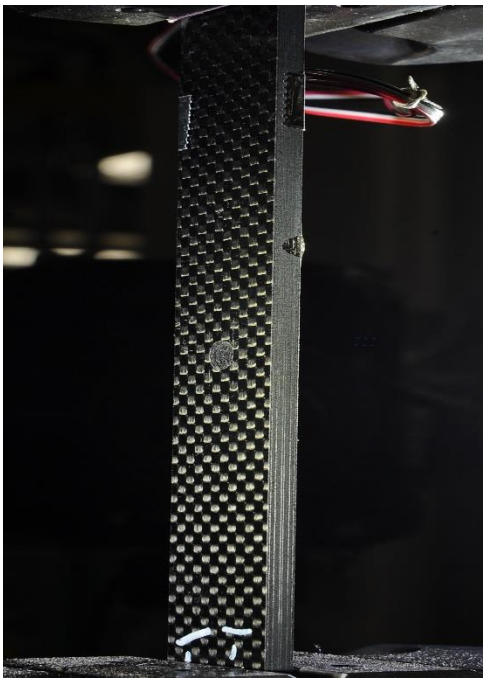

(A2-L-1) at 50k Cycles

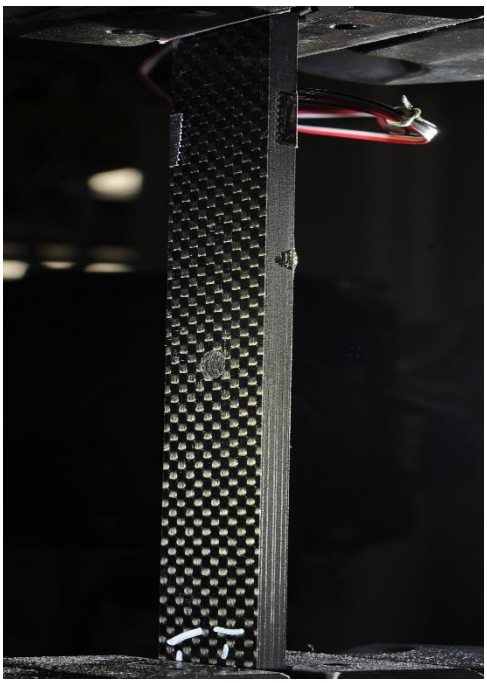

(A2-L-1) at 60k Cycles

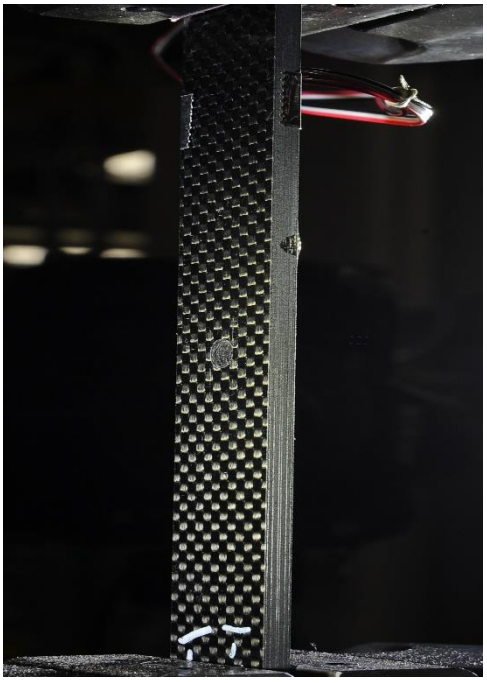

(A2-L-1) at 70k Cycles

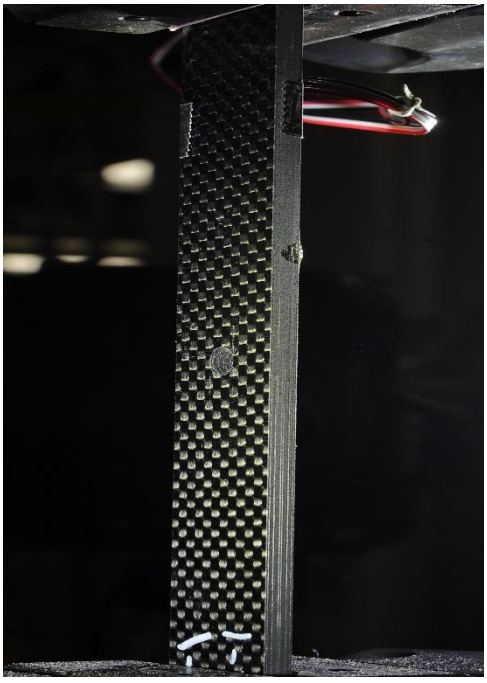

(A2-L-1) at 80k Cycles

Figure C 2-103 Damage Progression in (A2-L-1) Test specimen to 80k Cycles

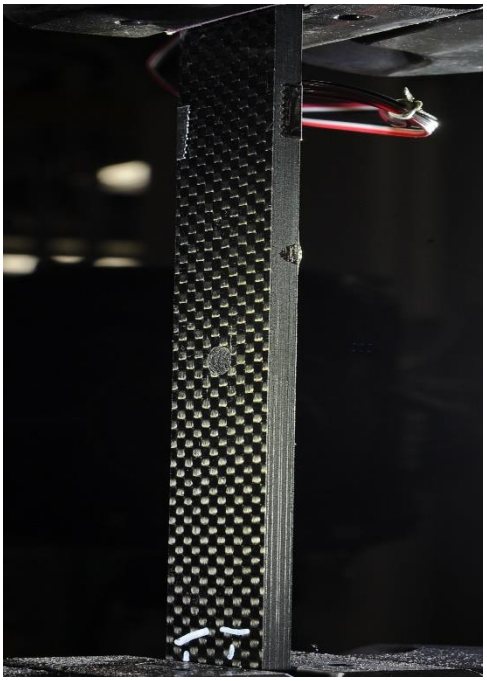

(A2-L-1) at 90k Cycles

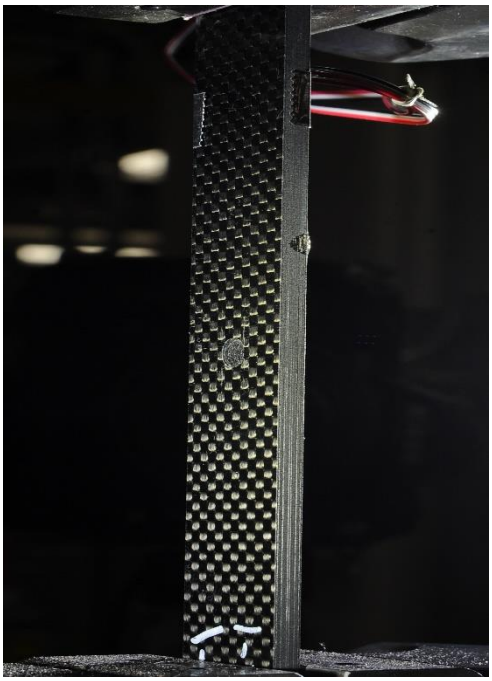

(A2-L-1) at 100k Cycles

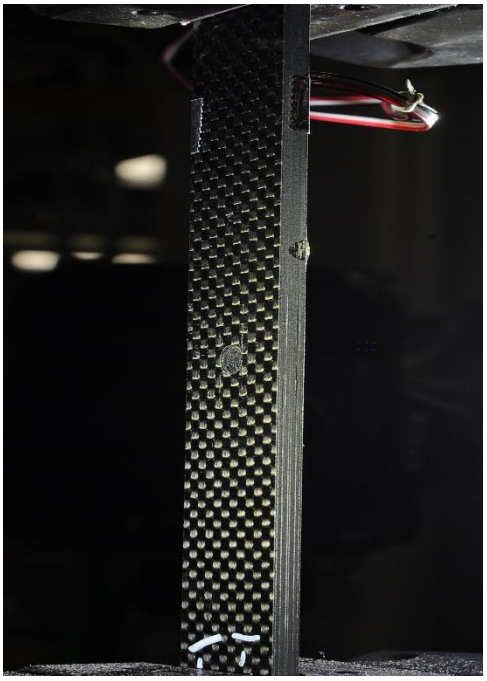

(A2-L-1) at 125k Cycles

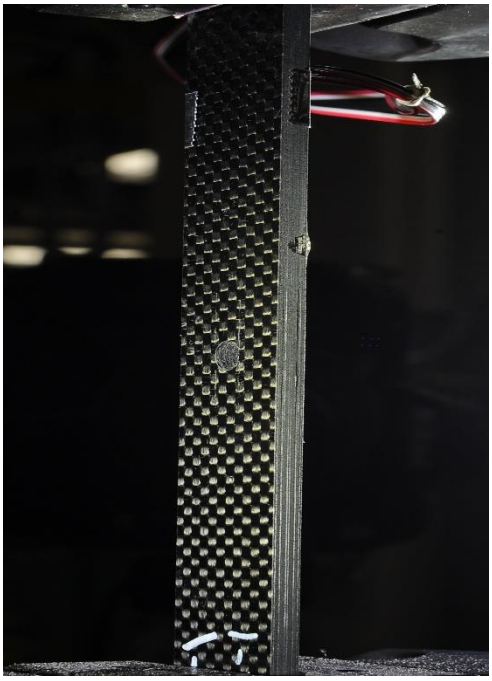

(A2-L-1) at 150k Cycles

Figure C 2-104 Damage Progression in (A2-L-1) Test specimen to 150k Cycles

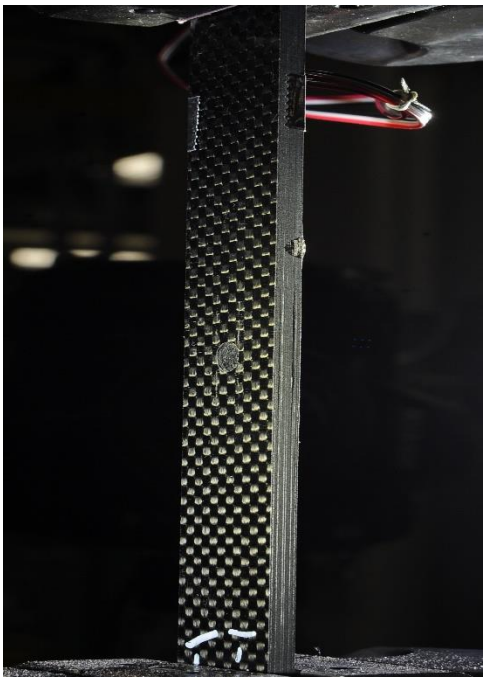

(A2-L-1) at 175k Cycles

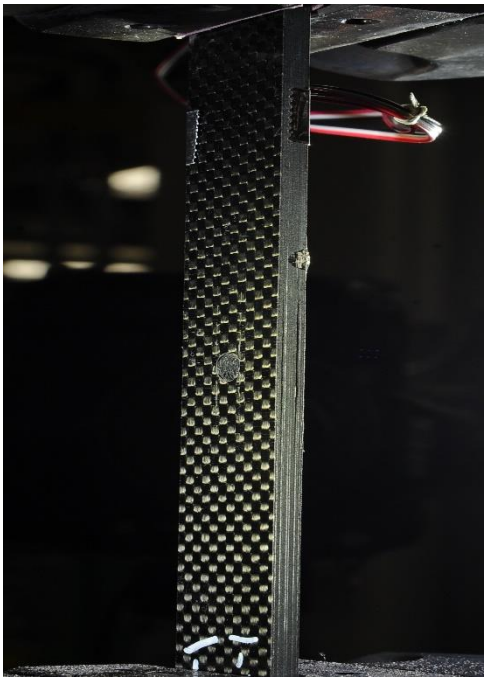

(A2-L-1) at 200k Cycles

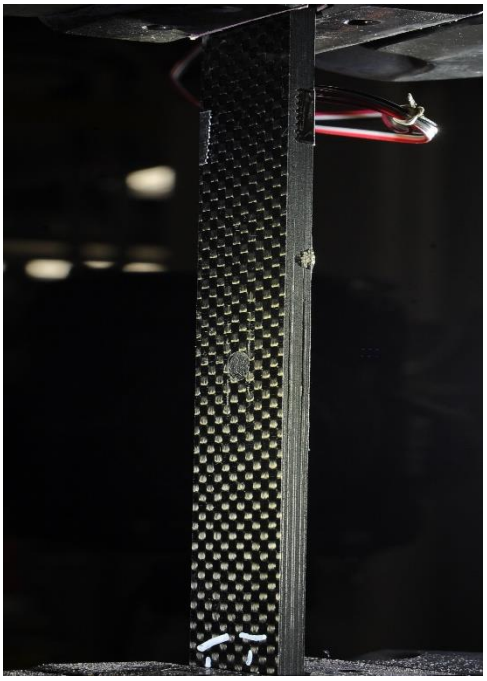

(A2-L-1) at 225k Cycles

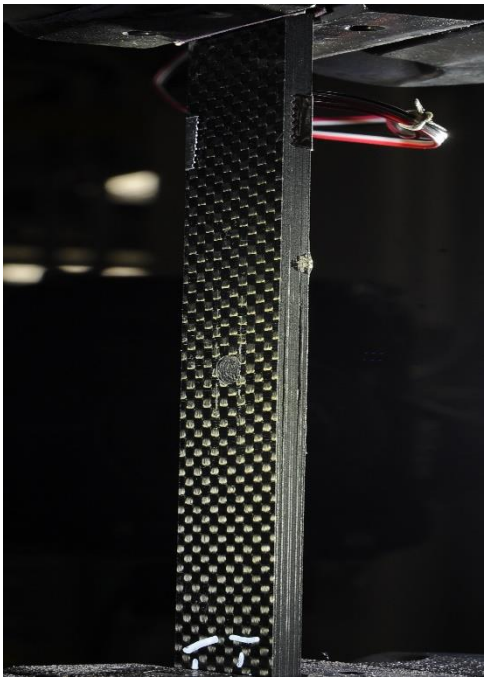

(A2-L-1) at 250k Cycles

Figure C 2-105 Damage Progression in (A2-L-1) Test specimen to 250k Cycles

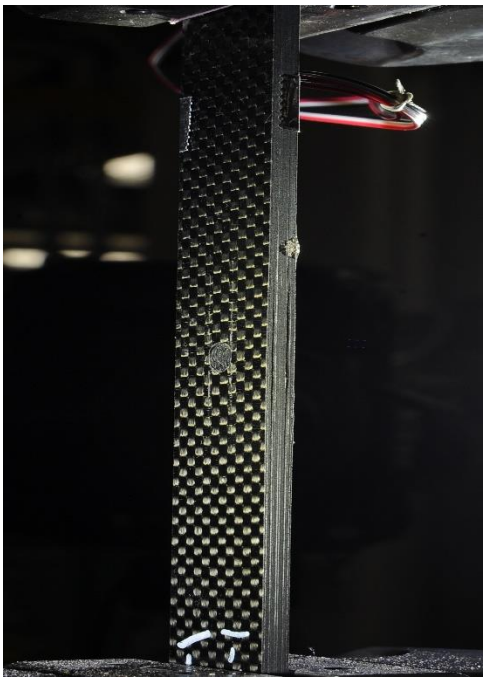

(A2-L-1) at 275k Cycles

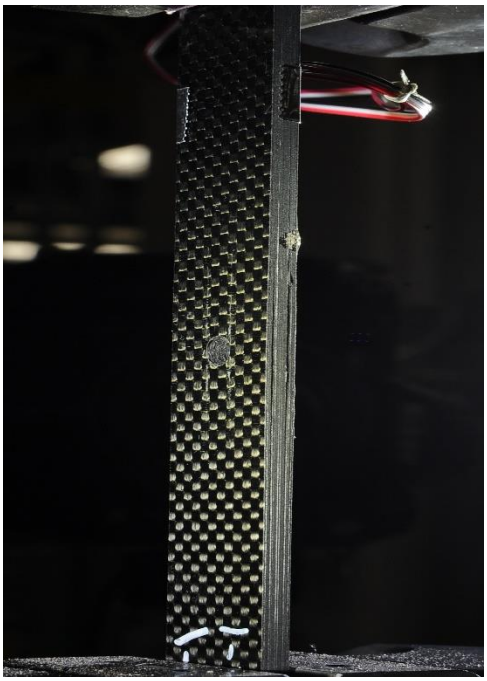

(A2-L-1) at 300k Cycles

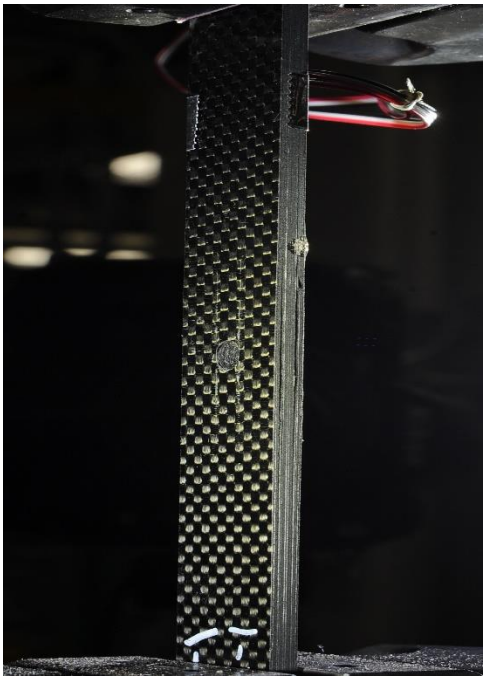

(A2-L-1) at 325k Cycles

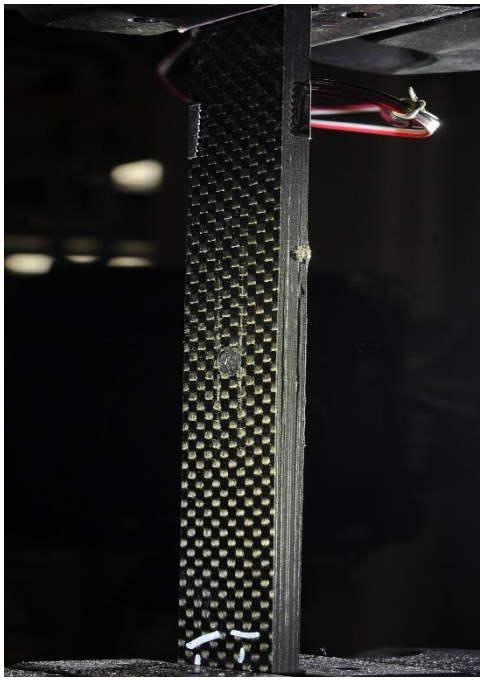

(A2-L-1) at 350k Cycles

Figure C 2-106 Damage Progression in (A2-L-1) Test specimen to 350k Cycles

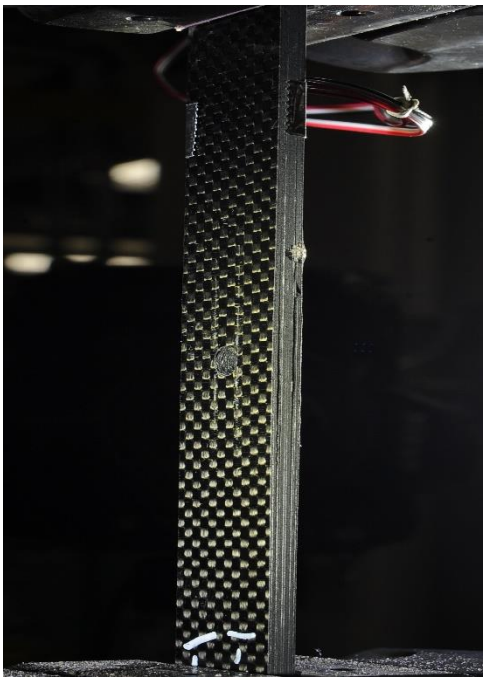

(A2-L-1) at 375k Cycles

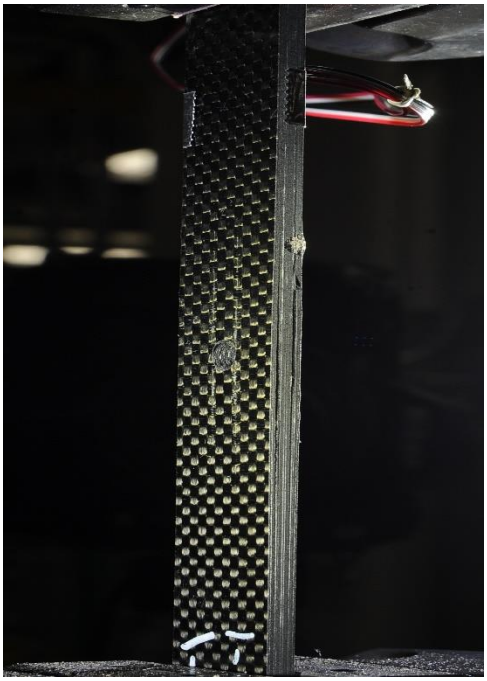

(A2-L-1) at 400k Cycles

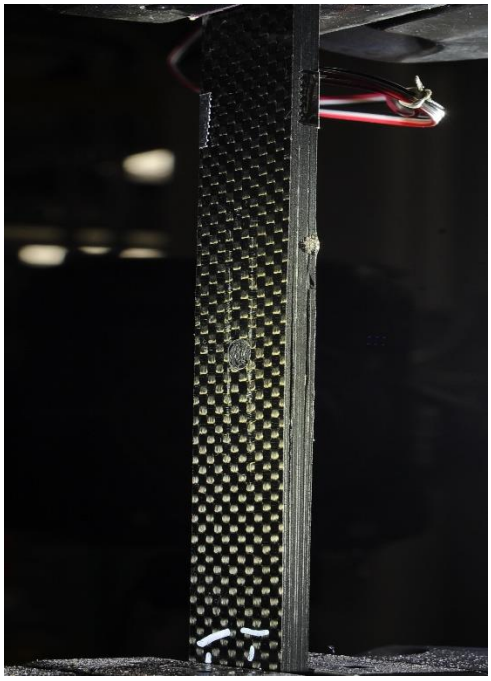

(A2-L-1) at 425k Cycles

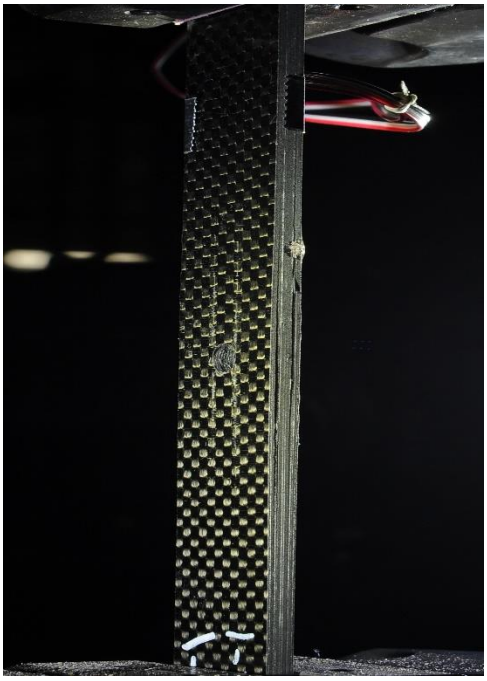

(A2-L-1) at 450k Cycles

Figure C 2-107 Damage Progression in (A2-L-1) Test specimen to 450k Cycles

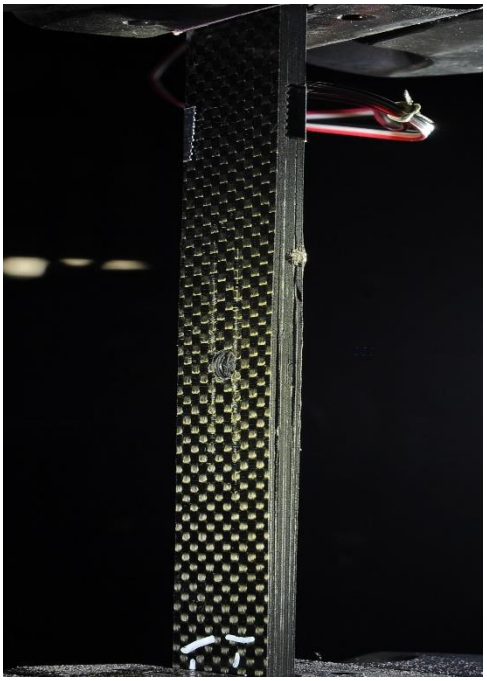

(A2-L-1) at 475k Cycles

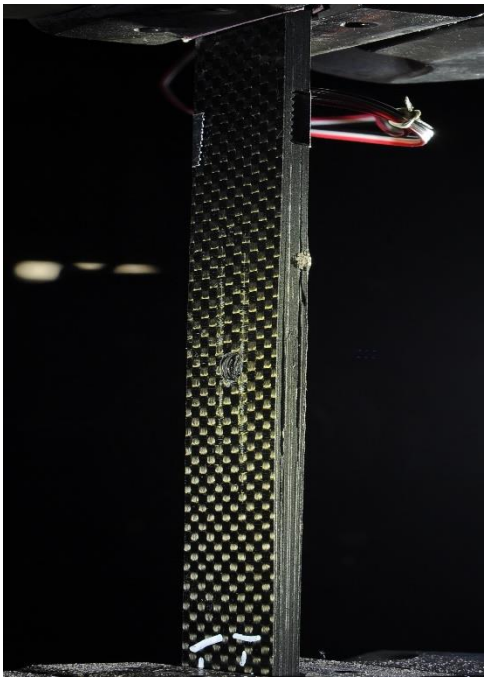

(A2-L-1) at 500k Cycles

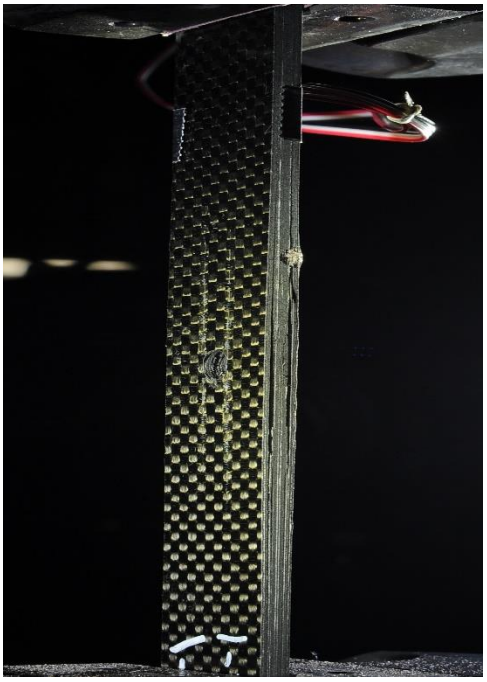

(A2-L-1) at 525k Cycles

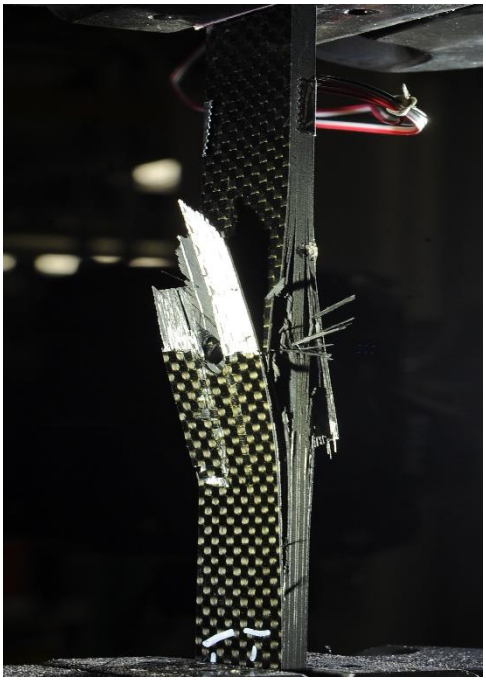

(A2-L-1) at Failure

Figure C 2-108 Damage Progression in (A2-L-1) Test specimen to Failure

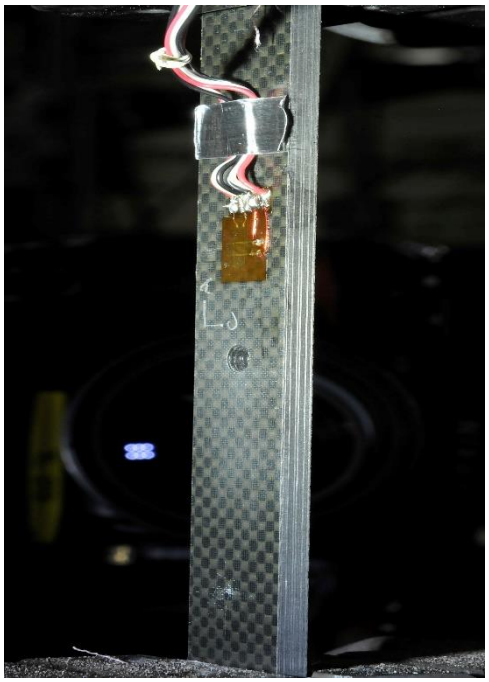

(A2-L-2) at 1 Cycle

(A2-L-2) at 100 Cycles

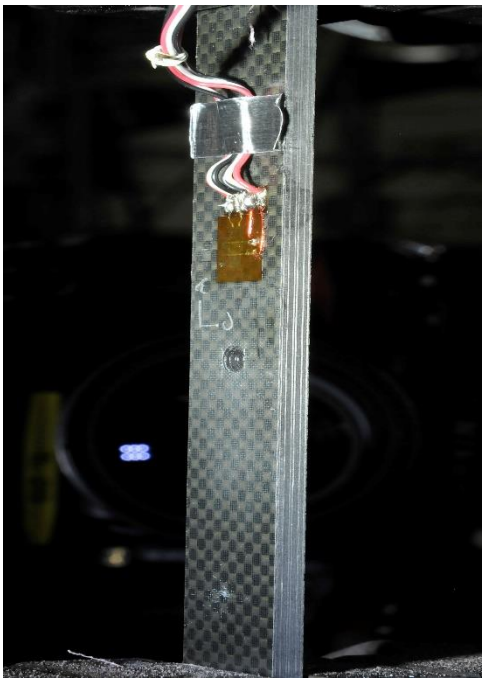

(A2-L-2) at 1k Cycles

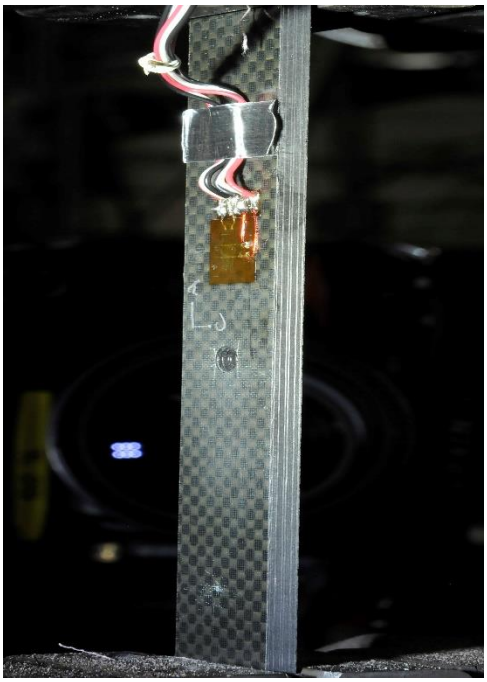

(A2-L-2) at 5k Cycles

Figure C 2-109 Damage Progression in (A2-L-2) Test specimen to 5k Cycles

(A2-L-2) at 10k Cycles

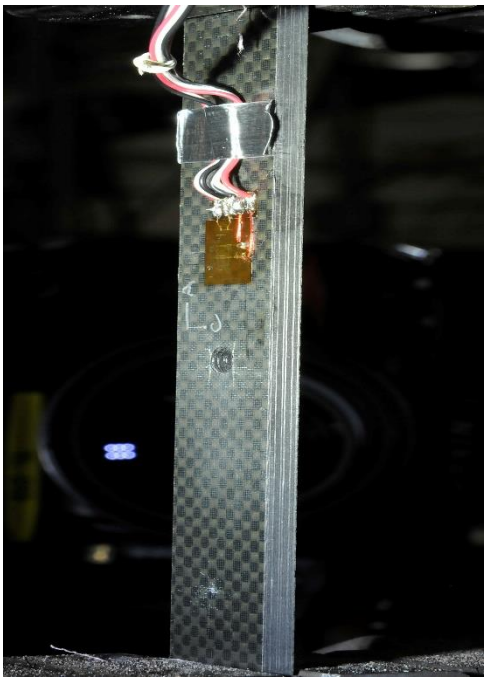

(A2-L-2) at 20k Cycles

(A2-L-2) at 30k Cycles

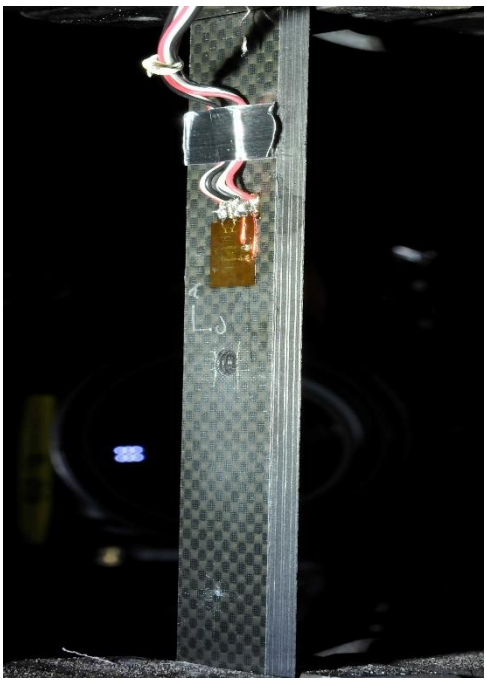

(A2-L-2) at 40k Cycles

Figure C 2-110 Damage Progression in (A2-L-2) Test specimen to 40k Cycles

(A2-L-2) at 50k Cycles

(A2-L-2) at 60k Cycles

(A2-L-2) at 70k Cycles

(A2-L-2) at 80k Cycles

Figure C 2-111 Damage Progression in (A2-L-2) Test specimen to 80k Cycles

(A2-L-2) at 90k Cycles

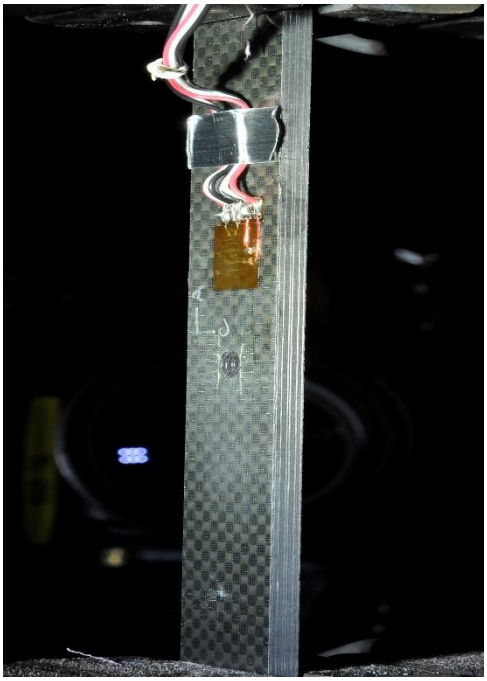

(A2-L-2) at 100k Cycles

(A2-L-2) at 125k Cycles

(A2-L-2) at 150k Cycles

Figure C 2-112 Damage Progression in (A2-L-2) Test specimen to 150k Cycles

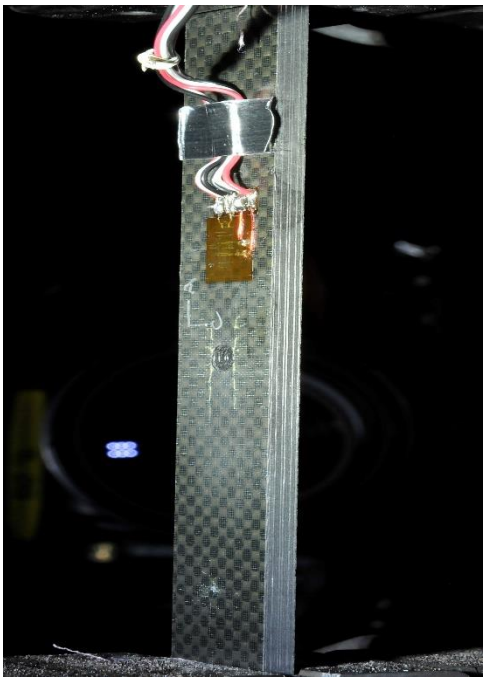

(A2-L-2) at 175k Cycles

(A2-L-2) at 200k Cycles

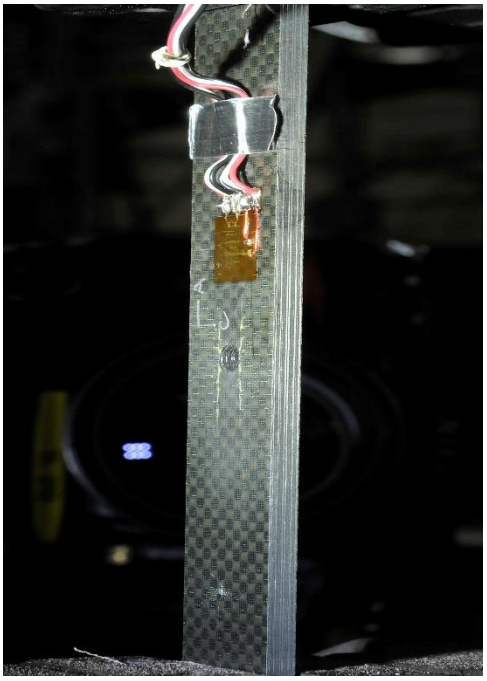

(A2-L-2) at 225k Cycles

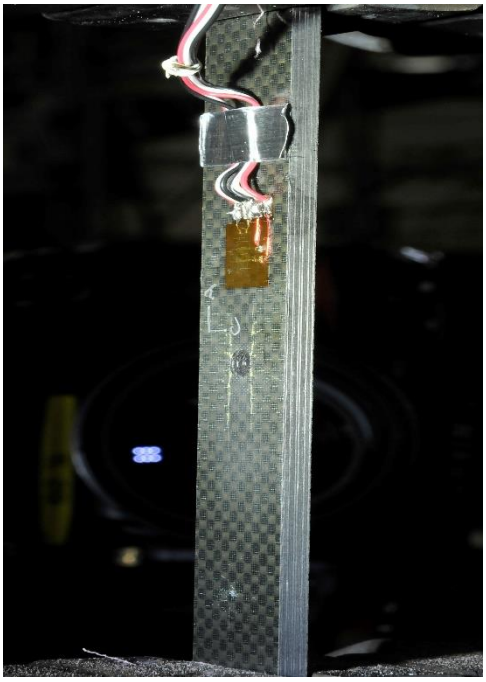

(A2-L-2) at 250k Cycles

Figure C 2-113 Damage Progression in (A2-L-2) Test specimen to 250k Cycles

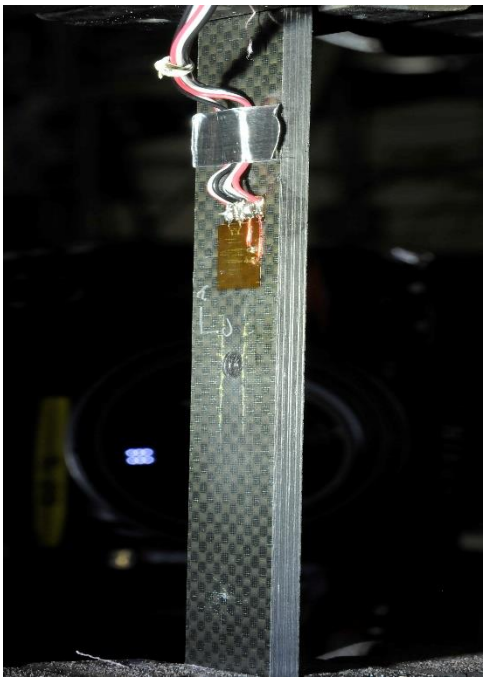

(A2-L-2) at 275k Cycles

(A2-L-2) at 300k Cycles

(A2-L-2) at 325k Cycles

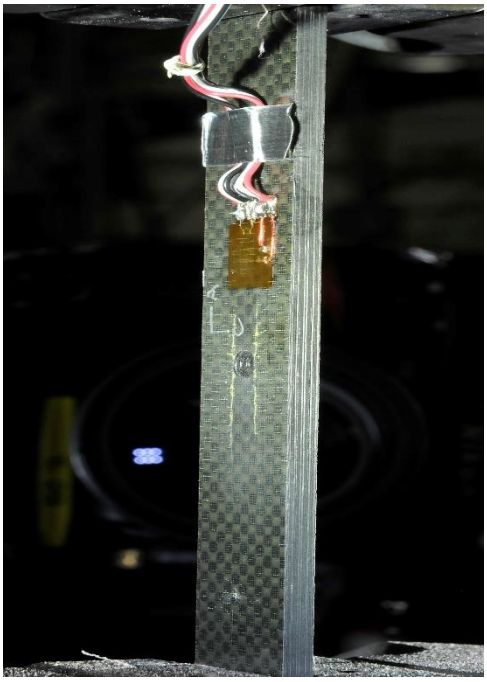

(A2-L-2) at 350k Cycles

Figure C 2-114 Damage Progression in (A2-L-2) Test specimen to 350k Cycles

(A2-L-2) at 375k Cycles

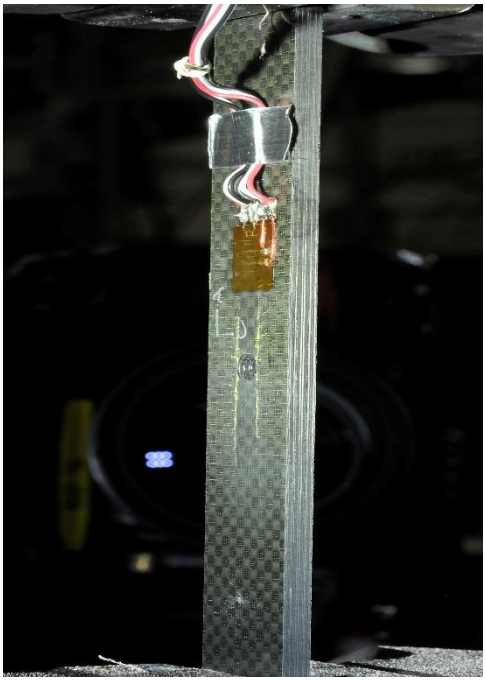

(A2-L-2) at 400k Cycles

(A2-L-2) at 425k Cycles

(A2-L-2) at 450k Cycles

Figure C 2-115 Damage Progression in (A2-L-2) Test specimen to 450k Cycles

(A2-L-2) at 475k Cycles

(A2-L-2) at 500k Cycles

(A2-L-2) at 525k Cycles

(A2-L-2) at 550k Cycles

Figure C 2-116 Damage Progression in (A2-L-2) Test specimen to 550k Cycles

(A2-L-2) at 575k Cycles

(A2-L-2) at 600k Cycles

(A2-L-2) at 625k Cycles

(A2-L-2) at 650k Cycles

Figure C 2-117 Damage Progression in (A2-L-2) Test specimen to 650k Cycles

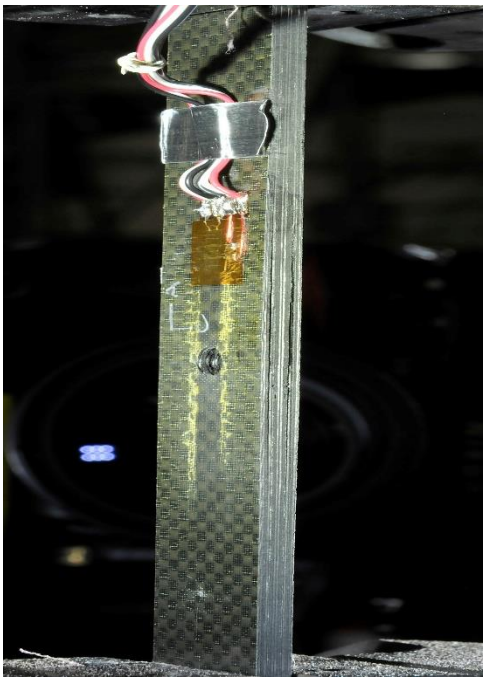

(A2-L-2) at 675k Cycles

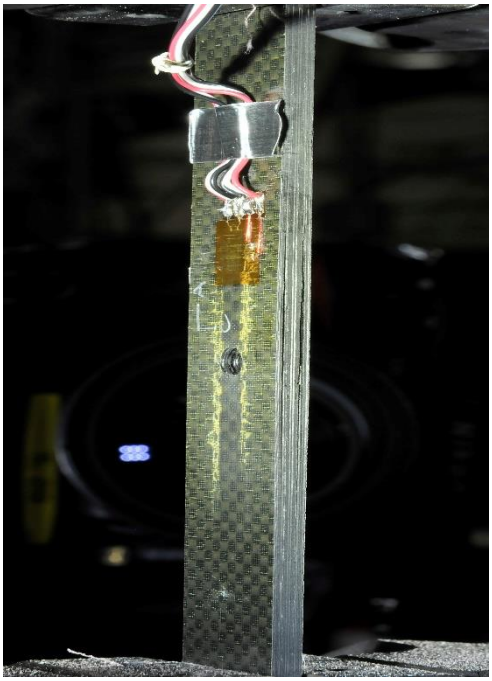

(A2-L-2) at 700k Cycles

(A2-L-2) at 725k Cycles

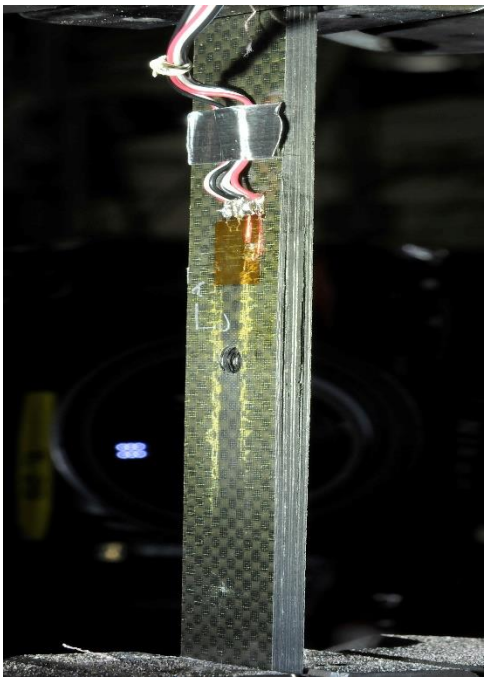

(A2-L-2) at 750k Cycles

Figure C 2-118 Damage Progression in (A2-L-2) Test specimen to 750k Cycles

(A2-L-2) at 775k Cycles

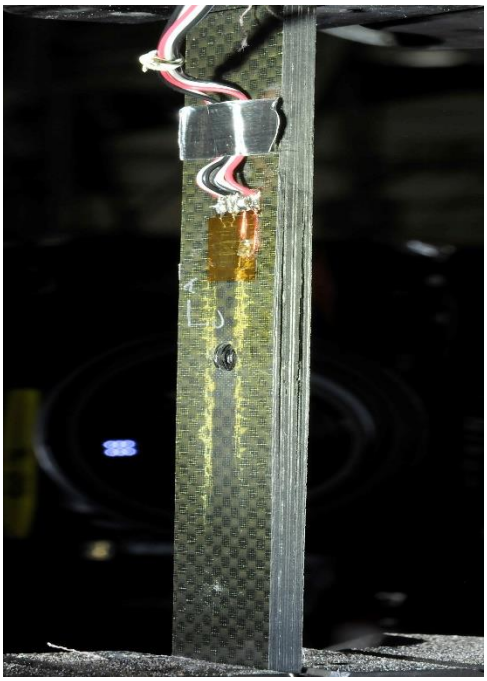

(A2-L-2) at 800k Cycles

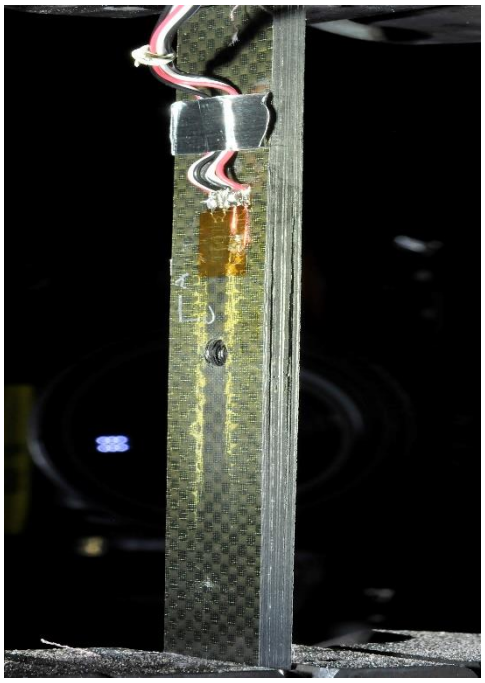

(A2-L-2) at 825k Cycles

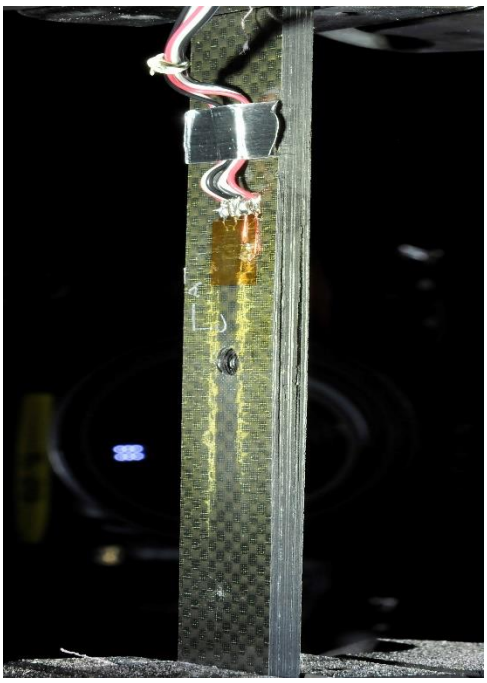

(A2-L-2) at 850k Cycles

Figure C 2-119 Damage Progression in (A2-L-2) Test specimen to 850k Cycles

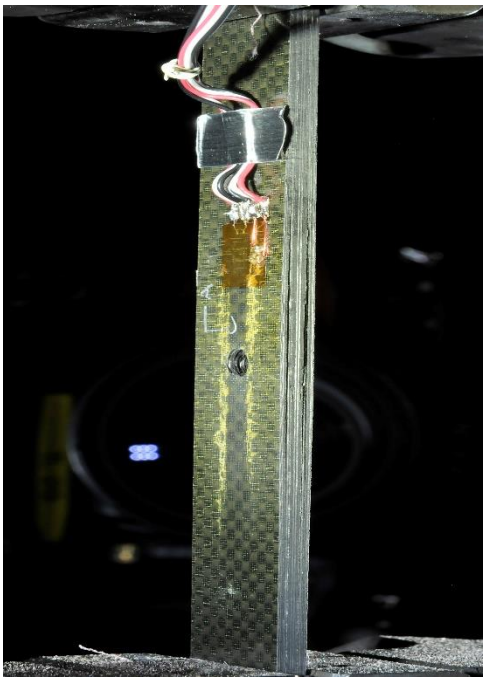

(A2-L-2) at 875k Cycles

(A2-L-2) at 900k Cycles

(A2-L-2) at 925k Cycles

(A2-L-2) at 950k Cycles

Figure C 2-120 Damage Progression in (A2-L-2) Test specimen to 950k Cycles

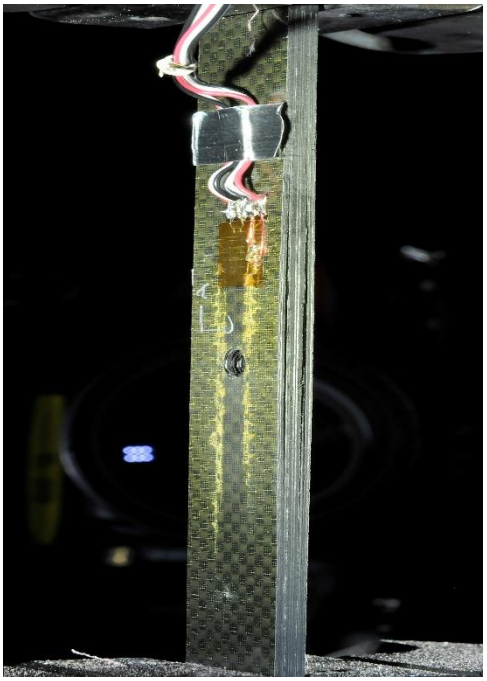

(A2-L-2) at 975k Cycles

(A2-L-2) at 1000k Cycles

(A2-L-2) at Pre RS

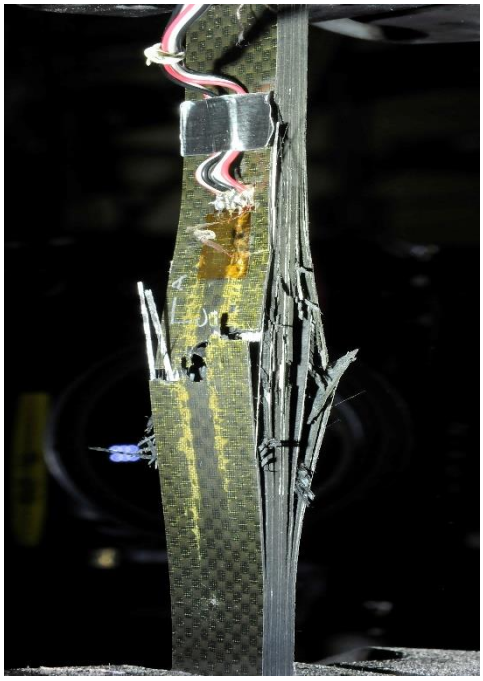

(A2-L-2) at Failure

Figure C 2-121 Damage Progression in (A2-L-2) Test specimen to Failure

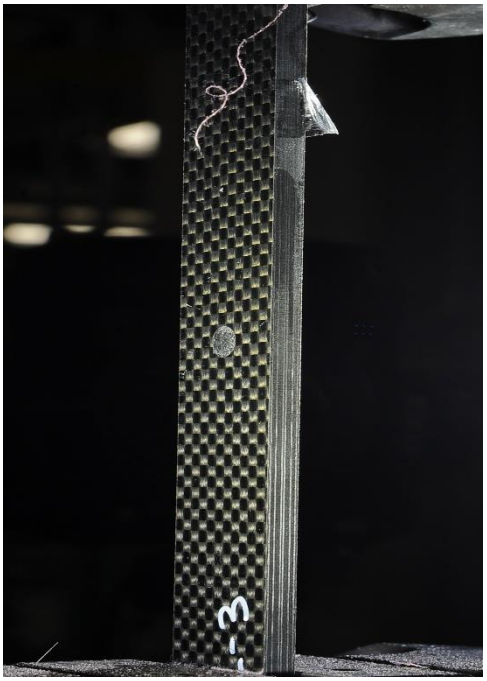

(A2-L-3) at 1 Cycle

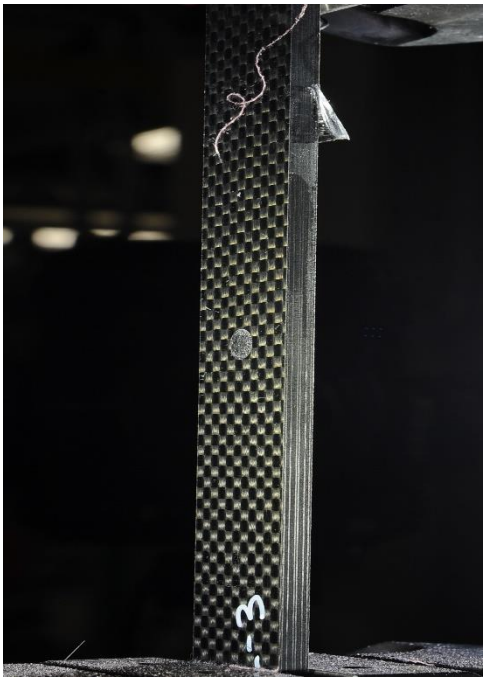

(A2-L-3) at 100 Cycles

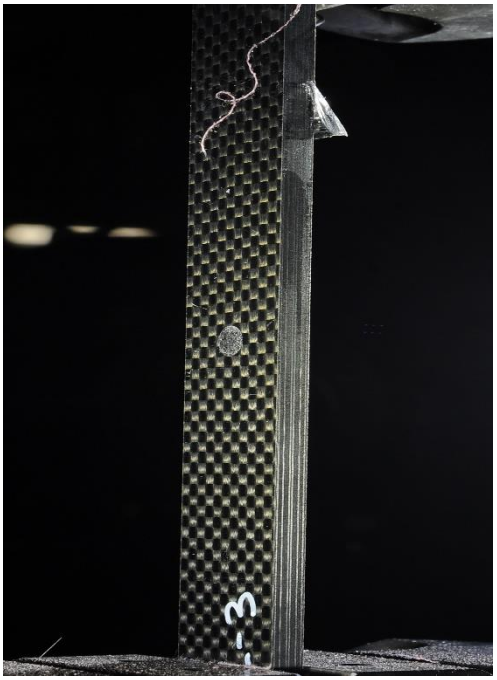

(A2-L-3) at 1k Cycles

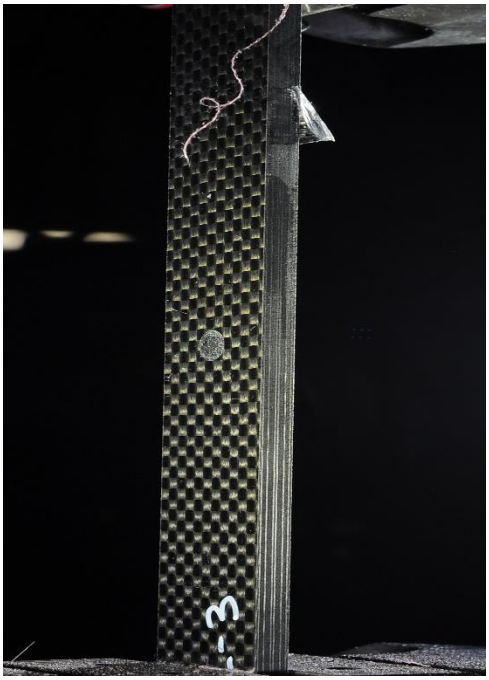

(A2-L-3) at 5k Cycles

Figure C 2-122 Damage Progression in (A2-L-3) Test specimen to 5k Cycles

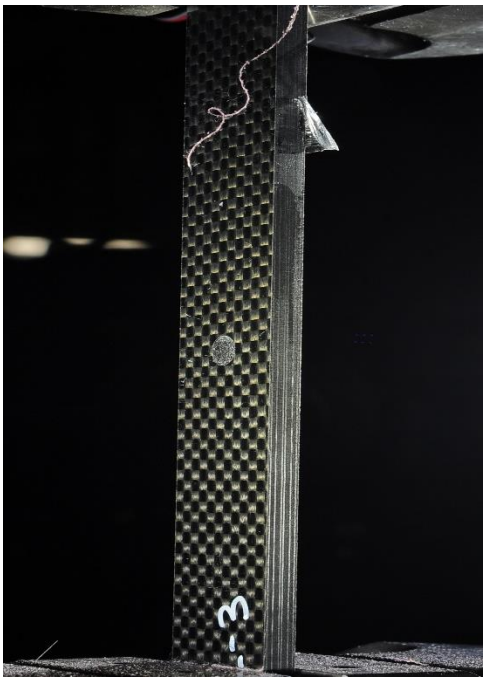

(A2-L-3) at 10k Cycles

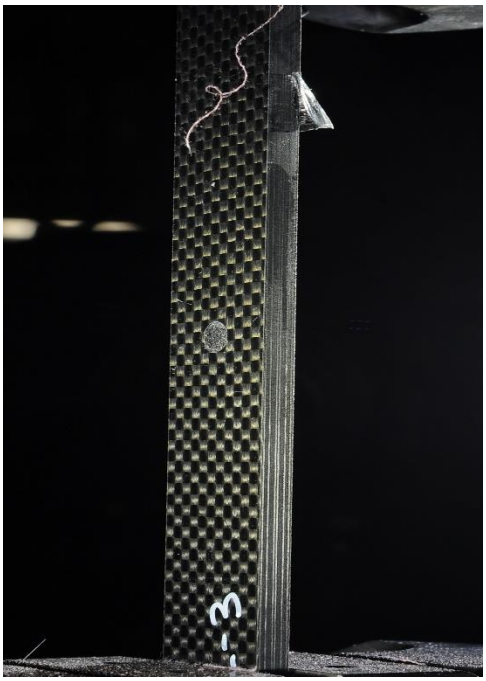

(A2-L-3) at 20k Cycles

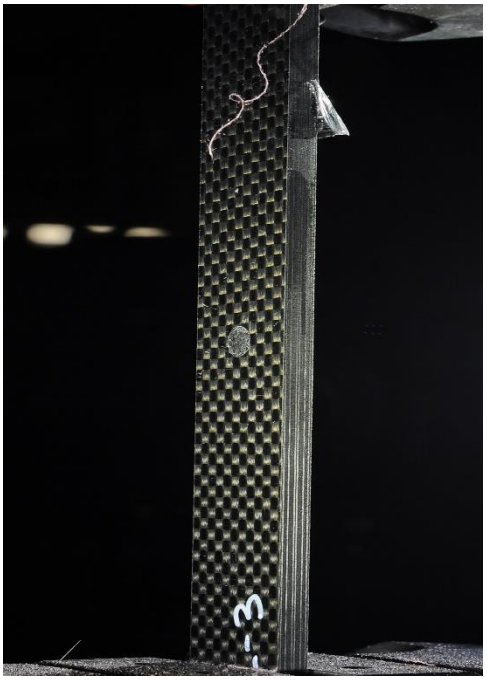

(A2-L-3) at 30k Cycles

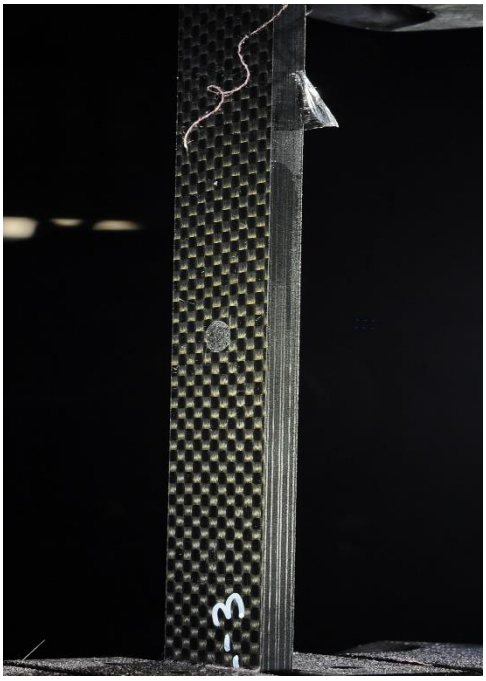

(A2-L-3) at 40k Cycles

Figure C 2-123 Damage Progression in (A2-L-3) Test specimen to 40k Cycles

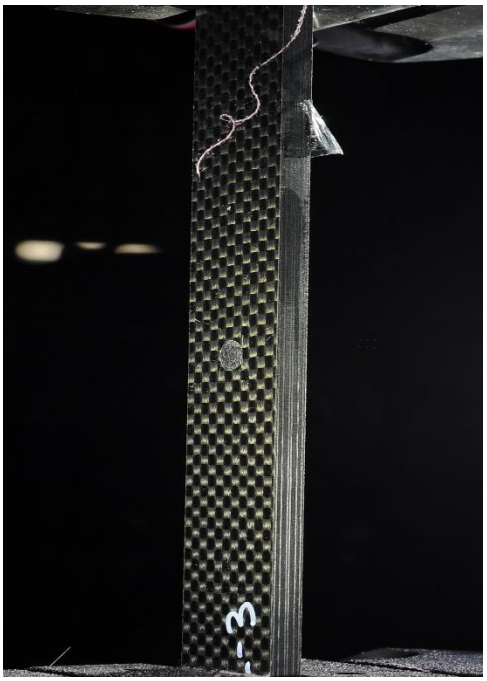

(A2-L-3) at 50k Cycles

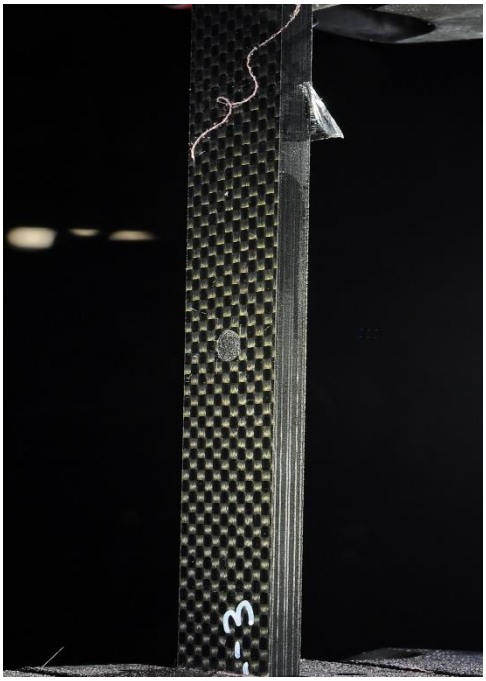

(A2-L-3) at 60k Cycles

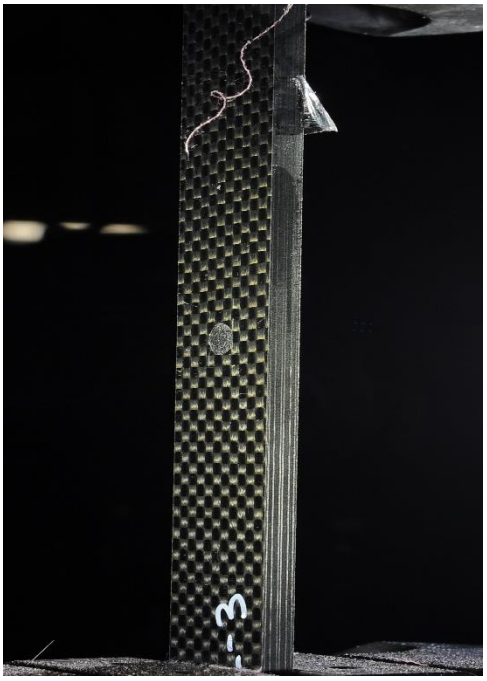

(A2-L-3) at 70k Cycles

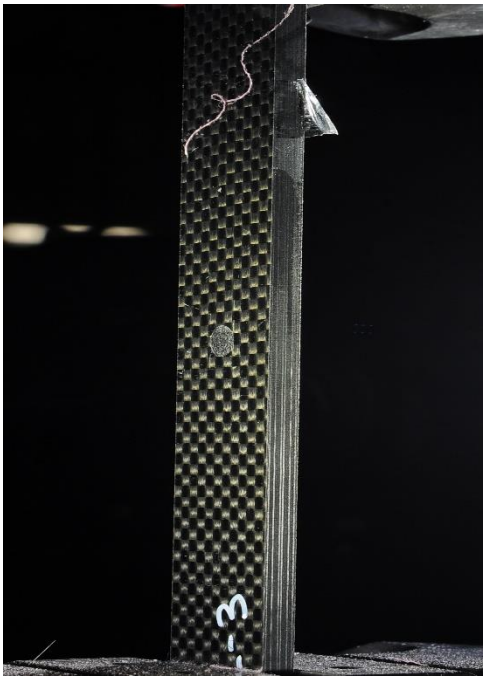

(A2-L-3) at 80k Cycles

Figure C 2-124 Damage Progression in (A2-L-3) Test specimen to 80k Cycles

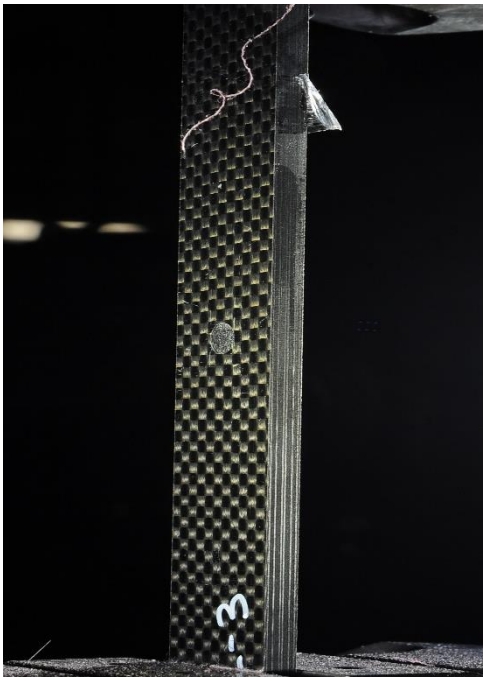

(A2-L-3) at 90k Cycles

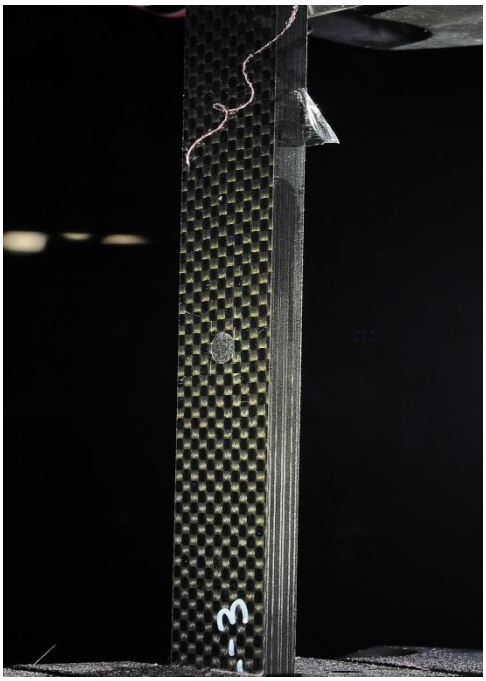

(A2-L-3) at 100k Cycles

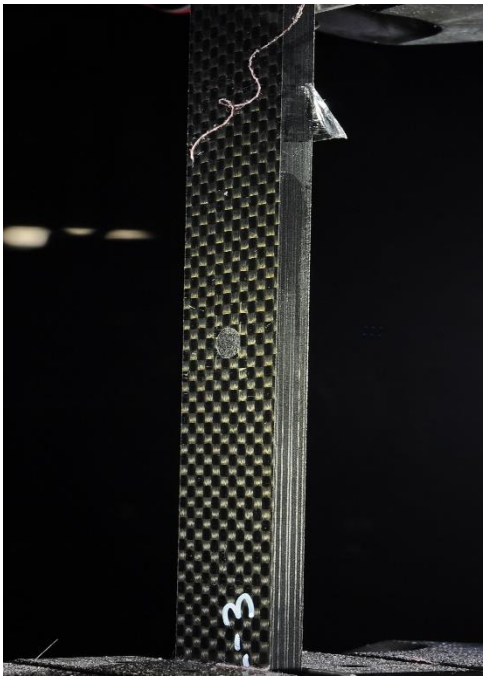

(A2-L-3) at 125k Cycles

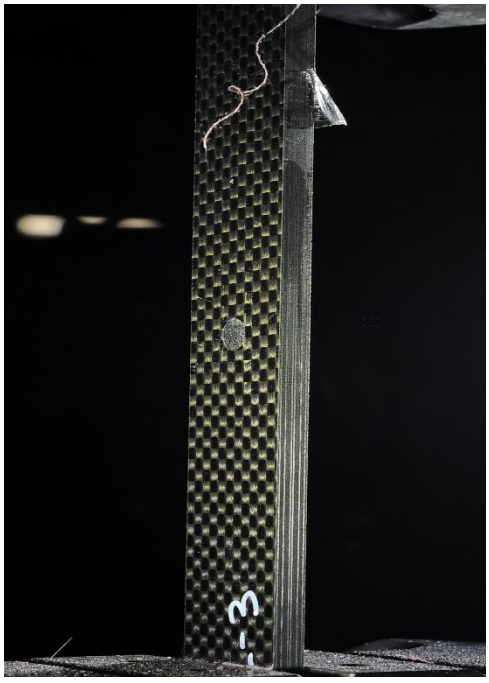

(A2-L-3) at 150k Cycles

Figure C 2-125 Damage Progression in (A2-L-3) Test specimen to 150k Cycles

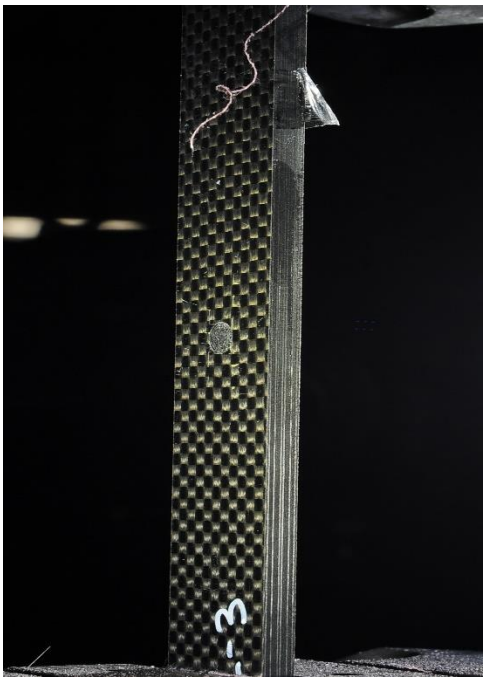

(A2-L-3) at 175k Cycles

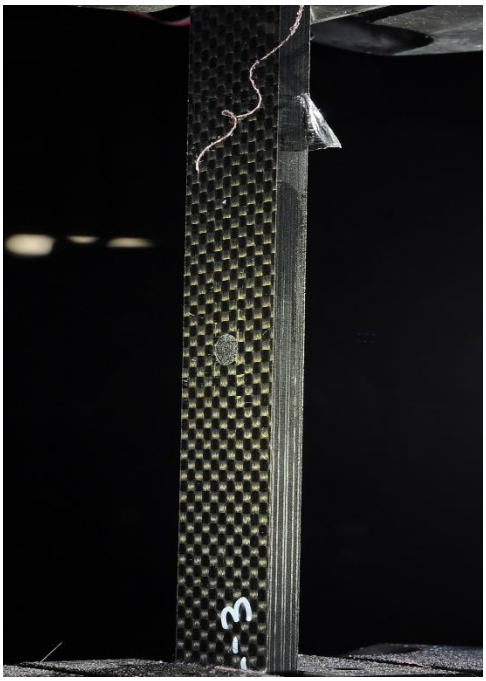

(A2-L-3) at 200k Cycles

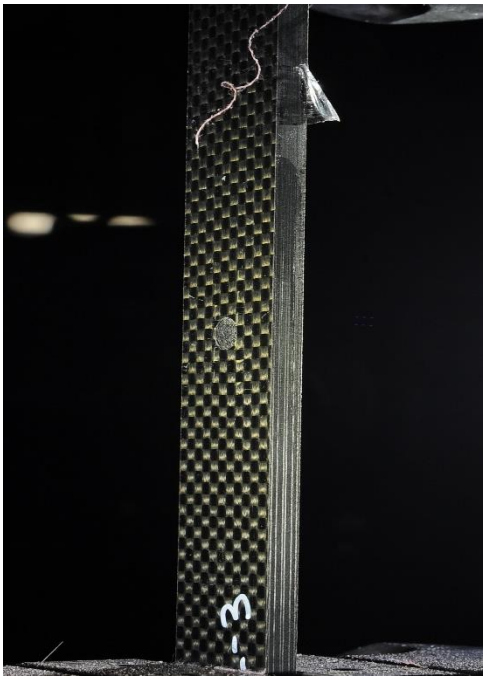

(A2-L-3) at 225k Cycles

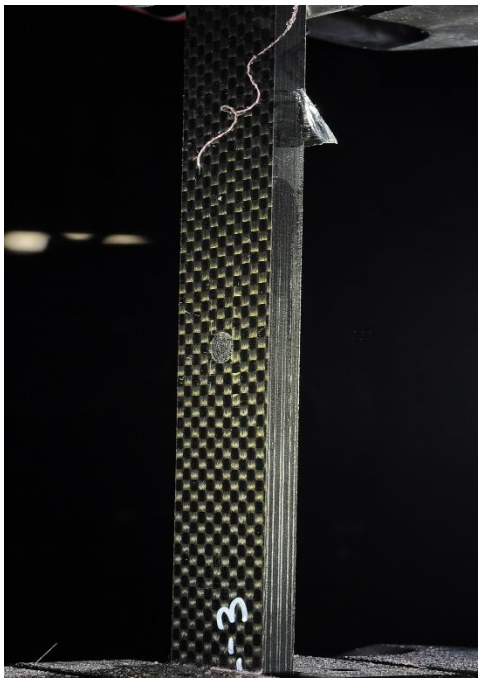

(A2-L-3) at 250k Cycles

Figure C 2-126 Damage Progression in (A2-L-3) Test specimen to 250k Cycles

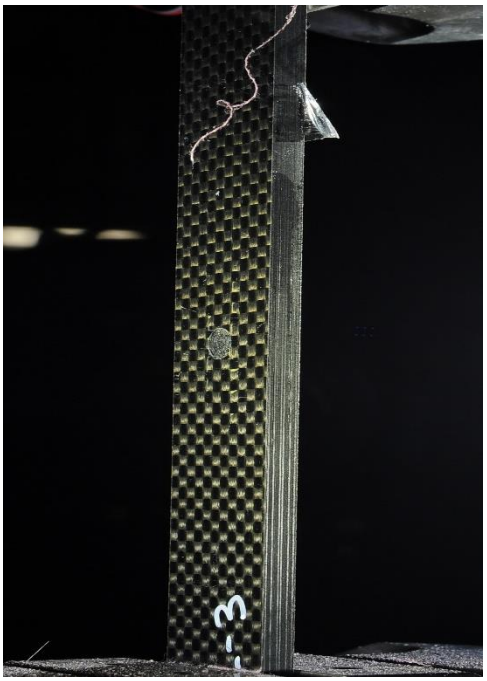

(A2-L-3) at 275k Cycles

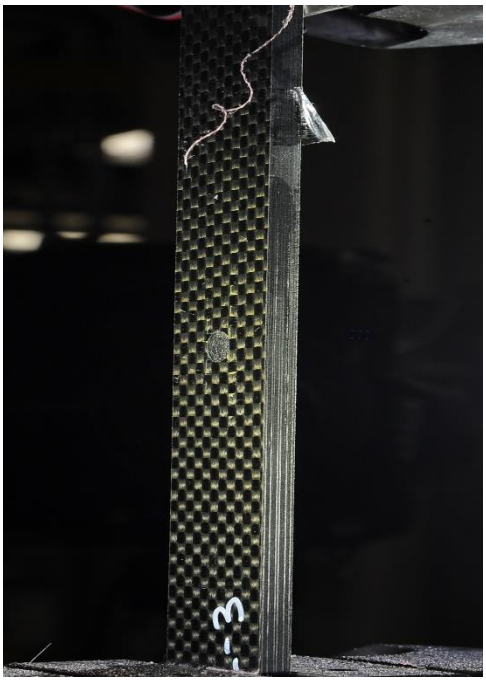

(A2-L-3) at 300k Cycles

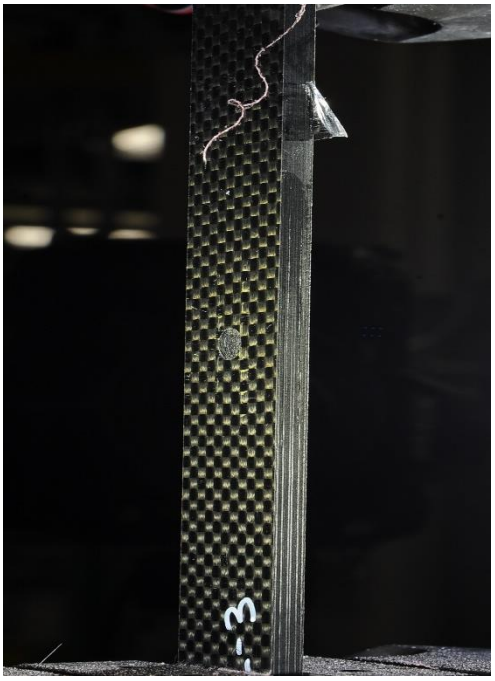

(A2-L-3) at 325k Cycles

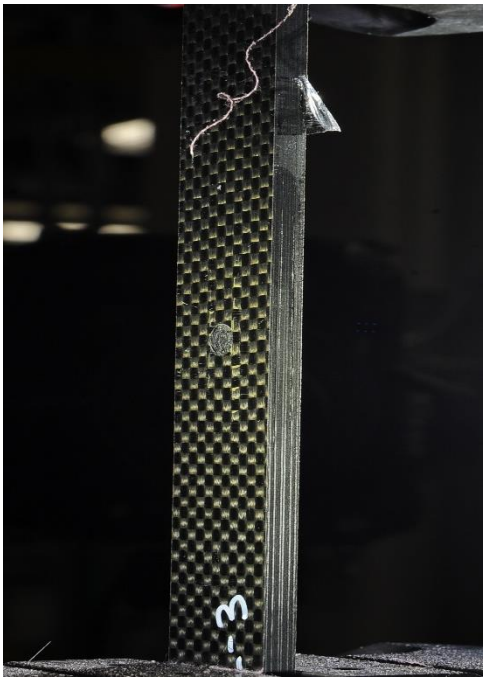

(A2-L-3) at 350k Cycles

Figure C 2-127 Damage Progression in (A2-L-3) Test specimen to 350k Cycles

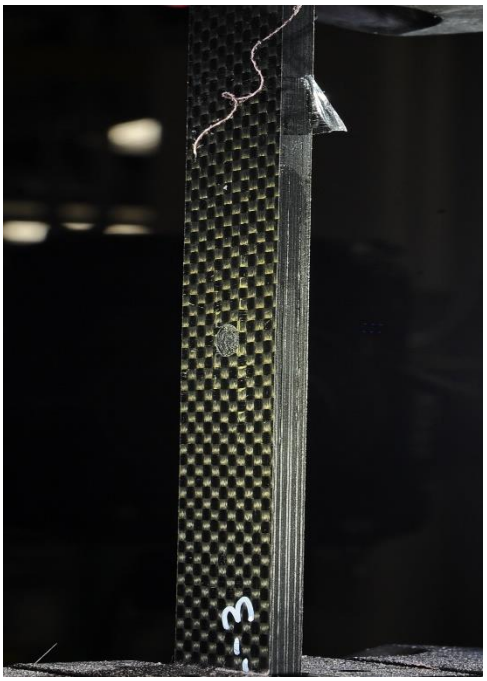

(A2-L-3) at 375k Cycles

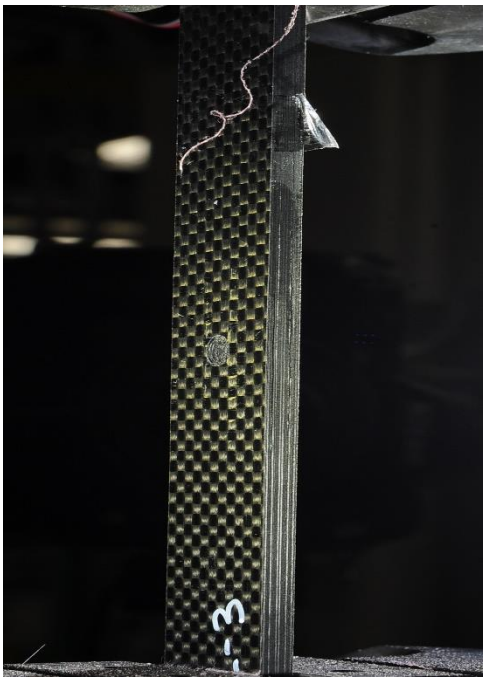

(A2-L-3) at 400k Cycles

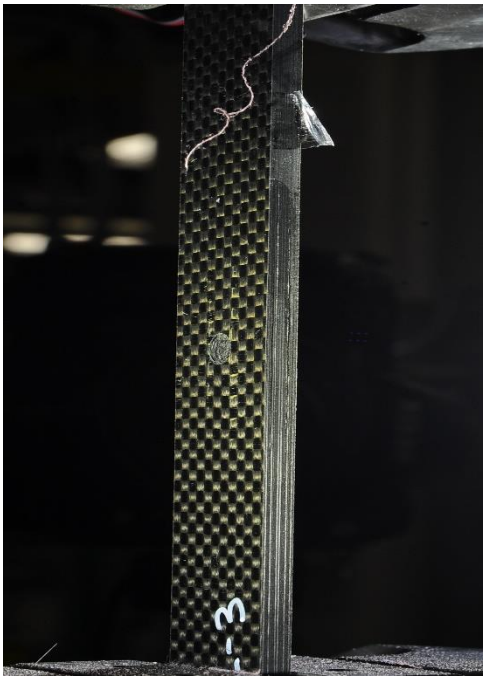

(A2-L-3) at 425k Cycles

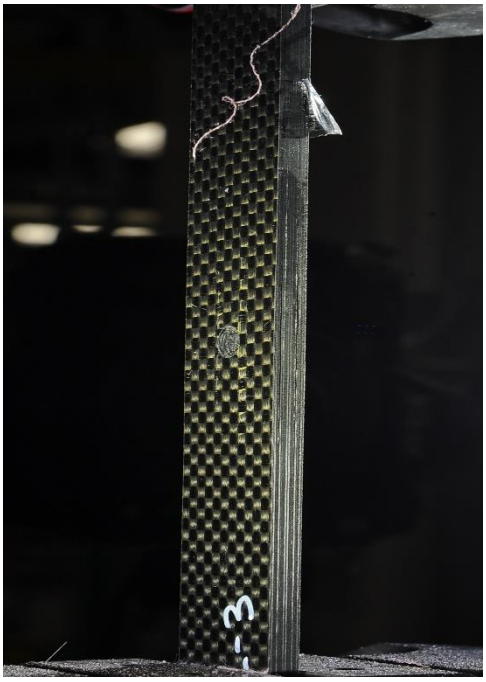

(A2-L-3) at 450k Cycles

Figure C 2-128 Damage Progression in (A2-L-3) Test specimen to 450k Cycles

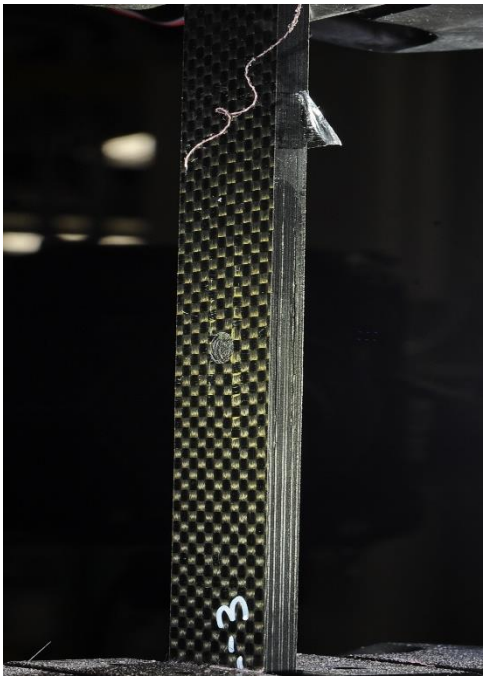

(A2-L-3) at 475k Cycles

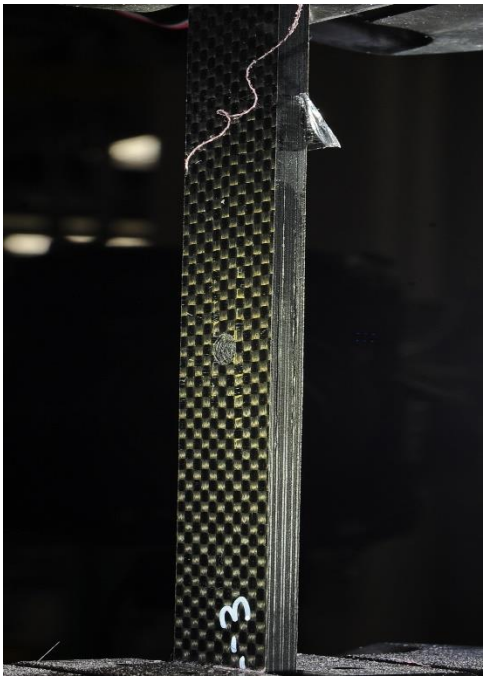

(A2-L-3) at 500k Cycles

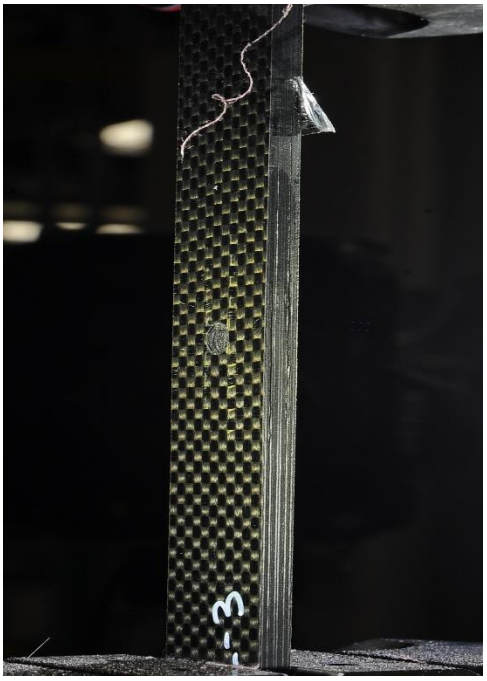

(A2-L-3) at 525k Cycles

(A2-L-3) at 550k Cycles

Figure C 2-129 Damage Progression in (A2-L-3) Test specimen to 550k Cycles

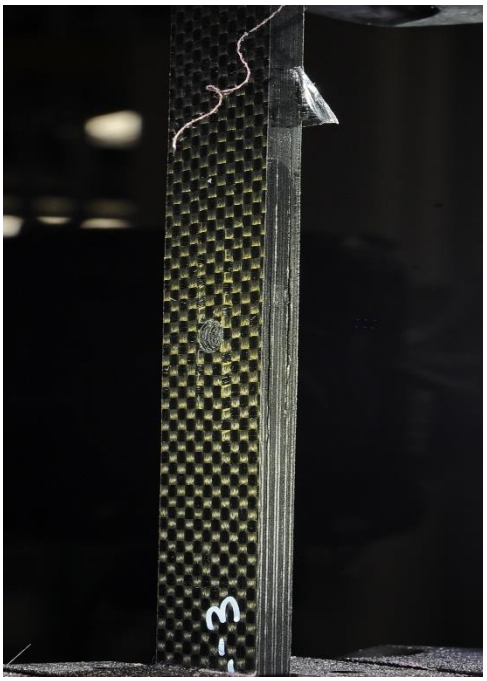

(A2-L-3) at 575k Cycles

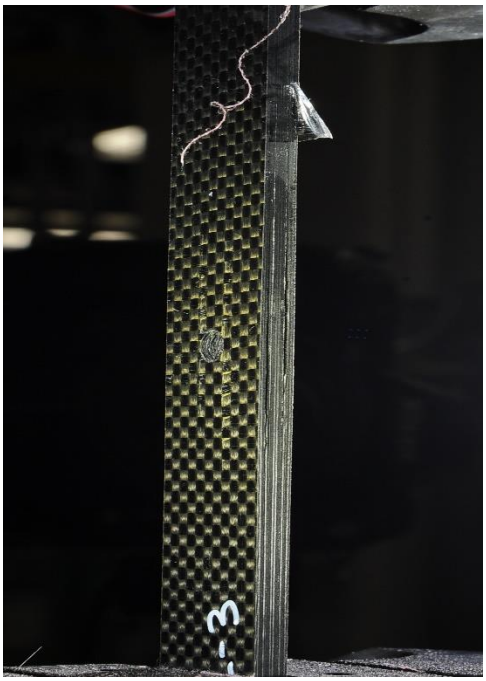

(A2-L-3) at 600k Cycles

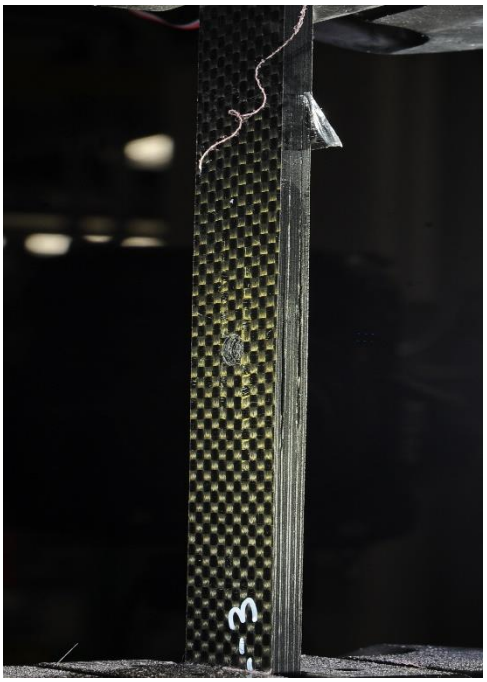

(A2-L-3) at 625k Cycles

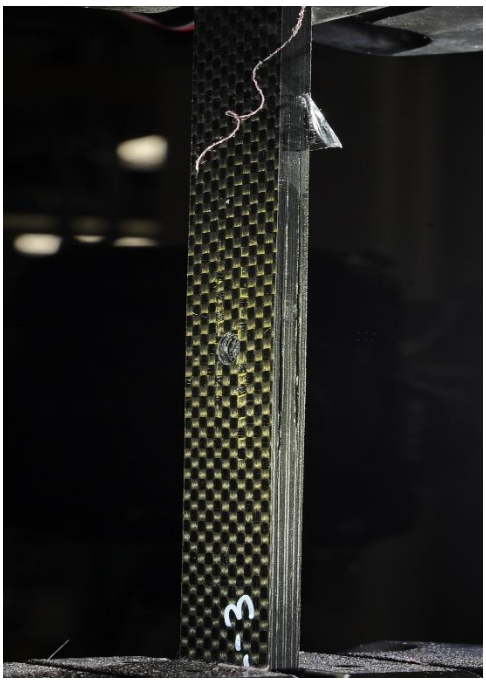

(A2-L-3) at 650k Cycles

Figure C 2-130 Damage Progression in (A2-L-3) Test specimen to 650k Cycles

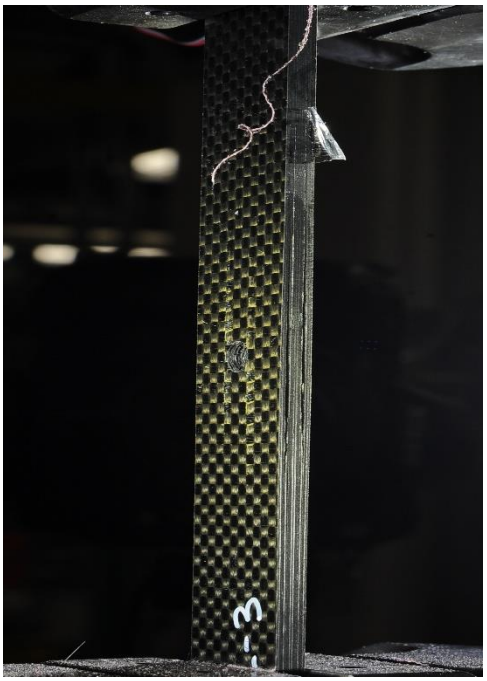

(A2-L-3) at 675k Cycles

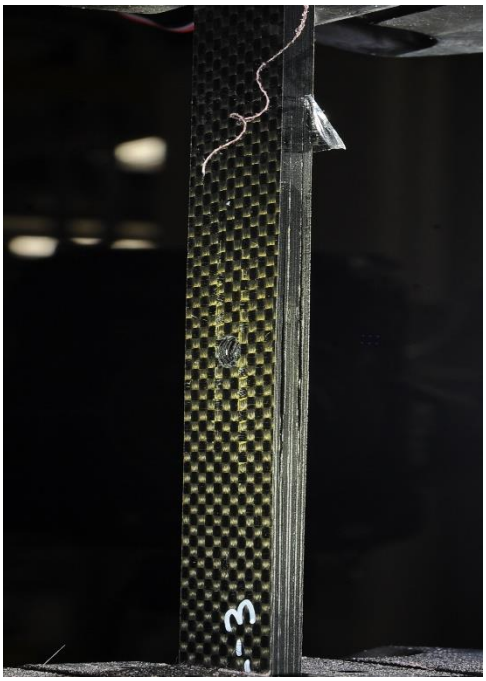

(A2-L-3) at 700k Cycles

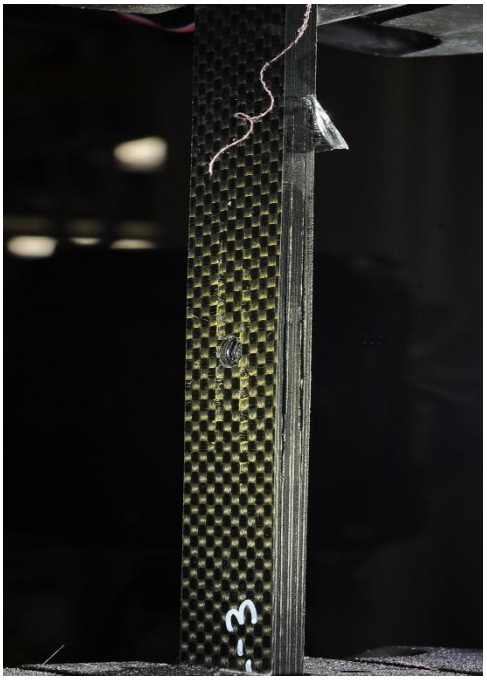

(A2-L-3) at 725k Cycles

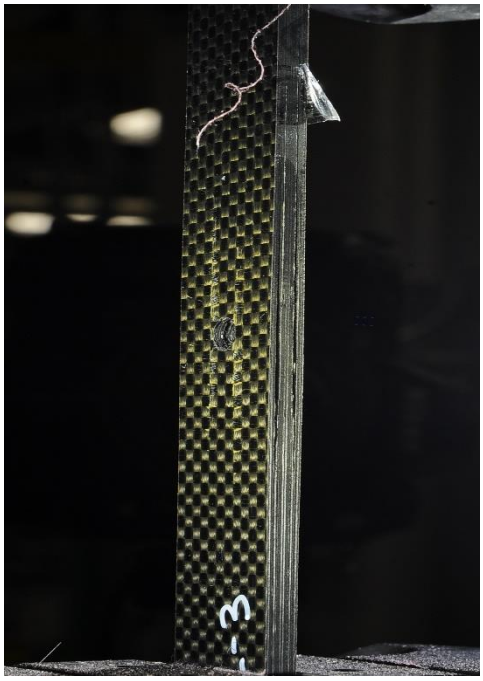

(A2-L-3) at 750k Cycles

Figure C 2-131 Damage Progression in (A2-L-3) Test specimen to 750k Cycles

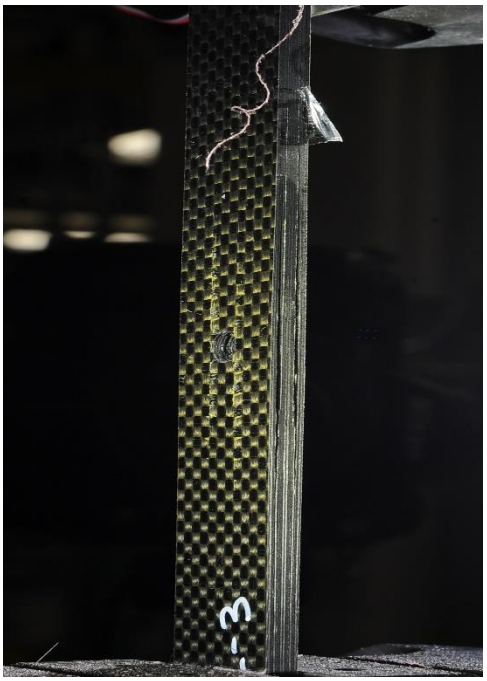

(A2-L-3) at 775k Cycles

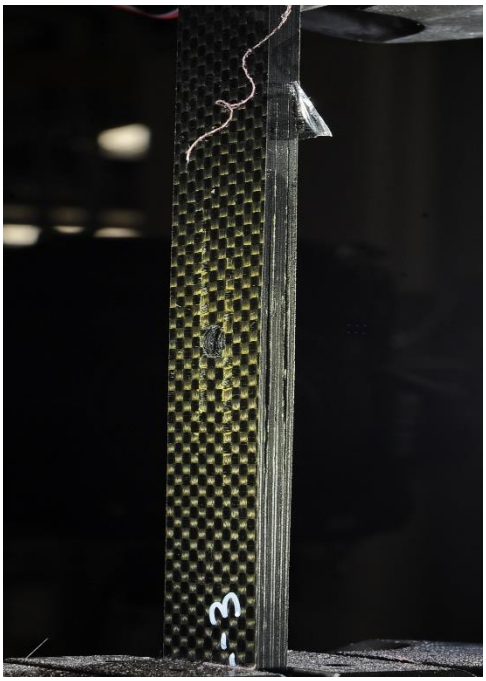

(A2-L-3) at 800k Cycles

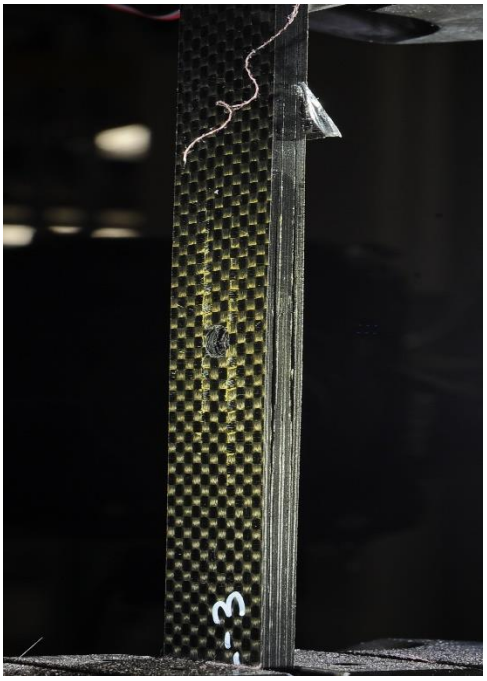

(A2-L-3) at 825k Cycles

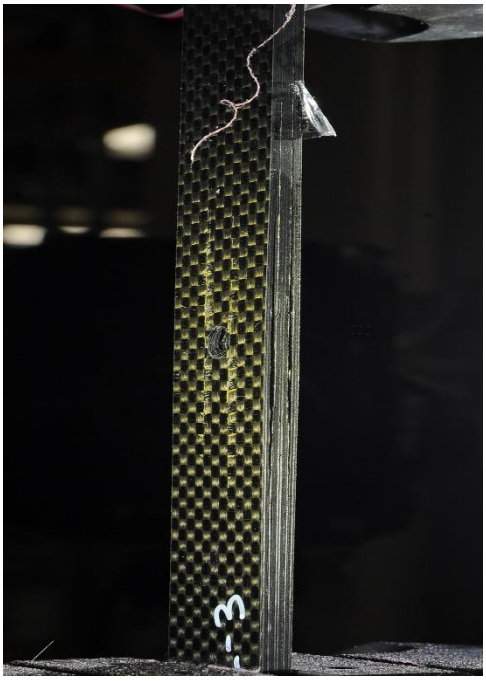

(A2-L-3) at 850k Cycles

Figure C 2-132 Damage Progression in (A2-L-3) Test specimen to 850k Cycles

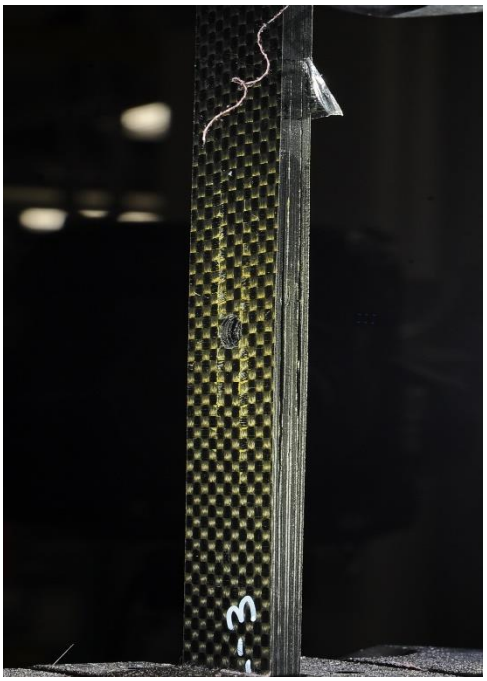

(A2-L-3) at 875k Cycles

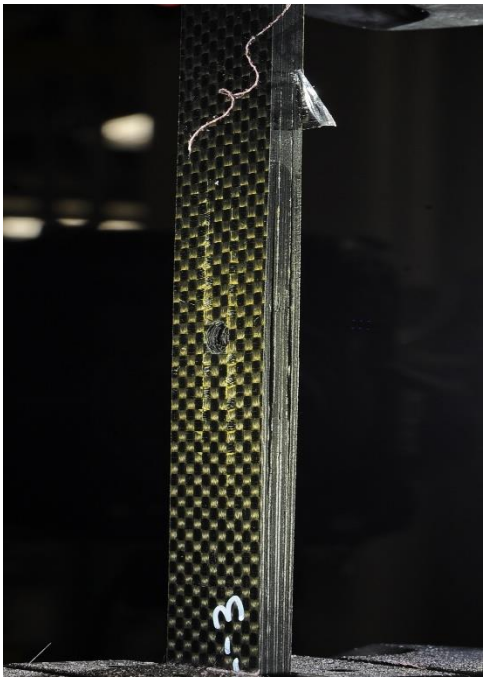

(A2-L-3) at 900k Cycles

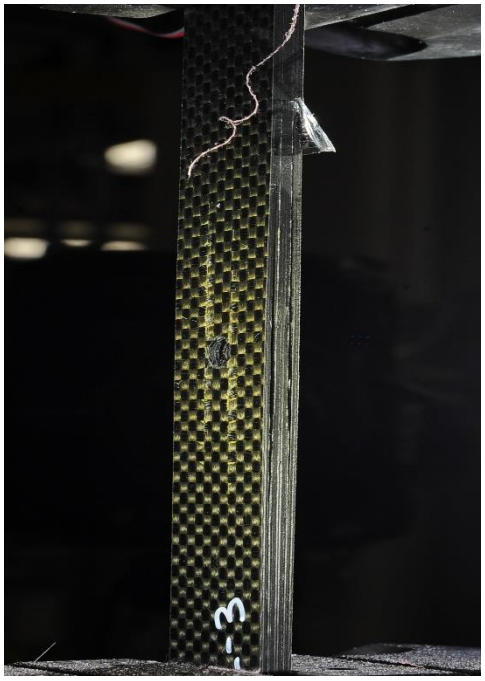

(A2-L-3) at 925k Cycles

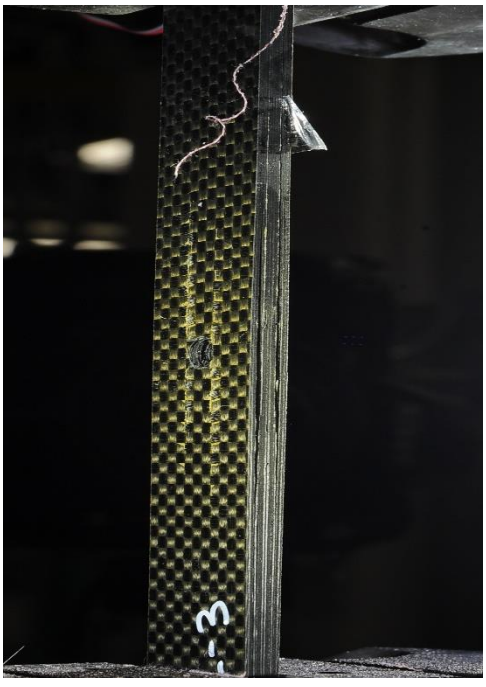

(A2-L-3) at 950k Cycles

Figure C 2-133 Damage Progression in (A2-L-3) Test specimen to 950k Cycles

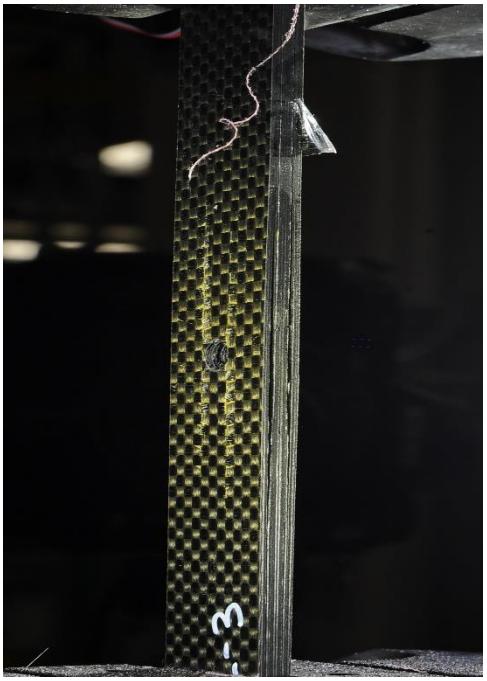

(A2-L-3) at 975k Cycles

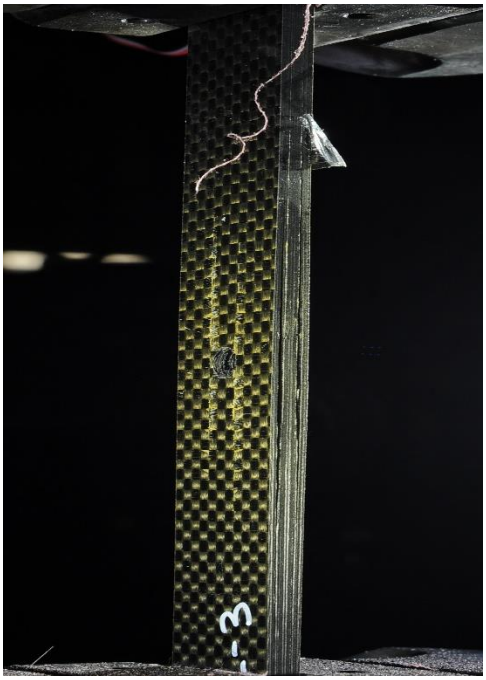

(A2-L-3) at 1000k Cycles

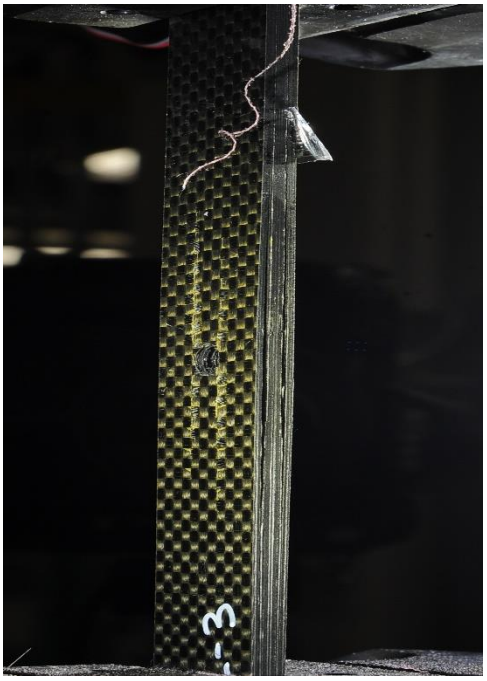

(A2-L-3) at Pre RS

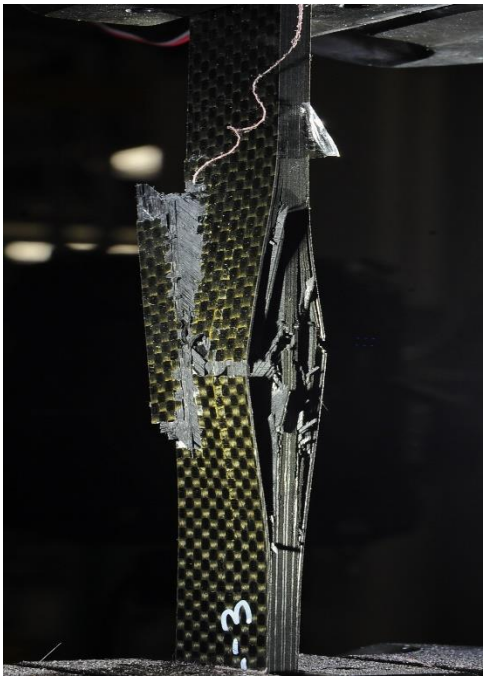

(A2-L-3) at Failure

Figure C 2-134 Damage Progression in (A2-L-3) Test specimen to Failure

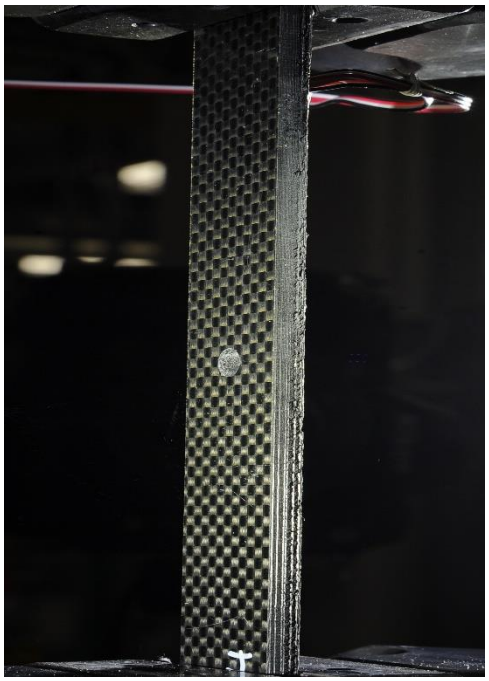

(A2-L-4) at 1 Cycle

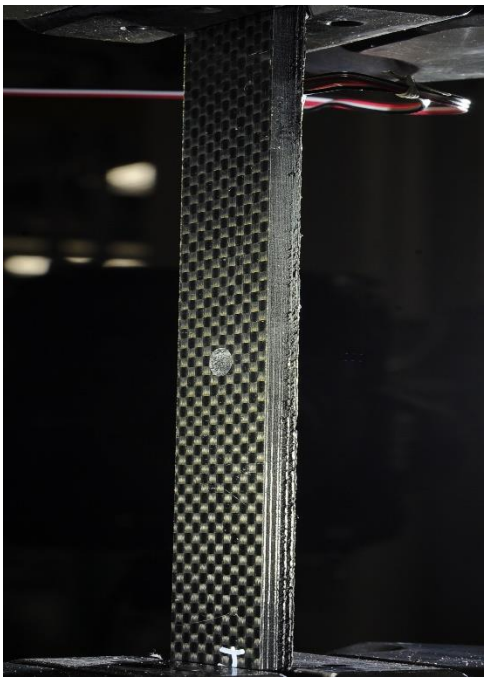

(A2-L-4) at 100 Cycles

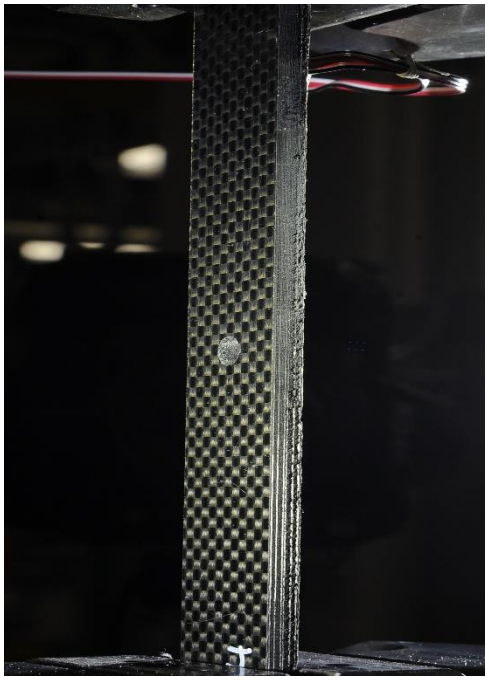

(A2-L-4) at 1k Cycles

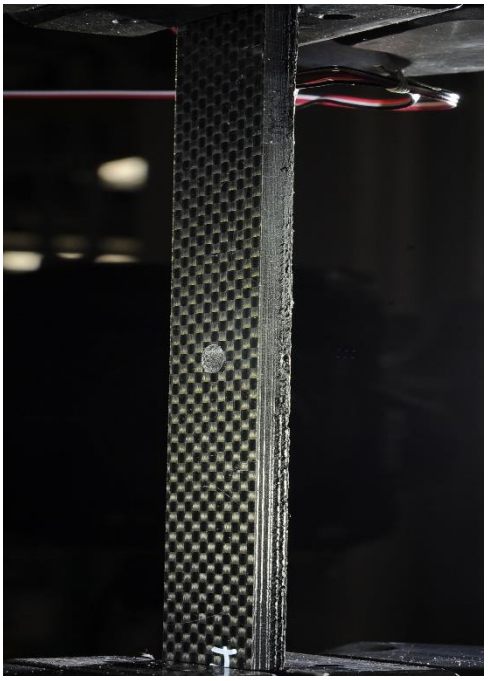

(A2-L-4) at 5k Cycles

Figure C 2-135 Damage Progression in (A2-L-4) Test specimen to 5k Cycles

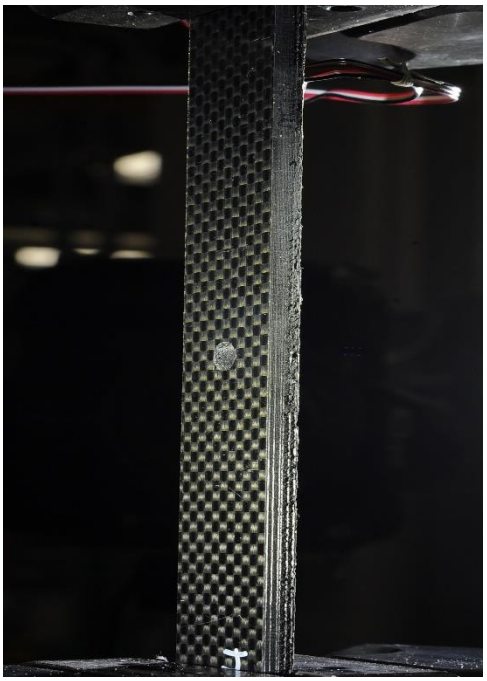

(A2-L-4) at 10k Cycles

(A2-L-4) at 20k Cycles

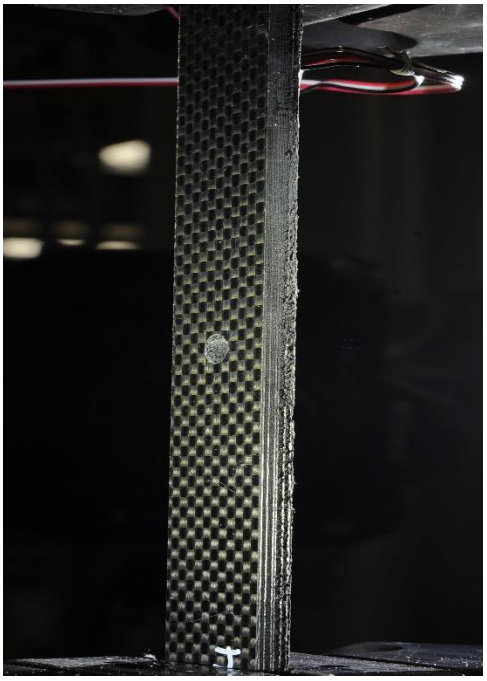

(A2-L-4) at 30k Cycles

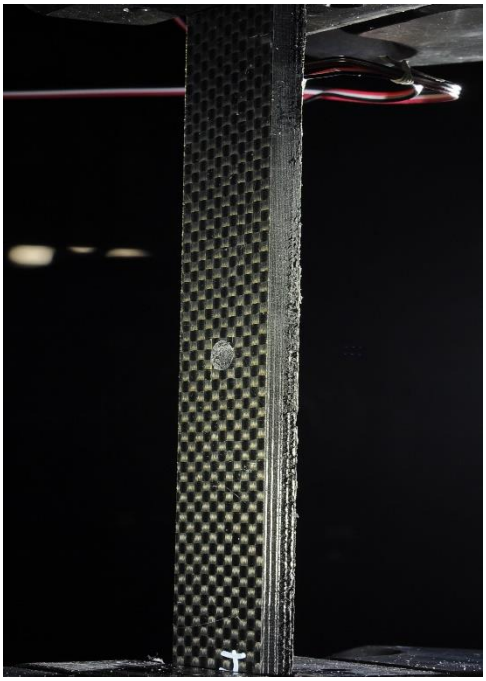

(A2-L-4) at 40k Cycles

Figure C 2-136 Damage Progression in (A2-L-4) Test specimen to 40k Cycles

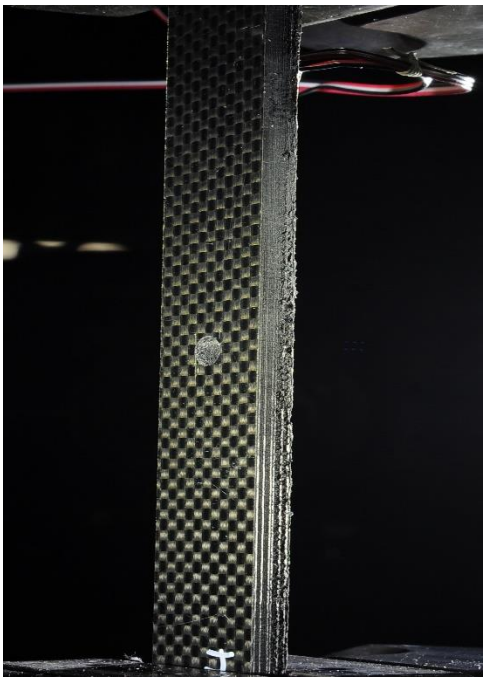

(A2-L-4) at 50k Cycles

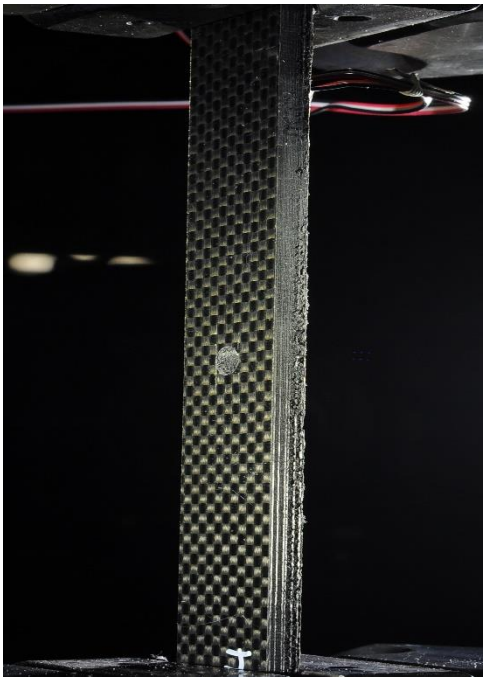

(A2-L-4) at 60k Cycles

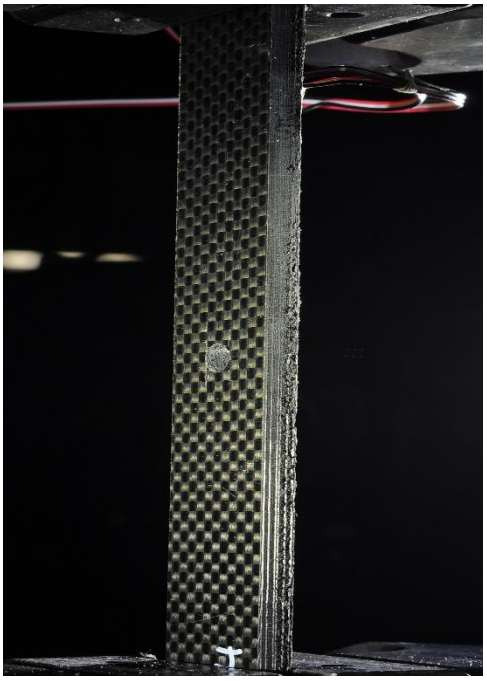

(A2-L-4) at 70k Cycles

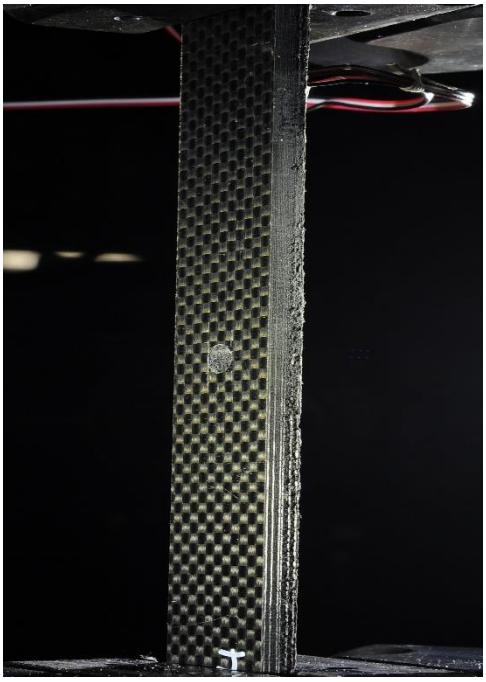

(A2-L-4) at 80k Cycles

Figure C 2-137 Damage Progression in (A2-L-4) Test specimen to 80k Cycles

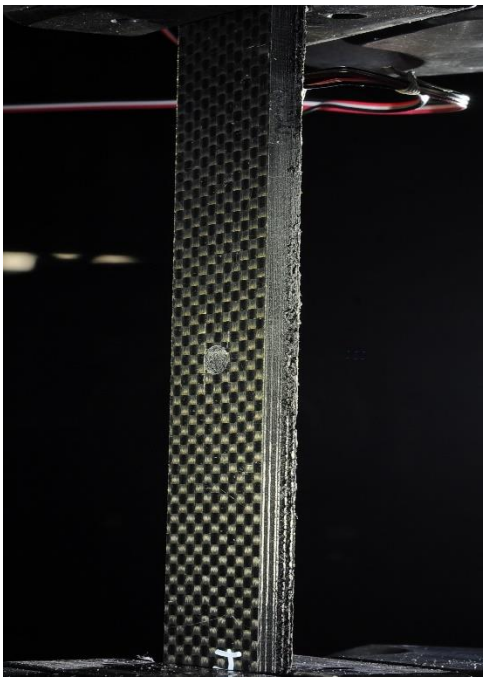

(A2-L-4) at 90k Cycles

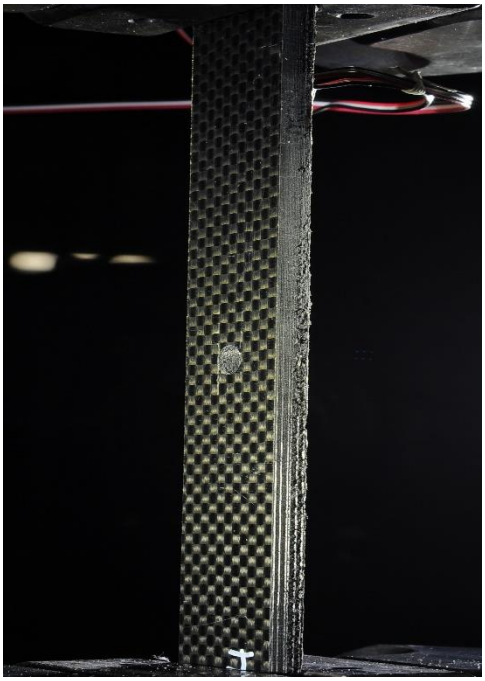

(A2-L-4) at 100k Cycles

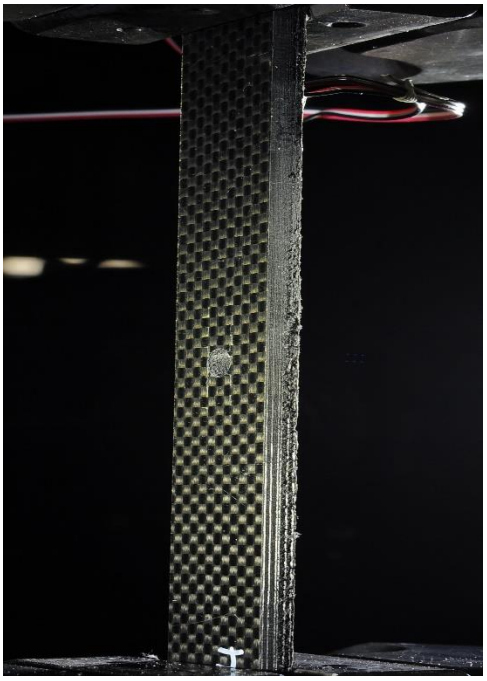

(A2-L-4) at 125k Cycles

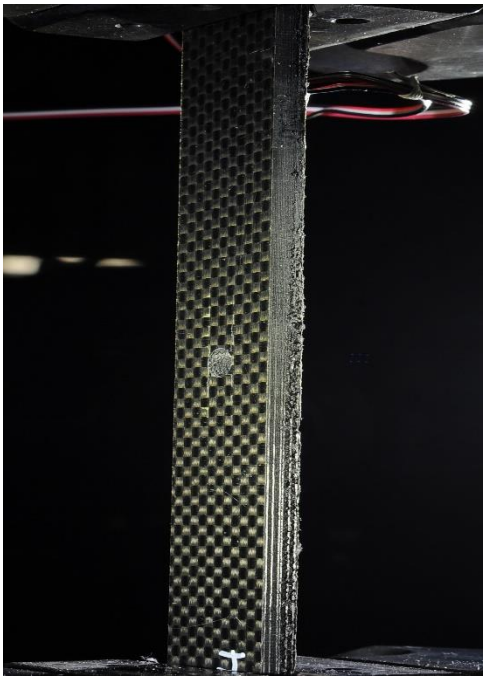

(A2-L-4) at 150k Cycles

Figure C 2-138 Damage Progression in (A2-L-4) Test specimen to 150k Cycles

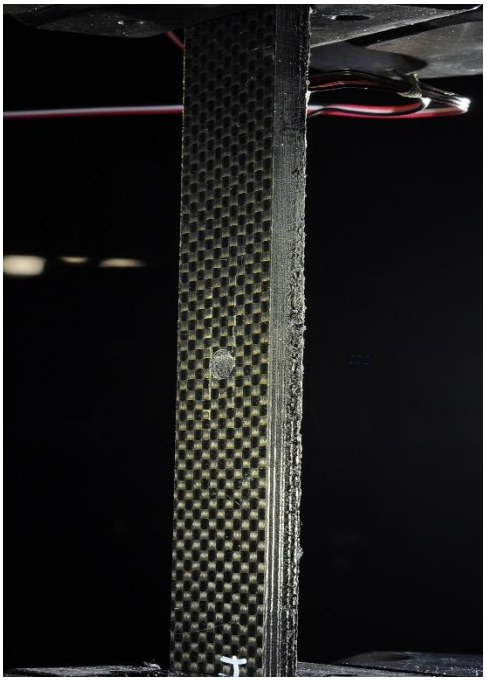

(A2-L-4) at 175k Cycles

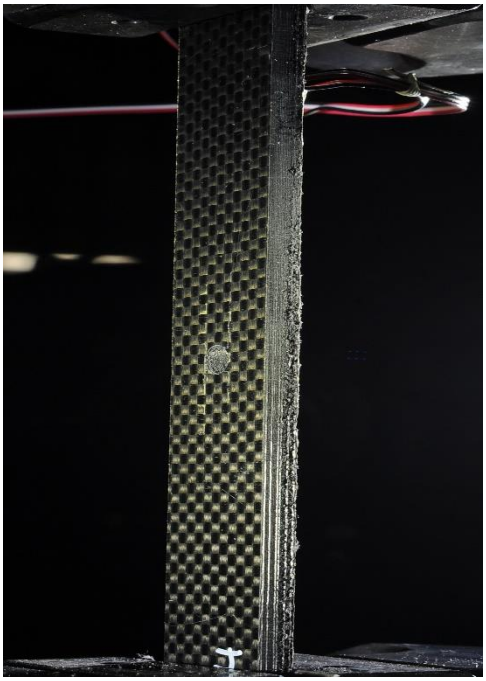

(A2-L-4) at 200k Cycles

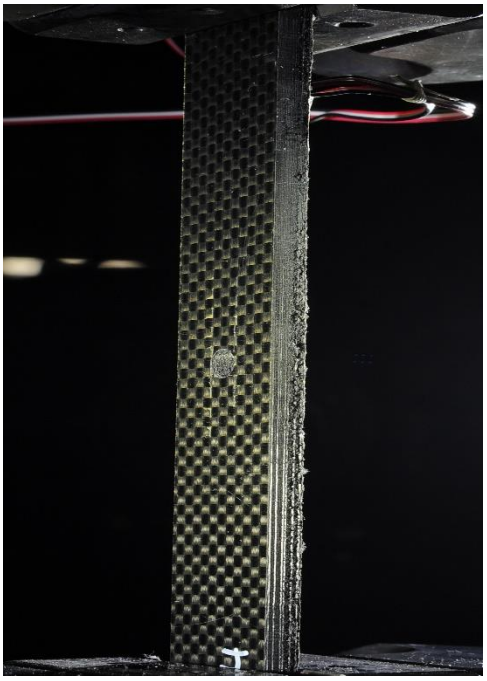

(A2-L-4) at 225k Cycles

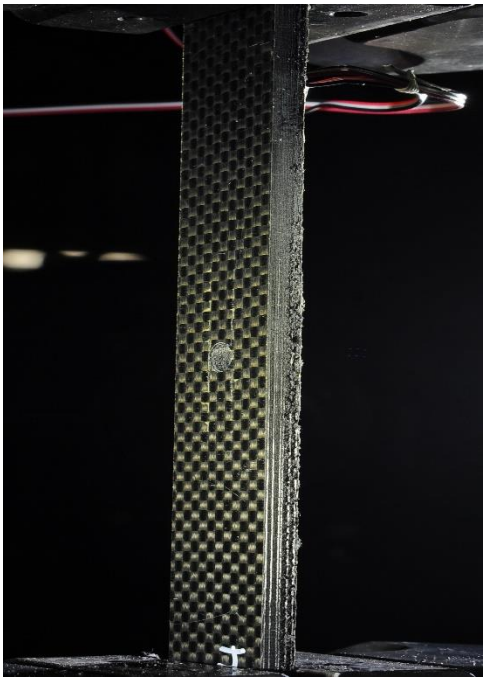

(A2-L-4) at 250k Cycles

Figure C 2-139 Damage Progression in (A2-L-4) Test specimen to 250k Cycles

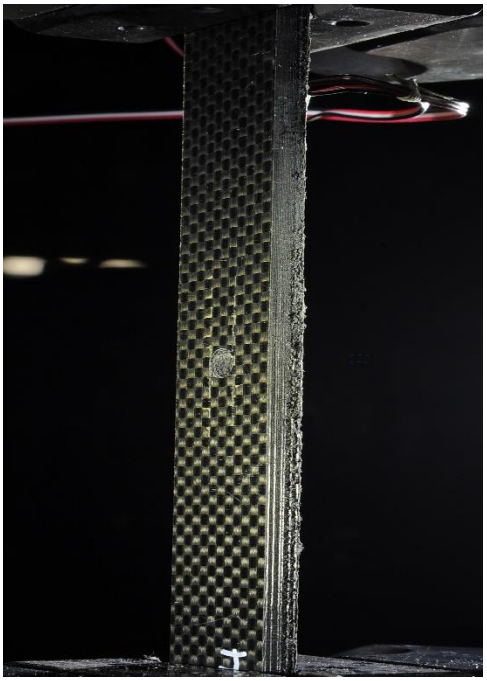

(A2-L-4) at 275k Cycles

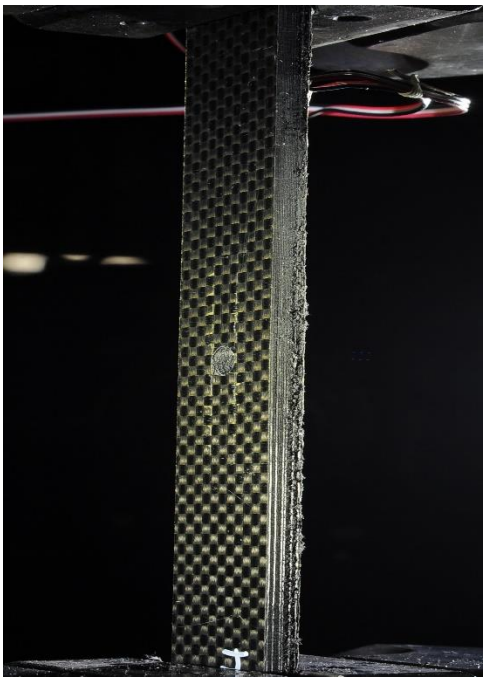

(A2-L-4) at 300k Cycles

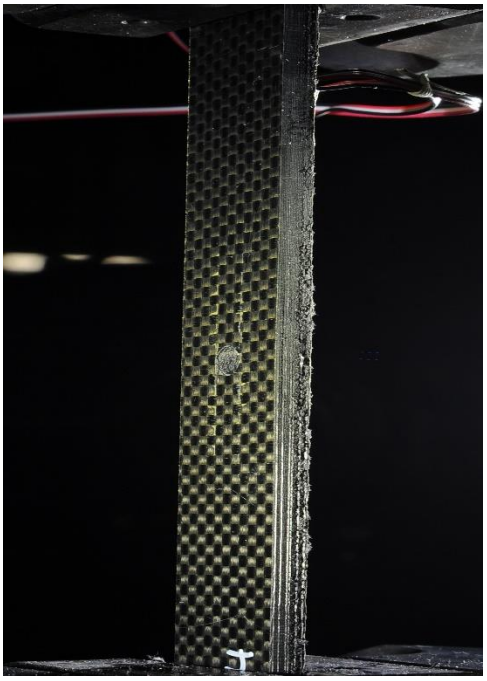

(A2-L-4) at 325k Cycles

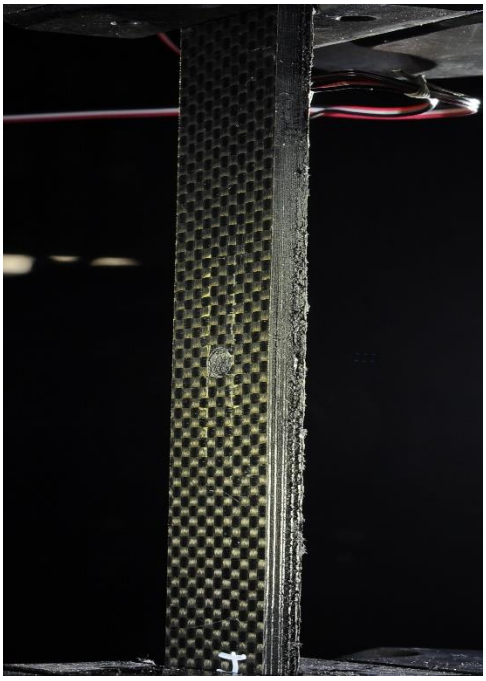

(A2-L-4) at 350k Cycles

Figure C 2-140 Damage Progression in (A2-L-4) Test specimen to 350k Cycles

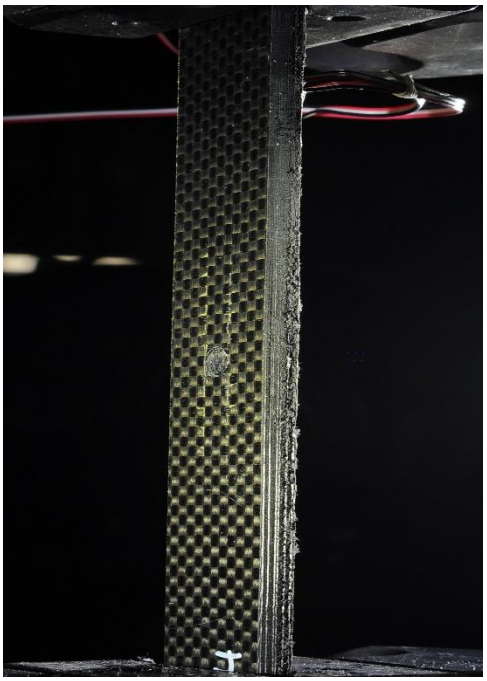

(A2-L-4) at 375k Cycles

(A2-L-4) at 400k Cycles

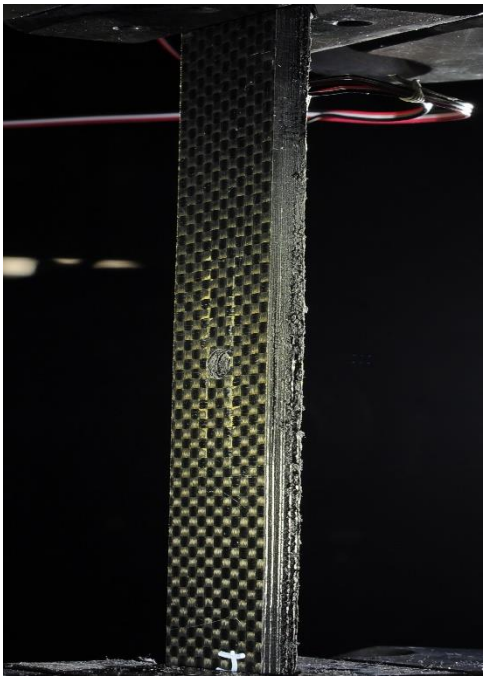

(A2-L-4) at 425k Cycles

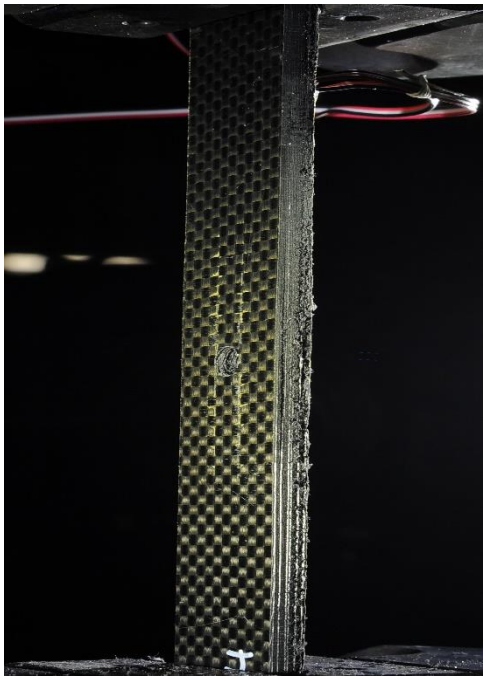

(A2-L-4) at 450k Cycles

Figure C 2-141 Damage Progression in (A2-L-4) Test specimen to 450k Cycles

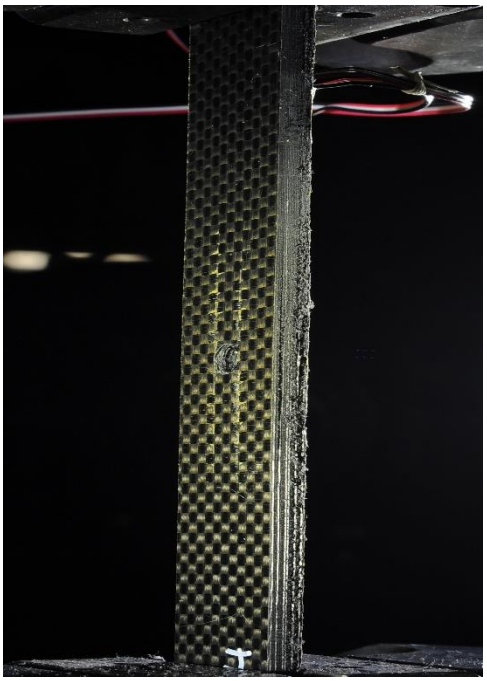

(A2-L-4) at 475k Cycles

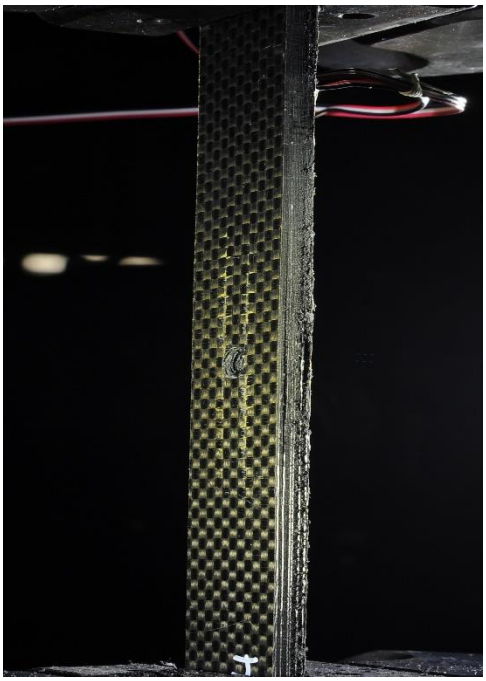

(A2-L-4) at 500k Cycles

(A2-L-4) at 525k Cycles

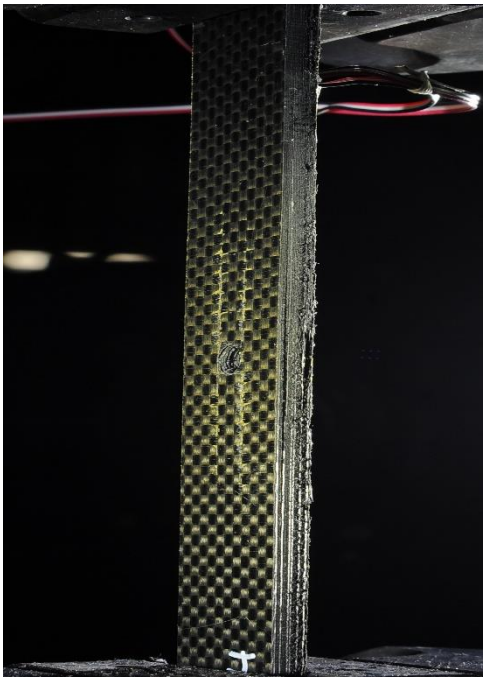

(A2-L-4) at 550k Cycles

Figure C 2-142 Damage Progression in (A2-L-4) Test specimen to 550k Cycles

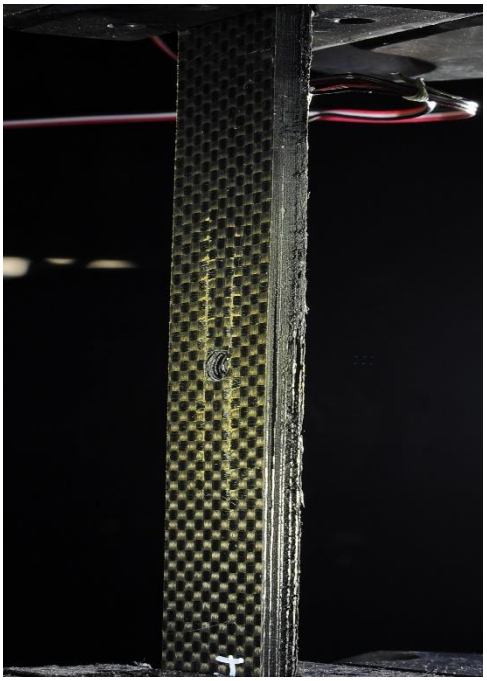

(A2-L-4) at 575k Cycles

(A2-L-4) at Failure

Figure C 2-143 Damage Progression in (A2-L-4) Test specimen to Failure

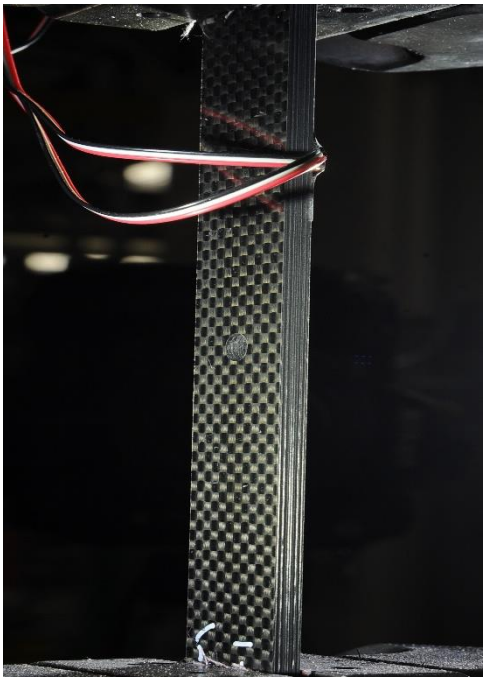

(B2-L-1) at 1 Cycle

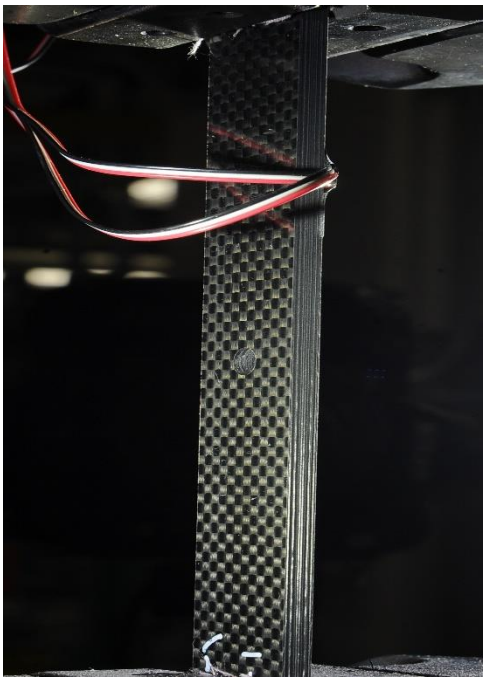

(B2-L-1) at 100 Cycles

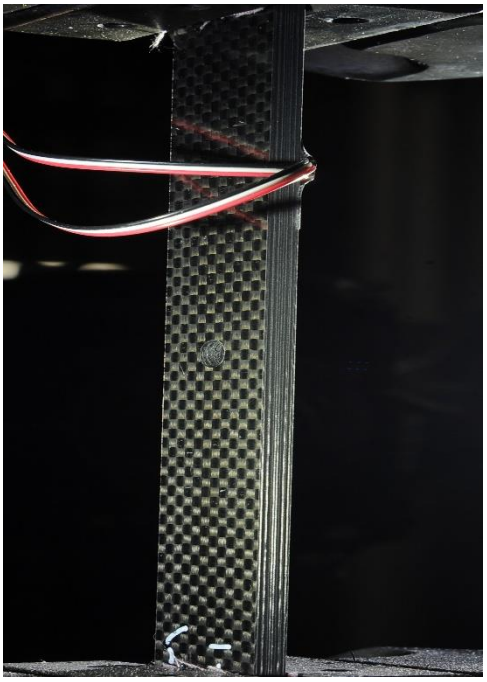

(B2-L-1) at 1k Cycles

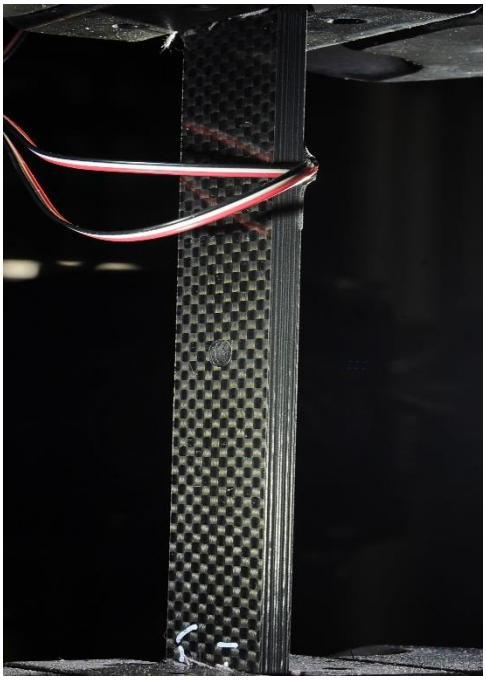

(B2-L-1) at 5k Cycles

Figure C 2-144 Damage Progression in (B2-L-1) Test specimen to 5k Cycles

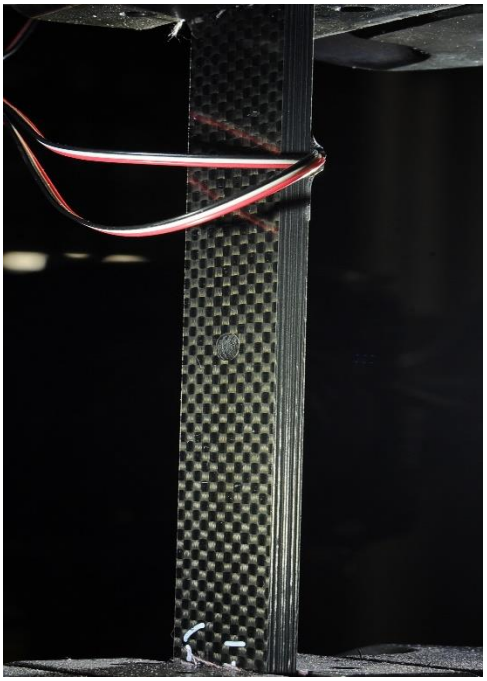

(B2-L-1) at 10k Cycles

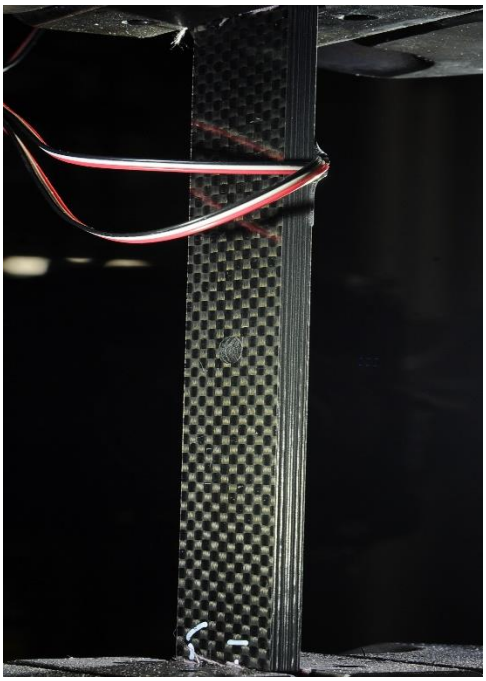

(B2-L-1) at 20k Cycles

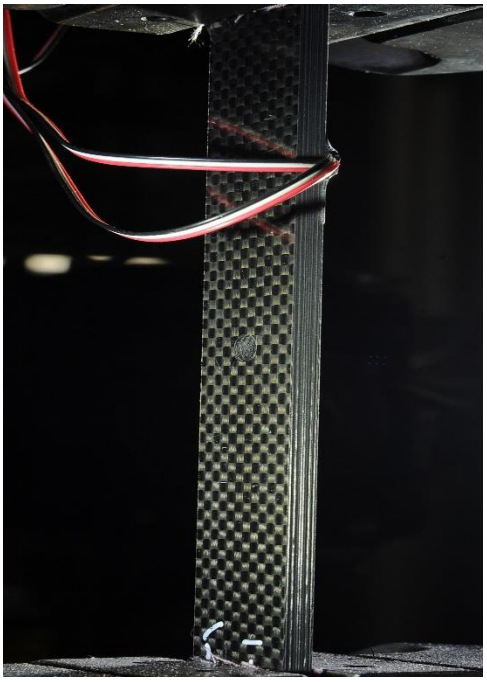

(B2-L-1) at 30k Cycles

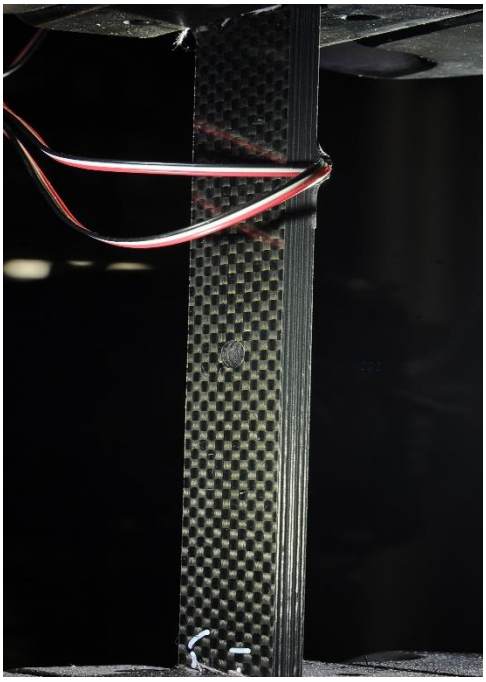

(B2-L-1) at 40k Cycles

Figure C 2-145 Damage Progression in (B2-L-1) Test specimen to 40k Cycles

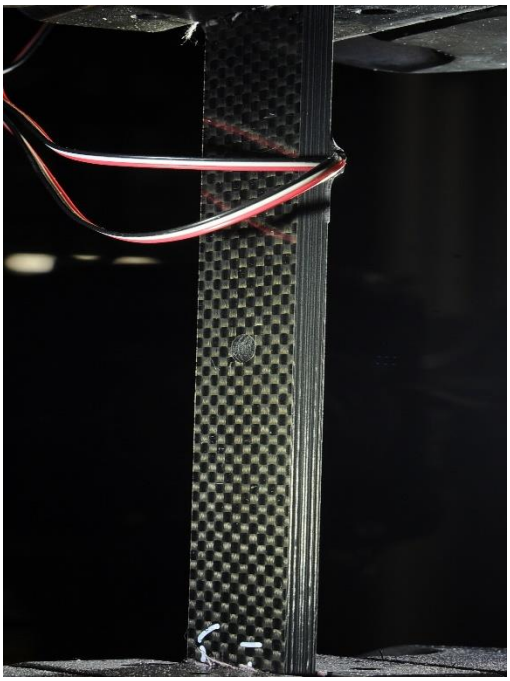

(B2-L-1) at 50k Cycles

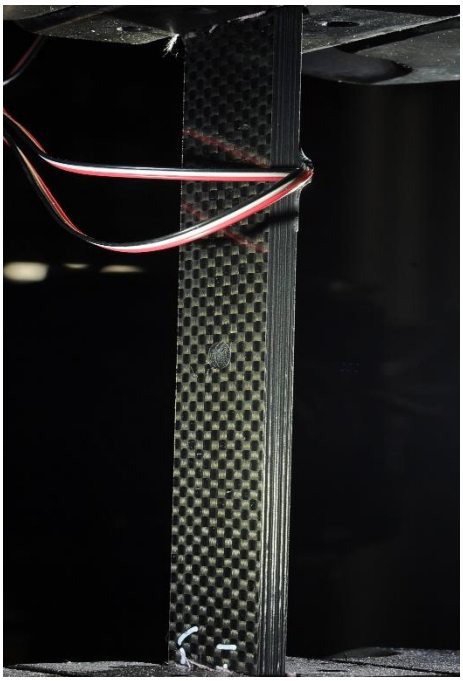

(B2-L-1) at 60k Cycles

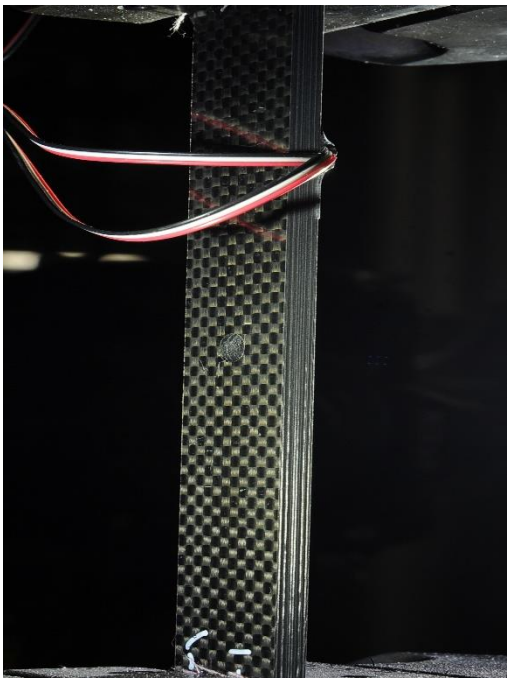

(B2-L-1) at 70k Cycles

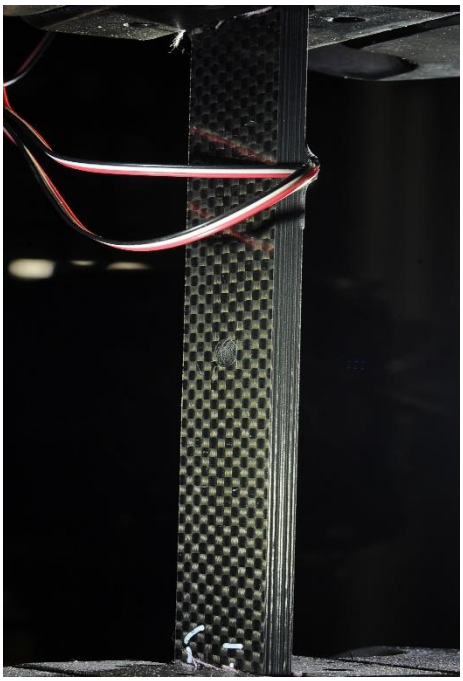

(B2-L-1) at 80k Cycles

Figure C 2-146 Damage Progression in (B2-L-1) Test specimen to 80k Cycles

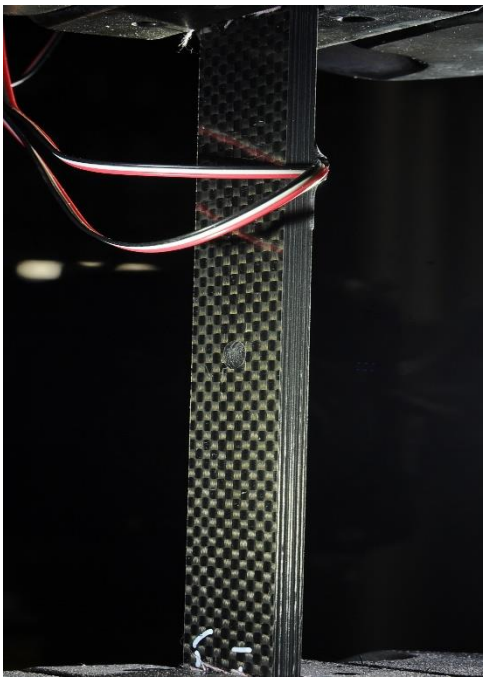

(B2-L-1) at 90k Cycles

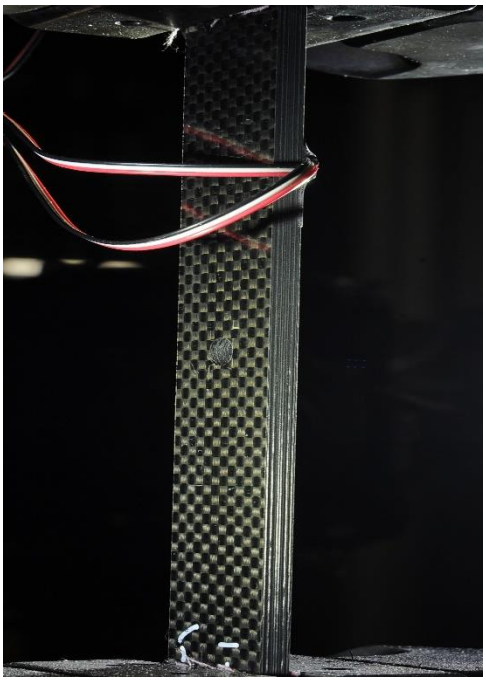

(B2-L-1) at 100k Cycles

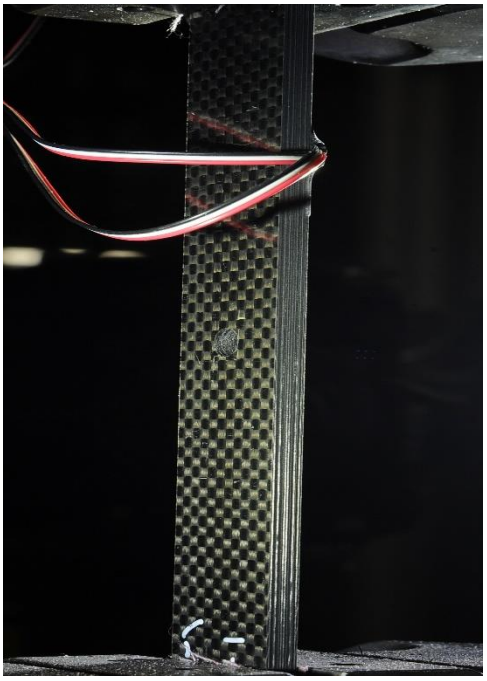

(B2-L-1) at 125k Cycles

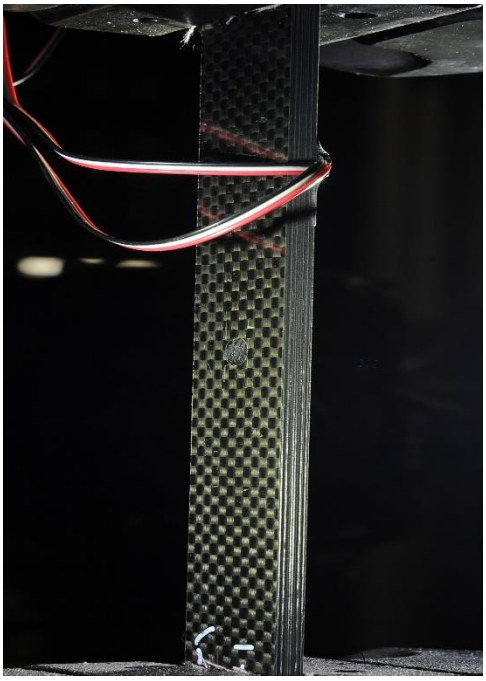

(B2-L-1) at 150k Cycles

Figure C 2-147 Damage Progression in (B2-L-1) Test specimen to 150k Cycles

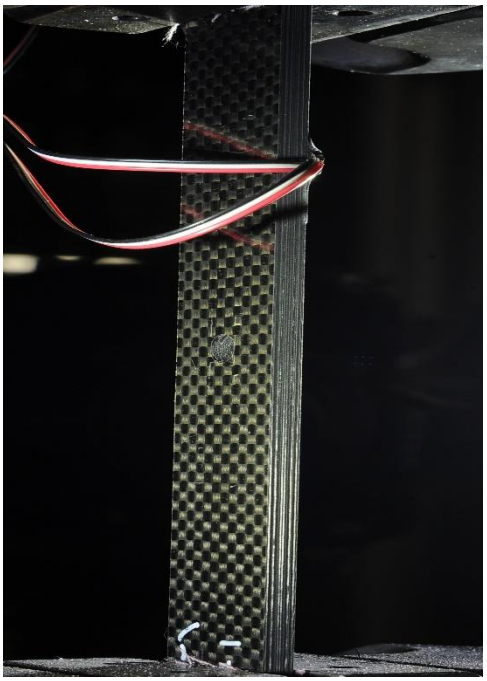

(B2-L-1) at 175k Cycles

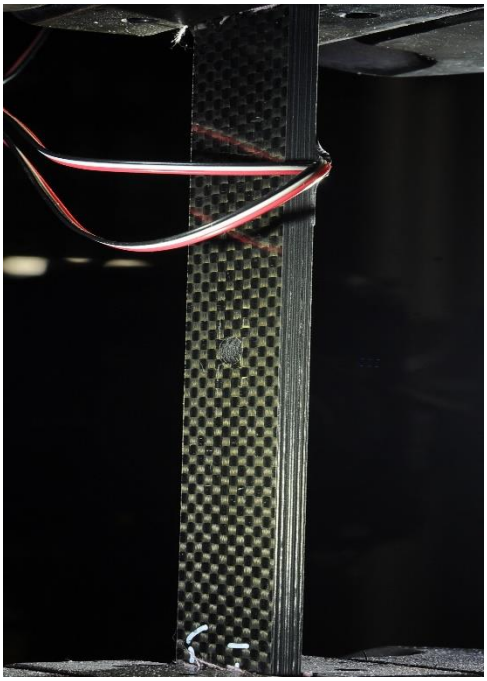

(B2-L-1) at 200k Cycles

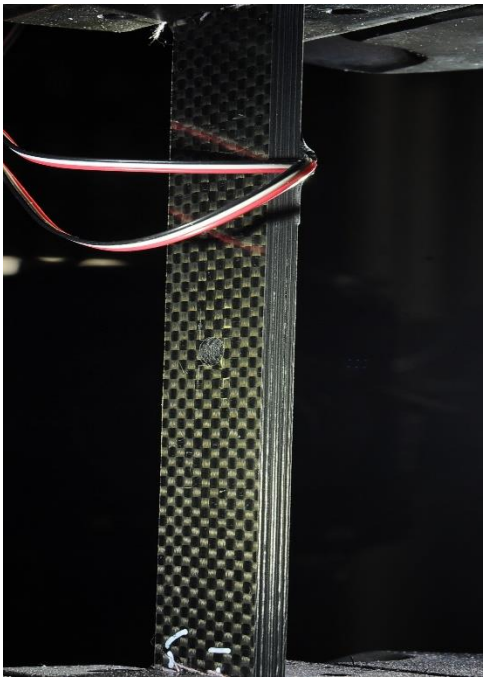

(B2-L-1) at 225k Cycles

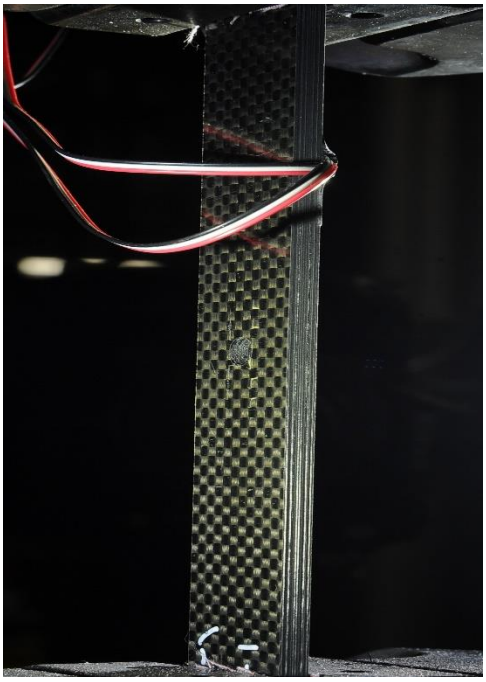

(B2-L-1) at 250k Cycles

Figure C 2-148 Damage Progression in (B2-L-1) Test specimen to 250k Cycles

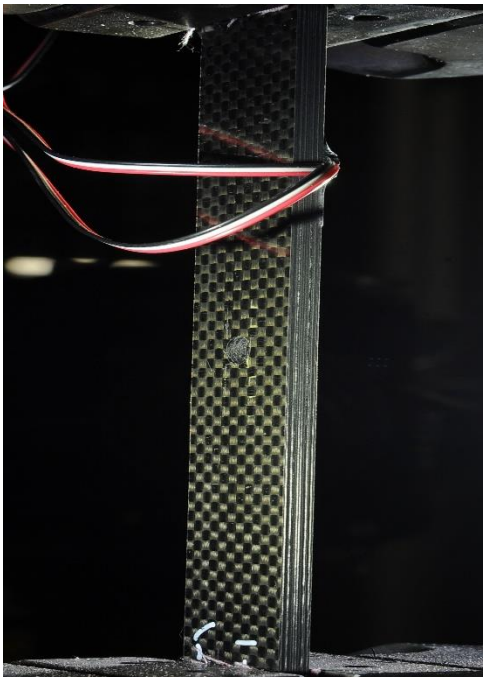

(B2-L-1) at 275k Cycles

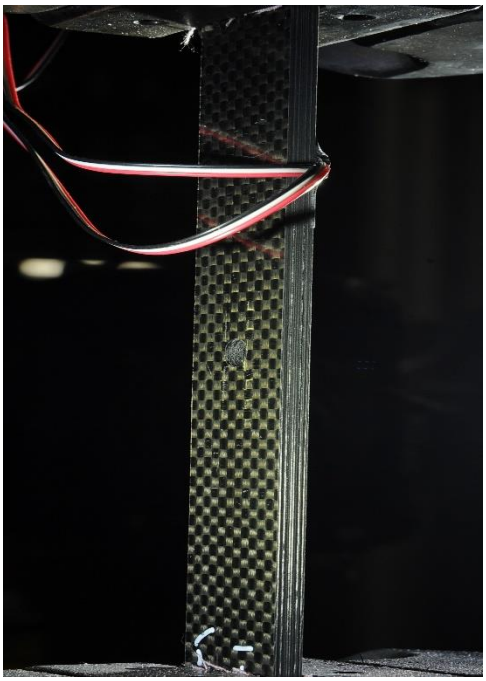

(B2-L-1) at 300k Cycles

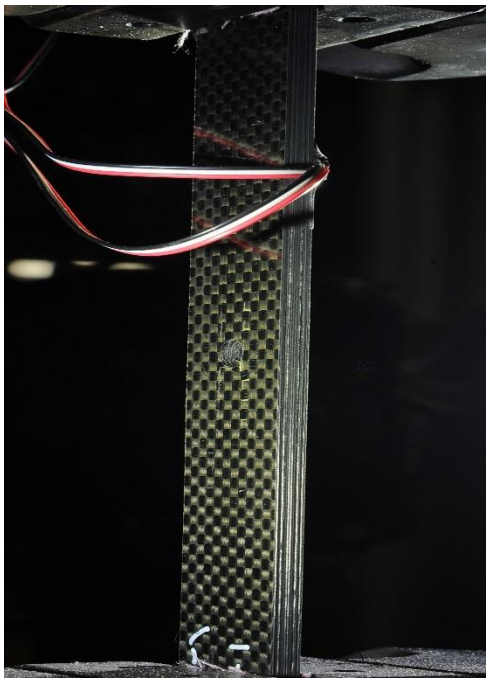

(B2-L-1) at 325k Cycles

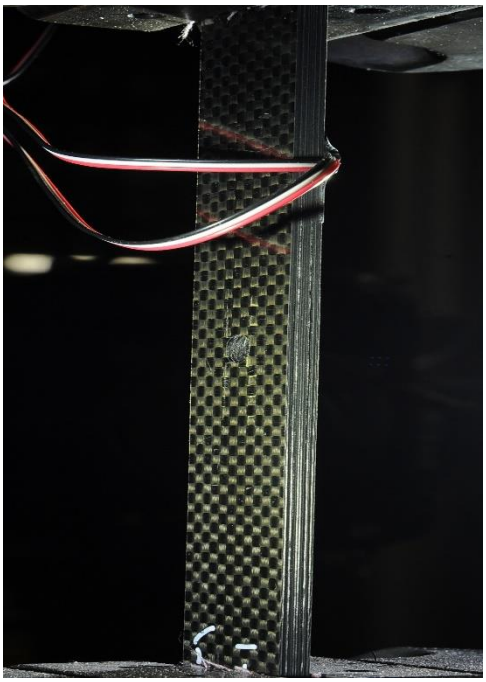

(B2-L-1) at 350k Cycles

Figure C 2-149 Damage Progression in (B2-L-1) Test specimen to 350k Cycles

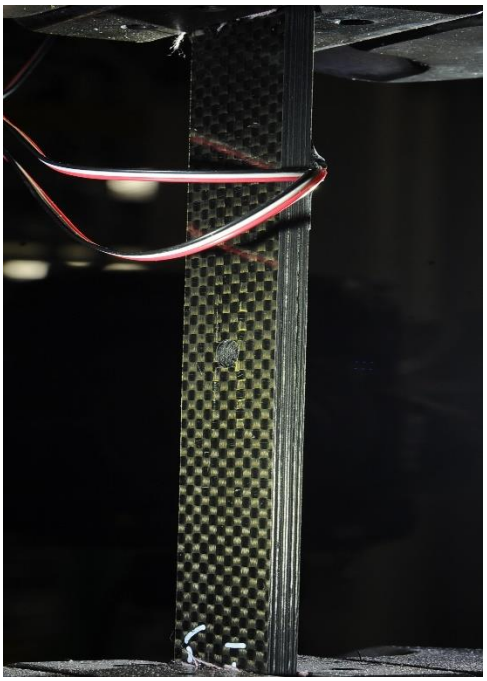

(B2-L-1) at 375k Cycles

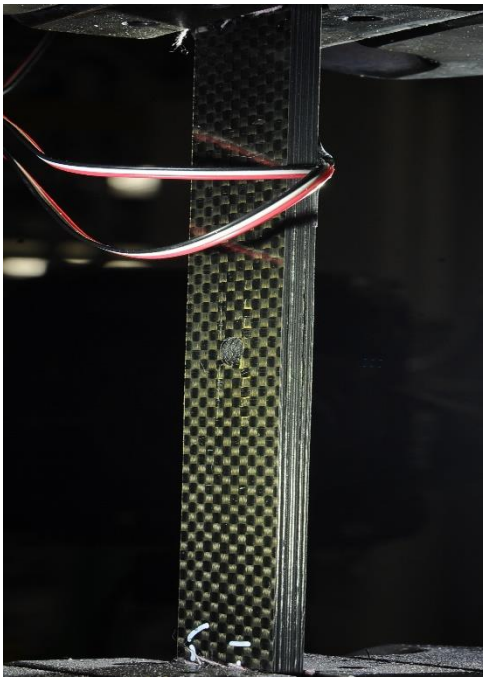

(B2-L-1) at 400k Cycles

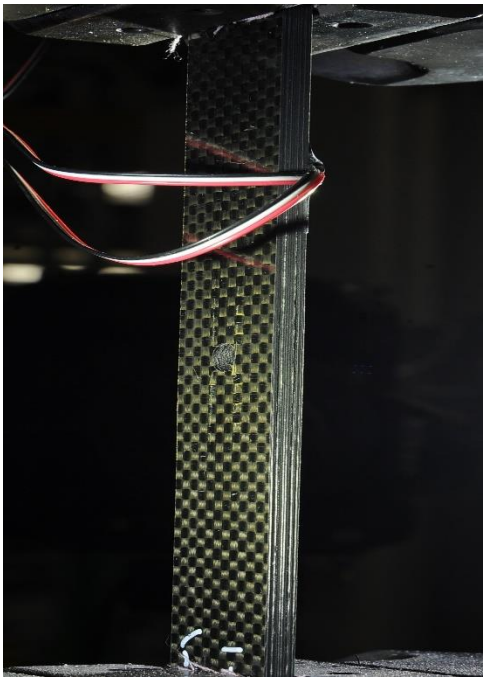

(B2-L-1) at 425k Cycles

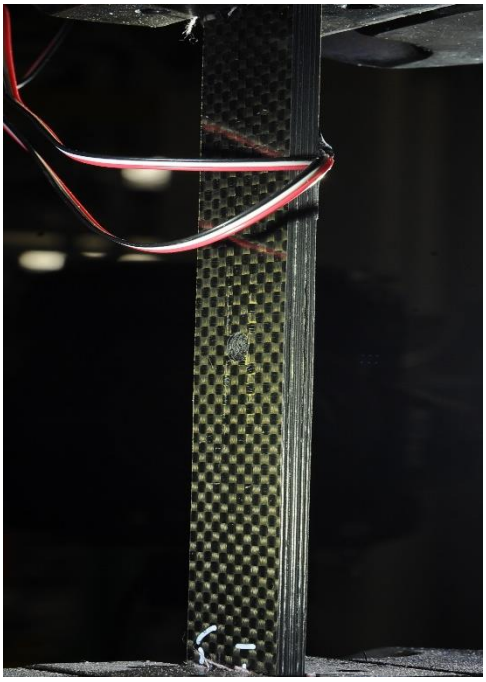

(B2-L-1) at 450k Cycles

Figure C 2-150 Damage Progression in (B2-L-1) Test specimen to 450k Cycles

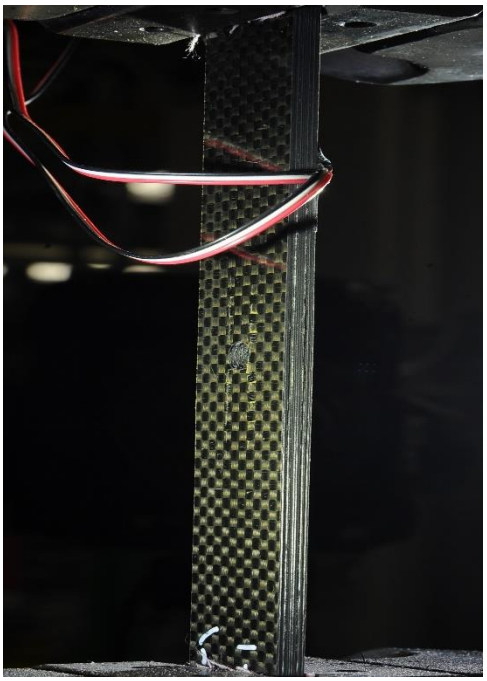

(B2-L-1) at 475k Cycles

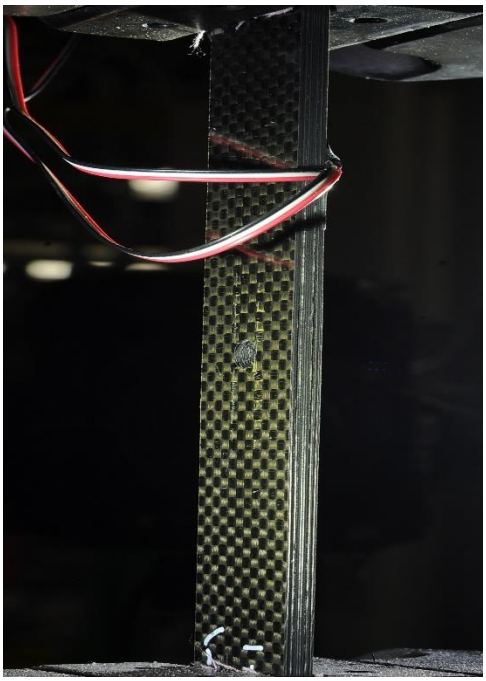

(B2-L-1) at 500k Cycles

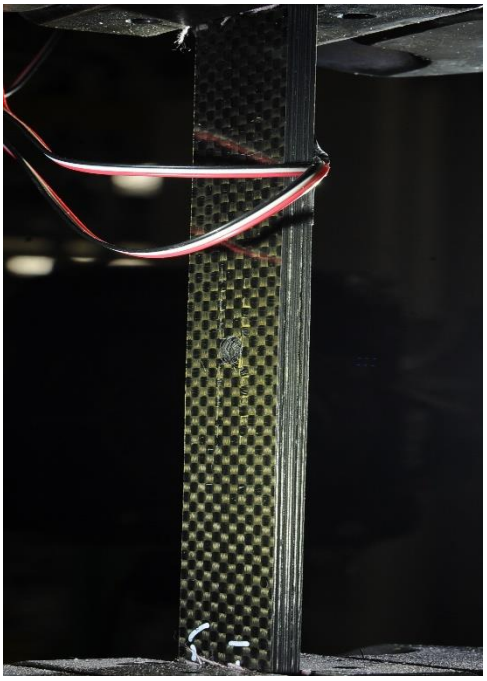

(B2-L-1) at 525k Cycles

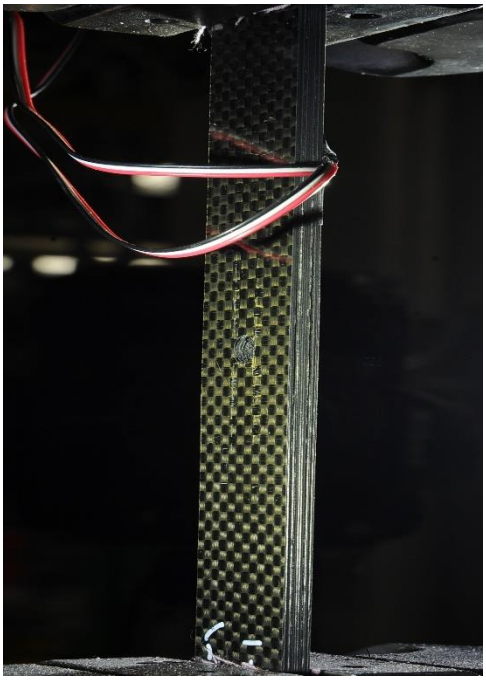

(B2-L-1) at 550k Cycles

Figure C 2-151 Damage Progression in (B2-L-1) Test specimen to 5k Cycles

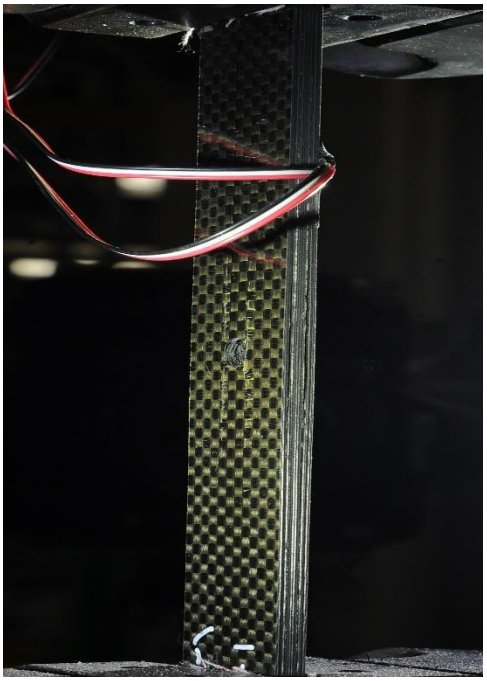

(B2-L-1) at 575k Cycles

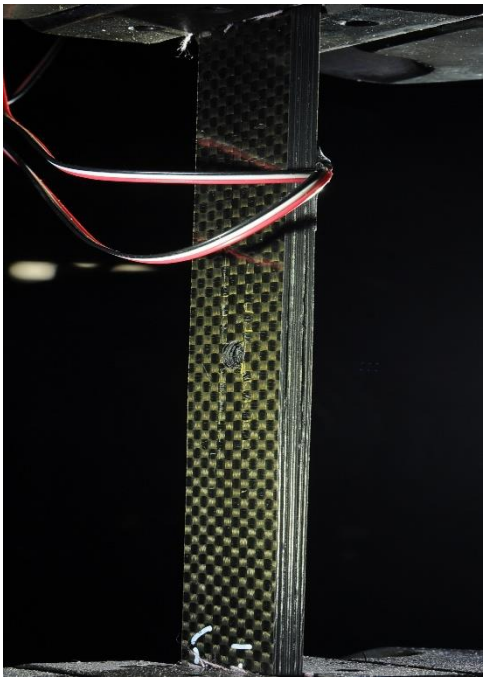

(B2-L-1) at 600k Cycles

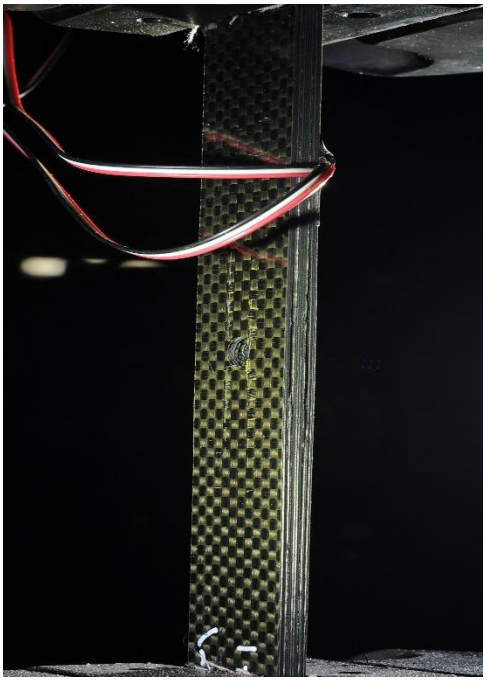

(B2-L-1) at 625k Cycles

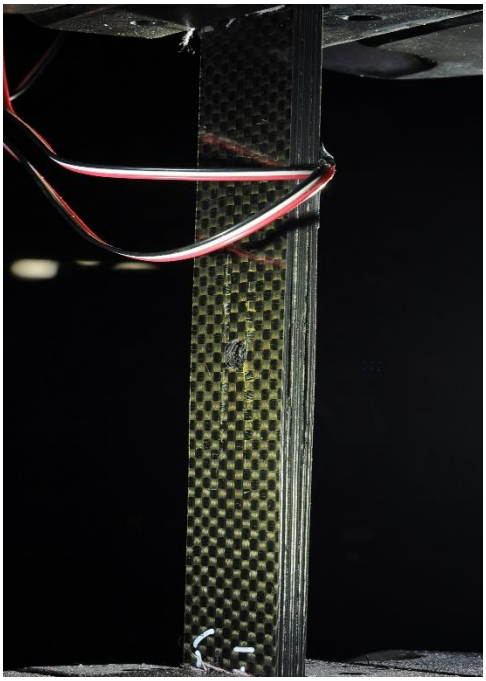

(B2-L-1) at 650k Cycles

Figure C 2-152 Damage Progression in (B2-L-1) Test specimen to 650k Cycles

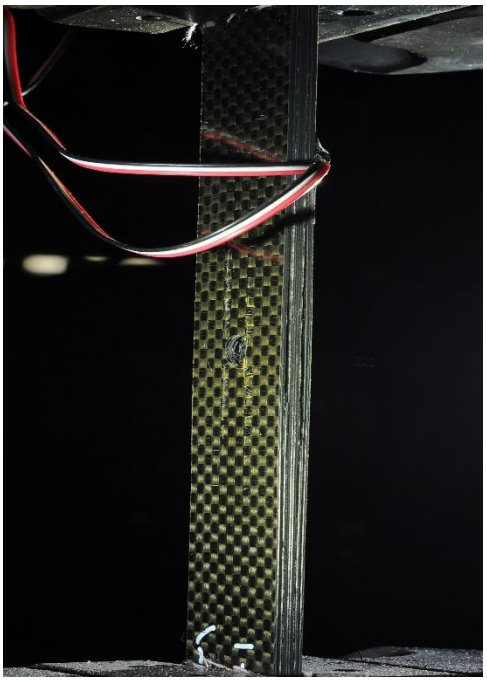

(B2-L-1) at 675k Cycles

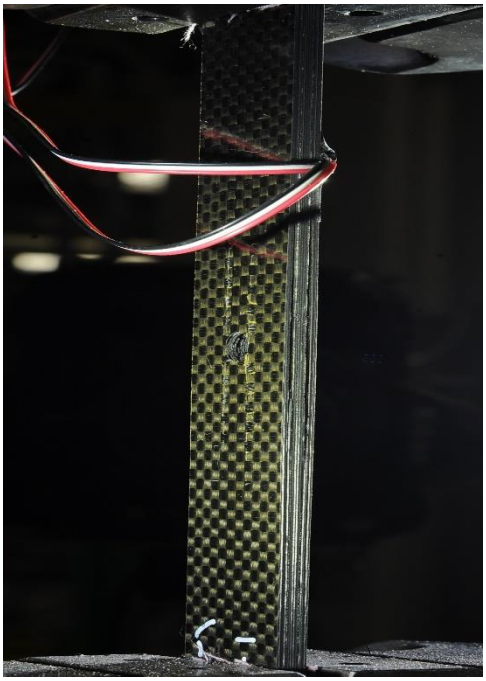

(B2-L-1) at 700k Cycles

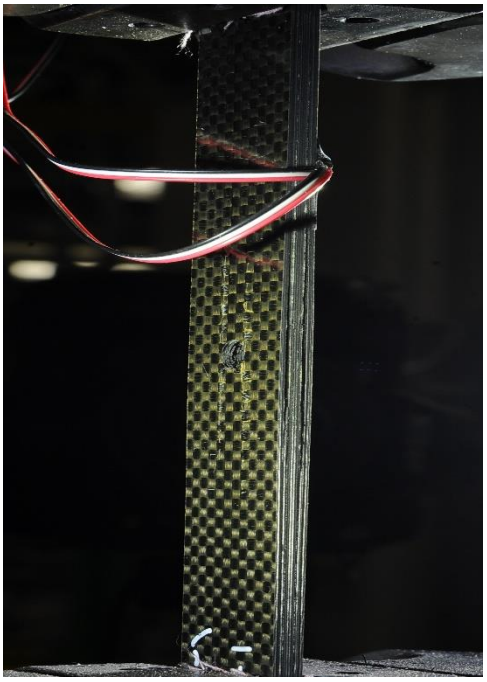

(B2-L-1) at 725k Cycles

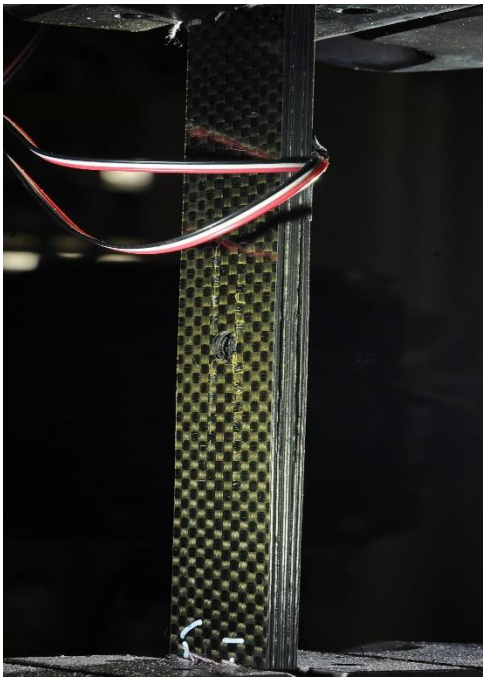

(B2-L-1) at 750k Cycles

Figure C 2-153 Damage Progression in (B2-L-1) Test specimen to 750k Cycles

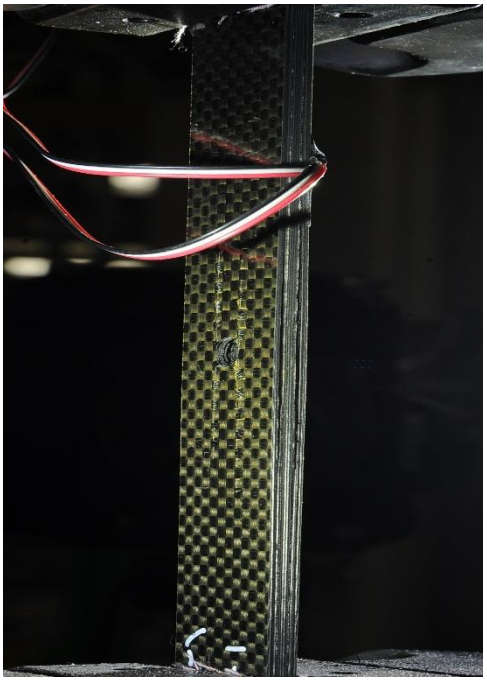

(B2-L-1) at 775k Cycles

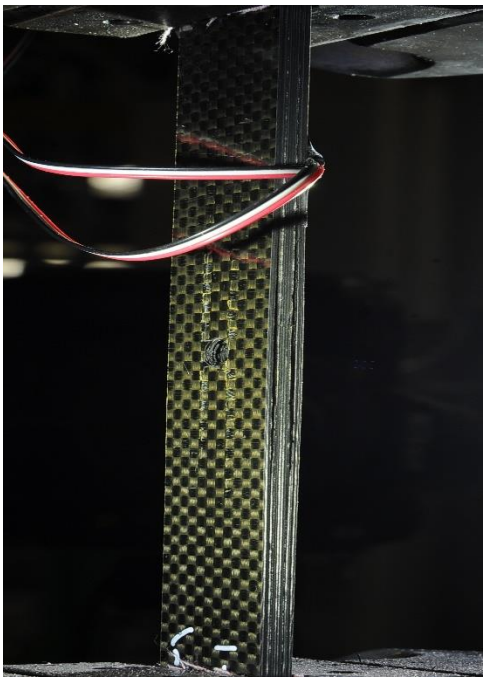

(B2-L-1) at 800k Cycles

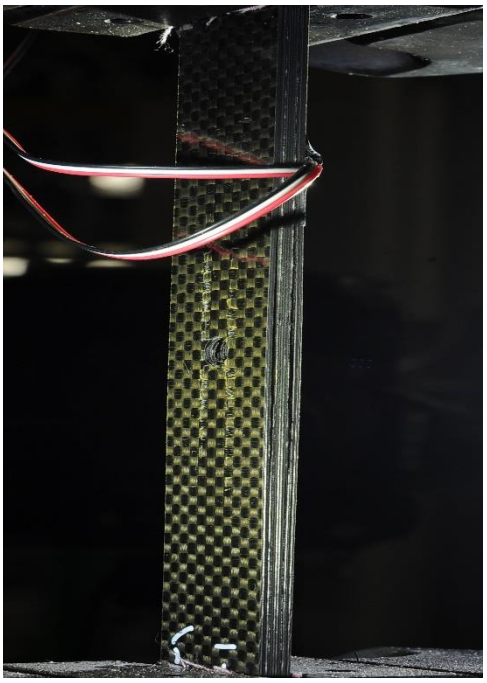

(B2-L-1) at 82k Cycles

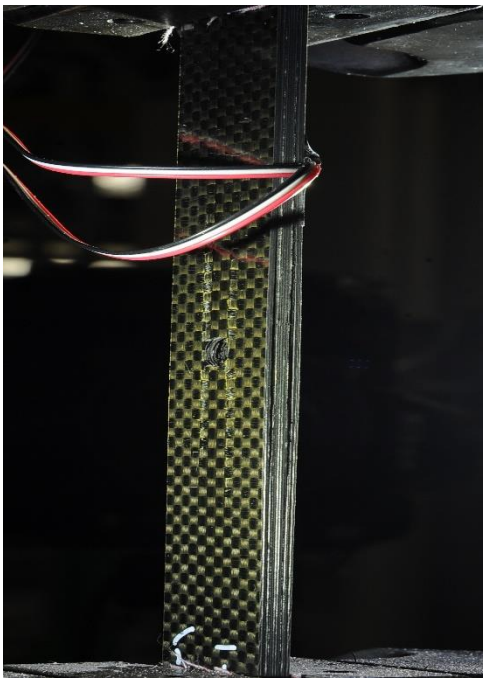

(B2-L-1) at 850k Cycles

Figure C 2-154 Damage Progression in (B2-L-1) Test specimen to 850k Cycles

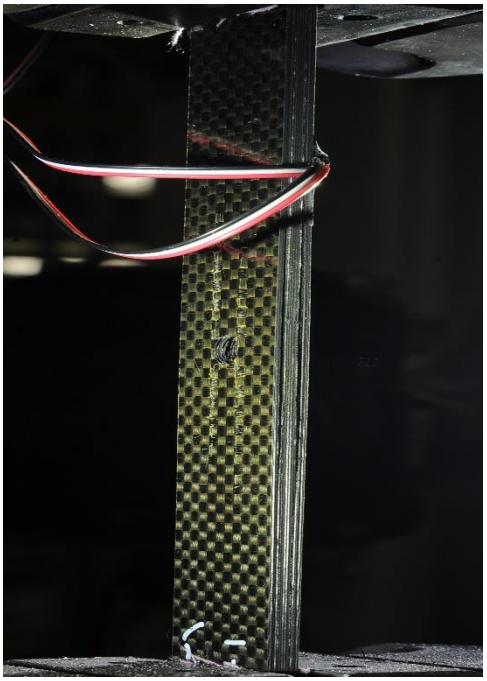

(B2-L-1) at 875k Cycles

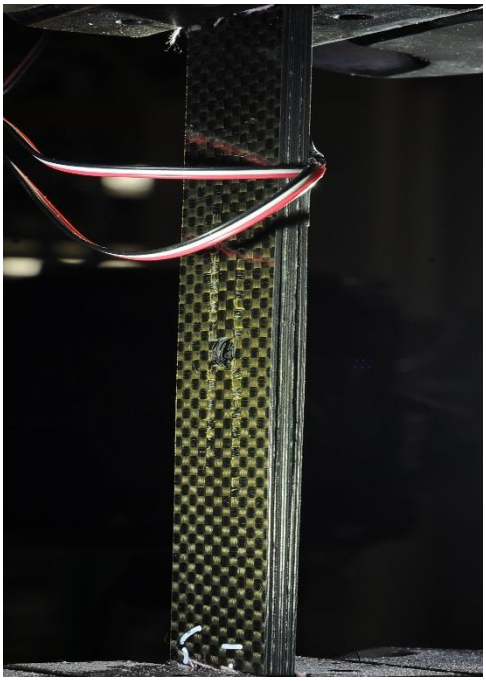

(B2-L-1) at 900k Cycles

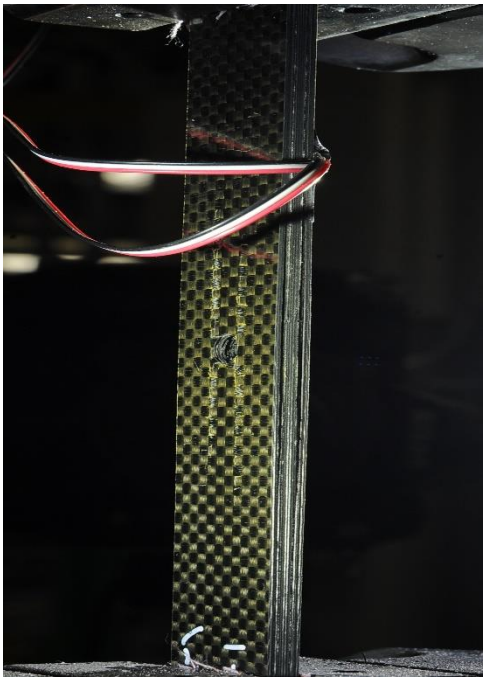

(B2-L-1) at 925k Cycles

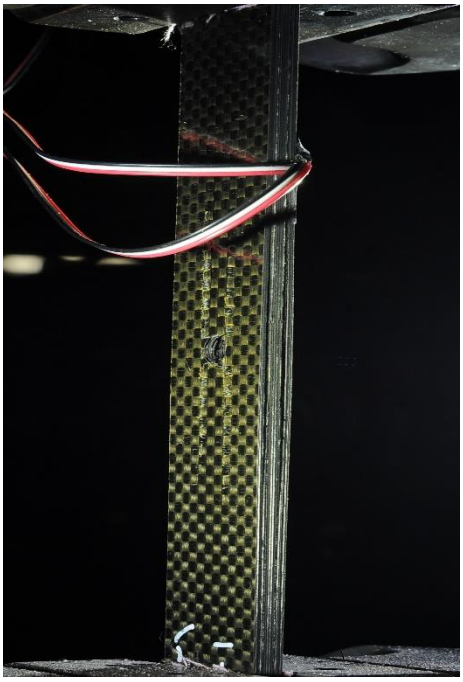

(B2-L-1) at 950k Cycles

Figure C 2-155 Damage Progression in (B2-L-1) Test specimen to 950k Cycles

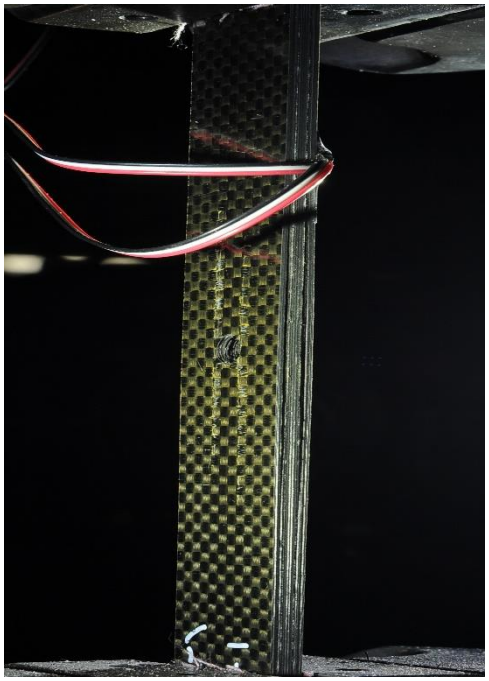

(B2-L-1) at 975k Cycles

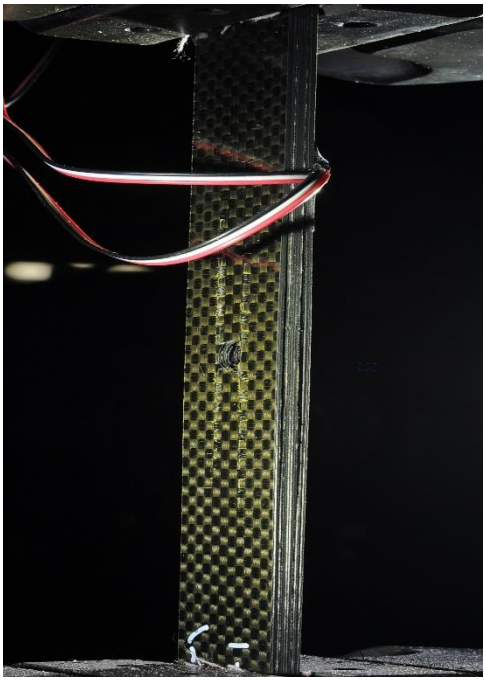

(B2-L-1) at 1000k Cycles

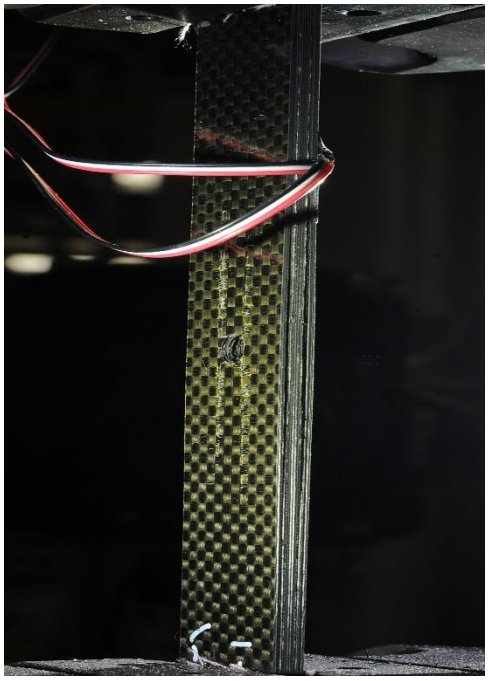

(B2-L-1) at Pre RS

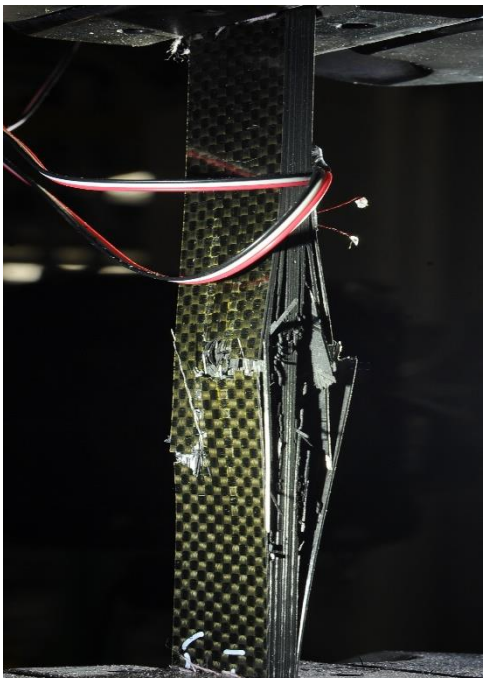

(B2-L-1) at Failure

Figure C 2-156 Damage Progression in (B2-L-1) Test specimen to Failure

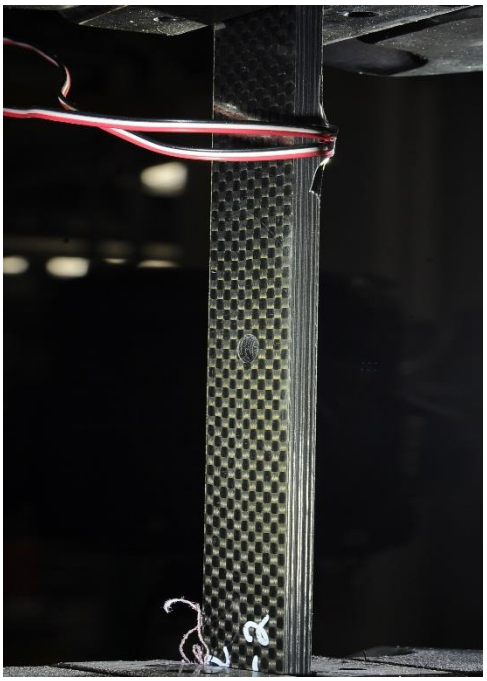

(B2-L-2) at 1 Cycle

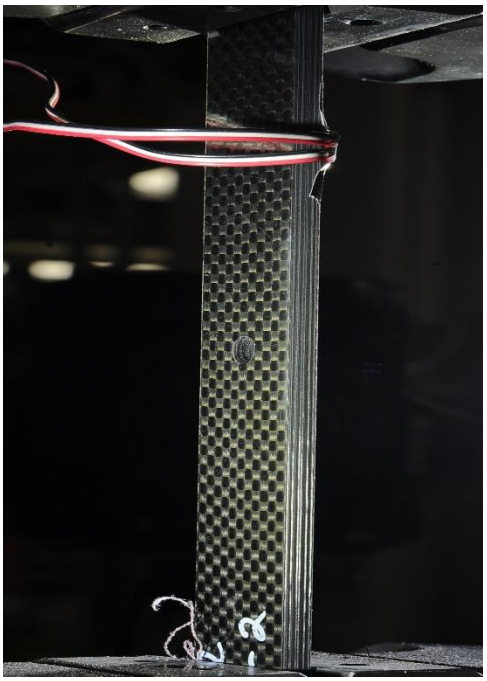

(B2-L-2) at 100 Cycles

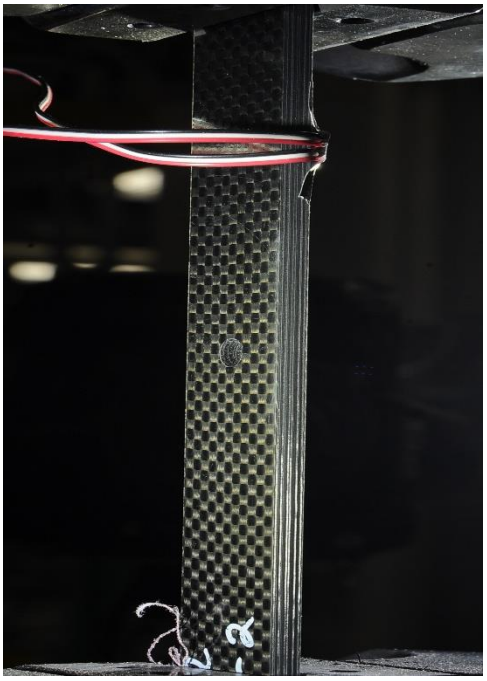

(B2-L-2) at 1k Cycles

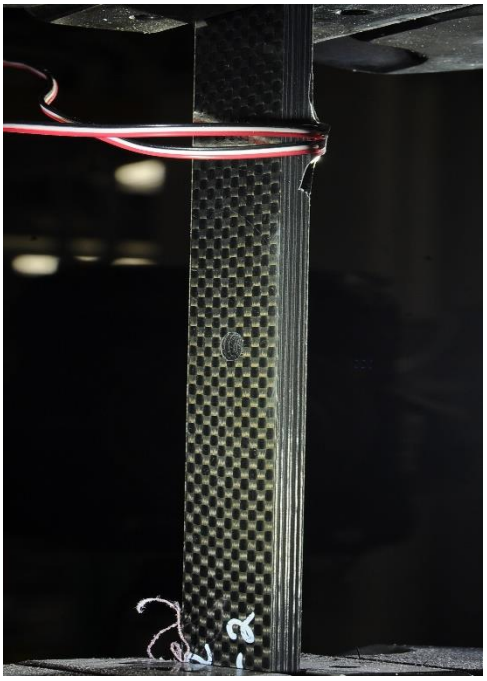

(B2-L-2) at 5k Cycles

Figure C 2-157 Damage Progression in (B2-L-2) Test specimen to 5k Cycles

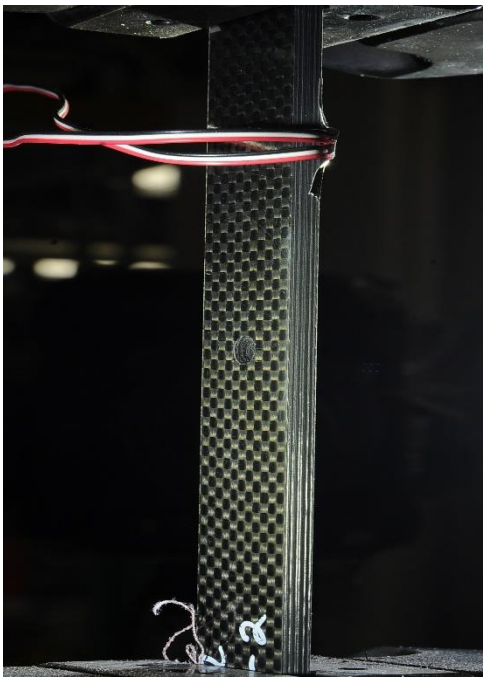

(B2-L-2) at 10k Cycles

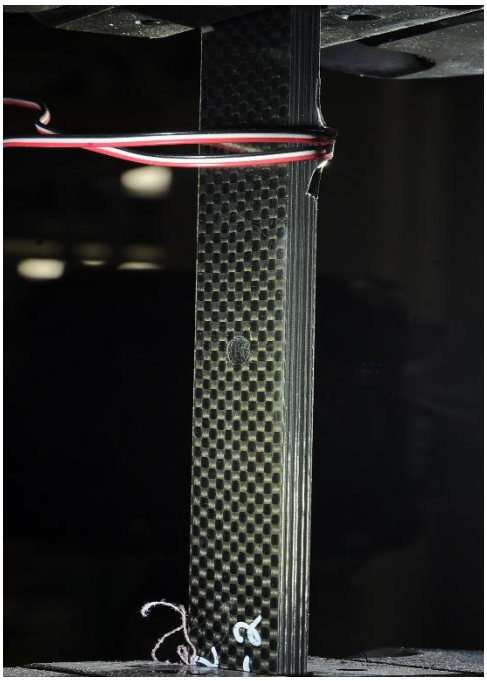

(B2-L-2) at 20k Cycles

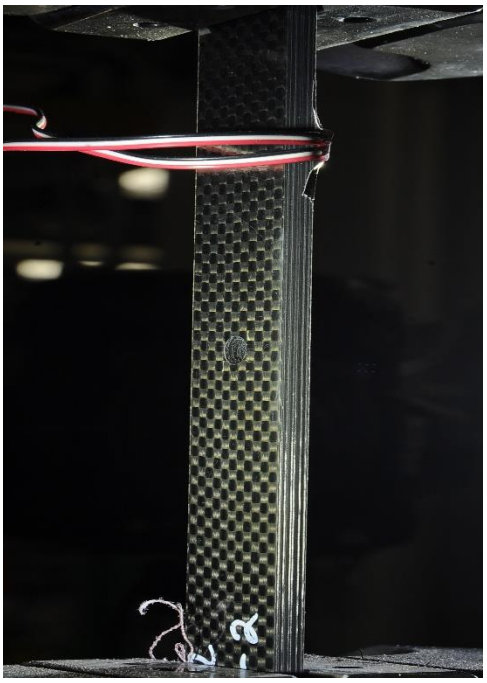

(B2-L-2) at 30k Cycles

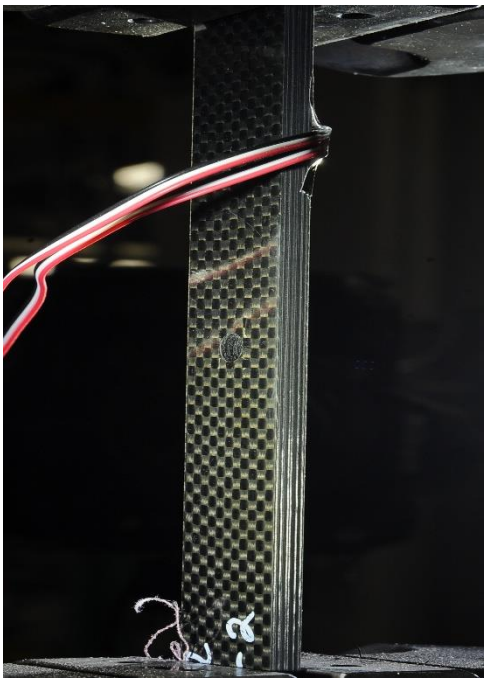

(B2-L-2) at 40k Cycles

Figure C 2-158 Damage Progression in (B2-L-2) Test specimen to 40k Cycles

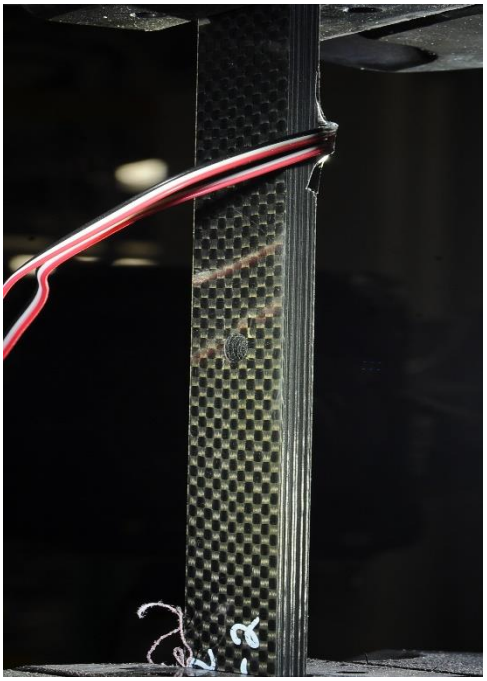

(B2-L-2) at 50k Cycles

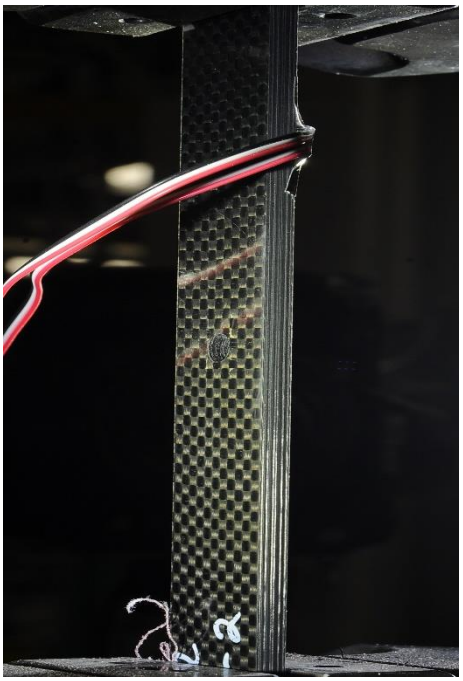

(B2-L-2) at 60k Cycles

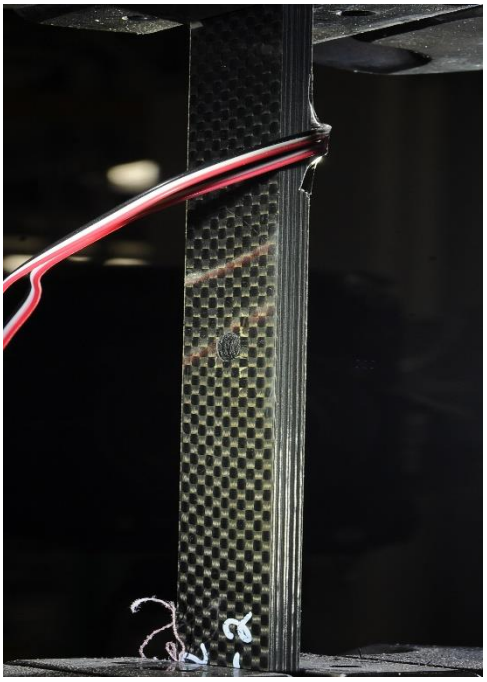

(B2-L-2) at 70k Cycles

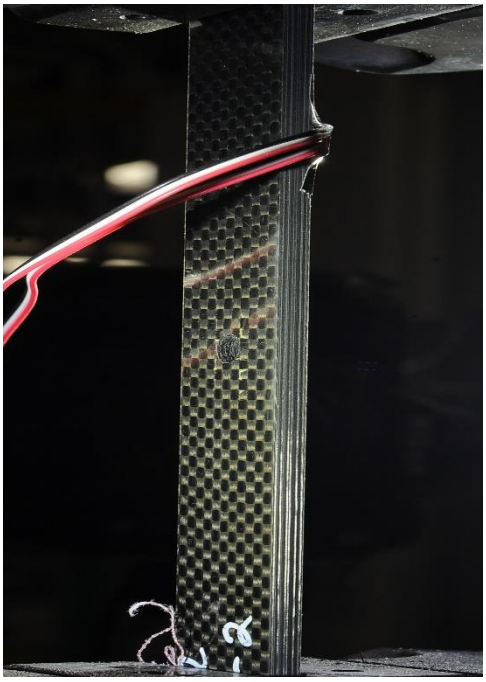

(B2-L-2) at 80k Cycles

Figure C 2-159 Damage Progression in (B2-L-2) Test specimen to 80k Cycles

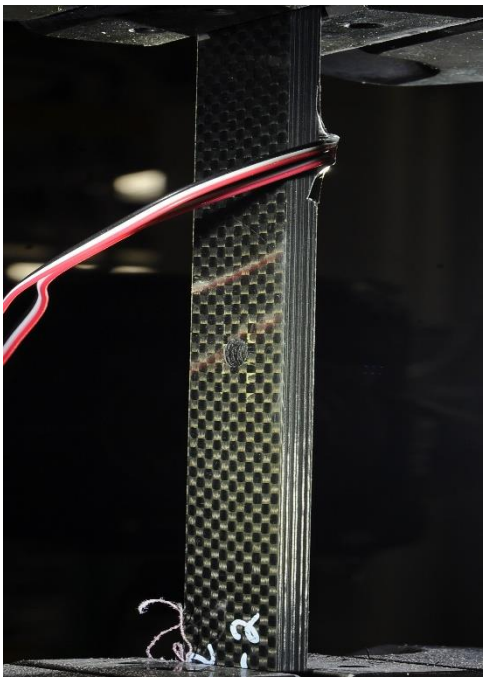

(B2-L-2) at 90k Cycles

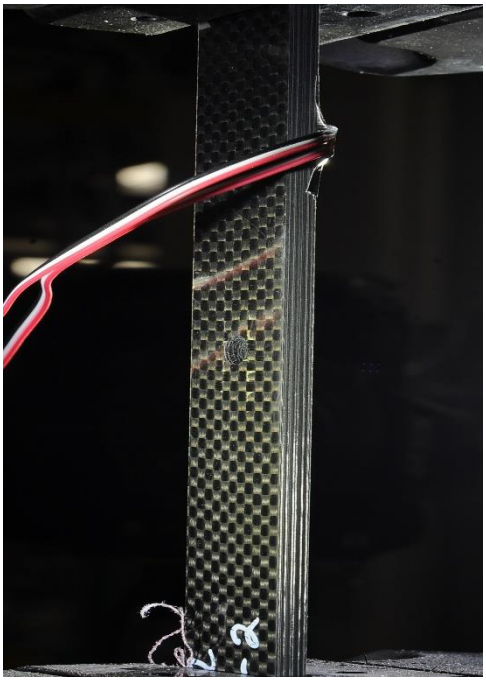

(B2-L-2) at 100k Cycles

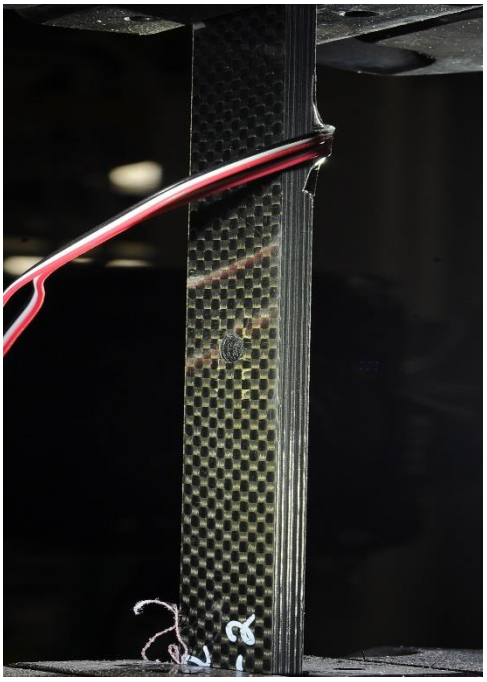

(B2-L-2) at 125k Cycles

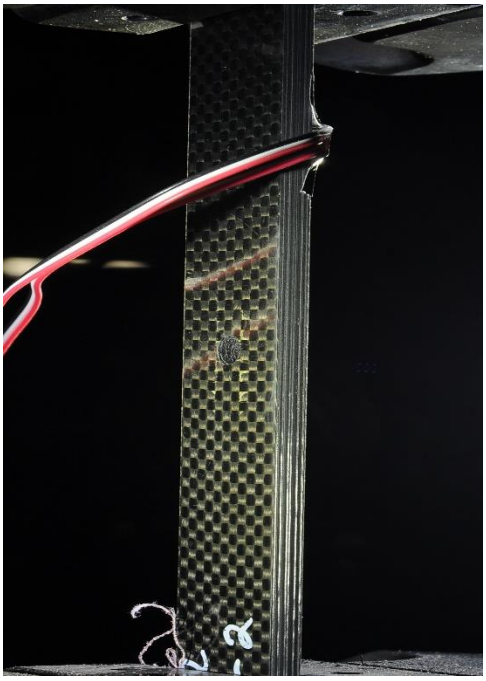

(B2-L-2) at 150k Cycles

Figure C 2-160 Damage Progression in (B2-L-2) Test specimen to 150k Cycles

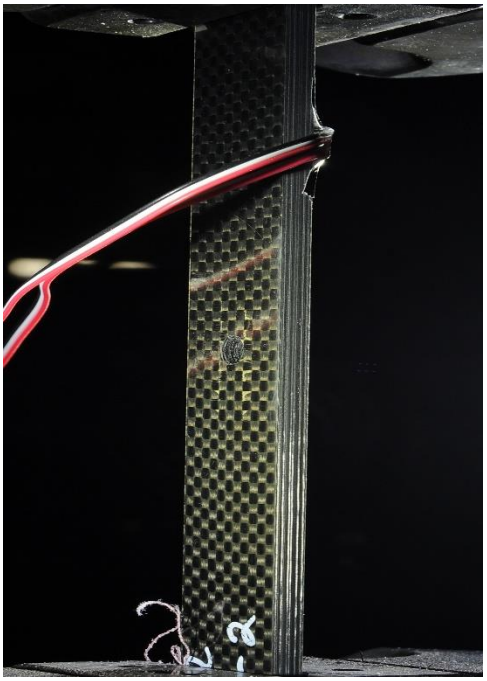

(B2-L-2) at 175k Cycles

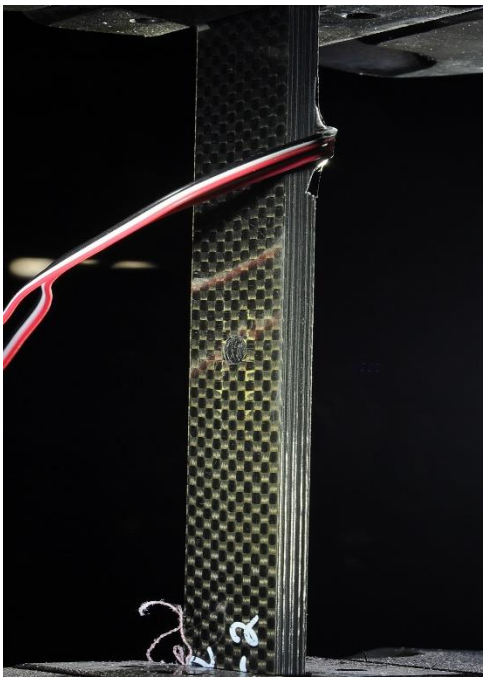

(B2-L-2) at 200k Cycles

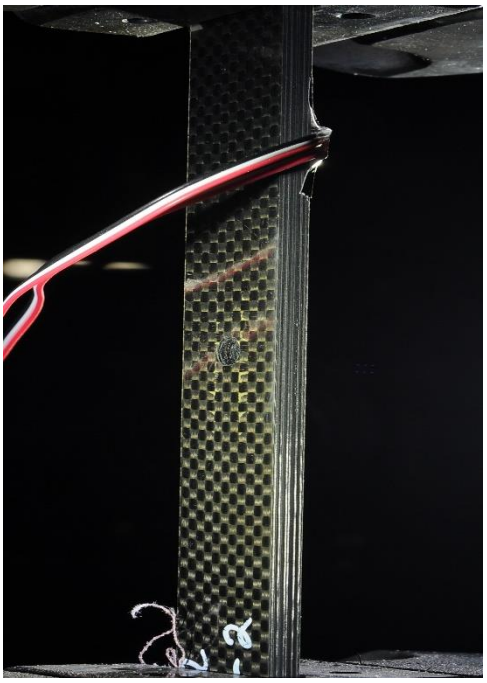

(B2-L-2) at 225k Cycles

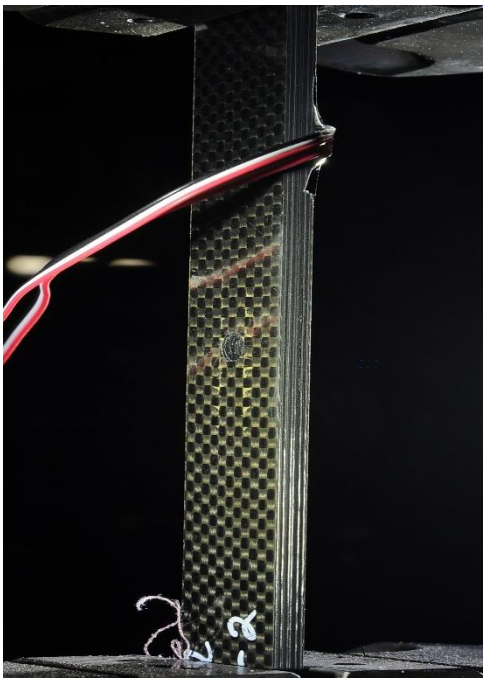

(B2-L-2) at 250k Cycles

Figure C 2-161 Damage Progression in (B2-L-2) Test specimen to 250k Cycles

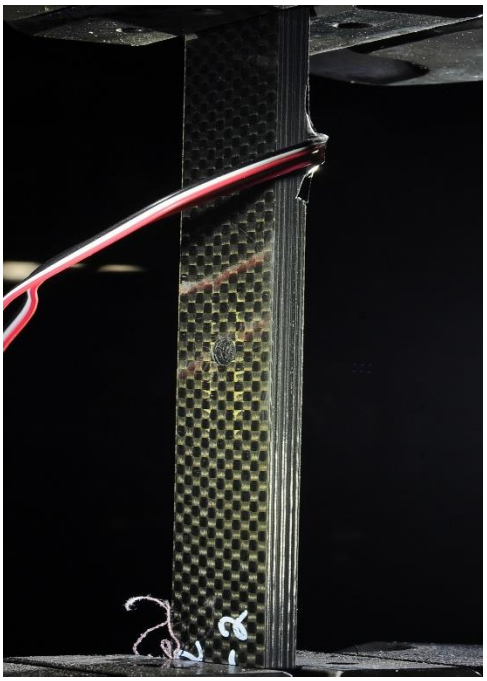

(B2-L-2) at 275k Cycles

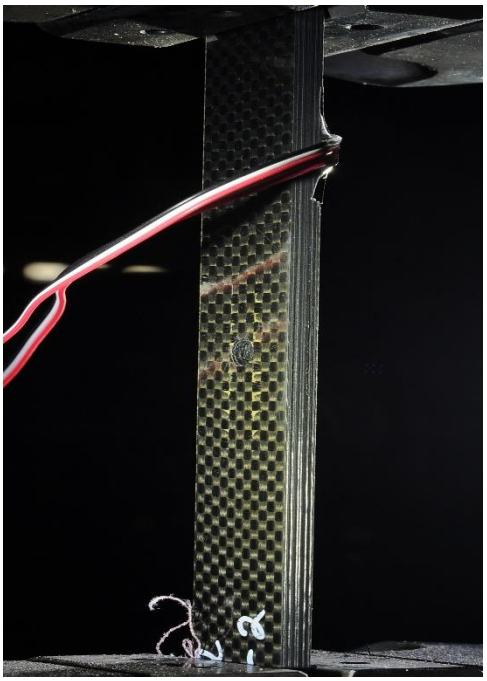

(B2-L-2) at 300k Cycles

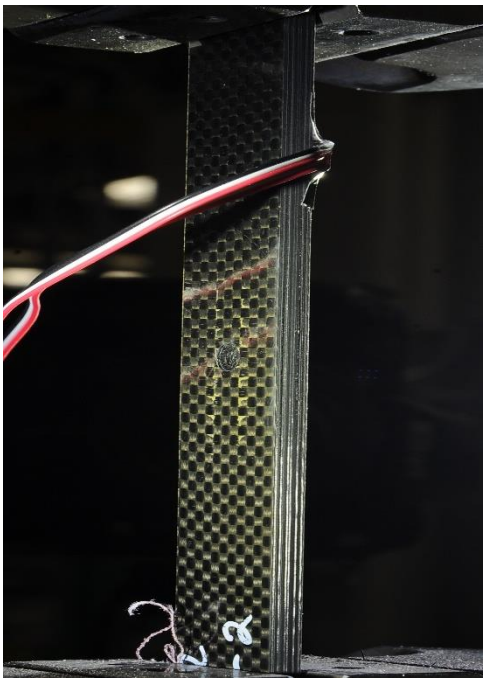

(B2-L-2) at 325k Cycles

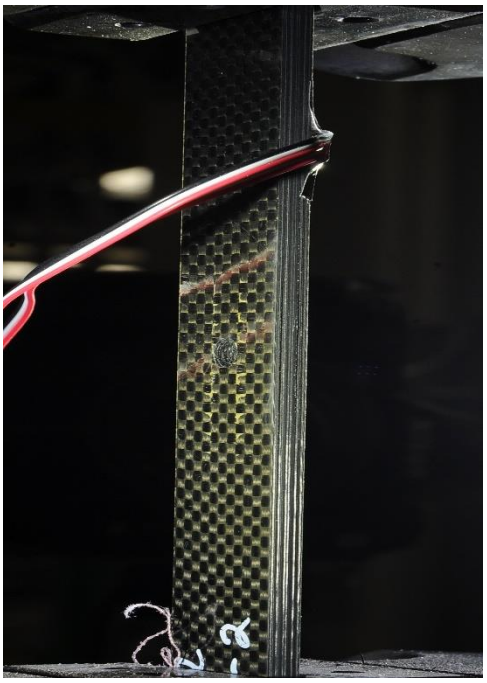

(B2-L-2) at 350k Cycles

Figure C 2-162 Damage Progression in (B2-L-2) Test specimen to 350k Cycles

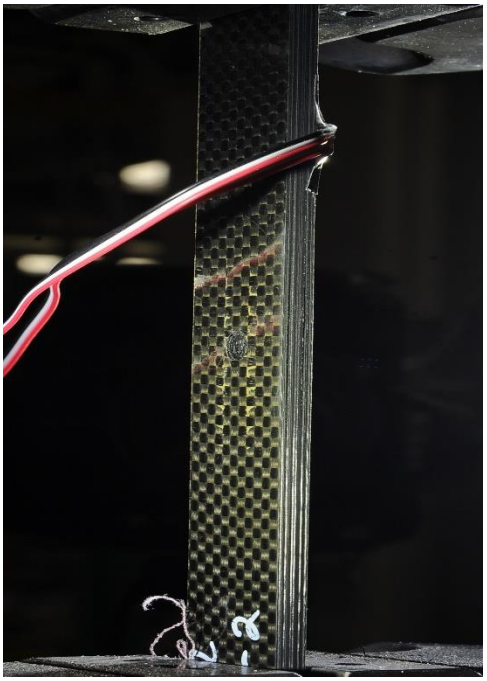

(B2-L-2) at 375k Cycles

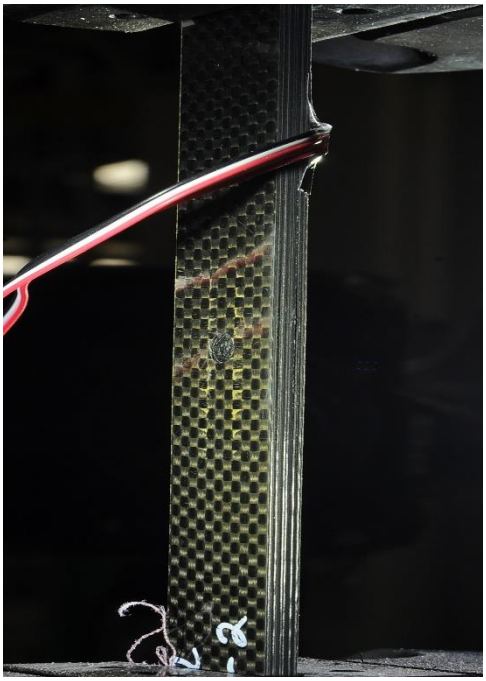

(B2-L-2) at 400k Cycles

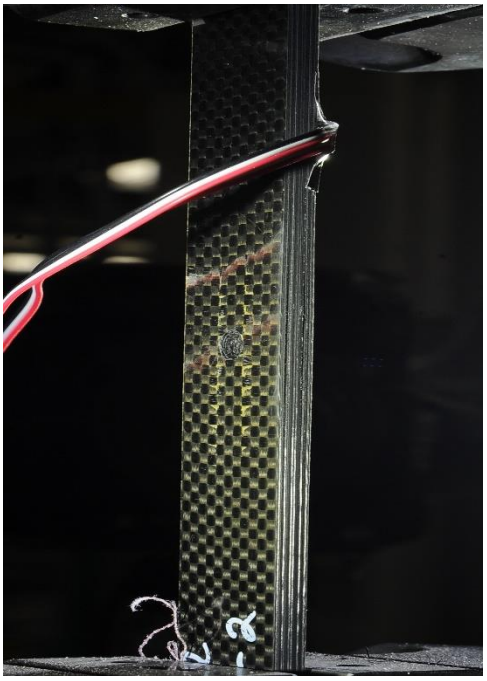

(B2-L-2) at 425k Cycles

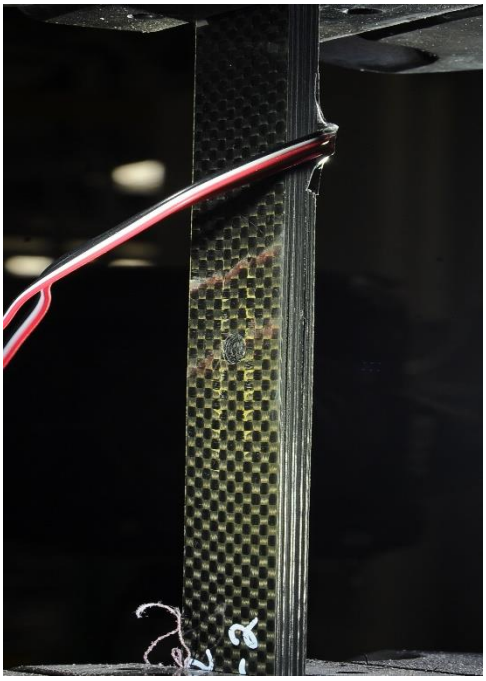

(B2-L-2) at 450k Cycles

Figure C 2-163 Damage Progression in (B2-L-2) Test specimen to 450k Cycles

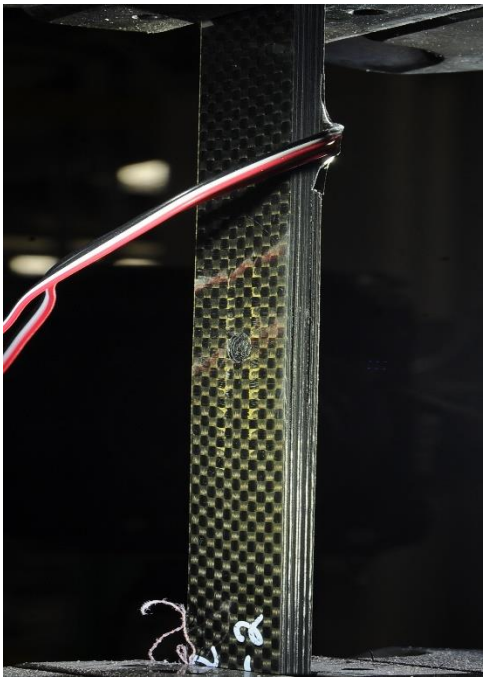

(B2-L-2) at 475k Cycles

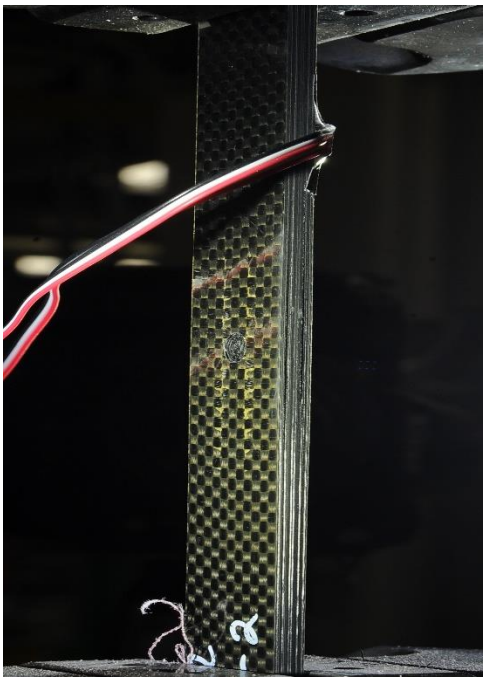

(B2-L-2) at 500k Cycles

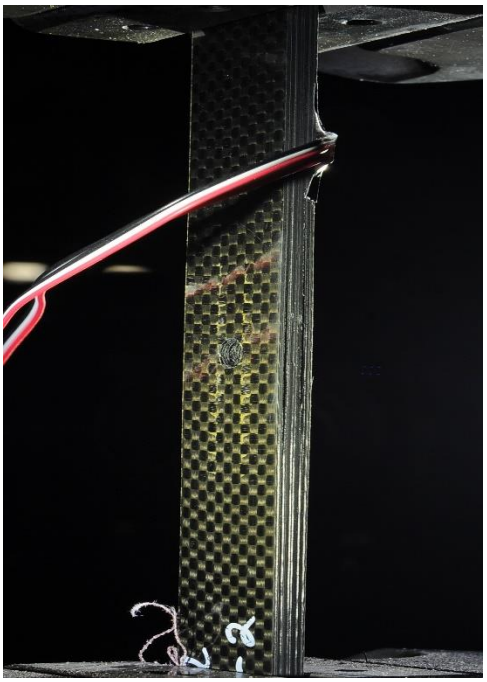

(B2-L-2) at 525k Cycles

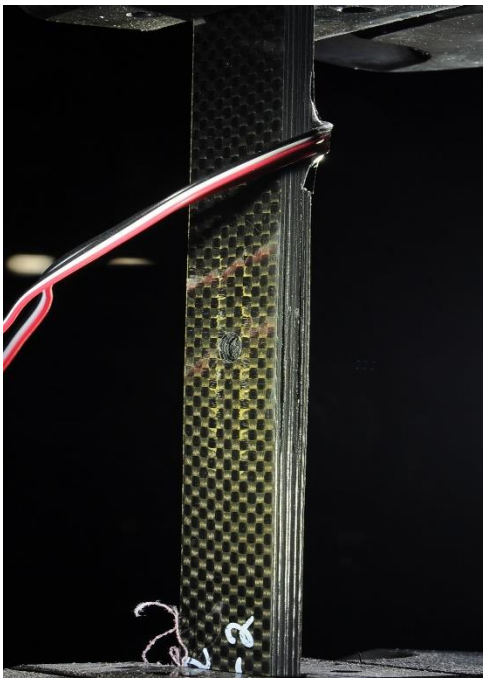

(B2-L-2) at 550k Cycles

Figure C 2-164 Damage Progression in (B2-L-2) Test specimen to 550k Cycles

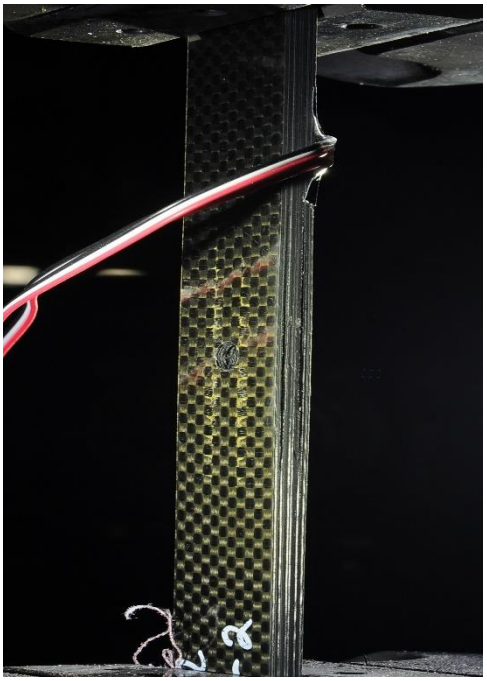

(B2-L-2) at 575k Cycles

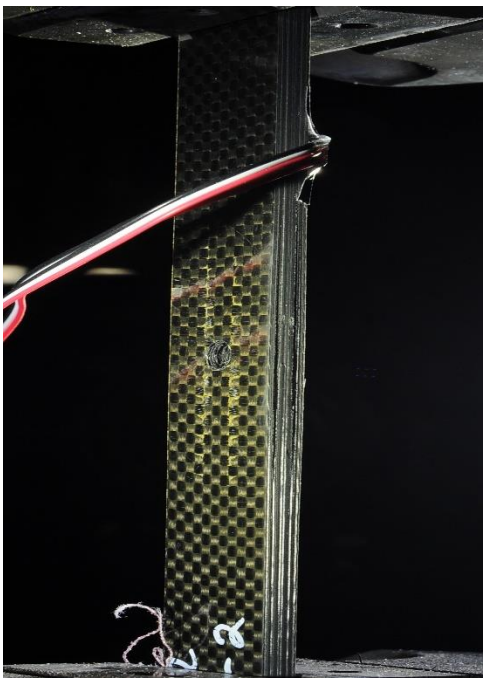

(B2-L-2) at 600k Cycles

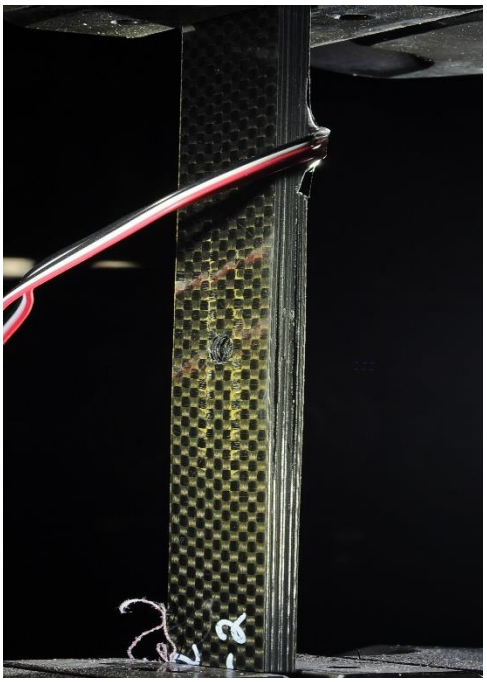

(B2-L-2) at 625k Cycles

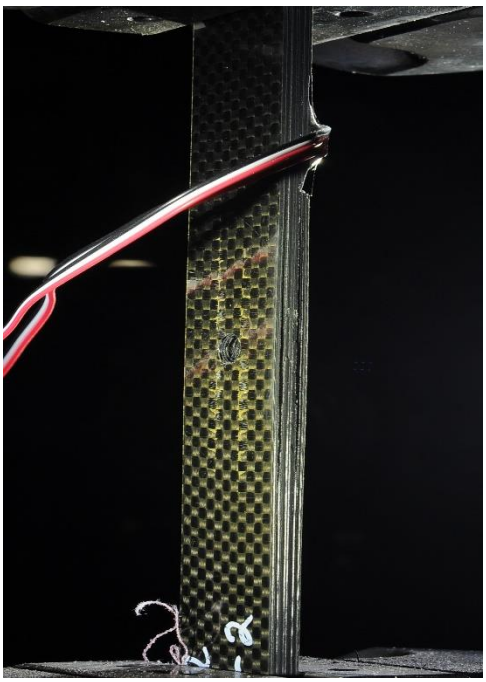

(B2-L-2) at 650k Cycles

Figure C 2-165 Damage Progression in (B2-L-2) Test specimen to 650k Cycles

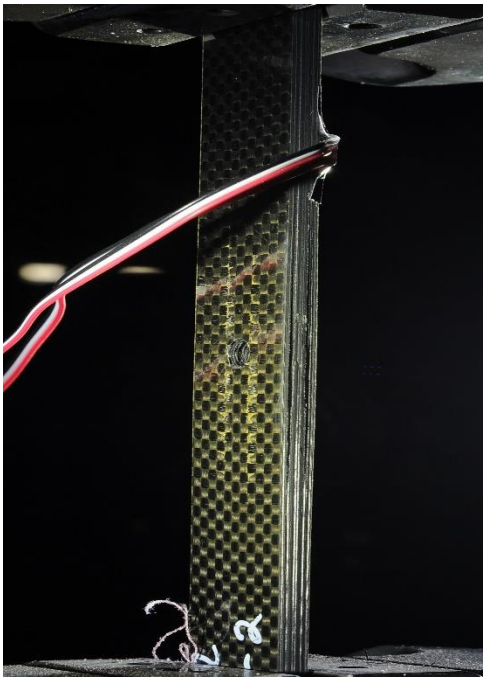

(B2-L-2) at 675k Cycles

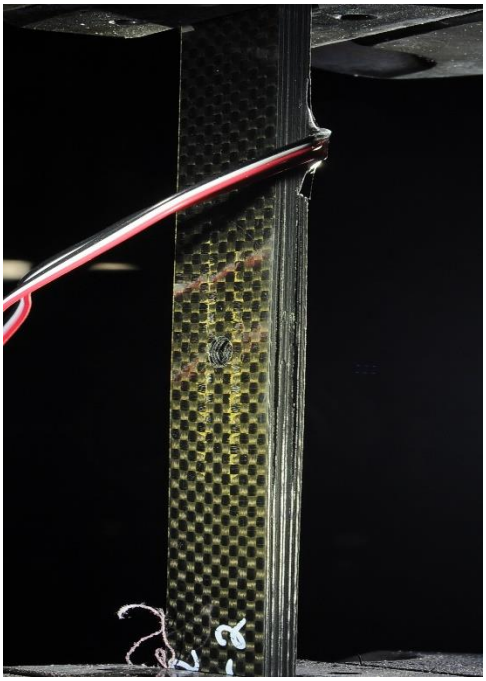

(B2-L-2) at 700k Cycles

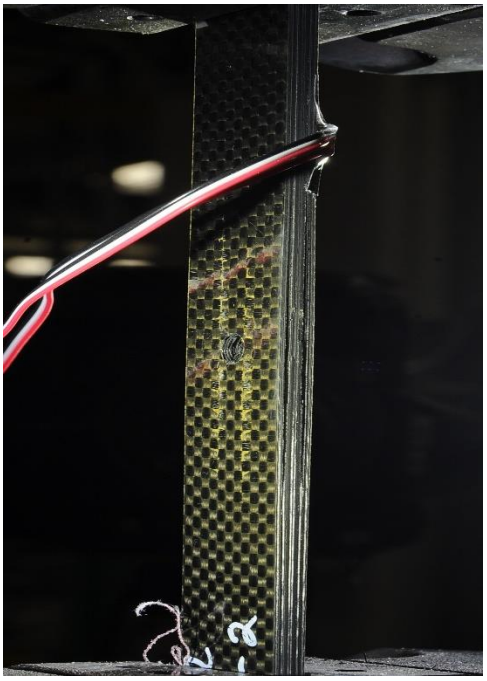

(B2-L-2) at 725k Cycles

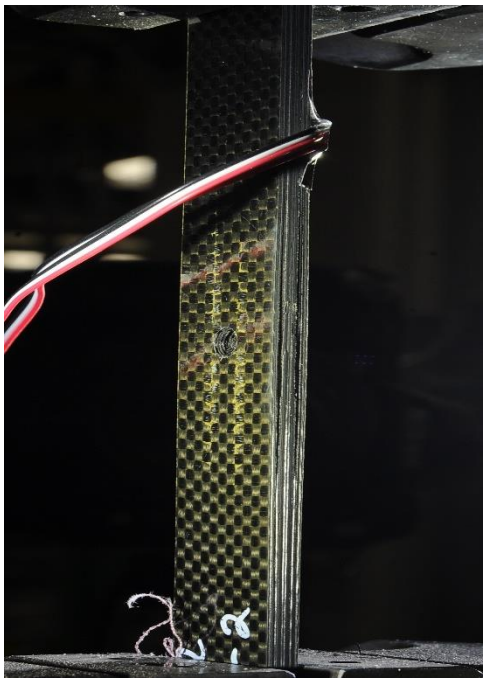

(B2-L-2) at 750k Cycles

Figure C 2-166 Damage Progression in (B2-L-2) Test specimen to 750k Cycles

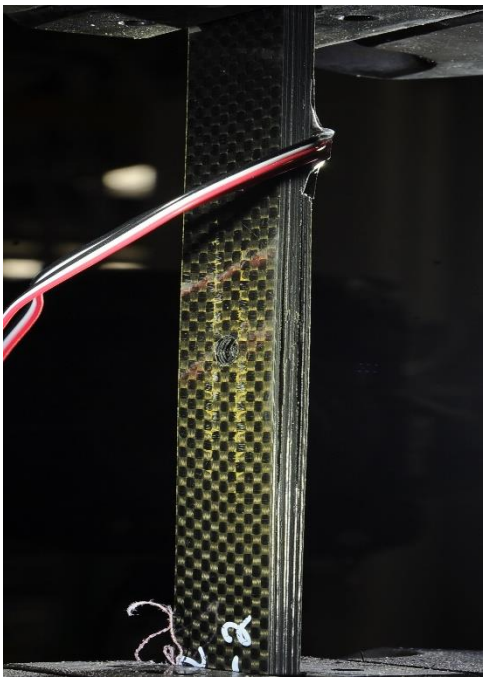

(B2-L-2) at 775k Cycles

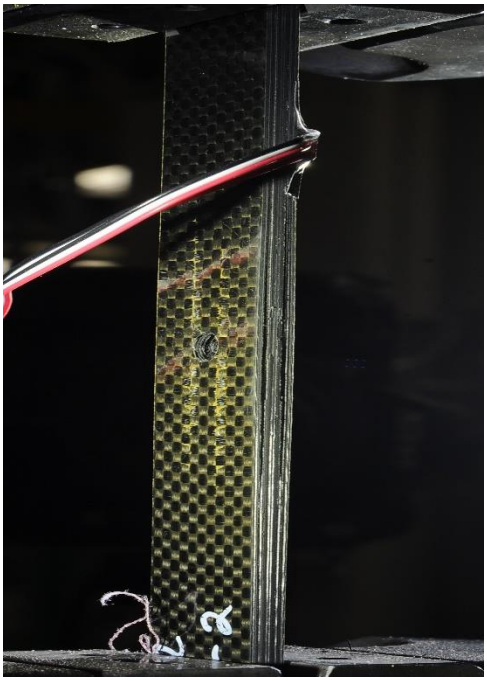

(B2-L-2) at 800k Cycles

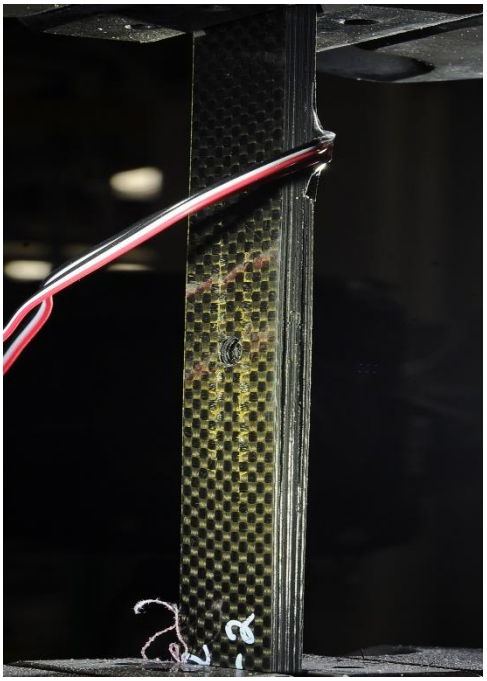

(B2-L-2) at 825k Cycles

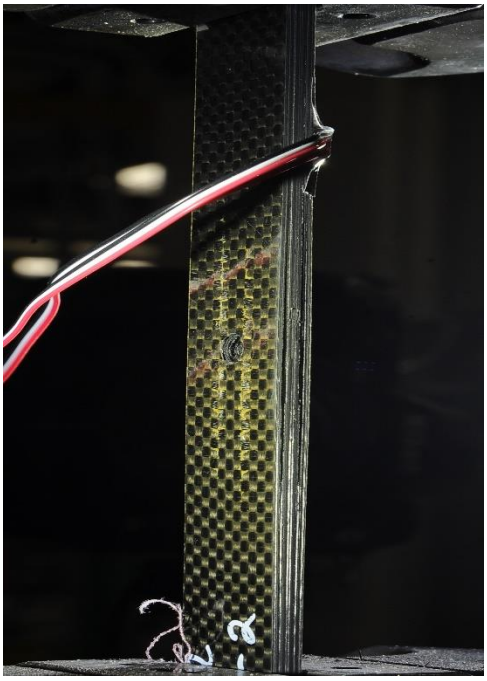

(B2-L-2) at 850k Cycles

Figure C 2-167 Damage Progression in (B2-L-2) Test specimen to 850k Cycles

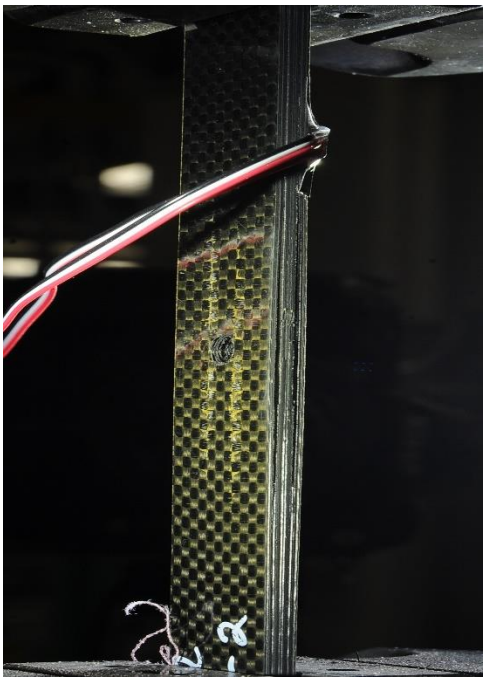

(B2-L-2) at 875k Cycles

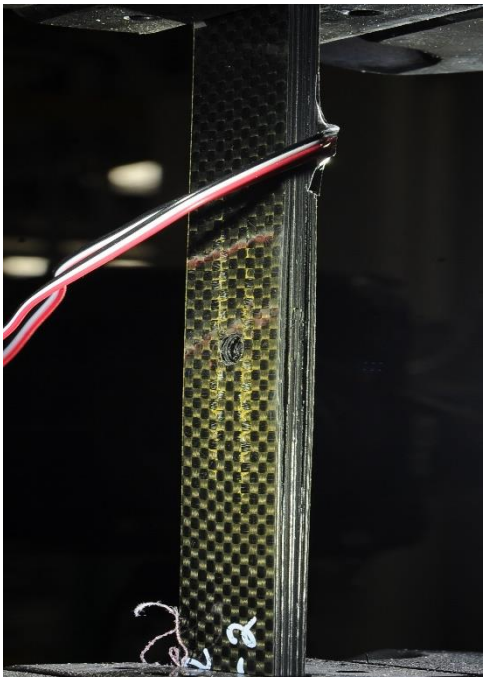

(B2-L-2) at 900k Cycles

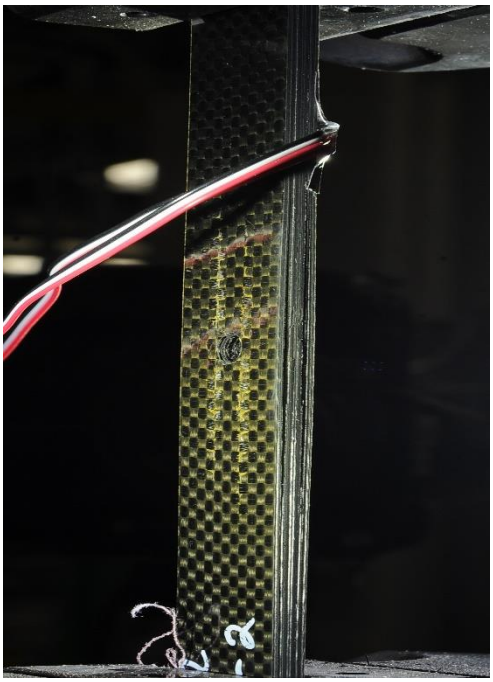

(B2-L-2) at 925k Cycles

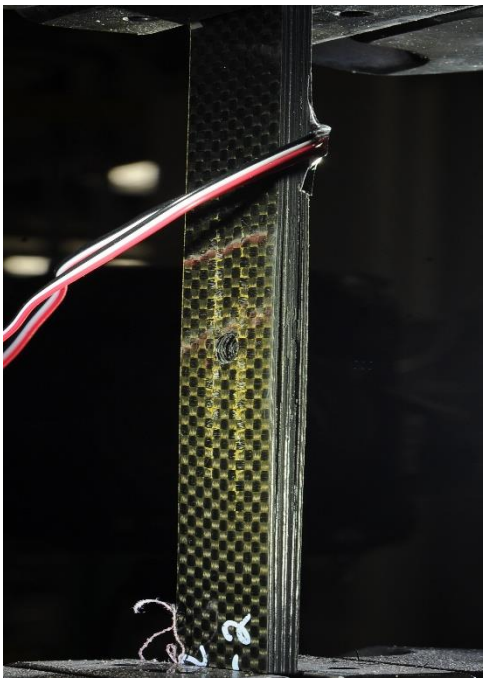

(B2-L-2) at 950k Cycles

Figure C 2-168 Damage Progression in (B2-L-2) Test specimen to 950k Cycles

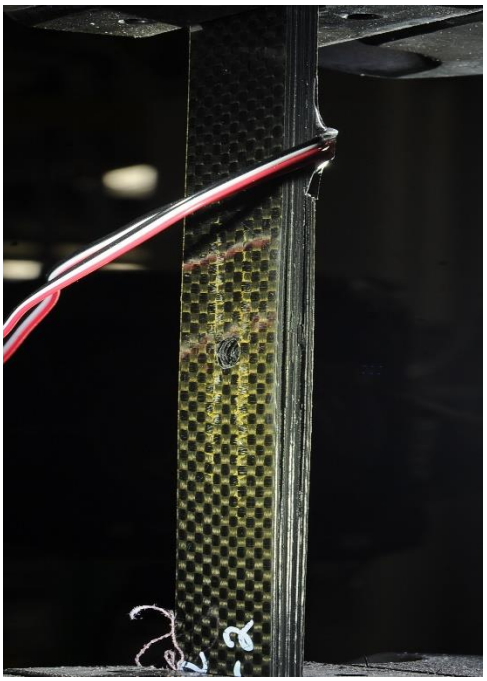

(B2-L-2) at 975k Cycles

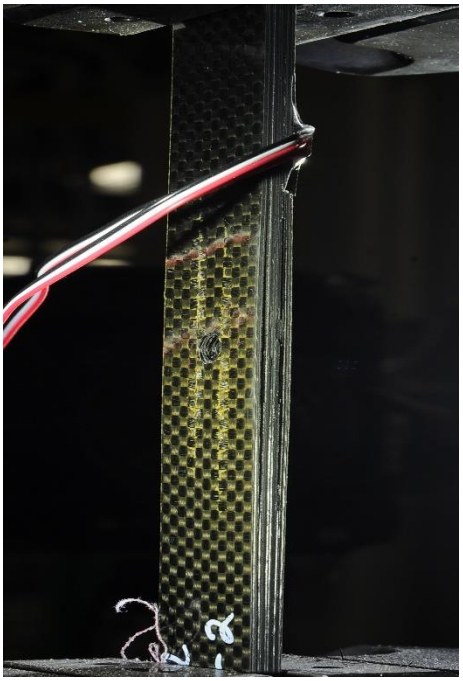

(B2-L-2) at 1000k Cycles

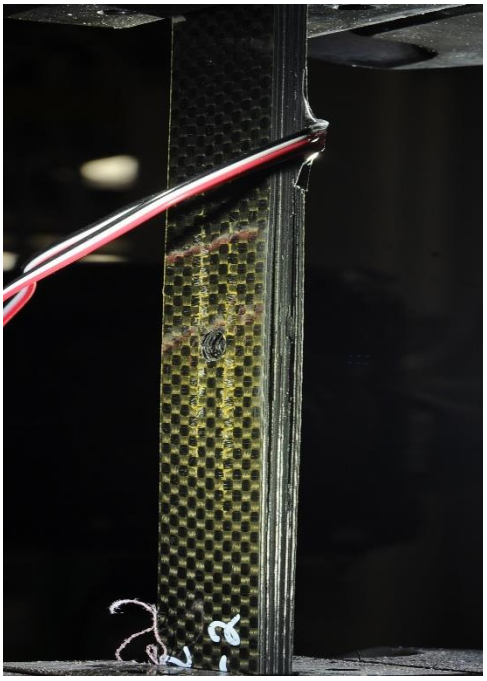

(B2-L-2) at Pre RS

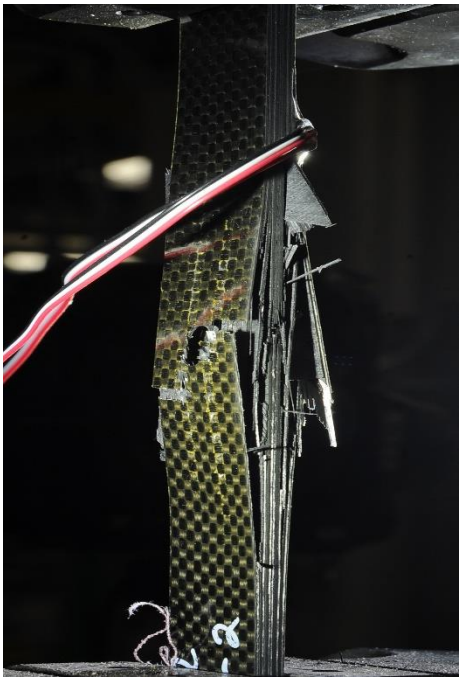

(B2-L-2) at Failure

Figure C 2-169 Damage Progression in (B2-L-2) Test specimen to Failure

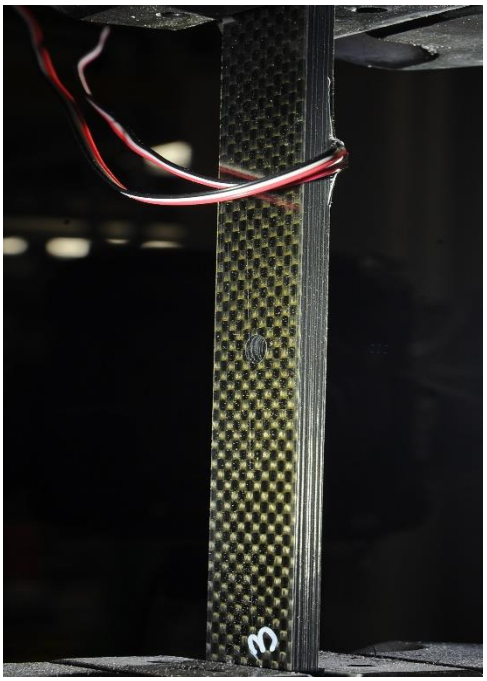

(B2-L-3) at 1 Cycle

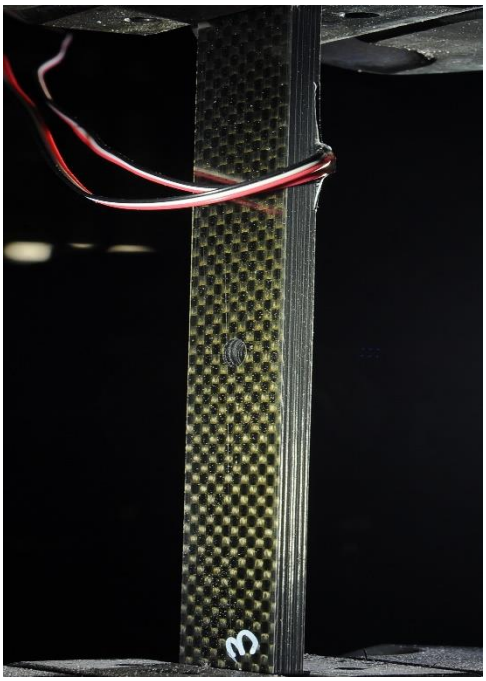

(B2-L-3) at 100 Cycles

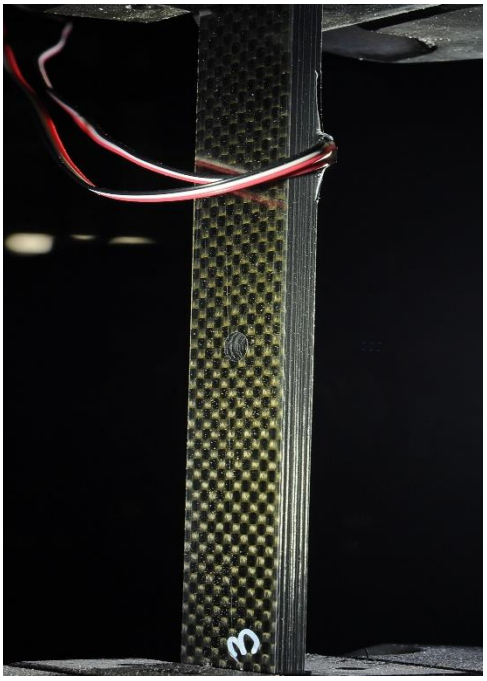

(B2-L-3) at 1k Cycles

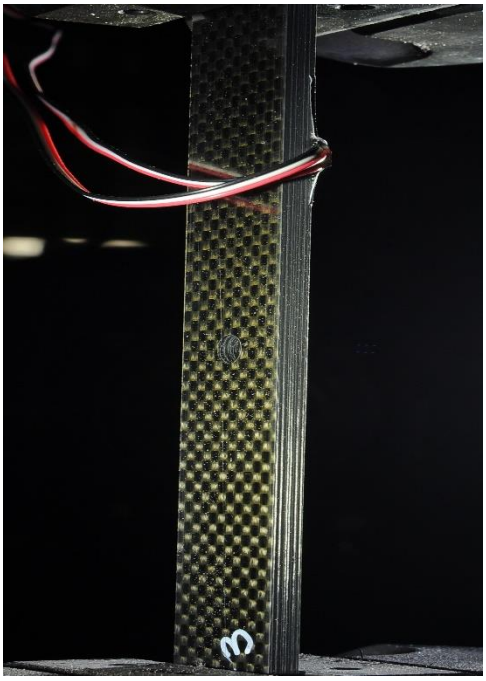

(B2-L-3) at 5k Cycles

Figure C 2-170 Damage Progression in (B2-L-3) Test specimen to 5k Cycles

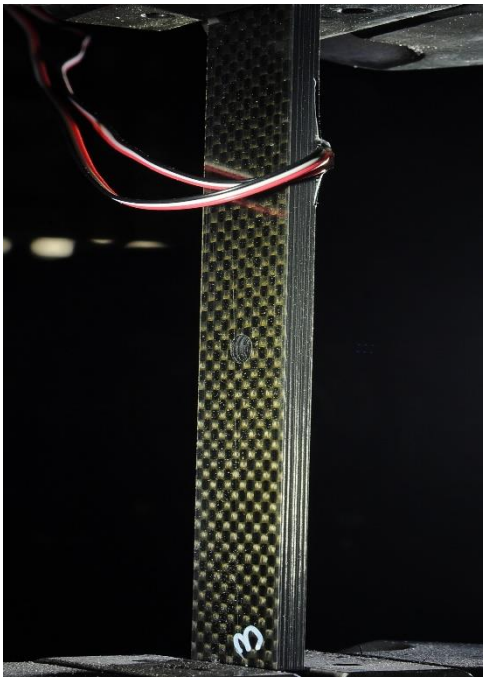

(B2-L-3) at 10k Cycles

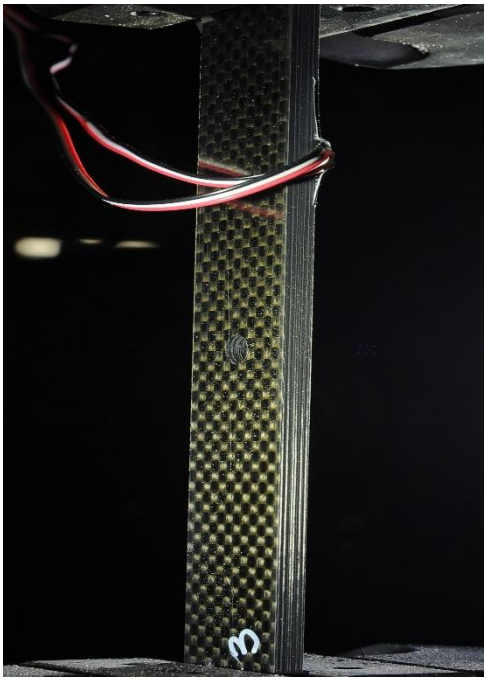

(B2-L-3) at 20k Cycles

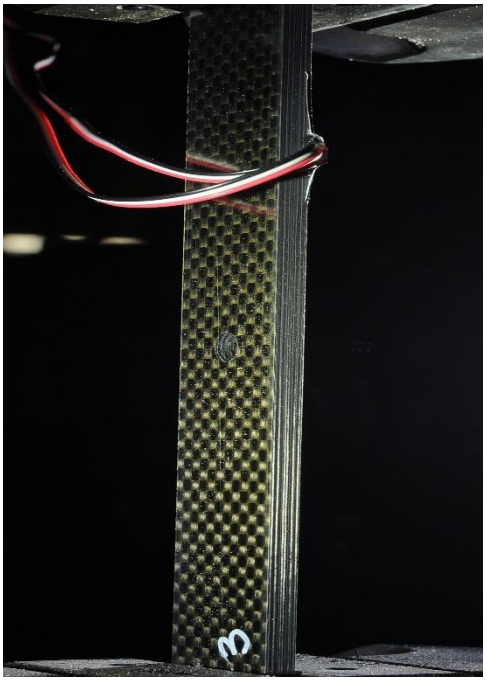

(B2-L-3) at 30k Cycles

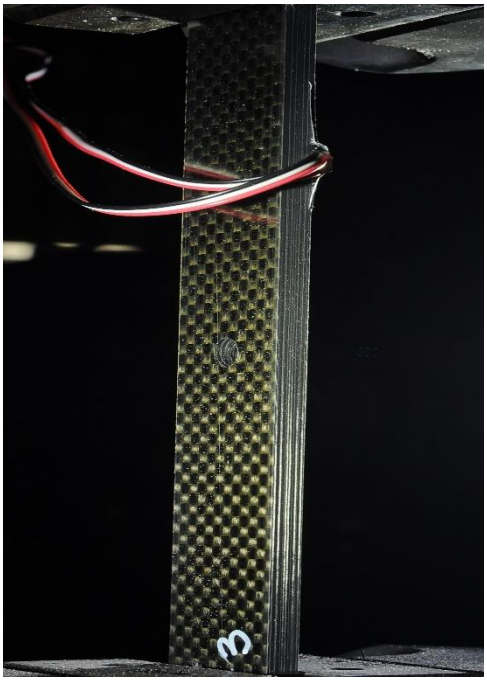

(B2-L-3) at 40k Cycles

Figure C 2-171 Damage Progression in (B2-L-3) Test specimen to 40k Cycles

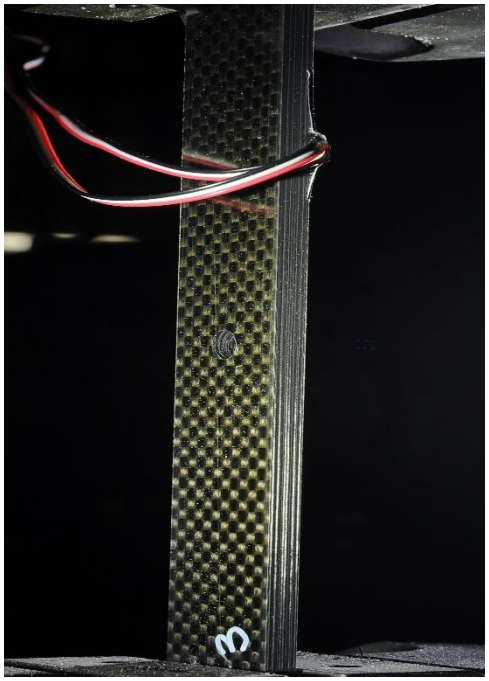

(B2-L-3) at 50k Cycles

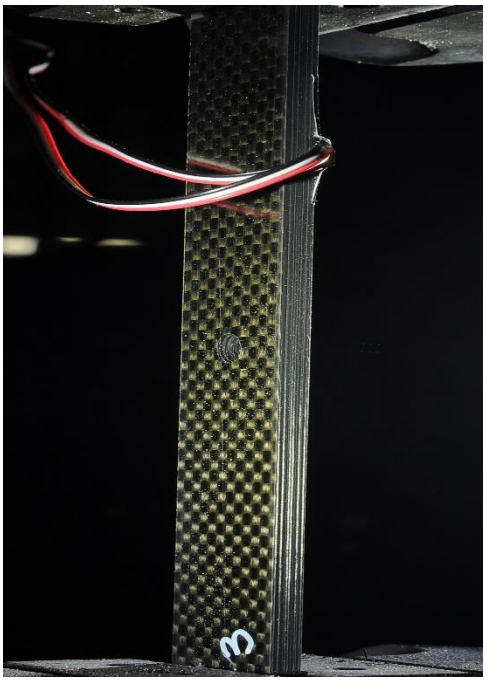

(B2-L-3) at 60k Cycles

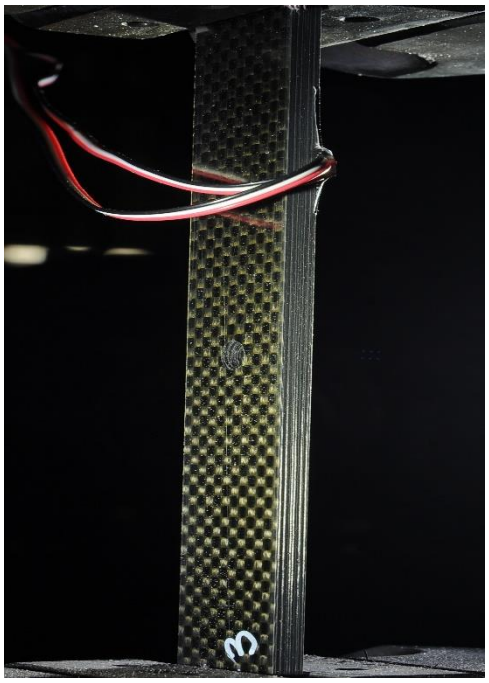

(B2-L-3) at 70k Cycles

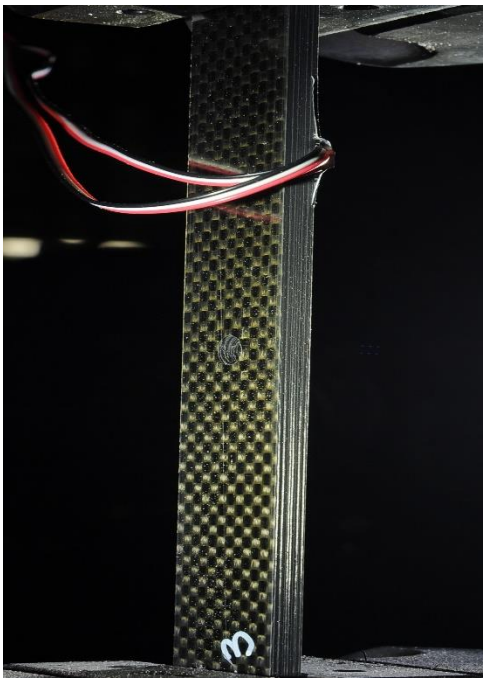

(B2-L-3) at 80k Cycles

Figure C 2-172 Damage Progression in (B2-L-3) Test specimen to 80k Cycles

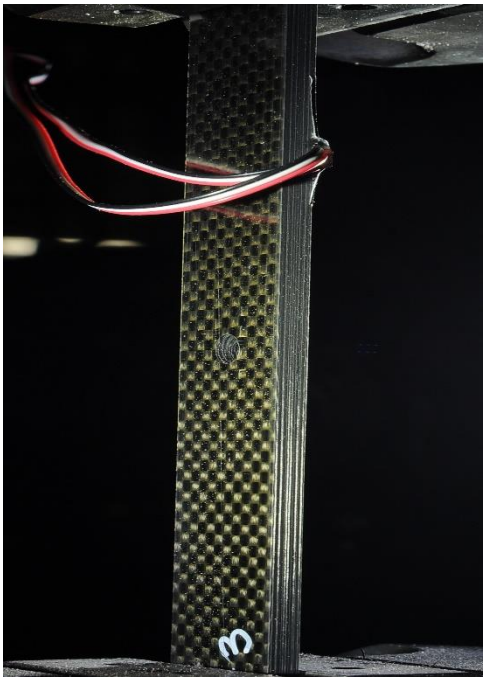

(B2-L-3) at 90k Cycles

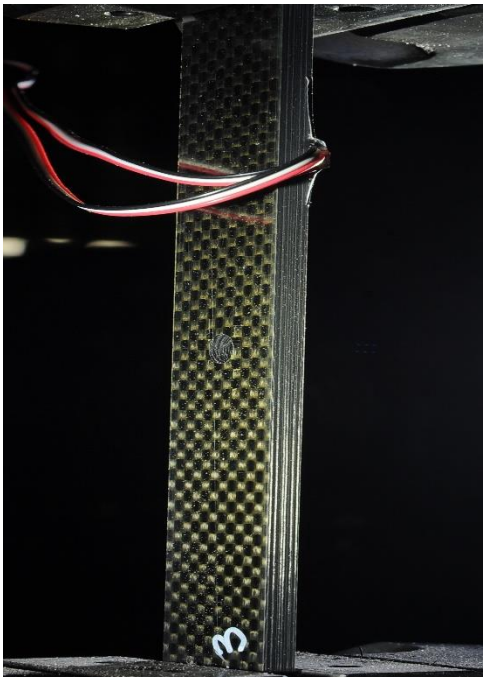

(B2-L-3) at 100k Cycles

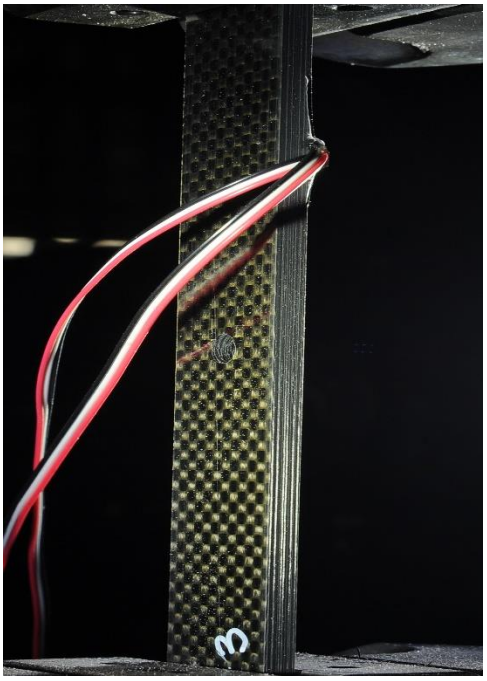

(B2-L-3) at 125k Cycles

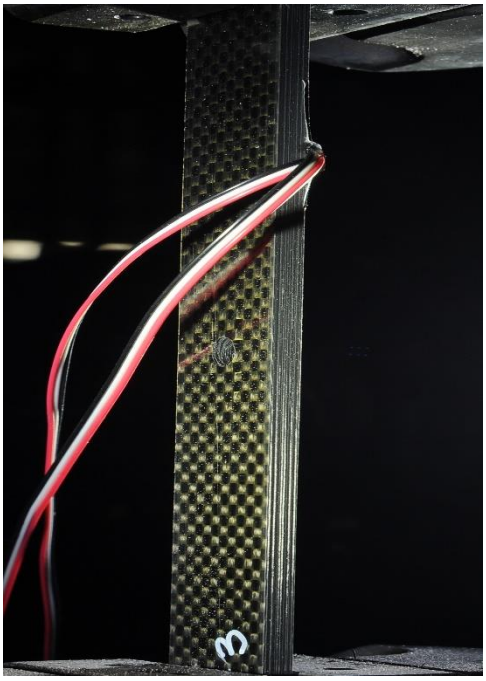

(B2-L-3) at 150k Cycles

Figure C 2-173 Damage Progression in (B2-L-3) Test specimen to 150k Cycles

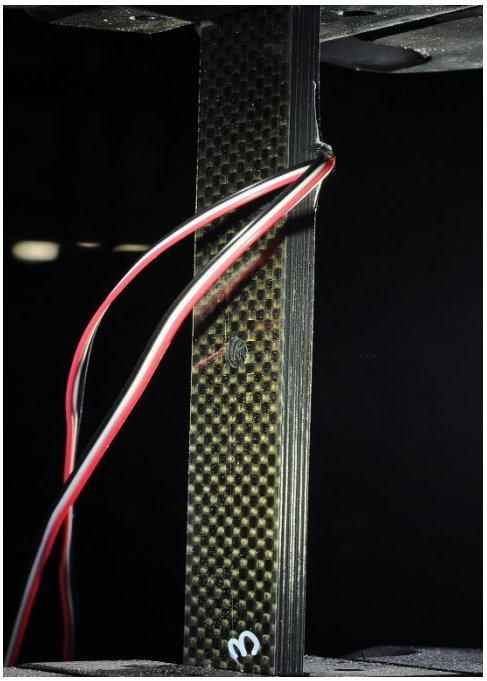

(B2-L-3) at 175k Cycles

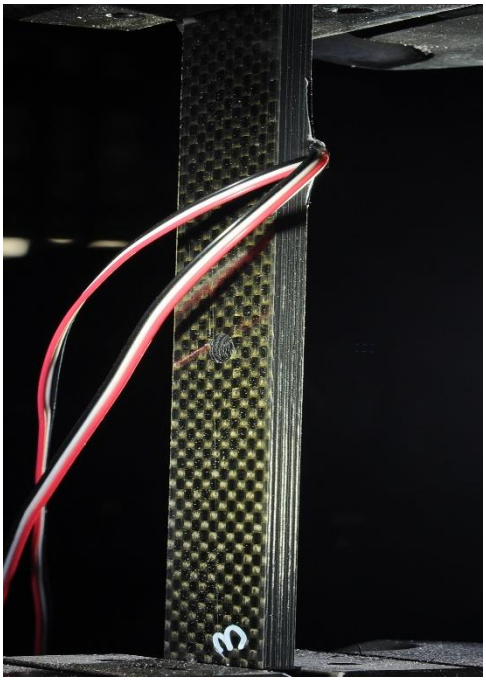

(B2-L-3) at 200k Cycles

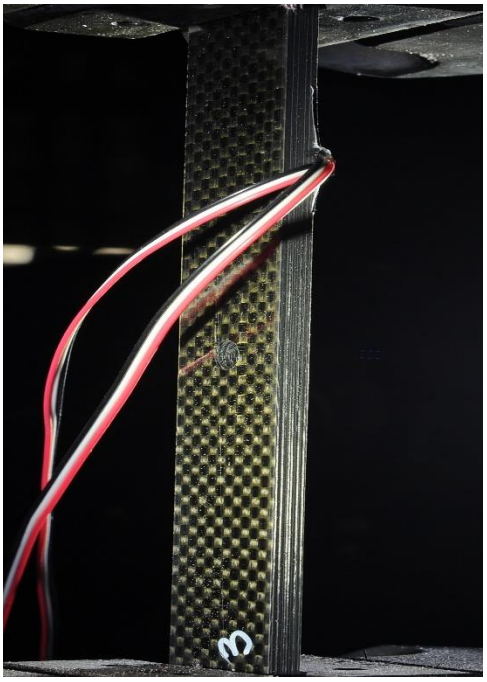

(B2-L-3) at 225k Cycles

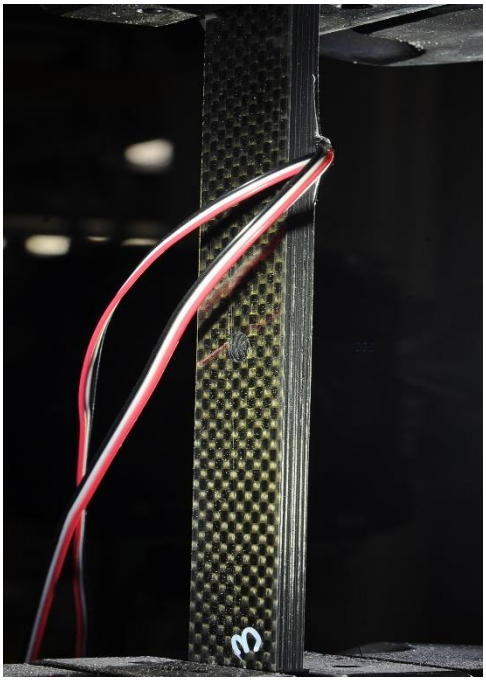

(B2-L-3) at 250k Cycles

Figure C 2-174 Damage Progression in (B2-L-3) Test specimen to 250k Cycles

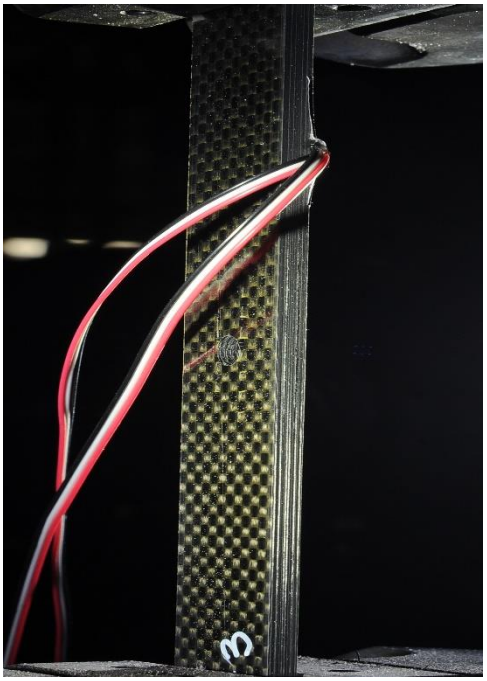

(B2-L-3) at 275k Cycles

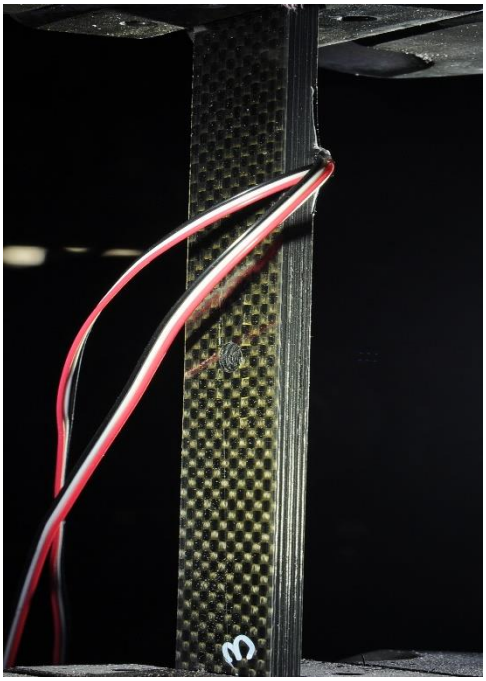

(B2-L-3) at 300k Cycles

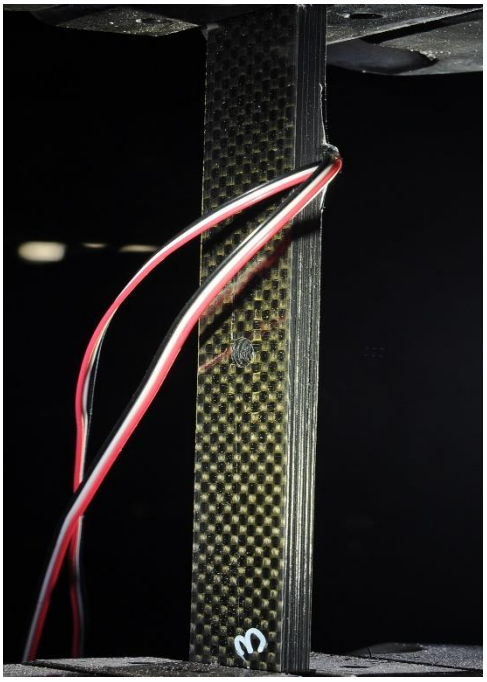

(B2-L-3) at 325k Cycles

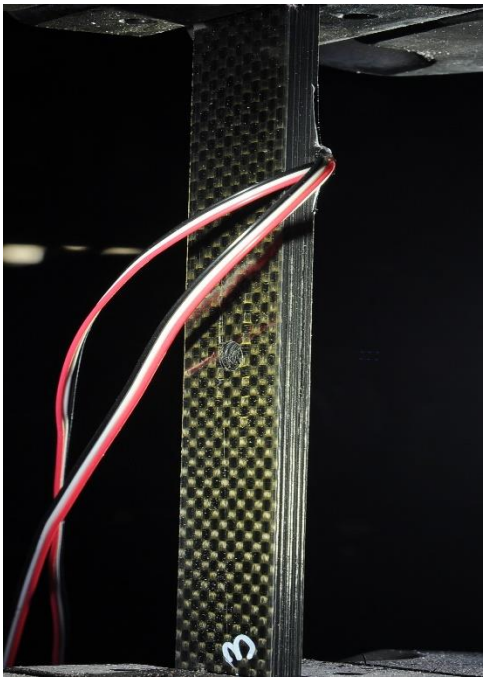

(B2-L-3) at 350k Cycles

Figure C 2-175 Damage Progression in (B2-L-3) Test specimen to 350k Cycles

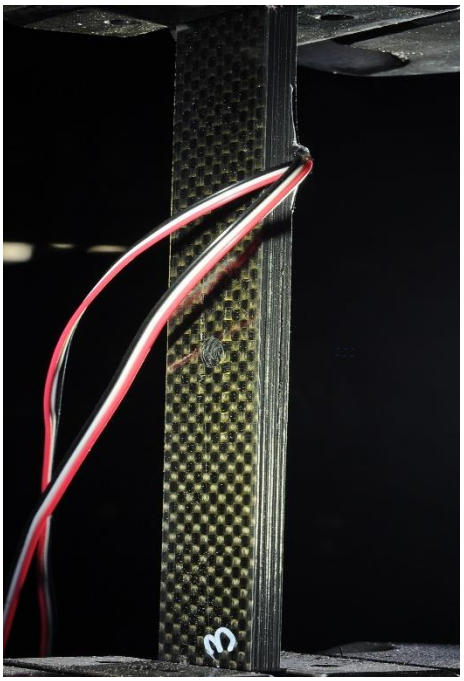

(B2-L-3) at 375k Cycles

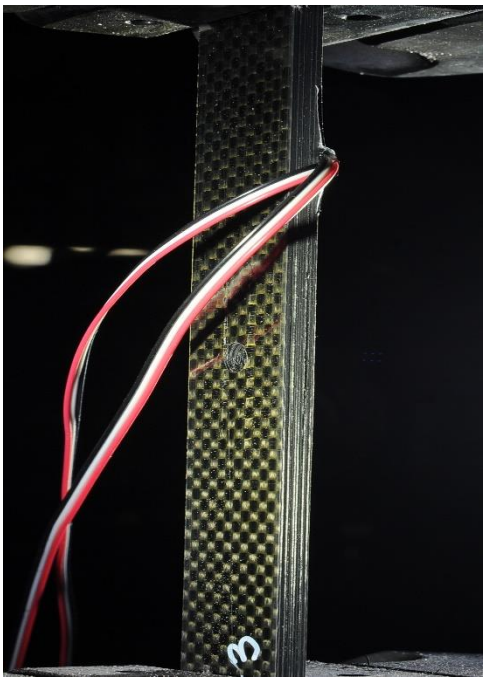

(B2-L-3) at 400k Cycles

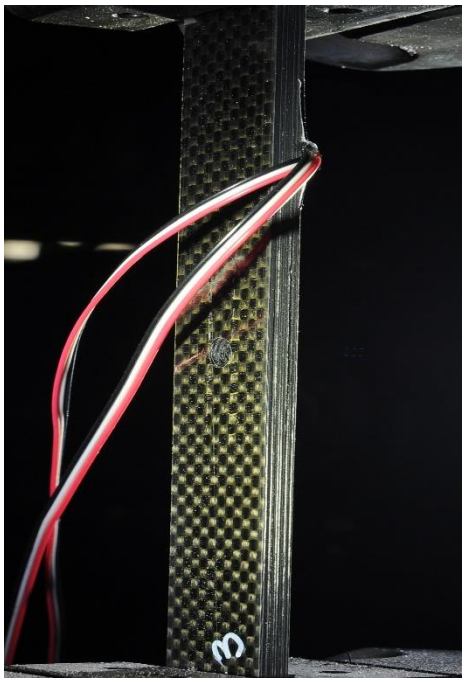

(B2-L-3) at 425k Cycles

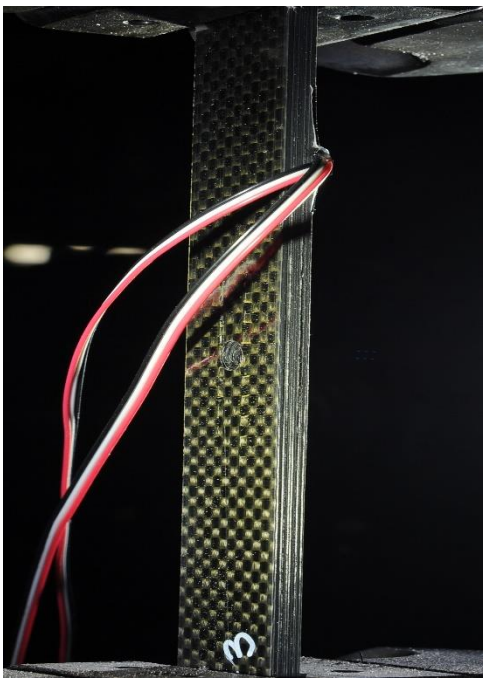

(B2-L-3) at 450k Cycles

Figure C 2-176 Damage Progression in (B2-L-3) Test specimen to 450k Cycles

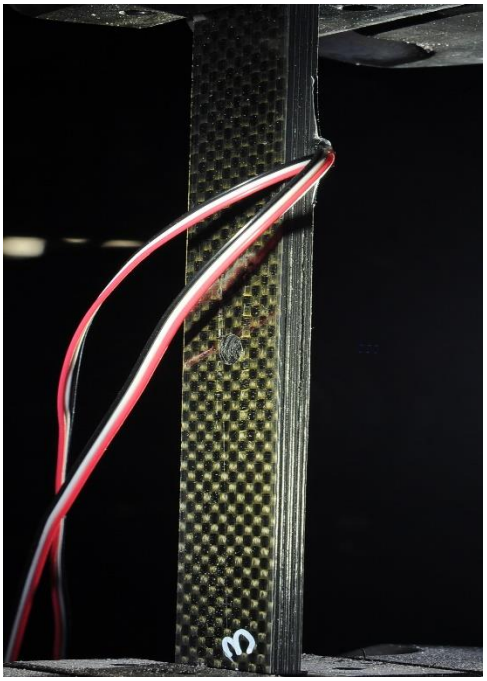

(B2-L-3) at 475k Cycles

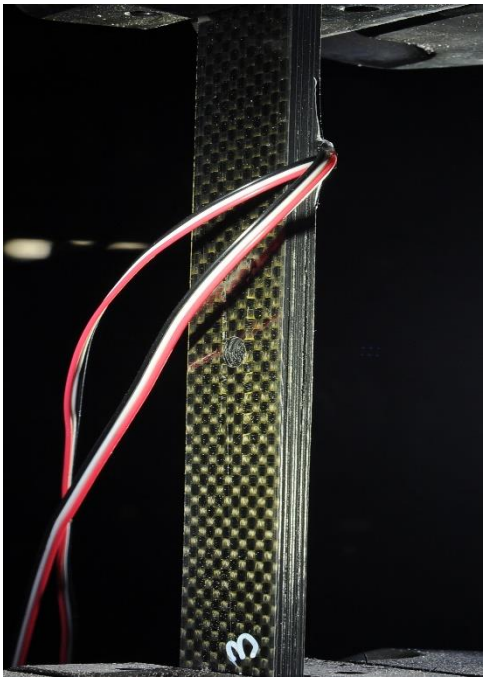

(B2-L-3) at 500k Cycles

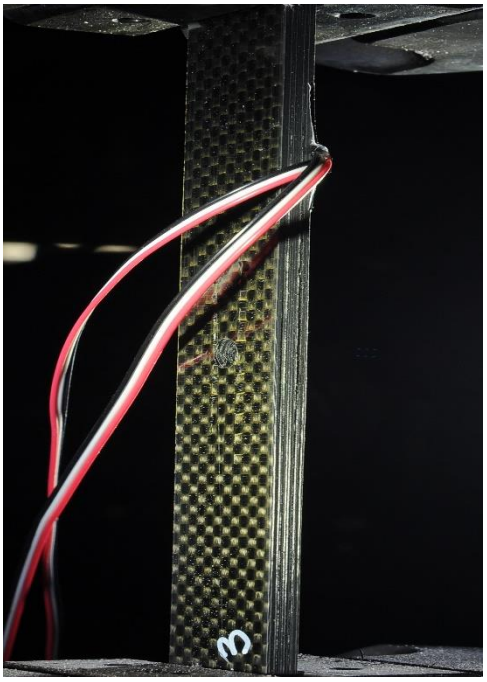

(B2-L-3) at 525k Cycles

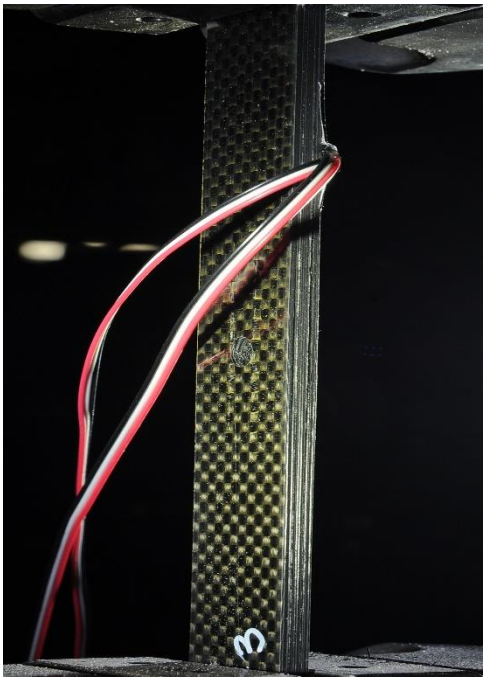

(B2-L-3) at 550k Cycles

Figure C 2-177 Damage Progression in (B2-L-3) Test specimen to 550k Cycles

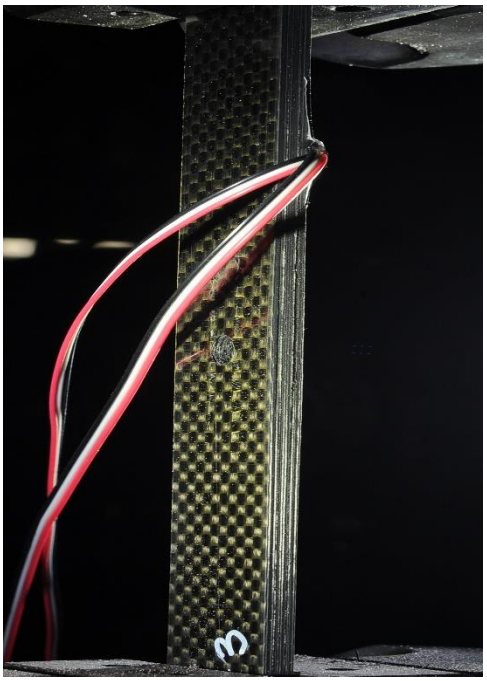

(B2-L-3) at 575k Cycles

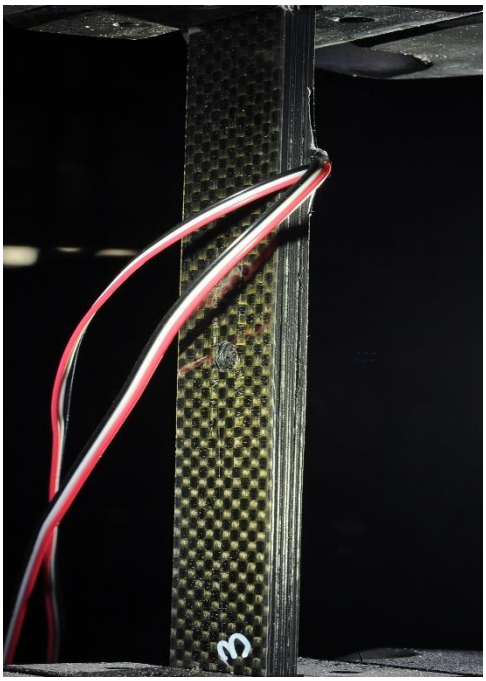

(B2-L-3) at 600k Cycles

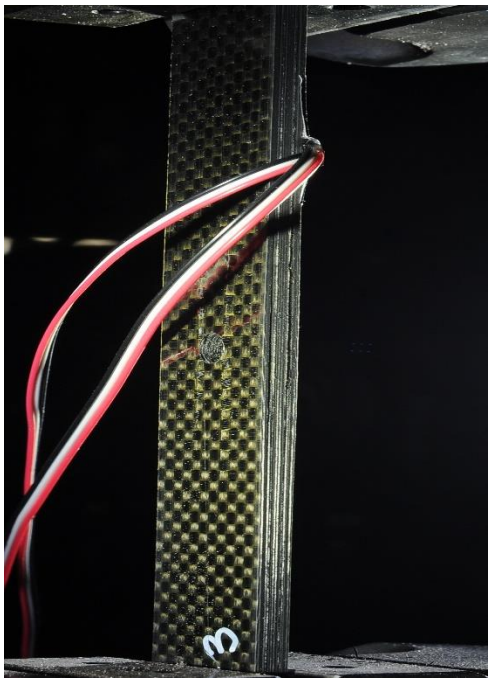

(B2-L-3) at 625k Cycles

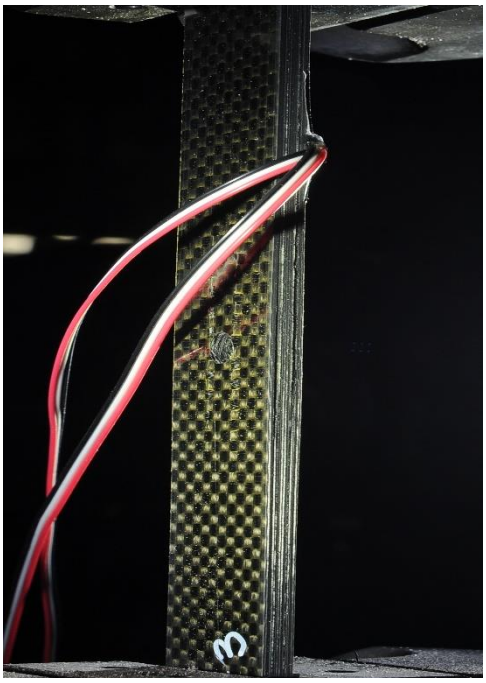

(B2-L-3) at 650k Cycles

Figure C 2-178 Damage Progression in (B2-L-3) Test specimen to 650k Cycles

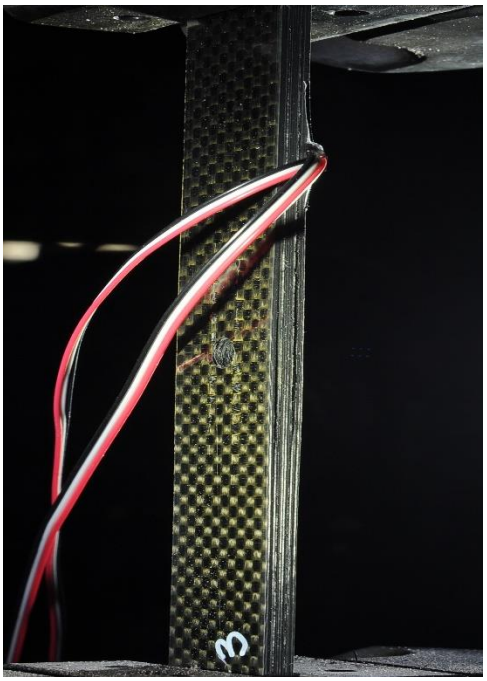

(B2-L-3) at 675k Cycles

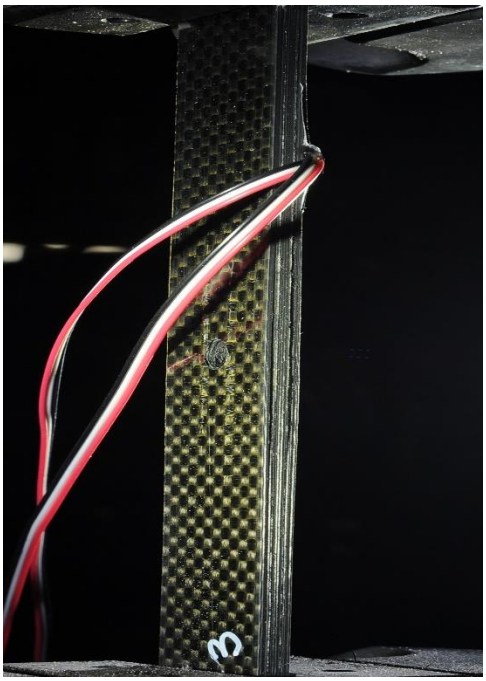

(B2-L-3) at 700k Cycles

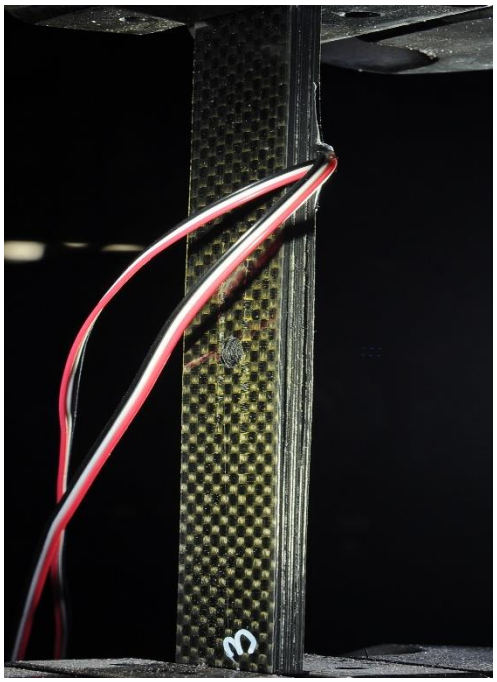

(B2-L-3) at 725k Cycles

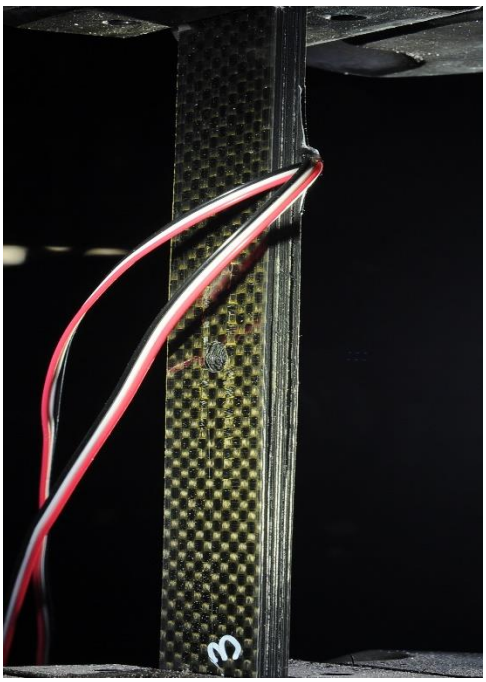

(B2-L-3) at 750k Cycles

Figure C 2-179 Damage Progression in (B2-L-3) Test specimen to 750k Cycles

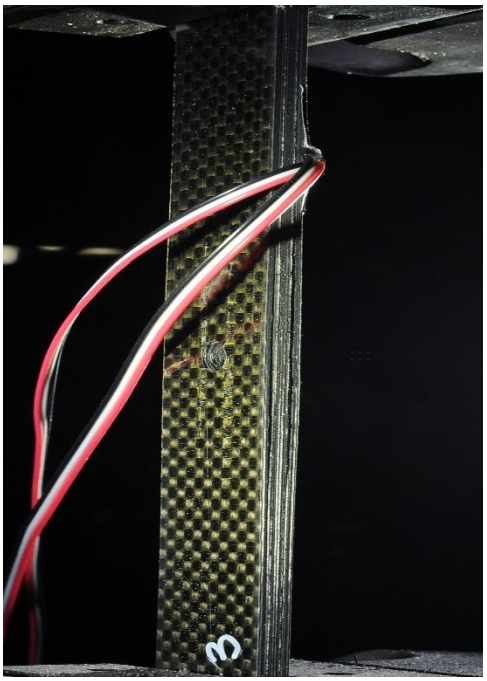

(B2-L-3) at 775k Cycles

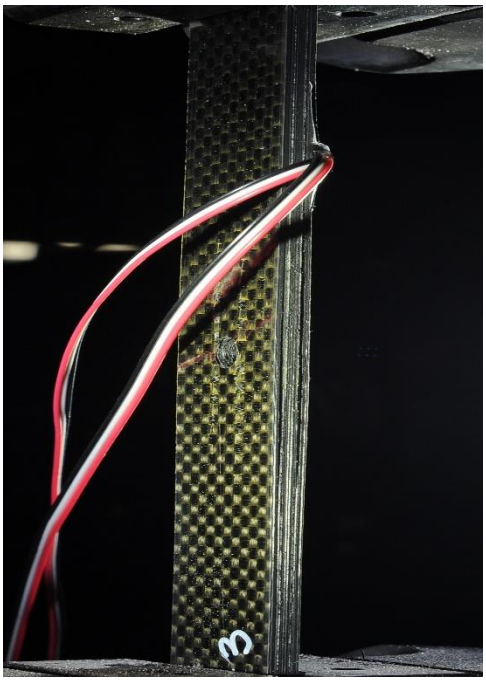

(B2-L-3) at 800k Cycles

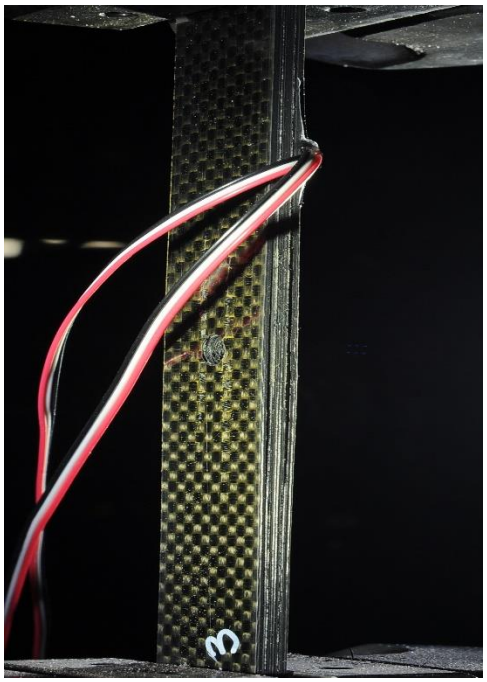

(B2-L-3) at 825k Cycles

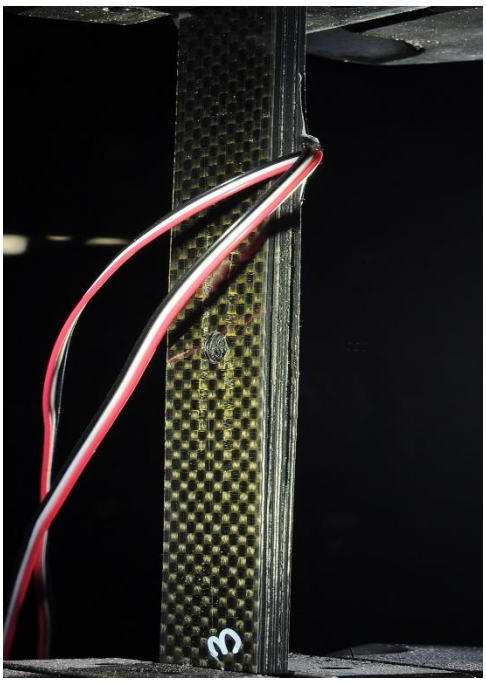

(B2-L-3) at 850k Cycles

Figure C 2-180 Damage Progression in (B2-L-3) Test specimen to 850k Cycles

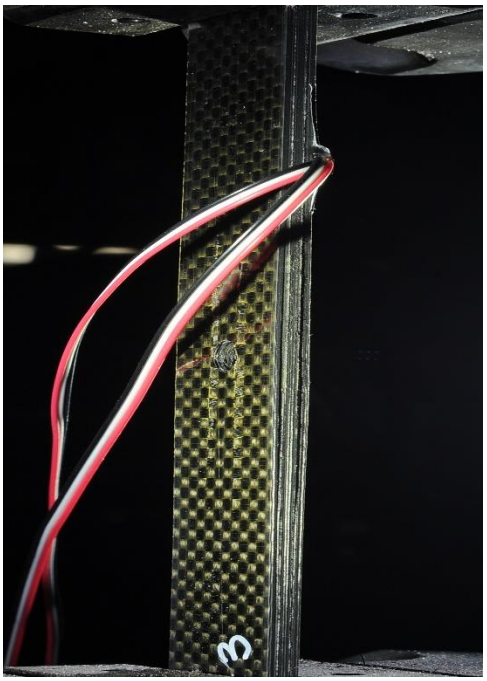

(B2-L-3) at 875k Cycles

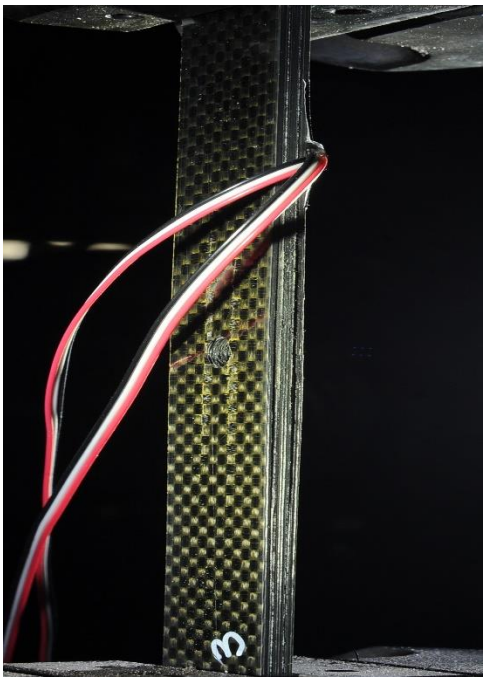

(B2-L-3) at 900k Cycles

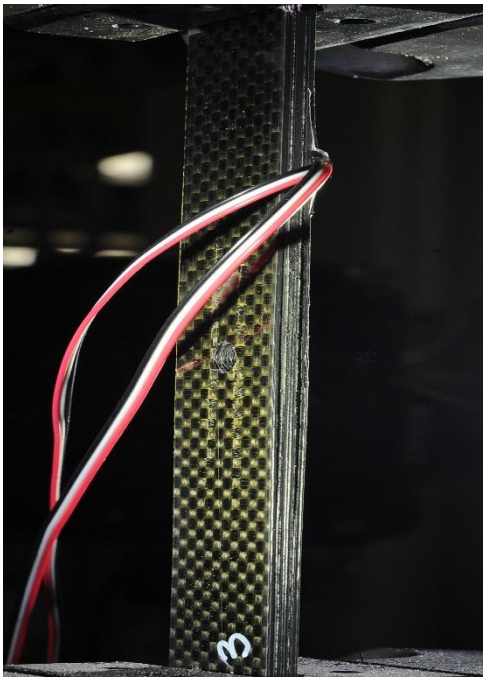

(B2-L-3) at 925k Cycles

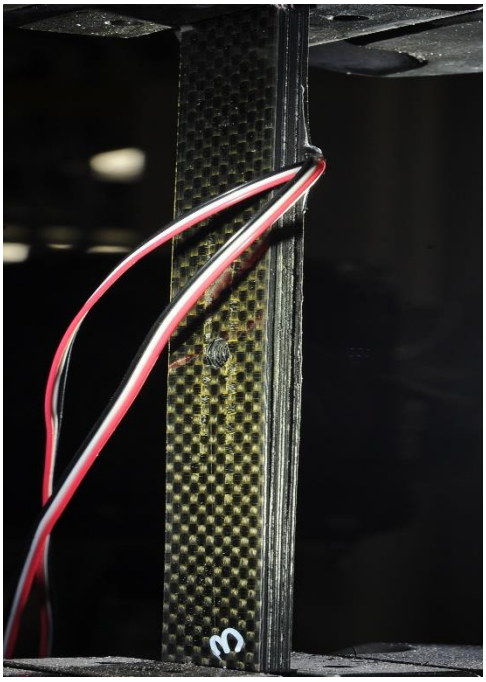

(B2-L-3) at 950k Cycles

Figure C 2-181 Damage Progression in (B2-L-3) Test specimen to 950k Cycles

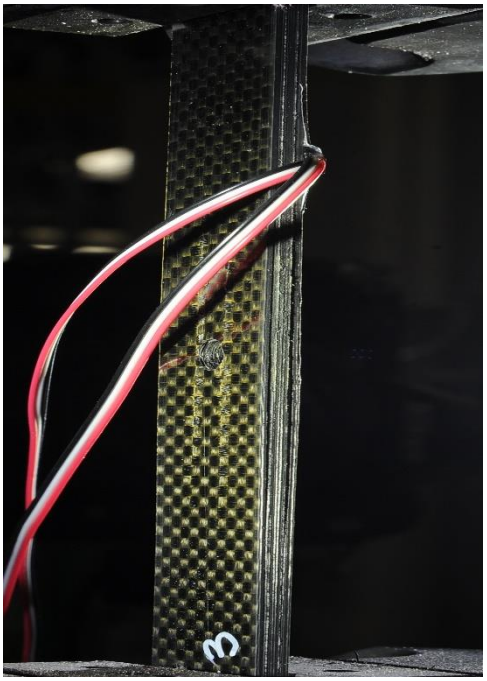

(B2-L-3) at 975k Cycles

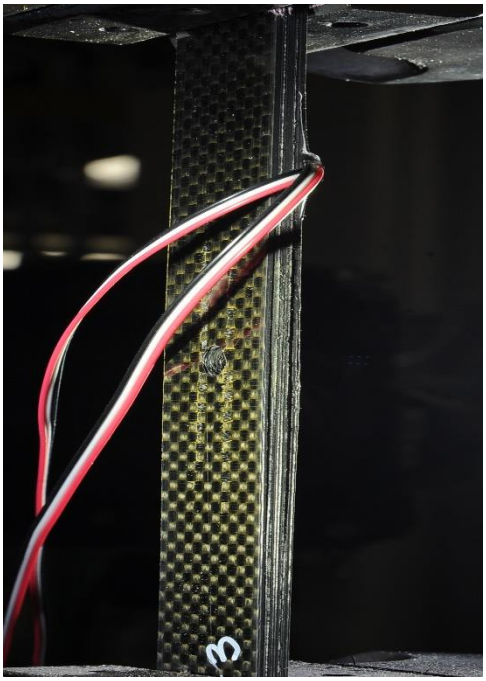

(B2-L-3) at 1000k Cycles

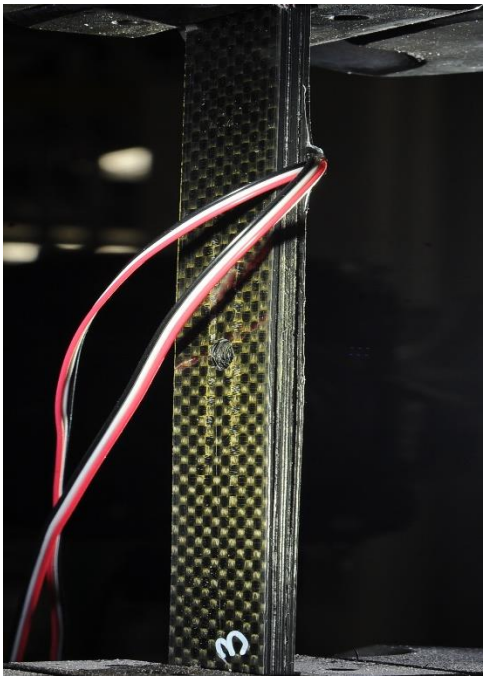

(B2-L-3) at Pre RS

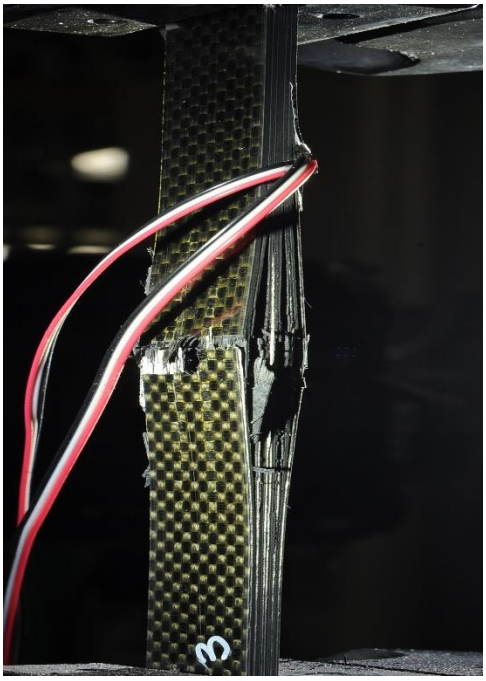

(B2-L-3) at Failure

Figure C 2-182 Damage Progression in (B2-L-3) Test specimen to Failure